AD_____

Award Number: W81XWH-10-1-0128

TITLE: Smart Prosthetic Hand Technology - Phase II

PRINCIPAL INVESTIGATOR: Desineni Subbaram Naidu, PhD

CONTRACTING ORGANIZATION: Idaho State University
Pocatello, ID 83209-8219

REPORT DATE: May 2011

TYPE OF REPORT: Annual

PREPARED FOR: U.S. Army Medical Research and Materiel Command
Fort Detrick, Maryland 21702-5012

DISTRIBUTION STATEMENT:

☒ Approved for public release; distribution unlimited

The views, opinions and/or findings contained in this report are those of the author(s) and should not be construed as an official Department of the Army position, policy or decision unless so designated by other documentation.

REPORT DOCUMENTATION PAGE

Form Approved
OMB No. 0704-0188

1. REPORT DATE *(DD-MM-YYYY)*
May 2011

2. REPORT TYPE
Annual

3. DATES COVERED *(From - To)*
21 April 2010 to 20 April 2011

4. TITLE AND SUBTITLE
Smart Prosthetic Hand Technology - Phase II

5a. CONTRACT NUMBER
W81XWH-10-1-0128

5b. GRANT NUMBER

5c. PROGRAM ELEMENT NUMBER

6. AUTHOR(S)
Desineni Subbaram Naidu, PhD, Marco P. Schoen, PhD, Alba Perez, PhD, Steve Chiu, PhD, Solomon Leung, PhD, Jim Lai, PhD, and Jim Creelman, PT, DPT, MS, OCS

email: naiduds@isu.edu

5d. PROJECT NUMBER

5e. TASK NUMBER

5f. WORK UNIT NUMBER

7. PERFORMING ORGANIZATION NAME(S) AND ADDRESS(ES)
Idaho State University
921 S.8th Avenue, Stop 8219
Pocatello, ID 83209-8219

8. PERFORMING ORGANIZATION REPORT NUMBER

9. SPONSORING / MONITORING AGENCY NAME(S) AND ADDRESS(ES)
U.S. Army Medical Research and Materiel Command,
Fort Detrick, Maryland 21702-5012

10. SPONSOR/MONITOR'S ACRONYM(S)

11. SPONSOR/MONITOR'S REPORT NUMBER(S)

12. DISTRIBUTION / AVAILABILITY STATEMENT
Approved for public release; distribution unlimited

13. SUPPLEMENTARY NOTES

14. ABSTRACT
The present Phase II of Smart Prosthetic Hand Technology focuses on the four closely connected areas of EMG signal identification and estimation, hand motion estimation, intelligent embedded systems and control, robotic hand and biocompatibility and signaling. The developed identification algorithm using a new sensor array, a proposed hybrid estimation algorithm will provide for the decomposition and inference of multiple signals. Different categories of amputation level will be simulated and the identification of EMG signals will be tested and adapted to these different cases. Next, the proposed sensing and actuation system for the artificial hand overcomes the limitations on dexterous manipulation of the prosthetic hands. Strategies on grasping and manipulation will be developed to complement the myoelectric signals. The proposed fusion of soft and hard embedded control systems strategy will alleviate the present problems associated with prosthetic devices. Finally, by investigating into the issues of the inflammatory responses of cells/tissues in response to an artificial implant and the interference with signaling of the artificial implant, the design of our in-vitro model will ultimately improve the design and construct a functional and biocompatible artificial limb.

15. SUBJECT TERMS Smart Prosthetics, Bio-Robotics, Intelligent EMG Signal Processing, Embedded Systems and Intelligent Control, Inflammatory Responses of Cells, Toxicity of Nano Materials

16. SECURITY CLASSIFICATION OF: U			**17. LIMITATION OF ABSTRACT**	**18. NUMBER OF PAGES**	**19a. NAME OF RESPONSIBLE PERSON**
a. REPORT	**b. ABSTRACT**	**c. THIS PAGE**			**19b. TELEPHONE NUMBER** *(include area code)*
U	U	U	UU	531	USAMRMC

Standard Form 298 (Rev. 8-98)
Prescribed by ANSI Std. Z39.18

Table of Contents

INTRODUCTION

Over 1.2 million people in America have missing limbs resulting from combat (e.g., wars and other conflicts) and non-combat (e.g., accidents, birth defects) operations. Thus, availability of artificial limbs will help these people to lead a more normal life. Although artificial devices have been around for the last 30 years, there are no artificial hands that fully simulate the various natural/human-like operations of moving, grasping, lifting, and twisting. Moreover, prosthetic devices still pose significant biocompatibility problems, that need to be addressed and tissues surrounding implants develop ―inflammatory reactions".

The present Phase II of Smart Prosthetic Hand Technology focuses on the four closely connected areas of EMG signal identification and estimation, hand motion estimation, intelligent embedded systems and control, robotic hand and biocompatibility and signaling. The developed identification algorithm using a new sensor array, a proposed hybrid estimation algorithm will provide for the decomposition and inference of multiple signals. Different categories of amputation level will be simulated and the identification of EMG signals will be tested and adapted to these different cases. Next, the proposed sensing and actuation system for the artificial hand overcomes the limitations on dexterous manipulation of the prosthetic hands. Strategies on grasping and manipulation will be developed to complement the myoelectric signals. The proposed fusion of soft and hard embedded control systems strategy will alleviate the present problems associated with prosthetic devices. Finally, by investigating into the issues of the inflammatory responses of cells/tissues in response to an artificial implant and the interference with signaling of the artificial implant, the design of our in-vitro model will ultimately improve the design and construct a functional and biocompatible artificial limb.

BODY

GOAL 1: EMG Signal Identification:

1. Overview

Prosthesis can be greatly useful for the amputees which can impact their life in a positive way. The objective of this research is to design a ‗Smart Prosthetic Hand' for the people with upper extremity amputations. In control part of the prosthesis we have two main objectives, force and position control. Therefore, to have an effective control of force and position we need to have the information of force and positions in advance. This makes it absolutely necessary to have an estimation scheme or model in place that can compute the required position and force to perform a specific task of grasping or manipulation. There has been active research in past towards prosthetic hand design that have similar functionality and appearance as human hands [1, 2]. Surface electromyographic (sEMG) signals are the sole control input for most of these research works where the recorded sEMG signal is used as an input to activate the prosthesis. sEMG signals depend on the flow of specific ions including sodium (Na^+), potassium (K^+) and calcium (Ca^{++}) resulting in the action potentials in nerves and their respective skeletal muscle fibres which get activated and controlled by the central nervous system. These ion exchanges cause a potential difference across neuronal membranes which can be measured as an electrical voltage change [3]. An EMG signal recorded on the surface of the limb is expressed as an electric voltage ranging, between -5 and +5 mV. The movement and force control of the prosthesis in [4, 5] uses sEMG signal as an input to the controller. Past research results show that EMG signal amplitude generally increases with skeletal muscle force. However, this relationship is not always same; as there are other factors that influence the muscular force. There are numerous factors such as the varying motor unit recruitments, crosstalk, and biochemical interaction within the muscular fibres that affect the sEMG signals. This makes EMG signals random, complex, and dynamic in nature and the control of the prosthesis difficult. Moreover, it changes continuously due to the onset and progression of muscle fatigue which results because of continuous high frequency stimulation or because of tetanic stimulation [6]. Synchronization of active motor units along the muscle fibres, and a decrease in conduction velocity are reflected in the EMG signal as an increase of amplitude in the time domain and a decrease of medium frequency in the frequency domain [6]. All these factors make the relationship between EMG and force nonlinear. Correct interpretation of EMG signal is vital to achieve precise motion and force control of prosthesis. EMG analysis is a well-accepted method for muscle fatigue assessment [7].

In 1977, L. Lindstrom, R. Kadefors and I. Petersen developed a method that measures the localized muscle fatigue based on the power spectrum analysis using myoelectric signals [8]. This approach permits real-time investigations and can yield statistically based criteria for the occurrence of fatigue. Rate of fatigue development and

changes in muscle action potential conduction velocity were used to interpret the findings in [8]. The joint analysis method using EMG amplitude and spectrum (JASA) allows distinguishing between the difference of fatigue-induced and force related EMG changes. Simultaneous changes in the EMG amplitude and spectrum are considered in the JASA approach. The JASA principle states that muscle force decreases because of the decrease in EMG amplitude. Fatigue can occur because of continuous high frequency stimulation or because of tetanic stimulation.
This part of the research addresses issues with the position and force estimation and their variations due to the muscle fatigue. The sEMG, skeletal muscle force and the angles of the proximal interphalangeal (PIP) joint of the index finger signals are filtered using different filters and modeled with linear and nonlinear System Identification techniques and adaptive neuro-fuzzy inference (ANFIS) systems. The outputs of obtained models are fused using an adaptive probability of Kullback Information Criterion (KIC) for model selection to achieve better force and angle estimates. Following part of the report presents ‗Experimental Set-Up and Signal Pre-Processing,' ‗Skeletal Muscle Fatigue and Spectral Analysis of sEMG Signals,' ‗Different Modeling Approaches,' ‗Data Fusion Algorithm,' ‗Results and Discussion,' and ‗Conclusion and Future Work.'

2. Classification of amputation

Individuals with amputations of either the upper or lower extremities are generally classified by the level of the amputation in relation to the most proximal joint. For example, a person having the hand amputated would be considered a trans-radial/ulnar amputee (below the elbow). If the amputation was through the humerus, this would be a trans-humeral (above the elbow) However, this classification only grossly defines amputations and makes no reference to the true length of the residual limb or the specific musculature that remains after appropriate surgical intervention. In line with our studies investigating sEMG signal identification and filtering, fatigue estimation and array sensor development, we have completed the measurements of specific muscle lengths of 16 fully dissected normal cadaver arms to determine the most appropriate and functional residuum length giving the best possible potential for sEMG signaling from the remaining musculature post amputation. It is well known that surgeons have the task of making decisions related to level of amputation in both traumatic and planned amputations and the general consensus is that the longer the residuum and proximal joint sparing, the better the potential for prosthetic function [9]. There is also the concern of muscle atrophy in limbs post amputation which may affect the potential for socket fit and myoelectric prosthetic use. The greater length of the residuum has clear functional benefits especially when the musculature the limb is relatively intact and has enough length to maintain motor point locations.

2.1 Physical classification

The arms of three female and four male cadaver specimens (16 arms) were procured from the existing cadaver holdings at Idaho State University. The mean height of the specimens was 171.175 cm (SD 9.114). Cadavers were neatly dissected with all superficial skin, adipose and fascia removed from the upper extremities and shoulder girdle. Measurements were taken by three researchers with an inter-tester reliability of r=.866 using both 200mm and 300 mm Vernier Aerospace® calipers as seen in Fig. 2.1.1. The measurements of the upper extremity musculature included the distance from the acromioclavicular (AC) joint to the medial and lateral condyles of the humerus, the distance from the medial humeral condyle to the distal myotendinous (MTJ) junction of the majority muscles of the flexor compartment of the forearm, and the distance from the lateral humeral condyle to the distal MTJ of the majority muscles in the extensor compartment of the forearm (see Fig. 2.1.2). In addition, all muscle length measurements of muscles of the upper arm on both posterior and anterior regions were taken from the AC joint to the distal MTJ. The muscles measured in the forearm are considered extrinsic movers of the hand and fingers. The muscles in the upper arm are considered movers of the elbow and, in part, the shoulder girdle. The measurement for the forearm and upper arm musculature in both the flexor and extensor compartments were analyzed for means, and standard deviations and ratios of the measurements to the mean AC to medical and epicondyle values. Table 2.1.1 includes the summary of measurements from the AC joint to the medial and lateral epicondyles. Table 2.1.2, 2.1.3 and 2.1.4 includes muscles which were measured at each compartment of the entire arm.

Fig. 2.1.1. Vernier Aerospace® Caliper used in Measurements.

Fig: 2.1.2. Example of Measurement Taken on the Extensor Carpi Ulnaris Muscle in Forearm of Extensor Compartment.

Fig: 2.1.3. Example of Measurement of Deltoid Muscle in Upper Arm.

TABLE 2.1.1
MEASUREMENT OF ACROMIOCLAVICULAR JOINT TO MEDIAL AND LATERAL EPICONDYLES

	Mean	SD
Medial Condyle	31.780 cm	2.118 cm
Lateral Epicondyle	32.638 cm	2.205 cm
Combined	32.209 cm	2.165 cm

TABLE 2.1.2
MUSCLE MEAN MEASUREMENTS OF FOREARM AND UPPER ARM
EXTENSOR GROUPING

Muscle	Mean (cm)	SD (cm)
Brachioradialis	17.873	3.221
Extensor carpi radialis longus	18.477	2.650
Extensor carpi radialis brevis	15.683	2.205
Extensor digitiorum	18.306	2.598
Extensor digitorum minimi	16.776	2.705
Extensor carpi ulnaris	17.820	2.854
Anconeus	6.960	1.872
Supinator	6.856	1.598
Abductor policis longus	15.545	2.111
Extensor policis longus	13.820	1.896
Extensor policis brevis	7.631	1.601

TABLE 2.1.3
MUSCLE MEAN MEASUREMENTS OF FOREARM AND UPPER ARM
FLEXOR GROUPING

Muscle	Mean (cm)	SD (cm)
Pronator teres	15.040	1.705
Flexor carpi radialis	17.942	3.050
Flexor carpi ulnaris	21.030	3.339
Flexor digitorum superficialis	20.726	3.201
Flexor digitorum profundus	18.303	1.211
Flexor policis longus	15.438	2.063

TABLE 2.1.4
MUSCLE MEAN MEASUREMENTS OF FOREARM AND UPPER ARM
UPPER ARM

Muscle	Mean (cm)	SD (cm)
Biceps brachii long head	25.821	2.603
Biceps brachii short head	23.832	3.126
Brachialis	24.765	2.652
Deltoid	16.272	2.212
Triceps long head	22.578	3.226
Triceps lateral head	16.671	2.716

Ratios of the mean muscle length values to the length of the mean AC to mean lateral and medial epicondyle measures were calculated to ascertain the level of the distal residuum where the majority of muscles and respective motor points would be located to enhance the potential for sEMG signal monitoring in individuals with amputations. The calculated ratios for the forearm musculature in both flexor and extensor groupings was .636 ± .0535. The ratio of the mean upper arm musculature length to the AC condylar distance is .505 ± .041. Given these ratios of length to a known distance, the measurements suggest that residuum arms that are distal (Zone 1) to the ratio measurement would be ideal for sEMG signaling since they would have almost all the forearm or upper arm musculature intact. If the residuum was proximal (Zone 2) to the ratio measurement it would still be appropriate for sEMG signaling since the motor points of the major movers of the hand would still be intact allowing for adequate signaling. Although individual variation will occur, motor point mapping of specific musculature has been documented [10]. However, residuum arm lengths that would be much shorter, would present some difficulty for detecting sEMG signaling. As an example, Fig. 2.1.4 and 2.1.5 show one of the cadaver specimens on which the Zones have been depicted. Arrows depict the Zone measurements as calculated per the derived ratios. The AC to mean condylar measurement of this specimen is 30.5 cm. In both cases, the demarcation of Zone 2 suggests that the

number of muscles and their motor points would be adequate for harvesting the sEMG signal in respective upper arm and forearm musculature. In Fig. 2.1.4 the demarcation of Zone 1 and 2 is measured at 19.39 cm distal to the elbow joint. In Fig. 2.1.5 the demarcation of the Zones is at 15.40 cm distal to the AC joint. In both cases it is evident that the bulk of the musculature is located proximal to the line of Zone delineation.

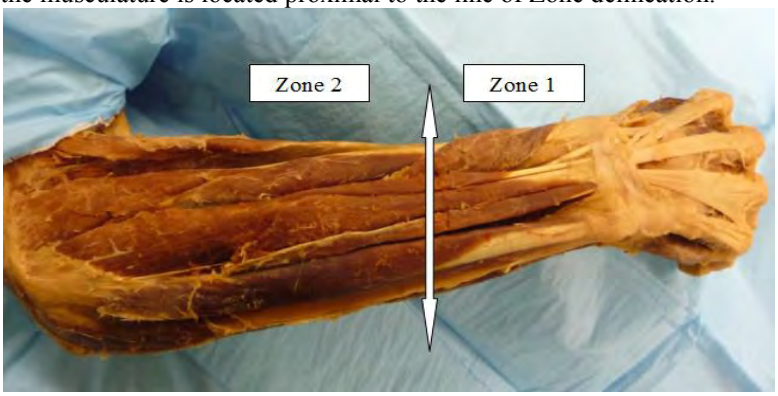

Fig. 2.1.4. Zone Delineation on Forearm Musculature.

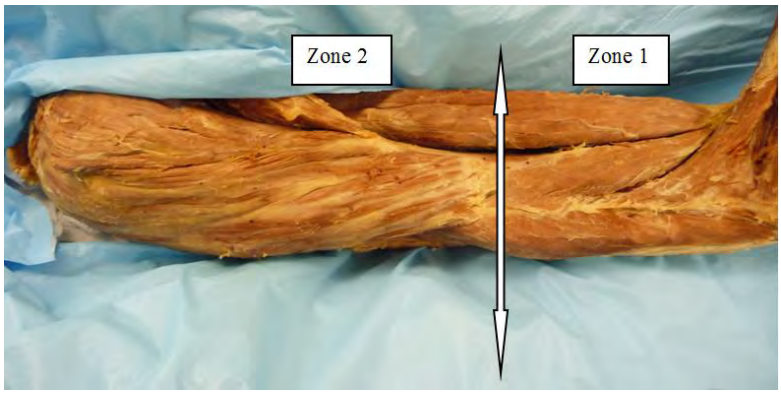

Fig: 2.1.5**.** Zone Delineation on Upper Arm.

With the development of this classification and the measurements of the distal Zones, we plan to move ahead in this next quarter with sEMG signaling from Zone 1 a 2 in the forearm to validate this amputation classification sEMG signaling. In addition, the array sensor experiments using this classification will also investigate the parameters of signal filtering and fatigue in the musculature in these zones. . Further, sEMG signaling of the arm musculature during the movements of forearm pronation and supination and force data in various normal subjects will also be tested.

2.2 **Experimental set-up and spatial filtering/signal pre-processing**

2.2.1 <u>Spatial Filtering</u>:

"Spatial filtering" is broadly defined as methods which compute spatial density estimates for events that have been observed at individual locations. Spatial filtering describes a set of tools for displaying functions estimated from these data points which are generally distributed in two-dimensional space. Spatial filtering can also be thought of as a form of data smoothing method which is designed to give us a clearer view of the general underlying information.

Spatial filtering is a non-parametric analysis method which belongs within the field of exploratory spatial analysis which relies, to a large degree, on graphical methods of analysis. Spatial filters are used when there is no a priori curve to fit to a data series. Instead, it relies on nearby or adjacent, values to estimate the value at a given point. These filters take out variability in a data set while retaining the local features of data. By varying the size of the filter, features in the data that vary at different spatial scales can be differentially removed. Spatial filtering is useful as an exploratory technique for identifying areas that are homogeneous or areas that have larger or smaller values than which generally occurs.

Spatial filtering is principally associated with digital image processing. This method may be applied to almost any type of grid/data set or image (which contains the gray scale values or pixel data in the form of a grid). This term can also be used, in a related manner, in the area of spatial statistics. The most commonly provided functions of spatial filtering are the so-called low-pass and high-pass spatial filters. These are focal functions whose operation is determined by a kernel or neighborhood of *N*x*N* cells around each pixel or grid position [11]. Grid cells –covered" by a kernel are multiplied by the matching kernel entry and then the weighted average is calculated and assigned as the value for the central cell, *G*. For example, asymmetric 3x3 kernel may look like the one shown in (1), or any combination of the weights. Typically *a, b* are positive integers. If *a*=*b*=1, then the kernel provides a simple smoothing or averaging operation. The weights in the kernel can be modified for specific cases or data sets. In any case the weighted average is divided by the sum of the elements of the kernel. Filters of this type are sometimes referred to as low-pass filters.

$$\text{Symmetric Kernel} = \begin{bmatrix} a & a & a \\ a & b & a \\ a & a & a \end{bmatrix} \quad (1)$$

If the weights in the kernel looks like the one in (2) and *a, b, and c* are positive integers.

$$\text{Symmetric Kernel with different weights} = \begin{bmatrix} c & a & c \\ a & b & a \\ c & a & c \end{bmatrix} \quad (2)$$

And if the following, *b*>*a*>*c*, is true then the kernel is described as a Gaussian filter which is symmetric but center-weighted.

The filtered grid value „*G*" of an *m*=*N*x*N* kernel matrix, with C_i set of coefficients and P_i - set of source grid values, is calculated as;

$$G = \frac{\sum_{i=1}^{m} C_i P_i}{\sum_{i=1}^{m} C_i} + B \quad (3)$$

Where, *B* is often set to 0. *B* is a bias term to increase or decrease the resulting value of „*G*"

There are many different forms of spatial filters depending on the weights and the symmetry associated with the kernel. This kernel is also sometimes referred to as the *„filter mask"*. Some of the other examples are given in Table 2.1.1.

Linear Spatial Filtering:

Linear spatial filtering modifies an image „*f*" by replacing the value at each pixel with a linear function of the values of nearby pixels (This same analogy can be applied to data set in a grid format; similar to the case of multiple sEMG sensors placed in grid). Moreover, this linear function is assumed to be independent of the pixel's location (*k, l*), where (*k, l*) are the indices of the pixels in *f*, which is represented by a data matrix. This kind of operation can be expressed as convolution or correlation. For spatial filtering, it's often more intuitive to work with correlation.

The filtered result *g(k, l)* is obtained by centering the mask over pixel (*k, l*) and multiplying the elements of *f* with the overlapping elements of the mask and then adding them up. A special case exists when the special when the center of the mask is on the boundary of *f*. The common assumption in this case is that the data matrix is periodic. But this assumption does not always hold true. In such cases the non-existing entries assumed to be zero.

TABLE 2.2.1
LINEAR SPATIAL FILTERS

Filter Type	Filter	Kernel	Description
Low-pass (symmetric)	Averaging	$\begin{bmatrix} a & a & a \\ a & b & a \\ a & a & a \end{bmatrix}, \begin{bmatrix} 0 & a & 0 \\ a & b & a \\ 0 & a & 0 \end{bmatrix}$	Smoothing, Noise Reduction or Blurring Filter (focal mean)
	Gaussian	$\begin{bmatrix} c & a & c \\ a & b & a \\ c & a & c \end{bmatrix}$	Smoothing, Noise Reduction or Blurring Filter (focal weighted mean)
High-pass (symmetric)	Sharpening	$\begin{bmatrix} -a & -a & -a \\ -a & +b & -a \\ -a & -a & -a \end{bmatrix}, \begin{bmatrix} 0 & a & 0 \\ -a & b & -a \\ 0 & -a & 0 \end{bmatrix}$	Mean effect removal/sharpening filter (focal sum). Provides limited edge detection. Typically entries sum to 1 but may be greater.
Gradient (asymmetric)	Edge Detection	$\begin{bmatrix} a & b & a \\ 0 & 0 & 0 \\ -a & -b & -a \end{bmatrix}, \begin{bmatrix} -a & 0 & a \\ -b & 0 & b \\ -a & 0 & a \end{bmatrix}$	Kernel highlights vertical and horizontal edges. Typically *a=1*, and *b=1* or 2 and entries sum to 0.
	Embossing	$\begin{bmatrix} 0 & +a & +a \\ -a & +a & +a \\ -a & -a & 0 \end{bmatrix}$	Enhance edges in a selected direction to provide embossed effect.
	Directional	$\begin{bmatrix} -1 & 1 & 1 \\ -1 & -2 & 1 \\ -1 & 1 & 1 \end{bmatrix}, \begin{bmatrix} 1 & 1 & 1 \\ 1 & -2 & 1 \\ -1 & -1 & -1 \end{bmatrix}, \begin{bmatrix} 1 & 2 & 1 \\ 0 & 0 & 0 \\ -1 & -2 & -1 \end{bmatrix}$	

Application of Spatial Filters to sEMG data Array:

Recording and analysis of Surface EMG (sEMG) has been around for almost a century now. Surface electrodes have been routinely used to record the gross electrical activity of skeletal muscles. However, when specific information about individual motor unit discharge rates or recruitment needs to be extracted, sEMG signal have been treated with some reservation. So previously, in most cases, intramuscular EMG recording using fine wire or needle electrodes were employed to selectively record the single motor unit activity. Unfortunately, invasive recordings of sEMG are inconvenient, do induce pain to the subject and may potentially damage muscle tissues and nerves. In recent years, considerable efforts have been directed towards effectively recording single motor unit activity noninvasively *i.e.* using surface EMG sensors.

The principle underlying this approach is to be increasingly selective in recording the information using surface EMG electrodes. In other words, the objective is to amplify the activity of motor unit/s located closest to the recording site (generally the actual motor location for the particular limb) and reducing the EMG signal generated by other motor units located further away. The selectivity of surface EMG recordings can be increased by reducing the electrode size (i.e., skin–electrode contact area or inter-electrode distance) [12, 13] and/or by applying temporal filters [14]. More recent work has focused on recent advances in the design of surface electrode arrays [15–17] to extract single motor unit information from sEMG. A large number of traditional [18–21] and adaptive [22, 23] linear spatial filters have been extensively used to glean more information out of sEMG signals and to understand it much better.

Many types of nonlinear spatial filters have also been studied in the past. In this study comparison of a few spatial filters is presented.

Experiments were performed using multiple sEMG sensors in the array configuration as shown in Fig. 2.2.1. Nine different experiments were conducted and the corresponding sEMG was measured simultaneously from all the different sensors. Information regarding the various experiments is given below:
Experiment 1 – Baseline – 30 sec – No Motion/ Force – Red Stress ball
Experiment 2 – Baseline – 30 sec – No Motion/ Force – Red Stress ball
Experiment 3 – 30 sec – Ring Finger Grasping Motion – Red Stress ball
Experiment 4 – 30 sec – Ring Finger Grasping Motion – Red Stress ball
Experiment 5 – 45 sec – Ring Finger Grasping Motion with Thumb Restrained – Red Stress ball
Experiment 6 – 45 sec – Ring Finger Grasping Motion with Thumb Restrained – Red Stress ball
Experiment 7 – 45 sec – Ring Finger Grasping Motion with Thumb Restrained – Yellow Stress ball
Experiment 8 – 45 sec – Ring Finger Grasping Motion with Thumb Restrained – Yellow Stress ball
Experiment 9 – 60 sec – Ring Finger Grasping Motion with Thumb Restrained – Red Stress ball

Experiments 1 and 2 were conducted to give insight into the sEMG generated by the subject's hand, in the absence of any motion or force. Also, a thumb restrain was used to limit the influence of thumb while application of force to the stress ball. A Force Sensitive Resistors (FSR) was mounted on the stress ball to record force levels for different grasping force levels.

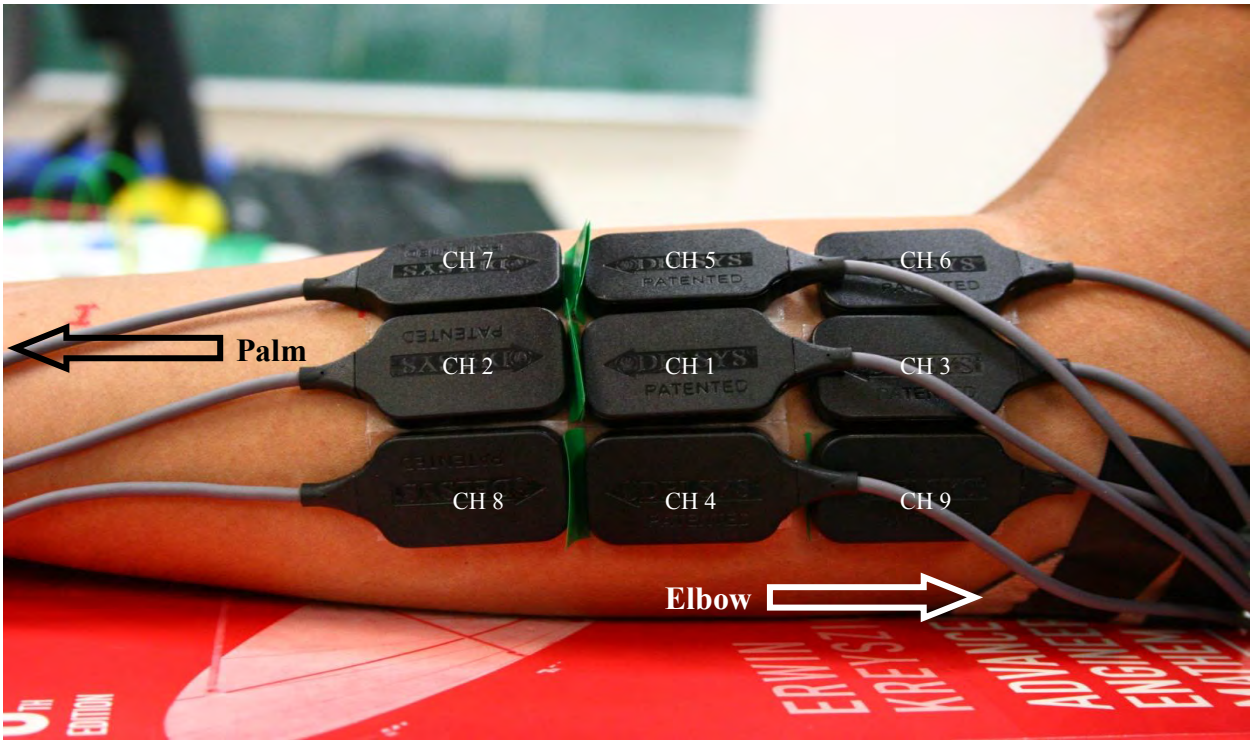

Fig. 2.2.1. Experimental Setup – Location of sEMG Sensors.
Fig. 2.2.1 shows the variable associated with the various sEMG locations. Fig. 2.2.2 shows the thumb-restrain in use during various contraction experiments. Fig. 2.2.3 also shows the location of the FSR. Fig. 2.2.4 shows the sEMG capture 16 channel Bagnoli measuring system.

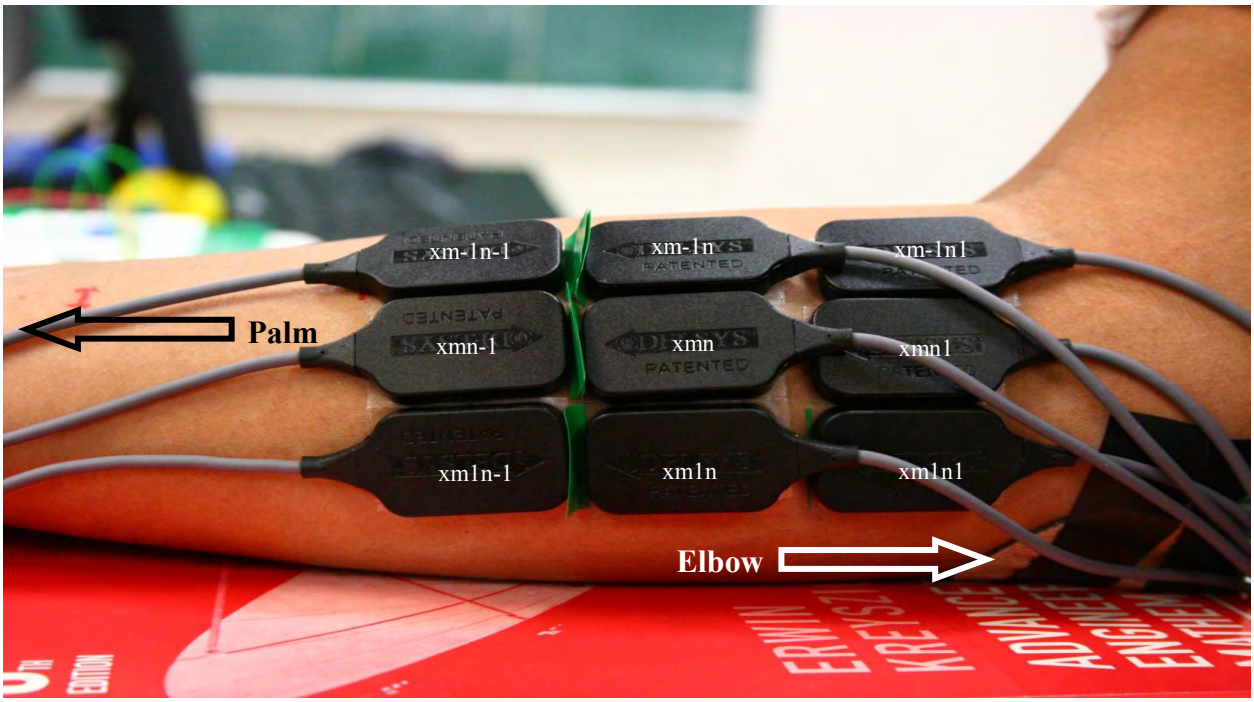

Fig. 2.2.2. Experimental Setup – Variables Associated with the sEMG Channels.

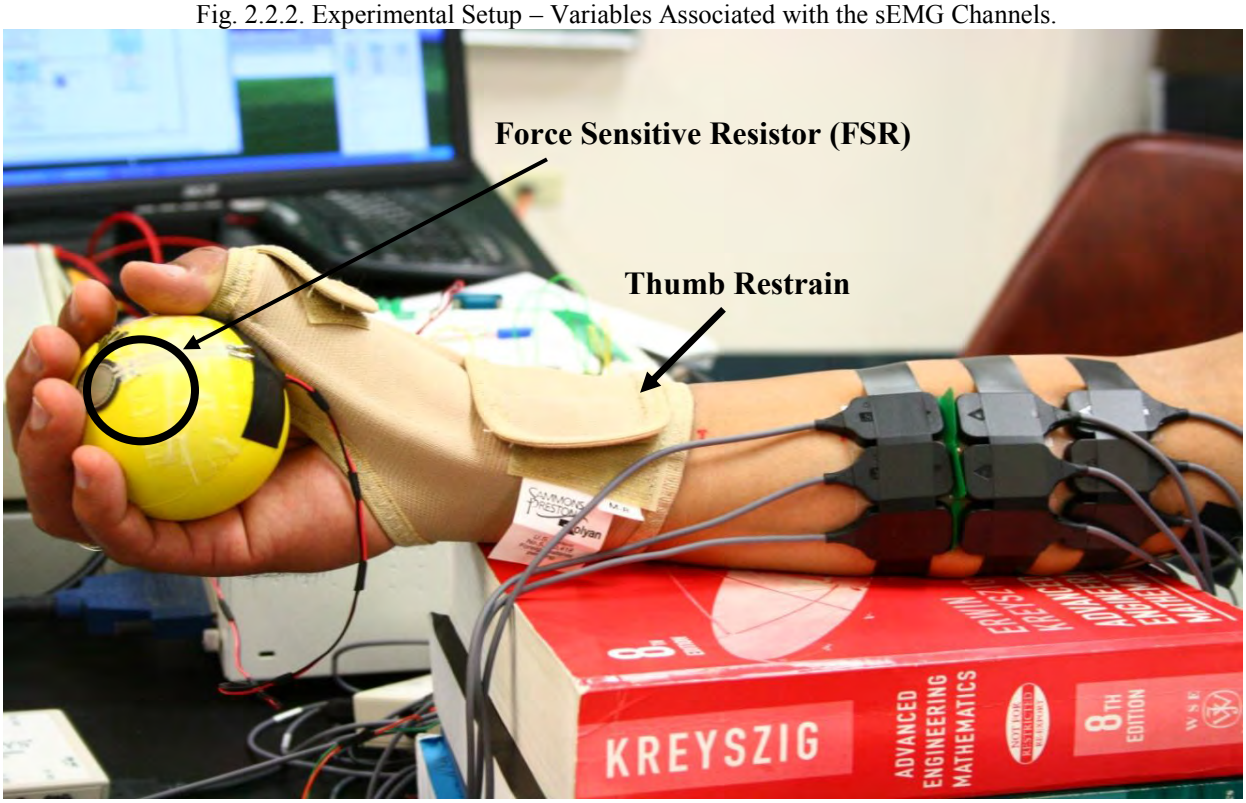

Fig. 2.2.3. Experimental Setup – Location of Force Sensitive Resistor (FSR) and Thumb Restrain.

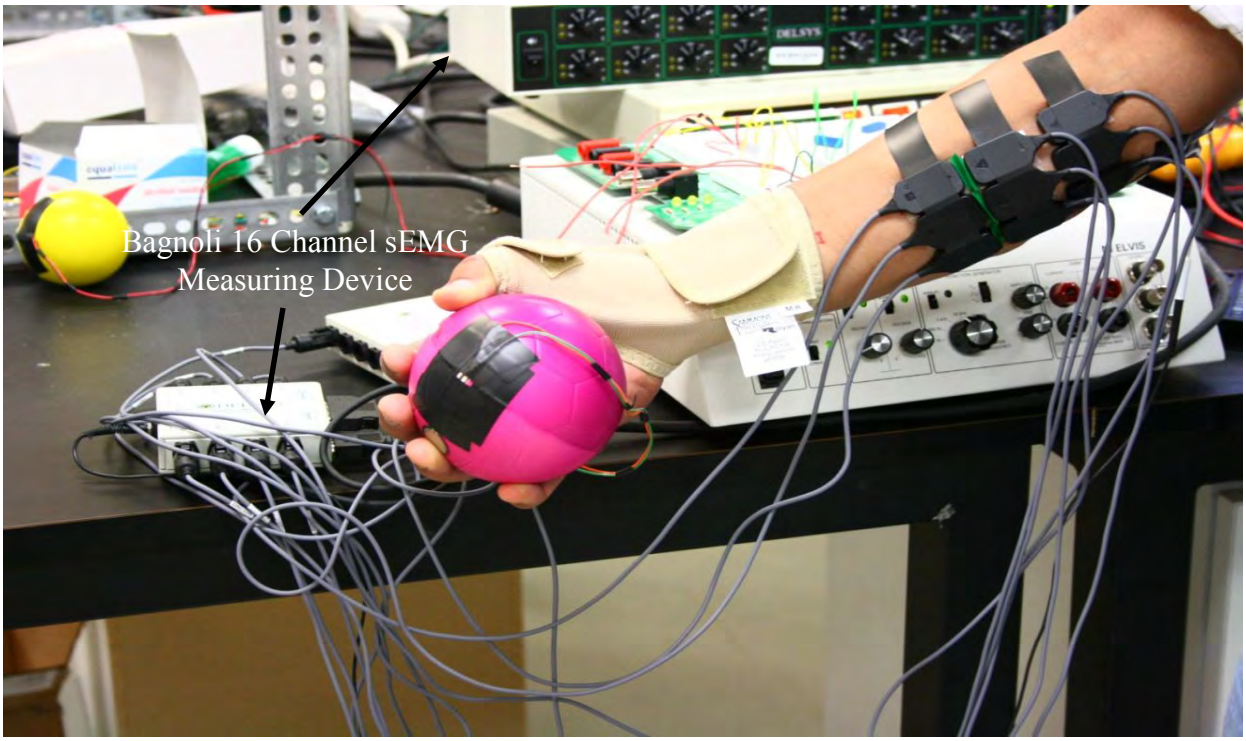

Fig. 2.2.4. Experimental Setup – Bagnoli 16 Channel sEMG Measuring Device.

The most commonly used Linear Spatial filters for isolating the motor unit action potentials (MUAPs) are:

1) Longitudinal Single Differential (LSD)
2) Transverse Single Differential (TSD)
3) Longitudinal Double Differential (LDD)
4) Transverse Double Differential (TDD)
5) Normal Double Differential (NDD)
6) Inverse Binomial (IB2) and the
7) Inverse Rectangular (IR) Filter

The mask of these filters and the corresponding resultant equations on application of the mask to the grid data obtained from the sEMG array arrangement are given below.

CASE 1

Longitudinal Single Differential (LSD)

EMG Array Information, Spatial Filter Mask

$$\text{LSD} = \begin{bmatrix} sEMG7 & sEMG5 & sEMG6 \\ 0 & 0 & 0 \\ sEMG2 & sEMG1 & sEMG3 \\ -1 & 1 & 0 \\ sEMG8 & sEMG4 & sEMG9 \\ 0 & 0 & 0 \end{bmatrix} \tag{4}$$

Result Equation: $-sEMG2 + sEMG1$

$$\text{TSD}=\begin{bmatrix} 0 & -1 & 0 \\ 0 & 1 & 0 \\ 0 & 0 & 0 \end{bmatrix}; \quad \text{LDD}=\begin{bmatrix} 0 & 0 & 0 \\ -1 & 2 & -1 \\ 0 & 0 & 0 \end{bmatrix}; \quad \text{TDD} = \begin{bmatrix} 0 & -1 & 0 \\ 0 & 2 & 0 \\ 0 & -1 & 0 \end{bmatrix} \tag{5}$$

LSD Equation = sEMG1-sEMG2; *TSD* Equation = *sEMG1-sEMG5*. We can similarly deduce the equations for the other spatial filters:

$$\text{NDD}=\begin{bmatrix} 0 & -1 & 0 \\ -1 & 4 & -1 \\ 0 & -1 & 0 \end{bmatrix};\quad \text{IB2}=\begin{bmatrix} -1 & -2 & -1 \\ -2 & 12 & -2 \\ -1 & -2 & -1 \end{bmatrix};\quad \text{IR}=\begin{bmatrix} -1 & -1 & -1 \\ -1 & 8 & -1 \\ -1 & -1 & -1 \end{bmatrix} \tag{6}$$

In contrast to the varied number of linear spatial filters which are available for multichannel surface EMG signal analysis and isolation of MUAP‘s there is a dearth of nonlinear spatial filters. Few of these have been reported in literature [24]. The nonlinear spatial filters used here are 1) 1-D Nonlinear Transverse Spatial Filter, 2) 1-D Nonlinear Longitudinal Spatial Filter, 3) 2-D Nonlinear spatial Filter in Two- Orthogonal Directions and 4) Nonlinear Spatial Filter in All Four possible Directions. The results of spatially filtered data for the linear case and the nonlinear case are compared based on the ―Kurtosis" criteria. *Kurtosis* is a measure of whether the data are peaked or flat relative to a normal distribution. That is, data sets with high kurtosis tend to have a distinct peak near the mean, decline rather rapidly, and have heavy tails. Data sets with low kurtosis tend to have a flat top near the mean rather than a sharp peak. A uniform distribution would be the extreme case. The mathematical expression for kurtosis is given in equation 11.

$$Kurt = \frac{E[x^4] - 3(E[x^2])^2}{E[x^2]^2} \tag{7}$$

The Nonlinear Spatial Filters use the Teager-Kaiser Energy (TKE) Operator [25], [26]. This operator is derived from Teager‘s experiments in 1983. This technique is a threshold ‗energy‘ based approach where outliers are first detected and then replaced by their estimated values. Based on Newton‘s law of motion, a nonlinear quadratic operator called Teager-Kaiser (TK) operator was first introduced by Teager and Kaiser [25], [26] to measure the real physical energy of a system. This nonlinear operator differs from the common way to calculate the energy of a discrete-time signal as the average sum of its squared magnitudes. The energy of a generating system of a simple oscillation signal was computed as the product of the square of the amplitude and the frequency of the signal. It was found that this nonlinear operator exhibits several attractive features such as simplicity, efficiency and ability to track instantaneously-varying special patterns. Since its introduction, several applications have been derived for one-dimensional [27], [28], and two dimensional signal processing [29].

Before the Teager-Kaiser operator was introduced, various filtering methods were proposed both linear and nonlinear alternatives. Filtering is often a trade-off between different features, such as performance in Gaussian and non-Gaussian environments, ability to adapt in case of non-stationary signals, edge preservation and computational complexity. Two typical methods were running mean and median filters, which exploit a sliding fixed length window. Mean filters are known to remove the additive Gaussian noise very well, but they tend to soften edges and cannot fully cope with impulsive noise. Median filters on the other hand are nonlinear, which involve sorting of the data, and are able to eliminate impulses at the expense of some streaking and edge jittering [30]. De-noising deals with the same problem of estimating the underlying signal from the noisy observations, but now the data is not needed to process online or is not time-dependent at all. De-noising is not restricted to the methods acting in time domain, the signal is often processed in some transform domain. Wavelet transform has recently gained research interest in several fields of signal processing, using thresholding of (orthogonal) wavelet coefficients and taking the inverse wavelet transform has been proposed to solve de-noising problem.

The nonlinear spatial filters with the TKE operator incorporated are given as follows:

a) General Form of Nonlinear Spatial Filter using the Teager-Kaiser (TKE) operator

$$\Psi[x(n)] = x^2(n) - x(n+1)x(n-1) \tag{8}$$

b) 1-D Nonlinear Transverse Spatial Filter

$$\Psi_{d,m}[x(m,n)] = x^2(m,n) - x(m-1,n)x(m+1,n) \tag{9}$$

c) 1-D Nonlinear Longitudinal Spatial Filter

$$\Psi_{d,n}[x(m,n)] = x^2(m,n) - x(m,n-1)x(m,n+1) \tag{10}$$

d) Nonlinear Spatial Filter in Two Orthogonal Directions

$$\Psi_{d,2}[x(m,n)] = \Psi_{d,2m}[x(m,n)] + \Psi_{d,n}[x(m,n)]$$

$$= 2x^2(m,n) - x(m-1,n)x(m+1,n) - x(m,n-1)x(m,n+1)$$

e) Nonlinear Spatial Filter in all Four Directions

$$\Psi_{d,4}[x(m,n)] = 4x^2(m,n) - x(m-1,n)x(m+1,n) \tag{11}$$
$$- x(m,n-1)x(m,n+1)$$
$$- x(m-1,n+1)x(m+1,n-1)$$
$$- x(m-1,n-1)x(m+1,n+1)$$

Fig. 2.2.5 and 2.2.6 show the plots of the raw sEMG signal for the experiment without any force being applied.

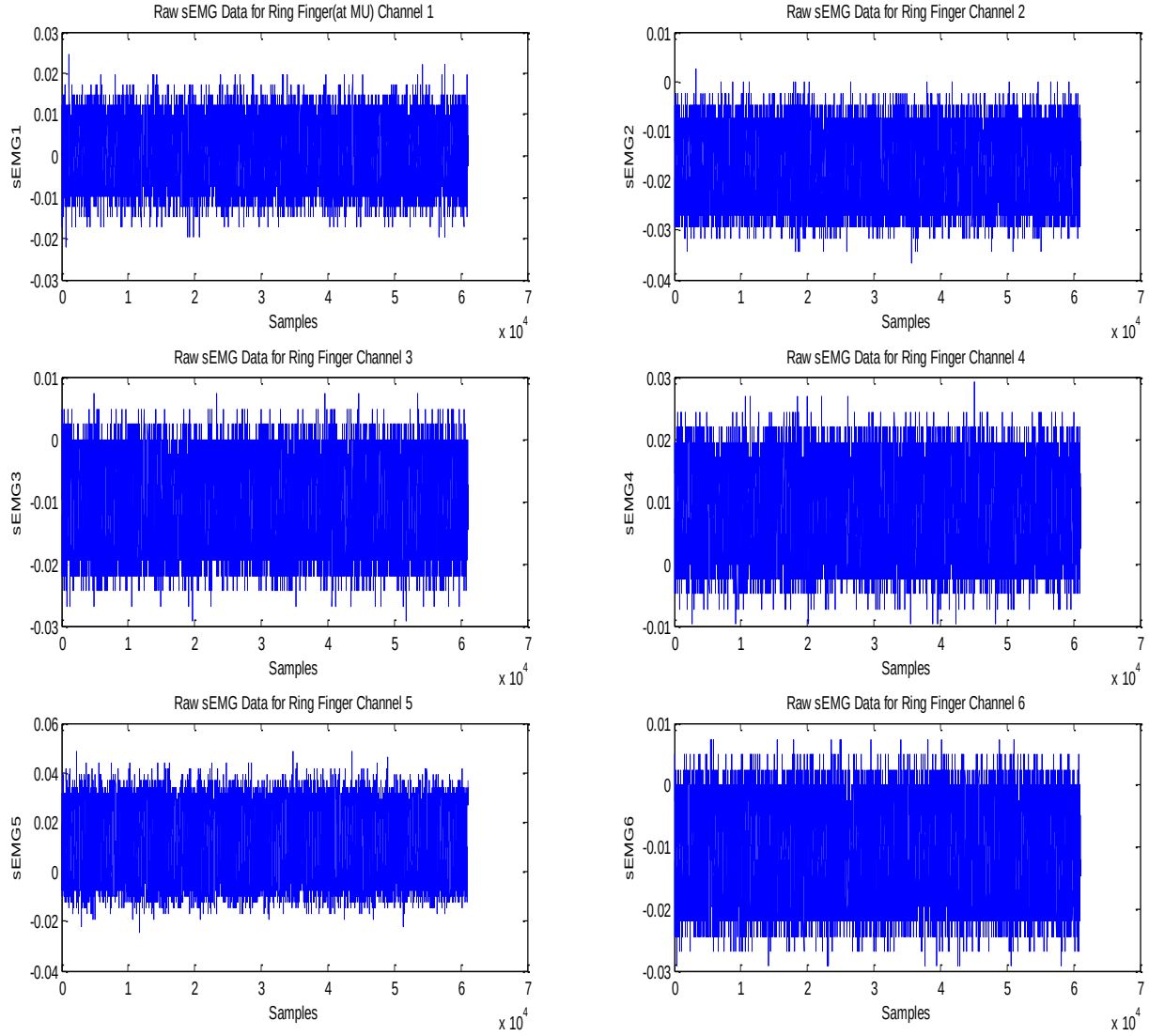

Fig. 2.2.5. Raw sEMG Data Plots Channels 1 to 6

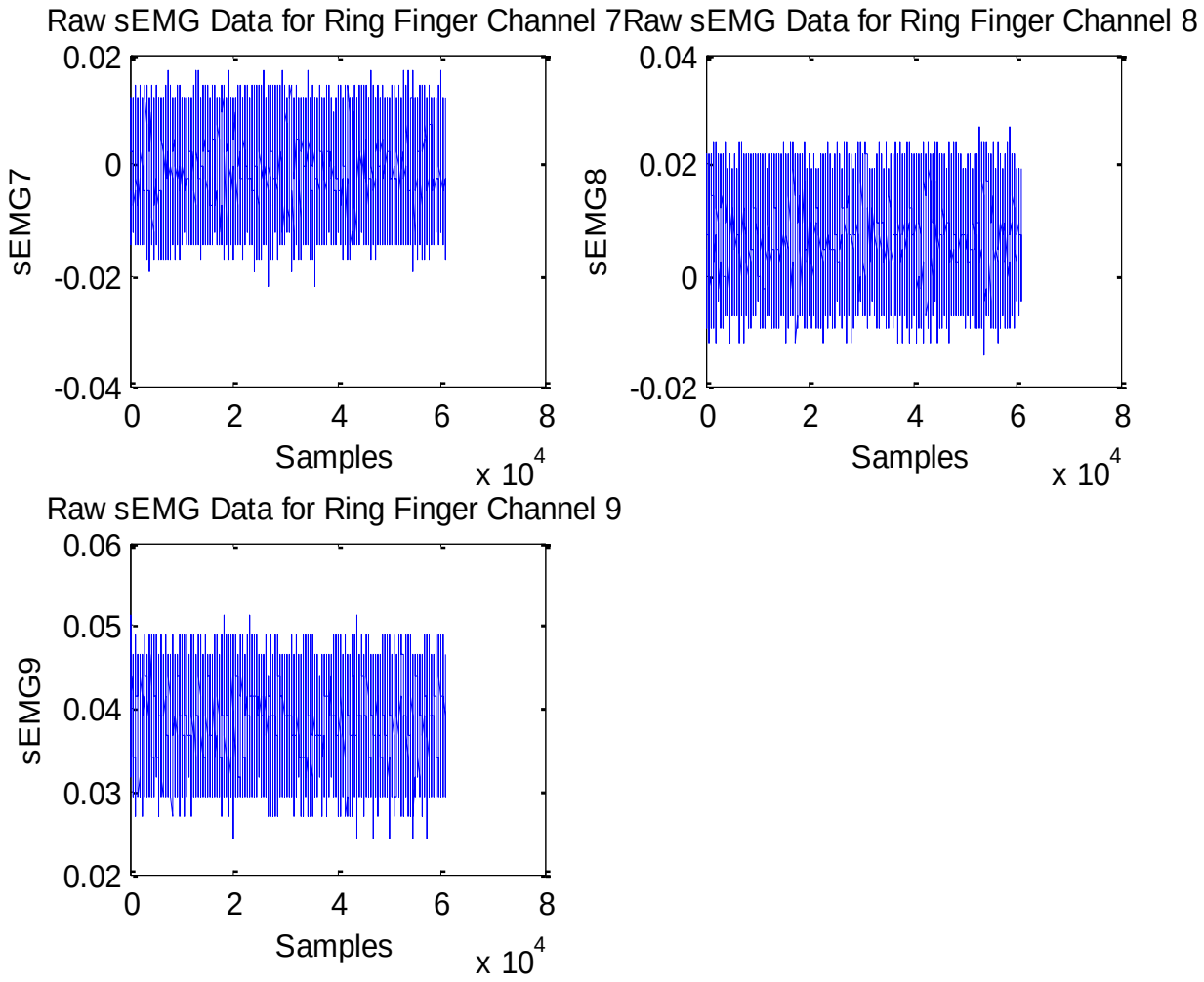

Fig. 2.2.6. Raw sEMG Data Plots Channels 7 to 9

The sEMG data was then filtered using a Chebyshev Type II filter with a pass-band frequency of 60-450 Hz. The force data was also filtered using a 3rd order Low-pass Butterworth filter with cutoff frequency of 10 Hz. The same filtering was carried out for all the experiments conducted. The plots of the filtered force and sEMG data are given in Fig. 2.2.7. Fig. 2.2.7 shows the baseline sEMG and force levels generated by the subject where no contractions were performed.

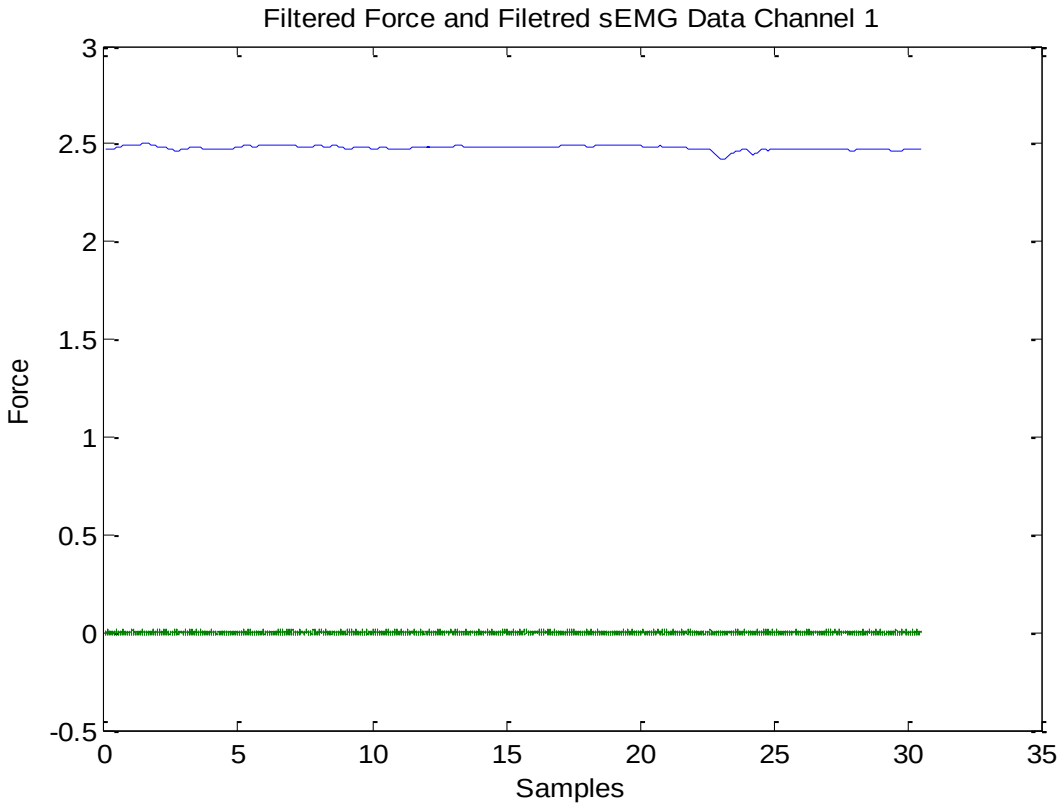

Fig. 2.2.7. Filtered sEMG and Force Data – No Force Generation

Fig. 2.2.8 and 2.2.9 plots the raw sEMG of all the channels (1-9) for another experiment where the subject was performing the action of squeezing the force ball with a force sensor attached to the ball.

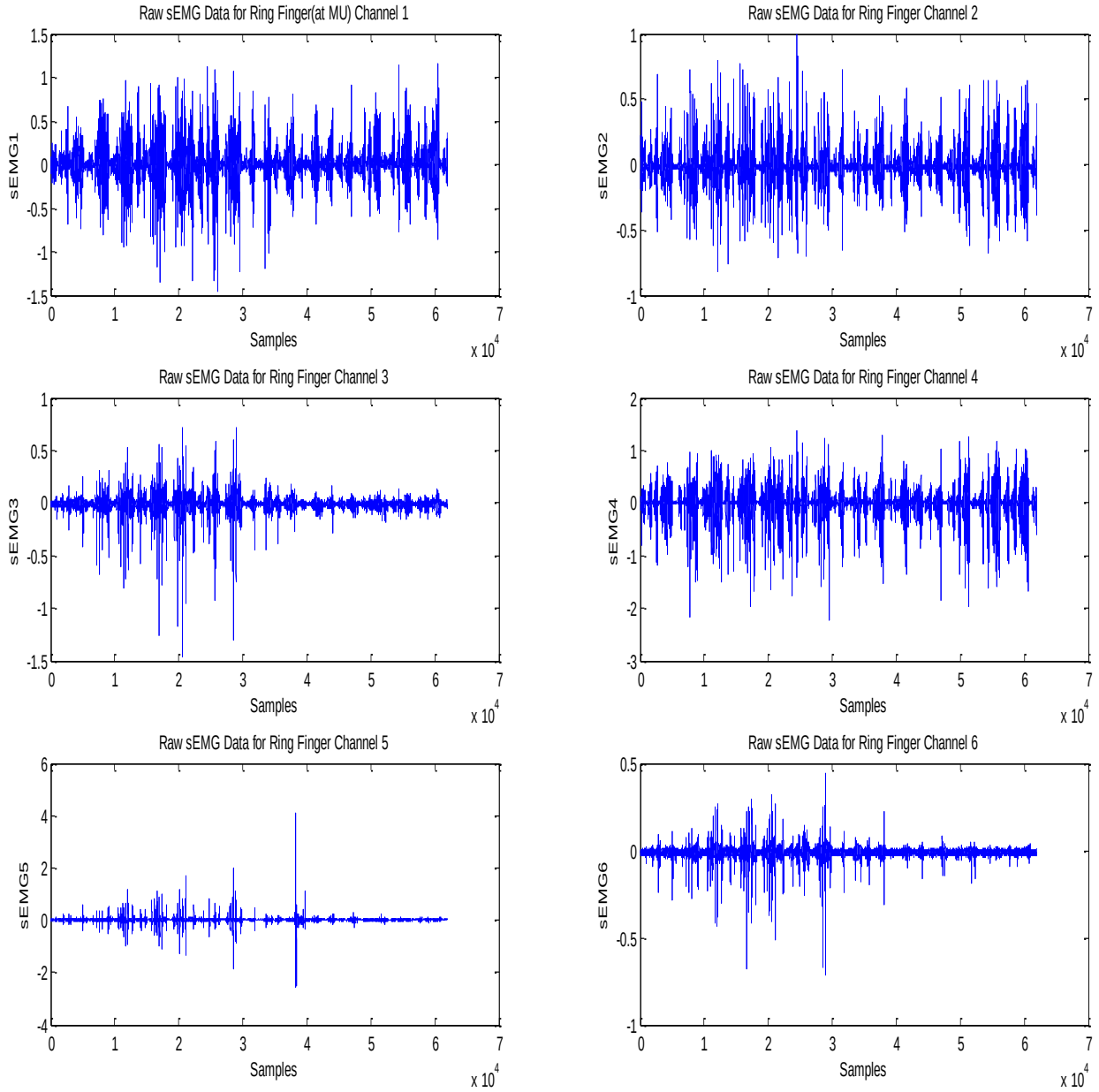

Fig. 2.2.8. Raw sEMG Data Plots Channels 1 to 6

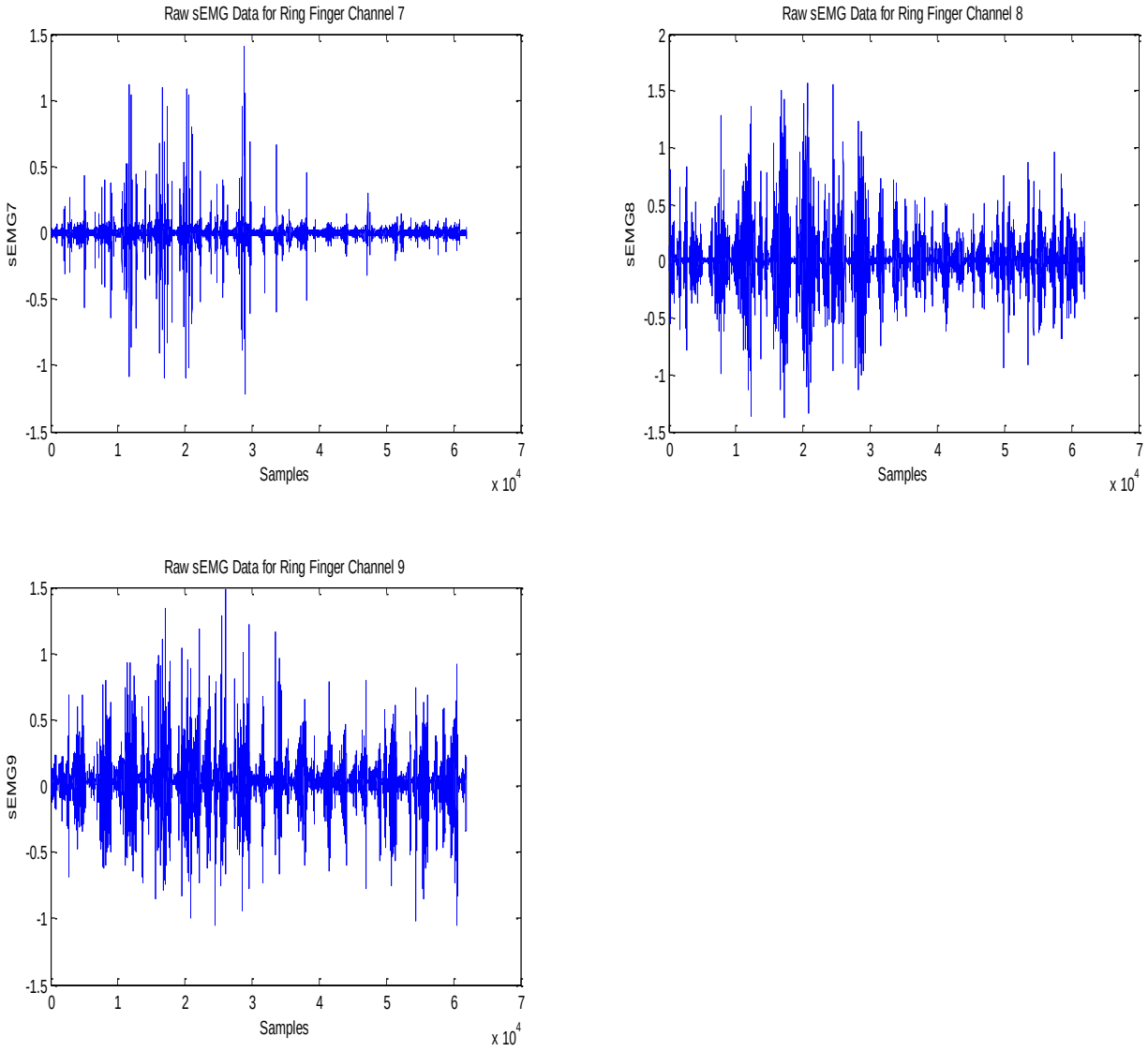

Fig. 2.2.9. Raw sEMG Data Plots Channels 7 to 9

Fig. 2.2.10 shows the sEMG and the force signal generated by the subject where the subject performed random variation of force by squeezing the stress ball.

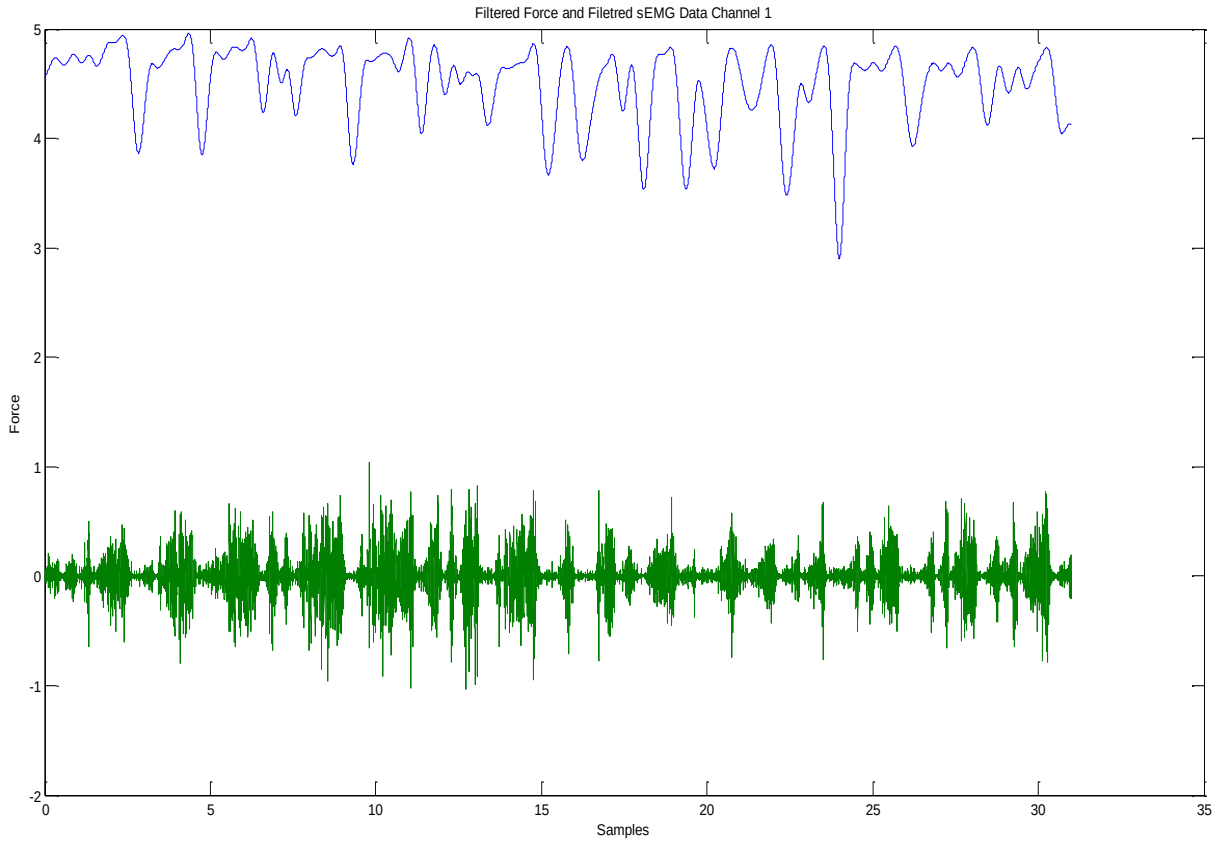

Fig. 2.2.10. Filtered sEMG and Force Data – Force Generated

Fig. 2.2.11 (a), (b), (c) and (d) show the results of the Non-linear Spatially Filtered sEMG data for the multi-sensor array setup shown in Fig. 2.2.1.

(a)

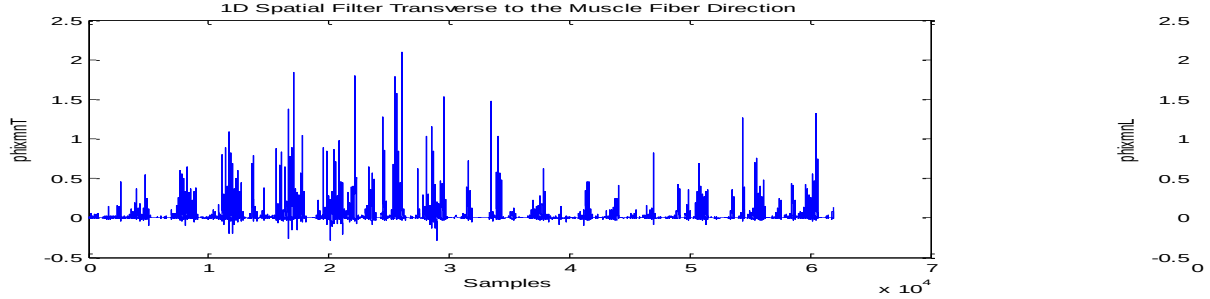

(b)

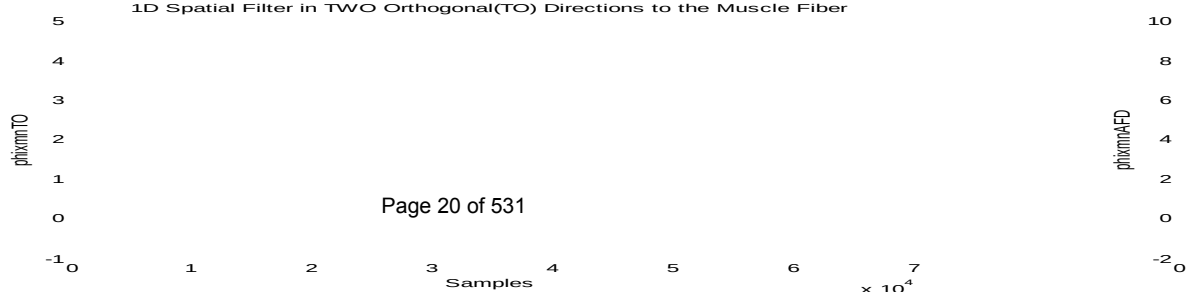

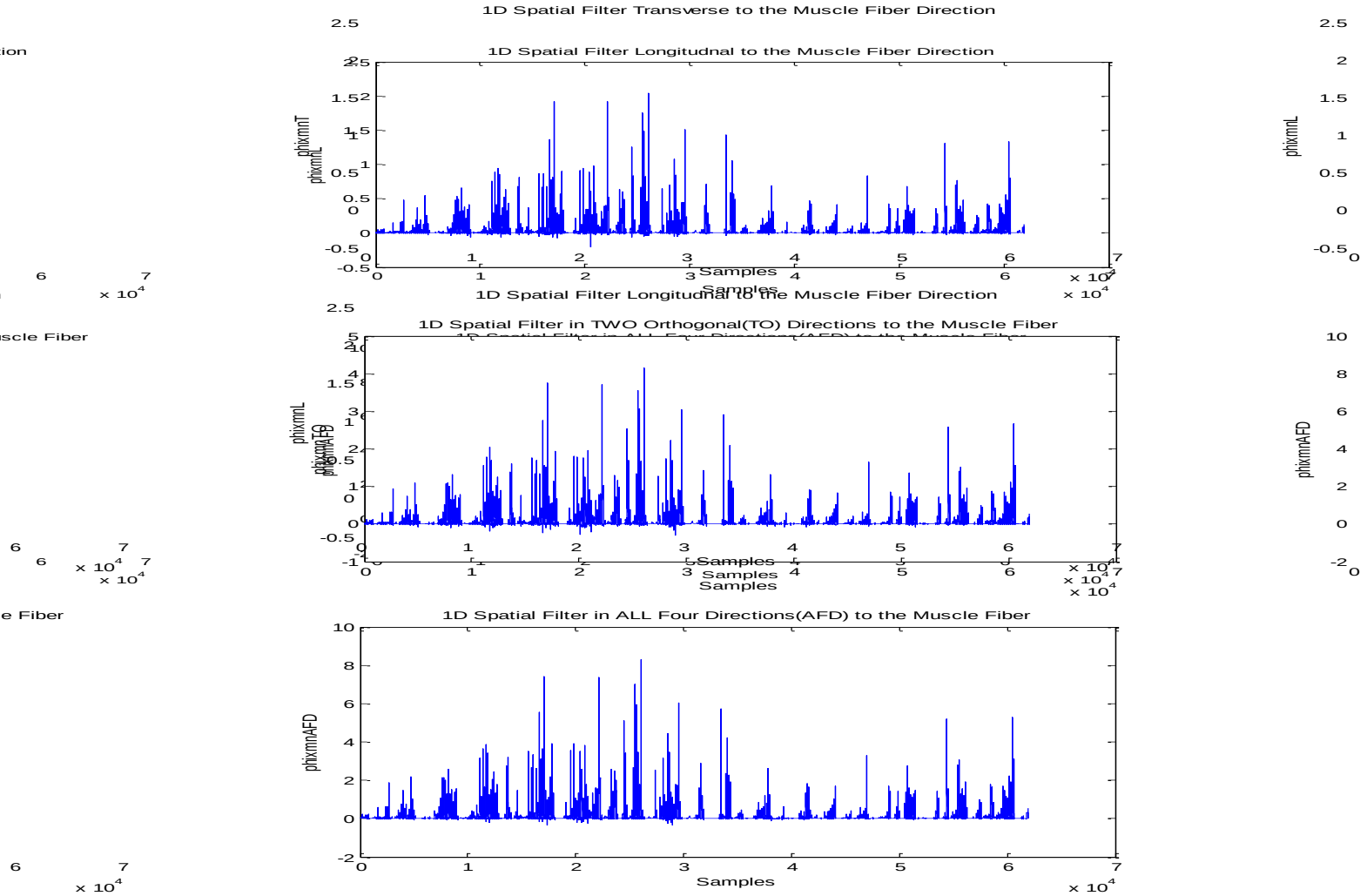

Fig. 2.2.11. Spatially Filtered sEMG a) 1-D Nonlinear Transverse Spatial Filter, b) 1-D Nonlinear Longitudinal Spatial Filter, c) Nonlinear Spatial Filter in Two Orthogonal Directions, d) Nonlinear Spatial Filter in All Four Directions

Fig. 2.2.12 shows the results of the various Linear Spatially Filtered sEMG data for the multi-sensor array setup shown in Fig. 2.2.1.

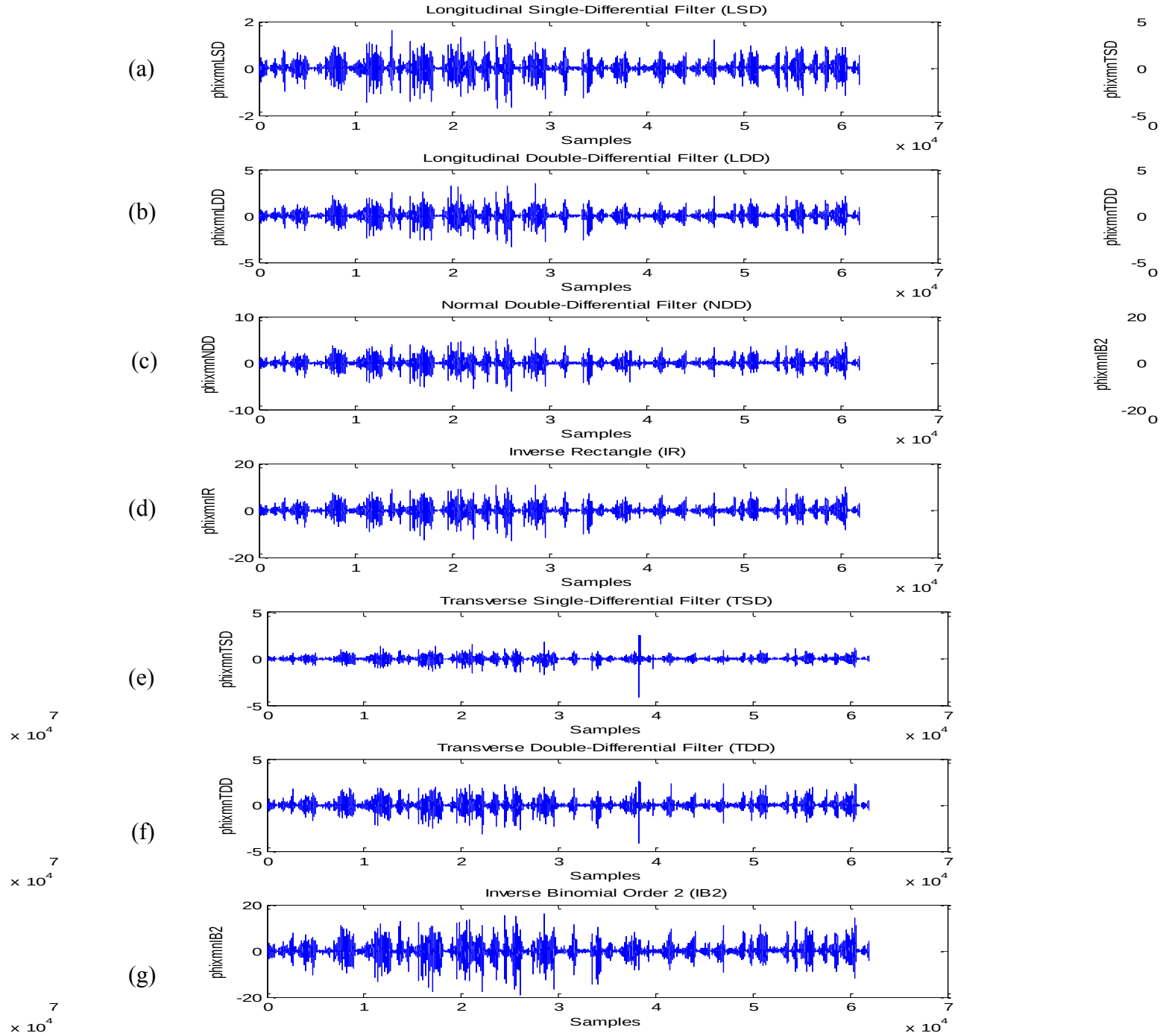

Fig. 2.2.12. Spatially Filtered sEMG a) Longitudinal Single Differential (LSD), b) Longitudinal Double Differential (LDD), c) Normal Double Differential (NDD), d) Inverse Rectangular (IR) Filter, e) Transverse Single Differential (TSD), f) Transverse Double Differential (TDD), g) Inverse Binomial (IB2)

The sEMG signal was subjected to various spatial filters as mentioned in the previous section. In addition to these 11 spatial filters, the sEMG data was also filtered using 4 other filters – Bessel, Butterworth, Chebyshev Type I and Chebyshev Type II filters. The filter characteristics of these 4 filters were in accordance to the ISEK standards. The relation of sEMG-Force was modeled using Non-Linear Hammerstein-Wiener models. This modeling method has been proven to work in the past, in assuming a black-box model structure for the system. In order to model the sEMG-Force relation, the filtered data from the various experiments was split into various four (4) time windows.

Equation (12) describes the general Hammerstein-Wiener model structure:

$$w(t) = f((g(t)), \quad b(t) = \frac{B_{j,i}(q)}{F_{j,i}(q)} w(t), \quad y(t) = h(x(t)), \qquad (12)$$

where, $w(t)$ and $b(t)$ are internal variables, $w(t)$ has the same dimensions as $u(t)$ - input, and $x(t)$ has the same dimensions as $y(t)$ - output. $g()$ and $h()$ are the input and output non-linearity functions respectively. $B(q)$ and $F(q)$ are regression polynomials. The model fit values are computed using Equation (13) as follows:

$$fit = 100 * \frac{1 - \|\hat{y} - y\|}{\|y - \hat{y}\|} \qquad (13)$$

where, $\hat{y}$ is the estimated output by the model.

The time windows used for estimation and validation of the models were called "ze" and "zv" respectively. "ze" contained 8000 sample points and "zv" contained data points shifted by 2000 sample points. For example, if "ze" was a time window between 2-6 seconds i.e. samples 4000-12000, then "zv" was between 3-7 seconds i.e. 6000-14000 samples. Thus the Hammerstein-Wiener method uses "ze" to estimate the model structure and based on this information predicts the next 2000 sample points. The data was filtered using the various filters mentioned in the previous sections. We would like to stress once again the point that the force was varied randomly and the subject was in no way trying to achieve maximum voluntary contractions during each cycle. A cycle is defined as the subject starting without any force on the stress ball, squeezing it (to any force level) and then going back to no force. The subject has to keep the finger in contact with the force ball throughout this cycle.

A plot of the variations in force achieved for 3 experiments is shown in Fig. 2.2.13. The Matlab® code for the Hammerstein-Wiener model is: *nlhw(ze,* [n_a n_b n_k], …., …). The modeling was carried out by varying n_a - the number of past output terms used to predict the current output, n_b - the number of past input terms used to predict the current output and n_k - the delay from input and output in terms of the number of samples for the various Hammerstein-Wiener models.

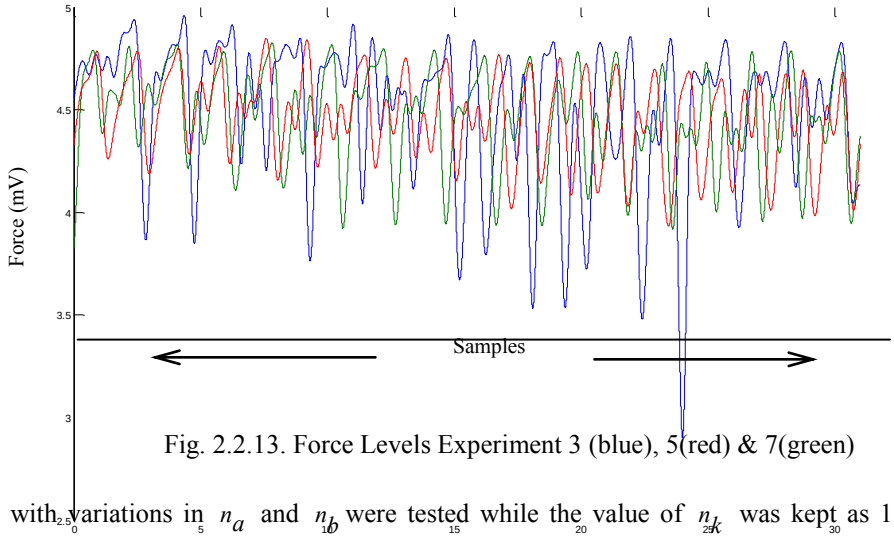

Fig. 2.2.13. Force Levels Experiment 3 (blue), 5(red) & 7(green)

42 models with variations in n_a and n_b were tested while the value of n_k was kept as 1. The total number of models estimated were 15 (filter types) x 4 (time windows) x 42 models per time window x 4 experiments = 10,080 models.

(Refer for additional details Publication – "Evaluation of Filtering Techniques Applied to Surface EMG Data and Comparison Based on Hammerstein-Wiener Models") [P1]

Table 2.2.2 and 2.2.3 show the results of modeling for the time window 0-9 sec. 42 models were estimated by varying n_a and n_b only 35 of those are shown here on account of page size limitation. The Hammerstein-Wiener models worked very well in capturing the dynamics of the force levels for the various experiments conducted. This method of modeling could help in improving the control over the motors used in prosthetic devices to mimic the actual changes force levels in a real hand. This method also performed very well in the scenarios where the subject

did fatigue but the affects were successfully modeled by the Hammerstein–Wiener models. The nonlinear and linear spatial filters (TDD, NDD and NLT, NLTO and NLAFD) did outperform the other filtering methods used especially for the later time windows. The only other filter which had a comparable performance to the spatial filters was the Bessel filter. Further investigation into reducing the wide range of the fit values obtained needs to be performed. One of the possible methods to pursue would be to use Genetic Algorithm to optimize the model parameters n_a and n_b and also the number of iterations used for the modeling of sEMG-force levels. One of the possible reasons for poor fit values could also be attributed to the model trying to over-fit the data sets.

We pursued optimization of the filter mask using GA and the details of this investigation are presented in detail in the paper titled ―Optimized Spatial Filter Mask Using Genetic Algorithm And sEMG-Force Modeling Using System Identification". [P2]

TABLE 2.2.2
EXAMPLE OF MODEL FIT VALUES FOR TIME WINDOW 0-9 SEC – VARIED *NA* AND *NB*

Model Number	na	nb	nk	Bessel	Butter-worth	Cheby I	Cheby II	NLT	NLL	NLTO
m1	2	3	1	40.67	10.37	34.65	13.09	34.17	17.52	60.13
m2	2	4	1	53.19	41.72	31.75	30.02	31.25	12.08	10.54
m3	2	5	1	51.32	29.32	13.5	1.644	35.51	37.41	32.78
m4	2	6	1	56.36	2.764	12.19	36.28	34.07	13.87	33.57
m5	2	7	1	54.23	11.82	31.93	35.53	39.7	28.23	28.91
m6	2	8	1	53.2	11.05	12.01	36.59	19.71	26.51	26.17
m7	2	9	1	46.88	32.3	32.7	-0.297	33.8	15.8	35
m8	3	3	1	52.05	31.56	30.21	36.3	34.64	19.16	17.8
m9	3	4	1	48.66	6.734	19.66	39	36.45	19.74	33.04
m10	3	5	1	13.79	34.23	32.11	36.06	17	17.92	16.44
m11	3	6	1	51.9	42.87	15.19	36.39	33.75	17.84	19.51
m12	3	7	1	50.05	18.56	2.805	36.66	34.7	29.34	34.02
m13	3	8	1	51.74	26.33	33.82	43.69	28.41	27.05	32.79
m14	3	9	1	33.48	34.44	25.83	37	32.56	27	18.55
m15	4	3	1	48.02	18.53	12.38	39.07	15.27	26.56	15.54
m16	4	4	1	52.36	35.9	15.09	3.257	14.95	26.84	32.16
m17	4	5	1	12.1	40.11	14.74	30.87	27.77	17.76	40.91
m18	4	6	1	54.11	1.436	14.84	38.77	27.45	30.69	16.55
m19	4	7	1	50.38	30.62	27.6	35.76	46.37	23.5	27.66
m20	4	8	1	44.06	-0.4972	9.644	36.71	36.58	26.63	11.47
m21	4	9	1	50.44	1.269	-0.0622	37.15	36.07	40.85	34.55
m22	5	3	1	48.26	34.89	13.48	17.98	26.48	18.41	58.38
m23	5	4	1	51.51	5.417	13.53	38.45	39.21	25.89	46.88
m24	5	5	1	52.61	43.02	12.5	36.78	33.26	17.92	25.49
m25	5	6	1	47.45	10.01	12.22	36.45	34.25	27.74	27.41
m26	5	7	1	52.25	30.03	14.07	36.29	33.95	30.69	27.12
m27	5	8	1	52.22	31.85	12.61	37.87	34	28.33	26.55
m28	5	9	1	55.21	33.96	12.32	31.98	57.96	26.95	25.52
m29	6	3	1	50.12	-0.3022	-0.1301	29.63	15.48	30.51	16.15

m30	6	4	1	43.39	21.07	30.2	2.117	34.32	25.46	37.36
m31	6	5	1	49.26	1.169	19.23	10.32	36.3	31.73	16.04
m32	6	6	1	53.1	15.03	14.63	9.181	26.98	14.11	26.16
m33	6	7	1	52.9	0.9796	15.35	0.6897	46.02	33.64	34.97
m34	6	8	1	51.92	5.604	11.16	1.212	27.86	46.24	16
m35	6	9	1	51.35	21.36	19.06	39.84	41.41	27.68	20.68

TABLE 2.2.3
EXAMPLE OF MODEL FIT VALUES FOR TIME WINDOW 0-9 SEC – VARIED NA AND NB

Model Number	na	nb	nk	NLAFD	LSD	TSD	LDD	TDD	NDD	IB2	IR
m1	2	3	1	17.21	41.39	-9.685	31.06	39.53	45.55	33.79	35.38
m2	2	4	1	16.75	17.4	43.19	31.86	39.36	36.84	16.88	23.89
m3	2	5	1	17.99	35.94	2.247	23.54	30.09	39.87	36.17	38.16
m4	2	6	1	20.51	41.99	43.46	3.266	41.28	10.83	36.41	36.7
m5	2	7	1	34.41	40.55	31.28	31.58	44.65	2.593	32.26	36.34
m6	2	8	1	12.24	4.259	20.08	37.84	21.89	8.036	36.22	36.57
m7	2	9	1	31.1	-0.1887	28.71	31.42	35.78	38.11	35.54	35.82
m8	3	3	1	18.97	40.04	12.33	36.59	36.17	4.478	41.09	35.81
m9	3	4	1	25.54	40.72	36.57	20.74	31.53	29.76	37.43	38.76
m10	3	5	1	22.03	11.53	30.24	39.87	39.83	39.25	35.15	37.9
m11	3	6	1	18.37	35.41	44.24	38.79	40.76	39.01	35.66	38.17
m12	3	7	1	17.87	41.67	42.69	35.54	39.93	36.81	31.31	35.6
m13	3	8	1	23.09	0.2404	2.988	37	39.6	37.4	36.18	15.24
m14	3	9	1	5.519	39.42	44.21	37.83	26.8	41.36	37.53	34.42
m15	4	3	1	21.62	41.48	15.21	34.4	43.01	39.58	0.8962	30.42
m16	4	4	1	35.08	37.8	29.57	37.76	40.12	-0.3683	36.65	36.9
m17	4	5	1	32.36	40.53	20.3	23.31	17.97	32.97	37.22	34.48
m18	4	6	1	31.55	41.86	33.33	33.27	22.13	30.85	38.48	39.23
m19	4	7	1	17.66	41.51	42.28	36.6	41	41.16	38.11	35.41
m20	4	8	1	20.88	42.04	29.77	35.3	40.65	18.03	37.3	37.03
m21	4	9	1	18.93	41.33	37.4	27.97	36.73	6.661	37.54	36.21
m22	5	3	1	18	14.08	41.46	2.748	42.14	41.36	33.82	34.69
m23	5	4	1	25.55	7.815	42.19	30.54	39.49	36.47	37.93	35.36
m24	5	5	1	17.81	38.31	30.71	39.16	41.95	36.29	34.53	16.75
m25	5	6	1	17.72	16.64	31.41	37.13	41.81	37.15	36.03	36.3
m26	5	7	1	20.48	33.97	37.15	38.43	34.96	34.03	29.84	35.49
m27	5	8	1	16.78	34.58	29.29	18.8	41.45	39.14	35.47	34.89
m28	5	9	1	15.89	35.33	36.44	37.96	42.36	40.24	21.59	35.36
m29	6	3	1	18.76	42.76	30.01	38.74	39.93	37.22	40.46	-0.1423
m30	6	4	1	22.08	38.44	29.07	38.81	39.93	29.86	33.32	33.93

m31	6	5	1	17.71	42.58	29.1	39.44	38.74	36.42	36.17	38.93
m32	6	6	1	16.67	38.6	41.18	19.42	40.12	40.96	35.99	35.34
m33	6	7	1	20.38	42.05	31.74	10.04	39.55	43.21	35.88	31.28
m34	6	8	1	17.05	3.922	25.66	28.73	39.85	39.5	31.34	13
m35	6	9	1	17.24	-0.4172	42.73	15.23	39.03	36.42	21.46	34.38

Some of the models for this time window were selected and then recomputed using GA to optimize the filter mask with the fitness function being the fit value of an identified model achieved for a given model order. Table 2.2.4 shows an example of the fits that were obtained on varying the parameters of the Hammerstein-Wiener model. The highlighted models (and a few other models) were selected randomly to be optimized using GA. We had two scenarios under GA –1) GA Constrained and 2) GA – Unconstrained. The first scenario GA constrained optimized only the mask entry a_{22} (location of the sEMG sensor on the motor unit). The other entries of the filter mask were then computed from this optimized value. In the second scenario, GA unconstrained we let GA optimize all the entries for various masks. The GA parameters for optimization were as follows: number of iterations: 50; initial population size Generation 0: 96; population size Generation 1: 48; Number of Chromosomes kept for mating: 24; and mutation rate was set to 4%.

TABLE 2.2.4
EXAMPLE OF SYSTEM IDENTIFICATION RESULTS USING FILTER MASK FROM LITERATURE – HIGHLIGHTED MODELS OPTIMIZED

Model Number	n_a	n_b	n_k	LDD	LSD	TDD	TSD	NDD	IB2	IR
m1	2	3	1	31.06	41.39	39.53	-9.685	45.55	33.79	35.38
m2	2	4	1	31.86	17.4	39.36	43.19	36.84	16.88	23.89
m3	2	5	1	23.54	35.94	30.09	2.247	39.78	36.17	38.16
m4	2	6	1	3.266	41.99	41.28	43.46	10.83	36.41	36.7
m5	2	7	1	31.58	40.55	44.65	31.28	2.593	32.26	36.34
m6	2	8	1	37.84	4.259	21.89	20.08	8.036	36.22	36.57
m7	2	9	1	31.42	-0.1887	35.78	28.71	38.11	35.54	35.82
m8	3	3	1	36.59	40.04	36.17	12.33	4.478	41.09	35.81
m9	3	4	1	20.74	40.72	31.53	36.57	29.76	37.43	38.76
m10	3	5	1	39.87	11.53	39.83	30.24	39.25	35.15	37.9
⋮	⋮	⋮	⋮	⋮	⋮	⋮	⋮	⋮	⋮	⋮
⋮	⋮	⋮	⋮	⋮	⋮	⋮	⋮	⋮	⋮	⋮
m40	7	7	1	34.91	10.18	40.79	35.21	35.24	33.42	37.92
m41	7	8	1	-0.1127	36.28	39.68	40.26	20.27	35.88	24.32
m42	7	9	1	36.55	-0.412	25.24	31.31	35.4	34.26	39.82

TABLE 2.2.5 (A)
RESULTS OF CONSTRAINED AND UNCONSTRAINED GA OF HIGHLIGHTED MODELS FROM TABLE 1

Longitudinal Double Differential (LDD)			
	Fit %		
	From Literature	GA Constrained	GA Unconstrained
m1	31.06	**42.8291**	**61.3475**
m6	37.84	**53.3134**	33.724
m12	35.54	**44.2513**	**51.7942**
m31	39.44	**47.0034**	**60.6489**

Longitudinal Single Differential (LSD)			
	Fit %		
	From Literature	GA Constrained	GA Unconstrained
m1	41.39	48.9135	59.8055
m4	41.99	41.5731	68.4191
m8	40.04	40.5924	63.8523
m9	40.72	45.2322	56.5113

Transverse Double Differential (TDD)			
	Fit %		
	From Literature	GA Constrained	GA Unconstrained
m1	39.53	**41.5297**	**59.8055**
m5	44.65	**49.4667**	**68.4191**
m10	39.83	**41.307**	**63.8523**
m15	43.01	43.3466	**56.5113**

Transverse Single Differential (TSD)			
	Fit %		
	From Literature	GA Constrained	GA Unconstrained
m2	43.19	**44.0017**	**65.9038**
m4	43.46	**43.0529**	**58.2755**
m11	44.24	39.7867	44.8431
m31	29.1	**43.5787**	**47.6688**

TABLE 2.2.5 (B)
RESULTS OF CONSTRAINED AND UNCONSTRAINED GA OF HIGHLIGHTED MODELS FROM TABLE 3

Normal Double Differential (NDD)			
	Fit %		
	From Literature	GA Constrained	GA Unconstrained
m1	45.55	53.1512	57.9496
m3	39.87	47.1084	60.7374
m7	38.11	51.8065	60.5535
m11	39.01	46.881	56.1193

Inverse Binomial 2 (IB2)			
	Fit %		
	From Literature	GA Constrained	GA Unconstrained
m1	33.79	38.6076	58.2365
m3	36.17	38.9074	58.1653
m4	36.41	38.9957	55.5179
m8	41.09	47.2971	55.0537

From the results in Table 2.2.5 (A) & (B) we can see that the optimization of the filter mask using GA worked in almost all the cases chosen. GA without constraints performed significantly better, in most cases, than the filter masks reported in literature and also the mask which we computed using GA, which only optimized the entry (a_{22}) i.e. the weight associated with the sEMG signal at the motor unit. This restriction on GA would leave the filter mask symmetrical. But looking at the results of the GA, we can conclude that the filter mask need not always be symmetrical for analysis of sEMG, especially for data recorded using an array. Examples of the filter mask that we obtained for TDD, model m5 and NDD, model 3 spatial filters are given below:

$$\text{TDD} = \begin{bmatrix} 0 & -41.5561 & 0 \\ 0 & 54.7329 & 0 \\ 0 & -22 & 0 \end{bmatrix}, \quad \text{NDD} = \begin{bmatrix} 0 & -11.5790 & 0 \\ -46.7773 & 36.9276 & -11.8061 \\ 0 & -70.0491 & 0 \end{bmatrix}.$$

The linear spatial filter masks reported in literature had poor *kurtosis* improvements which we optimized using GA, these were compared based on the model fit values achieved using Hammerstein-Wiener models. The fit values did improve significantly in the two GA scenarios – GA with and without constraints. The GA without constraints performed better than the GA with constrains, which brings into focus the possibility that the sEMG signal distribution over the entire grid cannot be assumed to be symmetrically distributed and that the weights associated with the sEMG signal at various locations need to be modified depending on probably the subject and also based on the experimental design. This is in contrast to the reported filter mask in the literature, which are all symmetric. Almost all the filter masks optimized resulted in a significant improvement over the masks reported in literature.

2.2.2 Signal Pre-processing:

An experimental set-up is designed with a 5" circular FSR from Interlink™ Electronics and a stress ball. The experimental set-up is shown in Fig. 2.2.2(a). Using this experimental set-up both sEMG and muscle force signals were acquired simultaneously using LabVIEW™ at a sampling rate of 2000 Hz. The sEMG data capturing was aided by a DELSYS® Bagnoli-16 EMG system with DE-2.1 differential EMG sensors. One sEMG sensor was placed on the motor point of the ring finger and two adjacent to the motor point of a healthy subject. Prior to placing the sEMG sensors, the skin surface of the subject was prepared according to International Society of Electrophysiology and Kinesiology (ISEK) protocols.

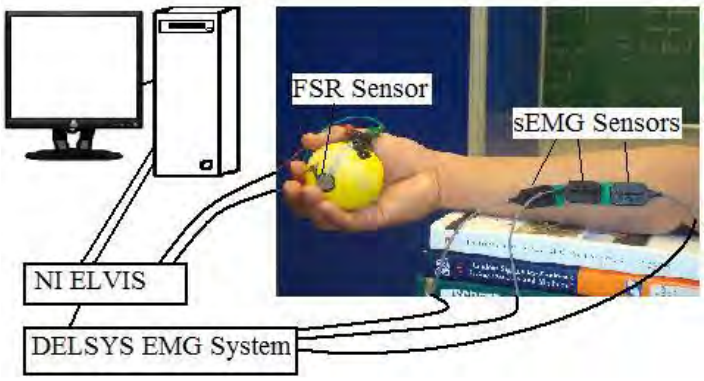

Fig. 2.2.2(a). Experimental Set-Up.

Pre-processing of the signals captured was done according to previous research based on [31], where the Bayesian based filtering method yields the most suitable sEMG signals. The nonlinear filter significantly reduces noise and extracts a signal that best describes EMG signals and may permit effective use in prosthetic control. An instantaneous conditional probability density $P(EMG \mid x)$ provides the resulting EMG for the latent driving signal x [31]. The model for the conditional probability of the rectified EMG signal $emg = |EMG|$ is used in this current estimation algorithm. EMG signals are usually described as amplitude-modulated zero mean Gaussian noise sequence [32]. For the rectified EMG signal, the "Half-Gaussian measurement model" in [31] is given by Equation (2.2.2.1).

$$P(emg \mid x) = 2 * exp(- [emg] \hat{} 2/(2 * x \hat{} 2))/ [(2 * \pi * x \hat{} 2)] \hat{} (1/2). \quad (2.2.2.1)$$

The EMG signal is modeled for the conditional probability of the rectified EMG signal as a filtered random process with random rate. The likelihood function for the rate evolves in time according to a Fokker–Planck partial differential equation [31]. The discrete time Fokker–Planck Equation is given by Equation (2.2.2.2).

$$p(x,t-)\alpha * p(x-\varepsilon,t-1) + (1-2*\alpha) * p(x,t-1) + \alpha * p(x+\varepsilon,t-1) + \beta + (1-\beta) * p(x,t-1). \quad (2..2.2.2)$$

Here, α and β are two free parameters, α is the expected rate of gradual drift in the signal, and β is the expected rate of sudden shifts in the signal. The unknown driving signal x is discretized into bins of width ε. These two free parameters of the non-linear Half-Gaussian filter model are optimized for the acquired EMG data using elitism based Genetic Algorithm (GA). GA belongs to a class of optimization algorithms that are based on observing nature and its corresponding processes to imitate solving complex problems, most often optimization or estimation problems, see [33-35]. A Chebyshev type II low pass filter with a 550 Hz pass frequency is used to filter the force signal. Fig. 2.2.2(b) depicts the raw and Chebyshev type-II low pass filtered force signals.

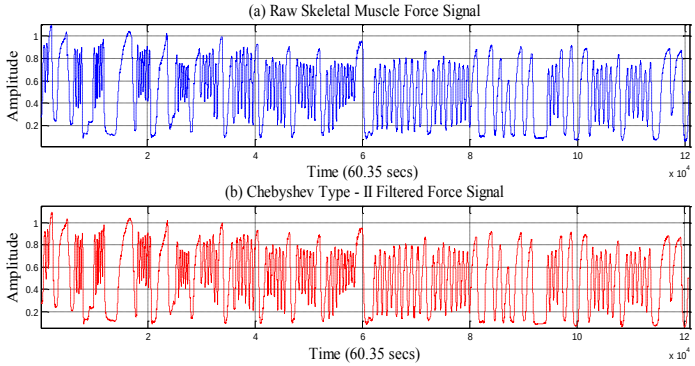

Fig. 2.2.2(b). (a) Raw and (b) Chebyshev Type-II Filtered Skeletal Muscle Force Signals.

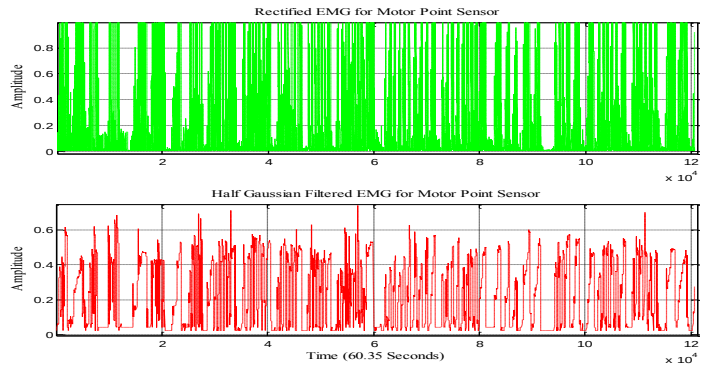

Fig. 2.2.2(c). Rectified EMG and Half-Gaussian Filtered EMG Signal for Motor Point Sensor.

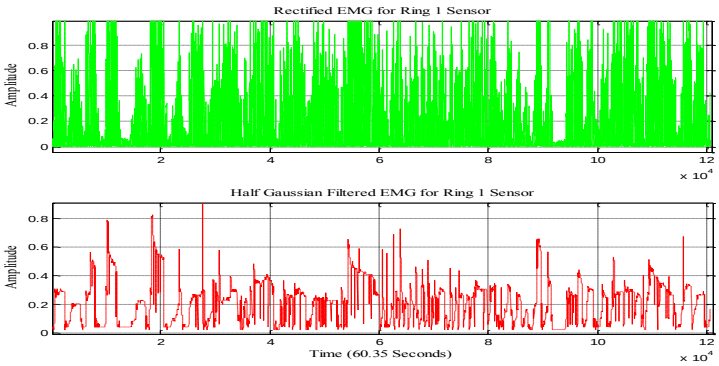

Fig. 2.2.2(d). Rectified EMG and Half-Gaussian Filtered EMG Signal for Ring 1 Sensor.

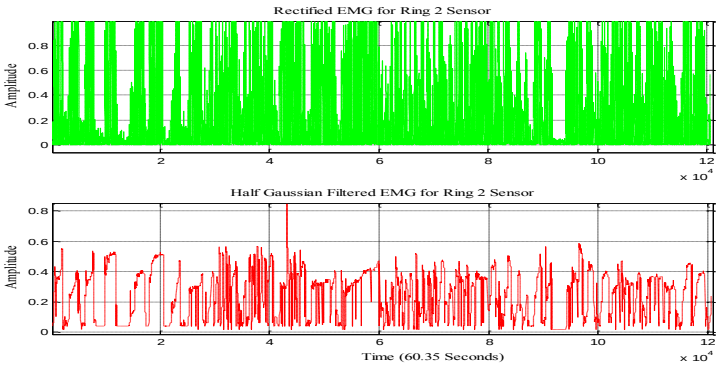

Fig. 2.2.2(e). Rectified EMG and Half-Gaussian Filtered EMG Signal for Ring 2 Sensor.

Fig. 2.2.2(c), (d) and (e) show the rectified EMG and Half-Gaussian Filtered EMG signal for three sensors. After this, experiments with an array of nine sensors were conducted. The experimental set-up for the ring finger experiment is shown in Fig. 2.2.2(f) and 2.2.2(g).

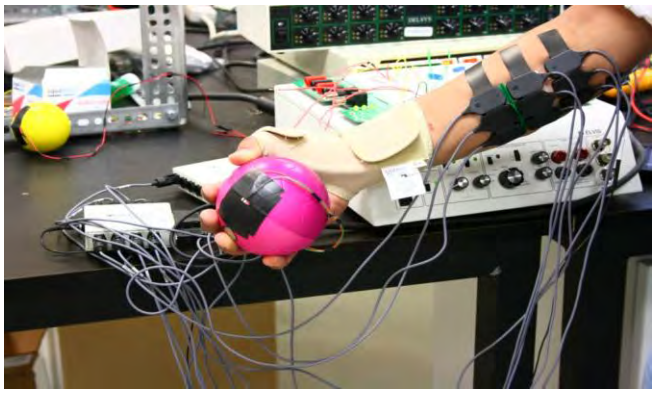

Fig. 2.2.2(f). Experimental Set-Up for Ring Finger with Nine sEMG Sensors and Red Stress Ball.

In this case, there is an array of nine sensors; where the motor point sensor is at the center of the array. With this experimental set-up, nine sets of experiments with different time duration and with two different stress balls of different stiffness and with and without of thumb restrictor were conducted. Fig. 2.2.2(h) shows the corresponding 30 seconds time-amplitude plot for the ring finger associated EMG signal and above-mentioned experimental set-up.

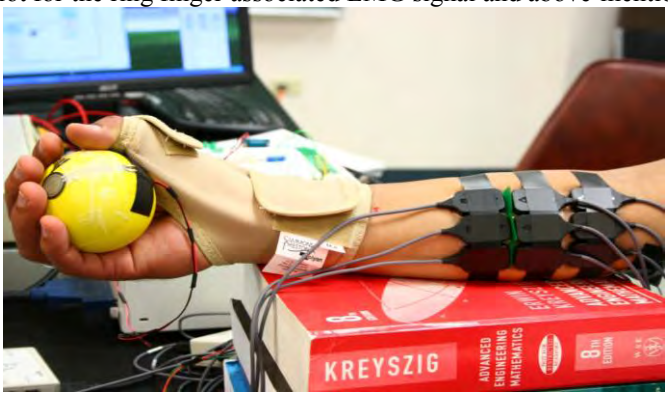

Fig. 2.2.2(g). Experimental Set-Up for Ring Finger with Nine sEMG Sensors and Yellow Stress Ball.

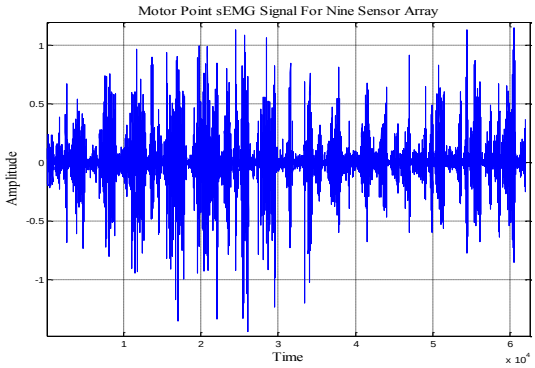

Fig. 2.2.2(h). Ring Finger Motor Point sEMG Signal for Nine-Sensor Array.

This sEMG signal is filtered using nonlinear spatial filtering for multichannel surface EMG. As given in [36], this nonlinear spatial filter is derived from ~~"~~Nonlinear Teager-Kaiser Energy (TKE) Operator." In [36], the schematic description of the multiple channel surface EMG recording is given in Fig. 2.2.2(i). Here the array is of nine sensors covers the four directional spatial distribution of the sEMG signal.

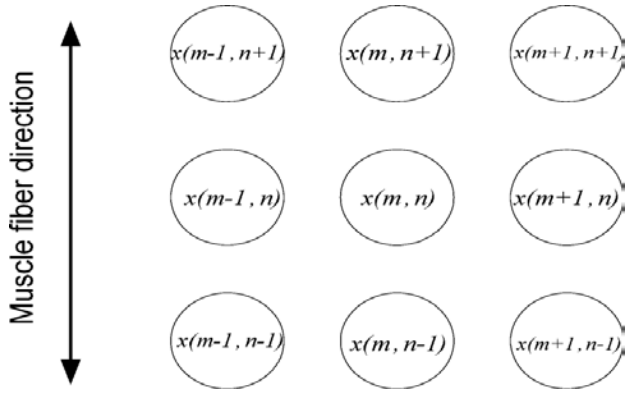

Fig 2.2.2(i). Schematic Description of the Multiple Channel Surface EMG Recording [36].

As given in [36], the TKE operator in time domain on sEMG signal is defined by Equation (2.2.2.3).

$$\Psi[x(n)] = x^2(n) - x(n+1) * x(n-1). \quad (2.2.2.3)$$

Here, Ψ is TKE operator and $x(n)$ is time domain sEMG signal. Based on the TKE operator, the one-dimensional nonlinear spatial filters are given by Equation (2.2.2.4) and (2.2.2.5). Two-dimensional and four-dimensional nonlinear spatial filters are given by Equation (2.2.2.6) and (2.2.2.7) respectively.

$$\Psi_{d,m}[x(m,n)] = x^2(m,n) - x(m-1,n) * x(m+1,n). \quad (2.2.2.4)$$

$$\Psi_{d,n}[x(m,n)] = x^2(m,n) - x(m,n-1) * x(m,n+1). \quad (2.2.2.5)$$

$$\Psi_{d,2}[x(m,n)] = 2 * x^2(m,n) - x(m-1,n) * x(m+1,n) - x(m,n-1) * x(m,n+1). \quad (2.2.2.6)$$

$$\Psi_{d,4}[x(m,n)] = 4 * x^2(m,n) - x(m-1,n) * x(m+1,n) - x(m,n-1) * x(m,n+1) - x(m-1,n+1) * x(m+1,n-1) - x(m-1,n-1) * x(m+1,n+1) \quad (2.2.2.7)$$

Fig. 2.2.2(j) and 2.2.2(k) shows the one-dimensional nonlinear spatially filtered data plots for ring finger. Fig. 2.2.2(l) and 2.2.2(m) shows the two and four-dimensional nonlinear spatially filtered data plots for ring finger signals respectively.

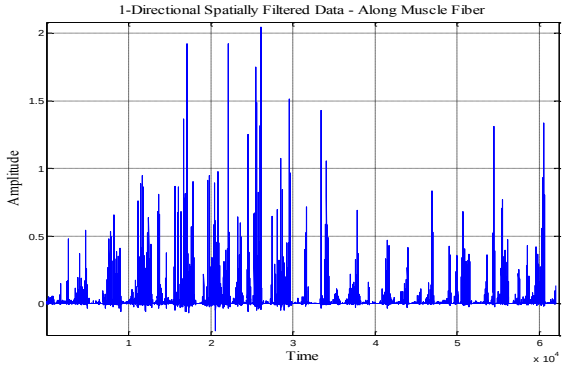

Fig. 2.2.2(j). One-Directional – Along the Muscle Fiber – Nonlinear Spatially Filtered Data for Ring Finger sEMG Signals.

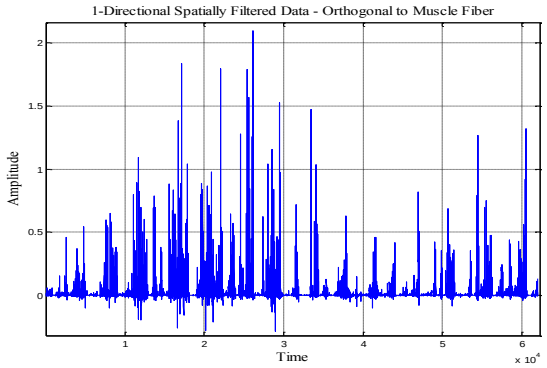

Fig. 2.2.2(k). One-Directional – Orthogonal to Muscle Fiber – Nonlinear Spatially Filtered Data for Ring Finger sEMG Signals.

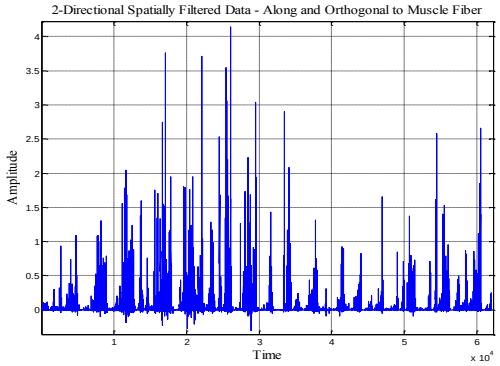

Fig. 2.2.2(l). Two-Dimensional Nonlinear Spatially Filtered Data for Ring Finger sEMG Signals.

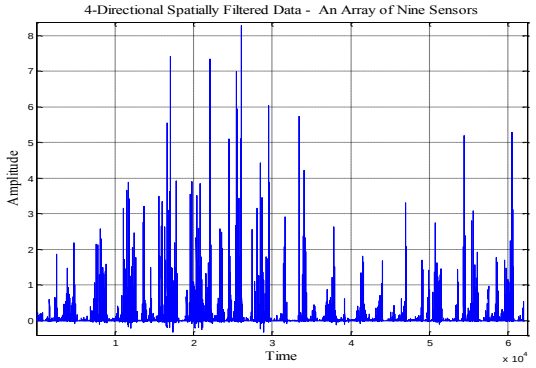

Fig. 2.2.2(m). Four-Dimensional Nonlinear Spatially Filtered Data for Ring Finger sEMG Signals.

These nonlinear spatially filtered data is not yet modeled using SI. In the future work, we will model these nonlinear spatially filtered data for different fingers and different time durations.

We designed a new experimental set-up to simultaneously acquire the sEMG from the motor point of the index finger and the joint angle of the PIP joint of the index finger. Nine DE-3.1 sEMG sensors of the DELSYS® Bagnoli-16 EMG system are placed in a three-by-three array [36]; the arrangement covers the four directional spatial distributions of the sEMG signal. The middle three sEMG sensors were attached directly on the skin surface above the motor point of the index finger of a healthy subject. Using a 10k-Ohm wheel potentiometer, an angle measurement device is designed to measure the joint angles of the PIP joint of the index finger of a healthy subject. Appropriate sEMG electrode attachment point for the motor point of the index finger was identified using a wet probe muscle stimulator at the FDS (RICH-MAR, HV 1000).

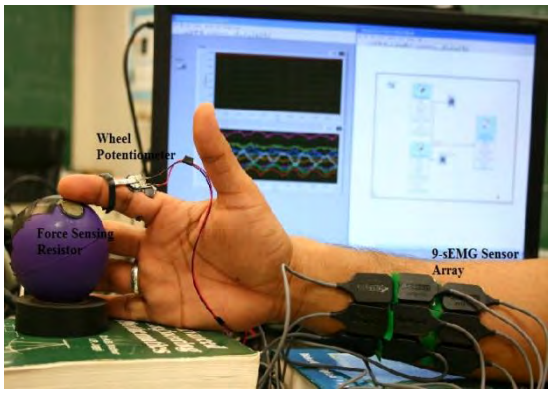

Fig. 2.2.2(n): Experimental Set-Up for Angle Measurement.

Prior to placing the sEMG sensors, the skin surface of the subject was prepared according to International Society of Electrophysiology and Kinesiology (ISEK) protocols. An Interlink™ Electronics FSR 0.5" circular force sensor on a stress ball is used to press with the movement to introduce some resistance to the movement of the PIP joint of the index finger. Experimental set-up is shown in Fig. 2.2.2(n) where nine sensors are shown on a healthy subject forearm, with an angle measurement device on the PIP joint of the index finger and having a stress ball for force measurements. The various signals are sampled at a rate of 2000 Hz using LabVIEW™ in conjunction with DELSYS® Bagnoli-16 EMG and NI ELVIS™. With this experimental set-up we conducted several experiments of 30 seconds, 45 seconds and 60 seconds durations.

To investigate the change in sEMG signal as a result of muscle fatigue we conducted two different sets of fatigue inducing experiments. One experiment using dynamic force variations and another with 50 pounds of static force was conducted. For the dynamic force variation we used an Interlink™ Electronics FSR 0.5" circular force sensor on a stress ball and for the static force experiment we used a cable tensionmeter (T5166) by ‗Pacific Scientific Company.' Fig. 2.2.2(n) and (o) shows the experimental set-up for dynamic force variations and static force level. For the dynamic force experiment we restricted the thumb movement using a thumb splint. For the static force experiment we held the force of the dynamometer at 50 pounds and tried to maintain this force level to induce fatigue in skeletal muscles. Force data for dynamic force experiments was captured using NI ELVIS™ with Interlink™ Electronics FSR 0.5" circular force sensor.

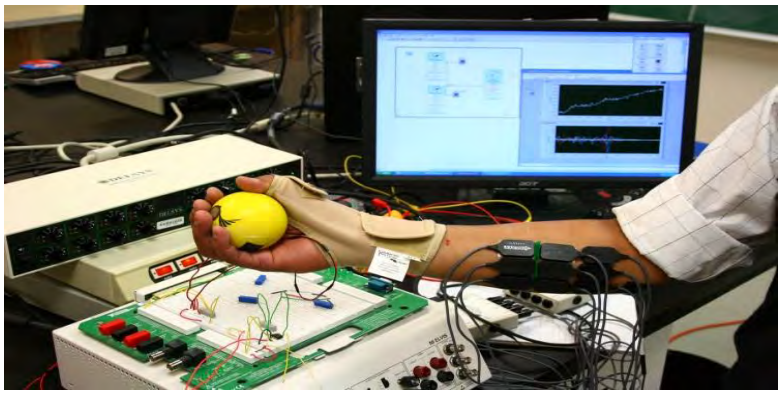
Fig. 2.2.2(n). Experimental Set-Up for Dynamic Force Levels.

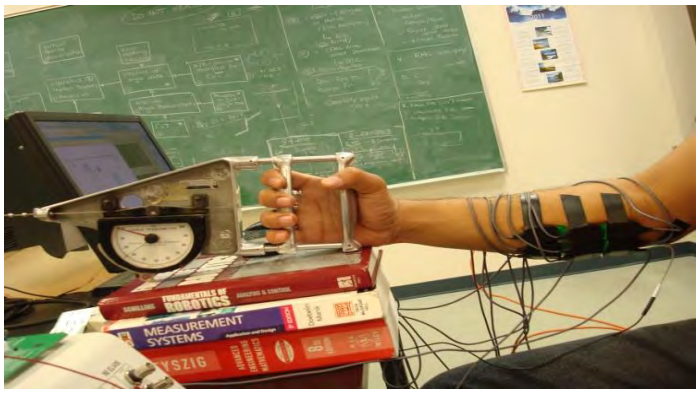

Fig. 2.2.2(o). Experimental Set-Up for 50 Pounds Static Force Levels.

3 Array sensors

3.1 Physical development

In this method we are using an array of 8 sensors which are arranged in such a way that they cover the maximum area and they are further attached to the sEMG sensors which are further connected to the Bagnoli system. The best part of this type of sensor is the ease of application but the drawback is the crosstalk which hinders the collection of EMG signals. But the results which we got during tests were very encouraging and removing the factor of crosstalk, it will be of great importance as it has 8 sensors on a single board and thus the area under observation increases, without increasing the number of sensors. The output is derived the same way as it is taken with sEMG sensors setup. So there is not much difference in the technique but the only factor is the number of sensors that a board comprises.

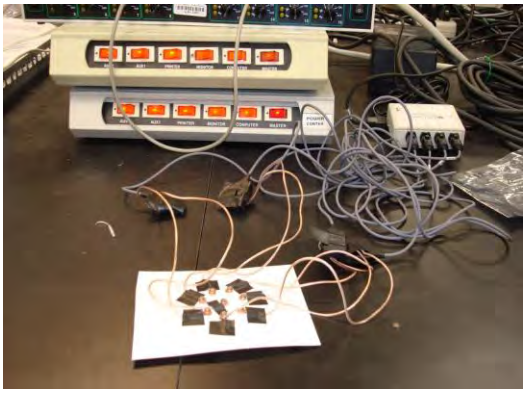
Fig. 3.1.1(a). Array Sensors Connected to the System.


Fig. 3.1.1(b): Array Sensors Tested on NI LabVIEW™.

Construction:

The array sensor is a group of 8 sensors arranged in a circular manner on a single board, the surface of the board should be something that prevents cross-talks between signals. So after choosing the surface the small sensors are placed and are further connected to the Bengali system which derives signals from sEMG signals and thus this is the way the whole set up is made. The connection between sEMG sensors is made with array sensors in a way that the output from them is easily derivable so they are connected with multithread wires so that the stable connection is maintained and the signal is continuous.

Scope:

The type of array sensor arrangement shown can be extremely useful as the area under the observation is increased and also the cost of this is very low as compared to the conventional array sensors. So if the problem of crosstalk is removed then this can be a huge step as it will not only help us to get excellent results but also at the same time reduce the count of array sensors applied as it has 8 sensors on board as compared to the 2 or 3 on board sensors available.

3.2 Fusion of data

In this part of the research work, array of three sEMG sensors as shown in Fig. 2.2.2(a) are used along with a proposed sensor fusion scheme that results in a simple Multi-Input-Single-Output (MISO) transfer function. Experimental data is used along with System Identification to find this MISO system. A Genetic Algorithm (GA) approach is employed to optimize the characteristics of the MISO system. The proposed fusion-based approach has promising results discussed in simulation results section.

Method I:

The data collected from multiple sensors are processed, estimated using sensor fusion technique. A data fusion technique, by combining the data from different sensors, enables one to achieve more specific inferences about the measured data. The sEMG sensors pick up the cross-talk from muscle fibers adjacent to motor units. In [P3], sensor fusion was done in the time domain, by taking sEMG as input and force signal as the output. We used combinations of different filters (Butterworth, Chebyshev, Exponential and Half-Gaussian filters) and different information criteria based on Akaike (AIC), Bayesian (BIC), and Kull-back (KIC) and concluded that the KIC criterion with Half Gaussian filtering gives the best EMG-Force model fit.

In the present work, sensor fusion is done in the frequency domain for the sEMG data. Fig. 3.2(a) gives the flow diagram of the fusion technique used based on the GA [P4].

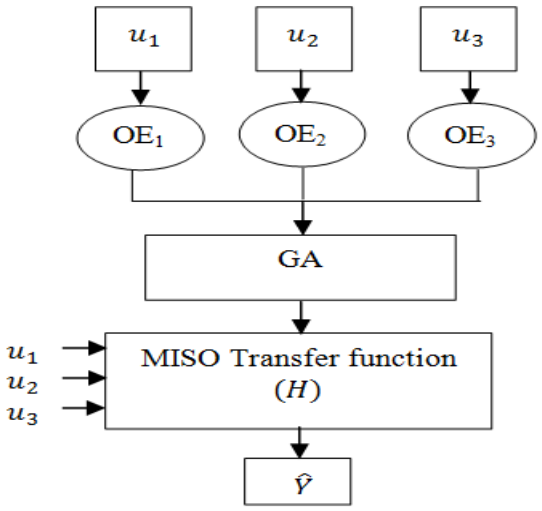

Fig. 3.2(a). Flow Diagram of the Fusion Technique.

The data from the three sensors around the individual motor unit are collected, rectified and then filtered using a Half-Gaussian filter. By using the system identification technique the dynamic relationship between the sEMG datau_1,u_2, and u_3 from the three sensors and their corresponding force are determined. In this proposed fusion algorithm, SI is achieved by utilizing an Output Error (OE) model first for each individual data set. The OE model structure is given as follows:

$$y(t) = \frac{B(q)}{F(q)}u(t - nk) + e(t) \quad (3.2.1)$$

where B, and F are the polynomials, q is shift operator, $e(t)$ is output error, $y(t)$ is system output, u is input, nk is the system delay and t is time index.

The corresponding continuous-time model is given by the transfer function in Equation (3.2.2).

$$G(s) = \frac{B(s)}{F(s)} = \frac{b_{nb}s^{(nb-1)}b_{nb-1}s^{(nb-2)}+\cdots+b_1}{s^{nf}+f_{nf}s^{nf-1}+\cdots+f_1} \quad (3.2.2)$$

Similar to the discrete-time case the orders of the numerator and denominator are determined by nb and nf. For multi-input systems, nb and nf are row vectors. b, f are the coefficients of the numerator and denominator polynomials respectively.

MISO transfer function (H) is constructed by using the poles of the three individual identified OE models, corresponding to each sensor, while the denominators of the respective individual transfer functions (corresponding to each OE model) are transferred over to the new MISO transfer function, the corresponding zeros are found through the use of a GA. Generally GA's can find global optimum points if elitism is used and sufficient number of generations is allowed in the algorithm. This optimization algorithm is rather computationally expensive, but since there was not a computational time requirement, one is free to use GA rather than other intelligent based algorithms. Chromosomes are constructed by designating each zero of a numerator as a gene. Since a discrete time model is utilized, the search area is limited to the unit circle (and the resulting MISO model is decreased to be minimum phase). The number of potential zeros was set to the order of the corresponding denominator because the number of zeros is at most the number of poles (for a causal system, can't predict the future). The objective function was set as the error squared of the resulting MISO system (H) can be constructed as follows:

From u_1 to output -

$$\frac{s^8 - 3.843s^7 + 7.729s^6 - 10.78s^5 + 10.6s^4 - 7.417s^3 + 3.603s^2 - 0.9795s + 0.1192}{s^8 - 4.028s^7 + 6.325s^6 - 4.121s^5 - 1.545s^4 + 5.87s^3 - 5.433s^2 + 2.28s - 0.3496}$$

From u_2 to output –

$$\frac{s^8 - 4.339s^7 + 9.005s^6 - 12.42s^5 + 12.22s^4 - 8.117s^3 + 3.427s^2 - 0.9134s + 0.1424}{s^8 - 4.028s^7 + 6.325s^6 - 4.121s^5 - 1.545s^4 + 5.87s^3 - 5.433s^2 + 2.28s - 0.3496}$$

From u_3 to output –

$$\frac{s^8 - 3.522s^7 + 6.655s^6 - 8.864s^5 + 8.183s^4 - 5.365s^3 + 2.423s^2 - 0.557s + 0.09585}{s^8 - 4.028s^7 + 6.325s^6 - 4.121s^5 - 1.545s^4 + 5.87s^3 - 5.433s^2 + 2.28s - 0.3496}$$

Method II:

In this method also, fusion algorithm was done in frequency domain. First sEMG was rectified and filtered using Half-Gaussian filter. Three output error models were obtained using the system identification toolbox. By plotting the bode plots of three models separately and combining the peaks of all three models using the fusion algorithm proposed in method I, we got the results as shown in the following section.

Simulation Results:

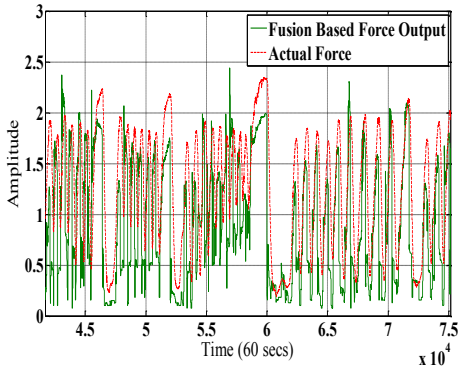

Fig. 3.2(b). Final Fusion Based Force Vs. Measured Force Signal.

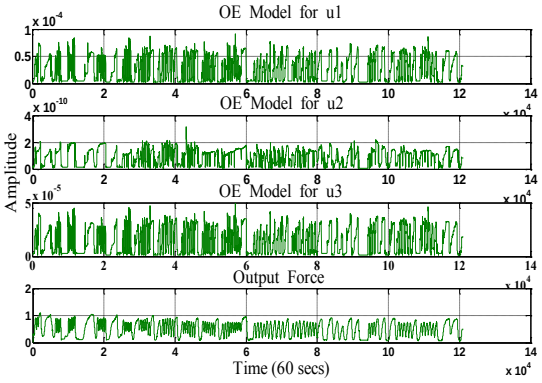

Fig. 3.2(c). Estimated Force Output for Individual OE Models and the Measured Force Signal.

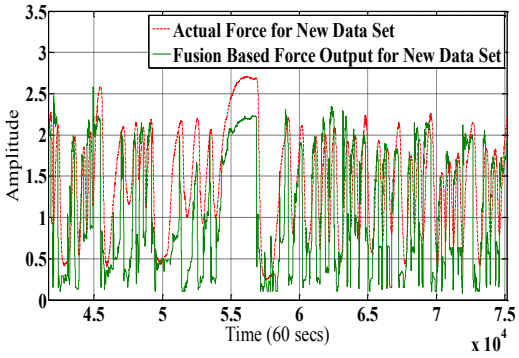

Fig. 3.2(d). Validation Plot for Data Set-I.

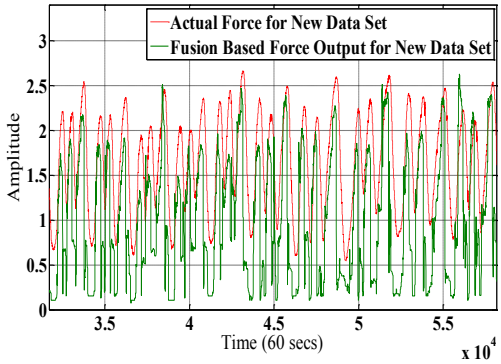

Fig. 3.2(e). Validation Plot for Data Set-II.

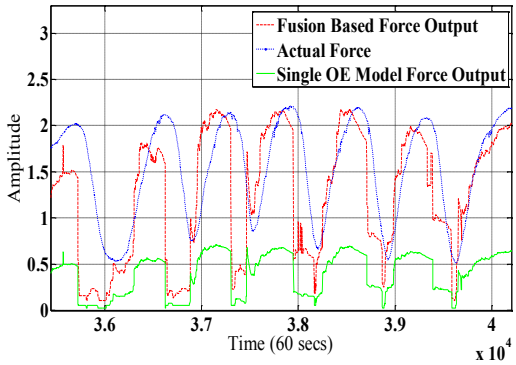

Fig. 3.2(f). Comparison between Measured, Fusion Based and Single OE Model Output Force.

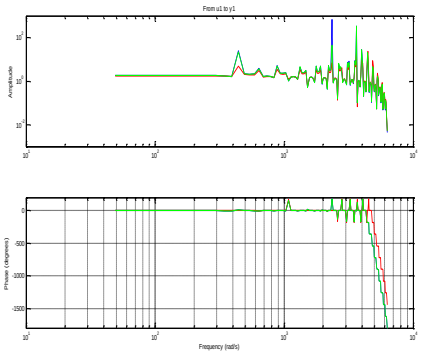

Fig. 3.2(g). Bode Plots of Three Different Sensors.

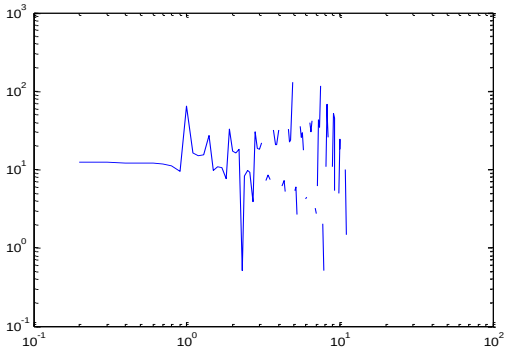

Fig. 3.2(h). Fusion Based Force Signal.

Conclusion:
Both the methods were done in frequency domain. Method I gave 82 % fit value and Method II needs to be improvised. In future, we want to compare the three different fusion techniques.

4. Skeletal Muscle Fatigue and Spectral Analysis of sEMG Signals
As it is explained in the earlier part of the report that muscle fatigue is a complex phenomenon and affects the sEMG signals as it progress. We conducted the experiments to capture the muscle fatigue as a change in sEMG as the muscle fatigue progress. sEMG signals are analyzed to investigate the change in frequency domain during skeletal muscle fatigue [P4]. Fig. 2.2.2(n) and (o) shows the experimental set-ups for dynamic and static force experiments to induce skeletal muscle fatigue. The sEMG signals are filtered with a nonlinear Teager–Kaiser Energy (TKE) operator-based nonlinear spatial filter [36]. Two sets of dynamic force data are segmented into three and five parts and two sets of static force data are segmented into five parts each. There is a 75% overlap between the two adjacent segments. A number of classical, model-based and eigenvector based spectral estimation techniques are used to study the change in the sEMG signals as a result of muscle fatigue. In classical methods Fast Fourier transform (FFT) and Welch‘s averaged modified periodogram methods are used. In case of model-based methods Yule-Walker (Y-W), Burg, Covariance (Cov.) and Modified Covariance (Mcov.) Autoregressive (AR) methods are applied. For eigenvector methods Multiple Signal Classification (MUSIC) and Eigenvector (EIG) spectral estimation methods were selected for processing sEMG signals. Using these spectrum analysis techniques, Power Spectral Density (PSD) estimates and detailed documentations of the sEMG signals were obtained. These methods were compared in terms of their frequency resolution and the effects in determination of skeletal muscle fatigue.

A. Discrete Fourier Transform (DFT):
DFT which is the computational basis of the spectral analysis transforms the time or space domain data into frequency domain data [37]. The DFT of a vector x of length N is given as

$X(k) = \sum_{j=1}^{N} x(j)\omega_N^{(j-1)(k-1)}$, (4.A.1)

where $\omega_N = e^{(-2\pi i)/N}$ is the N_{th} root of unity [37].

B. Welch's averaged modified periodogram method:

As the name suggests, the _Welch's averaged modified periodogram method' depends on the periodogram of the signal $\{x(n)_n^N\}$ which is given by Equation (4.B.1), [37].

$\hat{S}_{per}(f) = \frac{1}{N}|\sum_{n=1}^{N} x(n)\exp(-j2\pi fn)|^2$. (4.B.1)

In Welch method, the signal is segmented into eight parts of equal length with an overlapping ratio of 50% and each part is segmented using a Hamming window as given by Equation (4.B.2), [37].

$w(n) = 0.54 - 0.46\cos\left(2\pi\frac{n}{N}\right), 0 \le n \le N$. (4.B.2)

C. Yule-Walker (Y-W) autoregressive (AR) method:

The Yule-Walker autoregressive method, also called the autocorrelation method, estimates the power spectral density (PSD) of the input. This method fits an autoregressive (AR) model to the windowed input data by minimizing the forward prediction error in the least-squares sense. This formulation leads to the Yule-Walker equations, which are solved by Levinson-Durbin recursion [37].

D. Burg autoregressive (AR) method:

The Burg autoregressive (AR) method is a parametric spectral estimation method of the signal, x. The power spectral density is calculated in units of power per radians per sample. This method is based on the minimization of the forward and backward prediction error and on estimation of the reflection coefficients [37].

E. Covariance (Cov.) autoregressive (AR) method:

The covariance autoregressive (AR) method uses the covariance algorithm to estimate the parametric spectral density of the signal, x. Based on causal observation of the input signal, the covariance method minimizes the forward prediction error and fits an AR linear prediction filter model to the signal [37].

F. Modified covariance (Mcov.) autoregressive (AR) method:

Modified covariance autoregressive (AR) method estimates the PSD of the signal using the modified covariance method. Based on the causal information of the input signal, the modified covariance method fits an autoregressive (AR) linear prediction filter model to the signal by simultaneously minimizing the forward and backward prediction errors. The spectral estimate returned by this method is the magnitude squared frequency response of the AR model [37].

G. Multiple Signal Classification (MUSIC) spectral estimation method:

The MUSIC algorithm estimates the pseudospectrum (in rad/sample) at the corresponding vector of frequencies for the input signal x [37]. This algorithm uses the estimates of the eigenvectors of a correlation matrix associated with the input signal using Schmidt's eigenspace analysis method [37]. The MUSIC pseudospectrum estimate is given by Equation (4.G.1),

$P_{music}(f) = \frac{1}{e^H(f)(\sum_{k=p+1}^{N} v_k v_k^H)e(f)} = \frac{1}{\sum_{k=p+1}^{N}|v_k^H e(f)|^2}$, (4.G.1)

where N is the dimension of the eigenvectors and v_k is the k-th eigenvector of the correlation matrix [37]. The signal subspace has a dimension p and the eigenvectors v_k used in the sum corresponds to the smallest eigenvalues and also spans the noise subspace [37]. The vector $e(f)$ consists of the complex exponentials, so the inner product $v_k^H e(f)$ amounts to a Fourier transform. To estimates the pseudospectrum, the squared magnitudes are summed for FFT computed for each v_k [37].

H. Eigenvector (EIG) spectral estimation method:

The eigenvector spectral estimation method estimates the pseudospectrum (in rad/sample) at the corresponding vector of frequencies using estimates of the eigenvectors of a correlation matrix associated with the input signal x [37]. This method estimates the pseudospectrum from a signal or a correlation matrix using a weighted version of the MUSIC algorithm derived from Schmidt's eigenspace analysis method [38, 39]. To find the frequency content of the signal the algorithm performs eigenspace analysis of the signal's correlation matrix. Singular value decomposition is used to compute the eigenvalues and eigenvectors of the signal's correlation matrix [37]. This method computes the pseudospectrum estimate as given by Equation (4.H.1).

$P_{ev}(f) = \frac{1}{(\sum_{k=p+1}^{N}|v_k^H e(f)|^2)/\lambda_k}$, (4.H.1)

where the eigenvectors have a dimension of N and v_k is the k-th eigenvector of the correlation matrix [37]. The signal subspace has a dimension p and the eigenvectors v_k used in the sum corresponds to the smallest eigenvalues and also spans the noise subspace [37]. The vector $e(f)$ consists of the complex exponentials, so the inner product

$v_k^H e(f)$ amounts to a Fourier transform and to estimate the pseudospectrum, the squared magnitudes are summed for FFT computed for each v_k [37].

I. Selection of Model Orders for Model-Based and Eigenvector Based Methods:

Model-based and eigenvector-based methods need to have a specific model order which is an important aspect of the use in these methods. Using the sEMG and force data as input and outputs for three and five sets of the segments for different data sets, we created model structure matrices using ‗struc' function in MATLAB®, using ‗arxstruc' we compared a model order of 1 to 50th with varying delay of 1 to 50 using cross-validation on the second half of the data set. With this approach, it was possible to select the order that gives the best fit for the validation data set.

J. Results and Discussion:

sEMG signal changes as a consequence of muscle fatigue [40-45], the amplitude of the PSD of the signal increases and the median frequency shifts towards the lower frequency range [43-45]. In this study, PSDs of the different segments of each sEMG data set were obtained using FFT, Welch's averaged modified periodogram, Yule-Walker, Burg, Covariance, Modified Covariance autoregressive (AR), Multiple Signal Classification (MUSIC), and Eigenvector spectral estimation methods. The objective of this study was to determine preferred methods of signal processing that elevates the sensitivity of muscle fatigue as represented in the PSD of the sEMG signal. An increased sensitivity allows for better modeling of the fatigue phenomena and hence more accurate sEMG models. Ultimately this may lead to better prosthetic control.

Data of two experiments for dynamic force variations was segmented in three and five parts respectively. Each segment is with an overlap of 75% with its adjacent segment. Using different methods, we computed the PSDs for each segment. For the dynamic force experiments, the maximum value of PSDs of sEMG signal increases with muscle fatigue as time or segment number is increased. The classical methods (FFT and Welch) and eigenvector based methods (MUSIC and Eigenvector (EIG.)) are representing this change well in case of maximum PSD values and show a clear difference.

TABLE 4.1
MAXIMUM VALUE OF PSD FOR CLASSICAL METHODS AND EIGENVECTOR BASED METHODS – DYNAMIC VARYING FORCE – EXPERIMENT 2

Segment No.	Classical-Methods		Eigenvector-Methods	
	FFT	Welch	MUSIC	EIG
1st	4.1e+6	0.0082	371.59	1.0819
2nd	5.09e+6	0.0100	424.43	1.3892
3rd	5.74e+6	0.0111	480.71	1.4132
4th	6.79e+6	0.0133	508.64	1.4936
5th	2.13e+7	0.0379	695.08	10.2118

Table 4.1 lists the peak values of the PSDs of five segments using classical and eigenvector based methods for a dynamically varying force experiment. Fig. 4(a) shows the overlapping plot of PSDs for five segments using the MUSIC algorithm based spectral estimation method. The increase in the maximum PSD value is evident from the 1st to the 5th segment of the data.

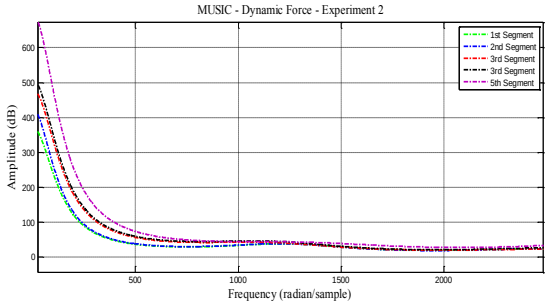

Fig. 4(a). PSD vs. Frequency Plot for MUSIC Algorithm – Dynamic Force Experiment.

Fig. 4(b) shows the resulting PSD using the Burg method. Comparing Fig. 4(a) and 4(b), the progression of fatigue influence shift in PSDs is evident in both plots. However, the MUSIC algorithm not only shows larger amplitudes,

but also a greater relative sensitivity to fatigue. The rather equal spacing between the lines of the PSD for the MUSIC algorithm compared to the Burg method indicates a rather more linear relationship of the fatigue progression.

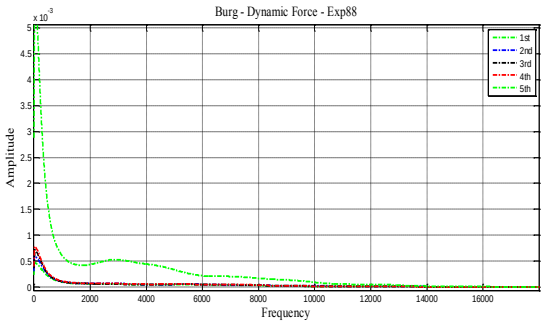

Fig. 4(b). PSD vs. Frequency Plot for Burg Method – Dynamic Force Experiment.

TABLE 4.2
MAXIMUM VALUE OF PSD FOR CLASSICAL METHODS – STATIC FORCE – 50 POUNDS - EXPERIMENT 1

Segment No.	Classical-Methods		Eigenvector-Methods	
	FFT	Welch	MUSIC	EIG
1st	1.03e+5	6.81e-5	1413	9.93e-4
2nd	1.80e+5	1.12e-4	1793	16e-4
3rd	3.21e+5	1.80e-4	2296	28e-4
4th	4.25e+5	2.62e-4	3102	37e-4
5th	6.23e+5	3.58e-4	7723	104e-4

TABLE 4.3
MAXIMUM VALUE OF PSD FOR CLASSICAL METHODS – STATIC FORCE – 50 POUNDS - EXPERIMENT 1

Segment No.	1st	2nd	3rd	4th	5th
Model-Based Methods	7.7e-7	1.3e-6	2.3e-6	3.1e-6	7.81-6

The sEMG data of two experiments for static force (50 pounds) were processed and the maximum PSDs of five segments using classical, model-based, and eigenvector based methods were computed. Data from both the experiments show similar results as the dynamic case. Table 4.2 lists the peak values of the PSDs of five segments using classical and eigenvector based methods for static force (50 pounds) for one experiment. Table 4.3 lists the maximum values of the PSD for model-based methods: Y-W, Burg, Covariance, and modified covariance. All of these methods resulted in the same maximum values for each segment. Comparing Table 4.2 and 4.3, we recognize the large difference in maximum value between the model-based methods and the corresponding values from the FFT and MUSIC method. Fig. 4(c) shows the overlapping plot of PSDs for five parts using eigenvector algorithm based spectral estimation method. The increase in the maximum PSD value is evident from the 1st to the 5th segment of the static force sEMG data.

The eigenvector method produces a similar characteristic as the MUSIC algorithm and distinguishes itself by also providing a more linear characteristic of the fatigue progression and a greater relative sensitivity. Fig. 4(d) depicts the PSD generated by using FFT method for the 1st and 5th segments of a static force experiment. While providing a large maximum value, the FFT method is limited by its own spectral resolution ($1/N$) and, due to windowing of the finite data set, results into spectral leaking.

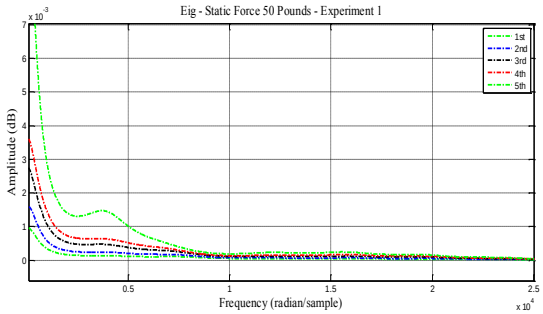

Fig. 4(c). PSD vs. Frequency Plot for Eigenvector Method – Static Force of 50 Pounds.

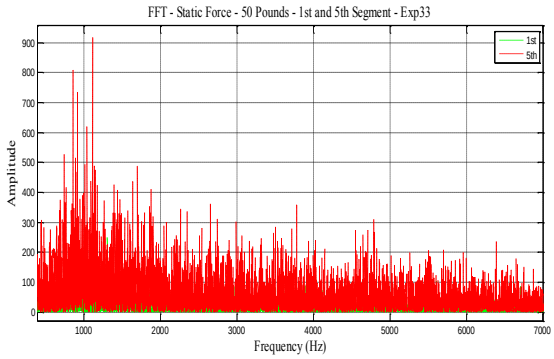

Fig. 4(d). PSD vs. Frequency Plot for FFT Method – Static Force of 50 Pounds.

All the model-based methods for both dynamic and static force levels produce the same peak values and the same PSD for the corresponding experiment. Since Burg and Y-W methods guarantee stability while the covariance and modified covariance methods have conditions for stability to be satisfied (i.e. min. order must be of certain length of the input frame size), Burg and Y-W should be the preferred methods for sEMG analysis. However, the Burg method is to be preferred if short data sets are used.

Comparing the eigenvector based methods (MUSIC and Eigenvector), both of these methods are frequency estimator techniques based on eigenanalysis of the autocorrelation matrix where the resulting estimate has sharp peaks at the frequencies of interest. The eigenvector method uses inverse eigenvector weighting whereas the MUSIC method uses unity weighting, implying that the eigenvector method gives fewer spurious peaks than the MUSIC algorithm [46]. As seen from the dynamic experiment results, the MUSIC method provides for a better spacing between the segments based PSDs compared to the Burg and eigenvector method. From static experiments, we conclude that all three (MUSIC, Burg, and Eigenvector) methods perform similarly if a linear relationship of the fatigue progression is desired.

Conclusion and Future Work

In this part of the research, we characterized muscle fatigue using a PSD representation of different segments of sEMG data. Classical (fast Fourier transform and Welch‘s averaged modified periodogram), model-based (Yule-Walker, Burg, Covariance, and Modified Covariance autoregressive (AR) method) and eigenvector based methods (Multiple Signal Classification (MUSIC) and eigenvector spectral estimation method) are used to compute the PSDs. Classical and eigenvector based methods are more sensitive than the model-based methods for analyzing the fatigue related changes in sEMG signal. However, the MUSIC algorithm provides good maximum value in the PSD as well as a clear distinction between the segmented sEMG data. The latter point is indicative of a relative linear fatigue progression in time for the same case when the MUSIC algorithm is utilized. In the future work these results can be used to design and improve the skeletal muscle _Force-sEMG-Fatigue‘ based models [P4] for prosthetic design and other rehabilitation research.

5. Force models

To model the skeletal muscle force and sEMG signals we tried all the possible models available in *MATLAB®*. For the data set acquired using the experimental set-up in Fig. 2(a).

5.1 Regular force model

5.1.1 Skeletal Muscle Force Estimation Using Nonlinear Models for an array of three Semg sensors

We tried multi nonlinear Auto Regressive eXogenous (ARX) and Wiener-Hammerstein models with different nonlinearity estimators/classes using System Identification (SI) for three sets of sensor data. For the motor point, ring 1 and ring 2 sensors we obtained seven, seven and eight nonlinear models respectively [P5, P6]. First, the outputs of these nonlinear models are fused separately and then the final fusion based outputs from three sensors are fused further to have better force estimates for an array of three sEMG sensors. Data fusion is done using an adaptive KIC probability.

Results and Discussion

This section deals with the results, discussion and future work. The following plots show the nonlinear (ARX and Wiener-Hammerstein) model and adaptive fusion algorithm based estimated force output for each sensor first and then finally combined adaptive fusion based output for all three sensors. Fig. 5.1.1(a) shows the overlapping plot of the original and adaptive fusion based force output for the motor point sensor. The output is the result of the adaptive fusion algorithm on three nonlinear ARX and four nonlinear Wiener-Hammerstein models for the motor point sensor signal. Fig. 5.1.1(b) shows the overlapping plot of the original and adaptive fusion based force output for ring1 sensor. This output is the result of adaptive fusion algorithm of three nonlinear ARX and four nonlinear Wiener-Hammerstein models for ring1 sensor signal. Fig. 5.1.1(c) shows the overlapping plot of the original and adaptive fusion based force output for ring2 sensor. This output is the result of adaptive fusion algorithm on three nonlinear ARX and five nonlinear Wiener-Hammerstein models for ring2 sensor signal.

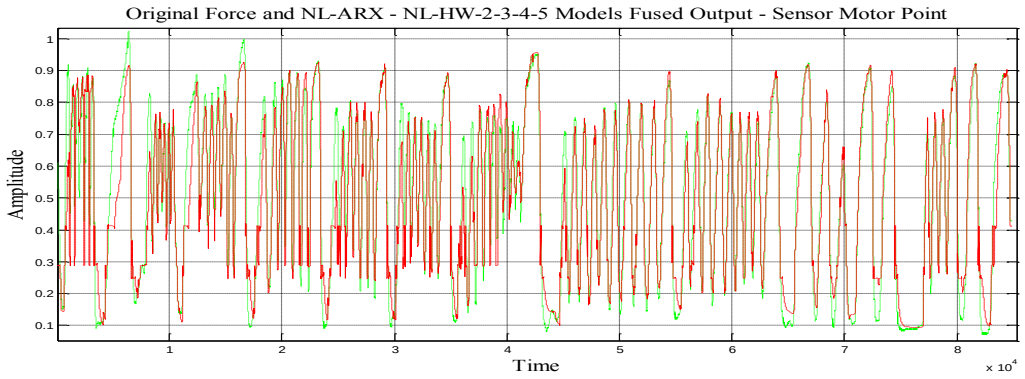

Fig. 5.1.1(a): Original and Fusion Based Output for Motor Point Sensor.

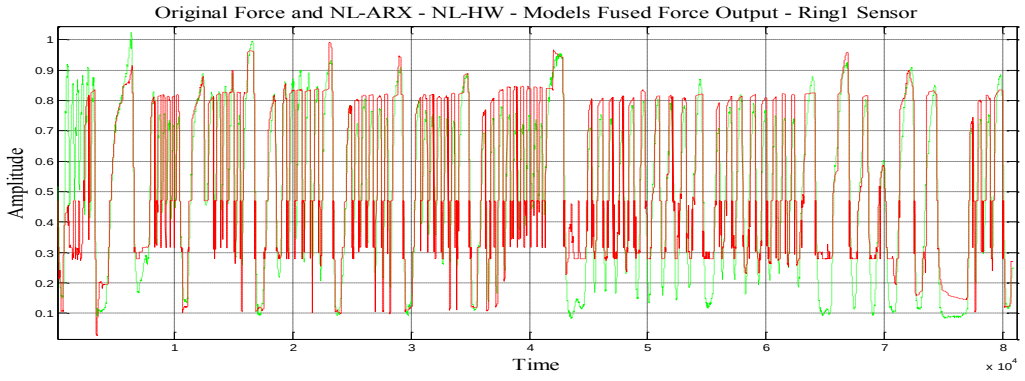

Fig. 5.1.1(b): Original and Fusion Based Output for Ring1 Sensor.

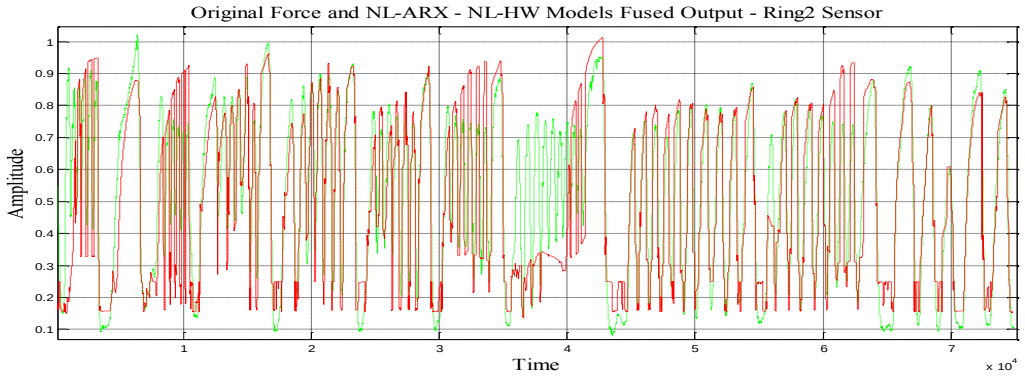

Fig. 5.1.1(c): Original and Fusion Based Output for Ring2 Sensor.

Fig. 5.1.1(d) shows the overlapping plot of the original and final combined adaptive fusion based force output for motor point, ring1 and ring2 sensors. The output is the result of adaptive fusion algorithm on the final outputs of three sensors i.e. motor point, ring1 and ring2 as shown in Fig. 5.1.1(a) to 5.1.1(c). Fig. 5.1.1(d) shows the best skeletal muscle force estimate, which is the result of the multi nonlinear ARX and Wiener-Hammerstein models and an adaptive hybrid data fusion on these nonlinear models.

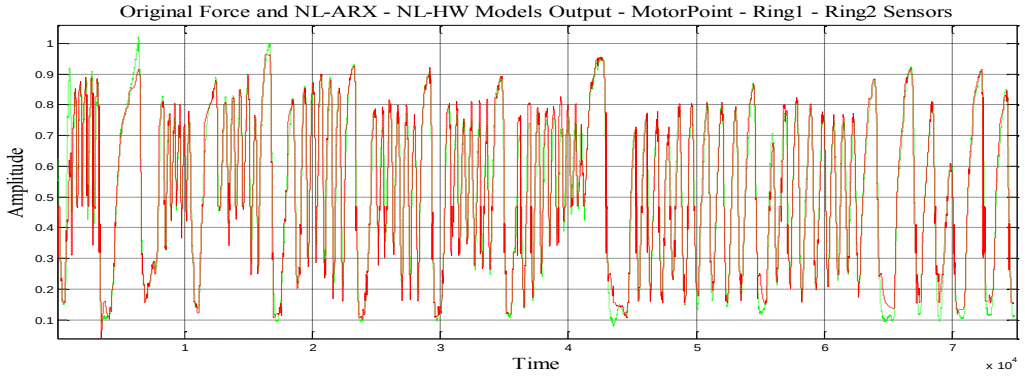

Fig. 5.1.1(d): Final Plot - Original and Fusion Based Output for All Three Sensors.

Fig. 5.1.1(e) shows the error plot of the original and best-estimated model output for the motor point sensor. Fig. 5.1.1(f) shows the error plot of original and final multi nonlinear modeled and adaptive hybrid data fusion based force estimate (results from three sensors, nonlinear modeling and adaptive data fusion algorithm). If we compare Fig. 5.1.1(e) and 5.1.1(f), it is very clear and conspicuous that the error has decreased remarkably and is very close to zero.

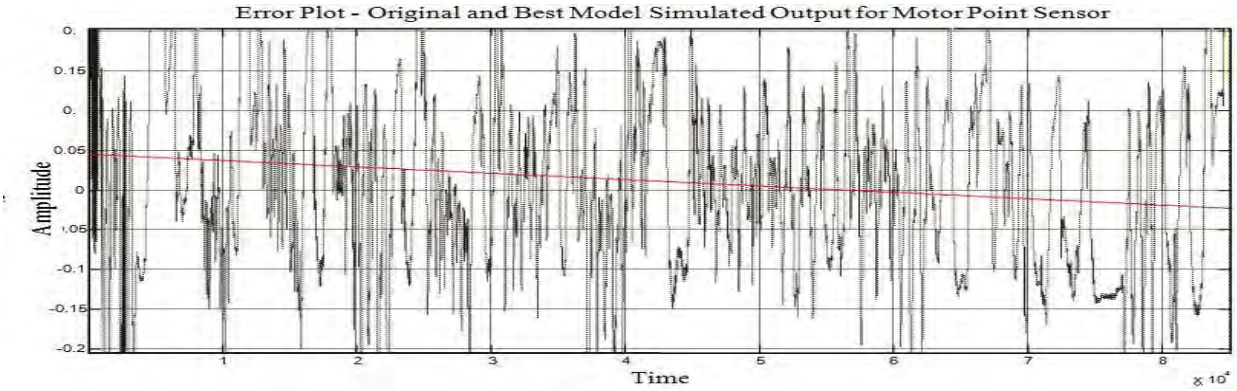

Fig. 5.1.1(e): Error Plot – Original and Best-Estimated Model Output for Motor Point Sensor.

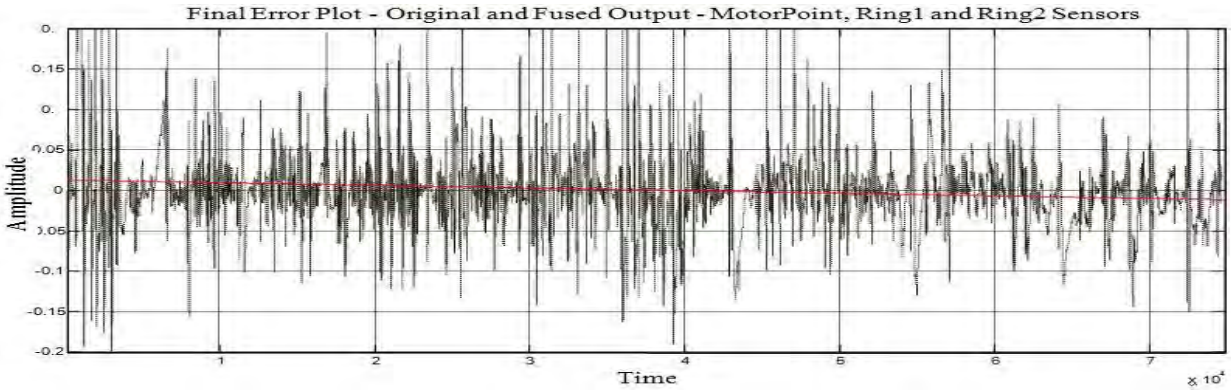

Fig. 5.1.1(f): Final Error Plot – Original and Fusion Based Output for Motor Point, Ring1 and Ring2 Sensors.

5.1.2 Skeletal Muscle Force Estimation Using Linear and Nonlinear Models for an array of three sEMG sensors

Once we tried all the possible nonlinear models available in *MATLAB®* to estimate the skeletal muscle force for three sensor array, we thought of using linear and nonlinear models together to model the relationship between the skeletal muscle force and sEMG [P7, P8]. First we tried this approach for the motor point sensor and then we tried this for the all three sensors as shown in the experimental set-up in Fig. 2.2.2(a). For three sensor array data set we obtained multi linear and nonlinear models for motor point, ring 1 and ring 2 data sets. For motor point, ring 1 and ring 2 sensors we obtained ‗six linear and three nonlinear models,' ‗three linear and five nonlinear models,' ‗six linear and five nonlinear models,' respectively.

Results and Discussion

An adaptive KIC probability based data fusion algorithm is applied to linear and nonlinear models separately for the models obtained using three sets of input and output data for three sEMG sensors. First the fusion based output for each sensor is obtained and then the three fusion based outputs from three sEMG sensors are fused to get the improved estimates of the skeletal muscle force. The following plots show the improvement in the force estimates in succession with different sensors separately and then combined. All the plots have the measured skeletal muscle force signal in green and the estimated force signal in red color. Fig. 5.1.2(a) is a plot of measured and Chebyshev type II filtered finger force data with the adaptive KIC probability fusion based force for the first sensor named as ring1. The two signals are very clear and the estimated signal shows good follow up of the measured signal. Fig. 5.1.2(b) shows the measured and Chebyshev type II filtered skeletal muscle force with the adaptive KIC probability fusion based force signals for the second sensor named as ring2. It is evident that the measured signal has a very close follow up by the estimated signal. Fig. 5.1.2(c) shows the measured and Chebyshev type II filtered skeletal muscle force with the adaptive KIC probability fusion based force signals for third sensor placed on the motor point of ring finger. The results for this sensor are best among the three based of the used three sensor data and it is evident that the measured signal has a very close follow up by the estimated signal.

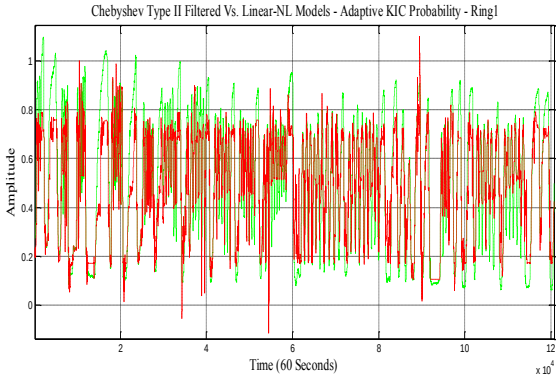

Fig. 5.1.2(a). Chebyshev Type II vs. Adaptive KIC Probability Based Force from Linear and Nonlinear Models for Ring1 Sensor.

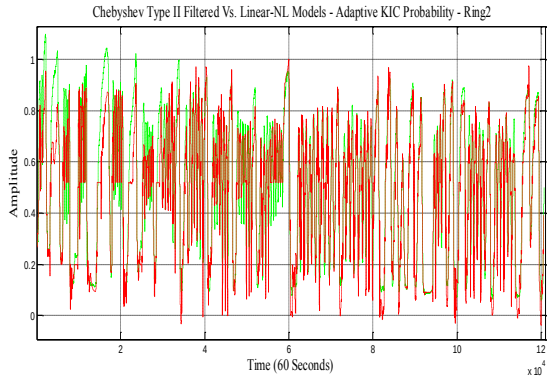

Fig. 5.1.2(b). Chebyshev Type II vs. Adaptive KIC Probability Based Force from Linear and Nonlinear Models for Ring2 Sensor.

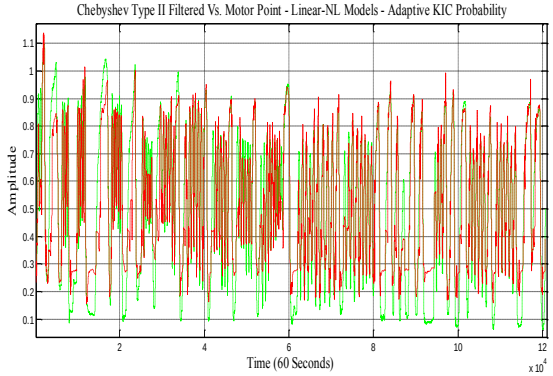

Fig. 5.1.2(c). Chebyshev Type II vs. Adaptive KIC Probability Based Force from Linear and Nonlinear Models for Motor Point Sensor.

Finally the estimated skeletal muscle force from three sEMG sensors is further fused with adaptive KIC probability based data fusion algorithm. Fig. 5.1.2(d) shows the comparison of the measured and Chebyshev type II filter with the final adaptive KIC probability based fusion skeletal muscle force estimate using three sEMG sensors. The final result for three sensors is the best estimate of skeletal muscle force and it is evident that the measured signal has a very close follow up by the estimated signal.

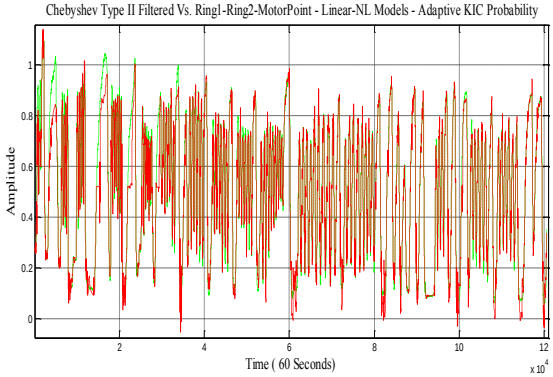

Fig. 5.1.2(d). Chebyshev Type II vs. Adaptive KIC Probability Based Force from Linear and Nonlinear Models for Ring1, Ring2 and Motor Point Sensor Combined.

The results show that there is a decrease in the percentage error from the linear and nonlinear model fusion based separate outputs to the fusion based combined output of linear and nonlinear models combined for all three sensors. However, these results show that there is a 16% improvement in the mean fit value of the motor point signal models with the adaptive KIC probability based data fusion algorithm for multi-sensors (three in this case). Fig. 5.1.2(e) and (f) show the validation plots of this approach for two separate sets of sEMG and skeletal muscle force data where

green signal is the Chebyshev type II filtered measured force signal and the blue signal is estimated using this approach.

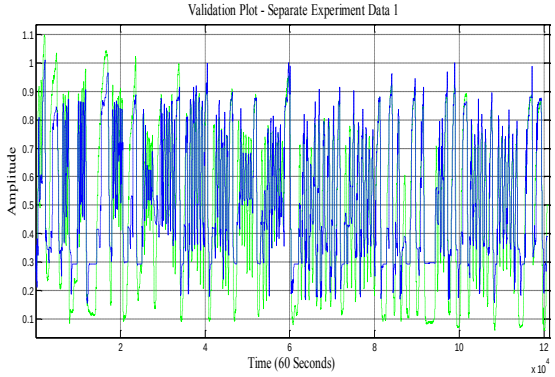

Fig. 5.1.2(e). Validation Plot 1 - Chebyshev Type II vs. Estimated Force Signal using Adaptive KIC Probability.

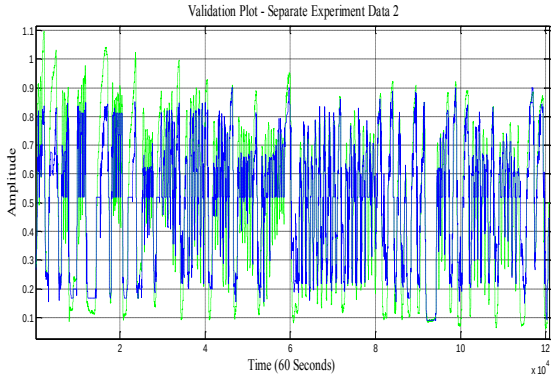

Fig. 5.1.2(f). Validation Plot 2 - Chebyshev Type II vs. Estimated Force Signal using Adaptive KIC Probability.

5.1.3 Adaptive Neuro Fuzzy Inference Systems (ANFIS) and Smoothing Spline Curve Fitting Based Estimation of Skeletal Muscle Force

Another method that we tried to estimate the skeletal muscle force using the sEMG signal is ‗ANFIS and Smoothing Spline Curve Fitting.' Here we used the data set captured using an array of nine sEMG sensors as shown in the experimental set-up of Fig. 2.2.2(f). Eight Takagi-Sugeno-Kang ANFIS with different membership functions each with a rule base of ten are designed. The training of each ANFIS is done using a hybrid optimization method with zero error tolerance and 40 epochs. Each of the force signals simulated using these ANFIS and measured force signals are applied to a smoothing spline curve fitting method [P9]. The outputs from the smoothing spline curve fitting are supplied to a data fusion algorithm with adaptive KIC probability. The final output of this approach gives improved estimates of the skeletal muscle force.

Results and Discussion

This method of skeletal muscle force estimation gives good estimation of the skeletal muscle force. A data set of 45 seconds is used to estimate the output. Fig.5.1.3(a) shows the measured and estimated skeletal muscle force using this method.

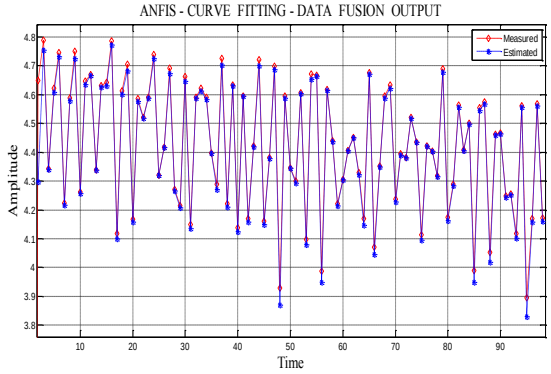

Fig. 5.1.3(a). Plot of Measured and Proposed Method Estimated Skeletal Muscle Force.

Fig. 5.1.3(b) and (c) are the validation plots for 45 seconds and 60 seconds of data sets respectively. All of these three plots show a very close follow up of the measured signal by the estimated signal using this approach. Fig. 5.1.3(d) shows the percentage error between the measured force signal and estimated finger force signal for 45 seconds of data set. The percentage error reduced to the lower values and the maximum percentage error value is 1.7 percent. The mean fit value between the measured and estimated output is 91.3 percent.

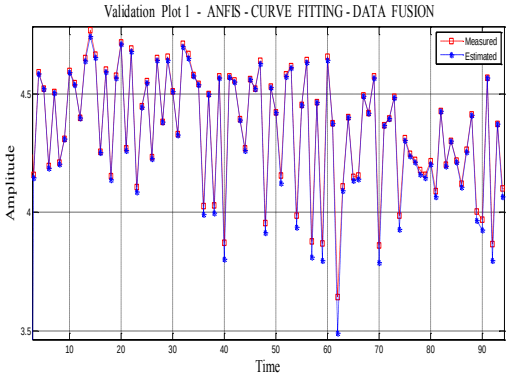

Fig. 5.1.3(b). Validation Plot 1 Using Different Data Set.

Fig. 5.1.3(e) shows the percentage error plot for different data set of 60 seconds duration. Percentage error reduced to lower values and the maximum percentage error value is 3.7 percent. The mean fit value between the measured and estimated output is 40 percent. The mean fit value for another 45 seconds of data set is 73 percent.

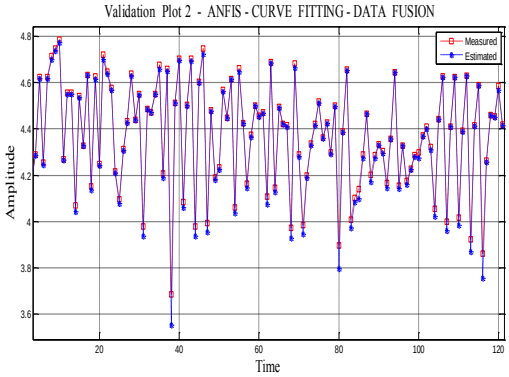

Fig. 5.1.3(c). Validation Plot 2 Using Different Data Set.

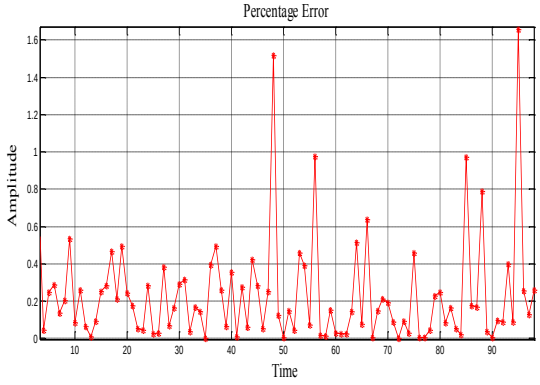

Fig. 5.1.3(d). Percentage Error Plot.

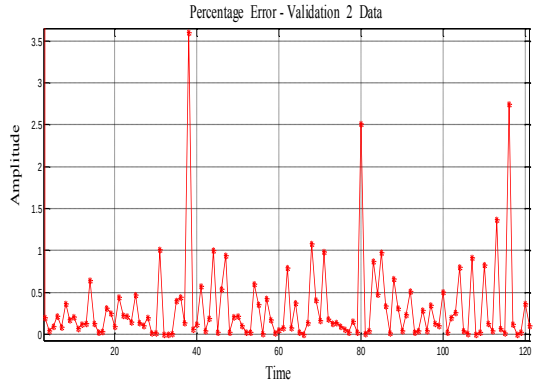

Fig. 5.1.3(e). Percentage Error Plot for 60 Seconds Data Set.

5.2 **Force-fatigue model**

As it is explained in earlier part of the report that muscle fatigue is a natural and dynamic phenomenon and cannot be avoided. So, it is equally important that while estimating the skeletal muscle force from sEMG we address the issue of muscle fatigue or have some compensation for the change in sEMG as a result of muscle fatigue. This part of the research deals with the issue of skeletal muscle fatigue and try to design the mathematical model that can capture the dynamics of muscle fatigue. Here we used the experimental set-up shown in Fig. 2.2.2(a), and the data is captured for a muscle fatiguing contraction for the dominant hand of a healthy subject. The data is pre-processed using nonlinear Half-Gaussian Bayesian filter. The data was segmented into five parts with 91 percent overlap among the adjacent data segments for three sEMG sensors. Output Error (OE) models for each segment is obtained and the state space matrices are transformed using Modal transformation. The eigenvalues are the transformed matrices are plotted and curve fitted to capture the dynamics of muscle fatigue. Finally using this method we obtained three discrete-time dynamic state space models for three sEMG sensors for the ring finger [P10].

Results and Discussion

Based on previous research results and after trying different model orders for sEMG/Force data, an optimal model order of $n_b = 2, n_f = 2, n_k = 1$ is used in this work. Equation (5.2.1), (5.2.2), and (5.2.3) give three resulting discrete time state-space sEMG-Force-Fatigue models for motor point sensor, sensor-1 and sensor-2 respectively.

$$x_m(h+1) = A_m x_m(h) + B_m EMG_m(h);$$
$$\hat{Y}_m(h) = C_m x_m(h) + D_m EMG_m(h). \quad (5.2.1)$$
$$x_1(h+1) = A_1 x_1(h) + B_1 EMG_1(h);$$
$$\hat{Y}_1(h) = C_1 x_1(h) + D_1 EMG_1(h). \quad (5.2.2)$$
$$x_2(h+1) = A_2 x_2(h) + B_2 EMG_2(h);$$
$$\hat{Y}_2(h) = C_2 x_2(h) + D_2 EMG_2(h). \quad (5.2.3)$$

In these case matrices D_m, D_1, and D_2 are zero matrices, whereas matrices $A_m, B_m, C_m, A_1, B_1, C_1, A_2, B_2$, and C_2 are given as: $A_m = \begin{bmatrix} a_{m1}(t) & 0 \\ 0 & a_{m2} \end{bmatrix}$; $B_m = \begin{bmatrix} b_{m1}(t) \\ b_{m2}(t) \end{bmatrix}$; $C_m = [c_{m1}(t) \;\; c_{m2}(t)]$; $A_1 = \begin{bmatrix} a_{11} & 0 \\ 0 & a_{12} \end{bmatrix}$;

$B_1 = \begin{bmatrix} b_{11} \\ b_{12} \end{bmatrix}$; $C_1 = [c_{11} \;\; c_{12}]$; $A_2 = \begin{bmatrix} a_{21}(t) & 0 \\ 0 & a_{22} \end{bmatrix}$; $B_2 = \begin{bmatrix} b_{21}(t) \\ b_{22}(t) \end{bmatrix}$; and $C_2 = [c_{21}(t) \;\; c_{22}(t)]$; where the elements of matrices A_m, B_m, C_m, A_2, B_2, and C_2 are function of time and the elements of matrices A_1, B_1, and C_1 are constants for this particular data set. The time variables $a_{m1}(t), a_{m2}(t), b_{m1}(t), b_{m2}(t), c_{m1}(t), c_{m2}(t)$, $a_{21}(t), a_{22}(t), b_{21}(t), b_{22}(t), c_{21}(t)$, and $c_{22}(t)$ are given by quadratic polynomials obtained by curve fitting the tracked modal transformed coefficients. These time variables are given as:

$a_{m1}(t) = 0.00026t^2 - 0.033t - 11;$
$a_{m2}(t) = -0.0018t^2 + 0.24t - 33;$
$b_{m1}(t) = -0.002t^2 + 0.33t + 42;$ $b_{m2}(t) = -0.0017t^2 + 0.33t + 25;$
$c_{m1}(t) = (3.2 * 10^{-7})t^2 - (4.2 * 10^{-5})t + 0.71;$
$c_{m2}(t) = (4.6 * 10^{-8})t^2 - (5.8 * 10^{-6})t - 0.71;$
$a_{21}(t) = -(1.2 * 10^{-5})t^2 + 0.0013t - 0.47;$
$a_{22}(t) = 0.001t^2 - 0.037t - 35;$
$b_{21}(t) = (6.4 * 10^{-6})t^2 - 0.001t + 0.3;$
$b_{22}(t) = 0.0023t^2 - 0.12t - 75;$

$c_{21}(t) = -(1.8 * 10^{-7})t^2 + (6.4 * 10^{-6})t + 0.71;$ and $c_{22}(t) = -(2.1 * 10^{-9})t^2 + (2.4 * 10^{-7})t - 0.71.$
Elements of matrices A_1, B_1, and C_1 are constants for this particular data set, they are given as:

$a_{11} = -0.0159;$ $a_{12} = -43.1883;$ $b_{11} = 0.0090;$ $b_{12} = -72.1875;$ $c_{11} = 0.7147;$ and $c_{12} = -0.7071.$

The discrete models have a sampling time of $\Delta t = 0.0005$ seconds.

Fig. 5.2(a) and (b) shows the measured and estimated fused output, depending on the error between the two later follows the measured signal very closely. This approach identifies a fused fatigue model and estimates an adaptive probability based output that follows the measured output very closely. The outcome of this research can be used to estimate the skeletal muscle force of a human hand for prosthetic hand design, application and improvement.

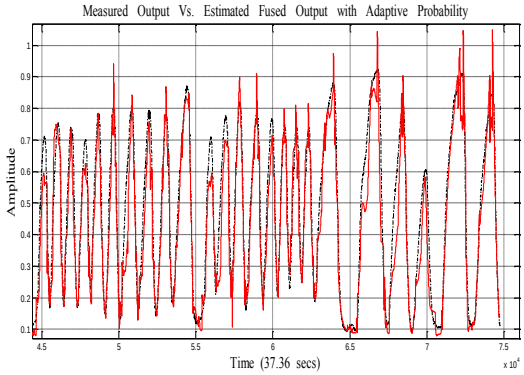

Fig. 5.2(a). Measured Output Vs. Estimated Fused Output with Adaptive Probability.

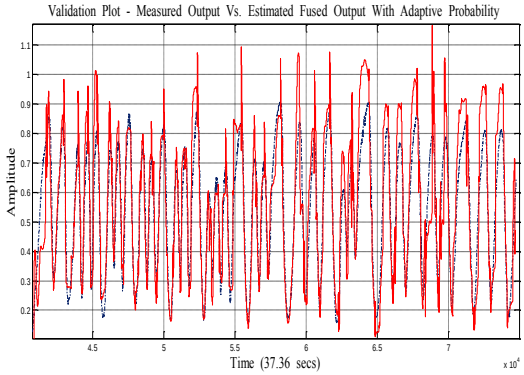

Fig. 5.2(b). Validation Plot - Measured Vs. Estimated Fused Output with Adaptive Probability.

6. Motion model

This part of the report presents a novel approach to dynamic modeling and estimation of the angles of the proximal interphalangeal (PIP) joint of the index finger with the corresponding sEMG signal. This can be used as an angle control signal for the controller and replace the need of pre-programmed motion sets, which are initiated when some threshold value of the measured sEMG signal is reached. Here we are using System Identification (SI) in order to obtain a dynamic finger angle model/estimation. The data for the simulation and modeling is captured using an experimental set-up as shown in Fig. 2.2.2(n) that we designed for this specific purpose.

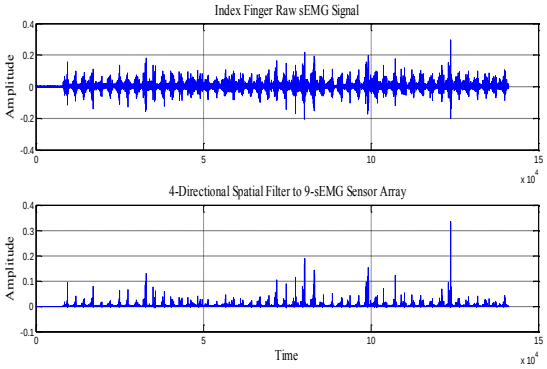

Fig. 6(a). Raw and Spatially Filtered sEMG Signal from Index Finger.

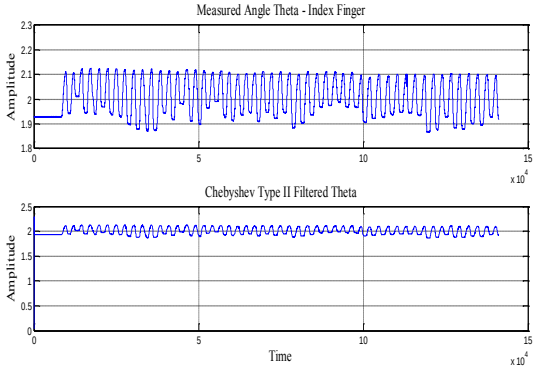

Fig. 6(b). Raw and Chebyshev Type II Filtered PIP Joint Angle for Index Finger.

The recorded sEMG signal for the index finger is filtered using nonlinear spatial filtering for nine channel surface EMG. The nonlinear spatial filter is obtained from the ~~"~~Nonlinear Teager-Kaiser Energy (TKE) Operator," [25]. Fig. 6(a) shows a comparison between the measured and nonlinear spatial filtered sEMG signals. A Chebyshev

type II infinite impulse response (IIR) low pass filter with a 550 Hz pass band frequency is used to filter the PIP joint angle data. Fig. 6(b) shows the comparison between the measured and Chebyshev type II filtered skeletal muscle force signal.

The filtered signals are smoothed using a smoothing spline curve fitting. The smoothed sEMG data is used as input and the respective smoothed finger angle data is used as output for a system identification routine to obtain multiple linear and nonlinear models. Five linear and three nonlinear models are obtained and to achieve better estimates of the finger angles, an adaptive probabilistic Kullback Information Criterion (KIC) for model selection based data fusion algorithm is applied to the linear and nonlinear model‘s outputs. Final fusion based output of this approach results in improved estimates of finger angles [P11].

Results and Discussion

The sEMG signals from the sensor array and angle signals of PIP joint of index finger are filtered; smoothing spline curve fitted and modeled using multiple linear and nonlinear models. First the outputs of linear and nonlinear models are fused separately and then the resultant outputs are fused using an adaptive KIC based probability. This approach gives improved estimates of the finger angles of the PIP joint of the index finger of the dominant hand of a healthy subject. Results are presented in the following figures.

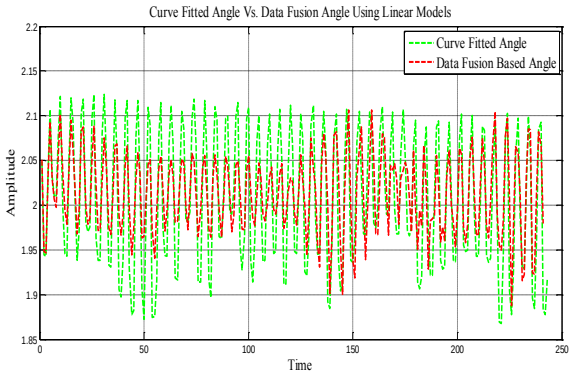

Fig. 6(c). Curve Fitted Vs. Data Fusion Based Angle Using Linear Models.

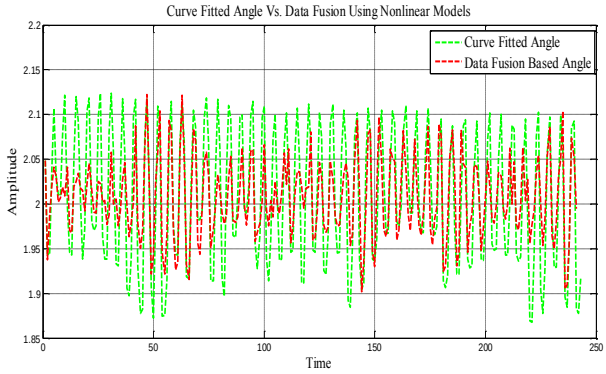

Fig. 6(d). Curve Fitted Vs. Data Fusion Based Angle Using Nonlinear Models.

Fig. 6(c) shows the overlapping plot of the measured-curve fitted angle vs. data fusion based angle using linear models. Fig. 6(d) shows the overlapping plot of the measured-curve fitted angle vs. data fusion based angle using nonlinear models. Fig. 6(e) shows the overlapping plot of the curve fitted angle vs. data fusion based angle using linear-nonlinear models. It is clearly evident that the data fusion based output follows the measured-curve fitted output. Mean percentage error of the linear, nonlinear and linear-nonlinear models data fusion based angles are 2.5191e-005, -4.5807e-006, and 8.1167e-006 respectively.

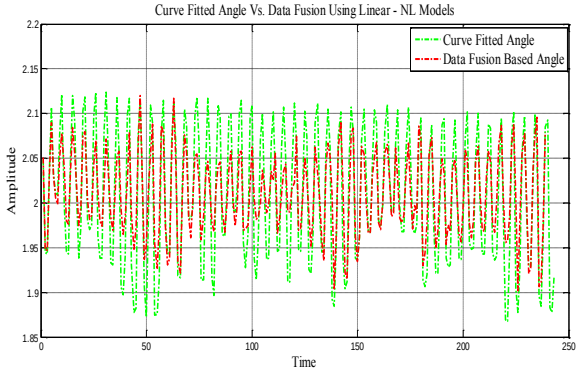

Fig. 6(e). Curve Fitted Vs. Data Fusion Based Angle Using Linear-Nonlinear Models.

Fig. 6(f) shows the validation plot for a different experimental data where the measured-curve fitted and the linear-nonlinear modeled data fusion based angle signal shows a close follow up. Mean percentage error of the linear, nonlinear and linear-nonlinear models data fusion based angles are 2.8202e-005, 3.3191e-005, and 6.8079e-006 respectively.

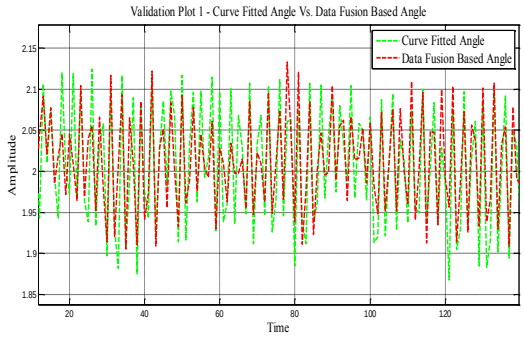

Fig. 6(f). Validation Plot - Curve Fitted Vs. Data Fusion Based Angle Using Linear-Nonlinear Models.

In addition to the research conducted on the sEMG-force and sEMG-angle modeling, we also investigated various optimization methods for improving the non-linear Hammerstein model fits for sEMG-force models. This research was published in 2010 [P15]. ~~–~~A Study on Hybridization of Particle Swarm and Tabu Search Algorithms for unconstrained Optimization and Estimation Problems."
Also, we learnt a great deal about the Hammerstein-Wiener models from our previous research which led to the classification of amputation utilizing various spatial filters. This research was published in 2010 [P16].

Goal 2A: Intelligent Control

The overall research is accomplished under four goals: Goal 1: EMG Signal Identification and Estimation, Hand Motion Estimation, Goal2: Intelligent Control of Prosthetics, Goal 3: Robotic Hand and Goal 4: Biocompatibility and Signaling.

The schematic diagram of the proposed work is shown in Figure 1 (see the works of Light et al. (2002); Rodriguez-Cheu and Casals (2006); Zhao et al. (2006)). The overall system, in brief, consists of electromyographic (EMG) signal acquisition from user arm for surface or implanted electrodes (in the implanted case we focus on biocomptibility based on nano-materials research). The EMG signal is then processed for feature extraction and classification or identification of EMG signal to correspond to different motions of the prosthetic hand. The classified signal is then used to control the prosthetic hand using actuators and driving mechanisms.

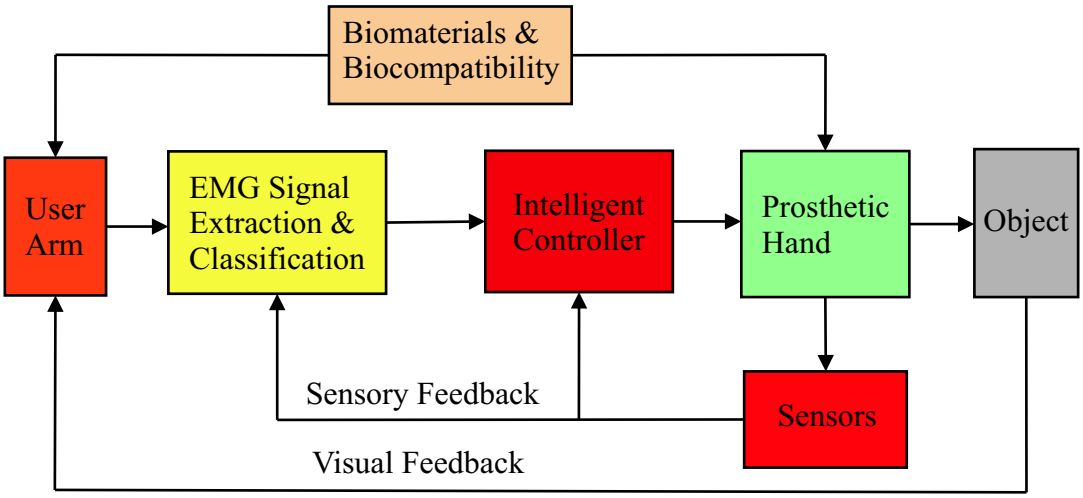

Figure 1: Schematic Diagram of Prosthetic Hand Technology

Soft computing (SC) or computational intelligence (CI) (Konar (2005)) is an emerging field based on synergy and seamless integration of neural networks (NN), fuzzy logic (FL) and genetic algorithms (GA) (Karray and De Silva (2004)). The previous works on prosthetic hand used artificial neural networks by Hudgins (1991); Christodooulu and Pattichis (1999); Light et al. (2002), fuzzy logic by Weir and Ajiboye (2003); Chan et al. (2000); Ajiboye and Weir (2005), genetic algorithms in (Fernandez et al. (2000)) etc mostly for EMG signal classification for various movements or functions of the prosthetic hand.

Goal 2: Intelligent Control of Prosthetics

The research accomplishments under Goal 2A: Intelligent Control of Prosthetics are

1. a comprehensive literature updated on the topic of control techniques for prosthetic hands was conducted,

2. trajectory planning, kinematics and dynamics of a prosthetic hand with a two-link thumb and four three-link fingers based on analytical models were investigated,

3. hard control techniques (feedback linearization, PD, PID, optimal and adaptive) to prosthetic hand,

4. soft computing strategies (neural networks, fuzzy logic, adaptive neural-fuzzy inference system and genetic algorithm) to prosthetic hand, and

5. fusion of hard and soft control techniques (fuzzy logic+PD and genetic algorithm+PID) to the five-fingered smart prosthetic hand.

Overview of Control Strategies for Smart Prosthetic Hand Technology

In research and development of a prosthetic hand using non-invasive techniques, the three basic problems are, first, electromyographic (EMG) signal acquisition, and classification to correspond to various human-like operations or features, second, conversion of EMG feature signals to control signals to input to actuators to operate the prosthetic hand, and third, design and building of a prosthetic hand with necessary sensors to operate according to the control signal that corresponds to the EMG signal intended for the particular identified hand operation. In this paper, a chronological overview of the applications of control theory to prosthetic hand is presented. The overview focuses on *hard* computing or control techniques such as multi-variable feedback, optimal, nonlinear, adaptive and robust and *soft* computing or control techniques such as artificial intelligence, neural networks, fuzzy logic, genetic algorithms and on the *fusion* of hard and soft control techniques. This overview is not intended to be an exhaustive survey on this topic and any omissions of other works is purely unintentional.

A hand is considered as an agent of human brain and is the most intriguing and versatile appendage to the human body. Over the last several years, attempts have been made to build a prosthetic hand to replace a human hand to fully simulate the various natural/human-like operations of moving, grasping, lifting, twisting and so on. Replicating the human hand in all its various functions is still a challenging task due to the extreme complexity of a human hand, which is 27 bones, controlled by about 38 muscles to provide the hand with 22 degrees of freedom (DOFs), and incorporates about 17,000 tactile units of 4 different types Kandel and Schartz (1985); Zecca et al. (2002). Parallels between dextrous robot and human hands were explored by examining sensor motor integration in the design and control of these robots through bringing together experimental psychologists, kinesiologists, computer scientists, and electrical and mechanical engineers.

Artificial hands have been around for the last several years developed by various researchers in the field and some of the prosthetic devices developed are given below (in chronological order) Zecca et al. (2002, 2006):

1. Russian arm - Kobrinski (1960); Sherman (1964); McKenzie (1965),

2. Waseda hand - Kato et al. (1967),

3. Boston arm[1] - Mann and Reimers (1970),

4. UNB hand (University of New Brunswick) - Rohland (1975); Hudgins (1991); Light et al. (2002),

5. Hanafusa hand - Hanafusa and Asada (1977),

6. Crossley hand - Crossley and Umholtz (1977),

[1]The "Boston Arm," project involved the Harvard Medical School, Massachusetts General Hospital, the Liberty Mutual Research and Rehabilitation Centers, and M.I.T.

7. Okada hand - Okada (1982),
8. Utah/MIT hand (University of Utah/Massachusetts Institute. of Technology) - Jacobsen et al. (1982, 1985); Iversen et al. (2005),
9. JPL/Stanford hand (Jet Propulsion Laboratory/Stanford University) - Salisbury (1982); Venkataraman and Djaferis (1987),
10. Minnesota hand - Lian et al. (1983),
11. Manus hand - Kyberd and Pons (2003); Pons et al. (2004),
12. Kobayashi hand - Kobayashi (1985),
13. Rovetta hand - Rovetta (1983),
14. UT/RAL hand - Kim et al. (1987),
15. Dextrous gripper - Van Brussel et al. (1989),
16. Belgrade/USC hand (University of Belgrade/University of Southern California)- Bekey et al. (1990),
17. Southampton hand (University of Southampton, Southampton, UK) - Kyberd and Chappell (1994),
18. MARCUS hand (Manipulation And Reaction Control under User Supervision) - Kyberd et al. (1995),
19. Kobe hand (Kobe University, Japan) - Okuno et al. (1996),
20. Robonaut hand (NASA Johnson Space Center) - Lovchik and Diftler (1999),
21. NTU hand (National Taiwan University) - Huang and Chen (1999),
22. Hokkaido hand - Nishikawa et al. (2001),
23. DLR hand (Deutschen Zentrums für Luft- und Raumfahrt-German Aerospace Center) - Liu et al. (1999); Butterfass et al. (2001),
24. TUAT/Karlsruhe hand (Tokyo University of Agriculture and Technology/University of Karlsruhe) - Fukaya et al. (1996),
25. BUAA hand (Beijing University of Aeronautics and Astronautics) - Zhang et al. (2001),
26. TBM hand (Toronto/Bloorview MacMillan) - Dechev et al. (2001),
27. ULRG System (University of Louisiana Robotic Gripper) - Kolluru et al. (2002),
28. Oxford hand - Kyberd and Pons (2003),
29. IOWA hand (University of Iowa) - Yang et al. (2004),
30. MA-I hand - Suárez and Grosch (2004),

31. RCH -1 (ROBO CASA hand 1 [2]) - Roccella et al. (2004),
32. UB hand (University of Bologna) - Lotti et al. (2005),
33. Ottoback SUVA hand - (www.ottobock.co.uk),
34. Northwestern University system - Farrell et al. (2005),
35. SKKU Hand II (Sungkyunkwan University, Korea) - Choi et al. (2006),
36. Applied Physics Laboratory (APL) at Johns Hopkins University (JHU) - DARPA06b (2006); APL-JHU-06 (2006); APL-JHU-07 (2007),

and some of the commercial web sites for prosthetic devices are

1. Sensor Hand^{TM} Speed from Otto Bock (www.ottobock.co.uk),
2. VASI (Variety Ability Systems Inc.), a company of the Otto Boch Group (http://www.vasi.on.ca/index.html),
3. Utah Arm from Motion Control (www.utaharm.com),
4. The i-LIMB Hand from Touch Bionics (www.touchbionics.com), and
5. so on.

A very useful comparison table between several hands listed above and human hand, adapted from Zecca et al. (2002, 2006), is updated and shown in Table 1.

However, about 35% of the amputees do not use their prosthetic hand regularly according to Atkins et al. (1996) due to various reasons such as poor functionality of the presently available prosthetic hands and psychological problems. To overcome this problem, one has to design and develop an artificial hand which "mimics the human hand as closely as possible" both in functionality and appearance.

There are a number of surveys, and/or state-of-the art articles that appeared over the years on the subject of myoelectric prosthetic hand including the work in USSR (Russian) given by Sherman (1964) and some of them are given by Childress (1980); Scott and Parker (1988); Grupen et al. (1989); Sears and Shaperman (1991); Shimoga (1996); Bicchi (2000); Okamura et al. (2000); Zecca et al. (2002); Kyberd et al. (2003); Muzumdar (2004); Cotton et al. (2006); Arimoto (2008); Birglen et al. (2008); Inoue and Hirai (2009).

The complete details are given in our book chapter attached as Appendix 2A-1.

Modeling of a Five-Fingered Smart Prosthetic Hand

Human Hand Anatomy

Figure 2 (a) shows a normal human hand composed of thumb (t), index (i), middle (m), ring (r), little (l) fingers and palm. The wrist is located between the forearm and the hand and consists of eight carpal bones organized in two rows of proximal (movable) and distal (immovable) carpal bones as shown in Figure 2 (b) Seeley et al. (2007). The proximal row (top) of carpal bones from lateral to medial is the *Scaphoid*, *Lunate*, *Triquetrum* and *Pisiform*; the distal row (bottom) of carpal bones from medial to lateral has the *Hamate*, *Capitate*, *Trapezoid* and *Trapezium*. The hand is composed

[2] the Italy-Japan joint laboratory for Research on Humanoid and Personal Robotics

Table 1: **comparison of Human Hand with Artificial Hands: Robotic and Prosthetic Hands: *Force* indicates power grasp *Speed* indicates the time required for a full closing and opening; *E*: stands for *external*; *I*: stands for *internal***

	Size (Norm)	# of Fingers	# of DOFs	# of Sensors	# of Actuators	Weight (gms)	Force (N)	Speed (sec)	Controls
Human hand	1.0	5	22	≈ 17,000	38(I+E)	≈ 400	>300	0.25	E
Russian arm		5		3	1		≈ 147		
Waseda hand									
UNB hand									
Hanafusa hand									
Crossley hand									
Utah/MIT hand	≈ 2.0	4	16	16	32(E)	-	31.8	-	E
JPL/Stanford hand	≈ 1.2	3	9	-	12(E)	1100	45	-	E
Minnesota hand									
Kobayashi hand									
Rovetta hand									
UT/RAL hand									
Dextrous gripper									
Belgrade/USC hand	≈1.1	4	4	23+4	4(E)	-	-	-	E
Southampton hand	≈ 1.0	5	6	-	6(E)	400	38	≈ 5	E
MARCUS hand	≈ 1.1	3	2	3	2(I)	-	-	-	I
Kobe hand									
Robonaut hand	≈ 1.5	5	12+2	43+	14(E)	-	-	-	E
NTU hand	≈ 1	5	17	35	17(E)	1570	-	-	E
Hokkaido hand	≈ 1	5	17	35	17(E)	1570	-	-	E
DLR hand II	>1	5	7	-	7(E)	125	-	-	E
TUAT/Karlsruhe hand	≈ 1	5	17	-	17(E)	≈ 120	12	0.1	E
BUAA hand		4			2				
TBM hand									
Oxford hand									
IOWA hand									
MA-I hand									
Robo Casa hand-1	≈ 1	5	16	24	6(E+I)	350	≈ 40	0.25	E
Ottobock SUVA	1	3	1	2	1(E)	600	-	-	I
UB hand									
Hokkaido hand	>1	5	7	-	7(E)	125	-	-	E
Northwestern									
SKKU Hand II	1.1	4	4	-	3	900			
APL-JHU System									

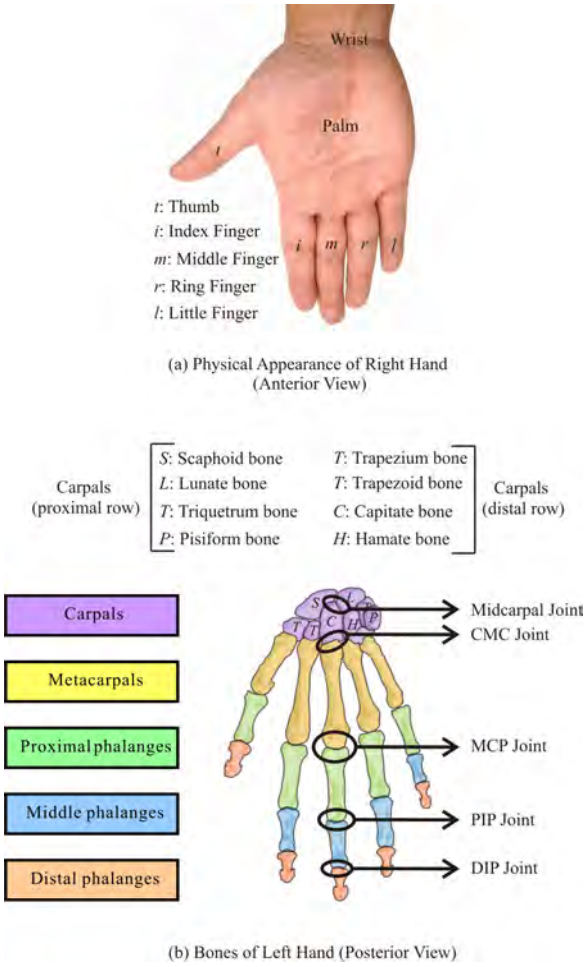

Figure 2: Human Wrist and Hand: (a) Physical Appearance of Right Hand (Anterior View) (b) Bones of Left Hand (Posterior View)

of five *Metacarpals* and five Digits. The metacarpals produce a curve, so the palm is concave in the resting position. The five digits contain one thumb (t) and four fingers, e.g. index (i), middle (m), ring (r), and little (l) fingers, respectively. The thumb has two bones, *Proximal phalanx* and *Distal phalanx*. Each finger consists of three bones, *Proximal phalanx*, *Middle phalanx* and *Distal phalanx*. In this work, we assumed that the palm is fixed, the thumb has two links (proximal phalanx and distal phalanx), and each finger has three links (proximal phalanx, middle phalanx and distal phalanx).

Synovial joints are formed at the surface of relative motion between two bones. The joints of thumb and four fingers contain two saddle-shaped articulating surfaces between two bones and can be classified as saddle joints. Index, middle, ring, and little fingers include three revolute joints in order to do the angular movements (Figure 2 (b)). Metacarpal-phalangeal (MCP) joint is located between metacarpal and proximal phalange bones; proximal and distal interphalangeal (PIP and DIP) joints separate the phalangeal bones. Thumb contains metacarpal-phalangeal (MCP) and interphalangeal (IP) joints Seeley et al. (2007). In this work, q_1^j, q_2^j and q_3^j ($j = i$, m, r and l) represent the angular positions (or joint angles) of the first joint MCP^j, the second joint PIP^j and the third joint DIP^j of index, middle, ring and little fingers, respectively; q_1^t and q_2^t are the angular positions of the first joint MCP^t and the second joint IP^t of thumb (t), respectively.

Trajectory Planning

The trajectory planning using cubic polynomial was discussed in our previous work Chen (2009); Chen et al. (2008a,b, 2009a,c, 2010) for a two-fingered (thumb and index finger) smart prosthetic hand. For three-link fingers, we present the same technique for fingertip orientation control. A time history of desired (d) fingertip orientation (ϕ) and its differentiation ($\dot{\phi}$ and $\ddot{\phi}$) is given as

$$\phi_d^j(t) = \omega_0 + \omega_1 t + \omega_2 t^2 + \omega_3 t^3, \quad (1)$$

$$\dot{\phi}_d^j(t) = \omega_1 + 2\omega_2 t + 3\omega_3 t^2, \quad (2)$$

$$\ddot{\phi}_d^j(t) = 2\omega_2 + 6\omega_3 t, \quad (3)$$

where ω_0-ω_3 are undetermined constants and the superscript j indicates the index of each finger ($j = i$, m, r and l). The relations (1) and (2) need to satisfy the constraint conditions at initial time t_0 and final time t_f. This can be written as

$$\mathbf{T}\ \mathbf{\Omega} = \mathbf{\Phi}. \quad (4)$$

Here, the matrices $\mathbf{T}$, $\mathbf{\Omega}$, and $\mathbf{\Phi}$ are

$$\mathbf{T} = \begin{bmatrix} 1 & t_0 & t_0^2 & t_0^3 \\ 0 & 1 & 2t_0 & 3t_0^2 \\ 1 & t_f & t_f^2 & t_f^3 \\ 0 & 1 & 2t_f & 3t_f^2 \end{bmatrix}, \quad (5)$$

$$\mathbf{\Omega} = \begin{bmatrix} \omega_0 & \omega_1 & \omega_2 & \omega_3 \end{bmatrix}', \quad (6)$$

$$\mathbf{\Phi} = \begin{bmatrix} \phi_0^j & \dot{\phi}_0^j & \phi_f^j & \dot{\phi}_f^j \end{bmatrix}'. \quad (7)$$

Therefore, the 4 unknown constants, ω_0-ω_3, can be computed by $\mathbf{\Omega} = \mathbf{T}^{-1}\mathbf{\Phi}$.

Kinematics

Kinematics is the study of geometry in motion and is restricted to a natural geometrical description of motion by the manners, including positions, orientations, and their derivatives (velocities and accelerations) Jazar (2007); Siciliano et al. (2009). Forward and inverse kinematics of articulated systems study the analytical relationship between the angular positions of joints and the positions and orientations of the fingertips. A desired trajectory is usually specified in *Cartesian* space and the trajectory controller is easily performed in the *joint* space. Therefore, conversion of Cartesian trajectory planning to the joint space Siciliano et al. (2009) is necessary. Using inverse kinematics, the joint angular positions of each finger need to be obtained from the known fingertip positions. Then the angular velocities and angular accelerations of joints can be obtained from the linear and angular velocities and accelerations of fingertips by differential kinematics. The inverse and differential kinematics of two-link thumb and three-link fingers were discussed in our previous publications Chen (2009); Chen et al. (2008a,b, 2009a,c, 2010) for a two-fingered (thumb and index finger) smart prosthetic hand.

For five fingers shown in Figure 3, X^G, Y^G, and Z^G are the three axes of global coordinate. Local coordinate x^t-y^t-z^t of thumb can be reached by rotating through angles α and β to X^G and Y^G of the global coordinate, subsequently. Local coordinate x^i-y^i-z^i of index finger can be obtained by rotating through angle α to X^G and then translating a vector $\mathbf{d^i}$ of the global coordinate; similarly, the local coordinate x^j-y^j-z^j of middle finger ($j = m$), ring finger ($j = r$), and little finger ($j = l$) can be obtained by rotating through angle α to X^G and then translating the vector $\mathbf{d^j}$ ($j = m$, r and l) of the global coordinate.

Figure 3: Relationship between Global Coordinate and Local Coordinates: Local coordinate x^t-y^t-z^t of thumb can be reached by rotating through angles α and β to X^G and Y^G of global coordinate, subsequently. Local coordinate x^i-y^i-z^i of index finger can be obtained by rotating through angle α to X^G and then translating a vector $\mathbf{d^i}$ of the global coordinate.

Adaptive Neuro-Fuzzy Inference System (ANFIS)

The inverse kinematics problems can be solved by using adaptive neuro-fuzzy inference system (ANFIS) method Jang et al. (1997) where the input of fuzzy-neuro system is the Cartesian space and the output is the joint space. ANFIS is a fuzzy inference system implemented in the framework of adaptive networks which provides the best optimization algorithm to find parameters in order to fit the data. ANFIS includes *premise parameters*, that defines membership functions, and *consequent parameters*, that defines the coefficients of each output equation. ANFIS tunes the membership function and identifies the coefficients by the backpropagation gradient descent and least-squares methods, respectively. ANFIS uses a hybrid learning algorithm to identify parameters of Sugeno-type fuzzy inference systems for fuzzy modeling procedures to learn information about a data set in order to compute the membership function and track the given input/output data. Figure 4 (a) shows a two input first-order Sugeno fuzzy model with two rules and Figure 4 (b) depicts the equivalent ANFIS structure for all the computation below. Sugeno-type fuzzy system has the following **Rule Base** Jang et al. (1997); Karray and De Silva (2004); Nguyen et al. (2003); Nandikolla and Naidu (2005); Nandikolla (2005).
If x is A_1 and y is B_1, then $f_1 = p_1x + q_1y + r_1$.
If x is A_2 and y is B_2, then $f_2 = p_2x + q_2y + r_2$.
Here, x and y are inputs to constitute the premise parameters A_1, A_2, B_1, and B_2 (Layer 1 in Figure 4 (b)). p_i, q_i, and r_i (i = 1,2) are the consequent parameters. We evaluate the rules by choosing *product* $\prod$ for T-Norm (Layers 2 and 3) which results in

$$w_i \quad = \quad \mu_{A_i}(x)\ \mu_{B_i}(y),\ i = 1, 2. \tag{8}$$

Here, $\mu_{A_i}(x)$ and $\mu_{B_i}(y)$ are designed fuzzy membership functions. Now after leaving the arguments (Layer 4), we get the output $f(x, y)$ by **Rule Consequences**.

$$f(x, y) \quad = \quad \frac{w_1(x, y)f_1(x, y) + w_2(x, y)f_2(x, y)}{w_1(x, y) + w_2(x, y)}. \tag{9}$$

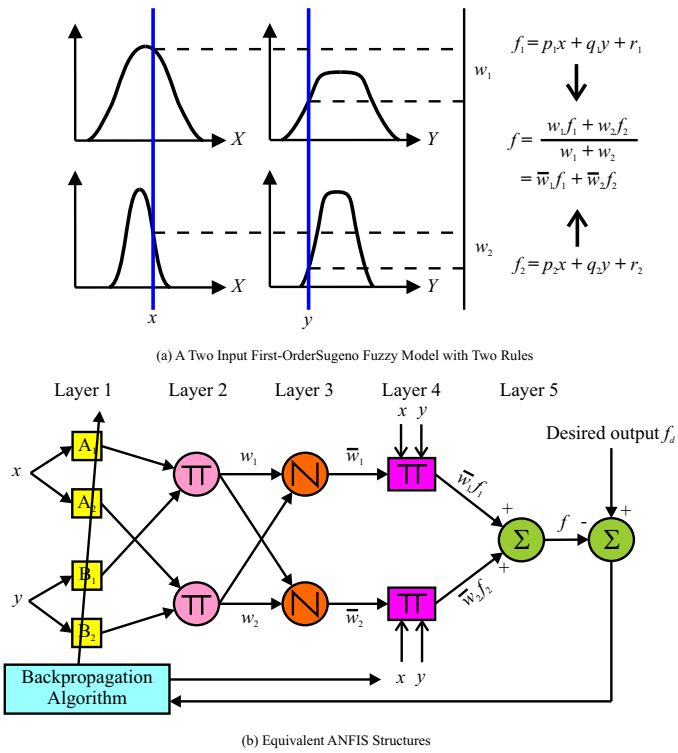

Figure 4: ANFIS Architecture: (a) A Two Input First-Order Sugeno Fuzzy Model with Two Rules (b) Equivalent ANFIS Structure Jang et al. (1997). The inverse kinematics problems are solved by using adaptive neuro-fuzzy inference system (ANFIS) method where the input of fuzzy-neuro system is the Cartesian space and the output is the joint space. ANFIS is a fuzzy inference system implemented in the framework of adaptive networks which provides the best optimization algorithm to find parameters in order to fit the data.

f (Layer 5) can be written as

$$\begin{aligned} f &= \frac{w_1 f_1 + w_2 f_2}{w_1 + w_2} \\ &= \bar{w}_1 f_1 + \bar{w}_2 f_2, \end{aligned} \tag{10}$$

where

$$\bar{w}_1 = \frac{w_1}{w_1 + w_2}, \quad \bar{w}_2 = \frac{w_2}{w_1 + w_2}. \tag{11}$$

Dynamics of Hand

The dynamic equations of hand motion are derived via Lagrangian approach using kinetic energy and potential energy as Lewis et al. (2004); Kelly et al. (2005); Jazar (2007); Siciliano et al. (2009); Chen (2009)

$$\frac{d}{dt}\left(\frac{\partial \mathcal{L}}{\partial \dot{\mathbf{q}}}\right) - \frac{\partial \mathcal{L}}{\partial \mathbf{q}} = \boldsymbol{\tau}, \tag{12}$$

where $\mathcal{L}$ is the Lagrangian; $\dot{\mathbf{q}}$ and $\mathbf{q}$ represent the angular velocities and angle vectors of joints, respectively; $\boldsymbol{\tau}$ is the given torque vector at joints. The Lagrangian $\mathcal{L}$ can be expressed as

$$\mathcal{L} = T - V, \tag{13}$$

where T and V denote kinetic and potential energies, respectively. Substituting (13) into (12), dynamic equations of thumb can be obtained as below.

$$\mathbf{M}(\mathbf{q})\ddot{\mathbf{q}} + \mathbf{C}(\mathbf{q}, \dot{\mathbf{q}}) + \mathbf{G}(\mathbf{q}) = \boldsymbol{\tau}, \tag{14}$$

where $\mathbf{M}(\mathbf{q})$ is the inertia matrix; $\mathbf{C}(\mathbf{q}, \dot{\mathbf{q}})$ is the Coriolis/centripetal vector and $\mathbf{G}(\mathbf{q})$ is the gravity vector. (14) can be also written as

$$\mathbf{M}(\mathbf{q})\ddot{\mathbf{q}} + \mathbf{N}(\mathbf{q}, \dot{\mathbf{q}}) = \boldsymbol{\tau}, \tag{15}$$

where $\mathbf{N}(\mathbf{q}, \dot{\mathbf{q}}) = \mathbf{C}(\mathbf{q}, \dot{\mathbf{q}}) + \mathbf{G}(\mathbf{q})$ represents nonlinear terms. The dynamic relations for the two-link thumb and the remaining three-link fingers are quite lengthy and omitted here due to lack of space Nikoobin and Haghighi (2008); Arslan et al. (2008); Chen (2009).

Control Techniques

Feedback Linearization

The nonlinear dynamics represented by (15) is to be converted into a linear state-variable system using feedback linearization technique Lewis et al. (2004). Alternative state-space equations of the dynamics can be obtained by defining the position/velocity state $\mathbf{x}(t)$ of the joints as

$$\mathbf{x}(t) = \left[\mathbf{q}'(t) \;\; \dot{\mathbf{q}}'(t)\right]'. \tag{16}$$

Let us repeat the dynamical model and rewrite (15) as

$$\frac{d}{dt}\dot{\mathbf{q}}(t) = -\mathbf{M}^{-1}(\mathbf{q}(t))\left[\mathbf{N}(\mathbf{q}(t), \dot{\mathbf{q}}(t)) - \boldsymbol{\tau}(t)\right]. \tag{17}$$

Thus, from (16) and (17), we can derive a linear system in *Brunovsky canonical form* as

$$\dot{\mathbf{x}}(t) = \begin{bmatrix} \mathbf{0} & \mathbf{I} \\ \mathbf{0} & \mathbf{0} \end{bmatrix} \mathbf{x}(t) + \begin{bmatrix} \mathbf{0} \\ \mathbf{I} \end{bmatrix} \mathbf{u}(t) \tag{18}$$

with its control input vector given by

$$\mathbf{u}(t) = -\mathbf{M}^{-1}(\mathbf{q}(t))\left[\mathbf{N}(\mathbf{q}(t), \dot{\mathbf{q}}(t)) - \boldsymbol{\tau}(t)\right]. \tag{19}$$

Let us suppose the prosthetic hand is required to track the desired trajectory $\mathbf{q}_d(t)$ described under path generation or tracking. Then, the tracking error $\mathbf{e}(t)$ is defined as

$$\mathbf{e}(t) = \mathbf{q}_d(t) - \mathbf{q}(t). \tag{20}$$

Here, $\mathbf{q}_d(t)$ is the *desired* angle vector of joints and can be obtained by trajectory planning Chen (2009); Chen et al. (2008a,b, 2009a,c); $\mathbf{q}(t)$ is the *actual* angle vector of joints. Differentiating (20) twice, to get

$$\dot{\mathbf{e}}(t) = \dot{\mathbf{q}}_d(t) - \dot{\mathbf{q}}(t), \quad \ddot{\mathbf{e}}(t) = \ddot{\mathbf{q}}_d(t) - \ddot{\mathbf{q}}(t). \tag{21}$$

Substituting (17) into (21) yields

$$\ddot{\mathbf{e}}(t) = \ddot{\mathbf{q}}_d(t) + \mathbf{M}^{-1}(\mathbf{q}(t))\left[\mathbf{N}(\mathbf{q}(t), \dot{\mathbf{q}}(t)) - \boldsymbol{\tau}(t)\right] \tag{22}$$

from which the control function can be defined as

$$\mathbf{u}(t) = \ddot{\mathbf{q}}_d(t) + \mathbf{M}^{-1}(\mathbf{q}(t))\left[\mathbf{N}(\mathbf{q}(t), \dot{\mathbf{q}}(t)) - \boldsymbol{\tau}(t)\right]. \tag{23}$$

This is often called the *feedback linearization* control law, which can also be inverted to express it as

$$\boldsymbol{\tau}(t) = \mathbf{M}(\mathbf{q}(t))\left[\ddot{\mathbf{q}}_d(t) - \mathbf{u}(t)\right) + \mathbf{N}(\mathbf{q}(t), \dot{\mathbf{q}}(t)\right]. \tag{24}$$

Using the relations (21) and (23), and defining state vector $\mathbf{x}(t) = [\mathbf{e}'(t) \;\; \dot{\mathbf{e}}'(t)]'$, the *tracking error dynamics* can be written as

$$\dot{\mathbf{x}}(t) = \begin{bmatrix} \mathbf{0} & \mathbf{I} \\ \mathbf{0} & \mathbf{0} \end{bmatrix} \mathbf{x}(t) + \begin{bmatrix} \mathbf{0} \\ \mathbf{I} \end{bmatrix} \mathbf{u}(t). \tag{25}$$

Note that this is in the form of a *linear* system such as

$$\dot{\mathbf{x}}(t) = \mathbf{A}\mathbf{x}(t) + \mathbf{B}\mathbf{u}(t). \tag{26}$$

Adaptive Control

The tracking error $\mathbf{e}(t)$ and the filtered tracking error $\mathbf{r}(t)$ are defined as

$$\mathbf{e}(t) = \mathbf{q}_d(t) - \mathbf{q}(t), \tag{27}$$

$$\mathbf{r}(t) = \dot{\mathbf{e}}(t) + \boldsymbol{\Lambda}\mathbf{e}(t). \tag{28}$$

Here, $\mathbf{q}_d(t)$ is the *desired* angle vector of joints; $\mathbf{q}(t)$ is the *actual* angle vector of joints; $\boldsymbol{\Lambda} = diag(\lambda_1, \lambda_2, \ldots, \lambda_n)$ is the positive-definite diagonal gain matrix. The filtered error (28) ensures stability of the overall system so that the tracking error (27) is bounded. Figure 5 shows the block diagram of the adaptive controller. Here, the filtered signal $\mathbf{r}(t)$ is derived from the tracking error $\mathbf{e}(t)$ and the trajectory planner and is fed to the adaptive controller of the prosthetic hand. Differentiating and substituting (28) into (14) gives the dynamic equation in terms of the filtered error $\mathbf{r}(t)$ as

$$\mathbf{M}(\mathbf{q}(t))\dot{\mathbf{r}}(t) = -\mathbf{C}_m(\mathbf{q}(t), \dot{\mathbf{q}}(t))\mathbf{r}(t) + \mathbf{f}(t) - \boldsymbol{\tau}(t), \tag{29}$$

where $\mathbf{C}(\mathbf{q}(t), \dot{\mathbf{q}}(t)) = \mathbf{C}_m(\mathbf{q}(t), \dot{\mathbf{q}}(t))\dot{\mathbf{q}}(t)$ and the nonlinear term $\mathbf{f}(t)$ can be defined as

$$\begin{aligned} \mathbf{f}(t) &= \mathbf{M}(\mathbf{q}(t))(\ddot{\mathbf{q}}_d(t) + \boldsymbol{\Lambda}\dot{\mathbf{e}}(t)) + \mathbf{G}(\mathbf{q}(t)) + \\ &\quad \mathbf{C}_m(\mathbf{q}(t), \dot{\mathbf{q}}(t))(\dot{\mathbf{q}}_d(t) + \boldsymbol{\Lambda}\mathbf{e}(t)) + \boldsymbol{\tau}_{dis}, \\ &= \mathbf{Y}\boldsymbol{\pi}. \end{aligned} \tag{30}$$

Here, $\boldsymbol{\tau}_{dis}$ is the unknown disturbance. $\mathbf{Y}$ is a regression matrix of known robot functions and $\boldsymbol{\pi}$ is a vector of unknown parameters Lewis et al. (1999). The regression matrix $\mathbf{Y}$ and the unknown parameter vector $\boldsymbol{\pi}$ of two-link thumb and three-link index finger are given in Appendix Chen (2009). The torque vector $\boldsymbol{\tau}(t)$ can be calculated by

$$\boldsymbol{\tau}(t) = \mathbf{f}(t) + \mathbf{K_D}\mathbf{r}(t). \tag{31}$$

The unknown parameter rate vector $\dot{\boldsymbol{\pi}}$ can be updated by

$$\dot{\boldsymbol{\pi}} = \boldsymbol{\Gamma}^{-1}\mathbf{Y}'\mathbf{r}(t) \tag{32}$$

where $\boldsymbol{\Gamma}$ is a tuning parameter diagonal matrix.

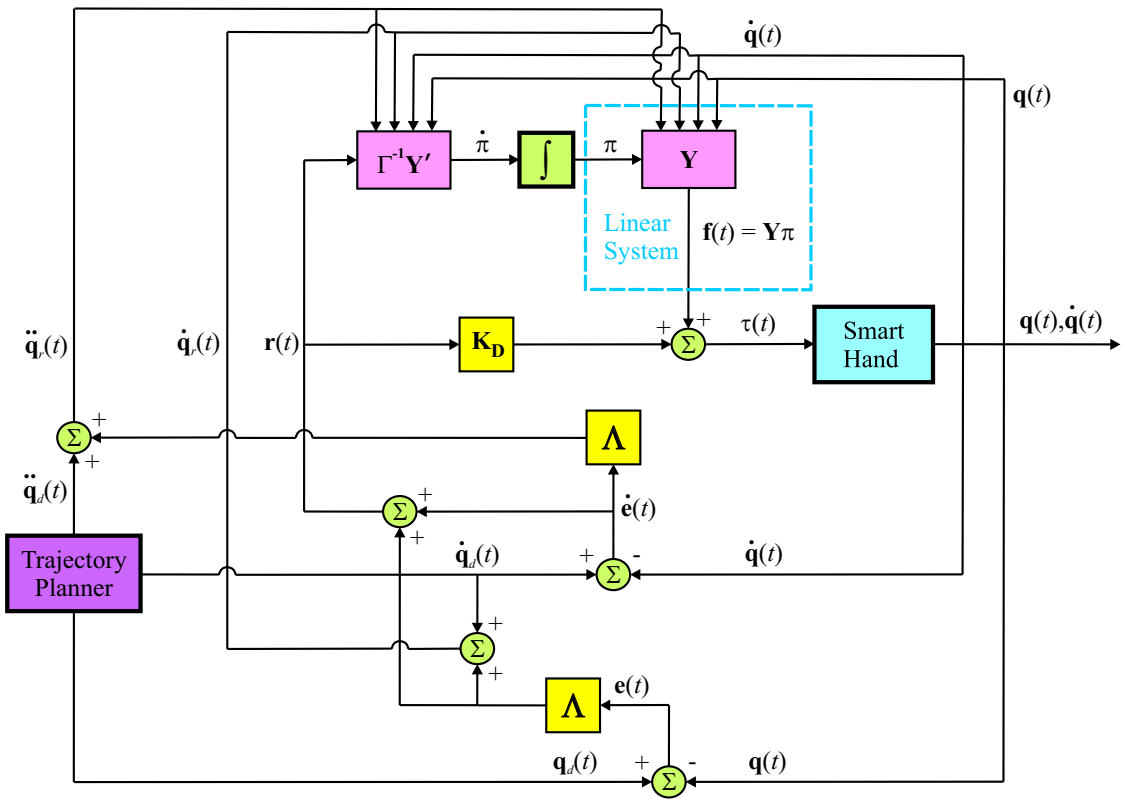

Figure 5: Block Diagram of Adaptive Control Technique

Finite-Time Linear Quadratic Optimal Control

Figure 6 shows the block diagram of finite-time linear quadratic optimal controller for prosthetic hand. For the linear system (26), we can formulate the well-known finite-time linear quadratic optimal control problem by defining a performance index J Naidu (2003) such as

$$\begin{aligned} J &= \frac{1}{2}\mathbf{x}'(t_f)\mathbf{F}(t_f)\mathbf{x}(t_f) \\ &\quad + \frac{1}{2}\int_{t_0}^{t_f} \left[\mathbf{x}'(t)\mathbf{Q}(t)\mathbf{x}(t) + \mathbf{u}'(t)\mathbf{R}(t)\mathbf{u}(t)\right] dt \end{aligned} \tag{33}$$

where the terminal cost matrix $\mathbf{F}(t_f)$ and the error weighted matrix $\mathbf{Q}(t)$ are positive *semidefinite* matrices, respectively; the control weighted matrix $\mathbf{R}(t)$ is a positive *definite* matrix. The optimal control $\mathbf{u}^*(t)$ is given by

$$\mathbf{u}^*(t) = -\mathbf{R}^{-1}(t)\mathbf{B}'\mathbf{P}(t)\mathbf{x}^*(t) = -\mathbf{K}(t)\mathbf{x}^*(t). \tag{34}$$

Here, $\mathbf{K}(t) = \mathbf{R}^{-1}(t)\mathbf{B}'\mathbf{P}(t)$ is called *Kalman gain* and $\mathbf{P}(t)$, the symmetric *positive definite* matrix (for all $t \in [t_0, t_f]$), is the solution of the matrix differential Riccati equation (DRE)

$$\dot{\mathbf{P}}(t) = -\mathbf{P}(t)\mathbf{A} - \mathbf{A}'\mathbf{P}(t) - \mathbf{Q}(t) + \mathbf{P}(t)\mathbf{B}\mathbf{R}^{-1}(t)\mathbf{B}'\mathbf{P}(t) \tag{35}$$

satisfying the *final* condition

$$\mathbf{P}(t = t_f) = \mathbf{F}(t_f). \tag{36}$$

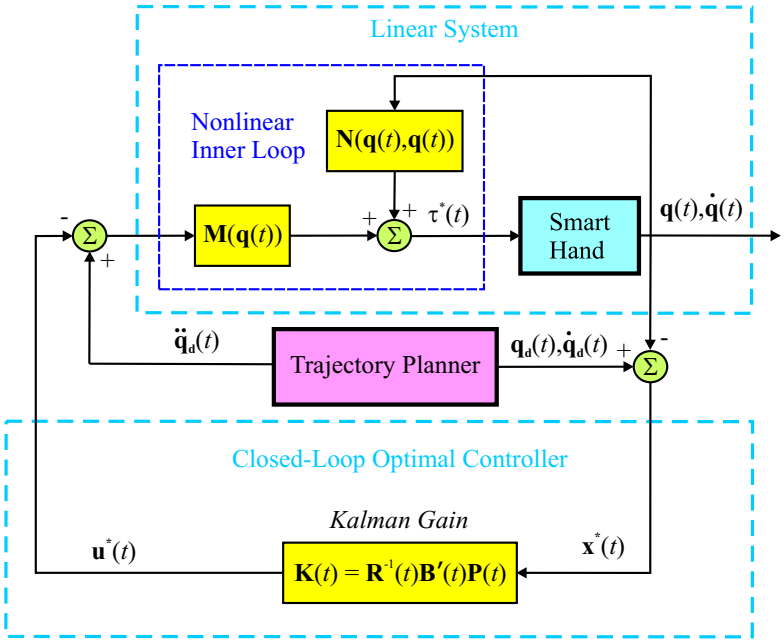

Figure 6: Block Diagram of Hybrid Optimal Controller for Prosthetic Hand

The optimal state $\mathbf{x}^*$ is the solution of

$$\dot{\mathbf{x}}^*(t) = \left[\mathbf{A} - \mathbf{B}\mathbf{R}^{-1}(t)\mathbf{B}'\mathbf{P}(t)\right]\mathbf{x}^*(t). \tag{37}$$

Therefore, the required torque $\boldsymbol{\tau}^*(t)$ can be calculated by the optimal control $\mathbf{u}^*(t)$.

$$\boldsymbol{\tau}^*(t) = \mathbf{M}(\mathbf{q}(t))(\ddot{\mathbf{q}}_d(t) - \mathbf{u}^*(t)) + \mathbf{N}(\mathbf{q}(t), \dot{\mathbf{q}}(t)). \tag{38}$$

The Stability of Finite-Time Optimal Control

Our previous work Chen (2009); Chen et al. (2009b,c) shows optimal control can avoid overshooting and get better results than PID control, but the regular optimal control takes time to be convergent. To study the convergent stability of the optimal control, we modify the performance index J Naidu (2003) as

$$\begin{aligned} J &= \frac{1}{2}\mathbf{x}'(t_f)\mathbf{F}(t_f)\mathbf{x}(t_f) + \\ &\quad \frac{1}{2}\int_{t_0}^{t_f} e^{2\alpha t}\left[\mathbf{x}'(t)\mathbf{Q}(t)\mathbf{x}(t) + \mathbf{u}'(t)\mathbf{R}(t)\mathbf{u}(t)\right]dt, \end{aligned} \tag{39}$$

where α is a positive parameter. To find the optimal control which minimizes the performance index (39) under the dynamical constraint (26). This problem can be solved by changing the previous system, so the following transformations can be developed as

$$\hat{\mathbf{x}}(t) = e^{\alpha t}\mathbf{x}(t); \quad \hat{\mathbf{u}}(t) = e^{\alpha t}\mathbf{u}(t). \tag{40}$$

Then, using the transformations (40), it is easy to see that the *modified* system becomes

$$\begin{aligned}\dot{\hat{\mathbf{x}}}(t) = \frac{d}{dt}\{e^{\alpha t}\mathbf{x}(t)\} &= \alpha e^{\alpha t}\mathbf{x}(t) + e^{\alpha t}\dot{\mathbf{x}}(t) \\ &= \alpha\hat{\mathbf{x}}(t) + e^{\alpha t}[\mathbf{A}\mathbf{x}(t) + \mathbf{B}\mathbf{u}(t)] \\ \dot{\hat{\mathbf{x}}}(t) &= (\mathbf{A} + \alpha\mathbf{I})\hat{\mathbf{x}}(t) + \mathbf{B}\hat{\mathbf{u}}(t). \end{aligned} \tag{41}$$

Considering the minimization of the modified system (41) and the performance index (39), we see that the optimal control Naidu (2003) is given by

$$\hat{\mathbf{u}}^*(t) = -\mathbf{R}^{-1}\mathbf{B}'\bar{\mathbf{P}}\hat{\mathbf{x}}^*(t) = -\bar{\mathbf{K}}\hat{\mathbf{x}}^*(t), \tag{42}$$

where $\bar{\mathbf{K}} = \mathbf{R}^{-1}\mathbf{B}'\bar{\mathbf{P}}$ and the matrix $\bar{\mathbf{P}}$ is the positive definite, symmetric solution of the algebraic Riccati equation

$$\bar{\mathbf{P}}(\mathbf{A} + \alpha\mathbf{I}) + (\mathbf{A}' + \alpha\mathbf{I})\bar{\mathbf{P}} - \bar{\mathbf{P}}\mathbf{B}\mathbf{R}^{-1}\mathbf{B}'\bar{\mathbf{P}} + \mathbf{Q} = 0. \tag{43}$$

Using the optimal control (42) in the modified system (41), we get the optimal closed-loop system as

$$\dot{\hat{\mathbf{x}}}^*(t) = (\mathbf{A} + \alpha\mathbf{I} - \mathbf{B}\mathbf{R}^{-1}\mathbf{B}'\bar{\mathbf{P}})\hat{\mathbf{x}}^*(t). \tag{44}$$

Hence, applying the transformations (41) in the modified system (42), the optimal control of the original system (26) and the associated performance measure (39) is given by

$$\begin{aligned}\mathbf{u}^*(t) &= e^{-\alpha t}\hat{\mathbf{u}}^*(t) = -e^{-\alpha t}\mathbf{R}^{-1}\mathbf{B}'\bar{\mathbf{P}}e^{\alpha t}\mathbf{x}^*(t) \\ &= -\mathbf{R}^{-1}\mathbf{B}'\bar{\mathbf{P}}\mathbf{x}^*(t) = -\bar{\mathbf{K}}\mathbf{x}^*(t). \end{aligned} \tag{45}$$

We see that the closed-loop optimal control system (44) has eigenvalues with real parts less than $-\alpha$. In other words, the state $\mathbf{x}^*(t)$ approaches zero at least as fast as $e^{-\alpha t}$.

GA-Based PID Hybrid Control

Figure 7 shows the block diagram of a hybrid GA-based PID controller for the presented five-fingered prosthetic hand with control signal as

$$\mathbf{u}(t) = -\mathbf{K_P}\mathbf{e}(t) - \mathbf{K_I}\int \mathbf{e}(t)dt - \mathbf{K_D}\dot{\mathbf{e}}(t) \tag{46}$$

with the proportional $\mathbf{K_P}$, integral $\mathbf{K_I}$, and derivative $\mathbf{K_D}$ diagonal gain matrices. We then rewrite (24) as

$$\begin{aligned}\boldsymbol{\tau}(t) &= \mathbf{M}(\mathbf{q}(t))[\ddot{\mathbf{q}}_d(t) + \mathbf{K_P}\mathbf{e}(t) + \mathbf{K_I}\int \mathbf{e}(t)dt \\ &\quad + \mathbf{K_D}\dot{\mathbf{e}}(t)) + \mathbf{N}(\mathbf{q}(t), \dot{\mathbf{q}}(t)]. \end{aligned} \tag{47}$$

Then we use GA to tune all gain coefficients $\mathbf{K_P}$, $\mathbf{K_D}$ and $\mathbf{K_D}$ of PID controller. Figure 8 shows the flowchart of GA and the procedure is briefly stated below.

1. Define the GA parameters: include initial population, population at the end of the first generation, number of chromosomes kept for mating, mutation rate, and tolerance ϵ so on.

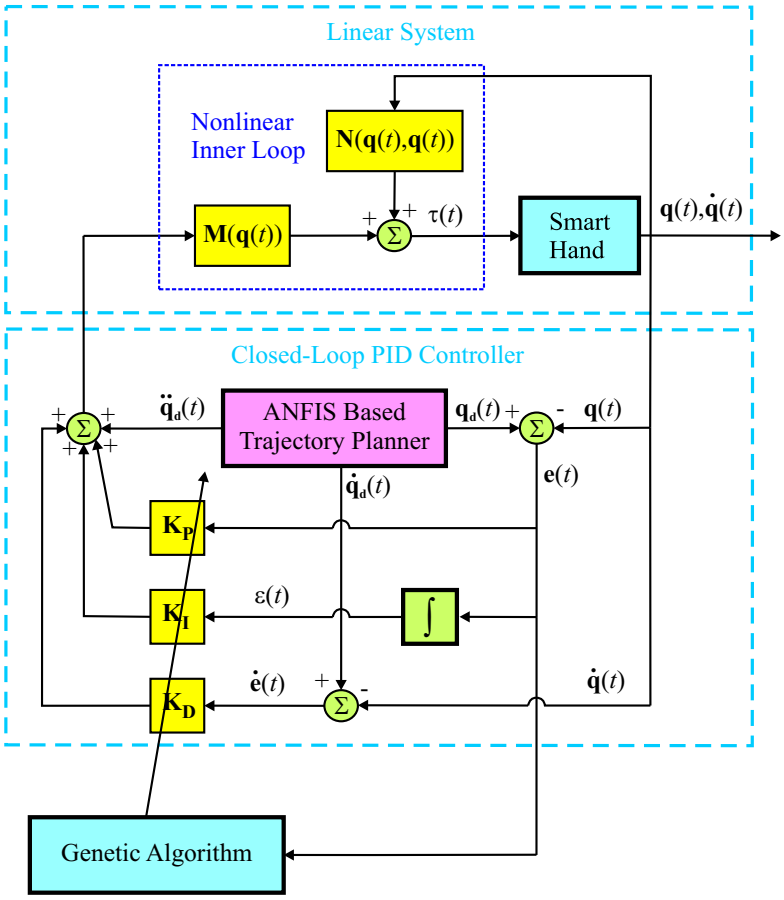

Figure 7: Block Diagram of the Hybrid GA-Based PID Controller for 14-DOF Five-Fingered Prosthetic Hand

2. Create a homogeneous population: generate N elements (chromosomes) and N is the initial population.

3. Evaluate cost (fitness) function of each chromosome: calculate the fitness value of the ith member in the population.

4. Select mate based on the performance of each gene: create a new population from the current population based on the ranking of the current fitness value, e.g. determine which parents participate in producing offspring for the next generation.

5. Reproduce the generation by crossover: use the single or multiple crossover points to generate new chromosomes that retain the good feature and discard the bad feature.

6. Mutate: utilize the mutation rate which can randomly mutate the gene to avoid falling into the local minima area.

7. Repeat steps 3 to 6 until it reaches the maximum number of iterations or stopping condition defined by ϵ is satisfied.

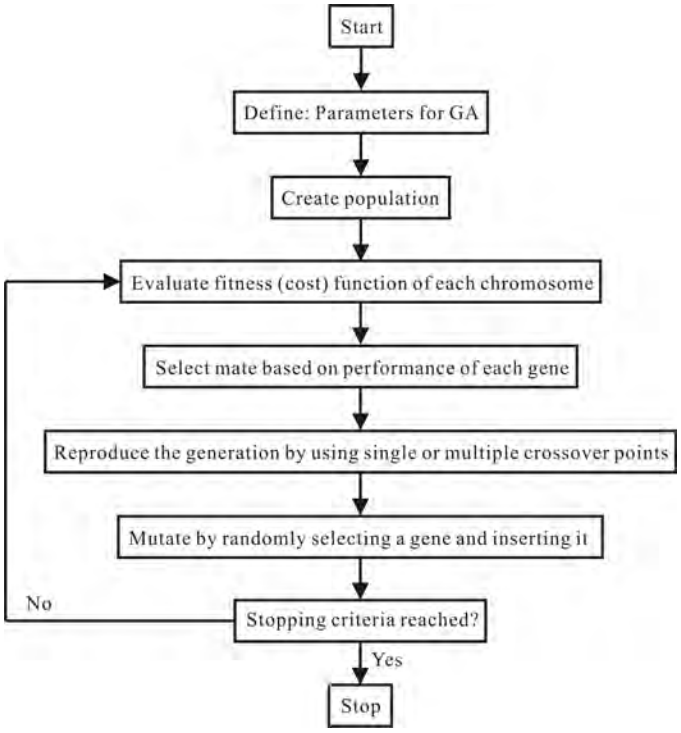

Figure 8: The Flowchart of Genetic Algorithm (GA)

Fuzzy Logic-Based PD Hybrid Control

Figure 9 shows the block diagram of the hybrid fuzzy logic-based PD controller for the presented five-fingered prosthetic hand with control signal as

$$\mathbf{u}(t) = -\mathbf{K_P}(t)\mathbf{e}(t) - \mathbf{K_D}(t)\dot{\mathbf{e}}(t) \tag{48}$$

with the proportional $\mathbf{K_P}(t)$ and derivative $\mathbf{K_D}(t)$ diagonal gain matrices with time varying. We then rewrite (24) as

$$\begin{aligned} \boldsymbol{\tau}(t) &= \mathbf{M}(\mathbf{q}(t))[\ddot{\mathbf{q}}_d(t) + \mathbf{K_P}(t)\mathbf{e}(t) + \mathbf{K_D}(t)\dot{\mathbf{e}}(t)) + \\ &\quad \mathbf{N}(\mathbf{q}(t), \dot{\mathbf{q}}(t)]. \end{aligned} \tag{49}$$

Then we use mamdani fuzzy inference system to tune the time-varying parameters $\mathbf{K_P}(t)$ and $\mathbf{K_D}(t)$ of PD controller. Figure 10 shows the structural characteristics of proposed fuzzy inference system, which includes two inputs (error $\mathbf{e}$ and error change $\dot{\mathbf{e}}$) on the left and one output ($\mathbf{K_P}$) on the right. Each input or output layer contains seven triangular membership functions as shown in Figure 11 and 49 logic rules as listed in Table 2. After using 49 logic rules, the output surface $\mathbf{K_P}$ of fuzzy inference system is generated as shown in Figure 12. Similarly, $\mathbf{K_D}$ can be computed by the same way.

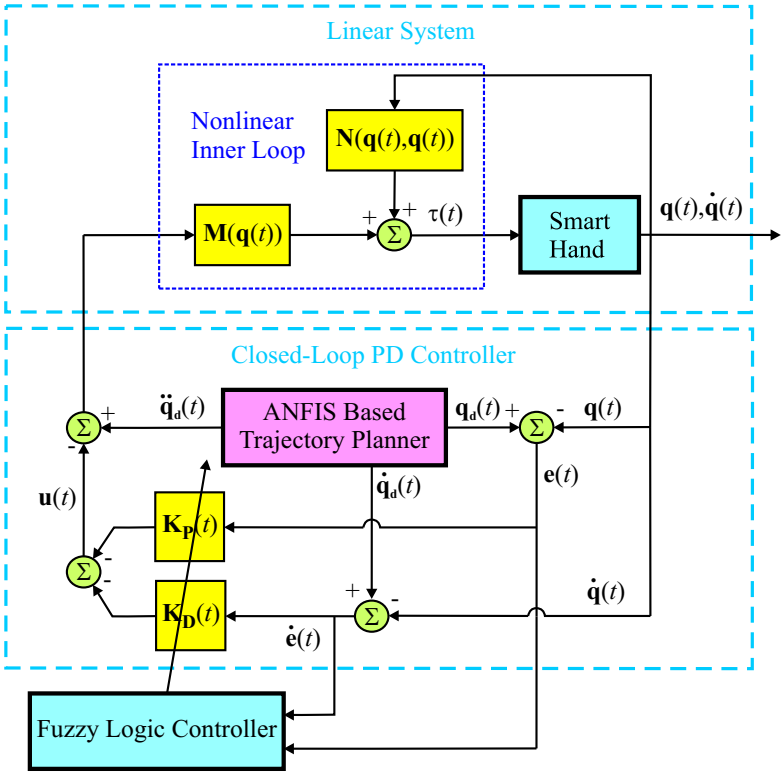

Figure 9: Block Diagram of the Presented Hybrid Fuzzy Logic-Based Proportional-Derivative (PD) Controller for a Five-Fingered Prosthetic Hand: Errors and error changes are calculated by actual and desired angles, which are based on adaptive neuro-fuzzy inference system (ANFIS) trajectory planner. Then fuzzy logic controller tunes all parameters of closed-loop PD control so that the required torque of the prosthetic hand nonlinear system is computed by control input.

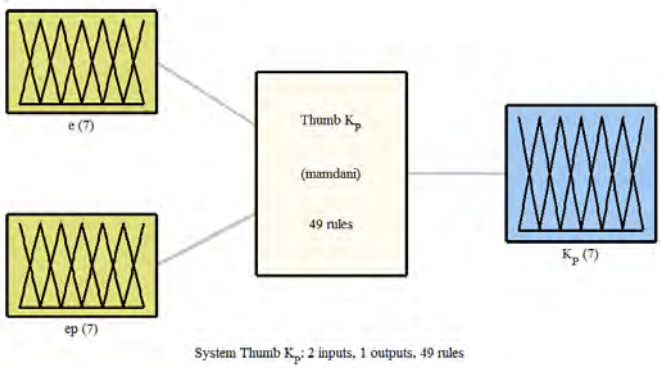

Figure 10: The Structural Characteristics of Proposed Fuzzy Inference System: Two inputs (error $\mathbf{e}$ and error change $\dot{\mathbf{e}}$) on the left and one output (tuned $\mathbf{K_P}$) on the right with 49 logic rules

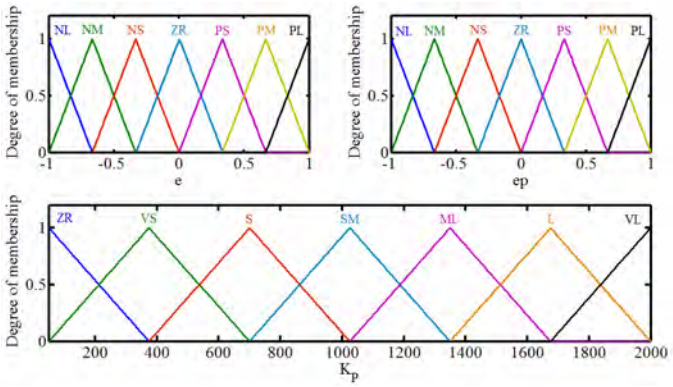

Figure 11: All Membership Functions: Each of Two Inputs (Upper Panel) and One Output (Lower Panel) Uses 7 Triangular Membership Functions

Table 2: A Complete Fuzzy Logic Rule Base

ė\e	**NL**	**NM**	**NS**	**ZR**	**PS**	**PM**	**PL**
NL	ZR	ZR	ZR	ZR	VS	S	SM
NM	ZR	ZR	ZR	VS	S	SM	ML
NS	ZR	ZR	VS	S	SM	ML	L
ZR	ZR	VS	S	SM	ML	L	VL
PS	VS	S	SM	ML	L	VL	VL
PM	S	SM	ML	L	VL	VL	VL
PL	SM	ML	L	VL	VL	VL	VL

N: negative; P: positive; ZR: zero; L: large; M: medium; S: small; V: very

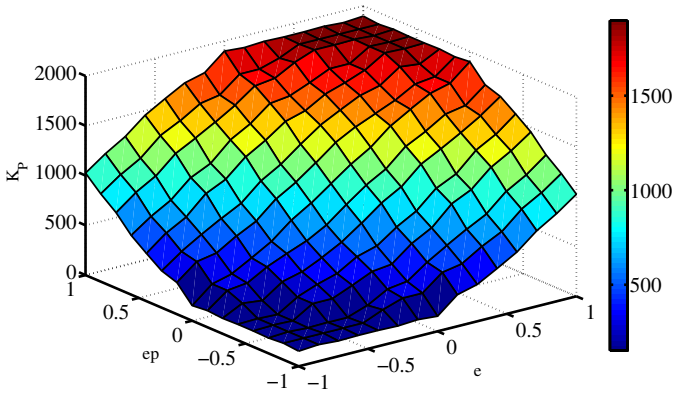

Figure 12: The Output Surface of Fuzzy Inference System with Two Inputs and 49 Logic Rules

Simulation Results and Discussion

Adaptive Control

Figure 13 shows that five-fingered prosthetic hand with 14 DOFs is reaching a rectangular rod in

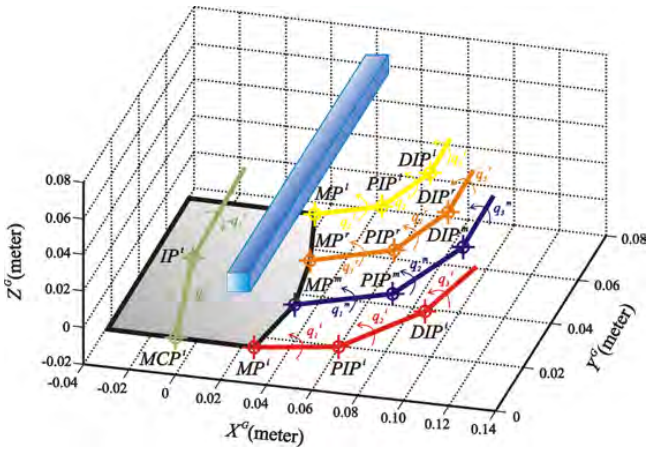

Figure 13: Five-Finger Prosthetic Hand Reaching a Rectangular Rod

order to grasp the object. When thumb and the other four fingers are performing extension/flexion movements, the workspace of fingertips is restricted to the maximum angles of joints. Referring to inverse kinematics, the first and second joint angles of the thumb fingertip are constrained in the ranges of [0,90] and [-80,0] (degrees). The first, second, and third joint angles of the other four fingers are constrained in the ranges of [0,90], [0,110] and [0,80] (degrees), respectively Lavangie and Norkin (2001).

Next, we present simulations with an adaptive controller for the 14 DOFs five-fingered smart prosthetic hand. The parameters of the two-link thumb/three-link fingers Arimoto (2008) were related to desired trajectory. All parameters of the smart prosthetic hand selected for the simulations are given in Table 3 and the side length and length of the target rectangular rod are 0.010 and 0.100 (m), respectively. All initial actual angles are zero. The relating parameters between the global coordinate and the local coordinates are defined in Table 4. Besides, in this work, we assumed that each link of all fingers is a circular cylinder with the radius (R) 0.010 (m), so the inertia I^j_{zzk} of each link k of all fingers j ($= t$, i, m, r and l) can be calculated as

$$I^j_{zzk} = \frac{1}{4} m^j_k R^2 + \frac{1}{3} m^j_k {L^j_k}^2. \tag{50}$$

Figure 14, Figure 16, Figure 18, Figure 20 and Figure 22 show the tracking errors of thumb, index, middle, ring, and little fingers for the proposed five-fingered smart prosthetic hand, respectively. Figure 15, Figure 17, Figure 19, Figure 21 and Figure 23 show the desired/actual angles of thumb, index, middle, ring, and little fingers for the proposed five-fingered smart prosthetic hand, respectively. The observation that all tracking errors dramatically drop within one second and are less than one degree after convergence provides the evidence that the adaptive controller for the 14-DOFs prosthetic hand enhances performance. The other observation that after convergence, all three-link fingers show more unstable errors than two-link thumb suggests that the more DOFs increase the difficulty of the adaptive controller without knowing the mass and inertia of the links of all fingers.

Table 3: Parameter Selection of the Smart Hand

Parameters	Values
Thumb	
Time (t_0,t_f)*	0, 20 (sec)
Desired Initial Position (X_0^t,Y_0^t)**	0.035, 0.060 (m)
Desired Final Position (X_f^t,Y_f^t)**	0.0495, 0.060 (m)
Desired Initial Velocity ($\dot{X}_0^t$,$\dot{Y}_0^t$)*	0, 0 (m/s)
Desired Final Velocity ($\dot{X}_f^t$,$\dot{Y}_f^t$)*	0, 0 (m/s)
Length (L_1^t,L_2^t)	0.040, 0.040 (m)
Mass (m_1^t,m_2^t)	0.043, 0.031 (kg)
Index Finger	
Desired Initial Position (X_0^i,Y_0^i)**	0.065, 0.080 (m)
Desired Final Position (X_f^i,Y_f^i)**	0.010, 0.060 (m)
Length (L_1^i,L_2^i,L_3^i)	0.040, 0.040, 0.030 (m)
Mass (m_1^i,m_2^i,m_3^i)	0.045, 0.025, 0.017 (kg)
Middle Finger	
Desired Initial Position (X_0^m,Y_0^m)**	0.065, 0.080 (m)
Desired Final Position (X_f^m,Y_f^m)**	0.005, 0.060 (m)
Length (L_1^m,L_2^m,L_3^m)	0.044, 0.044, 0.033 (m)
Mass (m_1^m,m_2^m,m_3^m)	0.050, 0.028, 0.017 (kg)
Ring Finger	
Desired Initial Position (X_0^r,Y_0^r)**	0.065, 0.080 (m)
Desired Final Position (X_f^r,Y_f^r)**	0.010, 0.060 (m)
Length (L_1^r,L_2^r,L_3^r)	0.040, 0.040, 0.030 (m)
Mass (m_1^r,m_2^r,m_3^r)	0.041, 0.023, 0.014 (kg)
Little Finger	
Desired Initial Position (X_0^l,Y_0^l)**	0.055, 0.080 (m)
Desired Final Position (X_f^l,Y_f^l)**	0.020, 0.060 (m)
Length (L_1^l,L_2^l,L_3^l)	0.036, 0.036, 0.027 (m)
Mass (m_1^l,m_2^l,m_3^l)	0.041, 0.023, 0.014 (kg)

*All fingers use same parameters

**All parameters are in local coordinates

Table 4: Parameter Selection of Conversion between Global and Local Coordinates

Parameters	Values
Rotating α	90 (deg)
Rotating β	45 (deg)
Translating $\mathbf{d^i}$	(0.035, 0, 0) (m)
Translating $\mathbf{d^m}$	(0.040, 0, -0.020) (m)
Translating $\mathbf{d^r}$	(0.035, 0, -0.040) (m)
Translating $\mathbf{d^l}$	(0.025, 0, -0.060) (m)

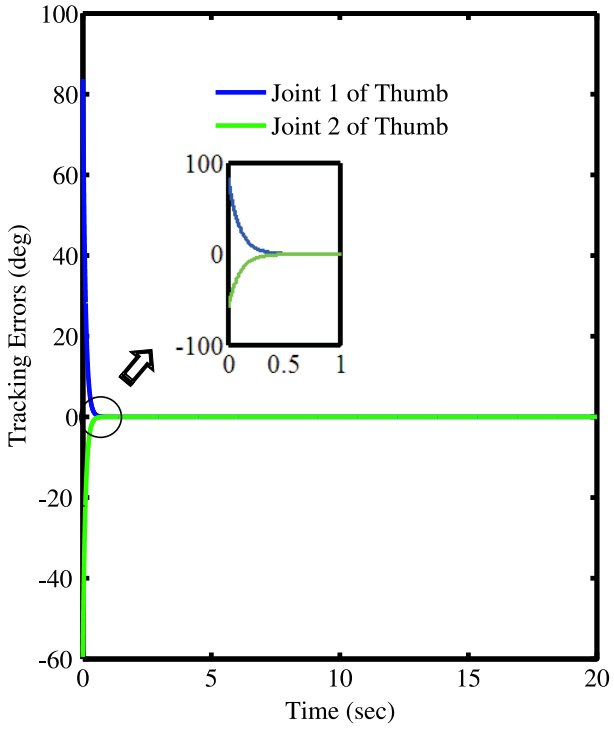

Figure 14: Tracking Errors of Adaptive Controller for Two-Link Thumb

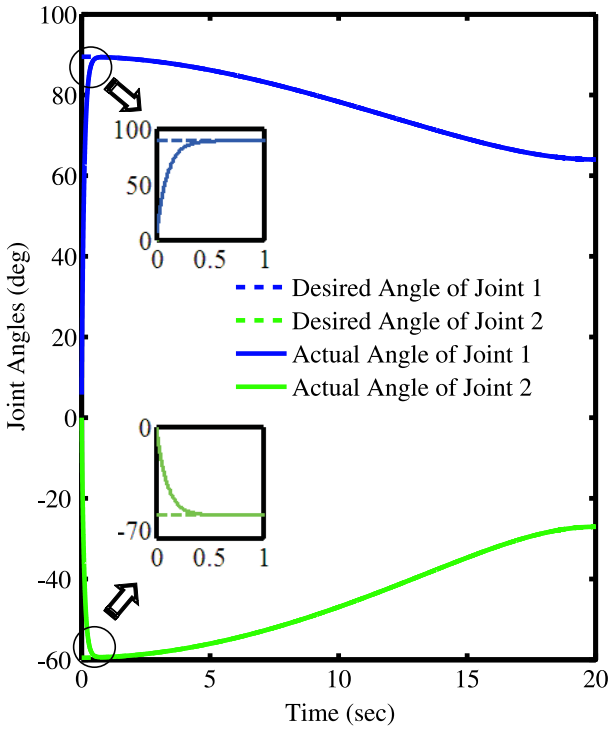

Figure 15: Tracking Angles of Adaptive Controller for Two-Link Thumb

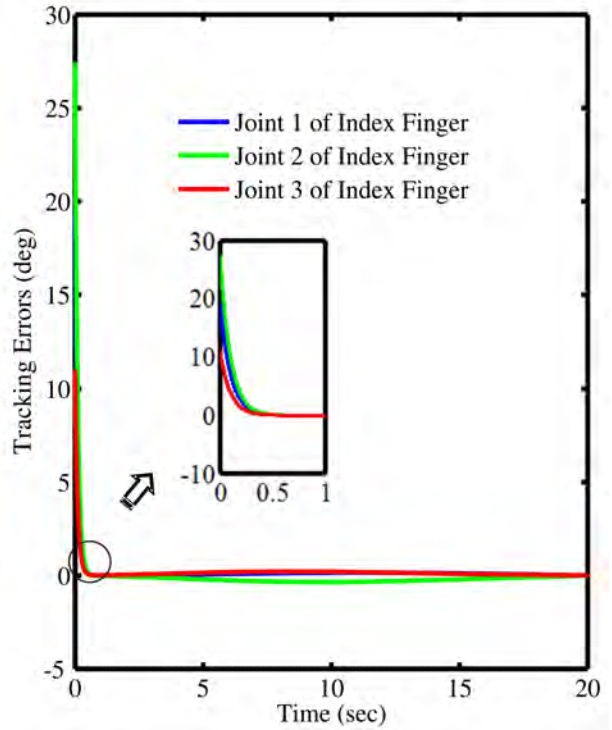

Figure 16: Tracking Errors of Adaptive Controller for Three-Link Index Finger

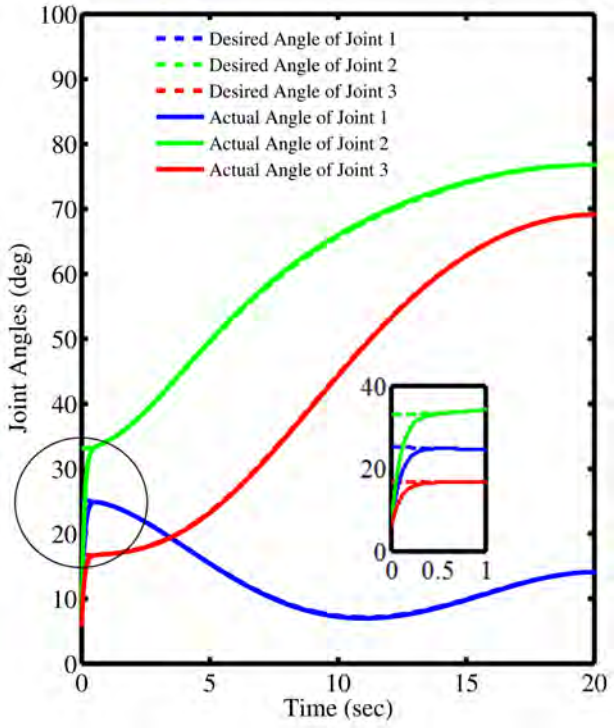

Figure 17: Tracking Angles of Adaptive Controller for Three-Link Index Finger

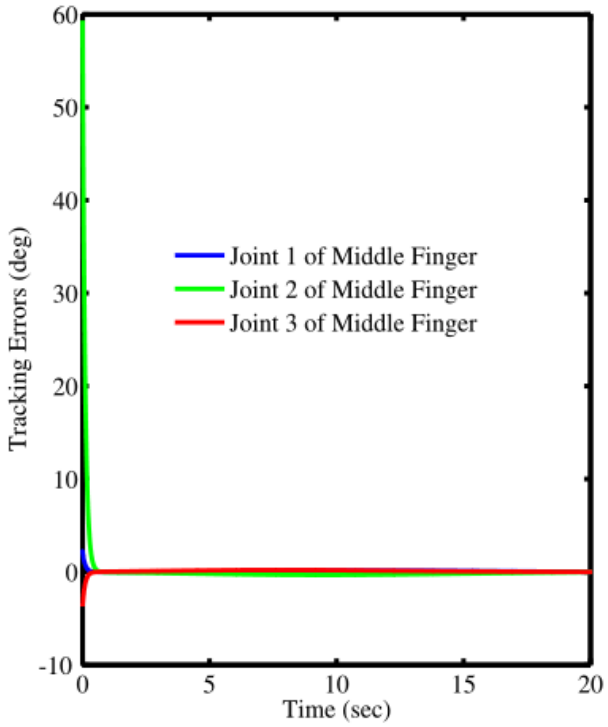

Figure 18: Tracking Errors of Adaptive Controller for Three-Link Middle Finger

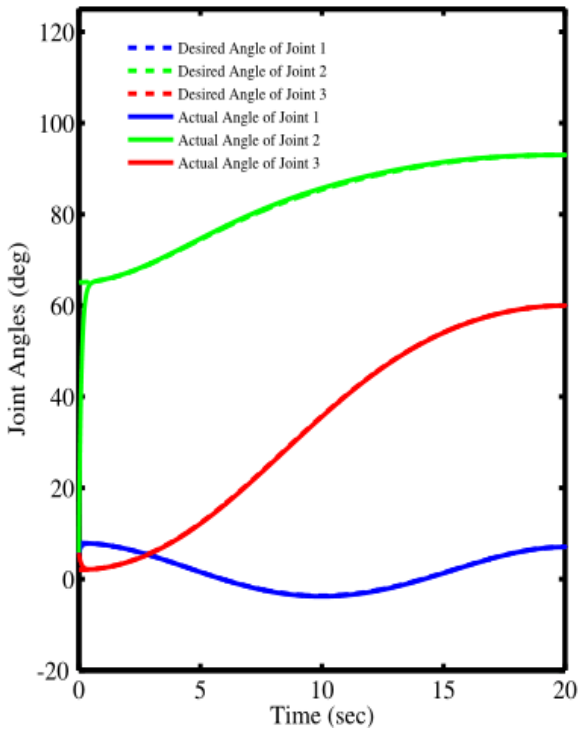

Figure 19: Tracking Angles of Adaptive Controller for Three-Link Middle Finger

Optimal Control

Referring to inverse kinematics, Figure 24 exhibits that the fingertip workspace of the thumb and index finger. We present simulations with the stability of optimal controller for the two-link thumb and three-link index finger of a smart prosthetic hand. All used parameters are the same to our previous work Chen et al. (2009c). The initial and final orientation ϕ_0 and ϕ_f are 75 and 160 degrees, respectively. Figure 25 displays the tracking errors and desired/actual angles of thumb for the smart prosthetic hand by using the presented optimal controller with the stability ($\alpha = 0$, 0.1, and 1). Figure 26 to Figure 28 are the tracking errors and desired/actual angles of index finger for the smart prosthetic hand ($\alpha = 0$, 1, and 10). To compare with the original system ($\alpha = 0$), these results demonstrate that the presented optimal controller behaves fast convergent and accurate as the stability α increases. For the three-link index finger, we design the orientation ϕ to calculate the angular positions via inverse kinematics. To compare with our previous works Chen (2009); Chen et al. (2009b,c,a) by using adaptive neuro-fuzzy inference system (ANFIS) and genetic algorithm (GA), the simulations show that the presented method is not time consuming.

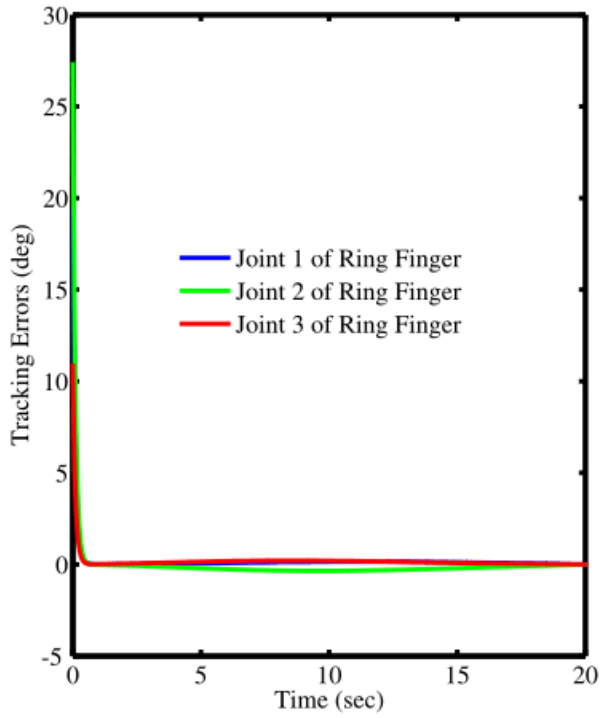

Figure 20: Tracking Errors of Adaptive Controller for Three-Link Ring Finger

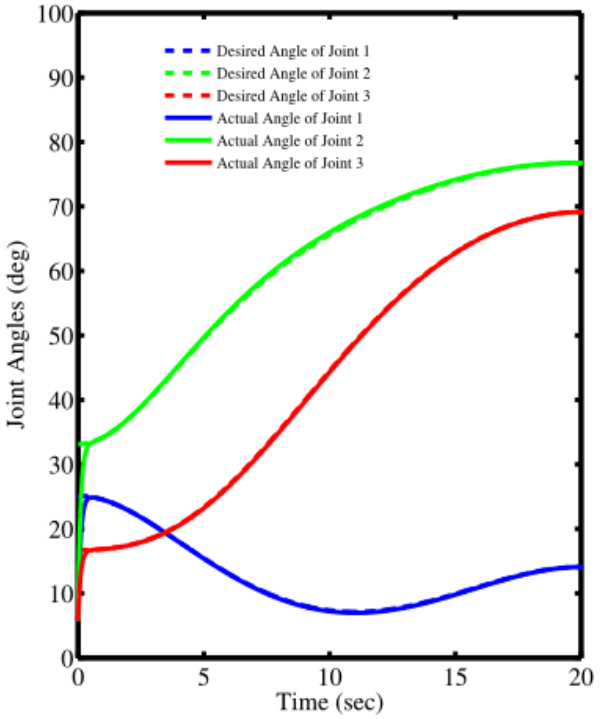

Figure 21: Tracking Angles of Adaptive Controller for Three-Link Ring Finger

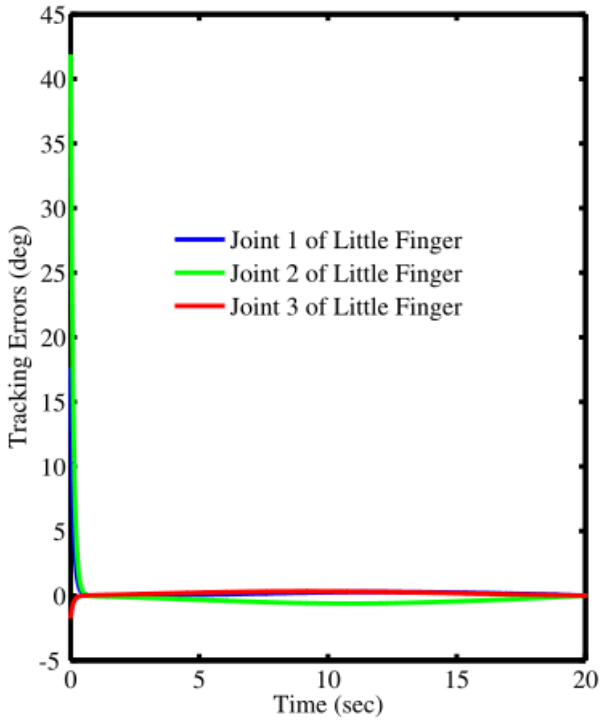

Figure 22: Tracking Errors of Adaptive Controller for Three-Link Little Finger

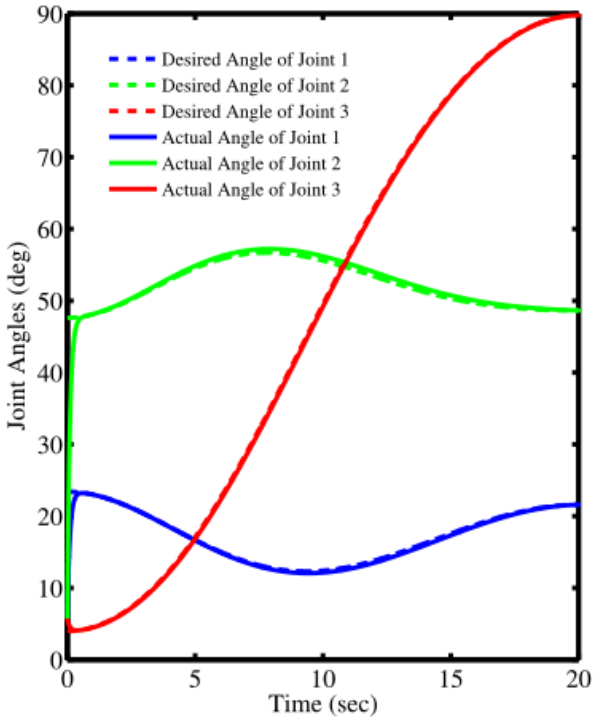

Figure 23: Tracking Angles of Adaptive Controller for Three-Link Little Finger

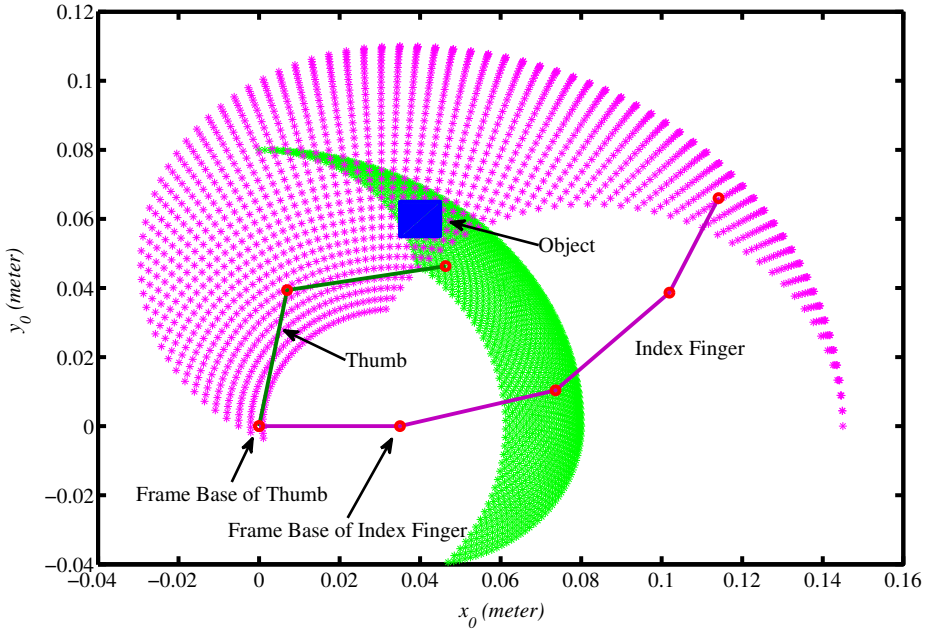

Figure 24: The Fingertip Workspace of Thumb and Index Finger and a Square Object

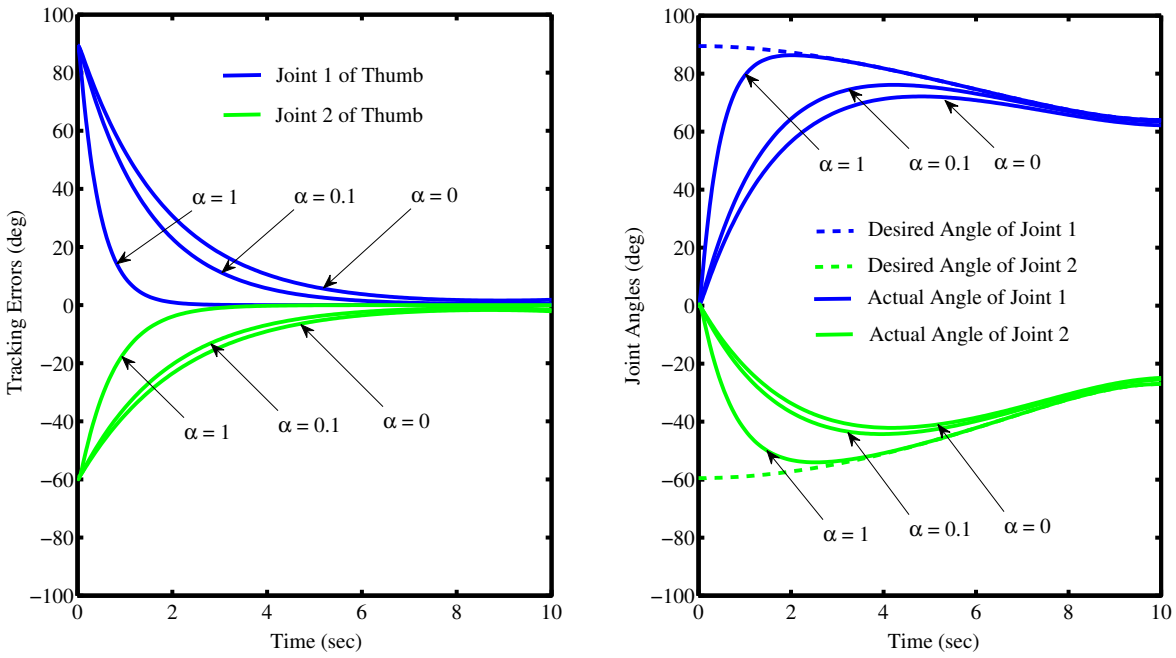

Figure 25: Tracking Errors (left) and Joint Angles (right) of Thumb for Optimal Control with the Stability ($\alpha = 0$, 0.1, and 1)

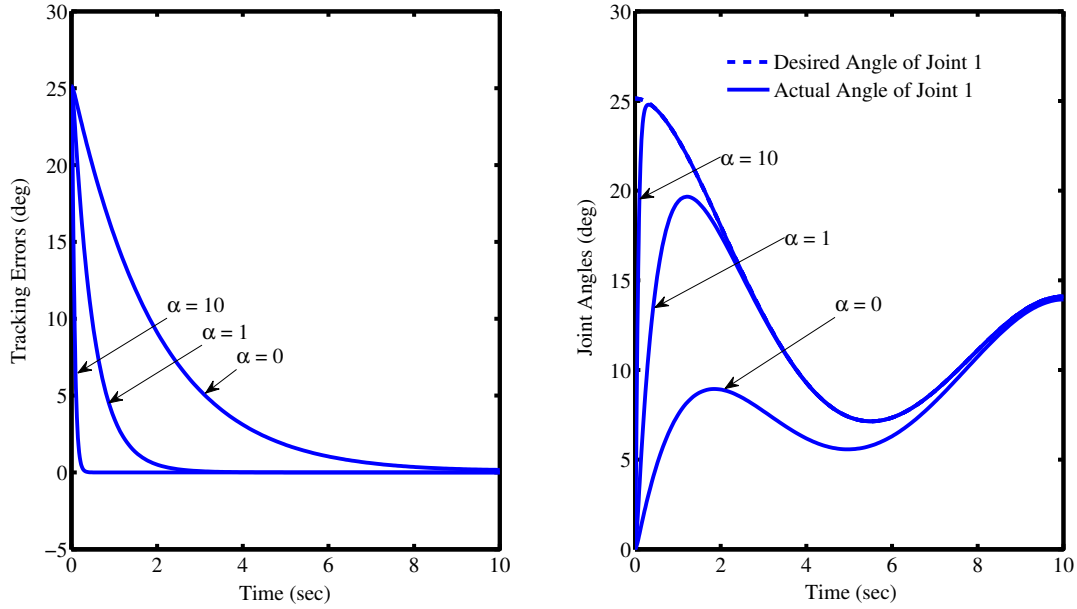

Figure 26: Tracking Errors (left) and Joint 1 Angles q_1^i (right) of Index Finger for Optimal Control with the Stability ($\alpha = 0$, 1, and 10)

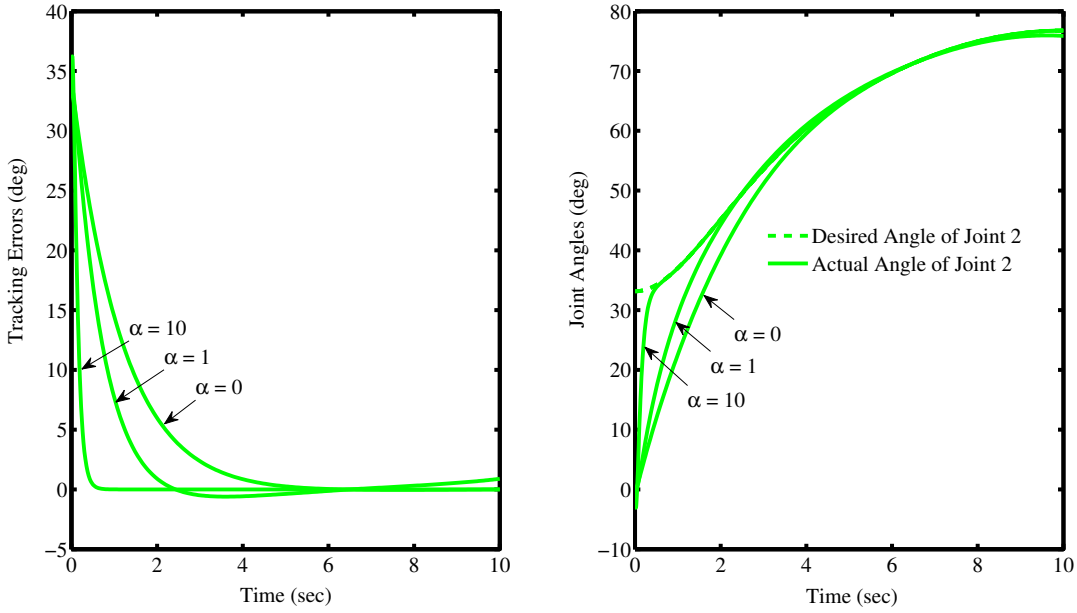

Figure 27: Tracking Errors (left) and Joint 2 Angles q_2^i (right) of Index Finger for Optimal Control with the Stability ($\alpha = 0$, 1, and 10)

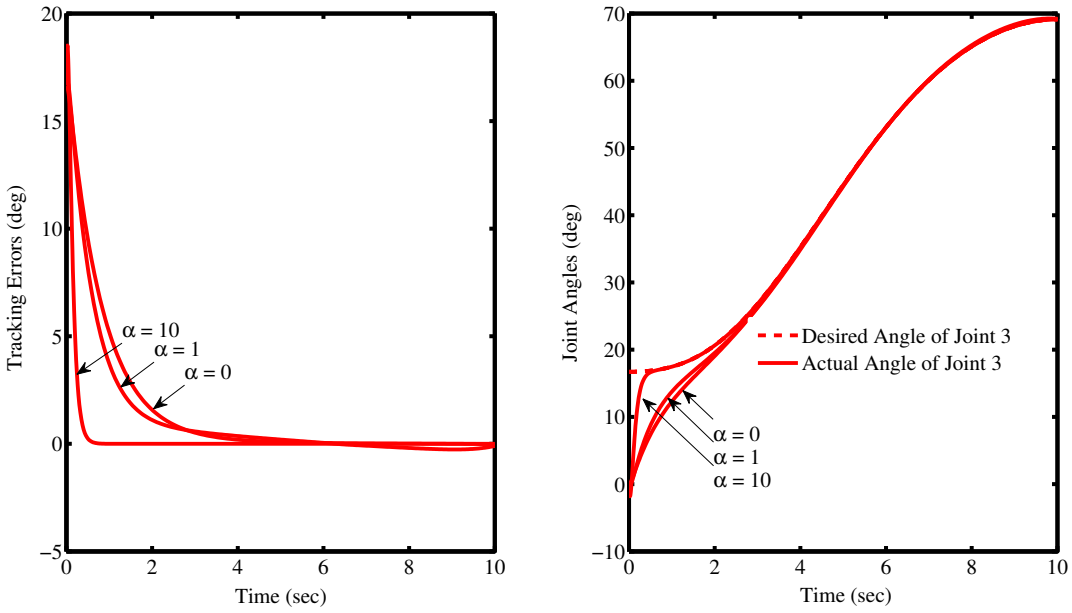

Figure 28: Tracking Errors (left) and Joint 3 Angles q_3^i (right) of Index Finger for Optimal Control with the Stability ($\alpha = 0$, 1, and 10)

GA-Based PID Hybrid Control

We present simulations with a PID controller and GA-tuned PID controller for the 14 DOFs five-fingered smart prosthetic hand grasping a rectangular object as shown in Figure 13. All parameters of the smart prosthetic hand selected for the simulations are the same as our previous works Chen et al. (2009b, 2010). All initial actual angles are zero and the diagonal coefficients, $\mathbf{K_P}$, $\mathbf{K_I}$ and $\mathbf{K_D}$, for the PID controller alone are arbitrarily chosen as 100. From the derived dynamic and control models, after the parameters ($\mathbf{K_P}$, $\mathbf{K_I}$ and $\mathbf{K_D}$) are determined, the torque matrix $\boldsymbol{\tau}$ can be computed, and then the squared-tracking errors $e_i^j(t)$ of the joint i of the finger j are obtained. Therefore, the total error $E(t)$, which is a time-dependent function, can be described as

$$E(t) = \int_{t_0}^{t_f} (e_i^j(t))^2 dt, \tag{51}$$

where t_0 and t_f are initial and terminal time, respectively. The tuned diagonal parameters ($\mathbf{K_P}$, $\mathbf{K_I}$ and $\mathbf{K_D}$) and the total error $E(t)$ of PID controller by GA are listed in Table 5. To study

Table 5: Parameter Selection of GA-Tuned PID Controller and Computed Total Errors

		Input		**Output**
Fingers	$\mathbf{K_P}$	$\mathbf{K_I}$	$\mathbf{K_D}$	$E(t)$
Case I	[976,956]	[779,279]	[170,236]	0.3107
Case II	[988,999]	[78,848]	[80,109]	0.1557
Case III	[199,198]	[127,157]	[104,102]	0.8100
Index	[794,398,960]	[960,918,914]	[15,59,242]	0.0465
Middle	[794,398,960]	[960,918,914]	[15,59,242]	0.1003
Ring	[794,398,960]	[960,918,914]	[15,59,242]	0.0465
Little	[794,398,960]	[960,918,914]	[15,59,242]	0.0607

whether the tuned parameter range influences total tracking errors, we design three different cases with altering lower and upper bounds of tuned parameter ranges for two-link thumb. Cases I, II, and III for the thumb represent that the PID parameters $\mathbf{K_P}$, $\mathbf{K_I}$ and $\mathbf{K_D}$ are constricted in three different bounded ranges [100,1000], [50,1000], and [100,200], respectively. Figure 29 and Figure 30 show that tracking errors and desired/actual angles of joints 1 and 2 of PID and GA-based PID controllers for Thumb. These simulations show that the large ranges [100,1000] (Case I) and [50,1000] (Case II) provide better results than the PID controller parameters arbitrarily chosen as 100. However, the small range [100,200] (Case III) gives worse result than the PID controller alone. These results suggest that the bigger parameter range, the smaller the total error. Cases I and II explain that GA finds some parameter values $\in$ [100,1000] and [50,100] escaping the local minimum area. Case III covers the value 100 in lower bound, but both total error and convergent speed are even worse than PID alone, suggesting that GA performs better for a large range, but is poor for searching on the boundary. To further consider the convergent speed, Case I gives smaller total error, but does not improve its convergent speed when comparing to PID control alone. Yet, Case II gives good total error and convergent speed. Case III gives poor total error and convergent speed. Taken together, these results imply that the global minimum could be located in the ranges [50,100] and [200,1000] and the parameter ranges play an important role in GA tuning. Based on these findings, we use the range [50,1000] for the remaining three-link fingers. Figures 31 to 34 show the simulations of PID and GA-based PID controllers for the remaining three-link fingers.

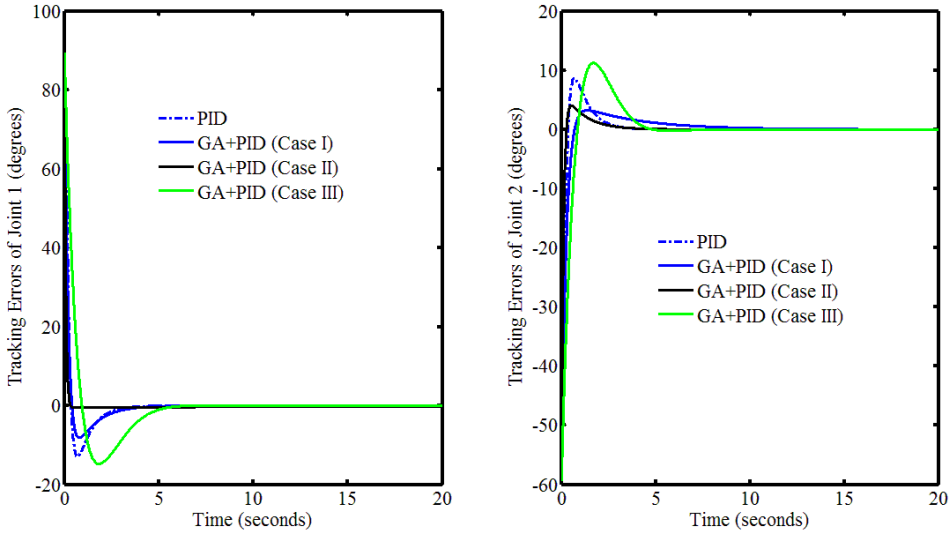

Figure 29: Tracking Errors of Joint 1 (left) and Joint 2 (right) of PID and GA-Based PID Controllers for Thumb

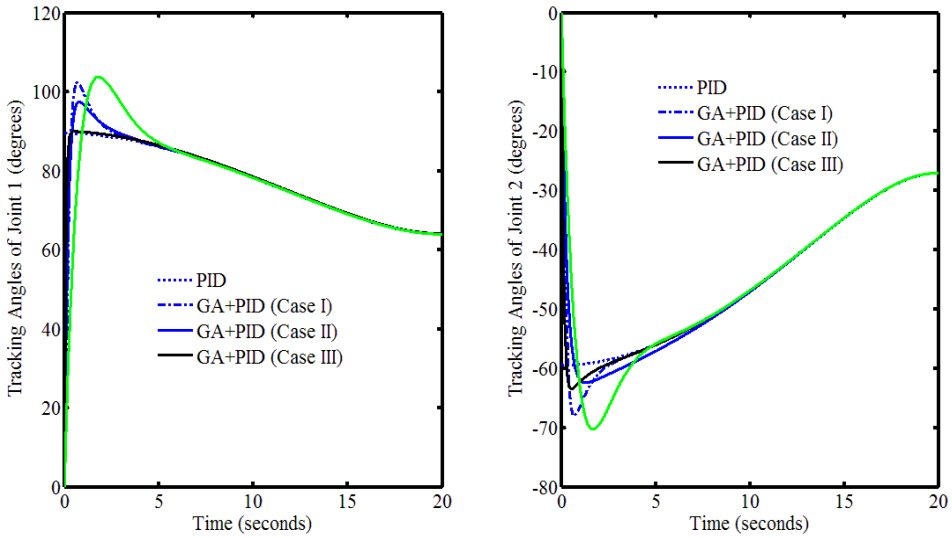

Figure 30: Tracking Angles of Joint 1 (left) and Joint 2 (right) of PID and GA-Based PID Controllers for Thumb

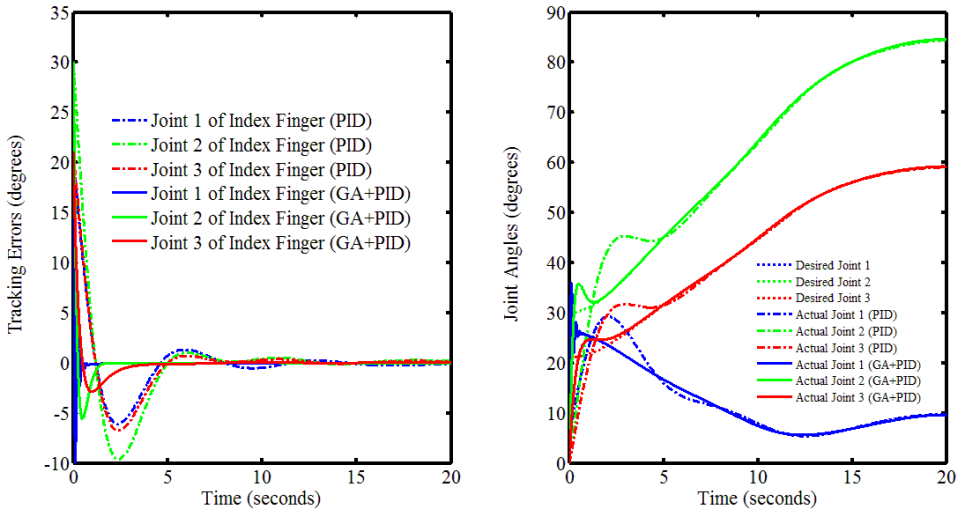

Figure 31: Tracking Errors (left) and Joint Angles (right) of PID and GA-Based PID Controllers for Index Finger

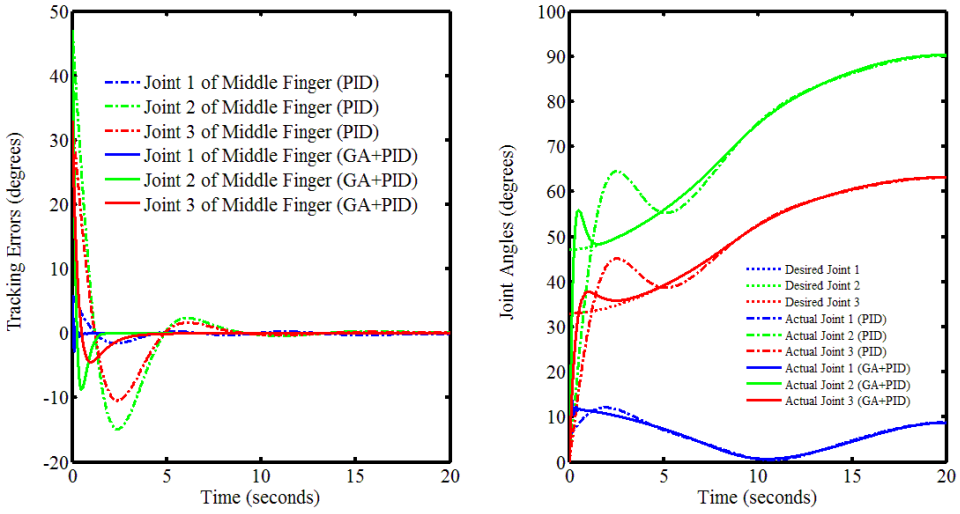

Figure 32: Tracking Errors (left) and Joint Angles (right) of PID and GA-Based PID Controllers for Middle Finger

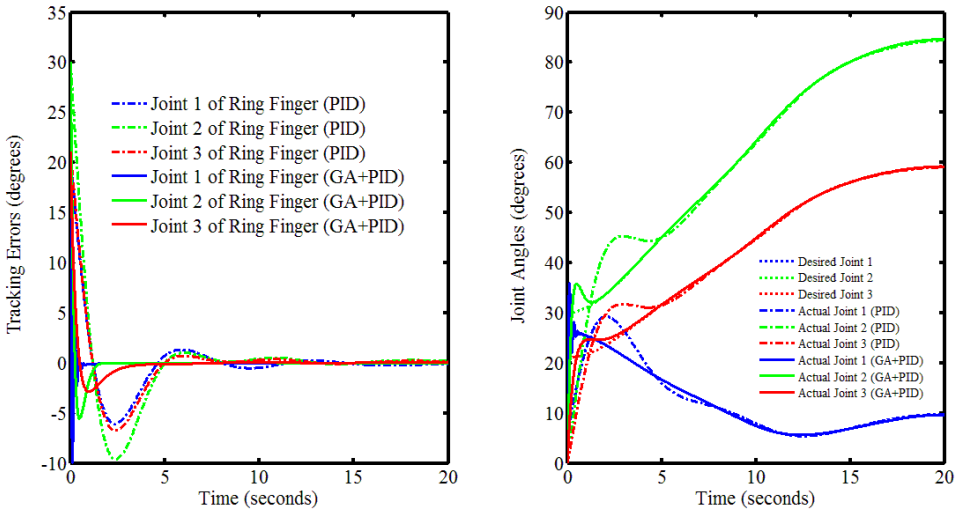

Figure 33: Tracking Errors (left) and Joint Angles (right) of PID and GA-Based PID Controllers for Ring Finger

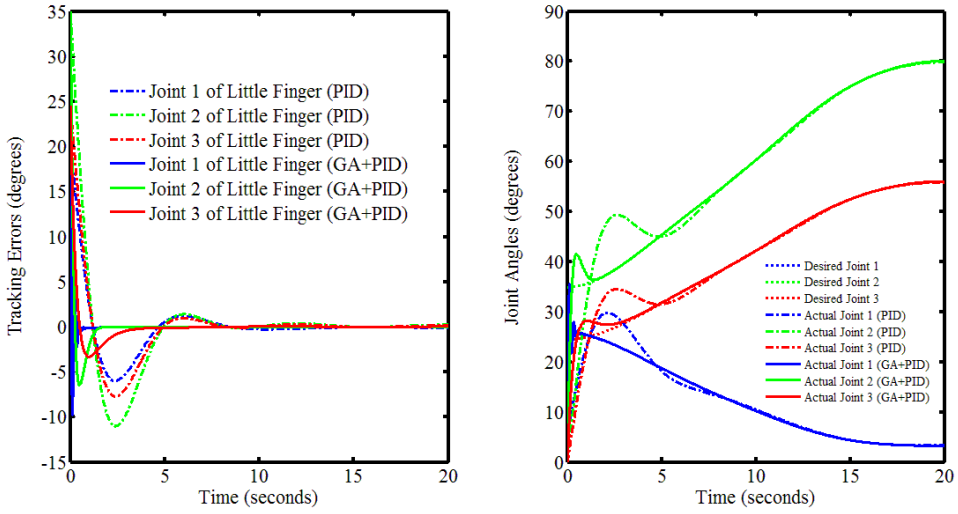

Figure 34: Tracking Errors (left) and Joint Angles (right) of PID and GA-Based PID Controllers for Little Finger

Fuzzy Logic-Based PD Hybrid Control

In this study, we assumed that each link of all fingers is a circular cylinder with the radius (R) 0.010 (m), so the inertia I^j_{zzk} of each link k of all fingers j (= t, i, m, r and l) can be calculated as

$$I^j_{zzk} = \frac{1}{4} m^j_k R^2 + \frac{1}{3} m^j_k {L^j_k}^2. \tag{52}$$

All initial actual angles are zero and the diagonal coefficients, $\mathbf{K_P}$, $\mathbf{K_I}$ and $\mathbf{K_D}$, for the PD or PID controller alone are arbitrarily chosen as 100. From the derived dynamic and control models, after the parameters ($\mathbf{K_P}$ and $\mathbf{K_D}$) are selected, the control signal $\boldsymbol{u}$ and torque $\boldsymbol{\tau}$ can be calculated.

Figure 35 shows tracking errors (e^t_1 and e^t_2 on the left column) and desired/actual angles (q^t_1 and

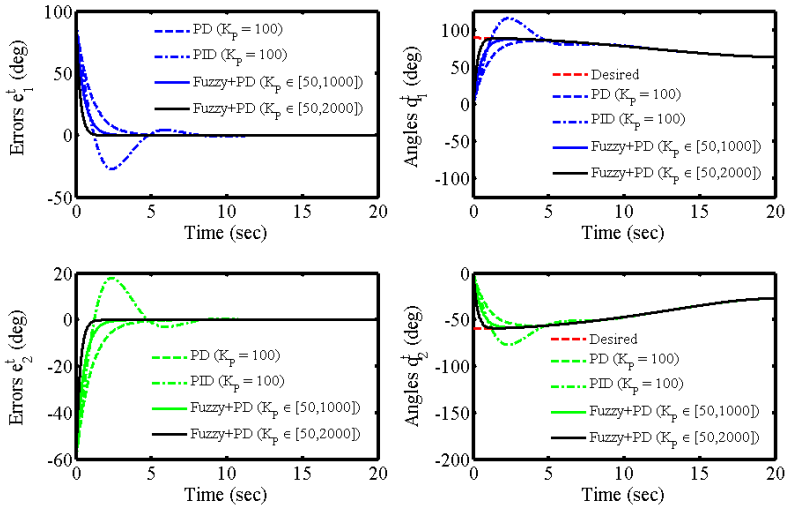

Figure 35: Tracking Errors (Left) and Desired/Actual Angles (Right) of Joints 1 (Upper) and 2 (Lower) for Two-Link Thumb Using PD (Dash Line), PID (Dot Line) and Fuzzy Logic Based PD (Solid Line) Controllers

q^t_2 on the right column) of joints 1 (the top row) and 2 (the bottom row) for two-link thumb using PD (dash line), PID (dot line) and fuzzy logic based PD (solid line) controllers. The tracking errors for PD control are convergent within 5 seconds without overshooting, but PID control acts longer (approximate 10 seconds) with overshooting and oscillation. The proposed hybrid fuzzy logic PD control using parameters $\mathbf{K_P} \in [50, 1000]$ and $\mathbf{K_D} \in [50, 500]$ provides faster convergence than both PD and PID controllers. To further study whether the parameter range influences tracking errors, we found that the larger parameter range, the faster convergent speed after altering $\mathbf{K_P} \in [50, 2000]$ without additional computational time. We also used fuzzy logic controller with two inputs (error and error rate) and one output (control signal), but the control system could not obtain convergent tracking errors (data not shown). These data suggest that fusion of soft computing (SC) and hard control (HC) is superior to either HC or SC methodology alone.

The time-variant computed control signals (u^t_1 and u^t_2) and torques (τ^t_1 and τ^t_2) for two-link thumb within the first 0.01 second are shown in Figure 36, suggesting that the presented hybrid fuzzy logic PD controller requires more power (torque) than PD and PID controllers in order to obtain faster convergent tracking errors.

Similarly, Figures 37, 39, 41 and 43 show tracking errors and desired/actual angles for all

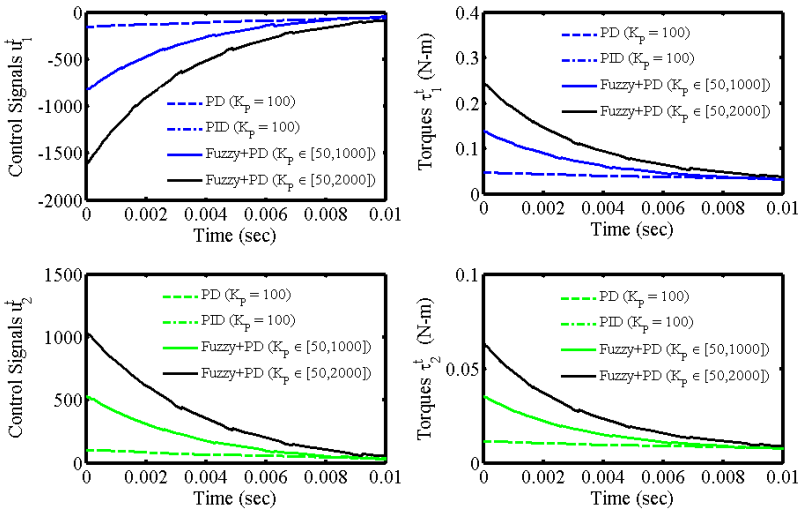

Figure 36: Control Signals (Left) and Actuated Torques (Right) of Joints 1 (Upper) and 2 (Lower) for Two-Link Thumb Using PD (Dash Line), PID (Dot Line) and Fuzzy Logic Based PD (Solid Line) Controllers in 0.01 Second

remaining three-link fingers. Figures 38, 40, 42 and 44 show control signals and torques for the mapping three-link fingers.

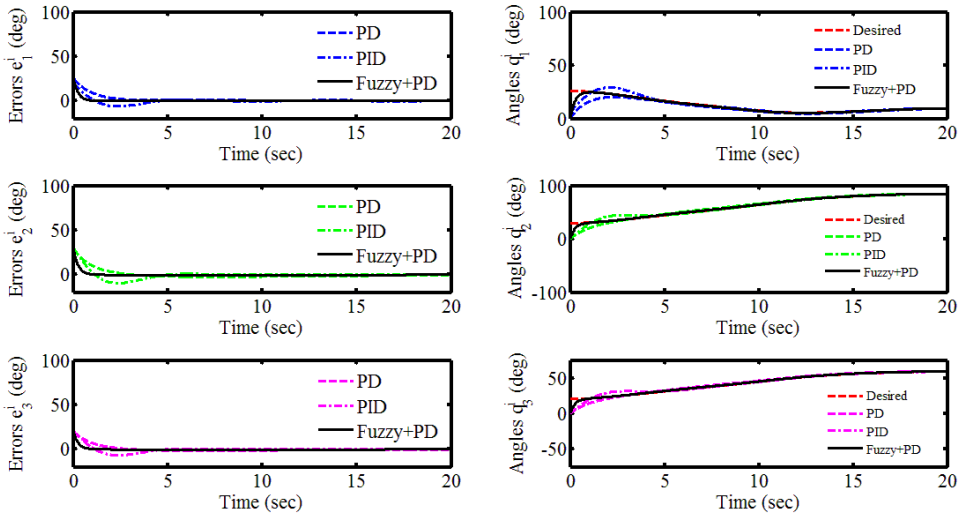

Figure 37: Tracking Errors (Left) and Desired/Actual Angles (Right) of Joints 1 (Top), 2 (Middle) and 3 (Bottom) for Three-Link Index Finger Using PD (Dash Line), PID (Dot Line) and Fuzzy Logic Based PD (Solid Line) Controllers

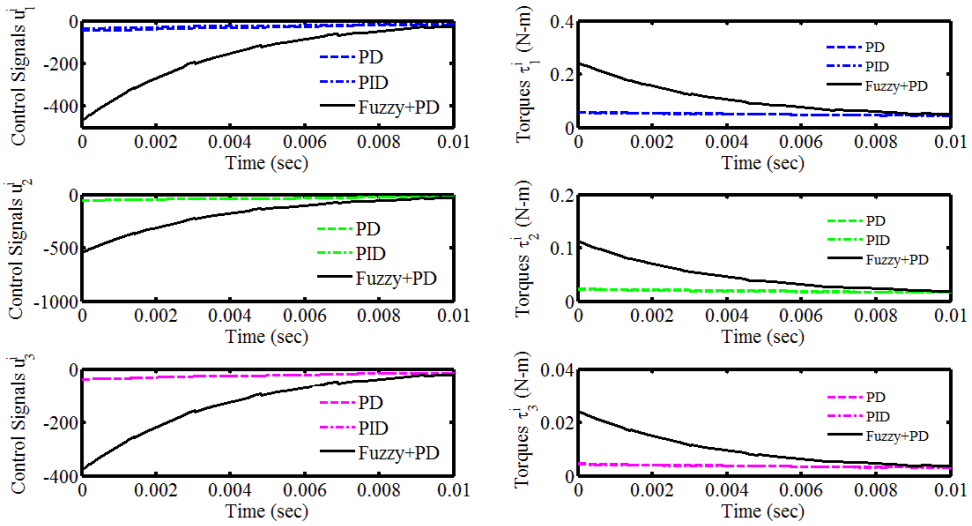

Figure 38: Control Signals (Left) and Actuated Torques (Right) of Joints 1 (Top), 2 (Middle) and 3 (Bottom) for Three-Link Index Finger Using PD (Dash Line), PID (Dot Line) and Fuzzy Logic Based PD (Solid Line) Controllers in 0.01 Second

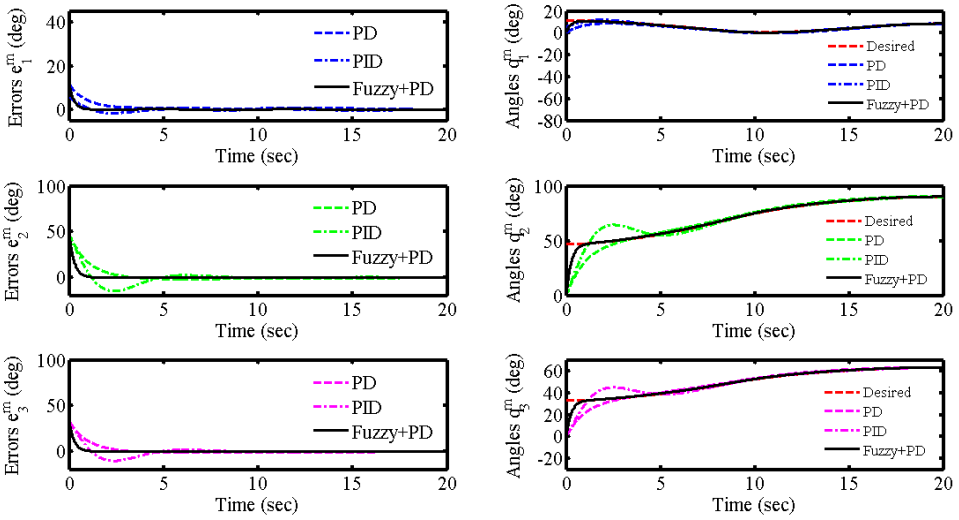

Figure 39: Tracking Errors (Left) and Desired/Actual Angles (Right) of Joints 1 (Top), 2 (Middle) and 3 (Bottom) for Three-Link Middle Finger Using PD (Dash Line), PID (Dot Line) and Fuzzy Logic Based PD (Solid Line) Controllers

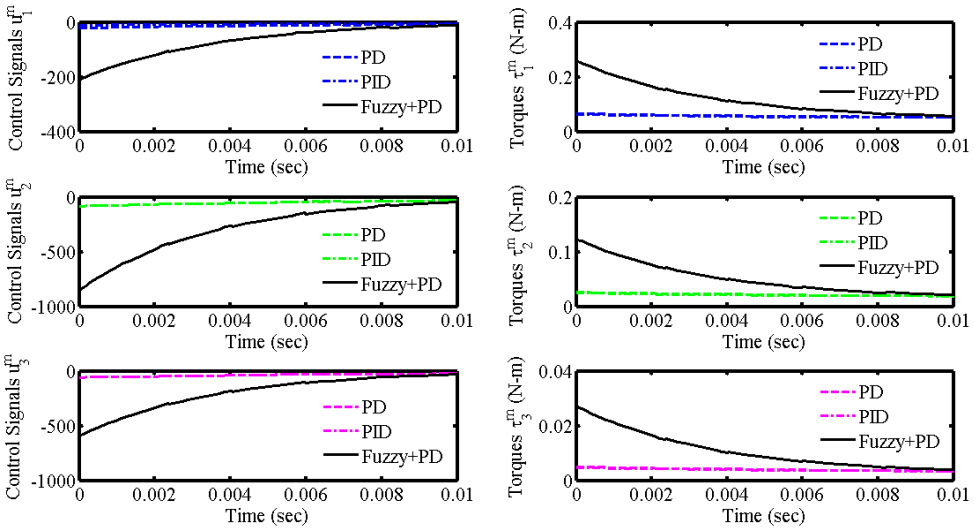

Figure 40: Control Signals (Left) and Actuated Torques (Right) of Joints 1 (Top), 2 (Middle) and 3 (Bottom) for Three-Link Middle Finger Using PD (Dash Line), PID (Dot Line) and Fuzzy Logic Based PD (Solid Line) Controllers in 0.01 Second

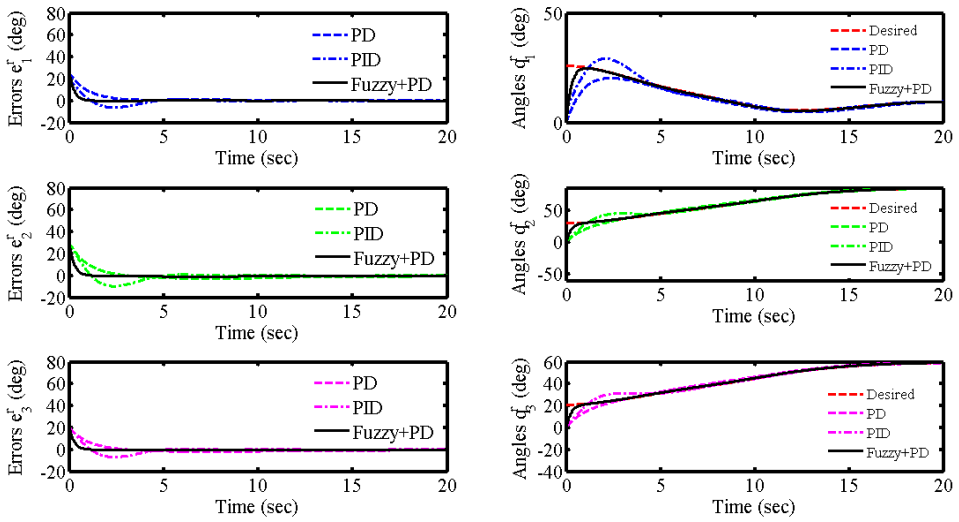

Figure 41: Tracking Errors (Left) and Desired/Actual Angles (Right) of Joints 1 (Top), 2 (Middle) and 3 (Bottom) for Three-Link Ring Finger Using PD (Dash Line), PID (Dot Line) and Fuzzy Logic Based PD (Solid Line) Controllers

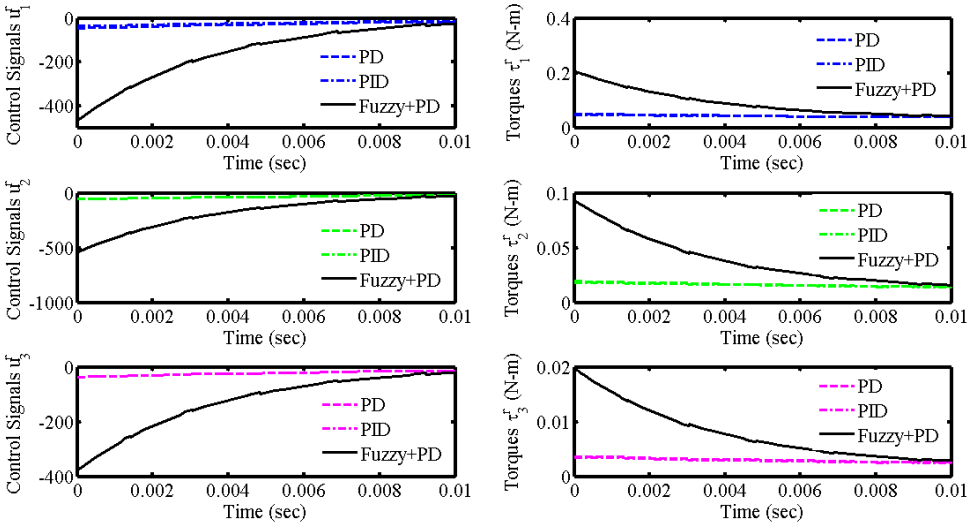

Figure 42: Control Signals (Left) and Actuated Torques (Right) of Joints 1 (Top), 2 (Middle) and 3 (Bottom) for Three-Link Ring Finger Using PD (Dash Line), PID (Dot Line) and Fuzzy Logic Based PD (Solid Line) Controllers in 0.01 Second

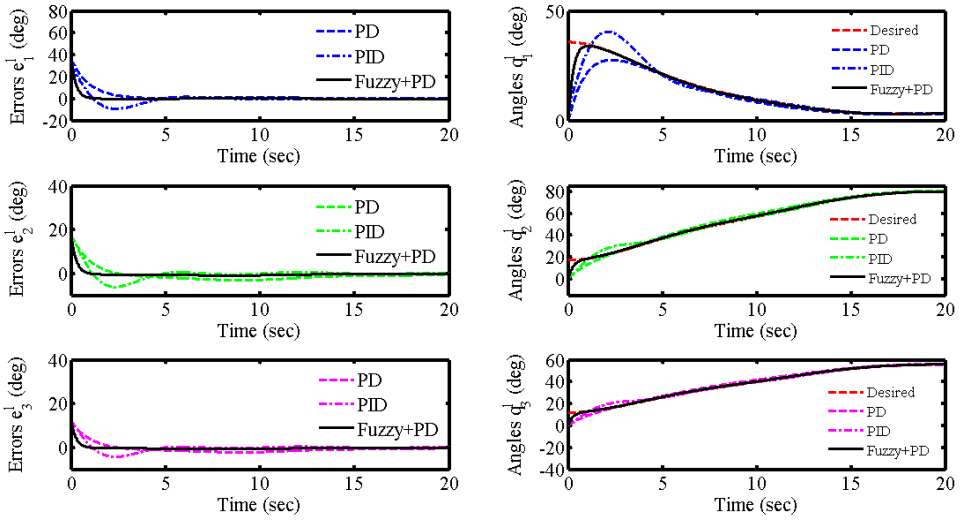

Figure 43: Tracking Errors (Left) and Desired/Actual Angles (Right) of Joints 1 (Top), 2 (Middle) and 3 (Bottom) for Three-Link Little Finger Using PD (Dash Line), PID (Dot Line) and Fuzzy Logic Based PD (Solid Line) Controllers

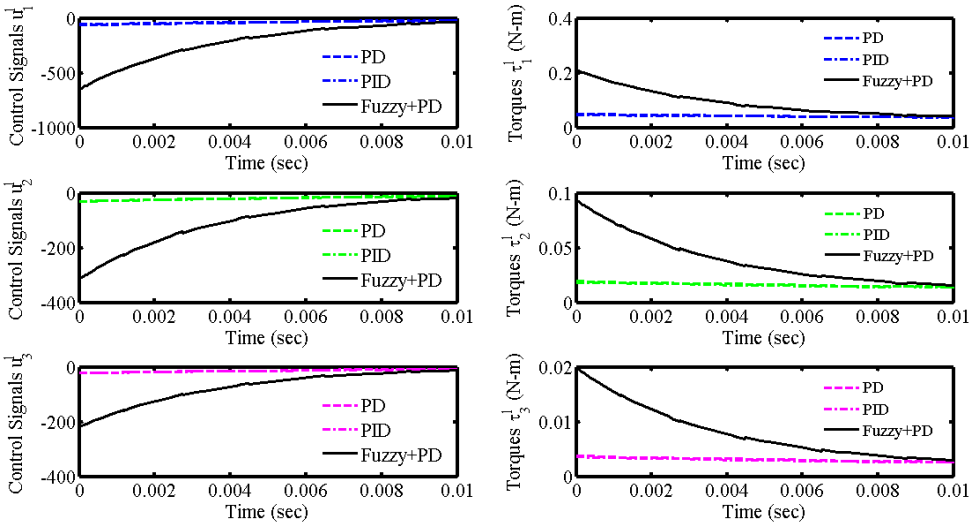

Figure 44: Control Signals (Left) and Actuated Torques (Right) of Joints 1 (Top), 2 (Middle) and 3 (Bottom) for Three-Link Little Finger Using PD (Dash Line), PID (Dot Line) and Fuzzy Logic Based PD (Solid Line) Controllers in 0.01 Second

1. Power grasping control for fully actuated prosthetic hand

1.1. Introduction

Human hand is one of the most important and complex parts of the body, which has the ability to handle different tasks. The ultimate goal of robotic hand is to achieve the functionality of a human hand. In the past three decades, there have been numerous investigations to achieve dexterity and ability of human hand, especially in the fields of humanoid robotics and prosthetic hand [1-6]. In spite of all these advances in this field, the current state of research on prosthetic hands is far from that objective of achieving the functionality of human hand. Commercially available prosthetic hands have very limited functionality and they are just simple grippers. The present research on prosthetic hands involves complex control schemes to achieve the most important functions of the hand [7-8].

Grasping can be categorized into two main groups: precision and power grasping. In precision grasping the object is held by tips of the fingers, while in power grasping, the whole the finger is active and in contact with the object [9]. Many research works addressed the precision grasping problem [12-15] mainly because of the well-established techniques for control of end effector; however the problem of power grasping is not studied in depth.

Many control methods require the knowledge of the shape of the object. For humans this information is available by visual feedback from eyes, while in case of a prosthetic hand this visual information is not directly available for hand controller, and the only available information is electromyographic (EMG) signal related to patient‘s arm muscle activities. However, normally the EMG signal is not available for all individual joints and besides, due to measurement noise, accessing high quality EMG signal is hard [10]. Moreover, using EMG signal to control all the movements requires lot of attention during grasping and leads to fatigue for the amputees [11]. Hence it is required for prosthetic hand to be semi-autonomous which means a part of command information will be provided by the EMG signal and the rest of the required command should be provided automatically by hand controller.

Defining finger trajectory without the knowledge of shape of object to be grasped is a challenging task for many path planning techniques. For multi DOFs robots there are two common methods for trajectory planning which are ―inverse kinematic‖ and ―inverse dynamic‖ [12-15]. Both these methods require object shape and are based on solving optimization problem which requires high computation, hence they are hard to implement for real-time applications.

To avoid solving the path planning problem for prosthetic hands, many researchers advocated under-actuated mechanisms, which are capable of adapting to object shape mechanically and without additional computation [16-18]. In these mechanisms, the number of actuators are less than the DOFs, and because of less actuators they have less weight. However fewer actuators result in less functionality, because fingers joints can‘t move independently.

Arimoto et al. [19] used ―virtual spring-damper hypothesis‖ for control of robotic arm-hand systems. A similar method called ―virtual model control‖ is also suggested by J.Pratt et al. [20] used for walking robots, and it is based on defining virtual forces between two points. Both methods are based on the use of Jacobian matrix to relate task space movement to joint space. In [20] it is shown that any kind of force can be defined between two points and the other study [19] shows that use of spring-damper forces will result in human like movement. From physiological point of view, human skilled multi-joint reaching movement has these characteristics that 1) endpoint trajectory become a quasi-straight line and less variable, 2)velocity profiles of the endpoint has a bell-shape, and 3) joint trajectories are rather variable from trial to trial [19].

In this report, a new control scheme is proposed that can efficiently address the problem of power grasping without complete knowledge of the shape of the object which may be called ―blind power grasping‖ for prosthetic hand. The proposed method is based on the works by Arimoto et al. [19] using virtual spring-damper (VSD) hypothesis used for control of robotic arm-hand systems. In our report, we use the above mentioned hypothesis, in particular for the

power grasping of a prosthetic hand. In this method, we define a virtual spring-damper between finger tip and desired point for control of movement of fingers. Further, in this method there is no need to introduce any performance indices to solve inverse kinematics uniquely and Jacobian pseudo-inverse or inverse dynamics which are common methods to define trajectories of redundant DOFs robots. Besides, in the present method, there is no need for any information on tactile or force sensing.

The report is organized as follows. In Section 2 modeling of prosthetic hand is discussed, Section 3 covers virtual spring damper method. Section 4 describes control strategy. Section 5 analyzes the efficiency of the proposed control scheme using numerical simulation. Finally, conclusion and discussion are presented in section 6.

1.2. Modeling of Prosthetic Hand

In this control method, controller is not derived directly from dynamic model of the system. Kinematics equation and Jacobian matrix are the required for controller design.

A model of a robotic hand system is shown in Fig.1. The model consists of a finger with 3DOF which represents three joints of a finger and palm.

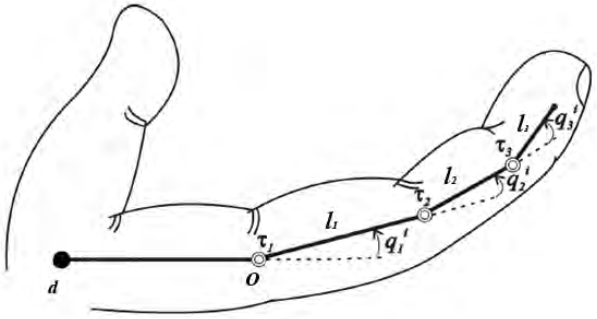

Fig. 1: Model of a Robotic Hand System.

In this report we assume the following:

1- Movement of both finger and object are confined to a two dimensional horizontal plane, and therefore there is no gravity effect.

2- The object is assumed to be initially stable in its position.

3- The initial movement toward object is handled by amputee, so the hand is close enough to the object before grasping.

The position of the tip of the finger is evaluated as (see Figure 1):

$$x = l_1 \cos q_1 + l_2 \cos(q_1 + q_2) + l_3 \cos(q_1 + q_2 + \quad (1)$$

$$y = l_1 \sin q_1 + l_2 \sin(q_1 + q_2) + l_3 \sin(q_1 + q_2 + \quad (2)$$

where, l_1, l_2, and l_3 are lengths of each finger and q_1, q_2, and q_3 are angles of each corresponding joint.

Based on above equation the Jacobian matrix is as:

$$J = \begin{bmatrix} j_{11} & j_{12} & j_{13} \\ j_{21} & j_{22} & j_{23} \end{bmatrix}, \quad (3)$$

$$j_{11} = -l_1 \sin q_1 - l_2 \sin(q_1 + q_2) - l_3 \sin(q_1 + \quad (4)$$

,

$$j_{12} = -l_2 \sin(q_1 + q_2) - l_3 \sin(q_1 + q_2 + q_3), \quad (5)$$

$$j_{12} = -l_2\ sin(q_1 + q_2) - l_3\ sin(q_1 + q_2 + q_3), \quad (6)$$

$$j_{13} = -l_3\ sin(q_1 + q_2 + q_3)\,, \quad (7)$$

$$j_{21} = l_1\ cos\ q_1 + l_2\ cos(q_1 + q_2) + l_3\ cos(q_1 + q \quad (8)$$
,

$$j_{22} = l_2\ cos(q_1 + q_2) + l_3\ cos(q_1 + q_2 + q_3), \quad (9)$$

$$j_{23} = l_3\ cos(q_1 + q_2 + q_3). \quad (10)$$

1.3. Virtual Spring-Damper Method

–Virtual model control" is a motion control scheme that uses simulations of virtual components to generate desired joint torques [20]. These joints produce the same effect that the virtual elements placed on robot would have created; hence they create the illusion that these virtual elements are connected to the real robot. Virtual elements can be any kind of real physical elements such as springs, dampers, gravity fields, nonlinear fields or any other components.

Virtual model control was proposed by J. Pratt et al [20] for biped walking robot. In a study by Arimoto [19] on robotic hand arm system, it is shown that using a virtual spring damper between robot end effector and desired point, and virtual dampers at each joint, human like movement can be achieved.

For power grasping by a prosthetic hand, one of the best options is the use of Virtual Spring-Damper (VSD) hypothesis. Some benefits of VSD control scheme are that it has a simple structure and requires relatively less computation. Besides, it doesn't need inverse dynamics to precisely define the robot movement. Thus, we use spring set points instead of commanded movement and robot automatically adapts its shape. Since finger joints at prosthetic hand work as virtual dampers, which is sensitive to velocity and not to position, they don't have a forced shape, instead just finger tip follow a defined path as will be discussed more in control strategy section.

The joint torques to virtual forces is given by:

$$\tau = J^T F, \quad (11)$$

where τ is the torque, and F is the force due to virtual spring damper given as

$$F = -(\xi\sqrt{k}\dot{x} + k\Delta x), \quad (12)$$

and

$$\tau_{spring-damper} = -J^T\left(\xi\sqrt{k}\dot{x} + k\Delta x\right), \quad (13)$$

where k represents the stiffness of the virtual spring, Δx is distance between finger tip and desired point, and ξ is the damping ratio. The damping force is defined at each joint as

$$\tau_{joints\ damping} = -C\dot{q}, \quad (14)$$

where, C denotes a diagonal positive definite matrix as follows:

$$C = \xi_0\ diag(c_1, \ldots, c_n). \quad (15)$$

Hence control signal would be sum of these two terms

$$u = -C\dot{q} - J^T(q)\left(\xi\sqrt{k}\dot{x} + k\Delta x\right). \quad (16)$$

Higher values of k result in more accurate and faster response to the desired point and higher C provides more stability. Thus k and C are chosen as design variables.

1.4. Control Strategy

Virtual spring-damper hypothesis is suitable for point to point control. Defining the desired trajectory as a semicircle (in order to have a full grasp of the object) given by,

$$x_d = (l_1 + l_2 + l_3)\ cos(t), \quad (17)$$

$$y_d = (l_1 + l_2 + l_3)\ sin(t), \quad (18)$$

Where t is proportional to EMG signal which is scaled to change between $0<t<\pi$.

As shown in Fig. 2, after passing this semi-circle, finger tip goes toward center to make a tighter grasping. This is achieved by defining a desired point close to center.

As mentioned earlier, the goal is not exactly following the defined path. If the object is big, due to contact of hand and object, it would be impossible to follow exact path and following this path is just to achieve grasping.

Fig. 3 illustrates the physical counterparts of the virtual forces for control strategy and Fig. 4 shows structure of the proposed control system. As shown, the command force comes from EMG signal, and controller provides the movement for hand which has dynamic interaction with the object.

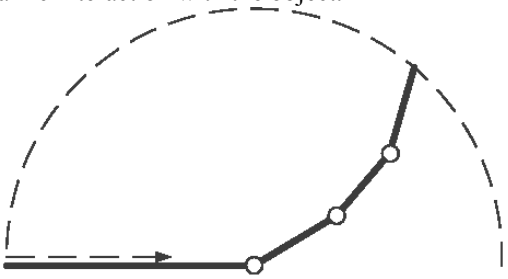

Fig. 2: Semi-Circle Path of Finger Tip

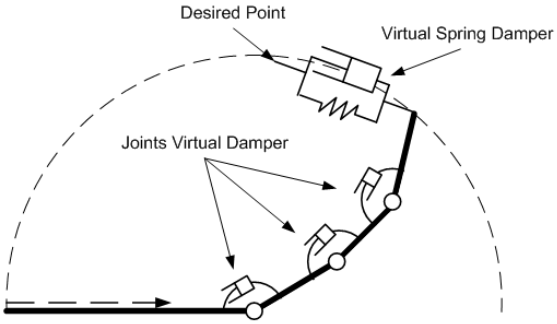

Fig 3: Physical Counterparts of the Virtual Forces

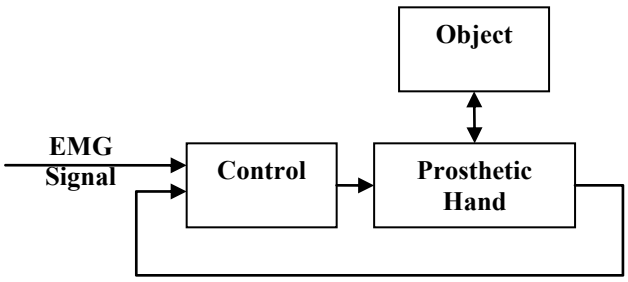

Fig. 4: Control Diagram of Prosthetic Hand System

1.5. Numerical Simulation

In order to show the effectiveness of the proposed control strategy, numerical simulations were conducted to grasp three different objects, based on the physical parameters of a hand system and objects summarized in Table 1.

In order to simulate dynamics of the hand and interaction with object, Adams software is used. This software is a multi-body analysis simulation program that solves the rigid body dynamic equilibrium equations and directly interfaces with Matlab/Simulink software in order to implement controller. The contact between object and hand is modeled and three sets of simulations with different objects are performed. In all three simulations the same control strategy is used which shows controller can handle grasping without information about physical parameters of object. Fingers and objects are assumed to be rigid. In these simulations the EMG signal is assumed to increase linearly with time.

Table 1. Parameters used for simulation

Index finger link 1	5 cm
Index finger link 2	2.5 cm
Index finger link 3	2.5 cm
Damping at joints	0.01 kg/s
Virtual damping ratio *(c)*	1
Virtual spring stiffness *(k)*	50 N/m
Rectangular object width	3 cm
Circular object radius	3 cm
Star shape object outer radius	2 cm

1.5.1 Simulation One

For first simulation a rectangular (cubic) object is used, and as mentioned earlier the movement is restricted to 2D movement. Object is not moving initially. Hand starts movement from open finger configuration. The hand positions at 1 second time interval are shown. Fig. 5 shows finger tip angle with respect to palm.
As it is shown in Fig. 6 the grasping is accomplished successfully.

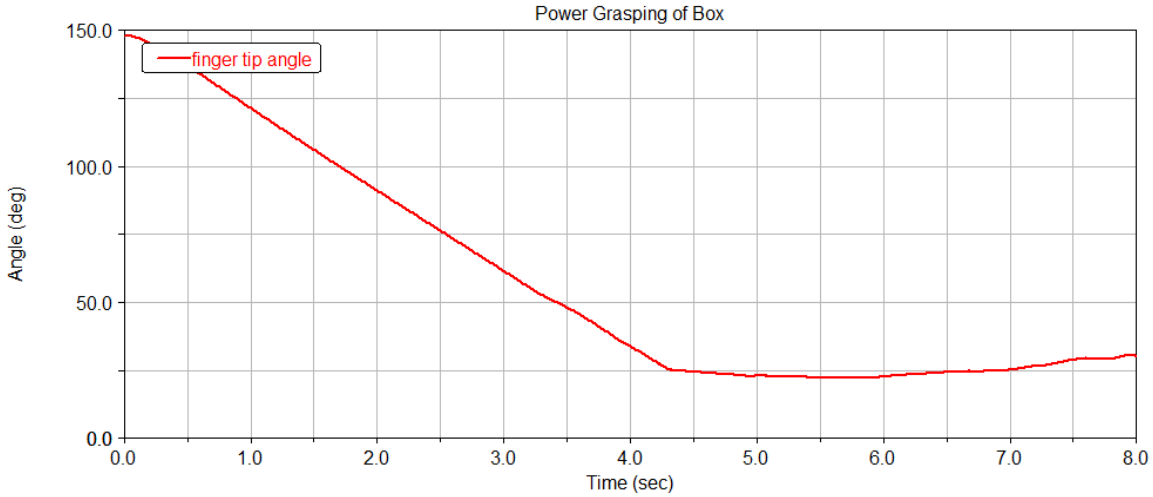

Fig. 5: Finger‘s Tip Angle at Rectangular Object Grasping

1.5.2 Simulation Two

For the second simulation a glass (circular object) is used. The control parameters are identical to previous simulation.
As shown in Fig. 7 the grasping is done successfully and the hand positions for 1 second time interval are depicted. Similarly the finger tip angle respect to palm is shown in Fig. 8.
Regardless of object shape, by use of proposed control scheme the hand can successfully grasp objects.

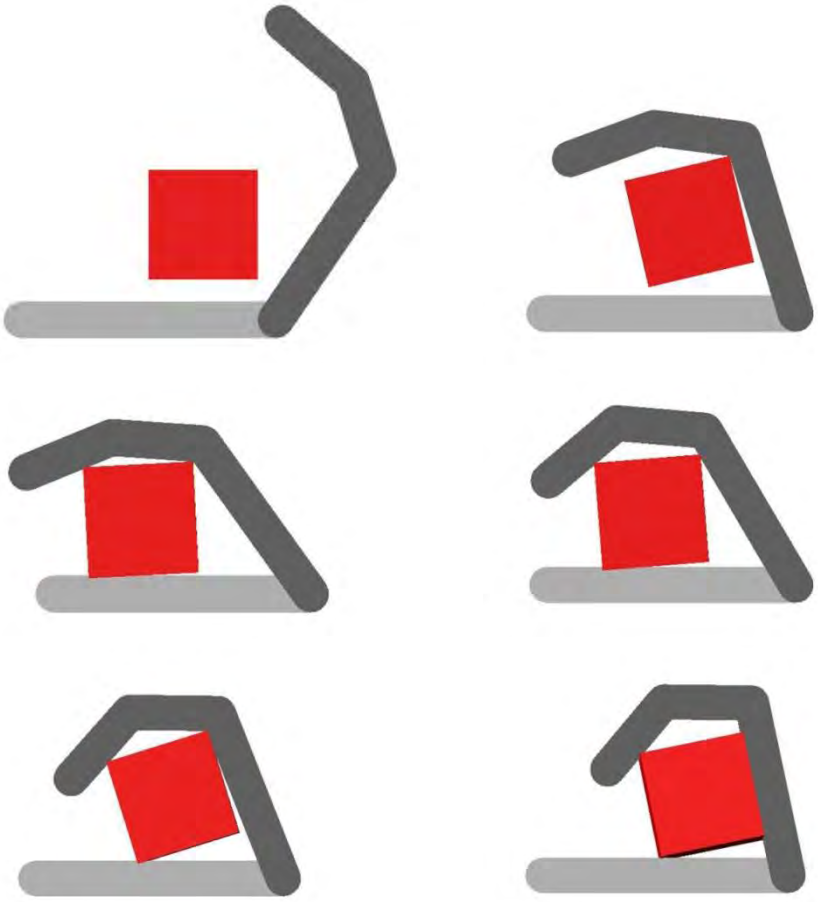

Fig. 6: Rectangular Object Grasping (1 Sec Intervals)

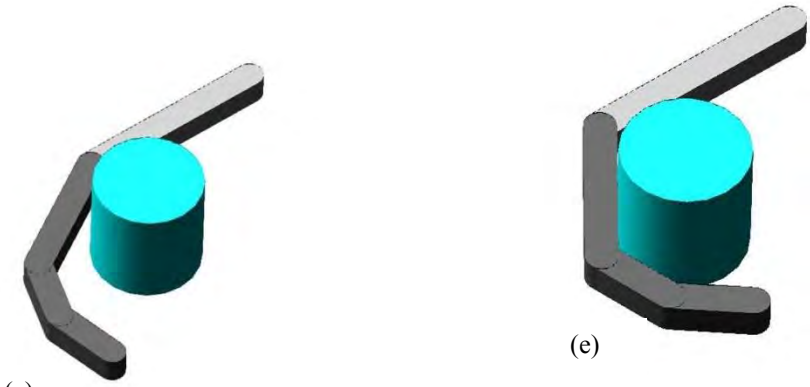

(a) (e)

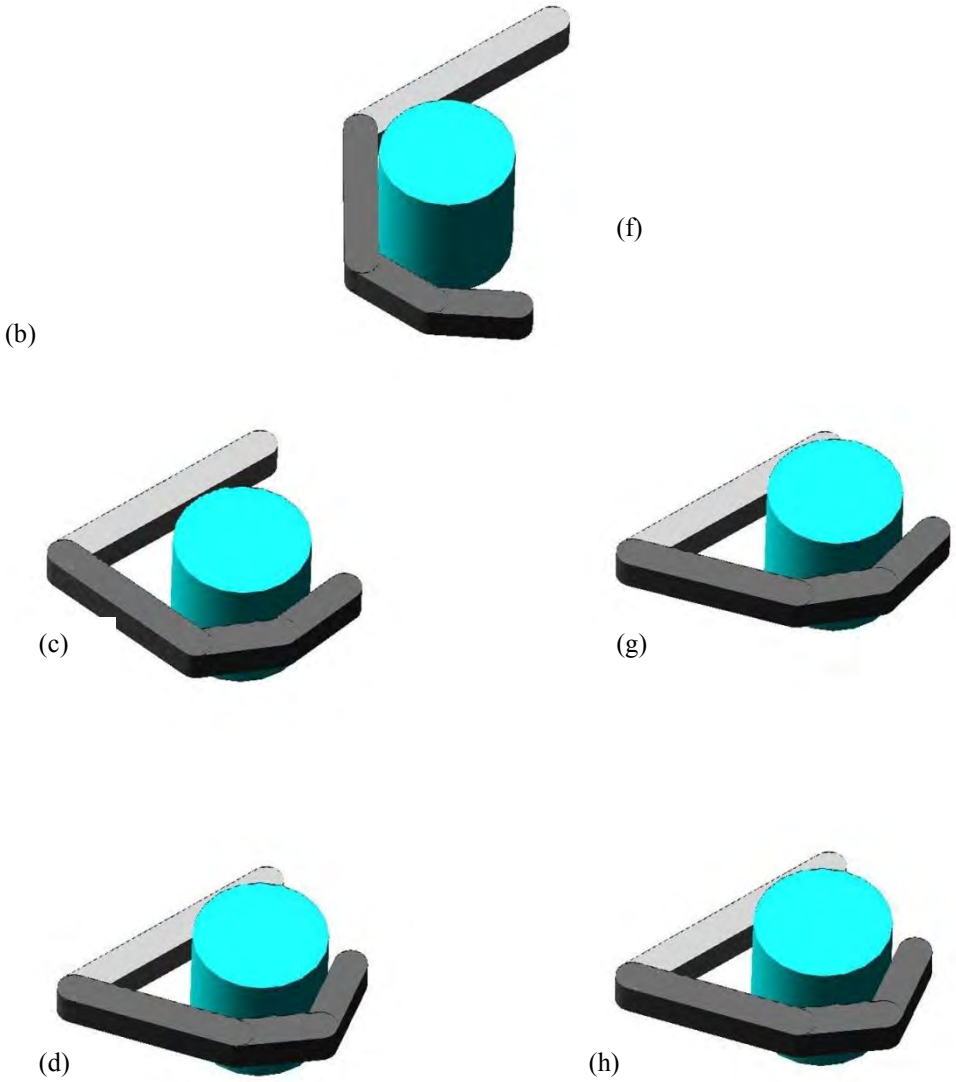

Fig. 7 (a-h) : Grasping of a Glass (1 sec. Intervals)

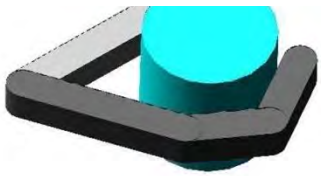

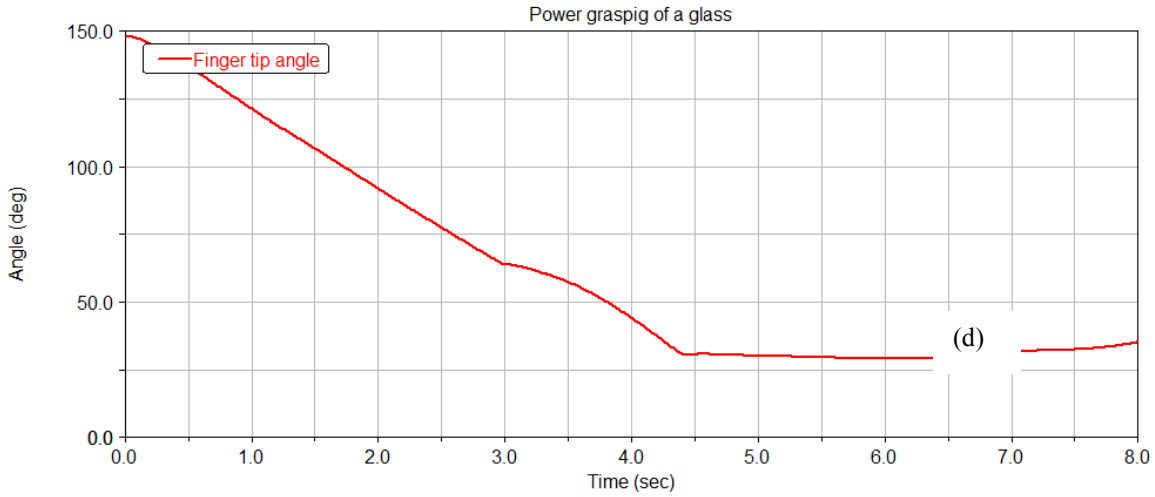

Fig. 8: Finger‘s Tip Angle at Grasping a Glass

1.5.3. Simulation Three

For the third simulation a star shape object is used. The control parameters are identical to (e) ; simulation. As shown in Fig. 9 the grasping is done successfully and the hand positions for 1 second time interval are illustrated. Final position of grasping in 3D (isometric) view is depicted in Fig. 10. Similarly the finger tip angle respect to palm is shown in Fig. 11.

The complicated shape of object shows that controller is able to handle grasp for wide variety of objects, without information of object shape.

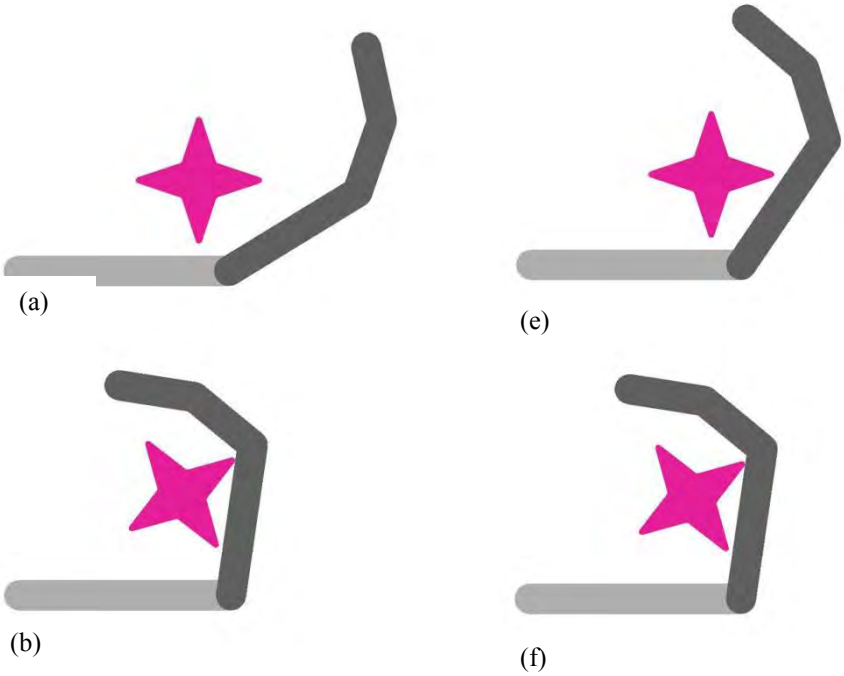

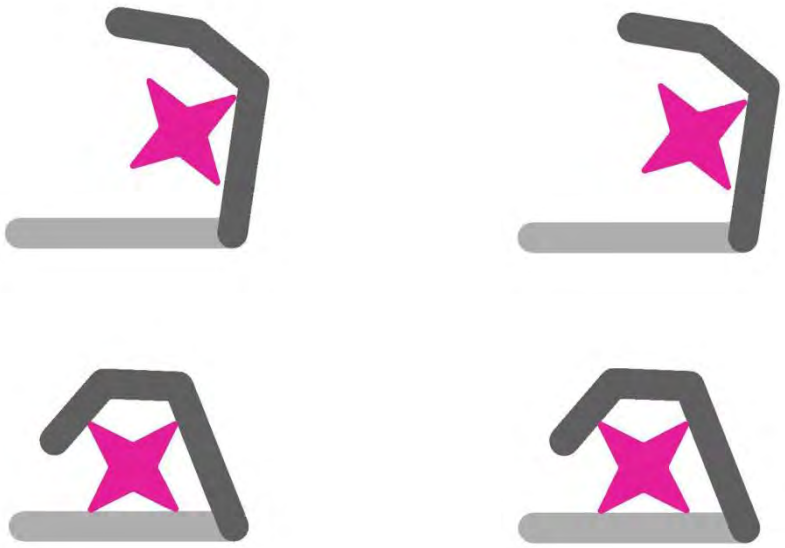

Fig. 9 (a-h) : Grasping of Star Shape Object (1 sec. Intervals)

Fig. 10 : 3D (Isometric) View of Star Shape Object After Grasping

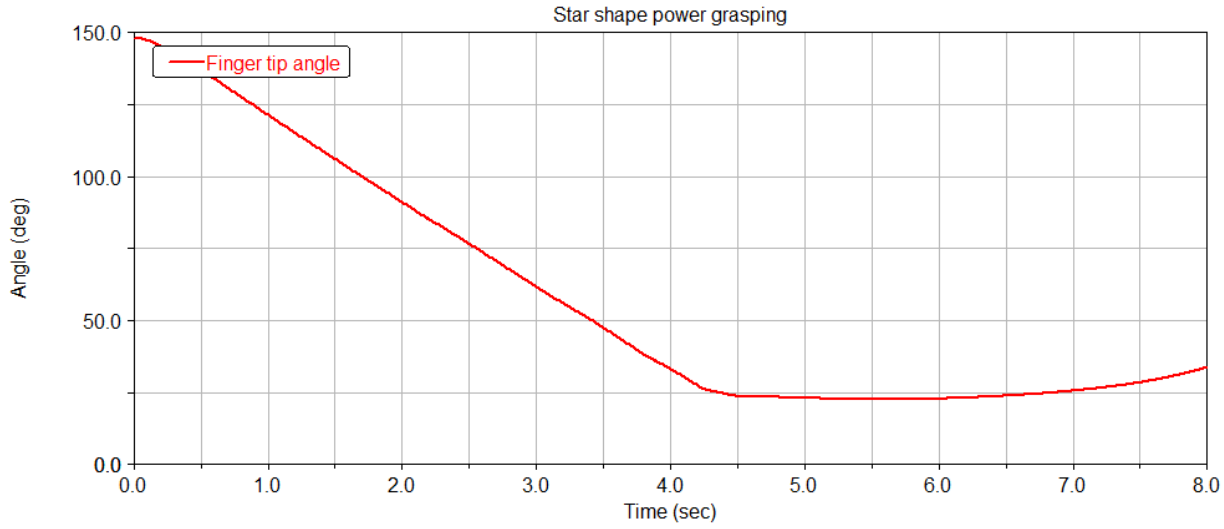

Fig. 11: Finger‘s Tip Angle at Star Shape Object Grasping

2. Precision grasping control for fully actuated prosthetic hand

Using the similar technique discussed in previous section for power grasping which is virtual spring damper hypothesis a control strategy is developed for precision grasping. In precision grasping the object is held by tips of the fingers, while in power grasping, the whole finger is active and in contact with the object. First a model is derived for kinematic of the hand, then the control strategy and numerical simulations are provided.

2.1. Modeling of Prosthetic Hand

In this control method, controller is not designed based on dynamic model of the system. Instead, kinematics equation and Jacobian matrix are used for controller design.

A model of a robotic hand system is shown in Fig.1. The model consists of a finger with 3DOF which represents three joints of index finger, palm and a finger with 2DOF which represents thumb.

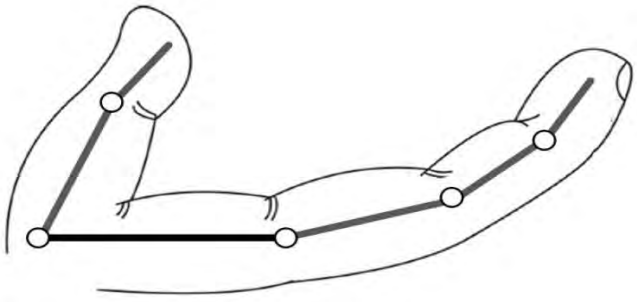

Fig. 1. Schematic of a robotic hand system

In this report we assume the following:

- Movement of both finger and object are confined to a 2 dimensional horizontal plane, and therefore there is no gravity effect.
- The object is assumed to be initially stable in its position.

- The initial movement toward object is handled by amputee, so the hand is close enough to the object before grasping.

The position of the tip of index fingers is evaluated as (see Fig. 1):

$$x_i = l_{i1}\ cos\ q_{i1} + l_{i2}\ cos(q_{i1} + q_{i2}) + l_{i3}\ cos(q_{i1} + q_{i2} + q_{i3}), \quad (1)$$

$$y_i = l_{i1}\ sin\ q_{i1} + l_{i2}\ sin(q_{i1} + q_{i2}) + l_{i3}\ sin(q_{i1} + q_{i2} + q_{i3}), \quad (2)$$

where, l_{i1}, l_{i2}, and l_{i3} are lengths of index finger and q_{i1}, q_{i2}, and q_{i3} are angles of each corresponding joint. Similarly the position of thumb finger is evaluated as:

$$x_t = l_{t1}\ cos\ q_{t1} + l_{t2}\ cos(q_{t1} + q_{t2}), \quad (3)$$

$$y_t = l_{t1}\ sin\ q_{t1} + l_{t2}\ sin(q_{t1} + q_{t2}), \quad (4)$$

where, l_{t1} and l_{t2} are lengths of thumb finger and q_{t1} and q_{t2}, are angles of corresponding joints.
Based on above equation the Jacobian matrix for index finger is as:

$$J_i = \begin{bmatrix} \frac{\partial x}{\partial q_{i1}} & \frac{\partial x}{\partial q_{i2}} & \frac{\partial x}{\partial q_{i3}} \\ \frac{\partial y}{\partial q_{i1}} & \frac{\partial y}{\partial q_{i2}} & \frac{\partial y}{\partial q_{i3}} \end{bmatrix}, \quad (5)$$

and Jacobian for thumb finger is as:

$$J_t = \begin{bmatrix} \frac{\partial x}{\partial q_{t1}} & \frac{\partial x}{\partial q_{t2}} \\ \frac{\partial y}{\partial q_{t1}} & \frac{\partial y}{\partial q_{t2}} \end{bmatrix}. \quad (6)$$

2.2. Control Strategy

Virtual spring-damper hypothesis is suitable for point to point control. In precision grasping two approaches can be considered. 1) Defining a virtual spring damper between fingers tip and geometrical center of the object, which requires information about the object position and shape, and this information is not available in case of a prosthetic hand for the controller which is used in [13] 2) Defining a virtual spring damper between tips of two fingers, then fingers attract together and grasp the object in between, without exact knowledge of object position and shape. In this case the amputee should place the hand close to the object and in appropriate position. Besides, a virtual damper force is considered at each finger joint. The latter method is used and physical counterpart of virtual forces are depicted at Fig. 2.

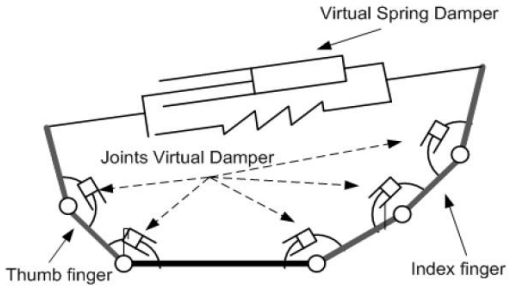

Fig. 2. Physical counterparts of the virtual forces

Higher values of k (virtual spring stiffness) results in faster movement of fingers as well as, higher grasping force. Thus by defining k proportional to EMG signal, amputee have control over speed of movement and grasping force. The damping coefficient of finger joints, can change the final shape of fingers. The joints with lower damping tends to move more, while higher damped joints move more. The appropriate values of damping are evaluated based on

trial and error to reach positions close to normal hand and they are held constant for further simulations.

2.3. Numerical Simulation

In order to show the effectiveness of the proposed control strategy, numerical simulations were conducted to grasp two different objects, based on the physical parameters of a hand system and objects summarized in Table I.

The Adams software which is multi-body dynamic simulation software is used for numerical analysis. The software is capable to conduct information between Matlab/ Simulink software environment, hence the plant is modeled by Adams and controller is implemented in Matlab/Simulnk.

TABLE I
PARAMETERS USED FOR SIMULATION

Parameter	Value
index finger link 1 length	5 cm
index finger link 2 length	2.5 cm
index finger link 3 length	2.5 cm
thumb finger link 1 length	4 cm
thumb finger link 2 length	3 cm
distance between thumb and index	6 cm
damping at joints	0.01 kg/s
virtual damping ratio	1
virtual spring stiffness	50 N/m
rectangular object width	2 cm
circular object radius	2 cm

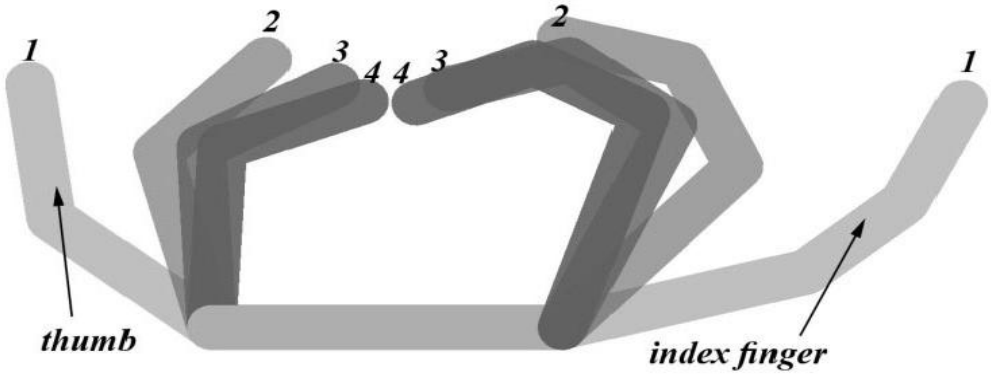

Fig. 3. Finger movements in 4 different position (0.25 sec. intervals)

For first simulation, two fingers are modeled without any object in between. As shown in Fig. 3, two fingers come together, and final position is close to normal hand coordination.

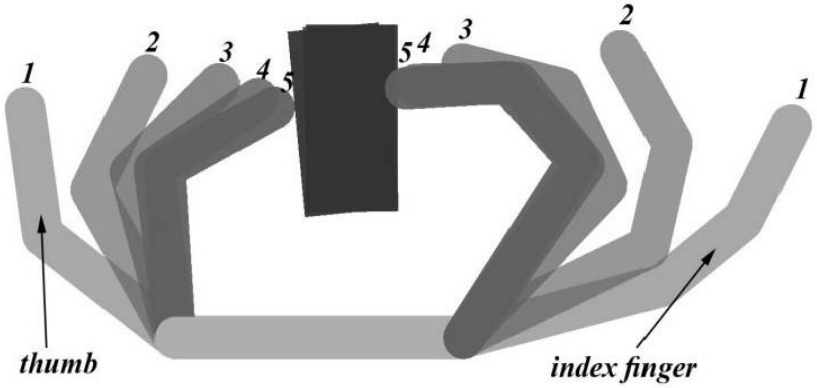

Fig. 4. Rectangular object grasping (0.25 sec intervals)

For the second simulation, a rectangular object is chosen to be grasped. The object is free to move in 2 dimensional plane, and contact and friction force are simulated between finger tip and the object. The object is placed at arbitrary final position of previous experiment. The finger movement at 0.25 sec time intervals and finger tip angles relative to palm are shown respectively in Figs. 4 and 5.

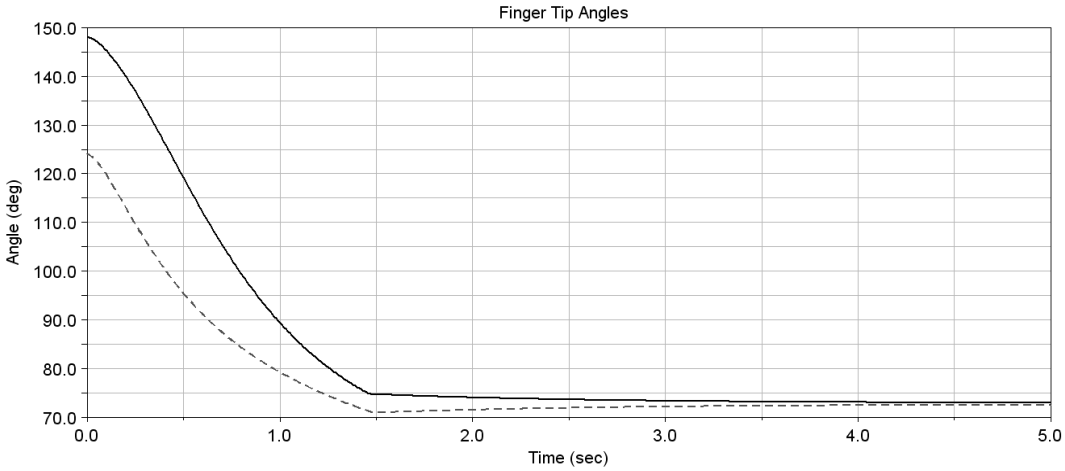

Fig. 5. Finger tips angle at rectangular object grasping
(index finger solid line and thumb finer dashed line)

As it is shown after contact with object at approximately 1.5 second the angles are not changing much. The small changes are due to object movements toward left.

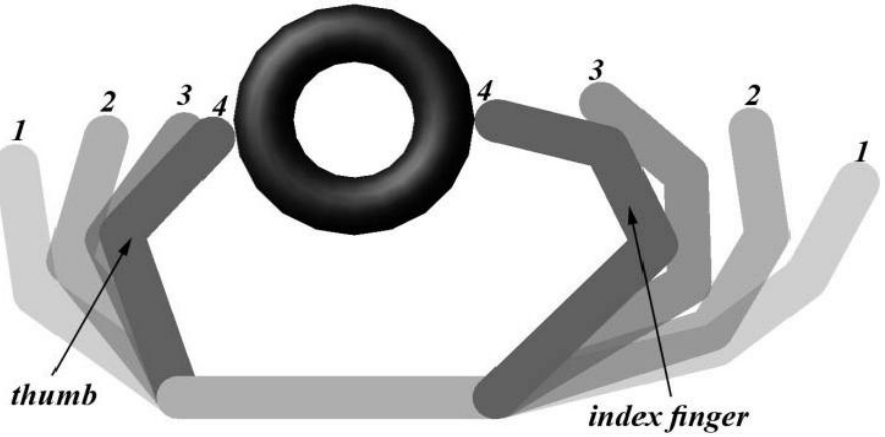

Fig. 6. Circular object grasping (0.25 sec intervals)

For third simulation a round object is selected. The object is not subjected to any constrain in 2 dimensional plane. The contact and friction force are defined between object and finger tip. The virtual spring coefficient which is proportional to EMG signal is assumed to be constant. Almost after 1 sec, the fingers contacted with the object. The finger movement at 0.25 sec time intervals and finger tip angles relative to palm are shown respectively in Figs. 6 and 7.

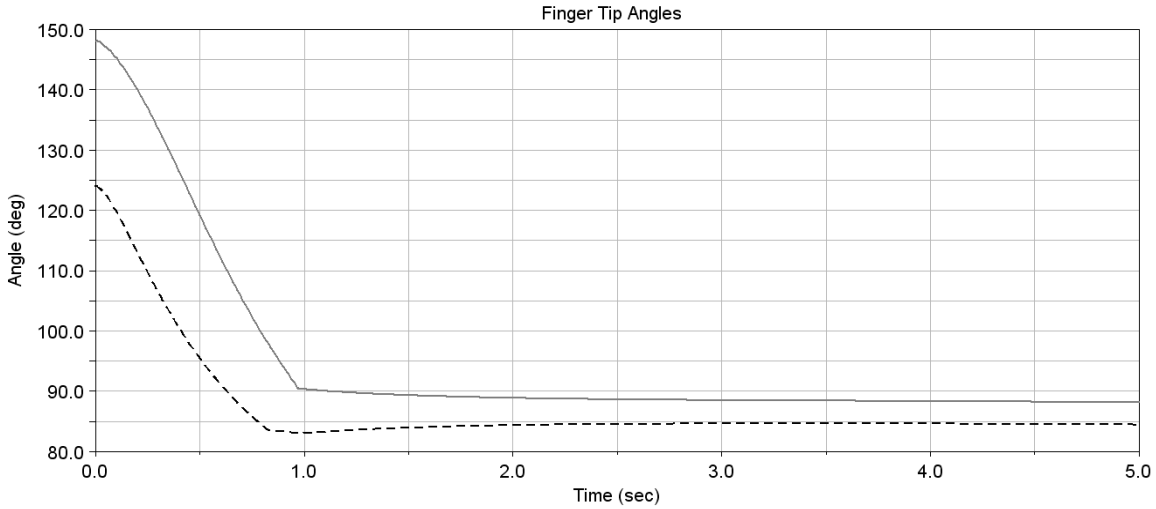

Fig. 7. Finger tips angle at circular object grasping
(index finger solid line and thumb finer dashed line)

Appropriate object position and friction force between fingers and object are important parameters that help successful grasping. For the case of a round object if the object has inappropriate position or friction is not enough, the grasping might be unstable, but guarantied successful grasping under all conditions require information about object shape and position which are not available for case of a prosthetic hand hence this control strategy is appropriate for most of the daily activities.

3. Underactuated prosthetic hand

3.1. Introduction

In underactuated mechanisms the number of actuators is less than their degree of freedom. These mechanisms are widely used in prosthetic hands because of two useful properties: the first advantage is less weight due to less actuator which is used in their design and the second advantage is easier control method.

Underactuation can be implemented through the use of passive elements like mechanical limits and springs leading to a mechanical adaptation of the finger to the shape of the object to be grasped. Underactuated robotic hands are the intermediate solution between fully actuated robotic hands for manipulation and simple grippers. It takes advantage of the mechanical intelligence embedded into the design of the hand allowing the shape adaptation of the fingers. In an underactuated finger, the actuation torque (or more generally wrench) is applied to the input of the finger and is transmitted to the phalanges through suitable mechanical design, e.g. linkages, pulleys and tendons, gears, etc.

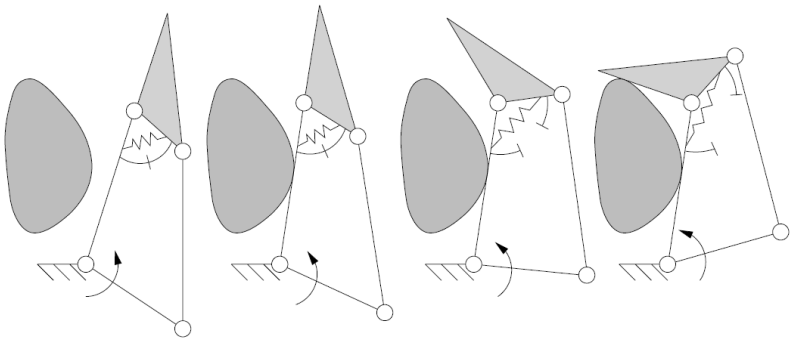

Fig 1.Closing sequence of a two-phalanx underactuated finger

An example of underactuated two-phalanx finger using linkages performing a typical closing sequence is illustrated in Fig. 1. The finger is actuated through the lower link, as shown by the arrow in the figure. Since there are two DOFs and one actuator, one (two minus one) elastic element is used. In the first two steps of the Figure, the finger behaves as a single rigid body in rotation about a fixed pivot. When the proximal phalanx makes contact with the object, the second phalanx is rotated away from the mechanical limit, and the finger is closing on the object since the proximal phalanx is constrained. During this phase, the actuator has to produce the force required to extend the spring. Finally, both phalanges are in contact with the object and the finger has completed the shape adaptation phase. The actuator force is distributed among the two phalanges in contact with the object. It should be noted that this sequence occurs with a continuous motion of the actuator. Notice also the mechanical limit that allows a pre-loading of the spring to prevent any undesirable motion of the second phalanx due to its own weight and/or inertial effects, and to prevent hyperextension of the finger. Springs are useful for keeping the finger from incoherent motion, but when the grasp sequence is complete, they still oppose the actuator force. Thus, they should be designed with the smallest stiffness possible, however sufficient to keep the finger from collapsing.

The basic property of the transmission system of an underactuated finger is to offer $n > 1$ DOF produced with fewer than n actuators. In Figure 2, the transmission stage consists of a five-bar linkage (the base joint is a double pivot) with two DOFs but one angle is initially constrained to a particular value with the spring and the mechanical limit.

3.2. Force analysis of underactuated finger

A two phalanx finger is considered in Fig.2. The input torque T_i is applied to the link a which transmits the torque to the whole finger trough phalanges. A rotational spring with force T is located at O which moves the phalanx back to its original position in absence of external force. The closing process is shown in Fig 2. Providing a mechanical limit can help in order to make pre-tension for the spring to prevent undesirable motion of the second phalanx and also hyper-flexion of the finger.

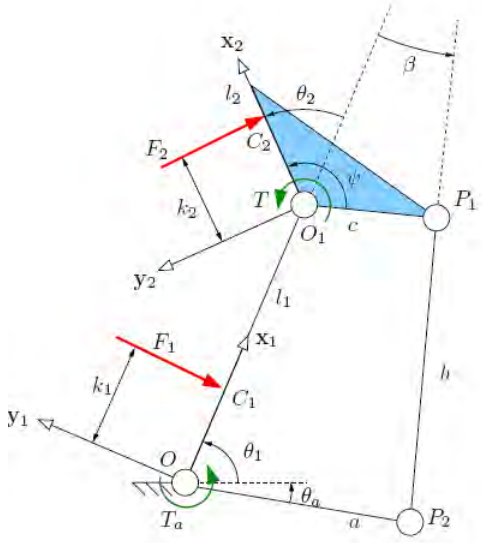

Fig.2. Underactuated hand model and exerted forces

To obtain the static model between inputs and outputs of the finger the virtual work principle is used. Equating the input and output virtual powers results

$$t^T \omega_i = f^T v \tag{1}$$

Where t is the input torque vector exerted by the actuator and the spring, ω_i is the rotational velocity vector, f is the vector of contact forces, and v is the velocity of the contact points along the normal vector of each phalanx. Contact forces are assumed to be normal to the phalanges and without friction. Each element in the above equation can be expressed as

$$t = \begin{bmatrix} T_i \\ T = -k\Delta\theta_2 \end{bmatrix} \tag{2}$$

$$\omega_i = \begin{bmatrix} \dot{\theta}_i \\ \dot{\theta}_2 \end{bmatrix} \tag{3}$$

$$f = \begin{bmatrix} f_1 \\ f_2 \end{bmatrix} \tag{4}$$

$$v = \begin{bmatrix} v_{C1}^T y1 \\ v_{C2}^T y2 \end{bmatrix} \tag{5}$$

The normal velocities of the contact point can be expressed as a Jacobian matrix J_T and the derivatives of the phalanx joint coordinates which is a natural choice, as $v = J_T \dot{\theta}$ or

$$\begin{bmatrix} v_{C1}^T y1 \\ v_{C2}^T y2 \end{bmatrix} = \begin{bmatrix} k_1 & 0 \\ k_2 + l_1 cos\ \theta_1 & k_2 \end{bmatrix} \begin{bmatrix} \dot{\theta}_i \\ \dot{\theta}_2 \end{bmatrix} \tag{6}$$

Through differential calculus, one also can relate vector ω_i to the derivatives of the phalanges joint coordinates defined previously with an actuation Jacobian matrix J_A as $\dot{\theta} = J_A \omega_a$ or

$$\begin{bmatrix} \dot{\theta}_i \\ \dot{\theta}_2 \end{bmatrix} = \begin{bmatrix} X & Y \\ 0 & 1 \end{bmatrix} \begin{bmatrix} \dot{\theta}_i \\ \dot{\theta}_2 \end{bmatrix} \tag{7}$$

Where X=1 and

$$Y = \frac{c[l_1 \sin(\theta_2 - \psi) - a \sin(\theta_1 - \theta_a + \theta_2 - \psi)]}{a[l_1 \sin(\theta_1 - \theta_a) + c \sin(\theta_1 - \theta_a + \theta_2 - \psi)]} \tag{8}$$

Finally, one obtains

$$f = J_T^{-T} J_A^{-T} t \tag{9}$$

which is the equation that provides a practical relationship between the actuator torque and contact forces. If the spring contribution is neglected the analytical expression are rather simple linear functions of the actuator torque,

$$f_1 = \frac{(k_2 - h\cos\theta_2) l_1}{a\, k_1 k_2 (\cot\beta \cos\alpha_1 + \sin\alpha_1)} T_a \tag{10}$$

$$f_2 = \frac{h}{a\, k_2 (\cot\beta \cos\alpha_1 + \sin\alpha_1)} T_a \tag{11}$$

where $h = c(\cos(\theta_2 - \psi) - \sin(\theta_2 - \psi)\cot\beta)$ is the distance between point O_1 and the intersection of lines (OO_1) and (P_1P_2). Also, α_1 is the angle between link *a* and the first phalanx. It can be shown that

$$\cot\beta\cos\alpha_1 + \sin\alpha_1 = \frac{\sin X}{\sin\beta} \quad (12)$$

where *X* is the angle between links *a* and *b*.

3.3. Design optimization

After obtaining the forces equation two consideration form the guidelines for design parameters selection: first grasp should be stable which means ejection should be prevented and differences between the phalanx forces should be minimum possible value. In Ejection phenomena the finger slide and push the object out instead of a secure grasping. To prevent ejection the exerted forces by each phalanx to the object should be positive. It is also desirable that forces at each phalanx to be close to their mean value and force distribute evenly between phalanxes which is referred to as force isotropy. So the conditions which should be satisfied can be expressed as:

$$\begin{cases} f_1 = f_2 \\ f_1 > 0 \quad and \quad f_2 > 0 \end{cases} \quad (13)$$

In order to have force isotropy it is necessary that forces by each phalanx are equal, but forces are function of contact position and θ_2 angle hence it is a local property. Therefore if the object moves these conditions are not true anymore. However in this case, another step is necessary since h is a function of the design parameters and the angle θ_2. Furthermore, many design variables are available to satisfy the latter equation, namely a, b, c, and d.
For instance, if one chooses *a* = *b*, a known *c* (e.g. resulting from minimal distance considerations) and $\psi = \frac{\pi}{2}$, a is completely defined as

$$a = \frac{2\,l_1 c\sin\theta_2 + c^2 + l_1^2}{2}\frac{\sqrt{A}}{B} \quad (14)$$

with ,

$$A = (C-1)((C-1)c^2 + 2cCl_1\sin\theta_2) + C^2 l_1^2 \quad (15)$$

$$B = -c^2 + Cc^2 - l_1 c\sin\theta_2 + 2Cl_1 c\sin\theta_2 + Cl_1^2 \quad (16)$$

$$C = -K\theta_2 + \frac{k_2}{k_2 + l_1\cos\theta_2 + k_1} \quad (17)$$

The above mentioned relationship can be used in order achieving isotropic design. However, the isotropic property is not very robust with respect to design parameters, so it suggests using the following method.
If one obtains an isotropic and therefore stable design for a particular contact set (k_1, k_2, θ_2), it may be of interest that the finger is also robust with respect to ejection around this isotropic point, in order to ensure that a deviation from this configuration does not lead to an unstable grasp. The final aim is to guaranty stability for all grasps if possible and satisfy certain ~~"~~quality" based indices like the isotropy. An index that can be used to ensure the grasp stability, even if the proximal contact is lost, is:

$$\mu = \frac{\int_W \delta(k_2,\theta_2)\,dk_2\,d\theta_2}{\int_W dk_2\,d\theta_2} \quad (18)$$

Where $\delta(k_2,\theta_2)$ is a Kronecker-like symbol for characterizing the stability of the contact situation:

$$\delta(k_2,\theta_2) = \begin{cases} 1 \; if \; the \; final \; grasp \; is \; stable \\ 0 \; otherwise \end{cases} \quad (19)$$

This index is the ratio between the stable and unstable areas in the grasp-state plane of the finger. Contour plots of the index μ is illustrated in Fig 3. for a mechanically actuated finger. The optimal design parameter values can be obtained using the following plot. In our design equal lengths are considered for both phalanxes (l_2/l_1=1), so the optimal value for c/a is around 0.6.

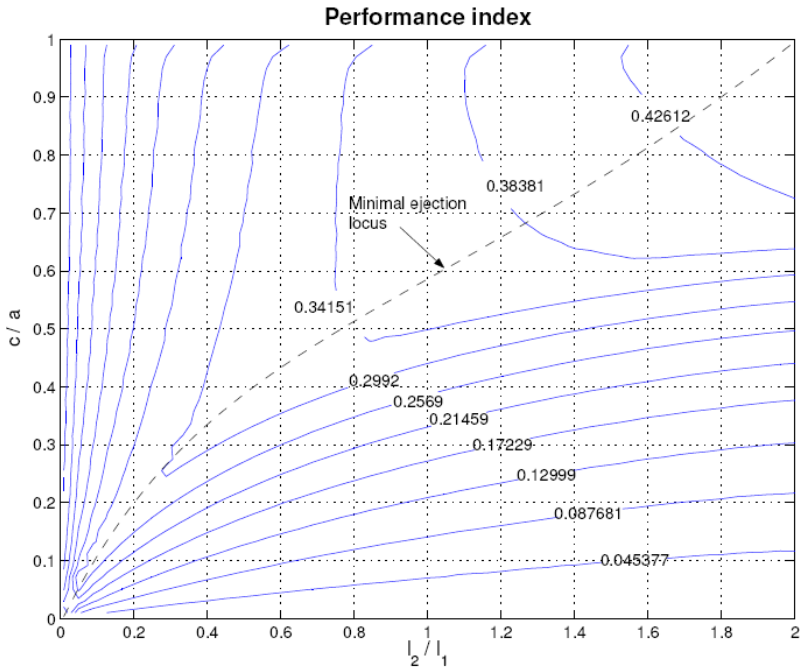

Fig 3. Performance index for linkage driven 2 phalanx underactuated hand3.4. Control system

The control is aimed at exploiting the main properties of underactuation to perform motion tasks close to reference angles obtained by EMG signal. The ordinary task considered for design and development of the motion control law is the finger preshaping for the palmar grasp of a cylindrical object.
Kinematic coupling among the joints is related by the relation

$$x_s = l_1\theta_1 + l_2(\theta_1 + \theta_2) \quad (20)$$

$$\ddot{x}_s = l_1\ddot{\theta}_1 + l_2(\ddot{\theta}_1 + \ddot{\theta}_2) \quad (21)$$

The dynamic relation among the joints are derived in equations (10) and (11).

3.4.1. PD Control in the joint space with elastic compensation

Dynamic relation (20) and (21) is used to actively control the first joint and passively move the second joint. The proposed control law is a modified version of the standard PD control in the joint space with gravity compensation and is expressed as

$$T_i = K_p\tilde{\theta} - K_D\dot{\theta} + g(\theta) + T_e \quad (22)$$

Where $\tilde{\theta} = \theta_D - \theta$ is the joint position error defined as the difference between the reference set point θ_D and the current joint angle θ, $g(\theta)$ is the estimation of joint gravitational torque, and K_p and K_D are the diagonal gain matrices for the proportional and derivative control actions, respectively. In addition to the standard PD control plus gravity compensation, an elastic term is introduced in order to compensate for the preload spring located between phalanxes joint.
The joint elastic torque is expressed as $T_e = k\Delta\theta_2$.

3.5. Numerical simulation

Based on results of optimal design a model of two phalanx finger is made in Adams software linked with Matlab/Simulink, which is shown in Fig. 3. Both phalanxes has the equal length and c/a ratio is 0.6 based on optimal design analysis. Torsion spring is located between two phalanxes. The revolute joint is located at joints and a motor is moving the finger which is shown by round arrow. A circular object is chosen to be grasped and the proposed controller is used to control finger movement.

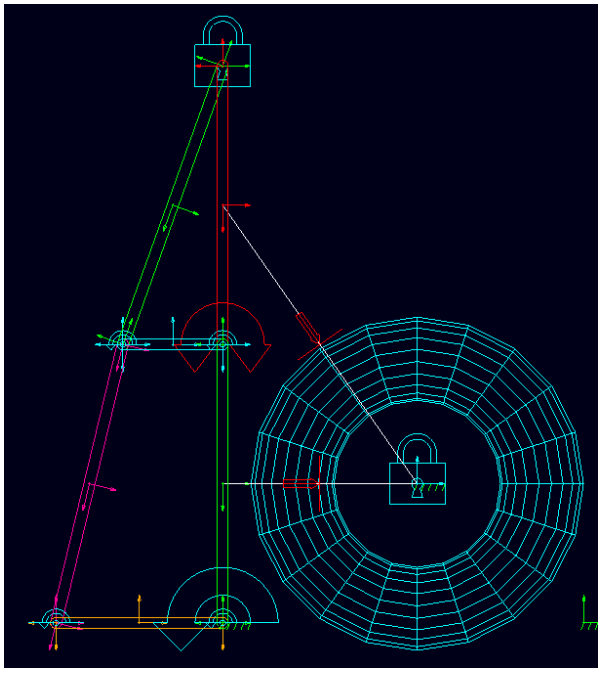

Fig.3. The two phalanx finger modeled in Adams software

By applying the control algorithm to the mechanism the finger can grasp the object. The grasping sequence is shown in Fig. 4 .

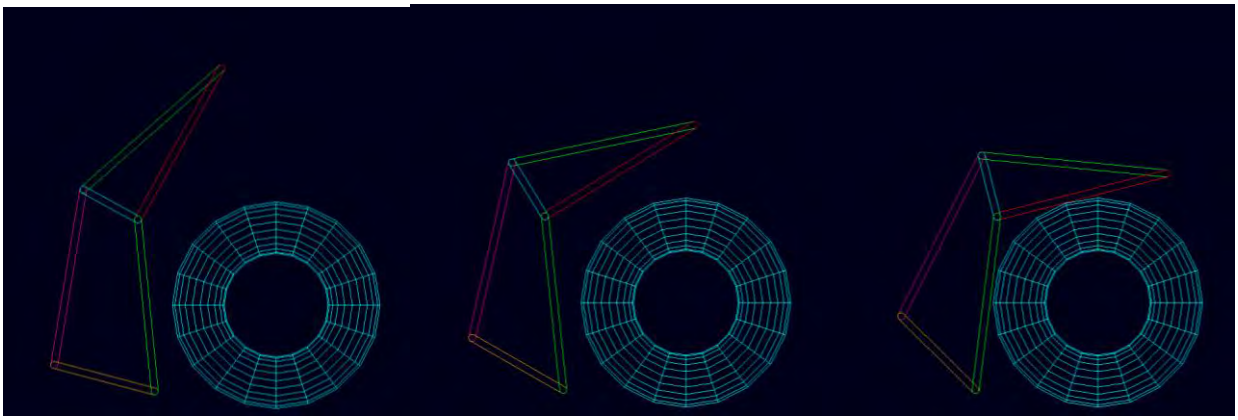

Fig. 4. The grasping sequence of a circular object by underactuated hand

The finger tip angle respect to horizontal plane is shown in Fig. 5. It starts from 90 degree and after first phalanx has contact with the object the rate of change of angle is changed.

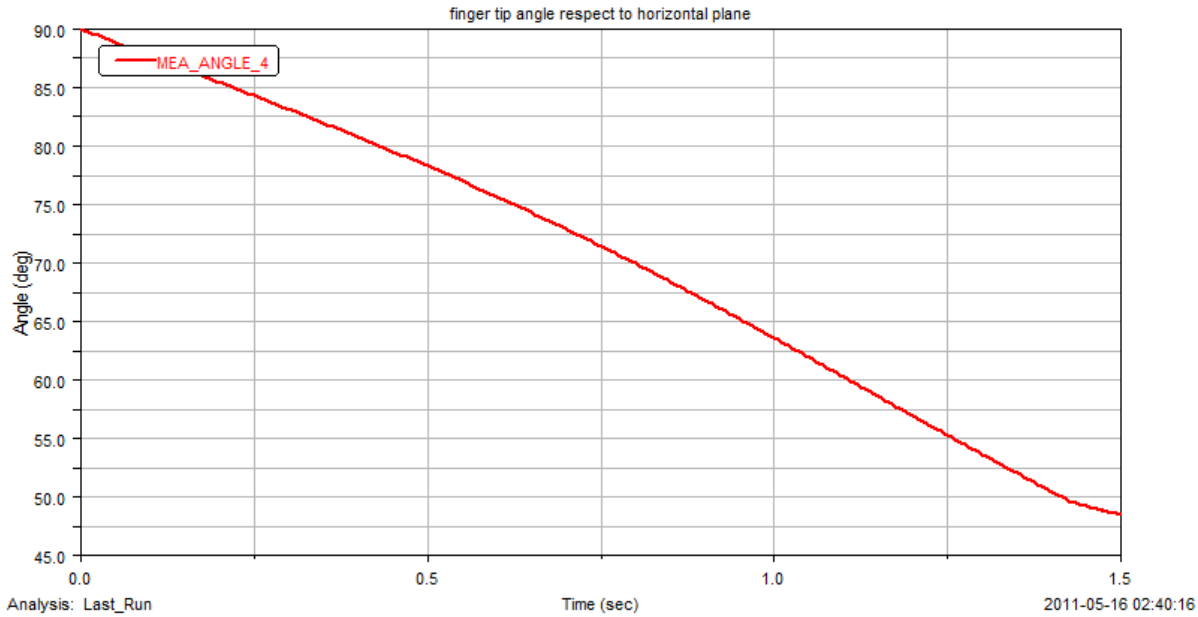

Fig. 5. Finger tip angle respect to horizontal plane for underactuated hand

Angle between two phalanxes is shown in Fig. 6. The angle starts from 180 degree and gradually changes until second phalanx touches the object.

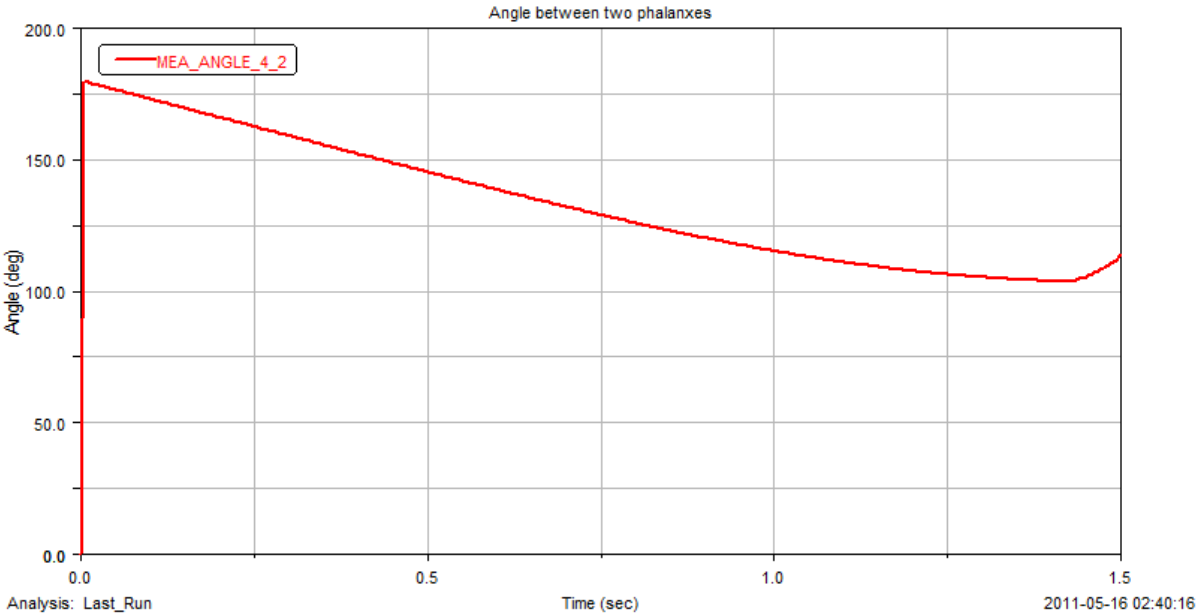

Fig.6. Angle between two phalanxes for underactuated hand

3.6. Comparison study between fully actuated and underactuated hand

Two general design which are fully actuated and underactuated and appropriate control methods for each of them are provided for prosthetic hand. In order to compare the functionality of these two methods a fully actuated finger with the same dimension and with a similar object to grasp is simulated. Power grasping algorithm which described before is used in order to control the movement. The sequence of movement is shown in Fig. 7. The finger tip angle respect to horizontal plane is shown in Fig. 8 and the angle between two joints is shown in Fig. 9.

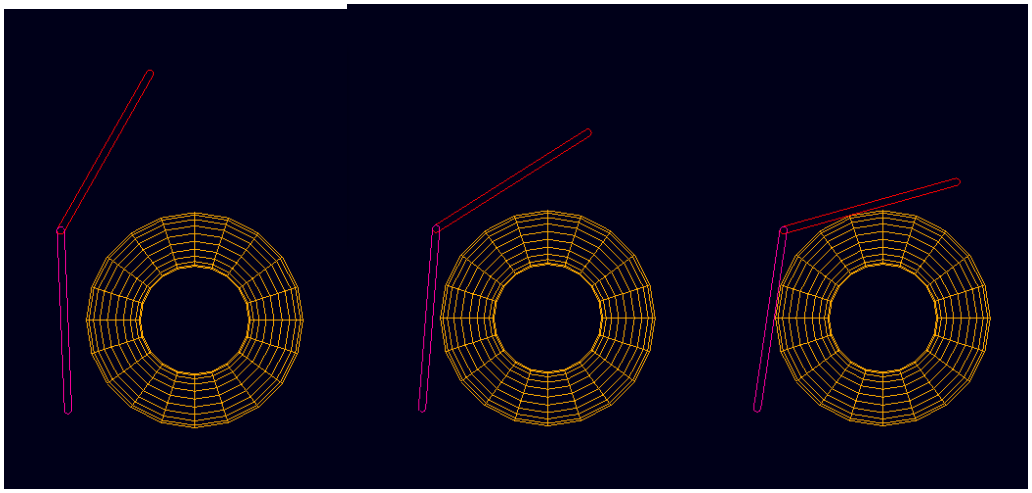

Fig. 7. The grasping sequence of a circular object by a fully actuated hand

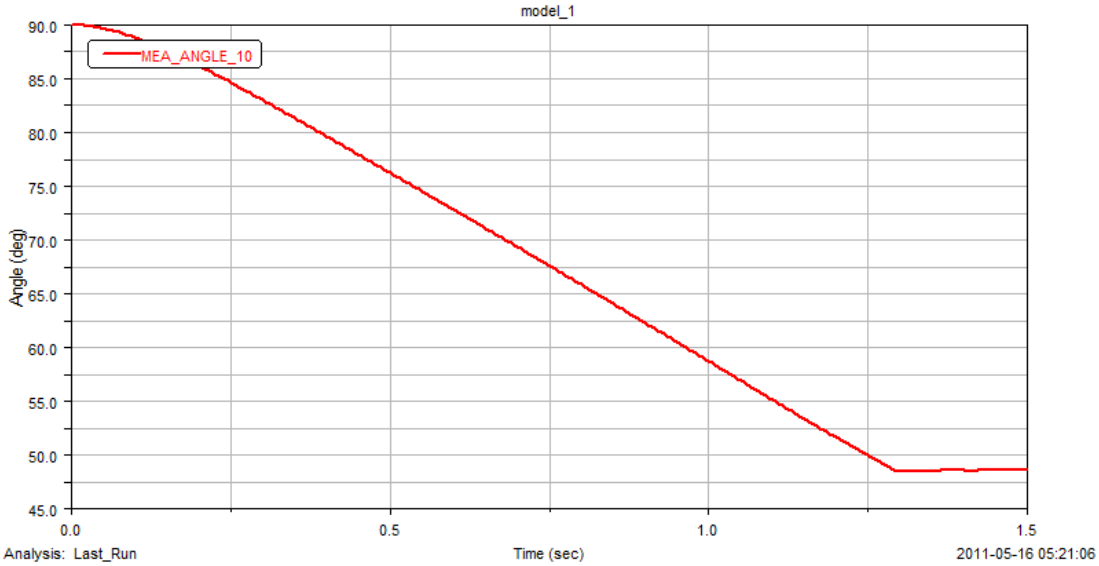

Fig.8. Finger tip angle respect to horizontal plane for fully actuated hand

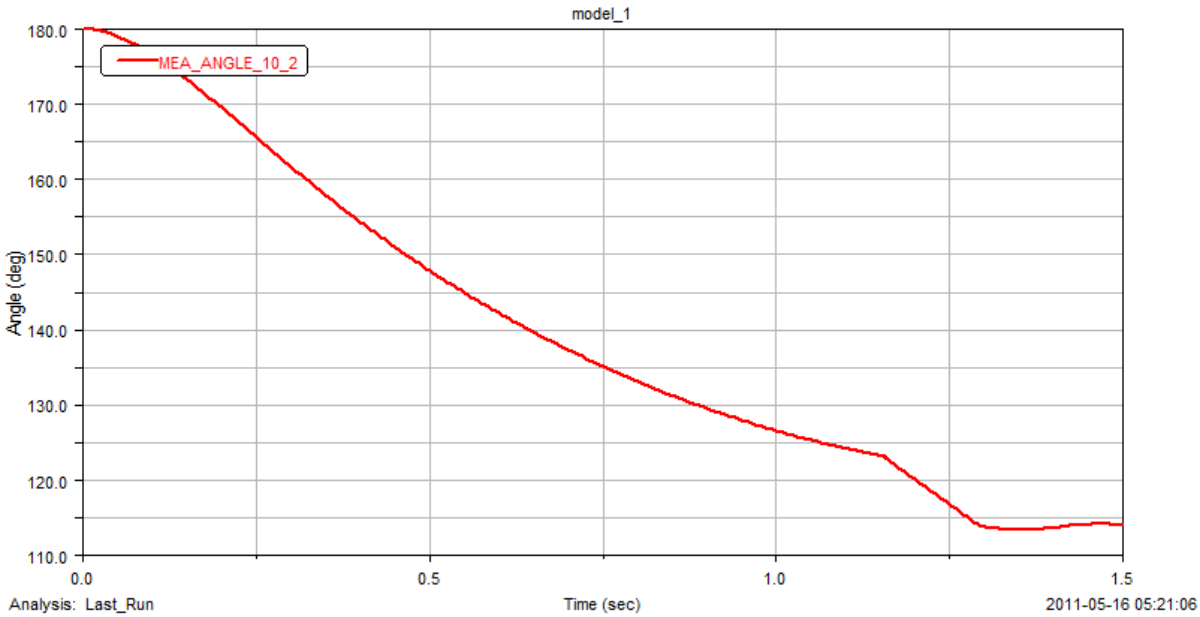

Fig.9. Angle between two phalanxes for fully actuated hand

As we can see both methods are capable to perform grasping and the graphs are very similar for both methods.

Goal 2B: Embedded Hierarchical Real-Time Systems

Overview: ***Narrative that briefly (one paragraph) describes the subject, purpose and scope of the research.*** The annual work under this Goal involved the following key tasks: (1) the construction of a test bed that integrates the software tool chain and prototype hardware (test bed); (2) the study on design and Implementation of the real-time control strategies on the embedded test bed, and the study and experimental set up of a real-time operating system on the embedded processor used in (1); (3) the study of integrating sEMG models on the embedded test bed for real-time control, signal processing and acquisition. The primary purpose of this work is to develop an embedded control system by researching, designing, testing, and prototyping the hardware and software for the system.

This section of the report shall describe the research accomplishments associated with each task outlined in the approved Statement of Work. Data presentation shall be comprehensive in providing a complete record of the research findings for the period of the report. Provide data explaining the relationship of the most recent findings with that of previously reported findings. Appended publications and/or presentations may be substituted for detailed descriptions of methodology but must be referenced in the body of the report. If applicable, for each task outlined in the Statement of Work, reference appended publications and/or presentations for details of result findings and tables and/or figures. The report shall include negative as well as positive findings. Include problems in accomplishing any of the tasks. Statistical tests of significance shall be applied to all data whenever possible. Figures and graphs referenced in the text may be embedded in the text or appended. Figures and graphs can also be referenced in the text and appended to a publication. Recommended changes or future work to better address the research topic may also be included, although changes to the original Statement of Work must be approved by the Army Contracting Officer Representative. This approval must be obtained prior to initiating any change to the original Statement of Work.

Initial System Design

The design is a multi-level hierarchical model with a rectified sine wave input. A flash memory interfaces with the high-level configuration, making it capable of holding the input functions and the control strategy. The flash memory interface is done by a Secure Digital (SD) card which enables quick retrieval and processing of data. The 32-bit PIC, memory interface and the Fuzzy controller constitutes the higher-level configuration. This level controls the lower-level configuration, depending on the input functions. Two 16-bit PICs, each associated with a stepper motor, makes up the lower-level configuration. Two lower-level PICs are programmed to control the stepper motors. The communication system in this design is unique. The two levels communicate through a full duplex distributed communication system. This communication system enables an effective coordination between the levels by distributing the traffic and therefore eliminates delay caused by any traffic congestion. This design provides flexibility in handling with a wide range of communication systems. This includes both the hard-wired and wireless communication based on the application. The stepper motors provide the necessary step changes in the output displacement based on the control signal which is a function of the input. Figure 1 depicts the overall design.

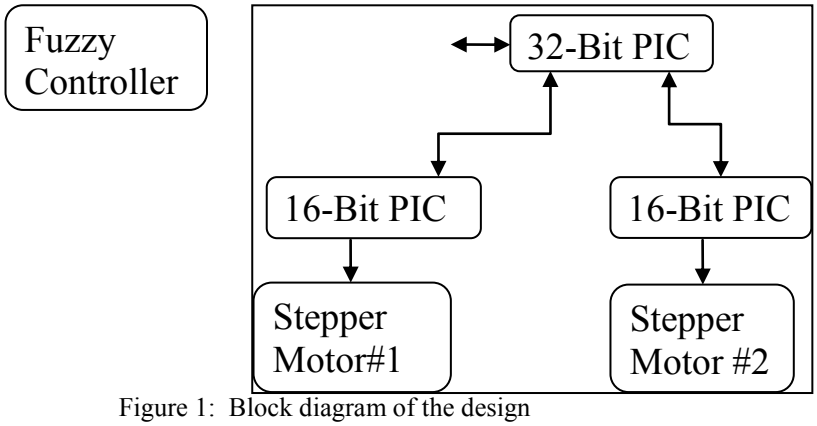

Figure 1: Block diagram of the design

Based on the input function, the fuzzy controller of the high-level configuration has its control signal, to which the 32-bit PIC has access to it through flash memory. The 32-bit PIC sends the encrypted data via the full duplex distributed communication channel to access the lower-level PICs. The encrypted data access the two 18-bit PICs to

control the two stepper motors for the desired angular displacements. The encrypted data has all the information for the control signal. It also contains the information regarding the desired step changes and the directions of them. The lower-level PICs are preprogrammed to control the stepper motors with necessary angular displacement. Synchronization plays an important role in the lower- level configuration. The encrypted data and the communication system make the synchronization easier. This type of communication system avoids traffic delay time. The encrypted data also has the information about the direction angular displacement for each motor. The key part of the model is the fuzzy controller. This gives the control signal to the high-level controller, which encrypts the data and send to the lower-level configuration the actuation signals for the motors.

The lower-level configuration involves two 16-bit PICs that contain the code to control respective stepper motors. When a message is received from the higher level, it will state which motor it wants to activate and what angular displacement it should make. One or both of the PIC16 will take its message and extract the angular displacement. Once this is done, the PIC will relay a message to the stepper motor, making it turn to the desired position. The PIC16 will then send a message to the PIC32 that lets the PIC32 know that it has completed its task. This information will be fed into the fuzzy controller.

The high-level configuration uses a PIC32. The PIC32 has an SD card reader attached to it. Having an SD card will allow large files to be read into the PIC. Another key part of the high-level configuration is a fuzzy controller. The fuzzy controller will be used to analyze the data and process it. The rectified sine wave is compared to the set of rules from the membership function of the intelligent controller. Once a result is determined, the controller will send a message to the lower-level controller [1].

[1] C. Potluri, P. Kumar, J. Molitor, M. Anugolu, A. Jensen, K. Hart, and S. Chiu, ―Multi-Level Motor Control for Prosthesis,‖ in the proceedings of the *2010 International Conference on Embedded Systems and Applications* (ESA, 07/2010).

Intial Controller Design (Related to EMG)

In this design, entropy is taken as the threshold value to initiate the motion by the fuzzy controller. The entropy values are extracted from the EMG signals of the index, middle and ring fingers, respectively when a power grip is done. Table 1 shows the entropy values for the EMG data taken for 11 different subjects. $Ring_1$ and $Middle_1$ in the Table 1 correspond to the entropy of the respective finger right next to its motor point location. Table 2 gives the threshold values. The threshold values are calculated as the difference between the mean and twice the standard deviation. The reason for taking the difference as the threshold value is that the controller should be initiated, even if the sensors are misplaced from the motor units or to eliminate the problems that are caused by the difficulty in identification of motor units in some cases.

Table 1: Entropy values of EMG signals for different fingers

Index	Ring	Middle	$Ring_1$	$Middle_1$
2.9792	2.9271	2.1554	2.3994	1.6711
2.6783	3.0008	1.9376	2.3947	1.5346
3.4943	2.9556	3.0277	2.9568	2.6673
3.679	3.1714	2.9268	3.1175	3.0581
3.2110	2.7015	1.9228	2.7997	1.2993
2.8451	2.9429	1.9555	3.0541	1.1095
1.4653	1.5559	3.7151	2.4827	1.6919
1.9371	1.4639	3.6648	3.2785	1.7955
2.7399	3.7132	3.0820	3.0425	2.3929
2.5421	3.5961	2.8593	2.6782	2.2040

Table 2: Threshold values for index, ring and middle finger EMG signals

Index	Ring	Middle

1.3724	1.5176	1.522

In this design [2], entropy values are used to establish a threshold value for initiation of finger motions. The fuzzy logic determines the correlation between the entropy and the corresponding force. The Mamdani type fuzzy logic is used for this design. The fuzzy logic implemented has four inputs and two outputs. The inputs are the threshold values for individual fingers (index, ring and middle) and the entropy values. The output of the fuzzy logic are the control signals to initiate the motion based on the threshold values and the control signal for the force based on the entropy values. Figure 2 shows the entire rule base for the developed fuzzy logic, which are given below:

1. If I_i is I_t, M_i is M_t, R_i is R_t then the control signal is power grip close.
2. If I_i is not I_t, M_i is not M_t and R_i is not R_t, then control signal is power grip open.
3. If I_i is I_t then control signal is index finger close.
4. If I_i is not I_t then control signal is index finger open.
5. If M_i is M_t then control signal is middle finger close.
6. If M_i is not M_t then control signal is middle finger open
7. If R_i is R_t then control signal is ring finger close.
8. If R_i is not R_t then control signal is ring finger open.
9. If entropy is low, then control signal is low force.
10. If entropy is medium, then the control signal is medium force.
11. If entropy is high, then the control signal is high force.

where I_i, M_i, R_i are the input entropy values and I_t, M_t, R_t are the threshold values for individual index, middle and ring fingers. In Figure 2, columns 1, 2, 3 show the rules for the sigmoidal membership function of input, i.e. index, middle and ring fingers respectively, and the corresponding threshold values. The sigmoidal function enables the initiation of movement for an entropy value which is greater than or equal to threshold value of individual fingers. The 4th and 6th columns give the rule base for the correlation of entropy with the corresponding force. The force is classified by the entropy range into three levels.

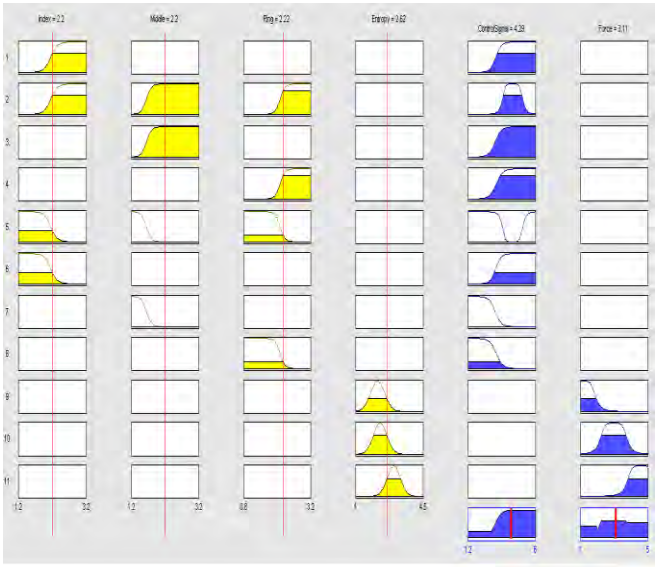

Figure 2: Rules for the Mamdani type fuzzy control

[2] C. Potluri, P. Kumar, M. Anugolu, S. Chiu, M. Schoen, A. Urfer, and D. S. Naidu, ―AnANFIS-Based Fuzzy Controller for Prosthetic Hand," in the proceedings of the *3rd IEEE RAS-EMBS International Conference on Biomedical Robotics and Biomechatronics* (BioRob, 09/2010).

Test Bed for Embedded Systems Prototyping

A test bed based on a 32-bit embedded processor (a.k.a. programmable intelligent controller, or PIC) was built. Figure 3 depicts the test bed, where Stage 1 represents the (micro-level) signal processing circuitry composed of the processor, its I/O expansion board, and the wiring needed to receive input sEMG signals and produce output actuation signals for the plant (the controlled one-finger device). Stage 2 consists of circuit elements and wiring for motor powering, actuation, and isolation of the motor circuit from the Stage 1 circuit for protection of the embedded processor against power surge.

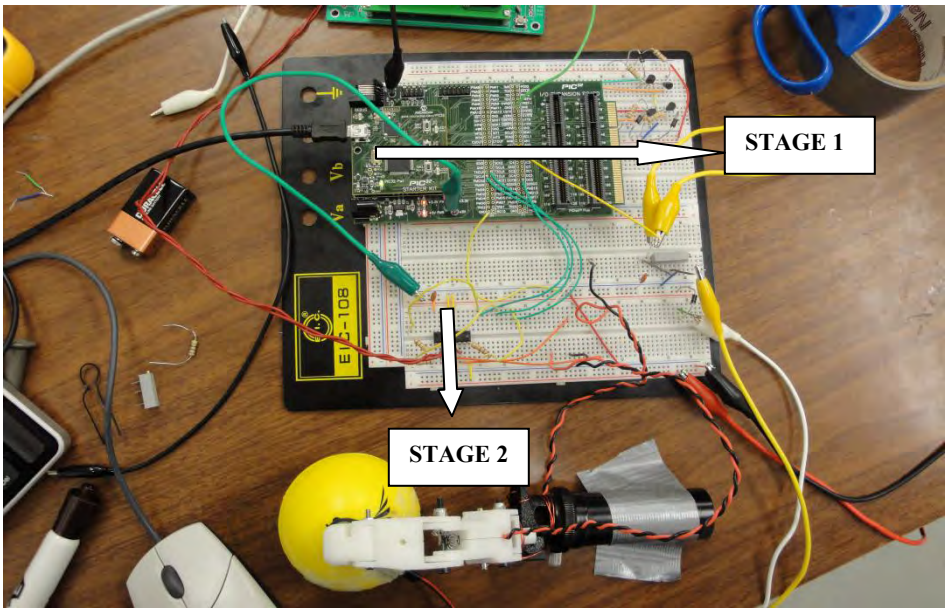

Figure 3. Overview of the test bed (omitting the software tool chain computer)

For Stage 1, a Microchip PIC32-I was used to implement our system. Based on this processor, we selected the dsPIC block set to generate the C code for PIC32-I from Simulink. The intent of this approach for the tool chain is due to the fact that our controller designs are being specified in Matlab models; and Simulink, along with its Real-Time Workshop toolbox, provides a logical and efficient path from model to prototype implementation and testing, for a given controller design. The processing flow of the various elements of the tool chain is shown in Figure 4, which builds and releases the executable of the controller to the PIC.

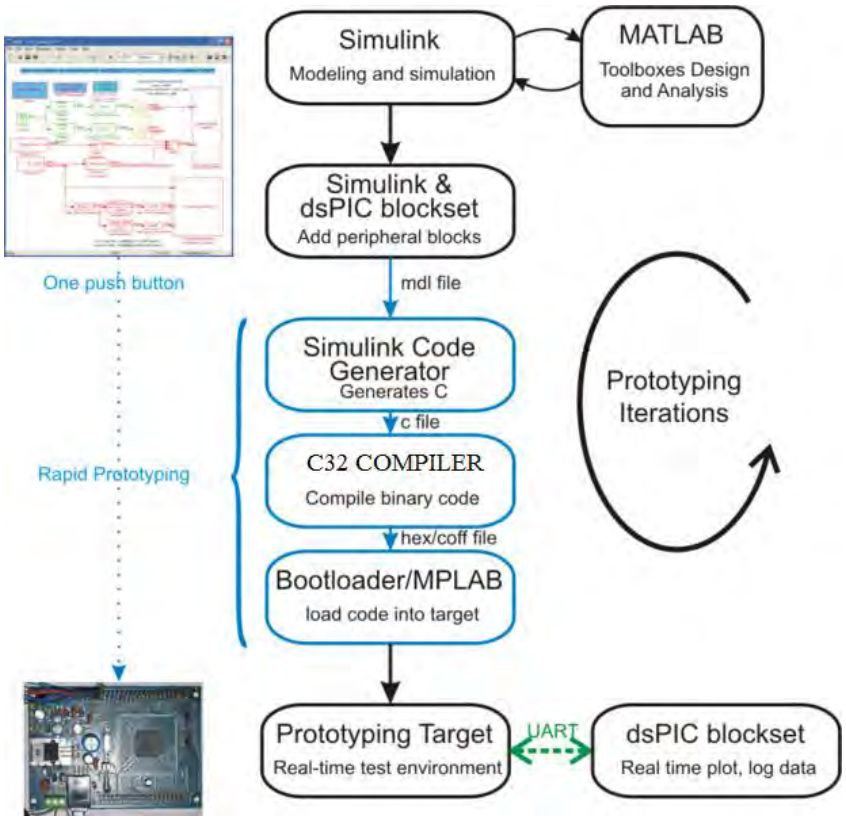

Figure 4. Processing flow for generating code to the processor

Several hardware modules within the PIC32-I were also used, including the Analog Input module, the Digital Output module, the Output Compare module, and the UART module. The Analog Input module was used for reading the input sEMG as well as sensory feedback data from the prototype hand. PIC32-I has an internal analog to digital converter. A real-time control strategy uses the data from the Analog Input module as a reference signal or the set point. Based on the control strategy, the Digital Output module generates digital control signals. The Output Compare module then generates a pulse width modulated (PWM) waveform with a specific duty cycle, based on the input analog signal (i.e. the sEMG). The UART module is used to transmit the signals from PIC32-I to a personal computer via the serial (i.e. RS-232) communication. This interface enabled us to debug and evaluate the performance of control strategies.

For Stage 2, we used the SN754410 quadruple half-H driver to actuate the motor with the control signal. The pin configuration for the H-driver is shown in Figure 5. The PWM signal from the Output Compare module is connected to pin1 (labeled ―1,2EN") of the H-driver. The digital outputs of the PIC32-I are connected to the direction pins of the H-driver (pins 2 and 7). By switching the digital outputs to 0 and 1 between the direction pins, the motor will rotate clockwise or counter-clock wise. Vcc_1 and Vcc_2 are connected to the 5-volt DC supply of the PIC32-I I/O expansion board.

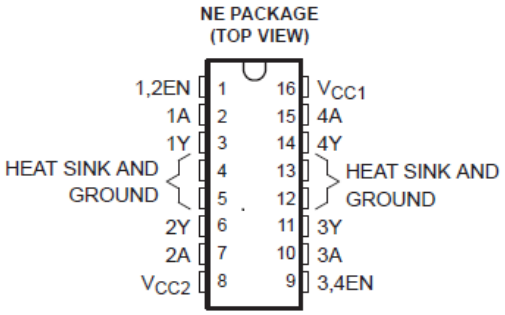

Figure 5. Pin configuration of the quadruple half-H driver.

The test bed and its operation was demonstrated, in the form of recorded video, to the researchers at the Applied Physics Laboratory of Johns Hopkins University, a major collaborator on the TATRC project with which ISU is a part of. The JHU APL researchers expressed their interest in further collaboration with ISU in several areas including this and the validation/verification of sEMG signal processing algorithms.

Design and Implementation of Real-Time Control Strategies:

In this work [3], the threshold values establish a correlation between the sEMG and the corresponding force required for the power grasp of an object. C.Potluri *et. al* [2] explained the correlation between sEMG entropy threshold values and skeletal muscle forces. These threshold values are fed as the reference or a set point to the controller. The signal flow is depicted as a block diagram in Figure 6.

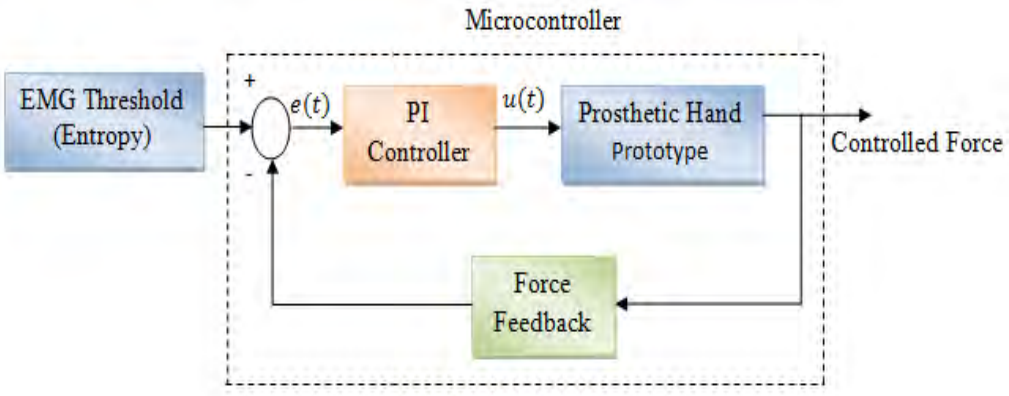

Figure 6. Block diagram of the real-time control signal flow.

The force feedback signal is acquired by a force sensitive resistor (FSR). The FSR is mounted on the fingertip of the prosthetic hand prototype as shown in Figure 8. The error $e(t)$ is computed as the difference between the reference value and the actual force from the FSR. A proportion-integral (PI) controller is employed to generate the actual force from the FSR, and make it equal to the reference force in order to reduce the error $e(t)$ to zero. The PI control action is given below in Equation (1).

$$u(t) = K_p * e(t) + K_i \int_0^t e(\tau)d\tau, \qquad (1)$$

In Equation (1), $u(t)$ is the control signal, K_p is the proportional gain, and K_i is the integral gain, $e(t)$is the error, and τ is the dummy integration variable. Gain parameters K_p and K_i are tuned using the Ziegler-Nichols method in MATLAB®.

Our proposed design was implemented on a PIC32-I microcontroller in two stages: ―Signal Processing" and ―Motor Actuation." The Signal Processing stage facilitates the implementation of real-time control strategies. A dsPIC

blockset was used to generate the C code for the PIC32 from Simulink®. The dsPIC blockset generates a .hex file, and this file is imported by MPLAB® to program the PIC.

Signal Processing Stage

We used the following modules of the PIC32 as a part of implementing our control strategies: the Analog Input module, the Digital Output module, the Output Compare module, and the UART module. The Analog Input module was used for reading the sEMG and sensory feedback data. The PIC32 has an internal analog to digital converter (ADC) which has a 10-bit resolution so that it can distinguish up to 1024 different voltages, usually in the range of 0 to 3.3 volts, and it yields 3mV resolution. A real-time control strategy was developed using the threshold value of the entropy of sEMG data as a reference or set point. The difference between the threshold of the sEMG entropy and the FSR feedback was fed in to the PI control loop to reduce the error to zero. The Digital Output module of the PIC32 was used to generate digital control signals. Depending on the error, a pulse width modulated (PWM) wave with a specific duty cycle was generated in the Output Compare module. The UART module in the PIC32 was used to transmit the signals from the microcontroller to the PC via serial communication. In this design, a virtual com port was created to feed the data via USB cable to the computer. MATLAB® was used to read the signals from the ports. This enables the user to troubleshoot and see the performance of the designed control strategy. The design is consistent with our initial system design and the embedded test bed.

Motor Actuation Stage

A SN754410 quadruple half-H driver is used to actuate the motor with the corresponding control signal. Fig. 3 shows the schematic of the pin configuration of the half-H driver. The PWM signal from the Output Compare module was connected to pin1 (1, 2EN) of the H driver. The PWM wave enables this H driver. The speed of the motor depends on the duty cycle of the PWM wave from the Output Compare module, which is a function of $e(t)$. The digital outputs of the PIC32 microcontroller are connected to the direction pins of the Hdriver (pins 2 and 7). Switching the digital outputs to 0 and 1 between the pins will makes the motor rotate in clockwise and counter-clockwise directions. V_{cc1} and V_{cc2} are connected to the 5V supply of the PIC32 I/O board. This proposed design was tested on an index finger of a prosthetic hand prototype. This part of the work made use of the embedded test bed as previously described.

Mechanical Structure of Hand Prototype

The robotic hand prototype finger has three degrees of freedom, and is actuated by two Pololu 35:1 mini metal gear motors and a bevel gear transmission system. The main characteristic of this prototype is its biologically-inspired parallel actuation system based on the behavior/strength space of the ”Flexor Digitorum Profundus (FDP)” and the ”Flexor Digitorum Superficialis (FDS)” muscles as explained in Figure 7. However this research work focuses on the ”Region 1” actuation system and it is interfacing with a microcontroller. Region 1 is populated by the more frequent dexterous tasks.

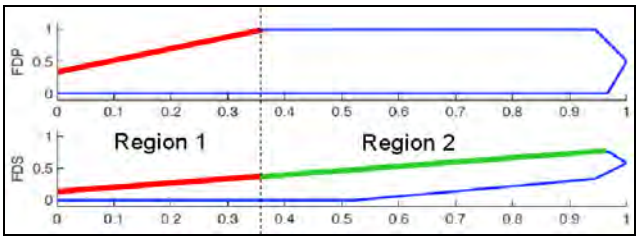

Figure 7. Strength space of FDS and FDP muscles

In our design, the movements associated with Region 1 are achieved by 2 DC motors. The motor in the metacarpal phalange of the finger actuates the PIP (Proximal Inter Phalangeal) joint and the motor at the base of the finger actuates the MCP (Meta Carpo Phalangeal) joint, as shown in Figure 8. As the main objective of this work is to

interface and control the two motors with a microcontroller, we have not considered the belt transmission system which is designed to drive the DIP (Distal Inter Phalangeal) joint as well.

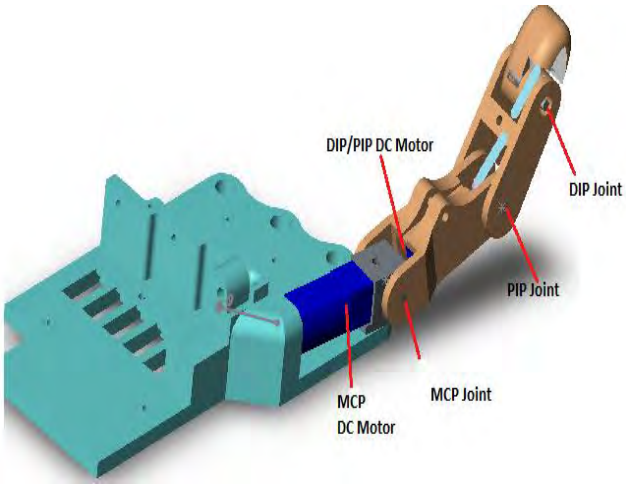

Figure 8. Region 1 actuation scheme for the finger

[3] C. Potluri, Y. Yihun, P. Kumar, J. Molitor, S. Chiu, D.S. Naidu, S. H. Mousavinezhad, ~~s~~EMG Based Real-Time Embedded Force Control Strategy for a Prosthetic Hand Prototype," Accepted in 2011 IEEE International Conference on Electro/Information technology (IEEE EIT, May 2011).

Reportable Outcomes

Results are acquired from the microcontroller through UART channel 2 of the PIC32 by a virtual com port via USB at 57600 baud rate. The data from the microcontroller is converted into unit16 data before it is transmitted through the UART. The PIC32 microcontroller is running 80 million instructions per second (MIPS) with its phase lock loop (PLL) activated. It is running at an external clock frequency of 8MHz with internal scaling enabled.

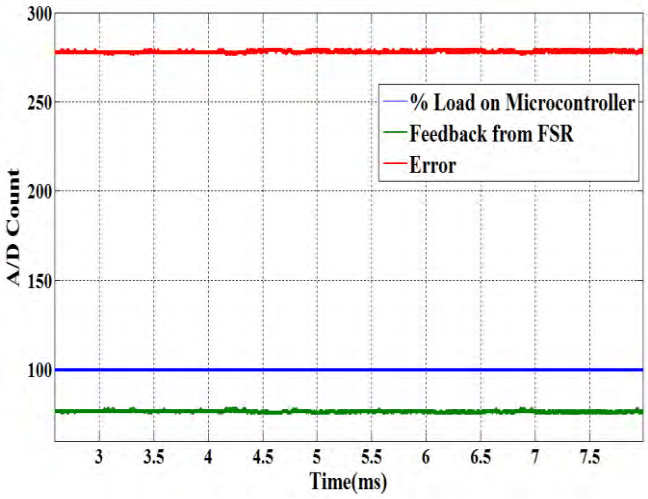

Figure 9. Feedback force and error before grasp

Figure 9 depicts the feedback force from the FSR and the error $e(t)$, before the grasp. As there is no contact between the object and the hand, the force is low and ideally should be zero. However, because the PIC32's ADC module has a high resolution, it shows some values even when the object is not in contact.

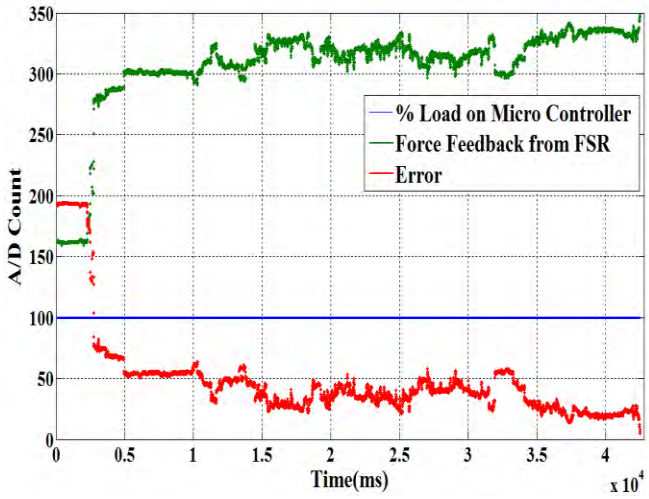

Figure 10. Feedback force and error after grasp

Figure 10 depicts the feedback force from the FSR plotted against the error $e(t)$ after the grasp. The error $e(t)$, i.e. the difference between the reference force from the sEMG threshold value and the actual force feedback from the FSR, is almost zero. From Figure 10, it is also evident that the actual force from the FSR is almost equal to the reference force value that is established from the sEMG threshold value, as the error approaches zero. Figure 11 shows the computational load on the PIC32 while performing this grasp. It indicates that the microcontroller completed the computation in approximately 12ms. The rest is handed over to the I/O blocks of the microcontroller and to the motor actuation stage.

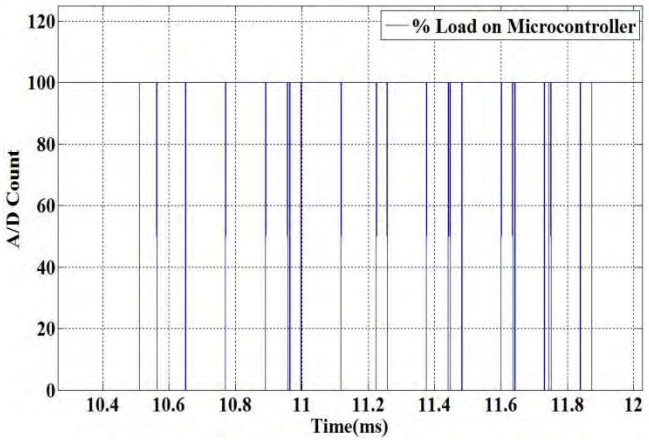

Figure 11. Computational load on the PIC32 during the grasp.

These results suggest an extensible design for increased load on the processing by the embedded system.

Real-Time Operating System for Embedded Control

For our work FreeRTOS is used to schedule several tasks that the microcontroller needs to do, based on their priority levels. These tasks include sEMG analysis, high-level control (i.e. the control strategy), low-level control

(i.e. the motor control), receive data from contact sensors, receive data from force sensors, and receive data from encoders, among others. All these tasks need not be done at the same frequency. Some of them might happen only occasionally. In case of contact an interrupt might happen and the controller algorithm might change, based on the event driven structure. Control load for each situation might be different. A task is an independent thread of execution that contains a sequence of independently schedulable instructions. Multitasking is the ability of the operating system to handle multiple activities within set deadlines. The Free RTOS multitasks in such a way that many threads of execution appear to be running concurrently; however, the OS is actually interleaving executions sequentially, based on a preset scheduling algorithm. The scheduler ensures that the appropriate task runs at the right time. FreeRTOS supports up to 256 priority levels, in which 0 is the highest and 255 the lowest. With a preemptive priority-based scheduler, each task has a priority, and the highest-priority task runs first. If a task with a priority higher than the current task becomes ready to run, the kernel immediately saves the current task‘s context and switches to the higher-priority task. When that is done, the control is returned to the original task.

An experimental setup similar to the one shown in Figure 3, but with Free RTOS installed on the PIC32-I, was built. For proof of concept, the embedded processor running a Free RTOS kernel was connected to two different sets of components: a DC motor and a group of LED‘s. An application program was built and released onto the PIC32-I, which drove the DC motor and flashed the LED‘s by way of interleaving the two separate tasks, with equal priority levels assigned to both tasks. The application performed as designed without any noticeable delay. While the computational loads of these tasks are insignificant, this experiment demonstrated the value of Free RTOS and its potential use at least in the low-level control, where multiple motors or sensing devices will likely be employed.

External Mass Storage of On-line EMG Data

Because embedded processors such as the PIC have limited on-chip storage, interfacing with external devices helps increase the data managing capability for our embedded control. In order to use these external devices such as the Secure Digital (SD) memory cards, we need to initialize the device. We tested a simple data sending and receiving pair as follows. For reading data from the SD card initially we sent a Read_Signal Command, then wait for the SD card to respond with a specific token DATA_START. Once the token is received we can confidently read in a rapid sequence all 512 bytes composing the requested block of data. This was followed by 16-bit Cyclic Redundancy Check (CRC) and finally we can retrieve data from device. Data sending worked as follows: Send a Write_Signal command and check the SD card‘s response to make sure that the command is accepted. Send DATA_START token and immediately after it, in a short loop, all 512 bytes of data. Send 2 bytes for the 16-bit CRC (with any dummy value). The token DATA_ACCEPT will confirm that the entire block of data has been received and the write operation has started. Wait for the completion of the write command. While the card is busy writing, it will keep the SDO (Send Data Out) line low. So we will wait for the SDO line to return high. We need to take care of the interrupts and communication path from the external device to the PIC to ensure both read and write operations are completed successfully.

Advance in technology helped to include a USB interface on the PIC32-II. With this we can directly accesses the USB for reading and writing the data from and to the USB. The USB module consists of the Clock Generator, USB Voltage Comparator, Transreceiver and SIE Dedicated DMA controller. The PIC32-II also includes a PIC32MX440F512H USB micro controller that provides debugged connectivity over USB. It provides 2 types of protocol translation debugging USB connectivity. The USB peripheral stack consists of the following layers:

Application Layer– Consists of the firmware needed to implement the device desired behavior.

Function Drivers– Function drivers implement the desired function behavior and provide function-specific control interfaces to the application. To access the USB and transfer data and control information, function drivers interact with the USB device layer.

USB Device Layer– Handles the protocol elements specified by the manufacturer. The device layer communicates with the Hardware Abstraction Layer as necessary to support interface.

Hardware Abstraction Layer (HAL)– Abstracts the USB controller hardware and provides accesses to all the features that the controller implement to support a USB peripheral Device.

We began preliminary work to build a look-up table of sEMG data based on the entropy corresponding to the ring, middle and index fingers. The next step is to implement a table and store it on USB-based storage devices, and programming the processor to read the data from USB and store the sEMG data during on-line acquisition of sEMG data.

Modeling and Simulation of the Embedded Control

One of the aspects that should be considered in this project is modeling and simulation of prosthetic hand. The simulation provides an environment to test the functionality of hand and evaluating performance of different control algorithms. A simulation environment can also provide visualization of hand which can be used in training the amputees before they use the actual prosthetic hand. A system design which has been used by Johns Hopkins University in order to simulate a prosthetic hand in an integrated environment is studied and the features of used elements is described and discussed.

Virtual Integrated Environment

The Virtual Integrated Environment (VIE) is a simulation system to model prosthetic hand as close as possible to a real hand in a virtual environment. This system is developed by Johns Hopkins University and it is a combination of different software which communicates with each other. The main elements of the system include: dynamic modeling, visualization, EMG data acquisition, and control. If it is required to model the prosthetic hand as a part of body, some optional parts might be added to the system. In this case it is necessary to track body movements, and an optical tracking system handles this part. The structure of VIE is shown in Figure 12.

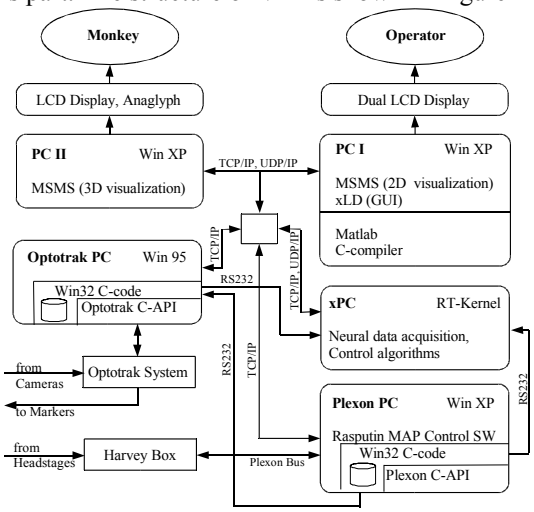

Figure 12. Block diagram of the VIE elements

Because the system is made of different software and elements, the TCP/IP and UDP/IP standard protocols are used to provide communication between these parts at the software level; and RS232 is used at hardware level for similar purposes. The VIE is capable of testing the functionality of the prosthetic hand and training amputees. However, the necessity of simulation is not limited to the above mentioned purpose and in design stage each design team might need to use some sort of simulation. One of the main simulation needs is dynamic modeling and visualization. The MSMS software is used for this purpose.

MSMS (Musculoskeletal Modeling Software)

MSMS is a software application for modeling and simulation of neural prostheses systems. It can be used to model and simulate human and prosthetic limbs, and the task environment they operate in. The simulations can be executed in a standalone computer to develop and test neural control systems or in a virtual reality environment where the human or animal subject can interact with and therefore affect the behavior of the simulated limb. MSMS is based on standard XML format for model description. It has some limited tools for creation, editing, and visualization of 3D models. To use more complicated models it has the ability to import models from SIMM and SolidWorks. Ability to model human limbs and prosthetic limbs and the task environments is a main feature of MSMS. The input commands to the hand can be stored in motion files or can be streamed in real-time from a simulation or motion

capture system. It also has the ability to playback animation sequences. The prosthetic hand can interact with the environment and finally the software can be used for virtual environment and subject in the loop simulation of prosthetic hand. The solver used in the software is SimMechanics which is part of the Matlab/Simulink software. SimMechanics is a multi-body mechanical simulation system. In this software instead of driving dynamic equation mechanical elements like joints, constraints and force elements are attached together and modeled as a system. MSMS provides a tree structure to make the model, which means each part can include some subparts. This feature makes the model easier to access and edit for later use, and it is based on XML description of the model. The structure of the software considering importing the CAD model from SolidWorks is shown in Figure 13.

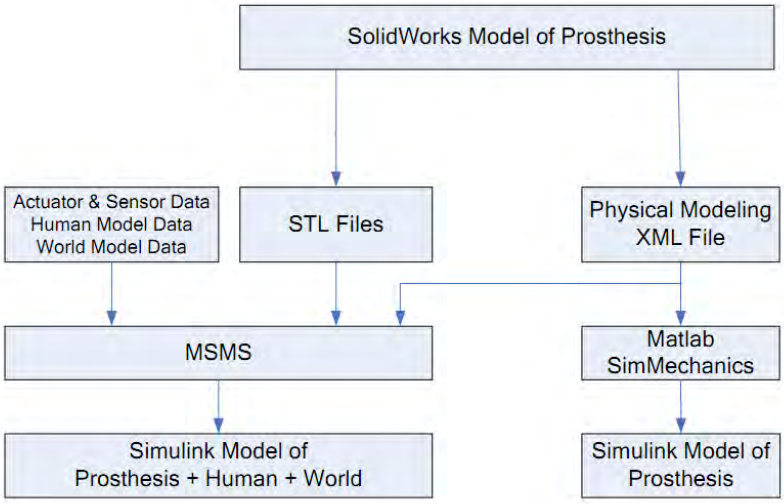

Figure 13. Importing models from SolidWorks to MSMS and from MSMS to Simulink

SolidWorks outputs a Physical Modeling XML file describing the mechanical linkage and STL files representing the appearance of each segment. Both sets of outputs are used by MSMS to create an accurate model of the prosthetic limb in MSMS. The final Simulink model can be built via Matlab/SimMechanics or MSMS. But the use of MSMS allows the users to attach the imported prosthetic limb to a human, add additional prosthetic components such as actuators, and simulate it in an appropriate task environment.

Simulation Mode

MSMS models can be automatically converted into Simulink for physics-based simulations of the model‘s behavior in response to control inputs and external forces. By defining the inputs and outputs, MSMS model converts as a block into the Simulink environment. By use of xPC target it is possible to run the model in real time and for virtual reality simulation and subject in the loop purposes. Figure 14 depicts this conversion process from MSMS to Simulink and xPC.

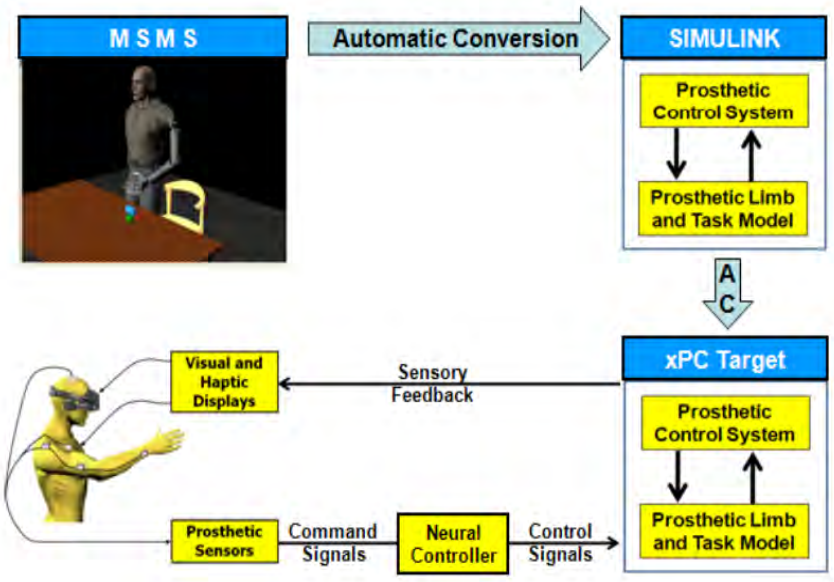

Figure 14. Model conversion from MSMS to Simulink and xPC target for real-time simulation

Solver Performance

As mentioned above, the solver uses SimMechanics. So the solver features are similar to Matlab/Simulink environment. The initial time, final time, and step size can be set; and simulation runs based on these parameters. The smaller steps means more accurate simulation which is necessary especially when the subject is interacting with the environment, and when modeling collision and grasping. On the other hand, the computation load increases and running simulation in real time might be impossible as the steps become very small – this suggests a computational performance bottleneck.

Goal 3: Robotic Hand

We proposed two deliverables within Goal 3 for Phase II, which can be divided in three objectives. The first one is the implementation and testing of the hand prototype developed in Phase I (Prototype 1), whose main characteristic is the parallel actuation system. The second one is the design of the new prototype (Prototype 2), combining the results of the testing with newly developed kinematic synthesis results, and with the results from the EMG signal identification. The third goal is to explore the manipulation of grasped objects from a theoretical point of view. Below find the detailed report of work and findings for each of these objectives.

Goal 3, Objective 1: Implementation and testing of hand Prototype 1

The outcome of the design from Phase I consisted of a two-finger plus thumb prototype with parallel actuation for mimicking the actions of the two main finger-flexing muscles, FDP and FDS (see final Report of Phase I). From now on, we will call this design Prototype 1.

Prototype 1 function

According to the results of the testing of the parallel actuation, and to the current findings of our Goal 1: EMG Signal Identification and Estimation, Prototype 1 will keep the parallel actuation structure, but its purpose has been modified: the parallel actuation system is to be used to drive separately the signals from position and force. The light, not-so-strong actuators at each finger limb will be driven by the motion, while this will be complemented, if needed, by the stronger, coupled actuators at the palm when more force is needed.

The manufacturing of Prototype 1 has been continued and extended for a full hand, with slight design modifications to correct flaws that were identified during the initial testing. The final version of Prototype 1 has the parallel actuation system and position / force feedback sensing.

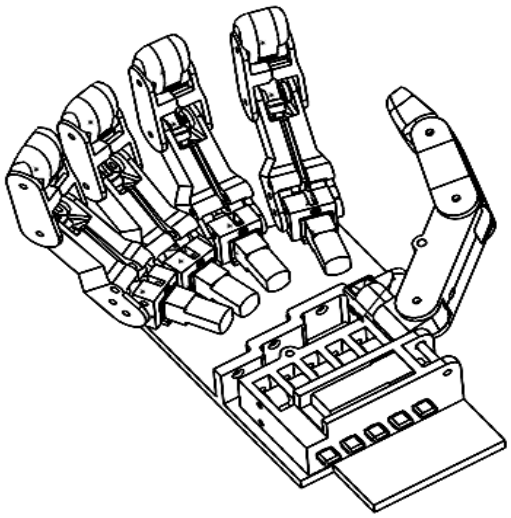

Figure 1: Hand Prototype 1 design

The refinement of the Phase I prototype has led to a five-fingered anthropomorphic hand (Figure 1) based on the design carried out at Phase I, has been manufactured and assembled with the electrical actuation structure (Figure 2). There has been some redesign for a better functionality and ease of assembly.

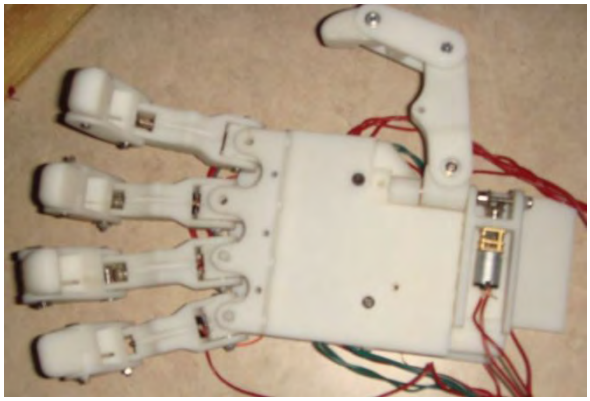

Figure 2: The assembled hand Prototype 1

Electrical actuators

The muscles of most interest for this research and most responsible for flexural grip of the finger are the FDS and FDP muscles. The FDP muscle reaches its maximum force exertion at approximately 35% of the total flexural effort; however, the FDS muscle continues to exert force until it reaches about 100% of the total flexural effort. It is to be noted that the actual act of gripping requires much less complex finger motion than that of manipulation. Based on these observations, the FDS and FDP strength space was divided into the region 1, which represents the more frequent dexterous tasks, and region 2 i.e. the less frequent and more strength based tasks. Having this concept the design of the actuation has been implemented accordingly.

The region-one actuation scheme for the fingers, i.e. DIP/PIP DC motors and the MCP DC motors, has been assembled and tested for different grasping configurations. Figure 3 shows the actuators within the hand. The actuators used in the prototype are Pololu 35:1 Mini Metal Gearmotors. The DC motors are coupled to the joints of the finger via two bevel gears.

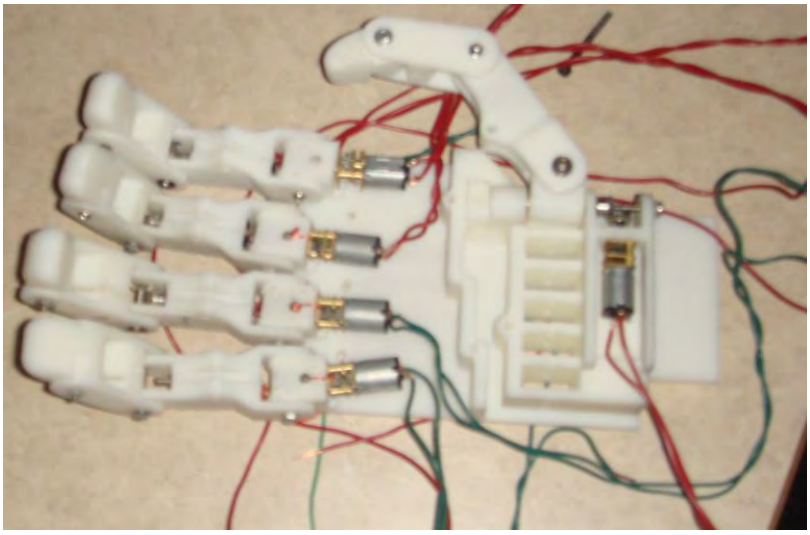

Figure 3: Region-1 actuation scheme for finger

Experimental setup and Testing

The basic requirements for a prosthetic hand are grasping functionality and simple controllability. These different requirements cannot be addressed separately because they are strictly connected and can be faced as different issues of one fundamental challenge to develop appropriate and suitable artificial hands able to ultimately replicate the characteristics and performance the human hand.

In order to assess whether a design is successful from a functional point of view, a well-defined set of tasks and performance indices are needed, see (Ellul and Saliba 2010). The development of the standards and benchmark tests for Prototypes 1 and 2 is a task that is currently being developed and we expect to finish in the next three months.

In parallel, some testing has been performed in order to assess basic functional aspects of Prototype 1 as well as its basic interaction with the EMG driving signals. This testing is described below and is partially covered in one of our publications (Crawford, et al. 2010).

Testing for Grasping Performance

The grasping ability and the reaching of each finger have been analyzed in the prototype. Fingers–thumb opposability enables the hand to carry out prehensile movements of the fingers to hold an object securely. Here we focus on two main patterns in prehensile grasping, the precision grip (or grasp), between the terminal digital pad of the opposed thumb and the pads of the fingertips, and the power grip (or grasp).

Holding large objects involves all the digits, while small objects require only the thumb, the index, and the middle digits. Smaller objects may be pinched specifically between the thumb and index (or middle) finger, which should be adapted to perform fine control. The power grip is executed between the surface of the fingers and the palm, which acts as a buttressing and reinforcing agent. All these grasping actions have been visually checked in the prototype; see Figure 4 as an example.

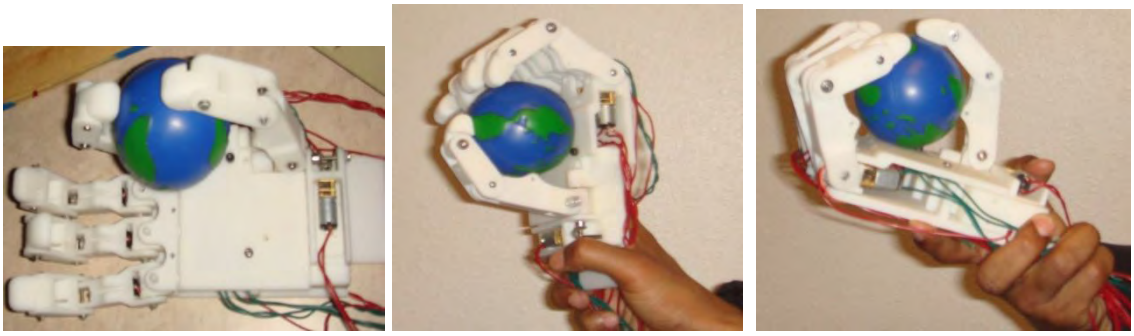

Figure 4: Prototype hand holding a spherical object.

Experiments on Force Control

In order to estimate the force exerted at the grasping, a system based on FSR has been designed. The experiment has been conducted as follow.

- The two pololu 35:1 mini metal gear motors in the finger are driven by PWM which is generated by the microcontroller.
- The FSR is attached to the tip of the finger or to the ball that we wanted to grasp and for feedback it is connected back to the micro controller (Figure 5).

The motors keep on rotating until the finger is in contact with the object; however, when it keeps on pressing further, the motors are commanded to rotate back and stop in contact position. It is a promising simple result that could be part of a strategy for the amputee to grasp different objects like, glass, egg, etc, with some control on the exerted force depending on the fragility of the object. Results and details of the control mechanism and algorithm will be further discussed in the control and embedded systems section.

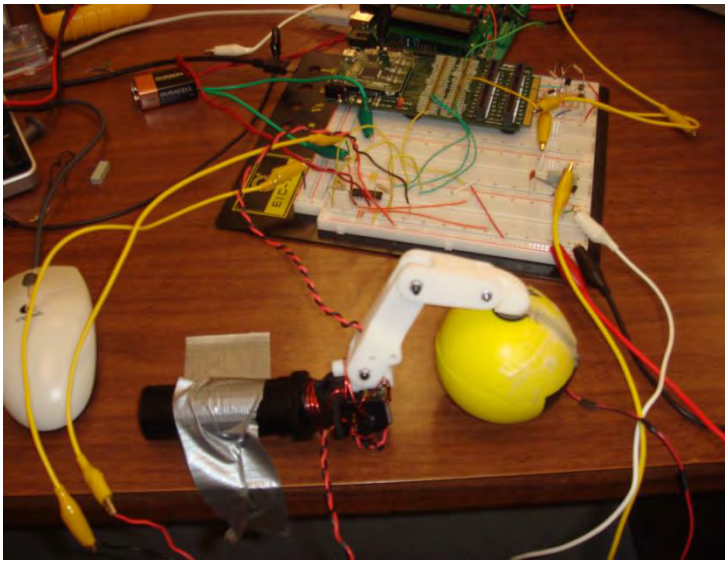

Figure 5: Contact position control experiment setup

Actuation Experiment with simple EMG Controller

In this experiment, EMG signal capturing capability was added to control the DC motors. The raw signals were processed by taking the maximum absolute value over a 100 sample interval and generating a new data set. In order to get the full flex and extend ability of the finger from this new data set two threshold levels where introduced. Above one threshold the motor would spin in one direction (flex) and below another the motor would spin in the opposite direction (extend). The deadzone was implemented as a buffer area to transition between the flexion and extension zones.

The EMG signal was acquired from the digit III FDP muscle and supplied as an analog voltage from a separate PC incorporating a Delsys Bagnoli EMG system. The analog voltage was sampled through a National Instruments data acquisition card installed in the motor control PC. The analog signal was then filtered and scaled using LabVIEW to a value representing the amplitude of the EMG signal, which was then used to control the direction of the motors. A sample of the filtered and scaled signal with thresholds is shown in Figure 6.

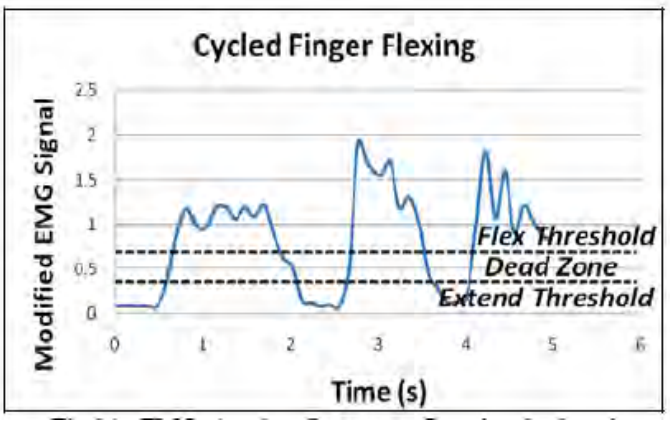

Figure 6: Thresholds used in the EMG driving signal

The controller was applied to the DC motors of finger and thumb only, in their close grip configurations. The objective of these tests is to obtain some preliminary data in order to setup the EMG-testing platform.

The EMG voltage and current outputs for both the finger and thumb were consistent with that of the direct power supply inputs. The EMG thumb test resulted in a DC motor force of 0.95N which agreed with the 1.24N + 0.35N generated by the direct power supply tests presented in the Final Report of Phase I.

Prototype 1 – Redesign of key parts

While testing the prototype, problems were identified and solutions are being developed. For some of them measures have already been taken. It is important to notice that this is an ongoing process, as more testing leads to the identification of further problems. Some of these will be implemented in Prototype 1, while some will be implemented in Prototype 2 once this is in a more mature stage.

The palm and fingers attachment point has been modified in such a way that the assembly is easier, while keeping its function in providing a passive DOF for the abduction of the fingers (Figure 7).

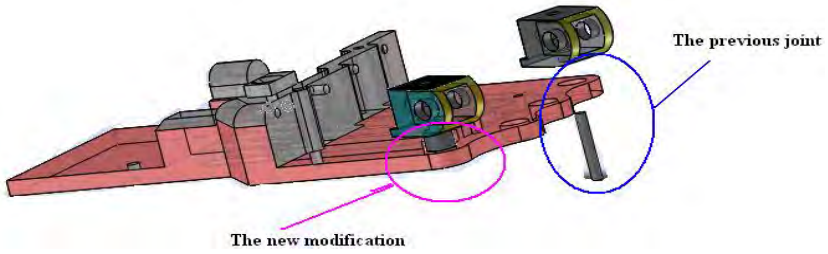

Figure 7: Knuckle jointed with the palm

As shown in the figure, in the first case the part was designed so that it will be attached by a screw, but as the part is loaded with torsion and bending moments the screw becomes loose; we also observed interference with the gears. We found this new approach is a good solution to keep the part in place and still provide access for maintenance of the gear pin.

Modification on the thumb, particularly on the actuator of the CMC joint has been also carried out. In the model, one of the CMC joint of the thumb (flexion motion) was designed so that it could be fully actuated by the SMA. However, due to the orientation of the thumb and due to the substantial hysteresis (due to energy dissipation) that could occur on the heating and cooling cycles, accurate control of SMAs could be difficult and hence variation of force in the thumb is expected. The thumb must generate much higher forces than any other finger when performing certain gripping actions due to the thumb opposing the total force generated by the four fingers. This thumb behavior is prevalent in common grip types such as a pinch grip and tripod grip. Therefore an alternative actuator is currently being characterized for this application.

In order to perform further experiments, and in order to drive the flexion motion of the CMC joint, the muscle-like string with a DC motor is implemented. This is the focus of ongoing work and on completion will be integrated with the current design. However, we will also implement the parallel actuation technique using SMA or similar actuators as it is designed to provide additional power to the other fingers, too.

Prototype 1 - Working principle of the newly proposed actuation scheme.

Here the approach is similar to SMA actuation mechanism designed before, however because of the above and some other reasons, we are experimenting with the use of DC motors and a belt system to actuate the specified joint. A pin is fixed with the thumb metacarpal and a muscle like string will be fixed to it, this string will be wind up on a wheel driven by a DC motor. To return to its original position there is a torsion spring mounted in the joint as shown in the Figure 8.

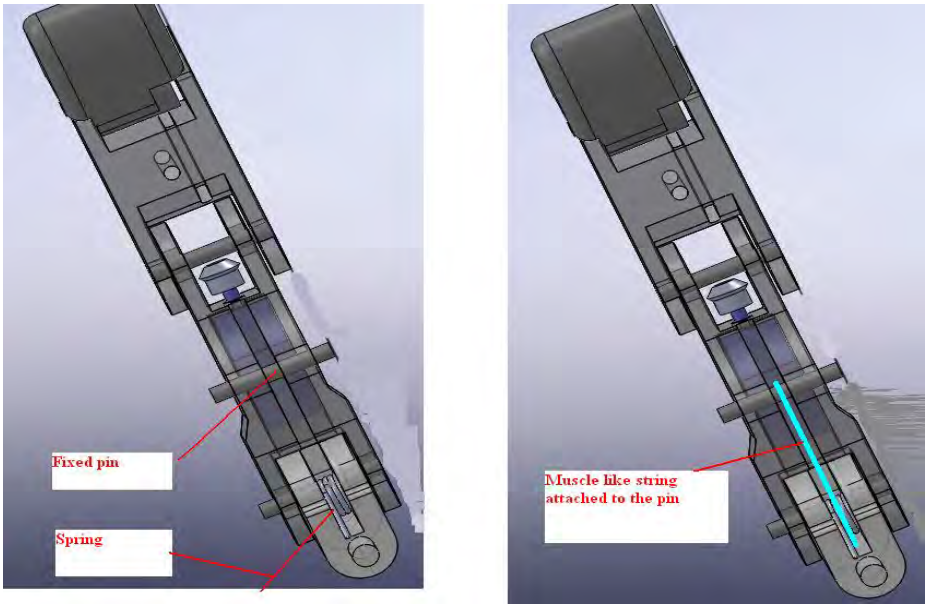

Figure 8: Actuation scheme for the CMC thumb joint

Summarizing the tasks for the testing, basic testing and redesign are being performed on Prototype 1. At the same time, a set of standards for testing is to be developed. We expect to have the final working version of Prototype 1 and the testing standards and testing results finalized within 3 months.

Goal 3, Objective 2: Design of hand Prototype 2

In parallel to the tasks being realized for Objective 1, and based on our experience with Prototype 1, we are working on developing Prototype 2. While conducting the experiment on Prototype 1, some problems were identified that will be considered in Prototype 2. To mention some of the issues, we list the noise coming from the gears, backlash problem in the gears and as the design was targeted in using parallel actuation, power supplied by the DC motor alone was not sufficient to hold things firmly. Some of the parts still need further modification, as it is not convenient for the artificial hand to be assembled and disassembled with relative ease. This will be a disadvantage for the end user, as these features of the design can only lead to enhanced user confidence in the prosthesis solution. Therefore, keeping the current prototype as a test bed for the control, EMG and interfacing experiments, further improvements on those problems and other prosthetic issues will be addressed in the new design for Prototype 2.

For this prototype, we are focusing on the design of the palm and thumb, the exploration of new actuation systems, and the use of kinematic synthesis in order to obtain novel designs.

Literature Review

The research on the state of the art in a field as dynamic as this one needs to be revisited on a short basis. Below we present the review performed during this first year of Phase II.

In the development of an appropriate multifunctional prosthesis, one must balance enhanced performance with the consequent increases in cost and complexity in the finding of more EMG channels that it may incur. However, the prosthetic hand still has to provide useful levels of force and appropriate speeds of motion relative to the native hand and possesses an anthropomorphic skeletal structure to promote natural function and appearance.

Several prosthetic hands have recently been described in engineering research papers (Dalley and Wiste 2009) - (Caldwell and Tsagarakis 2002). In each device, the discrepancy between the number of independent actuators and the number of joints is accommodated either by differential drives, which prescribe a given torque distribution between joints, kinematic linkages, which prescribe a given relative motion between joints, variable compliance couplings, which prescribe given relative compliance between joints, or by a combination of these.

Review of Kinematical Structures

Researchers have approached in different ways the design in order to mimic the human hand, using conventional linkages and other mechanical transmission systems. The prosthetic hand in (Dalley and Wiste 2009) is designed to provide selected functions with a less number of independent control inputs. It possesses five independent actuators and 16 joints, hence it is an underactuated design. The discrepancy between the number of joints and actuators is accommodated by moment isotropy, wherein each digit achieves static equilibrium when the moment in each joint is essentially equal to the other joints in the same actuation chain. Moment isotropy is realized by a combination of tendons spanning multiple joints and a differential pulley mechanism that distributes forces across tendons. In each joint spring has been used for compliance by then eliminate the need for position sensing, as the compliant joint map the finger positions to the tendon force. Back drivable force controlled actuation system has been also implemented so that the user can have a sense of feeling of the force. The muscle contraction sensed by the user concurrently generates the input for the prosthetic device through EMG signals. Backdriveablity then allows for a proportional mapping of this input to device output. Each fingers has three DOF, the thumb has one additional DOF for opposition. See Figure 9

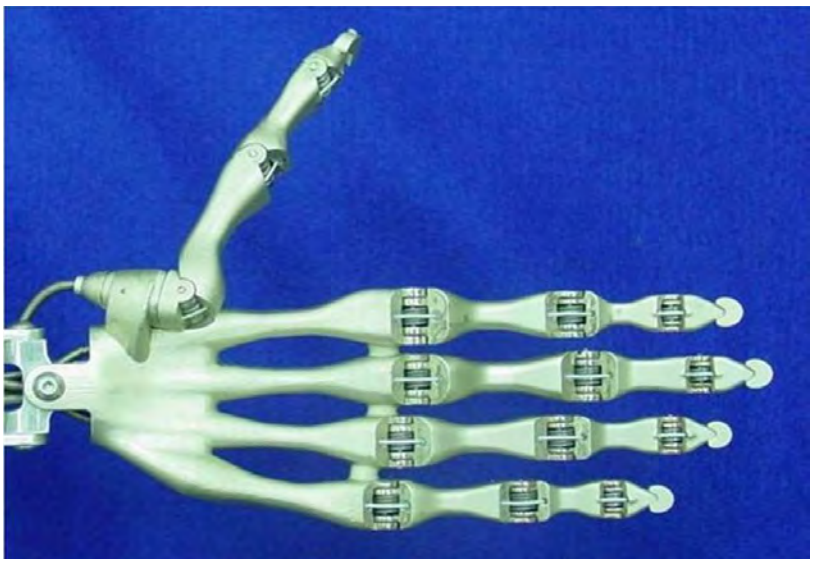

Figure 9: Sixteen-joint anthropomorphic hand

In (Oshima and Takayama 2009) a modular hand that can be inserted through trocars for robotic hand assisted laparoscopic surgery (HALS) has been proposed. The robot Hals has three fingers and nine active degrees of freedom and three passive DOF. Here tendons are also used for power transmission and as the design is targeted for manipulations these three fingers hold different configurations due to the middle finger has the freedom to translate forward and backward.

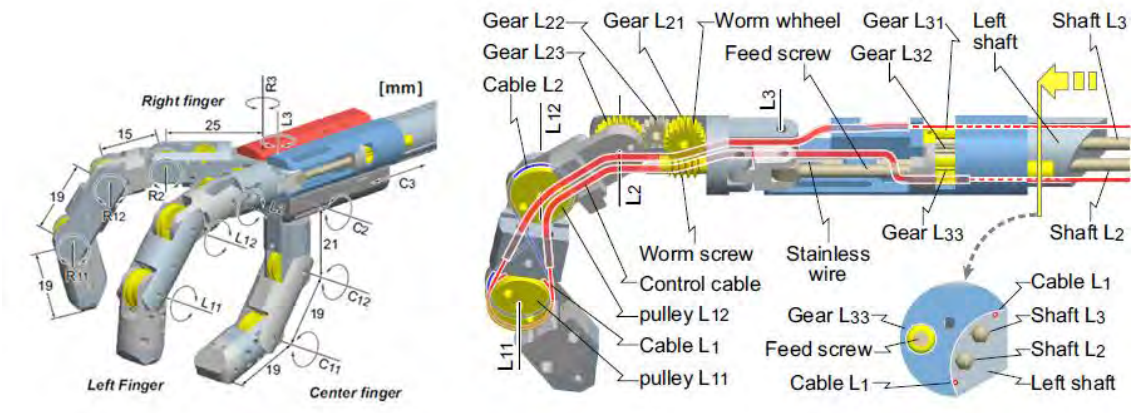

Figure 10: Assembled three-fingered nine-dof hand

Designed by the Robotic Systems Technology Branch at the NASA Johnson Space Center to reproduce the size, kinematics and strength of the space suited astronaut hand and wrist, the Robonaut Hand (Lovchik 1999) has an anthropomorphic configuration with 5 fingers and twelve degrees of freedom. The wrist has two DOF for a total of fourteen degrees of freedom. A forearm completes the structure, housing all fourteen motors, and other circuit boards. In order to match the size of an astronaut‘s gloved hand, the motors are mounted outside the hand, and mechanical power is transmitted through a flexible drive train. To avoid reliability problems associated with tendons when used in EVA space environment, the hand uses flex shafts to transmit power from the motors in the forearm to the fingers. The rotary motion of the flex shafts is converted into linear motion in the hand using small modular leadscrew assemblies resulting in a compact drive train, see Figure 11.

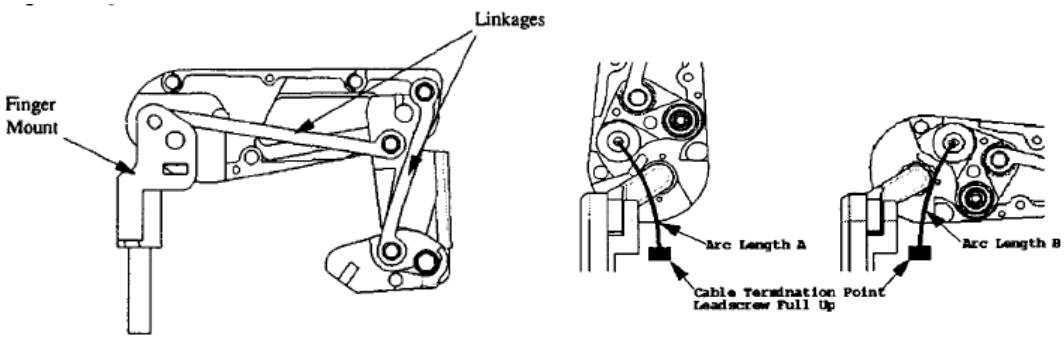

Figure 11: Grasping finger and decoupling link of the Robonaut Hand

Developed by the Shadow Robot Company, the Shadow Hand (Shadow Robot Company n.d.) has 24 degrees of freedom, distributed as follows: 4 DOF each for the first, middle and ring finger, 5 DOF for the little finger, 5 DOF for the thumb and 2 DOF for the wrist. The shadow hand utilizes 40 air muscles to actuate its 24 degrees of freedom in a volume resembling a very large forearm. In terms of speed, the Shadow Hand has a general movement at approximately half the speed of a human hand. Though the shadow hand looks bulky it has overall weight of approximately 4 kg only including sensors, muscles and valve manifold, due to the materials used to build it. Steel is only used for the forearm bone while other materials as aluminum, polycarbonate, rubber, etc are used to built fingers, palm and base. See **Error! Reference source not found.**Figure 12 and **Error! Reference source not found.**Figure 13.

Figure 12: The Shadow Dexterous Robot Hand

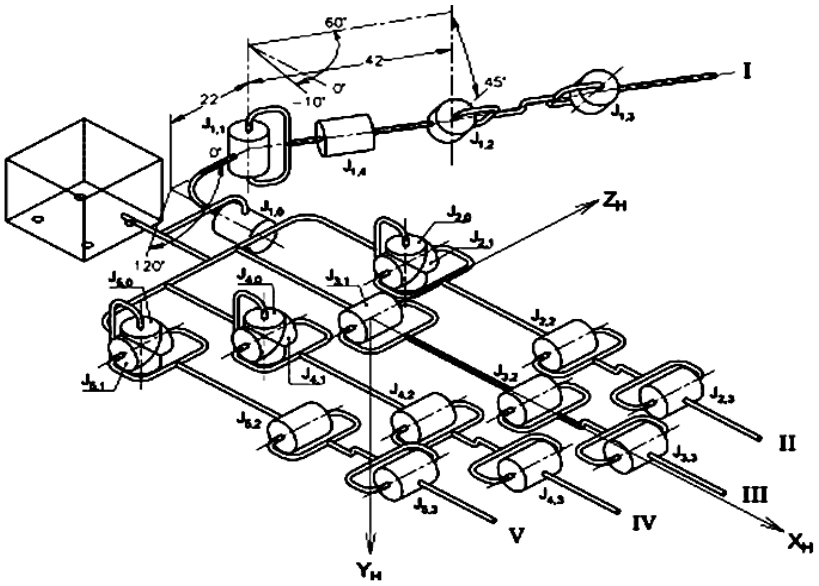

Figure 13: Configuration of joints for the Shadow Hand

Review of Sensing Technologies

Given the complexity of the human hand sensory system, the current technology is not enough to satisfy the prosthetic users. With some limitations, several sensor technologies have been applied to position and tactile sensing. One common technology is the force-sensing resistor (FSR), which are made of a resistive polymer film that responds in a non-linear way to pressure. Another technology is quantum-tunneling composite (QTC). When deformed, QTC material turns from a good insulator into a conductive material. Resistance drops exponentially as a function of pressure. Other force-sensing technologies are based on semiconductor strain gauges. These have been used to measure pressure and to create multi-dimensional load cells. Multi-dimensional load cells are particularly good for tactile sensing because they can be very sensitive and they can be used to localize a contact point on a fingertip. However, a drawback to using a load cell to sense forces in a robot hand has been size constraints.

In (Dalley and Wiste 2009), the user‘s musculature (from which the myoelectric command signals are measured) possesses force-sensing capabilities. By incorporating force-controlled, backdrivable actuation, some degree of force sensing can be reserved (i.e., the tendon forces retain some degree of proportionality with the EMG command). It was assumed (and is the case with myoelectric devices) that no conduit exists to bring sensory information to the user. Because of this, the device was designed to be force-controlled, such that the information contained in the

muscle contraction is, in essence, preserved in the prosthesis. Encoders are implemented to sense the motor position.

Prosthetic hands contain a sensory feedback device, for instance the Belgrade/USC Hand (Bekey, Tomovic and Zeljkovic 1990) has small conductive plastic potentiometers compact (35x10x3mm) with good resolution (320ohms/mm) of position sensors to indicate the rotation of the fingers base with respect to palm plane. The same hand also contains FSR located at the finger tips to detect contact with an object and the force being exerted in the range of 20 grams to 5 kg. These sensors can also report contact events when they sense a minimum normal force. Many hands, such as the Utah/MIT hand, contain internal sensors located at each joint to measure angular deflection and the sensor system is based on a Hall Effect. A magnetically sensitive Hall Effect device is located in the proximal link and two cobalt samarium magnets, operating in a dipole configuration, are attached to the distal link. Also semiconductor strain gage to detect the tendon tension. The Shadow Hand also contains a similar Hall Effect position sensor with resolution of 0.2 degrees.

The Robonaut hand contains forty three sensors not including tactile sensing. Each joint is equipped with an embedded absolute position sensor. Each motor is equipped with absolute encoders. Each of the lead screw assemblies as well as the wrist ball joint links are instrumented as load cells to provide force feedback.

Usually if we look for a prosthetic hand to perform a dexterous task we need a feedback from each joint to control the particular actuators, however while doing this the control complexity is also increased. Because of these and other reasons most of the prosthetic hands developed so far are limited to power grasping and use a more pragmatic and robust underactuated approach.

Review on Actuator Systems

The actuation units in (Dalley and Wiste 2009) are DC motors coupled with low-ratio gearheads and small-diameter pulleys to pull hand tendons. Each joint in the hand includes embedded torsional springs in parallel with the hand tendons. The compliant joints map joint motion to tendon force in free space gives advantages of 1) eliminating the need for position sensing in the hand, and 2) eliminating the need to switch between motion control and force control. Specifically, the hand frequently engages in both motion control (e.g., when gesturing or reaching) and force control (e.g., when grasping or squeezing). In the hand, the tendons are always under (open-loop) force control

Tendon paths are lined with Teflon tubing to reduce friction. Braided spectra cable of 0.75mm(0.03 in) diameter and 668 N (150 lbf) rated strength was chosen for tendon material due to its high strength, high-tensile fatigue resistance, low creep, and low stretch characteristics.

Progress in materials science, microcontrollers, batteries and cosmoses products made feasible the design of advanced prosthetic devices. However, due to the complexity and higher DOF of the hand prostheses have still restricted functions, mainly due to their conflicting design requirements (Caldwell and Tsagarakis 2002). Widely accepted problems of the underactuated DC motor solution are the low dexterity, weight and noise, as well as stiffness and size. Thus, finding alternative types of actuation and looking for a higher DOF mechanism becomes critical for enhancing prosthesis functionality and acceptance.

Literature Review Conclusions

Generally the problems or the limitations in the prosthetic hand design era can be seen in three ways

1. The mechanical structure / the mechanism to achieve all the DOF that the human hands possess: The problems that hinders researchers from proposing new design or mechanism are due to limitation of technology such as getting of actuators with low cost, miniature size, high power output, easy to control etc. the other problem also might be due to the high cost associated with the manufacturing of fancy shape and intricate objects.
2. The actuation system: as it is addressed above most of the available actuators are bulky and heavy to put them in the palm or in the fingers. Therefore people look a transmission mechanism to locate the motors remotely like in a forearm. While doing these a lot of issues will come like noise if we use gears, screws, and friction when we use belts and/or tendons, hence a lot of power loses and less life of mechanical members will result.
3. Control and sensory feed back problems.

Due to the above and other reasons most of the currently available designs are limited to underactuated type so that

to minimize control complexity, mainly using tendons; what makes them different is the actuation system they employ, the sensors and the control scheme. Even, if we see hands developed purely from kinematic links almost most of them are made from revolute or prismatic joints which can easily be actuated with conventional actuators. While trying to minimize control complexity the hands are also loosing dexterity.

Hence, based on supportive literature review and natural hand biomechanics and anatomical data we are working on studying and specifying prosthesis architecture.

We have structured our design approach in two ways,

1. Using real-time capturing of the fingers motion by camera system and applying image processing technique to filter out the required data points of the joint angels. Having these data as an input, a mechanism particularly to mimic the thumb motion will be developed. The study of the human hand kinematics can offer interesting solutions for the human hand prosthesis development or in fields like computer animation or gesture recognition that add a greatest value for the assistive medical device and upper limb rehabilitation engineering techniques as well. A kinematic synthesis based on the anthropomorphic data, having the same elements and approximated motions can successfully lead to develop a functional prototype capable to copy as much as possible the natural model.
2. Using a systematic approach based on modification of existing devices for the synthesis of possible structures of mechanisms for prosthetic applications (using the techniques used in (Chang and Tseng 2004), (Martell and Gini 2007) and others).

Prototype 2 Design: Thumb Design

A major factor in the evolutionary change in hand use was the development of the opposable thumb, which resulted in a remarkable increase in the versatility of hand function. Opposition involves flexion, abduction, and medial rotation of the thumb so that the pulp surface can make contact with the terminal phalanges of one or all of the remaining digits. The articulation of the thumb metacarpal (the proximal bone of the thumb) and the trapezium (a bone of the wrist), in what is known as a saddle joint, enables the thumb to rotate 45° around its longitudinal axis. This movement of opposition is essential for effective handling and exploration of small objects and greatly facilitated primate tool use and construction.

The kinematic properties of the thumb should mimic those of a human thumb. If the anatomical joints could be considered as revolute joints, matching the robotic thumb joints to the anatomic joints would create the proper relative motions between the bones. The human thumb has been described by a variety of kinematic models (Kapandji, 1970), (Landsmee 1989), (Callahan A. D 1990) and (Cooney 1981). Although several researchers describe the IP joint as having one rotational degree of freedom (Kapandji, 1970), (Landsmee 1989) and (Cooney 1981), there is less consensus on the characterization of the MCP and CMC joints. Previous research investigating thumb motion considered both the MCP and CMC joints to be universal joints, which have two perpendicular and intersecting axes.

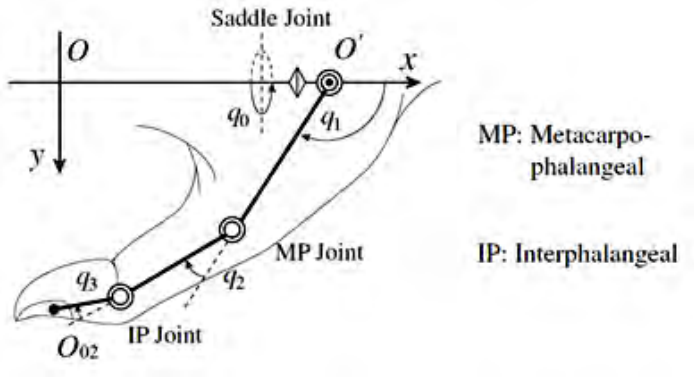

Figure 14: Configuration of the joint variables of the thumb (Arimoto 2007)]

(where q_0 denotes the angle of rotation around the x-axis and q_1, q_2 and q_3 denote the angles of rotation around the z-axis perpendicular to the xy-plane).

Most of the currently available hands have a thumb with four DOFs as shown in Figure 14. However, the human thumb is more realistically modeled with more than 4DOF ,and for this reason a number of researchers are still working on it to accurately replicate its DOFs and make ease of grasping and manipulating objects. In (J. Veronica 2004), five-hinge serial linkage model structure (Figure 15) has been used to model the thumb.

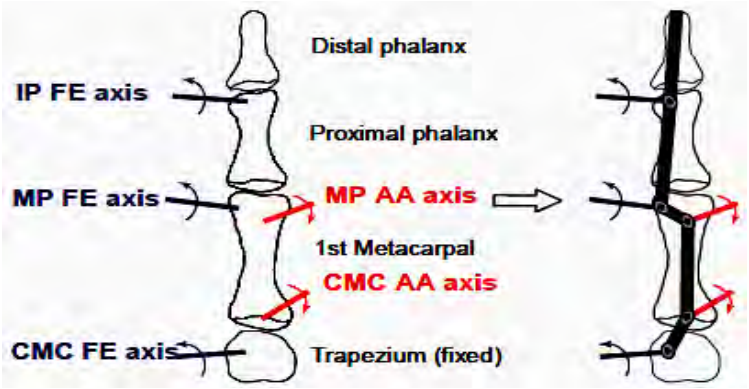

Figure 15: Thumb kinematics modeled as a serial chain of five hinges

The coupling mechanism-based prosthetic hand presented in (Yi-wei 2010) uses a four-bar linkage mechanism to design each finger and also to maximize the interaction between the thumb and other fingers, a spherical joint driven by 4-bar linkages has been used for the thumb.

Prototype 2 Design: Advances in Kinematic Synthesis of Tree-like Kinematic Chains for Exact Trajectories

Kinematic synthesis of articulated structures is a promising field for the design of complex systems. However, it is still at its first stages when we deal with spatial motion and go beyond simple serial chains. This is due to the great difficulty in stating meaningful equations, as well as the dimensionality of the problem, which renders most solvers useless.

Here we have attacked both these problems in order to develop a design tool to be used for anthropomorphic tasks. On one hand, we are developing a formulation based on finite screw theory, able to describe the geometry of the workspace or a trajectory within the workspace of any spatial chain. This procedure is used to perform exact synthesis and to simplify the formulation of the equations. On the other hand, a general kinematic solver has been developed that can deal with the synthesis of tree-like kinematic structures, such as that of the human hand. It is important to point out that this is the first time that the synthesis of tree-like articulated systems is attempted, with successful results and some surprising conclusions.

Finite-screw system kinematics

Given a trajectory such as the one presented in **Error! Reference source not found.**Figure 16 for a trajectory of the thumb, it is advantageous, from the synthesis point of view, to work with relative displacements. In Figure 17 we express the displacements of the thumb‘s proximal phalanx trajectory as screw axes with a pitch (the screw lengths are proportional to the pitch). We can see that the screw axes of the displacements with their pitches generate a screw surface. We use this description of the limb motion to minimize the difference with respect to the motion of a given linkage, the articulated system chosen to be used in the prosthetic hand.

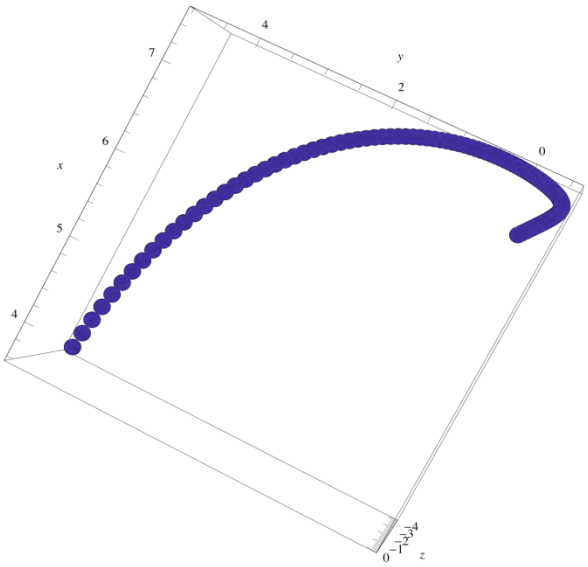

Figure 16: Thumb trajectory

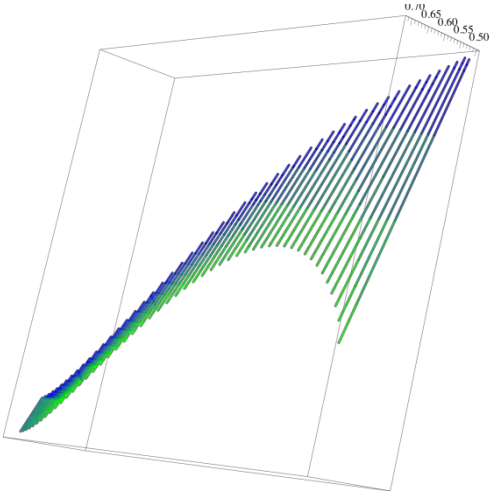

Figure 17: Screw surface corresponding to the previous thumb trajectory

Using screw systems such as the screw surface in the figure, we are able to extend the known theory of finite-position synthesis to the design of whole trajectories or subspaces.

The approach used in this paper for stating design equations is based on generalizing the standard inverse kinematics of robotics. We equate the forward kinematics of a serial chain to a set of goal displacements and consider the structural parameters also as variables. So far, the most efficient formulation for our purposes consists of stating the forward kinematics of relative displacements using the even Clifford subalgebra of the projective space C+(P3), also known as dual quaternions (Perez-Gracia 2011).

For a serial chain with n joints, in which each joint can rotate an angle θi and slide a distance di, around and along the axis Si, i = 1,...,n, the forward kinematics of relative displacements (with respect to a reference position) can be expressed as the composition of Clifford algebra elements corresponding to the motion of each joint. Let **θ0** and **d0** be the joint parameters of this chain when in the reference configuration. Then, the movement from this reference configuration is defined by

$$\hat{Q}(\vec{\Delta\hat{\theta}}) = e^{\frac{\Delta\hat{\theta}_1}{2}S_1} e^{\frac{\Delta\hat{\theta}_2}{2}S_2} \cdots e^{\frac{\Delta\hat{\theta}_n}{2}S_n} = (\cos\frac{\Delta\hat{\theta}_1}{2} + \sin\frac{\Delta\hat{\theta}_1}{2}S_1)(\cos\frac{\Delta\hat{\theta}_2}{2} + \sin\frac{\Delta\hat{\theta}_2}{2}S_2)\cdots(\cos\frac{\Delta\hat{\theta}_n}{2} + \sin\frac{\Delta\hat{\theta}_n}{2}S_n).$$

where the hat indicates dual joint variables. This formulation can be stated for any serial chain, and we will see later that it can be extended to other topologies.

In order to create design equations for the kinematic synthesis, we equate these forward kinematic equations to a set of positions that we want to reach,

$$\hat{P}_{1j} = e^{\frac{\Delta\hat{\theta}_{1j}}{2}\mathbf{s}_1} e^{\frac{\Delta\hat{\theta}_{2j}}{2}\mathbf{s}_2} \cdots e^{\frac{\Delta\hat{\theta}_{nj}}{2}\mathbf{s}_n}, \quad j = 2, \ldots, m$$

It is straightforward now to count for the number of equations and unknowns, in order to establish the maximum number of positions we can define. This is the formulation of the exact synthesis problem.

A finte-screw surface is a ruled surface in which the lines with their associated pitch correspond to relative displacements. A screw surface will be a screw system if it is closed under addition and scalar multiplication, that is, if every screw of the set can be written as a linear combination of screws belonging to it. The finite screw systems corresponding to serial chains can be obtained in a straightforward way from the dual quaternion formulation of the forward kinematics; in fact, they are subspaces of this algebra. Using this formulation, a formula can be worked out that relates the magnitude (in this case, unique) to the screw. When dealing with parallel robots, additional conditions must be added in order to define the screw surface.

It is easy now to generate trajectories and to transform them from displacement to screw in order to create trajectories. At the same time, given the fact that they are subspaces, using only a base for the system, we can apply a simplified finite-position dimensional synthesis algorithm. This method has been developed in (Perez-Gracia 2011) for the synthesis of a spatial overconstrained linkage, the spatial RPRP. A general procedure is being developed following this line.

When completed, this formulation will avoid the use of computationally-costly minimization procedure in order to synthesize articulated fingers to follow a trajectory of poses. It will be applied to the design of the thumb in the first place.

General kinematic synthesis solver for tree-like articulated system

For the first time we are developing a tool that will allow the kinematic synthesis of tree-like articulated systems with variable number and type of joints. This is the outcome of the job being developed in (Simo-Serra, Moreno-Noguer and Perez-Gracia 2011). The kinematic synthesis problem is again expressed equating the forward kinematics in Clifford algebra form to a set of finite positions. In this case, we are developing a mixed solver, based on genetic algorithms and paired with a local Levenberg-Marquardt solver. Currently this is being applied to a hand skeleton which is anthropomorphic in its degrees of freedom. However, the huge number of solutions of the problem poses an additional difficulty if we want to select something for prosthetic applications.

The raw application of the solver to fingertip trajectories from human hands leads to a big number of articulated structures, which are highly non-anthropomorphic. Figure… shows one of these results. In order to get anthropomorphic solutions, we are working on adding additional geometric constraints to the model. One important theoretical result out of this research is the proof that, despite common belief, the hand/wrist complex is not a redundant kinematic structure when the tasks of more than one fingertip are considered simultaneously.

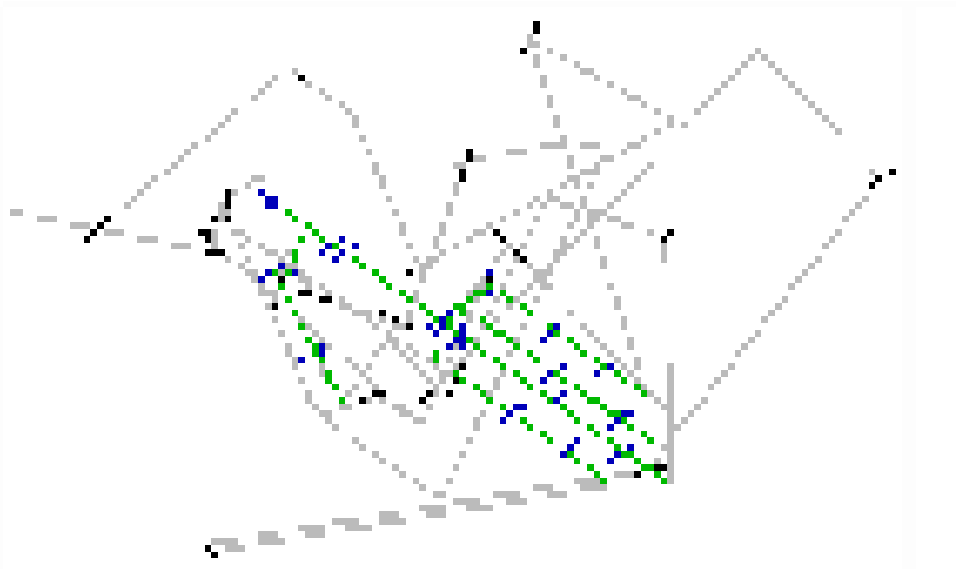

Figure 18: Input hand model (green) and one non-anthropomorphic solution (grey)

The actual model of the hand that the solver is working with has 26 degrees of freedom and handles 27 discrete poses of the hand for finding a solution set of dimension zero (that is, discrete number of solutions). This implies a system with more than 800 variables and more than 1000 equations, all highly nonlinear. The solution time for this model is about 60 hours on a single computer; it is now being implemented in a computer cluster.

This solver is an important tool to test different chain topologies in order to find new designs for some of the components of the hand. It has been implemented so that it can be applied to the design of any articulated system.

Goal 3, Objective 3: Manipulation of Grasped Objects

The main reason behind studying human grasping and manipulation characteristics within this project is to complement the input from the user when this is defective, noisy or just missing due to the degree of amputation. We are focusing on identifying implicit functions and workspace limits that will allow us to decrease the degree of the configuration space of the hand and the dimension and extension of its Cartesian manipulation manifold. In the study of finger‘s kinematics, it is obvious to consider the constraints as finger motion is constrained so that the hand cannot make arbitrary gestures. There are many examples of such constraints. For instance, fingers cannot bend backward too much and the pinky finger cannot be bent without bending the ring finger. The natural movements of human hands are implicitly defined by such motion constraints.

In order to do so, we are developing an experimental setup in order to obtain accurate data on limit angles for each degree of freedom, and in order to identify motion primitives. This last topics follows recent research, in which it is hypothesized that the hand motion is created on the hand structure and can be divided in a series of motion primitives, which could be identified using principal component analysis, see (M. Gabiccini, 2010)

The main problem with the experimental proof and finding of these synergies, or motion primitives, is the lack of a good system for hand data capture. Most of the existing systems either restrict the hand motion or miss some of its degrees of freedom. Due to this reason, we have focused our efforts in developing a non-contact, accurate motion capture and identification system for the hand.

Computer Vision System to Determine Kinematic Information

In order to create a prosthetic hand that mimics the human hand in every way, almost all hand motions and the related EMG signals need to be studied. The complex hand motion requires a sensing system capable of following its many degrees of freedom without interfering with the motion. This gives rise to a problem that can be solved using image processing and computer vision techniques.

The development of this system follows on the results obtained during Phase I of this project, and builds on the knowledge and the learning from the errors made during that first attempt.

To determine the articulation of fingers, the kinematical structure of the hand is modeled. In our research, the skeleton of a hand is abstracted as a stick figure with each finger as a kinematical chain with base frame at the palm and each fingertip as the end-effector. This model is constrained by constraints referred to the limits of the range of finger motions as a result of hand anatomy, and by constraints due to the limits imposed on joints during finger motion (intra and inter finger constraints). This initial skeleton will be adjusted to the real anatomy of the subject using a kinematic synthesis algorithm, and once the model of the hand is accurate, it is straightforward to calculate the joint angles for each position of the fingertips. The non-contact data will be obtained using a camera system.

Computer Vision System: Experimental Procedures and Analysis

The pose of a calibrated camera can be uniquely determined from a minimum of four coplanar but non-collinear points. In practice, there are many applications of camera pose tracking from planar targets and there are also a number of recent pose estimation algorithms, in our research, in order to compute pose for 3D to 2D correspondences of a planar target, the algorithm used is based on Schweighofer (Schweighofer 2006)

The whole experimental procedure is explained as follow, two squares with corners marked are attached to the thumb and to the base of the thumb/wrist/as shown in Figure 19 . Then the thumb moved to its different positions/reaches. While moving the thumb different frames are captured using the camera interfaced with computer and using LabVIEW block diagrams (Figure 20). This LabVIEW program captures and saves multiple images in to a data storage folder on the hard disk. Once the frames are saved, sample frames from different orientation of the thumb have been selected for processing.

The following set of data is provided to the algorithm in Matlab

1. 2D coordinates in pixels and 3D coordinates of the four points (corners of the square).
2. Intrinsic parameters of the camera

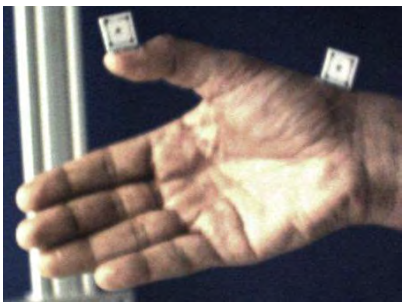

Figure 19: Square Placement for Studying Grasping Motion

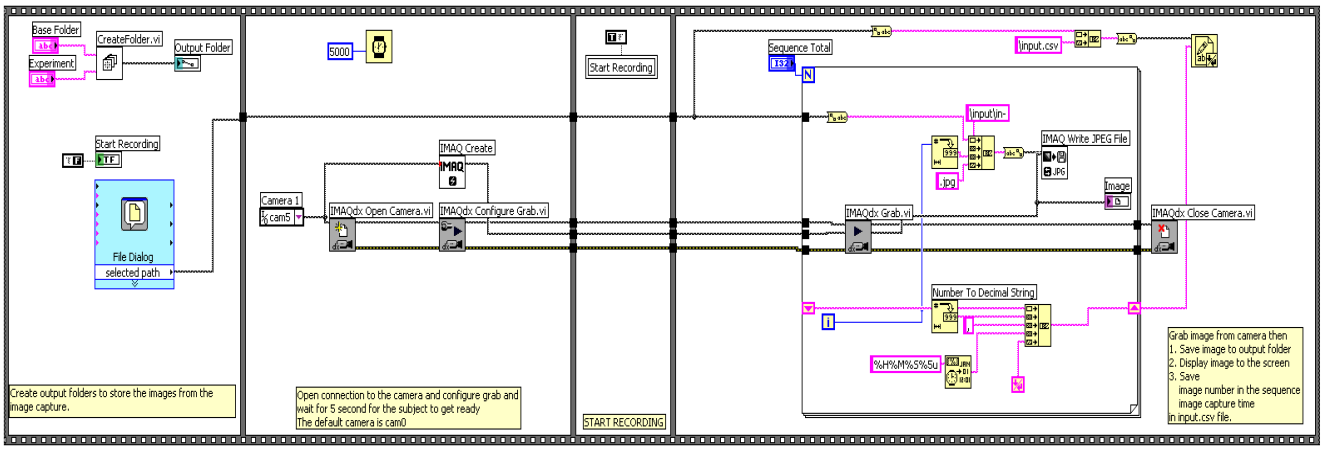

Figure 20: LabVIEW Block Diagram for Continuous Image Capture

For each squares attached to the hand we get the rotation and translation matrixes of the point with respect to the camera reference frame. Having this information the orientation of the tip of the thumb with respect to the wrist has been tabulated.

So far the system is working for a single marker on a single image. Current work is being developed in adding cameras to the system for greater resolution, and on the marker tracking algorithms. The results of this hand motion identification system will be used for identification of hand primitives and joint ranges, as input data for the synthesis algorithm in the design of Prototype 2, and also to study the correspondence between the EMG signals and the motion of each individual finger and degree of freedom.

Goal 4: Biocompatibility and Signaling

Overview: A major unresolved biocompatibility issue pertains to how tissue and cellular inflammatory responses are elicited by artificial implant material(s). We are developing a "Sensor on Cells on Skin Model" to facilitate the investigation of this biocompatibility issue. We have made significant progress in cell model development. We have developed new cell models of peripheral nervous system consisting of dorsal root ganglion neurons and Schwann cells. The new models are suitable for elucidating nerve degeneration and regeneration. We are characterizing these new models further. We have developed several "smart" biosensors for tissue engineering and biocompatibility studies and related biomedical engineering applications. In parallel with cell model and sensor development, we have investigated the molecular mechanisms underlying the cytotoxicity of silicon dioxide nanoparticles in neural cells. Our extensive literature survey indicates that our studies are truly novel and will lead to further ground-breaking discoveries because the whole important issue of how tissue and cellular inflammatory responses are elicited by implant material(s) have not been resolved and is poorly understood.

Current artificial organ and tissue engineering research (e.g., artificial bone and joint implants) reveals that over time the artificial implants fail to function even though over a short initial period after they were implanted, such devices appear to function as the biomedical engineers, who had designed them, expected. The findings of numerous studies indicate that the failure of the implants (despite their initial success) were attributed to the fact that, over time, the cells/tissues immediately surrounding and/or in contact with the implants appear to develop "inflammatory reactions" to the implants thereby compromising the implants' performance (see Lai et al., 2007a & ref. therein). Furthermore, if the implants act as sensors, the "inflammatory reactions" exhibited by the cells/tissues surrounding the implanted sensors induce interference of the signal transmission of the implants. However, "inflammatory reactions" exhibited by the cells/tissues surrounding the implanted sensors are poorly understood and remain to be major challenges for tissue engineers and other biomedical engineers who design such implant devices. Moreover, our extensive searching in the literature reveals that there is a paucity of literature on robotic implants and tissue inflammatory responses (Lai et al., 2007a). Nevertheless, nanoparticles and other nanomaterials have been increasing employed to manufacture implants and biosensors. There is emerging concerns that some nanomaterials may post health hazards to humans because of recent findings of nanotoxicology (Lai et al., 2007a,b). Consequently, in order to circumvent such biocompatibility issues in the design of robotic implants, it is imperative to elucidate the mechanisms by which such "inflammatory reactions" exhibited by the cells/tissues surrounding the implants arise and elucidate the putative nanotoxicity of nanomaterials employed to fabricate implants and biosensors. Thus, our in vitro model (see Fig. 1 below) allows us to address these physiologically and pathophysiologically important mechanistic issues. For phase II of our projects, the goals are to: (1) Continue to develop the "sensor on cells on skin model," especially stages two and three of the model development (see Addenda of Full Proposal); (2) Further characterize the putative nanotoxicity of nanoparticles and other nanomaterials commonly employed to fabricate biosensors and implants; (3) Detect signal mechanisms that influence cell growth and suppression such as apoptosis; (4) Couple enzymes on sensors for signal identifications and amplifications; and (5) Detect signals for biological growth and interferences with quantifiable parameters such as current, voltage, pH, etc. between various cell types of different organs of origin.

The following are the deliverables:

1) Continue to develop the "sensor on cells on skin model," especially stages two and three of the model development (see Addenda of Full Proposal);
2) Further characterize the putative nanotoxicity of nanoparticles and other nanomaterials commonly employed to fabricate biosensors and implants;
3) Detect signal mechanisms that influence cell growth and suppression such as apoptosis;
4) Couple enzymes on sensors for signal identifications and amplifications; and
5) Detect signals for biological growth and interferences with quantifiable parameters such as current, voltage, pH, etc. between various cell types of different organs of origin.

We have continued to make progress in studies outlined in Goal 4 of our proposal and have summarized the results obtained during this period in the following sections. We have been productive despite the gap in funding between the ending of Phase I and initiation of funding of Phase II: we have presented **seven** papers at national and international meetings and have **seven journal articles, one review, & seven conference proceedings papers** published or in press (see **Publications** below).

Set up of the "Sensor on Cells on Skin Model":

Based on our extensive experience in working with mammalian (including human) cells in culture (Dukhande et al., 2006; Hertz et al., 1998; Isaac et al., 2006; Isaac et al., 2007; Lai et al., 2008, 2010; Malthankar et al., 2004; Puli et al., 2006), we envisaged that we will undergo three stages to develop our "sensor on cells on skin model:" (i) stage one involves the development of different human and other mammalian cells (including nerve, muscle, and skin cells) in co-culture; (ii) stage two requires the juxtaposition of cells in relation to the membrane as illustrated in Figure 1. below (this figure was included in our proposal); and (iii) stage three involves designing the sensor(s) and fitting them into the "sensor on cells on skin model" (as shown in Fig. 1).

We successfully competed (i) stage one of setting up the model as depicted above. More recently, we have begun developing new cell models employing dorsal root ganglion neurons and Schwann cells, both are neural cells from the peripheral nervous system (see Appendices 2 & 6). Both dorsal root ganglion neurons and Schwann cells are important and relevant cell types for investigating biocompatibility of biomaterials. We have therefore started characterizing these cell types.

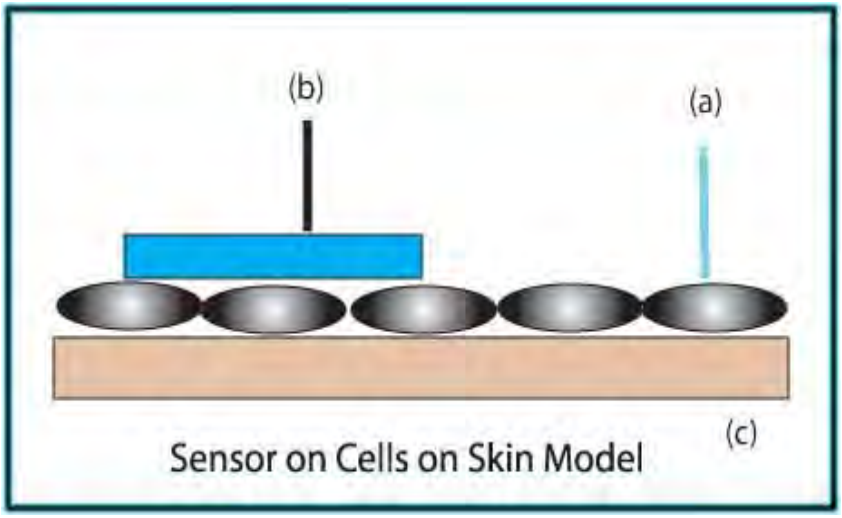

Fig. 1 "Sensor on Cells on Skin Model." The sensor (or implant: blue rectangle) is in contract with a monolayer of muscle or nerve cells (gray ovals), which are in contact with the artificial skin (an artificial membrane with specified pores: brown rectangle). (a) stimulating electrode; (b) sensor signal pick-up; (c) alternative position of sensor.

As shown in Figure 2, the population of dorsal root ganglion neurons showed exponential growth *in vitro* as a function of initial seeding density. Similarly, as shown in Figure 3, the S16 Schwann cells also showed exponential growth *in vitro* as a function of initial seeding density. Once we have established their growth patterns in culture, we are now in a position to further characterize them in terms of other physiological and cell biological functions.

We have continued the studies to address (ii) stage two of setting up the model and (iii) stage three of designing and characterizing the biosensors. We have summarized below our progress in developing and characterizing the biosensors.

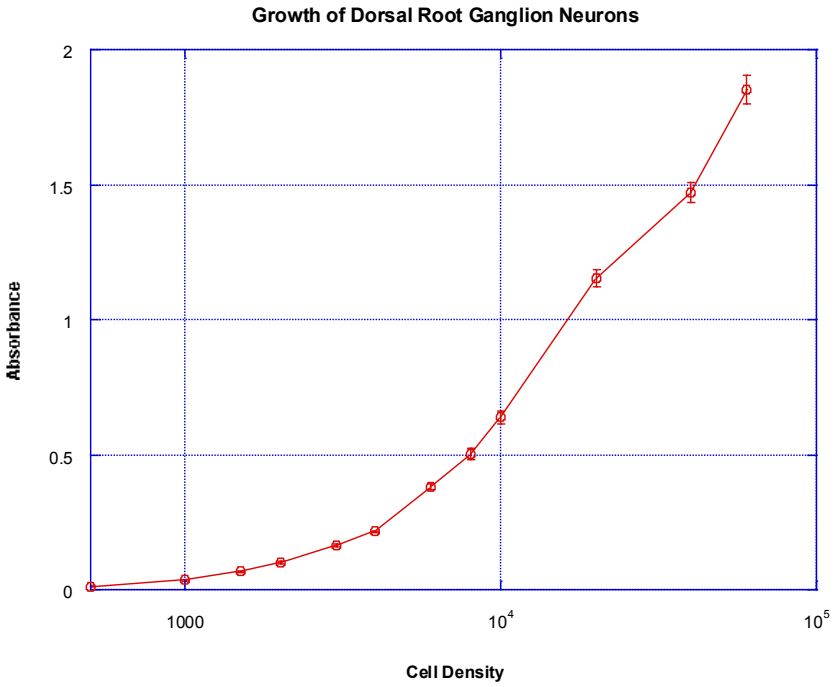

Figure 2. Growth of Dorsal Root Ganglion Neurons in Culture.

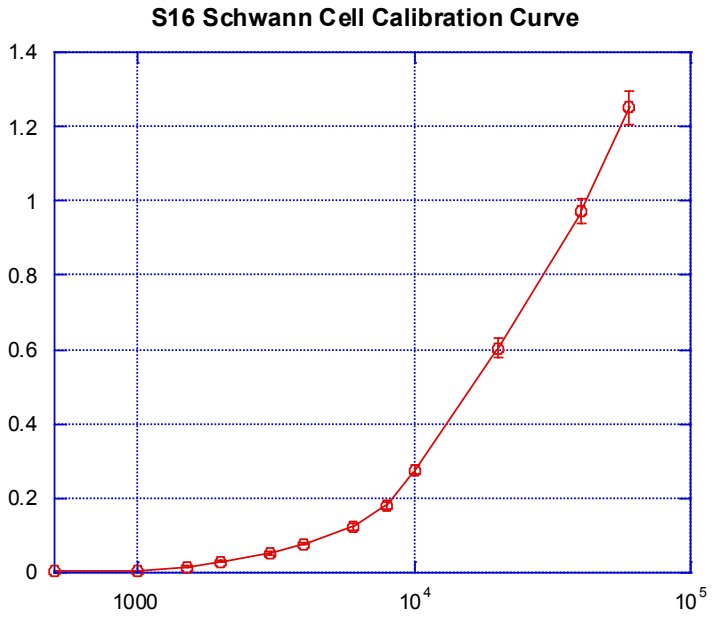

Figure 3. Growth of S16 Schwann Cells in Culture.

Sensor Development:

During Phase I of this project, we studied the development of biosensor platform that are capable of measuring biometabolites and environmental sensitive species, such as peroxide and nitrate/nitrate, to concentration in the order of ppb (parts per billion) or lower.

In our more recent development, we modified our platform with dendrimers to enhance its performance. Zero and second generation of dendrimers were coated on the surface of a carbon glassy platform electrode modified with GDH (glutamate dehydrogenase) and it was used to measured ammonium, a common biometabolite, at near neutral pH that is common for normal bioactivities. The resulting electrode was tested with ammonium concentrations ranged from 0.002 to 0.3 µM with satisfactory results. Figure 4 shows the cyclic voltammograms of various ammonium concentrations measured by the modified glassy carbon electrode, the lowest concentration was 2 nM. As indicated in the voltammogram in the reductive curves (upper lines), there was a big gap (current difference) between the blank (of buffer solution) and the first reductive curve (2 nM). Therefore, it is possible that the modified electrode can measure ammonium concentrations down to subnanomolar levels.

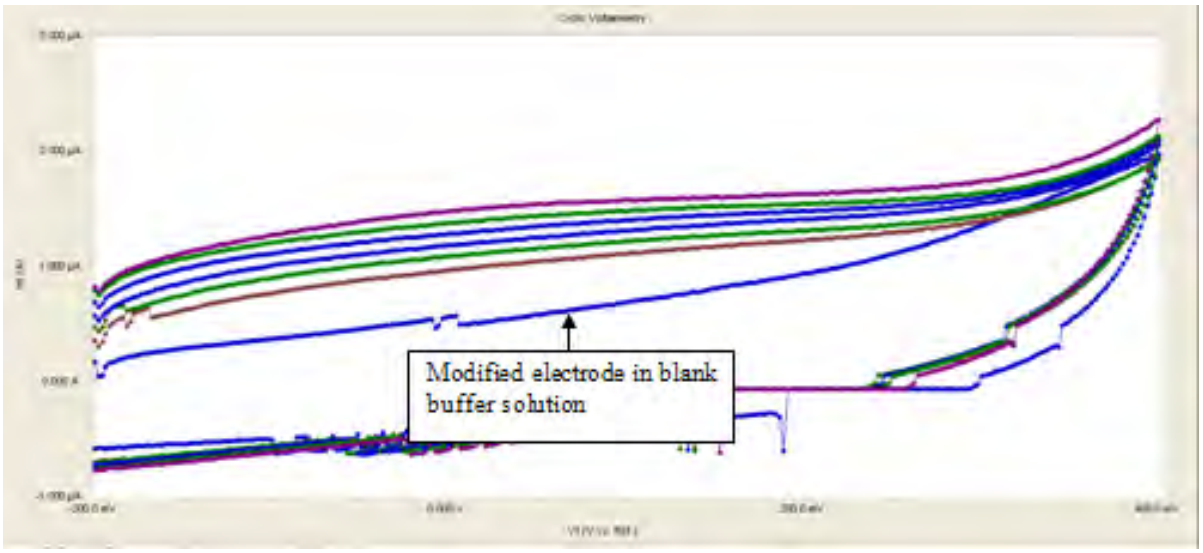

Figure 4. Cyclic voltammograms (i/v) of gold colloid-cysteamine/PAMAM_2ND-modified glassy carbon electrode measured from-0.2 to 0.4 V for the measurement of NH_4^+, the lowest concentration was 2 nM.

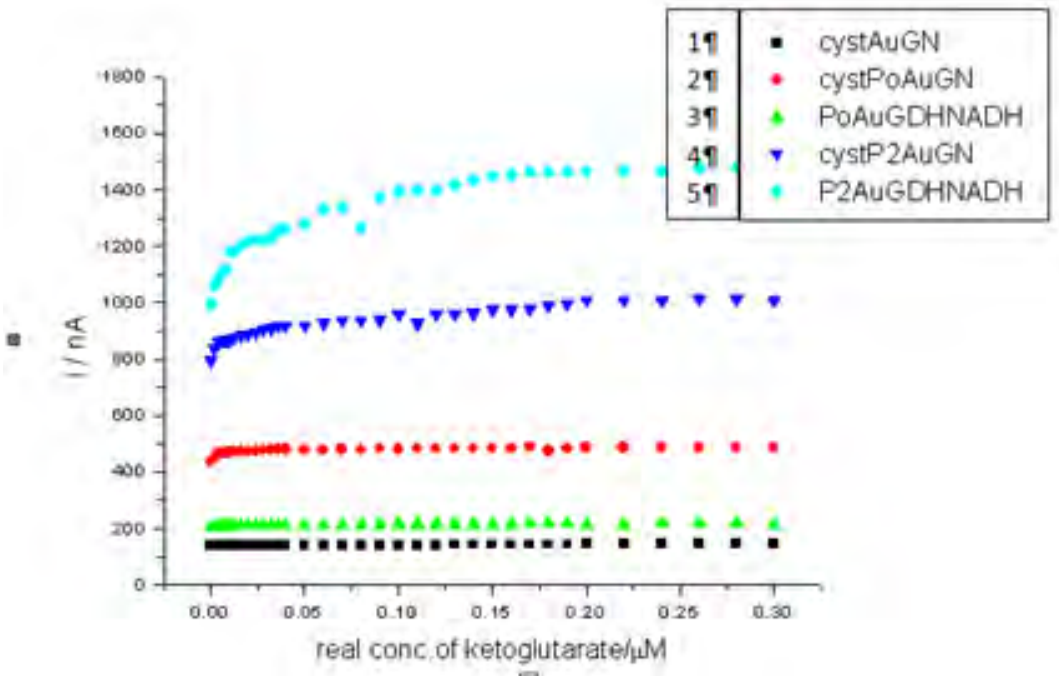

Figure 5. Performance differences of the glassy carbon electrode modified by different materials: 1. Modified with cysteamine-Au-GDH/NADH; 2. Cysteamine /PAMAM_0-Au-GDH/NADH; 3. PAMAM_0-Au-GDH/NADH; 4. Cysteamine /PAMAM_2nd-Au-GDH/NADH; 5. PAMAM_2nd -Au-GDH/NADH.

Figure 5 shows that there were distinctive current differences for the reaction of ammonium and α-ketoglutarate when the electrode was modified by different materials. From the stand point of detection, within the five modifications, sensor coated with second generation of PAMAM would have the highest sensitivity (current vs. concentration). The results were conceivably due to the higher branching property of PAMAM_2nd.

As shown in Figure 6, PAMAMs can be attached to cysteamine to enhance the available sites for the electrons transfer between reactions, in this case, ammonium and α-ketoglutarate, therefore increase the detection lower limit.

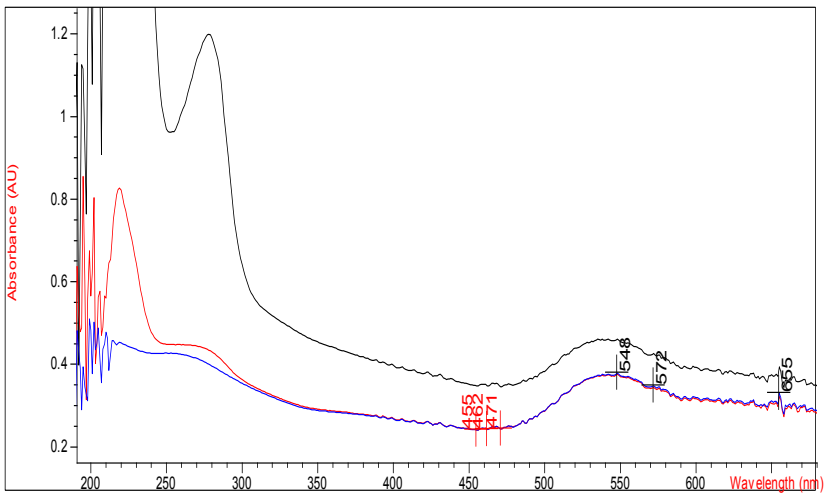

Figure 6. Cysteamine-PAMAM-Au-GDH coated on plastic UV-VIS cell with permanent absorption peak at 278 nm. Various lines indicated concentration differences.

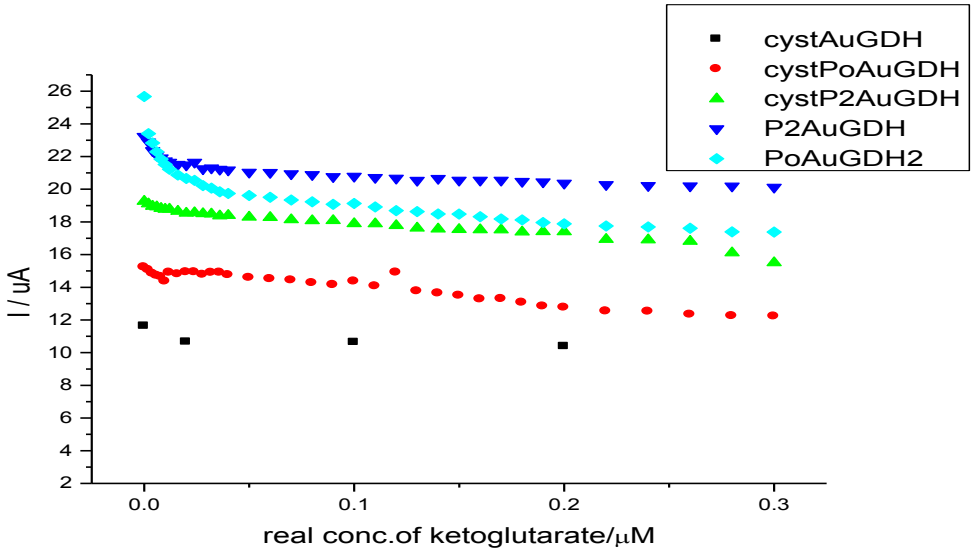

Figure 7. Cyclic voltammograms (i/v) of gold colloid-cysteamine/PAMAM_2ND-modified glassy carbon electrode measured for the measurement of α-ketoglutarate, which is an important tricarboxylic acid cycle intermediate and a common metabolite.

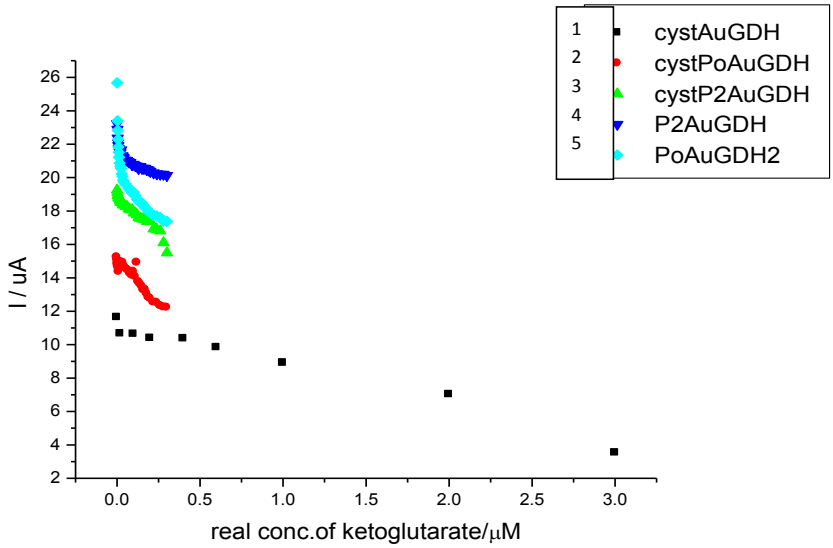

Figure 8. Cyclic voltammograms of GDH/NADH modified glassy carbon electrode (at low and high voltage range) for current vs. real concentration of α-ketoglutarate at low and high voltage for GDH and NADH modified electrodes. 1. Glassy carbon electrodes modified with cysteamine -Au-GDH. 2. Glassy carbon electrodes modified with cysteamine /PAMAM_0 -Au-GDH. 3. Glassy carbon electrodes modified with cysteamine /PAMAM_2nd -Au-GDH. 4. Glassy carbon electrodes modified with PAMAM_2nd -Au-GDH. 5. Glassy carbon electrodes modified with AMAM_0 -Au-GDH.

Figures 7 and 8 show that there were distinctive current differences for the reaction of ammonium and α-ketoglutarate when the electrode was modified by different materials. Because α-ketoglutarate is an important tricarboxylic acid cycle intermediate and a common metabolite, the modifications as indicated in the two figures suggested that the biosensor has good capacity for detecting a range of concentrations of this metabolite. However,

as shown in Figure 5, the current-voltage relationship is nearly linear after the initial extreme low concentrations. Thus, one should be cautious in selecting for the i/v ratio depending on the applications (for detection of extreme low and higher concentrations).

In our more recent development, we modified our platform to include the parallel development of biosensors and fuel cells. As in most biosensors, the detection principles are based on redox reactions of enzymatic reactions, which is the same principle used in most biofuel cell and how biological systems obtain energy to sustain live functions. For the sensors we previously developed that utilize the enzymes, LHD and GDH, for detections of various metabolites, biochemical reactions that involved these two enzymes can also be converted to a biofuel cell system:

For the biofuel cell system, the anodic half-cell was made by an Au electrode coated with lactate dehydrogenase (LDH) submerged in solution containing lactate and nicotinamide adenine dinucleotide (NAD+), thus, for the anodic half reaction:

Anode: $\text{Lactate} + NAD^+ \xrightarrow{LDH} \text{pyruvate} + NADH + 2H^+ + 2e^-$ (1)

As lactate was oxidized into pyruvate in the anode, the oxidative potential, E_0'(25 ˚C), would be 0.19 V.

The cathodic half-cell was made by a glassy carbon electrode (GCE) coated with glutamate dehydrogenase (GDH) submerged in solution containing ammonia and reduced nicotinamide adenine dinucleotide (NADH), the cathodic half reaction was:

Cathode: $\alpha\text{-Ketoglutarate} + NH_4^+ + NADH + H^+ + 2e^- \xrightarrow{GDH} \text{glutamate} + NAD^+ + H_2O$ (2)

As α-ketoglutarate was reduced into glutamate in the cathode, it generated a reductive potential, E_0'(25 ˚C), of -0.14 V.

Combining Equation (1) and (2), the total potential for the fuel cell with the anode and cathode above was 0.05 V (per mole). In general, biological reactions in nature do not release large amount of energy for each reaction step to preserve energy utilization efficiency. The overall reaction for the biofuel cell in our system was:

$\text{Lactate} + \alpha\text{-ketoglutarate} + NH_4^+ \xrightarrow{LDH,GDH} \text{pyruvate} + \text{glutamate} + H^+ + H_2O$ (3)

Since the ΔE_0' of Equation (3) was greater than 0, the reaction was spontaneous and would proceed as written from left to right.

Anodic half-cell

Figure 9 shows the oxidative responses of the modified Au electrode with nanogold particles, cysteamine and LDH. As seen, the characteristic peak of lactate conversion to pyruvate was detected at 250 mV and the accumulative current increased linearly with added lactate instantaneously [6]. It verified that the modified anodic electrode was functioning as expected in Equation (1).

Cathodic half-cell

Figure 10 is the reductive response of a GCE modified with 2nd generation of PAMAMs, nanogold particles, and GDH. The cathodic half-cell reaction functioned more efficiently at lower concentrations of α-ketoglutarate and became less effective as the accumulative concentration of α-ketoglutarate was higher (>0.025 mM).

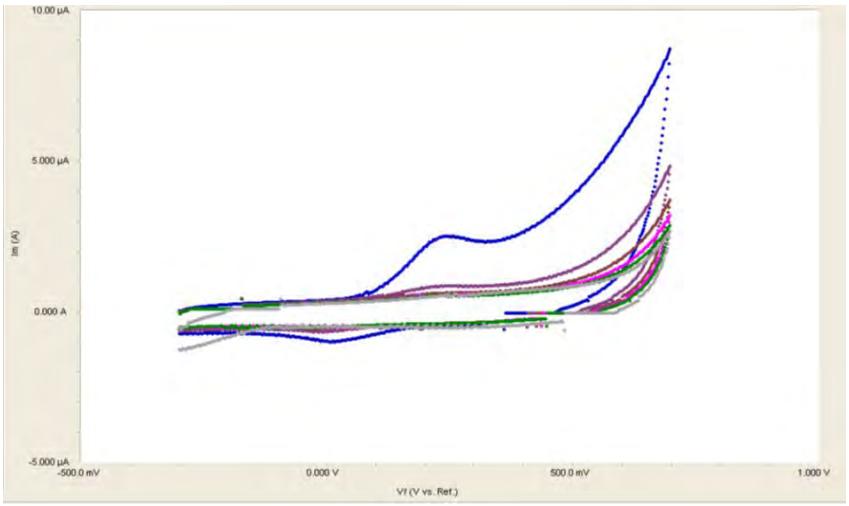

Figure 9. Voltammetric responses of an Au electrode coated with cysteamine, Au nanoparticles, and LDH at pH 8. Responses were stepwise additions of lactate at $1.0x^{-4}$ mol/ml with linear current increments (oxidative peaks) at 250 mV.

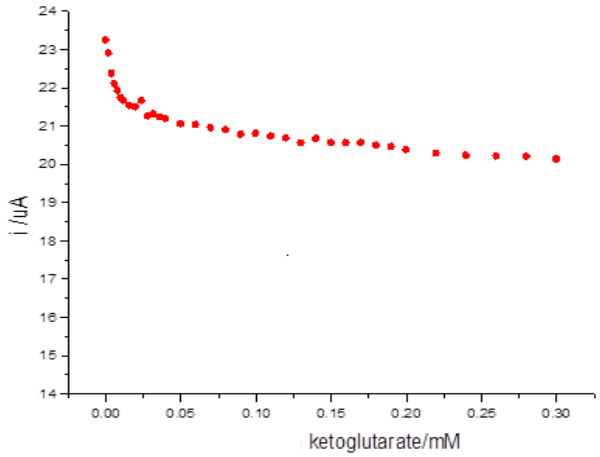

Figure 10. Reductive responses of a glassy carbon electrode modified with PAMAM, Au nanoparticle and GDH measured at 0.7 V in solution of ammonia and α-ketoglutarate.

Our biofuel cell system would generate a relative low potential (0.05V), but the reactants are all readily available from our body which make it closer to reality for the system to be implanted into our body as power source for biomedical devices. A similar approach can be used to explore enzymatic reactions within human body that can produce higher energy output. This biofuel cell can be used potentially to power the prosthetic hand this grant is developing.

The biosensor platform thus far was proven to be versatile and can be used in many biomedical and environmental applications. We continue to work on the development of these smart sensors: we are particularly focusing on the development of bionanosensors for tissue engineering and biocompatibility studies and related biomedical engineering applications (see Appendices 9 &13).

A. Investigate the biocompatibility of materials that are commonly used to fabricate sensors:

Introductory remarks. One established approach to investigate the biocompatibility of materials is to determine whether or not such materials exert cytotoxic effects on mammalian cells (Lai et al., 2008, 2010). Two

nanomaterials that are commonly used to fabricate nanobiosensors are silicon dioxide nanoparticles and titanium oxide nanoparticles (Lai et al., 2008, 2010).

Molecular and Signaling Mechanisms underlying the Cytotoxic Effects of Metallic Oxide Nanoparticles. Nanomaterials have been increasingly used in industrial applications (e.g., drug delivery, additives to drugs and cosmetics). Because of their wide use, occupational exposure to nanomaterials and nanoparticles may pose as health risks. Recent studies have suggested that exposure to nanoparticles may induce cytotoxic effects in some mammalian cell types (Lai et al., 2010; Puli et al., 2006) although these effects have not been systematically investigated.

In these studies, we have begun to systematically investigate the molecular and signaling mechanisms underlying the cytotoxic effects of nanomaterials, especially nanoparticles, on human neural and non-neural cell types. Here we report on some of the mechanisms responsible for the cytotoxic effects of silicon dioxide (SiO_2) nanparticles on human astrocytoma U87 cells that are astrocytes-like.

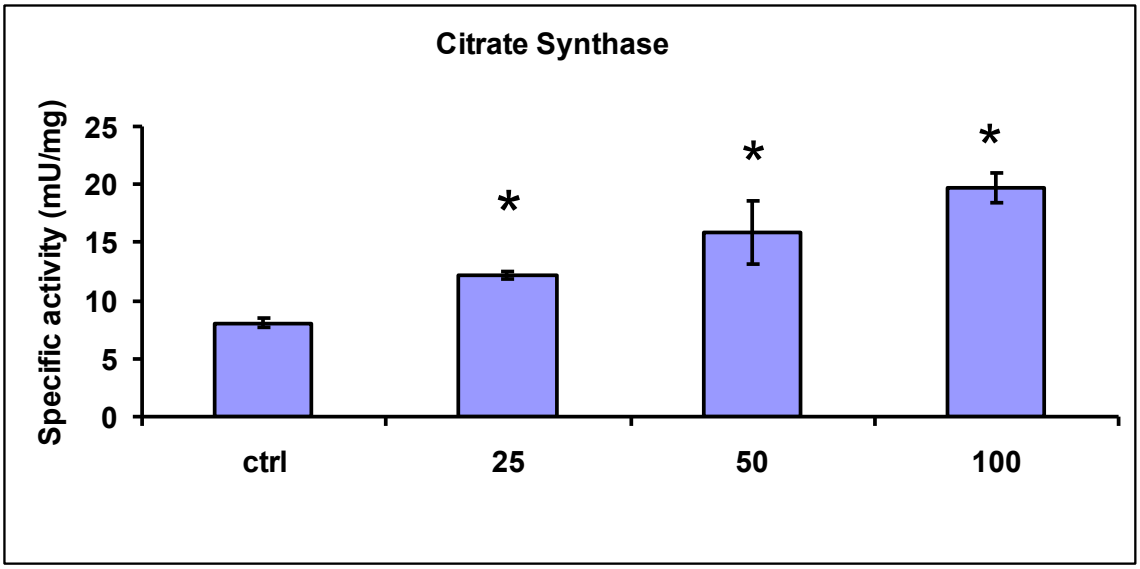

Figure 11. Effect of treatment with silicon dioxide nanoparticles on specific activities of citrate synthase in human astrocytoma U87 cells. U87 cells were treated at specified concentrations of silicon dioxide nanoparticles for 48 hours. Then the activities of citrate synthase in the homogenates of treated and untreated (i.e., control, ctrl) U87 cells were determined as described in Materials and Methods; the activities of citrate synthase were expressed per mg of homogenate protein as specific activities. The specific activities values were the mean ± SEM of at least three separate experiments; ctrl represented the value in untreated U87 cell homogenate; *$p < 0.05$ versus that of control cells.

Because cell survival critically depends on mitochondrial functions maintained at a normal physiological level, we determined the effect of SiO_2 nanoparticles on mitochondrial function in U87 cells by monitoring the activities of one key enzymes of the tricarboxylic acid (TCA) cycle namely, citrate synthase (CS). As shown in Figure 11, at treatment concentrations of 25-100 μg/mL for 48 hours, SiO_2 nanoparticles induced dose-related increases in CS activities in U87 cells.

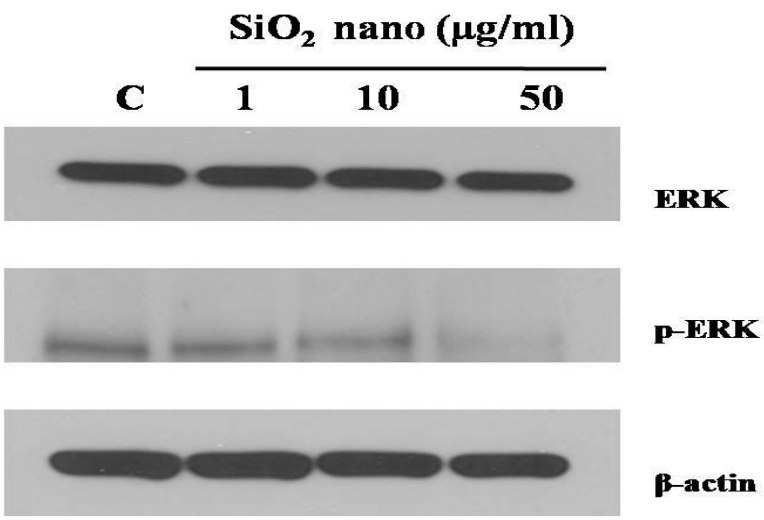

Figure 12. Effect of treatment with silicon dioxide nanoparticles on expression of ERK and phosphor-ERK in human astrocytoma U87 cells. U87 cells were treated at specified concentrations of silicon dioxide nanoparticles for 48 hours. Then cell lysates of treated and untreated (i.e., control) U87 cells were prepared as described in Materials and Methods. The expression of ERK and phosphor-ERK (p-ERK) was determined by Western blot analysis using β-actin as the loading control: Lane marked C, lysate of untreated or control U87 cells; lane marked 1, lysate of U87 cells treated with silicon dioxide nanoparticles at 1 μg/ml; lane marked 10, lysate of U87 cells treated with silicon dioxide nanoparticles at 10 μg/ml; lane marked 50, lysate of U87 cells treated with silicon dioxide nanoparticles at 50 μg/ml. The blots were from a typical experiment. Two other experiments yielded essential the same trend of results.

Treatment of U87 cells with SiO_2 nanoparticles could also lower the survival of U87 cells through altering cell signaling pathway(s) that regulate(s) cell survival and proliferation (7). We therefore investigated this possibility by examining the effect of these nanoparticles on expression of ERK and phospho-ERK proteins. We observed that when U87 cells were treated with 1-50 μg/mL of SiO_2 nanoparticles for 48 hours, their protein expression of phospho-ERK showed a dose-related decrease while that of ERK protein remained essentially unchanged (Figure 12), suggesting that a lowering of this cell survival/proliferation signaling mechanism could, at least in part, account for the dose-related decrease in U87 cell survival induced by these nanoparticles.

Taken together, the results of our ongoing studies on the molecular and signaling mechanisms underlying the cytotoxic effects of silicon dioxide (SiO_2) nanparticles indicate that alterations of mitochondrial bioenergetics and cell survival signaling underly the cytotoxic effects of these nanoparticles. Moreover, they suggest there may be other such mechanisms present. We are therefore continuing to pursue this interesting line of investigation.

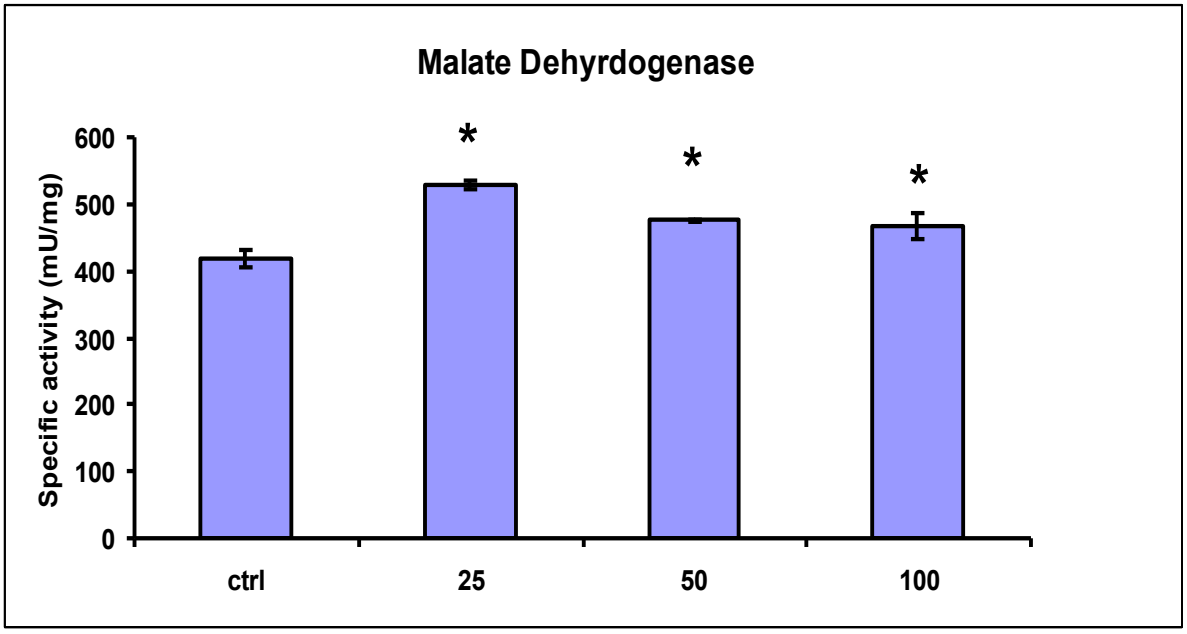

Figure 13. Effect of treatment with silicon dioxide nanoparticles on specific activities of citrate synthase in human astrocytoma U87 cells. U87 cells were treated at specified concentrations of silicon dioxide nanoparticles for 48 hours. Then the activities of malate dehydrogenase in the homogenates of treated and untreated (i.e., control, ctrl) U87 cells were determined as described in Materials and Methods; the activities of malate dehydrogenase were expressed per mg of homogenate protein as specific activities. The specific activities values were the mean ± SEM of at least three separate experiments; ctrl represented the value in untreated U87 cell homogenate; *$p < 0.05$ versus that of control cells.

Because cell survival critically depends on mitochondrial functions maintained at a normal physiological level, we determined the effect of SiO_2 nanoparticles on mitochondrial function in U87 cells by monitoring the activities of one key enzymes of the TCA cycle namely, malate dehydrogenase (MDH). As shown in Figure 13, at treatment concentrations of 25-100 μg/mL for 48 hours, SiO_2 nanoparticles induced dose-related increases in MDH activities in U87 cells.

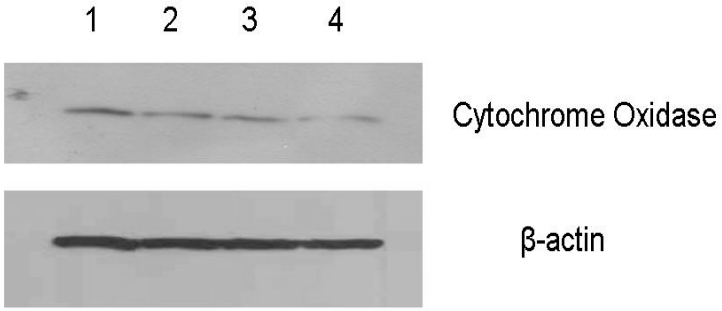

Figure 14. Effect of treatment with silicon dioxide nanoparticles on expression of cytochrome oxidase subunit II in human astrocytoma U87 cells. U87 cells were treated at specified concentrations of silicon dioxide nanoparticles for 48 hours. Then cell lysates of treated and untreated (i.e., control) U87 cells were prepared as described in Materials and Methods. The expression of cytochrome oxidase subunit II, encoded by mitochondrial DNA, was determined by Western blot analysis using β-actin as the loading control: Lane 1, lysate of untreated or control U87 cells; lane 2,

lysate of U87 cells treated with silicon dioxide nanoparticles at 25 µg/ml; lane 3 lysate of U87 cells treated with silicon dioxide nanoparticles at 50 µg/ml; lane 4, lysate of U87 cells treated with silicon dioxide nanoparticles at 100 µg/ml. The blots were from a typical experiment. Two other experiments yielded essential the same trend of results.

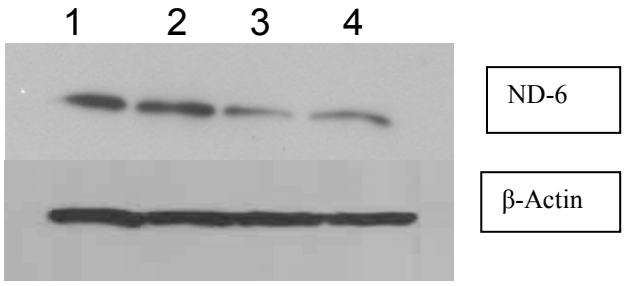

Figure 15. Effect of treatment with silicon dioxide nanoparticles on expression of NADH dehydrogenase subunit 6 (ND-6) in human astrocytoma U87 cells. U87 cells were treated at specified concentrations of silicon dioxide nanoparticles for 48 hours. Then cell lysates of treated and untreated (i.e., control) U87 cells were prepared as described in Materials and Methods. The expression of NADH dehydrogenase subunit 6 (ND-6), encoded by mitochondrial DNA, was determined by Western blot analysis using β-actin as the loading control: Lane 1, lysate of untreated or control U87 cells; lane 2, lysate of U87 cells treated with silicon dioxide nanoparticles at 25 µg/ml; lane 3 lysate of U87 cells treated with silicon dioxide nanoparticles at 50 µg/ml; lane 4, lysate of U87 cells treated with silicon dioxide nanoparticles at 100 µg/ml. The blots were from a typical experiment. Two other experiments yielded essential the same trend of results.

On the other hand, at treatment concentrations of 25-100 µg/mL for 48 hours, SiO_2 nanoparticles induced dose-related decreases in the expression of cytochrome C oxidase subunit II (a mitochondrial DNA-encoded peptide) in U87 cells (Figure 14). These results strongly suggested treatment with SiO_2 nanoparticles altered the normal functioning of the mitochondrial genome in U87 cells.

At treatment concentrations of 25-100 µg/mL for 48 hours, SiO_2 nanoparticles induced dose-related decreases in the expression of NADH dehydrogenase subunit 6 (ND 6) (a mitochondrial DNA-encoded peptide) in U87 cells (Figure 15). These results strongly suggested treatment with SiO_2 nanoparticles altered the normal functioning of the mitochondrial genome in U87 cells. A likely consequence of this effect of the nanoparticles is the impairment in the electron transport chain of the mitochondria in U87 cells: indeed, the nanoparticle–induced disruption of mitochondrial respiratory chain structure and function may be one cause of energy failure that ultimately led to the death of U87 cells.

Taken together, the results of our ongoing studies on the molecular mechanisms underlying the cytotoxic effects of silicon dioxide (SiO_2) nanparticles indicate that alterations of mitochondrial bioenergetics underly the cytotoxic effects of these nanoparticles. Moreover, they suggest there may be other such mechanisms present. Consequently, we are continuing to pursue this interesting line of investigation.

KEY RESEARCH ACCOMPLISHMENTS

Goal 1: EMG Signal Identification

The objectives that were accomplished for the Phase II of the ―Smart Prosthetic Hand Project" for the EMG group are as follows;

1) We proposed the expansion and development of dynamical models for relation between sEMG-force and sEMG and finger joint angle. We have successfully developed and published various articles on the different modeling methods and sEMG signal processing techniques that we investigated during this phase for various conferences (Please refer publications:)

2) Classification based on degree of amputation (physical classification) was completed using three female and four male cadaver specimens (16 arms) were procured from the existing cadaver holdings at Idaho State University. The measurements of various muscle bellies and lengths of forearm and upper arm flexor grouping made are reported in detail in section 2.1 of this draft.

3) A very thorough investigation of the different types of spatial filters was conducted during this phase. We investigated 11 types of spatial filters and 4 ISEK standard filters for sEMG signal processing. A detailed description of this research is provided under section 2.2 of this draft. We improved the capabilities of the existing spatial filters, available in the literature and optimized various filter masks, to obtain significantly higher values of model fits for the sEMG-force relation. In all under publication P1 and P2 we tested more than 10,000 different Hammerstein-Wiener models.

4) Development of an array sensor was also investigated under this phase. A detailed description of the research conducted is provided under section 3 of this draft.

5) A further extension to the development of the array sensor was developing our sensor fusion algorithm. This was also successfully completed and the research published under P3 and P4. A detailed report on this research is provided under section 3.2 of this draft.

6) Also, modeling of the fatigue in the modeling of sEMG-force was accomplished under this phase for an array based sensor arrangement. A detailed description of this research is provided under section 4 and 5 of this draft. Please also refer to publications

7) Along with the aforementioned research we also investigated the modeling of sEMG-joint angle of the index finger. A detailed report of this research is presented under section 6 of this draft. Also, the results of this investigation was published in shown under reportable outcomes.

Goal 2A: Intelligent Control

- A comprehensive literature updated on the topic of control techniques for prosthetic hands was conducted.
- Trajectory planning, kinematics and dynamics of a prosthetic hand with a two-link thumb and four three-link fingers based on analytical models were investigated.
- Hard computing or control techniques such as feedback linearization, proportional-derivative (PD), proportional-integral-derivative (PID), optimal and adaptive, were developed for the 14 degrees of freedom (DOFs), five-fingered smart prosthetic hand.
- Soft control techniques such as neural networks (NN), fuzzy logic (FL), adaptive neural-fuzzy inference system (ANFIS), and genetic algorithm (GA) were investigated.
- Finally, the fusion of hard and soft control techniques, such as FL+PD and GA+PID, was developed for the five-fingered smart prosthetic hand.
- Control method for power grasping for fully actuated hand
- Control method for precision grasping for fully actuated hand
- Optimal design for underactuated hand
- Control method for underactuated hand
- Comparison study of underactuated and fully actuated hands

Goal 2B: Embedded Hierarchical Real-Time Systems

- Fast prototyping test bed with common software tool chain and processors
- Design and Implementation of real-time control strategies on the test bed.
- Real-time operating system impact on the embedded control with multitasking
- Mass storage for on-line data access and management via external devices
- Investigation of modeling and simulation for the embedded control system

Goal 3: Robotic Hand

- Implementation of a working five-fingered prosthetic hand prototype (Prototype 1) based on a parallel actuation structure.
- Development of a general kinematic synthesis algorithm and solver for designing kinematic structures with the complexity of the human hand.
- Development of a synthesis theory for the exact design of articulated systems for full trajectories or workspaces.
- Development, setup and implementation of a camera system to recover finger pose from a single camera.

Goal 4: Biocompatibility and Signaling

- Development of a co-culture model for biocompatibility and other tissue engineering studies and applications
- Development of cell models of peripheral nervous system neural cells consisting of dorsal root ganglion neurons and Schwann cells for biocompatibility and other tissue engineering studies and applications
- Characterization of cell models consisting of dorsal root ganglion neurons and Schwann cells
- Development of ~~"s~~mart" biosensors for tissue engineering and biocompatibility studies and applications
- Characterization of cytotoxicity of silicon dioxide nanoparticles in human neural and non-neural cells
- Elucidation of cell death mechanisms underlying cytotoxic effects induced by silicon dioxide nanoparticles in human astrocytoma U87 (astrocytes-like) cells
- Initiation of a systematic examination of putative cytotoxicity of metallic oxide nanoparticles

REPORTABLE OUTCOMES

Goal 1: EMG Signal Identification

P1. A. Sebastian, P. Kumar, M. P. Schoen, "Evaluation of Filtering Techniques Applied to Surface EMG Data and Comparison Based on Hammerstein-Wiener Models", in *The 10th World Scientific and Engineering Academy and Society (WSEAS) International Conference on dynamical systems and control (CONTROL '11),* Iasi, Romania, July 1-3, 2011.

P2. A. Sebastian, P. Kumar, M. P. Schoen, "Optimized Spatial Filter Mask Using Genetic Algorithm And sEMG-Force Modeling Using System Identification", in *The 10th World Scientific and Engineering Academy and Society (WSEAS) International Conference on dynamical systems and control (CONTROL '11),* Iasi, Romania, July 1-3, 2011.

P3. M. Anugolu, A. Sebastian, P. Kumar, M. P. Schoen, A. Urfer, and D. S. Naidu, "Surface EMG Array Sensor Based Model Fusion Using Bayesian Approaches For Prosthetic Hands," 2009 ASME Dynamic Systems and Control Conference, Hollywood, California, USA, Oct. 12-14, 2009.

P4. C. Potluri, P. Kumar, M. Anugolu, A. Urfer, S. Chiu, D. S. Naidu, and M. P. Schoen, "Frequency Domain Surface EMG Sensor Fusion for Estimating Finger Forces," 32nd Annual International Conference of the IEEE Engineering in Medicine and Biology Society, Buenos Aires, Argentina, Aug. 31 – Sept. 4, 2010.

P5. P. Kumar, A. Sebastian, C. Potluri, Y. Yihun, A. Ilyas, M. Anugolu, R. Sharma, J. Creelman, A. Urfer, D. S. Naidu, and M. P. Schoen, "Spectral Analysis of sEMG Signals to Investigate Skeletal Muscle Fatigue," 50th IEEE Conference on Decision and Control and European Control Conference, Orlando (FL), USA, December 12-15, 2011 (Under Peer Review).

P6. P. Kumar, A. Sebastian, C. Potluri, A. Urfer, D. S. Naidu, and M. P. Schoen, "Towards Smart Prosthetic Hand: Adaptive Probability Based Skeletal Muscle Fatigue Model," 32nd Annual International Conference of the IEEE Engineering in Medicine and Biology Society, Buenos Aires, Argentina, Aug. 31 – Sept. 4, 2010.

P7. P. Kumar, C. Potluri, A. Sebastian, S. Chiu, A. Urfer, D. S. Naidu, and M. P. Schoen, "An Adaptive Multi Sensor Data Fusion with Hybrid Nonlinear ARX and Wiener-Hammerstein Models for Skeletal Muscle Force Estimation," The 14th World Scientific and Engineering Academy and Society (WSEAS) International Conference on Systems, Corfu Island, Greece, July 22-24, 2010.

P8. P. Kumar, C. Potluri, A. Sebastian, S. Chiu, A. Urfer, D. S. Naidu, and M. P. Schoen, Adaptive Multi Sensor Based Nonlinear Identification of Skeletal Muscle Force, WSEAS Transactions on Systems, Issue 10, Volume 9, October 2010, pp. 1051-1062, 2010.

P9. P. Kumar, C. Potluri, M. Anugolu, A. Sebastian, J. Creelman, A. Urfer, S. Chiu, D. S. Naidu, and M. P. Schoen, "A Hybrid Adaptive Data Fusion with Linear and Nonlinear Models for Skeletal Muscle Force Estimation," 5th Cairo International Conference on Biomedical Engineering, Cairo, Egypt, Dec. 16-18, 2010.

P10. P. Kumar, C. Potluri, A. Sebastian, Y. Yihun, A. Ilyas, M. Anugolu, R. Sharma, S. Chiu, J. Creelman, A. Urfer, D. S. Naidu, and M. P. Schoen, "A Hybrid Adaptive Multi Sensor Data Fusion for Estimation of Skeletal Muscle Force for Prosthetic Hand Control," The 2011 International Conference on Artificial Intelligence, ICAI'11, Las Vegas, Nevada, USA, July 18-21, 2011.

P11. P. Kumar, C. H. Chen, A. Sebastian, M. Anugolu, C. Potluri, A. Fassih, Y. S. Yihun, A. Jensen, Y. Tang, S. Chiu, K. Bosworth, D. S. Naidu, J. Creelman, A. Urfer and M. P. Schoen, "An Adaptive Hybrid Data Fusion Based Identification of Skeletal Muscle Force with ANFIS and Smoothing Spline Curve Fitting," 2011 IEEE International Conference on Fuzzy Systems, Taipei, Taiwan, June 27-30, 2011.

P12. P. Kumar, A. Sebastian, C. Potluri, A. Urfer, D. S. Naidu, and M. P. Schoen, "Towards Smart Prosthetic Hand: Adaptive Probability Based Skeletal Muscle Fatigue Model," 32nd Annual International Conference of the IEEE Engineering in Medicine and Biology Society, Buenos Aires, Argentina, Aug. 31 – Sept. 4, 2010.

P13. P. Kumar, A. Sebastian, C. Potluri, A. Ilyas, M. Anugolu, A. Urfer, and M. P. Schoen, "Adaptive Finger Angle Estimation form sEMG Data with Multiple Linear and Nonlinear Model Data Fusion," The 10th World Scientific and Engineering Academy and Society (WSEAS) International Conference on Dynamical Systems and Control, Iasi, Romania, July 1-3, 2011.

P14. P. Kumar, C. Potluri, N. Joshi, A. Jensen, M. P. Schoen, and S. Chiu, "Genetic Algorithm Running Time Optimization Using OpenMP Parallel Computing," International Conference on Parallel and Distributed Processing Techniques and Applications, PDPTA'10, Las Vegas, Nevada, USA, July 12-15, 2010.

P15. A. Sebastian, P. Kumar, M. P. Schoen, A Study on Hybridization of Particle Swarm and Tabu Search Algorithm for Unconstraint Optimization and Estimation, in The 14th World Scientific and Engineering Academy and Society (WSEAS) International Conference on Systems, Corfu Island, Greece, July 22-24, 2010.

P16. A. Sebastian, P. Kumar, M. P. Schoen, A. Urfer, Jim Creelman and D. S. Naidu, ―Analysis of EMG-force relation using system identification and Hammerstein-Wiener models," 2009 ASME Dynamic Systems and Control Conference, Hollywood, California, USA, Oct. 12-14, 2009.

Goal 2A: Intelligent Control

Portions of goal 2A have been accepted in one book chapter (attachment 2A-1), reviewed in one international journal paper (attachment 2A-2) and four international peer-reviewed conference papers (attachments 2A-3, 2A-4, 2A-5, and 2A-6); one poster (attachment 2A-7) have been presented as follows:

1. D. S. Naidu and C.-H. Chen. Control strategies for smart prosthetic hand technology: an overview, book chapter 12, to appear in a book titled –Distributed Diagnosis and Home Healthcare (D2H2): Volume 2", American Scientific Publishers, CA, 2011. (printed) (attachment 2A-1)

2. C.-H. Chen, D. S. Naidu, and M. P. Schoen. Adaptive control for a five-fingered prosthetic hand with unknown mass and inertia. *World Scientific and Engineering Academy and Society (WSEAS) Journal on* Systems, 2011. (under reviewed) (attachment 2A-2)

3. C.-H. Chen, D. S. Naidu, and M. P. Schoen. An adaptive control strategy for a five-fingered prosthetic hand. *In the 14th World Scientific and Engineering Academy and Society (WSEAS) International Conference on* Systems, Latest Trends on Systems (volume II), Corfu Island, Greece, July 22-24, pp. 405-410, 2010. (presented) (attachment 2A-3)

4. C.-H. Chen and D. S. Naidu. . Optimal control strategy for two-fingered smart prosthetic hand. *In Proceedings of the 15th International Association of Science and Technology for Development (IASTED) International Conference on Robotics and Applications (RA 2010)*, Cambridge, Massachusetts, USA, November 1-3, pp. 190-196, 2010. (presented) (attachment 2A-4)

5. C.-H. Chen and D. S. Naidu. Hybrid genetic algorithm based PID control for a five-fingered smart prosthetic hand. *In Proceedings of the 5th International Conference on Circuits, Systems and Signals (CSS'11)*, Corfu Island, Greece, July 14-16, 2011. (accepted) (attachment 2A-5)

6. C.-H. Chen and D. S. Naidu. Fusion of fuzzy logic and PD control for a five-fingered smart prosthetic hand. *In Proceedings of the 2011 IEEE International Conference on Fuzzy Systems (FUZZ-IEEE 2011)*, Taipei, Taiwan, June 27-30, 2011. (accepted) (attachment 2A-6)

7. C.-H. Chen and D. S. Naidu. Fusion of fuzzy logic and PD control for a five-fingered smart prosthetic hand. in Graduate Student Research and Creative Excellence Symposium, Idaho State University, Pocatello, Idaho, USA, April 8, 2011. (Poster presentation) (attachment 2A-7)

8. 1- Amir Fassih, D. Subbaram Naidu, Steve Chiu, and Marco P. Schoen , –Power grasping of a prosthetic hand based upon virtual spring-damper hypothesis", IASTED 2010, Massachusetts , Cambridge.

9. 2- Amir Fassih, D. Subbaram Naidu, Steve Chiu, and Marco P. Schoen , –Precision grasping of a prosthetic hand based on virtual spring damper hypothesis", CIBEC 2010, Egypt, Cairo.

Goal 2B: Embedded Hierarchical Real-Time Systems

The following related refereed publications were produced:

[1] Chandrasekhar Potluri, Yimesker Yihun, Parmod Kumar, Jeff Molitor, Steve Chiu, D. S. Naidu, S. H. Mousavinezhad, ―sEMG Based Real Time Embedded Force Control Strategy for a Prosthetic Hand Prototype," Accepted for publication in the IEEE International Conference on Electro/Information technology (IEEE EIT, 05/2011).

[2] Chandrasekhar Potluri, Parmod Kumar, Jeff Molitor, Madhavi Anugolu, Alex Jensen, Kenyon Hart, and Steve Chiu, ―Multi-Level Motor Control for Prosthesis," in the proceedings of the *2010 International Conference on Embedded Systems and Applications* (ESA, 07/2010).

[3] Chandrasekhar Potluri, Parmod Kumar, Madhavi Anugolu, Steve Chiu, Marco Schoen, Alex Urfer, and D. S. Naidu, ―AnANFIS Based Fuzzy Controller for Prosthetic Hand," in the proceedings of the *3rd IEEE RAS-EMBS International Conference on Biomedical Robotics and Biomechatronics* (BioRob, 09/2010).

[4]. H. Karepey, H. Ahsan, S. Chiu, and A. Perez-Gracia, ―3D Reconstruction for Hand Tracking and Estimation," in the proceedings of the *2010 International Conference on Image Processing, Computer Vision, and Pattern Recognition* (IPCV, 07/2010).

[5]. J. Manchala and S. Chiu, ―ANodal Feedback Model for Wireless Multi-Sensory Data Fusion," in the proceedings of the *2010 International Conference on Wireless Networks* (ICWN, 07/2010).

[6]. P. Kumar, N. Joshi, A. Jensen, C. Potluri, M. Schoen, and S. Chiu, ―Genetic Algorithm Running Time Optimization Using OpenMP Parallel Computing," in the proceedings of the *2010 International Conference on Parallel and Distributed Processing Techniques and Applications* (PDPTA, 07/2010).

Goal 3: Robotic Hand

Manuscripts published or in press (see Appendices –Goal3_1, Goal3_2, Goal3_3):

Perez Gracia, A., –Synthesis of Spatial RPRP Closed Linkages for a Given Screw System", *ASME Journal of Mechanisms and Robotics*, 2011, in press.

Simo-Serra, E., Moreno-Noguer, F., and Perez-Gracia, A., —Design of Non-anthropomorphic Robotic Hands for Anthropomorphic Tasks", *accepted at the ASME International Design Engineering Technical Conferences, IDETC 2011*, Washington DC, USA, August 29-31, 2011.

Crawford, A.L., Molitor, J., Perez Gracia, A., and Chiu, S., –Design of a Robotic Hand and Simple EMG Input Controller with a Biologically-Inspired Parallel Actuation System for Prosthetic Applications", *1st International Conference on Applied Bionics and Biomechanics (ICABB),* Venice, Italy, October 14-16, 2010.

Abstracts published:

Presentations:

A. Invited oral presentations:

B. Oral presentation:

C. Poster presentations:

D. Invitation to chair and/or organize sessions at national/international meetings:

Perez-Gracia: Symposium co-organizer at the 2011 ASME International Design Engineering Technical Conferences and Computers and Information in Engineering Conferences, Washington DC, USA, August 28-31, 2011.

Goal 4: Biocompatibility and Signaling

Our research has been very productive: to date, we have **7 journal articles, 1 review, and 7 conference proceedings papers** published or in press, published **7** abstracts, and given **3** oral and **4** poster presentations (see lists below for details).

Journal Articles published or in press:

1. Lai JCK, Ananthakrishnan G, Jandhyam S, Dukhande VV, Bhushan A, Gokhale M, Daniels CK & Leung SW (2010) Treatment of Human Astrocytoma U87 Cells with Silicon Dioxide Nanoparticles Lowers Their Survival and Alters Their Expression of Mitochondrial and Cell Signaling Proteins. International Journal of Nanomedicine 5:715-723.
2. Jaiswal AR, Bhushan A, Daniels CK & Lai JCK (2010) A Cell Culture Model for Diabetic Neuropathy Studies. Journal of the Idaho Academy of Science 46(1):58-63.
3. Wong YYW, Jaiswal AR, Bhushan A, Leung SW & Lai JCK (2010) Further Elucidation of Neuroprotective Properties of Astrocytoma (Astrocytes-like) Cells. Journal of the Idaho Academy of Science 46(1):52-57.
4. Patil PP, Lai MB, Leung SW, Lai JCK & Bhushan A (2010) Differential Cytotoxic Effects of Magnesium Oxide Nanoparticles on Cisplatin-sensitive and Cisplatin-resistant Leukemia Cancer Cells. Journal of the Idaho Academy of Science 46(1):70-75.
5. Wright GL, Lai JCK, Chan AWK, Minski MJ, Lim L & Leung SW (2010) Metallomic Distribution in Various Regions of the Brain as Influenced by Dietary Intakes and Their Implications. In Proceedings of the ISEIS 2010 International Conference on Ecological Informatics and Ecosystem Conservation, August 27-29, Beijing, China, published in Procedia Engineering 01 (2010) 0159-0171.
6. Leung SW, Siddhanti S, Williams B, Chan AWK, Minski MJ, Daniels CK & Lai JCK (2010) Effects of Diet Intake on Metal and Electrolyte Distributions in Various Organs. In Proceedings of the ISEIS 2010 International Conference on Ecological Informatics and Ecosystem Conservation, August 27-29, Beijing, China, published in Procedia Engineering 01 (2010) 0104-0108.
7. Leung SW, Wang Y & Lai JCK (2011) Biomedical Applications of Modified Carbon Glassy Electrode Sensor with Nanoparticles and Dendrimers. Sensors & Transducers (2011) Volume 11, Special Issue, April 2011, pp. 74-82.

Review Articles published or in press:

1. Bhushan A, Patil PP, Leung SW & Lai JCK (2011) Metallic Nanoparticles in Cancer Imaging and Therapy. In: CRC Biomedical Engineering Handbook, 4th Edition, CRC Press (in press).

Conference Proceedings Papers published or in press:

1. Jaiswal A, Wong YYW, Bhushan A, Daniels C & Lai JCK (2010) A Noncontact Co-Culture Model of Peripheral Neural Cells for Nanotoxicity, Tissue Engineering and Pathophysiological Studies. Technical Proceedings of the 2010 NSTI Nanotechnology Conference and Expo – Nanotech 2010, Vol. 3 Chapter 8: Environment, Health & Safety, Pages 527-531.
2. Wong YYW, Jaiswal AR, Dukhande VV, Bhushan A, Leung SW & Lai JCK (2010) Elucidation of Neuroprotective Properties of Astrocytoma (Astrocytes-like) Cells in Neural Cell Culture Models *In Vitro*: Applications in Tissue Engineering and Nanotoxicology. Technical Proceedings of the 2010 NSTI Nanotechnology Conference and Expo – Nanotech 2010, Vol. 3 Chapter 8: Environment, Health & Safety, Pages 561-564.
3. Leung SW, Gao W, Gu H, Bhushan A & Lai JCK (2010) Chitosan Membrane in Combinations with Nanoparticles and Adriamycin as a Treatment to Inhibit Glioma Growth and Migration. Technical Proceedings of the 2010 NSTI Nanotechnology Conference and Expo – Nanotech 2010, Vol. 3 Chapter 3: Nano for Biotech, Interfaces & Tissues, Pages 206-209.

4. Leung SW, Wang Y, Gu H & Lai JCK (2010) Biomedical Applications of Modified Carbon Glassy Electrode Sensor with Nanoparticles and Dendrimers. Technical Proceedings of the 2010 NSTI Nanotechnology Conference and Expo – Nanotech 2010, Vol. 3 Chapter 1: Bio Sensors, Diagnostics & Imaging, Pages 122-124.
5. Bhushan A, Patil PP, Bhardwaj V, Lai MB, Daniels CK, Leung SW & Lai JCK (2010) Cross Resistance of Magnesium Oxide Nanoparticles to Cisplatin in Leukemia Cells: Mechanistic Studies. In Seminar Proceedings of Institution of Mechanical Engineers Seminar on Nanotechnology in Medicine and Biotechnology, October 2010, London, UK, Chapt. 5, pp. 1-4.
6. Leung S & Lai J (2011) Advanced Dehydrogenase Biofuel Cell Modified with Highly Branched Polymers and Nanogold Sol-Gel. In Proceedings of 2011 International Conference on Agricultural and Biosystems Engineering (ICABE 2011). Lecture Notes in Information Technology Vols. 3-4, pp. 41-44.
7. Leung S, Williams B, Lai J, Chan A & Minski M (2011) Elemental Analyses in Organ Systems in a Small Animal after Life-Long Controlled Diet. In Proceedings of 2011 International Conference on Agricultural and Biosystems Engineering (ICABE 2011). Lecture Notes in Information Technology Vols. 3-4, pp. 45-48.

Abstracts published:

1. Jaiswal A, Wong YYW, Bhushan A, Daniels C & **Lai JCK** (2010) A Noncontact Co-Culture Model of Peripheral Neural Cells for Nanotoxicity, Tissue Engineering and Pathophysiological Studies. NSTI Nanotechnology Conference and Expo – Nanotech 2010, June 21-25, 2010, Anaheim, CA (in Abstracts Volume).
2. Wong YYW, Jaiswal AR, Dukhande VV, Bhushan A, Leung SW & Lai JCK (2010) Elucidation of Neuroprotective Properties of Astrocytoma (Astrocytes-like) Cells in Neural Cell Culture Models *In Vitro*: Applications in Tissue Engineering and Nanotoxicology. NSTI Nanotechnology Conference and Expo – Nanotech 2010, June 21-25, 2010, Anaheim, CA (in Abstracts Volume).
3. Leung SW, Gao W, Gu H, Bhushan A & Lai JCK (2010) Chitosan Membrane in Combinations with Nanoparticles and Adriamycin as a Treatment to Inhibit Glioma Growth and Migration. NSTI Nanotechnology Conference and Expo – Nanotech 2010, June 21-25, 2010, Anaheim, CA (in Abstracts Volume).
4. Leung SW, Wang Y, Gu H & Lai JCK (2010) Biomedical Applications of Modified Carbon Glassy Electrode Sensor with Nanoparticles and Dendrimers. NSTI Nanotechnology Conference and Expo – Nanotech 2010, June 21-25, 2010, Anaheim, CA (in Abstracts Volume).
5. Wright GL, Lai JCK, Chan AWK, Minski MJ, Lim L & Leung SW (2010) Metallomic Distribution in Various Regions of the Brain as Influenced by Dietary Intakes and Their Implications. ISEIS 2010 International Conference on Environmental Informatics, Beijing, China, August 27-29, 2010 (in Abstracts Volume).
6. Leung SW, Siddhanti S, Williams B, Chan AWK, Minski MJ, Daniels CK & Lai JCK (2010) Effects of Dietary Intake on Metal and Electrolyte Distributions in Various Organs. ISEIS 2010 International Conference on Environmental Informatics, Beijing, China, August 27-29, 2010 (in Abstracts Volume).
7. Bhushan A, Patil PP, Bhardwaj V, Lai MB, Daniels CK, Leung SW & Lai JCK (2010) Cross Resistance of Magnesium Oxide Nanoparticles to Cisplatin in Leukemia Cells: Mechanistic Studies. Institution of Mechanical Engineers Seminar on Nanotechnology in Medicine and Biotechnology, October 2010, London, UK (in Program & Abstracts).

Presentations:

E. **Invited oral presentations**:

1. Wright GL, Lai JCK, Chan AWK, Minski MJ, Lim L & Leung SW (2010) Metallomic Distribution in Various Regions of the Brain as Influenced by Dietary Intakes and Their Implications. ISEIS 2010 International Conference on Environmental Informatics, Beijing, China, August 27-29, 2010.
2. Leung SW, Siddhanti S, Williams B, Chan AWK, Minski MJ, Daniels CK & Lai JCK (2010) Effects of Dietary Intake on Metal and Electrolyte Distributions in Various Organs. ISEIS 2010 International Conference on Environmental Informatics, Beijing, China, August 27-29, 2010.
3. Bhushan A, Patil PP, Bhardwaj V, Lai MB, Daniels CK, Leung SW & Lai JCK (2010) Cross Resistance of Magnesium Oxide Nanoparticles to Cisplatin in Leukemia Cells: Mechanistic Studies. Institution of Mechanical Engineers Seminar on Nanotechnology in Medicine and Biotechnology, October 2010, London, UK.

F. **Poster presentations**:

1. Jaiswal A, Wong YYW, Bhushan A, Daniels C & Lai JCK (2010) A Noncontact Co-Culture Model of Peripheral Neural Cells for Nanotoxicity, Tissue Engineering and Pathophysiological Studies. NSTI Nanotechnology Conference and Expo – Nanotech 2010, June 21-25, 2010, Anaheim, CA.
2. Wong YYW, Jaiswal AR, Dukhande VV, Bhushan A, Leung SW & Lai JCK (2010) Elucidation of Neuroprotective Properties of Astrocytoma (Astrocytes-like) Cells in Neural Cell Culture Models *In Vitro*: Applications in Tissue Engineering and Nanotoxicology. NSTI Nanotechnology Conference and Expo – Nanotech 2010, June 21-25, 2010, Anaheim, CA.
3. Leung SW, Gao W, Gu H, Bhushan A & Lai JCK (2010) Chitosan Membrane in Combinations with Nanoparticles and Adriamycin as a Treatment to Inhibit Glioma Growth and Migration. NSTI Nanotechnology Conference and Expo – Nanotech 2010, June 21-25, 2010, Anaheim, CA.
4. Leung SW, Wang Y, Gu H & Lai JCK (2010) Biomedical Applications of Modified Carbon Glassy Electrode Sensor with Nanoparticles and Dendrimers. NSTI Nanotechnology Conference and Expo – Nanotech 2010, June 21-25, 2010, Anaheim, CA.

CONCLUSIONS

The EMG group of this project worked on the physical classification (ongoing), classification based on spatial filters (ongoing), development of sensors (to be tested), spatial filtering (completed), fatigue modeling (completed), spatial filters with fatigue (completed), motion model (on going). According to the stated timeline and milestones of the original proposal, we are well on track and making good progress to the final goals of Phase II.

A comprehensive literature updated on the topic of control techniques for prosthetic hands was conducted and one book chapter is printed. The forward and inverse kinematics of the system regarding the analytical relationship between the angular positions of joints and the positions and orientations of the end-effectors (fingertips), was obtained using a desired orientation □ □ for three-link fingers. The differential kinematics for a serial *n*-link revolute-joint planar prosthetic hand was derived to compute the angular velocities and angular accelerations of each finger. Besides, adaptive neuro-fuzzy inference system (ANFIS) was used for inverse kinematics of three-link fingers. Then, the cubic polynomial function was designed to track the orientation in order to calculate inverse kinematics and differential kinematics. An adaptive control strategy was developed for the 14 degrees of freedom (DOFs), five-fingered smart prosthetic hand with unknown mass and inertia of all the fingers. The simulations of the resulting adaptive controller showed good agreement between the reference and the actual trajectories. Work is in progress for developing an adaptive/robust controller for the five fingered hand with 14-DOFs. To make the optimal controller fast acting, the performance index J included an exponential term. The simulation results demonstrated a 30-fold increase in fast response compared to ANFIS or GA based trajectory planning. Work is underway to extend this methodology to five-fingered, three-dimensional prosthetic hand. A hybrid control technique combining soft control with ANFIS and genetic algorithm (GA) and hard control with proportional-integral-derivative (PID) was presented for a five-fingered smart prosthetic hand. The ANFIS is used for inverse kinematics and GA is used for tuning the PID parameters with the objective of minimizing the error squared between desired and actual angles of the links of the fingers. Simulation results for all the five fingers with GA-tuned PID controller showed superior performance compared to the PID control alone. A real-time implementation of this technique on a prototype of a prosthetic hand is planned for future work. For a five-fingered smart prosthetic hand, a hybrid control technique involving soft control with ANFIS and fuzzy logic (FL) and hard control with proportional-derivative (PD) was presented. The ANFIS is used for inverse kinematics and FL is used for tuning the PD parameters with two input layers (error and error change) using 7 triangular membership functions and 49 fuzzy logic rules. Simulation results with FL-tuned PD (hybrid) controller showed superior performance compared to the PD and PID control alone. Work is underway to extend this methodology to a real-time implementation on the prototype of a prosthetic hand. In this report two type of hand which are fully actuated and underactuated hand studied. Appropriate control methods are provided for precision and power grasping for fully actuated hand. For underactuated hand the optimal design condition derived and tested. Appropriate controller for hand movement proposed and tested through numerical simulation. Two methods of power grasping, based on fully actuated and underactuated hand compared and the results were close which means both method are capable of providing secure grasp for prosthetic hand.

The work demonstrated the usability of a fast prototyping test bed for the validation and verification of model-based controller designs. We were also able to study in more details the impact of implementation on the embedded control, including the use of CAN and RTOS. Furthermore, we began our investigation on the modeling and simulation of our embedded control through collaboration with Johns Hopkins University‘s Applied Physics Laboratory. Based on the promising test results obtained in the two- fingered (Thumb-index) prototype, mechanical design of the five-fingered, full-dof has been designed, and modeled in CAD software and validated through simulation. At this time, the five-fingered prosthetic hand prototype (Prototype 1) is finished in its prototype form. The actuators, particularly the region I actuation scheme, are also implemented. Using this actuation scheme, simple tasks, such as grasping spherical objects, have been tested. Similarly, the force at the tip of the finger while grasping has been tested using FSR; the implementation of position sensors is still in progress. During the next three to six months, the testing scheme will be developed and the full testing of Prototype 1 will be finished. The results will be useful to assess the need for the parallel actuation, and also as an input in the design of Prototype 2. For the design of Prototype 2 we are developing new kinematic synthesis results. A general algorithm, already implemented and in the phase of being refined, will allow us to size kinematic chains with the complexity of the human hand. Newly developed theory will also allows us to approximate or follow exactly whole trajectories of fingertips with new designs. This is complemented with a thorough study of actual designs. The focus of the Prototype 2 design will be on thumb and palm redesign, and on the underactuated/fully actuated duality scheme. An important tool for many of these activities is a hand motion identification and tracking system, which is being developed with good results and

will be ready to be used in the next three months. This system will be used not only on the synthesis process, but also for shedding some light on grasping and manipulation issues. Regarding this last topic, our efforts will be focused on identifying hand synergies and limits to allow us to lower the dimensionality of the hand motion space.

We have made significant progress in studies specified on biocompatibility and signaling. In the process of setting up the "Sensor on Cells on Skin Model," we have identified the three stages we need to undergo to achieve this goal: (i) stage one involves the development of different human and other mammalian cells (including nerve and skin cells) in co-culture; (ii) stage two requires the juxtaposition of cells in relation to the membrane; and (iii) stage three involves designing the sensor(s) and fitting them into the "sensor on cells on skin model". We have accomplished stages (i) and (ii) by developing the "co-culture" and the "on-contact" cell models and demonstrating that these models can be useful and relevant in facilitating studies to address various mechanistic issues in biocompatibility and other tissue engineering and nanotoxicity research. Furthermore, we have developed new cell models of peripheral nervous systems consisting of dorsal root ganglion neurons and Schwann cells. These models are particularly useful for elucidating nerve degeneration and regeneration. We are currently characterizing these models further. Our extensive literature survey indicates that our approaches are truly novel and will lead to further ground-breaking discoveries because, as we have already discussed above, the whole important issue of how tissue and cellular inflammatory responses are elicited by implant material(s) have not been resolved and is poorly understood. By way of heading towards completing stage (iii), we have developed several "smart" sensors that are pH sensitive and self-assembling with nanoparticles. Thus far, we are using glassy carbon, gold, or silver as anchor material for the sensor electrode. This type of "smart" sensor can be employed to detect many enzymatic and chemical reactions known to occur in different tissues/organs. Thus, we are focusing on the development of biosensors for tissue engineering and biocompatibility studies and related biomedical engineering applications. We also recently noted that some of the sensors we have designed can also be developed into fuel cells and related applications. One important but as yet poorly characterized facet of biocompatibility pertains to the putative nanotoxicity of nanoparticles and other nanomaterials employed to fabricate artificial implants. As part of our systematic studies to elucidate the cytotoxicity of nanoparticles of metallic oxides that are commonly found in composites in fabricating such implants, we have further characterized the effects of silicon dioxide nanoparticles on human neural cells and normal human fibroblasts. We have elucidated some of the cellular and molecular mechanisms underlying the cytotoxicity of these nanoparticles on human neural cells. These are important advances in nanotoxicity research because of the paucity of literature on the cytotoxicity of nanoparticles of metallic and non-metallic oxides in neural cells Thus, our findings may have toxicological and other pathophysiological implications on exposure of humans and other mammalian species to such nanoparticles.

REFERENCES

Goal 1: EMG Signal Identification

[1] Haruhisa Kawasaki, Tsuneo Komatsu, and Kazunao Uchiyama, Dexterous Anthropomorphic Robot Hand With Distributed Tactile Sensor: Gifu Hand II, *IEEE/ASME Transactions on Mechatronics,* Vol. 7, No. 3, September 2002, pp. 296-303.

[2] Northrop, R., Analysis and application of analogue electronic circuits to biomedical instrumentation. CRC Press, Boca Raton, Florida, 2004, pp. 6–9.

[3] M. Zecca, S. Micera, M. C. Carrozza, and P. Dario, Control of Multifunctional Prosthetic Hands by Processing the Electromyographic Signal, *Critical Reviews™ in Biomedical Engineering,* 30(4–6), 2002, pp. 459–485.

[4] Claudio Castellini and Patrick van der Smagt, Surface EMG in advanced hand prosthetics, *Biological Cybernetics,* (2009) 100, pp. 35–47.

[5] C. J. De Luca, Myoelectrical manifestations of localized muscular fatigue in humans, *Crit. Rev. Biomed. Eng.,* 11 (4), 1984, pp. 251-279.

[6] Merletti R, and Lo Conte LR, "Surface EMG signal processing during isometric contractions," Journal of Electromyography and Kinesiology, 7(4), pp. 241-250, 1997.

[7] Finsterer J., "EMG-interference pattern analysis," J Electromyogr Kinesiol, 11, pp. 231-246, 2001.

[8] A. Luttmann, M. Ja¨ger, J. So¨keland, and W. Laurig, "Electromyographical study on surgeons in urology, Part II: Determination of muscular fatigue," Ergonomics, 39, pp. 298-313, 1996.

[9] Clouse WD, Rassmussen E, Peristein J, Sutherlan MJ, Peck MA, Eliason JL, Jazerevic S, Jenkins D. Upper extremity vascular injury: A current in-theater wartime report from Operation Iraqi F. An of Vasc Surg. 2006; 20: 429-4343.N. Dechev, W. L. Cleghorn, and S. Naumann, Multiple finger, passive adaptive grasp prosthetic hand, *Mechanism and Machine Theory,* 36(2001), pp. 1157-1173.

[10] Warfel JW The Extremities: Muscles and Motor Points.6th ed. Philadelphia, PA: Lea and Febiger, 1993

[11] http://www.spatialanalysisonline.com/output/html/Linearspatialfiltering.html

[12] P. Zhou and W. Z. Rymer, "An evaluation of the utility and limitations of counting motor unit action potentials in the surface electromyogram," *Journal of Neural Engineering*, vol. 1, pp. 238–245, 2004.

[13] C. J. Deluca, A. Adam, R. Wotiz, L. D. Gilmore, and S. H. Nawab, "Decomposition of surface EMG signals," *Journal of Neurophysiology*, vol. 96,pp. 1646–1657, 2006.

[14] Z. Xu and S. Xiao, "Digital filter design for peak detection of surface EMG," *Journal of Electromyography & Kinesiology,* vol. 10, pp. 275–281, 2000.

[15] M. J. Zwarts and D. F. Stegeman, "Multichannel surface EMG: Basic aspects and clinical utility," *Muscle Nerve*, vol. 28, pp. 1–17, 2003.

[16] B. G. Lapatki, J. P. Van Dijk, I. E. Jonas, M. J. Zwarts, and D. F. Stegeman, "A thin, flexible multielectrode grid for high-density surface EMG," *Journal of Applied Physiology.*, vol. 96, pp. 327–336, 2004.

[17] M. Pozzo, A. Bottin, R. Ferrabone, and R. Merletti, "Sixty-four channel wearable acquisition system for long-term surface electromyogram recording with electrode arrays," *Medicine Biology Engineering and Computation*, vol. 42, pp. 455–466, 2004.

[18] H. Reucher, G. Rau, and J. Silny, "Spatial filtering of noninvasive multi-electrode EMG: Part I—Introduction to measuring technique and applications," *IEEE Transaction on Biomedical Engineering*, vol. BME-34, no. 2, pp. 98–105, Feb.1987.

[19] C. Disselhorst-Klug, J. Silny, and G. Rau, "Improvement of spatial resolution in surface-EMG: A theoretical and experimental comparison of different spatial filters," *IEEE Transactions on Biomedical Engineering*, vol. 44, no. 7, pp. 567–574, Jul. 1997.

[20] D. Farina, E. Schulte, R. Merletti, G. Rau, and C.Disselhorst-Klug, "Single motor unit analysis from spatially filtered surface electromyogram signals. Part I: Spatial selectivity," *Medicine Biology Engineering and Computation*, vol. 41, pp. 330–337, 2003.

[21] D. Farina, L. Mesin, S. Martina, and R. Merletti, ―Comparison of spatial filter selectivity in surface myoelectric signal detection: Influence of the volume conductor model," *Medicine Biology Engineering and Computation*, vol. 42, pp. 114–120, 2004.

[22] N. Ostlund, J. Yu, K. Roeleveld, and J. S. Karlsson, ―Adaptive spatial filtering of multichannel surface elelctromyogram signals," *Medicine Biology Engineering and Computation*, vol. 42, pp. 825–831, 2004.

[23] N. Ostlund, J. Yu, and J. S. Karlsson, ―Adaptive spatio-temporal filtering of multichannel surface EMG signals," *Medicine Biology Engineering and Computation*, vol. 44, pp. 209–215, 2006.

[24] P. Zhou, N. L. Suresh, M. Lowery, W. Z. Rymer, ―Nonlinear Spatial Filtering of Multichannel Surface Electromyogram Signals During Low Force Contractions", *IEEE Transactions on Biomedical Engineering*, vol. 56, no.7, pp. 1871-1879, July 2009.

[25] J. F. Kaiser, "On a simple algorithm to calculate the ‗energy' of a signal*", Proceedings of IEEE ICASSP'90,* Albuquerque, New Mexico, pp. 381-384, April 1990.

[26] J. F. Kaiser, "On Teager's energy algorithm and its generalization to continuous signals", *Proc. 4th IEEE Digital Signal Proc. Workshop, Mohonk* (New Paltz), NY, September 1990.

[27] P. Maragos, J. F. Kaiser, and T. F.Quatieri, "On amplitude and frequency demodulation using energy operators", *IEEE Transactions on Signal Processing*, Vol. 41, pp. 1532-1550, April 1993.

[28] R. Hamila, J. Astola, F. Alaya Cheikh, M. Gabbouj, and M. Renfors, "Teager Energy and the Ambiguity Function", *IEEE International Conference On Image Processing,* Vol. 47, No. 1, pp. 260-262, January 1999.

[29] F. Alaya Cheikh, R. Hamila, M. Gabbouj And J. Astola, "Impulse Noise Removal In Highly Corrupted Color Images," Proc. 1996 *IEEE International Conference On Image Processing,* Lausanne, Switzerland, Vol. I, pp. 997-1000, September, 1996.

[30] J. Astola and P. Kuosmanen, Fundamentals of Nonlinear Digital Filtering, *CRC Press LLC*, 1997.

[31] Terence D. Sanger, Bayesian Filtering of Myoelectric Signals, *J Neurophysiol,* 97, 2007, pp. 1839–1845.

[32] M. B. I. Reaz, M. S. Hussain and F. Mohd-Yasin, Techniques of EMG signal analysis: detection, processing, classification and applications, *Biol. Proced. Online*, 2006, 8(1), pp. 11-35.

[33] E. Kral, L. Vasek, V. Dolinay, P. Varacha, Usage of PSO Algorithm for Parameter Identification of District Heating Network Simulation Model, *The 14th World Scientific and Engineering Academy and Society (WSEAS) International Conference on Systems,* Corfu Island, Greece, July 22-24, 2010.

[34] A. Neubaur, The Intrinsic System Model of the Simple Genetic Algorithm with α-Selection, Uniform Crossover and Bitwise Mutation, *The 14th World Scientific and Engineering Academy and Society (WSEAS) International Conference on Systems,* Corfu Island, Greece, July 22-24, 2010.

[35] A. Sebastian, P. Kumar, M. P. Schoen, A Study on Hybridization of Particle Swarm and Tabu Search Algorithm for Unconstraint Optimization and Estimation, in *The 14th World Scientific and Engineering Academy and Society (WSEAS) International Conference on Systems,* Corfu Island, Greece, July 22-24, 2010.

[36] Ping Zhou, Nina L. Suresh, Madeleine M. Lowery, William Z. Rymer, ―Nonlinear Spatial Filtering of Multichannel Surface Electromyogram Signals During Low Force Contractions," IEEE Transactions on Biomedical Engineering, Vol. 56, No. 7, pp. 1871-1879, July 2009.

[37] ―Signal Processing Toolbox™ User's Guide," The MathWorks, Inc., 2010.

[38] Marple, S.L. Digital Spectral Analysis, Englewood Cliffs, NJ, Prentice-Hall, 1987, pp. 373-378.

[39] Schmidt, R.O, "Multiple Emitter Location and Signal Parameter Estimation," IEEE® Trans. Antennas Propagation, Vol. AP-34 (March 1986), pp.276-280.

[40] C.J. De Luca, 1984. ―Myoelectrical manifestations of localized muscular fatigue in humans". Crit. Rev. Biomed. Eng., 11 (4), pp. 251-279.

[41] B. Maton, and D. Gamet, 1989. ―The fatigability of two agonistic muscles in human isometric voluntary sub maximal contraction: an EMG study. II Motor unit firing rate and recruitment". Eur. J. Appl. Physiol., 58, pp. 369-374.

[42] A. Luttmann, M. Ja¨ger, J. So¨keland, and W. Laurig, 1996. ―Electromyographical study on surgeons in urology, Part II: Determination of muscular fatigue". Ergonomics, 39, pp. 298-313.

[43] K. J. Bennie, V.M. Ciriello, P.W. Johnson, and J.T. Dennerlein, 2002. –Electromyographic activity of the human extensor carpi ulnaris muscle changes with exposure to repetitive ulnar deviation". Eur. J. Appl. Physiol., 88, pp. 5-12.

[44] J. S. Petrofsky, 1979. –Frequency and amplitude analysis of the EMG during exercise on the bicycle ergometer". Eur. J. Appl. Physiol., 41, pp. 1-15.

[45] Basmajian JV, and DeLuca CJ., 1985. Muscle alive: their functions reviewed by electromyography. Williams & Wilkins, Baltimore.

[46] Johnson, D. H. and Dudgeon, D. E., –Array Signal Processing: Concepts and Techniques," Prentice-Hall, Englewood Cliffs, NJ, 1993.

Goal 2A: Intelligent Control

Ajiboye, A. B., Weir, R. F., September 2005. A heuristic fuzzy logic approach to EMG pattern recognition for multifunctional prosthesis control. IEEE Transactions on Neural Systems and Rehabilitation Engineering 13 (3), 280–291.

APL-JHU-06, February, 9 2006. APL to Lead Team Developing Revolutionary Prosthesis. Press Release: Dated February 9, 2006.

APL-JHU-07, April 26 2007. Revolutionizing Prosthetics 2009 Team Delivers First DARPA Limb Prototype. Press Release: Dated April 26, 2007.

Arimoto, S., 2008. Control Theory of Multi-fingered Hands: A Modeling and Analytical-Mechanics Approach for Dexterity and Intelligence. Springer-Verlag, London, UK.

Arslan, Y. Z., Hacioglu, Y., Yagiz, N., 2008. Prosthetic hand finger control using fuzzy sliding modes. Journal of Intelligent and Robotic Systems 52, 121–138.

Atkins, D. J., Heard, D. C. Y., Donovan, W. H., 1996. Epidemiologic overview of individuals with upper limb loss and their reported research priorities. Journal of Prosthetic and Orthotics 8 (1), 2–11.

Bekey, G. A., Tomovic, R., Zeljkovic, I., 1990. Control architecture for the belgrade/usc hand. In: Venkataraman, S., Iberall, T. (Eds.), Dextrous Robot Hands. Springer-Verlag, New York, NY, pp. 136–149.

Bicchi, A., December 2000. Hands for dexterous manipulation and robust grasping: a difficult road toward simplicity. IEEE Transactions on Robotics and Automation 16 (6), 652–662, (Summary article with 191 references).

Birglen, L., Laliberte, T., Gosselin, C., 2008. Underactuated Robotic Hands. Springer Tracts in Advanced Robotics. Springer-Verlag, Berlin, Germany.

Butterfass, J., Grebenstein, M., Liu, H., Hirzinger, G., 2001. DLR-Hand II: next generation of a dextrous robot hand. In: Proceedings of the IEEE International Conference on Robotics and Automation. pp. 109– 114.

Chan, F. H. Y., Yang, Y.-S., Lam, F. K., Y.-T., Zhang, Parker, P. A., 2000. Fuzzy EMG classification for prosthesis control. IEEE Transactions on Rehabilitation Engineering 8 (3), 305–311.

Chen, C.-H., May 2009. Hybrid control strategies for smart prosthetic hand. Ph.D. thesis, Measurement and Control Engineering, Idaho State University.

Chen, C.-H., Bosworth, K. W., Schoen, M. P., Bearden, S. E., Naidu, D. S., Perez, A., September 21-23 2008a. A study of particle swarm optimization on leukocyte adhesion molecules and control strategies for smart prosthetic hand. In: 2008 IEEE Swarm Intelligence Symposium (IEEE SIS08). St. Louis, Missouri, USA.

Chen, C.-H., Naidu, D. S., Perez, A., Schoen, M. P., November 16-18 2008b. Fusion of hard and soft control techniques for prosthetic hand. In: Proceedings of the International Association of Science and Technology for Development (IASTED) International Conference on Intelligent Systems and Control (ISC 2008). Orlando, Florida, USA, pp. 120–125.

Chen, C.-H., Naidu, D. S., Perez-Gracia, A., Schoen, M. P., September 2-6 2009a. A hybrid adaptive control strategy for a smart prosthetic hand. In: The 31st Annual International Conference of

the IEEE Engineering Medicine and Biology Society (EMBS). Minneapolis, Minnesota, USA, pp. 5056–5059.

Chen, C.-H., Naidu, D. S., Perez-Gracia, A., Schoen, M. P., December 16-18 2009b. A hybrid control strategy for five-fingered smart prosthetic hand. In: Joint 48th IEEE Conference on Decision and Control (CDC) and 28th Chinese Control Conference (CCC). Shanghai, P. R. China, pp. 5102–5107.

Chen, C.-H., Naidu, D. S., Perez-Gracia, A., Schoen, M. P., October 12-14 2009c. A hybrid optimal control strategy for a smart prosthetic hand. In: Proceedings of the ASME 2009 Dynamic Systems and Control Conference (DSCC). Hollywood, California, USA, (No. DSCC2009-2507).

Chen, C.-H., Naidu, D. S., Schoen, M. P., July 22-24 2010. An adaptive control strategy for a fivefingered prosthetic hand. In: The 14th World Scientific and Engineering Academy and Society (WSEAS) International Conference on Systems, Latest Trends on Systems (Volume II). Corfu Island, Greece, pp. 405–410.

Childress, D. S., July 1980. Closed-loop control in prosthetic systems: Historical perspective. Journal Annals of Biomedical Engineering 8 (4-6), 293–303, (45 references).

Choi, B., Lee, S., Choi, H. R., Kang, S., October 9-15 2006. Development of anthropomorphic robot hand with tactile sensor: SKKU Hand II. In: Proceedings of the 2006 IEEE/RSJ International Conference on Intelligent Robots and Systems. Beijing, China, pp. 3779–3784.

Christodooulu, C. I., Pattichis, C. S., 1999. Unsupervised pattern recognition for the classification of EMG signals. IEEE Transactions on Biomedical Engineering 46, 169–178.

Cotton, D. P. J., Cranny, A., Chappell, P. H.,White, N.M., Beeby, S. P., 2006. Control strategies for a multiple degree of freedom prosthetic hand. In: Proceedings of The Institution of Measurement and Control UK ACC Control 2006 Symposium. pp. 211–218.

Crossley, E. F. R., Umholtz, F. G., 1977. Design of a three-fingered hand. Journal of Mech. and Machine Theory 12, 85–93.

DARPA06b, February, 8 2006. DARPA - News Release: DARPA Initiates Revolutionary Prosthetic Programs. Press Release: Dated February 8, 2006.

Dechev, N., Cleghorn, W. L., Naumann, S., 2001. Multiple finger, passive adaptive grasp prosthetic hand. Mechanism and Machine Theory 36, 1157–1173.

Farrell, T. R., Weir, R. F., Heckathorne, C.W., Childress, D. S., May-June 2005. The effect of static friction and backlash on extended physiological proprioception control of a powered prosthesis. Journal of Rehabilitation Research & Development 42 (3), 327–342.

Fernandez, J. J., Farry, K. A., Cheatham, J. B., 2000.Waveform recognition using genetic programming: The myoelectric signal recognition problem. In: Proceedings of the first Annual Conference of Genetic Programming. pp. 1754–1759.

Fukaya, N., Toyama, S., Asfour, T., Diffmann, R., July 1996. Design of the TUAT/Karlsruhe humanoid hand. In: Proceedings of the 2000 IEEE/RSJ International Conference on Intelligent Robots and Systems. Stanford, CA, pp. 1–6.

Grupen, R. A., Henderson, T. C., McMammon, I. D., 1989. A survey of general purpose manipulation. International Journal of Robotics Research 8 (1), 38–62.
Hanafusa, H., Asada, H., 1977. Stable prehension by a robot hand with elastic fingers. In: Brady, M., Hollerbach, J., Johnson, T., Lozano-P´erez, T., Mason, M. (Eds.), Robot Motion: Planning

and Control. MIT Press, Cambridge, MA, pp. 322–335.

Huang, H., Chen, C., May 1999. Development of a myoelectric discrimination system for a multidegree prosthetic. In: Proceedings of the 1999 IEEE International Conference on Robotics & Automation. Detroit, MI, pp. 2392–2397.

Hudgins, B. S., 1991. A novel approach to multifunctional myoelectric control of prosthesis. Ph.D. thesis, University of New Brunswick, Fredericton, Canada.

Inoue, T., Hirai, S., 2009. Mechanics and Control of Soft-fingered Manipulation. Springer, New York, NY.
Iversen, E., Sears, H. H., Jacobsen, S. C., February 2005. Artificial arms evolve from robots, or vice versa? IEEE Control Systems Magazine 25 (1), 16–18, 20.

Jacobsen, S. C., Knutti, D. F., Johnson, R. T., Sears, H. H., April 1982. Development of the Utah artificial arm. IEEE Transactions on Biomedical Engineering BME-29 (4), 249–269.

Jacobsen, S. C., Wood, J. E., Knutti, D. F., Biggers, K. B., Iversen, E. K., 1985. The version I Utah/MIT dextrous hand. In: Hanafusa, H., Inoue, H. (Eds.), Robotics Research: The Second International Symposium. MIT Press, Cambridge, MA, pp. 301–308.

Jang, J.-S., Sun, C.-T., Mizutani, E., 1997. Neuro-Fuzzy and Soft Computing: A Computational Approach to Learning and Machine Intelligence. Prentice Hall PTR, Upper Saddle River, NJ.
Jazar, R. N., 2007. Theory of Applied Robotics. Kinematics, Dynamics, and Control. Springer, New York, USA.

Kandel, E. R., Schartz, J. H., 1985. Principles of Neural Science, Third Edition. Elsevier/North-Holland, New York, NY.

Karray, F., De Silva, C., 2004. Soft Computing and Intelligent Systems Design: Theory, Tools and Applications. Pearson Educational Limited, Harlow, England, UK.

Kato, I., Okazaki, E., Kikuchi, H., Iwanami, K., 1967. Electro-pneumatically controlled hand prosthesis using pattern recognition of myo-electric signals. In: Digest of 7th ICMBE. p. 367.

Kelly, R., Santibanez, V., Loria, A., 2005. Control of Robot Manipulators in Joint Space. Springer, New York, USA.

Kim, J. J., Blythe, D. R., Penny, D. A., Goldenberg, A. A., March 1987. Computer architecture and low level control of the PUMA/RAL-hand system. In: Proceedings of the IEEE Conference on Robotics and Automation. Raleigh, NC, pp. 1590–1594.

Kobayashi, H., 1985. Control and geometric considerations for an articulated robot hand. Journal of Robotic Research 1 (1), 3–12.

Kobrinski, A. E., 1960. Problems of bioelectric control. In: Proceedings of First IFAC. Moscow, USSR, p. 619.
Kolluru, R., Valavanis, K. P., Kimon, P., Smith, S., Tsourveloudis, N., 2002. An overview of the University of Louisiana robotic gripper system project. Transactions of the Institute of Measurement & Control 24 (1), 65–84.

Konar, A., 2005. Computational Intelligence: Principles, Techniques and Applications. Springer-Verlag, Berlin, Germany.

Kyberd, P., Chappell, P. H., 1994. The Southampton Hand: an intelligent myoelectric prosthesis. Journal of Rehabilitation Research & Development 31 (4), 326–334.

Kyberd, P., Chappell, P. H., Gow, D., 2003. Advances in the control of prosthetic arms: Guest Editorial. Technology and Disability 15 (2), 57–61.

Kyberd, P. J., Holland, O. E., Chappell, P. H., Smith, S., Tregidgo, R., Bagwell, P. J., Snaith, M., March 1995. MARCUS: a two degree of freedom hand prosthesis with hierarchical grip control. IEEE Transactions on Rehabilitation Engineering 3 (1), 70–76.

Kyberd, P. J., Pons, J. L., September 2003. A comparison of the Oxford and Manus intelligent hand prostheses. In: Proceedings of the 2003 IEEE International Conference on Robotics and Automation. Taipei, Taiwan, pp. 3231–3236.

Lavangie, P. K., Norkin, C. C., 2001. Joint Structure and Function: A Comprehensive Analysis, Third Edition. F. A. Davis Company, Philadelphia, PA.

Lewis, F., Dawson, D., Abdallah, C., 2004. Robot Manipulators Control: Second Edition, Revised and Expanded. Marcel Dekker, Inc., New York, NY.

Lewis, F., Jagannathan, S., Yesildirek, A., 1999. Neural Network Control of Robotic Manipulators and Nonlinear Systems. Taylor & Francis, London, UK.

Lian, D., Peterson, S., Donath, M., 1983. A three-fingered articulated hand. In: Proceedings of the 13th International Symposium on Industrial Robots. pp. 18.91–18.101.

Light, C. M., Chappell, P. H., Hudgins, B., Engelhart, K., July-August 2002. Intelligent multifunction myoelectric control of hand prostheses. Journal of Medical Engineering & Technology 26 (4), 139–146.

Liu, H., Butterfass, J., Knoch, S., Meusel, P., Hirzinger, G., April 1999. A new control strategy for DLR‘s multisensory articulated hand. IEEE Control Systems Magazine 19 (2), 47–54.

Lotti, F., Tiezzi, P., Vassura, G., Biagiotti, L., Palli, G., Melchiorri, C., April 2005. Development of UB hand 3: early results. In: Proceedings of the 2005 IEEE International Conference on Robotics and Automation. Barcelona, Spain, pp. 4488–4493.

Lovchik, C. S., Diftler, M. A., May 1999. The Robonaut hand: a dexterous robot hand for space. In: Proceedings of the IEEE International Conference on Robotics and Automation. pp. 907–912.

Mann, R. W., Reimers, S. D., 1970. Kinesthetic sensing for e.m.g. controlled Boston arm‘. IEEE Transactions on Man-Machine Systems MMS-11, 110–115.

McKenzie, D. S., August 1965. The Russian myo-electric arm. The Journal of Bone and Joint Surgery 47, 418–420.

Muzumdar, A. (Ed.), 2004. Powered Upper Limb Prostheses Control, Implementation and Clinical Application. Springer-Verlag, New York, NY.

Naidu, D., 2003. Optimal Control Systems. CRC Press, Boca Raton, FL.

Nandikolla, V., December 2005. Fusion of hard and soft control techniques in biomedical engineering. Ph.D. thesis, Measurement and Control Engineering, Idaho State University, Pocatello, Idaho, thesis Supervisor: D.S. Naidu.
Nandikolla, V., Naidu, D., November 5-11 2005. Blood glucose regulation for diabetic mellitus using a hybrid intelligent technique. In: Proceedings of the 2005 ASME International Mechanical Engineering Congress and Exposition (IMECE). Orlando, FL, pp. 1–6.

Nguyen, H., Prasad, N., Walker, C., Walker, E., 2003. A First Course in Fuzzy and Neural Control. Chapman & Hall/CRC, Boca Raton, FL.

Nikoobin, A., Haghighi, R., 2008. Lyapunov-based nonlinear disturbance observer for serial n-link robot manipulators. Journal of Intelligent and Robotic Systems(Published online on 11 December 2008).

Nishikawa, D., Yu, W., Yokoi, H., Kakazu, Y., 2001. On-line learning method for EMG prosthetic hand control. Electronics and Communications in Japan (Part III: Fundamental Electronic Science) 84 (10), 35–46, (Translated from Denshi Joho Tsushin Gakkai Ronbunshi, Vol.J82-D-II, No. 9, September 1999, pp.1510-1519).

Okada, T., 1982. Computer control of multijointed finger system for precise object-handling. IEEE Transaction on Systems, Man, and Cybernetics 12 (3), 289–299.

Okamura, A. M., Smaby, N., Cutkosky, M. R., April 2000. An overview of dexterous manipulation. In: Proceedings of the IEEE International C2000 conference on Robotics and Automation. San Francisco, CA, pp. 255–262, (52 references).

Okuno, R., Yoshida, M., Akazawa, K., March 1996. Development of biomimetic prosthetic hand controlled by electromyogram. In: 1996 4th International Workshop on Advanced Motion Control. Mie, Japan, pp. 103–108.

Pons, J. L., Rocon, E., Ceres, R., Reynaerts, D., Saro, B., Levin, S., Van Moorleghem, W., 2004. The MANUS-HAND dextrous robotics upper limb prosthesis: mechanical and manipulation aspects. Autonomous Robots 16, 143–163.

Roccella, S., Carrozza, M. C., Cappeiello, G., Zecca, M., Miwa, H., Itoh, K., Matsumoto, M., September 28-October 2 2004. Design, fabrication and preliminary results of a novel anthropomorphic hand for humanoid robotics: RCH-1. In: Proceedings of the 2004 IEEE/RSJ International Conference on Intelligent Robots and Systems. Sendal, Japan, pp. 266– 271.

Rodriguez-Cheu, L. E., Casals, A., February 20-22 2006. Sensing and control of a prosthetic hand with myoelectric feedback. In: Proceedings of the The First IEEE/RAS-EMBS 2006 International Conference on Biomedical Robotics and Biomechatronics. Pisa, Italy, pp. 607–612.

Rohland, T. A., March 1975. Sensory feedback for powered limb prostheses. Medical and Biological Engineering 12, 300–301.

Rovetta, A., March 1983. Sensors controlled multifingered robot hand. In: Proceedings of the IEEE Conference on Robotics and Automation. St. Louis, Missouri, pp. 1060–1063.

Salisbury, J. K., 1982. Kinematic and force analysis of articulated hands. Ph.D. thesis, Stanford University, Stanford, CA.

Scott, R. N., Parker, P. A., July/August 1988. Myoelectric prostheses: state of the art. Journal of Medical Engineering & Technology 12 (4), 143–151.

Sears, H. H., Shaperman, J., February 1991. Proportional myoelectric hand control: an evaluation. American Journal of Physical Medicine & Rehabilitation 70 (1), 20–28.

Seeley, R. R., Stephens, T. D., Tate, P., 2007. Anatomy & Physiology, Eighth Edition. TheMcGraw-Hill, New York, NY.

Sherman, E. D., December 12 1964. A Russian bioelectric-controlled prosthesis. Canadian Medical Association Journal (CMAJ) 91, 1268–1270.

Shimoga, K. B., 1996. Robot grasp synthesis algorithms: a survey. The International Journal of Robotics Research 15, 230–266, (Survey article with over 130 references).

Siciliano, B., Sciavicco, L., Villani, L., Oriolo, G., 2009. Robotics: Modelling, Planning and Control. Springer-Verlag, London, UK.

Su´arez, R., Grosch, P., 2004. Dexterous robotic hand MA-I software and hardware architecture. In: Proceedings of the Intelligent Manipulation and Grasping. Genova, pp. 91–96.

Van Brussel, H., Santoso, B., Reynaerts, D., January/February 1989. Design and control of a multifingered hand provided with tactile feedback. In: Proceedings of the NASA Conference on Space Telerobotics. Pasadena, CA, pp. 89–101.

Venkataraman, S. T., Djaferis, T. E., 1987. Multivariable feedback control of the JPL/stanford hand. In: Proceedings of the IEEE International Conference on Robotics and Automation. pp. 77–82.

Weir, R. F., Ajiboye, A. B., September 2003. A multifunction prosthesis controller based on fuzzylogic techniques. In: Proceedings of the 25th Annual International Conference of IEEE EMBS. Cancun, Mexico, pp. 17–21.

Yang, J., Pitarch, E., K.Abdel-Malek, Patrick, A., Lindkvist, L., June 2004. A multi-fingered hand prosthesis. Mechanism and Machine Theory 39 (6), 555–581.

Zecca, M., Micera, S., Carrozza, M., Dario, P., 2002. Control of multifunctional prosthetic hands by processing the electromyographic signal. Critical ReviewsTM in Biomedical Engineering 30, 459–485, (Review article with 96 references).

Zecca, M., Roccella, S., Cappiello, G., Ito, K., Imanishi, K., Miwa, H., Carrozza, C., Dario, P., Takanishi, A., 2006. From the human hand to a humanoid hand: Biologically-inspired approach for the development of robocasa hand #1. Tech. rep., 3ARTS Lab, Scuola Superiore Sant Anna, Pisa, Italy.

Zhang, Y., Han, Z., Zhang, H., Shang, X., Wang, T., Guo, W., May 2001. Design and control of the BUAA four-fingered hand. In: Proceedings of the 2001 IEEE International Conference on Robotics and Automation. Seoul, Korea, pp. 2517–2522.

Zhao, J., Xie, Z., Jiang, L., Cai, H. G., Liu, H., Hirzinger, G., February 20-22 2006. A five-fingered underactuated prosthetic hand control scheme. In: Proceedings of the The First IEEE/RASEMBS 2006 International Conference on Biomedical Robotics and Biomechatronics. Pisa, Italy, pp. 995–1000.

[1] Lynette A. Jones and Susan J. Lederman, *Human Hand Function*, New York: Oxford University Press, 2006, pp. 131-149.
[2] Amir Fassih, D. Subbaram Naidu, Steve Chiu, and Marco P. Schoen, ―power grasping of a prosthetic hand based upon virtual spring-damper hypothesis", *Proc. IASTED Int. Conf. Robotics and Applications,* Cambridge, Massachusetts, 2010, pp. 214-220.
[3] Mohammad Asghar Oskooei, Housheng Hu, ―Myoelectric control systems, a survey", *Biomedical Signal Processing and Control*, vol. 2, 2007, pp 275-294.
[4] Chiristian Cipriani, Franco Zaccone, Silvestro Micera, Chiara Carrozza, ―On the shared control of an emg-controlled prosthetic hand: analysis of user-prosthesis interaction", *IEEE Transaction on Robotics,* vol.24, No1, February 2008.
[5] Erik D Engeberg, Sanford G. Meek, ―Backsptepping and sliding mode control hybridized for a prosthetic hand", *IEEE Trans. on Neural Systems and Rehabilitation Engineering*, vol. 17, No.1, February 2009.
[6] D.E.Whitney, ―Resolved motion rate control of manipulators and human prostheses", *IEEE Trans. Man-Machine Syst.*, vol. MMS-10, No.2, 1969, pp.47– 53.
[7] Y. Nakamura, ―Advanced robotics: redundancy and optimization", Addison-Wesley, Reading, MA, 1991.
[8] N. Dechev, W.L. Cleghron, S. Naumann, Multiplefinger, ―Passive adaptive grasp prosthetic hand", *Mechanism and Machine Theory,* vol.36, 2001, pp.1157-1173.
[9] Ramiero Cabas, Luis Maria Cabas, Carlos Balaguer, ―Optimized design of the underactuated robotic hand", *Proceeding of the 2006 IEEE International Conferences on Robotics and Automation*, Orlando, Florida, May 2006.
[10] Da-Peng Yang, Jing-dong Zhao, Yi-kun Gu, Xin-qing Wang, Nan Li, Li Jiang, Hong Liu, Hai Huang, Da-wei Zhao, ―An anthropomorphic robot hand develeoped based on underactuated mechanism and controlled by EMG signals", *Journal of Bionic Engineering,* vol. 6, 2009, pp 255-263.
[11] Suguru Arimoto, Masahiro Sekimoto, ―Human-like movements of robotic arms with redundant dofs: virtual spring-damper hypothesis to tackle the brenestein problem", *Prec. of IEEE Int. Conf. on Robotics and Automation,* Orlando, Florida, May 2006.
[12] Jerry Pratt, Chee-Meng Chew, Ann Torres, Peter Dilworth, Gill Pratt, ―Virtual model control: an intuitive approach for bipedal locomotion", *The International Journal of Robotics Research,* vol. 20, No. 2, pp. 129-143, February 2001.
[13] Thomas Wimboeck, Christian Ott, Gerhard Hirzinger, ―Passivity-based object-level impedance control for a multifingered hand" *Proceedings of the 2006 IEEE/RSJ, International Conference on Intelligent Robots and Systems,* Beijing, China,2006.
[14] Lionel Brignel,Thiery Laliberte, Clement Gosselin, ―Underactuated robotic hand",Springer 2008.

Goal 3: Robotic Hand

Arimoto, Suguru. *Control Theory of Multi-fingered hands,A Modeling and Analtical-mechanics Approach for Dexterity and intelligence.* Springer, 2007.

Bekey, G. A., G.R. Tomovic, and I. Zeljkovic. "Control Architecture for the Belgrade/USC Hand." In *Dextrous Robot Hands*, by S.T. Venkataram and T. Iberall, 136-149. New York: Springer-Verlag, 1990.

Caldwell, D.G., and N. Tsagarakis. "Biomimetic actuators in prosthetic and rehabilitation applications." *Technology and Health Care* (IOS Press) 10 (2002): 107-120.

Callahan A. D, Hunter J. M. "Anatomic considerations for splinting the thumb." *Rehabilitation of the hand: surgery and therapy*, 1990.

Chang, W.-T., and C.-H. Tseng. "Creative mechanism design for a prosthetic hand." *Journal of Engineering in Medicine, part H* 218 (2004)

Cooney, W. P. "The kinesiology of the thumb trapeziometacarpal joint." 1981: 1371-81.

Crawford, A.L., J. Molitor, A. Perez-Gracia, and S.C. Chiu. "Design of a Robotic Hand and Simple EMG Input Controller with a Biologically-Inspired Parallel Actuation System for Prosthetic Applications." *1st International Conference on Applied Bionics and Biomechanics, ICABB 2010* . Venice, Italy, 2010.

Dalley, S.A., and T.E. Wiste. "Design of a Multifunctional Anthropomorphic Prosthetic Hand with Extrinsic Actuation." *IEEE International Conference on Rehabilitation Robotics, ICARR 2009.* : , 2009.

Ellul, Carmel, and Michael A. Saliba. "Comparative Analyis of Artificial Hands. The Need for Reporting and Test Standards." *1st International Conference on Applied Biomechanics and Bionics, ICABB 2010.* Venice, Italy: , 2010.

J. Veronica, J. Santos. "Thumb Kinematics With Non-Orthogonal And Non-Intersecting Axes Of Rotation May Be Necessary To Predict Realistic Isometric Thumbtip Forces In Multiple Directions." *the American Society of Biomechanics.* 2004.

Kapandji, I. A. *The Physiology of the Joints, Upper Limb2nd ed. London: E and S Livingstone.* 1970.

Kapandji, I. A. *The Physiology of the Joints, Upper Limb2nd ed. London: E and S Livingstone.* 1970.

Landsmee, F. J. Bejjani and J. M. F. "Biomechanics of the Hand in Basic Biomechanics of the Musculoskeletal System." 1989: 275- 289.

Landsmee, F. J. Bejjani and J. M. F. "Biomechanics of the Hand in Basic Biomechanics of the Musculoskeletal System." 1989: 275- 289.

Lovchik, C.S. "The Robonaut Hand: A dexterous robot hand for space." *1999 IEEE International Conference on Robotics and Automation.* Detroit, USA: , 1999.

M. Gabiccini, A. B. (2010). On the Role of Hand Synergies in the Optimal Choice of Grasping Forces. . *Autonomous Robots [special issue on RSS2010]* .

Martell, J.W. Soto, and G. Gini. "Robotic Hands: Design Review and Proposal of New Design Process." *World Academy of Science, Engineering and Technology* 26 (2007):

Oshima, R., and T. Takayama. "Assemblable Three-fingered Nine-degree of freedom hand for laparoscopic surgery." *2009 IEEE/RSJ International Conference on Intelligent Robots and Systems.* St. Louis, USA: , 2009.

Perez-Gracia, A. "Synthesis of RPRP Closed Linkages for a Given Screw System." *ASME Journal of Mechanisms and Robotics (in press)*, 2011.

Schweighofer, G. and Pinz, A. " Robust pose estimation from a planar target." *IEEE Transactions on Pattern Analysis and Machine Intelligence,*, 2006: 2024–2030.

Shadow Robot Company, "Dexterous Hand for Advanced CLAWAR Applications". *Shadow Robot Company.* www.shadowrobot.com/hand/papers.shtml (accessed 01 23, 2011).

Simo-Serra, E., F. Moreno-Noguer, and A. Perez-Gracia. "Design of Non-anthropomorphic Robotic Hands for Anthropomorphic Tasks." *ASME International Design Engineering Technical Conferences.* Washington DC, USA, 2011 .

Yi-wei, Wang xin-qing and lIU. "Design And Control Of A Coupling Mechanism –Based Prosthetic Hand ." 2010.

Goal 4: Biocompatibility and Signaling

Dukhande, V.V., Malthankar-Phatak, G.H., Hugus, J.J., Daniels, C.K. & Lai, J.C.K. (2006) Manganese Induced Neurotoxicity is Differentially Enhanced by Glutathione Depletion in Astrocytoma and Neuroblastoma Cells. *Neurochem Res* 31(11):1349-1357.

Hertz, L., Peng, L. & Lai, J.C.K. (1998) Functional Studies in Cultured Astrocytes. In *Techniques for the Purification, Functional Evaluation and Transplantation of Brain Cells (A Companion to Methods in Enzymology*, Vol. 16) (Rozental, R. & Chiu, F.-C., eds.), pp. 293-310, Academic, New York, NY.

Isaac, A.O., Kawikova, I., Bothwell, A.L.M., Daniels, C.K. & Lai, J.C.K. (2006) Manganese Treatment Modulates the Expression of Peroxisomal Proliferator Activated Receptors (PPARs) in Astrocytoma and Neuroblastoma Cells. *Neurochem Res* 31(11):1305-1316.

Isaac, A.O., Dukhande, V.V. & Lai, J.C.K. (2007) Metabolic and Antioxidant System Alterations in an Astrocytoma Cell Line Challenged with Mitochondrial DNA Deletion. *Neurochem Res* 32(11):1906-1918.

Lai, J.C.K., Schoen, M.P., Perez Gracia, A., Naidu, D.S. & Leung, S.W. (2007a) Prosthetic Devices: Challenges and Implications of Robotic Implants and Biological Interfaces. In *Proc I Mech E, Vol 221 Part H, J Engineering in Medicine, Special Issue entitled: "Micro and Nano Technologies in Medicine,"* pp 173-183.

Lai, J.C.K., Schoen, M.P., Ebrahimpour, A., Bhushan, A., Daniels, C.K. & Leung, S.W. (2007b) Fast-Response Smart Self-Assembling Biosensors For Biomarker Detection. In *Proceedings of IMECE International Mechanical Engineering Congress and Exposition, November 11-15, 2007, Seattle, Washington*, IMECE2007-42100.

Lai, J.C.K., Lai, M.B., Jandhyam, S., Dukhande, V.V., Bhushan, A., Daniels, C.K. & Leung, S.W. (2008) Exposure to Titanium Dioxide and Other Metallic Oxide Nanoparticles Induces Cytotoxicity on Human Neural Cells and Fibroblasts. *Int J Nanomed* 3(4):533-545.

Lai, J.C.K., Ananthakrishnan, G., Jandhyam, S., Dukhande, V.V., Bhushan, A., Gokhale, M., Daniels, C.K. & Leung, S.W. (2010) Treatment of Human Astrocytoma U87 Cells with Silicon Dioxide Nanoparticles Lowers Their Survival and Alters Their Expression of Mitochondrial and Cell Signaling Proteins. *Int J Nanomed* 5:715-723.

Malthankar, G.V., White, B.K., Bhushan, A., Daniels, C.K., Rodnick, K.J. & Lai, J.C.K. (2004) Differential Lowering by Manganese Treatment of Activities of Glycolytic and Tricarboxylic Acid Cycle Enzymes in Neuroblastoma and Astrocytoma Cells Is Associated with Manganese-Induced Cell Death. *Neurochem. Res.* 29:709-717.

Puli, S., Lai, J.C.K., Edgley, K.L., Daniels, C.K., & Bhushan, A. (2006) Signaling Pathways mediating Manganese-Induced Neurotoxicity in Human Glioblastoma Cells (U87) *Neurochem Res* 31: 1211-1218.

EVALUATION OF FILTERING TECHNIQUES APPLIED TO SURFACE EMG DATA AND COMPARISON BASED ON HAMMERSTEIN-WIENER MODELS

ANISH SEBASTIAN, PARMOD KUMAR, MARCO P. SCHOEN
Measurement and Control Engineering Research Center (MCERC)
Idaho State University
921 South 8th Ave., Stop 8060, Pocatello, Idaho 83209-8060
UNITED STATES OF AMERICA
schomarc@isu.edu http://www.isu.edu/~schomarc/

Abstract: - Electromyogram (EMG) signals have been used for control of prosthetic devices in the past. However, most of the control schemes currently used are based on threshold values of the EMG signal as reference to actuate the prosthetic hand. Using such a control strategy, it is not possible to capture the underlying dynamics of the relationship between EMG signals and the intended finger movements and forces. We propose to use system identification based dynamic models which are extracted from recorded EMG signals and the corresponding finger forces. A key influence on the resulting quality of such models is the filtering of the EMG signals. This paper presents a thorough analysis of spatial filtering and other filtering methods. The different filters are compared on the basis of the EMG-finger force model fit values obtained using System Identification using various Non-Linear Hammerstein-Wiener models. The nonlinear spatial filters gave better fit values as compared to the standard filtering techniques.

Key-Words: - Spatial Filtering, Hammerstein-Wiener, Surface Electromyogram (sEMG).

1 Introduction

About 50% of the people who need upper extremity prosthetics do not use them, [1]. This could be due any one of the common following reasons; a) Dexterity, b) Comfort, c) Cost. Despite advances in the fields of manufacturing, electronics, signal processing, sensor design, and our understanding of biological signals, we still face a huge challenge designing a prosthetic device. This is due to the fact that the competition of such a device is with one which nature has gifted us. A human hand is without doubt the best possible design. For a prosthetic hand, to encompass all of the human hands features and capabilities is as of now still a distant reality. Electromyogram (EMG) signals have been used for quite some time now in the control of prosthesis. The EMG signal is a small voltage signal (in mV), generated by skeletal muscles. This signal carries information of the objective the user would like to execute. Using surface EMG (sEMG) signals, researchers have been able to actuate motors on artificial prosthetic devices. EMG signals can be measured using intramuscular electrodes, needle electrodes, or by placing electrodes on the surface of the skin. The purpose for which the sEMG signal is being recorded generally determines whether it should be measured within the muscle using needle electrodes or surface measurement using electrodes on the skin would suffice. If, the purpose of recording the EMG signal is to look for diseases relating to a particular muscle, one might be better off using needle electrodes. On the other hand, if it is to be used to actuate motors on a prosthetic device, which a user might want to take off and wear without the need of medical supervision, surface EMG would suffice. Measuring the EMG signal on the surface of the skin is also less uncomfortable. This method is generally suited only for superficial muscles. Even though recording (sEMG) is favorable, it is plagued with many issues, such as crosstalk from firing of multiple motor points in the vicinity of the recording location, which can cause significant corruption of the signal at that site, motion artifacts, and poor signal if the motor unit is not identified correctly etc. Needle electrodes, on the other hand, require trained medical professionals for appropriate placement of the electrodes in the muscle. This paper investigates sEMG signals only with the objective to extract intended finger forces. The sEMG-force relationship is modeled using Hammerstein-Wiener models to characterize the dynamics. These models are required to characterize the controller dynamics for sEMG based prosthetic hands. We look to overcome the crosstalk issue in the measurement by using an array of nine (9) sEMG sensors, and utilizing spatial filters to isolate and improve the quality of the signals at the identified site for EMG recording. The sensor array was placed on the motor unit location, which was identified for the subject using an external stimulator. The sensors were then placed around the motor unit to form a 3x3 square matrix. The processed signal was then used for identifying various dynamical models for the prediction of the force, from the recorded sEMG signal, that was generated during various voluntary contractions of

the subjects' hand. A comparison of the various outcomes (model fit values computed) of the system identification process, using signal processing techniques stated in the ISEK [2] guidelines and the spatially filtered signals are presented in this paper. The experiments were conducted for long durations, in order to analyze the effects of the muscle fatigue on the model structures.

2 Problem Formulation

EMG signal should ideally be measured at a motor unit. A motor unit (MU) consists of an α-motoneuron in the spinal cord and the muscle fiber it innervates. sEMG signals are influenced by multiple factors, some of which are; a) shape of the volume conductor, b) the thickness of the subcutaneous tissue layers, c) tissue inhomogeneities, d) distribution of the motor unit territories in the muscle, e) size of the motor unit territories, f) distribution and the number of fibers in the motor unit territory, g) length of the fibers, h) spread of the endplates and tendon junctions within the motor units, and i) spread of the innervations zones and tendon regions among motor units. The type of detection system used also plays an important part in influencing the sEMG measurements. Some of the factors which need to be taken into account, with the detection systems, are a) skin electrode contact (impedance, noise), b) spatial filtering for signal detection, c) inter-electrode distance, d) electrode size and shape, and e) inclination of the detection system relative to the muscle fiber orientation, [3]. Since sEMG is plagued by a multitude of issues, as pointed out in this section, one cannot approach this problem realistically by trying to account for each of the variables in the measurement, nor oversimplify the problem at hand by assuming a simple linear or a non-linear relation between the sEMG signal and the corresponding finger force generated. Hence the approach presented in this paper is to assume a black-box model in order to deduce a suitable relation or model structure for the two signals. This approach has been found to be of merit in our previous studies and has been been reported in [4] & [5] to yield satisfactory fits.

3 Problem Solution

"Spatial filtering" is broadly defined as a method which computes spatial density estimates for events that have been observed at individual locations. These filters are used when there is no a priori curve to fit to a data series. Instead, it relies on nearby or adjacent values to estimate the value at a given point. These filters take out variability in a data set while retaining the local features of data. Spatial filtering is principally associated with digital image processing. This method may be applied to almost any data in the form of a grid. The most common spatial filters are the low-pass and high-pass spatial filters. These are focal functions whose operation is determined by a kernel or neighborhood of ***NxN*** cells around each pixel or grid position [6]. Grid cells "covered" by a kernel are multiplied by the matching kernel entry and then the weighted average is calculated and assigned as the value for the central cell, *G*. For example, an asymmetric 3x3 kernel may look like the one shown in Equation (1), or any combination of the weights. Typically *a, b* are positive integers. If *a=b=*1, then the kernel provides a simple smoothing or averaging operation. The weights in the kernel can be modified for specific cases or data sets. In any case the weighted average is divided by the sum of the elements of the kernel. Filters of this type are sometimes referred to as low-pass filters.

$$\text{Symmetric Kernel} = \begin{bmatrix} a & a & a \\ a & b & a \\ a & a & a \end{bmatrix}. \qquad (1)$$

If the weights in the kernel is similar to the one in Equation (2) and *a, b, c* are positive integers, and if the following, *b>a>c*, is true, then the kernel is described as a Gaussian filter which is symmetric but center-weighted.

$$\text{Symmetric Kernel} = \begin{bmatrix} c & a & c \\ a & b & a \\ c & a & c \end{bmatrix}. \qquad (2)$$

The filtered grid value '*G*' of an *m=**NxN*** kernel matrix, with C_i set of coefficients and P_i - set of source grid values, is calculated as:

$$G = \frac{\sum_{i=1}^{m} C_i P_i}{\sum_{i=1}^{m} C_i} + B, \qquad (3)$$

where *B* is often set to 0. *B* is a bias term to increase or decrease the resulting value of '*G'*. This kernel is also sometimes referred to as the '*filter mask'*.

Linear Spatial Filtering: Linear spatial filtering would modify the sEMG array data '*f*' by replacing the value at each location with a linear function of the values of nearby data points. Moreover, this linear function is assumed to be independent of the data point locations (*k, l*), where (*k, l*) are the indices of the data points in *f*, which is represented by a composite data matrix. This kind of operation can be expressed as convolution or correlation. For spatial filtering, it's often more intuitive to work with correlation. The filtered result *g(k, l)* is obtained by centering the mask over pixel (*k, l*) and multiplying the elements of *f* with the overlapping elements of the mask and then adding them up. In other words, the objective is to amplify the activity of motor unit/s located closest to the recording site (ideally the actual motor location for the particular finger) and reducing the EMG signal generated by other motor units located further away or motor nits of other fingers. The selectivity of surface EMG recordings can be increased by reducing the electrode size (i.e., skin–electrode contact area or inter-electrode distance) [7] and/or by applying temporal filters [8]. More recent work has focused on advances in the design of surface electrode arrays [9-10] to extract single motor unit information from sEMG. A large number of traditional [11–13] and adaptive [14] linear spatial filters have been extensively used to glean more information out of sEMG signals and to understand it much better.

For this paper, the experiments were carried out on a healthy male subject to extract dynamical models describing the relationship between sEMG-force signals. The motor points were located using a

Muscle Stimulator, manufactured by Rich-Mar Corporation (model number HV 1100). The motor location of the ring finger was chosen for the experiments. The EMG detection system used was a Delsys, Bagnoli-16 channel EMG (DS-160, S/N-1116). The sensors used for measuring the sEMG action potentials were three pronged DE 3.1 differential surface electrodes. The subjects' skin was prepared, according to the ISEK standards, before the sensors were placed over the motor point. The electrodes were placed along the muscle fibers (Flexor Digitorum Superficialis) for recording sEMG. Multiple sEMG sensors in an array configuration were mounted on and around the identified motor unit, as shown in Figure 1. The subjects' hand was placed on a flat surface; the reference electrode was placed on the elbow where there is no sEMG signal. Sensor *CH1* was placed on the identified motor unit location. *CH2* and *CH3* were placed along the muscle fiber in front and behind *CH1* respectively. Channels 4-9 were placed in the orientation as shown in Figure 1. Nine different experiments were conducted and the corresponding sEMG signal was measured simultaneously from all the nine sensors. The force generated by the subject's fingers, for a given motion, was measured using a stress ball with a force sensitive resistor (FSR) mounted on it.

Figure 1: Experimental Setup – Location of sEMG sensors

The change in the resistance of the FSR is directly proportional to the force being applied. Figure 2 shows the location of the FSR on the stress ball. Experiments 1 and 2 were used to check for any spurious signals that might be recorded due to the slight angle at which the subjects' hand was held. Experiments 3 to 6 were done using a stress ball with a lesser stiffness as compared to experiments 7, 8 & 9.

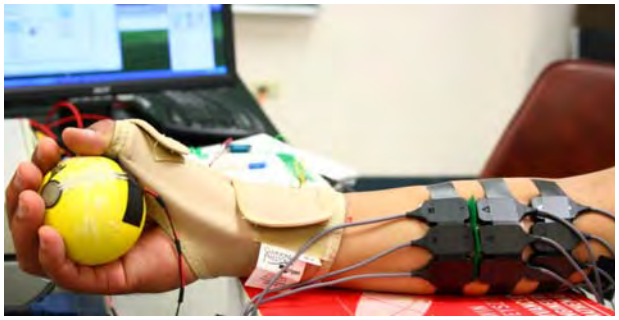

Figure 2: Force sensitive Resistor and Thumb Restrain

Also, a thumb restrain was used for experiments 5-9. The thumb restrain is showed in the Figure 2. The stress ball was changed as we were also interested in looking at the change in the sEMG signal when fatigue occurs, and also how it would affect the modeling for the relation between force-sEMG using System Identification (SI).

The linear spatial filters tested in this paper for isolating the motor unit action potentials (MUAPs) are; 1) Longitudinal Single Differential (LSD), 2) Transverse Single Differential (TSD), 3) Longitudinal Double Differential (LDD), 4) Transverse Double Differential (TDD), 5) Normal Double Differential (NDD), 6) Inverse Binomial (IB2) and 7) Inverse Rectangular (IR) Filter. The mask of these filters and the corresponding resultant equations on application of the mask to the grid data obtained from the sEMG array arrangement are given below.

EMG Array Information, Spatial Filter Mask

$$\text{LSD} = \begin{bmatrix} sEMG7 & sEMG5 & sEMG6 \\ 0 & 0 & 0 \\ sEMG2 & sEMG1 & sEMG3 \\ -1 & 1 & 0 \\ sEMG8 & sEMG4 & sEMG9 \\ 0 & 0 & 0 \end{bmatrix}$$

Result Equation: $-sEMG2 + sEMG1$

$$\text{TSD} = \begin{bmatrix} 0 & -1 & 0 \\ 0 & 1 & 0 \\ 0 & 0 & 0 \end{bmatrix};\ \text{LDD} = \begin{bmatrix} 0 & 0 & 0 \\ -1 & 2 & -1 \\ 0 & 0 & 0 \end{bmatrix};\ \text{TDD} = \begin{bmatrix} 0 & -1 & 0 \\ 0 & 2 & 0 \\ 0 & -1 & 0 \end{bmatrix}$$

LSD Equation = sEMG1-sEMG2; *TSD* Equation = *sEMG1-sEMG5*. We can similarly deduce the equations for the other spatial filters.

$$\text{NDD} = \begin{bmatrix} 0 & -1 & 0 \\ -1 & 4 & -1 \\ 0 & -1 & 0 \end{bmatrix};\ \text{IB2} = \begin{bmatrix} -1 & -2 & -1 \\ -2 & 12 & -2 \\ -1 & -2 & -1 \end{bmatrix};\ \text{IR} = \begin{bmatrix} -1 & -1 & -1 \\ -1 & 8 & -1 \\ -1 & -1 & -1 \end{bmatrix}$$

In this paper, nonlinear spatial filters have also been discussed these have been reported in literature [15]. These are 1) 1-D Nonlinear Transverse spatial filter (NLT), 2) 1-D Nonlinear Longitudinal spatial filter (NLL), 3) 2-D Nonlinear spatial filter in Two-Orthogonal Directions (NLTOD) and 4) Nonlinear spatial filter in All Four possible Directions (NLAFD). The nonlinear spatial filters use the Teager-Kaiser Energy (TKE) Operator, [16]. This technique is a threshold 'energy' based approach where outliers are first detected and then replaced by their estimated values. The nonlinear spatial filters with the TKE operator incorporated are given as follows; The general form of nonlinear spatial filter using the (TKE) operator is given in Equation (4);

$$\Psi[x(n)] = x^2(n) - x(n+1)x(n-1) \quad (4)$$

a) 1-D Nonlinear Transverse Spatial Filter (NLT); Equation (5)

$$\Psi_{d,m}[x(m,n)] = x^2(m,n) - x(m-1,n)x(m+1,n) \quad (5)$$

b) 1-D Nonlinear Longitudinal Spatial Filter (NLL); Equation (6)

$$\Psi_{d,n}[x(m,n)] = x^2(m,n) - x(m,n-1)x(m,n+1) \quad (6)$$

c) Nonlinear Spatial Filter in Two Orthogonal Directions (NLTOD): Equation (7)

$$\Psi_{d,2}[x(m,n)] = \Psi_{d,2m}[x(m,n)] + \Psi_{d,n}[x(m,n)] \quad (7)$$
$$= 2x^2(m,n) - x(m-1,n)x(m+1,n) - x(m,n-1)x(m,n+1)$$

d) Nonlinear Spatial Filter in all Four Directions (NLAFD): Equation (8)

$$\Psi_{d,4}[x(m,n)] = 4x^2(m,n) - x(m-1,n)x(m+1,n) \quad (8)$$
$$-x(m,n-1)x(m,n+1) - x(m-1,n+1)x(m+1,n-1)$$
$$-x(m-1,n-1)x(m+1,n+1)$$

4 Simulation Results

Plots of the raw data gathered are shown in Figure 3. The plots shown in Figure 3 represent the raw data collected from three channels of the grid, Channels 1, 4 & 5.

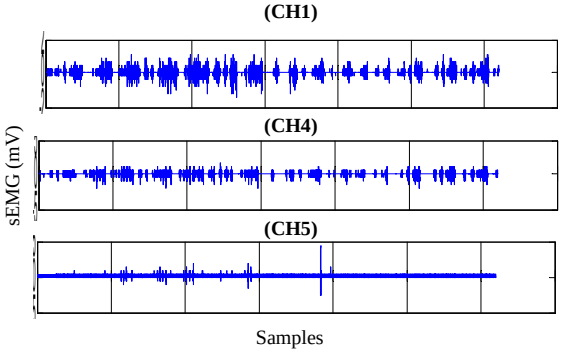

Figure 3: sEMG Raw Signal Channels 1, 4 and 5

The data shown above is for comparison of the sEMG obtained from various location of the subject's arm. Notice the change especially in the amplitude of the sEMG at Channel 1, 4 & 5. Figure 4 shows the plot of the filtered sEMG using the various spatial filters. In addition to these 11 spatial filters, the sEMG data was also filtered using 4 other filters – Bessel, Butterworth, Chebyshev Type I and Chebyshev Type II filters. The filter characteristics of these 4 filters were in accordance to the ISEK standards. The relation of sEMG-Force was modeled using Non-Linear Hammerstein-Wiener models. This modeling method has been proven to work in the past [4], [5] in assuming a black-box model structure for the system. In order to model the sEMG-Force relation, the filtered data from the various experiments was split into various four (4) time windows.

Equation 9 describes the general Hammerstein-Wiener model structure:

$$w(t) = f((g(t)), \quad b(t) = \frac{B_{j,i}(q)}{F_{j,i}(q)} w(t), \quad y(t) = h(x(t)), \quad (9)$$

where, $w(t)$ and $b(t)$ are internal variables, $w(t)$ has the same dimensions as $u(t)$ - input, and $x(t)$ has the same dimensions as $y(t)$ - output. $g()$ and $h()$ are the input and output non-linearity functions respectively. $B(q)$ and $F(q)$ are regression polynomials. The model fit values are computed using Equation (10) as follows;

$$fit = 100 * \frac{1 - \|\hat{y} - y\|}{\|y - \hat{y}\|} \quad (10)$$

where, $\hat{y}$ is the estimated output by the model.

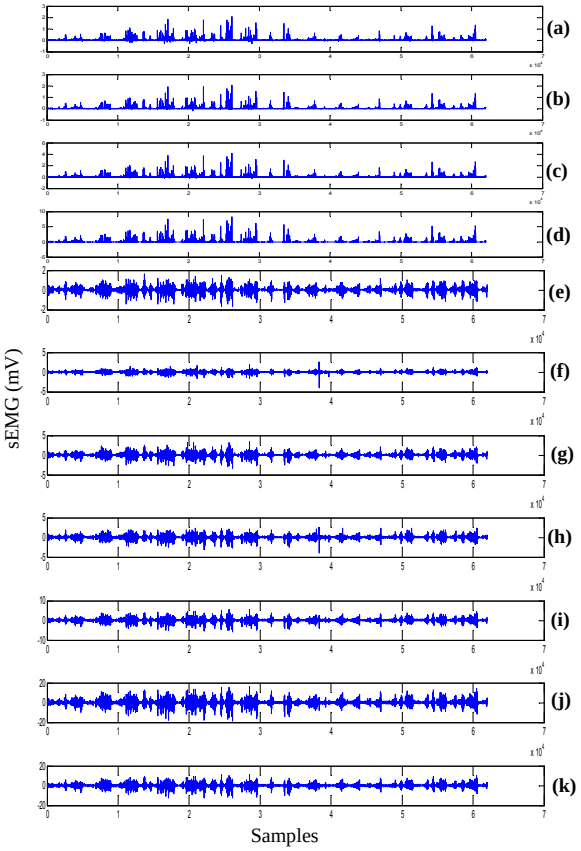

Figure 4: Spatially Filtered sEMG at Motor unit Ring Finger a) NLT, b) NLL, c) NLTOD, d) NLAFD, e) LSD, f) TSD, g) LDD, h) TDD, i) NDD, j) IB2, k) IR

The time windows used for estimation and validation of the models were called '*ze*' and '*zv*' respectively. '*ze*' contained 8000 sample points and '*zv*' contained data points shifted by 2000 sample points. For example, if '*ze*' was a time window between 2-6 seconds i.e. samples 4000-12000, then '*zv*' was between 3-7 seconds i.e. 6000-14000 samples. Thus the Hammerstein-Wiener method uses '*ze*' to estimate the model structure and based on this information predicts the next 2000 sample points. The data was filtered using the various filters mentioned in the previous sections. We would like to stress once again the point that the force was varied randomly and the subject was in no way trying to achieve maximum voluntary contractions during each cycle. A cycle is defined as the subject starting without any force on the stress ball, squeezing it (to any force level) and then going back

to no force. The subject has to keep the finger in contact with the force ball throughout this cycle.

A plot of the variations in force achieved for 3 experiments is shown in Figure 5. The Matlab™ code for the Hammerstein-Wiener model is: *nlhw(ze,* [n_a n_b n_k], …., …). The modeling was carried out by varying n_a - the number of past output terms used to predict the current output, n_b - the number of past input terms used to predict the current output and n_k - the delay from input and output in terms of the number of samples for the various Hammerstein-Wiener models.

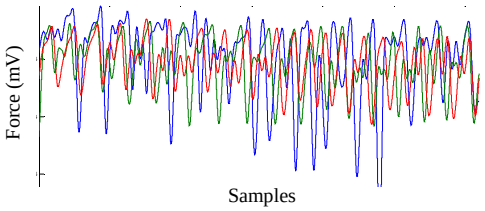

Figure 5: Force levels experiment 3 (blue), 5(red) & 7(green)

42 models with variations in n_a and n_b were tested while the value of n_k was kept as 1. The total number of models estimated were 15 (filter types) x 4 (time windows) x 42 models per time window x 4 experiments = 10,080 models. This paper does not list all these models but identifies and reports only the significant results of the analysis.

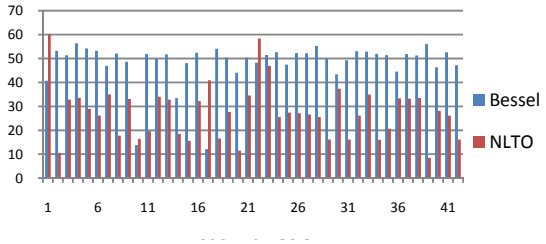

Figure 6: Fit % for Hammerstein-Wiener Models – Using Bessel and NLTO Filters (time window 2-7 sec, exp3)

As an example, for experiment 3, for time window of 2-7 sec, the fit values obtained by varying n_a between 2-7 and n_b between 3-9, are shown in Figure 6. The fit values ranged from 33-56% for the Bessel filter and from 20-60% for the NLTO filter. The best values obtained for this time window were 56.36% and 60.13% by the Bessel and the NLTO filters respectively. The model output plot for these values is shown in Figure 7. The large variation in the model fit values can be attributed to the fact that the two data sets have poor correlation between one another. The other filters used also predict the future variations in force but the fit percentages were in the range of 30-48%. A key objective of this research is help develop a control regime which in not based on threshold values of force can incorporate the dynamics in the force. This would help to control the response of the artificial limb to be closer to that of the actual hand. Similarly we tested various models for the other experiments too. Another set of results which gave very high values of fit was for the later time windows. This case was especially interesting as the subject had fatigued due to the repetitive experiments, but the Hammerstein-Wiener models did successfully capture the variations in the sEMG signal. The Hammerstein-Wiener models performed very well and we obtained fit values in the high sixties.

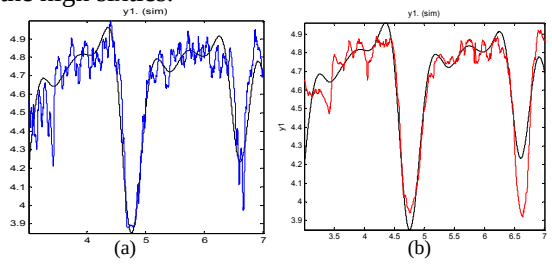

Figure 7: Measured data (black) a) Bessel (blue) 56.36% and b) NLTO (red) 60.13% for exp 3 time window 2-7seconds.

Figure 8 shows the model fit values obtained for these later data windows. As can be seen from the plots, contrary to our expectations the Hammerstein-Wiener Models performed very well and produced very good fit values.

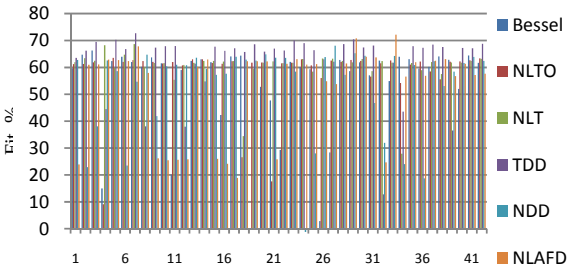

Figure 8: Fit Values Obtained for Different Hammerstein-Wiener Models – Bessel, NLTO NLT, TDD, NDD, NLAFD Filters (time window 20-25 sec, exp5)

Figure 9 shows the model output plots for some of the filters mentioned in Figure 8.

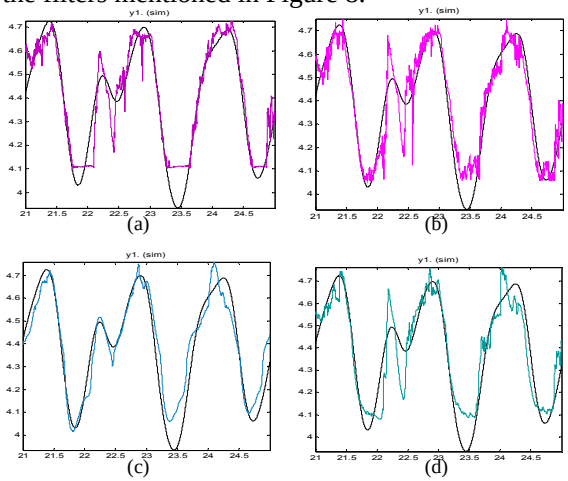

Figure 9: Measured Data Black – a) TDD (70.28%), b) NDD (68.09%), c) NLT (68.26%), d) NLAFD (72.16%), Filters

4 Conclusion

The Hammerstein-Wiener models worked very well in capturing the dynamics of the force levels for the various experiments conducted. This method of modeling could help in improving the control over the motors used in prosthetic devices to mimic the actual changes force levels in a real hand. This method also performed very well in the scenarios where the subject did fatigue but the affects were successfully modeled by the Hammerstein–Wiener models. The nonlinear and linear spatial filters (TDD, NDD and NLT, NLTO and NLAFD) did outperform the other filtering methods used especially for the later time windows. The only other filter which had a comparable performance to the spatial filters was the Bessel filter. Further investigation into reducing the wide range of the fit values obtained needs to be performed. One of the possible methods to pursue would be to use Genetic Algorithm to optimize the model parameters n_a and n_b and also the number of iterations used for the modeling of sEMG-force levels. One of the possible reasons for poor fit values could also be attributed to the model trying to over-fit the data sets.

Acknowledgement

This work was supported by a grant from the Telemedicine Advanced Technology Research Center (TATRC) of the US Department of Defense. The financial support is greatly appreciated.

References:

[1]http://www.army.mil/-news/2010/02/24/34906-the-future-of-prosthetics-is-in-your-mind/

[2] http://www.isek-online.org/standards_emg.html

[3] Farina, D., Merletti, R., and Enoka, M. R., 2004. "The extraction of neural strategies from the surface EMG". Journal of Applied Physiology, 96, pp. 1486-1495.

[4] Sebastian A., Parmod K., Anugolu M., Schoen P. M., Urfer A., Naidu S. D., 2009. "Optimization of Bayesian Filters and Hammerstein-Wierner Models for EMG-Force Signals Using Genetic Algorithm". Proceedings of the ASME 2009 Dynamic Systems and Control Conference DSCC 2009.

[5] Sebastian A., Parmod K., Schoen P. M., Urfer A., Creelman J., Naidu S. D., 2009. "Analysis of EMG-Force relation using System Identification and Hammerstein-Wiener Models". Proceedings of the ASME 2010 Dynamic Systems and Control Conference DSCC 2010.

[6]http://www.spatialanalysisonline.com/output/html/Linearspatialfiltering.html

[7] P. Zhou and W. Z. Rymer, "An evaluation of the utility and limitations of counting motor unit action potentials in the surface electromyogram," Journal of Neural Engineering, vol. 1, pp. 238–245, 2004.

[8] Z. Xu and S. Xiao, "Digital filter design for peak detection of surface EMG," Journal of Electromyography & Kinesiology, vol. 10, pp. 275–281, 2000.

[9] M. J. Zwarts and D. F. Stegeman, "Multichannel surface EMG: Basic aspects and clinical utility," Muscle Nerve, vol. 28, pp. 1–17, 2003.

[10] B. G. Lapatki, J. P. Van Dijk, I. E. Jonas, M. J. Zwarts, and D. F. Stegeman, "A thin, flexible multielectrode grid for high-density surface EMG," Journal of Applied Physiology, vol. 96, pp. 327–336, 2004.

[11] C. Disselhorst-Klug, J. Silny, and G. Rau, "Improvement of spatial resolution in surface-EMG: A theoretical and experimental comparison of different spatial filters," IEEE Transactions on Biomedical Engineering, vol. 44, no. 7, pp. 567–574, Jul. 1997.

[12] D. Farina, E. Schulte, R. Merletti, G. Rau, and C.Disselhorst-Klug, "Single motor unit analysis from spatially filtered surface electromyogram signals. Part I: Spatial selectivity," Medicine Biology Engineering and Computation, vol. 41, pp. 330–337, 2003.

[13] D. Farina, L. Mesin, S. Martina, and R. Merletti, "Comparison of spatial filter selectivity in surface myoelectric signal detection: Influence of the volume conductor model," Medicine Biology Engineering and Computation, vol. 42, pp. 114–120, 2004.

[14] N. Ostlund, J. Yu, and J. S. Karlsson, "Adaptive spatio-temporal filtering of multichannel surface EMG signals," Medicine Biology Engineering and Computation, vol. 44, pp. 209–215, 2006.

[15] P. Zhou, N. L. Suresh, M. Lowery, W. Z. Rymer, "Nonlinear Spatial Filtering of Multichannel Surface Electromyogram Signals During Low Force Contractions", IEEE Transactions on Biomedical Engineering, vol. 56, no.7, pp. 1871-1879, July 2009.

[16] J. F. Kaiser, "On Teager's energy algorithm and its generalization to continuous signals", Proc. 4th IEEE Digital Signal Proc. Workshop, Mohonk (New Paltz), NY, September 1990.

OPTIMIZED SPATIAL FILTER MASK USING GENETIC ALGORITHM AND SYSTEM IDENTIFICATION FOR MODELING SEMG AND FINGER FORCE SIGNALS

ANISH SEBASTIAN, PARMOD KUMAR, MARCO P. SCHOEN
Measurement and Control Engineering Research Center (MCERC)
Idaho State University
921 South 8th Ave., Stop 8060, Pocatello, Idaho 83209-8060
UNITED STATES OF AMERICA
schomarc@isu.edu http://www.isu.edu/~schomarc/

Abstract: - *This paper presents the investigation of the use of System Identification (SI) for modeling sEMG-Finger Force relation in the pursuit of improving the control of prosthetic hands. Finger force and sEMG data is generated by having the subject perform a number of random motions of the ring finger to simulate various force levels. Post-processing of the sEMG signal is performed using spatial filtering. The linear and nonlinear spatial filters are compared based on the 'kurtosis' improvements and also are based on the fit values of the models obtained using system identification. Some of the spatial filter masks are optimized using a Genetic Algorithm (GA) for the constrained and unconstrained cases. The resulting model fit value is utilized to serve as the cost function. The results are compared to the reported filter mask values in the literature. The unconstrained GA based filter mask values and in some instances the constrained GA based mask values performed better than the filter masks reported in literature.*

Key-Words: - Spatial Filtering, System Identification, Surface Electromyogram, Array Sensor.

1 Introduction

In the United States there are approximately 1.7 million people living with limb loss [1]. It is estimated that one out of every 200 people in the U.S. has had an amputation [2]. An ideal prosthetic hand has to be dexterous; easy to manufacture, must use little power and at the same time, must be of low cost. Building such a prosthetic hand, which can mimic the entire gamut of motions and have the functionality and dexterity of a human hand exactly, has eluded researchers so far. One of the main strategies used in making a prosthetic hand "user friendly" is to use the electromyogram (EMG) signal to control a prosthetic device. An EMG signal is a small voltage signal (in mV) which is generated by skeletal muscles. EMG is measured using fine wire intramuscular electrodes, needle electrodes, or on the surface of the skin over the motor point using surface electrodes. Surface electrodes are quick and easy to apply, do not need medical supervision, cause minimal discomfort and are generally suited for superficial muscles. Needle electrodes on the other hand require trained medical professionals for appropriate placement within the muscle. This paper looks only at surface electromyogram signals (sEMG). In the past, multiple methods have been investigated for extracting useful information from EMG signals. Some of these methods include employing low-pass or band-pass filtering; others have also used notch filtering to remove power line noise, [3]. Whitening filters can increase the quality of the amplitude estimates of the sEMG signals, [4]. Other methods include Markov models, [5] and fuzzy logic control, [6] – for classification of EMG, and wavelet processing, [7]. Currently, the accepted standardized method on how EMG signals must be recorded and analyzed is set by the International Society of Electromyography and Kinesiology (ISEK) [8]. sEMG signals are influenced by multiple factors, some of which are; a) shape of the volume conductor, b) the thickness of the subcutaneous tissue layers, c) tissue inhomogeneities, d) distribution of the motor unit territories in the muscle, e) size of the motor unit territories, f) distribution and the number of fibers in the motor unit territory, g) length of the fibers, h) spread of the endplates and tendon junctions within the motor units, and i) spread of the innervations zones and tendon regions among motor units. The type of detection system used also plays an important part in influencing the sEMG measurements. Some of the factors which need to be taken into account, with the detection systems, are a) skin electrode contact (impedance, noise), b) spatial filtering for signal detection, c) inter-electrode distance, d) electrode size and shape, and e) inclination of the detection system relative to the muscle fiber orientation, [9].

2 Problem Formulation

As multiple factors influence sEMG, it is impossible to account for each of these variables while modeling its relation to the force generated. Also, oversimplification of the problem at hand by neglecting some variables, which is a widely used common assumption, will cast doubt over the

usefulness of the results of modeling. Our approach is to assume a black-box model in order to deduce a suitable relation or model structure for the two signals. Here, the modeling of the sEMG-finger force relation is not based on root-mean-square, or average values of the sEMG signal, hence, we facilitate the capture of the dynamical changes in the force levels. Our approach of using Hammerstein-Wiener models has been found to be of merit in our previous studies [10, 11] to yield satisfactory fits.

3 Problem Solution

Spatial Filtering

The data collected is from a nine (3x3) sensor array and rather than analyzing the data only at the motor unit, we consider using spatial filters. Spatial filtering is a very attractive choice as it can be used to either amplify the signal at the motor unit or extract useful information from the entire grid. "Spatial filtering" is broadly defined as a method which computes spatial density estimates for events that have been observed at individual locations. These filters are used when there is no a priori curve to fit to a data series. Instead, it relies on nearby or adjacent, values to estimate the value at a given point. The most common spatial filters are the low-pass and high-pass spatial filters. These are focal functions whose operation is determined by a kernel or neighborhood of ***NxN*** cells around each pixel or grid position [12]. Grid cells "covered" by a kernel are multiplied by the matching kernel entry and then the weighted average is calculated and assigned as the value for the central cell, *G*. For example, an asymmetric 3x3 kernel may look like the one shown in Equation (1), or any combination of the weights. Typically *a, b* are positive integers. If *a=b=*1, then the kernel provides a simple smoothing or averaging operation. Filters of this type are sometimes referred to as low-pass filters.

$$\text{Symmetric Kernel} = \begin{bmatrix} a & a & a \\ a & b & a \\ a & a & a \end{bmatrix} \quad (1)$$

The filtered grid value '*G*' of an *m=**NxN*** kernel matrix, with C_i set of coefficients and P_i - set of source grid values, is calculated as;

$$G = \frac{\sum_{i=1}^{m} C_i P_i}{\sum_{i=1}^{m} C_i} + B \quad (2)$$

Where, *B* is often set to 0. *B* is a bias term to increase or decrease the resulting value of '*G*'. This kernel is also sometimes referred to as the '*filter mask*'. The linear spatial filters tested in this paper are; 1) Longitudinal Single Differential (LSD), 2) Transverse Single Differential (TSD), 3) Longitudinal Double Differential (LDD), 4) Transverse Double Differential (TDD), 5) Normal Double Differential (NDD), 6) Inverse Binomial (IB2) and 7) Inverse Rectangular (IR) Filter. The mask of these filters and the corresponding resultant equations on application of the mask to the grid data obtained from the sEMG array arrangement are given below.

EMG Array Information, Spatial Filter Mask

$$\text{LSD} = \begin{bmatrix} sEMG7 & sEMG5 & sEMG6 \\ 0 & 0 & 0 \\ sEMG2 & sEMG1 & sEMG3 \\ -1 & 1 & 0 \\ sEMG8 & sEMG4 & sEMG9 \\ 0 & 0 & 0 \end{bmatrix}$$

Result Equation: $-sEMG2 + sEMG1$

$$\text{TSD} = \begin{bmatrix} 0 & -1 & 0 \\ 0 & 1 & 0 \\ 0 & 0 & 0 \end{bmatrix};\ \text{LDD} = \begin{bmatrix} 0 & 0 & 0 \\ -1 & 2 & -1 \\ 0 & 0 & 0 \end{bmatrix};\ \text{TDD} = \begin{bmatrix} 0 & -1 & 0 \\ 0 & 2 & 0 \\ 0 & -1 & 0 \end{bmatrix}$$

LSD Equation = sEMG1-sEMG2; *TSD* Equation = *sEMG1-sEMG5*; we can similarly deduce the equations for the other spatial filters.

$$\text{NDD} = \begin{bmatrix} 0 & -1 & 0 \\ -1 & 4 & -1 \\ 0 & -1 & 0 \end{bmatrix};\ \text{IB2} = \begin{bmatrix} -1 & -2 & -1 \\ -2 & 12 & -2 \\ -1 & -2 & -1 \end{bmatrix};\ \text{IR} = \begin{bmatrix} -1 & -1 & -1 \\ -1 & 8 & -1 \\ -1 & -1 & -1 \end{bmatrix}$$

In this paper, some nonlinear spatial filters have also been discussed, these have been reported in the literature [13], these are 1) 1-D Nonlinear Transverse spatial filter (NLT), 2) 1-D Nonlinear Longitudinal spatial filter (NLL), 3) 2-D Nonlinear spatial filter in Two- Orthogonal Directions (NLTOD) and 4) Nonlinear spatial filter in All Four possible Directions (NLAFD). The Nonlinear Spatial Filters use the Teager-Kaiser Energy (TKE) Operator [14]. This technique is a threshold 'energy' based approach where outliers are first detected and then replaced by their estimated values. General Form of Nonlinear Spatial Filter using the Teager-Kaiser (TKE) operator is given in equation (4), where *x(n)* denotes the location of the sensor in the grid*;*

$$\Psi[x(n)] = x^2(n) - x(n+1)x(n-1) \quad (4)$$

a) 1-D Nonlinear Transverse Spatial Filter (NLT); equation (5)

$$\Psi_{d,m}[x(m,n)] = x^2(m,n) - x(m-1,n)x(m+1,n) \quad (5)$$

b) 1-D Nonlinear Longitudinal Spatial Filter (NLL); equation (6)

$$\Psi_{d,n}[x(m,n)] = x^2(m,n) - x(m,n-1)x(m,n+1) \quad (6)$$

c) Nonlinear Spatial Filter in Two Orthogonal Directions (NLTOD); equation (7)

$$\Psi_{d,2}[x(m,n)] = \Psi_{d,2m}[x(m,n)] + \Psi_{d,n}[x(m,n)] \quad (7)$$
$$= 2x^2(m,n) - x(m-1,n)x(m+1,n) - x(m,n-1)x(m,n+1)$$

d) Nonlinear Spatial Filter in all Four Directions (NLAFD); equation (8)

$$\Psi_{d,4}[x(m,n)] = 4x^2(m,n) - x(m-1,n)x(m+1,n) \quad (8)$$
$$-x(m,n-1)x(m,n+1) - x(m-1,n+1)x(m+1,n-1)$$
$$-x(m-1,n-1)x(m+1,n+1)$$

The experiments were carried out on a healthy male subject. The ring finger motor point was located using a Muscle Stimulator, manufactured by Rich-Mar Corporation (model number HV 1100). The EMG detection system used was a Delsys, Bagnoli-16 channel EMG (DS-160, S/N-1116). The sensors used for measuring the surface EMG action potentials were three pronged DE 3.1 differential surface electrodes. The material for the contacts of the electrode is 99.9% pure silver, the contacts are 10mm long, 1mm in diameter and spaced 10mm apart. The subjects' skin was prepared, according to the ISEK standards, before the sensors were placed over the motor point. The electrodes were placed along the muscle fibers (Flexor Digitorum Superficialis) for recording surface EMG. The reference electrode was placed on the elbow where there is no sEMG signal. Nine different experiments were conducted and the corresponding sEMG signal was measured simultaneously from all the 9 sensors. The force generated by the subject's fingers, for a given motion, was measured using a stress ball with a force sensitive resistor (FSR) mounted on it. Figure 1 shows the location of the FSR on the stress ball.

System Identification

Equation 9 describes the Hammerstein-Wiener model structure:

$$w(t) = f((g(t)), \quad b(t) = \frac{B_{j,i}(q)}{F_{j,i}(q)} w(t), \quad y(t) = h(x(t)), \quad (9)$$

where, $w(t)$ and $b(t)$ are internal variables, $w(t)$ has the same dimensions as $u(t)$ - input, and $x(t)$ has the same dimensions as $y(t)$ - output. $g()$ and $h()$ are the input and output non-linearity functions respectively. $B(q)$ and $F(q)$ are regression polynomials.

Figure 2A and 2B represent the Hammerstein-Wiener models individually and their combination respectively. The model fit values are computed using Equation (10) as follows;

$$fit = 100 * \frac{1 - \|\hat{y} - y\|}{\|y - \hat{y}\|} \quad (10)$$

where, $\hat{y}$ is the estimated output by the model.

The linear block is specified using the terms n_b - the number of zeros plus one, n_f - the number of poles and n_k - the delay from the input to the output in terms of the number of samples. The commonly used nonlinear estimators for Hammerstein-Wiener model are, a) Dead Zone, b) Piecewise Linear, c) Saturation, d) Sigmoid Network, and e) Wavelet Network, [15].

Genetic Algorithm (GA)

Genetic Algorithm is a class of evolutionary methods for solving both constrained and unconstrained optimization problems that are based on natural selection.

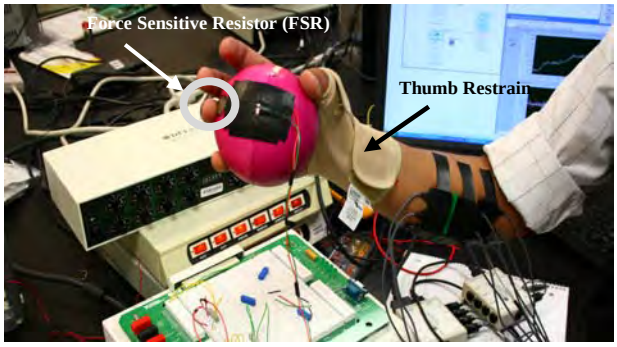

Figure 1: Force sensitive Resistor and Thumb Restrain

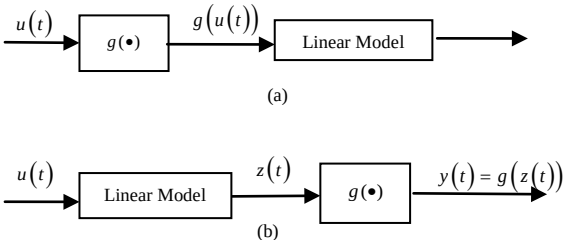

Figure 2A: a) Hammerstein model, b) Wiener model

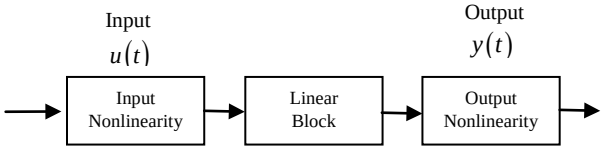

Figure 2B: Hammerstein-Wiener Model Structure

This is the same rule that governs biological systems. In GA, the population of individual solutions is modified repeatedly. A solution is given by a set of parameters (genes) and packaged as a chromosome. Each step or iteration the GA selects individuals (chromosomes) in a fashion that may include some randomness, from a given population, as parents, and uses them to produce offspring for the next generation. Over successive iterations or generations, the population evolves and finally reaches an optimal solution. The steps that make up GA are as follows:

1) Generate a random population of '*p*' chromosomes – these chromosomes carry information of the population and are confined in the feasible solution space. 2) Evaluate the objective or fitness function *f (p)* for each chromosome. 3) Create a new population or offspring from the initial population by using certain rules. These rules include a) Selection – selection of two parent chromosomes from the population according to their fitness. b) Crossover – crossover the parents to form new offspring, if no crossover is performed then the offspring is an exact copy of the parents. c) Mutation – involves the changing of a variable in a chromosome or some other change in the original chromosome as defined by the user. d) Acceptance Condition – if offspring satisfies the acceptance condition, include offspring in the new population or else discard. 4) Use the offspring as the parents for

the generation of a new population. 5) Continue until the end condition is satisfied. Figure 4 presents a graphical interpretation of the steps in GA. In this work, GA is used to assist in finding the optimal values of the filter mask for the filtration of the sEMG signal using the various spatial filters. The cost function that the GA tries to minimize, is the model fit obtained from system identification of the sEMG-force data that was collected.

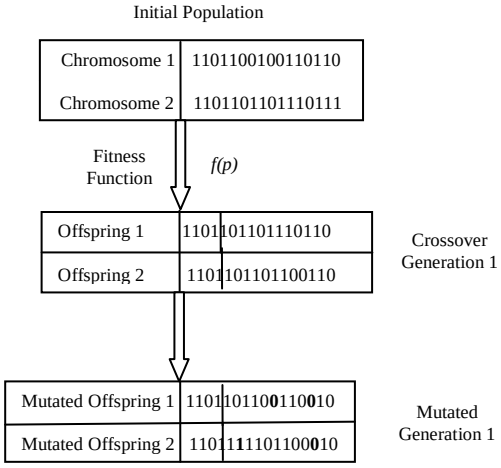

Figure 4: General steps in a binary genetic algorithm

4 Results

The results of spatially filtered data for the linear and the nonlinear spatial filters were first compared based on the "*Kurtosis*" criteria, [14]. '*Kurtosis'* is a measure of whether the data sets are peaked or flat relative to a normal distribution. That is, data sets with high kurtosis tend to have a distinct peak near the mean, decline rather rapidly, and have heavy tails. Data sets with low kurtosis tend to have a flat top near the mean rather than a sharp peak. A uniform distribution would be the extreme case. The mathematical expression for kurtosis is given in Equation 11.

$$Kurt = \frac{E[x^4] - 3(E[x^2])^2}{E[x^2]^2} \qquad (11)$$

Figure 5 shows the plot obtained for the various filters based on the *kurtosis* measure. The y-axis is the *kurtosis improvements* which is the ratio of the *output* to the *input kurtosis.* It is evident from the plot that the NLT, NLL, NLTO and the NLAFD spatial filters performed very well as compared to the linear spatial filters under investigation. The best *kurtosis improvements* were obtained for experiment 4 ≈ 44 for the nonlinear spatial filters. The x-axis in Figure 5 shows the numbers allotted to the various spatial filters investigated. Based on these results we focused our attention to the linear spatial filter masks for experiment 3, which exhibits poor *kurtosis* values. The filters were compared based on the model fit values obtained from various Hammerstein-Wiener models. The Matlab[R] code for the Hammerstein-Wiener model is: *nlhw(ze, [* n_b n_f n_k *], …., …).* The modeling was carried out by varying n_b - the number of zeros plus one, n_f - the number of poles and n_k - the delay from input and output in terms of the number of samples for the various Hammerstein-Wiener models.

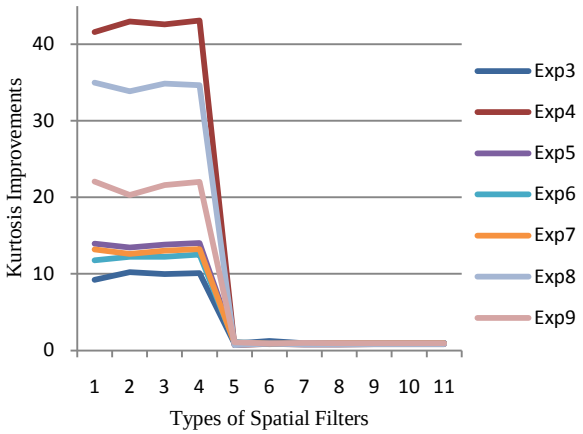

Figure 5: Kurtosis plots of various filters for exp3 – y-axis numbers are for the various filters 1-NLT, 2-NLL, 3-NLTO, 4-NLAFD, 5-LSD, 6-TSD, 7-LDD, 8-TDD, 9-NDD, 10-IB2, 11-IR

In all, 42 models with variations in n_a and n_b were tested while the value of n_k was kept as 1. The total number of models estimated were 7 (filter types) x 4 (time windows) x 42 models per time window = 1,176 models. The time windows used for estimation and validation of the models were called '*ze*' and '*zv*' respectively. '*ze*' contained 8000 sample points and '*zv*' contained data points shifted by 2000 sample points. For example, if '*ze*' was a time window between 2-6 seconds i.e. samples 4000-12000, then '*zv*' was between 3-7 seconds i.e. 6000-14000 samples. These models were computed using the filter masks available in literature. On examining the fit values closely we found them to have large variation from one model order to another. One of the reasons of this could be due to the poor correlation in the estimation and validation data sets, on account of the large variations that were achieved in the force. This paper does not list all these models tested but identifies and reports only the significant results of the analysis. We found that the filters tested performed poorly in the initial time window of 2-7 seconds for experiment 3. Some of the models for this time window were selected and then recomputed using GA to optimize the filter mask with the fitness function being the fit value of an identified model achieved for a given model order. Table 1 shows an example of the fits that were obtained on varying the parameters of the Hammerstein-Wiener model. The highlighted models (and a few other models) were selected randomly to be optimized using GA. We had two scenarios under GA –1) GA Constrained and 2) GA – Unconstrained. The first scenario GA constrained optimized only the mask entry a_{22} (location of the sEMG sensor on the motor unit). The other entries of the filter mask were then computed from this optimized value. In the second scenario, GA

unconstrained we let GA optimize all the entries for various masks. The GA parameters for optimization were as follows: number of iterations: 50; initial population size Generation 0: 96; population size Generation 1: 48; Number of Chromosomes kept for mating: 24; and mutation rate was set to 4%.

Model Number	n_a	n_b	n_k	LDD	LSD	TDD	TSD	NDD	IB2	IR
m1	2	3	1	31.06	41.39	39.53	-9.685	45.55	33.79	35.38
m2	2	4	1	31.86	17.4	39.36	43.19	36.84	16.88	23.89
m3	2	5	1	23.54	35.94	30.09	2.247	39.78	36.17	38.16
m4	2	6	1	3.266	41.99	41.28	43.46	10.83	36.41	36.7
m5	2	7	1	31.58	40.55	44.65	31.28	2.593	32.26	36.34
m6	2	8	1	37.84	4.259	21.89	20.08	8.036	36.22	36.57
m7	2	9	1	31.42	-0.1887	35.78	28.71	38.11	35.54	35.82
m8	3	3	1	36.59	40.04	36.17	12.33	4.478	41.09	35.81
m9	3	4	1	20.74	40.72	31.53	36.57	29.76	37.43	38.76
m10	3	5	1	39.87	11.53	39.83	30.24	39.25	35.15	37.9
⋮	⋮	⋮	⋮	⋮	⋮	⋮	⋮	⋮	⋮	⋮
m40	7	7	1	34.91	10.18	40.79	35.21	35.24	33.42	37.92
m41	7	8	1	-0.1127	36.28	39.68	40.26	20.27	35.88	24.32
m42	7	9	1	36.55	-0.412	25.24	31.31	35.4	34.26	39.82

Table 1: Example of System Identification Results Using Filter Mask from Literature – Highlighted Models Optimized

Longitudinal Double Differential (LDD)			
	Fit %		
	From Literature	GA Constrained	GA Unconstrained
m1	31.06	**42.8291**	**61.3475**
m6	37.84	**53.3134**	33.724
m12	35.54	**44.2513**	**51.7942**
m31	39.44	**47.0034**	**60.6489**

Longitudinal Single Differential (LSD)			
	Fit %		
	From Literature	GA Constrained	GA Unconstrained
m1	41.39	**48.9135**	**59.8055**
m4	41.99	41.5731	**68.4191**
m8	40.04	40.5924	**63.8523**
m9	40.72	**45.2322**	**56.5113**

Transverse Double Differential (TDD)			
	Fit %		
	From Literature	GA Constrained	GA Unconstrained
m1	39.53	**41.5297**	**59.8055**
m5	44.65	**49.4667**	**68.4191**
m10	39.83	**41.307**	**63.8523**
m15	43.01	43.3466	**56.5113**

Transverse Single Differential (TSD)			
	Fit %		
	From Literature	GA Constrained	GA Unconstrained
m2	43.19	**44.0017**	**65.9038**
m4	43.46	**43.0529**	**58.2755**
m11	44.24	39.7867	44.8431
m31	29.1	**43.5787**	**47.6688**

Normal Double Differential (NDD)			
	Fit %		
	From Literature	GA Constrained	GA Unconstrained
m1	45.55	**53.1512**	**57.9496**
m3	39.87	**47.1084**	**60.7374**
m7	38.11	**51.8065**	**60.5535**
m11	39.01	**46.881**	**56.1193**

Inverse Binomial 2 (IB2)			
	Fit %		
	From Literature	GA Constrained	GA Unconstrained
m1	33.79	**38.6076**	**58.2365**
m3	36.17	**38.9074**	**58.1653**
m4	36.41	**38.9957**	**55.5179**
m8	41.09	**47.2971**	**55.0537**

Table 2: Results of Constrained and Unconstrained GA of Highlighted Models from Table 1

From the results in Table 2 we can see that the optimization of the filter mask using GA worked in almost all the cases chosen. GA without constraints performed significantly better, in most cases, than the filter masks reported in literature and also the mask which we computed using GA, which only optimized the entry (a_{22}) i.e. the weight associated with the sEMG signal at the motor unit. This restriction on GA would leave the filter mask symmetrical. But looking at the results of the GA, we can conclude that the filter mask need not always be symmetrical for analysis of sEMG, especially for data recorded using an array. Examples of the filter mask that we obtained for TDD, model m5 and NDD, model 3 spatial filters are given below:

$$\text{TDD} = \begin{bmatrix} 0 & -41.5561 & 0 \\ 0 & 54.7329 & 0 \\ 0 & -22 & 0 \end{bmatrix},$$

$$\text{NDD} = \begin{bmatrix} 0 & -11.5790 & 0 \\ -46.7773 & 36.9276 & -11.8061 \\ 0 & -70.0491 & 0 \end{bmatrix}.$$

4 Conclusion

The linear spatial filter masks reported in literature had poor *kurtosis* improvements which we optimized using GA, these were compared based on the model fit values achieved using Hammerstein-Wiener models. The fit values did improve significantly in the two GA scenarios – GA with and without constraints. The GA without constraints performed better than the GA with constrains, which brings into focus the possibility that the sEMG signal distribution over the entire grid cannot be assumed to be symmetrically distributed and that the weights associated with the sEMG signal at various locations need to be modified depending on probably the subject and also based on the experimental design. This is in contrast to the reported filter mask in the literature, which are all symmetric. Almost all the filter masks optimized resulted in a significant improvement over the masks reported in literature.

Acknowledgement

This work was supported by a grant from the Telemedicine Advanced Technology Research Center (TATRC) of the US Department of Defense. The financial support is greatly appreciated.

References:

[1] Kathryn Ziegler-Graham, *et al*., "Estimating the Prevalence of Limb Loss in the United States - 2005 to 2050," Archives of Physical Medicine and Rehabilitation 89: 2008, pp. 422-429.

[2] Patricia F. Adams, et al, "Current Estimates from the National Health Interview Survey, 1996," Vital and Health Statistics 10:200, 1999.

[3] Mewett, D. T., Nazeran H., Reynolds, K., J., "Removing power line noise from recorded EMG". *Proceedings of the 23rd Annual IEEE/EMBS International Conference*, October, 2001, pp. 1-4.

[4]Clancy, A. E., Farry, A. K., "Whitening of the electromyogram to improve amplitude estimation". *IEEE Transactions on Biomedical Engineering*, 47(6), June 2000, pp. 709-719.

[5]Chan, D. C. A., Englehart, B. K., "Continuous myoelectric control for powered prostheses using hidden Markov models". *IEEE Transactions on Biomedical Engineering*, 52(1), January 2005, pp. 121-124.

[6]Chan, H. Y. F., Yang, Y., Lam, F. K., Zhang, Y., Parker, A. P., "Fuzzy EMG classification for Prosthesis control". *IEEE Transactions on Rehabilitation Engineering*, 8(3), September 2000, pp. 305-311.

[7] Reaz, I. B. M., Hussain, S. M., Yasin, M. F., "Techniques of EMG signal analysis: detection, processing, classification and application". *Biomedical Procedures Online*, 8(1), January 2006, pp. 11-35.

[8] http://www.isek-online.org/standards_emg.html

[9] Farina, D., Merletti, R., and Enoka, M. R., "The extraction of neural strategies from the surface EMG". Journal of Applied Physiology, 96, 2004, pp. 1486-1495.

[10] Sebastian A., Parmod K., Anugolu M., Schoen P. M., Urfer A., Naidu S. D., "Optimization of Bayesian Filters and Hammerstein-Wierner Models for EMG-Force Signals Using Genetic Algorithm". Proceedings of the ASME 2009 Dynamic Systems and Control Conference DSCC 2009.

[11] Sebastian A., Parmod K., Schoen P. M., Urfer A., Creelman J., Naidu S. D., "Analysis of EMG-Force relation using System Identification and Hammerstein-Wiener Models". Proceedings of the ASME 2010 Dynamic Systems and Control Conference DSCC 2010.

[12]http://www.spatialanalysisonline.com/output/html/Linearspatialfiltering.html

[13] P. Zhou, N. L. Suresh, M. Lowery, W. Z. Rymer, "Nonlinear Spatial Filtering of Multichannel Surface Electromyogram Signals During Low Force Contractions", *IEEE Transactions on Biomedical Engineering*, vol. 56, no.7, July 2009, pp. 1871-1879.

[14] J. F. Kaiser, "On a simple algorithm to calculate the 'energy' of a signal", *Proceedings of IEEE ICASSP'90*, Albuquerque, New Mexico, April 1990, pp. 381-384.

[15]http://www.mathworks.com/access/helpdesk/help/toolbox/ident/index.html?/access/helpdesk/help/toolbox/ident/gs/bq_ylq6.html

SURFACE EMG ARRAY SENSOR BASED MODEL FUSION USING BAYESIAN APPROACHES FOR PROSTHETIC HANDS

Madhavi Anugolu
Measurement and Control Engineering
Idaho State University
Pocatello, Idaho 83209
anugmadh@isu.edu

Anish Sebastian
Measurement and Control Engineering
Research Center (MCERC)
Idaho State University
Pocatello, Idaho 83209
sebaanis@isu.edu

Parmod Kumar
Measurement and Control Engineering
Idaho State University
Pocatello, Idaho 83209
kumaparm@isu.edu

Marco P. Schoen
MCERC
Department of Mechanical Engineering
Idaho State University
Pocatello, Idaho 83209
schomarc@isu.edu

Alex Urfer
Department of Physical and Occupational Therapy
Idaho State University
Pocatello, Idaho 83209
urfealex@isu.edu

D. Subbaram Naidu
Dept. of Electrical Engineering
MCERC
Idaho State University
Pocatello, Idaho 83209
naiduds@isu.edu

ABSTRACT

Traditional electromyopgrahic (EMG) measurements are based on single sensor information. Due to the arrangement of skeletal muscle fibers for hand motions, cross talk is an inherent problem when inferring motion/force potentials from EMG data. This paper studies means of using sensor arrays to infer better motion/force potential for prosthetic hands. In particular, a surface electromyographic (sEMG) sensor array is used to investigate multiple model fusion techniques. This paper provides a comparison between three statistical model selection criteria. The sEMG signals are pre-processed using four filters, Butterworth, Chebyshev type-II, as well as Bayesian filters such as the Exponential and Half-Gaussian filter. Output Error (OE) models were extracted from sEMG data and hand force data and compared using a Bayesian based fusion model. The four different filters effect were quantified based on the OE models performance in matching the actual measured data. The comparison indicates a preference for using the sensor fusion technique with preprocessed EMG data using the Half-Gaussian Bayesian filter and the Kullback Information Criterion (KIC).

NOMENCLATURE

$B(q)$, $F(q)$	Polynomials for parametric model.
$P(M_i \mid z)$	Probability of model M_i given data z
R	Residual norm.
Y	Force data (measured).
$\hat{Y}$	Predicted force (system output).
$\overline{Y}$	Mean value of force data (measured).
$e(t)$	Error sequence.
n	Number of data points.
p_i	Order of the i^{th} model (M_i).
$u(t)$	Measured sEMG data (system input).
Φ	EMG and Force data.
$\hat{\theta}$	Parameter vector.
ψ	Digamma function.

INTRODUCTION

According to the information provided by the National Center for Health Statistics, every year there will be 50,000 new amputations in the USA. In recent years, much progress has been made in developing prosthetics for individuals who have sustained hand amputation. A traditional approach to control hand prosthetics is based on surface myographic (sEMG) signals, gathered through electrodes placed on the skin's surface, and hence do not require the implementation of needle sensors, or the direct wiring of nerves to external devices. This paper details the data processing of sEMG recordings for the purpose of controlling smart hand prosthetics. Surface electromyography is an area of research that began some 60 years ago. Over time, many methods for filtering of EMG signals were proposed for different applications. Recently, a novel nonlinear recursive filter based on Bayesian estimation [1] was proposed in order to

overcome the limitation of the EMG signal usage in the fields of neural control, prosthetics and robotics. This filter allows the signal to maintain the same amplitude during the constant drive and allows the recording of rapid changes in the signal instead of smoothing the signal in the time domain.

Since sEMG sensors are prone to pick up cross talk from adjacent muscle groups, filtering of such data is an important step in order to infer the intended finger motion. Recently a multi-channel electrode approach was introduced to infer the EMG signal, [2]. This system consisted of 96 different EMG surface electrodes, where one line (16 channels) was selected based on the noise contents. The data from this line went through a canonical discriminate analysis to select the three first eigenvectors, which are used to classify the EMG signal. This approach allows tracking of 12 movements of the hand including four finger flexion movements with an 80% success rate. In this paper, we propose to use as well a sensor array. Though we are not interested in the classification of motion as done in the work by Natata et. al [2], rather we aim to extract dynamical models that describe the sEMG – finger force relationship. Also, we propose to use all sensor data within the array and apply a sensor fusion technique in order to maximize the model accuracy. Multiple model fusion, as detailed in [3], is based on assigning a particular probability to each individual model, which is extracted using System Identification (SI) from a single sEMG sensor. The probability is based on the SI model fit value, given by $\left[1-\left|Y-\hat{Y}\right|/\left|Y-\overline{Y}\right|\right]\times 100$.

Considering recorded sEMG signals as the input and the resulting force signal generated by the finger movements of the hand as the output, the raw signal will need to be processed. In this work we will investigate the effect of different filters such as Butterworth, Chebyshev, and nonlinear recursive filters that are based on Bayesian estimation using measurement models such as Exponential and Half –Gaussian, for details on these filters see [1]. In addition, we will be investigating the usage of different model selection criterion for the use of multiple model fusion.

THEORETICAL BACKGROUND

The low-pass Chebyshev type II filter in this work is constructed with a cutoff frequency of 550Hz, while the low pass Butterworth filter is of order 12. The Bayesian filter has the capability of recording the rapid changes in the sEMG signal instead of just smoothing it. It was shown in [1] that the processed data will have a high signal-to-noise ratio and a relatively low error as compared to low-pass 5Hz, low-pass 1Hz, or low-pass 0.1Hz linear filters. A Bayesian filtering method may potentially provide a good EMG signal for classification purposes. The filter has not been investigated in terms of the use for system identification, where the output force generated by the hand is modeled based on the measured sEMG data.

System Identification: The system identification is accomplished by utilizing Output Error (OE) models. The filtered and rectified EMG data is used to extract OE models, for more details see [4]. The corresponding equation for the OE model is given by

$$M_i \equiv \hat{Y}(t) = \frac{B(q)}{F(q)}u(t-nk) + e(t). \quad (1)$$

Model Fusion: Three different model selection criteria are used in this paper, i.e. the Akaike information criterion (AIC), Kullback information criterion (KIC) and the Bayesian information criterion (BIC), for more details on the specifics of these information criterions see [3]. AIC is relatively simple to apply because it requires only the maximum likelihood to be achieved within a given model. AIC is an asymptotically unbiased estimator of the Kullback's directed divergence between the true model and the estimated model. The dissimilarity between the two statistical models is called relative entropy or the I-divergence. AIC becomes a negatively biased estimator of the model when the dimension of the candidate model increases – when compared to the sample size. In order to overcome this shortcoming, biased corrected version of AIC was proposed in [5]. Akaike's asymptotic bias corrected form is given by

$$AIC = -2\ln R_i + 2p_i. \quad (2)$$

The biased corrected version by Hurvich is stated as

$$AIC(p_i) = \frac{n}{2}\log R_i + \frac{(p_i+1)n}{n-p_i-2}. \quad (3)$$

Kullback's information criterion is an asymmetric measure. The measure of the models dissimilarity can be obtained by the sum of two directed divergences, known as Kullback's symmetric or J-divergence [5].

$$KIC(p_i) = \frac{n}{2}\log R_i + \frac{(p_i+1)n}{n-p_i-2} - n\psi\left(\frac{n-p_i}{2}\right) + g(n), \quad (4)$$

where $g(n) = n\times\log(n/2)$. Bayesian inference is a preferred tool as it is precisely the quantity that updates the probability of the prior model to the posterior model probability. BIC was introduced by Schwarz in 1978, [6] and comes from approximating evidence ratios of models. This ratio is known as the Bayes factor, [6].

$$BIC(p_i) = \frac{n}{2}\log R_i + \frac{p_i+1}{2}\log n. \quad (5)$$

Fusion Algorithm

The following is the fusion technique based on [3] applied to sEMG – force identification models.

1.) Identify OE models $M_1, M_2, \ldots, M_k$ using sEMG data (u) as input and force data (Y) as output, for k number of sensors collecting data simultaneously.
2.) Compute the residual square norm

$R_i = \| Y - \Phi_i\hat{\theta}_i \|^2 = \left\|Y-\hat{Y}\right\|$, where $\hat{\theta}_i = \left\{\Phi_i^T\Phi_i\right\}^{-1}\Phi_i^T Y$,

and $\vec{\Phi} = \begin{bmatrix} Y_p^T & u_p^T & Y_{p-1}^T & \dots & u_1^T \\ Y_{p+1}^T & u_{p+1}^T & Y_p^T & \dots & u_2^T \\ \vdots & \vdots & \vdots & \ddots & \vdots \\ Y_{n-1}^T & u_{n-1}^T & Y_{n-2}^T & \dots & u_{n-p}^T \end{bmatrix}$

3.) Calculate the model criteria coefficient using Eqs. (3-5).

4.) Compute the model probability

$p(M_i \mid Z) = \frac{e^{-l_i}}{\sum_{j=1}^{k} e^{-l_j}}$, where l is the respective model selection criteria coefficient, i.e. $AIC(p_i)$, $BIC(p_i)$, or $KIC(p_i)$.

5.) Compute the fused model output $\hat{Y}_f = \sum_{i=1}^{k} p(M_i \mid Z)\hat{Y}_i$.

6.) Compute overall OE model from $\hat{Y}_f$ and Force data.

Experimental set up: In order to identify appropriate EMG electrode attachment points, a wet probe point stimulator was used at the forearm superficial musculature (flexor digitorum superficialis) (RICH-MAR, HV 1000) for collecting flexion of the ring finger (fourth digit). Surface EMG electrodes (model DE2.1; Delsys) were placed directly on the marked areas to record EMG actively. Force was measured using Interlink Electronics FSR 0.5" circle sensors. The sEMG and the force data were measured simultaneously at a sampling of 2000Hz for duration of 10 seconds.

TABLE 1: MODEL FUSION RESULTS

Criterion	Models	Butter-worth	Cheby-shev II	Bayes-Expon.	Bayes-Half G.
BIC	M_1	54.3	54.62	55.24	41.37
	M_2	61.24	61.15	55.24	54.27
	M_3	53.5	63.0	49.79	64.73
	$M\left(\hat{Y}_f\right)$	68.22	76.02	73.47	80.52
AIC	M_1	54.3	54.62	55.24	41.37
	M_2	61.24	61.15	55.24	54.27
	M_3	53.5	63.0	49.79	64.73
	$M\left(\hat{Y}_f\right)$	67.88	75.65	81.35	92.89
KIC	M_1	54.3	54.62	55.24	41.37
	M_2	61.24	61.15	55.24	54.27
	M_3	53.5	63.0	49.79	64.73
	$M\left(\hat{Y}_f\right)$	67.44	71.02	87.78	93.74

DISCUSSION

Table 1 details the obtained results using the different selection criteria for model fusion and filter options. The fit values describe how well the particular model (M_i), selected filter, and selection criteria predict the intended finger force. The numbers are given as percentages, where 100 represents a perfect fit and 0 no fit. It is evident that the general approach of combining data in order to produce an overall model ($M(\hat{Y}_f)$) improves the resulting force prediction, regardless of selection criteria or filtering method. From the results, it appears, regardless of the model selection criteria that the Half-Gaussian filter is performing better than the three other filters investigated with respect to model fusion. In addition, the KIC in connection with the Half-Gaussian filter yields the best fit of all the fused models. This is true also if the other Bayesian filter is used. The AIC is susceptible to over fitting and works well if the true model order of the system is used. Analogously, the BIC is receptive to the same over fitting issue as the AIC and is sensitive to increases in additional parameters. The used model fusion algorithm works well for sEMG-force relationships. The investigation presented here relay on one particular system identification routine. Its impact or its optimization in terms of model representation and/or estimation and its application to hand motion models without force will be investigated in future. The presented work is suitable for the use of array surface EMG sensors.

ACKNOWLEDGMENTS

This work was supported by a grant from the Telemedicine Advanced Technology Research Center (TATRC) of the U.S. – Department of Defense (DoD) and is greatly appreciated.

REFERENCES

[1] Terence D. Sanger., 2007. "Bayesian Filtering of Myoelectric Signals".See also URL http://jn.physiology.org/cgi/content/abstract/97/2/1839

[2] Natata K., Adno K., Yamada M., Magatani K., 2005, "*A Classification Method of Hand Movements using Multi Channel Electrode*," Proceedings of the 27th Annual Conference IEEE Engineering in Medicine, Shanghai, China, September 1-4, pp. 2375-2378.

[3] Huimin Chen, Shuqing Huang., 2005."*A Comparative study on Model Selection and Multiple Model Fusion*," 7th International Conference on Information Fusion, pp. 820-826.

[4] Jeffrey T. Bingham, Marco p. Schoen. "*Characterization of Myoelectric Signals using System Identification Techniques*", IMECE 2004, Anateim, CA, November 2004.

[5] Abd-Krim Seghouane, Maiza Bekara, Gilles Fleury, 2003, "*A Small Sample Model Selection Criterion Based on Kullback's symmetric Divergence*." IEEE Transaction, pp. 145-148.

[6] Andrew R. Liddle, 2008, "*Information Criteria for astrophysical model selection,*" astro-ph/071113, June 28, 2008, pp.1-5.

FREQUENCY DOMAIN SURFACE EMG SENSOR FUSION FOR ESTIMATING FINGER FORCES

Chandrasekhar Potluri, Parmod Kumar, Madhavi Anugolu, Alex Urfer, Steve Chiu, D. Subbaram Naidu, *Fellow, IEEE,* and Marco P. Schoen, *Member, IEEE*

***Abstract*---- Extracting or estimating skeletal hand/finger forces using surface electro myographic (sEMG) signals poses many challenges due to cross-talk, noise, and a temporal and spatially modulated signal characteristics. Normal sEMG measurements are based on single sensor data. In this paper, array sensors are used along with a proposed sensor fusion scheme that result in a simple Multi-Input-Single-Output (MISO) transfer function. Experimental data is used along with system identification to find this MISO system. A Genetic Algorithm (GA) approach is employed to optimize the characteristics of the MISO system. The proposed fusion-based approach is tested experimentally and indicates improvement in finger/hand force estimation.**

I. INTRODUCTION

The number of people with missing limbs due to combat and non-combat operations in the United States is over 1.2 million according to [1]. The recent wars in Afghanistan and Iraq substantially increased the number of amputees. To date there are no prosthetic devices available at an affordable cost and with the full functionality of a human hand. The need for such a device in these days is becoming more important. There are multiple types of hand prostheses. One of these types is based on measuring sEMG signals to initiate the actuation of the robotic hand. In this paper, surface based EMG sensors are used in order to avoid invasive methods of measuring EMG signals [2]. The major problem in capturing the sEMG signal is cross-talk from different motor units. As a muscle contracts several motor units fire simultaneously and hence make up the EMG signal [3].

Chandrasekhar Potluri is with Measurement and Control Engineering Research Center (MCERC), Idaho State University, Pocatello, Idaho 83201 USA (e-mail: potlchan@isu.edu).

Parmod Kumar is with MCERC, Idaho State University, Pocatello, Idaho 83201 USA (e-mail: kumaparm@isu.edu).

Madhavi Anugolu is with MCERC, Idaho State University, Pocatello, Idaho 83201 USA (e-mail: anugmadh@isu.edu).

Alex Urfer is with Department of Physical and Occupational Therapy, Idaho State University, Pocatello, Idaho 83201 USA (e-mail: urfealex@isu.edu).

Steve Chiu is with Department of Electrical Engineering and Computer Science, MCERC, Idaho State University, Pocatello, Idaho 83201 USA (e-mail:chiustev@isu.edu).

D. Subbaram Naidu is with Department of Electrical Engineering and Computer Science, MCERC, Idaho State University, Pocatello, Idaho 83201 USA (e-mail: naiduds@isu.edu).

Marco P. Schoen is with Department of Mechanical Engineering, MCERC, Idaho State University, Pocatello, Idaho 83201 USA (e-mail: schomarc@isu.edu).

The number of motor units in individual muscles varies from person to person and muscle fatigue begins at the onset of contraction and is ongoing throughout (i.e.) time to contraction failure or reduction in force generating capacity of the muscle. The EMG signal passes through several layers of tissues before reaching the skin surface [3]. This contributes to noise and interference in signal acquisition. The randomness of the EMG signal is an added difficulty in studying it. All of these factors make it rather complex to discriminate the content of the EMG signal against noise and interference. Identification of the content of the EMG signal should focus on the amplitude, frequency and amplitude-frequency content using distinct methods. Since the signal is amplitude modulated and time dependent, it is therefore spatially and temporally frequency encoded [4].

An approach to distinguish the onset of muscle contraction was introduced by Merlo et al. [5]. In their study, the sEMG sensors collect the action potential of individual motor units which are in turn identified by using a continuous wavelet transform. Accuracy of determining the intended force from the EMG signal is improved by using an array sensor. Array sensors use multi-channel EMG electrodes embedded into a small surface area in order to capture the electrical muscle activity from a set of muscles fibers at the skin level. The EMG sensor array approach produces a micro level and a macro level sensor network by utilizing several array sensors at different skin locations of the forearm. An array of micro sensors with the objective to extract signals from one motor unit corresponds to the micro level. The main objective of this arrangement is to use redundant data to infer the hand motion by including cross-talk. Also, a multi-channel methodology is proposed where elements of the sensor array is discarded based on the quality of the signal [6]. A simple sensor fusion scheme to improve the estimated hand/finger force from measured sEMG data based on Bayesian approaches was given [7].

In the following, Genetic Algorithm (GA) is used to accomplish the sensor fusion algorithm [8]. Briefly, GA's are evolutionary algorithms that simulate Darwin's survival of the fittest principle. The initial population of candidate solutions is randomly generated and represented as chromosomes in the form of genes. These chromosomes are evaluated based on an objective function and ranked in terms of its fitness. A subset of the next generation of candidate solutions is selected based on their performance with the objective function. The remaining set of the new generation is generated by a mating process, where the best performing candidate solution comprise the subset of the parents. In

addition to the mating process, a mutation rate is also embedded in the generation of the new population. The mutation rate enables the search for the optimum solution to overcome local minimums and locate the global minimum. This process of selection, mating, and mutation is repeated a number of times until the best performing candidate solution converges to some stationary value. GA's have the capability of overcoming local minima, some additional advantages of a genetic algorithm are the ease with which large numbers of parameters can be handled, the fact that they do not require the traditional approach of taking derivatives, the fact that they result in a set of optimum candidate solutions rather than a single candidate solution, and that they work well with experimental data as well as simulated data.

The approach presented in this paper is based on extracting useful information from all sensors in the array. To infer the intended motion from the sensor array, we propose to use an optimized non-linear filter. Optimization techniques are used as filters to fuse the EMG data from different sensors. The fusion process is done in the frequency domain.

The paper is structured as follows. The experimental set up is given in Section II and Section III provides background on sensor fusion. Section IV details the results and discussion and in the last section some conclusions are provided.

II. EXPERIMENTAL SET-UP

Experiments were carried out on a healthy male subject in order to collect EMG data from all the sensors corresponding to each individual motor unit. The mcheppuotor points of the subject and the appropriated EMG electrode attachment points were identified by using a wet probe point muscle stimulator (Rich-Mar Corporation, model number HV 1100.). For capturing the EMG data from the skin surface, a Delsys, Bagnoli-16 channel EMG, DS-160, S/N-1116 system is used. This capturing system has the capability of internally amplifying and reducing the acquired noise. Pronged DE 2.1 differential surface electrodes are used**.** For recording EMG at the forearm superficial musculature (flexor digitorum superficialis) electrodes are placed to extract EMG signals. The force data is measured by a force sensitive resistor (FSR). The data acquisition is set to a sampling rate of 2000 samples per second for force and EMG signal data.

III. SESNOR FUSION BACKGROUND

The sensor fusion process deals with association, correlation and estimation of data from multiple sensors. A data fusion technique, by combining the data from different sensors, enables one to achieve more specific inferences about the measured data. The sEMG sensors pick up the cross-talk from muscle fibers adjacent to motor units. In [7], sensor fusion was done in the time domain, by taking sEMG as input and force signal as the output. They used combinations of different filters (Butterworth, Chebyshev, Exponential and Half-Gaussian filters) and different information criteria based on Akaike (AIC), Bayesian (BIC), and Kull-back (KIC) and concluded that the KIC criterion with Half Gaussian filtering gives the best EMG-Force model fit.

In the present case, sensor fusion is done in the frequency domain for the sEMG data. Figure 1 depicts the flow diagram of the proposed fusion technique using a simple elitism based GA. The data from the three sensors around the individual motor unit are fused by first rectifying the data and then filtering it using a Half-Gaussian filter. The sEMG data u_1, u_2, and u_3 from the three sensors and their corresponding force signal is used to identify a dynamical relationship between the sEMG signals and the force signals using System Identification (SI). In this proposed fusion algorithm, SI is achieved by utilizing an Output Error (OE) model first for each individual data set [9]. The OE model structure is given as follows:

$$y(t) = \frac{B(q)}{F(q)}u(t - nk) + e(t), \quad (1)$$

where B, and F are the polynomials, q is shift operator, $e(t)$ is output error, $y(t)$ is system output, u is input, nk is the system delay and t is time index.

The corresponding continuous-time model is given by the transfer function.

$$G(s) = \frac{B(s)}{F(s)} = \frac{b_{nb}s^{(nb-1)}b_{nb-1}s^{(nb-2)}+\cdots+b_1}{s^{nf}+f_{nf}s^{nf-1}+\cdots+f_1}. \quad (2)$$

Similar to the discrete-time case the orders of the numerator and denominator are determined by nb and nf. For multi-input systems, nb and nf are row vectors. b, f are the coefficients of the numerator and denominator polynomials respectively.

Based on the poles of the three individual identified OE models, corresponding to each sensor, a MISO transfer function (H) is constructed. While the denominators of the respective individual transfer functions (corresponding to each OE model) are transferred over to the new MISO transfer function, the corresponding zeros are found through the use of a GA. Generally GA's can find global optimum points if elitism is used and sufficient number of generations are allowed in the algorithm. This optimization algorithm is rather computationally expensive, but since there was not a computational time requirement, one is free to use GA rather than other intelligent based algorithms. Chromosomes are constructed by designating each zero of a numerator as a gene. Since a discrete time model is utilized, the search area is limited to the unit circle (and the resulting MISO model is decreased to be minimum phase). The number of potential zeros was set to the order of the corresponding denominator because the number of zeros is at most the number of poles (for a causal system, can't predict the future). The objective

function was set as the error squared of the resulting MISO system (H) (see appendix) and the recorded force signal.

Here H is given as,

$$H(s) = \begin{pmatrix} \frac{Z_{1,1}s^n + Z_{1,2}s^{n-1} + \cdots Z_{1,n+1}}{P_{1,1}s^n + P_{1,2}s^{n-1} + \cdots P_{1,n+1}} \\ \frac{Z_{2,1}s^n + Z_{2,2}s^{n-1} + \cdots Z_{2,n+1}}{P_{2,1}s^n + P_{2,2}s^{n-1} + \cdots P_{2,n+1}} \\ \frac{Z_{3,1}s^n + Z_{3,2}s^{n-1} + \cdots Z_{3,n+1}}{P_{3,1}s^n + P_{3,2}s^{n-1} + \cdots P_{3,n+1}} \end{pmatrix}, \quad (3)$$

where $Z's$ and $P's$ are the zeros and poles respectively of individual transfer function and n is the order of the system.

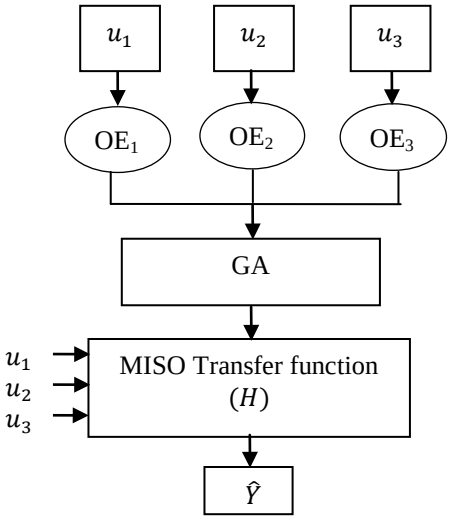

Figure 1: Flow Diagram.

IV. Results And Discussion

The actual force signal from the FSR sensor is filtered using a Chebyshev Type II high pass filter followed by a low pass filter. The EMG signal is rectified and filtered using a Half-Gaussian filter to minimize the noise content. The filter parameters for the Half-Gaussian filter are selected in such a way that the effective EMG signal frequency content is no more than 500 Hz, according to the ISEK standards [10]. Figure 2 shows the results of the fusion based force $\hat{Y}$ plotted against actual measured force. The predicted force matches the actual force characteristics well. Figure 3 shows the estimated force output, for the individual OE models which were used to construct the fusion model and the actual measured force. It is apparent that the individual force estimates from each OE model do not track the actual force as well as the estimated force from the fused model H. In particular, the magnitudes are substantially different. While not the most optimal identification was determined, the improvement indicated by the fused model output compared to the individual OE outputs is significant. The output of the fused model fits with peaks of the original force data. Several validation tests for the fused model are done by feeding new data sets to the MISO transfer function (H).

Figure 4 and 5 shows the plot between the actual force data and the predicted force data for two representative validation data sets. The output of the fused model exhibits an 82% fit with the actual force signal.

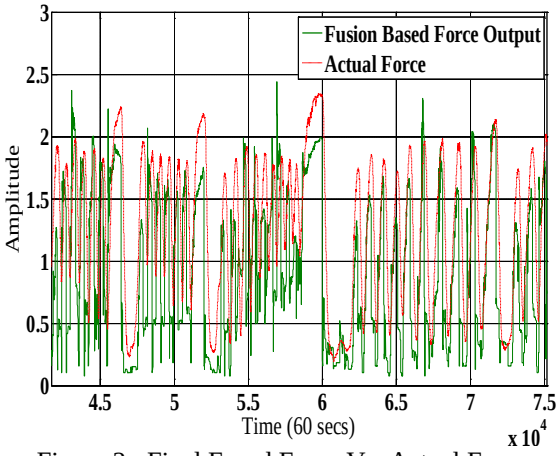

Figure 2 : Final Fused Force Vs. Actual Force.

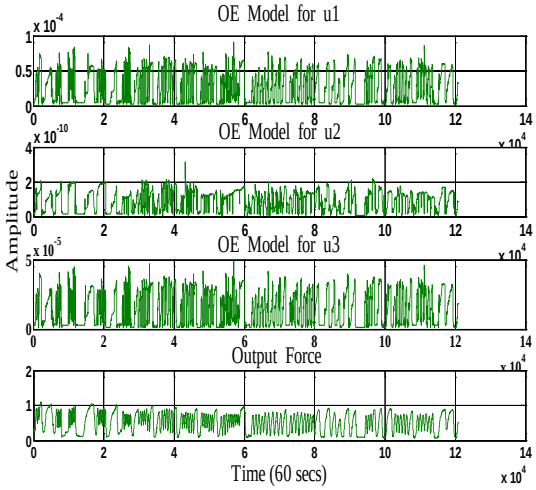

Figure 3: Estimated Force Output for Individual OE Model and the Actual Measured Force.

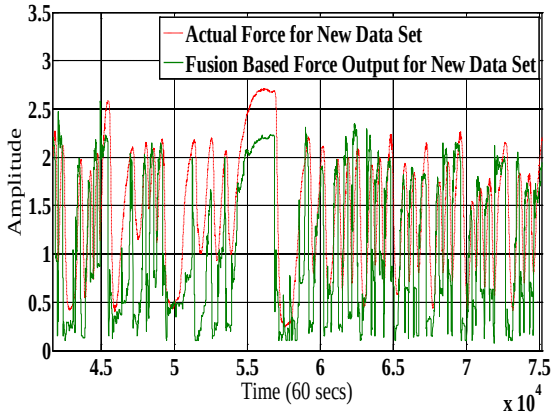

Figure 4: Validation Plot for Data Set-I.

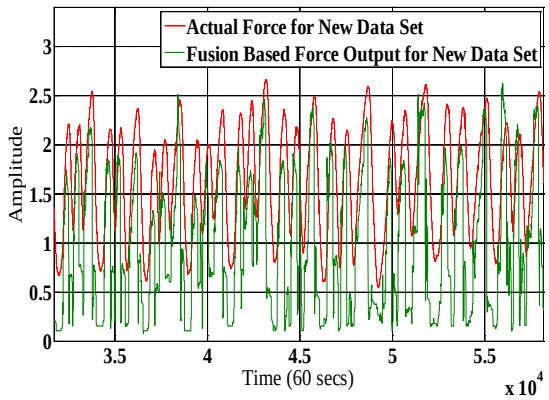

Figure 5: Validation Plot for Data Set-II.

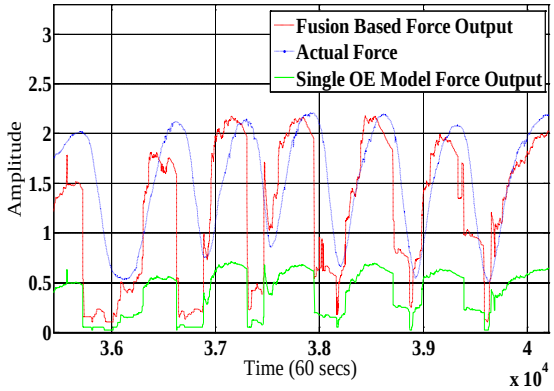

Figure 6: Comparison between Actual, Fusion Based and Single OE Model Output Force.

In order to visualize the improvement achieved with regard to the form of the predicted force, Figure 6 is generated to depict the actual force measured compared to the output of the fused model (predicted force) and the predicted force from one of the OE models used to construct the fused model. The amplitudes were modulated in order to show the different shapes of the wave forms. It is apparent that the fused model output matches the measured finger force better than an individual OE force estimate. While there are some additional higher frequency terms in the estimated finger force, the general trend and lower frequencies are well matched. The higher frequency elements are necessary parts of the MISO model since finger forces can change rather quickly, as indicated in Figure 2.

V. Conclusion

Although better individual models can be inferred using SI under perfect conditions, the proposed fusion algorithm improves the predicted force estimate consistency. The fusion algorithm results in a single MISO transfer function. Cross talk can be reduced by using filtering and in this work a Half-Gaussian filter is used. This also enables the smoothing of the fused signal. Several validation data sets were used to test the proposed fusion algorithm. Compared to single OE model, the proposed fusion-based force model is in good agreement with that of the actual force. Future work will address the optimization of the SI and the associated experimental conditions in order to arrive at better individual OE models. Also the optimization of the poles and the number of zeros will be undertaken in order to obtain a minimum realization of the MISO system. In addition, the MISO system is an ideal structure to incorporate dynamics related to muscle fatigue, which will be addressed in future work.

Appendix

The resulting MISO transfer function H is constructed as,
From u_1 to output,

$$\frac{s^8-3.843s^7+7.729s^6-10.78s^5+10.6s^4-7.417s^3+3.603s^2-0.9795s+0.1192}{s^8-4.028s^7+6.325s^6-4.121s^5-1.545s^4+5.87s^3-5.433s^2+2.28s-0.3496}$$

From u_2 to output,

$$\frac{s^8-4.339s^7+9.005s^6-12.42s^5+12.22s^4-8.117s^3+3.427s^2-0.9134\,s+0.1424}{s^8-4.028\,s^7+6.325\,s^6-4.121\,s^5-1.545\,s^4+5.87\,s^3-5.433\,s^2+2.28\,s-0.3496}$$

From u_3 to output,

$$\frac{s^8-3.522\,s^7+6.655\,s^6-8.864\,s^5+8.183\,s^4-5.365\,s^3+2.423\,s^2-0.557\,s+0.09585}{s^8-4.028\,s^7+6.325\,s^6-4.121s^5-1.545\,s^4+5.87\,s^3-5.433\,s^2+2.28\,s-0.3496}$$

Acknowledgement

The support by a grant from the Telemedicine Advanced Technology Research Center (TATRC) of the U.S. – Department of Defense (DoD) for pursuing this work is hereby acknowledged. Further, the technical help from Dr. Jim Creelman and Mr. Anish Sebastian is greatly appreciated.

References

[1] Amputee Coalition of America (ACA) National Limb Loss Information, Center (NLLIC) Limb Loss Facts in the United States, http://www.amputee-coalition.org, 2005.
[2] Northrop, R. *"Analysis and Application of Analog Electronic Circuits to Biomedical Instrumentation,"* CRC Press, Boca Raton, Florida, 2004, pp 6-9.
[3] Cram, J.R., Kasman G.S., and Holtz J. *"Introduction to Surface Electromyography,"* Aspen Publisher Inc., Gaithersburg, Maryland, 1998.
[4] Kandel E.R. and Schartz J.H., *"Principles of Neural Science,"* Elsevier/North-Holland, New York, 1981.
[5] Merlo A., Faina D., Merletti R., "A Fast and Reliable Technique for Muscle Activity Detection from Surface EMG Signals," *IEEE Transaction on Biomedical Engineering*, Vol. 50, No. 3, 2003, p. 316- 323.
[6] Natata K., Adno K., Yamada M., Magatani K., "A Classification Method of Hand Movements using Multi Channel Electrode," *Proceedings of the 27th Annual conference IEEE Engineering in Medicine Shanghai, China*, September 1-4, 2005, pp. 2375-2378.
[7] Madhavi Anugolu, Anish Sebastian, Parmod Kumar, Marco P. Schoen, Alex Urfer, and D. Subbaram Naidu, "Surface EMG Array Sensor Based Model Fusion using Bayesian Approaches for Prosthetic Hands," *Proceedings of the Dynamic Systems and Control Conference (DSCC), Hollywood, CA*, October 2009.
[8] R.L. Haupt, and S. E. Haupt, *"Practical Genetic Algorithms,"* John Wiley & Sons, Inc., New York, 1998.
[9] Jeffrey T. Bingham, and Marco P. Schoen, *"Characterization of Myoelectric signals using System Identification Techniques,"* IMECE2004, Anaheim, CA, November 2004.
[10] http://www.isek-online.org/standards_emg.html.

Spectral Analysis of sEMG Signals to Investigate Skeletal Muscle Fatigue

Parmod Kumar, Anish Sebastian, Chandrasekhar Potluri, Yimesker Yihun, Adnan Ilyas, Madhavi Anugolu, Rohit Sharma, Jim Creelman, Alex Urfer, D. Subbaram Naidu, *Fellow, IEEE,* and Marco P. Schoen, *Senior Member, IEEE*

***Abstract*— Recently, we focused our investigations on the dynamic modeling of the skeletal muscle of the human upper arm using surface electromyographic (sEMG) signals. The objective of these investigations is to develop models that dynamically compute the skeletal muscle force and finger angles for prosthetic hand control using sEMG as input. Since sEMG is temporal and spatially distributed and is influenced by various factors, muscle fatigue and its related sEMG becomes of importance. This study is an effort to spectrally analyze the sEMG signal during progression of muscle fatigue. The sEMG is captured using an array of nine sensors from the arms of healthy subjects during muscle fatiguing experiments for dynamic and static force levels. The sEMG signal is first filtered with a nonlinear Teager–Kaiser Energy (TKE) operator-based nonlinear spatial filter and segmented in five parts with 75% overlap between adjacent segments. The analysis is done using different classical (fast Fourier transform, Welch's averaged modified periodogram), model-based (Yule-Walker, Burg, Covariance and Modified Covariance autoregressive (AR) method), and eigenvector methods (Multiple Signal Classification (MUSIC) and eigenvector spectral estimation method) in frequency domain. Results show that the classical and eigenvector based methods are more sensitive than the model-based methods to fatigue related changes in sEMG signals.**

I. Introduction

THIS work focuses on the analysis of sEMG signals and investigates the effects of fatigue in the skeletal muscles. The sEMG signal is an electric voltage signal ranging between -5 to +5 mV and is generated by skeletal muscles. The motor units operate as a consequence of the central control strategies, signal transmission along nerve fibers and across neuromuscular junctions, electrical activation of the muscle fibers organized in elementary motors and, through a chain of complex biochemical events. The productions of the forces acting on the tendons of the agonist and/or antagonist muscles predict bone movement [1]. This mechanism also involves a number of feedback circuits relaying back to the spinal cord and the brain information concerning the length and velocity of shortening of the muscles and the forces acting on the tendons [1]. The EMG signal gives information about the motor points and their controller i.e. the central nervous system [2, 3]. The central nervous system activates and controls the EMG signals which depend on the flow of specific ions including sodium (Na^+), potassium (K^+) and calcium (Ca^{++}) resulting in the action potentials in nerves and their respective skeletal muscle fibers from which EMG signals are derived. Research efforts in the last few decades have focused on the prosthetic design where sEMG is a control input to activate the prosthesis. The sEMG is a dynamic signal with continual change in its pattern and strength and this becomes more complex with the fatigue induced in skeletal muscles.

Failure to maintain the required force level is termed as muscle fatigue, which is a complex phenomenon [4]. Reasons for fatigue can be the peripheral changes at the muscle level or an inadequate output from the central nervous system to stimulate motoneurons [4]. Intricacies of muscle fatigue are associated with several aspects where the relative importance of each depends on the fiber type and composition of the contracting muscle(s), as well as the intensity, type, and duration of contraction activity. Muscle cells are the focal points of fatigue and rarely involve the central nervous system or the neuromuscular junction [5]. The amount of force generated, duration of each contraction, and the rest period between two contractions has a direct influence on the muscle fatigue rate [6]. Muscle fiber-type distribution [7, 8], nerve conduction velocity of fatiguing muscles [9, 10], or even central factors within the central nervous system (CNS) will affect motivation to perform activities [11]. The EMG analysis is a well-accepted method for muscle fatigue assessment [8-10, 12-17]. Even though the sEMG has some limitations associated with the skin impedance, electrode placement, and cross-talk, it is used for the estimation of muscle fatigue of different muscles [16, 18, 19].

L. Lindstrom et al. developed a method that measures the

Manuscript received March 22, 2011. This work was supported in part by the US Department of the Army, under the award number W81XWH-10-1-0128.

Parmod Kumar is with Measurement and Control Engineering Research Center (MCERC), School of Engineering, Idaho State University, Pocatello, Idaho 83209, USA (email: kumaparm@isu.edu).

Anish Sebastian, Chandrasekhar Potluri, Yimesker Yihun, Adnan Ilyas, Madhavi Anugolu, and Rohit Sharma are with MCERC, School of Engineering, Idaho State University, Pocatello, Idaho 83209, USA (e-mail: sebaanis@isu.edu, potlchan@isu.edu, yihuyime@isu.edu, ilyaadna@isu.edu, anugmadh@isu.edu, sharrohi@isu.edu).

Jim Creelman and Alex Urfer are with Department of Physical and Occupational Therapy, Idaho State University, Pocatello, Idaho 83209, USA (email: creejame@isu.edu, urfealex@isu.edu).

D. Subbaram Naidu is with Department of Electrical Engineering and Computer Science, MCERC, Idaho State University, Pocatello, Idaho 83201 USA (email: naiduds@isu.edu).

Marco P. Schoen is with Department of Mechanical Engineering, MCERC, Idaho State University, Pocatello, Idaho 83209, USA (email: schomarc@isu.edu).

localized muscle fatigue based on the power spectrum analysis using myoelectric signals, [20]. This approach permits real-time investigations and can yield statistically based criteria for the occurrence of fatigue. Rate of fatigue development and changes in muscle action potential conduction velocity were used to interpret the findings [20-22]. Additional recruitment of motor units, synchronization of active motor units along the muscle fibers, and a decrease in conduction velocity is reflected in the EMG signal as an increase of amplitude in time domain and a decrease of medium frequency in frequency domain [23, 24].

The joint analysis method using sEMG amplitude and spectrum (JASA) allows distinguishing between the difference of fatigue-induced and force related EMG changes. Simultaneous changes in the EMG amplitude and spectrum is considered in the JASA approach [25]. According to traditional measurements, the EMG amplitude increases and median frequency (MF) decreases as a result of muscle fatigue [26-28]. Fatigue can occur because of continuous high frequency and tetanic stimulations. Decline in the force magnitude can be attributed to reduced Ca^{++} release from the sarcoplasmic reticulum (SR), reduced myofibrilllar Ca^{++} sensitivity, or because of reduced maximum Ca^{++}– activated tension. The main reason of the tension decline with continuous tetanic stimulation is decreased Ca^{++} release, which is due to impaired action potential propagation in the T tubules. Decrease in pH and increase in inorganic phosphate (Pi) concentration causes reduced Ca^{++} sensitivity and decline in maximum tension. This is the main contributing factor in decline of force with continual tetanic stimulation [29].

Increase in the inorganic phosphate in the myoplasm ([Pi]myo) results in reduced SR Ca^{++} release in both skinned and intact fibers. Muscle performance declines with rigorous activities which results in fatigue. Metabolic changes on either the contractile machinery or the activation process are also responsible for the fatigue of muscles. Myofibrillar proteins and activation process both are affected during fatigue with substantial increase in the concentration of inorganic phosphate (Pi) in myoplasm. Further, it has been shown that failure of the sarcoplasmic reticulum (SR) to release Ca^{++} also contributes to fatigue [30]. During intense exercise of skeletal muscles (less than 20 seconds), cells consume 100 of times more energy than during the rest period. The aerobic capacity of muscle cells falls short on energy demand and anaerobic metabolism must supply the majority of the adenosine triphosphate (ATP) required. Skeletal muscle fatigue results because of the high-intensity exercise. Hence, the anaerobic metabolism pathway results in a decline of contractile functionality [31].

The present work investigates the change in sEMG in frequency domain during skeletal muscle fatigue. The sEMG signals are acquired for multiple subjects for dynamic and static force experiments to induce skeletal muscle fatigue. The sEMG signals are filtered with a nonlinear Teager–Kaiser Energy (TKE) operator-based nonlinear spatial filter [32]. Two sets of dynamic force data are segmented into three and five parts and two sets of static force data are segmented into five parts each. There is a 75% overlap between the two adjacent segments. A number of classical, model-based and eigenvector based spectral estimation techniques are used to study the change in the sEMG signals as a result of muscle fatigue. In classical methods Fast Fourier transform (FFT) and Welch's averaged modified periodogram methods are used. In case of model-based methods Yule-Walker (Y-W), Burg, Covariance (Cov.) and Modified Covariance (Mcov.) Autoregressive (AR) methods are applied. For eigenvector methods Multiple Signal Classification (MUSIC) and Eigenvector (EIG) spectral estimation methods were selected for processing sEMG signals. Using these spectrum analysis techniques, Power Spectral Density (PSD) estimates and detailed documentations of the sEMG signals were obtained. These methods were compared in terms of their frequency resolution and the effects in determination of skeletal muscle fatigue.

II. Experimental Set-Up And Pre-Processing

An experiment set-up was developed using DELSYS® Bagnoli-16 EMG system with nine DE-3.1 sEMG sensors to capture the sEMG signals from skeletal muscles as given in [32]. This arrangement involves nine sensors covering four directional spatial distributions of the sEMG signal. The appropriate motor point of the flexor digitorum superficialis

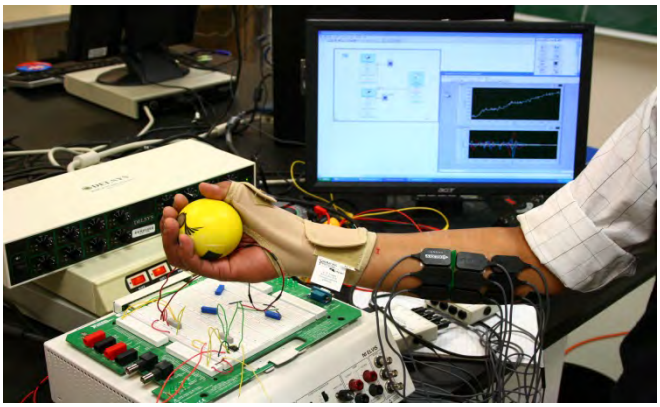

Fig. 1. Experimental set-up for dynamic force levels.

muscle (FDS), which controls the flexion of the ring finger, was identified using a wet probe muscle stimulator at the FDS (RICH-MAR, HV 1000). The middle three sEMG sensors were attached directly on the skin surface above the motor point of the ring finger. Prior to placing the sEMG sensors, the skin surface of the subject was prepared according to International Society of Electrophysiology and Kinesiology (ISEK) protocols. Two different sets of fatigue inducing experiments were conducted using this set-up of sEMG sensors. One experiment using dynamic force variations and another with a 50 pounds of static force. For the dynamic force variation we used an Interlink™ Electronics FSR 0.5" circular force sensor on a stress ball

and for the static force experiment we used a cable tensionmeter (T5166) by 'Pacific Scientific Company.'

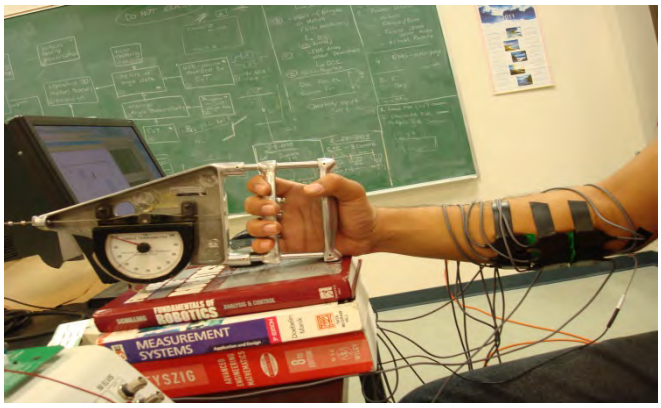

Fig. 2. Experimental set-up for 50 pounds static force levels.

For the dynamic force experiment we restricted the thumb movement using a thumb splint. For the static force experiment we held the force of the dynamometer at 50 pounds and tried to maintain this force level to induce fatigue in skeletal muscles. Force data for dynamic force experiments was captured using NI ELVIS™ with Interlink™ Electronics FSR 0.5" circular force sensor. Experimental set-up is shown in Fig. 1 and 2, where 9 sensors are shown on a healthy subject forearm, holding a stress ball and a tension dynamometer, respectively. The sEMG and finger force data was collected at a sampling rate of 2000 Hz using LabVIEW™ in conjunction with DELSYS® Bagnoli-16 EMG and NI ELVIS™. With these experimental set-ups, we conducted several experiments of 30 seconds, 45 seconds and 60 seconds durations.

III. Spectral Estimation Methods

Signals can be analyzed in the time and frequency domains and in some instances the frequency content of the signal is more useful than the time domain characteristics [33]. Various bio signals such as the heart rate, EMG, EEG, ECG, eye movements, and other motor responses, acoustic heart sounds, and stomach and intestinal sounds, show much richer information in the frequency domain [33]. Spectral analysis is a mathematical prism which finds the frequency content of a waveform by decomposing the signal into its constituent frequencies [33, 34]. There is a wide range of methods for spectral analysis, each having its own benefits and drawbacks. In this research we are using classical methods based on the Fourier transform, modern methods based on the estimation of model parameters, and eigenvector based methods [33] in order to characterize the muscle fatigue occurring in skeletal human muscles, in particular muscles of the forearm. To use the spectral analysis wisely, we need to have an understanding of the spectral features of interests and the best methods to accurately determine those features [33].

A. Discrete Fourier Transform (DFT)

DFT which is the computational basis of the spectral analysis transforms the time or space domain data into frequency domain data [35]. The DFT of a vector x of length N is given as

$$X(k) = \sum_{j=1}^{N} x(j)\omega_N^{(j-1)(k-1)}, \quad (1)$$

where $\omega_N = e^{(-2\pi i)/N}$ is the N_{th} root of unity [35].

B. Welch's averaged modified periodogram method:

As the name suggests, the 'Welch's averaged modified periodogram method' depends on the periodogram of the signal $\{x(n)_n^N\}$ which is given by Equation (2), [35].

$$\hat{S}_{per}(f) = \frac{1}{N}\left|\sum_{n=1}^{N} x(n)\exp(-j2\pi fn)\right|^2. \quad (2)$$

In Welch method, the signal is segmented into eight parts of equal length with an overlapping ratio of 50% and each part is segmented using a Hamming window as given by Equation (3), [35].

$$w(n) = 0.54 - 0.46\cos\left(2\pi\frac{n}{N}\right), 0 \le n \le N \ . \quad (3)$$

C. Yule-Walker (Y-W) autoregressive (AR) method:

The Yule-Walker autoregressive method, also called the autocorrelation method, estimates the power spectral density (PSD) of the input. This method fits an autoregressive (AR) model to the windowed input data by minimizing the forward prediction error in the least-squares sense. This formulation leads to the Yule-Walker equations, which are solved by Levinson-Durbin recursion [35].

D. Burg autoregressive (AR) method:

The Burg autoregressive (AR) method is a parametric spectral estimation method of the signal, x. The power spectral density is calculated in units of power per radians per sample. This method is based on the minimization of the forward and backward prediction error and on estimation of the reflection coefficients [35].

E. Covariance (Cov.) autoregressive (AR) method:

The covariance autoregressive (AR) method uses the covariance algorithm to estimate the parametric spectral density of the signal, x. Based on causal observation of the input signal, the covariance method minimizes the forward prediction error and fits an AR linear prediction filter model to the signal [35].

F. Modified covariance (Mcov.) autoregressive (AR) method:

Modified covariance autoregressive (AR) method estimates the PSD of the signal using the modified covariance method. Based on the causal information of the input signal, the modified covariance method fits an autoregressive (AR) linear prediction filter model to the signal by simultaneously minimizing the forward and backward prediction errors. The spectral estimate returned by this method is the magnitude squared frequency response of the AR model [35].

G. Multiple Signal Classification (MUSIC) spectral estimation method:

The MUSIC algorithm estimates the pseudospectrum (in rad/sample) at the corresponding vector of frequencies for the input signal x [35]. This algorithm uses the estimates of the eigenvectors of a correlation matrix associated with the input signal using Schmidt's eigenspace analysis method

[36]. The MUSIC pseudospectrum estimate is given by Equation (4),

$$P_{music}(f) = \frac{1}{e^H(f)(\Sigma_{k=p+1}^{N} v_k v_k^H)e(f)} = \frac{1}{\Sigma_{k=p+1}^{N}|v_k^H e(f)|^2}, \quad (4)$$

where N is the dimension of the eigenvectors and v_k is the k-th eigenvector of the correlation matrix [35]. The signal subspace has a dimension p and the eigenvectors v_k used in the sum corresponds to the smallest eigenvalues and also spans the noise subspace [35]. The vector $e(f)$ consists of the complex exponentials, so the inner product $v_k^H e(f)$ amounts to a Fourier transform. To estimates the pseudospectrum, the squared magnitudes are summed for FFT computed for each v_k [35].

H. Eigenvector (EIG) spectral estimation method:

The eigenvector spectral estimation method estimates the pseudospectrum (in rad/sample) at the corresponding vector of frequencies using estimates of the eigenvectors of a correlation matrix associated with the input signal x [35]. This method estimates the pseudospectrum from a signal or a correlation matrix using a weighted version of the MUSIC algorithm derived from Schmidt's eigenspace analysis method [36, 37]. To find the frequency content of the signal the algorithm performs eigenspace analysis of the signal's correlation matrix. Singular value decomposition is used to compute the eigenvalues and eigenvectors of the signal's correlation matrix [35]. This method computes the pseudospectrum estimate as given by Equation (5).

$$P_{ev}(f) = \frac{1}{(\Sigma_{k=p+1}^{N}|v_k^H e(f)|^2)/\lambda_k}, \quad (5)$$

where the eigenvectors have a dimension of N and v_k is the k-th eigenvector of the correlation matrix [35]. The signal subspace has a dimension p and the eigenvectors v_k used in the sum corresponds to the smallest eigenvalues and also spans the noise subspace [35]. The vector $e(f)$ consists of the complex exponentials, so the inner product $v_k^H e(f)$ amounts to a Fourier transform and to estimate the pseudospectrum, the squared magnitudes are summed for FFT computed for each v_k [35].

I. Selection of Model Orders for Model-Based and Eigenvector Based Methods

Model-based and eigenvector-based methods need to have a specific model order which is an important aspect of the use in these methods. Using the sEMG and force data as input and outputs for three and five sets of the segments for different data sets, we created model structure matrices using 'struc' function in MATLAB®, using 'arxstruc' we compared a model order of 1 to 50th with varying delay of 1 to 50 using cross-validation on the second half of the data set. With this approach, it was possible to select the order that gives the best fit for the validation data set.

IV. Results and Discussion

sEMG signal changes as a consequence of muscle fatigue [23-28], the amplitude of the PSD of the signal increases and the median frequency shifts towards the lower frequency range [26-28]. In this study, PSDs of the different segments of each sEMG data set were obtained using FFT, Welch's averaged modified periodogram, Yule-Walker, Burg, Covariance, Modified Covariance autoregressive (AR), Multiple Signal Classification (MUSIC) and Eigenvector spectral estimation methods. The objective of this study was to determine preferred methods of signal processing that elevates the sensitivity of muscle fatigue as represented in the PSD of the sEMG signal. An increased sensitivity allows for better modeling of the fatigue phenomena and hence more accurate sEMG models. Ultimately this may lead to better prosthetic control.

Data of two experiments for dynamic force variations was segmented in three and five parts respectively. Each segment is with an overlap of 75% with its adjacent segment. Using different methods, we computed the PSDs for each segment. For the dynamic force experiments, the maximum value of PSDs of sEMG signal increases with muscle fatigue as time or segment number is increased. The classical methods (FFT and Welch) and eigenvector based methods (MUSIC and Eigenvector (EIG.)) are representing this change well in case of maximum PSD values and show a clear difference.

TABLE I
MAXIMUM VALUE OF PSD FOR CLASSICAL METHODS AND EIGENVECTOR BASED METHODS – DYNAMIC VARYING FORCE – EXPERIMENT 2

Segment No.	Classical-Methods		Eigenvector-Methods	
	FFT	Welch	MUSIC	EIG
1st	4.1e+6	0.0082	371.59	1.0819
2nd	5.09e+6	0.0100	424.43	1.3892
3rd	5.74e+6	0.0111	480.71	1.4132
4th	6.79e+6	0.0133	508.64	1.4936
5th	2.13e+7	0.0379	695.08	10.2118

Table I lists the peak values of the PSDs of five segments using classical and eigenvector based methods for a dynamically varying force experiment. Fig. 1 shows the overlapping plot of PSDs for five segments using the MUSIC algorithm based spectral estimation method. The increase in the maximum PSD value is evident from the 1st to the 5th segment of the data.

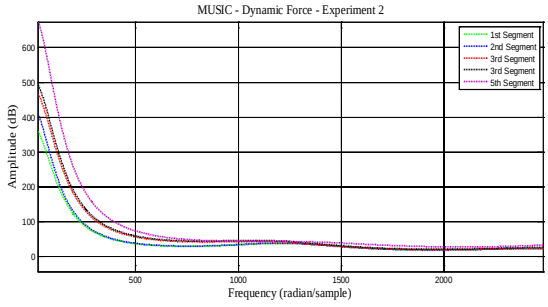

Fig. 3. PSD vs. Frequency Plot for MUSIC Algorithm – Dynamic Force Experiment.

Fig. 3 shows the resulting PSD using the Burg method. Comparing Fig. 3 and 4, the progression of fatigue influence shift in PSDs is evident in both plots. However, the MUSIC algorithm not only shows larger amplitudes, but also a greater relative sensitivity to fatigue. The rather equal spacing between the lines of the PSD for the MUSIC

algorithm compared to the Burg method indicates a rather more linear relationship of the fatigue progression.

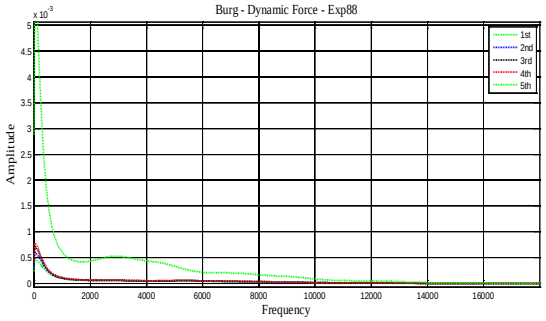

Fig. 4. PSD vs. Frequency Plot for Burg Method – Dynamic Force Experiment.

TABLE II
MAXIMUM VALUE OF PSD FOR CLASSICAL METHODS – STATIC FORCE – 50 POUNDS - EXPERIMENT 1

Segment No.	Classical-Methods		Eigenvector-Methods	
	FFT	Welch	MUSIC	EIG
1st	1.03e+5	6.81e-5	1413	9.93e-4
2nd	1.80e+5	1.12e-4	1793	16e-4
3rd	3.21e+5	1.80e-4	2296	28e-4
4th	4.25e+5	2.62e-4	3102	37e-4
5th	6.23e+5	3.58e-4	7723	104e-4

TABLE III
MAXIMUM VALUE OF PSD FOR CLASSICAL METHODS – STATIC FORCE – 50 POUNDS - EXPERIMENT 1

Segment No.	1st	2nd	3rd	4th	5th
Model-Based Methods	7.7e-7	1.3e-6	2.3e-6	3.1e-6	7.81-6

The sEMG data of two experiments for static force (50 pounds) were processed and the maximum PSDs of five segments using classical, model-based, and eigenvector based methods were computed. Data from both the experiments show similar results as the dynamic case. Table II lists the peak values of the PSDs of five segments using classical and eigenvector based methods for static force (50 pounds) for one experiment. Table III lists the maximum values of the PSD for model-based methods: Y-W, Burg, Covariance, and modified covariance. All of these methods resulted in the same maximum values for each segment. Comparing Table II and III, we recognize the large difference in maximum value between the model-based methods and the corresponding values from the FFT and MUSIC method. Fig. 5 shows the overlapping plot of PSDs for five parts using eigenvector algorithm based spectral estimation method. The increase in the maximum PSD value is evident from the 1st to the 5th segment of the static force sEMG data.

The eigenvector method produces a similar characteristic as the MUSIC algorithm and distinguishes itself by also providing a more linear characteristic of the fatigue progression and a greater relative sensitivity. Fig. 6 depicts the PSD generated by using FFT method for the five segments of a static force experiment. While providing a large maximum value, the FFT method is limited by its own spectral resolution ($1/N$) and, due to windowing of the finite data set, results into spectral leaking.

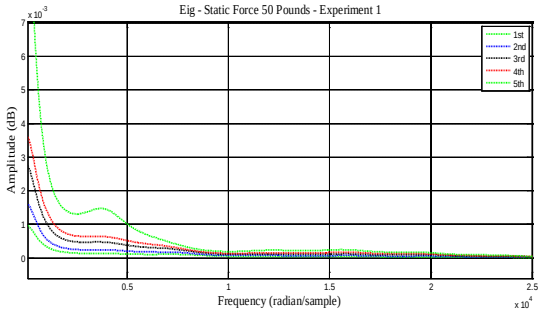

Fig. 5. PSD vs. Frequency Plot for Eigenvector Method – Static Force of 50 Pounds.

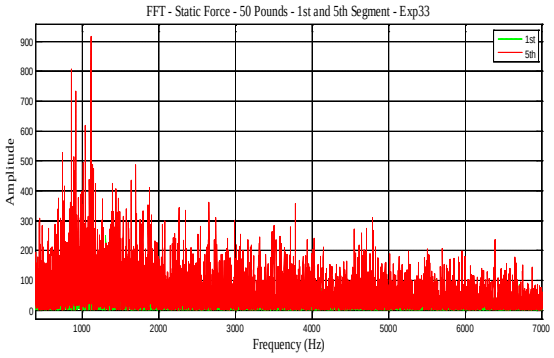

Fig. 6. PSD vs. Frequency Plot for FFT Method – Static Force of 50 Pounds.

All the model-based methods for both dynamic and static force levels produce the same peak values and the same PSD for the corresponding experiment. Since Burg and Y-W methods guarantee stability while the covariance and modified covariance methods have conditions for stability to be satisfied (i.e. min. order must be of certain length of the input frame size), Burg and Y-W should be the preferred methods for sEMG analysis. However, the Burg method is to be preferred if short data sets are used.

Comparing the eigenvector based methods (MUSIC and Eigenvector), both of these methods are frequency estimator techniques based on eigenanalysis of the autocorrelation matrix where the resulting estimate has sharp peaks at the frequencies of interest. The eigenvector method uses inverse eigenvector weighting whereas the MUSIC method uses unity weighting, implying that the eigenvector method gives fewer spurious peaks than, the MUSIC algorithm [38]. As seen from the dynamic experiment results, the MUSIC method provides for a better spacing between the segment PSDs compared to the Burg and eigenvector method. From static experiments, we conclude that all three (MUSIC, Burg, and Eigenvector) methods perform similarly if a linear relationship of the fatigue progression is desired.

V. Conclusion and Future Work

In this paper, we have shown the skeletal muscle fatigue related change in the sEMG signal in the frequency domain. Classical (fast Fourier transform and Welch's averaged modified periodogram), model-based (Yule-Walker, Burg, Covariance, and Modified Covariance autoregressive (AR) method) and eigenvector based methods (Multiple Signal Classification (MUSIC) and eigenvector spectral estimation method) are used to compute the PSDs. Classical and eigenvector based methods are more sensitive than the model-based methods for analyzing the fatigue related changes in sEMG signal. However, the MUSIC algorithm provides good maximum value in the PSD as well as a clear distinction between the segmented sEMG data. The latter point is indicative of a relative linear fatigue progression in time for the MUSIC algorithm. In future work these results can be used to design and improve the skeletal muscle 'Force-sEMG-Fatigue' based models [39] for prosthetic design and other rehabilitation research.

Acknowledgment

This research was sponsored by the US Department of the Army, under the award number W81XWH-10-1-0128 awarded and administered by the U.S. Army Medical Research Acquisition Activity, 820 Chandler Street, Fort Detrick MD 21702-5014. The information does not necessarily reflect the position or the policy of the Government, and no official endorsement should be inferred. For purposes of this article, information includes news releases, articles, manuscripts, brochures, advertisements, still and motion pictures, speeches, trade association proceedings, etc.

References

[1] R. Merletti, and P. Parker, "ELECTROMYOGRAPHY: Physiology, Engineering, and Noninvasive Applications," John Wiley & Sons, Inc., Hoboken, New Jersey, 2004, ch. 1.

[2] Merletti, R., D. Farina, M. Gazzoni, A. Merlo, P. Ossola, and A. Rainoldi, "Surface electromyography: A window on the muscle, a glimpse on the central nervous system," Europa Medicophysica 37, 57–68 (2001).

[3] Wolf, W., "The EMG as a window to the brain: signal processing tools to enhance the view," in I. Gath, and G. Inbar, eds., Advances in processing and pattern analysis of biological signals, Plenum Press, New York, 1996, pp. 339–356.

[4] S. C. Gandevia, 2001. "Spinal and Supraspinal Factors in Human Muscle Fatigue". Physiological Reviews, American Physiological Society 81(4), October.

[5] R. H. Fitts, 1994. "Cellular mechanisms of muscle fatigue". Physiological Reviews, American Physiological Society, 74, pp. 49-94.

[6] B R Bigland-Ritchie, N J Dawson, R S Johansson and O C Lippold, 1986. "Reflex origin for the slowing of motoneurone firing rates in fatigue of human voluntary contractions". Journal of Physiology, 379, pp. 451-459.

[7] Gerdle B, Edstrom M, Rahm M, 1993." Fatigue in the shoulder muscles during static work at two different torque levels". Clinical Physiology, 13(5), pp. 469-482.

[8] Paavo V. Komi, and Per Tesch, 1979. "EMG frequency spectrum, muscle structure, and fatigue during dynamic contractions in man". European Journal of Applied Physiology, 42(1), pp. 41-50.

[9] M. Hagberg, 1981. "Muscular endurance and surface electromyogram in isometric and dynamic exercise". Journal of Applied Physiology, 51, pp. 1-7.

[10] M. Hagberg, 1981. "Electromyographic signs of shoulder muscular fatigue in two elevated arm positions". American Journal of Physical Medicine, 60(3), pp.111-121.

[11] Enoka RM, 1995. "Morphological features and activation patterns of motor units". Journal of Clinical Neurophysiology, 12(6), pp. 538-559.

[12] L. G. Christova, A. S. Alexabdrov, and B. A. Ishpekova, 1999. "Single motor unit activity pattern in patients with Schwartz-Jampel syndrome". Journal of Neurology, Neurosurgery and Psychiatry, 66(2), pp. 252-253.

[13] Björn Gerdle, Jessica Elert, and Karin Henriksson-Larsén, 1989. "Muscular fatigue during repeated isokinetic shoulder forward flexions in young females". European Journal of Applied Physiology, 58(6), pp. 666-673.

[14] Paula M. Ludewig, and Thomas M. Cook, 1996. "The effect of head position on scapular orientation and muscle activity during shoulder elevation". Journal of Occupational Rehabilitation, 6(3), pp. 147-158.

[15] Merletti R, and Lo Conte LR, 1997. "Surface EMG signal processing during isometric contractions". Journal of Electromyography and Kinesiology, 7(4), pp. 241-250.

[16] T. Moritani, M. Muro and A. Nagata, 1986. "Intramuscular and surface electromyogram changes during muscle fatigue". Journal of Applied Physiology, 60(4), pp. 1179-1185.

[17] J. Bruce Moseley, Frank W. Jobe, Marilyn Pink, Jacquelin Perry, and James Tibone, 1992. "EMG analysis of the scapular muscles during a shoulder rehabilitation program". The American Journal of Sports Medicine, 20(2), pp. 128-134.

[18] D. David Ebaugh, Philip W. McClure, and Andrew R. Karduna, 2006. "Effects of shoulder muscle fatigue caused by repetitive overhead activities on scapulothoracic and glenohumeral kinematics". Journal of Electromyography and Kinesiology, 16, pp. 224-235.

[19] McQuade KJ, Dawson J, and Smidt GL, 1998. "Scapulothoracic muscle fatigue associated with alterations in scapulohumeral rhythm kinematics during maximum resistive shoulder elevation". The Journal of Orthopedic and Sports Physical Therapy, 28(2), pp. 74-80.

[20] L. Lindstrom, R. Kadefors and I. Petersen, 1977. "An electromyographic index for localized muscle fatigue". Journal of Applied Physiology, American Physiological Society, 43(4), pp. 750-754.

[21] Weytjens JLF, and van Steenberghe D, 1984. "The effects of motor unit synchronization on the power spectrum of the electromyogram". Biol Cybern, 51, pp. 71-77.

[22] Finsterer J., 2001. "EMG-interference pattern analysis". J Electromyogr Kinesiol, 11, pp. 231-246.

[23] C.J. De Luca, 1984. "Myoelectrical manifestations of localized muscular fatigue in humans". Crit. Rev. Biomed. Eng., 11 (4), pp. 251-279.

[24] B. Maton, and D. Gamet, 1989. "The fatigability of two agonistic muscles in human isometric voluntary sub maximal contraction: an EMG study. II Motor unit firing rate and recruitment". Eur. J. Appl. Physiol., 58, pp. 369-374.

[25] A. Luttmann, M. Ja¨ger, J. So¨keland, and W. Laurig, 1996. "Electromyographical study on surgeons in urology, Part II: Determination of muscular fatigue". Ergonomics, 39, pp. 298-313.

[26] K. J. Bennie, V.M. Ciriello, P.W. Johnson, and J.T. Dennerlein, 2002. "Electromyographic activity of the human extensor carpi ulnaris muscle changes with exposure to repetitive ulnar deviation". Eur. J. Appl. Physiol., 88, pp. 5-12.

[27] J. S. Petrofsky, 1979. "Frequency and amplitude analysis of the EMG during exercise on the bicycle ergometer". Eur. J. Appl. Physiol., 41, pp. 1-15.

[28] Basmajian JV, and DeLuca CJ., 1985. Muscle alive: their functions reviewed by electromyography. Williams & Wilkins, Baltimore.

[29] H. Westerblad, J. A. Lee, J. Lannergren and D. G. Allen, 1991. "Cellular mechanisms of fatigue in skeletal muscle". AJP - Cell Physiology, American Physiological Society, 261(2), pp. C195-C209.

[30] D. G. Allen and H. Westerblad, 2001. "Role of phosphate and calcium stores in muscle fatigue". Journal of Physiology, 536.3, pp. 657–665.

[31] Haken Westerblad, David G. Allen, and Jan Lannergren, 2002. "Muscle Fatigue: Lactic Acid or Inorganic Phosphate the Major

Cause?". News in Physiological Sciences, The American Physiological Society 17(1), February, pp. 17-21.
[32] P. Zhou, N. L. Suresh, M. M. Lowery, and W. Z. Rymer, "Nonlinear Spatial Filtering of Multichannel Surface Electromyogram Signals During Low Force Contractions," IEEE Transactions on Biomedical Engineering, Vol. 56, No. 7, pp. 1871-1879, July 2009.
[33] J. H. Semmlow, "Biosignal and Biomedical Image Processing: MATLAB-Based Applications," Marcel Dekker, Inc., New York, 2004, Ch. 3., pp. 79-162.
[34] Hubbard B. B., "The World According to Wavelets," 2nd ed., A.K. Peters, Ltd., Natick, MA, 1998.
[35] "Signal Processing Toolbox™ User's Guide," The MathWorks, Inc., 2010.
[36] Marple, S.L. Digital Spectral Analysis, Englewood Cliffs, NJ, Prentice-Hall, 1987, pp. 373-378.
[37] Schmidt, R.O, "Multiple Emitter Location and Signal Parameter Estimation," IEEE® Trans. Antennas Propagation, Vol. AP-34 (March 1986), pp.276-280.
[38] Johnson, D. H. and Dudgeon, D. E., "Array Signal Processing: Concepts and Techniques," Prentice-Hall, Englewood Cliffs, NJ, 1993.
[39] P. Kumar, A. Sebastian, C. Potluri, A. Urfer, D. S. Naidu, and M. P. Schoen, "Towards Smart Prosthetic Hand: Adaptive Probability Based Skeletal Muscle Fatigue Model," 32nd Annual International Conference of the IEEE Engineering in Medicine and Biology Society, Buenos Aires, Argentina, Aug. 31 – Sept. 4, 2010.

TOWARDS SMART PROSTHETIC HAND: ADAPTIVE PROBABILITY BASED SKELETAN MUSCLE FATIGUE MODEL

Parmod Kumar, Anish Sebastian, Chandrasekhar Potluri, Alex Urfer, D. Subbaram Naidu, *Fellow, IEEE*, and Marco P. Schoen, *Member, IEEE*

***Abstract* - Skeletal muscle force can be estimated using surface electromyographic (sEMG) signals. Usually, the surface location for the sensors is near the respective muscle motor unit points. Skeletal muscles generate a spatial EMG signal, which causes cross talk between different sEMG signal sensors. In this study, an array of three sEMG sensors is used to capture the information of muscle dynamics in terms of sEMG signals. The recorded sEMG signals are filtered utilizing optimized nonlinear Half-Gaussian Bayesian filters parameters, and the muscle force signal using a Chebyshev type-II filter. The filter optimization is accomplished using Genetic Algorithms. Three discrete time state-space muscle fatigue models are obtained using system identification and modal transformation for three sets of sensors for single motor unit. The outputs of these three muscle fatigue models are fused with a probabilistic Kullback Information Criterion (KIC) for model selection. The final fused output is estimated with an adaptive probability of KIC, which provides improved force estimates.**

I. INTRODUCTION

National Limb Loss Information Center [1] reported in 2002 that 1.2 million people live with amputations. Since then, this number is increasing due to ongoing wars in Iraq and Afghanistan. However, prostheses can significantly improve the lives for these people.

Recent research efforts have been active towards creating surface electromyographic (sEMG) based prosthetics for hand amputees. The recorded sEMG signal is used as an input to activate the prosthesis. The central nervous system activates and controls the EMG signals which depend on the flow of specific ions including sodium (Na^+), potassium (K^+) and calcium (Ca^{++}) resulting in the action potentials in nerves and their respective skeletal muscle fibres. A potential difference develops across neuronal membranes because of this ion exchange and this can be measured as an electrical voltage change [2]. sEMG signals are collected from the skin as an electric voltage ranging between -5 and +5 mV. The control of the myoelectric-based prosthesis is difficult because of the dynamic nature of the EMG signal [1] due to varying motor unit recruitment, crosstalk, and biochemical interaction within the muscular fibres. In addition, sEMG changes continuously due to the onset and progression of muscle fatigue [1].

Muscle fatigue is complex in nature and results in failure to maintain the required force level [3]. Reasons for fatigue can be the peripheral changes at the muscle level or an inadequate output from the central nervous system to stimulate motoneurons [3]. The amount of force generated, duration of each contraction, and the rest period between two contractions has a direct influence on the muscle fatigue rate [4]. Muscle fibre-type distribution [5], nerve conduction velocity of fatiguing muscles, or even factors within the central nervous system (CNS) affect EMG signals [6]. EMG analysis is a well-accepted method for muscle fatigue assessment [6].

In 1977, L. Lindstrom, R. Kadefors and I. Petersen developed a method that measures the localized muscle fatigue based on the power spectrum analysis using myoelectric signals [7]. This approach permits real-time investigations and can yield statistically based criteria for the occurrence of fatigue. Rate of fatigue development and changes in muscle action potential conduction velocity were used to interpret the findings [7]. Additional recruitment of motor units, synchronization of active motor units along the muscle fibres, and a decrease in conduction velocity are reflected in the EMG signal as an increase of amplitude in time domain and a decrease of medium frequency in frequency domain [8].

The joint analysis method using EMG amplitude and spectrum (JASA) allows distinguishing between the difference of fatigue-induced and force related EMG changes. Simultaneous changes in the EMG amplitude and spectrum are considered in the JASA approach [9]. The JASA principle states that muscle force decreases because of the decrease in EMG amplitude [9]. Fatigue can occur because of continuous high frequency stimulation or because of titanic stimulation. The Flow Chart of the work in this paper is shown in Figure 1.

This paper addresses the issue of skeletal muscle fatigue that is a dynamic phenomenon. The modeling is based on system identification, where mathematical relations are inferred from experimental data. The data consists of sEMG signals and hand/finger force generated by healthy subjects. The recorded three-sEMG signals are filtered using nonlinear Half-Gaussian Bayesian filters

Parmod Kumar is with Measurement and Control Engineering Research Center (MCERC), College of Engineering, Idaho State University, Pocatello, Idaho 83209, USA (email: kumaparm@isu.edu).

Anish Sebastian is with MCERC, College of Engineering, Idaho State University, Pocatello, Idaho 83209, USA (email: sebaanis@isu.edu).

Chandrasekhar Potluri is with MCERC, College of Engineering, Idaho State University, Pocatello, Idaho 83209, USA (e-mail: potlchan@isu.edu).

Alex Urfer is with Department of Physical and Occupational Therapy, Idaho State University, Pocatello, Idaho 83209, USA (email: urfealex@isu.edu).

D. Subbaram Naidu is with Department of Electrical Engineering, MCERC, Idaho State University, Pocatello, Idaho 83201 USA (email: naiduds@isu.edu).

Marco P. Schoen is with Department of Mechanical Engineering, MCERC, Idaho State University, Pocatello, Idaho 83209, USA (email: schomarc@isu.edu).

with optimized filter parameters, whereas the skeletal muscle force signal is pre-processed using a Chebyshev type-II filter [1, 10].

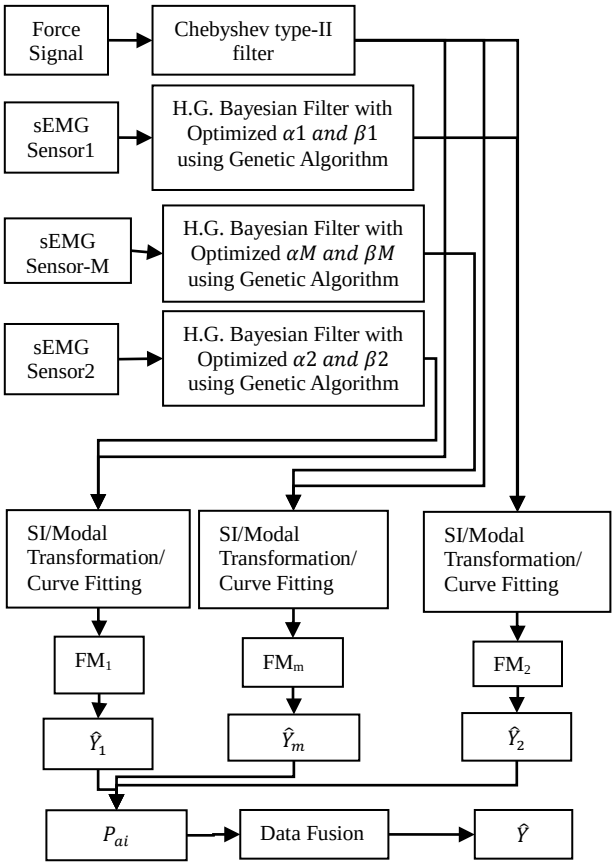

Figure 1: The Flow Chart of the Work in this Paper.

A simple Genetic Algorithm code is used to optimize the Bayesian filter parameters. Using an input/output approach, the EMG signal is the input to the skeletal muscle, and the produced hand/finger force constitutes the output. Three discrete time state-space models are obtained using system identification and modal transformation for three sets of sensors. One sensor is placed at the motor unit of the ring finger of the dominant hand and two sensors are located in its vicinity as shown in Figure 2. The extracted models from the data sets are fused with a probabilistic Kullback Information Criterion (KIC) for model selection. The final fused output is estimated with an adaptive probability of KIC that gives an improved skeletal muscle force estimates.

II. Experimental Set-up and Pre–processing

Both sEMG and muscle force signals were acquired simultaneously using LabVIEW™ 8.2 at a sampling rate of 2000 Hz. The sEMG data capturing was aided by a DELSYS® Bagnoli-16 EMG system with DE-2.1 differential EMG sensors. The corresponding force data was captured using NI ELVIS with Interlink Electronics FSR 0.5" circular force sensor. The experimental set-up is shown in Figure 2. One sEMG sensor was placed on the motor point of ring finger and two adjacent to the motor point of a healthy subject. Prior to placing the sEMG sensors, the skin surface of the subject was prepared according to International Society of Electrophysiology and Kinesiology (ISEK) protocols.

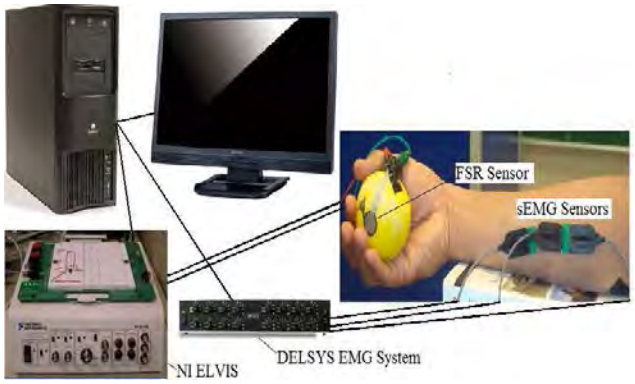

Figure 2: Experimental Set-Up.

The EMG signal is modeled for the conditional probability of the rectified EMG signal as a filtered random process with random rate. The likelihood function for the rate evolves in time according to a Fokker–Planck partial differential Equation [10]. Here, α and β are two free parameters, α is the expected rate of gradual drift in the signal, and β is the expected rate of sudden shifts in the signal. These two free parameters of the non-linear "Half-Gaussian filter model" are optimized for the acquired EMG data using an elitism based Genetic Algorithm. A Chebyshev type II low pass filter with a 550 Hz pass frequency is used to filter the force signal.

III. System Identification and Modal Transformation

An alternative to physically based mathematical modeling is data based -'system identification (SI)'- that can be applied to different systems where it needs sufficient experimental data [11]. The parametric system identification process yields a dynamical model such as the Auto Regressive with exogenous input (ARX) or Output Error (OE) model, this model gives us the system in mathematical form. In this work, the SI approach is used with the myolelectric signal as the input to the system and as the output is the intended finger/hand force. In this work, we are using an output error (OE) model structure for the modeling of EMG and hand/finger force signals, which has been documented in the literature to perform well for EMG signals among linear parametric models [1]. Each OE model takes the form of Equation (1),

$$y(t) = \frac{B(q)}{F(q)} u(t - n_k) + e(t), \qquad (1)$$

where t is time index, $y(t)$ is output, $u(t - n_k)$ is input, n_k is the delay, $e(t)$ is the error, and $B(q)$ and $F(q)$ are polynomials.

A common OE model is obtained for each sensor data set using one set of model parameters (polynomial order). The OE models then are converted into a state-space formulation. By doing this, the identification properties of

the OE model formulation are preserved and represented in the state-space form. A modal form is computed by using state-space matrices and following transformation:

$$\Lambda = \mathrm{T}^{-1}\mathrm{AT}, \Omega = \mathrm{T}^{-1}\mathrm{B}, \Gamma = C\mathrm{T}, \quad (2)$$

where T is the matrix composed of the eigenvectors of A, Λ, Ω and Γ are corresponding transformations for matrix A, B, and C. Matrix D came out to be a zero matrix for the cases treated in this work. Equation (2) refers to the continuous representation of the identified models. Using the modal form representation for each corresponding data set, the influence of fatigue can be observed by charting the modal coefficients in time for each matrix. For example, the coefficients contained in the transformed matrix Λ can be plotted in the complex *s*-plane. This tracking can then be used as the basis for constructing polynomials that connect each element of each matrix in time with the corresponding time stamp. Hence, a fatigue model in state-space description is constructed, where the input is the recorded EMG signal and the output the expected force generated by the hand motion all as a function of time.

IV. Fusion of Outputs and Adaptive Probability of KIC

Multiple model fusion is done by assigning a particular probability to each individual model [12]. These models are obtained using SI for three sEMG sensors for single motor unit. SI model fit value is used to compute the probability for each model. The fit value is given by $\left[1 - \frac{|Y-\hat{Y}|}{|Y-\bar{Y}|}\right] * 100$. The model selection criterion used in this paper is Kullback information criterion (KIC), which is an asymmetric measure. The sum of two directed divergences, which is the measure of the models dissimilarity, is known as Kullback's symmetric or J-divergence [13], as given by Equation (3).

$$KIC(p_i) = \frac{n}{2}\log R_i + \frac{(p_i+1)n}{n-p_i-2} - n\psi\left(\frac{n-p_i}{2}\right) + g(n), \quad (3)$$

where $g(n) = n * \log(n/2)$.

Following fusion technique is applied for sEMG – force identification models, which is based on [12].

1) Identify OE models $M_1,\ M_2, \ldots, M_{k1}$ using sEMG data (u) as input and force data (Y) as output, for $k1$ number of sensors collecting data simultaneously.
2) Compute the residual square norm

$R_i = \left\|Y - \Phi_i\widehat{\Theta}_i\right\|^2 = \left\|Y - \hat{Y}\right\|^2$,

where $\widehat{\Theta}_i = \{{\Phi_i}^T\Phi_i\}^{-1}{\Phi_i}^T Y$, and

$$\Phi = \begin{bmatrix} Y_p^T & u_p^T & Y_{p-1}^T & \ldots & u_1^T \\ Y_{p+1}^T & u_{p+1}^T & Y_p^T & \ldots & u_2^T \\ \vdots & \vdots & \vdots & \ddots & \vdots \\ Y_{n-1}^T & u_{n-1}^T & Y_{n-2}^T & \ldots & u_{n-p}^T \end{bmatrix}.$$

3) Calculate the model criteria coefficient using Equation (3).
4) Compute the model probability $p(M_i|Z) = \frac{e^{-l_i}}{\sum_{j=1}^{k1} e^{-l_j}}$, where l is model selection criterion, i.e. $KIC(p_i)$.
5) Compute the fused model output $\hat{Y}_f = \sum_{i=1}^{k1} p(M_i|Z)\hat{Y}_i$.
6) Compute the overall OE model from $\hat{Y}_f$ and force data.

Here all the computation from step 2) to step 6) is adaptive i.e. the residual square norm, $KIC(p_i)$, model probability $p(M_i|Z)$, and fused model output $\hat{Y}_f$ are being updated with time or for each data point.

V. Results, Conclusion and Future Work

Based on previous research results and after trying different model orders for sEMG/Force data, an optimal model order of $n_b = 2, n_f = 2, n_k = 1$ is used in this work. Equation (4), (5), and (6) give three resulting discrete time state-space sEMG-Force-Fatigue models for motor point sensor, sensor-1 and sensor-2 respectively.

$$x_m(h+1) = A_m x_m(h) + B_m EMG_m(h);$$
$$\hat{Y}_m(h) = C_m x_m(h) + D_m EMG_m(h). \quad (4)$$

$$x_1(h+1) = A_1 x_1(h) + B_1 EMG_1(h);$$
$$\hat{Y}_1(h) = C_1 x_1(h) + D_1 EMG_1(h). \quad (5)$$

$$x_2(h+1) = A_2 x_2(h) + B_2 EMG_2(h);$$
$$\hat{Y}_2(h) = C_2 x_2(h) + D_2 EMG_2(h). \quad (6)$$

In these case matrices D_m, D_1, and D_2 are zero matrices, whereas matrices $A_m, B_m, C_m, A_1, B_1, C_1, A_2, B_2$, and C_2 are given as: $A_m = \begin{bmatrix} a_{m1}(t) & 0 \\ 0 & a_{m2} \end{bmatrix}$; $B_m = \begin{bmatrix} b_{m1}(t) \\ b_{m2}(t) \end{bmatrix}$;

$C_m = [c_{m1}(t)\ \ c_{m2}(t)]$; $A_1 = \begin{bmatrix} a_{11} & 0 \\ 0 & a_{12} \end{bmatrix}$;

$B_1 = \begin{bmatrix} b_{11} \\ b_{12} \end{bmatrix}$; $C_1 = [c_{11}\ \ c_{12}]$; $A_2 = \begin{bmatrix} a_{21}(t) & 0 \\ 0 & a_{22} \end{bmatrix}$; $B_2 = \begin{bmatrix} b_{21}(t) \\ b_{22}(t) \end{bmatrix}$; and $C_2 = [c_{21}(t)\ \ c_{22}(t)]$; where the elements of matrices A_m, B_m, C_m, A_2, B_2, and C_2 are function of time and the elements of matrices A_1, B_1, and C_1 are constants for this particular data set. The time variables $a_{m1}(t), a_{m2}(t), b_{m1}(t), b_{m2}(t), c_{m1}(t), c_{m2}(t)$, $a_{21}(t), a_{22}(t), b_{21}(t), b_{22}(t), c_{21}(t)$, and $c_{22}(t)$ are given by quadratic polynomials obtained by curve fitting the tracked modal transformed coefficients. These time variables are given as:

$a_{m1}(t) = 0.00026t^2 - 0.033t - 11;$
$a_{m2}(t) = -0.0018t^2 + 0.24t - 33;$
$b_{m1}(t) = -0.002t^2 + 0.33t + 42;$
$b_{m2}(t) = -0.0017t^2 + 0.33t + 25;$
$c_{m1}(t) = (3.2 * 10^{-7})t^2 - (4.2 * 10^{-5})t + 0.71;$
$c_{m2}(t) = (4.6 * 10^{-8})t^2 - (5.8 * 10^{-6})t - 0.71;$
$a_{21}(t) = -(1.2 * 10^{-5})t^2 + 0.0013t - 0.47;$
$a_{22}(t) = 0.001t^2 - 0.037t - 35;$
$b_{21}(t) = (6.4 * 10^{-6})t^2 - 0.001t + 0.3;$
$b_{22}(t) = 0.0023t^2 - 0.12t - 75;$

$c_{21}(t) = -(1.8 * 10^{-7})t^2 + (6.4 * 10^{-6})t + 0.71$; and $c_{22}(t) = -(2.1 * 10^{-9})t^2 + (2.4 * 10^{-7})t - 0.71$.
Elements of matrices A_1, B_1, and C_1 are constants for this particular data set, they are given as:

$a_{11} = -0.0159$; $a_{12} = -43.1883$; $b_{11} = 0.0090$; $b_{12} = -72.1875$; $c_{11} = 0.7147$; and $c_{12} = -0.7071$.

The discrete models have a sampling time of $\Delta t = 0.0005$ seconds. The duration of the final estimated and fused output for three sensors is 37.36 seconds. Figure 3 depicts the probability and 10th degree curve fitting for motor point, ring2 and ring1 sensor signals.

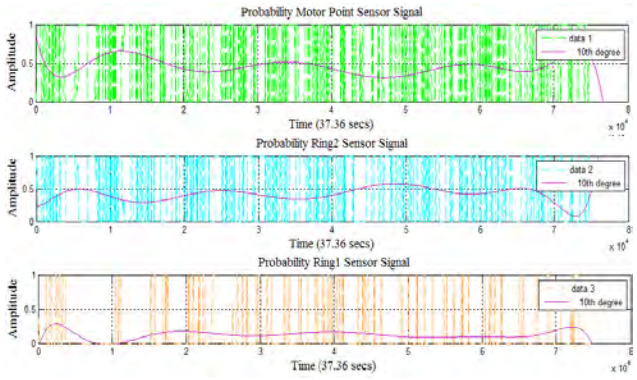

Figure 3: 10th Degree Curve Fitting – Probability Motor, Ring2 and Ring1 Sensor Signals.

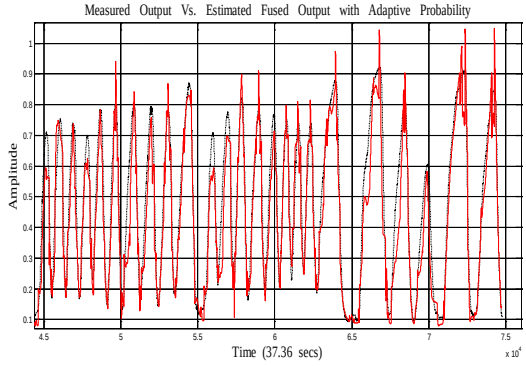

Figure 4: Measured Output Vs. Estimated Fused Output with Adaptive Probability.

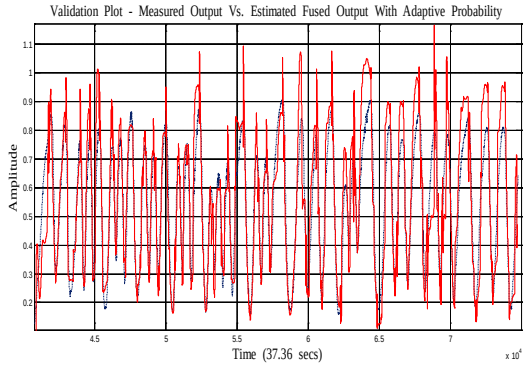

Figure 5: Validation Plot - Measured Vs. Estimated Fused Output with Adaptive Probability.

Figure 4 and Figure 5 shows the measured and estimated fused output, depending on the error between the two later follows the measured signal very closely. This approach identifies a fused fatigue model and estimates an adaptive probability based output that follows the measured output very closely. The outcome of this research can be used to estimate the skeletal muscle force of a human hand for prosthetic hand design, application and improvement.

In future work improvement of the data collection techniques and sEMG sensor design, may lead to improved force estimation.

ACKNOWLEDGMENT

This work was supported by a grant from the Telemedicine Advanced Technology Research Center (TATRC) – Department of Defense. The financial support is greatly appreciated.

REFERENCES

[1] Jeffrey T. Bingham and Marco P. Schoen, "Characterization of Myoelectric Signals using System Identification Techniques," *Proceedings of IMECE 2004: 2004 ASME International Mechanical Engineering Congress Anaheim, California*, November 13-19, 2004.

[2] Northrop, R., *Analysis and application of analogue electronic circuits to biomedical instrumentation.* CRC Press, Boca Raton, Florida, 2004, pp. 6–9.

[3] S. C. Gandevia, "Spinal and Supraspinal Factors in Human Muscle Fatigue," *Physiological Reviews, American Physiological Society*, 81(4), October 2001.

[4] B R Bigland-Ritchie, N J Dawson, R S Johansson and O C Lippold, "Reflex origin for the slowing of motoneurone firing rates in fatigue of human voluntary contractions," *Journal of Physiology*, 379, pp. 451-459, 1986.

[5] Gerdle B, Edstrom M, Rahm M, "Fatigue in the shoulder muscles during static work at two different torque levels," *Clinical Physiology, 13(5)*, pp. 469-482, 1993.

[6] Merletti R, and Lo Conte LR, "Surface EMG signal processing during isometric contractions," *Journal of Electromyography and Kinesiology*, 7(4), pp. 241-250, 1997.

[7] Finsterer J., "EMG-interference pattern analysis," *J Electromyogr Kinesiol*, 11, pp. 231-246, 2001.

[8] B. Maton, and D. Gamet, "The fatigability of two agonistic muscles in human isometric voluntary sub maximal contraction: an EMG study. II Motor unit firing rate and recruitment," *Eur. J. Appl. Physiol.*, 58, pp. 369-374, 1989.

[9] A. Luttmann, M. Ja¨ger, J. So¨keland, and W. Laurig, "Electromyographical study on surgeons in urology, Part II: Determination of muscular fatigue," *Ergonomics*, 39, pp. 298-313, 1996.

[10] Terence D. Sanger, "Bayesian Filtering of Myoelectric Signals," *J Neurophysiol* 97, pp. 1839–1845, 2007.

[11] Lennart Ljung, *System Identification: Theory for the User*. 2nd edition, Printice Hall PTR, 1999, Chap. 1, pp. 1-15.

[12] H. Chen and S. Huang, "A Comparative study on Model Selection and Multiple Model Fusion," *7th International Conference on Information Fusion*, pp. 820-826, 2005.

[13] Abd-Krim Seghouane, M. Bekara, G. Fleury, "A Small Sample Model Selection Criterion Based on Kullback's symmetric Divergence," *IEEE Transaction*, pp. 145-148, 2003.

An Adaptive Multi Sensor Data Fusion with Hybrid Nonlinear ARX and Wiener-Hammerstein Models for Skeletal Muscle Force Estimation

PARMOD KUMAR, CHANDRASEKHAR POTLURI, ANISH SEBASTIAN, STEVE CHIU, ALEX URFER, D. SUBBARAM NAIDU, and MARCO P. SCHOEN
Measurement and Control Engineering Research Center, College of Engineering
Idaho State University
921 South 8th Avenue, Stop 8060, Pocatello, Idaho
USA
schomarc@isu.edu http://isu.edu/~schomarc

Abstract: - Skeletal muscle force can be estimated using surface electromyographic (sEMG) signals. Usually, the sEMG location for the sensors is near the respective muscle motor unit points. Skeletal muscles generate a temporal and spatial distributed EMG signal, which causes cross talk between different sEMG signal sensors. In this paper, an array of three sEMG sensors is used to capture the information of muscle dynamics in terms of sEMG signals and generated muscle force. The recorded sEMG signals are filtered utilizing optimized nonlinear Half-Gaussian Bayesian filter, and a Chebyshev type-II filter prepares the muscle force signal. The filter optimization is accomplished using Genetic Algorithm (GA). Multi nonlinear Auto Regressive eXogenous (ARX) and Wiener-Hammerstein models with different nonlinearity estimators/classes are obtained using system identification (SI) for three sets of sensor data. The outputs of these models are fused with a probabilistic Kullback Information Criterion (KIC) for model selection and an adaptive probability of KIC. First, the outputs are fused for the same sensor and for different models and then the final outputs from each sensor. The final fusion based output of three sensors provides good skeletal muscle force estimates.

Key-Words: - sEMG, ARX, Weiner-Hammerstein, KIC, SI, GA

1 Introduction

Aftereffects of the loss of upper limbs are a reduction of functionality and psychological disturbance for the person. According to [1] there are 1.7 million peoples with amputation in the United States and this number is on rise after the Afghanistan and Iraq war in 2003 [2]. Conversely, a prosthetic limb can considerably increase the functionality of an amputee and benefit the person in everyday life.

In the past, there have been various research works towards prosthetic hand design, having similar functionality and appearance as human hand [3-4]. Most of these research works are based on electromyography (EMG). The EMG signal is activated and controlled by the central nervous system, which depends on the flow of specific ions such as sodium (Na^+), potassium (K^+) and calcium (Ca^{++}).

An EMG signal recorded on the surface of the limb is expressed as an electric voltage ranging between -5 and +5 mV. This method is known as surface electromyography (sEMG). sEMG is utilized as an input to the controller to realize the movements of the prosthesis and force control [5-6]. Past research results show that EMG signal amplitude generally increases with skeletal muscle force. However, this relationship is not always rigid; various factors affect this relationship. EMG signals are a result of the varying motor unit recruitments, crosstalk, and biochemical interaction within the muscular fibres. This makes EMG signals random, complex and dynamic in nature and the control of the prosthesis difficult. Moreover, it changes continuously due to the onset and progression of muscle fatigue which results because of continuous high frequency stimulation or because of titanic stimulation [7]. Synchronization of active motor units along the muscle fibres, and a decrease in conduction velocity are reflected in the EMG signal as an increase of amplitude in time domain and a decrease of medium frequency in frequency domain [8]. All these factors make the relationship between EMG and force nonlinear. Correct interpretation of EMG signal is vital to achieve precise motion and force control of prosthesis.

The present work presents a novel approach to estimate skeletal muscle force using an adaptive multi-sensor data fusion algorithm with hybrid nonlinear ARX and Wiener-Hammerstein models. Here, an array of three sEMG sensors is used to capture the information of muscle dynamics in terms of sEMG signals. The recorded sEMG signals are filtered utilizing optimized nonlinear Half-Gaussian Bayesian filter parameters, and the skeletal muscle force signal is filtered by using a Chebyshev type-II filter. A simple Genetic Algorithm

code is used to optimize the Bayesian filter parameters. Using an input/output approach, the EMG signal measured at the skin surface is considered as input to the skeletal muscle, whereas the resulting hand/finger force constitutes the output. Multi nonlinear ARX and Wiener-Hammerstein models with different nonlinearity estimators/classes are obtained using SI for three sets of sensor data obtained from the vicinity of a single motor unit. Different nonlinearity estimators/classes are used for nonlinear modeling as they capture the dynamics of the system differently. The outputs of estimated nonlinear models are fused with a probabilistic Kullback Information Criterion (KIC) for model selection and an adaptive probability of KIC. First, the outputs are fused for the same sensor and for different models and then the final outputs from each sensor. The final fused output of three sensors provides good skeletal muscle force estimates.

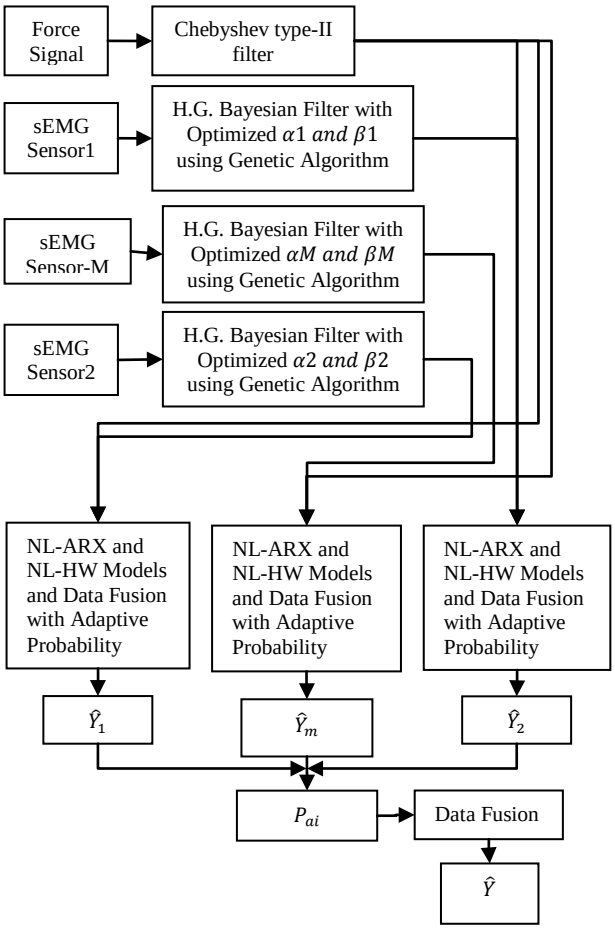

Fig. 1: The Flow Chart for Skeletal Muscle Force Estimation.

Fig. 1 shows the flow chart for skeletal muscle force estimation. This paper is structured as follows. First, the experimental set-up, pre-processing and filter parameter optimization for sEMG signals are discussed. Second, nonlinear ARX and Wiener-Hammerstein modeling are covered. Third, the fusion of various nonlinear model outputs using KIC and adaptive probability of KIC is covered. Finally, the results, discussion and future work are provided followed by a conclusion to summarize the importance of this work.

2 Experimental Set-Up and Pre-Processing

The experimental set-up is shown in Fig. 2. Both sEMG and muscle force signals were acquired simultaneously using LabVIEW™ at a sampling rate of 2000 Hz. The sEMG data capturing was aided by a DELSYS® Bagnoli-16 EMG system with DE-2.1 differential EMG sensors. The corresponding force data was captured using Interlink Electronics FSR 0.5" circular force sensor. One sEMG sensor was placed on the motor point of the ring finger and two adjacent to the motor point of a healthy subject. Prior to placing the sEMG sensors, the skin surface of the subject was prepared according to International Society of Electrophysiology and Kinesiology (ISEK) protocols.

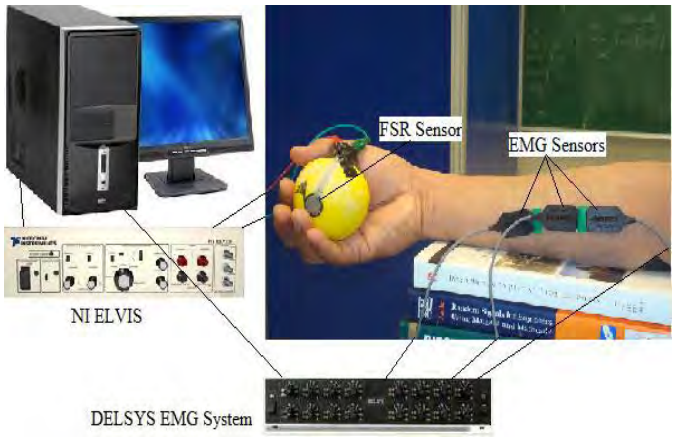

Fig. 2: Experimental Set-Up.

According to previous research, the Bayesian based filtering method yields the most suitable sEMG signals [9]. The nonlinear filter significantly reduces noise and extracts a signal that best describes EMG signals and may permit effective use in prosthetic control. An instantaneous conditional probability density $P(EMG|x)$ provides the resulting EMG for the latent driving signal x [9]. The model for the conditional probability of the rectified EMG signal $emg = |EMG|$ is used in this current estimation algorithm. EMG signals are usually described as amplitude-modulated zero mean Gaussian noise sequence [10]. For the rectified EMG signal, the "Half-Gaussian measurement model" in [9] is given by Equation (1).

$$P(emg|x) = 2 * exp(-\frac{emg^2}{2*x^2})/(2 * \pi * x^2)^{1/2}. \quad (1)$$

The EMG signal is modeled for the conditional probability of the rectified EMG signal as a filtered random process with random rate. The likelihood function for the rate evolves in time according to a

Fokker–Planck partial differential equation [9]. The discrete time Fokker–Planck Equation is given by equation (2).

$$p(x,t-) \approx \alpha * p(x-\varepsilon,t-1) + (1-2*\alpha) * p(x,t-1) + \alpha * p(x+\varepsilon,t-1) + \beta + (1-\beta) * p(x,t-1). \quad (2)$$

Here, α and β are two free parameters, α is the expected rate of gradual drift in the signal, and β is the expected rate of sudden shifts in the signal. The unknown driving signal x is discretized into bins of width ε. These two free parameters of the non-linear Half-Gaussian filter model are optimized for the acquired EMG data using elitism based GA.

A Chebyshev type II low pass filter with a 550 Hz pass frequency is used to filter the force signal. Fig. 3 depicts the raw and Chebyshev type-II low pass filtered force signals.

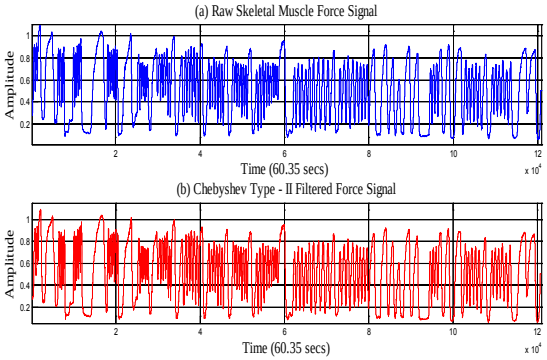

Fig. 3: (a) Raw and (b) Chebyshev Type-II Filtered Skeletal Muscle Force Signals.

3 Nonlinear ARX and Wiener-Hammerstein Modeling

In this paper, we are using nonlinear ARX and Wiener-Hammerstein models with different nonlinearity estimators/classes to model three sEMG sensors data as input and skeletal muscle force data as output. The nonlinear ARX model uses a parallel combination of nonlinear and linear blocks [11].

Fig. 4 shows the nonlinear ARX model structure. The nonlinear ARX model uses regressors as variables for nonlinear and linear functions. Regressors are functions of measured input-output data [11]. The predicted output $\hat{y}(t)$ of a nonlinear model at time t is given by the general Equation (3):

$$\hat{y}(t) = F(x(t)) \quad (3)$$

where $x(t)$ represents the regressors, F is a nonlinear regressor command, which is estimated by nonlinearity estimators/classes [11]. As shown in Fig. 4, the command F can include both linear and nonlinear functions of $x(t)$. Equation (4) gives the description of F.

$$F(x) = \sum_{k=1}^{d} \alpha_k \, \kappa(\beta_k(x-\gamma_k)) \quad (4)$$

where κ is the unit nonlinear command, d is the number of nonlinearity units, and α_k, β_k and γ_k are the parameters of the nonlinearity estimators/classes [11].

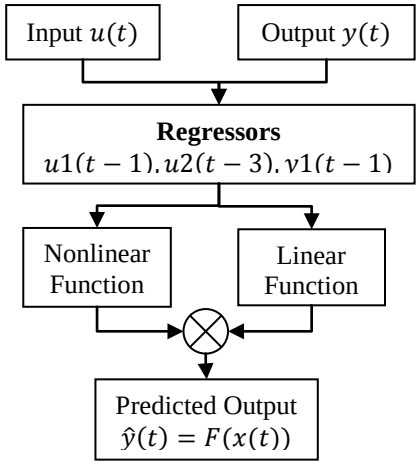

Fig. 4: Nonlinear ARX Model Structure.

The Wiener-Hammerstein model uses one or two static nonlinear blocks in series with a linear block. Structural representation of a nonlinear Wiener-Hammerstein is shown in Fig. 5 [11].

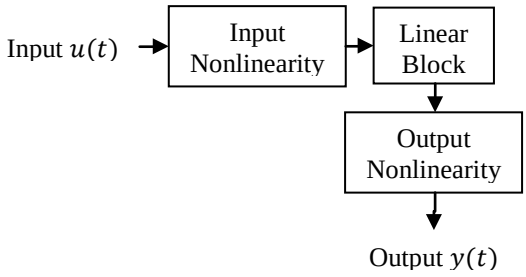

Fig. 5: Nonlinear Wiener-Hammerstein Model Structure.

The general Equations (5), (6), and (7) can describe the Wiener-Hammerstein structure [11].

$$w(t) = f(u(t)) \quad (5)$$

$$x(t) = \frac{B_{j,i}(q)}{F_{j,i}(q)} w(t) \quad (6)$$

$$y(t) = h(x(t)). \quad (7)$$

where $u(t)$ and $y(t)$ are input and output of the system, respectively, f and h are nonlinear functions, which corresponds to input and output nonlinearity, respectively, $w(t)$ and $x(t)$ are internal variables, where $w(t)$ has the same dimensions as $u(t)$ and $x(t)$ has the same dimensions as $y(t)$, and $B(q)$ and $F(q)$ corresponds to the linear dynamic block, these are polynomials in the backward shift operator.

The nonlinearity classes used in this work are Wavenet, Treepartition, Sigmoidnet, Pwlinear, Saturation, and Deadzone. For motor point and ring1 sensors, three nonlinear ARX and four nonlinear Wiener-Hammerstein models with different nonlinearity

estimators/classes are obtained. For ring2 sensor, three nonlinear ARX and five nonlinear Wiener-Hammerstein models with different nonlinearity estimators/classes are obtained.

4 Data Fusion and Adaptive KIC Probability

Data fusion of multiple outputs of nonlinear ARX and Wiener-Hammerstein models is done by assigning a particular probability to each individual model [12]. First, the fusion algorithm is applied to the outputs of different nonlinear ARX and Wiener-Hammerstein models for each sensor obtained using different nonlinearity estimators. Second, the fusion algorithm is again applied to the final fusion based outputs of each sensor; this gives good force estimate. SI model fit value gives the probability for each model, which is given by $\left[1-\frac{|Y-\hat{Y}|}{|Y-\bar{Y}|}\right]*100$. The model selection criterion used in this paper is KIC. The sum of two directed divergences, which is the measure of the models dissimilarity, is known as Kullback's symmetric or J-divergence [13], as given by Equation (8).

$$KIC(p_i) = \frac{n}{2}\log R_i + \frac{(p_i+1)n}{n-p_i-2} - n\psi\left(\frac{n-p_i}{2}\right) + g(n), \quad (8)$$

where $g(n) = n*\log(n/2)$.

The following fusion algorithm as given by [12] is applied for data fusion of the outputs of different nonlinear ARX and Wiener-Hammerstein models:

1) Identify models $M_1, M_2, \dots, M_k$ using sEMG data (u) as input and force data (Y) as output, for k number of sensors collecting data simultaneously.

2) Compute the residual square norm

$R_i = \left\|Y - \Phi_i\widehat{\Theta}_i\right\|^2 = \left\|Y - \hat{Y}\right\|$, where $\widehat{\Theta}_i = \{{\Phi_i}^T\Phi_i\}^{-1}{\Phi_i}^T Y$, and

$$\Phi = \begin{bmatrix} Y_p^T & u_p^T & Y_{p-1}^T & \dots & u_1^T \\ Y_{p+1}^T & u_{p+1}^T & Y_p^T & \dots & u_2^T \\ \vdots & \vdots & \vdots & \ddots & \vdots \\ Y_{n-1}^T & u_{n-1}^T & Y_{n-2}^T & \dots & u_{n-p}^T \end{bmatrix}.$$

3) Calculate the model criteria coefficient using Equation (8).

4) Compute the model probability $p(M_i|Z) = \frac{e^{-l_i}}{\sum_{j=1}^{k} e^{-l_j}}$, where l is model selection criterion, i.e. $KIC(p_i)$.

5) Compute the fused model output $\hat{Y}_f = \sum_{i=1}^{k} p(M_i|Z)\hat{Y}_i$.

6) Compute the overall model from $\hat{Y}_f$ and force data.

Here all the computation from step 2) to 6) is adaptive i.e. the residual square norm, $KIC(p_i)$, model probability $p(M_i|Z)$, and fused model output $\hat{Y}_f$ are being updated with time or for each data point. Fig. 6 shows the flow chart for fusion of outputs and adaptive probability of KIC.

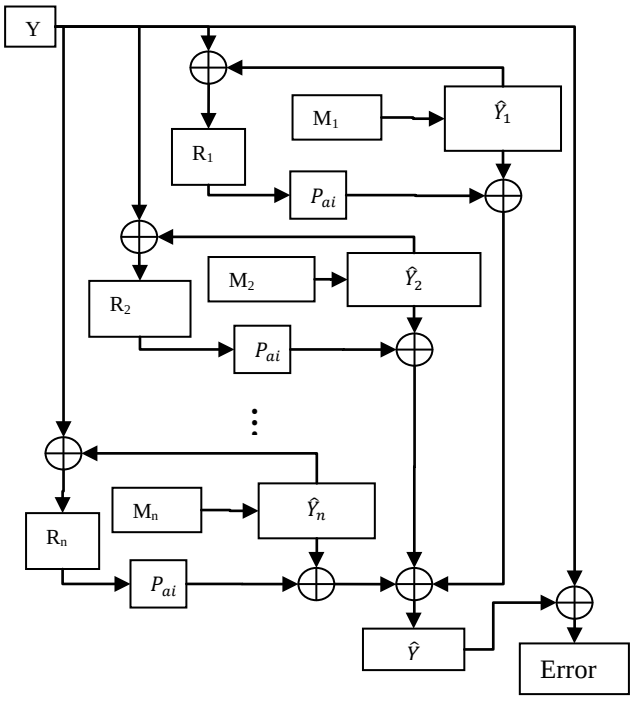

Fig. 6: Data Fusion and Adaptive KIC Probability.

5 Results, Discussion and Future Work

This section deals with the results, discussion and future work. The following plots show the nonlinear (ARX and Wiener-Hammerstein) model and adaptive fusion algorithm based estimated force output for each sensor first and then finally combined adaptive fusion based output for all three sensors. Fig. 7 shows the overlapping plot of the original and adaptive fusion based force output for the motor point sensor. The output is the result of the adaptive fusion algorithm on three nonlinear ARX and four nonlinear Wiener-Hammerstein models for the motor point sensor signal.

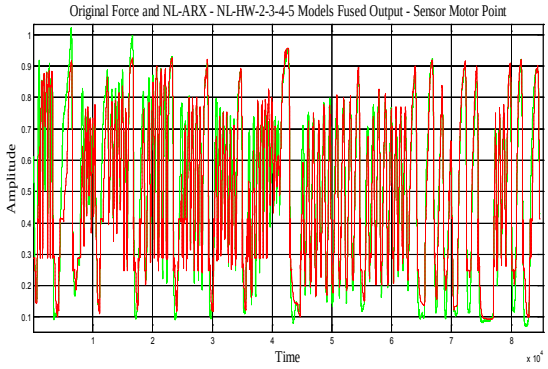

Fig. 7: Original and Fusion Based Output for Motor Point Sensor.

Fig. 8 shows the overlapping plot of the original and adaptive fusion based force output for ring1 sensor. The

output is the result of adaptive fusion algorithm of three nonlinear ARX and four nonlinear Wiener-Hammerstein models for ring1 sensor signal.

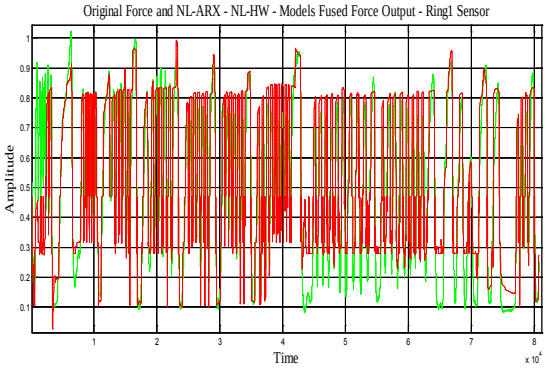

Fig. 8: Original and Fusion Based Output for Ring1 Sensor.

Fig. 9 shows the overlapping plot of the original and adaptive fusion based force output for ring2 sensor. The output is the result of adaptive fusion algorithm on three nonlinear ARX and five nonlinear Wiener-Hammerstein models for ring2 sensor signal.

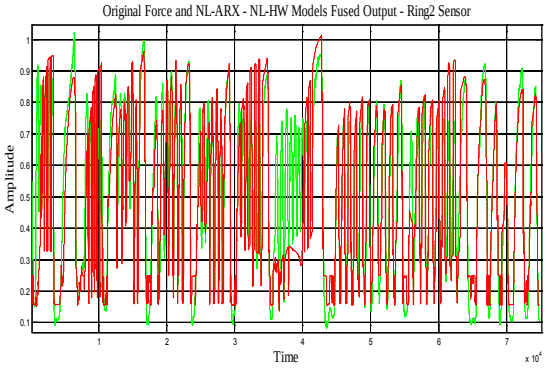

Fig. 9: Original and Fusion Based Output for Ring2 Sensor.

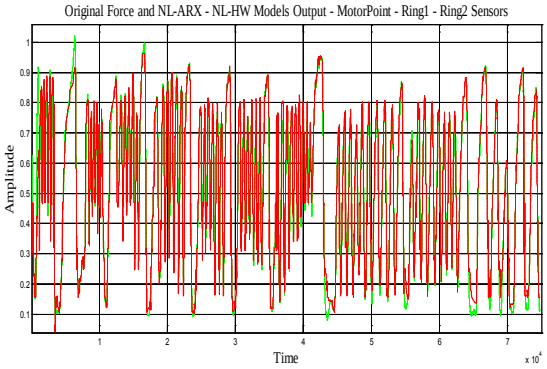

Fig. 10: Final Plot - Original and Fusion Based Output for All Three Sensors.

Fig. 10 shows the overlapping plot of the original and final combined adaptive fusion based force output for motor point, ring1 and ring2 sensors. The output is the result of adaptive fusion algorithm on the final outputs of three sensors i.e. motor point, ring1 and ring2 as shown in Fig. 7 to 9. Fig. 10 shows the best skeletal muscle force estimate, which is the result of the multi nonlinear ARX and Wiener-Hammerstein models and an adaptive hybrid data fusion on these nonlinear models. Fig. 11 shows the error plot of the original and best-estimated model output for the motor point sensor.

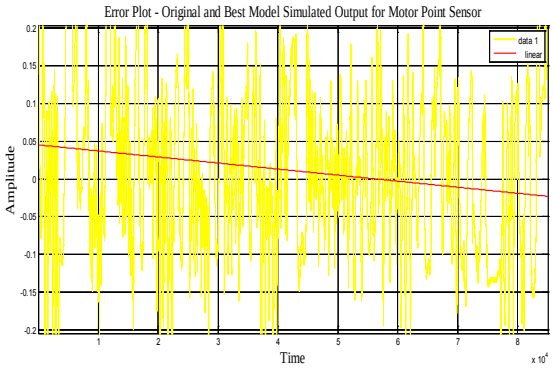

Fig. 11: Error Plot – Original and Best-Estimated Model Output for Motor Point Sensor.

Fig. 12 shows the error plot of original and final multi nonlinear modeled and adaptive hybrid data fusion based force estimate (results from three sensors, nonlinear modeling and adaptive data fusion algorithm). If we compare Fig. 11 and 12, it is very clear and conspicuous that the error has decreased remarkably and is very close to zero.

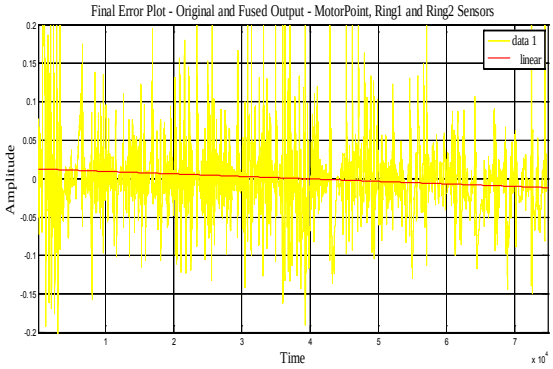

Fig. 12: Final Error Plot – Original and Fusion Based Output for Motor Point, Ring1 and Ring2 Sensors.

Future work will focus on the improvement of the data collection techniques and experimental set-up. By using the combination of linear and nonlinear modeling, and adaptive hybrid data fusion, the skeletal muscle force estimate can be improved further. Furthermore, the authors believe that by using different model selection criteria such as Akaike Information Criterion (AIC), Kullback Information Criterion (KIC) and the Bayesian

Information Criterion (BIC) together to obtain final skeletal muscle force estimate will give improved results.

6 Conclusion

sEMG and force data acquired using three EMG and one common FSR force sensor is modeled using nonlinear SI. Using different nonlinearity estimators/classes, multi nonlinear ARX and Wiener-Hammerstein models are obtained for each sensor. First, the outputs of different models for each sensor are fused with a data fusion algorithm and an adaptive KIC probability. Finally, the fused outputs from each sensor are again fused with same algorithm and adaptive KIC probability. The final estimated force using this technique gives the best estimate.

Acknowledgement

This work was supported by a grant from the Telemedicine Advanced Technology Research Center (TATRC) of the US Department of Defense. The financial support is greatly appreciated.

References:

[1] Kathryn Ziegler-Graham, PhD, et al., Estimating the Prevalence of Limb Loss in the United States - 2005 to 2050, *Archives of Physical Medicine and Rehabilitation,* 89 (2008): 422-429.

[2] O'Connor, P., Iraq war vet decides to have second leg amputated, *Columbia Missourian*, 2009.

[3] N. Dechev, W. L. Cleghorn, and S. Naumann, *Multiple finger, passive adaptive grasp prosthetic hand*, Mechanism and Machine Theory 36(2001), pp. 1157-1173.

[4] Haruhisa Kawasaki, Tsuneo Komatsu, and Kazunao Uchiyama, Dexterous Anthropomorphic Robot Hand With Distributed Tactile Sensor: Gifu Hand II, *IEEE/ASME TRANSACTIONS ON MECHATRONICS,* VOL. 7, NO. 3, SEPTEMBER 2002, pp. 296-303.

[5] M. Zecca, S. Micera, M. C. Carrozza, and P. Dario, Control of Multifunctional Prosthetic Hands by Processing the Electromyographic Signal, *Critical Reviews™ in Biomedical Engineering,* 30(4–6), 2002, pp. 459–485.

[6] Claudio Castellini and Patrick van der Smagt, Surface EMG in advanced hand prosthetics, *Biological Cybernetics*, (2009) 100, pp. 35–47.

[7] Jeffrey T. Bingham and Marco P. Schoen, Characterization of Myoelectric Signals using System Identification Techniques, *Proceedings of IMECE 2004: 2004 ASME International Mechanical Engineering Congress Anaheim, California,* November 13-19, 2004.

[8] C.J. De Luca, Myoelectrical manifestations of localized muscular fatigue in humans, *Crit. Rev. Biomed. Eng.*, 11 (4), 1984, pp. 251-279.

[9] Terence D. Sanger, Bayesian Filtering of Myoelectric Signals, *J Neurophysiol*, 97, 2007, pp. 1839–1845.

[10] M. B. I. Reaz, M. S. Hussain and F. Mohd-Yasin, Techniques of EMG signal analysis: detection, processing, classification and applications, *Biol. Proced. Online*, 2006, 8(1), pp. 11-35.

[11] Lennart Ljung, *System Identification Toolbox™ 7 User's Guide*, The MathWorks, Inc., 2010.

[12] Huimin Chen and Shuqing Huang, A Comparative study on Model Selection and Multiple Model Fusion, *7th International Conference on Information Fusion*, 2005, pp. 820-826.

[13] Abd-Krim Seghouane, Maiza Bekara, and Gilles Fleury, A Small Sample Model Selection Criterion Based on Kullback's symmetric Divergence, *IEEE Transaction*, 2003, pp. 145-148.

Adaptive Multi Sensor Based Nonlinear Identification of Skeletal Muscle Force

PARMOD KUMAR, CHANDRASEKHAR POTLURI, ANISH SEBASTIAN, STEVE CHIU, ALEX URFER, D. SUBBARAM NAIDU, and MARCO P. SCHOEN
Measurement and Control Engineering Research Center, College of Engineering
Idaho State University
921 South 8th Avenue, Stop 8060, Pocatello, Idaho
USA
{kumaparm, potlchan, sebaanis, chiustev, urfealex, naiduds, schomarc}@isu.edu
http://www.isu.edu/~schomarc

Abstract: - Skeletal muscle force and surface electromyographic (sEMG) signals are closely related. Hence, the later can be used for the force estimation. Usually, the location for the sEMG sensors is near the respective muscle motor unit points. EMG signals generated by skeletal muscles are temporal and spatially distributed which results in cross talk that is recorded by different sEMG sensors. This research focuses on modeling muscle dynamics in terms of sEMG signals and the generated muscle force. Here, an array of three sEMG sensors is used to capture the information of the muscle dynamics in terms of sEMG signals and generated muscle force. Optimized nonlinear Half-Gaussian Bayesian filters and a Chebyshev type-II filter are used for the filtration of the sEMG signals and the muscle force signal, respectively. A Genetic Algorithm is used for the optimization of the filter parameters. sEMG and skeletal muscle force is modeled using multi nonlinear Auto Regressive eXogenous (ARX) and Wiener-Hammerstein models with different nonlinearity estimators/classes using System Identification (SI) for three sets of sensor data. An adaptive probabilistic Kullback Information Criterion (KIC) for model selection is applied to obtain the fusion based skeletal muscle force for each sensor first and then for the final outputs from each sensor. The approach yields good skeletal muscle force estimates.

Key-Words: - sEMG, ARX, Weiner-Hammerstein, Prosthetic hand**,** KIC, System Identification,

1 Introduction

Aftereffects of the loss of upper limbs are a reduction of functionality and psychological disturbance for the person. According to [1] there are 1.7 million peoples with amputation in the United States and this number is on rise after the Afghanistan and Iraq war in 2003 [2]. Conversely, a prosthetic limb can considerably increase the functionality of an amputee and benefit the person in everyday life.

In the past, there have been various research works towards prosthetic hand design, having similar functionality and appearance as human hand [3-4]. Most of these research works are based on electromyography (EMG). The EMG signal is activated and controlled by the central nervous system, which depends on the flow of specific ions such as sodium (Na^+), potassium (K^+) and calcium (Ca^{++}).

An EMG signal recorded on the surface of the limb is expressed as an electric voltage ranging between -5 and +5 mV. This method is known as surface electromyography (sEMG). sEMG is utilized as an input to the controller to realize the movements of the prosthesis and force control [5-6]. Past research results show that EMG signal amplitude generally increases with skeletal muscle force. However, this relationship is not always rigid; various factors affect this relationship. EMG signals are a result of the varying motor unit recruitments, crosstalk, and biochemical interaction within the muscular fibres. This makes EMG signals random, complex and dynamic in nature and the control of the prosthesis difficult. Moreover, it changes continuously due to the onset and progression of muscle fatigue which results because of continuous high frequency stimulation or because of titanic stimulation [7]. Synchronization of active motor units along the muscle fibres, and a decrease in conduction velocity are reflected in the EMG signal as an increase of amplitude in time domain and a decrease of medium frequency in frequency domain [7]. All these factors make the relationship between EMG and force nonlinear. Correct interpretation of EMG signal is vital to achieve precise motion and force control of prosthesis.

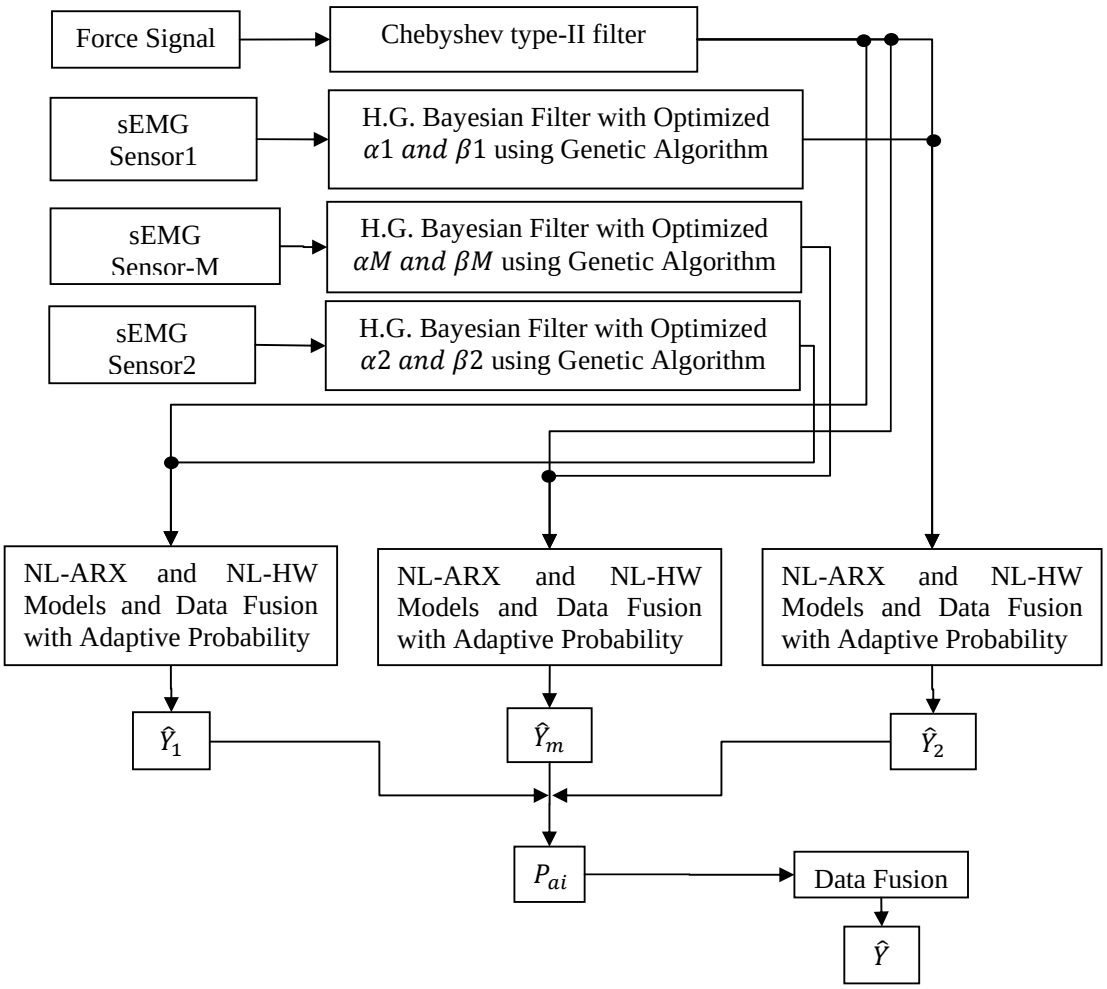

Fig. 1: The Flow Chart for Skeletal Muscle Force Estimation.

The present work presents a novel approach to estimate skeletal muscle force using an adaptive multi-sensor data fusion algorithm with hybrid nonlinear ARX and Wiener-Hammerstein models. Here, an array of three sEMG sensors is used to capture the information of muscle dynamics in terms of sEMG signals. The recorded sEMG signals are filtered utilizing optimized nonlinear Half-Gaussian Bayesian filter parameters, and the skeletal muscle force signal is filtered by using a Chebyshev type-II filter. A simple Genetic Algorithm code is used to optimize the Bayesian filter parameters. Using an input/output approach, the EMG signal measured at the skin surface is considered as input to the skeletal muscle, whereas the resulting hand/finger force constitutes the output. Multi nonlinear ARX and Wiener-Hammerstein models with different nonlinearity estimators/classes are obtained using SI for three sets of sensor data obtained from the vicinity of a single motor unit. Different nonlinearity estimators/classes are used for nonlinear modeling as they capture the dynamics of the system differently. The outputs of estimated nonlinear models are fused with a probabilistic Kullback Information Criterion (KIC) for model selection and an adaptive probability of KIC. First, the outputs are fused for the same sensor and for different models and then the final outputs from each sensor. The final fused output of three sensors provides good skeletal muscle force estimates.

Fig. 1 shows the flow chart for skeletal muscle force estimation. This paper is structured as follows. First, the experimental set-up, pre-processing and filter parameter optimization for sEMG signals are discussed. Second, nonlinear ARX and Wiener-

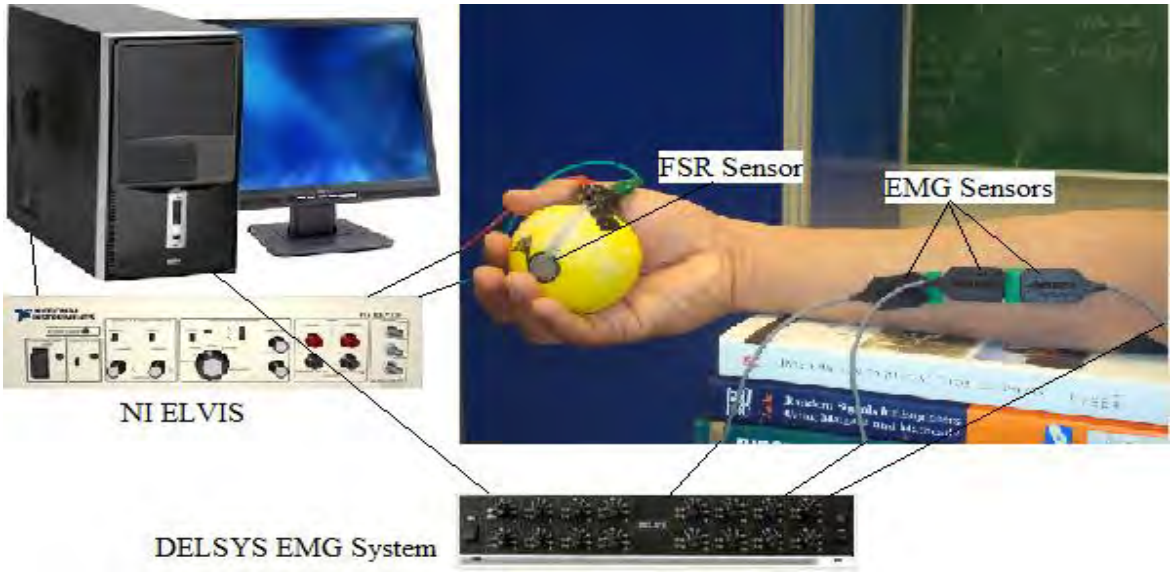

Fig. 2: Experimental Set-Up.

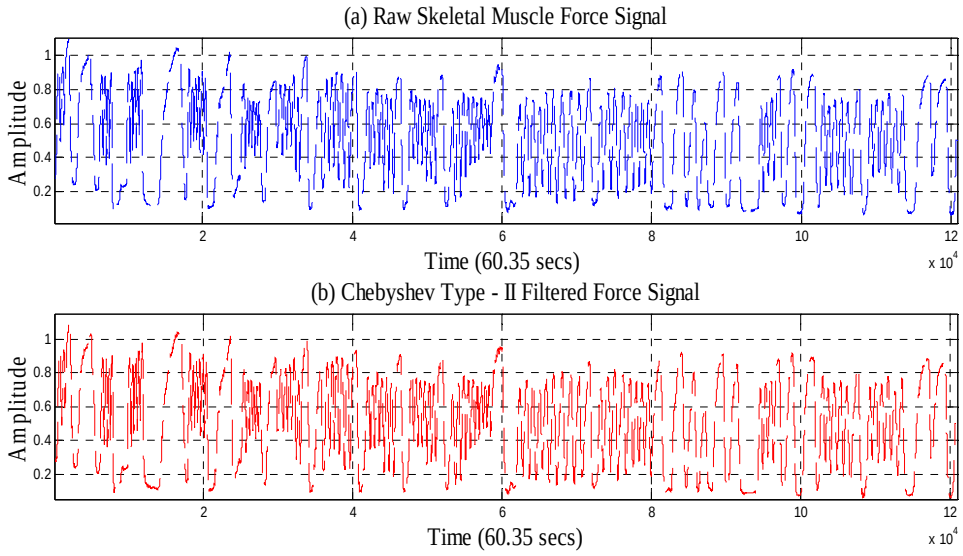

Fig. 3: (a) Raw and (b) Chebyshev Type-II Filtered Skeletal Muscle Force Signals.

Hammerstein modeling is covered. Third, the fusion of various nonlinear model outputs using KIC and adaptive probability of KIC is covered. Finally, the results, discussion and future work are provided followed by a conclusion to summarize the importance of this work.

2 Experimental Set-Up and Pre-Processing

The experimental set-up is shown in Fig. 2. Both sEMG and muscle force signals were acquired simultaneously using LabVIEW™ at a sampling rate of 2000 Hz. The sEMG data capturing was aided by a DELSYS® Bagnoli-16 EMG system with DE-2.1 differential EMG sensors. The

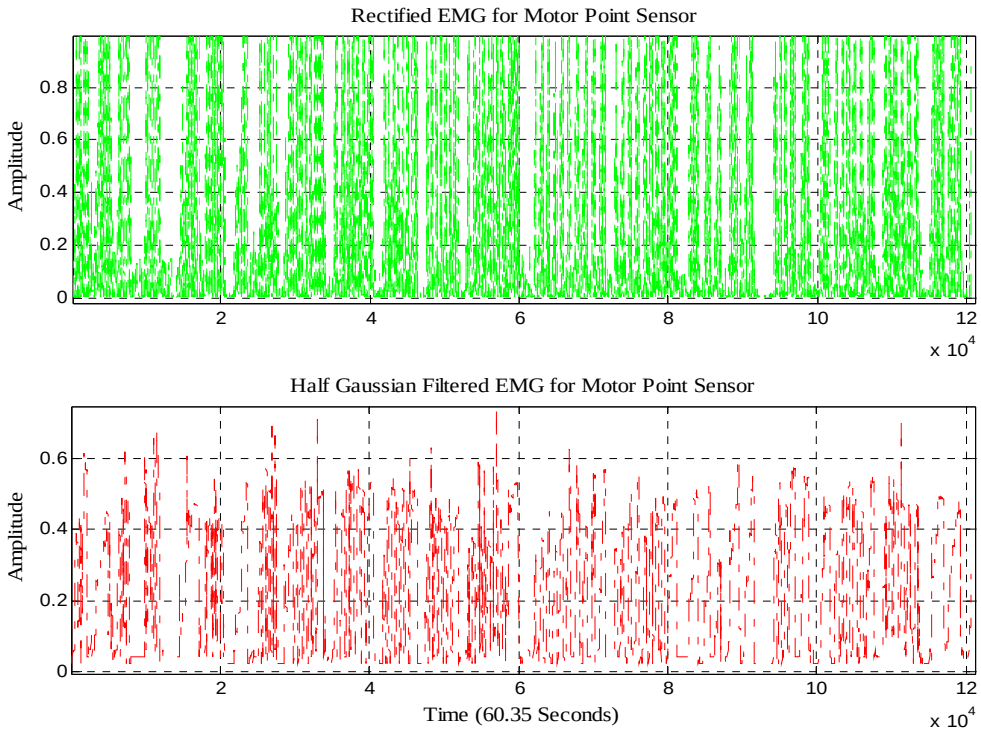

Fig. 4(a): Rectified EMG and Half-Gaussian Filtered EMG Signal for Motor Point Sensor.

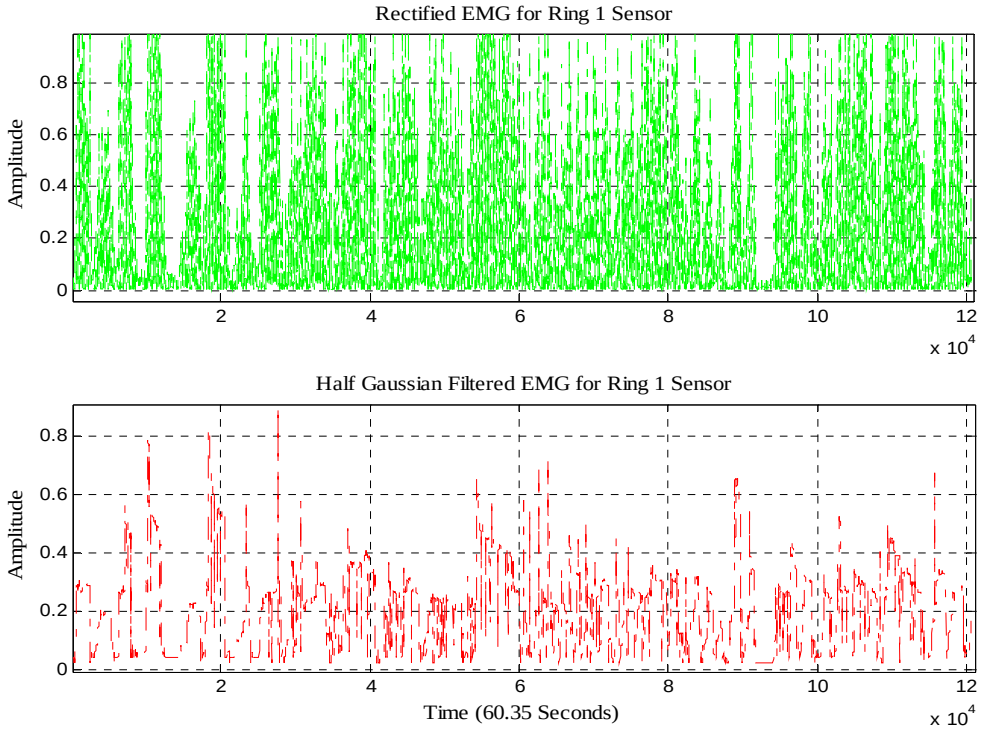

Fig. 4(b): Rectified EMG and Half-Gaussian Filtered EMG Signal for Ring 1 Sensor.

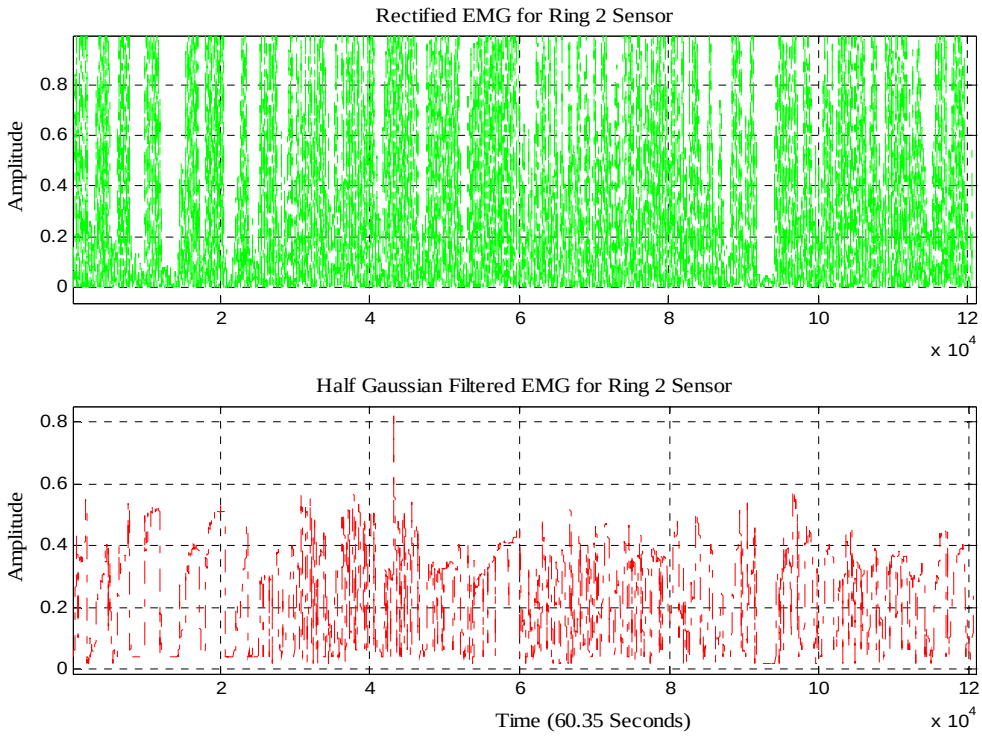

Fig. 4(c): Rectified EMG and Half-Gaussian Filtered EMG Signal for Ring 2 Sensor.

corresponding force data was captured using Interlink Electronics FSR 0.5" circular force sensor. One sEMG sensor was placed on the motor point of the ring finger and two adjacent to the motor point of a healthy subject. Prior to placing the sEMG sensors, the skin surface of the subject was prepared according to International Society of Electrophysiology and Kinesiology (ISEK) protocols. According to previous research, the Bayesian based filtering method yields the most suitable sEMG signals [8]. The nonlinear filter significantly reduces noise and extracts a signal that best describes EMG signals and may permit effective use in prosthetic control. An instantaneous conditional probability density $P(EMG|x)$ provides the resulting EMG for the latent driving signal x [8]. The model for the conditional probability of the rectified EMG signal $emg = |EMG|$ is used in this current estimation algorithm. EMG signals are usually described as amplitude-modulated zero mean Gaussian noise sequence [9]. For the rectified EMG signal, the "Half-Gaussian measurement model" in [8] is given by Equation (1).

$$P(emg|x) = \frac{2*exp\left(-\frac{emg^2}{2x^2}\right)}{\sqrt{2\pi x^2}}. \quad (1)$$

The EMG signal is modeled for the conditional probability of the rectified EMG signal as a filtered random process with random rate. The likelihood function for the rate evolves in time according to a Fokker–Planck partial differential equation [8]. The discrete time Fokker–Planck Equation is given by equation (2).

$$p(x,t-) \approx \alpha * p(x-\varepsilon,t-1) + (1-2*\alpha) * p(x,t-1) + \alpha * p(x+\varepsilon,t-1) + \beta + (1-\beta) * p(x,t-1). \quad (2)$$

Here, α and β are two free parameters, α is the expected rate of gradual drift in the signal, and β is the expected rate of sudden shifts in the signal. The unknown driving signal x is discretized into bins of width ε. These two free parameters of the non-linear Half-Gaussian filter model are optimized for the acquired EMG data using elitism based GA. GA belongs to a class of optimization algorithms that are based on observing nature and its corresponding processes to imitate solving complex problems, most often optimization or estimation problems, see [10-12]. A Chebyshev type II low pass filter with a 550 Hz pass frequency is used to filter the force signal. Fig. 3 depicts the raw and Chebyshev type-II low pass filtered force signals. Fig. 4(a), (b) and (c)

show the rectified EMG and Half-Gaussian Filtered EMG signal for three sensors.

3 Nonlinear ARX and Wiener-Hammerstein Modeling

In this paper, we are using nonlinear ARX and Wiener-Hammerstein models with different nonlinearity estimators/classes to model three sEMG sensors data as input and skeletal muscle force data as output. The nonlinear ARX model uses a parallel combination of nonlinear and linear blocks [13].

Fig. 5 shows the nonlinear ARX model structure. The nonlinear ARX model uses regressors as variables for nonlinear and linear functions. Regressors are functions of measured input-output data [13]. The predicted output $\hat{y}(t)$ of a nonlinear model at time t is given by the general Equation (3):

$$\hat{y}(t) = F(x(t)) \quad (3)$$

where $x(t)$ represents the regressors, F is a nonlinear regressor command, which is estimated by nonlinearity estimators/classes [13]. As shown in Fig. 5, the command F can include both linear and nonlinear functions of $x(t)$. Equation (4) gives the description of F.

$$F(x) = \sum_{k=1}^{d} \alpha_k \, \kappa(\beta_k(x - \gamma_k)) \quad (4)$$

where κ is the unit nonlinear command, d is the number of nonlinearity units, and α_k, β_k and γ_k are the parameters of the nonlinearity estimators/classes [13].

The Wiener-Hammerstein model uses one or two static nonlinear blocks in series with a linear block. Structural representation of a nonlinear Wiener-Hammerstein is shown in Fig. 6 [13].

The general Equations (5), (6), and (7) can describe the Wiener-Hammerstein structure [13].

$$w(t) = f(u(t)) \quad (5)$$

$$x(t) = \frac{B_{j,i}(q)}{F_{j,i}(q)} w(t) \quad (6)$$

$$y(t) = h(x(t)). \quad (7)$$

where $u(t)$ and $y(t)$ are input and output of the system, respectively, f and h are nonlinear functions, which corresponds to input and output nonlinearity, respectively, $w(t)$ and $x(t)$ are internal variables, where $w(t)$ has the same dimensions as $u(t)$ and $x(t)$ has the same dimensions as $y(t)$, and $B(q)$ and $F(q)$ corresponds to the linear dynamic block, these are polynomials in the backward shift operator.

The nonlinearity classes used in this work are Wavenet, Treepartition, Sigmoidnet, Pwlinear, Saturation, and Deadzone. For motor point and ring1 sensors, three nonlinear ARX and four nonlinear Wiener-Hammerstein models with different nonlinearity estimators/classes are obtained. For ring2 sensor, three nonlinear ARX and five nonlinear Wiener-Hammerstein models with different nonlinearity estimators/classes are obtained. Tables 1, 2 and 3 gives the nonlinearity estimators/classes for different sensors and their corresponding model fit values.

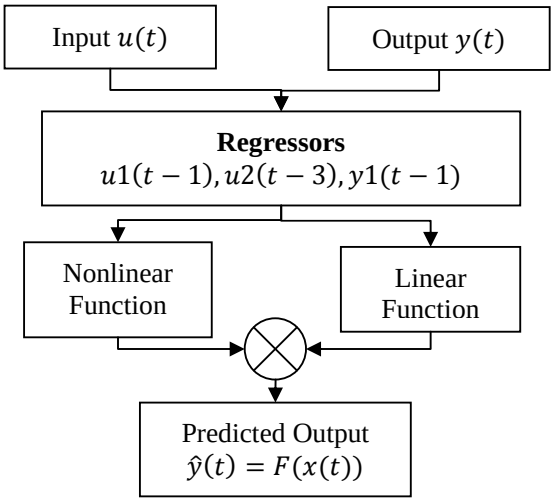

Fig. 5: Nonlinear ARX Model Structure.

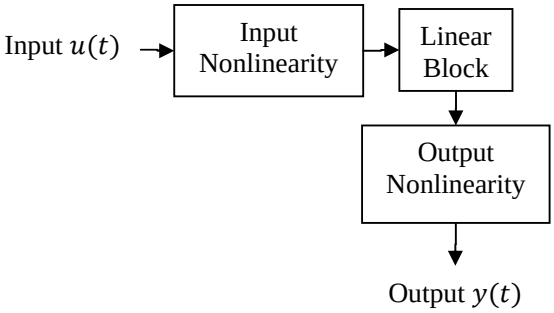

Fig. 6: Nonlinear Wiener-Hammerstein Model Structure.

4 Data Fusion and Adaptive KIC Probability

Data fusion of multiple outputs of nonlinear ARX and Wiener-Hammerstein models is done by assigning a particular probability to each individual model [14]. First, the fusion algorithm is applied to the outputs of different nonlinear ARX and Wiener-Hammerstein models for each sensor obtained using different nonlinearity estimators. Second, the fusion algorithm is again applied to the final fusion based

Table 1: Different Nonlinearity Estimators and Model Fit Values for Motor Point Sensor.

S. No.	Model	Nonlinearity Class	Model Fit
1.	$nlarx1$	Wavenet	24.78 %
2.	$nlarx2$	Treepartiton	40.46 %
3.	$nlarx3$	Sigmoidnet	48.75 %
4.	$nlhw2$	Wavenet	32.38 %
5.	$nlhw3$	Pwlinear	26.27 %
6.	$nlhw4$	Saturation	55.16 %
7.	$nlhw5$	Deadzone	42.45 %

Table 2: Different Nonlinearity Estimators and Model Fit Values for Ring1 Sensor.

S. No.	Model	Nonlinearity Class	Model Fit
1.	$nlarx31$	Wavenet	-60.76 %
2.	$nlarx32$	Treepartiton	-52.64 %
3.	$nlarx33$	Sigmoidnet	-39.36 %
4.	$nlhw31$	Pwlinear	31.06 %
5.	$nlhw32$	Sigmoidnet	10.05 %
6.	$nlhw33$	Saturation	31.57 %
7.	$nlhw35$	Wavenet	32.36 %

Table 3: Different Nonlinearity Estimators and Model Fit Values for Ring2 Sensor.

S. No.	Model	Nonlinearity Class	Model Fit
1.	$nlarx21$	Wavenet	-25.12 %
2.	$nlarx22$	Treepartiton	-22.31 %
3.	$nlarx23$	Sigmoidnet	-33.65 %
4.	$nlhw21$	Pwlinear	34.69 %
5.	$nlhw22$	Sigmoidnet	34.76 %
6.	$nlhw23$	Saturation	33.3 %
7.	$nlhw24$	Deadzone	34.94 %
8.	$nlhw25$	Wavenet	34.89 %

outputs of each sensor; this gives good force estimate. SI model fit value gives the probability for each model, which is given by $\left[1-\frac{|Y-\hat{Y}|}{|Y-\bar{Y}|}\right]*100$. The model selection criterion used in this paper is KIC. The sum of two directed divergences, which is the measure of the models dissimilarity, is known as Kullback's symmetric or J-divergence [15], as given by Equation (8).

$$KIC(p_i) = \frac{n}{2}\log R_i + \frac{(p_i+1)n}{n-p_i-2} - n\psi\left(\frac{n-p_i}{2}\right) + g(n), \quad (8)$$

where $g(n) = n * \log(n/2)$.

The following fusion algorithm as given by [14] is applied for data fusion of the outputs of different nonlinear ARX and Wiener-Hammerstein models:

1) Identify models $M_1, M_2, \ldots, M_k$ using sEMG data (u) as input and force data (Y) as output, for k number of sensors collecting data simultaneously.
2) Compute the residual square norm $R_i = \left\|Y - \Phi_i\widehat{\Theta}_i\right\|^2 = \left\|Y - \hat{Y}\right\|$, where $\widehat{\Theta}_i = \{{\Phi_i}^T\Phi_i\}^{-1}{\Phi_i}^T Y$, and $\Phi = \begin{bmatrix} Y_p^T & u_p^T & Y_{p-1}^T & \ldots & u_1^T \\ Y_{p+1}^T & u_{p+1}^T & Y_p^T & \ldots & u_2^T \\ \vdots & \vdots & \vdots & \ddots & \vdots \\ Y_{n-1}^T & u_{n-1}^T & Y_{n-2}^T & \ldots & u_{n-p}^T \end{bmatrix}$.

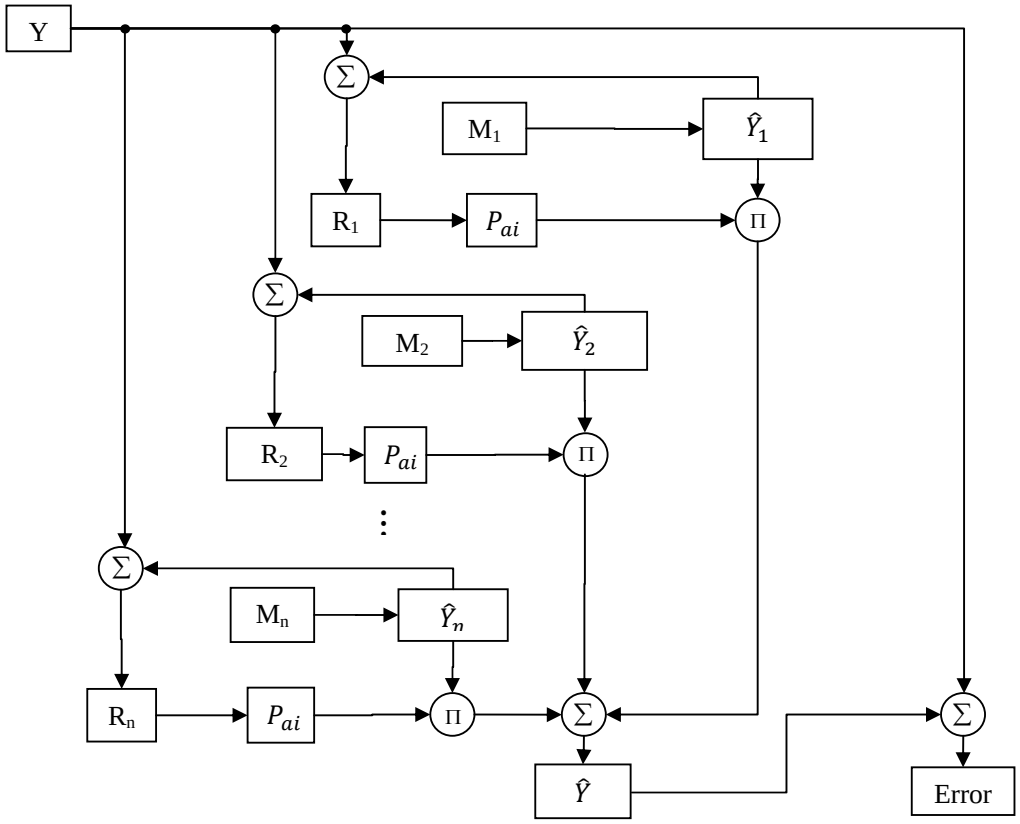

Fig. 7: Data Fusion and Adaptive KIC Probability.

3) Calculate the model criteria coefficient using Equation (8).
4) Compute the model probability $p(M_i|Z) = \frac{e^{-l_i}}{\sum_{j=1}^{k} e^{-l_j}}$, where l is model selection criterion, i.e. $KIC(p_i)$.
5) Compute the fused model output $\hat{Y}_f = \sum_{i=1}^{k} p(M_i|Z)\hat{Y}_i$.
6) Compute the overall model from $\hat{Y}_f$ and force data.

Here all the computation from step 2) to 6) is adaptive i.e. the residual square norm, $KIC(p_i)$, model probability $p(M_i|Z)$, and fused model output $\hat{Y}_f$ are being updated with time or for each data point. Fig. 7 shows the flow chart for fusion of outputs and adaptive probability of KIC.

5 Results, Discussion and Future Work

This section deals with the results, discussion and future work. The following plots show the nonlinear (ARX and Wiener-Hammerstein) model and adaptive fusion algorithm based estimated force output for each sensor first and then finally combined adaptive fusion based output for all three sensors. Fig. 8 shows the overlapping plot of the original and adaptive fusion based force output for the motor point sensor. The output is the result of the adaptive fusion algorithm on three nonlinear ARX and four nonlinear Wiener-Hammerstein models for the motor point sensor signal. Fig. 9 shows the overlapping plot of the original and adaptive fusion based force output for ring1 sensor. This output is the result of adaptive fusion algorithm of three nonlinear ARX and four nonlinear Wiener-Hammerstein models for ring1 sensor signal. Fig. 10 shows the overlapping plot of the original and adaptive fusion based force output for ring2 sensor. This output is the result of adaptive fusion algorithm on three nonlinear ARX and five nonlinear Wiener-Hammerstein models for ring2 sensor signal. Fig. 11 shows the overlapping plot of the original and final combined adaptive fusion based force output for motor point, ring1 and ring2 sensors. The output is the result of adaptive fusion algorithm on the final

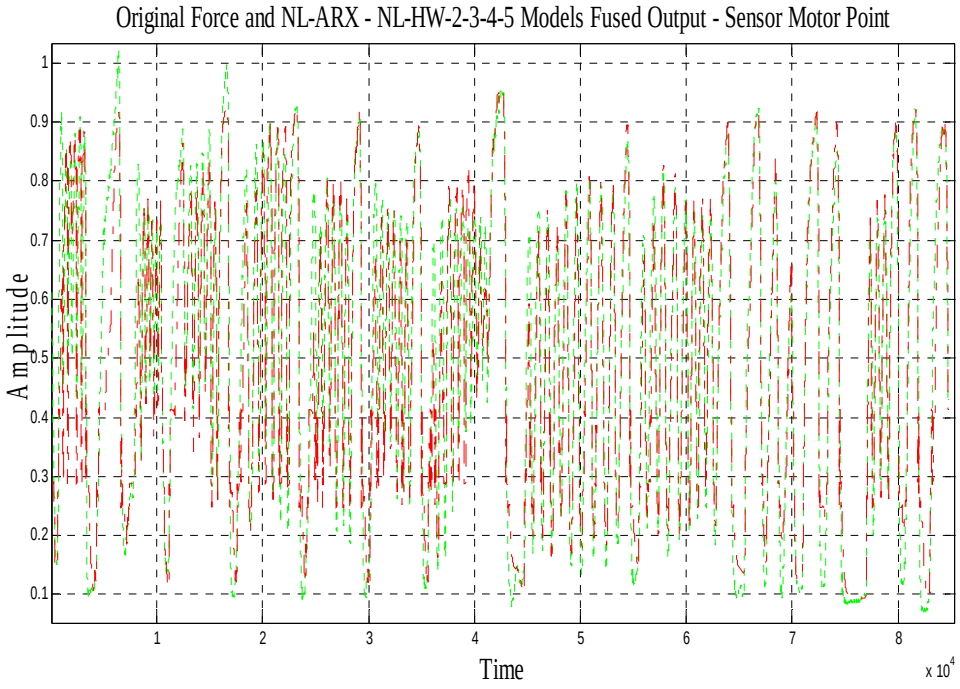

Fig. 8: Original and Fusion Based Output for Motor Point Sensor.

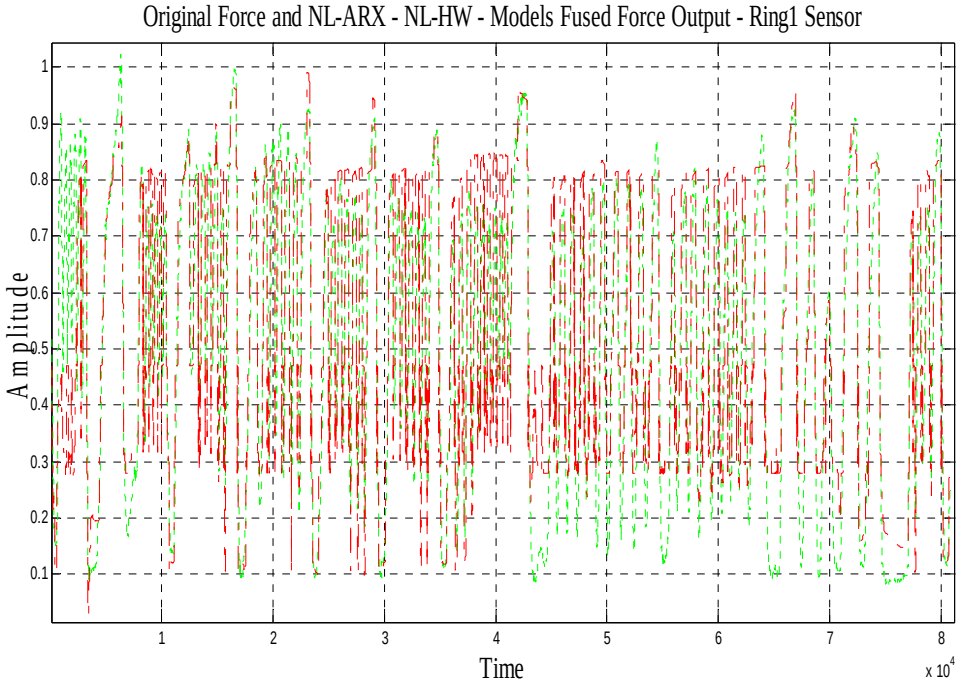

Fig. 9: Original and Fusion Based Output for Ring1 Sensor.

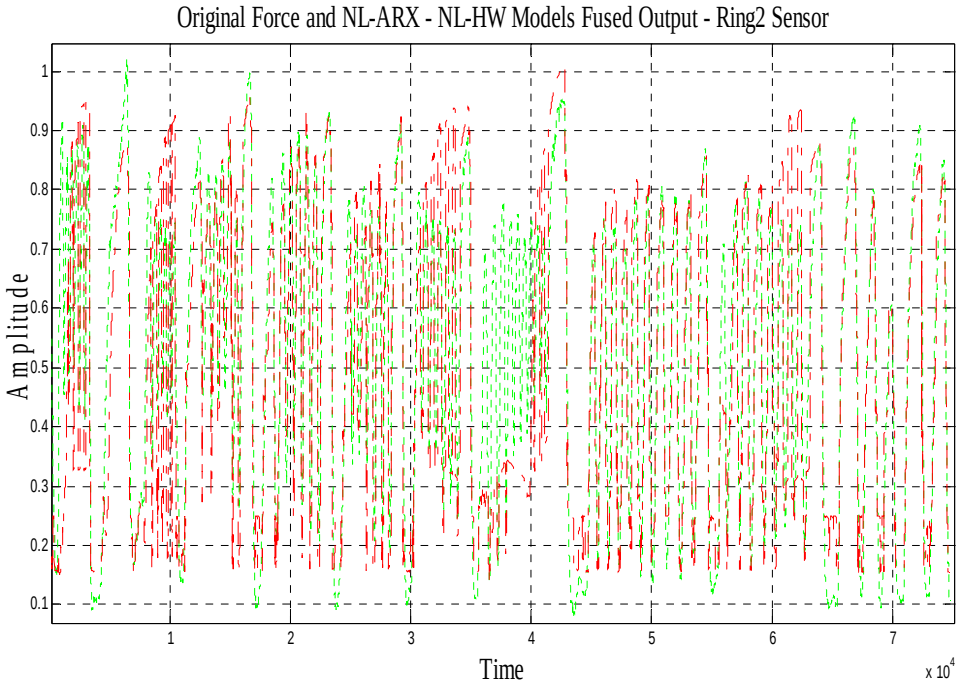

Fig. 10: Original and Fusion Based Output for Ring2 Sensor.

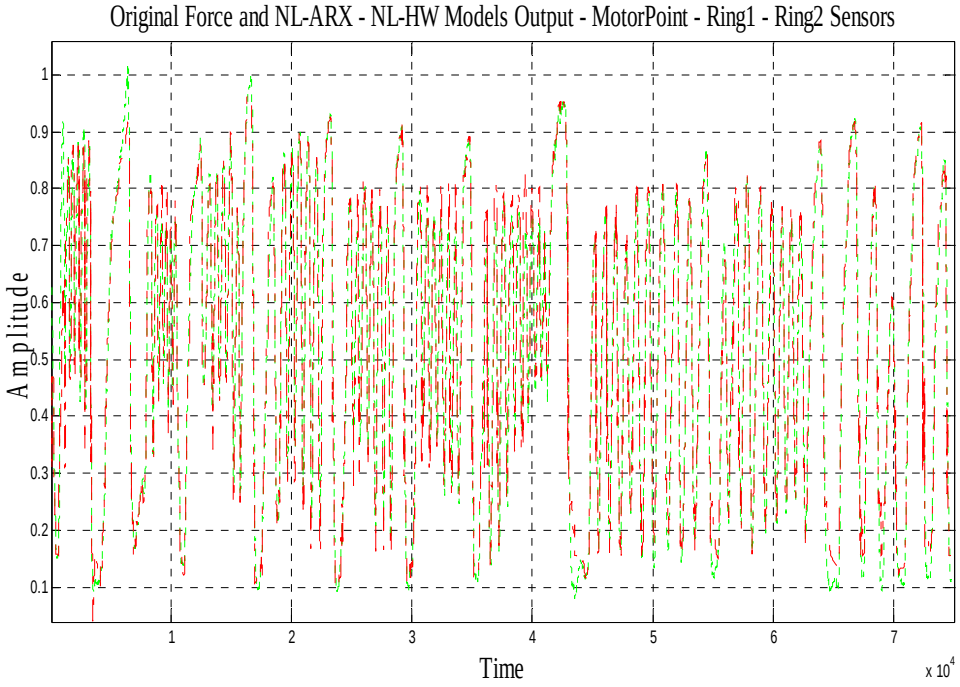

Fig. 11: Final Plot - Original and Fusion Based Output for All Three Sensors.

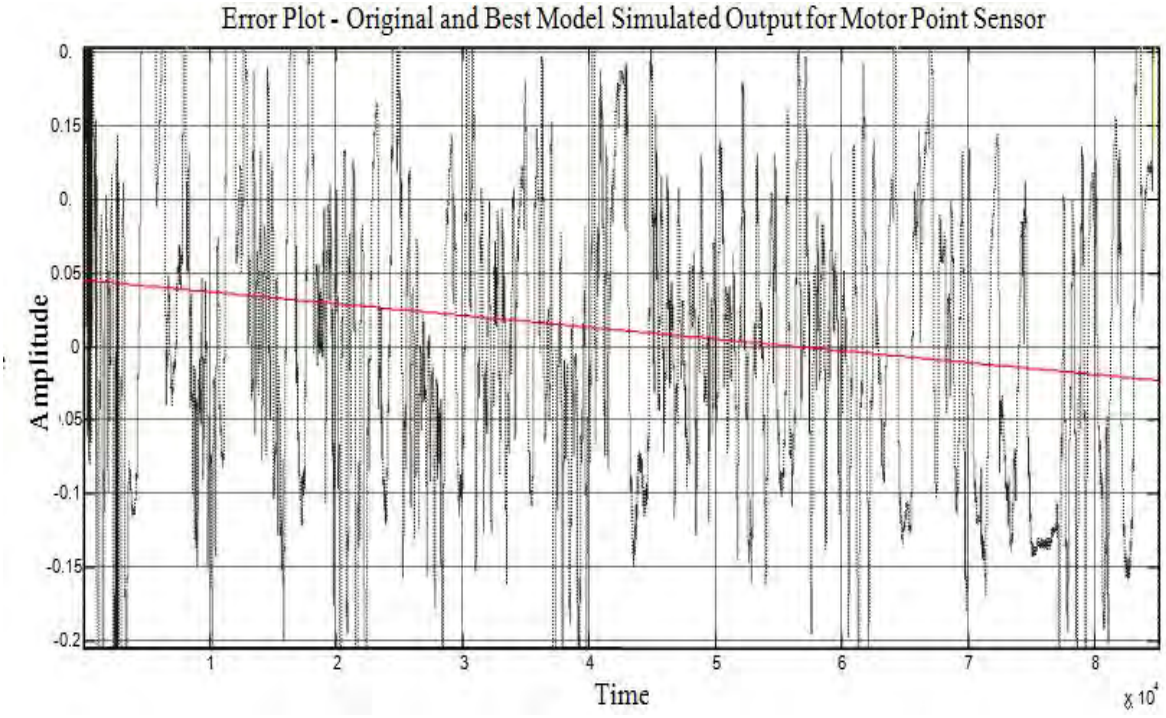

Fig. 12: Error Plot – Original and Best-Estimated Model Output for Motor Point Sensor.

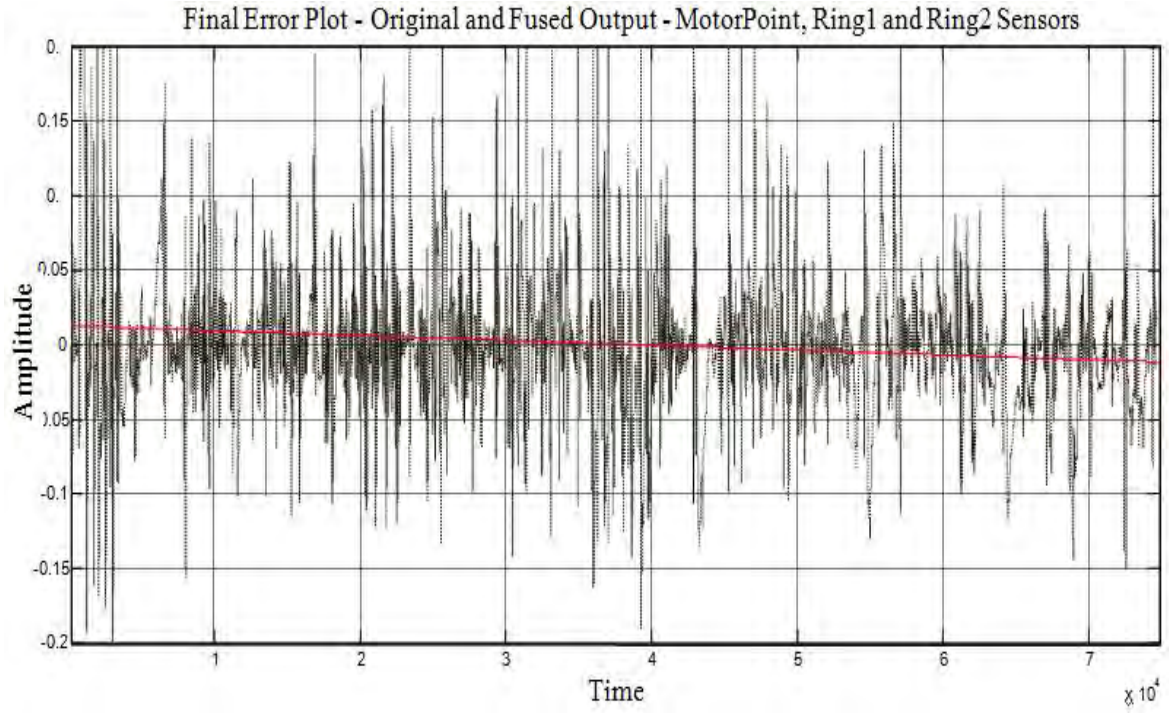

Fig. 13: Final Error Plot – Original and Fusion Based Output for Motor Point, Ring1 and Ring2 Sensors.

outputs of three sensors i.e. motor point, ring1 and ring2 as shown in Fig. 8 to 10. Fig. 11 shows the best skeletal muscle force estimate, which is the result of the multi nonlinear ARX and Wiener-Hammerstein models and an adaptive hybrid data fusion on these nonlinear models. Fig. 12 shows the error plot of the original and best-estimated model output for the motor point sensor.

Fig. 13 shows the error plot of original and final multi nonlinear modeled and adaptive hybrid data fusion based force estimate (results from three sensors, nonlinear modeling and adaptive data fusion algorithm). If we compare Fig. 12 and 13, it is very clear and conspicuous that the error has decreased remarkably and is very close to zero.

Future work will focus on the improvement of the data collection techniques and experimental set-up. By using the combination of linear and nonlinear modeling, and adaptive hybrid data fusion, the skeletal muscle force estimate can be improved further. Furthermore, the authors believe that by using different model selection criteria such as Akaike Information Criterion (AIC), Kullback Information Criterion (KIC) and the Bayesian Information Criterion (BIC) together to obtain final skeletal muscle force estimate will give improved results.

6 Conclusions

sEMG and force data acquired using three EMG and one common FSR force sensor is modeled using nonlinear SI. Using different nonlinearity estimators/classes, multi nonlinear ARX and Wiener-Hammerstein models are obtained for each sensor. First, the outputs of different models for each sensor are fused with a data fusion algorithm and an adaptive KIC probability. Finally, the fused outputs from each sensor are again fused with same algorithm and adaptive KIC probability. The final estimated force using this technique gives the best estimate. The presented approach can be utilized for controlling prosthetic hands [16].

Acknowledgement

The research was sponsored by the US Department of the Army, under the award number W81XWH-10-1-0128 awarded and administered by the U.S. Army Medical Research Acquisition Activity, 820 Chandler Street, Fort Detrick MD 21702-5014. The information does not necessarily reflect the position or the policy of the Government, and no official endorsement should be inferred. For purposes of this article, information includes news releases, articles, manuscripts, brochures, advertisements, still and motion pictures, speeches, trade association proceedings, etc.

References:

[1] Kathryn Ziegler-Graham, PhD, et al., Estimating the Prevalence of Limb Loss in the United States - 2005 to 2050, *Archives of Physical Medicine and Rehabilitation*, 89 (2008): 422-429.

[2] O'Connor, P., Iraq war vet decides to have second leg amputated, *Columbia Missourian*, 2009.

[3] N. Dechev, W. L. Cleghorn, and S. Naumann, Multiple finger, passive adaptive grasp prosthetic hand, *Mechanism and Machine Theory*, 36(2001), pp. 1157-1173.

[4] Haruhisa Kawasaki, Tsuneo Komatsu, and Kazunao Uchiyama, Dexterous Anthropomorphic Robot Hand With Distributed Tactile Sensor: Gifu Hand II, *IEEE/ASME Transactions on Mechatronics*, Vol. 7, No. 3, September 2002, pp. 296-303.

[5] M. Zecca, S. Micera, M. C. Carrozza, and P. Dario, Control of Multifunctional Prosthetic Hands by Processing the Electromyographic Signal, *Critical Reviews™ in Biomedical Engineering*, 30(4–6), 2002, pp. 459–485.

[6] Claudio Castellini and Patrick van der Smagt, Surface EMG in advanced hand prosthetics, *Biological Cybernetics*, (2009) 100, pp. 35–47.

[7] C.J. De Luca, Myoelectrical manifestations of localized muscular fatigue in humans, *Crit. Rev. Biomed. Eng.*, 11 (4), 1984, pp. 251-279.

[8] Terence D. Sanger, Bayesian Filtering of Myoelectric Signals, *J Neurophysiol*, 97, 2007, pp. 1839–1845.

[9] M. B. I. Reaz, M. S. Hussain and F. Mohd-Yasin, Techniques of EMG signal analysis: detection, processing, classification and applications, *Biol. Proced. Online*, 2006, 8(1), pp. 11-35.

[10] E. Kral, L. Vasek, V. Dolinay, P. Varacha, Usage of PSO Algorithm for Parameter Identification of District Heating Network Simulation Model, *The 14th World Scientific and Engineering Academy and Society (WSEAS) International Conference on Systems*, Corfu Island, Greece, July 22-24, 2010.

[11] A. Neubaur, The Intrinsic System Model of the Simple Genetic Algorithm with α-Selection, Uniform Crossover and Bitwise Mutation, *The 14th World Scientific and Engineering Academy and Society (WSEAS) International Conference*

on Systems, Corfu Island, Greece, July 22-24, 2010.

[12] A. Sebastian, P. Kumar, M. P. Schoen, A Study on Hybridization of Particle Swarm and Tabu Search Algorithm for Unconstraint Optimization and Estimation, in *The 14th World Scientific and Engineering Academy and Society (WSEAS) International Conference on Systems*, Corfu Island, Greece, July 22-24, 2010.

[13] Lennart Ljung, *System Identification Toolbox™ 7 User's Guide*, The MathWorks, Inc., 2010.

[14] Huimin Chen and Shuqing Huang, A Comparative study on Model Selection and Multiple Model Fusion, *7th International Conference on Information Fusion*, 2005, pp. 820-826.

[15] Abd-Krim Seghouane, Maiza Bekara, and Gilles Fleury, A Small Sample Model Selection Criterion Based on Kullback's symmetric Divergence, *IEEE Transaction on Signal Processing*, 2003, pp. 145-148.

[16] C. H. Chen, D. S. Naidu, M. P. Schoen, An Adaptive Control Strategy for a Five-Fingered Prosthetic Hand, *The 14th World Scientific and Engineering Academy and Society (WSEAS) International Conference on Systems*, Corfu Island, Greece, July 22-24, 2010.

A Hybrid Adaptive Data Fusion with Linear and Nonlinear Models for Skeletal Muscle Force Estimation

Parmod Kumar, Chandrasekhar Potluri, Madhavi Anugolu, Anish Sebastian, Jim Creelman, Alex Urfer,

Steve Chiu, D. Subbaram Naidu, *Fellow, IEEE*, and Marco P. Schoen, *Member, IEEE*

***Abstract* – Position and force control are two critical aspects of prosthetic control. Surface electromyographic (sEMG) signals can be used for skeletal muscle force estimation. In this paper, skeletal muscle is considered as a system and System Identification (SI) is used to model sEMG and skeletal muscle force. The recorded sEMG signal is filtered utilizing optimized nonlinear Half-Gaussian Bayesian filter, and a Chebyshev type-II filter prepares the muscle force signal. The filter optimization is accomplished using Genetic Algorithm (GA). Multi- linear and nonlinear models are obtained with sEMG as input and skeletal muscle force of a human hand as an output. The outputs of these models are fused with a probabilistic Kullback Information Criterion (KIC) for model selection and an adaptive probability of KIC. This approach gives good estimate of the skeletal muscle force.**

I. Introduction

The current incidence of amputation in the United States is approximately 1.7 million people [1] and this number is on rise with the U.S. involvement in both the Afghanistan and Iraq wars since 2003 [2]. Loss of upper limb results in reduction of functionality and presents numerous psychological issues for the individual.

Previous research was mainly based on the electromyography (EMG) signals and focus on the prosthetic hand design [3-4]. The EMG signal recorded at the surface of the limb is known as surface EMG (sEMG) which is an electric voltage ranging between -5 and +5 mV. sEMG can be used to control the position and force of the hand prosthesis [5-6]. Generally EMG signal amplitude increases with an increase in the skeletal muscle force, however, various factors affect this relationship. Since varying motor unit recruitments, crosstalk, and biochemical interaction within the muscular fibres contribute to generate EMG signals, hence the EMG signals are random, complex and dynamic in nature. Together all of these factors make the relationship between EMG and finger force nonlinear. Precise control of the prosthesis is critical, so the correct interpretation of the measured EMG signal is important. Previously authors have published similar work using multi sensor data fusion and Output Error (OE) model and modal transformation [7], and multi sensor data fusion using nonlinear models [8].

The present work presents a novel approach to estimate skeletal muscle force using an adaptive data fusion algorithm with hybrid multi linear and nonlinear models as shown in Figure 1. The recorded sEMG signals are filtered utilizing Genetic Algorithm (GA) based optimized nonlinear Half-Gaussian Bayesian filter parameters, and the skeletal muscle force signal is filtered by using a Chebyshev type-II filter. Using an input/output approach, the EMG signal measured at the skin surface is considered as input to the skeletal muscle, whereas the resulting hand/finger force constitutes the output. Multi linear and nonlinear models are obtained using System Identification (SI) for the motor point signals as they capture the dynamics of the system differently. The outputs of estimated linear and nonlinear models are fused with a probabilistic Kullback Information Criterion (KIC) for model selection and an adaptive probability of KIC. First, the outputs are fused for the linear models and then for nonlinear models and finally the resultant outputs of linear and nonlinear models are fused together. The final fused

Manuscript received August 27, 2010. This work was supported by the US Department of the Army, under the award number W81XWH-10-1-0128.

Parmod Kumar is with Measurement and Control Engineering Research Center (MCERC), College of Engineering, Idaho State University, Pocatello, Idaho 83209, USA (email: kumaparm@isu.edu).

Chandrasekhar Potluri is with MCERC, College of Engineering, Idaho State University, Pocatello, Idaho 83209, USA (e-mail: potlchan@isu.edu).

Madhavi Anugolu is with MCERC, Idaho State University, Pocatello, Idaho 83201 USA (e-mail: anugmadh@isu.edu).

Anish Sebastian is with MCERC, College of Engineering, Idaho State University, Pocatello, Idaho 83209, USA (email: sebaanis@isu.edu).

Jim Creelman is with Department of Physical and Occupational Therapy, Idaho State University, Pocatello, Idaho 83209, USA (email: urfealex@isu.edu).

Alex Urfer is with Department of Physical and Occupational Therapy, Idaho State University, Pocatello, Idaho 83209, USA (email: urfealex@isu.edu).

Steve Chiu is with Department of Electrical Engineering and Computer Science, MCERC, Idaho State University, Pocatello, Idaho 83201 USA (e-mail:chiustev@isu.edu).

D. Subbaram Naidu is with Department of Electrical Engineering, MCERC, Idaho State University, Pocatello, Idaho 83201 USA (email: naiduds@isu.edu).

Marco P. Schoen is with Department of Mechanical Engineering, MCERC, Idaho State University, Pocatello, Idaho 83209, USA (email: schomarc@isu.edu).

output of different linear and nonlinear models results in good skeletal muscle force estimates.

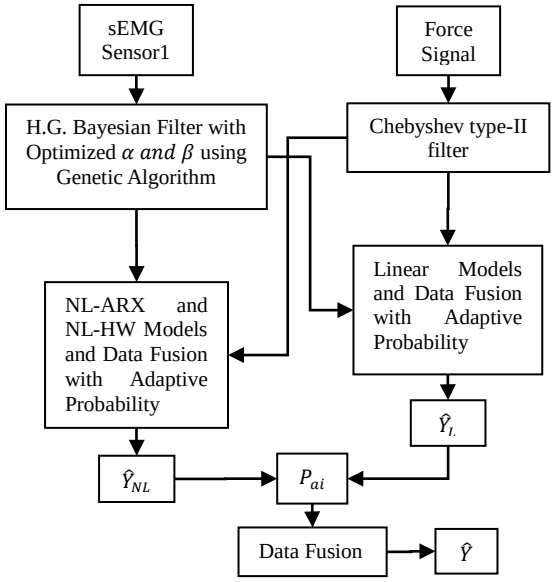

Fig. 1. Flow chart for estimation of skeletal muscle force using an adaptive data fusion algorithm.

II. Experimental Set-up and Pre–Processing

Data acquisition for EMG and skeletal muscle force is accomplished using LabVIEW™ 8.2 simultaneously at a sampling rate of 2000 Hz. A DELSYS® Bagnoli-16 EMG system with DE-2.1 differential EMG sensors is used for sEMG data capturing. However, the corresponding force data was captured using NI ELVIS with Interlink Electronics FSR 0.5" circular force sensor. Figure 2 explains the experimental set-up. One sEMG sensor was placed on the motor point of the ring finger and two adjacent to the motor point of a healthy subject. For the experiment, three sEMG sensors were used, but only the motor point signal is used for the force estimation in this research work. The International Society of Electrophysiology and Kinesiology (ISEK) protocol was followed to capture the sEMG signals.

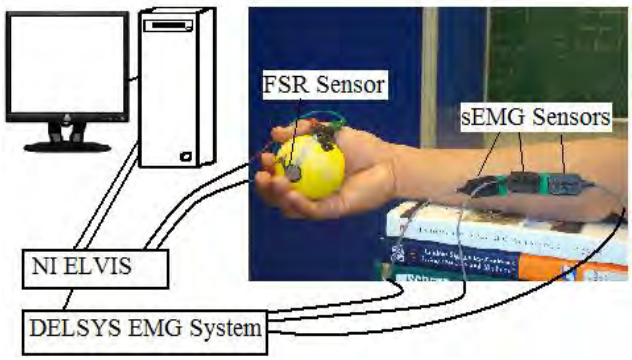

Fig. 2. Experimental set-up.

To model the sEMG signal, it is assumed that the conditional probability of the rectified EMG signal is a filtered random process with random rate. Fokker–Planck partial differential equation gives the likelihood function for the rate evolving in time [9]. In the Fokker–Planck partial differential equation, α and β are two free parameters, α is the expected rate of gradual drift in the signal, and β is the expected rate of sudden shifts in the signal. Optimization of these two free parameters is achieved using the GA. Skeletal muscle force signal is filtered with a Chebyshev type II low pass filter.

III. System Identification – Linear and Non-Linear Modeling

System Identification (SI) is based on the acquired experimental data and is an alternative to physically based mathematical modeling [10]. A dynamical model such as the Auto Regressive with eXogenous input (ARX) or Output Error (OE) gives the system in mathematical form which is the outcome of parametric system identification process. In this work, the SI approach is used with the myolelectric signal as the input to the system and as the output is the intended finger/hand force. In this work, mutli- linear and nonlinear models are obtained for modeling of EMG and hand/finger force signals. Six linear and three nonlinear models are obtained for the motor point sEMG signal.

TABLE I
LINEAR MODELS AND THEIR STRUCTURES

Linear Model Name	Linear Model Structure
Output Error	$y(t) = \frac{B(q)}{F(q)}u(t-n_k) + e(t)$
ARX	$A(q)y(t) = B(q)u(t-n_k) + e(t)$
ARMAX	$A(q)y(t) = B(q)u(t-n_k) + C(q)e(t)$
Box-Jenkins	$y(t) = \frac{B(q)}{F(q)}u(t-n_k) + \frac{C(q)}{D(q)}e(t)$
State-Space – subspace method	$x(t+Ts) = Ax(t) + Bu(t) + Ke(t)$ $y(t) = Cx(t) + Du(t) + e(t)$
State-Space – prediction error/maximum likelihood method	$x(t+Ts) = Ax(t) + Bu(t) + Ke(t)$ $y(t) = Cx(t) + Du(t) + e(t)$

For the linear models Output Error model of order 6, ARX model of order 6, ARMAX model of model order 5, Box-Jenkins model of order 18, State-Space model with subspace method of order 12 and a State-Space model with prediction error/maximum likelihood method of order 12 are obtained using SI as given in table I. In table I y is output, t is time, $B(q)$, $F(q)$, $A(q)$, $C(q)$, $D(q)$, are polynomials, q is a backward shift operator, u is input, n_k is delay and e is error [11]. For State-Space models:- x is state, t is time, Ts is sampling time, u is input, e is error, A, B, K, C, and D are system matrices, and y is output [11].

In contrary to six linear models as given in table I, nonlinear ARX with nonlinearity estimator as 'sigmoidnet' and nonlinear Wiener-Hammerstein models with nonlinearity estimators as 'piecewise linear - pwlinear' and 'saturation' are obtained, as given in table II.

TABLE II
NONLINEAR MODELS AND THEIR STRUCTURES

Nonlinear Model Name	Nonlinear Model Structure
Nonlinear ARX – Sigmoidnet	$y_p(t) = f(y(t-1), y(t-2), y(t-3), \dots, u(t-1), u(t-2), \dots);$ $f(z) = \frac{1}{e^{-z}+1}$ is sigmoid function.
Nonlinear HW – Piecewise Linear –pwlinear	$w(t) = f(u(t)),$ $x(t) = \frac{B_{ji}(q)}{F_{ji}(q)} w(t),$ $y(t) = h(x(t));$
Nonlinear HW – Saturation	$w(t) = f(u(t)),$ $x(t) = \frac{B_{ji}(q)}{F_{ji}(q)} w(t),$ $y(t) = h(x(t));$

In table II f is a nonlinear function for the nonlinear ARX model. Inputs to f are model regressors. $y_p(t)$ is the predicted output as a weighted sum of past output values and current and past input values. For the nonlinear Hammerstein-Wiener model $u(t)$ and $y(t)$ are the inputs and outputs for the system, respectively. f and h are nonlinear functions that corresponds to the input and output nonlinearity, respectively. $w(t)$ and $x(t)$ are internal variables. $w(t)$ has the same dimension as $u(t)$. $x(t)$ has the same dimension as $y(t)$. $B(q)$ and $F(q)$ in the linear dynamic block are polynomials in the backward shift operator. If only the input nonlinearity is present, the model is called the Hammerstein model. If only the output nonlinearity is present, the model is called the Wiener model [11].

IV. Fusion of Outputs and Adaptive Probability of KIC

The outputs of multiple models can be fused by assigning a particular probability to each individual model [12]. In this work, we are obtaining multi linear and nonlinear models using SI for the sEMG sensor for the motor unit. The probability of each model is computed using the SI model fit value. Model fit value is given by $\left[1 - \frac{|Y-\hat{Y}|}{|Y-\bar{Y}|}\right] * 100$. Kullback information criterion (KIC), which is an asymmetric measure for the model selection, is used for this research. Kullback's symmetric or J-divergence is the sum of two directed divergences, which is the measure of the models dissimilarity and given by Equation (1) [13].

$$KIC(p_i) = \frac{n}{2}\log R_i + \frac{(p_i+1)n}{n-p_i-2} - n\psi\left(\frac{n-p_i}{2}\right) + g(n), \qquad (1)$$

where $g(n) = n * \log(n/2)$.

Based on [10], the following fusion technique is applied for sEMG – force identification models.

1) Identify OE models $M_1, M_2, \dots, M_{k1}$ using sEMG data (u) as input and force data (Y) as output, for $k1$ number of sensors collecting data simultaneously.
2) Compute the residual square norm
$R_i = \left\|Y - \Phi_i\widehat{\Theta}_i\right\|^2 = \left\|Y - \hat{Y}\right\|^2,$
where $\widehat{\Theta}_i = \{{\Phi_i}^T\Phi_i\}^{-1}{\Phi_i}^T Y$, and
$$\Phi = \begin{bmatrix} Y_p^T & u_p^T & Y_{p-1}^T & \dots & u_1^T \\ Y_{p+1}^T & u_{p+1}^T & Y_p^T & \dots & u_2^T \\ \vdots & \vdots & \vdots & \ddots & \vdots \\ Y_{n-1}^T & u_{n-1}^T & Y_{n-2}^T & \dots & u_{n-p}^T \end{bmatrix}.$$
3) Calculate the model criteria coefficient using Equation (1).
4) Compute the model probability $p(M_i|Z) = \frac{e^{-l_i}}{\sum_{j=1}^{k1} e^{-l_j}}$, where l is model selection criterion, i.e. $KIC(p_i)$.
5) Compute the fused model output $\hat{Y}_f = \sum_{i=1}^{k1} p(M_i|Z)\hat{Y}_i$.
6) Compute the overall OE model from $\hat{Y}_f$ and force data.

In the above steps all the computation from step 2) to step 6) is adaptive i.e. the residual square norm, $KIC(p_i)$, model probability $p(M_i|Z)$, and fused model output $\hat{Y}_f$ are being updated with time or for each data point.

V. Results, Conclusion and Future Work

Adaptive KIC probability based data fusion algorithm is applied to linear and nonlinear models separately and then combined. Figures 3 and 4 show the results for the linear and nonlinear models respectively. Finally, both linear and nonlinear models are combined and adaptive KIC probability based data fusion algorithm is applied to obtain the final output that is given by Figure 5. Validation of this technique is confirmed with a separate data set. Figure 6 depicts the validation of the proposed technique. Future work will focus on the improved data collection techniques, use of spatial filters for sEMG signals filtration, and use of multi sensor data with this technique.

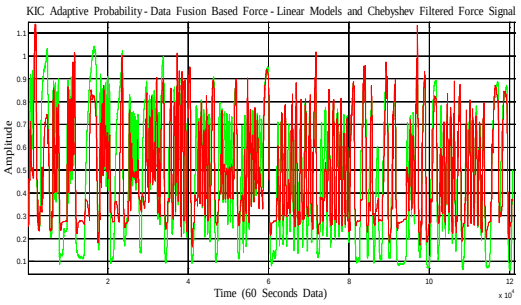

Fig. 3. For linear models: KIC adaptive probability data fusion based force vs. Chebyshev type II filtered force.

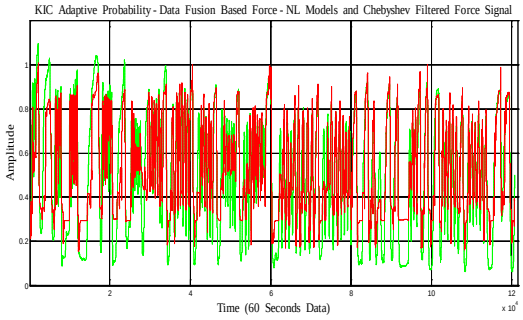

Fig. 4. For nonlinear models: KIC adaptive probability data fusion based force vs. Chebyshev type II filtered force.

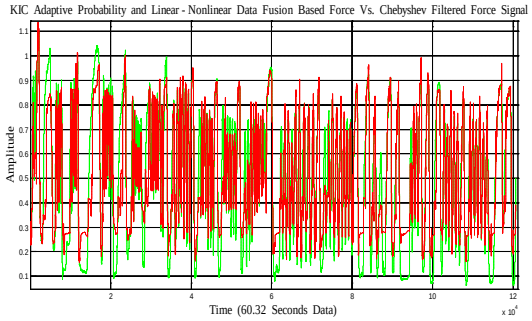

Fig. 5. For linear and nonlinear models combined: KIC adaptive probability data fusion based force vs. Chebyshev type II filtered force.

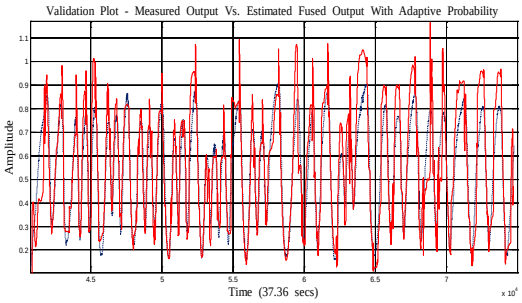

Fig. 6. Validation plot - for linear and nonlinear models combined: KIC adaptive probability data fusion based force vs. Chebyshev type II filtered force.

ACKNOWLEDGMENT

The research was sponsored by the US Department of the Army, under the award number W81XWH-10-1-0128 awarded and administered by the U.S. Army Medical Research Acquisition Activity, 820 Chandler Street, Fort Detrick MD 21702-5014. The information does not necessarily reflect the position or the policy of the Government, and no official endorsement should be inferred. For purposes of this article, information includes news releases, articles, manuscripts, brochures, advertisements, still and motion pictures, speeches, trade association proceedings, etc.

REFERENCES

[1] Kathryn Ziegler-Graham, PhD, et al., Estimating the Prevalence of Limb Loss in the United States - 2005 to 2050, *Archives of Physical Medicine and Rehabilitation*, 89 (2008): 422-429.

[2] O'Connor, P., Iraq war vet decides to have second leg amputated, *Columbia Missourian*, 2009.

[3] N. Dechev, W. L. Cleghorn, and S. Naumann, *Multiple finger, passive adaptive grasp prosthetic hand*, Mechanism and Machine Theory 36(2001), pp. 1157-1173.

[4] Haruhisa Kawasaki, Tsuneo Komatsu, and Kazunao Uchiyama, Dexterous Anthropomorphic Robot Hand With Distributed Tactile Sensor: Gifu Hand II, *IEEE/ASME TRANSACTIONS ON MECHATRONICS*, VOL. 7, NO. 3, SEPTEMBER 2002, pp. 296-303.

[5] M. Zecca, S. Micera, M. C. Carrozza, and P. Dario, Control of Multifunctional Prosthetic Hands by Processing the Electromyographic Signal, *Critical Reviews™ in Biomedical Engineering*, 30(4–6), 2002, pp. 459–485.

[6] Claudio Castellini and Patrick van der Smagt, Surface EMG in advanced hand prosthetics, *Biological Cybernetics*, (2009) 100, pp. 35–47.

[7] P. Kumar, A. Sebastian, C. Potluri, A. Urfer, D. S. Naidu, and M. P. Schoen, "Towards Smart Prosthetic Hand: Adaptive Probability Based Skeletan Muscle Fatigue Model," *32nd Annual International Conference of the IEEE EMBS Conference*, 2010.

[8] P. Kumar, C. Potluri, A. Sebastian, S. Chiu, A. Urfer, D. S. Naidu, and M. P. Schoen, "An Adaptive Multi Sensor Data Fusion with Hybrid Nonlinear ARX and Wiener-Hammerstein Models for Skeletal Muscle Force Estimation," *14th WSEAS Int. Conf. on SYSTEMS*, Vol. 1, pp. 186-191, July 2010.

[9] Terence D. Sanger, "Bayesian Filtering of Myoelectric Signals," *J Neurophysiol* 97, pp. 1839–1845, 2007.

[10] Lennart Ljung, *System Identification: Theory for the User*. 2nd edition, Printice Hall PTR, 1999, Chap. 1, pp. 1-15.

[11] Lennart Ljung, System Identification ToolboxTM 7 User's Guide, The MathWorks, Inc., 2010.

[12] H. Chen and S. Huang, "A Comparative study on Model Selection and Multiple Model Fusion," *7th International Conference on Information Fusion*, pp. 820-826, 2005.

[13] Abd-Krim Seghouane, M. Bekara, G. Fleury, "A Small Sample Model Selection Criterion Based on Kullback's symmetric Divergence," *IEEE Transaction*, pp. 145-148, 2003.

A Hybrid Adaptive Multi Sensor Data Fusion for Estimation of Skeletal Muscle Force for Prosthetic Hand Control

Parmod Kumar, Chandrasekhar Potluri, Anish Sebastian, Yimesker Yihun, Adnan Ilyas, Madhavi Anugolu, Rohit Sharma, Steve Chiu, Jim Creelman, Alex Urfer, D. Subbaram Naidu, *Fellow IEEE*, and Marco P. Schoen, *Senior Member IEEE*

Abstract – ***Effective use of upper extremity prostheses depends on the two critical aspects of precise position and force control. Surface electromyographic (sEMG) signals can be used as a control input for the position and force actions related to the prosthesis. In this paper, we use the measured sEMG signals to estimate skeletal muscle force. Further, we consider skeletal muscle as a system and System Identification (SI) is used to model multi-sensor sEMG and skeletal muscle force. The sEMG signals are filtered utilizing optimized nonlinear Half-Gaussian Bayesian filter, and a Chebyshev type-II filter provides the muscle force signal. The filter optimization is accomplished using a Genetic Algorithm (GA). Multi- linear and nonlinear models are obtained with sEMG data as input and skeletal muscle force of a healthy human hand as an output for three sensors. The outputs of these models for three sensors are fused with a probabilistic Kullback Information Criterion (KIC) for model selection and an adaptive probability of KIC. The final fusion based force for multi-sensor sEMG gives improved estimate of the skeletal muscle force.***

Keywords: *sEMG, SI, GA, KIC*

I. INTRODUCTION

In the last decade there have been active research efforts in the field of prosthetics. According to [1] the United States has 1.7 million of amputees and this figure is on the rise since 2003 due to the wars in Afghanistan and Iraq [2].

Manuscript received March 31, 2011. This work was supported in part by the US Department of the Army, under the award number W81XWH-10-1-0128.

Parmod Kumar is with Measurement and Control Engineering Research Center (MCERC), School of Engineering, Idaho State University, Pocatello, Idaho 83209, USA (email: kumaparm@isu.edu).

Chandrasekhar Potluri, Anish Sebastian, Yimesker Yihun, Adnan Ilyas, Madhavi Anugolu, and Rohit Sharma are with MCERC, School of Engineering, Idaho State University, Pocatello, Idaho 83209, USA (e-mail: potlchan@isu.edu, sebaanis@isu.edu, yihuyime@isu.edu, ilyaadna@isu.edu, anugmadh@isu.edu, sharrohi@isu.edu).

Steve Chiu is with Department of Electrical Engineering and Computer Science, MCERC, Idaho State University, Pocatello, Idaho 83201 USA (email: chiustev@isu.edu).

Jim Creelman and Alex Urfer are with Department of Physical and Occupational Therapy, Idaho State University, Pocatello, Idaho 83209, USA (email: creejame@isu.edu, urfealex@isu.edu).

D. Subbaram Naidu is with Department of Electrical Engineering and Computer Science, MCERC, Idaho State University, Pocatello, Idaho 83201 USA (email: naiduds@isu.edu).

Marco P. Schoen is with Department of Mechanical Engineering, MCERC, Idaho State University, Pocatello, Idaho 83209, USA (email: schomarc@isu.edu).

Individuals with upper extremity amputations not only have a reduction in function, but also struggle with numerous psychological issues which may further complicate the appropriate control and use of the prosthesis. Previous research on the prosthetic hand design was mainly based on the electromyography (EMG) signals [3-4]. The EMG signal recorded at the surface of the limb is known as surface EMG (sEMG). The sEMG is an electric voltage ranging between -5 and +5 mV, which reflects the electrical activity associated with voluntary muscle contraction and which has been used to control the position and force of the hand prosthesis [5-6]. The skeletal muscle force and the sEMG signals are related and higher sEMG amplitude generally correlates with greater force production. However, there are various other factors that affect this relationship. The sEMG signals are random, complex and dynamic in nature because of varying motor unit recruitment, crosstalk, and biochemical interaction within the muscular fibers. Hence all these factors contribute towards the nonlinear relationship between the two.

Since sEMG is the control input for the prosthesis, precise control and correct interpretation of the measured sEMG signal is important. In previous works, the authors have published similar work using multi sensor data fusion and Output Error (OE) model and modal transformation [7], and multi sensor data fusion using nonlinear models [8].

The present work is an extension of our previous work [9] where we proposed estimation of the skeletal muscle force using an adaptive data fusion algorithm with hybrid multi linear and nonlinear models. In [9] the sEMG data was based only from measuring the motor point sEMG signal, whereas in the present work we extend this to three sensors for the ring finger of the dominant hand of a healthy male subject. Figure 1 presents the flow chart of the work done in this paper. The sEMG signals are acquired from the forearm of a healthy subject and filtered utilizing Genetic Algorithm (GA) based optimized nonlinear Half-Gaussian Bayesian filter. On the other hand, the skeletal muscle force signal is filtered using a Chebyshev type-II filter. The sEMG is considered as input whereas force signal is considered as an output. Since each model captures the dynamics differently, we obtained multiple linear and nonlinear models using System Identification (SI) for the sEMG data corresponding to the three sensors. First, the outputs of all the linear and nonlinear models from the three sensors are fused separately and then

the resultant three outputs are fused with a probabilistic Kullback Information Criterion (KIC) for model selection and an adaptive probability of KIC. The final fused output using this approach gives improved skeletal muscle force estimates.

The paper is organized as follows, the present section covers the introduction and literature work, which is followed by the description of the experimental set-up and pre-processing, then system identification and linear and nonlinear modeling is discussed, followed by the data fusion algorithm. The paper is concluded by a section with, results and discussions, and followed by the conclusions and future work.

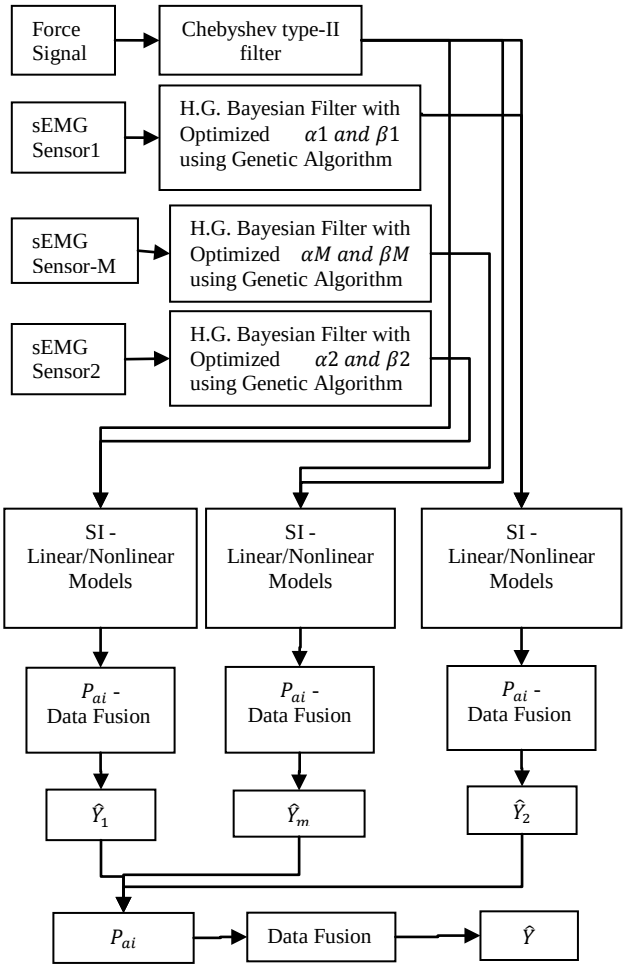

Figure 1. Flow chart for estimation of skeletal muscle force using an adaptive data fusion algorithm.

II. Experimental Set-Up and Pre-Processing

The sEMG and skeletal muscle force signals are acquired using LabVIEW™ 8.2 simultaneously at a sampling rate of 2000 Hz. A DELSYS® Bagnoli-16 EMG system with DE-2.1 differential EMG sensors is used for sEMG data capturing. However, the corresponding force data was captured using NI ELVIS with Interlink Electronics FSR 0.5" circular force sensor. The experimental set-up is shown in Figure 2. One sEMG sensor was placed on the motor point of the ring finger and two adjacent to the motor point of a healthy subject. Skin surface on the forearm of the subject was prepared with the International Society of Electrophysiology and Kinesiology (ISEK) protocol prior to placing sEMG sensors.

The nonlinear Bayesian filter yields good sEMG data and significantly reduces the influence of noise and it also extracts a signal that best describes the EMG signals and may permit effective use in prosthetic control [10]. The sEMG signal can be modeled with the assumption that the conditional probability of the rectified EMG signal is a filtered random process with random rate. The "Half-Gaussian measurement model" for the rectified EMG signal is given by Equation (1), [10].

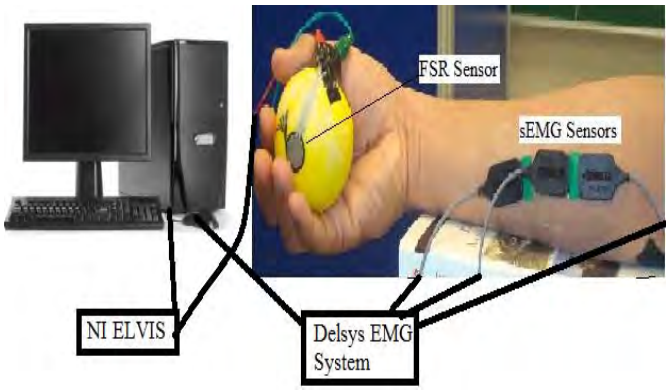

Figure 2. Experimental Set-Up.

$$P(emg|x) = 2 * exp(-\frac{emg^2}{2*x^2})/(2 * \pi * x^2)^{1/2}. \qquad (1)$$

The likelihood function for the rate evolving in time is given by the Fokker–Planck partial differential equation, where the two free parameters in the signal are the expected rate of gradual drift, α and the expected rate of sudden shifts β [10]. The two free parameters of the sEMG signal are optimized using an elitism based GA. On the other hand the skeletal muscle force signal is filtered with a Chebyshev type II low pass filter.

III. System Identification – Linear and Nonlinear Modeling

A system can be modeled either by using physics based mathematical models or by System Identification (SI) [11]. Parametric SI gives a dynamic model such as the Auto Regressive with eXogenous input (ARX) or Output Error (OE) of the system in mathematical form. In this research, we use the SI approach to model the two signals. The sEMG is the input to the system and the intended finger/hand force is output. In this work, mutli- linear and nonlinear models are obtained for modeling of sEMG and hand/finger force signals for three sensors for the ring finger of the dominant hand of a healthy subject. Six linear and three nonlinear models are obtained for the motor point sEMG signal, three linear and five nonlinear models are obtained for the ring1 sensor, and six linear and five nonlinear models are obtained for ring2

sensor data. Table I and II gives the structures of linear and nonlinear models respectively.

The model order of the various models used in this work are as follows: linear models for the motor point data, OE model of order 6, ARX model of order 6, ARMAX model of model order 5, Box-Jenkins (BJ) model of order 18, State-Space model with subspace method (N4SID) of order 12 and a State-Space model with prediction error/maximum likelihood method (PEM) of order 12 are obtained using SI. For ring1 sensor (sensor adjacent to the motor point sensor) data OE model of order 17, ARMAX model of order 35 and BJ model of order 11 are obtained. For ring2 sensor (sensor on opposite side of ring1 sensor) data OE model of order 45, ARX model of order 12, ARMAX model of order 17, BJ model of order 14, N4SID model of order 13 and PEM model of order 22 are obtained. Table I gives the structure of all the linear models. In table I y is output, t is time, $B(q)$, $F(q)$, $A(q)$, $C(q)$, $D(q)$, are polynomials, q is a backward shift operator, u is input, n_k is delay and e is error [12]. For State-Space models:- x is state, t is time, Ts is sampling time, u is input, e is error, A, B, K, C, and D are system matrices, and y is output [12].

TABLE I
LINEAR MODELS AND THEIR STRUCTURES

Linear Model Name	Linear Model Structure
Output Error	$y(t) = \frac{B(q)}{F(q)}u(t-n_k) + e(t)$
ARX	$A(q)y(t) = B(q)u(t-n_k) + e(t)$
ARMAX	$A(q)y(t) = B(q)u(t-n_k) + C(q)e(t)$
Box-Jenkins	$y(t) = \frac{B(q)}{F(q)}u(t-n_k) + \frac{C(q)}{D(q)}e(t)$
State-Space – subspace method	$x(t+Ts) = Ax(t) + Bu(t) + Ke(t)$ $y(t) = Cx(t) + Du(t) + e(t)$
State-Space – prediction error/maximum likelihood method	$x(t+Ts) = Ax(t) + Bu(t) + Ke(t)$ $y(t) = Cx(t) + Du(t) + e(t)$

Table II gives the structures of nonlinear models. The nonlinear models for the motor point data are obtained as, the nonlinear ARX with a sigmoidnet nonlinearity estimator, nonlinear Wiener-Hammerstein models with a piecewise linear nonlinearity estimator, and a saturation based estimator. For each ring1 and ring2 signal data sets, five nonlinear Wiener-Hammerstein models with nonlinearity estimators as 'piecewise linear – pwlinear,' 'sigmoidnet,' 'saturation,' 'deadzone,' and wavelet network' are obtained.

In table II f is a nonlinear function for the nonlinear ARX model. Inputs to f are model regressors. $y_p(t)$ is the predicted output as a weighted sum of past output values and current and past input values. For the nonlinear Hammerstein-Wiener model $u(t)$ and $y(t)$ are the inputs and outputs for the system, respectively. f and h are nonlinear functions that corresponds to the input and output nonlinearity, respectively. $w(t)$ and $x(t)$ are internal variables. $w(t)$ has the same dimension as $u(t)$. $x(t)$ has the same dimension as $y(t)$. $B(q)$ and $F(q)$ in the linear dynamic block are polynomials in the backward shift operator. For nonlinear Hammerstein-Weiner model with deadzone nonlinearity estimator, F is a nonlinear function of x with the properties given in the table II. For nonlinear Hammerstein-Weiner model with wavelet network as nonlinearity estimator, $\kappa(s)$ as a wavelet function, and β_k is a row vector such that $\beta_k(x-\gamma_k)$ is a scalar. If only the input nonlinearity is present, the model is called the Hammerstein model. If only the output nonlinearity is present, the model is called the Wiener model [12].

TABLE II
NONLINEAR MODELS AND THEIR STRUCTURES

Nonlinear Model Name	Nonlinear Model Structure
Nonlinear ARX – Sigmoidnet	$y_p(t) = f(y(t-1), y(t-2), y(t-3), \dots, u(t-1), u(t-2), \dots)$; $f(z) = \frac{1}{e^{-z}+1}$ is sigmoid function.
Nonlinear HW – Piecewise Linear – pwlinear	$w(t) = f(u(t))$, $x(t) = \frac{B_{ji}(q)}{F_{ji}(q)}w(t)$, $y(t) = h(x(t))$;
Nonlinear HW – Sigmoidnet	$y_p(t) = f(y(t-1), y(t-2), y(t-3), \dots, u(t-1), u(t-2), \dots)$; $f(z) = \frac{1}{e^{-z}+1}$ is sigmoid function.
Nonlinear HW – Saturation	$w(t) = f(u(t))$, $x(t) = \frac{B_{ji}(q)}{F_{ji}(q)}w(t)$, $y(t) = h(x(t))$;
Nonlinear HW – Deadzone	$y = F(x)$; $a \le x < b, \quad F(x) = 0$ $x < a, \quad F(x) = x - a$ $x \ge b, \quad F(x) = x - b$
Nonlinear HW – Wavelet Network	$g(x) = \sum_{k=1}^{n} \alpha_k \kappa(\beta_k(x-\gamma_k))$

IV. DATA FUSION ALGORITHM

A data fusion algorithm with an adaptive probability of the Kullback information criterion (KIC) is used to fuse the outputs of different models obtained [13]. Kullback information criterion (KIC) is an asymmetric measure for the model selection. Kullback's symmetric or J-divergence is the

sum of two directed divergences, which is the measure of the models dissimilarity and given by Equation (2), [14].

$$KIC(p_i) = \frac{n}{2}\log R_i + \frac{(p_i+1)n}{n-p_i-2} - n\psi\left(\frac{n-p_i}{2}\right) + g(n), \quad (2)$$

where $g(n) = n * \log(n/2)$.

In this research work, we are obtaining multi- linear and nonlinear models using SI for the sEMG sensor for the ring finger motor unit, and two adjacently placed sensors, ring1 and ring2. The probability of each model is computed using the SI model fit value, which is given by $[1 - |Y - \hat{Y}|/|Y - \bar{Y}|] * 100$. The fusion of outputs and adaptive KIC probability is shown in Figure 3 which is followed by the data fusion algorithm.

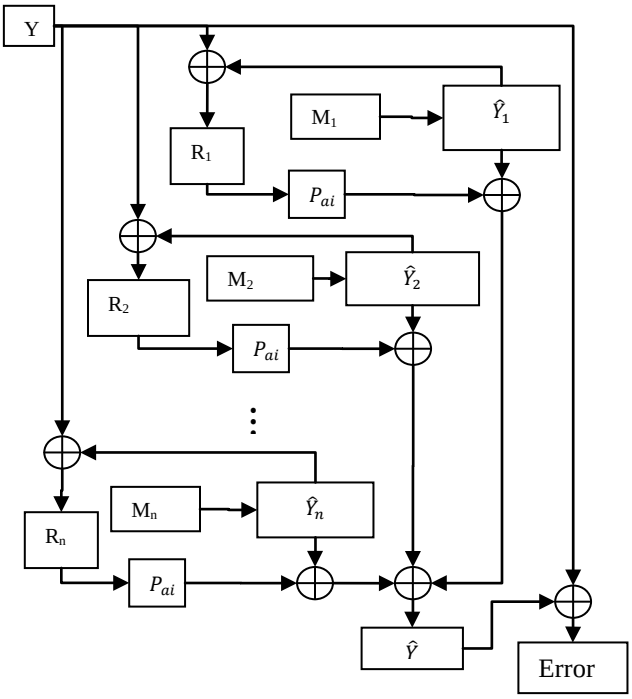

Figure 3. Adaptive KIC Probability Based Data Fusion.

The following fusion algorithm as given by [13] is applied for data fusion of the outputs of different linear and nonlinear models:

1) Identify models $M_1, M_2, \ldots, M_k$ using sEMG data (u) as input and force data (Y) as output, for k number of sensors collecting data simultaneously.
2) Compute the residual square norm

$R_i = \left\|Y - \Phi_i\widehat{\Theta}_i\right\|^2 = \left\|Y - \hat{Y}\right\|$, where $\widehat{\Theta}_i = \{{\Phi_i}^T\Phi_i\}^{-1}{\Phi_i}^T Y$, and

$$\Phi = \begin{bmatrix} Y_p^T & u_p^T & Y_{p-1}^T & \ldots & u_1^T \\ Y_{p+1}^T & u_{p+1}^T & Y_p^T & \ldots & u_2^T \\ \vdots & \vdots & \vdots & \ddots & \vdots \\ Y_{n-1}^T & u_{n-1}^T & Y_{n-2}^T & \ldots & u_{n-p}^T \end{bmatrix}.$$

3) Calculate the model criteria coefficient using Equation (2).
4) Compute the model probability $p(M_i|Z) = \frac{e^{-l_i}}{\sum_{j=1}^{k} e^{-l_j}}$, where l is model selection criterion, i.e. $KIC(p_i)$.
5) Compute the fused model output $\hat{Y}_f = \sum_{i=1}^{k} p(M_i|Z)\hat{Y}_i$.
6) Compute the overall model from $\hat{Y}_f$ and force data.

Here all the computation from step 2) to 6) is adaptive i.e. the residual square norm, $KIC(p_i)$, model probability $p(M_i|Z)$, and fused model output $\hat{Y}_f$ are being updated with time or for each data point.

V. Results and Discussion

An adaptive KIC probability based data fusion algorithm is applied to linear and nonlinear models separately for the models obtained using three sets of input and output data for three sEMG sensors. First the fusion based output for each sensor is obtained and then the three fusion based outputs from three sEMG sensors are fused to get the improved estimates of the skeletal muscle force. The following plots show the improvement in the force estimates in succession with different sensors separately and then combined. All the plots have the measured skeletal muscle force signal in green and the estimated force signal in red color. Figure 4 is a plot of measured and Chebyshev type II filtered finger force data with the adaptive KIC probability fusion based force for the first sensor named as ring1. The two signals are very clear and the estimated signal shows good follow up of the measured signal. Figure 5 shows the measured and Chebyshev type II filtered skeletal muscle force with the adaptive KIC probability fusion based force signals for the second sensor named as ring2. It is evident that the measured signal has a very close follow up by the estimated signal.

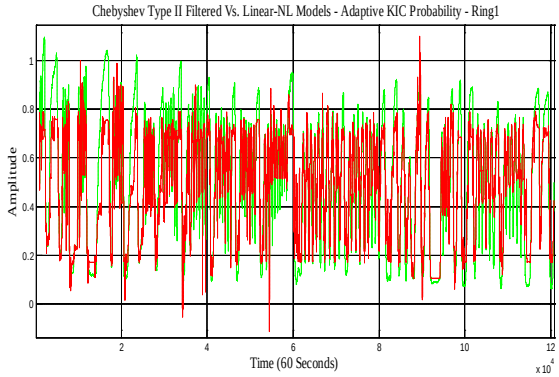

Figure 4. Chebyshev Type II vs. Adaptive KIC Probability Based Force from Linear and Nonlinear Models for Ring1 Sensor.

Figure 6 shows the measured and Chebyshev type II filtered skeletal muscle force with the adaptive KIC probability fusion based force signals for third sensor placed on the motor point of ring finger. The results for this sensor are best among the three based of the used three sensor data and it is evident that the measured signal has a very close follow up by the estimated signal.

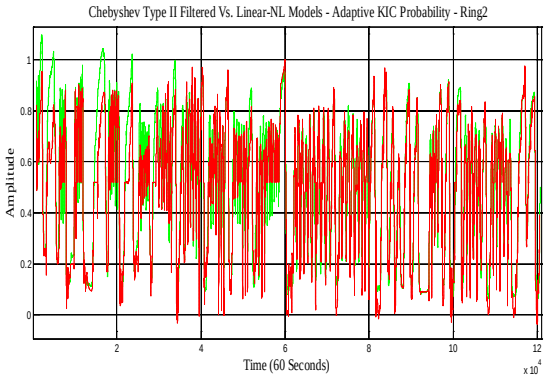

Figure 5. Chebyshev Type II vs. Adaptive KIC Probability Based Force from Linear and Nonlinear Models for Ring2 Sensor.

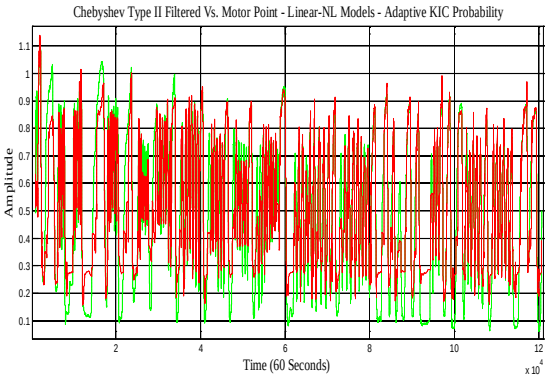

Figure 6. Chebyshev Type II vs. Adaptive KIC Probability Based Force from Linear and Nonlinear Models for Motor Point Sensor.

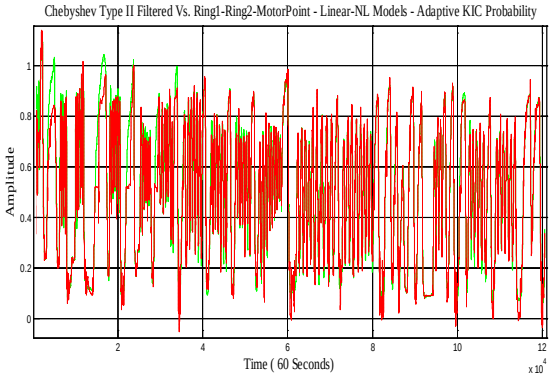

Figure 7. Chebyshev Type II vs. Adaptive KIC Probability Based Force from Linear and Nonlinear Models for Ring1, Ring2 and Motor Point Sensor Combined.

Finally the estimated skeletal muscle force from three sEMG sensors is further fused with adaptive KIC probability based data fusion algorithm. Figure 7 shows the comparison of the measured and Chebyshev type II filter with the final adaptive KIC probability based fusion skeletal muscle force estimate using three sEMG sensors. The final result for three sensors is the best estimate of skeletal muscle force and it is evident that the measured signal has a very close follow up by the estimated signal.

The results show that there is a decrease in the percentage error from the linear and nonlinear model fusion based separate outputs to the fusion based combined output of linear and nonlinear models combined for all three sensors. However, these results show that there is a 16% improvement in the mean fit value of the motor point signal models with the adaptive KIC probability based data fusion algorithm for multi-sensors (three in this case). Figure 8 and 9 show the validation plots of this approach for two separate sets of sEMG and skeletal muscle force data where green signal is the Chebyshev type II filtered measured force signal and the blue signal is estimated using this approach.

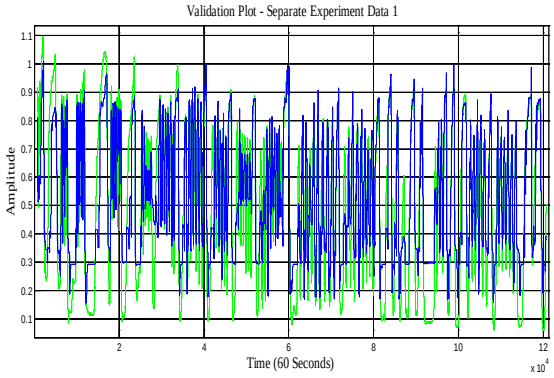

Figure 8. Validation Plot 1 - Chebyshev Type II vs. Estimated Force Signal using Adaptive KIC Probability.

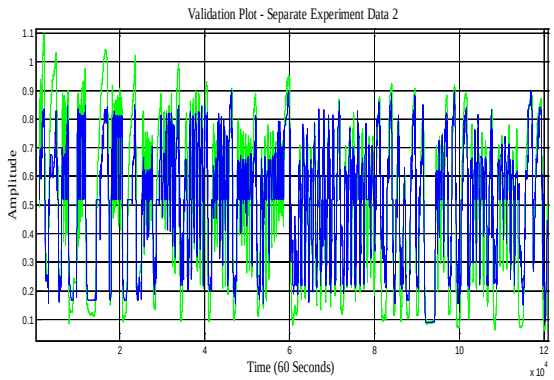

Figure 9. Validation Plot 2 - Chebyshev Type II vs. Estimated Force Signal using Adaptive KIC Probability.

VI. CONCLUSION AND FUTURE WORK

Different linear and nonlinear models are obtained using system identification (SI) for three sets of data. Linear and nonlinear models' outputs are fused separately for each sensor and then fused together to get the final force estimate for each sensor. The net force estimates for each sensor is then applied with adaptive KIC probability based data fusion algorithm.

The final estimates of the skeletal muscle force gives improved results. Future work will focus on the improved data collection techniques and capturing data at higher sampling rate (6000 samples per second). Also, we would design new model selection criteria using different model selection criteria such as Akaike Information Criterion (AIC), Kullback Information Criterion (KIC) and the Bayesian Information Criterion (BIC).

ACKNOWLEDGMENT

This research was sponsored by the US Department of the Army, under the award number W81XWH-10-1-0128 awarded and administered by the U.S. Army Medical Research Acquisition Activity, 820 Chandler Street, Fort Detrick MD 21702-5014. The information does not necessarily reflect the position or the policy of the Government, and no official endorsement should be inferred. For purposes of this article, information includes news releases, articles, manuscripts, brochures, advertisements, still and motion pictures, speeches, trade association proceedings, etc.

REFERENCES

[1] Kathryn Ziegler-Graham, PhD, et al., Estimating the Prevalence of Limb Loss in the United States - 2005 to 2050, Archives of Physical Medicine and Rehabilitation, 89 (2008): 422-429.

[2] O'Connor, P., Iraq war vet decides to have second leg amputated, Columbia Missourian, 2009.

[3] N. Dechev, W. L. Cleghorn, and S. Naumann, Multiple finger, passive adaptive grasp prosthetic hand, Mechanism and Machine Theory 36(2001), pp. 1157-1173.

[4] Haruhisa Kawasaki, Tsuneo Komatsu, and Kazunao Uchiyama, Dexterous Anthropomorphic Robot Hand With Distributed Tactile Sensor: Gifu Hand II, IEEE/ASME Transactions on Mechatronics, Vol. 7, No. 3, September 2002, pp. 296-303.

[5] M. Zecca, S. Micera, M. C. Carrozza, and P. Dario, Control of Multifunctional Prosthetic Hands by Processing the Electromyographic Signal, Critical Reviews™ in Biomedical Engineering, 30(4-6), 2002, pp. 459-485.

[6] Claudio Castellini and Patrick van der Smagt, Surface EMG in advanced hand prosthetics, Biological Cybernetics, (2009) 100, pp. 35-47.

[7] P. Kumar, A. Sebastian, C. Potluri, A. Urfer, D. S. Naidu, and M. P. Schoen, “Towards Smart Prosthetic Hand: Adaptive Probability Based Skeletal Muscle Fatigue Model,” 32nd Annual International Conference of the IEEE EMBS Conference, 2010.

[8] P. Kumar, C. Potluri, A. Sebastian, S. Chiu, A. Urfer, D. S. Naidu, and M. P. Schoen, "An Adaptive Multi Sensor Data Fusion with Hybrid Nonlinear ARX and Wiener-Hammerstein Models for Skeletal Muscle Force Estimation," 14th WSEAS Int. Conf. on Systems, Vol. 1, pp. 186-191, July 2010.

[9] P. Kumar, C. Potluri, M. Anugolu, A. Sebastian, J. Creelman, A. Urfer, S. Chiu, D. S. Naidu, and M. P. Schoen, “A Hybrid Adaptive Data Fusion with Linear and Nonlinear Models for Skeletal Muscle Force Estimation,” 5th Cairo International Conference on Biomedical Engineering, Cairo, Egypt, Dec. 16-18, 2010.

[10] Terence D. Sanger, Bayesian Filtering of Myoelectric Signals, J Neurophysiol, 97, 2007, pp. 1839–1845.

[11] Lennart Ljung, System Identification: Theory for the User. 2nd edition, Printice Hall PTR, 1999, Chap. 1, pp. 1-15.

[12] Lennart Ljung, System Identification ToolboxTM 7 User's Guide, The MathWorks, Inc., 2010.

[13] H. Chen and S. Huang, "A Comparative study on Model Selection and Multiple Model Fusion," 7th International Conference on Information Fusion, pp. 820-826, 2005.

[14] Abd-Krim Seghouane, M. Bekara, G. Fleury, "A Small Sample Model Selection Criterion Based on Kullback's symmetric Divergence," IEEE Transaction, pp. 145-148, 2003.

An Adaptive Hybrid Data Fusion Based Identification of Skeletal Muscle Force with ANFIS and Smoothing Spline Curve Fitting

Parmod Kumar, C. H. Chen, Anish Sebastian, Madhavi Anugolu, Chandrasekhar Potluri, Amir Fassih, Yimesker Yihun, Alex Jensen, Yi Tang, Steve Chiu, Ken Bosworth, D. S. Naidu and Marco P. Schoen
Measurement and Control
Engineering Research Center
College of Science and Engineering
Idaho State University
Pocatello, ID 83209, USA
Email: kumaparm@isu.edu, chenchen@isu.edu, sebaanis@isu.edu, anugmadh@isu.edu, potlchan@isu.edu, fassamir@isu.edu, yihuyime@isu.edu, jensalex@isu.edu, mrtang_42@hotmail.com, chiustev@isu.edu, boswkenn@isu.edu, naiduds@isu.edu, schomarc@isu.edu

Jim Creelman and Alex Urfer
Department of Physical and Occupational Therapy
Idaho State University
Pocatello, ID 83209, USA
Email: creejame@isu.edu, urfealex@isu.edu

***Abstract*—Precise and effective prosthetic control is important for its applicability. Two desired objectives of the prosthetic control are finger position and force control. Variation in skeletal muscle force results in corresponding change of surface electromyographic (sEMG) signals. sEMG signals generated by skeletal muscles are temporal and spatially distributed that result in cross talk between adjacent sEMG signal sensors. To address this issue, an array of nine sEMG sensors is used with a force sensing resistor to capture muscle dynamics in terms of sEMG and skeletal muscle force. sEMG and skeletal muscle force are filtered with a nonlinear Teager–Kaiser Energy (TKE) operator based nonlinear spatial filter and Chebyshev type-II filter respectively. Multiple Takagi-Sugeno-Kang Adaptive Neuro Fuzzy Inference Systems (ANFIS) are obtained using sEMG as input and skeletal muscle force as output. Outputs of these ANFIS systems are fitted with smoothing spline curve fitting. To achieve better estimate of the skeletal muscle force, an adaptive probabilistic Kullback Information Criterion (KIC) for model selection based data fusion algorithm is applied to the smoothing spline curve fitting outputs. Final fusion based output of this approach results in improved skeletal muscle force estimates.**

Keywords – sEMG; TKE; ANFIS; KIC

I. INTRODUCTION

In the United States, 1.6 million people lived with amputations during 2005 [1]. This increase reflects on the war effects in Afghanistan and Iraq since 2003 [2]. During the same period of time, the fields of prosthetic design and development research for prosthesis has received increased attention. Precise and timely control of prosthesis is critical for its applicability, which necessitates the replacement of conventional algorithms by intelligent systems and decision methods. Therefore, a natural means of interface between the user and prosthesis is required. sEMG signals from skeletal muscles are a convenient means for users who do not want to deal with additional surgeries and regular hygiene problems. sEMG signals are simply electric voltages ranging between -5 and +5 [mV] which can be recorded on the skin surface of a hand amputee's forearm. Skeletal muscles generate a base sEMG even without a limb movement which changes with different movements and applied forces. This makes sEMG signals useful for position and force control of prosthesis. Presently available prosthetic hands have no tactile or proprioceptive feedback for grasping and only user's direct vision as a sensory feedback is available for its position control. Afore mentioned reasons cause 30–50% of the upper extremity amputees to choose not to use their prosthetic hand on a regular bases [3-4].

Effective grasping of any object requires the knowledge of force and its feedback. Since the hand amputee uses only sEMG signals collected from skeletal muscles, there is no hand force information directly available. sEMG is a measure of the nervous excitation that ultimately is responsible for activating the skeletal muscles, which in turn generate the finger forces with the help of the link kinematics of human hand. Therefore, a model or estimation scheme is needed for the dynamic estimation of skeletal muscle force from sEMG

signals. There have been numerous efforts in this direction and some of the recent are evident in the research work of [5-10].

The present work proposes a novel scheme of skeletal muscle force identification using sEMG signals. An array of nine sEMG sensors is used to record sEMG signals and skeletal muscle force signals recorded with a force sensing resistor from the arm of a healthy subject, which respectively is explained in detail in Section II and III. Eight Takagi-Sugeno-Kang ANFIS with different membership functions each with a rule base of ten are designed. The training of each ANFIS is done using a hybrid optimization method with zero error tolerance and 40 epochs. Each of the force signals simulated using these ANFIS and measured force signals are applied to a smoothing spline curve fitting method. Figure 1 shows the flow chart of the proposed approach. Final estimated force signal shows good match with the measured signal. This approach is tested on two different data sets of 45 and 60 seconds duration and the results seem promising. The paper is organized in eight sections. Present section follows the experimental set-up and then signal processing, ANFIS modeling, smoothing spline curve fitting, data fusion, results and discussion and conclusion and future work is presented respectively.

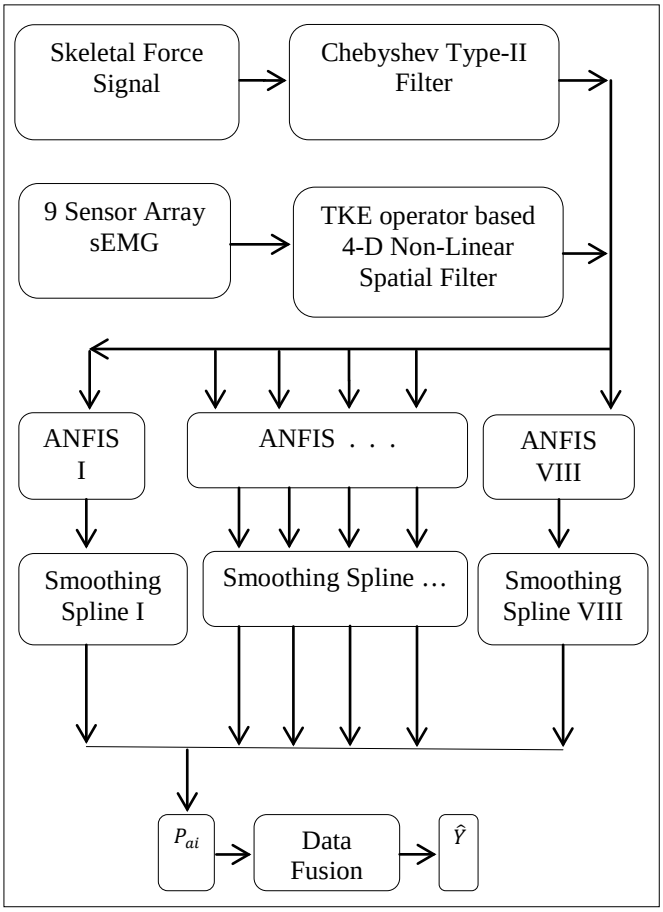

Figure 1. Flow chart of the approach used in this research work.

II. Experimental Set-Up

Based on the set-up of a sEMG sensor array in [11], an experiment set-up was developed using DELSYS® Bagnoli-16 EMG system with nine DE-3.1 sEMG sensors to capture sEMG signals from skeletal muscles. Here, the array involves nine sensors covering four directional spatial distributions of the sEMG signal. The middle three sEMG sensors were attached directly on the skin surface above the motor point of the flexor digitorum superficialis muscle (FDS) which controls the flexion of the ring finger. Appropriate sEMG electrode attachment point for the flexion of the ring finger was identified using a wet probe muscle stimulator at the FDS (RICH-MAR, HV 1000).

Prior to placing the sEMG sensors, the skin surface of the subject was prepared according to International Society of Electrophysiology and Kinesiology (ISEK) protocols. The thumb movement was restricted in this experiment using a thumb splint. However, the corresponding force data was captured using NI ELVIS™ with Interlink™ Electronics FSR 0.5” circular force sensor. Experimental set-up is shown in Figure 2, where 9 sensors are shown on a healthy subject forearm, holding a stress ball for force measurements. The sEMG and finger force data was collected at a sampling rate of 2000 Hz using LabVIEW™ in conjunction with DELSYS® Bagnoli-16 EMG and NI ELVIS™. With this experimental set-up we conducted several experiments of 30 seconds, 45 seconds and 60 seconds durations.

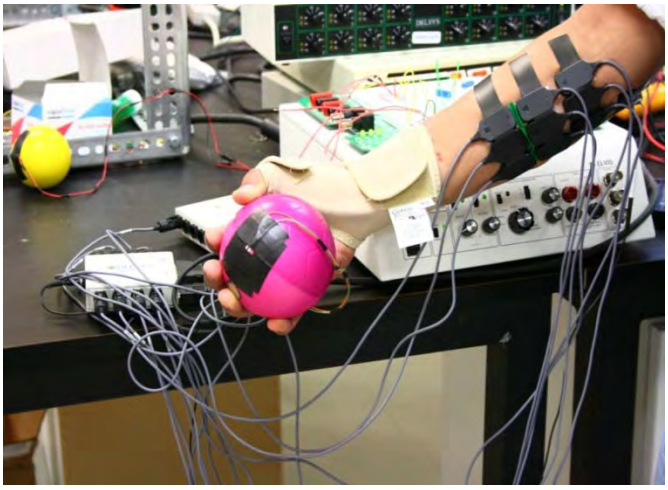

Figure 2. Experiment set-up.

III. Signal Processing

The recorded sEMG signal is filtered using nonlinear spatial filtering for multichannel surface EMG. As given in [11], this nonlinear spatial filter is derived from “Nonlinear Teager-Kaiser Energy (TKE) Operator.” As given in [11], the

TKE operator in the time domain on sEMG signal is defined by Equation (1).

$$\Psi[x(n)] = x^2(n) - x(n+1) * x(n-1). \quad (1)$$

Here, Ψ is the TKE operator and $x(n)$ is the time domain sEMG signal. Based on the TKE operator, the four-dimensional nonlinear spatial filter is given by Equation (2).

$$\Psi_{d,4}[x(m,n)] = 4 * x^2(m,n) - x(m-1,n) * x(m+1,n) - x(m,n-1) * x(m,n+1) - x(m-1,n+1) * x(m+1,n-1) - x(m-1,n-1) * x(m+1,n+1). \quad (2)$$

Figure 3 shows a comparison between the measured and nonlinear spatial filtered sEMG signals.

A Chebyshev type II infinite impulse response (IIR) low pass filter with a 550 Hz pass band frequency is used to filter the skeletal muscle force signal. Figure 4 shows the comparison between the measured and Chebyshev type II filtered skeletal muscle force signal.

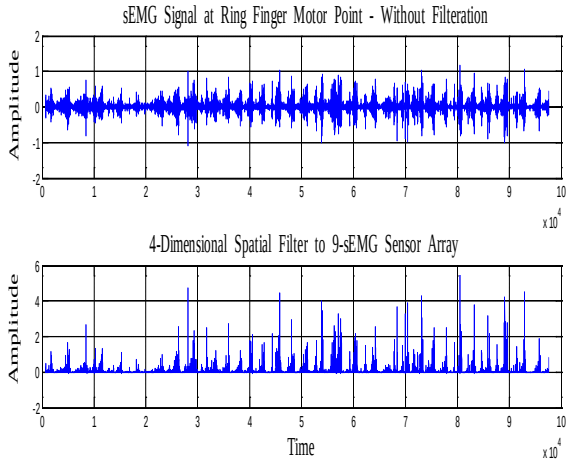

Figure 3. sEMG signal from ring finger.

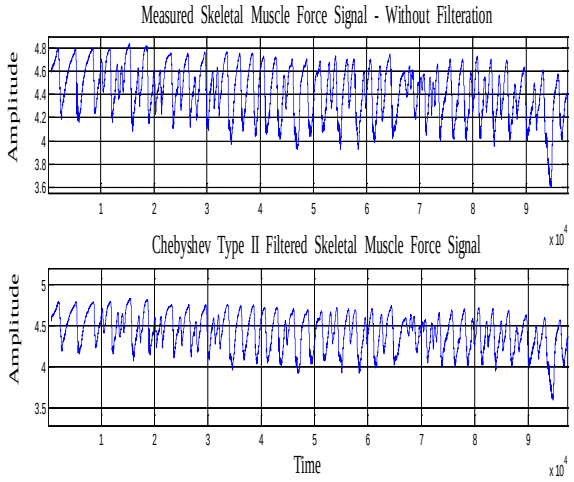

Figure 4. Skeletal muscle force signal from ring finger.

IV. ANFIS MODELING

In 1965 professor Lofti A. Zadeh introduced the concept of "*Fuzzy Sets*", which are sets with imprecise amplitudes [12]. Dr. Zadeh stated that the "*membership*" in a fuzzy set is a matter of degree and not a matter of affirmation or denial. For last four decades, this proposal has gained recognition as an important point in the evolution of modern concept of imprecision and uncertainty [12]. This innovation represents a paradigm shift from the classical sets or the crisp sets to "*Fuzzy Sets*" [12].

Fuzzy set and fuzzy logic theory can be used to capture the natural phenomenon of the imprecision and uncertainty [12]. The membership function is the characteristic of fuzzy set, which is a function whose range is an ordered membership set within the closed unit interval [12].

A crisp set which is a collection of distinct objects is defined in a way to partition objects in a given domain of discourse into two groups: members and non-members [12]. On the other hand, a fuzzy set can be formed by assigning a membership value (which represents the degree to which an object belongs to a fuzzy set) to each object in the interval of 0 to 1 [12]. Fuzzy membership functions can be of different forms such as triangular, trapezoidal, pi, bell and Gaussian form.

Fuzzy Inferance System (FIS) in fuzzy logic can be used to model a system which is an inference system based on empirical knowledge based linguistic rules [13]. The fuzzy inference system is composed of five steps: fuzzification of the input variables, application of the fuzzy operator (AND or OR) in the precedent, implication from the precedent to the subsequent, aggregation of the subsequents across the rules, and defuzzification. In the fuzzification process, the membership values coming from quantitative measurements are converted to linguistic values based on the membership functions [13].

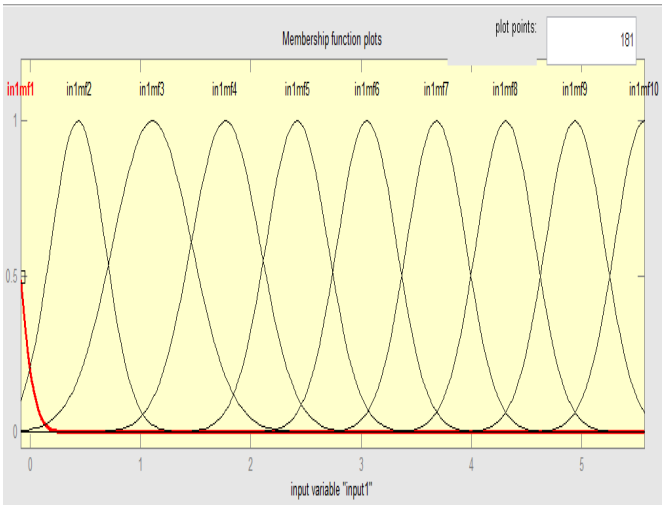

Figure 5. Gaussian membership functions for sEMG.

Figure 5 shows the plot of Gaussian membership functions for fuzzification of sEMG. The process of fuzzification followed by IF .. AND.. THEN ..OR ELSE type control or relation/estimation rules [13]. The output of the rules is computed as a max-min composition [13]. In the defuzzification process, the output of the rules has to be converted to a crisp value [13].

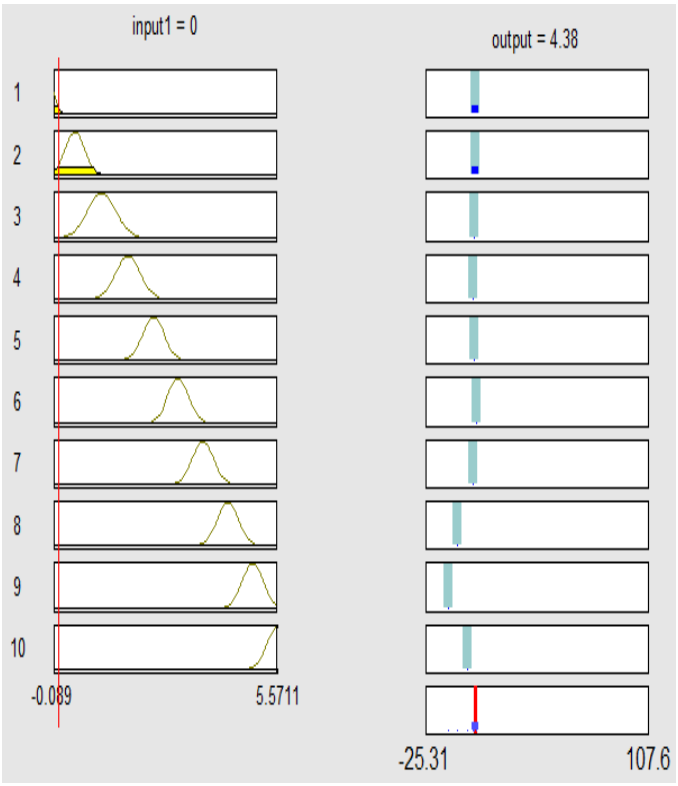

Figure 6. Illustration of ANFIS inference mechanism.

TABLE I. MEMBERSHIP FUNCTIONS

S. No.	Membership Function
1.	Gaussian (GAUSSMF)
2.	Gaussian combination (GAUSS2MF)
3.	Difference between two sigmoidal membership functions (DSIMF)
4.	Generalized bell-shaped (GBELLMF)
5.	Π-shaped (PIMF)
6.	Product of two sigmoidally shaped membership functions (PSIMF)
7.	Trapezoidal-shaped (TRAPMF)
8.	Triangular-shaped (TRIMF)

Using eight different membership functions types we designed eight single-output Sugeno-type adaptive neuro-fuzzy inference systems (ANFIS) using a grid partition on the data. The output membership function in each of these is linear. Each ANFIS has ten rules and connection type is 'And' with a weight of 1. For the 'And' method 'product' and for 'Or' method 'probabilistic' types are used for each ANFIS. Deffuzification is achieved using weighted average (wtaver) from each rule. Figure 6 shows the rules for ANFIS with Gaussian membership functions and illustrate the ANFIS inference mechanism. The membership functions used are tabulated in Table 1.

A Gaussian function is given by $f(x;\sigma,c) = e^{\frac{-(x-c)^2}{2\sigma^2}}$ for some real constants c and $\sigma > 0$, and $e = 2.718$. Gaussian combination membership function (GAUSS2MF) depends on the c and σ parameters [14]. The sigmoidal membership function is given as $f(x;a,c) = \frac{1}{1+e^{-a(x-c)}}$ and depends on the two parameters a and c. The difference between two sigmoidal membership function (DSIMF) which is the difference between two sigmoidal functions depends on the four parameters a_1, c_1, a_2, and c_2 [14]. Generalized bell-shaped membership function (GBELLMF) is given as $f(x;a,b,c) = \frac{1}{1+\left|\frac{x-c}{a}\right|^{2b}}$ and depends on three parameters a, b, and c where parameter a and b decide the width of the curve and parameter c locates the center, usually $b > 0$ [14]. Pi-shaped membership function (PIMF) is given by

$$f(x;a,b,c,d) = \begin{pmatrix} 0, & x \le a \\ 2\left(\frac{x-a}{b-a}\right)^2, & a \le x \le \frac{a+b}{2} \\ 1-2\left(\frac{x-b}{b-a}\right)^2, & \frac{a+b}{2} \le x \le b \\ 1, & b \le x \le c \\ 1-2\left(\frac{x-c}{d-c}\right)^2, & c \le x \le \frac{c+d}{2} \\ 2\left(\frac{x-d}{d-c}\right)^2, & \frac{c+d}{2} \le x \le d \\ 0, & x \ge d \end{pmatrix}, \quad \text{and}$$

evaluated at the points given by vector x. The "feet" of the curve is determined by parameters a and d whereas parameters b and c decides its "shoulders" [14]. The Product of two sigmoidally shaped membership functions (PSIMF) is simply the products of two sigmoidal functions as given before. The trapezoidal shaped membership function (TRAPMF) is given by

$$f(x;a,b,c,d) = \begin{pmatrix} 0, & x \le a \\ \frac{x-a}{b-a}, & a \le x \le b \\ 1, & b \le x \le c \\ \frac{d-x}{d-c}, & c \le x \le d \\ 0, & d \le x \end{pmatrix}$$ which depends on

four scalar parameters a, b, c, and d. The triangular shaped membership function (TRIMF) is given by

$$f(x;a,b,c) = \begin{pmatrix} 0, & x \le a \\ \frac{x-a}{b-a}, & a \le x \le b \\ \frac{c-x}{c-b}, & b \le x \le c \\ 0, & c \le x \end{pmatrix}$$ which depends on the scalar parameters a, b and c [14].

V. Smoothing Spline Curve Fitting

MATLAB® Curve Fitting Toolbox™ is a useful tool for fitting curves and surfaces to acquired data [15]. It can be used to do exploratory data analysis, preprocessing and post-processing of the data, comparing candidate models, and for removing outliers [15]. Weights for each smoothing spline curve fit are calculated by subtracting the ANFIS output from the measured skeletal muscle force output. A graphical user interface is used to fit the smoothing spline curve to each output from eight ANFIS with respective weights. Smoothing spline which is a piecewise polynomial computed from a smoothing parameter (p) of 0.92 is fitted to each of eight outputs of ANFIS. Smoothing parameter (p) is a number between 0 and 1. Change in the value of p from 0 to 1 results in the change in smoothing spline. For $p = 0$ the smoothing spline is a least-square straight-line approximation to the data whereas for $p = 1$ it gives the "natural" cubic spline interpolant to the data [15].

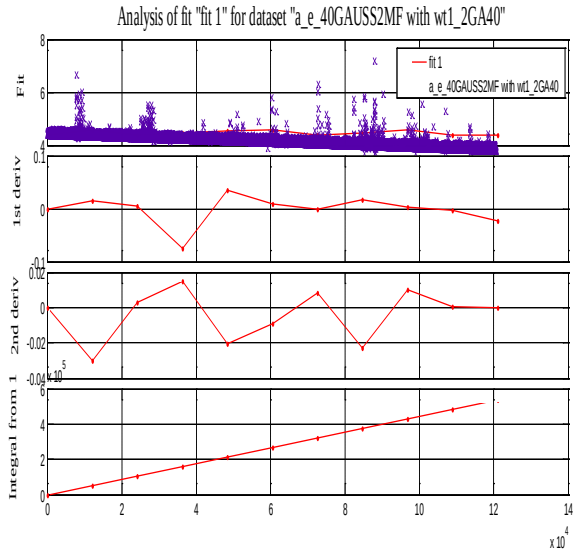

Figure 7. Analysis results for smoothing spline curve fitting to the output of ANFIS with Gaussian membership function.

For the specified weight (w_i) and smoothing parameter (p) a smoothing spline s is formed which minimizes the parameter J given by Equation (3).

$$J = p\sum_i w_i(y_i - s(x_i))^2 + (1-p)\int(\frac{d^2s}{dx^2})^2 dx, \qquad (3)$$

where x_i and y_i are predictor and response data respectively. The smoothing parameter p should be chosen to make the error $E(s) = \sum_i w_i(y_i - s(x_i))^2$ and roughness $\int(\frac{d^2s}{dx^2})^2 dx$ small. In this work the smoothing parameter p is chosen as 0.92 [15]. Figure 7 shows the analysis results for smoothing spline curve fitting to the output of ANFIS with Gaussian membership function.

VI. Data Fusion

Data fusion of multiple outputs of smoothing spline curve fittings is done by assigning a particular probability to each individual output [16]. This method gives good estimation of the skeletal muscle force. The goodness of the fit of each smoothing spline output can be measured using System Identification (SI) model fit value which is given by Equation (4).

$$FIT = [1 - |Y - \hat{Y}|/|Y - \bar{Y}|] * 100 \qquad (4)$$

In Equation (4) Y is measured, $\hat{Y}$ is estimated and $\bar{Y}$ is mean output signal. The model selection criterion used in this paper is Kullback Information Criterion (KIC) which has shown to perform well for sEMG sensor data fusion [7-10]. The sum of two directed divergences, which is the measure of the models dissimilarity, is known as Kullback's symmetric or J-divergence [17], as given by Equation (5).

$$KIC(p_i) = \frac{n}{2}logR_i + \frac{(p_i+1)n}{n-p_i-2} - n\psi\frac{(n-p_i)}{2}) + g(n), \qquad (5)$$

where $g(n) = n * log(n/2)$.

The fusion algorithm as given by [16] is applied for data fusion of the outputs of eight smoothing spline curve fit outputs which are obtained from eight different ANFIS models:

(I) Find smoothing spline curve fit outputs $M_1, M_2, \dots, M_k$ for k number of outputs.

(II) Compute the residual square norm

$R_i = \|Y - \Phi_i\,\hat{\Theta}_i\|^2 = \|Y - \hat{Y}\|^2$,
where $\hat{\Theta}_i = \{{\Phi_i}^T\Phi_i\}^{-1}{\Phi_i}^T Y$, and

$$\Phi = \begin{bmatrix} Y_p^T & u_p^T & Y_{p-1}^T & \dots & u_1^T \\ Y_{p+1}^T & u_{p+1}^T & Y_p^T & \dots & u_2^T \\ \vdots & \vdots & \vdots & \ddots & \vdots \\ Y_{n-1}^T & u_{n-1}^T & Y_{n-2}^T & \dots & u_{n-p}^T \end{bmatrix}.$$

(III) Calculate the model criteria coefficient using Equation (5).

(IV) Compute the model probability $p(M_i|Z) = \frac{e^{-l_i}}{\sum_{j=1}^{k1} e^{-l_j}}$, where l is model selection criterion, i.e. $KIC(p_i)$.

(V) Compute the fused model output $\hat{Y}_f = \sum_{i=1}^{k1} p(M_i|Z)\hat{Y}_i$.

(VI) Compute the overall model from $\hat{Y}_f$ and skeletal muscle force data.

Here all the computation from step (II) to (VI) is adaptive i.e. the residual square norm, $KIC(p_i)$, model probability

$p(M_i|Z)$, and fused model output $\hat{Y}_f$ are being updated with time or for each data point. Figure 8 shows the flow chart for fusion of outputs and adaptive probability of KIC.

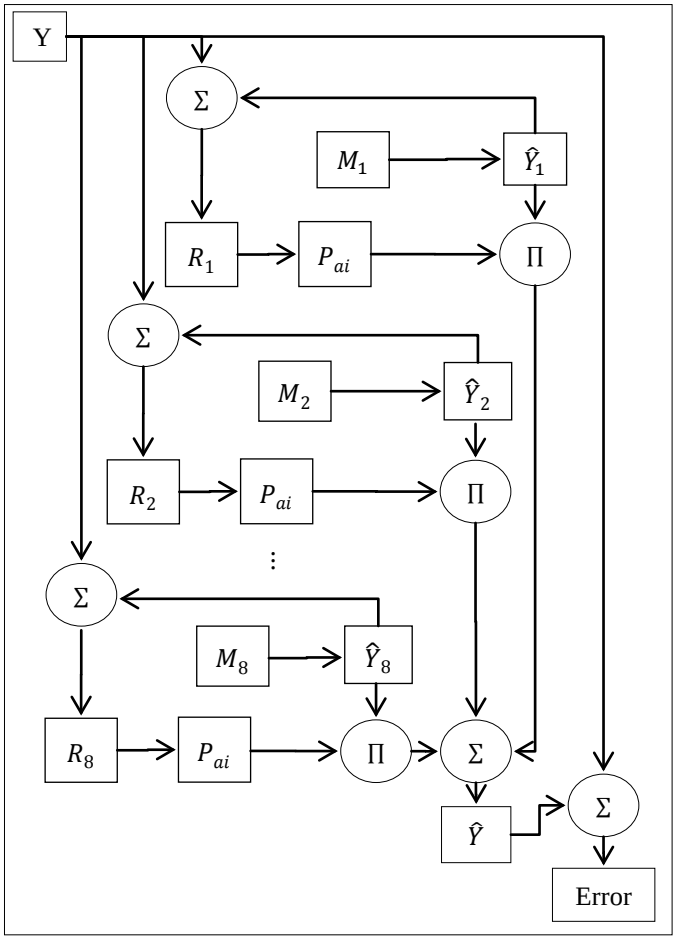

Figure 8. Flow chart for fusion of outputs and adaptive probability.

VII. Results and Discussion

The proposed method gives good estimation of the skeletal muscle force. A data set of 45 seconds is used to estimate the output. Figure 9 shows the measured and estimated skeletal muscle force using this method.

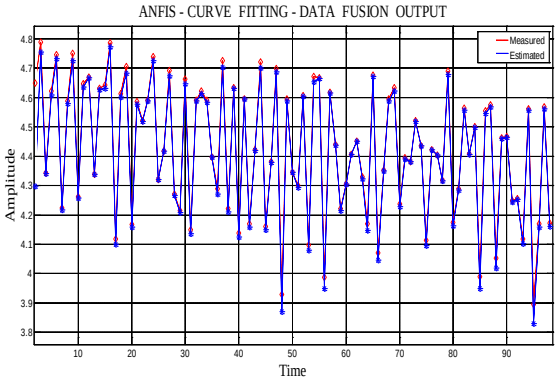

Figure 9. Plot of measured and proposed method estimated skeletal muscle force.

Figures 10 and 11 are the validation plots for 45 seconds and 60 seconds of data sets respectively. All of these three plots show a very close follow up of the measured signal by the estimated signal using this approach. Figure 12 shows the percentage error between the measured force signal and estimated finger force signal for 45 seconds of data set. The percentage error reduced to the lower values and the maximum percentage error value is 1.7 percent. The mean fit value between the measured and estimated output is 91.3 percent.

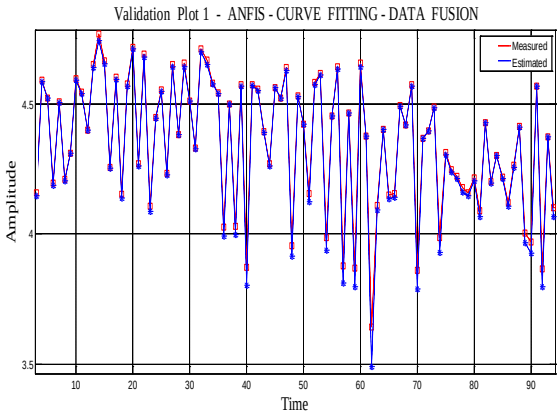

Figure 10. Validation plot 1 using different data set.

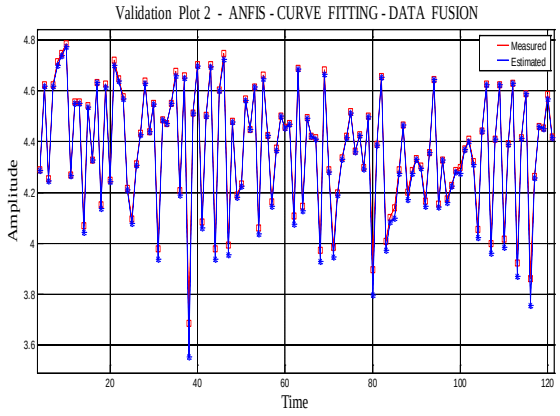

Figure 11. Validation plot 2 using different data set.

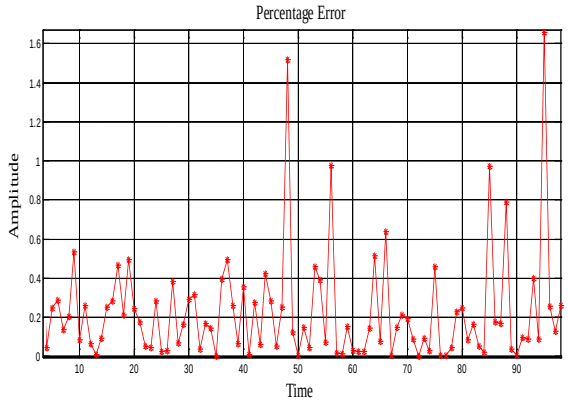

Figure 12. Percentage error plot.

Figure 13 shows the percentage error plot for different data set of 60 seconds duration. Percentage error reduced to lower values and the maximum percentage error value is 3.7 percent. The mean fit value between the measured and estimated output is 40 percent. The mean fit value for another 45 seconds of data set is 73 percent.

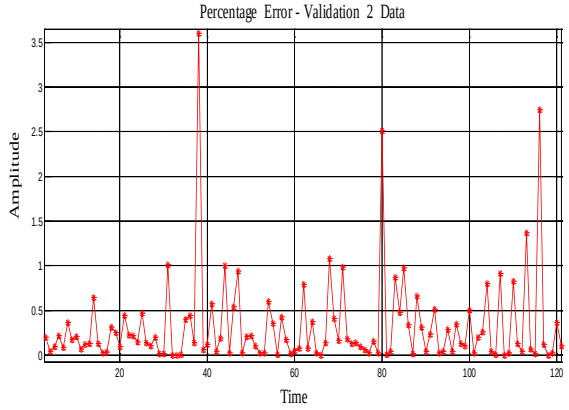

Figure 13. Percentage error plot for 60 seconds data set.

VIII. Conclusion and Future Work

Using sEMG and skeletal muscle force as input and output data, eight ANFIS were designed and tested. Output of these ANFIS were fitted with smoothing spline curve fit and resultant outputs were fused using a KIC based data fusion algorithm. This approach has been validated using two separate data sets. Results are promising and show good estimation of skeletal muscle force which can be applied to design, application and improvement of prosthetic hands for amputees.

Future work will address the improvement of data collection techniques, sEMG sensor design, use of this approach for finger angles and stiffness estimation from sEMG signals. Different modeling techniques with this approach and combined probability of different model selection criteria such as Akaike Information Criterion (AIC), Kullback Information Criterion (KIC) and the Bayesian Information Criterion (BIC) together will give improved results.

Acknowledgment

This research was sponsored by the US Department of the Army, under the award number W81XWH-10-1-0128 awarded and administered by the U.S. Army Medical Research Acquisition Activity, 820 Chandler Street, Fort Detrick MD 21702-5014. The information does not necessarily reflect the position or the policy of the Government, and no official endorsement should be inferred. For purposes of this article, information includes news releases, articles, manuscripts, brochures, advertisements, still and motion pictures, speeches, trade association proceedings, etc.

References

[1] K. Ziegler-Graham, E. J. MacKenzie, P. L. Ephraim, T. G. Travison, and R. Brookmeyer, "Estimating the Prevalence of Limb Loss in the United States - 2005 to 2050," Archives of Physical Medicine and Rehabilitation, vol. 89, pp. 422-429, March 2008.

[2] P. O'Connor. (2009, February 15). Iraq war vet decides to have second leg amputated [Online]. Available: http://www.columbiamissourian.com/stories/2009/02/15/soldier-who-lost-leg-iraq-may-lose-other/

[3] D. J. Atkins, D. C. Y. Heard, and W. H. Donovan, "Epidemiologic overview of individuals with upper-limb loss and their reported research priorities," Journal of Prosthetics and Orthotics, vol. 8, No. 1, pp. 2-11, 1996.

[4] D. H. Silcox, M. D. Rooks, R. R. Vogel, and L. L. Fleming, "Myoelectric prostheses. A long-term follow-up and a study of the use of alternate prostheses," The Journal of Bone and Joint Surgery, vol. 75-A, No. 12, pp. 1781–1789, December 1993.

[5] P. K. Artemiadis and K. J. Kyriakopoulos, "EMG-based position and force control of a robot arm: Application to teleoperation and orthosis," *in Conf. Rec. 2007 IEEE/ASME Int. Conf. on Advanced Intelligent Mechatronics*, Zurich, pp. 1-6, September 2007.

[6] P. K. Artemiadis and K. J. Kyriakopoulos, "EMG-Based Position and Force Estimates in Coupled Human-Robot Systems: Towards EMG-Controlled Exoskeletons," in *Experimental Robotics, Springer Tracts in Advanced Robotics*, vol. 54, Berlin Heidelberg: Springer-Verlag, 2009, pp. 241-250.

[7] P. Kumar, C. Potluri, A. Sebastian, S. Chiu, A. Urfer, D. S. Naidu, and M. P. Schoen, "A Adaptive Multi Sensor Data Fusion with Hybrid Nonlinear ARX and Wiener-Hammerstein Models for Skeletal Muscle Force Estimation," in *Proc. The 14th World Scientific and Engineering Academy and Society (WSEAS) International Conference on Systems*, Corfu Island, Greece, 2010, July 22-24.

[8] P. Kumar, A. Sebastian, C. Potluri, A. Urfer, D. S. Naidu, and M. P. Schoen, "Towards Smart Prosthetic Hand: Adaptive Probability Based Skeletal Muscle Fatigue Model," in *Conf. Rec. 32nd Annual International Conference of the IEEE Engineering in Medicine and Biology Society*, Buenos Aires, Argentina, Aug. 31 – Sept. 4, 2010.

[9] P. Kumar, C. Potluri, A. Sebastian, S. Chiu, A. Urfer, D. S. Naidu, and Marco P. Schoen, "Adaptive Multi Sensor Based Nonlinear Identification of Skeletal Muscle Force," *WSEAS Transactions on Systems*, vol. 9, Issue 10, pp. 1051-1062, October 2010.

[10] P. Kumar, C. Potluri, M. Anugolu, A. Sebastian, J. Creelman, A. Urfer, S. Chiu, D. S. Naidu, and M. P. Schoen, "A Hybrid Adaptive Data Fusion with Linear and Nonlinear Models for Skeletal Muscle Force Estimation," in *Proc. 5th Cairo International Conference on Biomedical Engineering*, Cairo, Egypt, Dec. 16-18, 2010.

[11] P. Zhou, N. L. Suresh, M. M. Lowery, and W. Z. Rymer, "Nonlinear Spatial Filtering of Multichannel Surface Electromyogram Signals During Low Force Contractions," *IEEE Transactions on Biomedical Engineering*, vol. 56, No. 7, pp. 1871-1879, July 2009.

[12] A. Celikyilmaz, and I. B. Turksen, *Modeling Uncertainty with Fuzzy Logic: With Recent Theory and Applications*. Berlin Heidelberg: Springer-Verlag, 2009, pp. 11-50.

[13] J. Espinosa, J. Vandewalle, and V. Wertz, *Fuzzy Logic, Identification and Predictive Control*. Springer-Verlag London Limited, 2005.

[14] *MATLAB® Fuzzy Logic Toolbox™ User's Guide*. The MathWorks, Inc. 2010.

[15] *MATLAB® Curve Fitting Toolbox™ User's Guide*. The MathWorks, Inc. 2010.

[16] H. Chen and S. Huang, "A Comparative study on Model Selection and Multiple Model Fusion," in *Proc. 7th International Conference on Information Fusion*, New Orlean, USA, July 25-28, 2005, pp. 820-826.

[17] A. K. Seghouane, and M. Bekara, "A Small Sample Model Selection Criterion Based on Kullback's symmetric Divergence," *IEEE Transactions on Signal Processing*, vol. 52, No. 12, pp. 3314-3323, 2004.

TOWARDS SMART PROSTHETIC HAND: ADAPTIVE PROBABILITY BASED SKELETAN MUSCLE FATIGUE MODEL

Kumar P., Sebastian A., Potluri C., Urfer A., Schoen M. P., and Naidu D.S., *Fellow, IEEE*

***Abstract* - Skeletal muscle force can be estimated using surface electromyographic (sEMG) signals. Usually, the surface location for the sensors is near the respective muscle motor unit points. Skeletal muscles generate a spatial EMG signal, which causes cross talk between different sEMG signal sensors. In this study, an array of three sEMG sensors is used to capture the information of muscle dynamics in terms of sEMG signals. The recorded sEMG signals are filtered utilizing optimized nonlinear Half-Gaussian Bayesian filters parameters, and the muscle force signal using a Chebyshev type-II filter. The filter optimization is accomplished using Genetic Algorithms. Three discrete time state-space models are obtained using system identification and modal transformation for three sets of sensors for single motor unit. The outputs of these three models are fused with a probabilistic Kullback Information Criterion (KIC) for model selection. The final fused output is estimated with an adaptive probability of KIC, which provides improved force estimates.**

I. INTRODUCTION

National Limb Loss Information Center [1] reported in 2002 that 1.2 million people live with amputations. Since then, this number is increasing due to ongoing wars in Iraq and Afghanistan. However, prostheses can significantly improve the lives for these people.

Recent research efforts have been active towards creating surface electromyographic (sEMG) based prosthetics for hand amputees. The recorded sEMG signal is used as an input to activate the prosthesis. The central nervous system activates and controls the EMG signals which depend on the flow of specific ions including sodium (Na^+), potassium (K^+) and calcium (Ca^{++}) resulting in the action potentials in nerves and their respective skeletal muscle fibres. A potential difference develops across neuronal membranes because of this ion exchange and this can be measured as an electrical voltage change [2]. sEMG signals are collected from the skin as an electric voltage ranging between -5 and +5 mV.

Kumar P., is with Measurement and Control Engineering Research Center (MCERC), College of Engineering, Idaho State University, Pocatello, Idaho 83209, USA (email: kumaparm@isu.edu).

Sebastian A., is with MCERC, College of Engineering, Idaho State University, Pocatello, Idaho 83209, USA (email: sebaanis@isu.edu).

Potluri C., is with MCERC, College of Engineering, Idaho State University, Pocatello, Idaho 83209, USA (e-mail: potlchan@isu.edu).

Urfer A., is with Department of Physical and Occupational Therapy, Idaho State University, Pocatello, Idaho 83209, USA (email: urfealex@isu.edu).

Schoen M. P., is with Department of Mechanical Engineering, MCERC, Idaho State University, Pocatello, Idaho 83209, USA (email: schomarc@isu.edu).

Naidu D. S., is with Department of Electrical Engineering, MCERC, Idaho State University, Pocatello, Idaho 83201 USA (email: naiduds@isu.edu).

The control of the myoelectric-based prosthesis is difficult because of the dynamic nature of the EMG signal [1] due to varying motor unit recruitment, crosstalk, and biochemical interaction within the muscular fibres. In addition, sEMG changes continuously due to the onset and progression of muscle fatigue [1].

Muscle fatigue is complex in nature and results in failure to maintain the required force level [3]. Reasons for fatigue can be the peripheral changes at the muscle level or an inadequate output from the central nervous system to stimulate motoneurons [3]. The amount of force generated, duration of each contraction, and the rest period between two contractions has a direct influence on the muscle fatigue rate [4]. Muscle fibre-type distribution [5], nerve conduction velocity of fatiguing muscles, or even factors within the central nervous system (CNS) affect EMG signals [6]. EMG analysis is a well-accepted method for muscle fatigue assessment [6-10].

In 1977, L. Lindstrom, R. Kadefors and I. Petersen developed a method that measures the localized muscle fatigue based on the power spectrum analysis using myoelectric signals [11]. This approach permits real-time investigations and can yield statistically based criteria for the occurrence of fatigue. Rate of fatigue development and changes in muscle action potential conduction velocity were used to interpret the findings [11-13]. Additional recruitment of motor units, synchronization of active motor units along the muscle fibres, and a decrease in conduction velocity are reflected in the EMG signal as an increase of amplitude in time domain and a decrease of medium frequency in frequency domain [14-15].

The joint analysis method using EMG amplitude and spectrum (JASA) allows distinguishing between the difference of fatigue-induced and force related EMG changes. Simultaneous changes in the EMG amplitude and spectrum are considered in the JASA approach [16]. The JASA principle states that muscle force decreases because of the decrease in EMG amplitude [16]. Fatigue can occur because of continuous high frequency stimulation or because of titanic stimulation. The Flow Chart of the work in this paper is shown in figure 1.

This paper addresses the issue of skeletal muscle fatigue that is a dynamic phenomenon. The modeling is based on system identification, where mathematical relations are inferred from experimental data. The data consists of sEMG signals and hand/finger force generated by healthy subjects. The recorded three-sEMG signals are filtered using nonlinear Half-Gaussian Bayesian filters with optimized filter parameters, whereas the skeletal muscle force signal is pre-processed using a Chebyshev type-II filter [1,17].

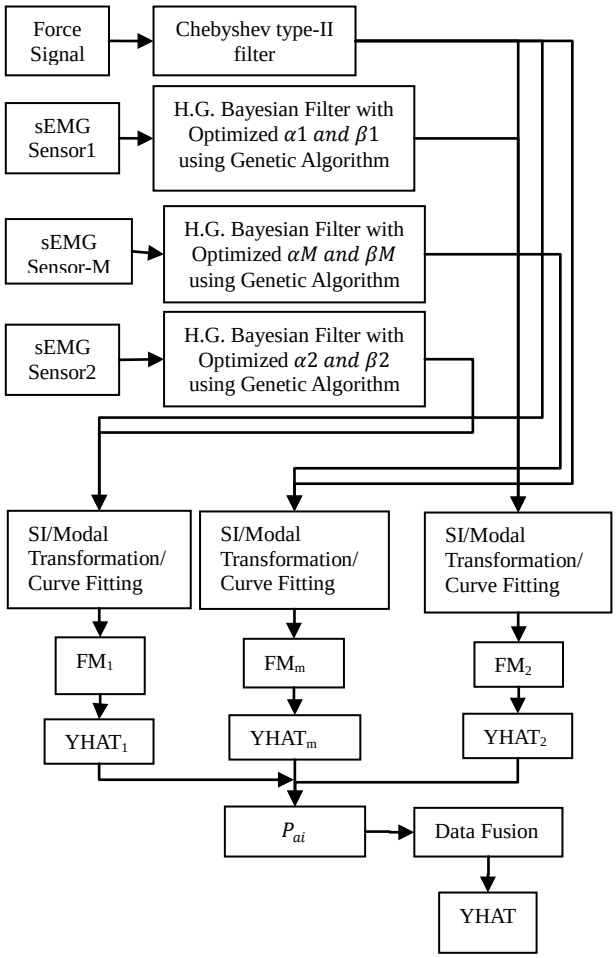

Figure 1: The Flow Chart of the Work in this Paper.

A simple Genetic Algorithm code is used to optimize the Bayesian filter parameters. Using an input/output approach, the EMG signal is input to the skeletal muscle, and the produced hand/finger force constitutes the output. Three discrete time state-space models are obtained using system identification and modal transformation for three sets of sensors. One sensor is placed at the motor unit of the ring finger of the dominant hand and two sensors are located in its vicinity as shown in Figure 2. The extracted models from the data sets are fused with a probabilistic Kullback Information Criterion (KIC) for model selection. The final fused output is estimated with an adaptive probability of KIC that gives an improved skeletal muscle force estimates.

II. EXPERIMENTAL SET-UP AND PRE–PROCESSING

Both sEMG and muscle force signals were acquired simultaneously using LabVIEW™ 8.2 at a sampling rate of 2000 Hz. The sEMG data capturing was aided by a DELSYS® Bagnoli-16 EMG system with DE-2.1 differential EMG sensors. The corresponding force data was captured using NI ELVIS with Interlink Electronics FSR 0.5" circular force sensor. The experimental set-up is shown in Figure 2. One sEMG sensor was placed on the motor point of ring finger and two adjacent to the motor point of a healthy subject. Prior to placing the sEMG sensors, the skin surface of the subject was prepared according to International Society of Electrophysiology and Kinesiology (ISEK) protocols.

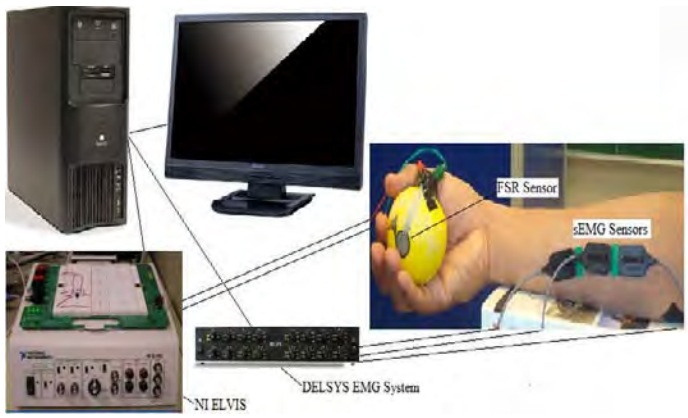

Figure 2: Experimental Set-Up.

EMG signal is modeled for the conditional probability of the rectified EMG signal as a filtered random process with random rate. The likelihood function for the rate evolves in time according to a Fokker–Planck partial differential Equation [17]. Here, α and β are two free parameters, α is the expected rate of gradual drift in the signal, and β is the expected rate of sudden shifts in the signal. These two free parameters of the non-linear "Half-Gaussian filter model" are optimized for the acquired EMG data using an elitism based Genetic Algorithm. A Chebyshev type II low pass filter with a 550 Hz pass frequency is used to filter the force signal.

III. SYSTEM IDENTIFICATION AND MODAL TRANSFORMATION

An alternative to physically based mathematical modeling is data based -'system identification (SI)'- that can be applied to different systems where it needs sufficient experimental data [18]. The parametric system identification process yields a dynamical model such as the Auto Regressive with exogenous input (ARX) or Output Error (OE) model, this model gives us the system in mathematical form. In this work, the SI approach is used with the myolelectric signal as the input to the system and as output the intended muscle force.

In this work, we are using an output error (OE) model structure for the modeling of EMG and force signals, which has been documented in the literature to perform well for EMG signals among linear parametric models [1]. The OE model is by Equation (1).

$$y(t) = \frac{B(q)}{F(q)} u(t - n_k) + e(t). \quad (1)$$

A common OE model is obtained for each sensor data set using one set of model parameters (polynomial order). The OE models then are converted into a state-space formulation. By

doing this, the identification properties of the OE model formulation are preserved and represented in the state-space form. A modal form is computed by using following transformation:

$$\Lambda = \mathrm{T}^{-1}, \Omega = \mathrm{T}^{-1}\mathrm{B}, \Gamma = C\mathrm{T}. \quad (2)$$

where T is the matrix composed of the eigenvectors of A, and D is came out to be a zero matrix for the cases treated in this work. Equation (2) refers to the continuous representation of the identified models. Using the modal form representation for each corresponding data set, the influence of fatigue can be observed by charting the coefficients in time for each matrix. For example, the coefficients contained in the transformed matrix Λ can be plotted in the complex s-plane. This tracking can then be used as the basis for constructing polynomials that connect each element of each matrix in time with the corresponding time stamp. Hence, a fatigue model in state-space description is constructed, where the input is the recorded EMG signal and the output the expected force generated by the hand motion.

IV. Fusion of Outputs and Adaptive Probability of KIC

Multiple model fusion is done by assigning a particular probability to each individual model [19]. These models are obtained using System Identification (SI) for three sEMG sensors for single motor unit. SI model fit value gives the probability for each model, which is given by $\left[1-\frac{|Y-\hat{Y}|}{|Y-\bar{Y}|}\right]*100$. The model selection criterion used in this paper is Kullback information criterion (KIC), which is an asymmetric measure. The sum of two directed divergences, which is the measure of the models dissimilarity, is known as Kullback's symmetric or J-divergence [20], as given by Equation (3).

$$KIC(p_i) = \frac{n}{2}\log R_i + \frac{(p_i+1)n}{n-p_i-2} - n\psi\left(\frac{n-p_i}{2}\right) + g(n), \quad (3)$$

where $g(n) = n * \log(n/2)$.

Following fusion technique is applied for sEMG – force identification models, which is based on [19].

1) Identify OE models $M_1, M_2, \ldots, M_k$ using sEMG data (u) as input and force data (Y) as output, for k number of sensors collecting data simultaneously.
2) Compute the residual square norm
   $R_i = \left\|Y - \Phi_i\widehat{\Theta}_i\right\|^2 = \left\|Y - \hat{Y}\right\|$,
   where $\widehat{\Theta}_i = \{{\Phi_i}^T\Phi_i\}^{-1}{\Phi_i}^T Y$, and
   $$\Phi = \begin{bmatrix} Y_p^T & u_p^T & Y_{p-1}^T & \ldots & u_1^T \\ Y_{p+1}^T & u_{p+1}^T & Y_p^T & \ldots & u_2^T \\ \vdots & \vdots & \vdots & \ddots & \vdots \\ Y_{n-1}^T & u_{n-1}^T & Y_{n-2}^T & \ldots & u_{n-p}^T \end{bmatrix}.$$
3) Calculate the model criteria coefficient using Equation (3).
4) Compute the model probability
   $p(M_i|Z) = \frac{e^{-l_i}}{\sum_{j=1}^{k} e^{-l_j}}$, where l is model selection criterion, i.e. $KIC(p_i)$.
5) Compute the fused model output $\hat{Y}_f = \sum_{i=1}^{k} p(M_i|Z)\hat{Y}_i$.
6) Compute the overall OE model from $\hat{Y}_f$ and force data.

Here all the computation from step 2) to step 6) is adaptive i.e. the residual square norm, $KIC(p_i)$, model probability $p(M_i|Z)$, and fused model output $\hat{Y}_f$ are being updated with time or for each data point.

V. Results, Conclusion and Future Work

Based on previous research results and after trying different model orders for sEMG/Force data an optimal model order of $n_b = 2, n_f = 2, n_k = 1$ is used in this work. Equation (4), (5), and (6) give three resulting discrete time state-space sEMG-Force-Fatigue models for three sensors.

$$x_m(k+1) = A_m(t)x_m(k) + B_m(t)EMG_m(k);$$
$$YHAT_m(k) = C_m(t)x_m(k) + D_m(t)EMG_m(k). \quad (4)$$
$$x_1(k+1) = A_1x_1(k) + B_1EMG_1(k);$$
$$YHAT_1(k) = C_1x_1(k) + D_1EMG_1(k). \quad (5)$$
$$x_2(k+1) = A_2(t)x_2(k) + B_2(t)EMG_2(k);$$
$$YHAT_2(k) = C_2(t)x_2(k) + D_2(t)EMG_2(k). \quad (6)$$

In these case matrices D_m, D_1, and D_2 are zero matrices, whereas matrices $A_m, B_m, C_m, A_1, B_1, C_1, A_2, B_2$, and C_2 are given as: $A_m = \begin{bmatrix} a_{m1}(t) & 0 \\ 0 & a_{m2} \end{bmatrix}$; $B_m = \begin{bmatrix} b_{m1}(t) \\ b_{m2}(t) \end{bmatrix}$; $C_m = [c_{m1}(t)\ c_{m2}(t)]$; $A_1 = \begin{bmatrix} a_{11} & 0 \\ 0 & a_{12} \end{bmatrix}$; $B_1 = \begin{bmatrix} b_{11} \\ b_{12} \end{bmatrix}$; $C_1 = [c_{11}\ c_{12}]$; $A_2 = \begin{bmatrix} a_{21}(t) & 0 \\ 0 & a_{22} \end{bmatrix}$; $B_2 = \begin{bmatrix} b_{21}(t) \\ b_{22}(t) \end{bmatrix}$; and $C_2 = [c_{21}(t)\ c_{22}(t)]$; where the elements of matrices A_m, B_m, C_m, A_2, B_2, and C_2 are function of time and the elements of matrices A_1, B_1, and C_1 are constants for this particular data set. The time variables $a_{m1}(t), a_{m2}(t), b_{m1}(t), b_{m2}(t), c_{m1}(t), c_{m2}(t), a_{21}(t), a_{22}(t), b_{21}(t), b_{22}(t)$, $c_{21}(t)$, and $c_{22}(t)$ are given by quadratic polynomials obtained by curve fitting the tracked modal transformed coefficients. These time variables are given as:

$a_{m1}(t) = 0.00026t^2 - 0.033t - 11$; $a_{m2}(t) = -0.0018t^2 + 0.24t - 33$;

$b_{m1}(t) = -0.002t^2 + 0.33t + 42$; $b_{m2}(t) = -0.0017t^2 + 0.33t + 25$;

$c_{m1}(t) = (3.2 * 10^{-7})t^2 - (4.2 * 10^{-5})t + 0.71$;

$c_{m2}(t) = (4.6 * 10^{-8})t^2 - (5.8 * 10^{-6})t - 0.71$;

$a_{21}(t) = -(1.2 * 10^{-5})t^2 + 0.0013t - 0.47$;

$a_{22}(t) = 0.001t^2 - 0.037t - 35$; $b_{21}(t) = (6.4 * 10^{-6})t^2 - 0.001t + 0.3$;

$b_{22}(t) = 0.0023t^2 - 0.12t - 75$;

$c_{21}(t) = -(1.8 * 10^{-7})t^2 + (6.4 * 10^{-6})t + 0.71$; and

$c_{22}(t) = -(2.1 * 10^{-9})t^2 + (2.4 * 10^{-7})t - 0.71$.

Elements of matrices A_1, B_1, and C_1 are constants for this particular data set, they are given as:

$a_{11} = -0.0159$; $a_{12} = -43.1883$; $b_{11} = 0.0090$; $b_{12} = -72.1875$; $c_{11} = 0.7147$; and $c_{12} = -0.7071$.

The discrete models have a sampling time of $\Delta t = 0.0005$ seconds. The duration of the final estimated and fused output for three sensors is 37.36 seconds. Figure 3 depicts the probability and 10th degree curve fitting for motor point, ring2 and ring1 sensor signals.

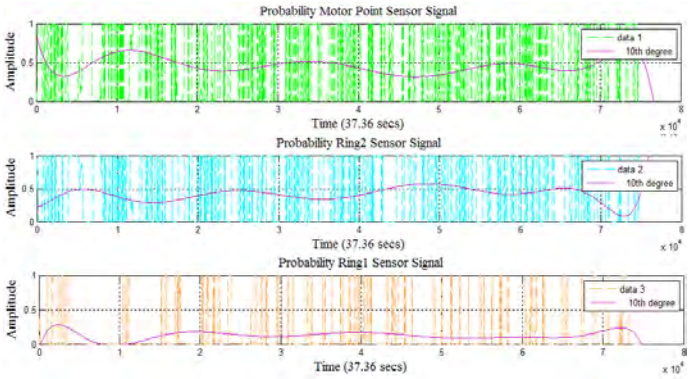

Figure 3: 10th Degree Curve Fitting – Probability Motor, Ring2 and Ring1 Sensor Signals.

Figure 4 shows the original and estimated fused output, depending on the error between the two later follows the original signal very closely. This approach identifies a fused fatigue model and estimate an adaptive probability based output that follows the original output very closely. Outcome of this research can be used to estimate the skeletal muscle force of human hand for prosthetic hand design, application and improvement.

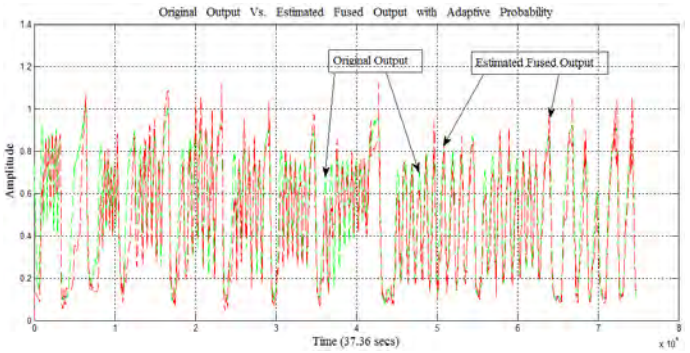

Figure 4: Original Output Vs. Estimated Fused Output with Adaptive Probability.

In future by improving the data collection techniques and sEMG sensor design, the estimated force can be improved further.

ACKNOWLEDGMENT

This work was supported by a grant from the Telemedicine Advanced Technology Research Center (TATRC) – Department of Defense. The financial support is greatly appreciated.

REFERENCES

[1] Jeffrey T. Bingham and Marco P. Schoen, "Characterization of Myoelectric Signals using System Identification Techniques". Proceedings of IMECE 2004: 2004 ASME International Mechanical Engineering Congress Anaheim, California, November 13-19, 2004.

[2] Northrop, R., 2004. Analysis and application of analogue electronic circuits to biomedical instrumentation, CRC Press, Boca Raton, Florida, pp. 6–9.

[3] S. C. Gandevia, "Spinal and Supraspinal Factors in Human Muscle Fatigue". Physiological Reviews, American Physiological Society 81(4), October, 2001.

[4] B R Bigland-Ritchie, N J Dawson, R S Johansson and O C Lippold, 1986. "Reflex origin for the slowing of motoneurone firing rates in fatigue of human voluntary contractions". Journal of Physiology, 379, pp. 451-459.

[5] Gerdle B, Edstrom M, Rahm M, 1993." Fatigue in the shoulder muscles during static work at two different torque levels". Clinical Physiology, 13(5), pp. 469-482.

[6] Enoka RM, 1995. "Morphological features and activation patterns of motor units". Journal of Clinical Neurophysiology, 12(6), pp. 538-559.

[7] L. G. Christova, A. S. Alexabdrov, and B. A. Ishpekova, 1999. "Single motor unit activity pattern in patients with Schwartz-Jampel syndrome". Journal of Neurology, Neurosurgery and Psychiatry, 66(2), pp. 252-253.

[8] Paula M. Ludewig, and Thomas M. Cook, 1996. "The effect of head position on scapular orientation and muscle activity during shoulder elevation". Journal of Occupational Rehabilitation, 6(3), pp. 147-158.

[9] Merletti R, and Lo Conte LR, 1997. "Surface EMG signal processing during isometric contractions". Journal of Electromyography and Kinesiology, 7(4), pp. 241-250.

[10] J. Bruce Moseley, Frank W. Jobe, Marilyn Pink, Jacquelin Perry, and James Tibone, 1992. "EMG analysis of the scapular muscles during a shoulder rehabilitation program". The American Journal of Sports Medicine, 20(2), pp. 128-134.

[11] L. Lindstrom, R. Kadefors and I. Petersen, 1977. "An electromyographic index for localized muscle fatigue". Journal of Applied Physiology, American Physiological Society, 43(4), pp. 750-754.

[12] Weytjens JLF, and van Steenberghe D, 1984. "The effects of motor unit synchronization on the power spectrum of the electromyogram". Biol Cybern, 51, pp. 71-77.

[13] Finsterer J., 2001. "EMG-interference pattern analysis". J Electromyogr Kinesiol, 11, pp. 231-246.

[14] C.J. De Luca, 1984. "Myoelectrical manifestations of localized muscular fatigue in humans". Crit. Rev. Biomed. Eng., 11 (4), pp. 251-279.

[15] B. Maton, and D. Gamet, 1989. "The fatigability of two agonistic muscles in human isometric voluntary sub maximal contraction: an EMG study. II Motor unit firing rate and recruitment". Eur. J. Appl. Physiol., 58, pp. 369-374.

[16] A. Luttmann, M. Ja¨ger, J. So¨keland, and W. Laurig, 1996. "Electromyographical study on surgeons in urology, Part II: Determination of muscular fatigue". Ergonomics, 39, pp. 298-313.

[17] Terence D. Sanger, 2007. "Bayesian Filtering of Myoelectric Signals." *J Neurophysiol* 97, pp. 1839–1845.

[18] Lennart Ljung, 1999. System Identification: Theory for the User, 2nd edition, Printice Hall PTR, Chap. 1, pp. 1-15.

[19] Huimin Chen, Shuqing Huang., 2005. *"A Comparative study on Model Selection and Multiple Model Fusion," 7th* International Conference on Information Fusion, pp. 820-826.

[20] Abd-Krim Seghouane, Maiza Bekara, Gilles Fleury, 2003, *"A Small Sample Model Selection Criterion Based on Kullback's symmetric Divergence." IEEE Transaction, pp. 145-148.*

Adaptive Finger Angle Estimation from sEMG Data with Multiple Linear and Nonlinear Model Data Fusion

PARMOD KUMAR, ANISH SEBASTIAN, CHANDRASEKHAR POTLURI, ADNAN ILYAS, MADHAVI ANUGOLU, ALEX URFER, and MARCO P. SCHOEN
Measurement and Control Engineering Research Center, School of Engineering
Idaho State University
921 South 8th Avenue, Stop 8060, Pocatello, Idaho
USA
schomarc@isu.edu http://isu.edu/~schomarc

Abstract: - This paper presents a novel approach to control the motion of a smart prosthesis using surface electromyographic (sEMG) signals. Currently, all sEMG based prosthetic hands are controlled based on pre-programmed motion sets, which are initiated when some threshold value of the measured sEMG signal is reached. In this paper, we present an approach that utilizes System Identification (SI) in order to obtain a dynamic finger angle model. Such a model allows for instantaneous control for the finger motions. The algorithm presented relays on an array of nine sEMG sensors. The sEMG and angle data is filtered using a nonlinear Teager–Kaiser Energy (TKE) operator based nonlinear spatial filter and a Chebyshev type-II filter respectively. The filtered signals are smoothed using a smoothing spline curve fitting. The smoothed sEMG data is used as input and the respective smoothed finger angle data is used as output for a system identification routine to obtain multiple linear and nonlinear models. To achieve better estimates of the finger angles, an adaptive probabilistic Kullback Information Criterion (KIC) for model selection based data fusion algorithm is applied to the linear and nonlinear model's outputs. Final fusion based output of this approach results in improved estimates of finger angles.

Key-Words: - sEMG, Prosthetics, System Identification, Teager–Kaiser Energy operator, KIC.

1 Introduction

The United States had 1.6 million people with amputations during 2005, [1]. This number is continuously on increase due to the ongoing wars in Afghanistan and Iraq, [2]. Hence, one of the prime reasons for the enlarged attention in the field of prosthetic is to facilitate the increased demand for efficiently and highly dexterous prosthesis. Because of the lack of tactile or proprioceptive feedback for grasping in prosthesis, almost 30–50% of the upper extremity amputees choose not to use their prosthetic hand on regular bases [3, 4]. The control of a prosthetic plays a key role in the usefulness and ultimately in the acceptance of the device by a user. Since full dexterity is still out of reach for current prosthetics, the precision and effectiveness of a prosthetics takes on greater value. The controller implemented must be capable of regulating the intended finger forces and finger motion of the artificial hand. The reference value for these outputs is given by the amputee's mind/intention, expressed by the generated surface electromyographic (sEMG) signal of the remaining skeletal arm muscles. In this work, we assume that the amputation is transradial, and hence sufficient muscle mass is accessible for sEMG data acquisition. EMG can be measured on the surface or by needle electrodes that are injected into the subjects arm. Choosing the sEMG as a control input eliminates the problems associated with surgeries and regular hygiene for the user of implanted electrodes. sEMG signal amplitudes range between -5 and +5 [mV]. The sEMG signal changes with different limb movements and applied forces. This justifies the use of sEMG signals for the position and force control of prosthesis. Current prosthetics using EMG or sEMG sensors utilize this data by computing some threshold value – for example the RMS value – to activate a pre-programmed motion and/or force set of the artificial hand. The resulting motion is only initiated by the user, but not controlled thereafter. This is quite different than what a healthy subject uses to control his/her hand. For non-amputees, the motion of the fingers is controlled at every instance, which allows for complex motion sets to be executed. To mimic this characteristic, we propose to use dynamic models relating sEMG data with finger motion. The potential of such models is obvious from the operational point of view, but also allows the incorporation of muscle fatigue dynamics to be included in the control algorithm [9-13].

Previous research works give different methods to extract the information from the sEMG signals [5]. These methods use wavelet analysis, artificial neural networks, and other feature extraction methods to make use of sEMG for prosthetic control [5]. Research work as reported in [6] presents sEMG as an autoregressive (AR) model with the delayed intramuscular EMG signal as the input. In our work, we rely only on sEMG since no injected electrodes will be used to obtain EMG signals. Hence the task is to develop a model and an estimation scheme for describing the dynamics of the skeletal muscle force and finger angles from the sEMG signals. Some of the recent efforts in this direction are evident in the research work of [7-13].

Present research focus on the dynamic modeling and estimation of the angles of the proximal interphalangeal (PIP) joint of the index finger with the corresponding sEMG signal. An array of nine sEMG sensors is used to record sEMG signals and joint angles are recorded using a wheel potentiometer from the arm of a healthy subject, which respectively is explained in detail in Section 2 and 3. Both the signals are filtered and smoothing spline curve fitted with 0.993 as smoothing parameter. The dynamic modeling is achieved using the approach of System Identification (SI) where smoothed sEMG data is the input and the smoothed joint angle data is the output. Multiple linear and nonlinear models are obtained. To achieve better estimate of the finger angles, an adaptive probabilistic Kullback Information Criterion (KIC) for model selection based data fusion algorithm is applied to the linear and nonlinear models outputs. Final fusion based output of this approach results in improved estimates of finger angles.

2 Experimental Set-Up

An experimental set-up is designed to simultaneously acquire the sEMG from the motor point of the index finger and the joint angle of the PIP joint of the index finger. Nine DE-3.1 sEMG sensors of the DELSYS® Bagnoli-16 EMG system are placed in a three-by-three array [14]; the arrangement covers the four directional spatial distributions of the sEMG signal. The middle three sEMG sensors were attached directly on the skin surface above the motor point of the index finger of a healthy subject. Using a 10k-Ohm wheel potentiometer, an angle measurement device is designed to measure the joint angles of the PIP joint of the index finger of a healthy subject. Appropriate sEMG electrode attachment point for the motor point of the index finger was identified using a wet probe muscle stimulator at the FDS (RICH-MAR, HV 1000).

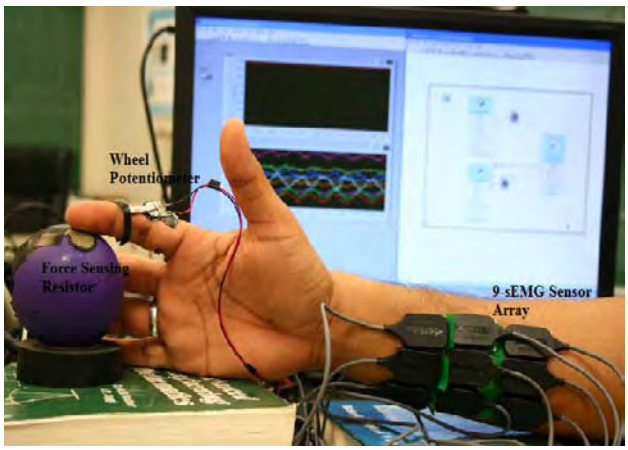

Fig. 1: Experimental Set-Up.

Prior to placing the sEMG sensors, the skin surface of the subject was prepared according to International Society of Electrophysiology and Kinesiology (ISEK) protocols. An Interlink™ Electronics FSR 0.5" circular force sensor on a stress ball is used to press with the movement to introduce some resistance to the movement of the PIP joint of the index finger. Experimental set-up is shown in Fig. 1 where nine sensors are shown on a healthy subject forearm, with an angle measurement device on the PIP joint of the index finger and having a stress ball for force measurements. The various signals are sampled at a rate of 2000 Hz using LabVIEW™ in conjunction with DELSYS® Bagnoli-16 EMG and NI ELVIS™. With this experimental set-up we conducted several experiments of 30 seconds, 45 seconds and 60 seconds durations.

3 Signal Pre-Processing

The recorded sEMG signal for the index finger is filtered using nonlinear spatial filtering for nine channel surface EMG. The nonlinear spatial filter is obtained from the "Nonlinear Teager-Kaiser Energy (TKE) Operator," [14]. Equation (1) gives the TKE operator in the time domain on sEMG signal [14].

$$\Psi[x(n)] = x^2(n) - x(n+1) * x(n-1). \quad (1)$$

Here, Ψ is the TKE operator and $x(n)$ is the time domain sEMG signal at location n. The four-directional nonlinear spatial filter can be derived from the TKE operator. Equation (2) gives the four-directional nonlinear spatial filter.

$$\Psi_{d,4}[x(m,n)] = 4 * x^2(m,n) - x(m-1,n) * x(m+1,n) - x(m,n-1) * x(m,n+1) - x(m-1,n+1) * x(m+1,n-1) - x(m-1,n-1) * x(m+1,n+1). \quad (2)$$

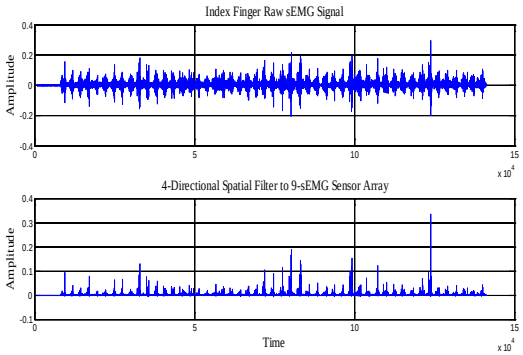

Fig. 2: Raw and Spatially Filtered sEMG Signal from Index Finger.

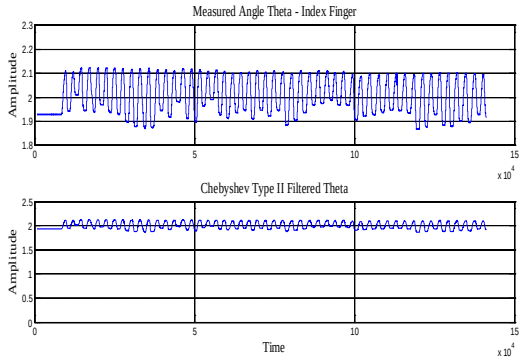

Fig. 3: Raw and Chebyshev Type II Filtered PIP Joint Angle for Index Finger.

Fig. 2 shows a comparison between the measured and nonlinear spatial filtered sEMG signals. A Chebyshev type II infinite impulse response (IIR) low pass filter with a 550 Hz pass band frequency is used to filter the PIP joint angle data. Fig. 3 shows the comparison between the measured and Chebyshev type II filtered skeletal muscle force signal.

4 Smoothing Spline Curve Fitting

Any data can be curve or surface fitted using the MATLAB® Curve Fitting Toolbox™ [15]. Smoothing spline which is a piecewise polynomial computed from a smoothing parameter (p) of 0.993 is fitted to the filtered sEMG and angle data. Smoothing parameter (p) is a number between 0 and 1. Change in the value of p from 0 to 1 results in the change in smoothing spline. For $p = 0$ the smoothing spline is a least-square straight-line approximation to the data, whereas for $p = 1$ it gives the "natural" cubic spline interpolant to the data [15].

For the specified weight (w_i) and smoothing parameter (p) a smoothing spline s is formed which minimizes the parameter J given by Equation (3).

$$J = p\sum_i w_i(y_i - s(x_i))^2 + (1-p)\int(\frac{d^2s}{dx^2})^2 dx, \quad (3)$$

where x_i and y_i are predictor and response data respectively. The smoothing parameter p should be chosen to make the error $E(s) = \sum_i w_i(y_i - s(x_i))^2$ and roughness $\int(\frac{d^2s}{dx^2})^2 dx$ small. Here in this work the smoothing parameter p is chosen as 0.993 [15].

5 System Identification

System Identification (SI) is a tool to model a dynamic system based on input-output data [16]. In this research, we use the SI to model two signals which are smoothing spline curve fitted. The sEMG is the input to the system and the intended PIP joint angle is the output. Multiple linear and nonlinear models are obtained for modeling of sEMG and PIP joint angle signals for the index finger of the dominant hand of a healthy subject. Five linear and three nonlinear models are obtained for the input and output data set. Table I and II gives the structures of the linear and nonlinear models respectively.

The model order of the various models used in this work are as follows: linear models for the input and output data set, OE model of order 16, ARX model of order 18, ARMAX model of model order 16, State-Space model with subspace method (N4SID) of order 18 and a State-Space model with prediction error/maximum likelihood method (PEM) of order 12 are obtained using SI. Table I gives the structure of all the linear models. In table I y is output, t is time, $B(q)$, $F(q)$, $A(q)$, $C(q)$, $D(q)$, are polynomials, q is a backward shift operator, u is input, n_k is delay and e is error [17]. For State-Space models:- x is state, t is time, Ts is sampling time, u is input, e is error, A, B, K, C, and D are system matrices, and y is output [17].

TABLE I
LINEAR MODELS AND THEIR STRUCTURES

Linear Model Name	Linear Model Structure
Output Error	$y(t) = \frac{B(q)}{F(q)}u(t-n_k) + e(t)$
ARX	$A(q)y(t) = B(q)u(t-n_k) + e(t)$
ARMAX	$A(q)y(t) = B(q)u(t-n_k) + C(q)e(t)$
State-Space – subspace method	$x(t+Ts) = Ax(t) + Bu(t) + Ke(t)$ $y(t) = Cx(t) + Du(t) + e(t)$
State-Space – prediction error/maximum likelihood method	$x(t+Ts) = Ax(t) + Bu(t) + Ke(t)$ $y(t) = Cx(t) + Du(t) + e(t)$

Table II gives the structures of nonlinear models. The nonlinear models for the input and output data set are obtained as, the nonlinear Wiener-Hammerstein models with nonlinearity estimators of 'piecewise linear – pwlinear,' 'sigmoidnet,' and 'wavelet network.'

In Table II, for the nonlinear Hammerstein-Wiener model $u(t)$ and $y(t)$ are the inputs and outputs for the system, respectively. f and h are nonlinear functions that corresponds to the input and output nonlinearity, respectively. $w(t)$ and $x(t)$ are internal variables. $w(t)$ has the same dimension as $u(t)$. $x(t)$ has the same dimension as $y(t)$. $B(q)$ and $F(q)$ in the linear dynamic block are polynomials in the backward shift operator. For nonlinear Hammerstein-Weiner model with wavelet network as nonlinearity estimator, $\kappa(s)$ as a wavelet function, and β_k is a row vector such that $\beta_k(x-\gamma_k)$ is a scalar. If only the input nonlinearity is present, the model is called the Hammerstein model. If only the output nonlinearity is present, the model is called the Wiener model [17].

TABLE II
NONLINEAR MODELS AND THEIR STRUCTURES

Nonlinear Model Name	Nonlinear Model Structure
Nonlinear HW – Piecewise Linear – pwlinear	$w(t) = f(u(t))$, $x(t) = \frac{B_{ji}(q)}{F_{ji}(q)} w(t)$, $y(t) = h(x(t))$;
Nonlinear HW – Sigmoidnet	$y_p(t) = f(y(t-1), y(t-2), y(t-3), \dots, u(t-1), u(t-2), \dots)$; $f(z) = \frac{1}{e^{-z}+1}$ is sigmoid function.
Nonlinear HW – Wavelet Network	$g(x) = \sum_{k=1}^{n} \alpha_k \kappa(\beta_k(x-\gamma_k))$

6 Adaptive Data Fusion

Data fusion of multiple outputs of the linear and nonlinear models is done by assigning a particular probability to each individual output [18]. This method gives good estimation of the PIP joint angles. The goodness of the fit of each linear and nonlinear model output can be computed using SI model fit value, which is given by Equation (4).

$$FIT = [1 - |Y - \hat{Y}\ |/|Y - \bar{Y}\ |\ ] * 100. \quad (4)$$

In Equation (4) Y is measured, $\hat{Y}$ is estimated and $\bar{Y}$ is mean output signal. The model selection criterion used in this paper is Kullback Information Criterion (KIC) which has shown to perform well for sEMG sensor data fusion [9-13]. The sum of two directed divergences, which is the measure of the models dissimilarity, is known as Kullback's symmetric or J-divergence [19], as given by Equation (5).

$$KIC(p_i) = \frac{n}{2} log R_i + \frac{(p_i+1)n}{n-p_i-2} - n\psi\frac{(n-p_i)}{2}) + g(n), \quad (5)$$

where $g(n) = n * log(n/2)$.

The fusion algorithm as given by [18] is applied for data fusion of the outputs of the linear and nonlinear models obtained using SI:

(I) Find the linear and nonlinear models outputs $M_1, M_2, \dots, M_k$ for k number of outputs.

(II) Compute the residual square norm

$R_i = \|Y - \Phi_i\, \widehat{\Theta}_i\|^2 = \|Y - \hat{Y}\ \|^2$,

where $\widehat{\Theta}_i = \{{\Phi_i}^T \Phi_i\}^{-1} {\Phi_i}^T Y$, and

$$\Phi = \begin{bmatrix} \mathrm{Y_p^T} & \mathrm{u_p^T} & \mathrm{Y_{p-1}^T} & \dots & \mathrm{u_1^T} \\ \mathrm{Y_{p+1}^T} & \mathrm{u_{p+1}^T} & \mathrm{Y_p^T} & \dots & \mathrm{u_2^T} \\ \vdots & \vdots & \vdots & \ddots & \vdots \\ \mathrm{Y_{n-1}^T} & \mathrm{u_{n-1}^T} & \mathrm{Y_{n-2}^T} & \dots & \mathrm{u_{n-p}^T} \end{bmatrix}.$$

(III) Calculate the model criteria coefficient using Equation (5).

(IV) Compute the model probability $p(M_i|Z) = \frac{\mathrm{e^{-l_i}}}{\sum_{\mathrm{j=1}}^{\mathrm{k1}} \mathrm{e^{-l_j}}}$, where l is model selection criterion, i.e. $KIC(p_i)$.

(V) Compute the fused model output $\widehat{\mathrm{Y}}_\mathrm{f} = \sum_{\mathrm{i=1}}^{\mathrm{k1}} \mathrm{p(M_i|Z)\widehat{Y}_i}$.

(VI) Compute the overall model from $\widehat{\mathrm{Y}}_\mathrm{f}$ and skeletal muscle force data.

In this algorithm the computation from step (II) to (VI) is adaptive i.e. the residual square norm, $\mathrm{KIC(p_i)}$, model probability $\mathrm{p(M_i|Z)}$, and fused model output $\widehat{\mathrm{Y}}_\mathrm{f}$ are being updated with time or for each data point.

7 Results and Discussion

The sEMG signals from the sensor array and angle signals of PIP joint of index finger are filtered; smoothing spline curve fitted and modeled using multiple linear and nonlinear models. First the outputs of linear and nonlinear models are fused separately and then the resultant outputs are fused using an adaptive KIC based probability. This approach gives improved estimates of the finger angles of the PIP joint of the index finger of the dominant hand of a healthy subject. Results are presented in the following figures. Fig. 4 shows the overlapping plot of the measured-curve fitted angle vs. data fusion based angle using linear models. Fig. 5 shows the overlapping plot of the measured-curve

fitted angle vs. data fusion based angle using nonlinear models.

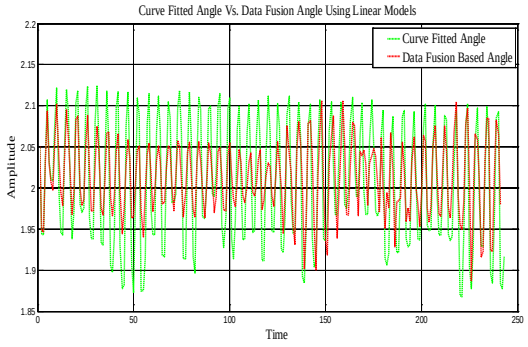

Fig. 4: Curve Fitted Vs. Data Fusion Based Angle Using Linear Models.

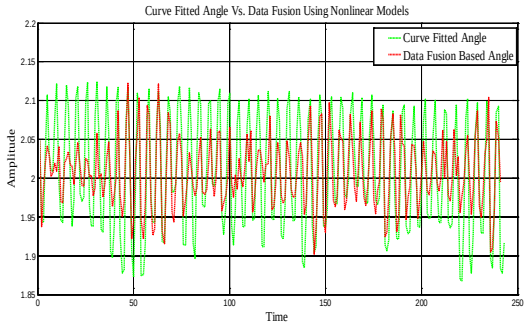

Fig. 5: Curve Fitted Vs. Data Fusion Based Angle Using Nonlinear Models.

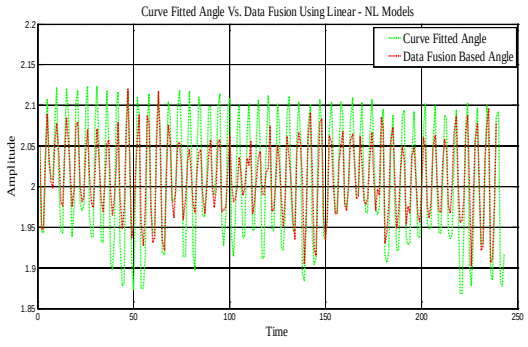

Fig. 6: Curve Fitted Vs. Data Fusion Based Angle Using Linear-Nonlinear Models.

Fig. 6 shows the overlapping plot of the curve fitted angle vs. data fusion based angle using linear-nonlinear models. It is clearly evident that the data fusion based output follows the measured-curve fitted output. Mean percentage error of the linear, nonlinear and linear-nonlinear models data fusion based angles are 2.5191e-005, -4.5807e-006, and 8.1167e-006 respectively.

Fig. 7 shows the validation plot for a different experimental data where the measured-curve fitted and the linear-nonlinear modeled data fusion based angle signal shows a close follow up. Mean percentage error of the linear, nonlinear and linear-nonlinear models data fusion based angles are 2.8202e-005, 3.3191e-005, and 6.8079e-006 respectively.

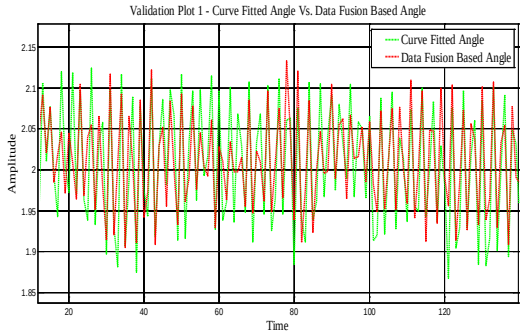

Fig. 7: Validation Plot - Curve Fitted Vs. Data Fusion Based Angle Using Linear-Nonlinear Models.

8 Conclusion and Future Work

The dynamic modeling of the filtered and smoothed sEMG and PIP joint angle of the index finger is achieved using SI with sEMG is the input and the joint angle is the output. Multiple linear and nonlinear models are obtained for the input and output data. To achieve a better estimate of the finger angles, an adaptive probabilistic Kullback Information Criterion (KIC) for model selection based data fusion algorithm is applied to the linear and nonlinear models outputs. Final fusion based output of this approach results in improved estimates of finger joint angles. The approach is validated using a different set of experimental data.

As this initial study shows potential in the pursuit of controlling an artificial hand on an instantaneous basis, we will further this work in the future by improving the data collection techniques and optimizing the experimental procedure as well as optimizing the smoothing parameter for the smoothing spline curve fitting.

Acknowledgement

This research was sponsored by the US Department of the Army, under the award number W81XWH-10-1-0128 awarded and administered by the U.S. Army Medical Research Acquisition Activity, 820 Chandler Street, Fort Detrick MD 21702-5014. The information does not necessarily reflect the position or the policy of the Government, and no official endorsement should be inferred. For purposes of this article, information includes news releases, articles, manuscripts, brochures, advertisements, still and motion pictures, speeches, trade association proceedings, etc.

References:

[1] K. Ziegler-Graham, E. J. MacKenzie, P. L. Ephraim, T. G. Travison, and R. Brookmeyer, Estimating the Prevalence of Limb Loss in the United States - 2005 to 2050, *Archives of Physical Medicine and Rehabilitation*, Vol. 89, March 2008, pp. 422-429.

[2]P. O'Connor. (2009, February 15). Iraq war vet decides to have second leg amputated [Online]. Available:http://www.columbiamissourian.com/stories/2009/02/15/soldier-who-lost-leg-iraq-may-lose-other/

[3] D. J. Atkins, D. C. Y. Heard, and W. H. Donovan, Epidemiologic overview of individuals with upper-limb loss and their reported research priorities, *Journal of Prosthetics and Orthotics*, Vol. 8, No. 1, 1996, pp. 2-11.

[4] D. H. Silcox, M. D. Rooks, R. R. Vogel, and L. L. Fleming, Myoelectric prostheses. A long-term follow-up and a study of the use of alternate prostheses, *The Journal of Bone and Joint Surgery*, Vol. 75-A, No. 12, December 1993, pp. 1781–1789.

[5] M. B. I. Reaz, M. S. Hussain and F. Mohd-Yasin, Techniques of EMG signal analysis: detection, processing, classification and applications, *Biological Procedures Online*, Vol. 8, March 2006, pp. 11-35.

[6] Y. Zhou, R. Chellappa, and G. Bekey, Estimation of intramuscular EMG signals from surface EMG signal analysis, *IEEE International Conference on Acoustics, Speech, and Signal Processing 1986*, Vol. 11, 1986, pp. 1805-1808.

[7] P. K. Artemiadis and K. J. Kyriakopoulos, EMG-based position and force control of a robot arm: Application to teleoperation and orthosis, *in Conf. Rec. 2007 IEEE/ASME Int. Conf. on Advanced Intelligent Mechatronics*, Zurich, Sept. 2007, pp. 1-6.

[8] P. K. Artemiadis and K. J. Kyriakopoulos, EMG-Based Position and Force Estimates in Coupled Human-Robot Systems: Towards EMG-Controlled Exoskeletons, *in Experimental Robotics, Springer Tracts in Advanced Robotics*, Vol. 54, Berlin Heidelberg: Springer-Verlag, 2009, pp. 241-250.

[9] P. Kumar, C. Potluri, A. Sebastian, S. Chiu, A. Urfer, D. S. Naidu, and M. P. Schoen, An Adaptive Multi Sensor Data Fusion with Hybrid Nonlinear ARX and Wiener-Hammerstein Models for Skeletal Muscle Force Estimation, *in Proc. The 14th World Scientific and Engineering Academy and Society (WSEAS) International Conference on Systems*, Corfu Island, Greece, 2010, July 22-24.

[10] P. Kumar, A. Sebastian, C. Potluri, A. Urfer, D. S. Naidu, and M. P. Schoen, Towards Smart Prosthetic Hand: Adaptive Probability Based Skeletal Muscle Fatigue Model, *in Conf. Rec. 32nd Annual International Conference of the IEEE Engineering in Medicine and Biology Society*, Buenos Aires, Argentina, Aug. 31 – Sept. 4, 2010.

[11] P. Kumar, C. Potluri, A. Sebastian, S. Chiu, A. Urfer, D. S. Naidu, and Marco P. Schoen, Adaptive Multi Sensor Based Nonlinear Identification of Skeletal Muscle Force, *WSEAS Transactions on Systems*, Vol. 9, Issue 10, October 2010, pp. 1051-1062.

[12] P. Kumar, C. Potluri, M. Anugolu, A. Sebastian, J. Creelman, A. Urfer, S. Chiu, D. S. Naidu, and M. P. Schoen, A Hybrid Adaptive Data Fusion with Linear and Nonlinear Models for Skeletal Muscle Force Estimation, *in Proc. 5th Cairo International Conference on Biomedical Engineering*, Cairo, Egypt, Dec. 16-18, 2010.

[13] P. Kumar, C. H. Chen, A. Sebastian, M. Anugolu, C. Potluri, A. Fassih, Y. Yihun, A. Jensen, Y. Tang, S. Chiu, K. Bosworth, D. S. Naidu, M. P. Schoen, J. Creelman and A. Urfer, An Adaptive Hybrid Data Fusion Based Identification of Skeletal Muscle Force with ANFIS and Smoothing Spline Curve Fitting, *in Proc. 2011 IEEE International Conference on Fuzzy Systems*, Taipei, Taiwan, June 27-30, 2011.

[14] P. Zhou, N. L. Suresh, M. M. Lowery, and W. Z. Rymer, Nonlinear Spatial Filtering of Multichannel Surface Electromyogram Signals During Low Force Contractions, *IEEE Transactions on Biomedical Engineering*, Vol. 56, No. 7, July 2009, pp. 1871-1879.

[15] *MATLAB® Curve Fitting Toolbox™ User's Guide*. The MathWorks, Inc. 2010.

[16] L. Ljung, *System Identification: Theory for the User. 2nd edition*, Printice Hall PTR, 1999, Chap. 1, pp. 1-15.

[17] L. Ljung, *System Identification Toolbox™ 7 User's Guide*, The MathWorks, Inc., 2010.

[18] H. Chen and S. Huang, A Comparative study on Model Selection and Multiple Model Fusion, *in Proc. 7th International Conference on Information Fusion*, New Orleans, USA, July 25-28, 2005, pp. 820-826.

[19] A. K. Seghouane, and M. Bekara, A Small Sample Model Selection Criterion Based on Kullback's symmetric Divergence, *IEEE Transactions on Signal Processing*, Vol. 52, No. 12, 2004, pp. 3314-3323.

Genetic Algorithm Running Time Optimization Using OpenMP Parallel Computing

Parmod Kumar[1], Nikesh Joshi[2], Jensen Alex[1], Chandrasekhar Potluri[1], Marco P. Schoen[1], Steve Chiu[2]

[1]Measurement and Control Engineering Research Centre, College of Engineering

[2]Department of Computer Science, College of Engineering

Idaho State University

Pocatello, Idaho, 83209 U.S.A.

[1]kumaparm@isu.edu, [2]joshnike@isu.edu, [1]jensalex@isu.edu, [1]potlchan@isu.edu, [1]schomarc@isu.edu, [2]chiustev@isu.edu

Abstract

Genetic Algorithm (GA) are biologically motivated evolutionary computation techniques used both as search methods for solving problems and for modelling evolutionary systems.GA has been used in a wide variety of optimization tasks, including numerical optimization and combinatorial optimization problems such as circuit design and job shop scheduling. Although there are many problems for which the genetic algorithm can evolve into a good solution in reasonable time, there are also problems for which it is inappropriate like the one in which it is important to find the exact global optimum. In addition, if the number of iteration increases the algorithm will take a long time to complete its computations. In this work, we are using GA to optimize the parameters of nonlinear Bayesian Filters for electromyographic (EMG) signal. OpenMP is a parallel programming model for shared memory and distributed shared memory multiprocessors. We are using OpenMP on four processors to improve the time of GA optimization for Bayesian Filter parameters.

Keywords: OpenMP**,** *Matlab*®, MPI, EMG**,** GA**,** Gene**,** Mother Chromosome, Father Chromosome, Pairing Operator, Mating Operator, Mutation, Population Size.

1. Introduction

Principles of natural selection and genetics has been used to deduce some efficient search algorithms, GA is one of them. GA is used in different fields to obtain solutions to different problems, e.g. engineering, science, business and economics [1, 2]. Some of the applications of GA are in automotive design, engineering design, robotics, evolvable hardware, optimized telecommunication routing, joke and pun generation, bio-mimetic invention, traffic and shipment routing, computer gaming, encryption and code breaking, computer-aided molecular design, gene expression profiling, optimizing chemical kinetic analysis, finance and investment strategies, and marketing and merchandising. Although, for a general problem of normal size, GA is a good option to get the optimal solution in appropriate amount of time, whereas for bigger and complex problems GA takes more time to find optimal solution. Researchers have explored different approaches to minimize this computational time and cost and parallel processing came out to be one of the most promising approaches.

GA is based on the principle of natural selection. It uses a random search technique to find the optimal solution of a problem by manipulating a population of candidate solutions. To form next generation, GA selects the best solutions from the evaluated population. Good solutions and time to reach them by GA depends on the population size [3, 4], because if the population is too small, then the search space will not be sufficient explored and it will be difficult to identify good solutions. In the case when the population is too big, the GA will waste computational resources processing unnecessary individuals. Each individual in the population has a fitness value, which is a payoff measure that depends on how well the

individual solves the problem. Crossover and mutation are the two operators used by GA to explore the search space, here crossover is a primary and mutation is a secondary search operator. The probability of crossover is much higher than the probability of mutation. GA can be stopped based on different conditions, one is by using a predetermined number of generations and function evaluations, second is the average quality of the population gets saturated after some number of generations, and the third is when all the individuals are identical, which can only occur when mutation is not used. We are using predetermined number of generations and function evaluations to stop the GA in this research work. The generic GA flow chart is shown in Figure 1.

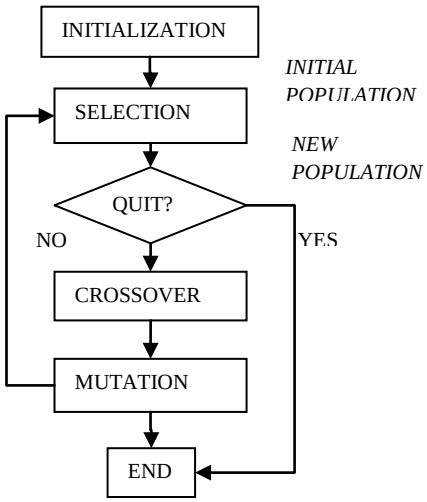

Figure 1: Generic GA Flow Chart.

The time taken by GA is directly proportional to the number of evaluations and generations, the more the number of evaluations the lager is the computational time for GA. On the other hand, this time can be minimized by paralleling the GA program on a parallel cluster. Most of the parallel programs divide the task in chunks and solve it simultaneously using multiple processors. On a parallel cluster, there are numerous processors, and they share the task, the larger the number of processors the faster the computation or lesser the time for the completion of the algorithm. In this research work we are using OpenMP parallel programming model and utilizing a cluster of four processors to run the GA and comparing its performance with the single processor in $Matlab^{®}$.

2. Background

Most of the parallel programs divide the task into chunks and solve it simultaneously using multiple processors. Similar approach can be used for GAs in different ways. These approaches can be using a single population, divide the population into several subpopulations, use of massively parallel architecture, or use of fewer multicomputer with fewer and more powerful processing units. Mainly there are three kinds of parallel GAs, and these are (a) global single-population master-slave GAs, (b) single-population fine grained, and (c) multiple-population coarse-grained GAs. The hierarchical parallel GAs combine the multiple demes with master-slave or fine-grained GAs. It has a higher level and a lower level, at the higher level they are multiple-deme algorithms and at the lower level they are single-population parallel GAs (either master-slave or fine-grained) [1].

The research work in [5] shows a method of parallel GA, in which a global parallel implementation of the conventional GA and a GA with a generation gap, where some part of the population is replaced. The efficiency of global parallel GA is close to 100 % in SIMD (single instruction multiple data) computers by [5]. Four prototypes for parallel GAs are proposed in [6] where the first three are variations of the master-slave GA, and the fourth is a multiple-population GA.

2.1 Master-Slave Parallelization

Same as in a simple GA, master-slave GA also have a single panmictic population. Figure 2 shows the schematic of master-slave GA, where the evaluation of fitness is distributed among the slave processors.

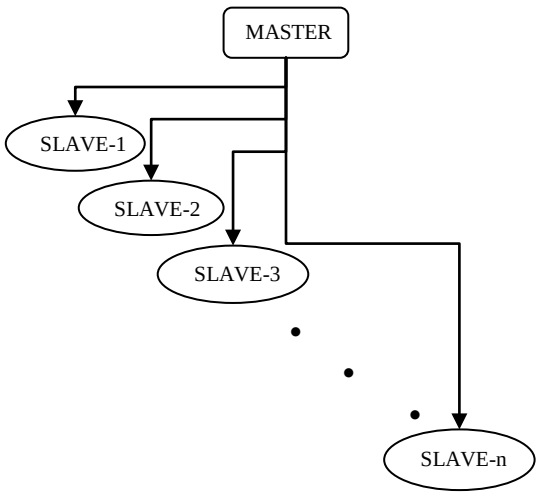

Figure 2: Master-Slave Parallel GA.

The master-slave GA considers full population size for selection and crossover, so it is known as global GA. The master-slave parallelization method for GA does not change the behavior of the algorithm while the single-population fine grained and multiple-population coarse-grained GA change the way the GA works [1]. The master-slave parallel GA considers all the population for selection, whereas the other parallel GAs considers only a subset of the population. In addition, in the master-slave parallel GA the mating is random, whereas in the other methods mating is restricted to a subset of individuals [1]. The majority of the global parallel GAs are implemented synchronously. If the multiprocessor architecture is of shared memory then each individual processor can share the information, reading and writing without any issue. In contrast, on distributed-memory architecture, the population is stored only at one processor and the master is responsible for sending the individuals to slaves for evaluation, collecting the results and applying GA for next generation. Encore Multimax is a shared-memory computer with 16 processors, a GA is implemented on this to search for efficient timetables for schools in [7]. This research in [7] gave a limited speed-up because of the critical path of the program serial code.

In 1993, Abramson, Mills, and Perkins added a distributed-memory machine "Fujitsu AP1000" with 128 processors to the experiments, changed the application to train timetables and modified the code [8]. In this research, the speed-up was significant up to 16 processors and then decreased because of the increase in communication as more processors are added.

Hauser and Männer used global GA on three different parallel processors and got good speed up only on NERV multiprocessor [9]. The speed-up of five using six processors is obtained with a very low communications overhead [9]. The reason of low performance on other processors a SparcServer and a KSR1 is because of the inadequate scheduling of computation threads to processors by the system. All the previous research results shows that the master-slave parallel GAs are easy to implement and very efficient method of parallelization especially when the evaluation needs considerable computations. Additionally the master-slave parallel GAs do not change the search behavior of the GA [1].

3. GA In *Matlab*®

The continuous number GA, which is used in this work, interprets the parameters of a problem as genes, where one set of parameters form a chromosome, $chromosome = \{gene_1, gene_2, \dots, gene_{Npar}\}$. Since one chromosome corresponds to a candidate solution, its evaluation is done by assessing the numerical value of that solution, which usually referred as the cost. Unlike traditional optimization, the function is not referred to as the cost function but as the fitness function or objective function. Using an initial population size with randomly generated chromosomes, where each gene is generated by a random number generator within the search space, the chromosome will take the dimension of $R^{Npar\ *population\ \ size}$. After evaluating each chromosome cost $c_i = f(chromosome_i), i = 1,2,\dots,population\ size$, the selection operator will select a subset of the chromosomes based on their cost value to survive for the next iteration.

For elitism based GA, the best performing chromosomes always survive. There are two options the population size, a steady-state or a performance based size. The first option maintains a certain number of chromosomes for each iteration – also referred to as a generation; while performance based size, selection sets a minimum criterion for chromosomes to survive. The latter option may cause the algorithm to end prematurely since not minimum criteria (cost value).

Pairing Operator: Genetic Algorithm may employ a number of pairing mechanisms. Among them are pairing from top to bottom, where the best performing chromosome is paired with the next best performing chromosome and so on; random pairing, where a uniform distribution is assumed to randomly pick the mother and father chromosome; weighted random pairing where the probability of selection is influenced by the performance of the individual chromosome; and rank weighing, where the probability of selection is influenced by the ranking of chromosome with respect to the others measured again by the performance. In this paper, the pairing is accomplished by determining the cumulative probability for each chromosome is

$P(n) = \frac{n}{\sum_{i=1}^{r} i}$, where

$r = \frac{population\ \ size - no.of\ chromosomes\ \ kept}{2}$,

and n is the index of chromosomes. Having computed the individual cumulative probabilities $P(n)$, the parent chromosomes are now selected by utilizing a

random number generator and indexing this with the cumulative probability. Hence, the best performing chromosome has the best chance of being selected, but also, all chromosomes in the mating pool have a chance of being selected.

Mating Operator: In this work, the next generation chromosomes are created from the mother and father chromosome (which were selected as described above) by following equations given as:

$$gene_{new\,1} = mother(\alpha) - \beta(mother(\alpha) - father(\alpha)),$$

$$gene_{new\,2} = father(\alpha) + \beta(mother(\alpha) - father(\alpha)),$$

Where, $\alpha = integer(rand * N_{par})$, $\beta = random\ number\ between\ 0-1$, and N_{par} is number of parameters for complete solution. In this α can also be viewed as equivalent to the cross-over point utilized in the binary GA. Hence, the offspring (new chromosomes) are found as

$$chrom_{new\,1} = (gene_{mother_1}, gene_{mother_2}, \dots, gene_{new\,1}, \dots, gene_{dad\,N_{par}}),$$

and

$$chrom_{new\,2} = (gene_{dad\,1}, gene_{dad\,2}, \dots, gene_{new\,2}, \dots, gene_{mother\,N_{par}}).$$

Mutation: Mutation is an important operator that allows the search to escape local minima in order to find better areas on cost surface. Too much mutation will do opposite, i.e. if a chromosome approach an optimum point, it might mutate and be placed at an entirely different location of the cost surface. Mutation is accomplished by randomly changing a gene, i.e. substitute it with a random numbers.

4. GA In OpenMP

OpenMP is a parallel programming model, which uses some compiler directives and library routines to express shared-memory parallelism [10]. OpenMP uses Fortran and C++ interfaces, which is a standard feature. OpenMP API is designed and developed by a group, which represents the major vendors of high-performance computing hardware and software. A set of compiler directives is the major part of OpenMP interface. The programmer adds these compiler directives to a sequential program. The programmer specifies the synchronization points and tells the compiler what parts of the program to execute concurrently. As the directives can be added in a incremental fashion, the OpenMP gives a path and platform for the parallelization of existing software. In contrary, the Pthreads and MPI approaches are library routines. Pthreads and MPI are linked with and called from a sequential program, and the programmer is required to divide the computational work manually [11].

Literature does not show any evidence of the use of OpenMP parallel programming model for GA in specific. This work is using OpenMP to optimize the filter parameters of Bayesian filters using GA technique. The parallel cluster has four processors. The idea of the research is to implement the GA using OpenMP on this four processors cluster and compare the results with the output on $Matlab^{®}$ on a single processor. The OpenMP parallel programming model is given in Figure 3, where sequential parts and parallel regions are labelled clearly.

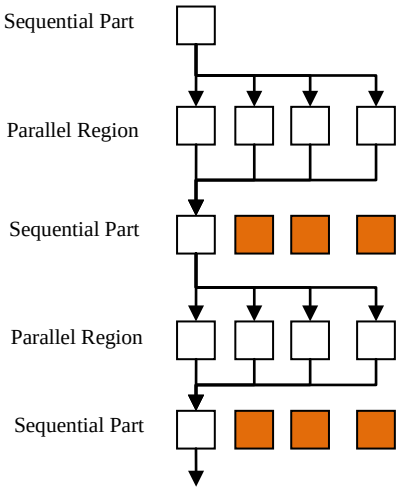

Figure 3: OpenMP Parallel Programming Model.

5. Results and Discussions

In this work, we are using GA to optimize the parameters of nonlinear Bayesian Filters for electromyographic (EMG) signals. OpenMP is a parallel programming model for shared memory and distributed shared memory multiprocessors. We are using OpenMP on four processors to improve the time of GA optimization for Bayesian Filter parameters. First $Matlab^{®}$ is used to run GA on one processor, and the same algorithm is applied on OpenMP parallel processing model using four processors. Two sets of data captured at a sampling rate of 2000Hz are used, first data is for 30 seconds and the second is for 60 seconds. The total simulation time taken by the

Matlab® and OpenMP is recorded precisely. Following tables shows the results obtained from simulations. Table 1, 2 and 3 shows the *Matlab*® simulation results for two different data sets of different lengths.

Table 1: Simulation time for 30 seconds and 60 seconds data sets in *Matlab*®.

No. of Iterations	Simulation time seconds – 30 seconds of data set.	Simulation time seconds – 60 seconds of data set.
10,000	7.13	2393.06
15,000	16.95	2403.52
20,000	28.05	2416.66
25,000	42.66	2432.89
30,000	60.61	2452.34
35,000	82.41	2475.94
40,000	108.21	2503.69
45,000	139.35	2535.91
50,000	175.45	2571.72

Table 2: Simulation time for 30 seconds and 60 seconds data sets in *Matlab*®.

No. of Iterations	Simulation time seconds – 30 seconds of data set.	Simulation time seconds – 60 seconds of data set.
60,000	208.65	2613.84
70,000	260.67	2741.73
80,000	331.85	2813.34
90,000	428.03	2913.25
100,000	550.89	3039.70

Table 3: Simulation time for 30 seconds and 60 seconds data sets in *Matlab*®.

No. of Iterations	Simulation time seconds – 30 seconds of data set.	Simulation time seconds – 60 seconds of data set.
125,000	704.54	3193.36
150,000	943.89	3433.06
175,000	1288.28	3775.16
200,000	1755.77	4236.28

Figures 1, 2 and 3 are graphical representation of the results from the Table 1, 2 and 3 respectively. It is evident from Figure 1, 2 and 3 that CPU time is directly proportional to the data size and number of iterations. Therefore, increase in the data size and the number of iterations results in the increase in CPU time.

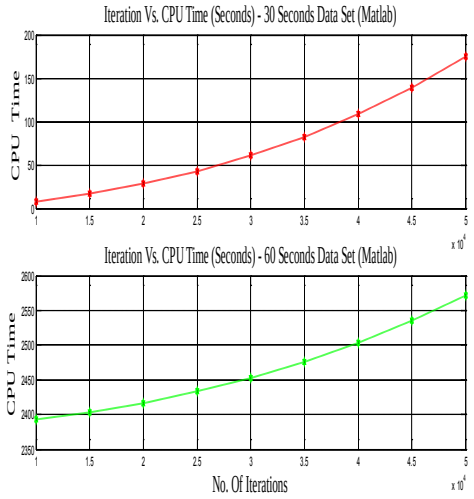

Figure 1: Iterations Vs. CPU Time – Table 1 Data.

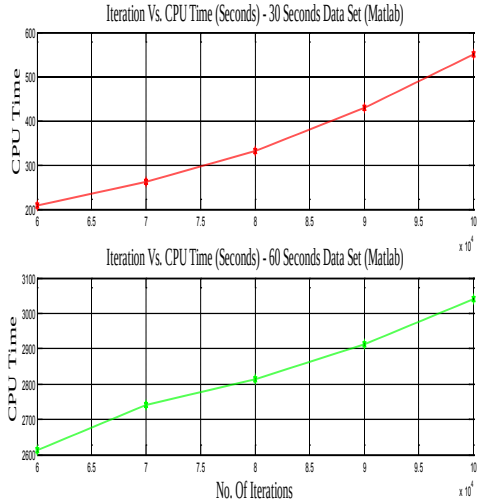

Figure 2: Iterations Vs. CPU Time – Table 2 Data.

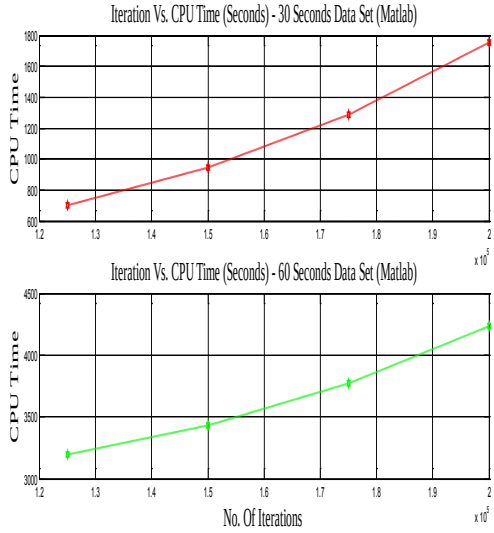

Figure 3: Iterations Vs. CPU Time – Table 3 Data.

The GA code from *Matlab*® is converted into C-code and OpenMP implementation is under pipeline. Results will be published in next reputed conferences.

The C-code can be found at http://www.isu.edu/~chiustev/research/FRC964.html.

6. Summary and Future Work

To conclude this work uses the idea of parallel processing and implement GA on OpenMP parallel programming model of four processors. First *Matlab*® GA code is converted to C code and then to OpenMP to implement on the parallel cluster. The algorithm is implemented both in OpenMP and *Matlab*® for 25, 50, 75 and 100 iterations and the time taken in execution is recorded. As expected the results shows the improvement of time in OpenMP implementation. In future work, similar approach will be applied using MPI and OpenMP and MPI combined for GA and more complex and advanced optimization algorithms.

Acknowledgement

The authors gratefully acknowledge the support of the Measurement and Control Engineering Research Center (MCERC) and College of Engineering, Idaho State University for using their recourses for this work.

References

[1] E. Cantú-Paz, "A survey of parallel genetic algorithms," *Calculateurs Parallèles,Réseaux et Systèmes Répartis*, vol. 10, no. 2, pp. 141–171, 1998.

[2] GOLDBERG D. E., « Genetic and evolutionary algorithms come of age ». *Communications of the ACM*, vol. 37, n 3, p. 113–119, 1994.

[3] GOLDBERG D. E., DEB K., CLARK J. H., « Genetic algorithms, noise, and the sizing of populations ». *Complex Systems*, vol. 6, p. 333–362, 1992.

[4] HARIK G., CANTÚ-PAZ E., GOLDBERG D. E., MILLER B. L., « The gambler's ruin problem, genetic algorithms, and the sizing of populations ». In *Proceedings of 1997 IEEE International Conference on Evolutionary Computation*, p. 7–12, IEEE Press (Piscataway, NJ), 1997.

[5] BETHKE A. D., « Comparison of Genetic Algorithms and Gradient-Based Optimizers on Parallel Processors: Efficiency of Use of Processing Capacity ». Tech. Rep. No. 197, University of Michigan, Logic of Computers Group, Ann Arbor, MI, 1976.

[6] GREFENSTETTE J. J., « Parallel adaptive algorithms for function optimization ». Tech. Rep. No. CS-81-19, Vanderbilt University, Computer Science Department, Nashville, TN, 1981.

[7] ABRAMSON D., ABELA J., « A parallel genetic algorithm for solving the school timetabling problem ». In *Proceedings of the Fifteenth Australian Computer Science Conference (ACSC-15)*, vol. 14, p. 1–11, 1992.

[8] ABRAMSON D., MILLS G., PERKINS S., « Parallelisation of a genetic algorithm for the computation of efficient train schedules ». *Proceedings of the 1993 Parallel Computing and Transputers Conference*, p. 139–149, 1993.

[9] HAUSER R., MÄNNER R., « Implementation of standard genetic algorithm on MIMD machines ». In DAVIDOR Y., SCHWEFEL H.-P., MÄNNER R., Eds., *Parallel Problem Solving fron Nature, PPSN III*, p. 504–513, Springer-Verlag (Berlin), 1994.

[10] [Online] Available: http://www.openmp.org.

[11] ENRIQUE A., MARCO T., << Parallelism and Evolutionary Algorithms >>. *IEEE Transactions on Evolutionary Computation, vol. 6, no. 5, October 2002.*

A Study on Hybridization of Particle Swarm and Tabu Search Algorithms for unconstrained Optimization and Estimation Problems

ANISH SEBASTIAN, PARMOD KUMAR, MARCO P. SCHOEN
Measurement and Control Engineering Research Center (MCERC)
Idaho State University
921 South 8th Ave., Stop 8060, Pocatello, Idaho 83209-8060
UNITED STATES OF AMERICA
schomarc@isu.edu http://www.isu.edu/~schomarc/

Abstract: - This paper presents a short study on the hybridization of a swarm based optimization algorithm with a single agent based algorithm. Swarm based algorithms and single agent based algorithms have each distinct advantages and disadvantages. One goal of the presented work is to combine the concepts of the two different algorithms such that a more effective optimization routine results. In particular, we used a Particle Swarm (PS) based optimization algorithm as basis and induce Tabu Search (TS) based operators. The developed hybrid algorithm is tailored such that has the capability to adapt to the given cost function during the optimization process. The proposed algorithm is tested on a set of different benchmark problems. In addition, the hybrid algorithm is utilized for solving the estimation problem encountered when colored noise is present and the Least Squares (LS) algorithm has bias problems.

Key-Words: - Particle Swarm, Optimization, Tabu Search, Parameter Estimation, Colored Noise

1 Introduction

Meta-heuristic approaches such as Particle Swarm Optimization (PSO) and Tabu Search (TS) algorithms have been around for a few years. They present alternative approaches to find optimality for a diverse set of optimization problems, such as estimation and system identification, among others. PSO and TS based approaches stand in contrast to hard computing methods such as gradient based methods by vastly reducing the computational complexity, especially for higher dimensional problems. A key motivation for using these soft-computing algorithms is the ability to escape local optimal points in pursuit of the global optimum during the search process.

PSO was first introduced by Kennedy and Eberhart as a stochastic global optimization routine, [1]. The algorithm searches the cost-surface with a set of individual particles, each representing a solution to the optimization problem. The particles orient themselves via influence components such as inertia, current best solution found by the entire flock, and the particle's best position. TS was presented by Glover, [2], as an iterative optimization procedure that attempts to avoid the shortfalls of the Local Search (LS) algorithm. TS is a single agent algorithm that progresses through the cost surface by creating a set of neighbors (which are potential new locations) and moves to a new location by evaluating these neighbors and comparing them to a list of previously visited locations. This list, the tabu list, ensures that no cycling will occur and local optimal points are overcome.

Recent efforts in improving PSO and TS have lead to a number of propositions that include concepts from other optimization philosophies. In [3] the authors proposed a TS-Genetic Algorithm based scheme to find best parameter estimates in colored noise environments. Higashitani et al., [4] proposed a predator-prey based PSO. The Constriction Factor Method (CFM) proposed by Clerc [5] reduces the velocity of the particles with duration of the search process in order to facilitate the intensification over the diversification mission with time. Combinations of PSO and TS have also been investigated, such as in [6], where PSO and TS are switched at each step to explore the vicinity of the particles, and in [7] where TS and PSO and sequential quadratic programming are combined. In [8] concepts of TS are used to create two swarms in PSO, one responsible for intensification, the other for diversification.

In this paper, we investigate various elements of the TS algorithm applied to the PSO scheme. In particular we investigate an alternative to the CFM method, were we use the TS concept to adapt the PSO parameters to the given problem using a parallel scheme of hybridization. The paper is organized as follows; Section 2 presents the problem formulation and basic background on PSO and TS. Section 3 introduces the proposed PSO-TS hybridization algorithm, while Section 4 will present

the results. Section 5 entails some conclusions based on the presented simulation results and prior works.

2 Problem Formulation

The optimization problems addressed in this paper are of the unconstrained type. Consider a real valued objective function $f(\mathbf{x})$ defined on a set $\mathbf{x} \in S$ in $\mathbb{R}^n$. We are tasked to find a point $\mathbf{x}^*$ corresponding to the value of $f(\mathbf{x}^*)$ such that

$$f(\mathbf{x}^*) = \min\{ f(\mathbf{x}) | \mathbf{x} \in S \} \quad (1)$$

The difficulty of finding such a point arises when $f(\mathbf{x})$ or the feasible domain S is non-convex. For such problems, gradient based methods will result in local optimums. Soft computing methods such as PSO and TS allow for an escape from local optimums and the continued search for a better optimum, in the extreme case the global optimum. For PSO algorithms, we consider a set of particles p and their associated location $\mathbf{x}^i$ where i is the index for the particles. The particles explore S in an incremental fashion. Their position is altered at each step by the following update rule:

$$\mathbf{x}^i(k+1) = \mathbf{x}^i(k) + \mathbf{v}^i(k+1), \quad (2)$$

where k is the increment number and $\mathbf{v}^i$ the velocity associated with the particle, which can be computed as follows:

$$\mathbf{v}^i(k+1) = w\mathbf{v}^i(k) + c_1 r_1 \left[\mathbf{b}_p^i - \mathbf{x}^i(k) \right] + c_2 r_2 \left[\mathbf{b}_g^i - \mathbf{x}^i(k) \right]. \quad (3)$$

In the velocity update formula, $\mathbf{b}_p^i$ and $\mathbf{b}_g^i$ represent the best ever position of the particle i and the global best position of the swarm up to iteration k, respectively. r_1 and r_2 are uniformly distributed random numbers between 0 and 1, while w, c_1 and c_2 are weighting coefficients that manage the three tendencies of Equation (3). These tendencies as given by the three terms in the velocity equation are characterized as: audacious for following your own way; conservative, for going back towards your best previous position; and sheep-like, for being pulled to the best overall position. The weighting coefficients help the balancing act of combining these tendencies in order to be globally efficient. The PSO scheme described so far is rather simple and computationally very efficient, especially when compared to a GA or any gradient based methods. To further this algorithm, a limitation on the maximum value of $\mathbf{v}$ can be imposed, say $v_{\max}$. This type of velocity clamping balances the exploration and intensification and also avoids excessive velocities that are responsible for particles overshooting their targets, [9]. Also, the CFM method can be employed, where the velocity update is modified – reduced – as the search progresses. For this, Equation (3) is altered as follows:

$$\mathbf{v}^i(k+1) = K \times \left[\mathbf{v}^i(k) + c_1 r_1 \left(\mathbf{b}_p^i - \mathbf{x}^i(k) \right) \right] + K \times \left[+ c_2 r_2 \left(\mathbf{b}_g^i - \mathbf{x}^i(k) \right) \right] \quad (4)$$

where $K = \dfrac{2}{\left| 2 - \varphi - \sqrt{\varphi^2 - 4\varphi} \right|}$ and $\varphi = c_1 + c_2$, as given by [5].

The inertia weight w has a competing purpose to the velocity clamping method [10], and is responsible for balancing the exploration and intensification part of the PSO. In [11] it is also shown that w is problem dependent. In this paper, we will investigate the option of adapting w using a TS based scheme such that the PSO algorithm becomes less problem dependent. Besides w, c_1 and c_2 control the stochastic influence, analogous to the mutation operator in GA. In [12], it is stated that for most problems one chooses $c_1 = c_2$, but the ratio is also problem dependent, i.e. for unimodal problems with smooth surfaces, usually one selects $c_2 > c_1$, while for multimodal problems these coefficients are chosen to be $c_1 > c_2$. In this paper, we also will investigate the optimization of these coefficients by implementing a TS scheme in parallel to the PSO.

The TS algorithm has the same objective as PSO-given by Equation 1. A TS algorithm employs one candidate point which moves incrementally on S. The moves between increments are defined by selecting the best update from a set of candidate points. This set is created by forming R n-dimensional spheres about the current position, and randomly place a point in each section (sphere). These points are evaluated on $f(\mathbf{x})$ and then compared to a list $T \in \mathbb{R}^{n \times q}$ of previously visited places. The list length q basically represents the memory of the algorithm. Around each element in T a n-dimensional sphere is created serving as a tabu-ball, where no new solution can be located. The best performing candidate point not violating the restricted spaces given by the q tabu balls is selected as the new position of the search. An aspiration criterion can be formulated as an escape clause to circumvent the restrictions imposed by the tabu-balls, often in the form of having an improved cost to the current solution. All of the past best solutions are stored in a new list – the promising list, which is assembled as the TS algorithm processes. The optimum of the entries of that list will be used as the final optimal value of the algorithm.

Usually, q, R, and the dimension of the individual R's are considered the control parameters of the TS algorithm, which are all problem dependent.

3 Problem Solution

The selection of w, c_1, and c_2 have rather large implication on the update of the new velocity vector $\mathbf{v}^i(k+1)$, as is illustrated in Fig. 1. Here, the three influence vectors with regard to the global best solution, $\mathbf{b}_g^i - \mathbf{x}^i(k)$, and with regard to the particles best solution $\mathbf{b}_p^i - \mathbf{x}^i(k)$ as well as the inertia vector $\mathbf{v}^i(k)$ are depicted for an instant k and a single

particle i. Each of these vectors are pre-multiplied by w, c_1, and c_2 respectively, resulting into some variation of the vectors, denoted by Δ in Fig. 1.

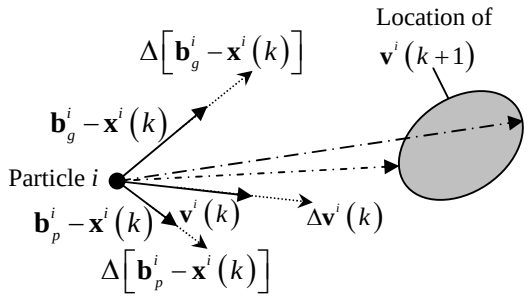

Fig. 1: Adaptation of proposed PSO-TS Algorithm.

As stated earlier, these three influence coefficients are problem dependent. In this paper, we propose to find the optimal coefficients by utilizing a TS. This is accomplished by using the variation of the influence vectors to describe a new search area, in which the original cost function $f(\mathbf{x})$ is prescribed. In Fig. 1, this area is symbolized in the shaded ellipsoid. The best combination of coefficient along with the influence vectors will then determine the velocity update $\mathbf{v}^i(k+1)$. This optimization is repeated at each increment. TS lends itself well for this purpose, since it is computationally very efficient. Since r_1 and r_2 are superimposed to the influence coefficients, we will investigate an option where this randomization is suppressed.

Parameter estimation is an important concept in engineering where a mathematical model of a system is identified with the help of input and output signals. The classical Least Squares (LS) algorithm gives an unbiased estimate of the parameters when the system noise is white. A bias result may occur if the residual $\varepsilon(k) = y(k) - \hat{y}(k)$ is not white, where y is the system output, $\hat{y}$ is the estimated output, and k is the discrete time index. For such instances, one can use a whitening filter, i.e. $C(q^{-1})\varepsilon(k) = e(k)$, where $C(z^{-1})$ is the coefficient polynomial of the whitening filter and z^{-1} is the backward shift operator. The corresponding cost function for the estimation becomes, [3]:

$$J = \sum e^2(k) = \sum [C(z^{-1})A(z^{-1})y(k) + C(z^{-1})B(z^{-1})u(k)]^2$$

where, $u(k)$ is the input sequence, $A(z^{-1})$ and $B(z^{-1})$ are the numerator and denominator polynomials of the system transfer function, respectively. As the signal to noise ratio becomes large, the cost function J may become multimodal. This was shown by Söderström et al. [13]. In order to obtain the global minimum an intelligent optimization technique needs to be employed. In this paper, we will utilize the proposed hybrid PSO-TS algorithm to such parameter estimation problems with a colored noise environment and compare it to the traditional LS method.

4 Simulation Results

The proposed hybrid algorithm is tested on a set of standard optimization benchmark problems, which are listed below:

Spherical: $f(\mathbf{x}) = \sum_{j=1}^{n} x_j^2$ and

Quadratic: $f(x) = \sum_{j=1}^{n} \left\{ \sum_{i=1}^{j} x_j \right\}^2$,

where $x_j \in [-100, 100]$ and $f(\mathbf{x}^*) = [0, 0]$.

Hyperellipsoid: $f(\mathbf{x}) = \sum_{j=1}^{n} j^2 x_j^2$ where $x_j \in [-1, 1]$ and $f(\mathbf{x}^*) = [0, 0]$.

Bohachevsky 1:

$f(\mathbf{x}) = x_1^2 + 2x_2^2 - 0.3\cos(3\pi x_1) - 0.4\cos(4\pi x_2) + 0.7$

where $x_j \in [-50, 50]$ and $f(\mathbf{x}^*) = [0, 0]$.

Rastrigin: $f(\mathbf{x}) = \sum_{j=1}^{n} \left(x_j^2 - 10\cos(2\pi x_j) + 10 \right)$

where $x_j \in [-5.12, 5.12]$ and $f(\mathbf{x}^*) = [0, 0]$.

Rosenbrock:

$f(\mathbf{x}) = \sum_{j=1}^{n/2} \left[100\left(x_{2j} - x_{2j-1}^2\right)^2 + \left(1 - x_{2j-1}\right)^2 \right]$, where $x_j \in [-2.048, 2.048]$ and $f(\mathbf{x}^*) = [1, 1]$.

Haupt & Haupt: $f(\mathbf{x}) = x_1 \sin(4x_1) + 1.1x_2 \sin(2x_2)$, where $x_j \in [0, 10]$ and $f(\mathbf{x}^*) = [9.0389, 8.6674]$.

In addition to these benchmark problems, we also will test the proposed algorithm to some parameter estimation problem with a colored noise environment. In particular, we will test the algorithm on one simple parametric model, which are given as follows:

$$y(k) = 0.5y(k-1) - 0.5y(k-2) + u(k) + \varepsilon(k) \quad (4)$$

The simulation was carried out by using the following set of parameters and conditions: uniformly distributed initial locations of particles, number of neighborhoods created at each step for each particle $R = 25$, uniform initial velocity of magnitude 1 for all particles, $p = 40$, $q = 5$, radius of the n dimensional Tabu balls: $r = 0.025(x_{\max} - x_{\min})$, where $x_{\max}$ and $x_{\min}$ are the dimensions of S, radius of neighborhood $r_N = 0.5r$, and radius of promising balls $r_p = 0.5r_N$. The PSO portion utilized 100 iterations, while the embedded

TS section used 10 iterations. Since randomness is a factor in the used and proposed algorithms, and in order to gain some kind of understanding of consistency, the simulations were carried out 100 times for each cost function listed above.

Table 1 lists the results for the unconstraint optimization problems in comparison with the original PSO algorithm. In this set of simulations, r_1 and r_2 were selected to be uniform random between 0 and 1.

Table 1: Simulation results

Cost Function	PSO	Hybrid PSOTS		
		w	w, c1	w,c_1c_2
Spherical	0.55135	***0.17214***	***0.0555***	***0.2216***
Quadratic	0.50718	***0.25637***	***0.12497***	***0.1347***
Bohachevsky	0.80852	***0.17689***	***0.15473***	***0.01617***
Hyperellipsoid	0.03252	***0.00436***	***0.00745***	***0.00069***
Rastrigin	***0.07168***	0.16678	0.16728	0.16021
Rosenbrock	1.4261	1.43255	1.47011	1.44042
Haupt	12.4736	***10.5563***	***10.5329***	***11.5222***

Table 2 lists the results for the unconstraint optimization problems in comparison with the original PSO algorithm. In this set of simulations, r_1 and r_2 were set equal, at all times, to 1. It is interesting to note that for almost all the cases, the proposed hybrid optimization algorithm, regardless of which set of coefficients are optimized, performs significantly better in comparison to the standard PSO for the Hyperellipsoid, the Bohachevsky cost function. For this case too, the spherical and the quadratic functions produced better results. In both the cases there was no improvement in the Rosenbrock function values and the Rastrigin still showed poor results as compared to the standard PSO algorithm.

The distinction between the characteristics of the cost function and the performance of the proposed algorithm can be made by associating the presented results with unimodal and multimodal cost functions. As listed above, the improved performance given by the proposed hybrid algorithm is found for unimodal cost functions. While the proposed algorithm does work well for multimodal cost functions, it does excel in comparison to the standard PSO algorithm with regard to unimodal functions.

Table 2: Simulation results

Cost Function	PSO	Hybrid PSOTS		
		w	w, c1	w,c_1c_2
Spherical	0.55135	***0.08975***	***0.19801***	***0.81325***
Quadratic	0.50718	***0.31023***	***0.14124***	***0.07529***
Bohachevsky	0.80852	***0.13091***	***0.20773***	***0.15158***
Hyperellipsoid	0.03252	***0.01464***	***0.01736***	***0.00278***
Rastrigin	***0.07168***	0.13648	0.23206	0.4902
Rosenbrock	1.4261	1.44026	1.44147	***1.39044***
Haupt	12.4736	***10.6342***	***10.8366***	***10.8408***

The hybrid algorithm was also tested to estimate the parameters of the system given by equation (4). The estimated system parameters are given in Table 3 for the two cases a) Random r_1 and r_2 and b) Fixed r_1 and r_2 to unity. In addition, we distinguished two cases where we either computed the instantaneous optimum value of the influence coefficients and the accumulated "averaged" optimum. The variance in the noise was set at 1%, while the input sequence was a white noise sequence with variance of 30%.

Table 3: Simulation Results for Estimation

Random			
Accumulative			
w	0.5898	-0.4583	1.0425
w,c1	0.5319	-0.3717	1.1217
w,c1,c2	0.4704	-0.4666	0.8921
Just Optimum			
w	0.5340	-0.5159	1.0025
w,c1	0.5339	-0.5234	1.0550
w,c1,c2	0.4820	-0.4622	1.0110
Fixed			
Accumulative			
w	0.5289	-0.3794	1.0061
w,c1	0.5018	-0.3799	1.0777
w,c1,c2	0.478	-0.4917	0.9182
Just Optimum			
w	0.4707	-0.4827	1.0515
w,c1	0.4797	-0.4397	1.0260
w,c1,c2	***0.5074***	***-0.5164***	***0.9794***

The hybrid algorithm gave the best estimated values of the system parameters for the following combination; Fixed r_1 and r_2, just optimum, w, c_1, c_2 optimized, and 40 particles. Table 3 is giving the average values based on 10 sample points. This combination was then used to compare the results of the hybrid algorithm with Least Squares (LS). Table 4 shows the comparison between LS and the proposed hybrid algorithm for various variances in the noise level. The hybrid PSOTS again outperforms the LS method in almost all the cases and in some estimated values. These cases are highlighted in bold italics. Simulation runs, for the hybrid algorithm, for variances 0.05, 0.09, 0.1 and 0.2 were increased from 10 to 30 which gave slightly better results once again in comparison to the LS.

A key objective of this paper is to make the proposed algorithm adaptive in nature to the subjected problem, i.e. cost function. As detailed in Section 2, the choice of the influence coefficients is dependent on the characteristics of the cost surface. The proposed hybrid algorithm optimizes these coefficients as well as the inertia coefficient w at each iteration. Hence we can plot these coefficients in order to determine if they show adaptation and consistency. This is done in Fig. 2. The plot is a representative characterization of the simulation

results obtained for the tested multimodal cost functions. We can recognize that the proposed algorithm adapts fast to the cost function and selects $c_1 > c_2$ as determined in the literature, indicating that each particle is dominated by its own personal best, and the algorithm is searching wider ranges. The rather non-smooth convergence plot is due to the fact that r_1 and r_2 are kept random and impose a perturbation to the optimal location of the influence coefficients. In comparison, the same plots are generated for some multimodal cost functions, i.e. the Hyperellipsoid in Fig. 3 and Spherical as depicted in Fig. 4. In both cases for the unimodal cost functions, the coefficients move quickly to the case where $c_2 > c_1$ as given in the literature, but after a few iterations, the weighting is switched and $c_1 > c_2$

Table 4: Comparison Hybrid PSOTS and LS

Simulation Options: Optimized w,c1,c2, Fixed r_1 and r_2 and Just Optimum, Simulation Runs :10	
Hybrid PSOTS	Least Squares
Variance: ***0.001***	
[0.5265,-0.4688,0.9695]	[-0.00640,-0.4238,0.8794]
Variance: ***0.005***	
[0.5256,-0.5206,1.0531]	[0.0005,-0.5050,0.8703]
Variance: ***0.009***	
[0.5289,-0.4394,0.9640]	[0.0640,-0.5395,0.8626]
Variance: ***0.01***	
[0.5074,-0.5164,0.9794]	[0.0208,-0.4711,0.8592]
Variance: ***0.05***	
[0.4183,-0.3988,***0.9539]***	[0.1354,***-0.5345***,0.8100]
Variance: ***0.09***	
[0.3300,-0.2699,***0.9840]***	[0.0981,***-0.7102***,0.9573]
Variance: ***0.1***	
[0.4035,-0.3056,***1.0322]***	[0.1276,***-0.6684***,0.8821]
Variance: ***0.2***	
[0.2952,-0.1684,***0.9861]***	[0.0418,***-0.7096***,0.9323]
Variance: ***0.05****, Simulation runs:****30***	
[0.4476,*-0.3844****,1.0049]***	[0.1354,***-0.5345***,0.8100]
Variance: ***0.09****, Simulation runs:****30***	
[0.3852,*-0.3505****,0.9672]***	[0.0981,*-0.7102*,0.9573]
Variance: ***0.1****, Simulation runs:****30***	
[0.4129,*-0.3550****,0.9922]***	[0.1276,***-0.6684***,0.8821]
Variance: ***0.2****, Simulation runs:****30***	
[0.3072,*-0.2769****,0.9970]***	[0.0418,***-0.7096***,0.9323]

This implies that the particles are no longer dominated by the global optimum, but rather by their own personal best performance and try to improve their performances. An explanation for this is found by considering the convergence plot, as detailed in Fig. 5. Here we can see that most of the convergence is achieved after the first few iterations. Once not much improvement is found, the algorithm tries to spread out and search larger regions rather than concentrating to the area dominated by the current global best solution. This adaptation may explain the cause for the improved performance of the proposed algorithm for unimodal functions compared to standard PSO algorithms.

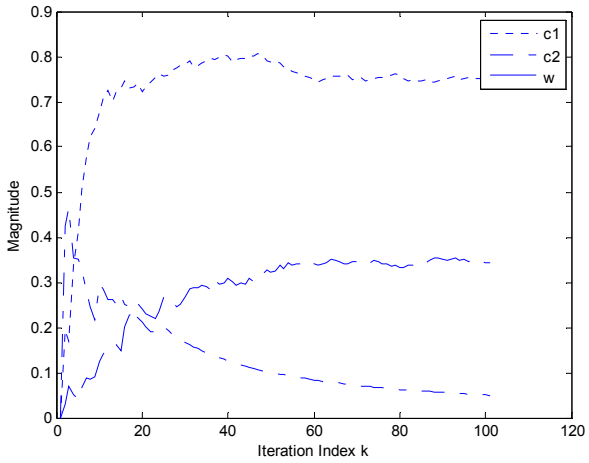

Fig. 2: Plot of optimized influence coefficients.

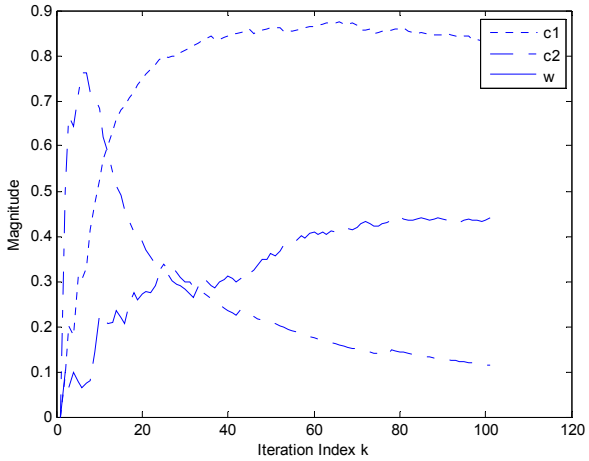

Fig. 3: Plot of optimized influence coefficients for Hyperellopsoid cost function.

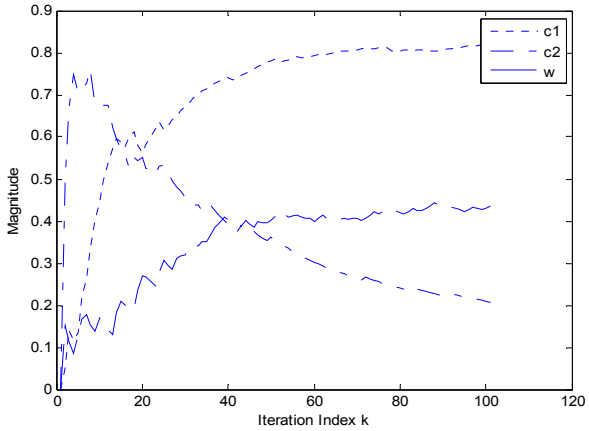

Fig. 4: Plot of optimized influence coefficients for the Spherical cost function.

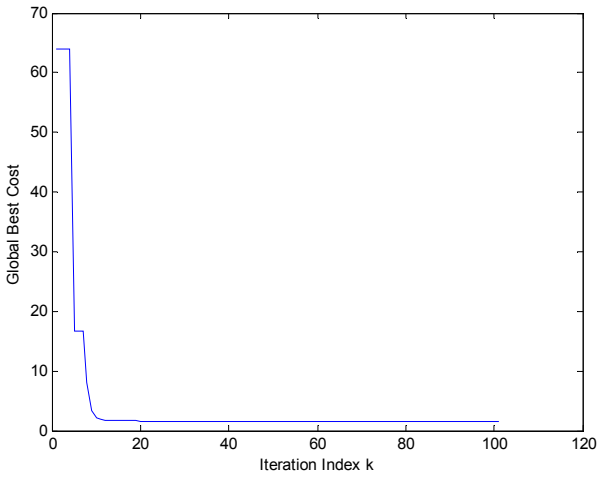

Fig. 5: Plot of global best cost vs. iteration index for the Spherical cost function.

4 Conclusion

In this paper, we propose a hybrid PSO-TS algorithm for optimization of unconstraint cost functions. The algorithm adapts to the underlying cost surface by adjusting the influence coefficients at each step. The proposed algorithm is tested on a series of benchmark problems and showed improved performance for unimodal cost functions. In addition, the hybrid PSO-TS algorithm is tested on two parameter estimation problems where colored noise influence causes bias estimates when the LS algorithm is used. The simulations indicate an improved estimate when the proposed PSO-TS algorithm is used.

Acknowledgement

This work was supported by a grant from the Telemedicine Advanced Technology Research Center (TATRC) of the US Department of Defense. The financial support is greatly appreciated.

References:

[1] Kennedy, J., Eberhart, R., Particle swarm optimization, *Proceedings of the IEEE First International Conference on Neural Networks*, Perth, Australia, 1995, pp. 1942-1948.

[2] Glover, F., Future paths for Integer programming and Links to Artificial Intelligence, *Computers & Operations Research*, Vol. 5, 1986, pp. 533-549.

[3] Ramkumar, B., Schoen, M. P., Lin, F., Application of an Intelligent Hybrid Optimization Technique for Parameter Estimation in the Presence of Colored Noise, *Proceedings of the IMECE*, 2007.

[4] Higashitami, M., Ishigame, A., Yasuda, K., Particle Swarm Optimization Considering the Concept of Predator-Prey Behavoir, *IEEE Congress on Evolutionary Computation*, 2006, pp. 434-437.

[5] Clerc, M., The swarm and the queen: Towards a deterministic and adaptive particle swarm optimization, *Proceedings of the Congress of Evolutionary Computation*, Vol. 3, 1999, pp. 1951-1957.

[6] Li, X., Cui, J.-F., Qu, J.-X., Yang, S.,D., Energy Transimssion Models Based on Tabu Search and Particel Swarm Hybrid Optimization Algorithm, *J. Cent. South Univ. Technol. 01-0144-05*, 2007.

[7] Boggs, P.T., Tolle, J.W., Sequential Quardratic programming, *Acta*, 1995, No. 4, pp. 1-52.

[8] Nakano, S., Ishigame, A., Yasuda, K., Paricle Swarm Optimization Based on the Concept of Tabu Search, IEEE Congress on Evolutionary Computation CEC 2007, pp. 3258-3263.

[9] Eberhart, R.C., Simpson, P.K., Dobbins, R.W., *Computational Intelligence PC Tools.*, Academic Press Professional, 1st Edition, 1996.

[10] Eberhart, R.C., Shi, Y., Particle Swarm Optimization: Developments, Applications and Resources, Proceedings of the IEEE Congress on Evolutionary Computation, Vol. 1, 2001, pp. 27-30.

[11] Shi, Y., Eberhart, R.C., A modified Particle Swarm Optimizer, Proceedings of the IEEE Congress on Evolutionary Computation, 1998, pp. 69-73.

[12] Engelbrecht, A.P., *Fundamentals of Computational Swarm Intelligence*, John Wiley & Sons, 2006.

[13] Söderström, T., Convergence Properties of Generalized Least Squares Idenficiation Method, Automatica, Vol. 10, pp. 617-626, 1974.

ANALYSIS OF EMG-FORCE RELATION USING SYSTEM IDENTIFICATION AND HAMMERSTEIN-WIENER MODELS

Anish Sebastian
Measurement and Control Engineering Research Center (MCERC)
Idaho State University, Pocatello, Idaho 83209, sebaanis@isu.edu

Parmod Kumar
MCERC
Idaho State University, Pocatello, Idaho 83209, kumaparm@isu.edu

Marco P. Schoen
Dept. of Mechanical Engineering, MCERC, Idaho State University, Pocatello, Idaho 83209, schomarc@isu.edu

Alex Urfer
Dept. of Physical and Occupational Therapy, Idaho State University, Pocatello, Idaho 83209, urfealex@isu.edu

Jim Creelman
Dept. of Physical and Occupational Therapy, Idaho State University, Pocatello, Idaho 83209, creejame@isu.edu

D. Subbaram Naidu
Dept. of Electrical Engineering, MCERC, Idaho State University, Pocatello, Idaho 83209, naiduds@isu.edu

ABSTRACT

Surface Electromyographic (sEMG) signals have been exploited for almost a century, for various clinical and engineering applications. One of the most compelling and altruistic applications being, control of prosthetic devices. The study conducted here looks at the modeling of the force and sEMG signals, using nonlinear Hammerstein-Weiner System Identification techniques. An extensive study has been conducted on the modeling of sEMG and corresponding force data to establish a relation which can mimic the actual force characteristics for a few particular hand motions. Analysis of the sEMG signals, obtained from specific Motor Unit locations corresponding to the index, middle and ring finger, and the force data led to the following deductions; a) Each motor unit location has to be treated as a separate system,(i.e. extrapolation of models for different fingers cannot be done) b) Fatigue influences the Hammerstein-Wiener model parameters and any control algorithm for implementing the force regimen will have to be adaptive in nature to compensate for the changes in the sEMG signal and c)The results also manifest the importance of the design of the experiments that need to be adopted to comprehensively model sEMG and force.

NOMENCLATURE

$B_{j,i}(s)$, $F_{j,i}(s)$	Polynomials in the linear block.
b_i,c_i	Coefficients of polynomials (Hammerstein Model).
fn^*	Objective function (PSO).
$g_i()$	Input nonlinearity function (Hammerstein Model).
$g(\bullet)$	Static nonlinear function.
$h()$	Output nonlinearity function.
n_b	Number of zeros plus one.
n_f	Number of poles.
n_k	Delay from the input to the output in terms of the number of samples.
$u(t)$	Input to a system.
$v(t)$, $w(t)$	Internal variables.
$x(t)$	Input nonlinearity (Hammerstein Model).
$y(t)$	Output of a system.
$\hat{y}(t)$	Predicted or estimated output.
$z(t)$	Output linear block (Wiener Model).
$x_i^j(t)$	The i^{th} component position of the j^{th} particle in time t.
$x_i^{j,lbest}(t)$	The local best position of the j^{th} particle in generation t.
$x_i^{j,gbest}(t)$	The global best position of the j^{th} particle in generation t.
$v_i^j(t)$	The i^{th} component velocity of the j^{th} particle in time t.
t	time.
H	Physical parameters of non-linear function g(•).
α	Expected rate of gradual drift.
β	Expected rate of sudden shifts in surface EMG.
ε	Tolerance.

θ Finite dimensional vector used to parameterize the mapping.

INTRODUCTION

For centuries man has been fascinated by the human body and it's working. A great number of scientists, doctors and engineers have spent a great deal of time and effort interpreting various biological signals and decoding the information contained within them. Though the task at hand was very complicated, it never deterred researchers from undertaking this challenge with great determination, which led to some ground breaking work in this field. But inspite of all the advances made in these fields, we still oftentimes find ourselves coming up short in understanding the complexities of the human body. One such field is rehabilitation engineering. The biological signal of interest here is the Surface Electromyogram signal (sEMG). We have come a long way since the first ever study conducted on EMG signals by H. Piper in 1912, [1]. About 50% of the people who need upper extremity prosthetics don't use them, [2] which puts into perspective the direction that research on in this area needs to focus on. The ideal scenario would be to mimic the real human hand with all its functionality and dexterity probably using EMG signals. This goal seems to be quite distant as of today.

EMG signals have been used for quite some time now in the control of prosthetic devices. Simply put, it is analogous to having small voltage signals, with coded information of the specific desired objective, to actuate motors which would translate this information into the desired force dynamics.

EMG signals are fairly complex to work with. In order to have a standardized method, on how EMG signals must be recorded and analyzed, the International Society of Electromyography and Kinesiology (ISEK) has a set of guidelines which are widely accepted. These guidelines for reporting EMG data are documented in, [3]. Other signal analysis techniques generally employed include low-pass or band-pass filtering; others have also employed notch filtering to remove power line noise, [4]. Whitening filters have also been employed in order to increase the quality of the amplitude estimates of the surface EMG signals, [5]. Some of the other signal processing methods include using Markov models, [6] and fuzzy logic control, [7] – for classification of EMG, wavelet processing, [8], and Bayesian estimators, [9]. Extensive research has also been carried out in obtaining a relationship between sEMG and force – for example, linear and non-linear sEMG-Force by Wood *et al.*, [10], EMG-Force relationships in skeletal muscles by Jacquelin *et al.*, [11], where a linear relationship was approximately quantified for the middle operating force range during an isometric effort. They also concluded that the presence of any movement, the algebraic relations estimated were not sufficient to describe the relation. They also concluded that considerable attention needs to be given to the data acquisition, the type of electrode, amplification, rectification, sampling, noise filtering etc. as all these elements do have an impact on the mathematical formulation of the sEMG-Force relation. The effects of joint position, gravity and recruitment have been studied by Solomonow *et al.* in [12]. The effects of fatigue on EMG-Force relation was investigated by Moxham *et al.* [13]. Studies investigating the fatigue of motor units in muscles that control the fingers of the hand were carried out by Fuglevand *et al.* This study showed that fatigue caused the force-frequency relation to be displaced to higher frequencies.

The work reported in this paper is focused on using non-linear System Identification techniques, to come up with a suitable model or models for the sEMG-Force relation. Also modeling for the effects of fatigue on the sEMG-Force relation is taken into consideration and a guideline is provided on the type of experiments that would be most beneficial to encompass the large number of variables which affects the sEMG signal over time. The results of a number of nonlinear models used for deducing the sEMG-Force relationship strongly indicate the need for an adaptive method to be developed to capture the dynamics of the two signals. The results also indicate that the modeling of the sEMG-Force relation should not be extrapolated to different fingers even though the experiments performed were almost the same to obtain very similar force signal patterns. Bayesian filters were also used in analyzing the sEMG signals as they have been shown to be beneficial in system identification [14]. Particle Swarm optimization was used to assist in identifying possible trends in the Bayesian filter parameters with the onset of fatigue.

THEORETICAL BACKGROUND

EMG, VARIABLES AFFECTING sEMG-FORCE RELATIONSHIP & PREVIOUS RESEARCH: An EMG signal is an electrical signal which is generated in a muscle contraction and is representative of neuromuscular activity. sEMG signals are measured at motor unit location. A motor unit (MU) consists of an α -motoneuron in the spinal cord and the muscle fiber it innervates. Many factors influence sEMG signals, some of which are; a) shape of the volume conductor, b) the thickness of the subcutaneous tissue layers, c) tissue inhomogeneities, d) distribution of the motor unit territories in the muscle, e) size of the motor unit territories, f) distribution and the number of fibers in the motor unit territory, g) length of the fibers, h) spread of the endplates and tendon junctions within the motor units, and i) spread of the innervations zones and tendon regions among motor units. The type of detection system used also plays an important part in influencing the sEMG measurements. Some of the factors which need to be taken into account, with the detection systems, are a) skin electrode contact (impedance, noise), b) spatial filtering for signal detection, c) inter-electrode distance, d) electrode size and shape, and e) inclination of the detection system relative to the muscle fiber orientation [15].

Some of the more recent studies suggest poor statistical trends between EMG amplitude and mean power spectral frequency, which indicate limitations in the use of EMG descriptors for fatigue assessment [16]. Mortiz *et al.* found evidence which supports the hypothesis that the EMG discharge rate variability is

a major determinant of the trends in isometric force variability across the working range of a muscle [17]. Studies also suggest that there is not a significant difference between the EMG-Force relations obtained using intramuscular EMG (iEMG) as compared to sEMG [18]. Extensive modeling for the simulating sEMG signals detected by surface electrodes has also been performed [19]. For the study conducted here, the sEMG signals were filtered using a Chebyshev Type II high pass filter and a Chebyshev Type II low pass filter. The sEMG signals were also filtered using a Bayesian Exponential, and a Half-Gaussian filter similar to the ones described in [20] and because it has previously been reported in [14] to yield better fits for non-linear Hammerstein-Wiener modeling.

Particle Swarm Optimization: Over the past few decades several algorithms have been used increasingly to find global minimum values in an optimization problem. Few of the well established optimization algorithms are; a) Genetic Algorithm (GA) – inspired by biological evolution, is at its core, survival of the fittest. The main drawback of GA being that it is computationally very expensive especially for large search spaces. GA has been paired with many other search methods in order to improve its overall performance. b) Tabu Search – which has a set of tabu balls and promising balls or a tabu list which helps it to reduce the search space, and is not very computationally expensive. Some of the other optimization algorithms are, Steepest Descent Method, Gradient Search Method, Ant Colony optimization, Simulated Annealing, Hill Climbing, Bees Algorithm, Quantum Annealing etc. In 1995, a new evolutionary algorithm was developed by J. Kennedy, a social psychologist, and R. Eberhart, known as Particle Swarm Optimization (PSO). This method is computationally less expensive and has been used in this paper to optimize the Bayesian filter parameters α and β. Particle swarm optimization has a simple procedure; 1) Defining the input parameters: This includes the swarm size (number of particles of the swarm), maximum number of iterations, the limiting velocity of the particles, the upper and lower bounds of the search space and the stopping tolerance. 2) Initializing the position of the particles – can be randomly assigned using a uniform or normal distribution [21]. 3) Evaluating the fitness function fn (objective function) for the j^{th} particle. This depends on the cost function, e.g. the local best and the global best values are compared and suitably updated. Moreover, the difference between $\left| fn^*(t) - fn^*(t-1) \right|$, i.e. the current (t) and $(t-1)$ is compared to the tolerance ε. If $\left| fn^*(t) - fn^*(t-1) \right| < \varepsilon$, then stop the loop; otherwise continue. Figures 1 and 2 show the particles of the PSO in the search space and the flow chart of the algorithm respectively.

System Identification (SI), Nonlinear SI, Hammerstein-Wiener Models:

The main aspect of SI involves modeling, which is, developing a concept or mathematical relation on how the system variables are related. If a model is constructed from observed data then it results into an estimation problem. The effort that needs to go behind modeling systems usually depends on the end application. Acceptable models are those which are defined by their "usefulness" rather than their "truthfulness". This means how closely the computed model is, in satisfactorily representing the true system. Modeling is divided into three components: 1) Accurately measuring a data set, e.g. the input and output of a system related in the time or the frequency domain.

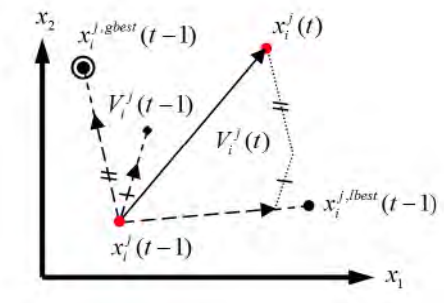

FIGURE 1: PREVIOUS AND UPDATED POSITON OF PARTICLES [21]

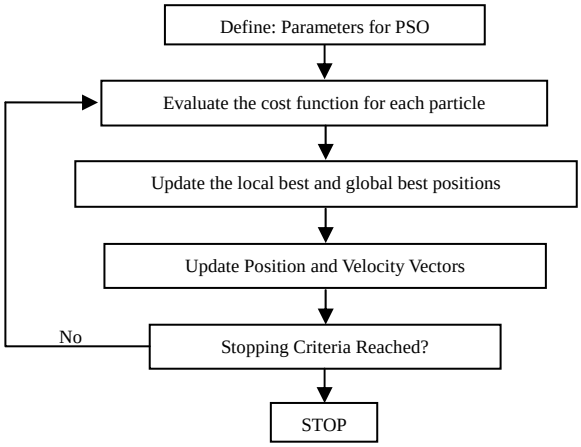

FIGURE 2: PARTICLE SWARM OPTIMIZATION LOOP

2) Defining a model structure and 3) A rule by which a model structure can be established from the measured data, such as Least-Squares. Looking closely at these components, the measured data may be recorded during a specifically designed experiment, so that the data carries maximum information, subject to any constraints, [22]. Choice of a model structure is one of the most important and difficult parts in system identification. Here *a priori* knowledge and engineering intuition coupled with formal properties of the system will prove to be invaluable. Models of systems with some unknown physical parameters can be constructed from basic physical laws and well established relations. These models are known as white box models. Models with unknown physical parameters and a large number of random variables, which cannot be satisfactorily represented by physical laws, are deduced using black box modeling. The third type of model is a gray box model; this represents a compromise and a combination between white and gray box modeling. The third component of modeling is assessment of the model quality and its ability to reproduce the measured data, also known as model validation. The process of System Identification is summarized in Figure 3. Modeling and identification of nonlinear systems is especially challenging, in the sense that the nonlinearity could be

in either the input, the output or in both. If modeling of the system is done using linear and/or non-linear blocks, to represent a system, careful combination of these needs to be formulated. In our study, the input is the sEMG and the output is the corresponding force signal generated by the human hand. The system is the particular subject's hand. The sEMG signal is affected by large number of variables, some of which have been mentioned in the EMG section of the theoretical background. The force signals too are non-linear, especially as time progresses and the muscle fatigues. It would be very difficult and complicated to take into account all the factors which plague these two signals. So with the assumption that the two signals are non-linear; the modeling for this system can be approached in a general sense. In SI the model structure that has been used previously for capturing the non-linear input and output system dynamics has been the Hammerstein-Wiener model.

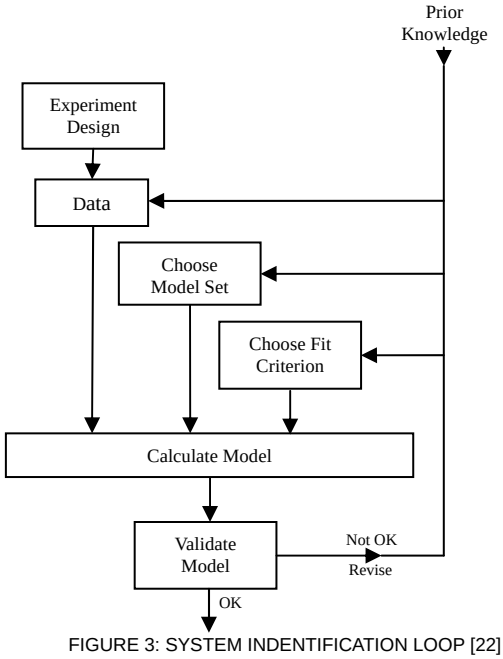

FIGURE 3: SYSTEM INDENTIFICATION LOOP [22]

Hammerstein models assume a separation between the non-linearity and the dynamics of the process [23]. The Hammerstein structure consists of a static non-linear block followed by a linear dynamic block. It is described by the following equations;

$$\begin{aligned} &x(t) = g(u(t)), \\ &y(t) = b_1 x(t-1) + \ldots + b_m x(t-m) - a_1 y(t-1) - \ldots - a_m y(t-m). \end{aligned} \quad (1)$$

Hammerstein models are popular in the field of control engineering as it is easy to compensate the non-linear process behavior by a controller that implements the inverse static nonlinearity $g^{-1}(\bullet)$ at its output (if the inverse exists). Another advantage of this model being that the stability is determined solely by the linear part of the model. Any assumption of the structure of the process is very restrictive and can be applied to only a limited class of systems. The static nonlinearity is usually approximated using a polynomial. For systems with multiple inputs the static nonlinearity $g(\bullet)$ becomes a higher dimensional function, say for $l = 2$, and $m = 2$ Equation (1) becomes;

$$\begin{aligned} &x(t) = c_0 + c_1 u(t) + c_2 u^2(t), \\ &y(t) = b_1 c_0 + b_1 c_1 u(t-1) + b_2 c_0 + b_2 c_1 u(t-2) + \\ &\quad b_1 c_2 u^2(t-1) + b_2 c_2 u^2(t-2) - a_1 y(t-1) - a_2 y(t-2). \end{aligned} \quad (2)$$

The generalized Hammerstein model is constructed by summarizing identical terms and re-parameterizing the model in a manner that yields linear parameters, for example, $b_1 c_0$ and $b_2 c_0$ both represent offsets and can be summarized. This leads to Equation (3);

$$\begin{aligned} y(t) = {} & \theta_1 + \theta_2 u(t-1) + \theta_3 u(t-2) + \\ & \theta_4 y(t-1) + \theta_5 y(t-2) + \theta_6 u^2(t-1) + \theta_7 u^2(t-2). \end{aligned} \quad (3)$$

The Wiener model structure is the Hammerstein model reversed. The linear dynamic block is followed by a static nonlinear block. This yields the equation given in (4)

$$\begin{aligned} &x(t) = b_1 u(t-1) + \ldots + b_m u(t-m) - a_1 x(t-1) - \ldots a_1 x(t-m), \\ &y(t) = g(x(t)). \end{aligned} \quad (4)$$

Eliminating x in (4) yields;

$$\begin{aligned} y(t) = {} & g(b_1 u(t-1) + \ldots + b_m u(t-m) \\ & - a_1 g^{-1}(y(t-1)) - \ldots - a_m g^{-1}(y(t-m)) \end{aligned} \quad (5)$$

The combination of the two is then the Hammerstein-Wiener model, [24] as given in Figure 4(a) Hammerstein b) Wiener models and Figure 5 Hammerstein-Wiener model. Consider the Hammerstein case where the static nonlinear function $g(\bullet)$ can be parameterized either in terms of physical parameters, such as saturation point and saturation level, or in black-box terms such as spline-function coefficients. This defines $g(\bullet, \eta)$. If the linear model is given by $G(q, \theta)$, the predicted output model will be in the following form:

$$\hat{y}(t \mid \theta, \eta) = G(q, \theta) g(u(t), \eta) \ . \quad (6)$$

Equation 7 describes the Hammerstein-Wiener model structure:

$$w(t) = f((g(t)), \quad b(t) = \frac{B_{j,i}(q)}{F_{j,i}(q)} w(t), \ \ y(t) = h(x(t)), \quad (7)$$

where, $w(t)$ and $b(t)$ are internal variables, $w(t)$ has the same dimensions as $u(t)$, and $x(t)$ has the same dimensions as $y(t)$.

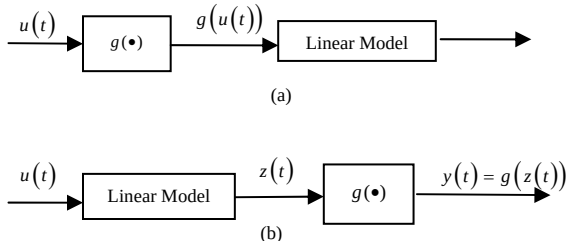

FIGURE 4 (A): A) HAMMERSTEIN MODEL, B) WIENER MODEL

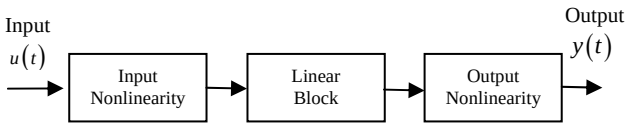

FIGURE 4 (B): HAMMERSTEIN-WIENER MODEL STRUCTURE

The linear block is specified using the terms n_b - the number of zeros plus one, n_f - the number of poles and n_k - the delay from the input to the output in terms of the number of samples. The commonly used nonlinear estimators for Hammerstein-Wiener model are, a) Dead Zone, b) Piecewise Linear, c) Saturation, d) Sigmoid Network, and e) Wavelet Network, [25-27].

EXPERIMENTAL SETUP

The experiments were carried out on a healthy male subject. The objective was to extract dynamical models describing the relationship between sEMG-Force signals. The motor point of the subject was located using a Muscle Stimulator, manufactured by Rich-Mar Corporation (model number HV 1100). The motor location of the ring finger was identified and chosen for the experiments. The EMG detection system used was a Delsys, Bagnoli-16 channel EMG (DS-160, S/N-1116), which has internal amplification and noise reduction technology built into it. The sensors used for measuring the surface EMG action potentials are two pronged DE 2.1 differential surface electrodes. The material for the contacts of the electrode is 99.9% pure silver, while the contacts are 10mm long, 1mm in diameter and spaced 10mm apart.

The subjects' skin was prepared before the sensors were placed over the motor point location of the forearm musculature being measured. Hair around the area was shaved and an alcohol swab was used to clean the skin. The Delsys Electrode Interface SC-FO2-3 was used which promotes the quality of the electrical connection between the electrode and the skin, minimizing motion artifacts and line interference. The electrodes were placed along the muscle fibers (Flexor Digitorum Superficialis) for recording surface EMG. The force was recorded using a force sensitive resistor (FSR) mounted on a stress ball. The data acquisition for the force and the sEMG signals was done at 2000 samples per second and the NI DAQ 6024 E Series boards were used. Experiments were conducted for three fingers, the index, middle and the ring finger. The motions simulated were a) pad to pad grip and b) a power grip, while measuring the force developed by individual fingers. For the ring finger, the motion to generate the force signal was randomized (the levels of force amplitude and frequency generated by the subject varied significantly over one experiment and for all six experiments that were carried out). This was done in order to have poor correlation between the sEMG-Force signals analyzed for various time windows. For the index and the ring finger four experiments were conducted for each. The motion to generate the force signal was made cyclic in order to have high correlation between the sEMG-Force signals. Cyclic motion was considered, in this case, to study the effects of fatigue as time progressed on system identification and the Hammerstein-Wiener modeling. Data, for the ring finger (random motion), was collected for 30, 45 and 60 seconds. Data for the middle and index fingers was collected for 30 and 45 seconds. The subject performed a cyclic and random series of flexions and contractions with the ring finger at constant and random speeds. The randomness – as depicted in Figure 5a) – was necessary in order to ensure that the system is excited at all modes. Figure 5a) shows the output of the random motion raw sEMG signal of the ring finger, 5b) Chebyshev filtered random motion sEMG-Force signals (ring finger), 5c) Half-Gaussian filtered sEMG, and also the data. 5d) cyclic sEMG-Force signals of the middle finger and 5e) cyclic sEMG-Force signals of the index finger. The x-axis in the figures is the number of samples and the y-axis is the amplitude of the sEMG and the force signal in milli-volts. During the experiment all fingers were flexed in order to generate the force and sEMG signal. A result of this was substantial cross talk in the measurement. This is closer to a real life situation. The fit values computed for the models uses the relation in equation, (8);

$$fit = 100 * (1 - norm(\hat{y} - y) / norm(y - mean(y))) \quad (8)$$

RESULTS AND DISCUSSION

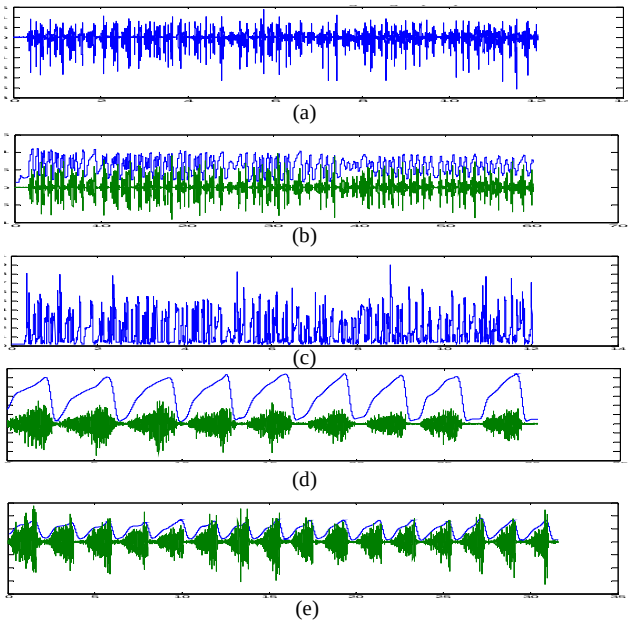

FIGURE 5: A) RANDOM RAW EMG RING FINGER, B) CHEBYSHEV FILTERED EMG AND FORCE (RING FINGER, RANDOM), C) HALF-GAUSSIAN FILTERED EMG (RING), D) CYCLIC EMG-FORCE MIDDLE FINGER, E) CYCLIC EMG-FORCE INDEX FINGER

The force signal was filtered using a low pass Butterworth filter using a cutoff frequency of 3Hz. The sEMG signal was also filtered using a Chebyshev Type II high pass filter with the following filter parameters, F_{stop}=60Hz, F_{pass}=70, A_{stop}=80, A_{pass}=1, match=stopband, to remove any line frequencies and followed by a low pass Chebyshev Type II high pass filter with the following filter parameters, F_{stop}=600Hz, F_{pass}=650, A_{stop}=80, A_{pass}=1, match=stopband. This was done since EMG signals have an effective frequency content of not more than 500Hz, according to the ISEK standards, [3].

Cyclic and Random Data Analysis: As mentioned earlier, experiments were carried out a) in a cyclic motion, to have a cyclic change in the sEMG and force signal so that the effects of fatigue could be characterized and b) in a random manner (with fatigue induced by repetition) to investigate how the Hammerstein-Wiener model parameters change with time. For the cyclic case, experiments were conducted on the index and the middle finger, while the ring finger was used for the random case. In all, for the cyclic case four experiments each were conducted on the index and middle finger and the data analyzed. The sEMG data was filtered using a Chebyshev filter and a Half-Gaussian filter. Hammerstein-Wiener models were tested by varying n_b and n_f values for both the cases. The data set was split into smaller windows; an example of the windows used for estimation and validation of the modeling is shown in Table 1, where ze is the time interval that was used for the model estimation and zv is the time interval used for model validation. A small overlapping time window, with the estimated model is used for the validation model.

TABLE 1: MODELING TIME WINDOWS CYCLIC MOTION (INDEX AND MIDDLE FINGERS)

ze (sec)	zv (sec)
0.5-6.5	2.5-8.5
6.5-13.5	9.5-16.5
13.5-19.5	16.5-22.5
17.0-23.0	20.0-26.0

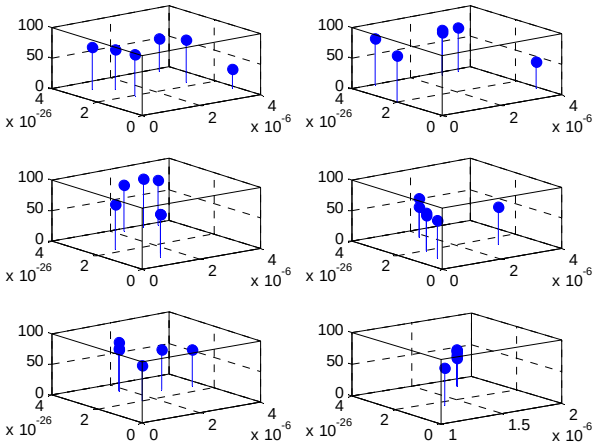

FIGURE 6: RESULTS OF PSO FOR SIX EXPERIMENTS. AXES ARE ALPHA, BETA AND FIT VALUES.

In all, the total time intervals for which models and fits were computed for the index finger alone, were 4 (time intervals per experiment) x 4(experiments) x 49 (models per window by varying n_b and n_f) x 2 (filtering methods) = 1,568 different models. This was also repeated for the middle finger (1,568 different models). For the random motion/force variation scenario; 8 (time intervals per experiment) x 7(experiments) x 49 (models per window by varying n_b and n_f) x 2 (filtering methods) x 2 (piecewise linearity function, 5 and 10)= 10,976 different models were analyzed. It would not be feasible to show all the results of all the models here, but examples are provided as to how the modeling was affected for the various time intervals and motion/force variations. Also, for the random scenario, PSO was used to investigate a relation between the filter parameters α and β and also to investigate the effect of fatigue on the model outputs. The results of the PSO optimization are summarized in Figure 6. From the results, it can be concluded that α values between 1.5 to 2.9e-6 and β values between 2.6-3.7e-26 are more likely to give better fits for nonlinear Hammerstein-Wiener models. The fits are not very conclusive, as the fit values for experiment 1 are not very high (probably the search space for α and β would need to be expanded) as compared to the other experiments for the initial time windows, where one would not expect any fatigue. But a trend can be observed that as fatigue sets in towards the last time window of almost all the experiments the fit % dropped, except for experiments 5 and 6 (not shown here) where the fits were relatively high about 67%. This was because the correlation between the signals for these two windows was much higher than the ones for the other experiments.

This indicates that as the muscle fatigue increases, it directly deteriorates the input sEMG signals relation to force. This casts a doubt on the effectiveness of the nonlinear blocks in the Hammerstein-Wiener models investigated. From these results, it could be concluded that a thorough investigation into the nonlinear block would be needed to capture the dynamics of fatigue and to compensate for the detrimental effects it has on modeling the sEMG-force signals. Also, the nonlinear block could be substituted for any of the blocks that have been discussed in, [28]. Figure 7 shows some of the results for the index finger nonlinear Hammerstein-Wiener models investigated for the experiments. The red plot is of the signal used for model estimation, the green plot is of the signal used for validation of the model and the blue plot is of the entire data spectrum for that experiment for Figure 7 (a) & (b). Figure 7(c) shows the auto-correlation of the model residuals for the output signal (force). This figure also plots the cross-correlation of the various models between the input (sEMG) and the residuals of the output (force). Figure 7 d) shows the results of the measured and the simulated model output signal, for the particular time window. The plots shown here are for the best fit scenarios. For example, nlhw1 with the following model parameters; $n_b = 2$; $n_f = 3$ and $n_k = 1$, with a piecewise linearity function value of 5, gives a fit of 80.51% for the time window 0.5-8.0sec window, which was split into 0.5-6.0 and 2.5-8.0for model estimation and validation. The model parameters were varied i.e. various n_b (from 2-9), and n_f (from 3-10) were investigated. **7**(e), (f) and (g) are the input nonlinearities, the linear block and the output nonlinearity blocks of the Hammerstein-Wiener models. The plot also shows the case where the simulated model failed for a set of parameters (the line in the input non-linearity which goes across the others). In the linear block plot there are a few lines which have a very large deviation from the others; these too are the cases where the modeling resulted in poor fit values.

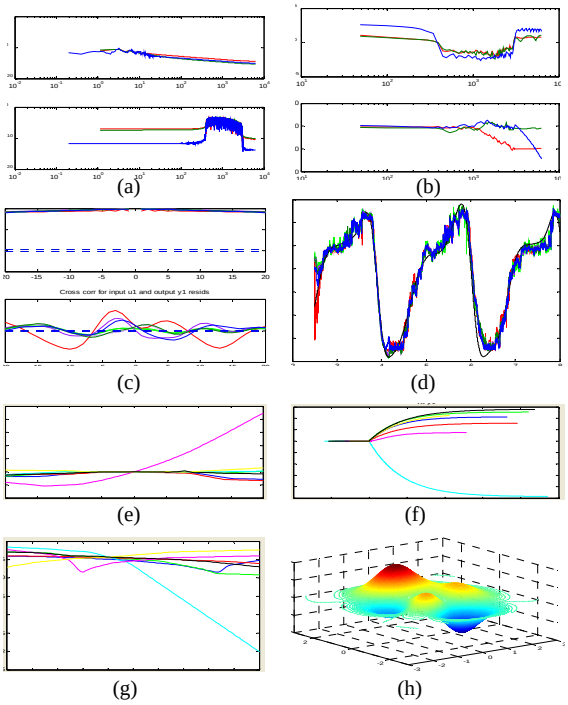

FIGURE 7: A) EMG INDEX FINGER DATA SPECTRUM, B) FREQUENCY CONTENT OF SIGNALS. C) MODEL RESIDUALS AND AUTO-CORRELATION AND CORSS-CORRELATION OF SIGNALS, D) MODEL OUTPUTS, E) INPUT NONLINEARITY, F) LINEAR BLOCK, G) OUTPUT NONLINEARITY, H) CONTOUR PLOT OF MODEL FITS

7(h) represents a contour plot of the fit values for the various models. The description here, is applicable to Figure 8 also, only the results shown are for the Middle finger.

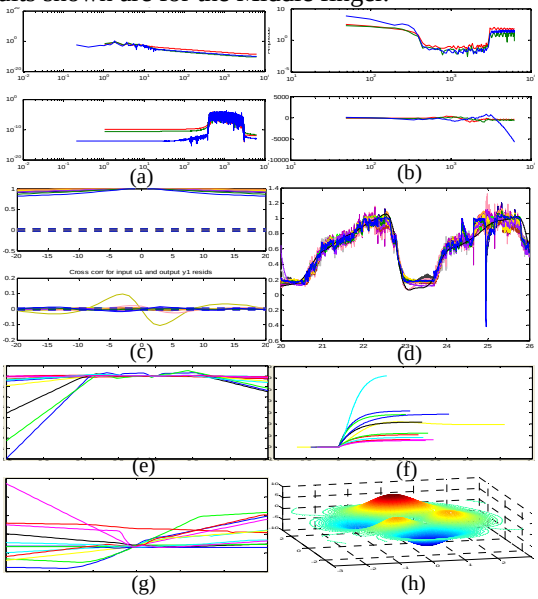

FIGURE 8: A) EMG MIDDLE FINGER DATA SPECTRUM, B) FREQUENCY CONTENT OF SIGNALS. C) MODEL RESIDUALS AND AUTO-CORRELATION AND CORSS-CORRELATION OF SIGNALS, D) MODEL OUTPUTS, E) INPUT NONLINEARITY, F) LINEAR BLOCK, G) OUTPUT NONLINEARITY, H) CONTOUR PLOT OF MODEL FITS

Figure 9 shows a distribution of the fit values for the various model parameters for a single time window.

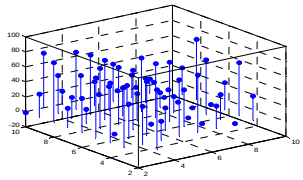

FIGURE 9: DISTRIBUTION OF MODEL PARAMETRS AND THE FIT VALUES (ONE TIME WINDOW)

CONCLUSION

From the experiments and the Hammerstein-Wiener modeling it can be concluded that, a) the Hammerstein-Wiener models do capture the dynamics of the sEMG-Force data, very well, for all the three fingers tested (in the range of 65 to 82% model fits). This statement holds true for all the initial time windows in the experiments. But the model fits deteriorate (between 17-25%) as fatigue in the muscle increases. In order, to capture and to account for the changes in the sEMG-force signals due to fatigue, further investigation will be needed into the non-linear block of the model structure. Also the size of the windows chosen for estimation and validation needs to have a fairly high degree of correlation. For the random motion case, where the force was varied randomly, added analysis of the frequency and amplitude of the two signals was needed. The selection of the size of the window could be automated using correlation coefficients. b) The Half-Gaussian filtering of the sEMG signal, used for modeling, yielded slightly better results than the Chebyshev filtering of sEMG (about 7-12% more). c) A change in the piecewise linearity function in the Hammerstein-Wiener modeling did also have a significant effect on the model fit value. Though a clear trend could not be seen from the results, an adaptive optimization scheme if applied could help in arriving to more concrete conclusions about the effect of this parameter on the model fits. d) Although the PSO did not offer concrete results about the effect of fatigue on the filter parameters α and β, it did throw some light on the direction in which the search space for these parameters needs to be further investigated, which could assist in modeling the sEMG-force signals, especially with muscle fatigue.

ACKNOWLEDGEMENTS

This work was supported by a grant from the Telemedicine Advanced Technology Research Center (TATRC) of the U.S. – Department of Defense (DoD) and is greatly appreciated.

REFERENCES

1. Piper, H., 1912. “Elektrophysiologie Menschlicher Muskeln”. *Springer Verlag*.
2. http://www.army.mil/-news/2010/02/24/34906-the-future-of-prosthetics-is-in-your-mind/
3. http://www.isek-online.org/standards_emg.html

4. Mewett, D. T., Nazeran H., Reynolds, K., J., 2001. "Removing power line noise from recorded EMG". *Proceedings of the 23rd Annual EMBS international Conference*.Light,
5. Clancy, A. E., Farry, A. K., 2000. "Whitening of the electromyogram to improve amplitude estimation". *IEEE Transactions on Biomedical Engineering*, 47(6), June, pp. 709-719.
6. Chan, D. C. A., Englehart, B. K., 2005. "Continuous myoelectric control for powered prostheses using hidden Markov models". *IEEE Transactions on Biomedical Engineering*, 52(1), January, pp. 121-124.
7. Chan, H. Y. F., Yang, Y., Lam, F. K., Zhang, Y., Parker, A. P., 2000. "Fuzzy EMG classification for Prosthesis control". *IEEE Transactions on Rehabilitation Engineering*, 8(3), September, pp. 305-311.
8. Reaz, I. B. M., Hussain, S. M., Yasin, M. F., 2006. "Techniques of EMG signal analysis: detection, processing, classification and application". *Biomedical Procedures Online*, 8(1), January, pp. 11-35.
9. Johnson, T. D., Elashoff, R. M., Harkema S. J., 2003. "Bayesian change-point analysis of electromyographic data: detecting muscle activation patterns and associated applications". *Biostatistics*, 4(1), pp. 143-164.
10. Woods J. J., Bigland-Ritchie B., 1983. "Linear and non-linear surface EMG/force relationships in human muscles. Anatomical/functional argument for the existence of both". *American Journal of Physical Medicine*, 62(6), December, pp. 287-299.
11. Jacquelin P., George A. B., 1981. "EMG-Force relationships in skeletal muscle". *CRC Critical Reviews in Biomedical Engineering*, 7(1), pp. 1-22.
12. Solomonow M., Guzzi A., Baratta R. Shoji H., D'Ambrosia R., 1986. "EMG-force model of the elbows antagonistic muscle pair. The effect of joint position, gravity and recruitment". *American Journal of Physical Medicine*, 65(5), October, pp. 223-244.
13. Moxham J., Edwards R. H., Aubier M., Troyer De. A., Farkas G., Macklem P.T., Roussos C. 1982. "Changes in EMG power spectrum (high-to-low ratio) with force fatigue in humans". *Journal of Applied Physiology*, 53(5), pp. 1094-1099.
14. Sebastian A., Parmod K., Anugolu M., Schoen P. M., Urfer A., Naidu S. D., 2009. "Optimization of Bayesian Filters and Hammerstein-Wierner Models for EMG-Force Signals Using Genetic Algorithm". *Proceedings of the ASME 2009 Dynamic Systems and Control Conference DSCC 2009.*
15. Farina, D., Merletti, R., and Enoka, M. R., 2004. "The extraction of neural strategies from the surface EMG". *Journal of Applied Physiology*, 96, pp. 1486-1495.
16. Clancy A. E., Bertolina V. M., Merletti R., Farina D., 2008. "Time-and frequency-domain monitoring of the myoelectric signal during long-duration, cyclic, force varying, fatiguing hand-grip task". *Journal of Electromyography and Kinesiology*, 18(5), October, pp. 789-797.
17. Mortiz T. C., Barry K. B., Pascoe A. M., Enoka M. R., 2004. "Discharge rate variability in force fluctuations across the working range of a hand muscle". *Journal of Neurophysiology*, 93, December, pp. 2449-2459.
18. Kamavuako N. E., Farina M., Yoshida K., Jensen W., 2009. "Relationship between grasping force and features of single-channel intramuscular EMG signals". *Journal of Neuroscience Methods*, 185(1), December, pp. 143-150.
19. Farina D., Merletti R., 2001. "A novel approach for precise simulation of EMG signal detected by surface electrodes". *IEEE Transactions on Biomedical Engineering*, 48(6), June, pp. 637-646.
20. Sanger, D. T., 2007. "Bayesian Filtering of Myoelectric signals". *Journal of Neurophysiology*, 97, pp. 1839-1845.
21. Chen, C.-H., Bosworth, K. W., and Schoen, M. P., 2007. "Investigation of particle swarm optimization dynamics". *In Proceedings of International Mechanical Engineering Congress and Exposition (IMECE).*
22. Ljung, L., 2nd ed., "System Identification: theory for the user". Prentice Hall Information and System Sciences Series, 1995, Chap. 13, pp. 409-453.
23. Nelles O., "Nonlinear System Identification: From classical approaches to neural networks and fuzzy models". Springer. Chap. 18, pp. 583-586
24. Ljung, L., 2nd ed., "System Identification: theory for the user". Prentice Hall Information and System Sciences Series, 1995, Chap. 5, pp. 140-145.
25. http://www.mathworks.com/access/helpdesk/help/toolbox/ident/index.html?/access/helpdesk/help/toolbox/ident/gs/bq_ylq6.html
26. Westwick, T. D., Kearney, E. R., 2000. "Identification of a Hammerstein Model of the stretch reflex EMG using separable least squares". *Proceedings of the 22nd Annual EMBS Conference*, July, pp. 1901-1904.
27. Dempsey, J. E., Westwick, T. D., 2001. "Identification of a Hammerstein Model of the stretch reflex EMG using cubic splines". *Proceedings of the 23rd Annual EMBS Conference*, October, pp. 1244-1247.
28. Juditsky A., Hjalmarsson H, Benveniste A., Delyon B., Ljung L., 1995. "Nonlinear black-box models in system identification: Mathematical Founddations". *Automatica* IFAC, 31(12), December, pp. 1725-1750.

CHAPTER 12

Automatic Control Techniques for Smart Prosthetic Hand Technology: An Overview

D. Subbaram Naidu, Cheng-Hung Chen

Measurement and Controls Engineering Research Center, School of Engineering, Idaho State University, Pocatello, Idaho, 83209-8060, USA

CONTENTS

1. INTRODUCTION

The human hand is considered to be an agent of the human brain and is the most intriguing and versatile appendages of the human body. Over the last several years, attempts have been made to build a prosthetic hand to replace the human hand that fully simulates the various natural/human-like operations of moving, grasping, lifting, twisting and so on. Replicating the human hand in all its various functions is still a challenging task due to its extreme complexity. It has 27 bones, controlled by about 38 muscles to provide the hand with 22 degrees of freedom (DOF) and incorporates about 17,000 tactile units of 4 different units [99, 207]. Parallels between dextrous robot and human hands were explored by studying sensor motor integration in the design and

ISBN: x-xxxxx-xxx-x

Distributed Diagnosis and Home Healthcare
Edited by U. Rajendra Acharya, Filippo Molinari, Toshiyo Tamura, D. Subbaram Naidu, and Jasjit S. Suri
Volume 2: Pages 1–23

control of these robots by bringing together experimental psychologists, kinesiologists, computer scientists, and electrical and mechanical engineers.

1.1. Relevance to the Military

"In the United States, there are approximately 1.9 million people living with limb loss" due to combat operations (such as conflicts, wars, etc.) and non-combat operations such as accidents, or birth defects, according to the Amputee Coalition of America (ACA) [3]. Further, during the recent wars in Afghanistan and Iraq, "at least 251,102 were killed and 532,715 seriously wounded" [192].

The following documents reveal the intense interest by military in the area of smart prosthetics.

1. First, according to [131], recognizing that "arm amputees rely on old devices" and that the existing technology for arm and hand amputees hasn't changed significantly in the past six decades, the Defense Department is embarking on a research program to "fund prosthetics research" according to [132] to revolutionalize upper-body prosthetics and to develop artificial arms that will "feel, look and perform" like a real arm guided by the central nervous system.
2. According to [55, 56], Bio-Revolution is one of the eight strategic research thrusts that DARPA is emphasizing in response to emerging trends and national security. In particular, the Human Assisted Neural Devices program under Bio-Revolution will have "immediate benefit to injured veterans, who would be able to control prosthetics. . . ." A related area of interest in Bio-Revolution is Cell and Tissue Engineering.
3. Next, according to the Defense Science Office (DFO) of DARPA [57], emerging technologies for combat casualties care with dual-usage for both military and civilian medical care, focus on programs in Revolutionizing Prosthetics, Human Assisted Neural Devices, Biologically Inspired Multi-functional Dynamic Robotics, and so on. In particular, according to [58], "today one of the most devastating battlefield injuries is loss of a limb . . . at DARPA, the vision of a future is to . . . regain full use of that limb again."

In research and development of a prosthetic hand using non-invasive techniques, the basic problems are

1. acquising and classifying electromyographic (EMG) signals to correspond to various human-like operations or features,
2. converting EMG feature signals to control signals to input to actuators to operate the prosthetic hand, and
3. designing and building a prosthetic hand with necessary sensors to operate according to the control signal that corresponds to the EMG signal intended for the particular identified hand operation.

This overview was first prepared in 2006 [138] when the first author and his colleagues at Idaho State University submitted a proposal on *Smart Prosthetic Hand Technology—Phase I of III* to the Telemedicine Advanced Technology Research Center (TATRC), which is the corporate or central laboratory for advanced technology research of the U.S. Army Medical Research and Material Command (USAMRMC) of U.S. Department of Defense. Since the proposal was funded by the TATRC in July 2007, the overview has been continuously updated and was then completed in the present form. In this chapter, a chronological overview of the applications of control theory to prosthetic hand is presented. The overview focuses on *hard* computing or control techniques, such as multi-variable feedback, optimal, nonlinear, adaptive and robust, and *soft* computing or control techniques, such as artificial intelligence, neural networks, fuzzy logic, genetic algorithms, and on the *fusion* of hard and soft control techniques. This overview, focusing on recent developments, is intended to supplement the already existing excellent survey articles [50, 112, 207], and is not intended to be an exhaustive survey on this topic. Any omissions of other works is purely unintentional.

2. CONTROL STRATEGIES

2.1. Prosthetic Hands

Over the last several years artificial hands have been developed by various researchers in the field and some of the prosthetic devices developed are given below (in chronological order) [207, 208]:

1. Russian arm – [108, 128, 177]
2. Waseda hand – [103]
3. Boston arm[a] – [125]
4. UNB hand (University of New Brunswick) – [88, 120, 162]
5. Hanafusa hand – [79]
6. Crossley hand – [51]
7. Okada hand – [146]
8. Utah/MIT hand (University of Utah/Massachusetts Institute of Technology) – [95, 96, 94]
9. JPL/Stanford hand (Jet Propulsion Laboratory/Stanford University) – [167, 195]
10. Minnesota hand – [119]
11. Manus hand – [114, 157]
12. Kobayashi hand – [107]
13. Rovetta hand – [165]
14. UT/RAL hand – [105]
15. Dextrous gripper – [193]
16. Belgrade/USC hand (University of Belgrade/University of Southern California) – [18]
17. Southampton hand (University of Southampton, Southampton, UK) – [111]
18. MARCUS hand (Manipulation And Reaction Control under User Supervision) – [113]
19. Kobe hand (Kobe University, Japan) – [148]
20. Robonaut hand (NASA Johnson Space Center) – [124]
21. NTU hand (National Taiwan University) – [86]
22. Hokkaido hand – [145]
23. DLR hand (Deutschen Zentrums für Luft- und Raumfahrt-German Aerospace Center) – [26, 121]
24. TUAT/Karlsruhe hand (Tokyo University of Agriculture and Technology/University of Karlsruhe) – [74]
25. BUAA hand (Beijing University of Aeronautics and Astronautics) – [209]
26. TBM hand (Toronto/Bloorview MacMillan) – [59]
27. ULRG System (University of Louisiana Robotic Gripper) – [109]
28. Oxford hand – [114]
29. IOWA hand (University of Iowa) – [205]
30. MA-I hand – [182]
31. RCH -1 (ROBO CASA hand 1[b]) – [159]
32. UB hand (University of Bologna) – [123]
33. Ottobock SUVA hand – (www.ottobock.co.uk)
34. Northwestern University system – [72]
35. SKKU Hand II (Sungkyunkwan University, Korea) – [44]
36. Applied Physics Laboratory (APL) at Johns Hopkins University (JHU) – [7, 8, 58]

Some of the commercial web sites for prosthetic devices are:

1. Sensor Hand™ Speed from Otto Bock (www.ottobock.co.uk),
2. VASI (Variety Ability Systems Inc.), a company of the Otto Boch Group (http://www.vasi.on.ca/index.html),

[a]The "Boston Arm," project involved the Harvard Medical School, Massachusetts General Hospital, the Liberty Mutual Research and Rehabilitation Centers, and M.I.T.
[b]The Italy-Japan joint laboratory for Research on Humanoid and Personal Robotics.

3. Utah Arm from Motion Control (www.utaharm.com),
4. The i-LIMB Hand from Touch Bionics (www.touchbionics.com), and so on.

A very useful comparison table between several hands listed above and the human hand, adapted from [207, 208], is updated and shown in Table 1.

However, about 35% of the amputees do not use their prosthetic hand regularly according to [14] due to various reasons such as poor functionality of the presently available prosthetic hands and psychological problems. To overcome this problem, one has to design and develop an artificial hand that "mimics the human hand as closely as possible" both in functionality and appearance.

There are a number of surveys, and/or state-of-the art articles that appeared over the years on the subject of myoelectric prosthetic hand including the work in USSR (Russian) [177] and other places [10, 19, 21, 43, 50, 77, 93, 112, 137, 147, 173, 174, 178, 207].

2.2. Chronological Overview

Up to 1970:

Electromyographic (EMG) signal is a simple and easily obtainable source of information about the various movements to be used for artificial/prosthetic hands. The EMG extraction using surface electrodes is a very attractive method from the point of view of the user compared to implants requiring surgery. Research activity in the field of

Table 1. Comparison of human hand with artificial hands: robotic and prosthetic hands. *Force* indicates power grasp, *Speed* indicates the time required for a full closing and opening, *E*, stands for *external*, *I*, stands for *internal*.

	Size (Norm)	# of fingers	# of DOF	# of sensors	# of actuators	Weight (gms)	Force (N)	Speed (sec)	Controls
Human hand	1.0	5	22	≈17,000	38(I+E)	≈400	>300	0.25	E
Russian arm		5		3	1		≈147		
Waseda hand									
[illegible] hand									
[illegible]afusa hand									
Crossley hand									
Utah/MIT hand	≈2.0	4	16	16	32(E)	—	31.8	—	E
JPL/Stanford hand	≈1.2	3	9	—	12(E)	1100	45	—	E
Minnesota hand									
[illegible]yashi hand									
[illegible]ovetta hand									
UT/RAL hand									
Dextrous gripper									
Belgrade/USC hand	≈1.1	4	4	23+4	4(E)	—	—	—	E
Southampton hand	≈1.0	5	6	—	6(E)	400	38	≈5	E
MARCUS hand	≈1.1	3	2	3	2(I)	—	—	—	I
Kobe hand									
Robonaut hand	≈1.5	5	12+2	43+	14(E)	—	—	—	E
NTU hand	≈1	5	17	35	17(E)	1570	—	—	E
Hokkaido hand	≈1	5	17	35	17(E)	1570	—	—	E
DLR hand II	>1	5	7	—	7(E)	125	—	—	E
TUAT/Karlsruhe hand	≈1	5	17	—	17(E)	≈120	12	0.1	E
BUAA hand		4			2				
[illegible] hand									
[illegible]rd hand									
IOWA hand									
MA-I hand									
Robo Casa hand-1	≈1	5	16	24	6(E+I)	350	≈40	0.25	E
Ottobock SUVA	1	3	1	2	1(E)	600	—	—	I
UB hand									
Hokkaido hand	>1	5	7	—	7(E)	125	—	—	E
Northwestern									
SKKU Hand II	1.1	4	4	—	3	900			
APL-JHU System									

prosthetic limbs was initiated by the US National Academy of Sciences in response to the needs of a large number of casualties in World War II [135]. Researchers reporting in Refs. [16, 203] first proposed the concept of EMG signals for the control of a prosthetic hand for amputees. A proportional (open-loop) control systems in which the amplitude of the hand motor voltage and hence its speed and force measured from strain gauges varies in direct proportion (linearly) to the amplitude of the EMG signal generated by the prosthetic hand, was first reported in Refs. [24, 25]. In addition, the system added force and velocity feedback controls so the users could feel more natural when using this device. An adaptive control scheme was developed by [187] for the Southampton Hand.

1971–79:

The work reported in Ref. [162] studied the effect of sensory feedback based on semiconductor strain gauges on either edge of thumb of the prosthetic hand to adjust the stimulus magnitude to target value and avoid dropping or crushing objects for control of a prosthesis and found this acceptable for patients. When the strain gauges received the stimulus, the system amplified and transferred the signals to comparator, and then the comparator modified the range of amplitude of stimulus to the level that the users needed. However, the device with feedback is two or three times larger than the normal hand. A hierarchical method consisting of analytical control theory, such as performance-adaptive self-organizing control algorithm and artificial intelligence using fuzzy automaton, was presented in Ref. [169] to drive a prosthetic hand.

1980–89:

In providing a historical perspective, the contribution in Ref. [43] presented the status of the closed-loop (feedback) control principles for the application of prosthetic devices. Three concepts relating to supplemental sensory feedback, artificial reflexes, and feedback through control interfaces were discussed, and it was concluded that "we have not moved very far in the last 65 years in the clinical application of these concepts." A statistical analysis involving the study of zero-crossings, second to fifth moments and correlation functions and pattern classification of EMG signals was given in Ref. [168]. A probabilistic model of the EMG pattern was formulated in the feature space of integral absolute value (IAV) to provide the relation between a command, represented by motion and speed variables and the location and shape of the pattern for real-time control of a prosthetic arm as given in Ref. [118]. Using kinematic relationships for dynamic model of fingers, multi-variable feedback control strategies using pole assignment in frequency domain were employed by [195] to guarantee local stability for controlling one finger of the JPL/Stanford hand. The work in Ref. [195] produced the dynamic models of three fingers (thumb, index, and middle) and three joints first, and then used Laplace transform to work in frequency domain. To get a guaranteed stability of control system, the roots/poles had to be located in the left half plane. Hence, they could get a desired steady movement of fingers by controlling the positions of the roots. The works reported by the groups in Refs. [49, 136] were the first to investigate various aspects such as kinematics, prehensility, dynamics, and control of multi-fingered hands manipulating objects of arbitrary shape in three dimensions.

1990–99:

Design, implementation, and experimental verification of an improved cybernetic elbow prosthesis was presented in Refs. [1, 2] that mimics the natural limb to both internal (voluntary) inputs from the amputee and external inputs from the environment. The work in Ref. [181] considered a dextrous hand employing a systematic approach to achieve the object stiffness control by actuator position control, tendon tension control, joint torque control, joint stiffness control, and Cartesian fingertip stiffness control. The work in Ref. [174] conducted a survey of 33 patients wearing the proportional myoelectric hand grouped into 3 categories based on previous experience with a terminal device: digital (on-off) myoelectric hand, body-powered terminal device, and no terminal device. The survey results showed that the group of patients having experience with the digital hand "were most impressed with proportionally controlled hand," because it has the advantages: comfortable, cosmetic acceptance, more natural, superior pinch force

(11–25 lb) compared to voluntary opening (7–8 lb), a greater range of function but less energy, sensory feedback, force feedback, and short below-elbow.

The research work in Ref. [81] developed three tests for evaluation of input-output properties of patient control of neuroprosthetic hand grasp, which can compensate or enrich the function of a damaged peripheral nervous system. The first test was for static input-output properties of the hand grasp, the second one was for control of hand grasp outputs while tracking step and ramp functions, and the final test was to obtain the input-output frequency response of the hand grasp system dynamics to estimate the transfer function using spectral analysis. Each test used visual feedback when the users controlled the grasp force and grasp position tracking of the hand. It was shown in Ref. [89] that the myoelectric signal is not random during the initial phase of muscle contraction thus providing a means of classifying patterns from different contraction types. The means is to establish the 60 records of an isometric contraction of the subjects and then produce some anisometric contraction types, like flexion and extension. This information was useful in designing a new multi-function myoelectric control system using artificial neural networks (ANN) for classifying myoelectric patterns. Additionally, the hidden layer size, segment length, and EMG electrode positions were studied. See related works in Refs. [68, 69, 75, 76] on multi-functional myoelectric control systems using pattern recognition methods for myoelectric signal extraction and classification. The control philosophy of a multi-fingered robotic hands for possible adaptation and use in prosthetics and rehabilitation was discussed in Refs. [90–92] with respect to the Belgrade/USC robot hand [18], called PRESHAPE (Programmable Robotic Experimental System for Hands and Prosthetics Evaluation), which can estimate a system that translates task commands to motor commands using pressure sensors, force sensors and pressure feedback, which is very useful to detect small contact forces.

Using the dynamic model of the nonlinear neuromuscular (motor servo) control system of human finger muscles including mechanical properties (such as viscoelasticity) of the muscle and stretch reflex, a surface-based myoelectrically-controlled biomimetic prosthetic hand (called the Kobe hand) with three fingers (thumb, index and middle fingers) was developed at Kobe University, Japan [148] with a system consisting of an EMG signal processing unit, the dynamic model, a positional control unit, and the prosthetic device. A survey of four important properties—dexterity, equilibrium, stability, and dynamic behavior relating to autonomous multi-fingered robotic hands—was presented [178]. An interesting aspect of this literature survey is a series of tables relating to existing multi-fingered robotic hands, force closure, dexterity in kinematically redundant robotic hands, equilibrium, in robotic grasp, and stability. As reported in Ref. [15], an intelligent prosthesis control system, developed by Animated Prosthetics, consists of two parts: the animation control system (ACS) residing in prosthesis and a remote prosthesis configuration unit (PCU) capable of on/off to variable speed/grip. Dynamic control of two arms to manipulate cooperatively an object with rolling contacts was addressed [170] using a nonlinear feedback control methodology that decouples and linearizes the system.

A sensory control system based on a force sensing resistor (FSR) was developed [191] at The National Institute for Accidents at Work (INAIL), Bologna, Italy, to control the strength of the grip on objects for a commercial prosthetic hand having two main functions: the automatic search for contact with the object and the detection of the object possibly slipping the grip by involuntary feedback (force sensors and slipping sensors). Further, automatic tuning of control parameters of the prostheses was investigated [23] using fuzzy logic expert systems resulting in a software package called the microprocessor controlled arm auto tuning. The automatic tuning software works as follows:

- the client connects the prosthesis hardware
- the program needs both sensor signals as client input the program combines the above qualitative and quantitative information stored in the fuzzy logic database to calculate the prosthesis parameter values
- the program enables the new parameter values to be down-loaded into the prosthesis control system memory.

Dynamic modeling of a robotic hand was proposed [172] using a hybrid approach with a discrete event aspect of grasping and continuous-time part with a variable structure impedance control algorithm. A novel on-line learning method was reported in Ref. [145] for prosthetic hand control based on EMG measurements with a system consisting of three units:

- an analysis unit for generating feature vectors containing useful information for discriminating motions from EMG signals
- an adaptation unit for adapting to the amputee's individual variation and for discriminating motions from the feature vector and at the same time generating the necessary control commands to the prosthetic hand
- a trainer unit for directing the adaptation unit to learn in real time based on the amputee's teaching signal and the feature vector.

In Ref. [191] researchers built a sensory control system based on the force-sensing resistor (FSR) for an upper limb prosthesis and an optical sensor for detecting movement. The prostheses produced were of the "all or nothing" (opening or closing) and proportional control type (the relationship between force and EMG signal is linear). For traditional control, it used voluntary (visual) feedback, but the users had to pay close attention. This work developed an involuntary feedback control that uses two kinds of sensors, strength and slipping sensors. If the prosthesis hand is slipping, the control system can automatically order the actuator of the prosthesis to increase the grip strength. On receiving the EMG signal, the hand begins a closing action and goes on closing until the FSRs produce a signal that is greater than or equal to a "contact threshold" value. Then it stops because the object has been grasped with the required strength of grip. The automatic grip mechanism is very useful in grasping delicate objects.

The investigation in Ref. [130] showed that the proposed neuro-fuzzy classifier known as Abe-Lan network, is able to identify correctly all the EMG signals related to different movements of the human hand. A highly anthropomorphic human hand, called Robonaut Hand consisting of five fingers and fourteen independent degrees of freedom, was built at NASA Johnson Space Center to interface with extra-vehicular activity (EVA) crew interfaces onboard the International Space Station (ISS) [124].

2000–2007:

In Ref. [190], estimating muscular contraction levels of flexors and extensors using neural networks, a new *impedance control* technique [83] was developed to control impedance parameters such as the moment of inertia, joint stiffness, and viscosity of a skeletal muscle model of a prosthetic hand. An overview of dextrous manipulation gave [147] an interesting time-line chart for the development of robotic dextrous manipulation during the period 1960s to 2000. An excellent survey [19] summarizing the evolution and state of the art in the robotic hands focusing mainly on functional requirements of manipulative dexterity, grasp robustness, and human operability. Also, the work in Ref. [126] exploited the nonholonomic character of a pair of bodies with regular rigid surfaces rolling onto each other, to study the constructive controllability algorithm for planning rolling motions for dextrous robot hands. A control system architecture was proposed [133, 134] with a feedforward loop based on EMG measurements consisting of a low-pass filter and neural network to provide the actual torque signal and a feedback loop based on the desired angle consisting of a proportional-derivative (PD) controller to provide the desired torque signal and the error signal between these torques drives the prosthetic hand to achieve the desired angle while the neural network learns based on feedback error.

Peckham et al. [155] studied finger extension, external control, overhead reach, and forearm pronation. For finger extension, they used two electrodes: one placed between the 2nd and 3rd metacarpals and the other between the 3rd and 4th metacarpals. They could provide full extension of the index, long, and ring fingers. For external control, a new form of control was developed by using retained voluntary wrist extension to control grasp opening and closing. Overhead reach can be provided by stimulation of the triceps muscle, so elbow position can be controlled by voluntary activation of biceps as

an antagonist. As for forearm pronation, the main issues are an increased number of stimulus channels to allow stimulation of the finger intrinsic muscles, triceps, and forearm pronator, an implanted control source, bidirectional communication between sensor and body, reduced size, and reduction of all external cables. The work in Ref. [207] presents a review of the traditional methods for control of artificial hands using EMG signals in both clinical and research areas and points out future developments in the control strategy of the prosthetics, in particular advocating neuroprosthesis with biocompatible neural interface for providing sensory feedback to the user leading to electroneurographic (ENG) based control in place of electromyographic (EMG) control.

Collaboration between the University of Southampton and University of New Brunswick (UNB) [120] resulted in a hybrid control system using a multilayer perceptron (MLP) artificial neural network as a classifier of time-domain features set (zero-crossings, mean absolute value, mean absolute slope, and trace length) extracted from myoelectric signals (MES) and a digital signal processor (DSP) controlling the grip pressure of the prosthetic hand without visual feedback (voluntary feedback). Design and development of an underactuated (the number of actuators less than the degrees-of-freedom) mechanism applicable to prosthetic hand was presented in Ref. [127] based on dynamic model of fingers leading to adaptive grasp (that is, being able to conform to the shape of an object held within the hand).

Although an adaptive control scheme was developed [187] for a Southampton Hand, further developments were made in the research first generation [22, 112] producing their IP (intelligent prosthesis) according to Ref. [111]. The investigation [116] provided an evolution of microprocessor-based control systems for prosthetics classified as (based on digital systems), second generation (with low power), and third generation (based on microprocessors and digital signal processors). The work in Ref. [114] conducted a comparison of Oxford and Manus hand prostheses with respect to:

1. hand mechanisms
2. control electronics: EMG analog amplifiers, A/D converters, digital signal processors
3. sensors: force, position and slip sensors based on Hall effect
4. manipulation or control schemes: Oxford hand used Southampton Adaptive Manipulation Scheme consisting of a three-level hierarchical scheme and Manus used a two-level scheme.

The scheme suggested in Ref. [30] consisted of five modules, including an artificial muscoskeletal system, position and force sensors, 3D force sensors, low-level control loop dedicated to control slipping and grasping, and an EMG control unit. Further, the scheme used two semiconductor strain gauges as the force sensor and the sensor in SS496B by Honeywell International, Inc. as the position sensor, which is the linear slider and small magnets. Moreover, the control system receives three signals: activation (EDG used to identify whether there is a movement), direction (SGN decides opening or closing), and amplitude of the movement (AMP controls the seed of the movement in a proportional means). As for the control scheme, it uses a simple proportional open-loop control.

A cylindrical grasp of a cylindrical object and a parallel force/position control is studied by [171] to ensure the stability. The work in Ref. [156] presented a feedback control system for hand prosthesis with elbow control. Using a concept of extended physiological proprioception (EPP) (i.e., using natural physiological sensors), both the work [156] and the investigation in Ref. [6] developed microprocessor-based controllers for upper limb prostheses. A systematic literature review [194] is useful for prosthetic hand, although the survey was done for lower-limb prosthesis. Scherillo et al. [171] developed a procedure to obtain maximum load and contact force distribution for a given grasp task and a parallel force/position control to ensure stability of the grasp. The goal of this control scheme is to specify a set of joint torque inputs so that the desired grasping forces along the constrained directions, and the desired position trajectory along the unconstrained directions are realized.

Several researchers showed [9–11] that sensory feedback signals are obtained for multi-fingered robot hands to perform the function of grasping an object and that dynamic force/torque closure can be constructed without knowing object kinematic parameters and location of the mass center. Further, the convergence of motion of the overall fingers-object system was proved using the concepts of "stability and asymptotic stability on a manifold." Mechanical design and manipulation (control) issues were addressed [157] for a multi-fingered dextrous hand for upper limb prosthetics using the underactuated kinematics enhancing the performance and providing four grasping modes (cylindrical, precision, hook, and lateral) with just two actuators, one for the thumb and one for the remaining fingers. In particular, the hierarchical control architecture consists of a host (or master) controller for EMG management and definition of grasp set points (for position and torque/force) and three local (or slave) controllers for low-level implementation of stiffness control of the joints. In Ref. [205], design and analysis was presented for a multi-fingered prosthetic hand consisting of a thumb with three joints and the rest of the four fingers having two joints using Haringx and element stiffness models, which enables the location of actuators far away from the hand to a belt around the waist and further enabling actuation and control with relatively high degrees of freedom. Robotic hand MA-I was designed and built [182] at the Institute of Industrial and Control Engineering (IOC) at the Polytechnic University of Catalonia (UPC) with 16 degrees of freedom and the control system consisting of 16 position control loops, independently controlling each of the 16 DC motors. Visual hand motion capture is a multiple-dimension and multiple-objective searching optimization problem and the work reported in Ref. [53] used pose estimation and a motion-tracking scheme with genetic algorithms (GA) embedded particle filter (PF) to navigate visual hand gesture, such as virtual environment and control of a robot arm.

The fabrication of a compliant, under-actuated prosthetic hand (both palm and fingers) molded as a soft polymeric single part for providing *adaptive* grasp was reported [28, 29]. The analysis and synthesis are "so complex and only experimental analysis of the solution adapted validate our works." It was shown [154] that an object with parallel surfaces in a horizontal plane could be controlled by a pair of robotic fingers to achieve stable grasping, angle and position control without the need for the object parameters or object sensors such as tactile, force, or visual sensors.

At Northwestern University Prosthetics Laboratory (NUPL), the researchers [199, 201] developed multi-function prosthetic hand/arm controller system receiving signals from as many as sixteen implantable myoelectric sensors (IMES) and a heuristic fuzzy logic approach to EMG signal pattern recognition [5, 200]. In particular, fuzzy logic was explored for discriminating between multiple surface EMG control signals and classifying them to user intention. The multi-functional hand mechanism consisted of a three-motor hand (one motor for driving the thumb, one motor for the index finger, and the third motor for the middle, ring and little finger) and a two-motor wrist (one motor for wrist extension/flexion and the other motor for wrist rotation). Further, the research [72] demonstrated that in implementing the extended physiological proprioception (EPP) control for a powered prosthesis, the backlash is determined by the stiffness of the control cable as well as mass located at the distal end of the forearm and that reduction of static friction and backlash in the system could prevent the limit cycle.

It was demonstrated [60] that by implanting electrodes within individual fascicles of peripheral nerve stumps, appropriate, distally referred sensory feedback about joint position and grip force from an artificial arm could be provided to an amputee through stimulation of the severed peripheral nerves, which also provide appropriate signals. It is interesting to note [100] the mechanism, design, and control system of a humanoid-type hand with human-like manipulation capabilities as a part of the development of service robots and the comparison (shown by [101, 158]) of natural and prosthetic hands. In Ref. [211], the EMG motion pattern classifier was developed using a parametric autoregressive (AR) model and Levenberg-Marquardt (LM)-based neural networks to identify three types of motion of thumb, index, and middle fingers to control a five-fingered underactuated prosthetic hand.

The work in Ref. [161] focused on the "optimal" delay as the maximum amount of time from command to hand movement, for a prosthesis controller with a delay of 200 to 400 ms as the range acceptable by users. A bypass prosthesis, called the Prosthetic Hand for Able-Bodied Subjects (PHABS), was developed to allow able-bodied subjects to operate a prosthetic terminal device. The controller is a commercially available Myo-pulse control, which combines pulse width modulation (PWM) and pulse period modulation (PPM) because it provides a linear relation between motor speed and the pulse width and timing of a digital control signal. In addition, it also used a mechanical low-pass filter to smooth the pulse train and movement. If the EMG reaches the threshold, the motor will be turned "on"; otherwise, it will be turned "off." Furthermore, the experimental controller was created in Matlab's Simulink and executed using Simulink's Real Time and XPC Target Toolboxes. Finally, this work summarized seven time-delay sources, including:

1. the time from the intent of movement to the development of EMG
2. the time constant of the analog filters contained in the EMG pre-amplifiers
3. the analog to digital sampling period
4. the time required to collect the EMG signal for feature extraction
5. the time required to perform the EMG signal for feature extraction
6. the time required to execute the pattern recognition on the extracted features
7. the time required to actuate the component

In Ref. [50], a review of the traditional methods of control as well as the current state of new control techniques was provided. A newly developed intelligent flexible hand system with 3 fingers and 10 joints, fitted with a small harmonic drive gear and a high power mini actuator, providing 12 DOF applied to a catching task was developed [117]. The authors [212] developed an EMG-based (using electrodes and torque and angle sensors) prosthetic hand control system composed of a human operator, a five-fingered under-actuated prosthetic hand system, the prosthetic hand controller (with analog-to-digital converters, a digital signal processing (DSP) board, and stepper motors) and visual feedback. In particular, the EMG signals undergo feature extraction and feature classification using neural networks with parametric autoregressive (AR) model and wavelet transforms. In an under-actuated system, there is a lower number of actuators compared to the number of degrees-of-freedom of the system. Further in Ref. [210], a hierarchical control system was proposed with a high-level supervisory controller for implementing the EMG signal acquisition and pattern recognition and also providing a set of commands (for operations such as close, open, position, etc.) to a low-level controller. A sensor-based hybrid control strategy (using normal feedback control based on EMG signals from sensors and feedback to the user) was presented [160] where a digital controller operating from prosthetic signals converts the user grasping intention (EMG signal) into an order to control the prosthesis.

Choi et al. [44] investigated developed a robot hand with tactile sensors (slip sensor and force sensor), called SKKU Hand II, having two functional units: a polyvinylidene fluoride (PVDF)-based slip sensor designed to detect slippage and a thin flexible force sensor that can read the contact force of and geometrical information on the object using a pressure variable resistor ink. A biomechatronic approach to the design and control of an anthropomorphic artificial hand was studied [216] for closing the hand finger while grasping an object using a reference trajectory and using two different versions (joint space and slider space) of proportional-derivative (PD) control system. In particular the artificial hand consists of three under-actuated fingers (index, middle, and thumb), which are actuated by three cable-driven DC motors placed in the lower part of the arm.

Farrell and Weir [71] studied large controller delays created by multi-functional prosthesis controllers. A device called PHABS (Prosthetic Hand for Able Bodied Subjects) was utilized to test the performance of 20 able-bodied subjects on the Box and Block Test. To estimate and compare the performance of prosthetic hands, a functionality index has been proposed [161]. An underwater flexible robot manipulation (called HEU Hand II)

that utilized PBNNIC (position-based neural network impedance control) for the force tracking control was studied in Ref. [129].

This work from [129] developed a dexterous underwater robot hand, called the HEU Hand II. The sensor system mainly includes 12 strain gauges at different locations. When the robot hand is under water, the control system is more complicated because the complete dynamic model is not known exactly. Hence, the control system considers the uncertainty of the robot dynamic model. The controller of the hand force tracking is designed by the PBNNIC scheme. Using biologically-inspired principles for design and control of a bionic robot arm [106], several control approaches were presented such as trajectory planning and optimization based on robot dynamics.

An alternate learning control strategy was proposed [163] based on the working assumptions that both human motor commands and sensory information are passed on in a discrete, episodic manner, quantized in time with a learning algorithm, called S-learning, based on *sequences* arguing against the traditional control approaches due to the highly nonlinear robot's dynamics and large number of degrees of freedom.

In the work in Ref. [206], the first prototype of a five-fingered prosthetic hand fitted with only 3 motors and achieving 20 degrees of freedom was described using a new "strings and springs" mechanism and a continuous wavelet transform (CWT) for extraction of EMG inputs for a feed-forward, back-propagation neural network to recognize the type of grip.

The work in Ref. [215] focuses on the control system of the hand and on the optimization of the hand design. It proposes the control action as proportional to the superficial EMG signals extracted by surface electrodes applied to a couple of antagonistic user's residual muscles. This work first explains designs of the hand prototype, such as biomechatronic design approach, under-actuated artificial hand, 3D CAD model (by ProEngineer) and dynamic analysis (by ANSYS). Second, it builds the model of control system, including the kinetics and dynamics of hand, in PD control in the joint space and slider space with elastic compensation. Third, it validates and optimizes the hand design in four multiple objective problems (or goals). The first two goals are related to the closed-loop control performance and the remaining two goals are part of joint trajectories. It develops the simulation in MATLAB/Simulink. Finally, it compares the experimental results with the simulation.

The dynamic system of a nonlinear flexible robot arm with a tip mass was introduced in Ref. [198]. Here, the proposed intelligent optimal controller, in which the fuzzy neural network controller and robust controller were designed to learn a nonlinear function and compensate the approximation errors respectively, could control the coupling of bending vibration and torsional vibration for the periodic motion. To overcome the traditional fuzzy logic difficulties, such as large rule bases and long training times, researchers [17] proposed a self-learning dynamic fuzzy network (DFN) with dynamic equality constraints to speed up the trajectory calculations for intelligent nonlinear optimal control. For a five-finger under-actuated prosthetic hand with tendon transmission, Cipriani et al. [46] presented a robust controller that implemented two subsequent and different phases, including the pre-shaping of the hand and the involved fingers rapidly closing around the object.

2.3. Main Control Technique Overview Since 2007

2.3.1. Hard Computing Techniques

1. **PD Controller**: Rong et al. [164] presented one kind of PD controller with feed-forward control based on adaptive theory for 2 DOF direct driven robot with uncertain parameters.
2. **Adaptive Controller**: Cai et al. [27] developed an observer back-stepping adaptive control scheme for a two-link manipulator under unmeasured velocity and uncertain environment. The adaptive velocity observer was designed independently from the state-feedback controller in order to compensate the estimation errors. Seo and Akella [175] derived the novel adaptive control solution involving a new filter

design for the regressor matrix for n DOF robot manipulator systems. By developing the Fourier series expansion from input reference signals of every joint, Liuzzo and Tomei [122] designed a global output error feedback adaptive learning control for 2 DOF planar robot with uncertain dynamics. To achieve the tracking control objective, Chen et al. [41] proposed an adaptive sliding-mode dynamic controller for wheeled mobile robots with system uncertainties and disturbances to make the real velocity of the wheeled mobile robot reach the desired velocity command.

3. **Robust Controller**: Because of the visco-elastic properties of manipulator links, Torabi and Jahed [189] utilized the loop-shaping method, which can decrease the order of the robust control model of a single-link manipulator examined in time and frequency domains. To enhance control of powered prosthetic hands, Engeberg and Meek [64–67] proposed robust sliding mode, back-stepping, and hybrid sliding mode-back-stepping (HSMBS) parallel force-velocity controllers that enabled the humans to more easily control a fine object by ten able-bodied test subjects. Ziaei et al. [214] developed the modeling, system identification adopting generalized orthonormal basis functions (GOBFs), and robust position and force controllers for single flexible link (SFL) manipulators required to operate the contact motion. Jiang and Ge [97] transformed the nonlinear kinematic models of 3 DOF wheels mobile robot with uncertain disturbance into linear control systems through an approximate linearization algorithm and then designed a partial feedback H_∞ robust controller through linear matrix inequality (LMI).
4. **Optimal Controller**: Vitiello et al. [196] synthesized the position controller and the Kalman filter to perform the planar movements, such as reaching and catching, of the NEURARM hydraulic piston actuation with nonlinear springs connected on the cable. Vrabie et al. [197] designed an online method via a biological inspired Actor/Critic structure to solve the adaptive optimal continuous-time control problem by the solution of the algebraic Riccati equation without using knowledge of the system internal dynamics. To minimize the positioning time (traveling between two specific points) of an under-actuated 2 DOF robot manipulator restricted to the input constraint and the structural parameter constraint, Cruz-Villar et al. [52] developed a concurrent structure-control redesign method that combined the structural parameters and a bang-bang control law. Duchaine et al. [62] derived the position tracking and velocity control, the dynamic model of the robot, the prediction and control horizons, and the constraints by a general predictive control law and also derived an analytical solution for the optimal control by a computationally-efficient-model-based predictive control scheme for a 6 DOF cable-driven parallel manipulator.
4. **Hierarchical Controller**: Fainekos et al. [70] proposed a hierarchical control law addressing the temporal logic motion planning problem for mobile robots modeled by second order dynamics to track a simpler kinematic model with a globally bounded error, and then solved the new robust temporal logic path planning problem for the kinematic model using automata theory and simple local vector fields.

2.3.2. Soft Computing Techniques

1. **Fuzzy Logic**: According to the human anatomy, Arslan et al. [13] developed the biomechanical model with a tendon configuration of the 3 DOF index finger of the human hand. The fuzzy sliding mode controller in which a fuzzy logic unit tuned the slope of the sliding surface was introduced to generate the required tendon forces during closing and opening motions.
2. **Artificial Neural Networks**: Onozato and Maeda [149] utilized two neural networks learning inverse kinematic and inverse dynamic to control the positions of 2 DOF SCARA robot. Aggarwal et al. [4] obtained the neural recordings from rhesus monkeys with three different movements, the flexion/extension of each finger, the rotation of wrist, and dexterous grasps. They also designed the separate decoding filters for each movement by using multilayer feed-forward artificial neural

network (ANN) (implemented in real-time MATLAB/Simulink). An online decentralized neural network control design without deriving the dynamic model for a class of large-scale uncertain robot manipulator systems was proposed by Tan et al. [184]. Kato et al. [104] expressed the reaction of brains to the adaptable prosthetic system for a 13 DOF EMG signal controlled prosthetic hand with an EMG pattern recognition learning by artificial neural networks. In addition, functional magnetic resonance imaging (f-MRI) was used to analyze the reciprocal adaptation between the human brain and the prosthetic hand by the plasticity of the motor and sensory cortex area in brains based on the variations in the phantom upper limb.

3. **Genetic Algorithm**: Marcos et al. [54] proposed the closed-loop pseudo-inverse method with genetic algorithms (CLGA) to minimize the largest joint displacement between two adjacent configurations, the total level of joint velocities, the joint accelerations, the total joint torque, and the total joint power consumption for the trajectory planning of 3 DOF redundant robots. Kamikawa and Maeno [98] used a genetic algorithm to optimize locations of pivots and grasping force and designed one ultrasonic motor to move 15 compliant joints for an under-actuated five-finger prosthetic hand.

2.3.3. Hybrid of Soft and Hard Computing Techniques

1. **PID Controller and Robust Controller**: Dieulot and Colas [61] presented a case study of the design of robust parametric methods for flexible axes and an heuristic initial tuning of the PID controller from additional pole placement constraints on the rigid mode.
2. **Adaptive Controller and Robust Controller**: To implement the trajectory tracking mission under the influence of unknown friction and uncertainty, Chen et al. [40] utilized a composite tracking scheme, including the adaptive friction estimation to determine Coulomb friction, viscous friction, and the Stribeck effect and a robust controller to enhance the overall stability and robustness for a 2 DOF planar robot manipulator.
3. **Robust Controller and Optimal Controller**: Huang et al. [87] designed the robust control systems with some uncertainties, including the unknown payload and unknown modeling of objects, and the unknown dynamic parameters, such as the performance index that was optimized by the optimal control method for the space robot to capture unknown objects.
4. **Robust Controller and Fuzzy Logic**: Tootoonchi et al. [188] combined a robust quantitative feedback theory (QFT) designed to follow the desired trajectory tracking with the fuzzy logic controller (FLC) designed to reduce the complexities of the system dynamics for 2 DOF arm manipulator. The control gain of the sliding mode controller tuned according to error states of the system by a fuzzy controller and a moving sliding surface whose slope is dynamically changed by a fuzzy logic algorithm for a 3 DOF spatial robot were presented by Yagiz and Hacioglu [204].
5. **Robust Controller and Artificial Neural Networks**: Siqueira and Terra [180] developed a neural network-based H_∞ controller that approximated the uncertain factors of an actual under-actuated cooperative manipulator. They robustly controlled the position and squeeze force errors between the manipulator end-effectors and the object, although one joint was not actuated.
6. **Sliding Mode Controller and Genetic Algorithm**: Chen and Chang [42] utilized the multiple-crossover genetic algorithm to estimate the unknown system parameters and the sliding mode control method to overcome the uncertainty for a two-link robot control.
7. **Sliding Mode Controller and Particle Swarm Optimization**: Salehi et al. [166] used an online particle swarm optimization to tune the parameters of sliding mode control at the contact moments of end effector and unknown environments for the 2 DOF planar manipulator.
8. **Fuzzy Logic and Artificial Neural Networks**: Subudhi and Morris [183] proposed a hybrid fuzzy neural control (HFNC) scheme containing a fuzzy logic controller

and a neural network controller to balance the coupling effects for the multi-link flexible manipulator with both rigid and flexible motions.

9. **Artificial Neural Networks and Particle Swarm Optimization**: Wen et al. [202] addressed the hybrid particle swarm optimization neural network (HPSONN) to compute the pseudo-inverse Jacobian of 2 DOF planar manipulator inverse kinematic control.

2.4. Revolutionary Prosthesis

Recently (see the press releases [7, 58]) the Applied Physics Laboratory (APL) of Johns Hopkins University (JHU) in Baltomore, MD, USA received funding for the Revolutionary Prosthesis 2009 program from DARPA (Defense Advanced Research Projects Agency), the U.S. Department of Defense, to "develop a next-generation mechanical arm that mimics the properties and sensory perception of the real thing." The APL leads an international team of about 30 organizations from Austria, Canada, Germany, Italy, Sweden, and USA. The APL team delivered its first DARPA Limb Proto 1 (see Ref. [8], which "is a complete limb system that also includes a virtual environment used for patient training, clinical configuration, and to record limb movements and control signals during clinical investigations").

3. HYBRID INTELLIGENT CONTROL STRATEGIES

Here we present the recent research activities on hybrid control strategies for a smart prosthetic hand conducted at Idaho State University (ISU). The schematic diagram of the work is shown in Figure 1 (see Refs. [120, 160, 212]). The overall system, in brief, consists of electromyographic (EMG) signal acquisition from the user arm for surface or implanted electrodes (in the implanted case we focus on biocompatibility based on nano-materials research). The EMG signal is then processed for feature extraction and classification or identification of EMG signal to correspond to different motions of the prosthetic hand. The classified signal is then used to control the prosthetic hand using actuators and driving mechanisms. It is to be noted in this proposal that the EMG signal extraction and identification and the control algorithm are investigated using the fusion of soft computing (SC) and hard computing (HC) techniques.

3.1. Fusion of Soft and Hard Computing Techniques

Soft computing (SC) or computational intelligence (CI) is an emerging field based on synergy and seamless integration of neural networks (NN), fuzzy logic (FL), and genetic algorithms (GA) [102]. The previous works on prosthetic hands used artificial neural networks [45, 88, 120], fuzzy logic [5, 31, 200], genetic algorithms [73], etc. mostly for EMG signal classification for various movements or functions of the prosthetic hand.

In hybrid intelligent control strategies, we look at the integrated structure by blending [153, 186] soft computing (SC) techniques and conventional hard computing (HC)

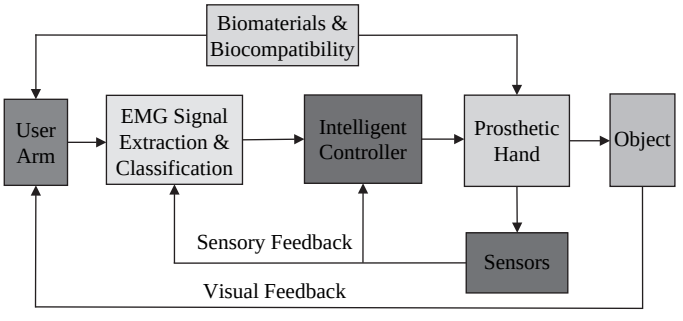

Figure 1. Schematic diagram of prosthetic hand technology.

techniques comprising optimal control [140], robust control [213], nonlinear control [110] and/or adaptive control [185] with specific applications to prosthetics.

The integration of SC and HC methodologies shown in Figure 2 has the following attractive features [153, 186]:

1. The methodology based on SC can be used, in particular with fuzzy logic, at upper levels of the overall mission where human involvement and decision making is of primary importance. Whereas, the HC can be used at lower levels for accuracy, precision, stability and robustness.
2. In another situation using a hybrid scheme, a neural network of the SC is used to supplement the control provided by a linear, fixed gain controller for a missile autopilot.
3. Further, the SC-based GA can be used for parameter tuning of a PID controller to achieve good performance and robustness for a wide range of operating conditions.
4. The SC and HC are potentially complementary methodologies.
5. The fusion could solve problems that cannot be solved satisfactorily by using either methodology alone.
6. Novel synergetic combinations of SC and HC lead to high performance, robust, autonomous, and cost-effective missions.

The research at Idaho State University (ISU) focuses on developing intelligent autonomous strategies for EMG signal extraction, analysis, and control of prosthetics by fusion of soft computing techniques comprising NN, FL, and GA [141, 153] and hard computing (HC) techniques. The proposal takes advantage of our in-house research experience with problems in prosthetics [20, 63] in particular, and with problems in biomedical engineering [142, 143] in general.

An overview of nine papers was presented using the techniques in industrial and engineering applications [152]. For the fusion techniques, Sick and Ovaska [179] described a multidimensional categorization scheme in five aspects: the degree of interconnection of soft and hard computing components (fusion grade), the topology of fusion skills (fusion structure), the time when fusion happens (fusion time), the layer of a system architecture (fusion level), and the motivation for the application (fusion incentive). Further, Ovaska et al. [151] classified the fusion techniques into twelve main categories and six supplementary categories.

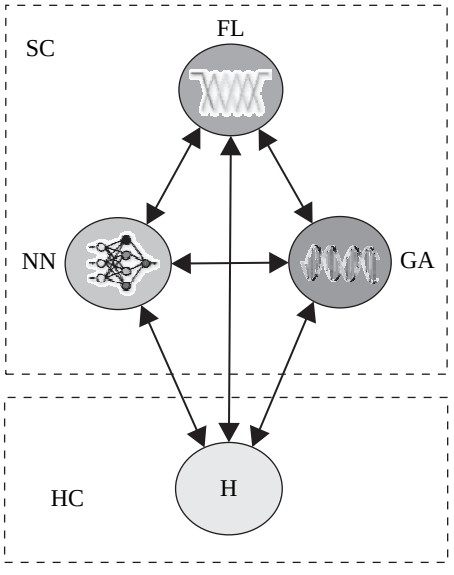

Figure 2. Principle behind fusion of soft and hard computing.

4. OVERVIEW OF RESEARCH AT ISU

A chronological overview of the research at Idaho State University is provided below.

A short review by Lai et al. [115] notes the importance of the biological interfaces between robotic implants and other prosthetic devices and notes an interdisciplinary team of biomedical and tissue engineers, and biomaterial and biomedical scientists is needed to work together holistically and synergistically.

In addressing the particle swarm optimization technique, a set of operators for a Particle Swarm Optimization (PSO)-based algorithm is investigated for the purpose of finding optimal values for some of the classical benchmark problems. Particle swarm algorithms are implemented as mathematical operators inspired by the social behaviors of bird flocks and fish schools. In addition, particle swarm algorithms utilize a small number of relatively less complicated rules in response to complex behaviors, such that they are computationally inexpensive in terms of memory requirements and processing time. In particle swarm algorithms, particles in a continuous variable space are linked with neighbors, therefore the updated velocity ~~means~~ the particles influence the simulation results. The work presents a statistical investigation on the velocity update rule for continuous variable PS algorithm. In particular, the probability density function influencing the particle velocity update is investigated along with the components used to construct the updated velocity vector of each particle within a flock. The simulation results of several numerical benchmark examples indicate that a small amount of negative velocity is necessary to obtain good optimal values near global optimality [32].

A chronological overview of the applications of control theory to prosthetic hand is presented by Naidu et al. [139] focusing on hard computing or control techniques, such as multi-variable feedback, optimal, nonlinear, adaptive and robust, and soft computing or control techniques, such as artificial intelligence, neural networks, fuzzy logic, genetic algorithms, particle swarm, and on the fusion of hard and soft control techniques. The work [34] presents the PSO algorithm for identifying the rupture force for leukocyte adhesion molecules and the problem of finding the correct control parameters of a robotic hand. Other work at ISU is the fusion of soft computing or control technique of genetic algorithm (GA) and hard computing technique of proportional integral derivative (PID) control with application to prosthetic hand. In particular, an adaptive neuro-fuzzy inference system (ANFIS) is used for inverse kinematics of the three-link index finger, and feedback ~~linearization~~ is used for the dynamics of the hand. The GA is used to find the optimal parameters of the PID controller [35]. An adaptive PSO (APSO) approach based on altering the maximum velocity at each iteration for two thirty-dimensional benchmark problems is used [33].

A hybrid of a soft computing technique of adaptive neuro-fuzzy inference system (ANFIS) and a hard computing technique of adaptive control for a two-dimensional movement of a prosthetic hand with a thumb and index finger was investigated [38]. The results of this hybrid controller, when compared with the PID controller showed enhanced performance. A novel condensed hybrid optimization (CHO) algorithm using enhanced continuous tabu search (ECTS) and the PSO was examined [39]. The proposed CHO algorithm combines the respective strengths of ECTS and the PSO. In particular, the ECTS is utilized to define smaller search spaces that are used in a second stage by the basic PSO to find the respective local optimum. The ECTS covers the global search space by using a TS concept called diversification and then selects the most promising areas in the search space. Once the promising regions in the search space are defined, the proposed CHO algorithm employs another TS concept called intensification in order to search the promising area thoroughly. The proposed CHO algorithm is tested with the multi-dimensional Hyperbolic and Rosenbrock problems. Compared to the other four algorithms, the results indicate that the accuracy and effectiveness of the proposed CHO algorithm were enhanced. Another hybrid of a soft computing technique using the ANFIS and a hard computing or control technique using finite-time linear quadratic optimal control for a two-fingered (thumb and index) prosthetic hand was investigated [37]. In particular, the ANFIS is used for inverse kinematics, and the optimal control is used

to minimize tracking errors utilizing feedback linearized dynamics. The simulations of this hybrid controller, when compared with the proportional-integral-derivative (PID) controller, showed enhanced performance. This work was extended to a five-fingered, three-dimensional prosthetic hand [36].

5. RECENT DEVELOPMENTS IN NEUROPROSTHETICS

It is worth noting some of the recent developments in neuroprosthesis [85, 84, 144, 176].

An interesting study was made by Hart et al. [80] on implanted neuroprostheses employing functional electric simulation (FES) to provide grasp and release to individuals with tetraplegia and comparing three control methods for shoulder position, wrist position, and myoelectric wrist extensors. To improve the control of grasp strength, forearm pronation, and elbow extension to people with spinal cord injury at C5 and C6, the investigation by Peckham et al. [155] developed an advanced neuroprosthesis that includes implanted components, including a 10-channel stimulator, leads, electrodes, and a joint angle transducer, and external components, such as a control unit and transmitter-receiver coil.

A particularly interesting case was reported [48, 78, 150] regarding Jesse Sullivan, who lost both arms in an electrical accident. He could move his bionic arm with his brain—basically rewiring the severed live nerves that control arm and hand movements by redirecting the nerves to pectoral muscles in his chest. Electrodes attached to the chest muscles produce an electrical signal that controls the robotic arm depending upon the nature of muscle movement, which in itself is characterized by "thinking" in the brain what is to be done with arms. However, the demonstrated bionic arm is only a "prototype and for research only."

More interesting news appeared [47, 82] regarding implantation of an electronic chip into the brain of a quadripledge man to use a computer to operate a robotic arm.

6. FUTURE DIRECTIONS

During the last three decades, investigations have been carried out on the use of EMG signals to develop a prosthetic hand to perform as many functions as possible. However, the use of EMG signals is limited in the number of possible human-like functions with as few electrodes as possible and also for the prosthetic hand to ultimately have a natural "cosmetic" appearance. Further, the EMG signal cannot provide any kind of feedback to the user [207]. One of several possible solutions to overcome the limitations of surface-based EMG approach is neuroprosthesis. Here, we use an interface between the peripheral nervous system (PNS) and the "natural" neural interface to extract, record, and simulate the PNS in a selective way. Further, advances in biocompatible neural interfaces can provide some sensory feedback to the user by stimulating the afferent nerves and allowing motor control of the prosthesis leading to a "natural" EMG-based control. Based on this, two possible ways of controlling prosthetic hands are the simple and non-intrusive EMG-based control and the more complicated, implantable EMG-based control.

In a recent conference of the National Academies *Keck Futures Initiative*, "Smart Prosthetics: Exploring Assistive Devices for Body and Mind," [12], it was pointed out, "We can make smarter prostheses when we are smarter in integrating state-of-the-art neuroscience with state-of-the-art engineering, medicine, and social science."

ACKNOWLEDGMENTS

This overview was first prepared in 2006 when the first author and his colleagues at Idaho State University submitted a proposal on *Smart Prosthetic Hand Technology - Phase I of III* to the Telemedicine Advanced Technology Research Center (TATRC), which is the corporate or central laboratory for advanced technology research of the U.S. Army Medical Research and Material Command (USAMRMC) of the U.S. Department of Defense.

Since the proposal was funded by the TATRC in July 2007, the overview has been continuously updated. The financial support from the TATRC is hereby acknowledged. The overview was then completed in the present form in April 2008 while the first author was visiting the School of the Electrical, Electronics and Computer Engineering (EECE) at the University of Western Australia (UWA), Crawley, near Perth, Australia. The financial support for and the excellent hospitality during the visit are greatefully acknowledged.

REFERENCES

1. C. J. Abu-Haj and N. Hogen, *IEEE Trans. on Biomed. Eng.* 37, 1025 (1990).
2. C. J. Abu-Haj and N. Hogen, *IEEE Trans. on Biomed. Eng.* 37, 1037 (1990).
3. Amputee Coalition of America (ACA) National Limb Loss Information Center (NLLIC) Limb Loss Facts in the United States. http://www.amputee-coalition.org, 2006.
4. V. Aggarwal, G. Singhal, J. He, M. H. Schieber, and N. V. Thakor, "30th Ann. Int. IEEE Engi. in Med. and Bio. Soc. Conf. (EMBC 2008)," p. 1703. Vancouver, British Columbia, Canada, August, 2008.
5. A. B. Ajiboye and R. F. Weir, *IEEE Trans. on Neural Sys. and Rehab. Eng.* 13, 280 (2005).
6. H. M. Al-angari, R. F. ff. Weir, C. W. Heckanthorne, and D. S. Childress, *Tech. and Disability* 15, 113 (2003).
7. APL to Lead Team Developing Revolutionary Prosthesis. Press Release: Dated February, 9 2006.
8. Revolutionizing Prosthetics 2009 Team Delivers First DARPA Limb Prototype. Press Release: Dated April 26 2007.
9. S. Arimoto, *Ann. Reviews in Control* 28, 75 (2004).
10. S. Arimoto, "Control Theory of Multi-Fingered Hands: A Modeling and Analytical-Mechanics Approach for Dexterity and Intelligence." Springer-Verlag, London, UK, 2008.
11. S. Arimoto, P. T. A. Nguyen, H.-Y. Han, and Z. Doulgeri, *Robotica* 18, 71 (2000).
12. Arnold and Mabel Beckman Center of the National Academies. "NAKFI: Smart Prosthetics: Exploring Assistive Devices for Body and Mind: Task Group Summaries." Irvine, CA, November 9–11, 2007.
13. Y. Z. Arslan, Y. Hacioglu, and N. Yagiz, *J. Intell. and Robotic Sys.* 52, 121 (2008).
14. D. J. Atkins, D. C. Y. Heard, and W. H. Donovan, *J. Prosth. and Orth.* 8, 2 (1996).
15. D. J. Bak, *Design News* 68 (1997).
16. C. K. Battye, A. Nightingale, and J. Whillis, *J. Bone and Joint Surgery* 37-B, 506 (1955).
17. Y. Becerikli, Y. Oysal, and A. F. Konar, *IEEE Trans. on Neural Networks* 15, 383 (2004).
18. G. A. Bekey, R. Tomovic, and I. Zeljkovic, "Dextrous Robot Hands" (S. T. Venkataraman and T. Iberall, Eds.), p. 136. Springer-Verlag, New York, NY, 1990.
19. A. Bicchi, *IEEE Trans. on Robotics and Automation* 16, 652 (2000), (Summary article with 191 references).
20. J. T. Bingham and M. P. Schoen, "Proc. of the 2004 ASME Int. Mech. Eng. Congress and Exposition (IMECE)," p. 123. Anaheim, CA, November, 2004.
21. L. Birglen, T. Laliberte, and C. Gosselin, "Underactuated Robotic Hands." Springer Tracts in Advanced Robotics, Springer-Verlag, Berlin, Germany, 2008.
22. Blatchford intelligent prosthesis. http://www.blatchford.co.uk, 1994.
23. C. Bonivento and A. Davalli, *J. Rehab. Res. & Dev.* 35, 294 (1998).
24. A. H. Bottomley, *The J. Bone and Joint Surgery* 47-B, 411 (1965).
25. A. H. Bottomley, G. Kingshill, P. Robert, D. Styles, P. H. Jilbert, J. W. Birtill, and J. R. Truscott, Prosthetic hand with improved control system for activation by electromyogram signals, Technical report, National Research Development Corporation, London, UK, December 1968, US Patent 3418662.
26. J. Butterfass, M. Grebenstein, H. Liu, and G. Hirzinger, "Proc. of the IEEE Int. Conf. on Robotics and Automation," p. 109. 2001.
27. J. Cai, X. Ruan, and X. Li, "2008 Int. Conf. on Intell. Computation Tech. and Auto. (ICICTA 2008)," p. 404. Changhsa, Hunan, China, October, 2008.
28. M. C. Carrozza, G. Cappiello, G. Stellin, F. Zaccone, F. Vechhi, S. Micera, and P. Dario, "Proc. of the IEEE/RSJ Int. Conf. on Intell. Robots and Systems," p. 1271. August, 2005.
29. M. C. Carrozza, B. Massa, S. Micera, R. Lazzarini, and M. Zecca, *IEEE/ASME Trans. on Mechatronics* 7, 108 (2002).
30. M. C. Carrozza, F. Vecchi, F. Sebastiani, G. Cappiello, S. Roccella, M. Zecca, R. Lazzarini, and P. Dario, "Proc. of the 2003 IEEE Int. Conf. on Robotics & Automation," p. 2230. September, 2003.
31. F. H. Y. Chan, Y.-S. Yang, F. K. Lam, Y.-T., Zhang, and P. A. Parker, *IEEE Trans. on Rehab. Eng.* 8, 305 (2000).
32. C.-H. Chen, K. W. Bosworth, and M. P. Schoen, "Proc. of Int. Mech. Eng. Cong. and Exposition (IMECE) 2007," Seattle, Washington, USA, November, 2007 (No. IMECE2007-41343).
33. C.-H. Chen, K. W. Bosworth, and M. P. Schoen, "Proc. of the Int. Assoc. of Sci. and Tech. for Dev. (IASTED) Int. Symp. on Computational Bio. and Bioinformatics (CBB 2008)," p. 260. Orlando, Florida, USA, November, 2008.
34. C.-H. Chen, K. W. Bosworth, M. P. Schoen, S. E. Bearden, D. S. Naidu, and A. Perez, "2008 IEEE Swarm Intelligence Symp. (IEEE SIS08)," St. Louis, Missouri, USA, September, 2008.
35. C.-H. Chen, D. S. Naidu, A. Perez, and M. P. Schoen, "Proc. of the Int. Assoc. of Sci. and Tech. for Dev. (IASTED) Int. Conf. on Intell. Sys. and Control (ISC 2008)," p. 120. Orlando, Florida, USA, November, 2008.

36. C.-H. Chen, D. S. Naidu, A. Perez-Gracia, and M. P. Schoen, "The 48th IEEE Conf. on Dec[illegible] and Control (CDC) and 28th Chinese Control Conf. (CCC)." Shanghai, P. R. China, December, 2009 (Accepted).
37. C.-H. Chen, D. S. Naidu, A. Perez-Gracia, and M. P. Schoen, "[illegible] of ASME 2009 Dynamic Sys. and Cont. Conf. (DSCC)," Hollywood, California, USA, October, 2009 (Accepted).
38. C.-H. Chen, D. S. Naidu, A. Perez-Gracia, and M. P. Schoen, "The 31st Ann. Int. Conf. of the IEEE Eng. Med. and Bio. Soc. (EMBC)," Minneapolis, Minnesota, USA, September, 2009 (Accepted).
39. C.-H. Chen, M. P. Schoen, and K. W. Bosworth. "Proc. of ASME 2009 Dynamic Sys. and Cont. Conf. (DSCC)," Hollywood, California, USA, October, 2009 (Accepted).
40. C.-Y. Chen, M. H.-M. Cheng, C.-F. Yang, and J.-S. Chen, "The 3rd Int. Conf. on Innovative Computing Info. and Cont. (ICICIC '08)," p. 422. Dalian, Liaoning, China, June, 2008.
41. C.-Y. Chen, T.-H. S. Li, Y.-C. Yeh, and C.-C. Chang, *Mechatronics* 19, 156 (2009).
42. J. L. Chen and W.-D. Chang, *Expert Systems with Applications* 36, 4154 (2009).
43. D. S. Childress, *J. Annals of Biomed. Eng.* 8, 293 (1980), (45 references).
44. B. Choi, S. Lee, H. R. Choi, and S. Kang, "Proc. of the 2006 IEEE/RSJ Int. Conf. on Intel. Robots and Sys.," p. 3779. Beijing, China, October, 2006.
45. C. I. Christodooulu and C. S. Pattichis, *IEEE Trans. on Biomed. Eng.* 46, 169 (1999).
46. C. Cipriani, F. Zaccone, G. Stellin, L. Beccai, G. Cappiello, M. C. Carrozza, and P. Dario, "Proc. 2006 IEEE Int. Conf. on Robotics and Auto. (ICRA 2006)," p. 2111. Orlando, Florida, USA, May, 2006.
47. CNN-News: Brain chip heralds neurotech dawn, July 17, 2006.
48. CNN-News: Bionic arm provides hope for amputees, September 14, 2006.
49. A. A. Cole, J. E. Hauser, and S. S. Sastry, *IEEE Trans. on Auto. Cont.* 34, 398 (1989).
50. D. P. J. Cotton, A. Cranny, P. H. Chappell, N. M. White, and S. P. Beeby, "Proc. of the Insti. of Measurement and Cont. UK ACC Cont. 2006 Symp.," p. 211. 2006.
51. E. F. R. Crossley and F. G. Umholtz, *J. Mech. and Machine Theory* 12, 85 (1977).
52. C. A. Cruz-Villar, J. Alvarez-Gallegos, and M. G. Villarreal-Cervantes, *Mechatronics* 19, 178 (2009).
53. J. Cui and Z. Sun, "Proc. of the Sixth IEEE Int. Conf. on Auto. Face and Gesture Recog. (FGR'04)," p. 729. May, 2004.
54. M. da G. Marcos, J. A. T. Machado, and T.-P. Azevedo-Perdicoulis, *Comm. in Nonlinear Sci. and Numer. Simul.* 14, 2858 (2009).
55. Director of Defense Advanced Research Projects Agency (DARPA) Presentation to Subcommittee on Terrorism, Unconventional Threats and Capabilities, House Armed Services Committee, US House of Representatives - Bridging the Gap. Press Release: Dated March 25, 2004.
56. Director of Defense Advanced Research Projects Agency (DARPA): Bridging The Gap Powered by Ideas. Press Release, February (2005).
57. Director of Defense Advanced Research Projects Agency (DARPA): Defense Sciences Office (2006).
58. DARPA - News Release: DARPA Initiates Revolutionary Prosthetic Programs. Press Release: Dated February 8, 2006.
59. N. Dechev, W. L. Cleghorn, and S. Naumann, *Mech. and Machine Theory* 36, 1157 (2001).
60. G. S. Dhillon and K. W. Horch, *IEEE Trans. on Neural Sys. and Rehab. Eng.* 13, 468 (2005).
61. J.-Y. Dieulot and F. Colas, *Mechatronics* 19, 269 (2009).
62. V. Duchaine, S. Bouchard, and C. M. Gosselin, *IEEE/ASME Trans. on Mechatronics* 12, 570 (2007).
63. K. Duraisamy, O. Isebor, A. Perez, M. P. Schoen, and D. S. Naidu, "Proc. of the First IEEE/RAS-EMBS 2006 Int. Conf. on Biomed. Robotics and Biomechatronics," p. 1135. Pisa, Italy, February, 2006.
64. E. D. Engeberg and S. G. Meek, "Proc. of the 2008 IEEE/RSJ Int. Conf. on Intell. Robots and Sys.," p. 1940. Nice, France, September, 2008.
65. E. D. Engeberg and S. G. Meek, *IEEE Trans. on Biomed. Eng.* 55, 817 (2008).
66. E. D. Engeberg and S. G. Meek, *IEEE Trans. on Neural Sys. and Rehab. Eng.* 17, 70 (2009).
67. E. D. Engeberg, S. G. Meek, and M. A. Minor, *IEEE Trans. on Biomed. Eng.* 55, 1572 (2008).
68. K. Englehart and B. Hudgins, *IEEE Trans. on Biomed. Eng.* 50, 848 (2003).
69. K. Englehart, B. Hudgins, and A. D. C. Chan, *Tech. and Disability* 15, 95 (2003).
70. G. E. Fainekos, A. Girard, H. Kress-Gazit, and G. J. Pappas, *Automatica* 45, 343 (2009).
71. T. R. Farrell and R. F. Weir, *IEEE Trans. on Neural Sys. and Rehab. Eng.* 15, 111 (2007).
72. T. R. Farrell, R. F. Weir, C. W. Heckathorne, and D. S. Childress, *J. Rehab. Res. & Dev.* 42, 327 (2005).
73. J. J. Fernandez, K. A. Farry, and J. B. Cheatham, "Proc. of the First Ann. Conf. of Genetic Prog." p. 1754. 2000.
74. N. Fukaya, S. Toyama, T. Asfour, and R. Diffmann, "Proc. of the 2000 IEEE/RSJ Int. Conf. on Intell. Robots and Sys.," p. 1. Stanford, CA, July, 1996.
75. D. Graupe, R. W. Liu, and G. S. Moschytz, "Proc. of the 27th IEEE Conf. on Dec. and Cont.," p. 343. Austin, TX, December, 1988.
76. D. Graupe, J. Magnussen, and A. A. Beex, *IEEE Trans. on Auto. Cont.* 23, 538 (1978).
77. R. A. Grupen, T. C. Henderson, and I. D. McMammon, *Int. J. Robotics Res.* 8, 38 (1989).
78. P. Guinnessy, *Physics Today* 59, 24 (2006).
79. H. Hanafusa and H. Asada, "Robot Motion: Planning and Control" (M. Brady, J. M. Hollerbach, T. L. Johnson, T. Lozano-Pérez, and M. T. Mason, Eds.), p. 322. MIT Press, Cambridge, MA, 1977.
80. R. L. Hart, K. L. Kilgore, and P. H. Peckham, *IEEE Trans. on Rehab. Eng.* 6, 208 (1998).
81. A. E. Hines, N. E. Owens, and P. E. Crago, *IEEE Trans. on Biomed. Eng.* 39, 610 (1992).

82. L. R. Hochberg, M. D. Serruya, G. M. Friehs, A. Mukand, M. Saleh, A. H. Caplan, A. Branner, D. Chen, R. D. Penn, and J. P. Donoghue, *Nature* 442, 164 (2006).
83. N. Hogan, *Trans. of ASME, J. Dynamic Sys., Measurement, and Cont.* 107, 1 (1985).
84. K. W. Horch and G. S. Dhillon, "Neuroprosthesis: Theory and Practice." World Scientific, River Edge, NJ, 2004.
85. K. W. Horch and G. S. Dhillon, "Proc. of the First IEEE/RAS-EMBS 2006 Int. Conf. on Biomed. Robotics and Biomechanics," p. 1. Pisa, Italy, February, 2006.
86. H. Huang and C. Chen, "Proc. of the 1999 IEEE Int. Conf. on Robotics & Automation," p. 2392. Detroit, MI, May, 1999.
87. P. Huang, J. Yan, J. Yuan, and Y. Xu, "Proc. of the 2007 Int. Conf. on Infor. Acquis. (ICIA '07)," p. 397. Jeju City, Korea, July, 2007.
88. B. S. Hudgins, A Novel Approach to Multifunctional Myoelectric Control of Prosthesis, Ph.D. Thesis, University of New Brunswick, Fredericton, Canada, 1991.
89. B. S. Hudgins, P. Parker, and R. N. Scott, *IEEE Trans. on Biomed. Eng.* 40, 82 (1993).
90. T. Iberall, G. Sukhatme, D. Beattie, and G. A. Bekey, "Proc. of the Rehab. Eng. and Assist. Tech. Soc. of N. Amer. (RESNA)," p. 12. Los Vegas, NV, June, 1993.
91. T. Iberall, G. Sukhatme, D. Beattie, and G. A. Bekey, "Proc. of the 1994 IEEE Int. Conf. on Robotics and Automation," p. 1753. San Diego, CA, May, 1994.
92. T. Iberall, G. Sukhatme, D. Beattie, and G. A. Bekey, "Proc. of the 1993 IEEE/RSJ Int. Conf. on Intell. Robots and Sys.," p. 824. Yokohama, Japan, July, 1993.
93. T. Inoue and S. Hirai, "Mechanics and Control of Soft-Fingered Manipulation." Springer, New York, NY, 2009.
94. E. Iversen, H. H. Sears, and S. C. Jacobsen, *IEEE Cont. Sys. Mag.* 25, 16 (2005).
95. S. C. Jacobsen, D. F. Knutti, R. T. Johnson, and H. H. Sears, *IEEE Trans. on Biomed. Eng.* BME-29, 249 (1982).
96. S. C. Jacobsen, J. E. Wood, D. F. Knutti, K. B. Biggers, and E. K. Iversen, "Robotics Research: The Second International Symposium" (H. Hanafusa and H. Inoue, Eds.), p. 301. MIT Press, Cambridge, MA, 1985.
97. W. Jiang and W. Ge, "2008 IEEE Conf. on Robotics, Auto. and Mechatronics (RAM 2008)," p. 1108. Chengdu, China, September, 2008.
98. Y. Kamikawa and T. Maeno, "Proc. of the 2008 IEEE/RSJ Int. Conf. on Intel. Robots and Sys.," p. 717. Nice, France, September, 2008.
99. E. R. Kandel and J. H. Schartz, "Principles of Neural Science," 3rd Edition. Elsevier/North-Holland, New York, NY, 1985.
100. A. Kargov, T. Asfour, C. Pylatiuk, R. Oberle, H. Klosek, S. Schulz, K. Regenstein, G. Bretthauer, and R. Dillmann, "9th Int. Conf. Rehab. Robotics (ICORR)," p. 182. Chicago, IL, June–July 2005.
101. A. Kargov, C. Pylatiuk, J. Martin, S. Schulz, and L. Derlein, *Disability and Rehab.* 26, 705 (2004).
102. F. O. Karray and C. De Silva, "Soft Computing and Intelligent Systems Design: Theory, Tools and Applications." Pearson Educational Limited, Harlow, England, UK, 2004.
103. I. Kato, E. Okazaki, H. Kikuchi, and K. Iwanami, "Digest of 7th ICMBE," p. 367. 1967.
104. R. Kato, H. Yokoi, A. H. Arieta, W. Yub, and T. Arai, *Robotics and Auto. Sys.* 57, 161 (2009).
105. J. J. Kim, D. R. Blythe, D. A. Penny, and A. A. Goldenberg, "Proc. of the IEEE Conf. on Robotics and Auto.," p. 1590. Raleigh, NC, March, 1987.
106. S. Klug, O. von Stryk, and B. Mohl, "The First IEEE/RAS-EMBS Int. Conf. on Biomed. Robo. and Biomechatronics," p. 450. Pisa, Italy, February, 2006.
107. H. Kobayashi, *J. Robotic Res.* 1, 3 (1985).
108. A. E. Kobrinski, "Proc. of First IFAC," p. 619. Moscow, USSR, 1960.
109. R. Kolluru, K. P. Valavanis, P. Kimon, S. Smith, and N. Tsourveloudis, *Trans. of the Instit. of Measurement & Cont.* 24, 65 (2002).
110. M. Kristic, I. Kanellakopoulos, and P. Kokotović, "Nonlinear and Adaptive Control Design." John Wiley & Sons, New York, NY, 1995.
111. P. Kyberd and P. H. Chappell, *J. Rehab. Res. & Dev.* 31, 326 (1994).
112. P. Kyberd, P. H. Chappell, and D. Gow, *Tech. and Disability* 15, 57 (2003).
113. P. J. Kyberd, O. E. Holland, P. H. Chappell, S. Smith, R. Tregidgo, P. J. Bagwell, and M. Snaith, *IEEE Trans. on Rehab. Eng.* 3, 70 (1995).
114. P. J. Kyberd and J. L. Pons, "Proc. of the 2003 IEEE Int. Conf. on Robotics and Auto.," p. 3231. Taipei, Taiwan, September 2003.
115. J. C. K. Lai, M. P. Schoen, A. Perez-Gracia, D. S. Naidu, and S. W. Leung, *Proc. of the Insti. of Mech. Eng. (IMechE), Part H: J. Eng. in Med.* 221, 173 (2007). Special Issue on Micro and Nano Technologies in Medicine.
116. C. Lake and J. M. Miguelez, *Tech. and Disability* 15, 63 (2003).
117. X.-T. Le, W.-G Kim, B.-C. Kim, S.-H. Han, J.-G. Ann, and Y.-H. Ha, "Proc. of the SICE-ICASE Int. Joint Conf.," p. 1. Bexco, Busan, Korea, October, 2006.
118. S. Lee and G. N. Saridis, *IEEE Trans. on Auto. Cont.* 29, 290 (1984).
119. D. Lian, S. Peterson, and M. Donath, "Proc. of the 13th Int. Symp. on Indus. Robots," p. 18.91. 1983.
120. C. M. Light, P. H. Chappell, B. Hudgins, and K. Engelhart, *J. Med. Eng. & Tech.* 26, 139 (2002).
121. H. Liu, J. Butterfass, S. Knoch, P. Meusel, and G. Hirzinger, *IEEE Cont. Sys. Mag.* 19, 47 (1999).
122. S. Liuzzo and P. Tomei, *Int. J. Adapt. Control Signal Process.* 23, 97 (2009).
123. F. Lotti, P. Tiezzi, G. Vassura, L. Biagiotti, G. Palli, and C. Melchiorri, "Proc. of the 2005 IEEE Int. Conf. on Robotics and Auto.," p. 4488. Barcelona, Spain, April, 2005.

124. C. S. Lovchik and M. A. Diftler, "Proc. of the IEEE Int. Conf. on Robotics and Auto.," p. 907. May, 1999.
125. R. W. Mann and S. D. Reimers, *IEEE Trans. on Man-Machine Sys.* MMS-11, 110 (1970).
126. A. Marigo and A. Bicchi, *IEEE Trans. on Auto. Control* 45, 1586 (2000).
127. B. Massa, S. Roccella, M. C. Carrozza, and P. Dario, "Proc. of the 2002 IEEE Int. Conf. on Robotics and Auto.," p. 3374. Washington, DC, May, 2002.
128. D. S. McKenzie, *The J. Bone and Joint Surg.* 47, 418 (1965).
129. Q. Meng, H. Wang, P. Li, L. Wang, and Z. He, "Proc. of the 2006 IEEE Int. Conf. on Mechatronics and Auto.," p. 1477. Luoyang, China, June, 2006.
130. S. Micera, A. M. Sabatini, P. Dario, and B. Rossi, *Med. Eng. Physics* 21, 303 (1999).
131. D. Moniz, Arm Amputees Rely on Old Devices, USA Today, 10-06-2005, June 2005.
132. D. Moniz, Military to Fund Prosthetics Research, USA Today, 10-06-2005, June 2005.
133. S. Morita, T. Kondo, and K. Ito, "Proc. of the 2001 ICRA/IEEE Int. Conf. on Robotics and Auto.," p. 1477. Seoul, Korea, May, 2001.
134. S. Morita, K. Shibata, X. Z. Zheng, and K. Ito, "Proc. of the 2000 IEEE/RSJ Int. Conf. on Intel. Robots and Sys.," p. 389. Takamatsu, Japan, October–November, 2000.
135. E. F. Murphy and A. B. Wilson, "Biomedical Engineering Systems" (M. Clynes and J. H. Milsum, Eds.), p. 489. McGraw-Hill, New York, NY, 1970.
136. R. M. Murray, Z. Li, and S. S. Sastry, "A Mathematical Introduction to Robotic Manipulation." CRC Press, Boca Raton, FL, 1994.
137. A. Muzumdar, Ed., "Powered Upper Limb Prostheses Control, Implementation and Clinical Application." Springer-Verlag, New York, NY, 2004.
138. D. S. Naidu, Control strategies for prosthetic hand technology. Technical report, Measurement and Control Engineering Research Center, Idaho State University, Pocatello, ID, November 2006. (Over 100 references).
139. D. S. Naidu, C.-H. Chen, A. Perez, and M. P. Schoen, "Proc. of the 30th Ann. Int. IEEE EMBS Conf.," p. 4314. Vancouver, Canada, August, 2008.
140. D. S. Naidu, "Optimal Control Systems." CRC Press, Boca Raton, FL, 2003.
141. D. S. Naidu, Intelligent Control Systems. Graduate Course Class Notes, 2007.
142. D. S. Naidu and V. K. Nandikolla, "Proc. of the Auto. Cont. Conf. (ACC)," p. 1575. Portland, OR, June, 2005.
143. V. K. Nandikolla and D. S. Naidu, "Proc. of the 2005 ASME Int. Mech. Eng. Congress and Exposition (IMECE)," p. 1. Orlando, FL, November, 2005.
144. X. Navarro, T. B. Krueger, N. Lago, S. Micera, T. Stieglitz, and P. Dario, *J. the Peripheral Nervous Sys.* 10, 229 (2005). (Review article with over 300 references).
145. D. Nishikawa, W. Yu, H. Yokoi, and Y. Kakazu, *Electronics and Communications in Japan (Part III: Fundamental Electronic Science)* 84, 35 (2001). (Translated from Denshi Joho Tsushin Gakkai Ronbunshi, Vol. J82-D-II, No. 9, September 1999, pp. 1510–1519).
146. T. Okada, *IEEE Trans. on Sys., Man, and Cybernetics* 12, 289 (1982).
147. A. M. Okamura, N. Smaby, and M. R. Cutkosky, "Proc. of the IEEE Int. C2000 Conf. on Robotics and Auto.," p. 255. San Francisco, CA, April, 2000 (52 references).
148. R. Okuno, M. Yoshida, and K. Akazawa, "1996 4th Int. Workshop on Adv. Motion Cont.," p. 103. Mie, Japan, March, 1996.
149. K. Onozato and Y. Maeda, "The Soc. of Instrument and Cont. Eng. (SICE) Ann. Conf. 2007," p. 1031. Kagawa University, Takamatsu, Japan, September, 2007.
150. K. Oppenheim, Jess Sullivan powers robotic arms with his mind, CNN, March 23, 2006.
151. S. J. Ovaska, A. Kamiya, and Y. Chen, *IEEE Trans. on Sys., Man, and Cybernetics—Part C: Appl. and Reviews* 36, 439 (2006).
152. S. J. Ovaska and H. F. VanLandingham, *IEEE Trans. on Sys., Man, and Cybernetics—Part C: Appl. and Rev.* 32, 69 (2002).
153. S. J. Ovaska, H. F. VanLandingham, and A. Kamiya, *IEEE Trans. on Sys., Man, and Cybeernetics—Part C: Appl. and Rev.* 32, 72 (2002).
154. R. Ozawa, S. Arimoto, S. Nakamura, and J.-H. Bae, *IEEE Trans. on Robotics* 21, 965 (2005).
155. P. H. Peckham, K. L. Kilgore, M. W. Keith, A. M. Bryden, N. Bhadra, and F. W. Montague, *The J. Hand Surgery* 27A, 265 (2002).
156. D. H. Plettenburg and J. L. Herder, *Tech. and Disability* 15, 85 (2003).
157. J. L. Pons, E. Rocon, R. Ceres, D. Reynaerts, B. Saro, S. Levin, and W. Van Moorleghem, *Autonomous Robots* 16, 143 (2004).
158. C. Pylatiuk, S. Mounier, A. Kargov, S. Schulz, and G. Bretthauer, "Proc. of the 26th Ann. Int. Conf. of the IEEE EMBS," p. 4260. San Francisco, CA, September, 2004.
159. S. Roccella, M. C. Carrozza, G. Cappeiello, M. Zecca, H. Miwa, K. Itoh, and M. Matsumoto, "Proc. of the 2004 IEEE/RSJ Int. Conf. on Intel. Robots and Sys.," p. 266. Sendal, Japan, September–October, 2004.
160. L. E. Rodriguez-Cheu and A. Casals, "Proc. of the The First IEEE/RAS-EMBS 2006 Int. Conf. on Biomed. Robotics and Biomechatronics," p. 607. Pisa, Italy, February, 2006.
161. L. E. Rodriguez-Cheu, A. Casals, A. Cuxart, and A. Parra, "2005 IEEE/RSJ Int. Conf. on Intel. Robots and Sys. (IROS)," p. 541. August, 2005.
162. T. A. Rohland, *Med. and Bio. Eng.* 12, 300 (1975).
163. B. Rohrer and S. Hulet, "Proc. of the The First IEEE/RAS-EMBS 2006 Int. Conf. on Biomed. Robotics and Biomechatronics," p. 57. Pisa, Italy, February, 2006.

164. P. X. Rong, Z. J. He, C. D. Zong, and N. Liu, "2008 Int. Conf. on Intel. Computation Tech. and Auto. (ICICTA 2008)," p. 298. Changhsa, Hunan, China, October, 2008.
165. A. Rovetta, "Proc. of the IEEE Conf. on Robotics and Auto.," p. 1060. St. Louis, Missouri, March, 1983.
166. M. Salehi, G. R. Vossoughi, M. Vajedi, and M. Brooshaki, "Proc. of the 2008 IEEE Int. Conf. on Info. and Auto.," p. 458. Zhangjiajie, China, June, 2008.
167. J. K. Salisbury, Kinematic and Force Analysis of Articulated Hands, Ph.D. Thesis, Stanford University, Stanford, CA, 1982.
168. G. N. Saridis and T. P. Gootee, *IEEE Trans. on Biomed. Eng.* BME-29, 403 (1982).
169. G. N. Saridis and H. E. Stephanou, *IEEE Trans. on Sys., Man and Cybernetics* 7, 407 (1977).
170. N. Sarkar, X. Yun, and V. Kumar, *IEEE Trans. on Robotics and Auto.* 13, 364 (1977).
171. P. Scherillo, B. Siciliano, L. Zollo, M. C. Carrozza, E. Guglielmelli, and P. Dario, "Proc. of the 2003 IEEE/ASME Int. Conf. on Adv. Intell. Mechatronics (AIM 2003)," p. 920. 2003.
172. T. Schlegl and M. Buss, "Proc. of the 1998 IEEE Int. Conf. on Robotics and Auto.," p. 3026. Leuven, Belgium, May, 1998.
173. R. N. Scott and P. A. Parker, *J. Med. Eng. & Tech.* 12, 143 (1988).
174. H. H. Sears and J. Shaperman, *Amer. J. Phys. Med. & Rehab.* 70, 20 (1991).
175. D. Seo and M. R. Akella, *Sys. & Cont. Lett.* 58, 304 (2009).
176. K. Shenoy, Toward High-Performance Neural Control of Prosthetic Devices. Technical Report, Stanford University, Stanford, CA, May (2007).
177. E. D. Sherman, *Canadian Med. Assoc. J. (CMAJ)* 91, 1268 (1964).
178. K. B. Shimoga, *The Int. J. Robotics Res.* 15, 230 (1996), (Survey article with over 130 references).
179. B. Sick and S. J. Ovaska, "2005 IEEE Mid-Summer Workshop on Soft Computing in Ind. Appl.," p. 57. Espoo, Finland, June, 2005.
180. A. A. G. Siqueira and M. H. Terra, *Cont. Eng. Practice* 17, 418 (2009).
181. G. P. Starr, *IEEE Trans. on Robotics and Auto.* 6, 342 (1990).
182. R. Suárez and P. Grosch, "Proc. of the Intel. Manipulation and Grasping," p. 91. Genova, 2004.
183. B. Subudhi and A. S. Morris, *Applied Soft Computing* 9, 149 (2009).
184. K. K. Tan, S. Huang, and T. H. Lee, *Automatica* 45, 161 (2009).
185. G. Tao, Ed., "Adaptive Control Design and Analysis." Wiley-Interscience, New York, NY, 2003.
186. A. Tettamanzi and M. Tomassini, "Soft Computing: Integrating Evolutionary, Neural, and Fuzzy Systems." Springer-Verlag, Berlin, Germany, 2001.
187. R. W. Todd, Adaptive Control of a Human Prosthesis, Ph.D. Thesis, University of Southampton, Southampton, UK, 1969.
188. A. A. Tootoonchi, M. R. Gharib, and Y. Farzaneh, "2008 IEEE Conf. on Robotics, Auto. and Mechatronics (RAM 2008)," p. 649. Chengdu, China, September, 2008.
189. M. Torabi and M. Jahed, "Tenth Int. Conf. on Computer Modeling and Simulation (UKSIM 2008)," p. 685. Cambridge, UK, April, 2008.
190. T. Tsuji, O. Fukuda, H. Shigeyoshi, and M. Kaneko, "Proc. of the 2000 IEEE/RSJ Int. Conf. on Intel. Robots and Systems," p. 377. Takamatsu, Japan, 2000.
191. A. Tura, C. Lamberti, A. Davalii, and R. Sacchetti, *J. Rehab. Res. & Dev.* 35, 14 (1998).
192. Casualties in Afganistan & Iraq. www.unknownnews.net, June 5 2006.
193. H. Van Brussel, B. Santoso, and D. Reynaerts, "Proc. of the NASA Conf. on Space Telerobotics," p. 89. Pasadena, CA, January/February, 1989.
194. H. van der Linde, C. J. Hofstad, A. C. H. Geurts, K. Postema, J. H. B. Geertzen, and J. van Limbeek, *J. Rehab. Res. & Dev.* 41, 555 (2004). (Review article with 91 references).
195. S. T. Venkataraman and T. E. Djaferis, "Proc. of the IEEE Int. Conf. on Robotics and Auto.," p. 77. 1987.
196. N. Vitiello, E. Cattin, S. Roccella, F. Giovacchini, F. Vecchi, M. C. Carrozza, and P. Dario, "Proc. of the 2007 IEEE/RSJ Int. Conf. on Intel. Robots and Systems," p. 1852. San Diego, California, USA, October–November, 2007.
197. D. Vrabie, F. Lewis, and M. Abu-Khalaf, *Trans. of the Inst. of Measurement and Cont.* 30, 207 (2008).
198. R.-J. Wai and M.-C. Lee, *IEEE Trans. on Indust. Elect.* 51, 201 (2004).
199. R. F. Weir, Direct Muscle Attachment as a Control Input for a Position-Servo Prosthesis Controller, Ph.D. Thesis, Northwestern University, Evanston, IL, 1995.
200. R. F. Weir and A. B. Ajiboye, "Proc. of the 25th Ann. Int. Conf. of IEEE EMBS," p. 17. Cancun, Mexico, September, 2003.
201. R. F. Weir, P. R. Troyk, G. DeMichele, and D. Kerns, "Proc. of the 25th IEEE Eng. in Med. and Bio. 27th Ann. Conf.," p. 7337. Shanghai, China, September, 2005.
202. X. Wen, D. Sheng, and J. Huang, "A Hybrid Particle Swarm Optimization for Manipulator Inverse Kinematics Control," Lecture Notes in Computer Science, Vol. 5226. Springer-Verlag, Berlin, Heidelberg, 2008.
203. N. Wiener, "Cybernetics or Cont. and Comm. in the Animal and the Machine." MIT Press, Cambridge, MA, 1948; 2nd Edition, 1961.
204. N. Yagiz and Y. Hacioglu, *Math. and Computer Modelling* 49, 114 (2009).
205. J. Yang, E. P. Pitarch, K. Abdel-Malek, A. Patrick, and L. Lindkvist, *Mechanism and Machine Theory* 39, 555 (2004).
206. J. Žajdlik, "Proc. of the 2006 Int. Conf. on Intel. Eng. Systems," p. 202. 2006.
207. M. Zecca, S. Micera, M. C. Carrozza, and P. Dario, *Crit. Rev.™ in Biomed. Eng.* 30, 459 (2002). (Review article with 96 references).

208. M. Zecca, S. Roccella, G. Cappiello, K. Ito, K. Imanishi, H. Miwa, C. Carrozza, P. Dario, and A. Takanishi, From the human hand to a humanoid hand: Biologically-inspired approach for the development of robocasa hand #1. Technical report, 3ARTS Lab, Scuola Superiore Sant Anna, Pisa, Italy, 2006.
209. Y. Zhang, Z. Han, H. Zhang, X. Shang, T. Wang, and W. Guo, "Proc. of the 2001 IEEE Int. Conf. on Robotics and Auto.," p. 2517. Seoul, Korea, May, 2001.
210. D. W. Zhao, L. Jiang, H. Huang, M. H. Jin, H. G. Cai, and H. Liu, "Proc. of the 2006 IEEE Int. Conf. on Robotics and Biomimetics," p. 1. Kunming, China, December, 2006.
211. J. Zhao, Z. Xie, L. Jiang, H. G. Cai, H. Liu, and G. Hirzinger, "Proc. of the 2005 IEEE Int. Conf. on Robotics and Auto.," p. 1. Barcelona, Spain, April, 2005.
212. J. Zhao, Z. Xie, L. Jiang, H. G. Cai, H. Liu, and G. Hirzinger, "Proc. of the First IEEE/RAS-EMBS 2006 Int. Conf. on Biomed. Robot. and Biomechatronics," p. 995. Pisa, Italy, February, 2006.
213. K. Zhou and J. C. Doyle, "Essentials of Robust Control." Prentice Hall, Upper Saddle River, NJ, 1998.
214. K. Ziaei, L. Ni, and D. W. L. Wang, *Cont. Eng. Prac.* 17, 329 (2009).
215. L. Zollo, S. Roccella, E. Guglielmelli, M. C. Carrozza, and P. Dario, *IEEE/ASME Trans. on Mechatronics* 12, 418 (2007).
216. L. Zollo, S. Roccella, R. Tucci, B. Siciliano, E. Guglielmelli, M. C. Carrozza, and P. Dario, "Proc. of the First IEEE/RAS-EMBS 2006 Int. Conf. on Biomed. Robo. and Biomechatronics," p. 402. Pisa, Italy, February, 2006.

Adaptive Control for a Five-Fingered Prosthetic Hand with Unknown Mass and Inertia

CHENG-HUNG CHEN[1,2], D. SUBBARAM NAIDU[1,3], MARCO P. SCHOEN[1,4]
[1]Measurement and Control Engineering Research Center
[2]Department of Biological Sciences
[3]Department of Electrical Engineering
[4]Department of Mechanical Engineering
School of Engineering, Idaho State University
921 S. 8th Avenue, Pocatello, ID 83209, USA
{chenchen; naiduds; schomarc}@isu.edu

Abstract: An adaptive control strategy for the 14 degrees of freedom (DOFs), five-fingered smart prosthetic hand with unknown mass and inertia of all the fingers is developed in this work. In modeling, the various links used for the five fingers of the prosthetic hand are shown. A cubic polynomial for the trajectory planning is used. In particular, using a desired orientation for three-link fingers, the forward and inverse kinematics of the prosthetic hand system regarding the analytical solutions between the angular positions of joints and the positions and orientations of the end-effectors (fingertips) have been obtained. The simulations of the resulting adaptive controller with five-fingered prosthetic hand show enhanced performance.

Key–Words: adaptive control, prosthetic hand, hard control, five finger hand, feedback linearization, trajectory planning

1 Introduction

Due to the extreme complexity of human hand that has 27 bones, controlled by about 38 muscles to provide the hand with 22 degrees of freedom (DOFs), and incorporates about 17,000 tactile units of 4 different units, reproducing the human hand in all its various functions and appearance is still a challenging task [1]. Prosthetic hands have been built to replace human hands that can fully operate the various motions, such as holding, moving, grasping, lifting, twisting and so on [1–6]. However, about 35% of the users do not regularly use their prosthetic hands because of several reasons, including poor functionality of the presently available prosthetic hands and psychological problems. Thus, designing and developing an artificial hand which can "mimic the human hand as closely as possible" both in functionality and appearance can overcome these problems.

Hard computing/control (HC) techniques are used at lower levels for accuracy, precision, stability and robustness. HC comprises proportional-integral (PI) control [7], proportional-integral-derivative (PID) control [8–10], optimal control [11, 12], adaptive control [13–16], robust control [17], etc. with specific applications to prosthetic devices. However, our previous work [15] for a two-fingered (thumb and index finger) prosthetic hand showed that adaptive controller can overcome overshooting and oscillation. However, a five-fingered prosthetic hand with adaptive control technique has not been developed yet.

In this work, we first describe briefly the trajectory planning problem, human hand anatomy and the inverse kinematics for two-link thumb and the remaining three-link fingers (index, middle, ring and little). Next, the dynamics of the prosthetic hand is derived and feedback linearization technique is used to obtain *linear* tracking error dynamics. Then the adaptive controller is designed to minimize the tracking error. The simulation results show that the five-fingered prosthetic hand with the proposed adaptive controller can grasp an object without overshooting and oscillation. The last section provides conclusions and future work.

2 Modeling

2.1 Human Hand Anatomy

Figure 1 (a) shows a normal human hand composed of thumb (t), index (i), middle (m), ring (r), little (l) fingers and palm. The wrist is located between the forearm and the hand and consists of eight carpal bones organized in two rows of proximal (movable) and distal (immovable) carpal bones as shown in Figure 1 (b)

(a) Physical Appearance of Right Hand (Anterior View)

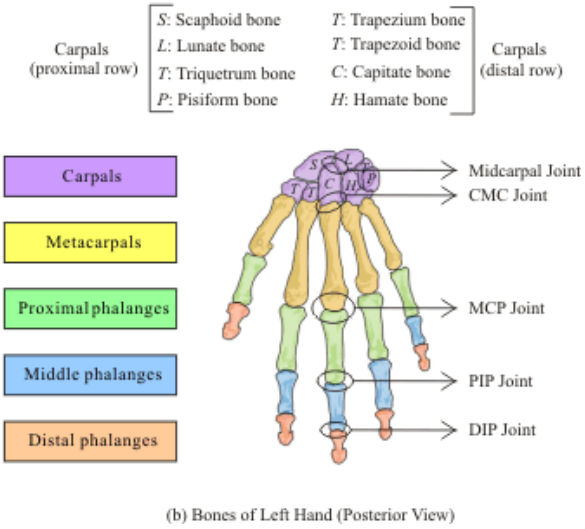

(b) Bones of Left Hand (Posterior View)

Figure 1: Human Wrist and Hand: (a) Physical Appearance of Right Hand (Anterior View) (b) Bones of Left Hand (Posterior View)

[18]. The proximal row (top) of carpal bones from lateral to medial is the *Scaphoid*, *Lunate*, *Triquetrum* and *Pisiform*; the distal row (bottom) of carpal bones from medial to lateral has the *Hamate*, *Capitate*, *Trapezoid* and *Trapezium*. The hand is composed of five *Metacarpals* and five Digits. The metacarpals produce a curve, so the palm is concave in the resting position. The five digits contain one thumb (t) and four fingers, e.g. index (i), middle (m), ring (r), and little (l) fingers, respectively. The thumb has two bones, $Proximal\ phalanx$ and $Distal\ phalanx$. Each finger consists of three bones, *Proximal phalanx*, *Middle phalanx* and *Distal phalanx*. In this work, we assumed that the palm is fixed, the thumb has two links (proximal phalanx and distal phalanx), and each finger has three links (proximal phalanx, middle phalanx and distal phalanx).

Synovial joints are formed at the surface of relative motion between two bones. The joints of thumb and four fingers contain two saddle-shaped articulating surfaces between two bones and can be classified as saddle joints. Index, middle, ring, and little fingers include three revolute joints in order to do the angular movements (Figure 1 (b)). Metacarpal-phalangeal (MCP) joint is located between metacarpal and proximal phalange bones; proximal and distal interphalangeal (PIP and DIP) joints separate the phalangeal bones. Thumb contains metacarpal-phalangeal (MCP) and interphalangeal (IP) joints [18]. In this work, q_1^j, q_2^j and q_3^j ($j = i$, m, r and l) represent the angular positions (or joint angles) of the first joint MCP^j, the second joint PIP^j and the third joint DIP^j of index, middle, ring and little fingers, respectively; q_1^t and q_2^t are the angular positions of the first joint MCP^t and the second joint IP^t of thumb (t), respectively.

2.2 Trajectory Planning

The trajectory planning using cubic polynomial for fingertip position control was discussed in our previous work [5, 8, 15, 19, 20] for a two-fingered (thumb and index finger) smart prosthetic hand. For three-link fingers, we present the same technique for fingertip orientation control. A time history of desired (d) fingertip orientation (ϕ) and its differentiation ($\dot{\phi}$ and $\ddot{\phi}$) is given as

$$\phi_d^j(t) = \omega_0 + \omega_1 t + \omega_2 t^2 + \omega_3 t^3, \quad (1)$$

$$\dot{\phi}_d^j(t) = \omega_1 + 2\omega_2 t + 3\omega_3 t^2, \quad (2)$$

$$\ddot{\phi}_d^j(t) = 2\omega_2 + 6\omega_3 t, \quad (3)$$

where ω_0-ω_3 are undetermined constants and the superscript j indicates the index of each finger ($j = i$, m, r and l). The relations (1) and (2) need to satisfy the constraint conditions at initial time t_0 and final time t_f. This can be written as

$$\mathbf{T}\ \mathbf{\Omega} = \mathbf{\Phi}. \quad (4)$$

Here, the matrices $\mathbf{T}$, $\mathbf{\Omega}$, and $\mathbf{\Phi}$ are

$$\mathbf{T} = \begin{bmatrix} 1 & t_0 & t_0^2 & t_0^3 \\ 0 & 1 & 2t_0 & 3t_0^2 \\ 1 & t_f & t_f^2 & t_f^3 \\ 0 & 1 & 2t_f & 3t_f^2 \end{bmatrix}, \quad (5)$$

$$\mathbf{\Omega} = \begin{bmatrix} \omega_0 & \omega_1 & \omega_2 & \omega_3 \end{bmatrix}', \quad (6)$$

$$\mathbf{\Phi} = \begin{bmatrix} \phi_0^j & \dot{\phi}_0^j & \phi_f^j & \dot{\phi}_f^j \end{bmatrix}'. \quad (7)$$

Therefore, the 4 unknown constants, ω_0-ω_3, can be computed by $\mathbf{\Omega} = \mathbf{T}^{-1}\mathbf{\Phi}$.

2.3 Kinematics

Kinematics is the study of geometry in motion and is restricted to a natural geometrical description of motion by the manners, including positions, orientations, and their derivatives (velocities and accelerations) [21, 22]. Forward and inverse kinematics of articulated systems study the analytical relationship between the angular positions of joints and the positions and orientations of the end-effectors (fingertips). A desired trajectory is usually specified in *Cartesian* space and the trajectory controller is easily performed in the *joint* space. Hence, conversion of Cartesian trajectory planning to the joint space [22] is necessary. Using inverse kinematics, the joint angular positions of each finger need to be obtained from the known fingertip positions. Then the angular velocities and angular accelerations of joints can be obtained from the linear and angular velocities and accelerations of fingertips (end-effectors) by differential kinematics. The inverse and differential kinematics of two-link thumb and three-link fingers were discussed in our previous publications [5,8,15,19,20] for a two-fingered (thumb and index finger) smart prosthetic hand.

For five fingers shown in Figure 2, X^G, Y^G, and

Figure 2: The Relationship between Global Coordinate and Local Coordinates

Z^G are the three axes of the global coordinate. The local coordinate x^t-y^t-z^t of thumb can be reached by rotating through angles α and β to X^G and Y^G of the global coordinate, subsequently. The local coordinate x^i-y^i-z^i of index finger can be obtained by rotating through angle α to X^G and then translating the vector $\mathbf{d^i}$ of the global coordinate; similarly, the local coordinate x^j-y^j-z^j of middle finger ($j = m$), ring finger ($j = r$), and little finger ($j = l$) can be obtained by rotating through angle α to X^G and then translating the vector $\mathbf{d^j}$ ($j = m$, r and l) of the global coordinate.

2.4 Dynamics of Hand

The dynamic equations of hand motion are derived via Lagrangian approach using kinetic energy and potential energy as [5]

$$\frac{d}{dt}\left(\frac{\partial \mathcal{L}}{\partial \dot{\mathbf{q}}}\right) - \frac{\partial \mathcal{L}}{\partial \mathbf{q}} = \boldsymbol{\tau}, \tag{8}$$

where $\mathcal{L}$ is the Lagrangian; $\dot{\mathbf{q}}$ and $\mathbf{q}$ represent the angular velocities and angle vectors of joints, respectively; $\boldsymbol{\tau}$ is the given torque vector at joints. The Lagrangian $\mathcal{L}$ can be expressed as

$$\mathcal{L} = T - V, \tag{9}$$

where T and V denote kinetic and potential energies, respectively. Substituting (9) into (8), dynamic equations of thumb can be obtained as below.

$$\mathbf{M}(\mathbf{q})\ddot{\mathbf{q}} + \mathbf{C}(\mathbf{q}, \dot{\mathbf{q}}) + \mathbf{G}(\mathbf{q}) = \boldsymbol{\tau}, \tag{10}$$

where $\mathbf{M}(\mathbf{q})$ is the inertia matrix; $\mathbf{C}(\mathbf{q}, \dot{\mathbf{q}})$ is the Coriolis/centripetal vector and $\mathbf{G}(\mathbf{q})$ is the gravity vector. (10) can be also written as

$$\mathbf{M}(\mathbf{q})\ddot{\mathbf{q}} + \mathbf{N}(\mathbf{q}, \dot{\mathbf{q}}) = \boldsymbol{\tau}, \tag{11}$$

where $\mathbf{N}(\mathbf{q}, \dot{\mathbf{q}}) = \mathbf{C}(\mathbf{q}, \dot{\mathbf{q}}) + \mathbf{G}(\mathbf{q})$ represents nonlinear terms. The dynamic relations for the two-link thumb and the remaining three-link fingers are quite lengthy and omitted here due to lack of space [5].

3 Control Techniques

3.1 Feedback Linearization

The nonlinear dynamics represented by (11) is to be converted into a linear state-variable system using feedback linearization technique [14]. Alternative state-space equations of the dynamics can be obtained by defining the position/velocity state $\mathbf{x}(t)$ of the joints as

$$\mathbf{x}(t) = \left[\mathbf{q}'(t) \quad \dot{\mathbf{q}}'(t)\right]'. \tag{12}$$

Let us repeat the dynamical model and rewrite (11) as

$$\frac{d}{dt}\dot{\mathbf{q}}(t) = -\mathbf{M}^{-1}(\mathbf{q}(t))\left[\mathbf{N}(\mathbf{q}(t), \dot{\mathbf{q}}(t)) - \boldsymbol{\tau}(t)\right]. \tag{13}$$

Thus, from (12) and (13), we can derive a linear system in *Brunovsky canonical form* as

$$\dot{\mathbf{x}}(t) = \begin{bmatrix} \mathbf{0} & \mathbf{I} \\ \mathbf{0} & \mathbf{0} \end{bmatrix} \mathbf{x}(t) + \begin{bmatrix} \mathbf{0} \\ \mathbf{I} \end{bmatrix} \mathbf{u}(t) \tag{14}$$

with its control input vector given by

$$\mathbf{u}(t) = -\mathbf{M}^{-1}(\mathbf{q}(t))\left[\mathbf{N}(\mathbf{q}(t), \dot{\mathbf{q}}(t)) - \boldsymbol{\tau}(t)\right]. \tag{15}$$

Let us suppose the prosthetic hand is required to track the desired trajectory $\mathbf{q}_d(t)$ described under path generation or tracking. Then, the tracking error $\mathbf{e}(t)$ is defined as

$$\mathbf{e}(t) = \mathbf{q}_d(t) - \mathbf{q}(t). \quad (16)$$

Here, $\mathbf{q}_d(t)$ is the *desired* angle vector of joints and can be obtained by trajectory planning [5,8,15,19,20]; $\mathbf{q}(t)$ is the *actual* angle vector of joints. Differentiating (16) twice, to get

$$\dot{\mathbf{e}}(t) = \dot{\mathbf{q}}_d(t) - \dot{\mathbf{q}}(t), \quad \ddot{\mathbf{e}}(t) = \ddot{\mathbf{q}}_d(t) - \ddot{\mathbf{q}}(t). \quad (17)$$

Substituting (13) into (17) yields

$$\ddot{\mathbf{e}}(t) = \ddot{\mathbf{q}}_d(t) + \mathbf{M}^{-1}(\mathbf{q}(t)) \left[\mathbf{N}(\mathbf{q}(t), \dot{\mathbf{q}}(t)) - \boldsymbol{\tau}(t)\right] \quad (18)$$

from which the control function can be defined as

$$\mathbf{u}(t) = \ddot{\mathbf{q}}_d(t) + \mathbf{M}^{-1}(\mathbf{q}(t)) \left[\mathbf{N}(\mathbf{q}(t), \dot{\mathbf{q}}(t)) - \boldsymbol{\tau}(t)\right]. \quad (19)$$

This is often called the *feedback linearization* control law, which can also be inverted to express it as

$$\boldsymbol{\tau}(t) = \mathbf{M}(\mathbf{q}(t)) \left[\ddot{\mathbf{q}}_d(t) - \mathbf{u}(t)\right) + \mathbf{N}(\mathbf{q}(t), \dot{\mathbf{q}}(t)\right]. \quad (20)$$

Using the relations (17) and (19), and defining state vector $\mathbf{x}(t) = [\mathbf{e}'(t) \;\; \dot{\mathbf{e}}'(t)]'$, the *tracking error dynamics* can be written as

$$\dot{\mathbf{x}}(t) = \begin{bmatrix} \mathbf{0} & \mathbf{I} \\ \mathbf{0} & \mathbf{0} \end{bmatrix} \mathbf{x}(t) + \begin{bmatrix} \mathbf{0} \\ \mathbf{I} \end{bmatrix} \mathbf{u}(t). \quad (21)$$

Note that this is in the form of a *linear* system such as

$$\dot{\mathbf{x}}(t) = \mathbf{A}\mathbf{x}(t) + \mathbf{B}\mathbf{u}(t). \quad (22)$$

3.2 Adaptive Control Technique

The tracking error $\mathbf{e}(t)$ and the filtered tracking error $\mathbf{r}(t)$ are defined as

$$\mathbf{e}(t) = \mathbf{q}_d(t) - \mathbf{q}(t), \quad (23)$$
$$\mathbf{r}(t) = \dot{\mathbf{e}}(t) + \boldsymbol{\Lambda}\mathbf{e}(t). \quad (24)$$

Here, $\mathbf{q}_d(t)$ is the *desired* angle vector of joints; $\mathbf{q}(t)$ is the *actual* angle vector of joints; $\boldsymbol{\Lambda} = diag(\lambda_1, \lambda_2, \ldots, \lambda_n)$ is the positive-definite diagonal gain matrix. The filtered error (24) ensures stability of the overall system so that the tracking error (23) is bounded. Figure 3 shows the block diagram of the adaptive controller. Here, the filtered signal $\mathbf{r}(t)$ is derived from the tracking error $\mathbf{e}(t)$ and the trajectory planner and is fed to the adaptive controller of the prosthetic hand. Differentiating and substituting (24) into (10) gives the dynamic equation in terms of the filtered error $\mathbf{r}(t)$ as

$$\mathbf{M}(\mathbf{q}(t))\dot{\mathbf{r}}(t) = -\mathbf{C}_m(\mathbf{q}(t), \dot{\mathbf{q}}(t))\mathbf{r}(t) + \mathbf{f}(t) - \boldsymbol{\tau}(t), \quad (25)$$

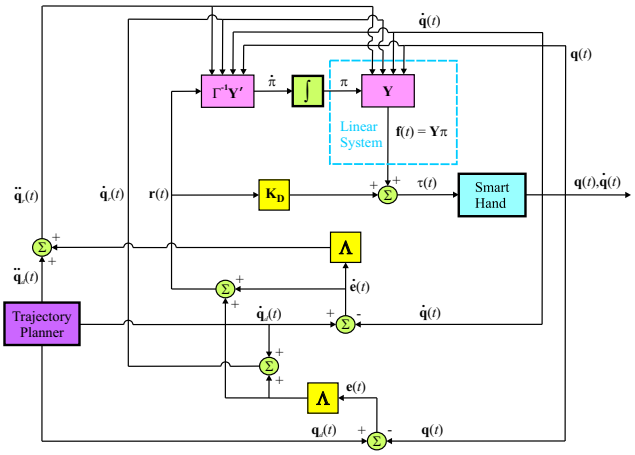

Figure 3: Block Diagram of Adaptive Control Technique

where $\mathbf{C}(\mathbf{q}(t), \dot{\mathbf{q}}(t)) = \mathbf{C}_m(\mathbf{q}(t), \dot{\mathbf{q}}(t))\dot{\mathbf{q}}(t)$ and the nonlinear term $\mathbf{f}(t)$ can be defined as

$$\begin{aligned} \mathbf{f}(t) &= \mathbf{M}(\mathbf{q}(t))(\ddot{\mathbf{q}}_d(t) + \boldsymbol{\Lambda}\dot{\mathbf{e}}(t)) + \mathbf{G}(\mathbf{q}(t)) + \\ &\quad \mathbf{C}_m(\mathbf{q}(t), \dot{\mathbf{q}}(t))(\dot{\mathbf{q}}_d(t) + \boldsymbol{\Lambda}\mathbf{e}(t)) + \boldsymbol{\tau}_{dis}, \\ &= \mathbf{Y}\boldsymbol{\pi}. \end{aligned} \quad (26)$$

Here, $\boldsymbol{\tau}_{dis}$ is the unknown disturbance. $\mathbf{Y}$ is a regression matrix of known robot functions and $\boldsymbol{\pi}$ is a vector of unknown parameters [13]. The regression matrix $\mathbf{Y}$ and the unknown parameter vector $\boldsymbol{\pi}$ of two-link thumb and three-link index finger are given in Appendix [5]. The torque vector $\boldsymbol{\tau}(t)$ can be calculated by

$$\boldsymbol{\tau}(t) = \mathbf{f}(t) + \mathbf{K_D}\mathbf{r}(t). \quad (27)$$

The unknown parameter rate vector $\dot{\boldsymbol{\pi}}$ can be updated by

$$\dot{\boldsymbol{\pi}} = \boldsymbol{\Gamma}^{-1}\mathbf{Y}'\mathbf{r}(t) \quad (28)$$

where $\boldsymbol{\Gamma}$ is a tuning parameter diagonal matrix.

4 Simulation Results and Discussion

Figure 4 shows that five-fingered prosthetic hand with 14 DOFs is reaching a rectangular rod in order to grasp the object. When thumb and the other four fingers are performing extension/flexion movements, the workspace of fingertips is restricted to the maximum angles of joints. Referring to inverse kinematics, the first and second joint angles of the thumb fingertip are constrained in the ranges of [0,90] and [-80,0] (degrees). The first, second, and third joint angles of the other four fingers are constrained in the ranges of [0,90], [0,110] and [0,80] (degrees), respectively [23].

Next, we present simulations with an adaptive controller for the 14 DOFs five-fingered smart prosthetic hand. The parameters of the two-link thumb/three-link fingers [24] were related to desired trajectory. All parameters of the smart prosthetic hand selected for the simulations are

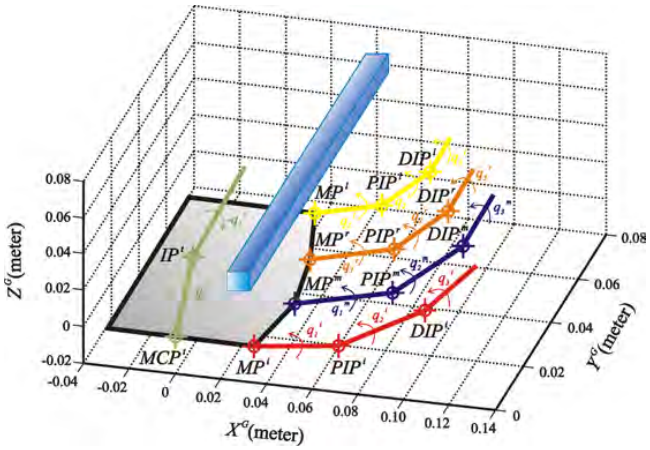

Figure 4: Five-Finger Prosthetic Hand Reaching a Rectangular Rod

given in Table 1 and the side length and length of the target rectangular rod are 0.010 and 0.100 (m), respectively. All initial actual angles are zero. The relating parameters between the global coordinate and the local coordinates are defined in Table 2.

Besides, in this work, we assumed that each link of all fingers is a circular cylinder with the radius (R) 0.010 (m), so the inertia I^j_{zzk} of each link k of all fingers j (= t, i, m, r and l) can be calculated as

$$I^j_{zzk} = \frac{1}{4} m^j_k R^2 + \frac{1}{3} m^j_k {L^j_k}^2. \tag{29}$$

Figure 5, Figure 7, Figure 9, Figure 11 and Figure 13 show the tracking errors of thumb, index, middle, ring, and little fingers for the proposed five-fingered smart prosthetic hand, respectively. Figure 6, Figure 8, Figure 10, Figure 12 and Figure 14 show the desired/actual angles of thumb, index, middle, ring, and little fingers for the proposed five-fingered smart prosthetic hand, respectively. The observation that all tracking errors dramatically drop within one second and are less than one degree after convergence provides the evidence that the adaptive controller for the 14-DOFs prosthetic hand enhances performance. The other observation that after convergence, all three-link fingers show more unstable errors than two-link thumb suggests that the more DOFs increase the difficulty of the adaptive controller without knowing the mass and inertia of the links of all fingers.

Table 1: Parameter Selection of the Smart Hand

Parameters	Values
Thumb	
Time (t_0,t_f)*	0, 20 (sec)
Desired Initial Position**	0.035, 0.060 (m)
Desired Final Position**	0.0495, 0.060 (m)
Desired Initial Velocity*	0, 0 (m/s)
Desired Final Velocity*	0, 0 (m/s)
Length	0.04, 0.04 (m)
Index Finger	
Desired Initial Position**	0.065, 0.080 (m)
Desired Final Position**	0.010, 0.060 (m)
Desired Initial ϕ_0***	75 (deg)
Desired Final ϕ_f***	160 (deg)
Desired Initial $\dot{\phi}_0$***	0 (m/s)
Desired Final $\dot{\phi}_f$***	0 (m/s)
Length	0.04, 0.04, 0.03 (m)
Middle Finger	
Desired Initial Position**	0.065, 0.080 (m)
Desired Final Position**	0.005, 0.060 (m)
Length	0.04, 0.04, 0.03 (m)
Ring Finger	
Desired Initial Position**	0.065, 0.080 (m)
Desired Final Position**	0.010, 0.060 (m)
Length	0.04, 0.04, 0.03 (m)
Little Finger	
Desired Initial Position**	0.055, 0.080 (m)
Desired Final Position**	0.020, 0.060 (m)
Length	0.04, 0.04, 0.03 (m)

*All fingers use same parameters
**Local coordinates
***All 3-link fingers use same parameters

5 Conclusions and Future Work

An adaptive control strategy was developed for the 14 degrees of freedom (DOFs), five-fingered smart prosthetic hand with unknown mass and inertia of all the fingers. Further, the forward and inverse kinematics of the system regarding the analytical relationship between the angular positions of joints and the positions and orientations of the end-effectors (fingertips), was obtained using a desired orientation for three-link fingers. The simulations of the resulting adaptive controller showed good agreement between the reference and the actual trajectories. Work is in progress for developing an adaptive/robust controller for the five fingered hand with 14-DOFs.

Acknowledgments: The research was sponsored by the U.S. Department of the Army, under the award number W81XWH-10-1-0128 awarded and administered by the U.S. Army Medical Research Acquisition Activity, 820 Chandler Street, Fort Detrick, MD 21702-5014. The information does not necessarily reflect the position or the policy of the Government, and no official endorsement should be inferred. For purposes of this article, information includes news releases, articles, manuscripts, brochures, advertisements, still and motion pictures, speeches, trade as-

Table 2: Parameter Selection of the Conversion from Global to Local Coordinates

Parameters	Values
Rotating α	90 (deg)
Rotating β	45 (deg)
Translating $\mathbf{d^i}$	(0.035, 0, 0) (m)
Translating $\mathbf{d^m}$	(0.040, 0, -0.020) (m)
Translating $\mathbf{d^r}$	(0.035, 0, -0.040) (m)
Translating $\mathbf{d^l}$	(0.025, 0, -0.060) (m)

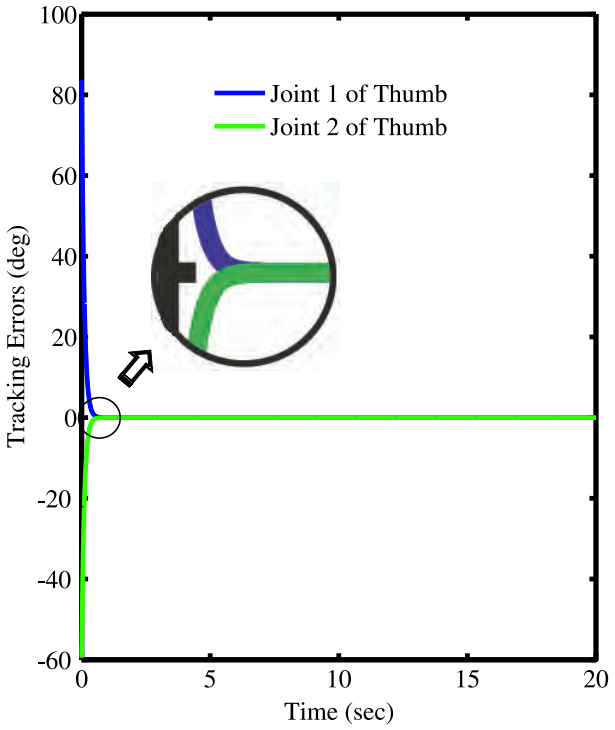

Figure 5: Tracking Errors of Adaptive Controller for Two-Link Thumb

sociation proceedings, etc.

Appendix: Regression Matrix Y and Unknown Parameter Vector π

In Section 3.2, the regression matrix $\mathbf{Y}^t$ and the unknown parameter vector $\boldsymbol{\pi}^t$ of two-link thumb can be expressed as

$$\begin{aligned}\mathbf{Y}^t &= \begin{bmatrix} Y_{11}^t & Y_{12}^t & Y_{13}^t & Y_{14}^t \\ Y_{21}^t & Y_{22}^t & Y_{23}^t & Y_{24}^t \end{bmatrix}, \\ \boldsymbol{\pi}^t &= \begin{bmatrix} m_1^t & m_2^t & I_{zz1}^t & I_{zz2}^t \end{bmatrix}',\end{aligned}$$

where

$$Y_{11}^t = l_1^t l_1^t(\ddot{q}_{d1} + \lambda_1 \dot{e}_1) + g l_1^t C_1,$$

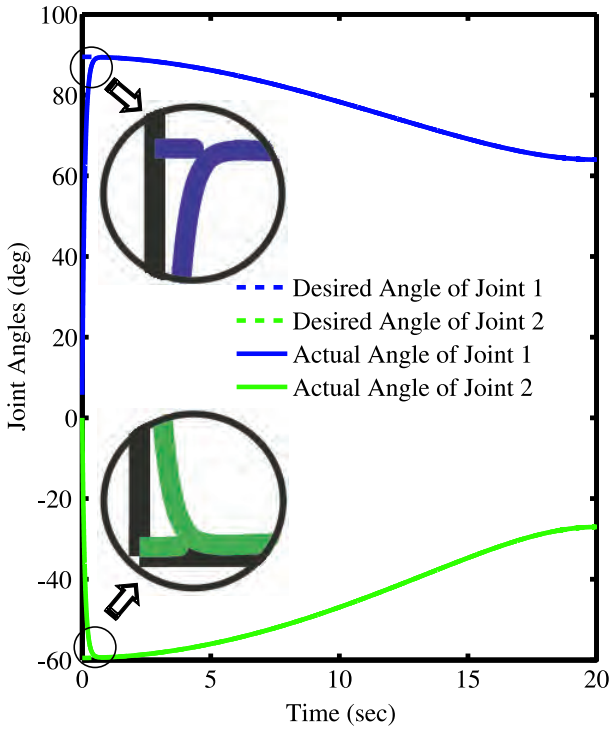

Figure 6: Tracking Angles of Adaptive Controller for Two-Link Thumb

$$\begin{aligned}
Y_{12}^t &= (2L_1^t l_2^t C_2 + L_1^t L_1^t + l_2^t l_2^t)(\ddot{q}_{d1} + \lambda_1 \dot{e}_1) \\
&\quad + (L_1^t l_2^t C_2 + l_2^t l_2^t)(\ddot{q}_{d2} + \lambda_2 \dot{e}_2) \\
&\quad - L_1^t l_2^t S_2 \dot{q}_2 (\dot{q}_{d1} + \lambda_1 e_1) \\
&\quad - L_1^t l_2^t S_2 (\dot{q}_1 + \dot{q}_2)(\dot{q}_{d2} + \lambda_2 e_2) + g l_2^t C_{12}, \\
Y_{13}^t &= \ddot{q}_{d1} + \lambda_1 \dot{e}_1, \\
Y_{14}^t &= \ddot{q}_{d1} + \lambda_1 \dot{e}_1 + \ddot{q}_{d2} + \lambda_2 \dot{e}_2, \\
Y_{21}^t &= Y_{23}^t = 0, \\
Y_{22}^t &= (L_1^t l_2^t C_2 + l_2^t l_2^t)(\ddot{q}_{d1} + \lambda_1 \dot{e}_1) + l_2^t l_2^t (\ddot{q}_{d2} + \lambda_2 \dot{e}_2) \\
&\quad + L_1^t l_2^t S_2 \dot{q}_1 (\dot{q}_{d1} + \lambda_1 e_1) \\
&\quad - L_1^t l_2^t S_2 \dot{q}_1 (\dot{q}_{d2} + \lambda_2 e_2) + g l_2^t C_{12}, \\
Y_{24}^t &= \ddot{q}_{d1} + \lambda_1 \dot{e}_1 + \ddot{q}_{d2} + \lambda_2 \dot{e}_2, \\
C_1 &= \cos(q_1), C_2 = \cos(q_2), \\
S_2 &= \sin(q_2), C_{12} = \cos(q_1 + q_2).
\end{aligned}$$

Similarly, the regression matrix $\mathbf{Y}^i$ and the unknown parameter vector $\boldsymbol{\pi}^i$ of three-link index finger can be written as

$$\begin{aligned}\mathbf{Y}^i &= \begin{bmatrix} Y_{11}^i & Y_{12}^i & Y_{13}^i & Y_{14}^i & Y_{15}^i & Y_{16}^i \\ Y_{21}^i & Y_{22}^i & Y_{23}^i & Y_{24}^i & Y_{25}^i & Y_{26}^i \\ Y_{31}^i & Y_{32}^i & Y_{33}^i & Y_{34}^i & Y_{35}^i & Y_{36}^i \end{bmatrix}, \\ \boldsymbol{\pi}^i &= \begin{bmatrix} m_1^i & m_2^i & m_3^i & I_{zz1}^i & I_{zz2}^i & I_{zz3}^i \end{bmatrix}'.\end{aligned}$$

Here,

$$Y_{11}^i = l_1^i l_1^i(\ddot{q}_{d1} + \lambda_1 \dot{e}_1) + g l_1^i C_1 + g l_2^i C_{12},$$

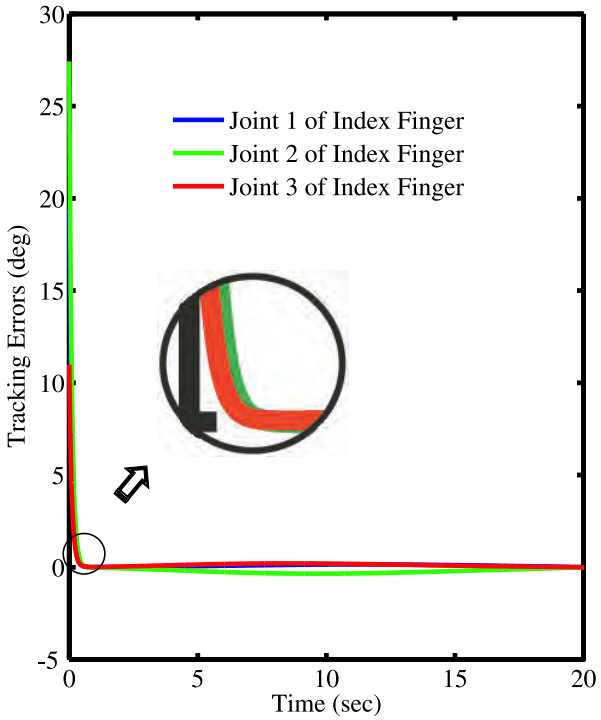

Figure 7: Tracking Errors of Adaptive Controller for Three-Link Index Finger

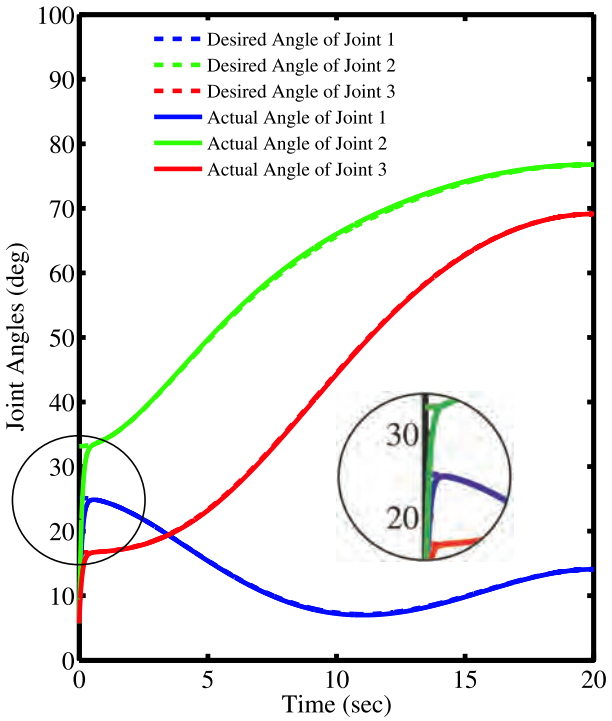

Figure 8: Tracking Angles of Adaptive Controller for Three-Link Index Finger

$$
\begin{aligned}
Y_{12}^i &= (2L_1^i l_2^i S_1 S_{12} + 2L_1^i l_2^i C_1 C_{12} + L_1^i L_1^i + l_2^i l_2^i)(\ddot{q}_{d1} + \lambda_1 \dot{e}_1) \\
&\quad + (L_1^i l_2^i S_1 S_{12} + L_1^i l_2^i C_1 C_{12} + l_2^i l_2^i)(\ddot{q}_{d2} + \lambda_2 \dot{e}_2) + g L_1 C_1 \\
&\quad + (L_1^i l_2^i S_1 C_{12} - L_1^i l_2^i C_1 S_{12}) \dot{q}_1 (\dot{q}_{d2} + \lambda_2 e_2) \\
&\quad + (L_1^i l_2^i S_1 C_{12} - L_1^i l_2^i C_1 S_{12}) \dot{q}_2 (\dot{q}_{d1} + \lambda_1 e_1) \\
&\quad + (L_1^i l_2^i S_1 C_{12} - L_1^i l_2^i C_1 S_{12}) \dot{q}_2 (\dot{q}_{d2} + \lambda_2 e_2),
\end{aligned}
$$

$$
\begin{aligned}
Y_{13}^i &= (2L_1^i L_2^i S_1 S_{12} + 2L_1^i L_2^i C_1 C_{12} + 2L_1^i l_3^i S_1 S_{123} \\
&\quad + 2L_1^i l_3^i C_1 C_{123} + 2L_2^i l_3^i S_{12} S_{123} + 2L_2^i l_3^i C_{12} C_{123} \\
&\quad + L_1^i L_1^i + L_2^i L_2^i + l_3^i l_3^i)(\ddot{q}_{d1} + \lambda_1 \dot{e}_1) \\
&\quad + (2L_2^i l_3^i S_{12} S_{123} + 2L_2^i l_3^i C_{12} C_{123} + L_1^i L_2^i S_1 S_{12} \\
&\quad + L_1^i L_2^i C_1 C_{12} + L_1^i l_3^i S_1 S_{123} + L_1^i l_3^i C_1 C_{123} \\
&\quad + L_2^i L_2^i + l_3^i l_3^i)(\ddot{q}_{d2} + \lambda_2 \dot{e}_2) \\
&\quad + (L_1^i l_3^i S_1 S_{123} + L_1^i l_3^i C_1 C_{123} + L_2^i l_3^i S_{12} S_{123} \\
&\quad + L_2^i l_3^i C_{12} C_{123} + l_3^i l_3^i)(\ddot{q}_{d3} + \lambda_3 \dot{e}_3) \\
&\quad + g L_1 C_1 + g L_2 C_{12} + g l_3 C_{123} \\
&\quad + (L_1^i L_2^i S_1 C_{12} - L_1^i L_2^i C_1 S_{12}) \dot{q}_1 (\dot{q}_{d2} + \lambda_2 e_2) \\
&\quad + (L_1^i L_2^i S_1 C_{12} - L_1^i L_2^i C_1 S_{12}) \dot{q}_2 (\dot{q}_{d1} + \lambda_1 e_1) \\
&\quad + (L_1^i l_3^i S_1 C_{123} - L_1^i l_3^i C_1 S_{123}) \dot{q}_1 (\dot{q}_{d2} + \lambda_2 e_2) \\
&\quad + (L_1^i l_3^i S_1 C_{123} - L_1^i l_3^i C_1 S_{123}) \dot{q}_2 (\dot{q}_{d1} + \lambda_1 e_1) \\
&\quad + (L_1^i l_3^i S_1 C_{123} - L_1^i l_3^i C_1 S_{123}) \dot{q}_1 (\dot{q}_{d3} + \lambda_3 e_3) \\
&\quad + (L_1^i l_3^i S_1 C_{123} - L_1^i l_3^i C_1 S_{123}) \dot{q}_3 (\dot{q}_{d1} + \lambda_1 e_1) \\
&\quad + (L_2^i l_3^i S_{12} C_{123} - L_2^i l_3^i C_{12} S_{123}) \dot{q}_1 (\dot{q}_{d3} + \lambda_3 e_3) \\
&\quad + (L_2^i l_3^i S_{12} C_{123} - L_2^i l_3^i C_{12} S_{123}) \dot{q}_3 (\dot{q}_{d1} + \lambda_1 e_1) \\
&\quad + (L_1^i l_3^i S_1 C_{123} - L_1^i l_3^i C_1 S_{123}) \dot{q}_2 (\dot{q}_{d3} + \lambda_3 e_3) \\
&\quad + (L_1^i l_3^i S_1 C_{123} - L_1^i l_3^i C_1 S_{123}) \dot{q}_3 (\dot{q}_{d2} + \lambda_2 e_2) \\
&\quad + (L_2^i l_3^i S_{12} C_{123} - L_2^i l_3^i C_{12} S_{123}) \dot{q}_2 (\dot{q}_{d3} + \lambda_3 e_3) \\
&\quad + (L_2^i l_3^i S_{12} C_{123} - L_2^i l_3^i C_{12} S_{123}) \dot{q}_3 (\dot{q}_{d2} + \lambda_2 e_2) \\
&\quad + (L_1^i L_2^i S_1 C_{12} - L_1^i L_2^i C_1 S_{12}) \dot{q}_2 (\dot{q}_{d2} + \lambda_2 e_2) \\
&\quad + (L_1^i l_3^i S_1 C_{123} - L_1^i l_3^i C_1 S_{123}) \dot{q}_2 (\dot{q}_{d2} + \lambda_2 e_2) \\
&\quad + (L_1^i l_3^i S_1 C_{123} - L_1^i l_3^i C_1 S_{123}) \dot{q}_3 (\dot{q}_{d3} + \lambda_3 e_3) \\
&\quad + (L_2^i l_3^i S_{12} C_{123} - L_2^i l_3^i C_{12} S_{123}) \dot{q}_3 (\dot{q}_{d3} + \lambda_3 e_3),
\end{aligned}
$$

$$
\begin{aligned}
Y_{14}^i &= \ddot{q}_{d1} + \lambda_1 \dot{e}_1, \\
Y_{15}^i &= \ddot{q}_{d1} + \lambda_1 \dot{e}_1 + \ddot{q}_{d2} + \lambda_2 \dot{e}_2, \\
Y_{16}^i &= \ddot{q}_{d1} + \lambda_1 \dot{e}_1 + \ddot{q}_{d2} + \lambda_2 \dot{e}_2 + \ddot{q}_{d3} + \lambda_3 \dot{e}_3, \\
Y_{21}^i &= Y_{24}^i = Y_{31}^i = Y_{32}^i = Y_{34}^i = Y_{35}^i = 0, \\
Y_{22}^i &= (L_1^i l_2^i S_1 S_{12} + L_1^i l_2^i C_1 C_{12} + l_2^i l_2^i)(\ddot{q}_{d1} + \lambda_1 \dot{e}_1) \\
&\quad + l_2^i l_2^i (\ddot{q}_{d2} + \lambda_2 \dot{e}_2) + g l_2 C_{12} \\
&\quad + (L_1^i l_2^i S_1 C_{12} - L_1^i l_2^i C_1 S_{12}) \dot{q}_2 (\dot{q}_{d1} + \lambda_1 e_1) \\
&\quad + (L_1^i l_2^i C_1 S_{12} - L_1^i l_2^i S_1 C_{12}) \dot{q}_1 (\dot{q}_{d1} + \lambda_1 e_1),
\end{aligned}
$$

$$
\begin{aligned}
Y_{23}^i &= (2L_2^i l_3^i S_{12} S_{123} + 2L_2^i l_3^i C_{12} C_{123} + L_1^i L_2^i S_1 S_{12} \\
&\quad + L_1^i L_2^i C_1 C_{12} + L_1^i l_3^i S_1 S_{123} + L_1^i l_3^i C_1 C_{123} \\
&\quad + L_2^i L_2^i + l_3^i l_3^i)(\ddot{q}_{d1} + \lambda_1 \dot{e}_1) + (2L_2^i l_3^i S_{12} S_{123} \\
&\quad + 2L_2^i l_3^i C_{12} C_{123} + L_2^i L_2^i + l_3^i l_3^i)(\ddot{q}_{d2} + \lambda_2 \dot{e}_2) \\
&\quad + (L_2^i l_3^i S_{12} S_{123} + L_2^i l_3^i C_{12} C_{123} + l_3^i l_3^i)(\ddot{q}_{d3} + \lambda_3 \dot{e}_3) \\
&\quad + g L_2 C_{12} + g l_3 C_{123} \\
&\quad + (L_1^i L_2^i S_1 C_{12} - L_1^i L_2^i C_1 S_{12}) \dot{q}_1 (\dot{q}_{d2} + \lambda_2 e_2) \\
&\quad + (L_1^i l_3^i S_1 C_{123} - L_1^i l_3^i C_1 S_{123}) \dot{q}_1 (\dot{q}_{d2} + \lambda_2 e_2)
\end{aligned}
$$

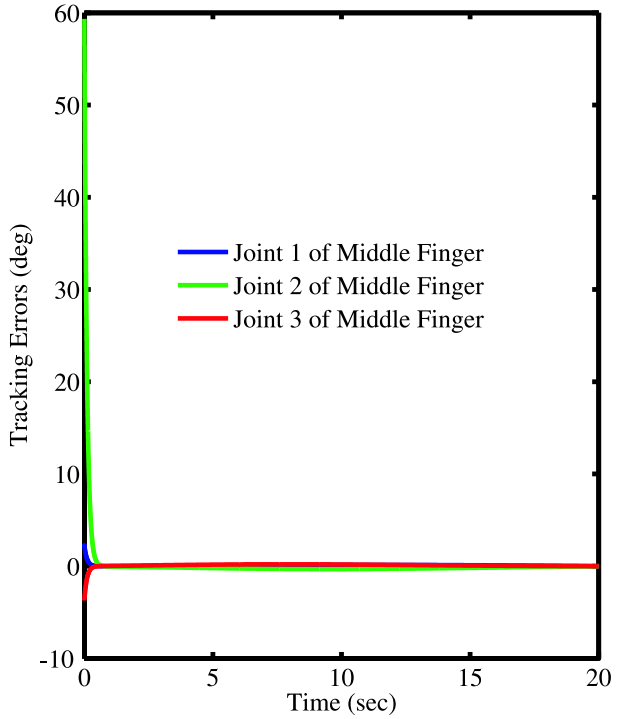

Figure 9: Tracking Errors of Adaptive Controller for Three-Link Middle Finger

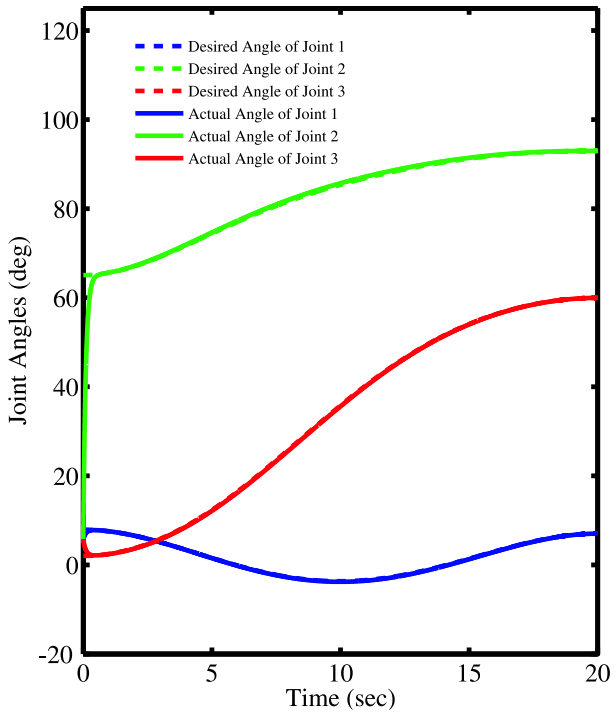

Figure 10: Tracking Angles of Adaptive Controller for Three-Link Middle Finger

$$
\begin{aligned}
&+(L_2^i l_3^i S_{12}C_{123} - L_2^i l_3^i C_{12}S_{123})\dot{q}_1(\dot{q}_{d3} + \lambda_3 e_3)\\
&+(L_2^i l_3^i S_{12}C_{123} - L_2^i l_3^i C_{12}S_{123})\dot{q}_3(\dot{q}_{d1} + \lambda_1 e_1)\\
&+(L_2^i l_3^i S_{12}C_{123} - L_2^i l_3^i C_{12}S_{123})\dot{q}_2(\dot{q}_{d3} + \lambda_3 e_3)\\
&+(L_2^i l_3^i S_{12}C_{123} - L_2^i l_3^i C_{12}S_{123})\dot{q}_3(\dot{q}_{d2} + \lambda_2 e_2)\\
&+(L_1^i L_2^i C_1 S_{12} - L_1^i L_2^i S_1 C_{12})\dot{q}_1(\dot{q}_{d1} + \lambda_1 e_1)\\
&+(L_1^i l_3^i C_1 S_{123} - L_1^i l_3^i S_1 C_{123})\dot{q}_1(\dot{q}_{d1} + \lambda_1 e_1)\\
&+(L_2^i l_3^i S_{12}C_{123} - L_2^i l_3^i C_{12}S_{123})\dot{q}_3(\dot{q}_{d3} + \lambda_3 e_3),
\end{aligned}
$$

$$
\begin{aligned}
Y_{25}^i &= \ddot{q}_{d1} + \lambda_1\dot{e}_1 + \ddot{q}_{d2} + \lambda_2\dot{e}_2,\\
Y_{26}^i &= \ddot{q}_{d1} + \lambda_1\dot{e}_1 + \ddot{q}_{d2} + \lambda_2\dot{e}_2 + \ddot{q}_{d3} + \lambda_3\dot{e}_3,
\end{aligned}
$$

$$
\begin{aligned}
Y_{33}^i = \;&(L_1^i l_3^i S_1 S_{123} + L_1^i l_3^i C_1 C_{123} + L_2^i l_3^i S_{12}S_{123}\\
&+L_2^i l_3^i C_{12}C_{123} + l_3^i l_3^i)(\ddot{q}_{d1} + \lambda_1\dot{e}_1)\\
&+(L_2^i l_3^i S_{12}S_{123} + L_2^i l_3^i C_{12}C_{123} + l_3^i l_3^i)(\ddot{q}_{d2} + \lambda_2\dot{e}_2)\\
&+l_3^i l_3^i(\ddot{q}_{d3} + \lambda_3\dot{e}_3) + g l_3 C_{123}\\
&+(L_2^i l_3^i C_{12}S_{123} - L_2^i l_3^i S_{12}C_{123})\dot{q}_1(\dot{q}_{d2} + \lambda_2 e_2)\\
&+(L_2^i l_3^i C_{12}S_{123} - L_2^i l_3^i S_{12}C_{123})\dot{q}_2(\dot{q}_{d1} + \lambda_1 e_1)\\
&+(L_1^i l_3^i S_1 C_{123} - L_1^i l_3^i C_1 S_{123})\dot{q}_1(\dot{q}_{d3} + \lambda_3 e_3)\\
&+(L_2^i l_3^i S_{12}C_{123} - L_2^i l_3^i C_{12}S_{123})\dot{q}_1(\dot{q}_{d3} + \lambda_3 e_3)\\
&+(L_2^i l_3^i S_{12}C_{123} - L_2^i l_3^i C_{12}S_{123})\dot{q}_2(\dot{q}_{d3} + \lambda_3 e_3)\\
&+(L_1^i l_3^i C_1 S_{123} - L_1^i l_3^i S_1 C_{123})\dot{q}_1(\dot{q}_{d1} + \lambda_1 e_1)\\
&+(L_2^i l_3^i C_{12}S_{123} - L_2^i l_3^i S_{12}C_{123})\dot{q}_1(\dot{q}_{d1} + \lambda_1 e_1)\\
&+(L_2^i l_3^i C_{12}S_{123} - L_2^i l_3^i S_{12}C_{123})\dot{q}_2(\dot{q}_{d2} + \lambda_2 e_2),
\end{aligned}
$$

$$
Y_{36}^i = \ddot{q}_{d1} + \lambda_1\dot{e}_1 + \ddot{q}_{d2} + \lambda_2\dot{e}_2 + \ddot{q}_{d3} + \lambda_3\dot{e}_3,
$$

$$
\begin{aligned}
C_1 &= \cos(q_1), C_{12} = \cos(q_1 + q_2),\\
S_1 &= \sin(q_1), S_{12} = \sin(q_1 + q_2),\\
C_{123} &= \cos(q_1 + q_2 + q_3),\\
S_{123} &= \sin(q_1 + q_2 + q_3).
\end{aligned}
$$

References:

[1] M. Zecca, S. Micera, M. Carrozza, and P. Dario, "Control of multifunctional prosthetic hands by processing the electromyographic signal," *Critical Reviews^{TM} in Biomedical Engineering*, vol. 30, pp. 459–485, 2002, (Review article with 96 references).

[2] J. C. K. Lai, M. P. Schoen, A. Perez-Gracia, D. S. Naidu, and S. W. Leung, "Prosthetic devices: Challenges and implications of robotic implants and biological interfaces," *Proceedings of the Institute of Mechanical Engineers (IMechE), Part H: Journal of Engineering in Medicine*, vol. 221, no. 2, pp. 173–183, January 2007, special Issue on Micro and Nano Technologies in Medicine.

[3] L. Zollo, S. Roccella, E. Guglielmelli, M. C. Carrozza, and P. Dario, "Biomechatronic design and control of an anthropomorphic artificial hand for prosthetic and robotic applications," *IEEE/ASME Transactions on Mechatronics*, vol. 12, no. 4, pp. 418–429, August 2007.

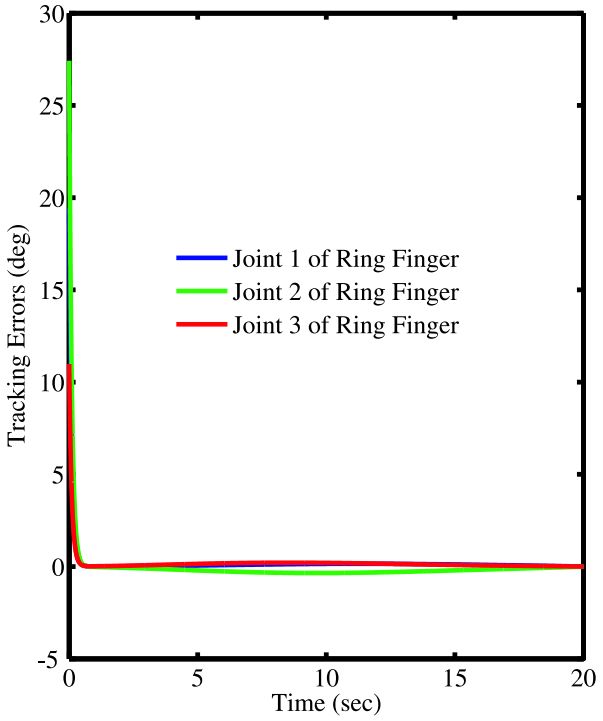

Figure 11: Tracking Errors of Adaptive Controller for Three-Link Ring Finger

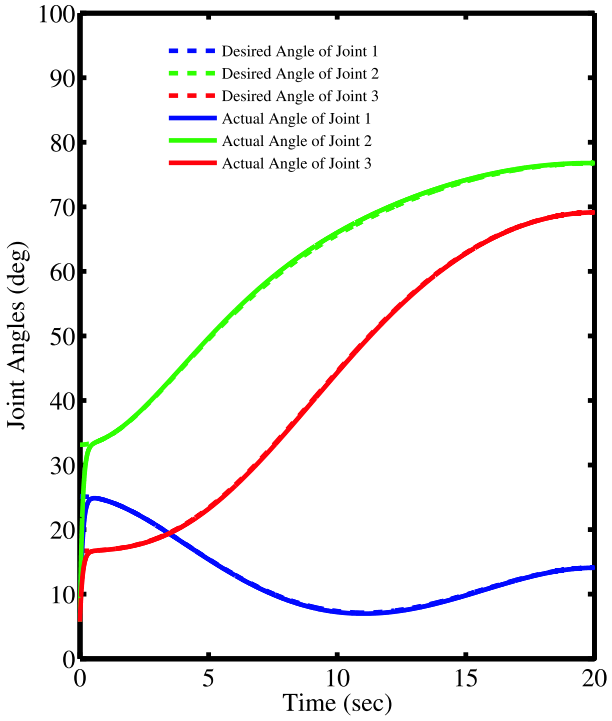

Figure 12: Tracking Angles of Adaptive Controller for Three-Link Ring Finger

[4] D. S. Naidu, C.-H. Chen, A. Perez, and M. P. Schoen, "Control strategies for smart prosthetic hand technology: An overview," in *Proceedings of the 30th Annual International IEEE EMBS Conference*, Vancouver, Canada, August 20-24 2008, pp. 4314–4317.

[5] C.-H. Chen, "Hybrid control strategies for smart prosthetic hand," Ph.D. dissertation, Measurement and Control Engineering, Idaho State University, May 2009.

[6] D. S. Naidu and C.-H. Chen., *Control strategies for smart prosthetic hand technology: an overview, book chapter 14, to appear in a book titled "Distributed Diagnosis and Home Healthcare (D2H2): Volume 2"*. California, USA: American Scientific Publisherss, February 2010.

[7] J. Zavacka, M. Bakosova, and K. Vanekova, "Design of robust pi controllers for control of an exothermic chemical reactor," in *The 14th World Scientific and Engineering Academy and Society (WSEAS) International Conference on Systems, Latest Trends on Systems (Volume II)*, Corfu Island, Greece, July 22-24 2010, pp. 387–392.

[8] C.-H. Chen, D. S. Naidu, A. Perez, and M. P. Schoen, "Fusion of hard and soft control techniques for prosthetic hand," in *Proceedings of the International Association of Science and Technology for Development (IASTED) International Conference on Intelligent Systems and Control (ISC 2008)*, Orlando, Florida, USA, November 16-18 2008, pp. 120–125.

[9] P. Dostalek, L. Pekar, V. Vasek, and J. Dolinay, "Microcontroller based self-tuning digital pid controller," in *The 14th World Scientific and Engineering Academy and Society (WSEAS) International Conference on Systems, Latest Trends on Systems (Volume I)*, Corfu Island, Greece, July 22-24 2010, pp. 248–251.

[10] L. Macku and D. Samek, "Two step, pid and model predictive control applied on fed batch process," in *The 14th World Scientific and Engineering Academy and Society (WSEAS) International Conference on Systems, Latest Trends on Systems (Volume II)*, Corfu Island, Greece, July 22-24 2010, pp. 470–473.

[11] D. Naidu, *Optimal Control Systems*. Boca Raton, FL: CRC Press, 2003.

[12] C.-H. Chen, D. S. Naidu, A. Perez-Gracia, and M. P. Schoen, "A hybrid control strategy for five-fingered smart prosthetic hand," in *Joint 48th IEEE Conference on Decision and Control (CDC) and 28th Chinese Control Conference (CCC)*, Shanghai, P. R. China, December 16-18 2009, pp. 5102–5107.

[13] F. Lewis, S. Jagannathan, and A. Yesildirek, *Neural Network Control of Robotic Manipulators and Nonlinear Systems*. London, UK: Taylor & Francis, 1999.

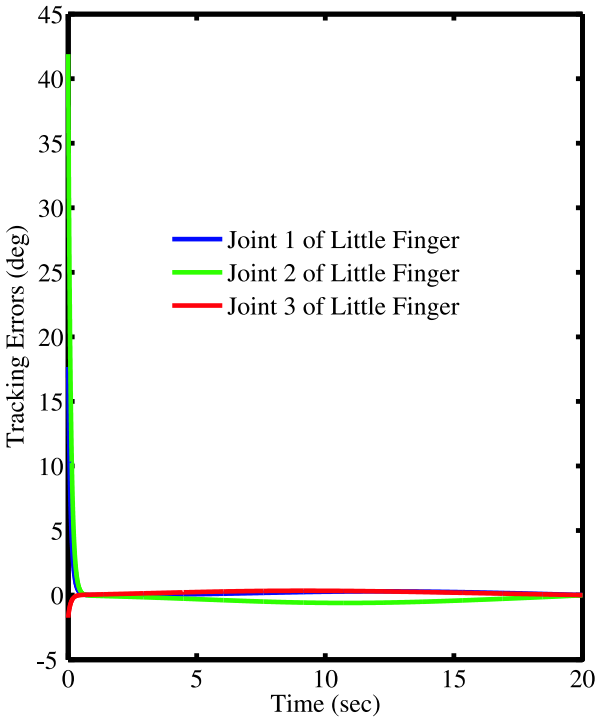

Figure 13: Tracking Errors of Adaptive Controller for Three-Link Little Finger

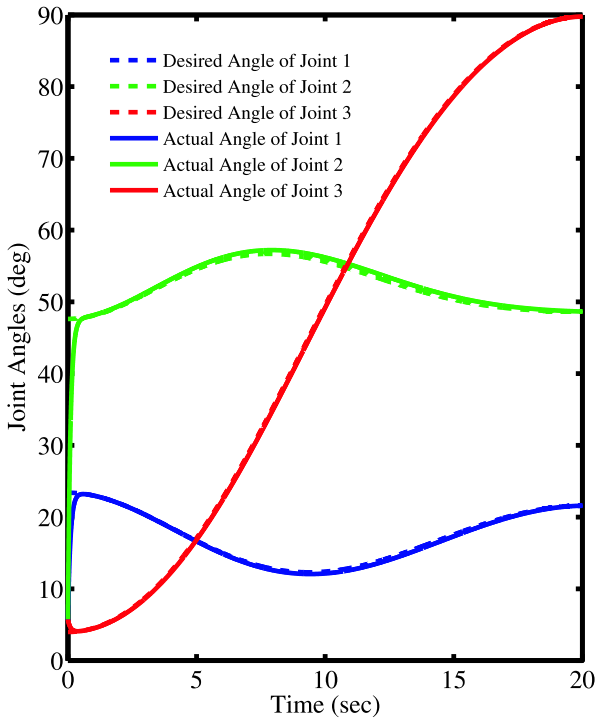

Figure 14: Tracking Angles of Adaptive Controller for Three-Link Little Finger

[14] F. Lewis, D. Dawson, and C. Abdallah, *Robot Manipulators Control: Second Edition, Revised and Expanded*. New York, NY: Marcel Dekker, Inc.,, 2004.

[15] C.-H. Chen, D. S. Naidu, A. Perez-Gracia, and M. P. Schoen, "A hybrid adaptive control strategy for a smart prosthetic hand," in *The 31st Annual International Conference of the IEEE Engineering Medicine and Biology Society (EMBS)*, Minneapolis, Minnesota, USA, September 2-6 2009, pp. 5056–5059.

[16] C.-H. Chen, D. S. Naidu, and M. P. Schoen, "An adaptive control strategy for a five-fingered prosthetic hand," in *The 14th World Scientific and Engineering Academy and Society (WSEAS) International Conference on Systems, Latest Trends on Systems (Volume II)*, Corfu Island, Greece, July 22-24 2010, pp. 405–410.

[17] M. Bakosova, A. Vasickaninova, and M. Karsaiova, "Robust static output feedback stabilization of an exothermic chemical reactor with input constraints," in *the 14th World Scientific and Engineering Academy and Society (WSEAS) International Conference on Systems, Latest Trends on Systems (Volume I)*, Corfu Island, Greece, July 22-24 2010, pp. 341–346.

[18] R. R. Seeley, T. D. Stephens, and P. Tate, *Anatomy & Physiology, Eighth Edition*. New York, NY: The McGraw-Hill, 2007.

[19] C.-H. Chen, K. W. Bosworth, M. P. Schoen, S. E. Bearden, D. S. Naidu, and A. Perez, "A study of particle swarm optimization on leukocyte adhesion molecules and control strategies for smart prosthetic hand," in *2008 IEEE Swarm Intelligence Symposium (IEEE SIS08)*, St. Louis, Missouri, USA, September 21-23 2008.

[20] C.-H. Chen, D. Naidu, A. Perez-Gracia, and M. P. Schoen, "A hybrid optimal control strategy for a smart prosthetic hand," in *Proceedings of the ASME 2009 Dynamic Systems and Control Conference (DSCC)*, Hollywood, California, USA, October 12-14 2009, (No. DSCC2009-2507).

[21] R. N. Jazar, *Theory of Applied Robotics. Kinematics, Dynamics, and Control*. New York, USA: Springer, 2007.

[22] B. Siciliano, L. Sciavicco, L. Villani, and G. Oriolo, *Robotics: Modelling, Planning and Control*. London, UK: Springer-Verlag, 2009.

[23] P. K. Lavangie and C. C. Norkin, *Joint Structure and Function: A Comprehensive Analysis, Third Edition*. Philadelphia, PA: F. A. Davis Company, 2001.

[24] S. Arimoto, *Control Theory of Multi-fingered Hands: A Modeling and Analytical-Mechanics Approach for Dexterity and Intelligence*. London, UK: Springer-Verlag, 2008.

An Adaptive Control Strategy for a Five-Fingered Prosthetic Hand

CHENG-HUNG CHEN
Measurement and Control
Engineering Research Center
Dept. of Biological Sciences
Idaho State University
Pocatello, ID 83209
USA
chenchen@isu.edu

D. SUBBARAM NAIDU
Measurement and Control
Engineering Research Center
Dept. of Electrical Engineering
Idaho State University
Pocatello, ID 83209
USA
naiduds@isu.edu

MARCO P. SCHOEN
Measurement and Control
Engineering Research Center
Dept. of Mechanical Engineering
Idaho State University
Pocatello, ID 83209
USA
schomarc@isu.edu

Abstract: In this paper, an adaptive control strategy is developed for the 14 degrees of freedom (DOFs), five-fingered smart prosthetic hand with unknown mass and inertia of all the fingers. In particular, the forward and inverse kinematics of the system regarding the analytical relationship between the angular positions of joints and the positions and orientations of the end-effectors (fingertips) have been obtained using a desired orientation for three-link fingers. The simulations of the resulting adaptive controller with five-fingered prosthetic hand show enhanced performance.

Key–Words: adaptive control, prosthetic hand, hard control, five finger hand, feedback linearization, trajectory planning

1 Introduction

Due to the extreme complexity of human hand, that has 27 bones, controlled by about 38 muscles to provide the hand with 22 degrees of freedom (DOFs), and incorporates about 17,000 tactile units of 4 different units, reproducing the human hand in all its various functions and appearance is still a challenging task [1]. Prosthetic hands have been built to replace human hands that can fully operate the various motions, such as holding, moving, grasping, lifting, twisting and so on [1–5]. However, about 35% of the users do not regularly use their prosthetic hands because of several reasons, including poor functionality of the presently available prosthetic hands and psychological problems. Thus, designing and developing an artificial hand which can "mimics the human hand as closely as possible" both in functionality and appearance can overcome these problems.

Hard computing/control (HC) techniques can be used at lower levels for accuracy, precision, stability and robustness. HC comprises proportional-integral-derivative (PID) control [6], optimal control [7, 8], adaptive control [9–11] etc. with specific applications to prosthetic devices. However, our previous work [11] for a two-fingered, thumb and index finger, prosthetic hand showed that adaptive controller can overcome overshooting and oscillation. However, a five-fingered prosthetic hand with adaptive control technique has not been developed yet.

In this work, we first describe briefly the trajectory planning problem, human hand anatomy and the inverse kinematics for two-link thumb and the remaining three-link fingers (index, middle, ring and little). Next, the dynamics of the prosthetic hand is derived and feedback linearization technique is used to obtain *linear* tracking error dynamics. Then the adaptive controller is designed to minimize the tracking error. The simulation results show that the five-fingered prosthetic hand with the presented adaptive controller can grasp an object without overshooting and oscillation. Conclusions and future work are provided in the last section.

2 Modeling

2.1 Trajectory Planning and Inverse Kinematics

The trajectory planning using cubic polynomial was discussed in our previous work [5, 6, 11, 12] for a two-fingered (thumb and index finger) smart prosthetic hand. Figure 1 shows that index finger, middle finer, ring finer and little finger contain three revolute joints in order to do the angular movements. Metacarpal-phalangeal (MCP) joint is located between metacarpal and proximal phalange bone; proximal and distal interphalangeal (PIP and DIP) joints separate the phalangeal bones. Thumb contains metacarpal-phalangeal (MCP) and interphalangeal (IP) joints. In this work, q_1^j, q_2^j and q_3^j repre-

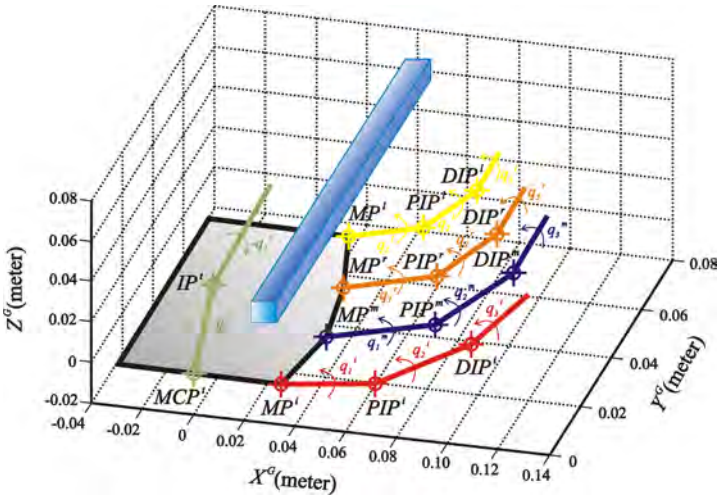

Figure 1: The Joints of Five-Finger Prosthetic Hand Reaching a Rectangular Rod

Figure 2: The Definition of Global Coordinate and Local Coordinates

sent the angular positions (or joint angles) of the first joint MCP^j, the second joint PIP^j and the third joint DIP^j of index finger ($j = i$), middle finger ($j = m$), ring finger ($j = r$) and little finger ($j = l$), respectively; q_1^t and q_2^t are the angular positions of the first joint MCP^t and the second joint IP^t of thumb (t).

Forward and inverse kinematics of articulated systems study the analytical relationship between the angular positions of joints and the positions and orientations of the end-effectors (fingertips). A desired trajectory is usually specified in *Cartesian* space and the trajectory controller is easily performed in the *joint* space. Hence, to convert Cartesian trajectory planning to the joint space [13] is necessary. Using inverse kinematics, the joint angular positions of each finger need to be obtained from the known fingertip positions (*joint space*). Then the angular velocities and angular accelerations of joints can be obtained from the linear and angular velocities and accelerations of fingertips (end-effectors) by the *geometric Jocobian*. As shown in Figure 2, X^G, Y^G, and Z^G are the three axes of the global coordinate. The local coordinate x^t-y^t-z^t of the thumb can be reached by rotating through angles α and β to X^G and Y^G of the global coordinate, subsequently. The local coordinate x^i-y^i-z^i of index finger can be obtained by rotating through angle α to X^G and then translating the vector $\mathbf{d^i}$ of the global coordinate; similarly, the local coordinate x^j-y^j-z^j of middle finger ($j = m$), ring finger ($j = r$), and little finger ($j = l$) can be obtained by rotating through angle α to X^G and then translating the vector $\mathbf{d^j}$ ($j = m$, r and l) of the global coordinate. The inverse kinematics of two-link thumb and three-link fingers was discussed in our previous publications [5,6,11,12] for a two-fingered (thumb and index finger) smart prosthetic hand.

2.2 Dynamics of Hand

The dynamic equations of hand motion are derived via Lagrangian approach using kinetic energy and potential energy as [5]

$$\frac{d}{dt}\left(\frac{\partial \mathcal{L}}{\partial \dot{\mathbf{q}}}\right) - \frac{\partial \mathcal{L}}{\partial \mathbf{q}} = \boldsymbol{\tau}, \tag{1}$$

where $\mathcal{L}$ is the Lagrangian; $\dot{\mathbf{q}}$ and $\mathbf{q}$ represent the angular velocity and angle vectors of joints, respectively; $\boldsymbol{\tau}$ is the given torque vector at joints. The Lagrangian $\mathcal{L}$ can be expressed as

$$\mathcal{L} = T - V, \tag{2}$$

where T and V denote kinetic and potential energies, respectively. Substitute (2) into (1) and dynamic equations of thumb can be obtained as below.

$$\mathbf{M}(\mathbf{q})\ddot{\mathbf{q}} + \mathbf{C}(\mathbf{q}, \dot{\mathbf{q}}) + \mathbf{G}(\mathbf{q}) = \boldsymbol{\tau}, \tag{3}$$

where $\mathbf{M}(\mathbf{q})$ is the inertia matrix; $\mathbf{C}(\mathbf{q}, \dot{\mathbf{q}})$ is the Coriolis/centripetal vector and $\mathbf{G}(\mathbf{q})$ is the gravity vector. (3) can be also written as

$$\mathbf{M}(\mathbf{q})\ddot{\mathbf{q}} + \mathbf{N}(\mathbf{q}, \dot{\mathbf{q}}) = \boldsymbol{\tau}, \tag{4}$$

where $\mathbf{N}(\mathbf{q}, \dot{\mathbf{q}})$=$\mathbf{C}(\mathbf{q}, \dot{\mathbf{q}})$+$\mathbf{G}(\mathbf{q})$ represents nonlinear terms. The dynamic relations for the two-link thumb and the remaining three-link fingers are quite lengthy and omitted here due to lack of space [5].

3 Control Techniques

3.1 Feedback Linearization

The nonlinear dynamics represented by (4) is to be converted into a linear state-variable system by finding a transformation using feedback linearization technique [10]. Alternative state-space equations of the dynamics can be obtained by defining the position/velocity state $\mathbf{x}(t)$ of the joints as

$$\mathbf{x}(t) = \left[\mathbf{q}(t)' \;\; \dot{\mathbf{q}}(t)'\right]'. \tag{5}$$

Let us repeat the dynamical model and rewrite (4) as

$$\frac{d}{dt}\dot{\mathbf{q}}(t) = -\mathbf{M}(\mathbf{q}(t))^{-1}\left[\mathbf{N}(\mathbf{q}(t), \dot{\mathbf{q}}(t)) - \boldsymbol{\tau}(t)\right]. \tag{6}$$

Thus, from (5) and (6), we can derive a linear state-variable equation in *Brunovsky canonical form* as

$$\dot{\mathbf{x}}(t) = \begin{bmatrix} \mathbf{0} & \mathbf{I} \\ \mathbf{0} & \mathbf{0} \end{bmatrix} \mathbf{x}(t) + \begin{bmatrix} \mathbf{0} \\ \mathbf{I} \end{bmatrix} \mathbf{u}(t) \tag{7}$$

with its control input vector given by

$$\mathbf{u}(t) = -\mathbf{M}(\mathbf{q}(t))^{-1}\left[\mathbf{N}(\mathbf{q}(t), \dot{\mathbf{q}}(t)) - \boldsymbol{\tau}(t)\right]. \tag{8}$$

Let us suppose the prosthetic hand is required to track the desired trajectory $\mathbf{q}_d(t)$ described under path generation or tracking. Then, the tracking error $\mathbf{e}(t)$ is defined as

$$\mathbf{e}(t) = \mathbf{q}_d(t) - \mathbf{q}(t). \tag{9}$$

Here, $\mathbf{q}_d(t)$ is the *desired* angle vector of joints and can be obtained by trajectory planning [5, 6, 11, 12]; $\mathbf{q}(t)$ is the *actual* angle vector of joints. Differentiating (9) twice, to get

$$\dot{\mathbf{e}}(t) = \dot{\mathbf{q}}_d(t) - \dot{\mathbf{q}}(t), \quad \ddot{\mathbf{e}}(t) = \ddot{\mathbf{q}}_d(t) - \ddot{\mathbf{q}}(t). \tag{10}$$

Substituting (6) into (10) yields

$$\ddot{\mathbf{e}}(t) = \ddot{\mathbf{q}}_d(t) + \mathbf{M}(\mathbf{q}(t))^{-1}\left[\mathbf{N}(\mathbf{q}(t), \dot{\mathbf{q}}(t)) - \boldsymbol{\tau}(t)\right] \tag{11}$$

from which the control function can be defined as

$$\mathbf{u}(t) = \ddot{\mathbf{q}}_d(t) + \mathbf{M}(\mathbf{q}(t))^{-1}\left[\mathbf{N}(\mathbf{q}(t), \dot{\mathbf{q}}(t)) - \boldsymbol{\tau}(t)\right]. \tag{12}$$

This is often called the *feedback linearization* control law, which can also be inverted to express it as

$$\boldsymbol{\tau}(t) = \mathbf{M}(\mathbf{q}(t))\left[\ddot{\mathbf{q}}_\mathbf{d}(t) - \mathbf{u}(t)\right) + \mathbf{N}(\mathbf{q}(t), \dot{\mathbf{q}}(t)\right]. \tag{13}$$

Using the relations (10) and (12), and defining state vector $\mathbf{x}(t) = [\mathbf{e}(t)' \;\; \dot{\mathbf{e}}(t)']'$, the *tracking error dynamics* can be written as

$$\dot{\mathbf{x}}(t) = \begin{bmatrix} \mathbf{0} & \mathbf{I} \\ \mathbf{0} & \mathbf{0} \end{bmatrix} \mathbf{x}(t) + \begin{bmatrix} \mathbf{0} \\ \mathbf{I} \end{bmatrix} \mathbf{u}(t). \tag{14}$$

Note that this is in the form of a *linear* system such as

$$\dot{\mathbf{x}}(t) = \mathbf{A}\mathbf{x}(t) + \mathbf{B}\mathbf{u}(t). \tag{15}$$

3.2 Adaptive Control Technique

The tracking error $\mathbf{e}$ and the filtered tracking error $\mathbf{r}$ are defined as

$$\mathbf{e} = \mathbf{q_d} - \mathbf{q}, \tag{16}$$

$$\mathbf{r} = \dot{\mathbf{e}} + \boldsymbol{\Lambda}\mathbf{e}. \tag{17}$$

Here, $\mathbf{q_d}$ is the *desired* angle vector of joints; $\mathbf{q}$ is the *actual* angle vector of joints; $\boldsymbol{\Lambda}$ is the positive-definite diagonal gain matrix. The filtered error (17) ensures stability of the overall system so that the tracking error (16) is bounded. Figure 3 shows the block diagram of the adaptive controller. Here, the filtered signal $\mathbf{r}(t)$ is derived from the tracking error $\mathbf{e}(t)$ and the trajectory planner and is fed to the adaptive controller of the prosthetic hand.

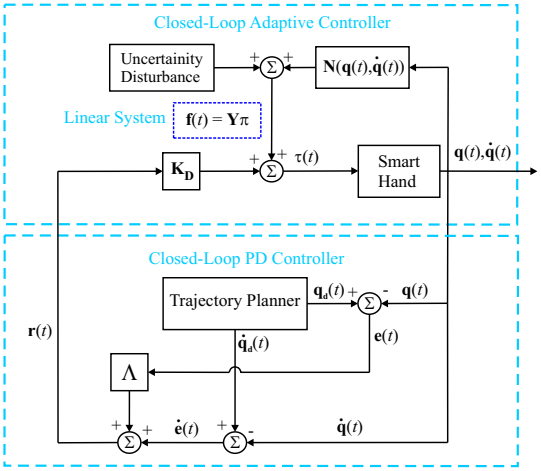

Figure 3: Block Diagram of Adaptive Control Technique

Differentiating and substituting (17) into (3) gives the dynamic equation in terms of the filtered error $\mathbf{r}$ as

$$\mathbf{M}(\mathbf{q})\dot{\mathbf{r}} = -\mathbf{C}_m(\mathbf{q}, \dot{\mathbf{q}})\mathbf{r} + \mathbf{f} - \boldsymbol{\tau} \tag{18}$$

where $\mathbf{C}(\mathbf{q}, \dot{\mathbf{q}}) = \mathbf{C}_m(\mathbf{q}, \dot{\mathbf{q}})\dot{\mathbf{q}}$ and the nonlinear term $\mathbf{f}$ can be defined as

$$\begin{aligned} \mathbf{f} &= \mathbf{M}(\mathbf{q})(\ddot{\mathbf{q}}_d + \boldsymbol{\Lambda}\dot{\mathbf{e}}) + \mathbf{C}_m(\mathbf{q}, \dot{\mathbf{q}})(\dot{\mathbf{q}}_d + \boldsymbol{\Lambda}\mathbf{e}) \\ &\quad + \mathbf{G}(\mathbf{q}) + \boldsymbol{\tau}_{dis} \\ &= \mathbf{Y}\boldsymbol{\pi}. \end{aligned} \tag{19}$$

Here, the regression matrix $\mathbf{Y}$ is a matrix of known robot functions and $\boldsymbol{\pi}$ is a vector of unknown parameters [9]. The regression matrix $\mathbf{Y}$ and the unknown parameter vector $\boldsymbol{\pi}$ of two-link thumb and three-link index finger are expressed in [5]. The torque vector $\boldsymbol{\tau}$ can be calculated by

$$\boldsymbol{\tau} = \mathbf{Y}\boldsymbol{\pi} + \mathbf{K_D}\mathbf{r}. \tag{20}$$

The unknown parameter rate vector $\dot{\boldsymbol{\pi}}$ can be updated by

$$\dot{\boldsymbol{\pi}} = \boldsymbol{\Gamma}^{-1}\mathbf{Y}'\mathbf{r} \tag{21}$$

where $\boldsymbol{\Gamma}$ is a tuning parameter diagonal matrix.

4 Simulation Results and Discussion

When thumb and the other four fingers are doing extension/flexion movements, the workspace of fingertips is restricted to the maximum angles of joints. Referring to inverse kinematics, the first and second joint angles of the thumb fingertip are constrained in the ranges of [0,90] and [-80,0] (degrees). The first, second, and third joint angles of the other four fingers are constrained in the ranges of [0,90], [0,110] and [0,80] (degrees), respectively [14]. Next, we present simulations with an adaptive controller for the 14 DOFs five-fingered smart prosthetic hand. The parameters of the two-link thumb/three-link index finger [15] were related to desired trajectory. All parameters of the smart prosthetic hand selected for the simulations are given in Table 1 and the side length and length of the target rectangular rod are 0.010 and 0.100 (m), respectively. The relating parameters between the global coordinate and the local coordinates are defined in Table 2. Besides, all links are assumed as a circular cylinder with the radius (R) 0.010 (m), so the inertia I^j_{zzk} of each link k of each finger j (j = t, i, m, r, and l) can be calculated as

$$I^j_{zzk} = \frac{1}{4}m^j_k R^2 + \frac{1}{3}m^j_k {L^j_k}^2. \tag{22}$$

All initial actual angles are zero.

Figure 4 to Figure 8 are the tracking errors and desired/actual angles of thumb, index finger, middle finger, ring finger, and little finger for the proposed five-fingered smart prosthetic hand.

Table 1: Parameter Selection of the Smart Hand

Parameters	Values
Thumb	
Time (t_0,t_f)*	0, 20 (sec)
Desired Initial Position**	0.035, 0.060 (m)
Desired Final Position**	0.0495, 0.060 (m)
Desired Initial Velocity*	0, 0 (m/s)
Desired Final Velocity*	0, 0 (m/s)
Length	0.04, 0.04 (m)
Index Finger	
Desired Initial Position**	0.065, 0.080 (m)
Desired Final Position**	0.010, 0.060 (m)
Length	0.04, 0.04, 0.03 (m)
Middle Finger	
Desired Initial Position**	0.065, 0.080 (m)
Desired Final Position**	0.005, 0.060 (m)
Length	0.04, 0.04, 0.03 (m)
Ring Finger	
Desired Initial Position**	0.065, 0.080 (m)
Desired Final Position**	0.010, 0.060 (m)
Length	0.04, 0.04, 0.03 (m)
Little Finger	
Desired Initial Position**	0.055, 0.080 (m)
Desired Final Position**	0.020, 0.060 (m)
Length	0.04, 0.04, 0.03 (m)

*All fingers use same parameters
**Local coordinates

5 Conclusions and Future Work

An adaptive control strategy was developed for the 14 degrees of freedom (DOFs), five-fingered smart prosthetic hand with unknown mass and inertia of all the fingers. Further, the forward and inverse kinematics of the system regarding the analytical relationship between the angular positions of joints and the positions and orientations of the end-effectors (fingertips), was obtained using a desired orientation for three-link fingers. The simulations of for the resulting adaptive controller with five-fingered prosthetic hand showed good agreement between the reference and the actual trajectories. Work is in progress for developing an adaptive/robust controller for the five fingered hand with 14-DOFs.

Acknowledgements: The financial support for this research from the Telemedicine Advanced Technology Research Center (TATRC) of the U.S. Department of Defense (DoD) is gratefully acknowledged.

References:

[1] M. Zecca, S. Micera, M. Carrozza, and P. Dario, "Control of multifunctional prosthetic hands by processing the electromyographic signal," *Critical Reviews^{TM} in Biomedical Engineering*, vol. 30, pp. 459–485, 2002, (Review article with 96 references).

[2] J. C. K. Lai, M. P. Schoen, A. Perez-Gracia, D. S. Naidu, and S. W. Leung, "Prosthetic devices: Challenges and implications of robotic implants and biological interfaces," *Proceedings of the Institute of Mechanical Engineers*

Table 2: Parameter Selection of the Relation between Global and Local Coordinates

Parameters	Values
α	90 (degrees)
β	45 (degrees)
$\mathbf{d^i}$	(0.035, 0, 0) (m)
$\mathbf{d^m}$	(0.040, 0, -0.020) (m)
$\mathbf{d^r}$	(0.035, 0, -0.040) (m)
$\mathbf{d^l}$	(0.025, 0, -0.060) (m)

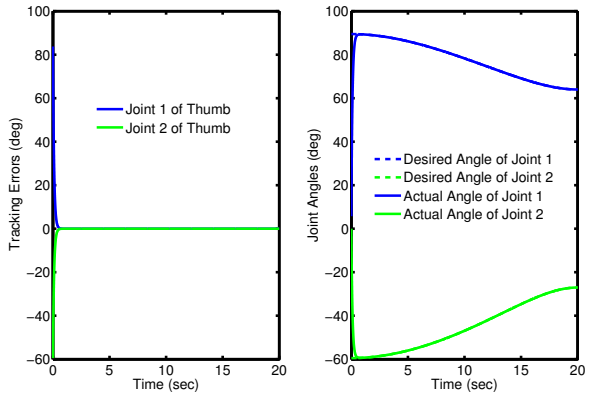

Figure 4: Tracking Errors (left) and Joint Angles (right) for Adaptive Controller of Thumb

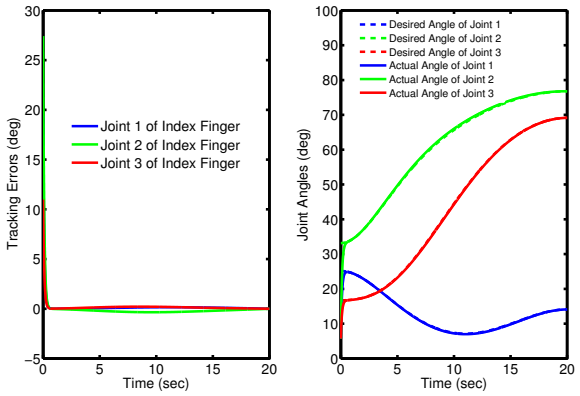

Figure 5: Tracking Errors (left) and Joint Angles (right) for Adaptive Controller of Index Finger

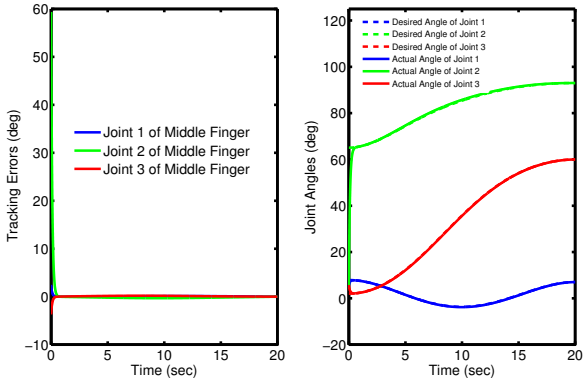

Figure 6: Tracking Errors (left) and Joint Angles (right) for Adaptive Controller of Middle Finger

(IMechE), Part H: Journal of Engineering in Medicine, vol. 221, no. 2, pp. 173–183, January 2007, special Issue on Micro and Nano Technologies in Medicine.

[3] L. Zollo, S. Roccella, E. Guglielmelli, M. C. Carrozza, and P. Dario, "Biomechatronic design and control of an anthropomorphic artificial hand for prosthetic and robotic applications," *IEEE/ASME Transactions on Mechatronics*, vol. 12, no. 4, pp. 418–429, August 2007.

[4] D. S. Naidu, C.-H. Chen, A. Perez, and M. P. Schoen, "Control strategies for smart prosthetic hand technology: An overview," in *Proceedings of the 30th Annual International IEEE EMBS Conference*, Vancouver, Canada, August 20-24 2008, pp. 4314–4317.

[5] C.-H. Chen, "Hybrid control strategies for smart prosthetic hand," Ph.D. dissertation, Measurement and Control Engineering, Idaho State University, May 2009.

[6] C.-H. Chen, D. S. Naidu, A. Perez, and M. P. Schoen, "Fusion of hard and soft control techniques for prosthetic hand," in *Proceedings of the International Association of Science and Technology for Development (IASTED) International Conference on Intelligent Systems and Control (ISC 2008)*, Orlando, Florida, USA, November 16-18 2008, pp. 120–125.

[7] D. Naidu, *Optimal Control Systems*. Boca Raton, FL: CRC Press, 2003.

[8] C.-H. Chen, D. S. Naidu, A. Perez-Gracia, and M. P. Schoen, "A hybrid control strategy for five-fingered smart prosthetic hand," in *Joint 48th IEEE Conference on Decision and Control (CDC) and 28th Chinese Control Conference (CCC)*, Shanghai, P. R. China, December 16-18 2009, pp. 5102–5107.

[9] F. Lewis, S. Jagannathan, and A. Yesildirek, *Neural Network Control of Robotic Manipulators and Nonlinear Systems*. London, UK: Taylor & Francis, 1999.

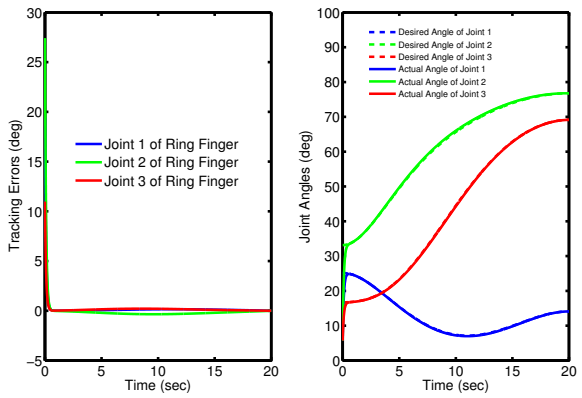

Figure 7: Tracking Errors (left) and Joint Angles (right) for Adaptive Controller of Ring Finger

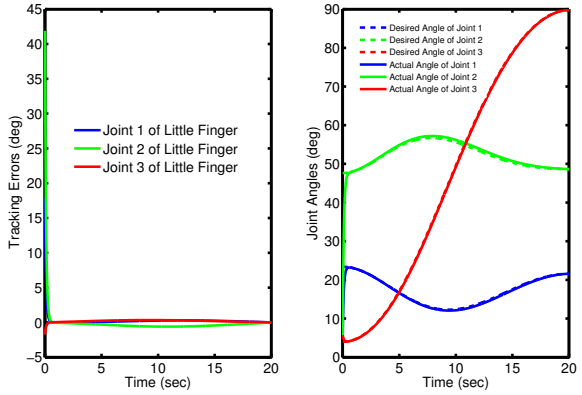

Figure 8: Tracking Errors (left) and Joint Angles (right) for Adaptive Controller of Little Finger

[10] F. Lewis, D. Dawson, and C. Abdallah, *Robot Manipulators Control: Second Edition, Revised and Expanded*. New York, NY: Marcel Dekker, Inc.,, 2004.

[11] C.-H. Chen, D. S. Naidu, A. Perez-Gracia, and M. P. Schoen, "A hybrid adaptive control strategy for a smart prosthetic hand," in *The 31st Annual International Conference of the IEEE Engineering Medicine and Biology Society (EMBS)*, Minneapolis, Minnesota, USA, September 2-6 2009, pp. 5056–5059.

[12] C.-H. Chen, D. Naidu, A. Perez-Gracia, and M. P. Schoen, "A hybrid optimal control strategy for a smart prosthetic hand," in *Proceedings of the ASME 2009 Dynamic Systems and Control Conference (DSCC)*, Hollywood, California, USA, October 12-14 2009, (No. DSCC2009-2507).

[13] B. Siciliano, L. Sciavicco, L. Villani, and G. Oriolo, *Robotics: Modelling, Planning and Control*. London, UK: Springer-Verlag, 2009.

[14] P. K. Lavangie and C. C. Norkin, *Joint Structure and Function: A Comprehensive Analysis, Third Edition*. Philadelphia, PA: F. A. Davis Company, 2001.

[15] S. Arimoto, *Control Theory of Multi-fingered Hands: A Modeling and Analytical-Mechanics Approach for Dexterity and Intelligence*. London, UK: Springer-Verlag, 2008.

Proceedings of the IASTED International Conference
Robotics and Applications (RA 2010)
November 1 - 3, 2010 Cambridge, Massachusetts, USA

OPTIMAL CONTROL STRATEGY FOR TWO-FINGERED SMART PROSTHETIC HAND

Cheng-Hung Chen
Measurement and Control
Engineering Research Center
Department of Biological Sciences
College of Science and Engineering
Idaho State University
Pocatello, Idaho 83209, USA
Email: chenchen@isu.edu

D. Subbaram Naidu
Measurement and Control
Engineering Research Center
Department of Electrical Engineering
School of Engineering
Idaho State University
Pocatello, Idaho 83209, USA
Email: naiduds@isu.edu

ABSTRACT
This paper addresses the optimal control for a two-fingered (thumb and index finger) prosthetic hand. To speed up the performance and improve the accuracy, we modified the performance index by including an exponential term. First, we developed the differential kinematics for a serial n-link revolute-joint planar manipulator to computer the angular velocities and angular accelerations of each finger. Further, the trajectory planning of the orientation was designed by using cubic polynomial. Simulations show that the proposed technique provides fast action with high accuracy and 30-fold faster than ANFIS or GA based trajectory planning.

KEY WORDS
Prosthetic Hand, Optimal Control, Stability, ANFIS

1 Introduction

Hard control (HC) techniques comprise proportional-integral-derivative (PID) control [1–3], optimal control [4–6], adaptive control [7–9] etc. with specific applications to prosthetic devices. However, our previous works [2, 3] for smart prosthetic hand showed that PID controller results in overshooting and oscillation. Optimal controller can obtain a high performance [5,6]. However, this control technique takes time to be convergent. To overcome the overshooting and convergent problems, studying the stability of the optimal controller is precisely the main goal of this work. In addition, the adaptive neuro-fuzzy inference system (ANFIS) and genetic algorithm (GA) based trajectory planning [5, 6, 10] take much time to train the neural layers, especially for high degree-of-freedom (DOF) problems. To improve the performance, it is also the goal of this paper.

In this paper, we first consider briefly forward kinematics and inverse kinematics for a serial n-link revolute-joint planar manipulator and two-link thumb and three-link index finger, respectively. Then, by using differential kinematics, the angular velocities and angular accelerations of a serial n-link revolute-joint planar manipulator are derived. Moreover, the trajectory planning of the orientation is designed by using cubic polynomial. The dynamic models of the smart prosthetic hand and linearization technique were briefly introduced. Finally, the stability of finite-time linear quadratic optimal controller are investigated by changing cost function J. The simulation results show the presented technique can be fast convergence and hold the high performance for the two-fingered smart prosthetic hand.

2 Modeling

Forward and inverse kinematics of articulated systems study the analytical relationship between the angular positions of joints and the positions and orientations of the end-effectors (fingertips). A desired trajectory is usually specified in *Cartesian* space and the trajectory controller is easily performed in the *joint* space. Hence, conversion of Cartesian trajectory planning to the joint space [11] is necessary. Using inverse kinematics, the joint angular positions of each finger need to be obtained from the known fingertip positions. Then the angular velocities and angular accelerations of joints can be obtained from the linear and angular velocities and accelerations of fingertips (end-effectors) by differential kinematics. The inverse kinematics of two-link thumb and three-link fingers were discussed in our previous publications [2,3,6,10,12] for a two-fingered (thumb and index finger) smart prosthetic hand. Here, we derive the general form of forward and differential kinematics for a serial n-link revolute-joint planar manipulator.

2.1 Forward Kinematics

Figure 1 shows the illustration of a serial n-link revolute-joint planar manipulator. L_i is the length of the link i and q_i is the angle of the joint i ($i = 1, 2, \cdots, n$). τ_i is the actuator of the joint i. The position $\mathbf{P}_n\ (X_n, Y_n)$ of the end-effector and the orientation ϕ_n of the end-effector frame have been

DOI: 10.2316/P.2010.706-014

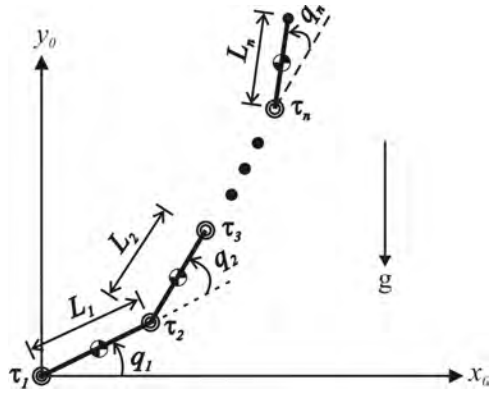

Figure 1. Illustration of a Serial n-Link Revolute-Joint Planar Manipulator

derived [12] as

$$X_n = \sum_{j=1}^{n} L_j \cos\left(\sum_{i=1}^{j} q_i\right),$$

$$Y_n = \sum_{j=1}^{n} L_j \sin\left(\sum_{i=1}^{j} q_i\right),$$

$$\phi_n = \sum_{i=1}^{n} q_i. \quad (1)$$

2.2 Inverse Kinematics

2.2.1 Two-Link Thumb

As shown in Figure 2, thumb is assumed as the two-link ($n = 2$) finger and the other four fingers, such as index finger, middle finger, ring finger, and little finger, are considered as three-link fingers. Hence, the angular positions, angular velocities, and angular accelerations of each finger can be deduced as follows. According to equation (1), the

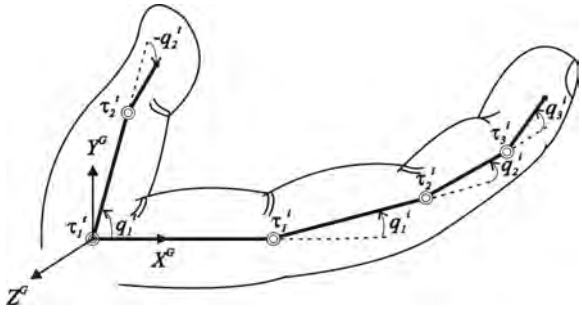

Figure 2. Schematic Diagram of Thumb and Index Finger

fingertip coordinate (X^t,Y^t) of thumb (t) can be described as

$$X^t = L_1^t cos(q_1^t) + L_2^t cos(q_1^t + q_2^t), \quad (2)$$

$$Y^t = L_1^t sin(q_1^t) + L_2^t sin(q_1^t + q_2^t). \quad (3)$$

Here L_1^t and L_2^t are the lengths of the links 1 and 2 of the thumb, respectively; q_1^t and q_2^t are the angular positions (or called angles) of joints 1 and 2 of the thumb. Choosing the *elbow up* configuration, the angle q_2^t of the joint 2 can be obtained from [11]

$$q_2^t = -\cos^{-1}\left(\frac{X^{t2} + Y^{t2} - {L_1^t}^2 - {L_2^t}^2}{2L_1^t L_2^t}\right). \quad (4)$$

Notice that in this paper, all positive angles are defined counterclockwise. When choosing the *elbow up* configuration, the angle q_2^t is clockwise, so the sign of q_2^t is negative. Based on the geometry, we can get

$$q_1^t = \tan^{-1}\left(\frac{Y^t}{X^t}\right) - \tan^{-1}\left(\frac{L_2^t \sin(q_2^t)}{L_1^t + L_2^t \cos(q_2^t)}\right). \quad (5)$$

2.2.2 Three-Link Index Finger

Figure 3 shows the illustration of three-link ($n = 3$) index

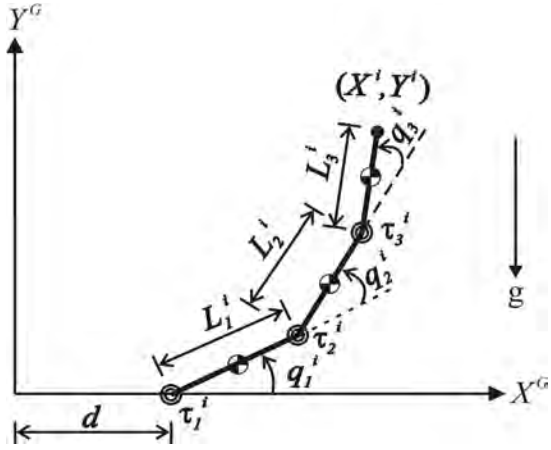

Figure 3. Three-Link Index Finger Illustration

finger. d is the distance between the global (G) frame and index finger (i) local frame base (zero); L_1^i, L_2^i, and L_3^i are the lengths of the links 1, 2 and 3 of the index finger (i), respectively; q_1^i, q_2^i, and q_3^i are the angles of the joints 1, 2, and 3 of the index finger. Using *Denavit-Hartenberg* (DH) [11–15] transformation matrices, the fingertip (end-effector) coordinate $\mathbf{P}^i$ (X^i, Y^i) and the orientation ϕ^i of the index finger (i) can be written as

$$X^i = d + L_1^i \cos(q_1^i) + L_2^i \cos(q_1^i + q_2^i) + L_3^i \cos(\phi^i),$$

$$Y^i = L_1^i \sin(q_1^i) + L_2^i \sin(q_1^i + q_2^i) + L_3^i \sin(\phi^i),$$

$$\phi^i = q_1^i + q_2^i + q_3^i. \quad (6)$$

The local coordinate $\mathbf{P}_2^i$ (X_2^i, Y_2^i) of the joint 2 can be obtained as

$$\begin{aligned} X_2^i &= X^i - L_3^i \cos(\phi^i) - d, \\ Y_2^i &= Y^i - L_3^i \sin(\phi^i). \end{aligned} \tag{7}$$

Choosing the *elbow down* configuration, the angles q_2^i and q_1^i can be obtained as

$$q_2^i = \cos^{-1}\left(\frac{{X_2^i}^2 + {Y_2^i}^2 - {L_1^i}^2 - {L_2^i}^2}{2L_1^i L_2^i}\right),$$

$$q_1^i = \tan^{-1}\left(\frac{Y^i}{X^i}\right) - \tan^{-1}\left(\frac{L_2^i \sin(q_2^i)}{L_1^i + L_2^i \cos(q_2^i)}\right). \tag{8}$$

Then we can get the angle q_3^i of the joint 3 as

$$q_3^i = \phi^i - q_1^i - q_2^i. \tag{9}$$

2.3 Differential Kinematics

The *linear* velocity ${}^0\dot{\mathbf{P}}_n$ and *angular* velocity ${}^0\boldsymbol{\omega}_n$ of the origin of the end-effector frame are linear relations to the joint angular velocities $\dot{\mathbf{q}}$ [12]. The *linear* relation represents the differential kinematics equation and can be expressed as

$${}^0\mathbf{V}_n = \mathbf{J}(\mathbf{q})\ \dot{\mathbf{q}}. \tag{10}$$

Here, ${}^0\mathbf{V}_n = [{}^0\dot{\mathbf{P}}_n \quad {}^0\boldsymbol{\omega}_n]'$ is the (6×1) end-effector velocity vector. $\mathbf{J}(\mathbf{q}) = [\mathbf{J_P}(\mathbf{q}) \quad \mathbf{J_O}(\mathbf{q})]'$ is the $(6 \times n)$ geometric Jacobian matrix of a serial n-link revolute-joint planar manipulator; both position Jacobian $\mathbf{J_P}(\mathbf{q})$ and orientation Jacobian $\mathbf{J_O}(\mathbf{q})$ are the $(3 \times n)$ matrices which contribute the joint angular velocities $\dot{\mathbf{q}}$ to the linear velocity ${}^0\dot{\mathbf{P}}_n$ and angular velocity ${}^0\boldsymbol{\omega}_n$ of the end-effector, respectively. The entry J_{ij} $(i, j \in N)$ of the geometric Jacobian $\mathbf{J}(\mathbf{q})$ in (10) can be rewritten as

$$J_{ij} = \begin{cases} -\sum_{j=1}^{n} L_j \sin\left(\sum_{k=1}^{j} q_k\right) & \text{if } i = 1, j \in [1,6]; \\ \sum_{j=1}^{n} L_j \cos\left(\sum_{k=1}^{j} q_k\right) & \text{if } i = 2, j \in [1,6]; \\ 0 & \text{if } i \in [3,5], j \in [1,6]; \\ 1 & \text{if } i = 6, j \in [1,6]. \end{cases}$$

Then, the angular velocities $\dot{\mathbf{q}}$ can be written as

$$\dot{\mathbf{q}} = \mathbf{J}^{-1}(\mathbf{q})\ {}^0\mathbf{V}_n. \tag{11}$$

Similarly, the angular accelerations $\ddot{\mathbf{q}}$ can be obtained as

$$\ddot{\mathbf{q}} = \mathbf{J}^{-1}(\mathbf{q})\left({}^0\mathbf{A}_n - \dot{\mathbf{J}}(\mathbf{q})\dot{\mathbf{q}}\right). \tag{12}$$

Here, ${}^0\mathbf{A}_n = [{}^0\ddot{\mathbf{P}}_n \quad {}^0\boldsymbol{\alpha}_n]'$ is the (6×1) end-effector acceleration vector, including linear acceleration ${}^0\ddot{\mathbf{P}}_n$ and angular acceleration ${}^0\boldsymbol{\alpha}_n$. The differential Jacobian $\dot{\mathbf{J}}(\mathbf{q})$ can be also written as

$$\dot{J}_{ij} = \begin{cases} -\sum_{j=1}^{n} L_j \cos\left(\sum_{k=1}^{j} q_k\right)\left(\sum_{k=1}^{j} \dot{q}_k\right) & \text{if } i = 1, j \in [1,6]; \\ -\sum_{j=1}^{n} L_j \sin\left(\sum_{k=1}^{j} q_k\right)\left(\sum_{k=1}^{j} \dot{q}_k\right) & \text{if } i = 1, j \in [1,6]; \\ 0 & \text{if } i \in [3,6], j \in [1,6]. \end{cases}$$

2.4 Trajectory Planning

The trajectory planning using cubic polynomial for fingertip position control was discussed in our previous work [2, 3, 6, 10, 12] for a two-fingered (thumb and index finger) smart prosthetic hand. For the three-link index finger, we present the same technique for fingertip orientation control. A time history of desired (d) fingertip orientation (ϕ) and its differentiation $(\dot{\phi}$ and $\ddot{\phi})$ is given as

$$\phi_d^j(t) = \omega_0 + \omega_1 t + \omega_2 t^2 + \omega_3 t^3, \tag{13}$$

$$\dot{\phi}_d^j(t) = \omega_1 + 2\omega_2 t + 3\omega_3 t^2, \tag{14}$$

$$\ddot{\phi}_d^j(t) = 2\omega_2 + 6\omega_3 t, \tag{15}$$

where ω_0-ω_3 are undetermined constants and the superscript j indicates the index of each finger ($j = i$, m, r and l). The relations (13) and (14) need to satisfy the constraint conditions at initial time t_0 and final time t_f. This can be written as

$$\mathbf{T}\ \boldsymbol{\Omega} = \boldsymbol{\Phi}. \tag{16}$$

Here, the matrices $\mathbf{T}$, $\boldsymbol{\Omega}$, and $\boldsymbol{\Phi}$ are

$$\mathbf{T} = \begin{bmatrix} 1 & t_0 & t_0^2 & t_0^3 \\ 0 & 1 & 2t_0 & 3t_0^2 \\ 1 & t_f & t_f^2 & t_f^3 \\ 0 & 1 & 2t_f & 3t_f^2 \end{bmatrix}, \tag{17}$$

$$\boldsymbol{\Omega} = \begin{bmatrix} \omega_0 & \omega_1 & \omega_2 & \omega_3 \end{bmatrix}', \tag{18}$$

$$\boldsymbol{\Phi} = \begin{bmatrix} \phi_0^j & \dot{\phi}_0^j & \phi_f^j & \dot{\phi}_f^j \end{bmatrix}'. \tag{19}$$

Therefore, the 4 unknown constants, ω_0-ω_3, can be computed by $\boldsymbol{\Omega} = \mathbf{T}^{-1}\boldsymbol{\Phi}$.

2.5 Dynamics of Hand

The dynamic equations of hand motion are derived via Lagrangian approach using kinetic energy and potential energy as [8, 11, 12, 14, 15]

$$\frac{d}{dt}\left(\frac{\partial \mathcal{L}}{\partial \dot{\mathbf{q}}}\right) - \frac{\partial \mathcal{L}}{\partial \mathbf{q}} = \boldsymbol{\tau}, \tag{20}$$

where $\mathcal{L}$ is the Lagrangian; $\dot{\mathbf{q}}$ and $\mathbf{q}$ represent the angular velocity and angle vectors of joints, respectively; $\boldsymbol{\tau}$ is the given torque vector at joints. The Lagrangian $\mathcal{L}$ can be expressed as

$$\mathcal{L} = T - V, \tag{21}$$

where T and V denote kinetic and potential energies, respectively. Substituting (21) into (20), dynamic equations can be obtained as below.

$$\mathbf{M}(\mathbf{q})\ddot{\mathbf{q}} + \mathbf{C}(\mathbf{q}, \dot{\mathbf{q}}) + \mathbf{G}(\mathbf{q}) = \boldsymbol{\tau}, \tag{22}$$

where $\mathbf{M}(\mathbf{q})$ is the inertia matrix; $\mathbf{C}(\mathbf{q}, \dot{\mathbf{q}})$ is the Coriolis/centripetal vector and $\mathbf{G}(\mathbf{q})$ is the gravity vector. (22) can be also written as

$$\mathbf{M}(\mathbf{q})\ddot{\mathbf{q}} + \mathbf{N}(\mathbf{q}, \dot{\mathbf{q}}) = \boldsymbol{\tau}, \tag{23}$$

where $\mathbf{N}(\mathbf{q}, \dot{\mathbf{q}}) = \mathbf{C}(\mathbf{q}, \dot{\mathbf{q}}) + \mathbf{G}(\mathbf{q})$ represents nonlinear terms. The dynamic relations for the two-link thumb and the three-link index finger are quite lengthy and omitted here due to lack of space [12, 16, 17].

3 Control Techniques

3.1 Feedback Linearization

The nonlinear dynamics represented by (23) is to be converted into a linear state-variable system using feedback linearization technique [8]. Alternative state-space equations of the dynamics can be obtained by defining the position/velocity state $\mathbf{x}(t)$ of the joints as

$$\mathbf{x}(t) = [\mathbf{q}'(t) \quad \dot{\mathbf{q}}'(t)]'. \tag{24}$$

Let us repeat the dynamical model and rewrite (23) as

$$\frac{d}{dt}\dot{\mathbf{q}}(t) = -\mathbf{M}^{-1}(\mathbf{q}(t))\left[\mathbf{N}(\mathbf{q}(t), \dot{\mathbf{q}}(t)) - \boldsymbol{\tau}(t)\right]. \tag{25}$$

Thus, from (24) and (25), we can derive a linear system in *Brunovsky canonical form* as

$$\dot{\mathbf{x}}(t) = \begin{bmatrix} \mathbf{0} & \mathbf{I} \\ \mathbf{0} & \mathbf{0} \end{bmatrix} \mathbf{x}(t) + \begin{bmatrix} \mathbf{0} \\ \mathbf{I} \end{bmatrix} \mathbf{u}(t) \tag{26}$$

with its control input vector given by

$$\mathbf{u}(t) = -\mathbf{M}^{-1}(\mathbf{q}(t))\left[\mathbf{N}(\mathbf{q}(t), \dot{\mathbf{q}}(t)) - \boldsymbol{\tau}(t)\right]. \tag{27}$$

Let us suppose the prosthetic hand is required to track the desired trajectory $\mathbf{q}_d(t)$ described under path generation or tracking. Then, the tracking error $\mathbf{e}(t)$ is defined as

$$\mathbf{e}(t) = \mathbf{q}_d(t) - \mathbf{q}(t). \tag{28}$$

Here, $\mathbf{q}_d(t)$ is the *desired* angle vector of joints and can be obtained by trajectory planning [2, 3, 6, 10, 12]; $\mathbf{q}(t)$ is the *actual* angle vector of joints. Differentiating (28) twice, to get

$$\dot{\mathbf{e}}(t) = \dot{\mathbf{q}}_d(t) - \dot{\mathbf{q}}(t), \quad \ddot{\mathbf{e}}(t) = \ddot{\mathbf{q}}_d(t) - \ddot{\mathbf{q}}(t). \tag{29}$$

Substituting (25) into (29) yields

$$\ddot{\mathbf{e}}(t) = \ddot{\mathbf{q}}_d(t) + \mathbf{M}^{-1}(\mathbf{q}(t))\left[\mathbf{N}(\mathbf{q}(t), \dot{\mathbf{q}}(t)) - \boldsymbol{\tau}(t)\right] \tag{30}$$

from which the control function can be defined as

$$\mathbf{u}(t) = \ddot{\mathbf{q}}_d(t) + \mathbf{M}^{-1}(\mathbf{q}(t))\left[\mathbf{N}(\mathbf{q}(t), \dot{\mathbf{q}}(t)) - \boldsymbol{\tau}(t)\right]. \tag{31}$$

This is often called the *feedback linearization* control law, which can also be inverted to express it as

$$\boldsymbol{\tau}(t) = \mathbf{M}(\mathbf{q}(t))\left[\ddot{\mathbf{q}}_d(t) - \mathbf{u}(t)\right) + \mathbf{N}(\mathbf{q}(t), \dot{\mathbf{q}}(t)\right]. \tag{32}$$

Using the relations (29) and (31), and defining state vector $\mathbf{x}(t) = [\mathbf{e}'(t) \quad \dot{\mathbf{e}}'(t)]'$, the *tracking error dynamics* can be written as

$$\dot{\mathbf{x}}(t) = \begin{bmatrix} \mathbf{0} & \mathbf{I} \\ \mathbf{0} & \mathbf{0} \end{bmatrix} \mathbf{x}(t) + \begin{bmatrix} \mathbf{0} \\ \mathbf{I} \end{bmatrix} \mathbf{u}(t). \tag{33}$$

Note that this is in the form of a *linear* system such as

$$\dot{\mathbf{x}}(t) = \mathbf{A}\mathbf{x}(t) + \mathbf{B}\mathbf{u}(t). \tag{34}$$

3.2 Finite-Time Linear Quadratic Optimal Control

Figure 4 shows the block diagram of finite-time linear

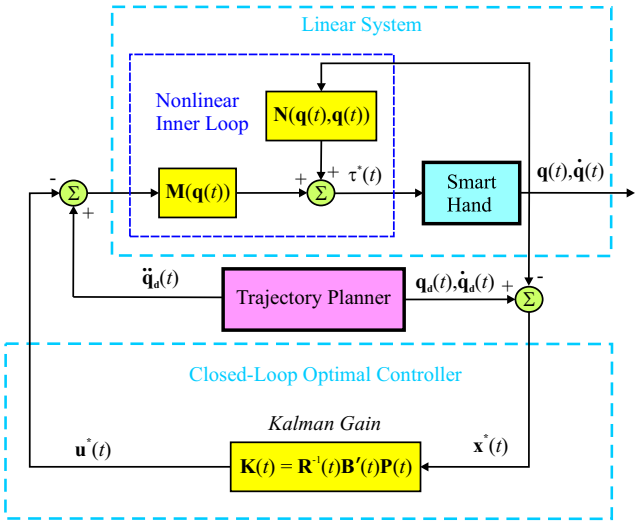

Figure 4. Block Diagram of Hybrid Optimal Controller for Prosthetic Hand

quadratic optimal controller for prosthetic hand. For the linear system (34), we can formulate the well-known finite-time linear quadratic optimal control problem by defining a performance index J [4] such as

$$J = \frac{1}{2}\mathbf{x}'(t_f)\mathbf{F}(t_f)\mathbf{x}(t_f) + \frac{1}{2}\int_{t_0}^{t_f}\left[\mathbf{x}'(t)\mathbf{Q}(t)\mathbf{x}(t) + \mathbf{u}'(t)\mathbf{R}(t)\mathbf{u}(t)\right]dt \tag{35}$$

where the terminal cost matrix $\mathbf{F}(t_f)$ and the error weighted matrix $\mathbf{Q}(t)$ are positive *semidefinite* matrices, respectively; the control weighted matrix $\mathbf{R}(t)$ is a positive *definite* matrix. The optimal control $\mathbf{u}^*(t)$ is given by

$$\mathbf{u}^*(t) = -\mathbf{R}^{-1}(t)\mathbf{B}'\mathbf{P}(t)\mathbf{x}^*(t) = -\mathbf{K}(t)\mathbf{x}^*(t). \tag{36}$$

Here, $\mathbf{K}(t) = \mathbf{R}^{-1}(t)\mathbf{B}'\mathbf{P}(t)$ is called *Kalman gain* and $\mathbf{P}(t)$, the symmetric *positive definite* matrix (for all $t \in [t_0, t_f]$), is the solution of the matrix differential Riccati equation (DRE)

$$\dot{\mathbf{P}}(t) = -\mathbf{P}(t)\mathbf{A} - \mathbf{A}'\mathbf{P}(t) - \mathbf{Q}(t) + \mathbf{P}(t)\mathbf{B}\mathbf{R}^{-1}(t)\mathbf{B}'\mathbf{P}(t) \quad (37)$$

satisfying the *final* condition

$$\mathbf{P}(t = t_f) = \mathbf{F}(t_f). \quad (38)$$

The optimal state $\mathbf{x}^*$ is the solution of

$$\dot{\mathbf{x}}^*(t) = \left[\mathbf{A} - \mathbf{B}\mathbf{R}^{-1}(t)\mathbf{B}'\mathbf{P}(t)\right]\mathbf{x}^*(t). \quad (39)$$

Therefore, the required torque $\boldsymbol{\tau}^*(t)$ can be calculated by the optimal control $\mathbf{u}^*(t)$.

$$\boldsymbol{\tau}^*(t) = \mathbf{M}(\mathbf{q}(t))(\ddot{\mathbf{q}}_d(t) - \mathbf{u}^*(t)) + \mathbf{N}(\mathbf{q}(t), \dot{\mathbf{q}}(t)). \quad (40)$$

3.3 The Stability of Finite-Time Optimal Control

Our previous work [5, 6, 12] shows optimal control can avoid overshooting and get better results than PID control, but the regular optimal control takes time to be convergent. To study the convergent stability of the optimal control, we modify the performance index J [4] as

$$\begin{aligned} J &= \frac{1}{2}\mathbf{x}'(t_f)\mathbf{F}(t_f)\mathbf{x}(t_f) + \\ &\quad \frac{1}{2}\int_{t_0}^{t_f} e^{2\alpha t}\left[\mathbf{x}'(t)\mathbf{Q}(t)\mathbf{x}(t) + \mathbf{u}'(t)\mathbf{R}(t)\mathbf{u}(t)\right]dt, \end{aligned} \quad (41)$$

where α is a positive parameter. To find the optimal control which minimizes the performance index (41) under the dynamical constraint (34). This problem can be solved by changing the previous system, so the following transformations can be developed as

$$\hat{\mathbf{x}}(t) = e^{\alpha t}\mathbf{x}(t); \qquad \hat{\mathbf{u}}(t) = e^{\alpha t}\mathbf{u}(t). \quad (42)$$

Then, using the transformations (42), it is easy to see that the *modified* system becomes

$$\begin{aligned} \dot{\hat{\mathbf{x}}}(t) = \frac{d}{dt}\{e^{\alpha t}\mathbf{x}(t)\} &= \alpha e^{\alpha t}\mathbf{x}(t) + e^{\alpha t}\dot{\mathbf{x}}(t) \\ &= \alpha\hat{\mathbf{x}}(t) + e^{\alpha t}[\mathbf{A}\mathbf{x}(t) + \mathbf{B}\mathbf{u}(t)] \\ \dot{\hat{\mathbf{x}}}(t) &= (\mathbf{A} + \alpha\mathbf{I})\hat{\mathbf{x}}(t) + \mathbf{B}\hat{\mathbf{u}}(t). \end{aligned} \quad (43)$$

Considering the minimization of the modified system (43) and the performance index (41), we see that the optimal control [4] is given by

$$\hat{\mathbf{u}}^*(t) = -\mathbf{R}^{-1}\mathbf{B}'\bar{\mathbf{P}}\hat{\mathbf{x}}^*(t) = -\bar{\mathbf{K}}\hat{\mathbf{x}}^*(t), \quad (44)$$

where $\bar{\mathbf{K}} = \mathbf{R}^{-1}\mathbf{B}'\bar{\mathbf{P}}$ and the matrix $\bar{\mathbf{P}}$ is the positive definite, symmetric solution of the algebraic Riccati equation

$$\bar{\mathbf{P}}(\mathbf{A} + \alpha\mathbf{I}) + (\mathbf{A}' + \alpha\mathbf{I})\bar{\mathbf{P}} - \bar{\mathbf{P}}\mathbf{B}\mathbf{R}^{-1}\mathbf{B}'\bar{\mathbf{P}} + \mathbf{Q} = 0. \quad (45)$$

Using the optimal control (44) in the modified system (43), we get the optimal closed-loop system as

$$\dot{\hat{\mathbf{x}}}^*(t) = (\mathbf{A} + \alpha\mathbf{I} - \mathbf{B}\mathbf{R}^{-1}\mathbf{B}'\bar{\mathbf{P}})\hat{\mathbf{x}}^*(t). \quad (46)$$

Hence, applying the transformations (43) in the modified system (44), the optimal control of the original system (34) and the associated performance measure (41) is given by

$$\begin{aligned} \mathbf{u}^*(t) &= e^{-\alpha t}\hat{\mathbf{u}}^*(t) = -e^{-\alpha t}\mathbf{R}^{-1}\mathbf{B}'\bar{\mathbf{P}}e^{\alpha t}\mathbf{x}^*(t) \\ &= -\mathbf{R}^{-1}\mathbf{B}'\bar{\mathbf{P}}\mathbf{x}^*(t) = -\bar{\mathbf{K}}\mathbf{x}^*(t). \end{aligned} \quad (47)$$

We see that the closed-loop optimal control system (46) has eigenvalues with real parts less than $-\alpha$. In other words, the state $\mathbf{x}^*(t)$ approaches zero at least as fast as $e^{-\alpha t}$.

4 Simulation Results and Discussion

Referring to inverse kinematics, Figure 5 exhibits that the

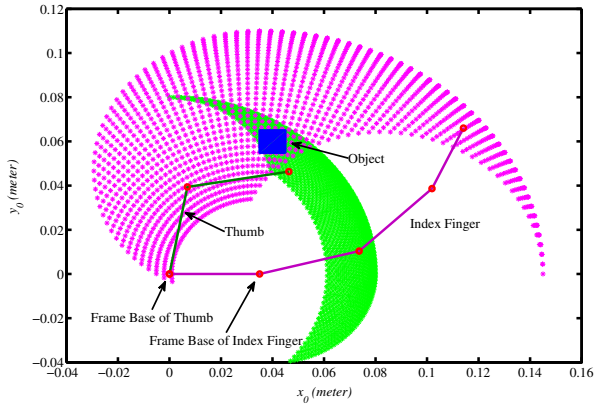

Figure 5. The Fingertip Workspace of Thumb and Index Finger and a Square Object

fingertip workspace of the thumb and index finger. We present simulations with the stability of optimal controller for the two-link thumb and three-link index finger of a smart prosthetic hand. All used parameters are the same to our previous work [6]. The initial and final orientation ϕ_0 and ϕ_f are 75 and 160 degrees, respectively. Figure 6 displays the tracking errors and desired/actual angles of thumb for the smart prosthetic hand by using the presented optimal controller with the stability (α = 0, 0.1, and 1). Figure 7 to Figure 9 are the tracking errors and desired/actual angles of index finger for the smart prosthetic hand (α = 0, 1, and 10). To compare with the original system (α = 0), these results demonstrate that the presented optimal controller behaves fast convergent and accurate as the stability α increases. For the three-link index finger, we design the orientation ϕ to calculate the angular positions via inverse kinematics. To compare with our previous works [5,6,10,12] by using adaptive neuro-fuzzy inference system (ANFIS) and genetic algorithm (GA), the simulations show that the presented method is not time consuming.

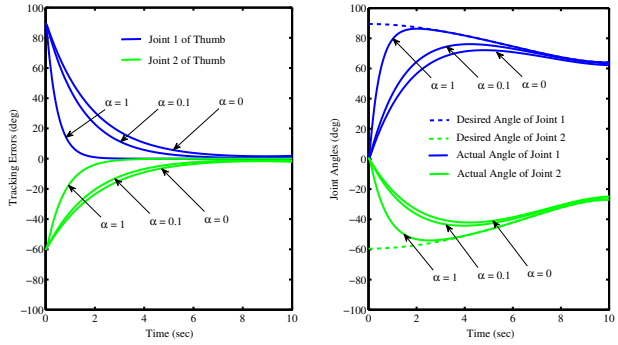

Figure 6. Tracking Errors (left) and Joint Angles (right) of Thumb for Optimal Control with the Stability (α = 0, 0.1, and 1)

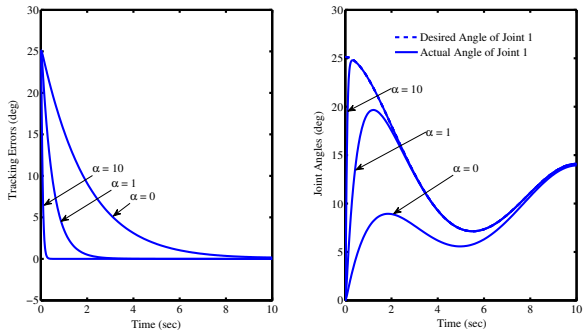

Figure 7. Tracking Errors (left) and Joint 1 Angles q_1^i (right) of Index Finger for Optimal Control with the Stability (α = 0, 1, and 10)

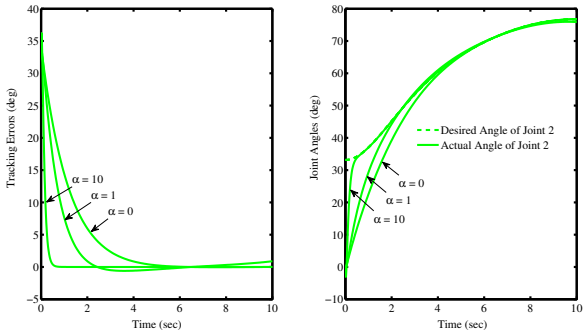

Figure 8. Tracking Errors (left) and Joint 2 Angles q_2^i (right) of Index Finger for Optimal Control with the Stability (α = 0, 1, and 10)

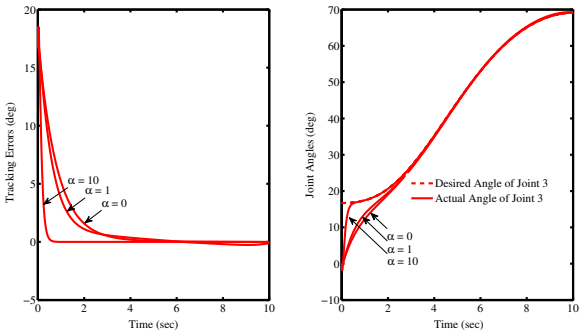

Figure 9. Tracking Errors (left) and Joint 3 Angles q_3^i (right) of Index Finger for Optimal Control with the Stability (α = 0, 1, and 10)

5 Conclusion and Future Work

This paper developed the differential kinematics for a serial n-link revolute-joint planar prosthetic hand to compute the angular velocities and angular accelerations of each finger. Then, the cubic polynomial function was designed to track the orientation ϕ in order to calculate inverse kinematics and differential kinematics. To make the optimal controller fast acting, the performance index J included an exponential term. The simulation results demonstrated a 30-fold increase in fast response compared to ANFIS or GA based trajectory planning [6]. Work is underway to extend this methodology to five-fingered, three-dimensional prosthetic hand.

Acknowledgments

The research was sponsored by the U.S. Department of the Army, under the award number W81XWH-10-1-0128 awarded and administered by the U.S. Army Medical Research Acquisition Activity, 820 Chandler Street, Fort Detrick, MD 21702-5014. The information does not necessarily reflect the position or the policy of the Government, and no official endorsement should be inferred. For purposes of this article, information includes news releases, articles, manuscripts, brochures, advertisements, still and motion pictures, speeches, trade association proceedings, etc.

References

[1] B. Subudhi and A. S. Morris, "Soft computing methods applied to the control of a flexible robot manipulator," *Applied Soft Computing*, vol. 9, pp. 149–158, 2009.

[2] C.-H. Chen, K. W. Bosworth, M. P. Schoen, S. E. Bearden, D. S. Naidu, and A. Perez, "A study of particle swarm optimization on leukocyte adhesion molecules and control strategies for smart prosthetic hand," in *2008 IEEE Swarm Intelligence Symposium (IEEE SIS08)*, St. Louis, Missouri, USA, September 21-23 2008.

[3] C.-H. Chen, D. S. Naidu, A. Perez, and M. P. Schoen, "Fusion of hard and soft control techniques for prosthetic hand," in *Proceedings of the International Association of Science and Technology for Development (IASTED) International Conference on Intelligent Systems and Control (ISC 2008)*, Orlando, Florida, USA, November 16-18 2008, pp. 120–125.

[4] D. Naidu, *Optimal Control Systems*. Boca Raton, FL: CRC Press, 2003.

[5] C.-H. Chen, D. S. Naidu, A. Perez-Gracia, and M. P. Schoen, "A hybrid control strategy for five-fingered smart prosthetic hand," in *Joint 48th IEEE Conference on Decision and Control (CDC) and 28th Chinese Control Conference (CCC)*, Shanghai, P. R. China, December 16-18 2009, pp. 5102–5107.

[6] C.-H. Chen, D. Naidu, A. Perez-Gracia, and M. P. Schoen, "A hybrid optimal control strategy for a smart prosthetic hand," in *Proceedings of the ASME 2009 Dynamic Systems and Control Conference (DSCC)*, Hollywood, California, USA, October 12-14 2009, (No. DSCC2009-2507).

[7] F. L. Lewis, S. Jagannathan, and A. Yesildirek, *Neural Network Control of Robotic Manipulators and Nonlinear Systems*. London, UK: Taylor & Francis, 1999.

[8] F. L. Lewis, D. M. Dawson, and C. T. Abdallah, *Robot Manipulators Control: Second Edition, Revised and Expanded*. New York, NY: Marcel Dekker, Inc.,, 2004.

[9] C.-H. Chen, D. S. Naidu, and M. P. Schoen, "An adaptive control strategy for a five-fingered prosthetic hand," in *The 14th World Scientific and Engineering Academy and Society (WSEAS) International Conference on Systems, Latest Trends on Systems (Volume II)*, Corfu Island, Greece, July 22-24 2010, pp. 405–410.

[10] C.-H. Chen, D. S. Naidu, A. Perez-Gracia, and M. P. Schoen, "A hybrid adaptive control strategy for a smart prosthetic hand," in *The 31st Annual International Conference of the IEEE Engineering Medicine and Biology Society (EMBS)*, Minneapolis, Minnesota, USA, September 2-6 2009, pp. 5056–5059.

[11] B. Siciliano, L. Sciavicco, L. Villani, and G. Oriolo, *Robotics: Modelling, Planning and Control*. London, UK: Springer-Verlag, 2009.

[12] C.-H. Chen, "Hybrid control strategies for smart prosthetic hand," Ph.D. dissertation, Measurement and Control Engineering, Idaho State University, May 2009.

[13] R. J. Schilling, *Fundamentals of Robotics: Analysis and Control*. Englewood Cliffs, NJ: Prentice Hall, 1990.

[14] R. Kelly, V. Santibanez, and A. Loria, *Control of Robot Manipulators in Joint Space*. New York, USA: Springer, 2005.

[15] R. N. Jazar, *Theory of Applied Robotics. Kinematics, Dynamics, and Control*. New York, USA: Springer, 2007.

[16] A. Nikoobin and R. Haghighi, "Lyapunov-based nonlinear disturbance observer for serial n-link robot manipulators," *Journal of Intelligent and Robotic Systems*, 2008, (Published online on 11 December 2008).

[17] Y. Z. Arslan, Y. Hacioglu, and N. Yagiz, "Prosthetic hand finger control using fuzzy sliding modes," *Journal of Intelligent and Robotic Systems*, vol. 52, pp. 121–138, 2008.

Hybrid Genetic Algorithm PID Control for a Five-Fingered Smart Prosthetic Hand

CHENG-HUNG CHEN
Measurement and Control
Engineering Research Center
Department of Biological Sciences
School of Science and Engineering
Idaho State University
Pocatello, ID 83209, USA
chenchen@isu.edu

D. SUBBARAM NAIDU
Measurement and Control
Engineering Research Center
Department of Electrical Engineering
and Computer Science
School of Engineering
Idaho State University
Pocatello, ID 83209, USA
naiduds@isu.edu

Abstract: A hybrid of soft control technique of adaptive neuro-fuzzy inference system (ANFIS) and genetic algorithm (GA) and hard control technique of proportional-integral-derivative (PID) for a five-fingered, smart prosthetic hand is presented. The ANFIS is used for inverse kinematics and GA is used for tuning the PID parameters with the objective of minimizing the error squared between desired and actual angles of the links of the fingers of the prosthetic hand. Simulation results for all the five fingers with GA-tuned PID controller exhibit superior performance compared to the PID control without GA.

Key–Words: Prosthetic Hand, PID Control, Genetic Algorithm, Adaptive Neuro-Fuzzy Inference System, Hybrid Control

1 Introduction

Hard control (HC) methodologies are used at lower levels for accuracy, precision, stability and robustness. HC comprises proportional-derivative (PD) control [1], proportional-integral-derivative (PID) control [2, 3], optimal control [3–6], adaptive control [7–9] etc. with specific applications to prosthetic devices. However, our previous works [1–3, 10] for a smart prosthetic hand showed that PID controller resulted in overshooting and oscillation because the system dynamics are sensitive to the rigidity of the target object and the used gain parameters of PD or PID controller [11].

Soft computing (SC) or computational intelligence (CI) is an emerging field based on synergy and seamless integration of neural networks (NN), fuzzy logic (FL) and optimization methods, such as genetic algorithms (GA), particle swarm (PS) [1, 12, 13], tabu search (TS) [13] and so on. The methodology based on SC can be used at upper levels of the overall mission whereas the HC can be used at lower levels for accuracy, precision, stability and robustness. Hence, we propose the GA-based PID controller to solve problems that cannot be solved satisfactorily by using either HC or SC methodology alone with specific applications to prosthetics.

In this paper, we first consider briefly trajectory planning and kinematics problems. Then, adaptive neuro-fuzzy inference system (ANFIS) is used to solve inverse kinematics problem for three-link fingers (index, middle, ring, and little). Next, the dynamics of the hand is derived and feedback linearization technique is used to obtain linear tracking error dynamics. Then we propose the GA-based PID control, which uses GA to tune all PID parameters by minimizing the tracking errors, for the five-fingered prosthetic hand. The resulting overall hybrid system incorporating both soft and hard control techniques is simulated with practical data for the hand and found to be superior to that using PID alone. We finally provide conclusions and future work.

2 Modeling

2.1 Trajectory Planning and Kinematics

The trajectory planning using cubic polynomial was discussed in our previous work [1, 2, 5, 8, 9, 14] for a two-fingered (thumb and index finger) smart prosthetic hand. The inverse and differential kinematics of two-link thumb and three-link fingers were discussed in our previous publications [1,2,5,8,9,14] for a two-fingered (thumb and index finger) smart prosthetic hand.

For five fingers shown in Figure 1, X^G, Y^G, and

Figure 1: The Relationship between Global Coordinate and Local Coordinates

Z^G are the three axes of the global coordinate. The local coordinate x^t-y^t-z^t of thumb can be reached by rotating through angles α and β to X^G and Y^G of the global coordinate, subsequently. The local coordinate x^i-y^i-z^i of index finger can be obtained by rotating through angle α to X^G and then translating the vector $\mathbf{d^i}$ of the global coordinate; similarly, the local coordinate x^j-y^j-z^j of middle finger ($j = m$), ring finger ($j = r$), and little finger ($j = l$) can be obtained by rotating through angle α to X^G and then translating the vector $\mathbf{d^j}$ ($j = m$, r and l) of the global coordinate.

2.2 Adaptive Neuro-Fuzzy Inference System (ANFIS)

The inverse kinematics problems can be solved by using adaptive neuro-fuzzy inference system (ANFIS) method [15] where the input of fuzzy-neuro system is the Cartesian space and the output is the joint space. ANFIS tunes the membership function and identifies the coefficients by the backpropagation gradient descent and least-squares methods, respectively. Figure 2 (a) shows a two input first-order Sugeno fuzzy model with two rules and Figure 2 (b) depicts the equivalent ANFIS structure for all the computation below. Sugeno-type fuzzy system has the following **Rule Base** [15].
If x is A_1 and y is B_1, then $f_1 = p_1x + q_1y + r_1$.
If x is A_2 and y is B_2, then $f_2 = p_2x + q_2y + r_2$.
Here, x and y are inputs to constitute the premise parameters A_1, A_2, B_1, and B_2 (Layer 1 in Figure 2 (b)). p_i, q_i, and r_i (i = 1,2) are the consequent parameters. We evaluate the rules by choosing *product* $\prod$ for T-Norm (Layers 2 and 3) which results in

$$w_i = \mu_{A_i}(x)\ \mu_{B_i}(y),\ \ i = 1, 2. \tag{1}$$

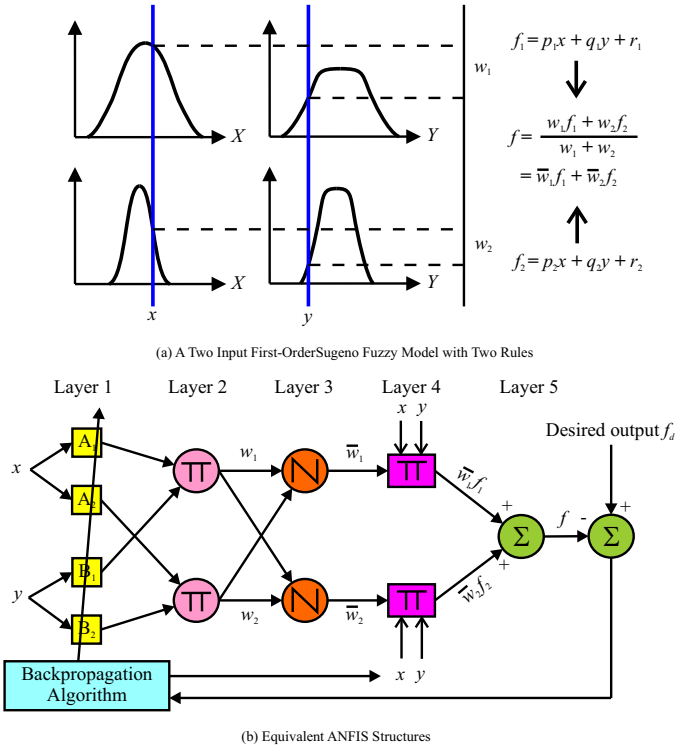

(a) A Two Input First-OrderSugeno Fuzzy Model with Two Rules

(b) Equivalent ANFIS Structures

Figure 2: ANFIS Architecture: (a) A Two Input First-Order Sugeno Fuzzy Model with Two Rules (b) Equivalent ANFIS Structure [15]

Here, $\mu_{A_i}(x)$ and $\mu_{B_i}(y)$ are designed fuzzy membership functions. Now after leaving the arguments (Layer 4), we get the output $f(x, y)$ by **Rule Consequences**.

$$f(x, y) = \frac{w_1(x, y)f_1(x, y) + w_2(x, y)f_2(x, y)}{w_1(x, y) + w_2(x, y)}. \tag{2}$$

f (Layer 5) can be written as

$$f = \frac{w_1f_1 + w_2f_2}{w_1 + w_2} = \bar{w}_1f_1 + \bar{w}_2f_2, \tag{3}$$

where

$$\bar{w}_1 = \frac{w_1}{w_1 + w_2},\quad \bar{w}_2 = \frac{w_2}{w_1 + w_2}. \tag{4}$$

2.3 Dynamics of the Prosthetic Hand

The dynamic equations of hand motion are derived via Lagrangian approach using kinetic energy and potential energy as [7, 14, 16] and can be written as below.

$$\mathbf{M}(\mathbf{q})\ddot{\mathbf{q}} + \mathbf{N}(\mathbf{q}, \dot{\mathbf{q}}) = \boldsymbol{\tau}, \tag{5}$$

where $\mathbf{M}(\mathbf{q})$ is the inertia matrix and $\mathbf{N}(\mathbf{q}, \dot{\mathbf{q}}) = \mathbf{C}(\mathbf{q}, \dot{\mathbf{q}}) + \mathbf{G}(\mathbf{q})$ represents nonlinear terms, including

Coriolis/centripetal vector $\mathbf{C}(\mathbf{q}, \dot{\mathbf{q}})$ and gravity vector $\mathbf{G}(\mathbf{q})$. The dynamic relations for the two-link thumb and the remaining three-link fingers are quite lengthy and omitted here due to lack of space [14].

3 Control Techniques

3.1 Feedback Linearization

The nonlinear dynamics represented by (5) is to be converted into a linear state-variable system using feedback linearization technique [7]. Let us suppose the prosthetic hand is required to track the desired trajectory $\mathbf{q}_d(t)$ described under path generation or tracking. Then, the tracking error $\mathbf{e}(t)$ is defined as

$$\mathbf{e}(t) = \mathbf{q}_d(t) - \mathbf{q}(t). \quad (6)$$

Here, $\mathbf{q}_d(t)$ is the *desired* angle vector of joints and can be obtained by trajectory planning [1, 2, 5, 8, 14]; $\mathbf{q}(t)$ is the *actual* angle vector of joints. Differentiating (6) twice, to get

$$\dot{\mathbf{e}}(t) = \dot{\mathbf{q}}_d(t) - \dot{\mathbf{q}}(t), \quad \ddot{\mathbf{e}}(t) = \ddot{\mathbf{q}}_d(t) - \ddot{\mathbf{q}}(t). \quad (7)$$

Substituting (5) into (7) yields

$$\ddot{\mathbf{e}}(t) = \ddot{\mathbf{q}}_d(t) + \mathbf{M}^{-1}(\mathbf{q}(t)) \left[\mathbf{N}(\mathbf{q}(t), \dot{\mathbf{q}}(t)) - \boldsymbol{\tau}(t)\right] \quad (8)$$

from which the control function can be defined as

$$\mathbf{u}(t) = \ddot{\mathbf{q}}_d(t) + \mathbf{M}^{-1}(\mathbf{q}(t)) \left[\mathbf{N}(\mathbf{q}(t), \dot{\mathbf{q}}(t)) - \boldsymbol{\tau}(t)\right]. \quad (9)$$

This is often called the *feedback linearization* control law, which can also be inverted to express it as

$$\boldsymbol{\tau}(t) = \mathbf{M}(\mathbf{q}(t)) \left[\ddot{\mathbf{q}}_d(t) - \mathbf{u}(t)\right) + \mathbf{N}(\mathbf{q}(t), \dot{\mathbf{q}}(t)\right]. \quad (10)$$

Using the relations (7) and (9), and defining state vector $\mathbf{x}(t) = [\mathbf{e}'(t) \quad \dot{\mathbf{e}}'(t)]'$, the *tracking error dynamics* in the form of a *linear* system can be written as

$$\dot{\mathbf{x}}(t) = \begin{bmatrix} \mathbf{0} & \mathbf{I} \\ \mathbf{0} & \mathbf{0} \end{bmatrix} \mathbf{x}(t) + \begin{bmatrix} \mathbf{0} \\ \mathbf{I} \end{bmatrix} \mathbf{u}(t). \quad (11)$$

3.2 GA-Based PID Hybrid Control

Figure 3 shows the block diagram of a hybrid GA-based PID controller for the presented five-fingered prosthetic hand with control signal as

$$\mathbf{u}(t) = -\mathbf{K_P}\mathbf{e}(t) - \mathbf{K_I} \int \mathbf{e}(t)dt - \mathbf{K_D}\dot{\mathbf{e}}(t) \quad (12)$$

with the proportional $\mathbf{K_P}$, integral $\mathbf{K_I}$, and derivative $\mathbf{K_D}$ diagonal gain matrices. We then rewrite (10) as

$$\begin{aligned} \boldsymbol{\tau}(t) \quad = \quad & \mathbf{M}(\mathbf{q}(t))[\ddot{\mathbf{q}}_d(t) + \mathbf{K_P}\mathbf{e}(t) + \mathbf{K_I} \int \mathbf{e}(t)dt \\ & + \mathbf{K_D}\dot{\mathbf{e}}(t)) + \mathbf{N}(\mathbf{q}(t), \dot{\mathbf{q}}(t)]. \end{aligned} \quad (13)$$

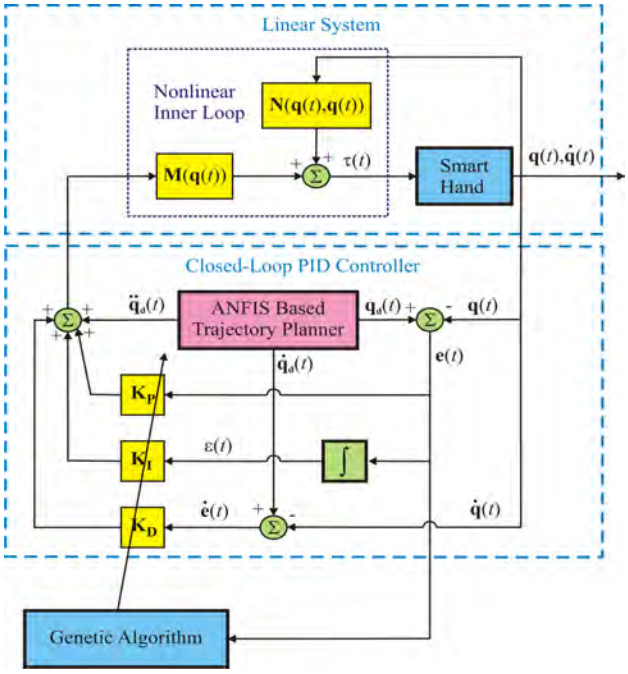

Figure 3: Block Diagram of the Hybrid GA-Based PID Controller for 14-DOF Five-Fingered Prosthetic Hand

Then we use GA to tune all gain coefficients $\mathbf{K_P}$, $\mathbf{K_D}$ and $\mathbf{K_D}$ of PID controller. Figure 4 shows the flowchart of GA and the procedure is briefly stated below.

1. Define the GA parameters: include initial population, population at the end of the first generation, number of chromosomes kept for mating, mutation rate, and tolerance ϵ so on.

2. Create a homogeneous population: generate N elements (chromosomes) and N is the initial population.

3. Evaluate cost (fitness) function of each chromosome: calculate the fitness value of the ith member in the population.

4. Select mate based on the performance of each gene: create a new population from the current population based on the ranking of the current fitness value, e.g. determine which parents participate in producing offspring for the next generation.

5. Reproduce the generation by crossover: use the single or multiple crossover points to generate new chromosomes that retain the good feature and discard the bad feature.

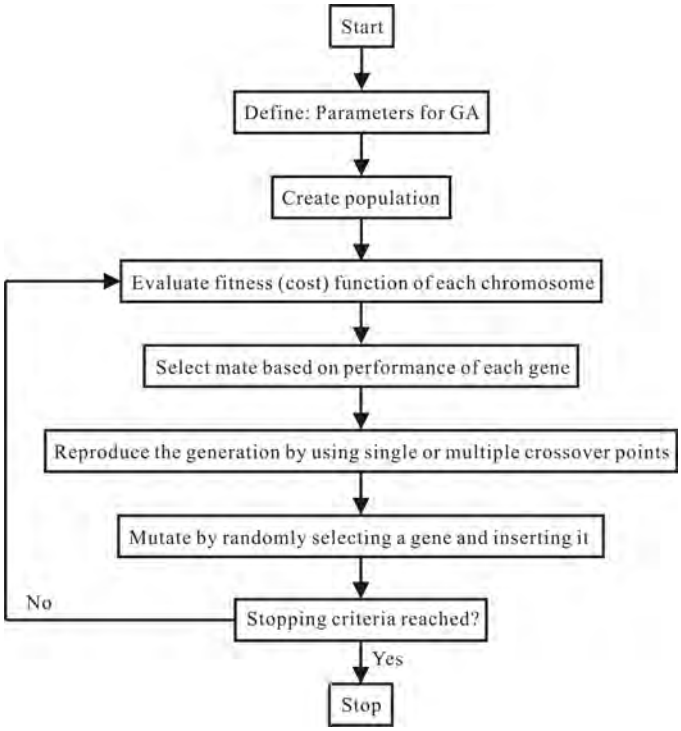

Figure 4: The Flowchart of Genetic Algorithm (GA)

6. Mutate: utilize the mutation rate which can randomly mutate the gene to avoid falling into the local minima area.

7. Repeat steps 3 to 6 until it reaches the maximum number of iterations or stopping condition defined by ϵ is satisfied.

4 Simulation Results and Discussion

We present simulations with a PID controller and GA-tuned PID controller for the 14 DOFs five-fingered smart prosthetic hand grasping a rectangular object as shown in Figure 5. All parameters of the smart prosthetic hand selected for the simulations are the same as our previous works [3, 9]. All initial actual angles are zero and the diagonal coefficients, $\mathbf{K_P}$, $\mathbf{K_I}$ and $\mathbf{K_D}$, for the PID controller alone are arbitrarily chosen as 100. From the derived dynamic and control models, after the parameters ($\mathbf{K_P}$, $\mathbf{K_I}$ and $\mathbf{K_D}$) are determined, the torque matrix $\boldsymbol{\tau}$ can be computed, and then the squared-tracking errors $e_i^j(t)$ of the joint i of the finger j are obtained. Therefore, the total error $E(t)$, which is a time-dependent function, can be described as

$$E(t) = \int_{t_0}^{t_f} (e_i^j(t))^2 dt, \qquad (14)$$

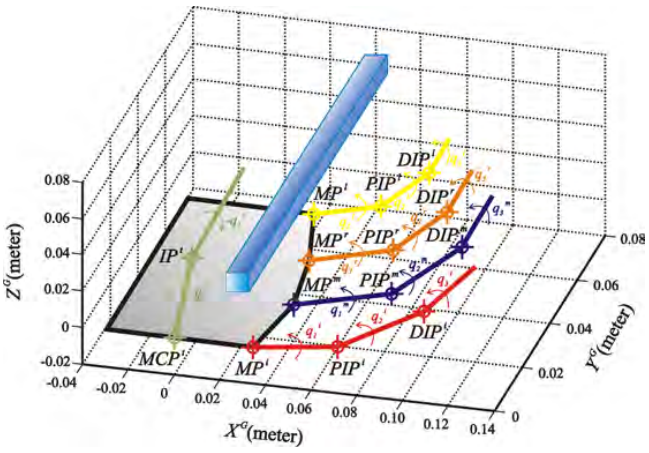

Figure 5: A Five-Finger Prosthetic Hand Grasping a Rectangular Object

where t_0 and t_f are initial and terminal time, respectively. The tuned diagonal parameters ($\mathbf{K_P}$, $\mathbf{K_I}$ and $\mathbf{K_D}$) and the total error $E(t)$ of PID controller by GA are listed in Table 1. To study whether the tuned parameter range influences total tracking errors, we design three different cases with altering lower and upper bounds of tuned parameter ranges for two-link thumb. Cases I, II, and III for the thumb represent that the PID parameters $\mathbf{K_P}$, $\mathbf{K_I}$ and $\mathbf{K_D}$ are constricted in three different bounded ranges [100,1000], [50,1000], and [100,200], respectively. Figure 6 and Figure 7 show that tracking errors and desired/actual angles of joints 1 and 2 of PID and GA-based PID controllers for Thumb. These simulations show that the large ranges [100,1000] (Case I) and [50,1000] (Case II) provide better results than the PID controller parameters arbitrarily chosen as 100. However, the small range [100,200] (Case III) gives worse result than the PID controller alone. These results suggest that the bigger parameter range, the smaller the total error. Cases I and II explain that GA finds some parameter values $\in$ [100,1000] and [50,100] escaping

Table 1: Parameter Selection of GA-Tuned PID Controller and Computed Total Errors

	Input			Output
Fingers	$\mathbf{K_P}$	$\mathbf{K_I}$	$\mathbf{K_D}$	$E(t)$
Case I	[976,956]	[779,279]	[170,236]	0.3107
Case II	[988,999]	[78,848]	[80,109]	0.1557
Case III	[199,198]	[127,157]	[104,102]	0.8100
Index	[794,398,960]	[960,918,914]	[15,59,242]	0.0465
Middle	[794,398,960]	[960,918,914]	[15,59,242]	0.1003
Ring	[794,398,960]	[960,918,914]	[15,59,242]	0.0465
Little	[794,398,960]	[960,918,914]	[15,59,242]	0.0607

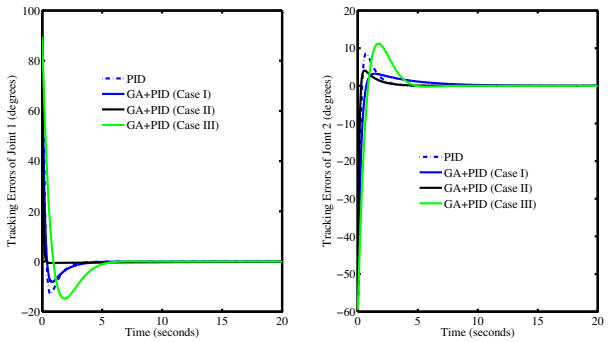

Figure 6: Tracking Errors of Joint 1 (left) and Joint 2 (right) of PID and GA-Based PID Controllers for Thumb

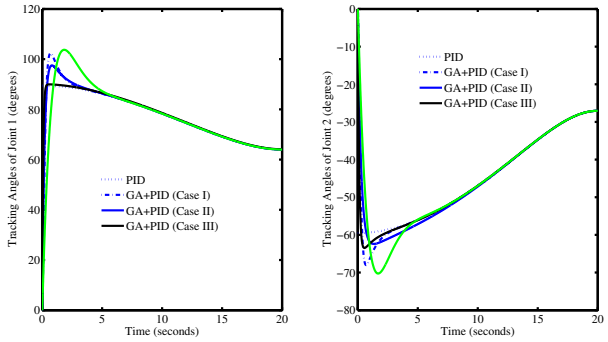

Figure 7: Tracking Angles of Joint 1 (left) and Joint 2 (right) of PID and GA-Based PID Controllers for Thumb

the local minimum area. Case III covers the value 100 in lower bound, but both total error and convergent speed are even worse than PID alone, suggesting that GA performs better for a large range, but is poor for searching on the boundary. To further consider the convergent speed, Case I gives smaller total error, but does not improve its convergent speed when comparing to PID control alone. Yet, Case II gives good total error and convergent speed. Case III gives poor total error and convergent speed. Taken together, these results imply that the global minimum could be located in the ranges [50,100] and [200,1000] and the parameter ranges play an important role in GA tuning. Based on these findings, we use the range [50,1000] for the remaining three-link fingers. Figures 8 to 11 show the simulations of PID and GA-based PID controllers for the remaining three-link fingers.

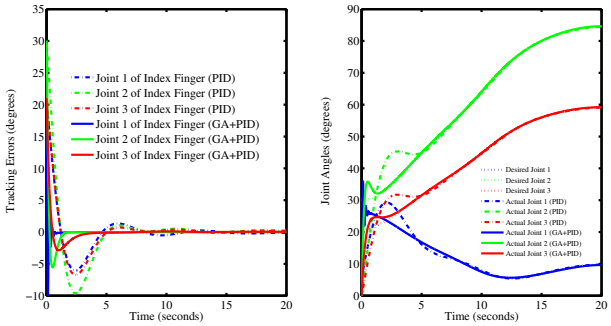

Figure 8: Tracking Errors (left) and Joint Angles (right) of PID and GA-Based PID Controllers for Index Finger

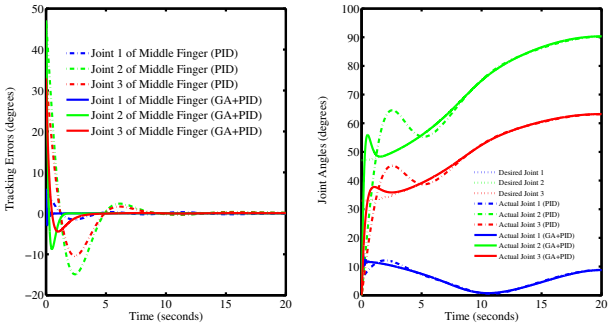

Figure 9: Tracking Errors (left) and Joint Angles (right) of PID and GA-Based PID Controllers for Middle Finger

5 Conclusions and Future Work

A hybrid control technique combining soft control with adaptive neuro-fuzzy inference system (ANFIS) and genetic algorithm (GA) and hard control with proportional-integral-derivative (PID) was presented for a five-fingered smart prosthetic hand. The ANFIS is used for inverse kinematics and GA is used for tuning the PID parameters with the objective of minimizing the error squared between desired and actual angles of the links of the fingers. Simulation results for all the five fingers with GA-tuned PID controller showed superior performance compared to the PID control alone. A real-time implementation of this technique on a prototype of a prosthetic hand is planned for future work.

Acknowledgements: The research was sponsored by the U.S. Department of the Army, under the award number W81XWH-10-1-0128 awarded and administered by the U.S. Army Medical Research Acquisition Activity, 820 Chandler Street, Fort Detrick, MD 21702-5014. The information does not necessarily

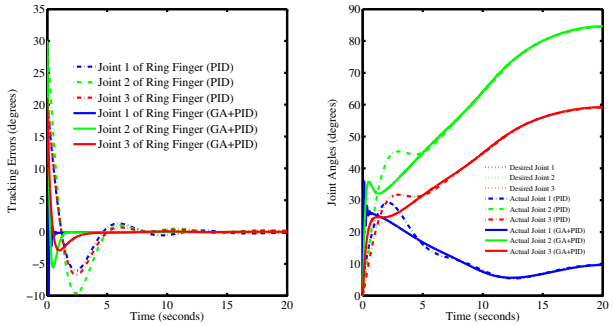

Figure 10: Tracking Errors (left) and Joint Angles (right) of PID and GA-Based PID Controllers for Ring Finger

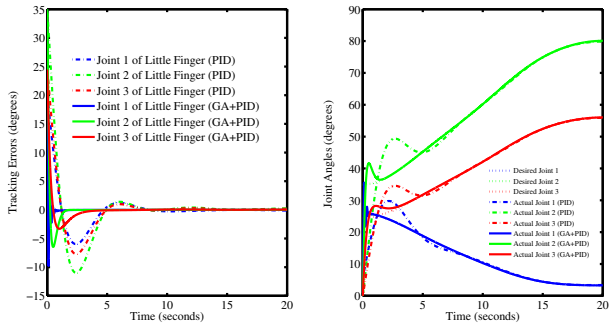

Figure 11: Tracking Errors (left) and Joint Angles (right) of PID and GA-Based PID Controllers for Little Finger

reflect the position or the policy of the Government, and no official endorsement should be inferred. For purposes of this article, information includes news releases, articles, manuscripts, brochures, advertisements, still and motion pictures, speeches, trade association proceedings, etc.

References:

[1] C.-H. Chen, K. W. Bosworth, M. P. Schoen, S. E. Bearden, D. S. Naidu, and A. Perez, "A study of particle swarm optimization on leukocyte adhesion molecules and control strategies for smart prosthetic hand," in *2008 IEEE Swarm Intelligence Symposium (IEEE SIS08)*, St. Louis, Missouri, USA, September 21-23 2008.

[2] C.-H. Chen, D. S. Naidu, A. Perez, and M. P. Schoen, "Fusion of hard and soft control techniques for prosthetic hand," in *Proceedings of the International Association of Science and Technology for Development (IASTED) International Conference on Intelligent Systems and Control (ISC 2008)*, Orlando, Florida, USA, November 16-18 2008, pp. 120–125.

[3] C.-H. Chen, D. S. Naidu, A. Perez-Gracia, and M. P. Schoen, "A hybrid control strategy for five-fingered smart prosthetic hand," in *Joint 48th IEEE Conference on Decision and Control (CDC) and 28th Chinese Control Conference (CCC)*, Shanghai, P. R. China, December 16-18 2009, pp. 5102–5107.

[4] D. Naidu, *Optimal Control Systems*. Boca Raton, FL: CRC Press, 2003.

[5] C.-H. Chen, D. S. Naidu, A. Perez-Gracia, and M. P. Schoen, "A hybrid optimal control strategy for a smart prosthetic hand," in *Proceedings of the ASME 2009 Dynamic Systems and Control Conference (DSCC)*, Hollywood, California, USA, October 12-14 2009, (No. DSCC2009-2507).

[6] C.-H. Chen and D. S. Naidu, "Optimal control strategy for two-fingered smart prosthetic hand," in *Proceedings of the International Association of Science and Technology for Development (IASTED) International Conference on Robotics and Applications (RA 2010)*, Cambridge, Massachusetts, USA, November 1-3 2010, pp. 190–196.

[7] F. Lewis, D. Dawson, and C. Abdallah, *Robot Manipulators Control: Second Edition, Revised and Expanded*. New York, NY: Marcel Dekker, Inc.,, 2004.

[8] C.-H. Chen, D. S. Naidu, A. Perez-Gracia, and M. P. Schoen, "A hybrid adaptive control strategy for a smart prosthetic hand," in *The 31st Annual International Conference of the IEEE Engineering Medicine and Biology Society (EMBS)*, Minneapolis, Minnesota, USA, September 2-6 2009, pp. 5056–5059.

[9] C.-H. Chen, D. S. Naidu, and M. P. Schoen, "An adaptive control strategy for a five-fingered prosthetic hand," in *The 14th World Scientific and Engineering Academy and Society (WSEAS) International Conference on Systems, Latest Trends on Systems (Volume II)*, Corfu Island, Greece, July 22-24 2010, pp. 405–410.

[10] C.-H. Chen, M. P. Schoen, and K. W. Bosworth, "A condensed hybrid optimization algorithm using enhanced continuous tabu search and particle swarm optimization," in *Proceedings of the*

ASME 2009 Dynamic Systems and Control Conference (DSCC), Hollywood, California, USA, October 12-14 2009, (No. DSCC2009-2526).

[11] R. Andrecioli and E. D. Engeberg, "Grasped object stiffness detection for adaptive force control of a prosthetic hand," in *Proceedings of the 2010 3rd IEEE RAS and EMBS International Conference on Biomedical Robotics and Biomechatronics (BioRob)*, Tokyo, Japan, September, 26-29 2010, pp. 197–202.

[12] C.-H. Chen, K. W. Bosworth, and M. P. Schoen, "Investigation of particle swarm optimization dynamics," in *Proceedings of International Mechanical Engineering Congress and Exposition (IMECE) 2007*, Seattle, Washington, USA, November 11-15 2007, (No. IMECE2007-41343).

[13] C.-H. Chen, K. Bosworth, and M. P. Schoen, "An adaptive particle swarm method to multiple dimensional problems," in *Proceedings of the International Association of Science and Technology for Development (IASTED) International Symposium on Computational Biology and Bioinformatics (CBB 2008)*, Orlando, Florida, USA, November 16-18 2008, pp. 260–265.

[14] C.-H. Chen, "Hybrid control strategies for smart prosthetic hand," Ph.D. dissertation, Measurement and Control Engineering, Idaho State University, May 2009.

[15] J.-S. Jang, C.-T. Sun, and E. Mizutani, *Neuro-Fuzzy and Soft Computing: A Computational Approach to Learning and Machine Intelligence*. Upper Saddle River, NJ: Prentice Hall PTR, 1997.

[16] B. Siciliano, L. Sciavicco, L. Villani, and G. Oriolo, *Robotics: Modelling, Planning and Control*. London, UK: Springer-Verlag, 2009.

TABLE I

PARAMETER SELECTION OF THE SMART HAND

Parameters	Values
Thumb	
Time (t_0,t_f)*	0, 20 (sec)
Desired Initial Position (X_0^t,Y_0^t)**	0.035, 0.060 (m)
Desired Final Position (X_f^t,Y_f^t)**	0.0495, 0.060 (m)
Desired Initial Velocity ($\dot{X}_0^t$,$\dot{Y}_0^t$)*	0, 0 (m/s)
Desired Final Velocity ($\dot{X}_f^t$,$\dot{Y}_f^t$)*	0, 0 (m/s)
Length (L_1^t,L_2^t)	0.040, 0.040 (m)
Mass (m_1^t,m_2^t)	0.043, 0.031 (kg)
Index Finger	
Desired Initial Position (X_0^i,Y_0^i)**	0.065, 0.080 (m)
Desired Final Position (X_f^i,Y_f^i)**	0.010, 0.060 (m)
Length (L_1^i,L_2^i,L_3^i)	0.040, 0.040, 0.030 (m)
Mass (m_1^i,m_2^i,m_3^i)	0.045, 0.025, 0.017 (kg)
Middle Finger	
Desired Initial Position (X_0^m,Y_0^m)**	0.065, 0.080 (m)
Desired Final Position (X_f^m,Y_f^m)**	0.005, 0.060 (m)
Length (L_1^m,L_2^m,L_3^m)	0.044, 0.044, 0.033 (m)
Mass (m_1^m,m_2^m,m_3^m)	0.050, 0.028, 0.017 (kg)
Ring Finger	
Desired Initial Position (X_0^r,Y_0^r)**	0.065, 0.080 (m)
Desired Final Position (X_f^r,Y_f^r)**	0.010, 0.060 (m)
Length (L_1^r,L_2^r,L_3^r)	0.040, 0.040, 0.030 (m)
Mass (m_1^r,m_2^r,m_3^r)	0.041, 0.023, 0.014 (kg)
Little Finger	
Desired Initial Position (X_0^l,Y_0^l)**	0.055, 0.080 (m)
Desired Final Position (X_f^l,Y_f^l)**	0.020, 0.060 (m)
Length (L_1^l,L_2^l,L_3^l)	0.036, 0.036, 0.027 (m)
Mass (m_1^l,m_2^l,m_3^l)	0.041, 0.023, 0.014 (kg)

*All fingers use same parameters

**All parameters are in local coordinates

TABLE II

PARAMETER SELECTION OF THE CONVERSION FROM GLOBAL TO LOCAL COORDINATES

Parameters	Values
Rotating α	90 (deg)
Rotating β	45 (deg)
Translating $\mathbf{d^i}$	(0.035, 0, 0) (m)
Translating $\mathbf{d^m}$	(0.040, 0, -0.020) (m)
Translating $\mathbf{d^r}$	(0.035, 0, -0.040) (m)
Translating $\mathbf{d^l}$	(0.025, 0, -0.060) (m)

TABLE III

GA-TUNED PARAMETER SELECTION OF PID CONTROL AND EVALUATED TOTAL ERROR

	Input			Output
Fingers	$\mathbf{K_P}$	$\mathbf{K_I}$	$\mathbf{K_D}$	$E(t)$
Case I	[976,956]	[779,279]	[170,236]	0.3107
Case II	[988,999]	[78,848]	[80,109]	0.1557
Case III	[199,198]	[127,157]	[104,102]	0.8100
Index	[794,398,960]	[960,918,914]	[15,59,242]	0.0465
Middle	[794,398,960]	[960,918,914]	[15,59,242]	0.1003
Ring	[794,398,960]	[960,918,914]	[15,59,242]	0.0465
Little	[794,398,960]	[960,918,914]	[15,59,242]	0.0607

Fusion of Fuzzy Logic and PD Control for a Five-Fingered Smart Prosthetic Hand

Cheng-Hung Chen
Measurement and Control
Engineering Research Center
Department of Biological Sciences
College of Science and Engineering
Idaho State University
Pocatello, ID 83209, USA
Email: chenchen@isu.edu

D. Subbaram Naidu
Measurement and Control
Engineering Research Center
Department of Electrical Engineering
School of Engineering
Idaho State University
Pocatello, ID 83209, USA
Email: naiduds@isu.edu

***Abstract*—A hybrid of soft control technique of adaptive neuro-fuzzy inference system (ANFIS) and fuzzy logic (FL) and hard control technique of proportional-derivative (PD) for a five-fingered, smart prosthetic hand is presented. The ANFIS is used for inverse kinematics and FL is used for tuning the PD parameters with two input layers (error and error change) using 7 triangular membership functions and 49 fuzzy logic rules. Simulation results with FL-tuned PD controller exhibit superior performance compared to the PD and PID control alone.**

***Index Terms*—Prosthetic Hand, Fuzzy Logic, PD Control, Adaptive Neuro-Fuzzy Inference System, Hybrid Control**

I. Introduction

During the recent wars in Afghanistan and Iraq, "at least 251,102 people have been killed and 532,715 people have been seriously wounded" [1]. Further, in the United States, the Amputee Coalition of America (ACA) [2] reports that there are approximately 1.9 million people living with limb loss, due to combat operations (such as conflicts, wars etc.), and non-combat operations such as accidents, or birth defects. According to a study of the 1996 National Health Interview Survey (NHIS) published by Vital and Health Statistics [3], it is estimated that one out of every 200 people in the U.S. has had an amputation. In other words, about one in every 2,000 new born babies will have limb deficiency and over 3,000 people lose a limb every week in America. By the year 2050, the projected number of Americans living with limb amputation will become 3.6 million [4]. In the past several decades, prosthetic hands have been developed by various researchers in the field [5]–[9], but reproducing the human hand in all its various functions, appearance, visibility, and weight is still a challenging task [5].

Hard computing/control (HC) techniques are used at lower levels for accuracy, precision, stability and robustness. HC comprises proportional-derivative (PD) control [10], proportional-integral-derivative (PID) control [11], [12], optimal control [12]–[15], adaptive control [16]–[19] etc. with specific applications to prosthetic devices. However, our previous works [10]–[12], [20] for a smart prosthetic hand showed that PID controller resulted in overshooting and oscillation. Soft computing (SC) or computational intelligence (CI) [21] is an emerging field based on synergy and seamless integration of neural networks (NN), fuzzy logic (FL) and optimization methods, such as genetic algorithms (GA), particle swarm (PS) [10], [22], [23], tabu search (TS) [23] and so on. The methodology based on SC can be used, in particular with FL, at upper levels of the overall mission where human involvement and decision making is of primary importance, whereas the HC can be used at lower levels for accuracy, precision, stability and robustness. Hence, we present the integration of SC and HC to solve problems that cannot be solved satisfactorily by using either HC or SC methodology alone with specific applications to prosthetics.

In this paper, we first consider briefly trajectory planning and kinematics problems associated with a five-fingered prosthetic hand. Then, adaptive neuro-fuzzy inference system (ANFIS) is used to solve inverse kinematics problem for three-link fingers (index, middle, ring, and little). Next, the dynamics of the hand is derived and feedback linearization technique is used to obtain *linear* tracking error dynamics. Then we propose the fuzzy logic-based PD (hybrid) controller, which uses fuzzy logic with 7 triangular membership functions in each input/output layer and 49 logic rules to tune PD gain parameters. The resulting overall hybrid system incorporating both soft and hard control techniques is simulated with practical data for the hand and found the performance to be superior to PD or PID alone. Finally, we provide conclusions and future work.

II. Modeling

A. Trajectory Planning and Kinematics

The trajectory planning using cubic polynomial was discussed in our previous work [10], [11], [14], [18], [19], [24] for a two-fingered (thumb and index finger) smart prosthetic hand.

Kinematics is the study of geometry in motion and is restricted to a natural geometrical description of motion by

the manners, including positions, orientations, and their derivatives (velocities and accelerations) [25], [26]. Forward and inverse kinematics of articulated systems study the analytical relationship between the angular positions of joints and the positions and orientations of the fingertips. A desired trajectory is usually specified in *Cartesian* space and the trajectory controller is easily performed in the *joint* space. Therefore, conversion of Cartesian trajectory planning to the joint space [26] is necessary. Using inverse kinematics, the joint angular positions of each finger need to be obtained from the known fingertip positions. Then the angular velocities and angular accelerations of joints can be obtained from the linear and angular velocities and accelerations of fingertips by differential kinematics. The inverse and differential kinematics of two-link thumb and three-link fingers were discussed in our previous publications [10], [11], [14], [18], [19], [24] for a two-fingered (thumb and index finger) smart prosthetic hand.

For five fingers shown in Figure 1, X^G, Y^G, and Z^G are

Fig. 1. Relationship between Global Coordinate and Local Coordinates: Local coordinate x^t-y^t-z^t of thumb can be reached by rotating through angles α and β to X^G and Y^G of global coordinate, subsequently. Local coordinate x^i-y^i-z^i of index finger can be obtained by rotating through angle α to X^G and then translating a vector $\mathbf{d^i}$ of the global coordinate.

the three axes of global coordinate. Local coordinate x^t-y^t-z^t of thumb can be reached by rotating through angles α and β to X^G and Y^G of the global coordinate, subsequently. Local coordinate x^i-y^i-z^i of index finger can be obtained by rotating through angle α to X^G and then translating a vector $\mathbf{d^i}$ of the global coordinate; similarly, the local coordinate x^j-y^j-z^j of middle finger ($j = m$), ring finger ($j = r$), and little finger ($j = l$) can be obtained by rotating through angle α to X^G and then translating the vector $\mathbf{d^j}$ ($j = m$, r and l) of the global coordinate.

B. Adaptive Neuro-Fuzzy Inference System (ANFIS)

The inverse kinematics problems can be solved by using adaptive neuro-fuzzy inference system (ANFIS) method [27] where the input of fuzzy-neuro system is the Cartesian space and the output is the joint space. ANFIS is a fuzzy inference system implemented in the framework of adaptive networks which provides the best optimization algorithm to find parameters in order to fit the data. ANFIS includes *premise parameters*, that defines membership functions, and *consequent parameters*, that defines the coefficients of each output equation. ANFIS tunes the membership function and identifies the coefficients by the backpropagation gradient descent and least-squares methods, respectively. ANFIS uses a hybrid learning algorithm to identify parameters of Sugeno-type fuzzy inference systems for fuzzy modeling procedures to learn information about a data set in order to compute the membership function and track the given input/output data. Figure 2 (a) shows a two input first-order Sugeno fuzzy model with two rules and Figure 2 (b) depicts the equivalent ANFIS structure for all the computation below. Sugeno-type fuzzy

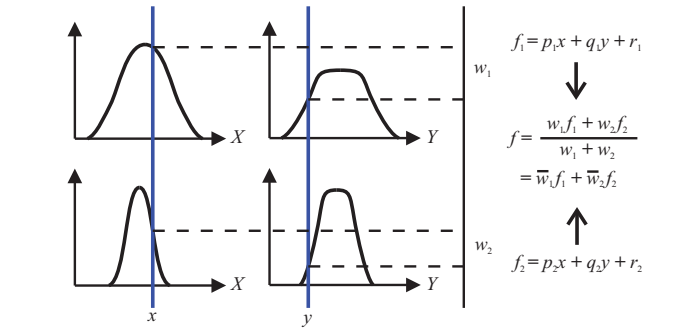

(a) A Two Input First-OrderSugeno Fuzzy Model with Two Rules

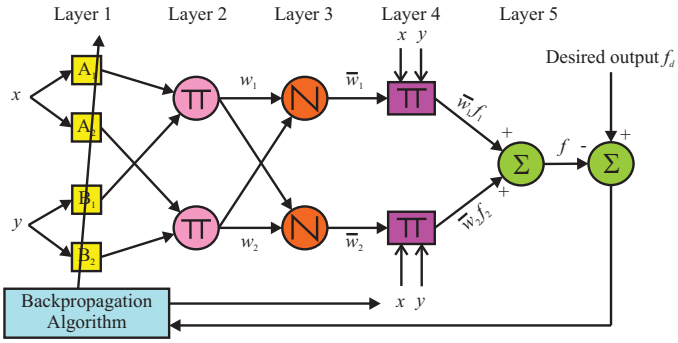

(b) Equivalent ANFIS Structures

Fig. 2. ANFIS Architecture: (a) A Two Input First-Order Sugeno Fuzzy Model with Two Rules (b) Equivalent ANFIS Structure [27]. The inverse kinematics problems are solved by using adaptive neuro-fuzzy inference system (ANFIS) method where the input of fuzzy-neuro system is the Cartesian space and the output is the joint space. ANFIS is a fuzzy inference system implemented in the framework of adaptive networks which provides the best optimization algorithm to find parameters in order to fit the data.

system has the following **Rule Base** [27]–[31].
If x is A_1 and y is B_1, then $f_1 = p_1x + q_1y + r_1$.
If x is A_2 and y is B_2, then $f_2 = p_2x + q_2y + r_2$.
Here, x and y are inputs to constitute the premise parameters A_1, A_2, B_1, and B_2 (Layer 1 in Figure 2 (b)). p_i, q_i, and r_i (i = 1,2) are the consequent parameters. We evaluate the rules by choosing *product* $\prod$ for T-Norm (Layers 2 and 3) which results in

$$w_i = \mu_{A_i}(x)\ \mu_{B_i}(y),\ i = 1, 2. \quad (1)$$

Here, $\mu_{A_i}(x)$ and $\mu_{B_i}(y)$ are designed fuzzy membership functions. Now after leaving the arguments (Layer 4), we get the output $f(x,y)$ by **Rule Consequences**.

$$f(x,y) = \frac{w_1(x,y)f_1(x,y) + w_2(x,y)f_2(x,y)}{w_1(x,y) + w_2(x,y)}. \quad (2)$$

f (Layer 5) can be written as

$$\begin{aligned} f &= \frac{w_1 f_1 + w_2 f_2}{w_1 + w_2} \\ &= \bar{w}_1 f_1 + \bar{w}_2 f_2, \end{aligned} \quad (3)$$

where

$$\bar{w}_1 = \frac{w_1}{w_1 + w_2}, \quad \bar{w}_2 = \frac{w_2}{w_1 + w_2}. \quad (4)$$

C. Dynamics of Hand

The dynamic equations of hand motion are derived via Lagrangian approach using kinetic energy and potential energy as [17], [24]–[26], [32]

$$\frac{d}{dt}\left(\frac{\partial \mathcal{L}}{\partial \dot{\mathbf{q}}}\right) - \frac{\partial \mathcal{L}}{\partial \mathbf{q}} = \boldsymbol{\tau}, \quad (5)$$

where $\mathcal{L}$ is the Lagrangian; $\dot{\mathbf{q}}$ and $\mathbf{q}$ represent the angular velocities and angle vectors of joints, respectively; $\boldsymbol{\tau}$ is the given torque vector at joints. The Lagrangian $\mathcal{L}$ can be expressed as

$$\mathcal{L} = T - V, \quad (6)$$

where T and V denote kinetic and potential energies, respectively. Substituting (6) into (5), dynamic equations of thumb can be obtained as below.

$$\mathbf{M}(\mathbf{q})\ddot{\mathbf{q}} + \mathbf{C}(\mathbf{q}, \dot{\mathbf{q}}) + \mathbf{G}(\mathbf{q}) = \boldsymbol{\tau}, \quad (7)$$

where $\mathbf{M}(\mathbf{q})$ is the inertia matrix; $\mathbf{C}(\mathbf{q}, \dot{\mathbf{q}})$ is the Coriolis/centripetal vector and $\mathbf{G}(\mathbf{q})$ is the gravity vector. (7) can be also written as

$$\mathbf{M}(\mathbf{q})\ddot{\mathbf{q}} + \mathbf{N}(\mathbf{q}, \dot{\mathbf{q}}) = \boldsymbol{\tau}, \quad (8)$$

where $\mathbf{N}(\mathbf{q}, \dot{\mathbf{q}}) = \mathbf{C}(\mathbf{q}, \dot{\mathbf{q}}) + \mathbf{G}(\mathbf{q})$ represents nonlinear terms. The dynamic relations for the two-link thumb and the remaining three-link fingers are quite lengthy and omitted here due to lack of space [24], [33], [34].

III. Control Techniques

A. Feedback Linearization

The nonlinear dynamics represented by (8) is to be converted into a linear state-variable system using feedback linearization technique [17]. Alternative state-space equations of the dynamics can be obtained by defining the position/velocity state $\mathbf{x}(t)$ of the joints as

$$\mathbf{x}(t) = \left[\mathbf{q}'(t) \quad \dot{\mathbf{q}}'(t)\right]'. \quad (9)$$

Let us repeat the dynamical model and rewrite (8) as

$$\frac{d}{dt}\dot{\mathbf{q}}(t) = -\mathbf{M}^{-1}(\mathbf{q}(t))\left[\mathbf{N}(\mathbf{q}(t), \dot{\mathbf{q}}(t)) - \boldsymbol{\tau}(t)\right]. \quad (10)$$

Thus, from (9) and (10), we can derive a linear system in *Brunovsky canonical form* as

$$\dot{\mathbf{x}}(t) = \begin{bmatrix} \mathbf{0} & \mathbf{I} \\ \mathbf{0} & \mathbf{0} \end{bmatrix}\mathbf{x}(t) + \begin{bmatrix} \mathbf{0} \\ \mathbf{I} \end{bmatrix}\mathbf{u}(t) \quad (11)$$

with its control input vector given by

$$\mathbf{u}(t) = -\mathbf{M}^{-1}(\mathbf{q}(t))\left[\mathbf{N}(\mathbf{q}(t), \dot{\mathbf{q}}(t)) - \boldsymbol{\tau}(t)\right]. \quad (12)$$

Let us suppose the prosthetic hand is required to track the desired trajectory $\mathbf{q}_d(t)$ described under path generation or tracking. Then, the tracking error $\mathbf{e}(t)$ is defined as

$$\mathbf{e}(t) = \mathbf{q}_d(t) - \mathbf{q}(t). \quad (13)$$

Here, $\mathbf{q}_d(t)$ is the *desired* angle vector of joints and can be obtained by trajectory planning [10], [11], [14], [18], [24]; $\mathbf{q}(t)$ is the *actual* angle vector of joints. Differentiating (13) twice, to get

$$\dot{\mathbf{e}}(t) = \dot{\mathbf{q}}_d(t) - \dot{\mathbf{q}}(t), \quad \ddot{\mathbf{e}}(t) = \ddot{\mathbf{q}}_d(t) - \ddot{\mathbf{q}}(t). \quad (14)$$

Substituting (10) into (14) yields

$$\ddot{\mathbf{e}}(t) = \ddot{\mathbf{q}}_d(t) + \mathbf{M}^{-1}(\mathbf{q}(t))\left[\mathbf{N}(\mathbf{q}(t), \dot{\mathbf{q}}(t)) - \boldsymbol{\tau}(t)\right] \quad (15)$$

from which the control function can be defined as

$$\mathbf{u}(t) = \ddot{\mathbf{q}}_d(t) + \mathbf{M}^{-1}(\mathbf{q}(t))\left[\mathbf{N}(\mathbf{q}(t), \dot{\mathbf{q}}(t)) - \boldsymbol{\tau}(t)\right]. \quad (16)$$

This is often called the *feedback linearization* control law, which can also be inverted to express it as

$$\boldsymbol{\tau}(t) = \mathbf{M}(\mathbf{q}(t))\left[\ddot{\mathbf{q}}_d(t) - \mathbf{u}(t)\right) + \mathbf{N}(\mathbf{q}(t), \dot{\mathbf{q}}(t)\right]. \quad (17)$$

Using the relations (14) and (16), and defining state vector $\mathbf{x}(t) = [\mathbf{e}'(t) \quad \dot{\mathbf{e}}'(t)]'$, the *tracking error dynamics* can be written as

$$\dot{\mathbf{x}}(t) = \begin{bmatrix} \mathbf{0} & \mathbf{I} \\ \mathbf{0} & \mathbf{0} \end{bmatrix}\mathbf{x}(t) + \begin{bmatrix} \mathbf{0} \\ \mathbf{I} \end{bmatrix}\mathbf{u}(t). \quad (18)$$

Note that this is in the form of a *linear* system such as

$$\dot{\mathbf{x}}(t) = \mathbf{A}\mathbf{x}(t) + \mathbf{B}\mathbf{u}(t). \quad (19)$$

B. Fuzzy Logic-Based PD Hybrid Control

Figure 3 shows the block diagram of the hybrid fuzzy logic-based PD controller for the presented five-fingered prosthetic hand with control signal as

$$\mathbf{u}(t) = -\mathbf{K_P}(t)\mathbf{e}(t) - \mathbf{K_D}(t)\dot{\mathbf{e}}(t) \quad (20)$$

with the proportional $\mathbf{K_P}(t)$ and derivative $\mathbf{K_D}(t)$ diagonal gain matrices with time varying. We then rewrite (17) as

$$\begin{aligned} \boldsymbol{\tau}(t) &= \mathbf{M}(\mathbf{q}(t))[\ddot{\mathbf{q}}_d(t) + \mathbf{K_P}(t)\mathbf{e}(t) + \mathbf{K_D}(t)\dot{\mathbf{e}}(t)) + \\ &\quad \mathbf{N}(\mathbf{q}(t), \dot{\mathbf{q}}(t)]. \end{aligned} \quad (21)$$

Then we use mamdani fuzzy inference system to tune the time-varying parameters $\mathbf{K_P}(t)$ and $\mathbf{K_D}(t)$ of PD controller. Figure 4 shows the structural characteristics of proposed fuzzy inference system, which includes two inputs (error $\mathbf{e}$ and error change $\dot{\mathbf{e}}$) on the left and one output ($\mathbf{K_P}$) on the right. Each input or output layer contains seven triangular membership

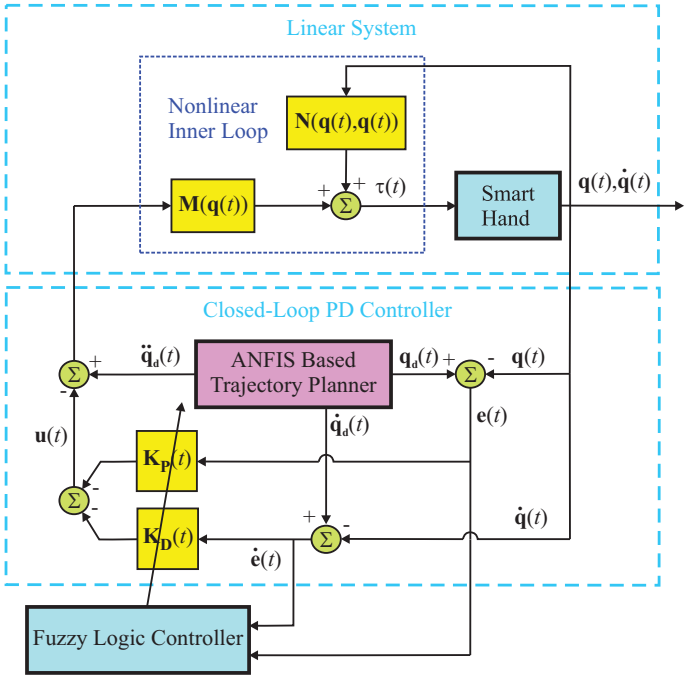

Fig. 3. Block Diagram of the Presented Hybrid Fuzzy Logic-Based Proportional-Derivative (PD) Controller for a Five-Fingered Prosthetic Hand: Errors and error changes are calculated by actual and desired angles, which are based on adaptive neuro-fuzzy inference system (ANFIS) trajectory planner. Then fuzzy logic controller tunes all parameters of closed-loop PD control so that the required torque of the prosthetic hand nonlinear system is computed by control input.

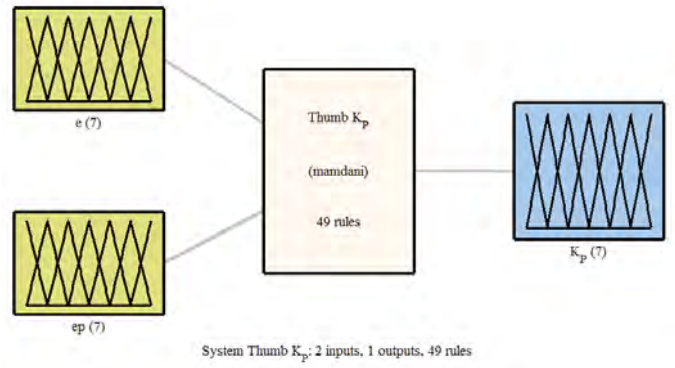

Fig. 4. The Structural Characteristics of Proposed Fuzzy Inference System: Two inputs (error $\mathbf{e}$ and error change $\dot{\mathbf{e}}$) on the left and one output (tuned $\mathbf{K_P}$) on the right with 49 logic rules

functions as shown in Figure 5 and 49 logic rules as listed in Table I. After using 49 logic rules, the output surface $\mathbf{K_P}$ of fuzzy inference system is generated as shown in Figure 6. Similarly, $\mathbf{K_D}$ can be computed by the same way.

IV. Simulation Results and Discussion

Figure 7 shows that a five-fingered prosthetic hand with 14 DOFs is reaching a rectangular rod in order to grasp the object. When thumb and the other four fingers are performing extension/flexion movements, the workspace of fingertips is restricted to the maximum angles of joints. Referring to inverse

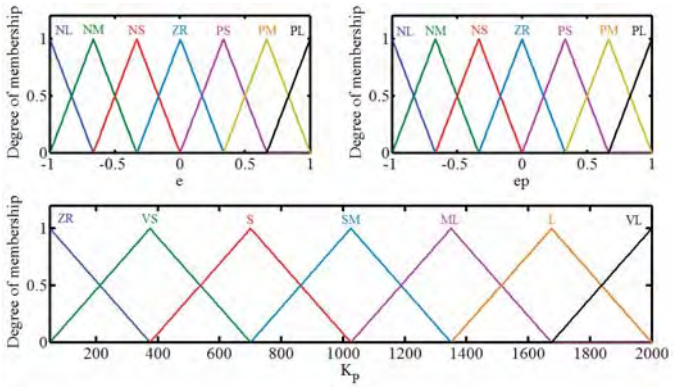

Fig. 5. All Membership Functions: Each of Two Inputs (Upper Panel) and One Output (Lower Panel) Uses 7 Triangular Membership Functions

TABLE I
A Complete Fuzzy Logic Rule Base

ė\e	NL	NM	NS	ZR	PS	PM	PL
NL	ZR	ZR	ZR	ZR	VS	S	SM
NM	ZR	ZR	ZR	VS	S	SM	ML
NS	ZR	ZR	VS	S	SM	ML	L
ZR	ZR	VS	S	SM	ML	L	VL
PS	VS	S	SM	ML	L	VL	VL
PM	S	SM	ML	L	VL	VL	VL
PL	SM	ML	L	VL	VL	VL	VL

N: negative; P: positive; ZR: zero; L: large; M: medium; S: small; V: very

kinematics, the first and second joint angles of the thumb fingertip are constrained in the ranges of [0,90] and [-80,0] (degrees). The first, second, and third joint angles of the other four fingers are constrained in the ranges of [0,90], [0,110] and [0,80] (degrees), respectively [35].

Next, we present simulations with PD and PID controllers and fuzzy inference system tuned PD controller for the 14 DOFs five-fingered smart prosthetic hand. The parameters of the two-link thumb/three-link fingers [36] were related to desired trajectory. All parameters of the smart prosthetic hand selected for the simulations are given in Table II and the

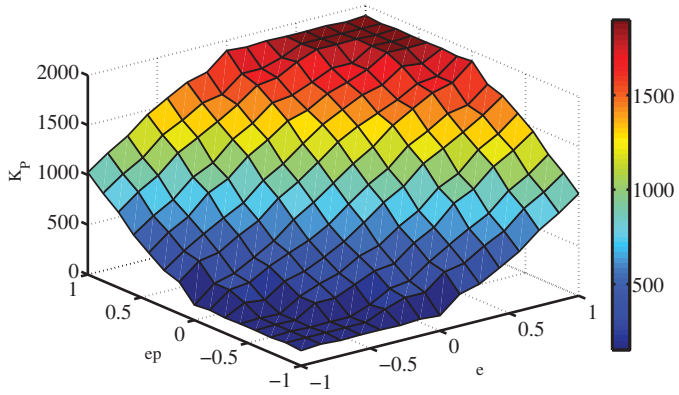

Fig. 6. The Output Surface of Fuzzy Inference System with Two Inputs and 49 Logic Rules

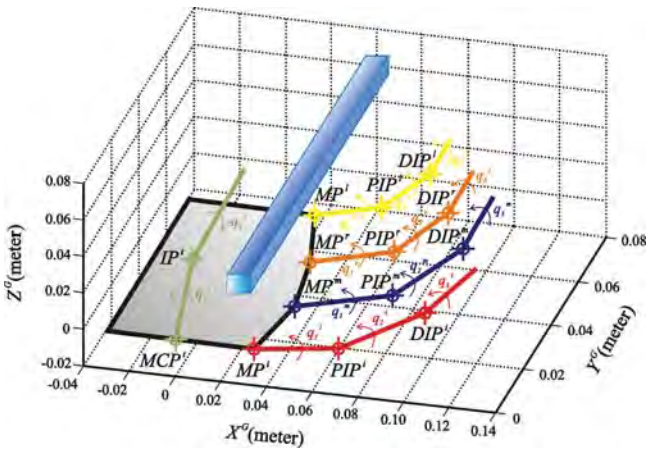

Fig. 7. Five-Fingered Prosthetic Hand Grasping a Rectangular Object

side length and length of the target rectangular rod are 0.010 and 0.100 (m), respectively. The relating parameters between the global coordinate and the local coordinates are defined in Table III. Moreover, in this work, we assumed that each link

TABLE II
PARAMETER SELECTION OF THE SMART HAND

Parameters	Values
Thumb	
Time $(t_0,t_f)^*$	0, 20 (sec)
Desired Initial Position $(X_0^t,Y_0^t)^{**}$	0.035, 0.060 (m)
Desired Final Position $(X_f^t,Y_f^t)^{**}$	0.0495, 0.060 (m)
Desired Initial Velocity $(\dot{X}_0^t,\dot{Y}_0^t)^*$	0, 0 (m/s)
Desired Final Velocity $(\dot{X}_f^t,\dot{Y}_f^t)^*$	0, 0 (m/s)
Length (L_1^t,L_2^t)	0.040, 0.040 (m)
Mass (m_1^t,m_2^t)	0.043, 0.031 (kg)
Index Finger	
Desired Initial Position $(X_0^i,Y_0^i)^{**}$	0.065, 0.080 (m)
Desired Final Position $(X_f^i,Y_f^i)^{**}$	0.010, 0.060 (m)
Length (L_1^i,L_2^i,L_3^i)	0.040, 0.040, 0.030 (m)
Mass (m_1^i,m_2^i,m_3^i)	0.045, 0.025, 0.017 (kg)
Middle Finger	
Desired Initial Position $(X_0^m,Y_0^m)^{**}$	0.065, 0.080 (m)
Desired Final Position $(X_f^m,Y_f^m)^{**}$	0.005, 0.060 (m)
Length (L_1^m,L_2^m,L_3^m)	0.044, 0.044, 0.033 (m)
Mass (m_1^m,m_2^m,m_3^m)	0.050, 0.028, 0.017 (kg)
Ring Finger	
Desired Initial Position $(X_0^r,Y_0^r)^{**}$	0.065, 0.080 (m)
Desired Final Position $(X_f^r,Y_f^r)^{**}$	0.010, 0.060 (m)
Length (L_1^r,L_2^r,L_3^r)	0.040, 0.040, 0.030 (m)
Mass (m_1^r,m_2^r,m_3^r)	0.041, 0.023, 0.014 (kg)
Little Finger	
Desired Initial Position $(X_0^l,Y_0^l)^{**}$	0.055, 0.080 (m)
Desired Final Position $(X_f^l,Y_f^l)^{**}$	0.020, 0.060 (m)
Length (L_1^l,L_2^l,L_3^l)	0.036, 0.036, 0.027 (m)
Mass (m_1^l,m_2^l,m_3^l)	0.041, 0.023, 0.014 (kg)

*All fingers use same parameters
**All parameters are in local coordinates

of all fingers is a circular cylinder with the radius (R) 0.010 (m), so the inertia I_{zzk}^j of each link k of all fingers j ($= t$, i, m, r and l) can be calculated as

$$I_{zzk}^j = \frac{1}{4} m_k^j R^2 + \frac{1}{3} m_k^j {L_k^j}^2. \quad (22)$$

All initial actual angles are zero and the diagonal coefficients, $\mathbf{K_P}$, $\mathbf{K_I}$ and $\mathbf{K_D}$, for the PD or PID controller alone are arbitrarily chosen as 100. From the derived dynamic and control models, after the parameters ($\mathbf{K_P}$ and $\mathbf{K_D}$) are selected, the control signal $\boldsymbol{u}$ and torque $\boldsymbol{\tau}$ can be calculated.

Figure 8 shows tracking errors (e_1^t and e_2^t on the left

TABLE III
PARAMETER SELECTION OF CONVERSION BETWEEN GLOBAL AND LOCAL COORDINATES

Parameters	Values
Rotating α	90 (deg)
Rotating β	45 (deg)
Translating $\mathbf{d^i}$	(0.035, 0, 0) (m)
Translating $\mathbf{d^m}$	(0.040, 0, -0.020) (m)
Translating $\mathbf{d^r}$	(0.035, 0, -0.040) (m)
Translating $\mathbf{d^l}$	(0.025, 0, -0.060) (m)

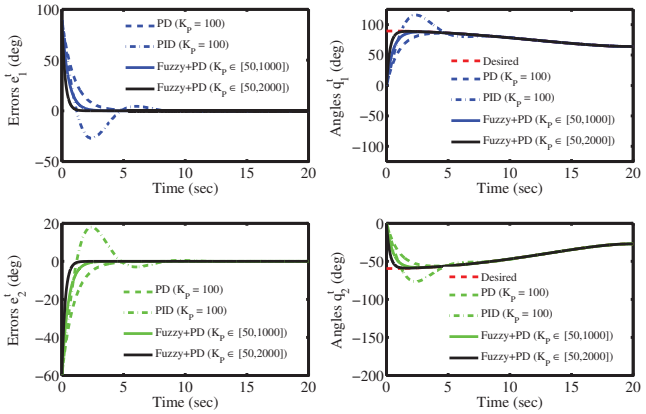

Fig. 8. Tracking Errors (Left) and Desired/Actual Angles (Right) of Joints 1 (Upper) and 2 (Lower) for Two-Link Thumb Using PD (Dash Line), PID (Dot Line) and Fuzzy Logic Based PD (Solid Line) Controllers

column) and desired/actual angles (q_1^t and q_2^t on the right column) of joints 1 (the top row) and 2 (the bottom row) for two-link thumb using PD (dash line), PID (dot line) and fuzzy logic based PD (solid line) controllers. The tracking errors for PD control are convergent within 5 seconds without overshooting, but PID control acts longer (approximate 10 seconds) with overshooting and oscillation. The proposed hybrid fuzzy logic PD control using parameters $\mathbf{K_P} \in [50, 1000]$ and $\mathbf{K_D} \in [50, 500]$ provides faster convergence than both PD and PID controllers. To further study whether the parameter range influences tracking errors, we found that the larger parameter range, the faster convergent speed after altering $\mathbf{K_P} \in [50, 2000]$ without additional computational time. We also used fuzzy logic controller with two inputs (error and error rate) and one output (control signal), but the control system could not obtain convergent tracking errors (data not shown). These data suggest that fusion of soft computing (SC) and

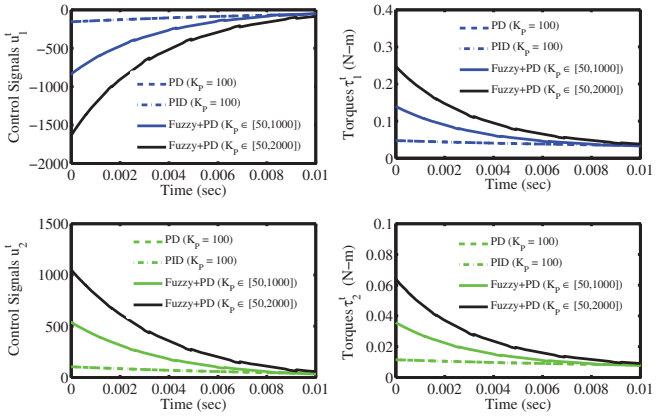

Fig. 9. Control Signals (Left) and Actuated Torques (Right) of Joints 1 (Upper) and 2 (Lower) for Two-Link Thumb Using PD (Dash Line), PID (Dot Line) and Fuzzy Logic Based PD (Solid Line) Controllers in 0.01 Second

hard control (HC) is superior to either HC or SC methodology alone.

The time-variant computed control signals (u_1^t and u_2^t) and torques (τ_1^t and τ_2^t) for two-link thumb within the first 0.01 second are shown in Figure 9, suggesting that the presented hybrid fuzzy logic PD controller requires more power (torque) than PD and PID controllers in order to obtain faster convergent tracking errors.

Similarly, Figures 10, 12, 14 and 16 show tracking errors and desired/actual angles for all remaining three-link fingers. Figures 11, 13, 15 and 17 show control signals and torques for the mapping three-link fingers.

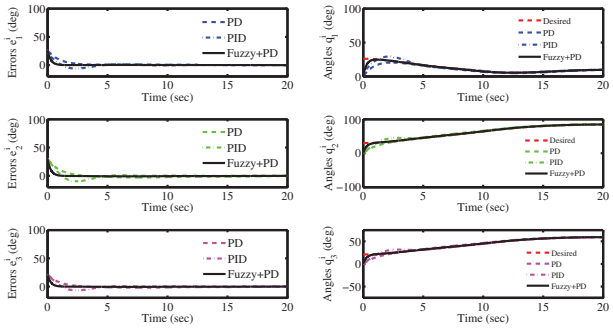

Fig. 10. Tracking Errors (Left) and Desired/Actual Angles (Right) of Joints 1 (Top), 2 (Middle) and 3 (Bottom) for Three-Link Index Finger Using PD (Dash Line), PID (Dot Line) and Fuzzy Logic Based PD (Solid Line) Controllers

V. Conclusions and Future Work

For a five-fingered smart prosthetic hand, a hybrid control technique involving soft control with adaptive neuro-fuzzy inference system (ANFIS) and fuzzy logic (FL) and hard control with proportional-derivative (PD) was presented. The ANFIS is used for inverse kinematics and FL is used for tuning the PD parameters with two input layers (error and

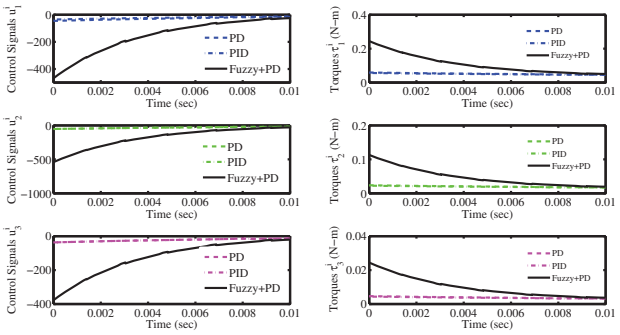

Fig. 11. Control Signals (Left) and Actuated Torques (Right) of Joints 1 (Top), 2 (Middle) and 3 (Bottom) for Three-Link Index Finger Using PD (Dash Line), PID (Dot Line) and Fuzzy Logic Based PD (Solid Line) Controllers in 0.01 Second

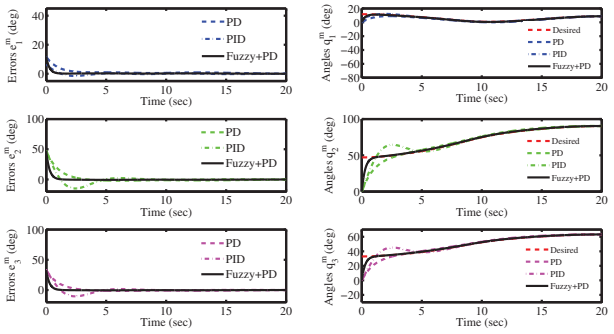

Fig. 12. Tracking Errors (Left) and Desired/Actual Angles (Right) of Joints 1 (Top), 2 (Middle) and 3 (Bottom) for Three-Link Middle Finger Using PD (Dash Line), PID (Dot Line) and Fuzzy Logic Based PD (Solid Line) Controllers

error change) using 7 triangular membership functions and 49 fuzzy logic rules. Simulation results with FL-tuned PD (hybrid) controller showed superior performance compared to the PD and PID control alone. Work is underway to extend this methodology to a real-time implementation on the prototype of a prosthetic hand.

Acknowledgment

The research was sponsored by the U.S. Department of the Army, under the award number W81XWH-10-1-0128 awarded and administered by the U.S. Army Medical Research Acquisition Activity, 820 Chandler Street, Fort Detrick, MD 21702-5014. The information does not necessarily reflect the position or the policy of the Government, and no official endorsement should be inferred. For purposes of this article, information includes news releases, articles, manuscripts, brochures, advertisements, still and motion pictures, speeches, trade association proceedings, etc.

References

[1] "Casualties in Afghanistan & Iraq," www.unknownnews.net, June 5 2006.

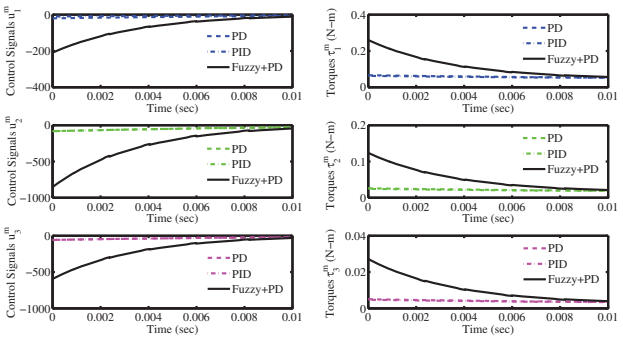

Fig. 13. Control Signals (Left) and Actuated Torques (Right) of Joints 1 (Top), 2 (Middle) and 3 (Bottom) for Three-Link Middle Finger Using PD (Dash Line), PID (Dot Line) and Fuzzy Logic Based PD (Solid Line) Controllers in 0.01 Second

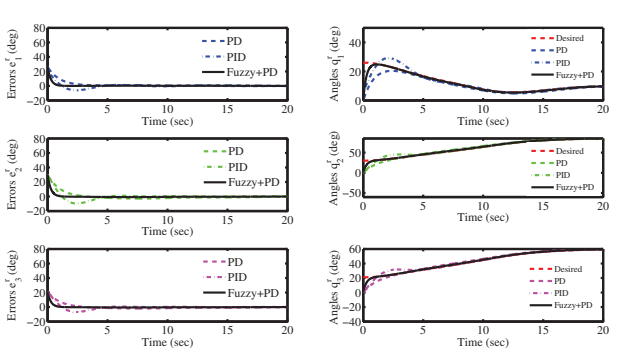

Fig. 14. Tracking Errors (Left) and Desired/Actual Angles (Right) of Joints 1 (Top), 2 (Middle) and 3 (Bottom) for Three-Link Ring Finger Using PD (Dash Line), PID (Dot Line) and Fuzzy Logic Based PD (Solid Line) Controllers

[2] "Amputee Coalition of America (ACA) National Limb Loss Information Center (NLLIC) Limb Loss Facts in the United States," http://www.amputee-coalition.org, 2006.

[3] P. F. Adams, G. E. Hendershot, and M. A. Marano, "Current estimates from the national health interview survey, 1996." *National Center for Health Statistics. Vital and Health Statistics*, vol. 200, no. 10, pp. 1–203, 1999.

[4] K. Ziegler-Graham, E. J. MacKenzie, P. L. Ephraim, T. G. Travison, and R. Brookmeyer, "Estimating the prevalence of limb loss in the united states: 2005 to 2050," *Archives of Physical Medicine and Rehabilitation*, vol. 89, pp. 422–429, March 2008.

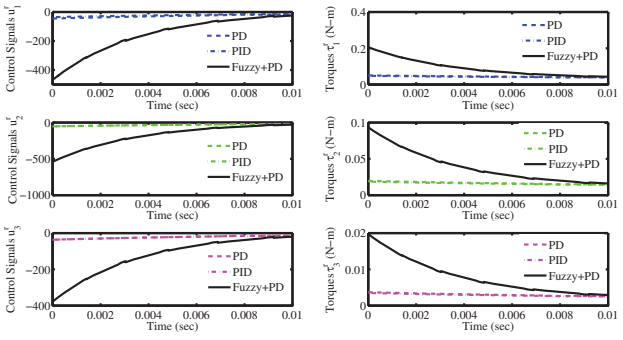

Fig. 15. Control Signals (Left) and Actuated Torques (Right) of Joints 1 (Top), 2 (Middle) and 3 (Bottom) for Three-Link Ring Finger Using PD (Dash Line), PID (Dot Line) and Fuzzy Logic Based PD (Solid Line) Controllers in 0.01 Second

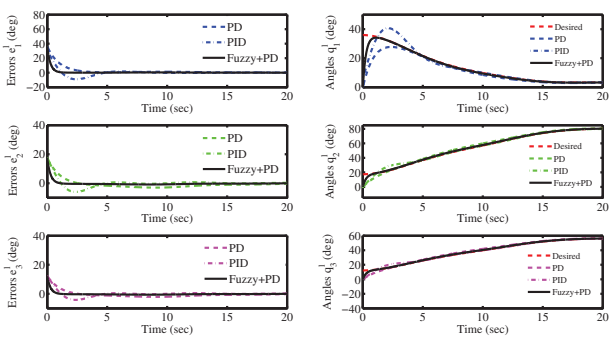

Fig. 16. Tracking Errors (Left) and Desired/Actual Angles (Right) of Joints 1 (Top), 2 (Middle) and 3 (Bottom) for Three-Link Little Finger Using PD (Dash Line), PID (Dot Line) and Fuzzy Logic Based PD (Solid Line) Controllers

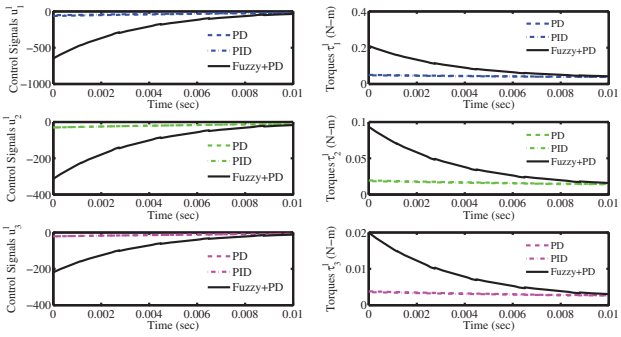

Fig. 17. Control Signals (Left) and Actuated Torques (Right) of Joints 1 (Top), 2 (Middle) and 3 (Bottom) for Three-Link Little Finger Using PD (Dash Line), PID (Dot Line) and Fuzzy Logic Based PD (Solid Line) Controllers in 0.01 Second

[5] M. Zecca, S. Micera, M. Carrozza, and P. Dario, "Control of multifunctional prosthetic hands by processing the electromyographic signal," *Critical Reviews^{TM} in Biomedical Engineering*, vol. 30, pp. 459–485, 2002, (Review article with 96 references).

[6] J. C. K. Lai, M. P. Schoen, A. Perez-Gracia, D. S. Naidu, and S. W. Leung, "Prosthetic devices: Challenges and implications of robotic implants and biological interfaces," *Proceedings of the Institute of Mechanical Engineers (IMechE), Part H: Journal of Engineering in Medicine*, vol. 221, no. 2, pp. 173–183, January 2007, special Issue on Micro and Nano Technologies in Medicine.

[7] L. Zollo, S. Roccella, E. Guglielmelli, M. C. Carrozza, and P. Dario, "Biomechatronic design and control of an anthropomorphic artificial hand for prosthetic and robotic applications," *IEEE/ASME Transactions on Mechatronics*, vol. 12, no. 4, pp. 418–429, August 2007.

[8] D. S. Naidu, C.-H. Chen, A. Perez, and M. P. Schoen, "Control strategies for smart prosthetic hand technology: An overview," in *Proceedings of the 30th Annual International IEEE EMBS Conference*, Vancouver, Canada, August 20-24 2008, pp. 4314–4317.

[9] D. S. Naidu and C.-H. Chen., *Automatic Control Techniques for Smart Prosthetic Hand Technology: An Overview, book chapter 12, to appear in a book titled "Distributed Diagnosis and Home Healthcare (D2H2): Volume 2"*. California, USA: American Scientific Publishers, 2011, (in printed).

[10] C.-H. Chen, K. W. Bosworth, M. P. Schoen, S. E. Bearden, D. S. Naidu, and A. Perez, "A study of particle swarm optimization on leukocyte adhesion molecules and control strategies for smart prosthetic hand," in *2008 IEEE Swarm Intelligence Symposium (IEEE SIS08)*, St. Louis, Missouri, USA, September 21-23 2008.

[11] C.-H. Chen, D. S. Naidu, A. Perez, and M. P. Schoen, "Fusion of hard and soft control techniques for prosthetic hand," in *Proceedings of the International Association of Science and Technology for Development (IASTED) International Conference on Intelligent Systems and Control (ISC 2008)*, Orlando, Florida, USA, November 16-18 2008, pp. 120–125.

[12] C.-H. Chen, D. S. Naidu, A. Perez-Gracia, and M. P. Schoen, "A hybrid control strategy for five-fingered smart prosthetic hand," in *Joint 48th IEEE Conference on Decision and Control (CDC) and 28th Chinese Control Conference (CCC)*, Shanghai, P. R. China, December 16-18 2009, pp. 5102–5107.

[13] D. Naidu, *Optimal Control Systems*. Boca Raton, FL: CRC Press, 2003.

[14] C.-H. Chen, D. S. Naidu, A. Perez-Gracia, and M. P. Schoen, "A hybrid optimal control strategy for a smart prosthetic hand," in *Proceedings of the ASME 2009 Dynamic Systems and Control Conference (DSCC)*, Hollywood, California, USA, October 12-14 2009, (No. DSCC2009-2507).

[15] C.-H. Chen and D. S. Naidu, "Optimal control strategy for two-fingered smart prosthetic hand," in *Proceedings of the International Association of Science and Technology for Development (IASTED) International Conference on Robotics and Applications (RA 2010)*, Cambridge, Massachusetts, USA, November 1-3 2010, pp. 190–196.

[16] F. Lewis, S. Jagannathan, and A. Yesildirek, *Neural Network Control of Robotic Manipulators and Nonlinear Systems*. London, UK: Taylor & Francis, 1999.

[17] F. Lewis, D. Dawson, and C. Abdallah, *Robot Manipulators Control: Second Edition, Revised and Expanded*. New York, NY: Marcel Dekker, Inc.,, 2004.

[18] C.-H. Chen, D. S. Naidu, A. Perez-Gracia, and M. P. Schoen, "A hybrid adaptive control strategy for a smart prosthetic hand," in *The 31st Annual International Conference of the IEEE Engineering Medicine and Biology Society (EMBS)*, Minneapolis, Minnesota, USA, September 2-6 2009, pp. 5056–5059.

[19] C.-H. Chen, D. S. Naidu, and M. P. Schoen, "An adaptive control strategy for a five-fingered prosthetic hand," in *The 14th World Scientific and Engineering Academy and Society (WSEAS) International Conference on Systems, Latest Trends on Systems (Volume II)*, Corfu Island, Greece, July 22-24 2010, pp. 405–410.

[20] C.-H. Chen, M. P. Schoen, and K. W. Bosworth, "A condensed hybrid optimization algorithm using enhanced continuous tabu search and particle swarm optimization," in *Proceedings of the ASME 2009 Dynamic Systems and Control Conference (DSCC)*, Hollywood, California, USA, October 12-14 2009, (No. DSCC2009-2526).

[21] A. Konar, *Computational Intelligence: Principles, Techniques and Applications*. Berlin, Germany: Springer-Verlag, 2005.

[22] C.-H. Chen, K. W. Bosworth, and M. P. Schoen, "Investigation of particle swarm optimization dynamics," in *Proceedings of International Mechanical Engineering Congress and Exposition (IMECE) 2007*, Seattle, Washington, USA, November 11-15 2007, (No. IMECE2007-41343).

[23] C.-H. Chen, K. Bosworth, and M. P. Schoen, "An adaptive particle swarm method to multiple dimensional problems," in *Proceedings of the International Association of Science and Technology for Development (IASTED) International Symposium on Computational Biology and Bioinformatics (CBB 2008)*, Orlando, Florida, USA, November 16-18 2008, pp. 260–265.

[24] C.-H. Chen, "Hybrid control strategies for smart prosthetic hand," Ph.D. dissertation, Measurement and Control Engineering, Idaho State University, May 2009.

[25] R. N. Jazar, *Theory of Applied Robotics. Kinematics, Dynamics, and Control*. New York, USA: Springer, 2007.

[26] B. Siciliano, L. Sciavicco, L. Villani, and G. Oriolo, *Robotics: Modelling, Planning and Control*. London, UK: Springer-Verlag, 2009.

[27] J.-S. Jang, C.-T. Sun, and E. Mizutani, *Neuro-Fuzzy and Soft Computing: A Computational Approach to Learning and Machine Intelligence*. Upper Saddle River, NJ: Prentice Hall PTR, 1997.

[28] F. Karray and C. De Silva, *Soft Computing and Intelligent Systems Design: Theory, Tools and Applications*. Harlow, England, UK: Pearson Educational Limited, 2004.

[29] H. Nguyen, N. Prasad, C. Walker, and E. Walker, *A First Course in Fuzzy and Neural Control*. Boca Raton, FL: Chapman & Hall/CRC, 2003.

[30] V. Nandikolla and D. Naidu, "Blood glucose regulation for diabetic mellitus using a hybrid intelligent technique," in *Proceedings of the 2005 ASME International Mechanical Engineering Congress and Exposition (IMECE)*, Orlando, FL, November 5-11 2005, pp. 1–6.

[31] V. Nandikolla, "Fusion of hard and soft control techniques in biomedical engineering," Ph.D. dissertation, Measurement and Control Engineering, Idaho State University, Pocatello, Idaho, December 2005, thesis Supervisor: D.S. Naidu.

[32] R. Kelly, V. Santibanez, and A. Loria, *Control of Robot Manipulators in Joint Space*. New York, USA: Springer, 2005.

[33] A. Nikoobin and R. Haghighi, "Lyapunov-based nonlinear disturbance observer for serial n-link robot manipulators," *Journal of Intelligent and Robotic Systems*, 2008, (Published online on 11 December 2008).

[34] Y. Z. Arslan, Y. Hacioglu, and N. Yagiz, "Prosthetic hand finger control using fuzzy sliding modes," *Journal of Intelligent and Robotic Systems*, vol. 52, pp. 121–138, 2008.

[35] P. K. Lavangie and C. C. Norkin, *Joint Structure and Function: A Comprehensive Analysis, Third Edition*. Philadelphia, PA: F. A. Davis Company, 2001.

[36] S. Arimoto, *Control Theory of Multi-fingered Hands: A Modeling and Analytical-Mechanics Approach for Dexterity and Intelligence*. London, UK: Springer-Verlag, 2008.

2010 5th Cairo International Biomedical Engineering Conference
Cairo, Egypt, December 16-18, 2010

Precision Grasping of a Prosthetic Hand Based on Virtual Spring Damper Hypothesis

Amir Fassih, D. Subbaram Naidu, *Fellow*, Steve Chiu, *Member* and Marco P. Schoen, *Member, IEEE*

***Abstract*— A control strategy for achieving object precision grasping by a prosthetic hand is proposed. The control strategy is based on defining virtual spring-damper between two finger tips and damping force at each finger joint. It is shown that the proposed control strategy provides a satisfactory performance in precision grasping of a prosthetic hand, without the need for additional complexity regarding equations for inverse kinematics, or inverse dynamics, and the information on tactile or force sensing or even object shape.**

I. Introduction

HUMAN hand is one of the most important and complex parts of the body, which has the ability to handle different tasks. Loss of hand can highly affect the quality of life; hence there is a high demand among amputees for prosthetic hands. The goal is to design an anthropomorphic prosthetic hand which is capable to be controlled through mind and has functionality close to normal human hand.

The muscle movements in humans are controlled by electromyographic (EMG) signal which comes from brain to the body. In case of a lower hand amputee the remaining part of muscles are capable to measure EMG and through it find the subject's intention.

Grasping can be categorized into two main groups: precision and power grasping. In precision grasping the object is held by tips of the fingers, while in power grasping, the whole finger is active and in contact with the object [1]. Our previous work [2] addressed the problem of power grasping and here we study the problem of precision grasping of a prosthetic hand.

Many control methods require the knowledge of the shape of the object. For humans this information is available by visual feedback from eyes, while in case of a prosthetic hand this visual information is not directly available for hand controller, and the only available information is electromyographic (EMG) signal related to patient's arm muscle activities. However, normally the EMG signal is not available for all individual joints and besides, due to measurement noise, accessing high quality EMG signal is hard [3]. Moreover, using EMG signal to control all the movements requires lot of attention during grasping and leads to fatigue for the amputees [4]. Hence it is required for prosthetic hand to be semi-autonomous which means a part of command information will be provided by the EMG signal and the rest of the required command should be provided automatically by hand controller.

Defining finger trajectory without the knowledge of shape of object to be grasped is a challenging task for many path planning techniques. For multi DOFs robots there are two common methods for trajectory planning which are "inverse kinematics" and "inverse dynamics" [5]-[7]. Both these methods require object shape and are based on solving optimization problem which requires high computation, hence they are hard to implement for real-time applications.

To avoid solving the path planning problem for prosthetic hands, many researchers advocated under-actuated mechanisms, which are capable of adapting to object shape mechanically and without additional computation [8]-[10]. In these mechanisms, the number of actuators is less than the DOFs, and because of less number of actuators they have less weight. However fewer actuators result in less functionality, because fingers joints can't move independently.

Arimoto *et al.* [11] used "virtual spring-damper hypothesis" for control of robotic arm-hand systems. A similar method called "virtual model control" is also suggested by J.Pratt *et al.* [12] used for walking robots, and it is based on defining virtual forces between two points. Both methods are based on the use of Jacobian matrix to relate task space movement to joint space. In [12] it is shown that any kind of force can be defined between two points and the other study [11] shows that use of spring-damper forces will result in human like movement. From physiological point of view, human skilled multi-joint reaching movement has these characteristics: 1) endpoint trajectory become a quasi-straight line and less variable, 2)velocity profiles of the endpoint has a bell-shape, and 3) joint trajectories are rather variable from trial to trial [11].

In this paper, a new control scheme is proposed that can efficiently address the problem of precision grasping without complete knowledge of the shape of the object which may be called "blind precision grasping" for prosthetic hand. The proposed method is based on the works by Arimoto *et al.* [11] using virtual spring-damper (VSD) hypothesis for control of robotic arm-hand systems. In our paper, we use the above mentioned hypothesis, in particular for the precision grasping of a prosthetic hand. In this method, we define a virtual spring-damper between finger tip and desired point for control of movement of fingers. Further, in this method there is no need to introduce any performance indices to solve inverse kinematics uniquely

Manuscript received August 25, 2010. The research was sponsored by the US Department of the Army, under the award number W81XWH-10-1-0128 awarded and administered by the U.S. Army Medical Research Acquisition Activity, 820 Chandler Street, Fort Detrick MD 21702-5014.

Authors are with School of Engineering, Idaho State University, 921 S, 8th Ave, Pocatello, Idaho, ID 83209 USA (e-mail : naiduds@isu.edu).

978-1-4244-7169-0/10/$26.00 ©2010 IEEE

and Jacobian pseudo-inverse or inverse dynamics which are common methods to define trajectories of redundant DOFs robots. Besides, in the present method, there is no need for any information on tactile or force sensing.

The paper is organized as follows. In Section 2 modeling of prosthetic hand is discussed, Section 3 covers virtual spring damper method. Section 4 describes control strategy. Section 5 analyzes the efficiency of the proposed control scheme using numerical simulation. Finally, conclusion and discussion are presented in section 6.

II. Modeling of Prosthetic Hand

In this control method, controller is not designed based on dynamic model of the system. Instead, kinematics equation and Jacobian matrix are used for controller design.

A model of a robotic hand system is shown in Fig.1. The model consists of a finger with 3DOF which represents three joints of index finger, palm and a finger with 2DOF which represents thumb.

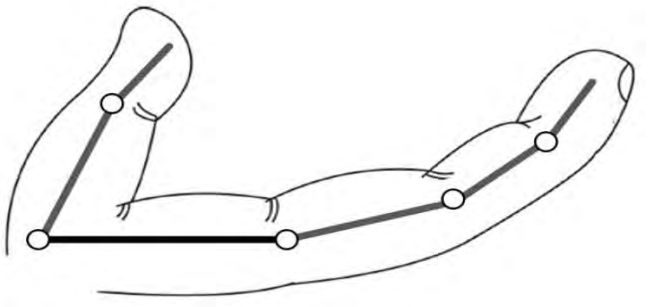

Fig. 1. Schematic of a robotic hand system

In this paper we assume the following:

1) Movement of both finger and object are confined to a 2 dimensional horizontal plane, and therefore there is no gravity effect.
2) The object is assumed to be initially stable in its position.
3) The initial movement toward object is handled by amputee, so the hand is close enough to the object before grasping.

The position of the tip of index fingers is evaluated as (see Fig. 1):

$$x_i = l_{i1}\ cos\, q_{i1} + l_{i2}\ cos(q_{i1} + q_{i2}) + l_{i3}\ cos(q_{i1} + qi2+qi3), \quad (1)$$

$$y_i = l_{i1}\ sin\, q_{i1} + l_{i2}\ sin(q_{i1} + q_{i2}) + l_{i3}\ sin(q_{i1} + qi2+qi3), \quad (2)$$

where, l_{i1}, l_{i2}, and l_{i3} are lengths of index finger and q_{i1}, q_{i2}, and q_{i3} are angles of each corresponding joint. Similarly the position of thumb finger is evaluated as:

$$x_t = l_{t1}\ cos\, q_{t1} + l_{t2}\ cos(q_{t1} + q_{t2}), \quad (3)$$

$$y_t = l_{t1}\ sin\, q_{t1} + l_{t2}\ sin(q_{t1} + q_{t2}), \quad (4)$$

where, l_{t1} and l_{t2} are lengths of thumb finger and q_{t1} and q_{t2}, are angles of corresponding joints.

Based on above equation the Jacobian matrix for index finger is as:

$$J_i = \begin{bmatrix} \frac{\partial x}{\partial q_{i1}} & \frac{\partial x}{\partial q_{i2}} & \frac{\partial x}{\partial q_{i3}} \\ \frac{\partial y}{\partial q_{i1}} & \frac{\partial y}{\partial q_{i2}} & \frac{\partial y}{\partial q_{i3}} \end{bmatrix}, \quad (5)$$

and Jacobian for thumb finger is as:

$$J_t = \begin{bmatrix} \frac{\partial x}{\partial q_{t1}} & \frac{\partial x}{\partial q_{t2}} \\ \frac{\partial y}{\partial q_{t1}} & \frac{\partial y}{\partial q_{t2}} \end{bmatrix}. \quad (6)$$

III. Virtual Spring Damper Method

Virtual model control was first proposed by J. Pratt *et al* [12] for biped walking robot. This method is a motion control scheme that uses simulations of virtual components to generate desired joint torques [12]. These joints produce the same effect that the virtual elements placed on robot would have created; hence they create the illusion that these virtual elements are connected to the real robot. Virtual elements can be any kind of real physical elements such as springs, dampers, gravity fields, nonlinear fields or any other components. In a study by Arimoto [11] on robotic hand arm system, it is shown that using a virtual spring damper between robot end effecter and desired point, and virtual dampers at each joint, human like movement can be achieved.

For precision grasping by a prosthetic hand, one of the best options is the use of Virtual Spring-Damper (VSD) hypothesis. Some benefits of VSD control scheme are that it has a simple structure and requires relatively less computation. Besides, it doesn't need inverse dynamics to precisely define the robot movement. Thus, we use spring set points instead of commanded movement and robot automatically adapts its shape. Since finger joints at prosthetic hand work as virtual dampers, which is sensitive to velocity and not to position, they don't have a forced shape, instead just finger tip follow a defined path as will be discussed more in control strategy section.

The joint torques to virtual forces is given by:

$$\tau = J^T F, \quad (7)$$

where τ is the torque, and *F* is the force due to virtual spring damper given as

$$F = -(\xi\sqrt{k}\dot{x} + k\Delta x), \quad (8)$$

and

$$\tau_{spring-damper} = -J^T\left(\xi\sqrt{k}\dot{x} + k\Delta x\right), \quad (9)$$

where *k* represents the stiffness of the virtual spring, Δx is distance between finger tip and desired point, and ξ is the damping ratio. The damping force is defined at each joint as

$$\tau_{joints\ damping} = -C\dot{q}, \quad (10)$$

where, C denotes a diagonal positive definite matrix as follows:

$$C = \xi_0\ diag(c_1, \dots, c_n). \quad (11)$$

Hence control signal would be sum of these two terms:

$$u = -C\dot{q} - J^T(q)\left(\xi\sqrt{k}\dot{x} + k\Delta x\right). \quad (12)$$

IV. Control Strategy

Virtual spring-damper hypothesis is suitable for point to point control. In precision grasping two approaches can be considered. 1) Defining a virtual spring damper between fingers tip and geometrical center of the object, which requires information about the object position and shape, and this information is not available in case of a prosthetic hand for the controller which is used in [13] 2) Defining a virtual spring damper between tips of two fingers, then fingers attract together and grasp the object in between, without exact knowledge of object position and shape. In this case the amputee should place the hand close to the object and in appropriate position. Besides, a virtual damper force is considered at each finger joint. The latter method is used and physical counterpart of virtual forces are depicted at Fig. 2.

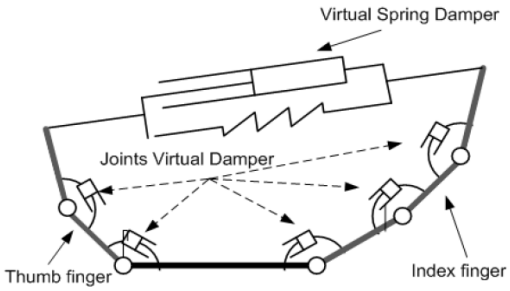

Fig. 2. Physical counterparts of the virtual forces

Higher values of k (virtual spring stiffness) results in faster movement of fingers as well as, higher grasping force. Thus by defining k proportional to EMG signal, amputee have control over speed of movement and grasping force.
The damping coefficient of finger joints, can change the final shape of fingers. The joints with lower damping tends to move more, while higher damped joints move more. The appropriate values of damping are evaluated based on trial and error to reach positions close to normal hand and they are held constant for further simulations.

V. Numerical Simulation

In order to show the effectiveness of the proposed control strategy, numerical simulations were conducted to grasp two different objects, based on the physical parameters of a hand system and objects summarized in Table I.

The Adams software which is multi-body dynamic simulation software is used for numerical analysis. The software is capable to conduct information between Matlab/ Simulink software environment, hence the plant is modeled by Adams and controller is implemented in Matlab/Simulnk.

TABLE I
Parameters Used for Simulation

Parameter	Value
index finger link 1 length	5 cm
index finger link 2 length	2.5 cm
index finger link 3 length	2.5 cm
thumb finger link 1 length	4 cm
thumb finger link 2 length	3 cm
distance between thumb and index	6 cm
damping at joints	0.01 kg/s
virtual damping ratio	1
virtual spring stiffness	50 N/m
rectangular object width	2 cm
circular object radius	2 cm

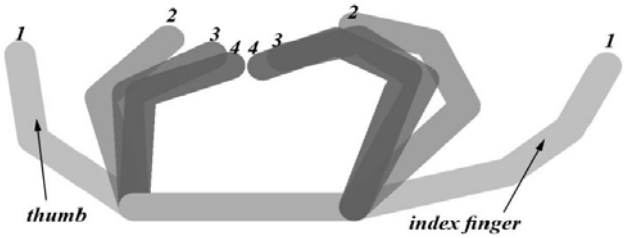

Fig. 3. Finger movements in 4 different position (0.25 sec. intervals)

For first simulation, two fingers are modeled without any object in between. As shown in Fig. 3, two fingers come together, and final position is close to normal hand coordination.

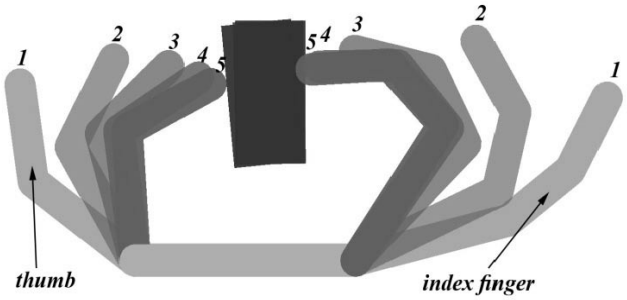

Fig. 4. Rectangular object grasping (0.25 sec intervals)

For the second simulation, a rectangular object is chosen to be grasped. The object is free to move in 2 dimensional plane, and contact and friction force are simulated between finger tip and the object. The object is placed at arbitrary final position of previous experiment. The finger movement at 0.25 sec time intervals and finger tip angles relative to palm are shown respectively in Figs. 4 and 5.

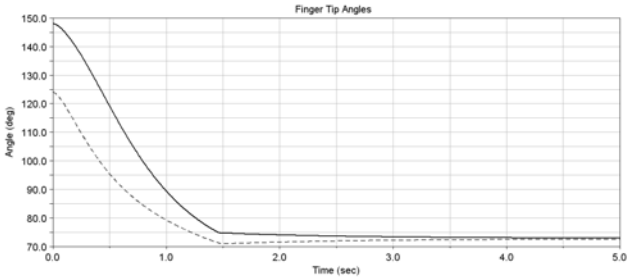

Fig. 5. Finger tips angle at rectangular object grasping
(index finger solid line and thumb finer dashed line)

As it is shown after contact with object at approximately 1.5 second the angles are not changing much. The small changes are due to object movements toward left.

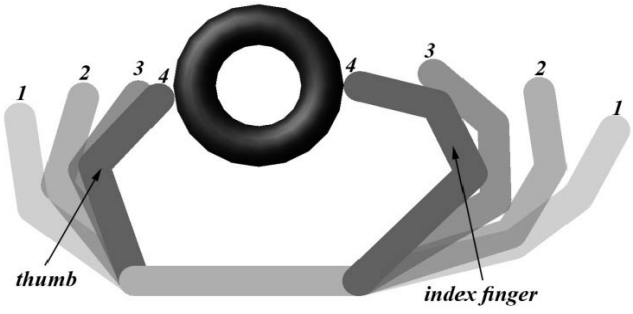

Fig. 6. Circular object grasping (0.25 sec intervals)

For third simulation a round object is selected. The object is not subjected to any constrain in 2 dimensional plane. The contact and friction force are defined between object and finger tip. The virtual spring coefficient which is proportional to EMG signal is assumed to be constant. Almost after 1 sec, the fingers contacted with the object. The finger movement at 0.25 sec time intervals and finger tip angles relative to palm are shown respectively in Figs. 6 and 7.

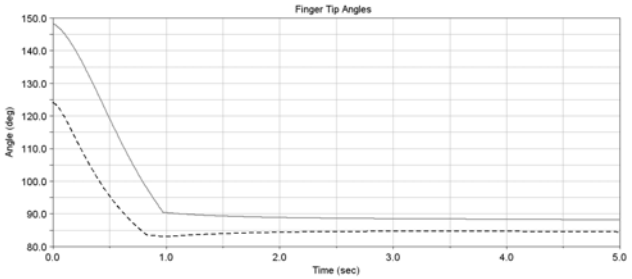

Fig. 7. Finger tips angle at circular object grasping
(index finger solid line and thumb finer dashed line)

Appropriate object position and friction force between fingers and object are important parameters that help successful grasping. For the case of a round object if the object has inappropriate position or friction is not enough, the grasping might be unstable, but guarantied successful grasping under all conditions require information about object shape and position which are not available for case of a prosthetic hand hence this control strategy is appropriate for most of the daily activities.

VI. Conclusion

Based on virtual spring damper hypothesis, a control strategy for precision grasping of a prosthetic hand was proposed. The controller doesn't require extensive computation of inverse kinematic or inverse dynamics to describe finger movement and hence the method is appropriate for real-time applications. The control strategy is independent of object shape or force and contact sensor. By numerical simulation, the capability and effectiveness of control strategy are shown. The same strategy was used for two different objects and grasping was successful.

The future work will focus on precision grasping by gravity cancelation and analysis in three-dimensional space and experimental implementation with EMG signals.

References

[1] Lynette A. Jones and Susan J. Lederman, *Human Hand Function*, New York: Oxford University Press, 2006, pp. 131-149.

[2] Amir Fassih, D. Subbaram Naidu, Steve Chiu, and Marco P. Schoen, "power grasping of a prosthetic hand based upon virtual spring-damper hypothesis", *Proc. IASTED Int. Conf. Robotics and Applications*, Cambridge, Massachusetts, 2010, pp. 214-220.

[3] Mohammad Asghar Oskooei, Housheng Hu, "Myoelectric control systems, a survey", *Biomedical Signal Processing and Control*, vol. 2, 2007, pp 275-294.

[4] Chiristian Cipriani, Franco Zaccone, Silvestro Micera, Chiara Carrozza, "On the shared control of an emg-controlled prosthetic hand: analysis of user-prosthesis interaction", *IEEE Transaction on Robotics*, vol.24, No1, February 2008.

[5] Erik D Engeberg, Sanford G. Meek, "Backsptepping and sliding mode control hybridized for a prosthetic hand", *IEEE Trans. on Neural Systems and Rehabilitation Engineering*, vol. 17, No.1, February 2009.

[6] D.E.Whitney, "Resolved motion rate control of manipulators and human prostheses", *IEEE Trans. Man-Machine Syst.*, vol. MMS-10, No.2, 1969, pp.47– 53.

[7] Y. Nakamura, "Advanced robotics: redundancy and optimization", Addison-Wesley, Reading, MA, 1991.

[8] N. Dechev, W.L. Cleghron, S. Naumann, Multiplefinger, "Passive adaptive grasp prosthetic hand", *Mechanism and Machine Theory*, vol.36, 2001, pp.1157-1173.

[9] Ramiero Cabas, Luis Maria Cabas, Carlos Balaguer, "Optimized design of the underactuated robotic hand", *Proceeding of the 2006 IEEE International Conferences on Robotics and Automation*, Orlando, Florida, May 2006.

[10] Da-Peng Yang, Jing-dong Zhao, Yi-kun Gu, Xin-qing Wang, Nan Li, Li Jiang, Hong Liu, Hai Huang, Da-wei Zhao, "An anthropomorphic robot hand develeoped based on underactuated mechanism and controlled by EMG signals", *Journal of Bionic Engineering*, vol. 6, 2009, pp 255-263.

[11] Suguru Arimoto, Masahiro Sekimoto, "Human-like movements of robotic arms with redundant dofs: virtual spring-damper hypothesis to tackle the brenestein problem", *Prec. of IEEE Int. Conf. on Robotics and Automation*, Orlando, Florida, May 2006.

[12] Jerry Pratt, Chee-Meng Chew, Ann Torres, Peter Dilworth, Gill Pratt, "Virtual model control: an intuitive approach for bipedal locomotion", *The International Journal of Robotics Research*, vol. 20, No. 2, pp. 129-143, February 2001.

[13] Thomas Wimboeck, Christian Ott, Gerhard Hirzinger, "Passivity-based object-level impedance control for a multifingered hand" *Proceedings of the 2006 IEEE/RSJ, International Conference on Intelligent Robots and Systems*, Beijing, China,2006.

Fusion of Fuzzy Logic and Proportional-Derivative Control for a Five-Fingered Smart Prosthetic Hand

Cheng-Hung Chen and D. Subbaram Naidu

Measurement and Control Engineering Research Center (MCERC)

School of Engineering, Idaho State University, Pocatello, ID 83209, USA

Abstract

A hybrid of soft control technique of adaptive neuro-fuzzy inference system (ANFIS) and fuzzy logic (FL) and hard control technique of proportional-derivative (PD) for a five-fingered, smart prosthetic hand is presented. The ANFIS is used for inverse kinematics and FL is used for tuning the PD parameters with two input layers (error and error change) using 7 triangular membership functions and 49 fuzzy logic rules. Simulation results with FL-tuned PD controller exhibit superior performance compared to the PD and PID control alone.

Methods

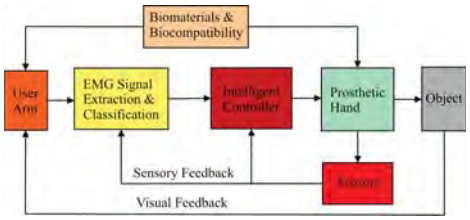

Figure 1. Schematic Diagram of Prosthetic Hand Technology: The overall system consists of electromyographic (EMG) signal acquisition from the user arm for surface or implanted electrodes (in the implanted case we focus on biocompatibility based on nano-materials research). The EMG signal is then processed for feature extraction and classification or identification of EMG signal to correspond to different motions of the prosthetic hand. The classified signal is then used to control the prosthetic hand using actuators and driving mechanisms.

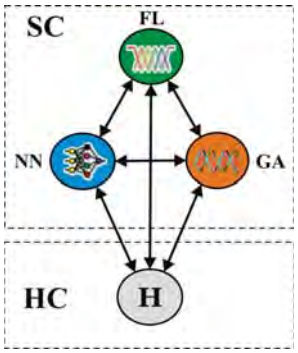

Figure 2. Principle behind Fusion of Soft and Hard Computing: The present research focuses on developing intelligent autonomous strategies for EMG signal, extraction, analysis and control prosthetics by fusion of soft computing (SC) techniques comprising neural network (NN), fuzzy logic (FL), and genetic algorithm (GA) and hard control (HC) techniques, such as proportional-derivative (PD), optimal control, adaptive control and so on. We present the integration of SC and HC to solve problems that cannot be solved satisfactorily by using either HC or SC methodology alone with specific applications to prosthetics.

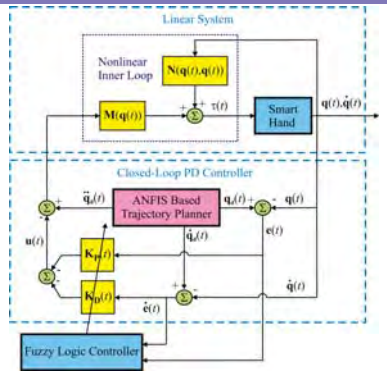

Figure 3. Block Diagram of the Presented Hybrid Fuzzy Logic-Based Proportional-Derivative (PD) Controller for a Five-Fingered Prosthetic Hand: Errors and error changes are calculated by actual and desired angles, which are based on adaptive neuro-fuzzy inference system (ANFIS) trajectory planner. Then fuzzy logic controller tunes all parameters of closed-loop PD control so that the required torque of the prosthetic hand nonlinear system is computed by control input.

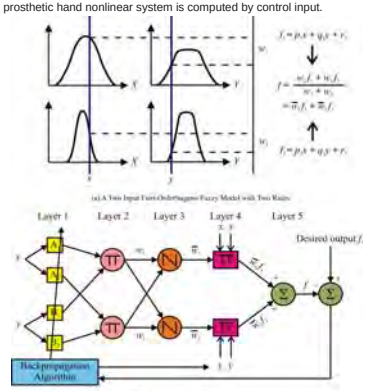

Figure 4. ANFIS Architecture: (a) A Two Input First-Order Sugeno Fuzzy Model with Two Rules (b) Equivalent ANFIS Structure. The inverse kinematics problems are solved by using adaptive neuro-fuzzy inference system (ANFIS) method where the input of fuzzy-neuro system is the Cartesian space and the output is the joint space. ANFIS is a fuzzy inference system implemented in the framework of adaptive networks which provides the best optimization algorithm to find parameters in order to fit the data.

Figure 5. Relationship between Global and Local Coordinates: Local coordinate x^l-y^l-z^l of thumb can be reached by rotating through angles α and β to X^G and Y^G of global coordinate, subsequently. Local coordinate x^l-y^l-z^l of index finger can be obtained by rotating through angle α to X^G and then translating a vector $\mathbf{d}^l$ of the global coordinate.

Figure 6. The Structural Characteristics of Proposed Fuzzy Inference System: Two inputs (error and error change) on the left and one output (tuned K_P) on the right with 49 logic rules

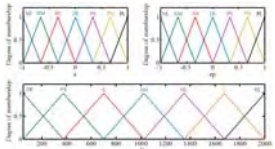

Figure 7. Each of Two Inputs (Upper Panel) and One Output (Lower Panel) Uses 7 Triangular Membership Functions

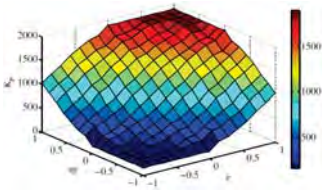

Figure 8. The Output Surface of Fuzzy Inference System with Two Inputs and 49 Logic Rules

Results

Table 1. Parameter Selection of Conversion between Global and Local Coordinates

Parameters	Values
Rotating α	90 (deg)
Rotating β	45 (deg)
Translating $\mathbf{d}^1$	(0.035, 0, 0) (m)
Translating $\mathbf{d}^{III}$	(0.040, 0, -0.020) (m)
Translating $\mathbf{d}^{IV}$	(0.035, 0, -0.040) (m)
Translating $\mathbf{d}^{V}$	(0.025, 0, -0.060) (m)

Table 2. A Complete Fuzzy Logic Rule Base

ė \ e	NL	NM	NS	ZR	PS	PM	PL
NL	ZR	ZR	ZR	ZR	VS	S	SM
NM	ZR	ZR	ZR	VS	S	SM	ML
NS	ZR	ZR	VS	S	SM	ML	L
ZR	ZR	VS	S	SM	ML	L	VL
PS	VS	S	SM	ML	L	VL	VL
PM	S	SM	ML	L	VL	VL	VL
PL	SM	ML	L	VL	VL	VL	VL

N: negative, P: positive, ZR: zero, L: large, M: medium, S: small, V: very

Table 3. Parameter Selection of the Smart Hand

Parameters	Value
Thumb	
Time (t_0, t_f)	0, 20 (sec)
Desired Initial Position (X_0^T, Y_0^T)*	0.035, 0.060 (m)
Desired Final Position (X_f^T, Y_f^T)*	0.0495, 0.060 (m)
Desired Initial Velocity ($\dot{X}_0^T, \dot{Y}_0^T$)*	0, 0 (m/s)
Desired Final Velocity ($\dot{X}_f^T, \dot{Y}_f^T$)*	0, 0 (m/s)
Length (L_1^T, L_2^T)	0.040, 0.040 (m)
Mass (m_1^T, m_2^T)	0.043, 0.031 (kg)
Index Finger	
Desired Initial Position (X_0^{II}, Y_0^{II})*	0.065, 0.080 (m)
Desired Final Position (X_f^{II}, Y_f^{II})*	0.010, 0.060 (m)
Length ($L_1^{II}, L_2^{II}, L_3^{II}$)	0.040, 0.040, 0.030 (m)
Mass ($m_1^{II}, m_2^{II}, m_3^{II}$)	0.045, 0.025, 0.017 (kg)
Middle Finger	
Desired Initial Position (X_0^{III}, Y_0^{III})*	0.065, 0.080 (m)
Desired Final Position (X_f^{III}, Y_f^{III})*	0.005, 0.060 (m)
Length ($L_1^{III}, L_2^{III}, L_3^{III}$)	0.044, 0.044, 0.033 (m)
Mass ($m_1^{III}, m_2^{III}, m_3^{III}$)	0.050, 0.028, 0.017 (kg)
Ring Finger	
Desired Initial Position (X_0^{IV}, Y_0^{IV})*	0.065, 0.080 (m)
Desired Final Position (X_f^{IV}, Y_f^{IV})*	0.010, 0.060 (m)
Length ($L_1^{IV}, L_2^{IV}, L_3^{IV}$)	0.040, 0.040, 0.030 (m)
Mass ($m_1^{IV}, m_2^{IV}, m_3^{IV}$)	0.041, 0.023, 0.014 (kg)
Little Finger	
Desired Initial Position (X_0^{V}, Y_0^{V})*	0.055, 0.080 (m)
Desired Final Position (X_f^{V}, Y_f^{V})*	0.020, 0.060 (m)
Length ($L_1^{V}, L_2^{V}, L_3^{V}$)	0.036, 0.036, 0.027 (m)
Mass ($m_1^{V}, m_2^{V}, m_3^{V}$)	0.041, 0.023, 0.014 (kg)

* All fingers use same parameters.
** All parameters are in local coordinates.

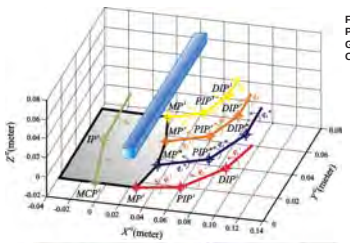

Figure 9. Five-Fingered Prosthetic Hand Grasping a Rectangular Object

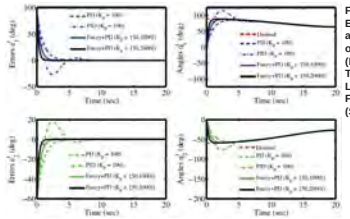

Figure 10. Tracking Errors (Left) and Desired and Actual Angles (Right) of Joints 1 (Upper) and 2 (Lower) for Two-Link Thumb Using PD (Dash Line), PID (Dot Line) and Fuzzy Logic Based PD (Solid Line) Controllers

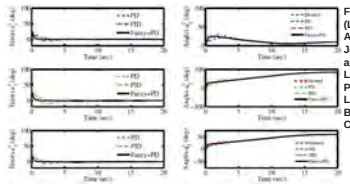

Figure 11. Tracking Errors (Left) and Desired and Actual Angles (Right) of Joints 1 (Top), 2 (Middle) and 3 (Bottom) for Three-Link Index Finger Using PD (Dash Line), PID (Dot Line) and Fuzzy Logic Based PD (Solid Line) Controllers

Conclusions and Future Work

1. For a five-fingered, smart prosthetic hand, a hybrid control technique involving soft control with adaptive neuro-fuzzy inference system (ANFIS) and fuzzy logic (FL) and hard control with proportional-derivative (PD) was presented.

2. The ANFIS is used for inverse kinematics and FL is used for tuning the PD parameters with two input layers (error and error change) using 7 triangular membership functions and 49 fuzzy logic rules.

3. Simulation results with FL-tuned PD controller showed superior performance compared to the PD and PID control alone.

4. Work is underway to extend this methodology to a real-time prosthetic hand.

Acknowledgment: **The research was sponsored by the U.S. Department of the Army, under the award number W81XWH-10-1-0128 awarded and administered by the U.S. Army Medical Research Acquisition Activity, 820 Chandler Street, Fort Detrick, MD 21702-5014, USA. The information does not necessarily reflect the position or the policy of the Government, and no official endorsement should be inferred.**

POWER GRASPING OF A PROSTHETIC HAND BASED UPON VIRTUAL SPRING-DAMPER HYPOTHESIS

Amir Fassih, D. Subbaram Naidu, Steve Chiu, and Marco P. Schoen
Measurement and Control Engineering Research Center, Idaho State University
921 South 8th Ave, Stop 8060, Pocatello, Idaho
USA
fassamir@isu.edu, naiduds@isu.edu, chiustev@isu.edu, and schomarc@isu.edu

ABSTRACT
A control scheme for achieving object power grasping by a prosthetic hand is proposed. The control scheme is based on defining virtual spring-damper between finger tip and desired point, and a semi circular path for finger tip. It is shown that the suggested control scheme provides satisfactory performance in power grasping of prosthetic hand, without the need for additional complexity regarding equations for inverse kinematics, or inverse dynamics, and the information on tactile or force sensing or even object shape.

KEY WORDS
Medical Robotics, Control, Power Grasping, Prosthetic Hand Control.

1. Introduction

Human hand is one of the most important and complex parts of the body, which has the ability to handle different tasks. The ultimate goal of robotic hand is to achieve the functionality of a human hand. In the past three decades, there have been numerous investigations to achieve dexterity and ability of human hand, especially in the fields of humanoid robotics and prosthetic hand [1-6]. In spite of all these advances in this field, the current state of research on prosthetic hands is far from that objective of achieving the functionality of human hand. Commercially available prosthetic hands have very limited functionality and they are just simple grippers. The present research on prosthetic hands involves complex control schemes to achieve the most important functions of the hand [7-8].

Grasping can be categorized into two main groups: precision and power grasping. In precision grasping the object is held by tips of the fingers, while in power grasping, the whole the finger is active and in contact with the object [9]. Many research works addressed the precision grasping problem [12-15] mainly because of the well-established techniques for control of end effector; however the problem of power grasping is not studied in depth.

Many control methods require the knowledge of the shape of the object. For humans this information is available by visual feedback from eyes, while in case of a prosthetic hand this visual information is not directly available for hand controller, and the only available information is electromyographic (EMG) signal related to patient's arm muscle activities. However, normally the EMG signal is not available for all individual joints and besides, due to measurement noise, accessing high quality EMG signal is hard [10]. Moreover, using EMG signal to control all the movements requires lot of attention during grasping and leads to fatigue for the amputees [11]. Hence it is required for prosthetic hand to be semi-autonomous which means a part of command information will be provided by the EMG signal and the rest of the required command should be provided automatically by hand controller.

Defining finger trajectory without the knowledge of shape of object to be grasped is a challenging task for many path planning techniques. For multi DOFs robots there are two common methods for trajectory planning which are "inverse kinematic" and "inverse dynamic" [12-15]. Both these methods require object shape and are based on solving optimization problem which requires high computation, hence they are hard to implement for real-time applications.

To avoid solving the path planning problem for prosthetic hands, many researchers advocated under-actuated mechanisms, which are capable of adapting to object shape mechanically and without additional computation [16-18]. In these mechanisms, the number of actuators are less than the DOFs, and because of less actuators they have less weight. However fewer actuators result in less functionality, because fingers joints can't move independently.

Arimoto et al. [19] used "virtual spring-damper hypothesis" for control of robotic arm-hand systems. A similar method called "virtual model control" is also suggested by J.Pratt et al. [20] used for walking robots, and it is based on defining virtual forces between two points. Both methods are based on the use of Jacobian matrix to relate task space movement to joint space. In [20] it is shown that any kind of force can be defined between two points and the other study [19] shows that use of spring-damper forces will result in human like movement. From physiological point of view, human skilled multi-joint reaching movement has these

characteristics that 1) endpoint trajectory become a quasi-straight line and less variable, 2)velocity profiles of the endpoint has a bell-shape, and 3) joint trajectories are rather variable from trial to trial [19].

In this paper, a new control scheme is proposed that can efficiently address the problem of power grasping without complete knowledge of the shape of the object which may be called "blind power grasping" for prosthetic hand. The proposed method is based on the works by Arimoto et al. [19] using virtual spring-damper (VSD) hypothesis used for control of robotic arm-hand systems. In our paper, we use the above mentioned hypothesis, in particular for the power grasping of a prosthetic hand. In this method, we define a virtual spring-damper between finger tip and desired point for control of movement of fingers. Further, in this method there is no need to introduce any performance indices to solve inverse kinematics uniquely and Jacobian pseudo-inverse or inverse dynamics which are common methods to define trajectories of redundant DOFs robots. Besides, in the present method, there is no need for any information on tactile or force sensing.

The paper is organized as follows. In Section 2 modeling of prosthetic hand is discussed, Section 3 covers virtual spring damper method. Section 4 describes control strategy. Section 5 analyzes the efficiency of the proposed control scheme using numerical simulation. Finally, conclusion and discussion are presented in section 6.

2. Modeling of Prosthetic Hand

In this control method, controller is not derived directly from dynamic model of the system. Kinematics equation and Jacobian matrix are the required for controller design.

A model of a robotic hand system is shown in Fig.1. The model consists of a finger with 3DOF which represents three joints of a finger and palm.

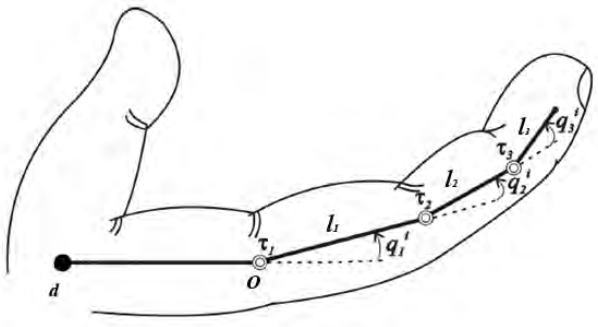

Fig. 1: Model of a Robotic Hand System.

In this paper we assume the following:

1- Movement of both finger and object are confined to a two dimensional horizontal plane, and therefore there is no gravity effect.

2- The object is assumed to be initially stable in its position.

3- The initial movement toward object is handled by amputee, so the hand is close enough to the object before grasping.

The position of the tip of the finger is evaluated as (see Figure 1):

$$x = l_1\ cos\, q_1 + l_2\ cos(q_1 + q_2) + l_3\ cos(q_1 + q_2 + q_3) \quad (1)$$

$$y = l_1\ sin\, q_1 + l_2\ sin(q_1 + q_2) + l_3\ sin(q_1 + q_2 + q_3) \quad (2)$$

where, l_1, l_2, and l_3 are lengths of each finger and q_1, q_2, and q_3 are angles of each corresponding joint.

Based on above equation the Jacobian matrix is as:

$$J = \begin{bmatrix} j_{11} & j_{12} & j_{13} \\ j_{21} & j_{22} & j_{23} \end{bmatrix}, \quad (3)$$

$$j_{11} = -l_1\ sin\, q_1 - l_2\ sin(q_1 + q_2) - l_3\ sin(q_1 + q_2 + q_3), \quad (4)$$

$$j_{12} = -l_2\ sin(q_1 + q_2) - l_3\ sin(q_1 + q_2 + q_3), \quad (5)$$

$$j_{12} = -l_2\ sin(q_1 + q_2) - l_3\ sin(q_1 + q_2 + q_3), \quad (6)$$

$$j_{13} = -l_3\ sin(q_1 + q_2 + q_3)\,, \quad (7)$$

$$j_{21} = l_1\ cos\, q_1 + l_2\ cos(q_1 + q_2) + l_3\ cos(q_1 + q_2 + q_3)\,, \quad (8)$$

$$j_{22} = l_2\ cos(q_1 + q_2) + l_3\ cos(q_1 + q_2 + q_3), \quad (9)$$

$$j_{23} = l_3\ cos(q_1 + q_2 + q_3). \quad (10)$$

3. Virtual Spring-Damper Method

"Virtual model control" is a motion control scheme that uses simulations of virtual components to generate desired joint torques [20]. These joints produce the same effect that the virtual elements placed on robot would have created; hence they create the illusion that these virtual elements are connected to the real robot. Virtual elements can be any kind of real physical elements such as springs, dampers, gravity fields, nonlinear fields or any other components.

Virtual model control was proposed by J. Pratt et al [20] for biped walking robot. In a study by Arimoto [19] on robotic hand arm system, it is shown that using a virtual spring damper between robot end effector and desired point, and virtual dampers at each joint, human like movement can be achieved.

For power grasping by a prosthetic hand, one of the best options is the use of Virtual Spring-Damper (VSD) hypothesis. Some benefits of VSD control scheme are that it has a simple structure and requires relatively less computation. Besides, it doesn't need inverse dynamics to precisely define the robot movement. Thus, we use spring set points instead of commanded movement and robot automatically adapts its shape. Since finger joints at prosthetic hand work as virtual dampers, which is sensitive to velocity and not to position, they don't have a forced shape, instead just finger tip follow a defined path as will be discussed more in control strategy section.

The joint torques to virtual forces is given by:

$$\tau = J^T F, \quad (11)$$

where τ is the torque, and F is the force due to virtual spring damper given as

$$F = -(\xi\sqrt{k}\dot{x} + k\Delta x), \quad (12)$$

and

$$\tau_{spring-damper} = -J^T\left(\xi\sqrt{k}\dot{x} + k\Delta x\right), \quad (13)$$

where k represents the stiffness of the virtual spring, Δx is distance between finger tip and desired point, and ξ is the damping ratio. The damping force is defined at each joint as

$$\tau_{joints\ damping} = -C\dot{q}, \quad (14)$$

where, C denotes a diagonal positive definite matrix as follows:

$$C = \xi_0\ diag(c_1, \dots, c_n). \quad (15)$$

Hence control signal would be sum of these two terms

$$u = -C\dot{q} - J^T(q)\left(\xi\sqrt{k}\dot{x} + k\Delta x\right). \quad (16)$$

Higher values of k result in more accurate and faster response to the desired point and higher C provides more stability. Thus k and C are chosen as design variables.

4. Control Strategy

Virtual spring-damper hypothesis is suitable for point to point control. Defining the desired trajectory as a semicircle (in order to have a full grasp of the object) given by,

$$x_d = (l_1 + l_2 + l_3)\ cos(t), \quad (17)$$
$$y_d = (l_1 + l_2 + l_3)\ sin(t), \quad (18)$$

Where t is proportional to EMG signal which is scaled to change between $0<t<\pi$.

As shown in Fig. 2, after passing this semi-circle, finger tip goes toward center to make a tighter grasping. This is achieved by defining a desired point close to center.

As mentioned earlier, the goal is not exactly following the defined path. If the object is big, due to contact of hand and object, it would be impossible to follow exact path and following this path is just to achieve grasping.

Fig. 3 illustrates the physical counterparts of the virtual forces for control strategy and Fig. 4 shows structure of the proposed control system. As shown, the command force comes from EMG signal, and controller provides the movement for hand which has dynamic interaction with the object.

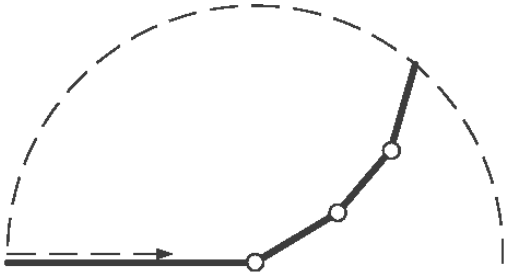

Fig. 2: Semi-Circle Path of Finger Tip

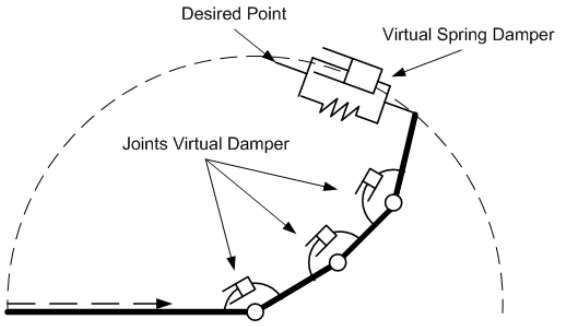

Fig 3: Physical Counterparts of the Virtual Forces

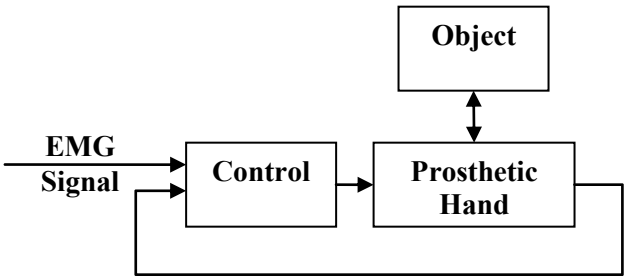

Fig. 4: Control Diagram of Prosthetic Hand System

5. Numerical Simulation

In order to show the effectiveness of the proposed control strategy, numerical simulations were conducted to grasp three different objects, based on the physical parameters of a hand system and objects summarized in Table 1.

In order to simulate dynamics of the hand and interaction with object, Adams software is used. This software is a multi-body analysis simulation program that solves the rigid body dynamic equilibrium equations and directly interfaces with Matlab/Simulink software in order to implement controller. The contact between object and hand is modeled and three sets of simulations with different objects are performed. In all three simulations

the same control strategy is used which shows controller can handle grasping without information about physical parameters of object. Fingers and objects are assumed to be rigid. In these simulations the EMG signal is assumed to increase linearly with time.

Table 1. Parameters used for simulation

Index finger link 1	5 cm
Index finger link 2	2.5 cm
Index finger link 3	2.5 cm
Damping at joints	0.01 kg/s
Virtual damping ratio *(c)*	1
Virtual spring stiffness *(k)*	50 N/m
Rectangular object width	3 cm
Circular object radius	3 cm
Star shape object outer radius	2 cm

5.1 Simulation One

For first simulation a rectangular (cubic) object is used, and as mentioned earlier the movement is restricted to 2D movement. Object is not moving initially. Hand starts movement from open finger configuration. The hand positions at 1 second time interval are shown. Fig. 5 shows finger tip angle with respect to palm.
As it is shown in Fig. 6 the grasping is accomplished successfully.

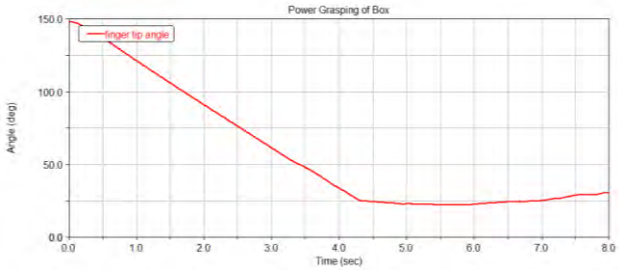

Fig. 5: Finger's Tip Angle at Rectangular Object Grasping

5.2 Simulation Two

For the second simulation a glass (circular object) is used. The control parameters are identical to previous simulation.
As shown in Fig. 7 the grasping is done successfully and the hand positions for 1 second time interval are depicted. Similarly the finger tip angle respect to palm is shown in Fig. 8.
Regardless of object shape, by use of proposed control scheme the hand can successfully grasp objects.

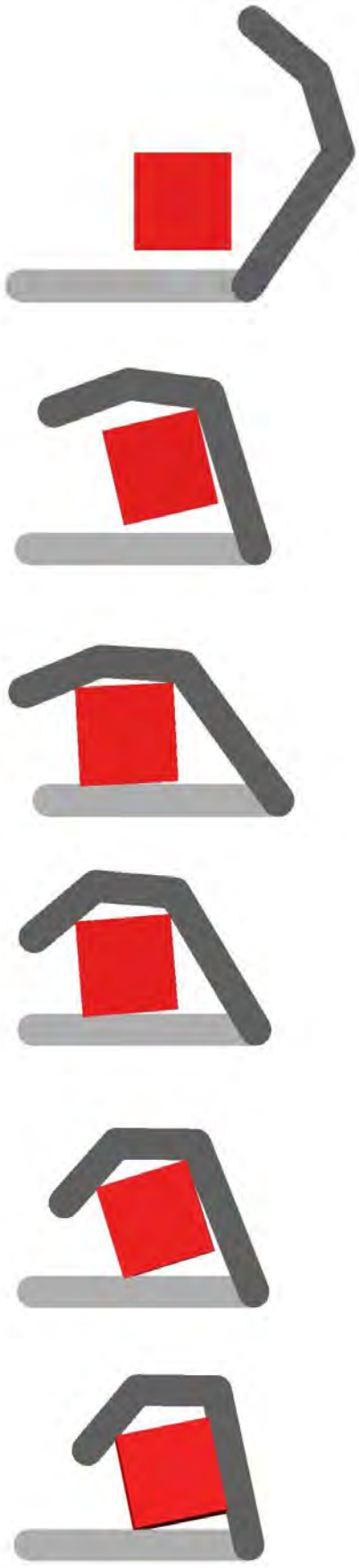

Fig. 6: Rectangular Object Grasping (1 Sec Intervals)

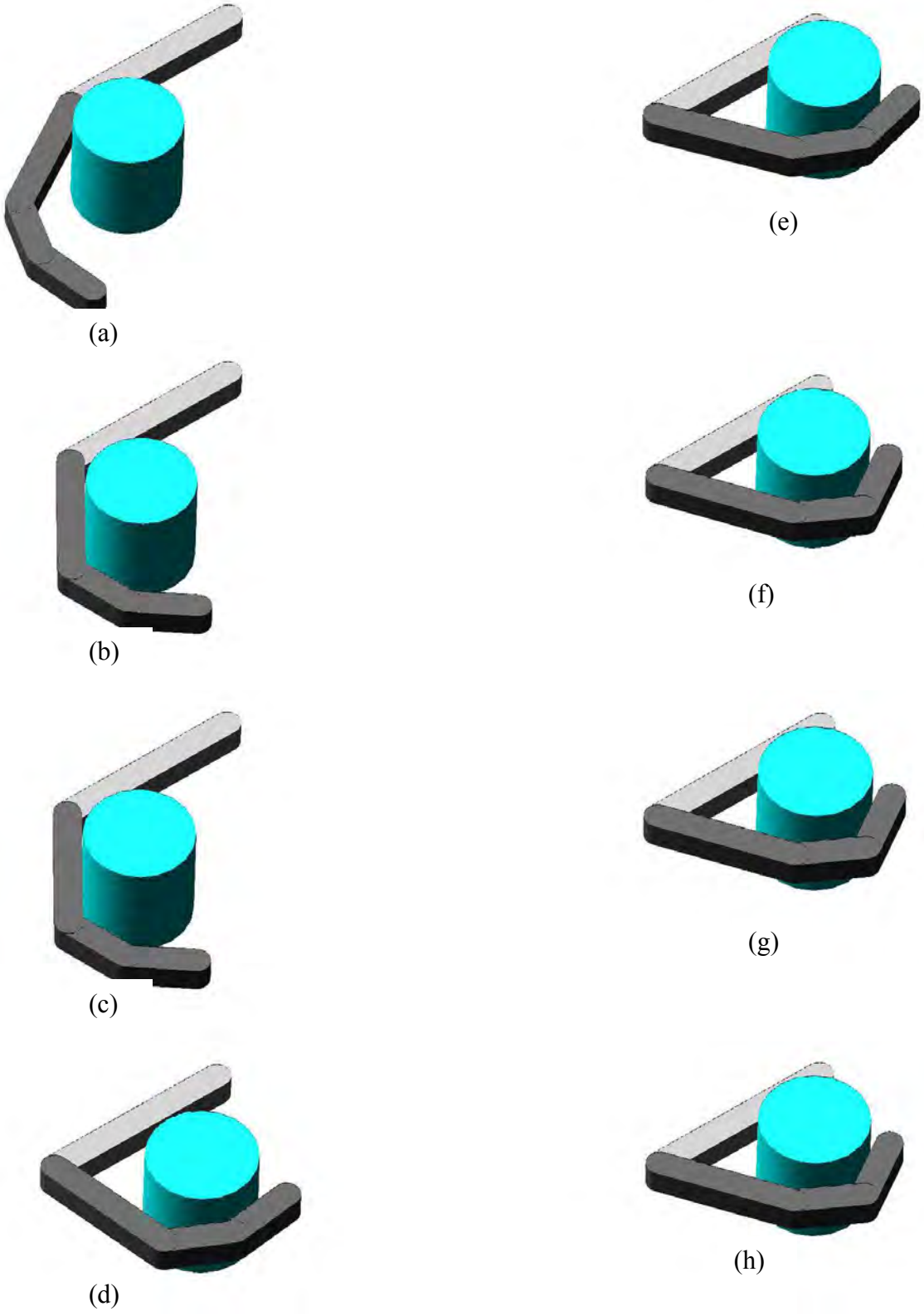

Fig. 7 (a-h) : Grasping of a Glass (1 sec. Intervals)

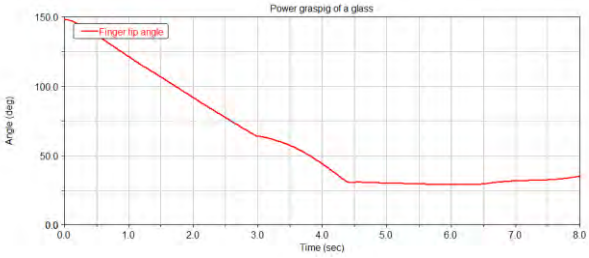

Fig. 8: Finger's Tip Angle at Grasping a Glass

5.3 Simulation Three

For the third simulation a star shape object is used. The control parameters are identical to previous simulation.
As shown in Fig. 9 the grasping is done successfully and the hand positions for 1 second time interval are illustrated. Final position of grasping in 3D (isometric) view is depicted in Fig. 10. Similarly the finger tip angle respect to palm is shown in Fig. 11.
The complicated shape of object shows that controller is able to handle grasp for wide variety of objects, without information of object shape.

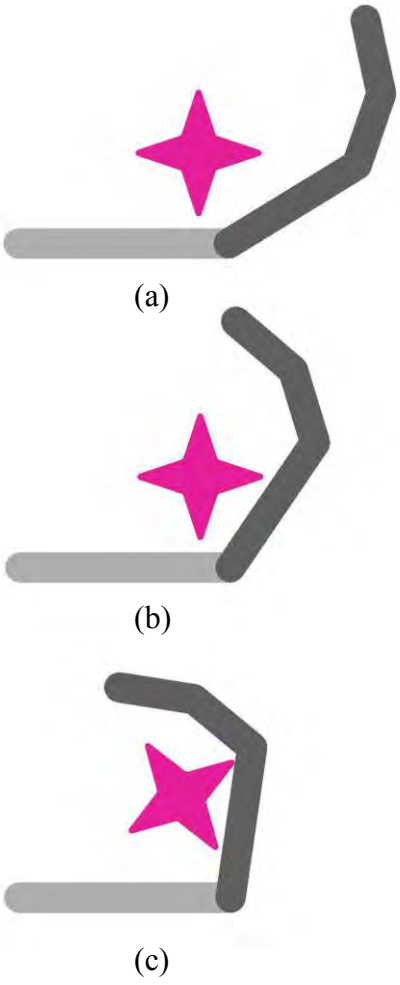

Fig. 9 (a-h) : Grasping of Star Shape Object (1 sec. Intervals)

Fig. 10 : 3D (Isometric) View of Star Shape Object After Grasping

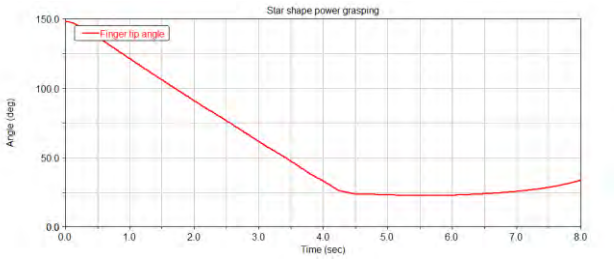

Fig. 11: Finger's Tip Angle at Star Shape Object Grasping

6. Conclusion

In this paper a control scheme for achieving object power grasping by a prosthetic hand was proposed. The control scheme was based on defining virtual spring-damper between finger tip and desired point, as well as, damping at finger joints, and a semi circular path for finger tip. It was shown through three sets of numerical simulations for different objects that the proposed control scheme can effectively be used for power grasping of prosthetic hand. It is shown that regardless of object shape proposed control method is successful for wide variety of situations. The proposed method did not rely on complex equations of inverse kinematics, or inverse dynamic and hence this method is better suitable for real-time applications. The immediate future investigation is the application of the proposed method to precision grasping of prosthetic hand.

Acknowledgements

The research was sponsored by the US Department of the Army, under the award number W81XWH-10-1-0128 awarded and administered by the U.S. Army Medical Research Acquisition Activity, 820 Chandler Street, Fort Detrick MD 21702-5014. The information does not necessarily reflect the position or the policy of the Government, and no official endorsement should be inferred. For purposes of this article, information includes news releases, articles, manuscripts, brochures, advertisements, still and motion pictures, speeches, trade association proceedings, etc.

References

[1] Z. Li, P. Hsu, and S. Sastry, Grasping and Coordinated Manipulation by a Multifingered Robot Hand," *J. of Robotics Research*, Vol. 8, No. 4, 1989, pp. 33-50.

[2] T. Yoshikawa and K. Nagai, Manipulating and Grasping Forces in Manipulation by Multifingered Robot Hands, *IEEE Trans. on Robotics and Automation*, Vol. 7, No. 1, 1991, pp. 67-77.

[3] A. M. Okamura, N. Smaby, and M. R. Cutkosky, An Overview of Dexterous Manipulation, *Proc. of the 2000 IEEE Int. Conf.* on Robotics *and Automation*, San Francisco, CA, April 2000, pp. 255-262.

[4] S. C. Jacobsen, E. K. Iversen, D. F. Knutti, and R. T. Johnson, Design of the Utah/MIT Dextrous Hand, *Proc. of the 1986 IEEE Int. Conf. on Robotics and Automation*, San Francisco, April, 1986, pp. 96-102.

[5] M. V. Weghe, M. Rogers, M. Weissert, and Y. Matsuoka, The ACT Hand: Design of the Skeletal Structure, *Proc. of the 2004 IEEE Int.Conf. on Robotics & Automation*, New Orleans, LA, USA, April 26-May 1, 2004, pp. 3375-3379.

[6] M. Higashimori, H. Jeong, I. Ishii, M. Kaneko, A. Namiki, and M. Ishikawa, A New Four-fingered Robot Hand with Dual Turning Mechanism, *Proc. of the 2005 IEEE Int. Conf. on Robotics & Automation,* Barcelona, Spain, April 18-22, 2005, pp.2690-2695.

[7] Erik D Engeberg, Sanford G. Meek, Backsptepping and Sliding Mode Control Hybridized for a Prosthetic Hand, *IEEE Transaction on Neural Systems and RehabilitationEngineering,* Vol. 17, No.1, February 2009.

[8] Lorendana Zollo, Stefano Rocella, Eugenio Guglielmelli, M. Chiara Carrozza, Paolo Dario, Biomechatronic Design and Control of an Anthromorphic Artificial Hand for Prosthetic and Robotic Application, *IEEE/ASME Transaction on Mechatronics,* Vol.12, No.4, August 2007.

[9] Lynette A. Jones and Susan J. Lederman, *Human Hand Function,* Oxford University Press, New York, 2006, pp. 131-149.

[10] Mohammad Asghar Oskooei, Housheng Hu, Myoelectric control systems, A survey, *Biomedical Signal Processing and Control,* Vol. 2, 2007, pp 275-294.

[11] Chiristian Cipriani, Franco Zaccone, Silvestro Micera, Chiara Carrozza, On the Shared Control of an EMG-Controlled Prosthetic Hand: Analysis of User-Prosthesis Interaction, *IEEE Transaction on Robotics,* Vol.24, No1, February 2008.

[12] D.E.Whitney, Resolved motion rate control of manipulators and human prostheses, *IEEE Trans. Man-Machine Syst*., Vol.MMS-10, No.2, 1969, pp.47– 53.

[13] Y. Nakamura, *Advanced Robotics: Redundancy and Optimization*, Addison-Wesley, Reading, MA, 1991.
[14] T. Yoshikawa, M. Brady and R. Paul Eds. Analysis and control of robot manipulators with redundancy, *in Robotics Research: The 1st Int. Symp.* , Cambridge, MA: MIT Press, 1984, pp.735–747.
[15] J.M. Hollerbach and K.C. Suh, Redundancy resolution of manipulators through torque optimization, *IEEE J. of Robotics and Automation*, Vol.RA-3, No.4, 1987, pp. 308–316.
[16] N. Dechev, W.L. Cleghron, S. Naumann, Multiplefinger, Passive Adaptive Grasp Prosthetic Hand, *Mechanism and Machine Theory,* Vol.36, 2001, pp.1157-1173.
[17] Ramiero Cabas, Luis Maria Cabas, Carlos Balaguer, Optimized Design of the Underactuated Robotic Hand, *Proceeding of the 2006 IEEE International Conferences on Robotics and Automation,* Orlando, Florida, May 2006.
[18] Da-Peng Yang, Jing-dong Zhao, Yi-kun Gu, Xin-qing Wang, Nan Li, Li Jiang, Hong Liu, Hai Huang, Da-wei Zhao, An Anthropomorphic Robot Hand Develeoped Based on Underactuated Mechanism and Controlled by EMG Signals, *Journal of Bionic Engineering,* Vol. 6, 2009, pp 255-263.
[19] Suguru Arimoto, Masahiro Sekimoto, Human-like Movements of Robotic Arms with Redundant DOFs: Virtual Spring-Damper Hypothesis to Tackle the Brenestein Problem, *Preceding of the 2006 IEEE International Conference on Robotics and Automation,* Orlando, Florida, May 2006.
[20] Jerry Pratt, Chee-Meng Chew, Ann Torres, Peter Dilworth, Gill Pratt, Virtual Model Control: An Intuitive Approach for Bipedal Locomotion, *The International Journal of Robotics Research*, Vol. 20, No. 2, pp. 129-143, February 2001.

Multi-Level Embedded Motor Control for Prosthesis

Chandrasekhar Potluri[1] potlchan@isu.edu
Parmod Kumar[1] kumaparm@isu.edu
Jeff Molitor[1] jdmolitor@gmail.com
Madhavi Anugolu[1] anugmadh@isu.edu
Alex Jensen[1] jensalex@isu.edu
Kenyon Hart[1] hartkeny@isu.edu
Steve C. Chiu[1, 2] chiustev@isu.edu

[1]Measurement and Control Engineering Research Center (MCERC), Idaho State University, Pocatello, ID 83209, U.S.A.
[2]Department of Electrical Engineering and Computer Science, Idaho State University, Pocatello, ID 83209, U.S.A.

Abstract *– This paper presents a novel approach for hierarchical multi-level motor control for prosthesis and prosthetic applications. This approach hierarchically clusters the work distribution among the levels to enable high computational speed and processing. Three PICs (peripheral interface controllers) were used: one 32-bit PIC and two 16-bit PICs. These made up the multi-level hierarchical model. Communication between the levels was established by full-duplex distributed communication. This model facilitates to modify the communication system between the levels as for the application. An intelligent fuzzy controller associated with the higher-level configuration provides a control strategy for the lower-level configuration to control the end device, in our case the stepper motor. The stepper motor provides desired step changes in the output angular displacement, depending on the application. A rectified sine wave input was fed to the controller, which pulled up a set of rules from the membership function of the intelligent fuzzy controller to initiate a desired angular displacement.*

Keywords – *Fuzzy Controller, Multi-Level Control, Embedded Systems, Full Duplex Distributed Communication*

I. NOMENCLATURE

The following acronyms are used in this paper to represent the motor actuation signals associated with our proposed control strategy:

NB – Negative Big,
NM – Negative Minimum,
PB – Positive Big,
PM – Positive Minimum.

II. INTRODUCTION

The work by Liu *et. al* [1] summarized the current tools used for the design and implementation of embedded systems, which lacked some important phases, e.g. supervision logic, real-time scheduling, design modeling of communication, etc. However, in today's real world there is more concentration on the design and simulation tools. Usually for hybrid control systems, there will be sub-controllers and switching logic. The complete controller will be defined with a set of equations. This paper attempts to address design and implementation of heterogeneous hierarchical control systems. In order to capture

different design perspectives, to demonstrate design principles, various software tools were used.

Self-configuring robust embedded systems seek to achieve graceful degradation, and this could be achieved by software reconfiguration. To accomplish this, the system must automatically reconfigure or upgrade itself despite any node failure. This paper gives architecture for the typical distributed embedded control systems to employ real-time, reliable data transmission using control area network (CAN) [2].

PIC

PIC is for Programmable Interface Controller. Owing to its low cost, often free development tools, serial programmable capability, PICs are used in many applications.

PIC32 was introduced by Microchip Technology Inc., a leading vendor of microcontroller and analog semiconductors. PIC uses Harvard architecture. In Harvard architecture, it has separate code space and data space. The code space is often implemented by EPROM, ROM or Flash ROM. Addressable data space was extended through banking. A program counter is also integrated into the data space and writable. In PIC32, the highest execution speed is 80 MIPS, one instruction will be executed per one clock cycle. Generally 512 K bytes of flash memory is used. It can be programmed by using the Microchip MPLAB C Compiler. In our design, the MPLAB ICD2 (with USB 2.0 interface) was used.

Stepper Motor

Stepper motor is an open-loop controller. It is an electric motor which can divide the full rotation into number of steps depending upon the application. In a unipolar stepper motor there are two windings per phase, one for corresponding direction of the magnetic field. As the magnetic field can be changed without making any changes in the current flow direction, it's easy to make the circuit for winding. In the design, for a given phase, one end of winding will be kept as common giving three leads per phase. In order to activate the driver transistors, stepper motor controllers are used. They are used to get the angular displacements.

III. BACKGROUND

Recent research shows a conjunction of design strategies characteristic of robot control [3]. A suite of continuous processes is used by many architectures. This uses local low-level control for particular motions [3]. Aboveboard, a task-level control is required so that lower-level processes can be assigned to the particular tasks [3]. Therefore, there is a requirement for a higher-level planned layer to grant a planned vision for other required tasks [3].

Robot systems, such as autonomous mobile robots, are required to organize their resources (sensors, actuators, and computation), and need to recover elegantly from exceptions [10]. Some of the previous research by [4] decomposed the problem into different levels. In [4] a number of levels of competence are defined for an autonomous mobile robot.

The approach in [5] is to design robot systems as a collection of behaviours that is independent, action-generating entities. Uncertainty and unpredictable changes are handled well in [5], but how it scales as tasks and environments increase in diversity is hazy. The capabilities in [5] are related to *task-level control*. These capabilities form the basis of the *executive* layer of the three-tiered robot control architectures in [6], [7], [8], and [9].

The architectures in [6], [7], [8], and [9], included three layers: planning layer, executive layer, and behaviour layer. The behaviour layer interacts with the physical world and is responsible for real-time control by controlling actuators and collecting information from sensors. How to realize goals and how to handle goal interactions is stated by the *planning* layer, whereas the *executive* layer facilitate between the symbolic level of the planner and the continuous level of the behaviours. Evidences in [6, 11, 12, 13, 14, 15, 16] show that hybrid architectures are the most recent research outcomes. The combination of the reactive and deliberative control is the advantage of hybrid architectures. Hybrid architecture takes the advantage of efficient low-level control with a connection to high-level reasoning. Most of the time the connection between the two levels is difficult . Therefore, special attention must be given to designing and implementing this connection to achieve the right blend of reactivity and deliberation [17].

The need to manage the complexity of interactions – both interactions between the system and its environment, and interactions between different parts of the system is one of the definite issues while designing a robotic system. The best way to deal with this complexity is divide it in smaller parts and levels with different levels of abstractions [17]. Therefore, by using modularity within a given structure of the architecture – the complexity of the overall system *c*an be simplified by ranking it into smaller modules [17]. The data flow style architectures facilitates this by giving independence to the upstream and downstream levels of the system [17].

Our objective of this design is to give the computational load to the higher-level processer so that the lower-level processors can perform the required motor function tasks.

IV. Proposed Design

The proposed design is a multi-level hierarchical model with a rectified sine wave input. A flash memory interfaces with the high-level configuration, making it capable of holding the input functions and the control strategy. The flash memory interface is done by a Secure Digital (SD) card which enables quick data retrieval and processing. The 32-bit PIC, memory interface and the Fuzzy controller constitutes the higher-level configuration. This level controls the lower-level configuration depending on input function. Two 16-bit PICs each associated with a stepper motor makes up the lower-level configuration. Two lower-level PICs are programmed to control the stepper motors. The communication system in this design is unique. The two levels are communicated through a full duplex distributed communication protocol. Such a communication system enables an effective coordination between the levels by distributing the traffic, and therefore eliminates delay caused often by traffic congestion. This design provides flexibility in handling with a wide range of communication systems, which could include both hard-wired and wireless communication based on the application. The end product, i.e. stepper motors, provides the necessary step changes in the output displacement based on the control signal, a function of input. The proposed design is shown in Figure 1.

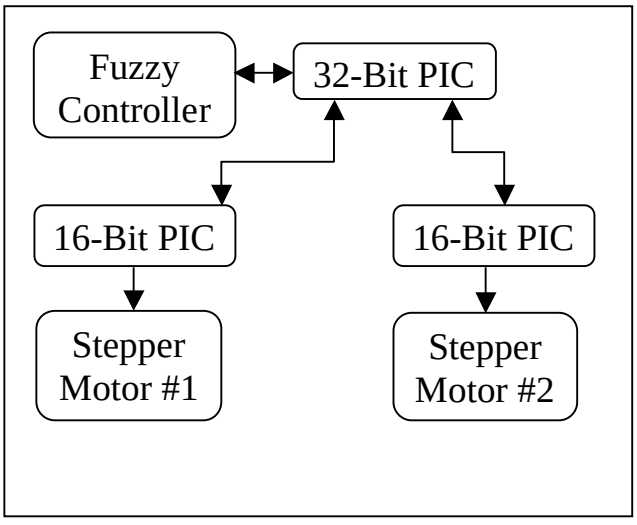

Figure 1: Block Diagram of the Proposed Design

Based on the input function, the fuzzy controller of the high-level configuration has its control signal, to which the 32-bit PIC has access to it through the flash memory. The 32-bit PIC sends the encrypted data via the fully duplex distributed communication channel to accesses the programed lower-level PICs. The encrypted data access the two 16-bit PICs to control the two stepper motors for the desired angular displacement. The encrypted data contains all the information of the control signal. It also contains the information regarding the desired step changes and the direction of them. The lower-level PICs are preprogramed to control the stepper motors with necessary angular displacement. Synchronization plays an important role in the lower-level configuration. The encrypted data and the communication system make the synchronization easier. This type of communication systems avoids traffic delay time. The encrypted data also has the information about the direction and angular displacement for each motor. The critical part of the model is the fuzzy controller. This gives the control signal to the high-level controller, which encrypts the data and send it to the lower-level configuration.

More specifically the lower-level configuration involves two 16-bit PICs that contain the code to control respective stepper motors. When a message is received from the higher-level, it will state which motor it wants to activate and what angular displacement it will make. One or both of the PIC16s will take its message and extract the angular displacement. Once this is done, the PIC will relay a message to the stepper motor making it turn to the desired position. Once this is done the PIC16 will then send a message to the PIC32 that lets the PIC32 know that it has completed its task. This information will be fed into the fuzzy controller that will continue with processing the data.

The higher-level configuration will include a PIC32. The PIC32 will have a SD card reader attached to it. Having an SD card will allow large files to be read into the PIC. Another key part of the high-level configuration is a fuzzy controller. The fuzzy controller will be used to analyze the data and process it. The rectified sine wave is compared to the set of rules specified in the membership function of the intelligent controller. Once a result is determined, the controller will send a message to the lower-level controller. The message will specify which PIC16 will be getting the instruction and the desired angular displacement of the stepper motor.

V. CONTROL STRATEGY

Fuzzy controller works on a fuzzy logic. Fuzzy logic can be described as computing with words rather than numbers. Therefore, fuzzy controller can be defined as controller with sentences rather than equations. The main components of the fuzzy control structure include: Fuzzification, Rule Base and Inference Engine, and Defuzzification, as in Figure 2 [1, 18].

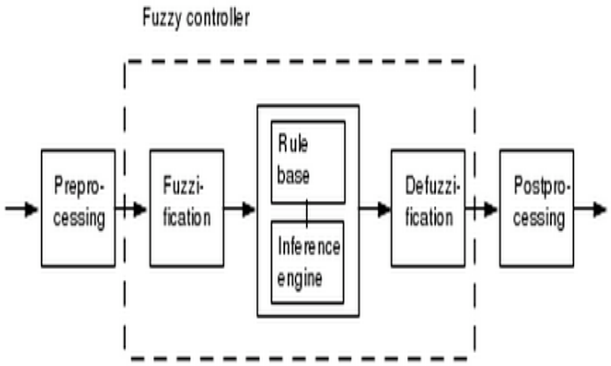

Figure 2: Fuzzy Controller System Diagram

Fuzzification is defined as taking out the rules from rule base given an input function. The rule base is a set of rules, which are defined by the user, depending upon the application. The resulting control signal, which is a function of the rule base and input, is called Defuzzification.

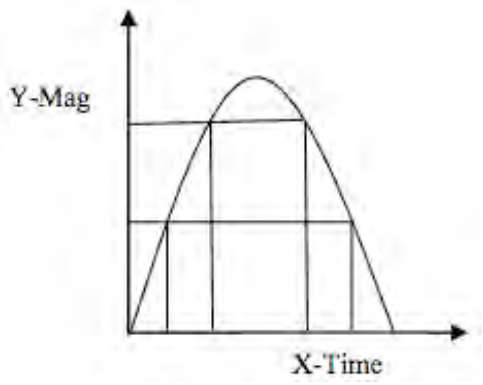

Figure 3: Input Signal (Rectified Sine Wave)

In this proposed design, the rectified sine wave is fed as an input signal as shown in figure [2]. The rectified sine wave is sampled at regular intervals of time based on the degrees of freedom.

Membership Function:

If 'x' is too small and 'y' is too small then output is 'NB'
If 'x' is small and 'y' is small then output is 'NM'
If 'x' is large and 'y' is large then output is 'PB'
If 'x' is too large and 'y' small then output is 'PM'

The control signals are fed to the lower-level configuration as inputs. The lower-level configuration outputs them to the end user, i.e. the stepper motors as angular displacements. The control signals and their corresponding angular displacements are shown in Table 1.

Table 1: Rules for Fuzzy Controller

Control Signal	Angular Displacement
NB	Anti clock wise 90^0
NM	Anti clock wise 45^0
PB	Clock wise 90^0
PM	Clock wise 45^0

Either the change in the time or magnitude pulls up a rule in the Rule Base from which a corresponding fuzzy controller signal is sent to the PIC32. For this design, the degree of freedom is four. Therefore the membership function consists of four rules. Enhancements of degree of freedom make the membership function contain more rules. Table 2 shows the synchronization chart for the individual control signal for the lower-level configuration. This synchronizes the two stepper motors for the application.

Table 2: Synchronization Chart

Control Signal	PIC 1	PIC2
NB	NB	PB
NM	NM	PM
PB	PB	NB
PM	PM	NM

VI. EXPERIMENTAL RESULTS AND DISCUSSION

Figures 4 and 5 show the state diagrams for the higher-level and lower-level configurations. Table 1 tabulates the control signal for the lower-level configuration sent in the form of encrypted data by the higher-level. This encrypted data access the preprogrammed lower-level configuration for a necessary angular displacement by the stepper motor. Table 2 shows the synchronization chart for the two lower-level PICs, which between the two PICs can be done by a unique control signal. The chart can be changed based on individual applications.

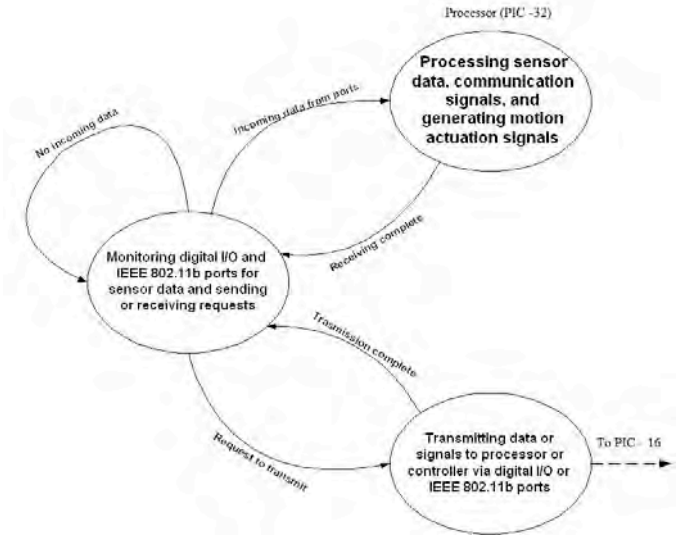

Figure 4: State Diagram for the Processor (PIC32)

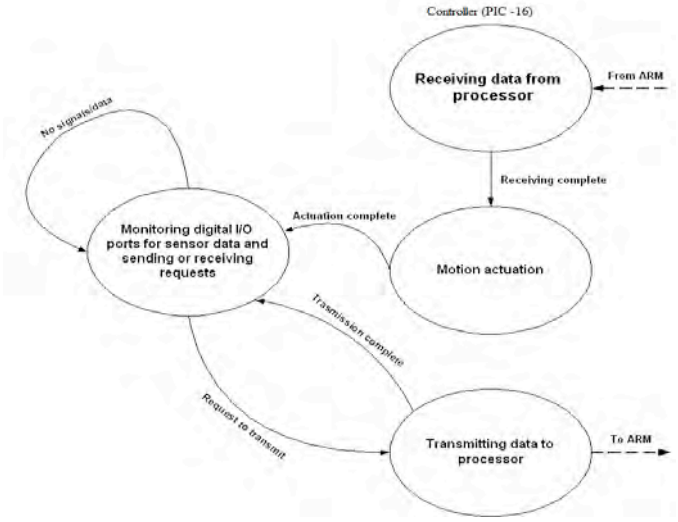

Figure 5: State Diagram for the Controller (PIC16)

The encrypted data access the program in the lower-level configuration. This enables the lower-level configuration to make necessary angular displacement in steps. The step change and the direction of the angular rotation is function of the input. So finally, this model becomes an independent finite state machine, which generates a directed step changes in output for the corresponding input function. The encrypted data is a series of characters communicated through a full duplex communication system, and these characters alter the direction and step changes in the output. Controlling the embedded platform through hyper terminal also involves control of the end device through characters. This permits serial transmission of data. The same concept is used in this configuration. However, using hyper terminal to control an embedded platform for prosthetic application is not efficient, because the platform should be independent.

For programming the two-level configuration, MPLAB along with the ICD2 (in circuit debugger) is used. ICD2 helps in programming the microcontrollers while in the circuit. This enabled us to make changes in the membership functions and the synchronization rules quickly according to the user applications. After the programming, the MPLAB is set to release mode and this enables the two-level configuration to discard from the computer and be independent, and work independently to its input function. For programming, CCS C compilers are used.

Table 3: Experimental Results

Control Signal	Motor1 Angular Displacement	Motor2 Angular Displacement
NB	Counter-Clockwise 90^0	Clockwise 90^0
NM	Counter-Clockwise 45^0	Clockwise 45^0
PB	Clockwise 90^0	Counter-Clockwise 90^0
PM	Clockwise 45^0	Clockwise 45^0

From Table 3, we see that each control signal contributes a synchronized angular displacement for the individual stepper motors in either the clockwise or counter-clockwise directions.

VII. CONCLUSIONS AND FUTURE WORK

This paper proposed a multi-level embedded platform for the control of prosthesis. In this model, we used a 32-bit PIC with a fuzzy controller and memory interface as a higher-level configuration and 2 16-bit PICs for lower-level configuration. The encrypted data from the higher-level configuration is send to the lower-level configuration. This is transmitted through a full duplex distributed communication system. This increases the transmission speed without any congestion. Based on the encrypted data, lower-level configuration makes the stepper motors generate the resulting angular displacement. Therefore the resulting angular displacement of the stepper motor was a function of the input, a rectified sine wave in this case.

For future work, it will be interesting to implement this design with even more powerful processors. This will improve the computational speed. It is challenging to implement this design with a hybrid fuzzy controller with a bio signal, e.g. EMG (or electromyogram). The hybrid fuzzy controller should be integrated with a feedback loop for further improvements.

VIII. REFERENCES

[1] Realistic Simulations of Embedded control Systems , “Jie Liu, Johan Eker, Jorn W. Janneck, Edward A. Lee.”

[2] Jini Embedded Control Networking : a case study in portability failure, “Meredith Beveridge, Philip Koopman.

[3] II-1 Charge Balance Control Scheme for Cascade Multilevel Converter in Hybrid Electric Vehicles– Leon M. Tolbert, IEEE Transaction on Industrial Electronics, Vol. 49, No. 5, October 2002.

[4] High-level Control of a Mobile Manipulator for Door Opening. “Lars Petersson, David Austin, Danica Kragic,” Proceedings of the 2000 IEEE/RSJ, International Conference on Intelligent Robots and Systems.

[5] A Procedural Knowledge Approach to Task-level Control, “Karen L. Myers,” AIPS 1996 Proceedings.

[6] A Robust Layered Control System for a Mobile Robot, “Rodney A. Brooks,” A. I. Memo 864, September, 1985.

[7] Structured Control for Autonomous Robots, “Reid G. Simmons,” IEEE Transactions on Robotics and Automation, Vol. 10, No. 1, Feb. 1994.

[8] P. Bonasso, J. Firby, E. Gat, D. Kortenkamp, D. Miller, and M. Slack. A Proven Three-Tiered Architecture for Programming Autonomous Robots, *Journal of Experimental and Theoretical Artificial Intelligence*, 9:2, 1997.

[9] An Investigation into Reactive Planning in Complex Domains, "R. James Firby," Proc. National Conference on Artificial Intelegence, pp 202-206, Seattle, WA, July, 1987.

[10] Integrating Planning and Reacting in a Heterogeneous Asynchronous Architecture for Controlling Real-World Mobile Robots, “E. Gat.,” Proc. National Conference on Artificial Inteligence, pp. 809-815, San Jose, CA, July 1992.

[11] Designed for Autonomy: Remote Agent for the New Millennium Program, “D. Bernard and B. Pell,” Proc. i-SAIRAS ’97, Tokyo Japan, October 1997.

[12] A Task Description Language for Robot Control, “Reid Simmons and David Apfelbaum,” Proceedings Conference on Intelligent Robotics and Systems, October, 1998.

[13] CIRCA: A cooperative intelligent real-time control architecture, “D. Musliner, E. Durfee, and K. Shin,” *IEEE Transactions on Systems, Man, and Cybernetics 23(6), 1993.*

[14] The New Millenium Remote Agent: To boldly go where no AI system has gone before, “N. Muscettola, P. Nayak, B. Pell, and B. Williams,” In *Proc of the 15th Intl Joint Conf on Artificial Intelligence, 1997.* Abstract of Invited Talk.

[15] State configured layered control, “J. G. Bellingham and T. R. Consi,” In *1st Worshop on Mobile Robots for Subsea Environments, pages 75-80, October 1990.*

[16] Controlshell: A software architecture for complex electro-mechanical systems, “S. Schneider, V. Chen, G. Pardo-Castellote, and H. Wang,” *International Journal of Robotics Research, special issue on Integrated Architectures for Robot Control and Programming, Spring 1998.*

[17] The orccad architecture, “J.-J. Borrelly, E. Coste-Maniere, B. Espiau, K. Kapelos, R. Pissard-Gibollet, D. Simon, and N. Turro,” *International Journal of Robotics Research, 17(4):338-359, April 1998.*

A NODAL FEEDBACK MODEL FOR WIRELESS MULTISENSORY DATA FUSION

Jamie Manchala
Measurement and Control Engineering Research Center
College of Engineering
Idaho State University
Pocatello, Idaho 83209
mancjami@isu.edu

Steve C. Chiu, Ph.D.
Department of Electrical Engineering and Computer Science
College of Engineering
Idaho State University
Pocatello, Idaho 83209
chiustev@isu.edu

ABSTRACT

Multi-sensor data fusion has an incredible impact in the field of wireless sensor networks since the last couple of decades. Many theories and statistical proofs have been made to enhance the design and system in view of accuracy and reliability in particular. Researchers have always looked into these two factors by modeling and computing for better accuracy, according to user application. But not much emphasis is given to feedback and memory. A novel approach for a sensor network that provides a feedback is proposed, keeping energy conservation in mind. A look into some possible energy concerns are discussed, visualizing different scenarios that can occur. This paper proposes a distributed de-centralized feedback system with energy conservation schemes, especially for data fusion networks in a wireless remote environment. It presents an innovative node-based model in a data flow chart, introducing feedback into the wireless world of sensor networks. It also looks into various scenarios that can cause inaccuracy, redundancy and other glitches in certain events, and proposes solutions to these issues. The model in this paper is designed for a broad perspective of applications that depend on data fusion for accuracy. If accuracy is not satisfied, a feedback is produced from the node level itself to request further data from the sensors.

Keywords: Sensor Networks, Data Fusion, Node Selection, Multisensory Feedback, Wireless Sensors

INTRODUCTION

Fusion of multisensory data provides a substantial benefit over a single source of data. Information from additional data sources, when fused, delivers precision when compared to a single data source [11]. Though originally developed for military purposes, multisensory data fusion soon took its place in many other evolving applications. This paper focuses its contribution in wireless sensor networks.

Multisensory data fusion in wireless network environments can cover a broad spectrum of applications such as battlefield surveillance, remote sensing, automatic target tracking and detection, [3]. This paper challenges applications related to exploration. Few examples that can be thought of are forest habitat research, underwater exploration, outer space discovery or its related fields.

This paper explains the concept of the “node” architecture. It looks into important blocks in the process flow, explaining their functions in the process. It also visualizes scenarios that could take place in the basic process of its operation. An illustration of the node-to-node snap and its immediate network recovery is presented. As limited power is one of the major concerns in the wireless network environment, a look into the possible power related issues is given. Considering the power issues, our “node” model tries to diffuse and spread the workload over the entire network. This provides an energy aware routing scheme for the system. Thus, the entire sensor network is balanced with respect to traffic load, and longevity of the system is enhanced.

PROPOSED NODE-BASED ARCHITECTURE

Our proposed node architecture consists of a Sensor module, a Data Fusion module, a Fetch Trigger, a Knowledge Base and Reference module, and the Network. The Sensor module is the main source of information to the entire network. It consists of a sensor (raw data measurement) and an event interrupt device, which self-triggers the node for any changes in the environment. The Data Fusion module provides two processes: data fusion and data aggregation. These two processes work on energy threshold levels that decide if the

node should perform data fusion or data aggregation. Data aggregation is considered a subset of data fusion. This process is only chosen if it falls under a certain threshold level. If energy levels are above this threshold level, data fusion (including data aggregation) will be performed. The working of the entire system is explained in latter sections of this paper. The architecture for our model is depicted in Figure 1.

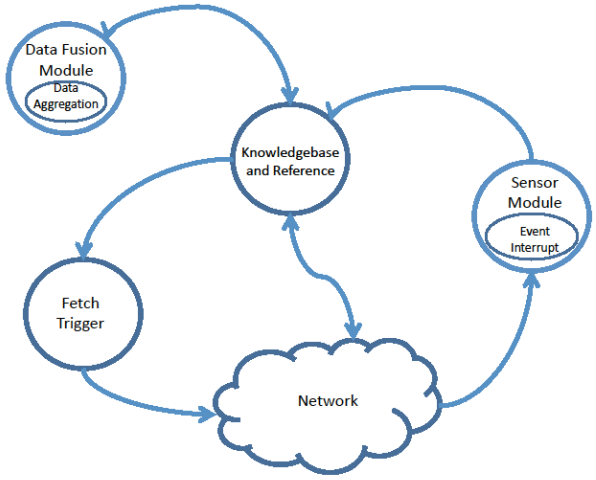

Fig. 1: Node-based architecture showing all node modules

This architecture introduces a feedback to the node-based model through a module called the Fetch Trigger. A Fetch signal is only triggered (to its lower nodes) if the measured values do not meet the required accuracy level. The Knowledge Base and Reference module is regarded as the chief central command, and provides reference for the node. It checks if the node has to operate as a sensor, or fuse data, or check for interrupts, or simply relay data into the network. The network cloud decides which node to route, according to the routing protocols programmed (i.e., application specific). It also decides if the signal needs to be modulated or demodulated into a Data signal or a Fetch signal. All these are explained as below.

PROPOSED NODE-BASED DATA FLOW

As technology enhances, it is becoming more possible for faster processors and large sized memory to work with low power consumption. Consider each of the sensor nodes built with these features, thus allowing a faster throughput for a data fusion setup. As we look into the proposed node model, the structure of this network system supports a de-centralized, distributed architecture. This node structure is mainly designed to keep work distributed between nodes, and spread them throughout the network. We look into an environment where all these sensor nodes are spread out in an ad hoc manner. Assuming each node in the network has a unique identity, same functionality, and consists of a built-in timer already synchronized before dispatch. We now examine the model as the user initiates the network.

The Sink sends out the Fetch signal to all the nodes, with the request of the location address to visualize the network. Each node then passes the Fetch data till the end node is reached. The final node basically plays the role of the sensor, which is to measure data. Then, the reverse path takes place from the source sensor back to the Sink. This measured data is then sent to the Network module. It is the Network that decides which path and direction to take, and which node to transfer its information. Figure 2 shows the data flow diagram of our proposed model.

It should be observed that there are two different signal types that run through each sensor node. The Fetch and Data are the two signals used in this paper to differentiate the direction of flow. The Fetch signal is only used to find the end sensor node in the network. This Fetch signal does not carry any data, but is rather used to request lower nodes to reply back with data. Hence, Fetch can be modulated as a low power signal with lesser bandwidth range. This signal keeps going through the network until it reaches its end node. Once the end node is detected (as the end node will have no possible lower branch nodes), the Fetch signal is converted into a Data signal through the Modulator/De-modulator unit of the network cloud. From Figure 2, at the end node check block, if the Modulator/De-modulator recognizes the signal as Fetch, then the system will operate in search for the end node. And if Modulator/De-modulator recognizes the signal as a Data signal, it will search for the Sink, as it moves in the opposite direction.

After the end sensor nodes sense information, they send raw measured data to their respective immediate parent nodes. These nodes check with their lower nodes for measured values. If there are no other nodes carrying the same data type, then its current value and location address is stored and sent to the Network module to be transmitted to the next node. If there is more than one node having measured values, then it is sent to a checker for data fusion. This is explained later in this paper. If Data Fusion (depicted as DF in the flow chart) was not able to take place because of node energy constraints, then Data Aggregation takes place. Data Aggregation will only collect data from its lower nodes and pass it onto the next node which gets routed by the Network module.

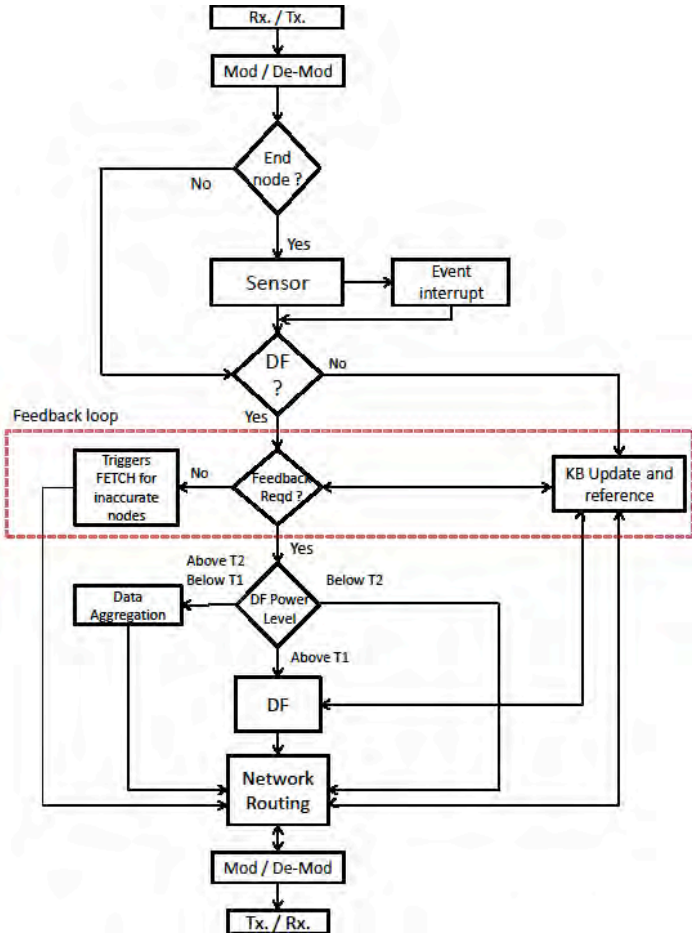

Fig. 2: Data flow for the nodal feedback model

We introduce an event interrupt into the system as a software program. It is part of the Sensor module, and is programmed to trigger a self-initiated request to the Sink. Once the sensor detects a change in the environment worthy to report, an interrupt gets generated. After the Sink knows how its network structure is distributed, it can individually send a Fetch request to a particular node when needed. This process of node selection is enhanced from its traditional algorithm, using the relevant node selection algorithm [10]. This algorithm claims energy efficient querying. Thus overall, there are three ways this network communicates – *Sink-all sources-Sink, Sink-single source-Sink,* and *self-interrupt driven source-Sink.*

We look into a scenario where two end sensor nodes are in close proximity with each other (shown in Figure 3). Then a misperception occurs as to which node should act as a sensor. In this case, both must act as Sensors and reply back to its respective branched parents. Considering this dynamic environment, where A and D are two end nodes. Node E keeps drifting away from its child node D, then a network snap occurs.

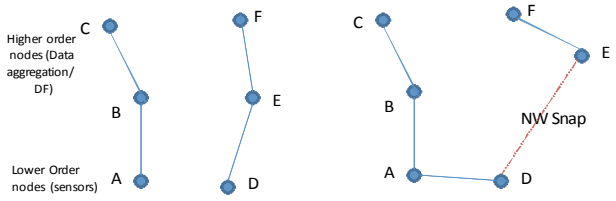

Fig. 3: An example of a network snap

Here now, A becomes the adopted parent for D, and E becomes the end sensor. E will sense information and send it through F while D sends its measured information through A. The advantage for all nodes equipped with the same functionality promotes reliability of the entire system. Anywhere down its data flow path, if any failure occurs, the system can stabilize and retrieve information back to the network. This is a benefit for this kind of network models in the dynamic environment.

POWER CHECK FOR DATA FUSION

Power in wireless sensor networks is one of the major concerns, as they run remotely on just battery. Introducing data fusion on these systems will call for more processing power. One way to manage power levels for each node is by introducing power threshold levels into *each* node. Targeting data fusion applications, we introduce two threshold levels, T1 and T2, into the power check scheme for each node.

Below T2	>	T2	>	T1
(Data transfer)		(Data Aggregation)		(Data Fusion)

Power check resulting over threshold level T1 is considered for data fusion of previous nodes (if any). Power levels less than T1, or equal to T1, will call for data to be aggregated or collected. Power levels less than or equal to T2 will only send raw, unprocessed data over to the next node. These threshold levels can be set after testing the node for power performance. This block, as depicted in Figure 2, compares its own health with reported health of its neighbors [4].

Apart from the Data Fusion process, other areas that cause a lot of power consumption are data storage in memory [9] and signal transmission between nodes [4]. Typically, there are two ways to store the collected data: one is to store them in the network nodes; the other is to store them in the Sink node [9]. This paper supports data storage in all the network nodes for its significance in data fusion. Likewise, when a particular node is selected (assuming any node in the network but the end nodes) to send data back to the Sink, it will already hold previously fused data, and can compare it with the currently measured data. With this, accurate values can be derived from only one data source.

It should be noted that data fusion will not always take place. Chances are, most of the data fusion that take place will be at the Sink node, or the user, where power is not a limitation. This occurs when only one node is called to process information and send back the data through the rest of the relay nodes. The other possibility is when two or more nodes are called to retrieve data, and they follow separate node paths. Data Fusion occurs during power up of the system, where the Sink wants to know the distributed location of the network nodes. Furthermore, it occurs when multiple signals (Data or Fetch) intersect at a common node. Power consumption can also be minimized by communicating only when necessary. Some of these basic power awareness schemes should be considered to drastically improve node power conservation [1].

KNOWLEDGEBASE AND REFERENCE

This module controls all processing of the node and keeps refreshing the knowledgebase. The importance of this unit is to update the respective node with recent information, location of its neighboring nodes and hop counts. This will update each successive parent node respectively, as Data signals are called back by the Sink. It becomes evident that higher order nodes (towards Sink) will have an updated Knowledge Base, because of already fused data from different paths. This in turn forces lower order nodes to perform data fusion at earlier stages. Emphasis is given on lower order node data fusion so that higher order node energy levels can be maintained. Higher order nodes mostly get a knowledgebase update and check for further data fusion. The higher the node's order, the greater its priority, as it holds a string of network nodes. They are also valued because of their proximity to the Sink. It balances load at each node and a smoother traffic is obtained. A Data Fusion power level unit checks to see if the node has enough energy to perform data fusion. If energy is insufficient then it simply passes the data fusion task on to the next node.

During initial stages or right after the dispatch of the network nodes, data fusion would take place at much lower node levels as power is assumed to be maximal. This would still not cause early power drain at lower node levels. Considering the first iteration that caused data fusion at lower nodes. The next iteration would only send raw data back to parent nodes as it would be at T2 (threshold level 2) or below. So the power drain is also watched at the lower level nodes. Overall, the lower levels keep pushing more work toward the higher levels as time progresses. This not only balances the work load of the network but also provides timeliness (fast enough to use) by distributing small processes per node over the network. Also, if the nodes are dispatched in the hundreds or thousands, an accurate, balanced traffic load and long lasting network system is created preliminarily.

Studies show that a central control or a centralized network where all the collected data is fused at a single processor helps to avoid the possibility of duplication [5]. However on the proposed de-centralized network, this should not be a concern, as each node is updated with the source address and trajectory node addresses. The node that actually performs the data fusion will check for redundant node addresses and simply disregard them if any such addresses exist.

The Knowledge Base and References module already has a set of predefined function values. It is application specific, as moisture sensors would have a different reference than light sensors. Another important function of the Knowledge Base is to keep updating itself on the location addresses or previous nodes. This helps the network to recognize the dynamic change in the system. It also keeps updating itself with the hop count from each node, which is essential to calculate the power levels so as to minimize the transmission cost [4].

MODULATOR / DE-MODULATOR

Considering that each node is able to transmit two types of signals, namely Data signals and Fetch signals. The assignment for this module is to modulate signals based on the direction of its travel. If a Fetch signal is sent from the Sink, then all the nodes will only search for the final node, and that node will only act as the sensor. On its return path back to the Sink, the modulator then changes the frequency of the return signal and calls it the Data signal. Only Data signals can be processed for Data Fusion. The introduction of the modulator/de-modulator

provides the security for the system. The Mod/De-Mod can be designed according to the application requirements.

The Mod/De-Mod promotes its signal over the transmitter/ receiver unit. The Mod/De-Mod unit converts the signal into three instances, namely:

- *End node conversion:* Once the Fetch signal reaches the end node, this node converts the Fetch signal into a Data signal (i.e. coming back).
- *Event interrupt:* If a sensor detects a change to report, this unit requests a Data signal conversion at the Mod/De-mod.
- *Feedback for inaccurate nodes:* Checks for accuracy criteria in lower order nodes and triggers inaccurate nodes by generating Fetch signal at the Mod/De-Mod unit.

FEEDBACK

This paper introduces a feedback system into data fusion, for the wireless sensor network environment. As we have assumed that each node is equally equipped with the same functionality, each node should be able to trigger a feedback to its lower level node or nodes. This feedback is only generated, based on the decision criteria of the data fusion algorithm implemented as per the application. The feedback loop consists of three blocks that check to see if a feedback is required. The Data Fusion module checks sensed data for accuracy or any requirement with respect to the Knowledgebase. If any node disagrees with the sensed data before fusing, it sends out a Fetch to its lower nodes for a reconfirmation. Then it compares it with the previous values of the Knowledgebase, and passes a Data signal on backward to the higher order node. For a clearer understanding, we look at an example considering three nodes A, B, C, where C is the parent node for both A and B (Figure 4). Considering a decision criterion based on a probability data fusion model, where A provides 70% accuracy and B provides only 50% accuracy (for a knowledgebase accuracy of 80%). Since both the expected values are below the accuracy requirement, a feedback will be triggered. But if the accuracy level is say 60%, then C only triggers B. This is again based on the Knowledgebase requirements to set the accuracy percentage in this case. If the accuracy from both A and B are met with the Knowledgebase of C, data fusion will be performed.

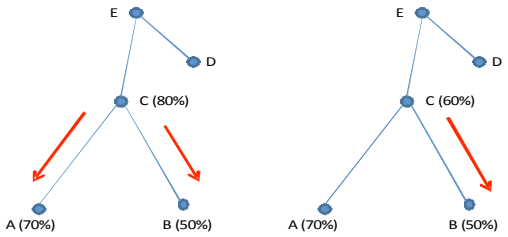

Fig. 4: Feedback in two scenarios: (a) Both A, B are inaccurate with C, (b) Only B is inaccurate with C

It can be thought that the power of the overall system may drain, especially for higher order node levels. As they are peers for lower order nodes, sending Fetch from this point all the way to end nodes can dramatically drain the power, especially for a large number of iterations. But this should not be a concern as feedback should take place only at the lower order. This is because at lower levels the accuracy requirement is already met. Otherwise the data fusion would not take place. This is the main rationale behind our proposed nodal feedback model.

DATAFUSION AND NETWORK ROUTING

Data fusion is preferred and is a valued process because of its accuracy in complex scenarios and ability to work in the wireless sensor network [2]. It has already succeeded in many applications in the wireless area [2][3]. There are many types of data fusion models, proposed and enhanced since last few decades [2][5]. Some models work well for a certain type of applications, while other models work better for some other applications. While, one fusion model looks into Active perception (SeFMAP) for Human Identification [7], other fusion model looks into Bayesian approaches for Prosthetic hands [8]. Subsequently, the Data Fusion block, the Network Routing block, and the Knowledgebase block are application specific. These are left open for flexibility, according to the application's design and specific requirements.

The Network Routing block processes information about the node address, identification, and itinerary or each node, as discussed previously. This paper looked into adaptive and probabilistic routing algorithms, because of each node being updated of node address, hop count, etc. [6]. But, this block is also left open to programmers for best routing schemes.

SYNCHRONIZATION

The synchronization of this network is interrupt driven. Each node is triggered only when: (a) Sink calls a particular node, (b) when the Sensor module detects an interrupt, and (c) a feedback is generated due to lack of accuracy in a node. Apart from this, synchronization of nodes takes place when the entire sensor network is powered up or when a data fusion is expected. As our objective does not include synchronization techniques, it is left for implementers to choose the appropriate synchronization algorithm to suit this nodal model.

CONCLUSION AND FUTURE WORK

In this paper we presented a feedback based nodal model for wireless sensor networks. We proposed an architecture design in the viewpoint of each node and its contributions to successfully fuse data along its reverse path to the sink. We discussed some power issues and provided solutions. Our model also emphasized the distribution of workload over the network, so as to balance and preserve the longevity of the overall system. Security can be provided to the system by modulating and demodulating Fetch signal and Data signal. These signals give the direction of flow and provide the itinerary for the next node.

A node-based data processing flow, in the form of a flow chart, was proposed and explained. The concept of how the feedback works in these systems is illustrated with examples. The persistence to keep our model generalized was to challenge new application approaches that may suit this concept. Future work on this concept is to produce a prototype or simulation of this model.

REFERENCES

[1] Prof. Anura Jayasumana, 2008. "Sensor Networks-Technologies, Protocols and applications", Worldcomp '08, Las Vegas, NV, July14, 2008.

[2] David Macii, Andrea Boni, Mariolino De Cecco, Dario Petri, 2008, "*Tutorial 14: Multisensor Data Fusion*," IEEE Instrumentation & Measurement Magazine, June, 2008.

[3] Hairong Qi, Xiaoling Wang, S. Sitharama Iyengar, 2001."*Multisensor Data Fusion* in *Distributed Sensor Net works Using Mobile Agents*" In Proceedings of 5th International Conference on Information Fusion.

[4] Rajnish Kumar, Matthew Wolenetz, Bikash Agarwalla, JunSuk Shin, Philip Hutto, Arnab Paul, and Umakishore Ramachandran, 2004, "*DFuse: A Framework for Distributed Data Fusion*." College of Computing, Georgia Institute of Technology

[5] Mark Bedworth and Jane O'Brien, 2000, "*The Omnibus Model: A New Model of Data Fusion?"* IEEE AES Systems Magazine, April 2000.

[6] Tom Parker, Koen Langndoen, 2005, "*Guesswork: Robust Routing in an Uncertain World."* IEEE MASS Magazine, 2005.

[7] Lena Biel and Peter Wide, 2002, *"An Intelligent Model approach for Combination of sensor information."* IEEE Magazine, 2002.

[8] Madhavi Anugolu, Anish Sabastian, Parmod Kumar, Marco P. Schoen, Alex Urfer, D. Subbaram Naidu, 2009, *"Surface EMG array sensor based model fusion using Bayesian approaches for prosthetic hand."* March, 2009.

[9] Wang, Yang: Fu, Xiong; Huang, Liusheng; 2009, "A Storage Node Placement Algorithm in Wireless Sensor Networks" Frontier of Computer Science and Technology, 2009. FCST'09. Fourth International Conference, Page(s): 267-271.

[10] Guilin Li; Jianzhong Li;2007, "An Energy Efficient Query Processing Algorithm Based on Relevant Node Selection for Wireless Sensor Networks,", Software Engineering, Artificial Intelligence, Networking, and Parallel/Distributed Computing, 2007. SNPD 2007. Eight ACIS International Conference, Page(s): 149-154.

[11] David L. Hall; James Llinas, 1997, "An Introduction to Multisensor data fusion" PROCEEDINGS OF THE IEEE, VOL. 85, NO. 1, JANUARY 1997.

3D Reconstruction for Hand Tracking and Estimation

Himabindu Karepey
Measurement and Control Engineering Research Center
College of Engineering, Idaho State University
Pocatello, ID 83209 U.S.A.

Hidayatullah Ahsan
Department of Electrical and Computer Engineering
College of Engineering, Boise State University
Boise, ID 83725 U.S.A.

Steve C. Chiu, Ph.D.
Measurement and Control Engineering Research Center
College of Engineering, Idaho State University
Pocatello, ID 83209 U.S.A.

Alba Perez-Gracia, Ph.D.
Measurement and Control Engineering Research Center
College of Engineering, Idaho State University
Pocatello, ID 83209 U.S.A.

Abstract - *In this paper we developed a framework for a computer vision system to determine kinematic information of the human hand motion, i.e., joint motion in discrete intervals of time. Since a 2D computer vision system developed does not provide complete kinematic information of the human hand, to overcome this we need a 3D vision system that uses multiple cameras and reconstructs a 3D image using reconstruction techniques. The resulting 3D image is used to determine the joint angles for all joints in the human hand. The vision system obtained is relatively inexpensive compared to commercial applications available, and can be used by persons who do not have expert knowledge of vision systems.*

Keywords: *Computer Vision, 3D Reconstruction (3D-RCon), Hand Tracking Analysis, and Motion Capture.*

1 Introduction

In recent years, image processing and human hand motion tracking have seen an increased interest in human-computer interaction (HCI) related applications. Hand motion is mainly defined by movement of underlying skeleton. This skeleton can be modelled as an articulated structure of rigid links connected at rotational joints forming a kinematic chain. The information from a vision system based on this kinematics can work with electromyogram (EMG) signals from the forearm muscles to provide better insight into how the hand moves.

Suppose when images are captured depth information of scene is lost, we need a 3D vision system to find this depth information. According to Hong Zhang *et. al* [1], for a 3D vision based hand motion tracking system to be successful, it has to be widely available, simple, accurate, and inexpensive. The system should be fast, since most human hand tracking applications are real-time in performance ; and should be able to deal with occlusions that occur while computation .

This paper focuses on the design and evaluation of a vision system for hand motion tracking and capturing. We propose a vision system that captures multiple view-point images, which provides three-dimensional data in real time. To elaborate on this work, Section 2 reviews the background research in 3D imaging and motion tracking methods, such as hand pose estimation for HCI. Section 3 describes our 3D vision system design. Section 4 discusses the experimental input and results for our six-camera system, followed by Section 5, conclusion and future work. Acknowledgement and References are given in Sections 6 and 7, respectively.

2 Background

In a 3D vision system, imaging and motion tracking of human hand are important research problems. Their various applications such as human body, hands, and face animation, pose gesture analysis and automatic detection of human activities, and other information such as articulated objects modeling, are often necessary. Vision based systems can be categorized as appearance-based and model-based. Example: the main idea behind appearance-based approach is detecting the shape of the hand. Hoshino and Tanimoto [2] identified the hand posture by shape detection and searching it from a database of already stored hand postures, which construct a 3D model of the hand to obtain all positional and kinematic information of hand. But in this case it is a tedious procedure since hand is a complex object with a high number of degrees of freedom. Vlasic, Baran, Matusiky, and Jovan Popovi´c [3]

developed a practical software system for capturing mesh animation details from multi-view-point video recordings, which captures the motion of both the skeleton and the shape and the result of this output mesh animation is enhanced with the details observed in the image silhouettes. But this method cannot reproduce the surface accurately from the contours, since it has to rely on the template to interpolate geometric information. This is especially problematic for unarticulated objects such as long scarves, faces, or flowing hair, it is also sensitive to errors in the silhouettes, and will likely produce incorrect geometry when visual hulls are noisy. In [4], Ueda, Matsumoto, Imai, and Ogasawara proposed a novel method for hand pose estimation that can be used as input interface. The system estimates all joint angles to manipulate objects in the virtual space. In that method, a hand pose is reconstructed as a "voxel model" by a multi-view point camera system, then all joint angles are estimated using 3D model fitting between the hand model and voxel model. But their system used an estimation that caused errors in the hand model. Processing speed of system was slow. The research in [5] by Duraisamy, Perez, and Schoen proposed that each finger is described as a serial robot expressed as Clifford algebra exponentials. This allows us to perform kinematic synthesis to obtain the angles at each joint, and to adapt the model to the dimensions of the hand of the subject being captured, based on the visual data obtained from the motion tracking system. The kinematic model obtained quantifies the motion of the natural hand. The experimental data obtained from the 3 cameras has been used to obtain some simplified results for the index finger. In our approach, we are using 6 cameras and for synthesizing model for whole hand for any arbitrary motion. However, all above mentioned approaches have their specific concerns.

In our research, we are continuing the work performed by Hidayatullah Ahsan [6]. His approach was to develop a 2D vision system with a marker-based semi-automatic tracking system to provide the joint angles of the index finger, which under certain assumptions can be used to study the complex grasping motion. Though effective, this approach does not provide complete kinematic information of the human hand. To overcome this, we developed a 3D vision system.

3 3D Vision System

A 3D vision system concerns the science and technology of machines. As a scientific discipline, computer vision is concerned with the theory behind artificial systems that extract information from images. The image data can take many forms, such as video sequences, views from multiple cameras, or multi-dimensional data. The hand model in [5] consists of links and joints that have specified locations and orientations drawn from anatomic data. These joint locations and orientations can be adapted to the actual dimensions of the subject via the kinematic synthesis. In order to both adapt the hand model to the geometry of the captured hand, and to track the angle at each joint, the procedure follows that of real-time model-based human motion tracking and analysis for human computer interaction systems. Applying kinematic synthesis expressing the motion as elements of Clifford algebra seems to produce a very good-behaved system of equations for the numerical solution. The equations are solved hierarchically using a Levenberg-Marquardt solver. The preliminary results of kinematics for smart prosthetics show that it is possible to recover the hand geometry and motion quickly and accurately when using synthetic data.

3.1 System Requirements

Our vision motion tracking system runs on a workstation using Intel® Core™ 2 Quad CPU at 2.40 GHz, and uses 6 DragonFly®2 cameras, model DR2-BW/COL-XX by point Grey Research Inc., which can capture black and white and color images. This system is connected to the computer with 6-pin IEEE1394a interface. These cameras can be used with National Instruments (NI) LabVIEW software [8][9]. For a multiple-camera vision system such as this one, it is important to have these cameras synchronized with a maximal deviation of 125µs between the cameras [9]. Fujinon HF9HA-1B 9mm model lens are used for our system due to its affordability and availability. Accuracy of 3D object reconstruction depends on camera configuration, lens, resolution, and speed [7]. Figure 1 gives the camera component specifications of our system.

Model	DR2-BW/COL-XX
Sensor	1/3" Progressive Scan CCD
Sensor Pixel Size	7.4µm Square Pixel
Color Modes	Black and White (Mono 8 and Mono 16)
	Color (RGB, YUV)
Resolution	Up to 648x488
Frame Rate	Black and White (Up to 60 fps)
	Color (Up to 30 fps)

DragonFly® 2 by Point Grey Research Inc.

Model	HF9HA1B 9mm
Mount Type	C/CS – Mount
Imager Size	2/3" CCD
Aperture	f/1.4 to f/1.6
Iris	Manual
Focus	Manual

Lens by Fujinon

Figure 1: Camera and lens specifications

3.2 Overview of the System

Our system exploits several computer vision techniques and multiple camera views of hand to find the depth information. It is important to know about the scene's background. This information helps in extracting the foreground object from an image. For our computer vision system we use a solid blue color sheet so the background is smooth and distinguishable from the human hand. For a multiple camera vision system, the cameras can be placed randomly or at a uniform distance from each other, as shown in Figure 3. The cameras should be pointing to the same region in the three-dimensional space. The process of 3D scene reconstruction depends on accurate camera calibration and background subtraction [7], and can be divided into the following steps:

1. Camera calibration
2. Image acquisition
3. Background subtraction
4. 3D object reconstruction

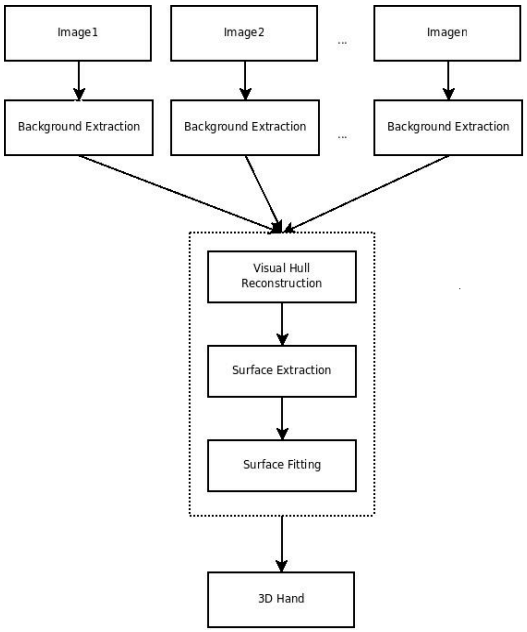

Figure 2: Steps involved in 3D reconstruction

3.3 Details of the 3D Reconstruction

The details of the 3D reconstruction are described below. Figure 2 illustrates the steps involved:

Camera calibration: The first step for 3D reconstruction using multiple images is to find a viewpoint for each camera, which results in a projection model [10] that is first used to determine the viewpoint of each image and then to find the approximate volume in space that contains the 3D object [11]. This gives the intrinsic/extrinsic parameters. For calibrating multiple cameras simultaneously, the method described in [10] was used, which relies on correspondence of a set of optical markers between images, where the optical marker can be a source of light such as a laser pointer.

Image acquisition: As discussed in Section 2, for image capturing we used the DragonFly®2 cameras and LabVIEW 8.2 package developed for capturing multiple view of hand motion. We captured gray-scale images, since the frame rate is much slower for color images.

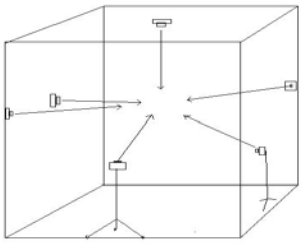

Figure 3: Camera setup for image acquisition

Background subtraction: We used the SACON method [12] developed by Wang and Sutter for segmenting images for tracking applications in cluttered or dynamic background, with an input of sequence images $i = 1, 2\ldots, N$. The SACON method involves the following steps:

A. Sampling: In this step the absolute difference between the pixel intensities of image i and all background images $t = 1\ldots, N$ is used to determine if a pixel m in image i is part of the background or the object of interest. Such an observation can be expressed by formula 3.1:

$$\Gamma_i = \begin{cases} 1 & if\ |x_i(m) - x_t(m)| \le T_r\ \ or\ \ \beta < \dfrac{x_i(m)}{x_t(m)} < \gamma \\ 0 & otherwise \end{cases} \quad (3.1)$$

where $x_i\ (m)$ represents the intensity of the pixel location m in image i. Here T_r is the error tolerance that needs to be found experimentally. The ratio $x_i\ (m) / x_t\ (m)$ is used to remove the influence of shadow in an image.

B. Consensus: The information from the above step is used to create a mask by summing the sampling results of an image i with all background images as shown in formula 3.2:

$$B_t(m) = \begin{cases} 1 & \sum_{i=1}^{N} \Gamma_i(m) \ge T_m \\ 0 & otherwise \end{cases} \quad (3.2)$$

where T_n is a threshold for the data points that are within the error tolerance. T_n is a function of T_r and can be found using formula 3.3:

$$T_n = \tau T_r N \quad (3.3)$$

where τ is a constant found experimentally.

C. Visual hull: Silhouettes for all images at a particular instance in time will be created, which have the projection transformation of the camera. Then they can be used to back project the foreground region into the 3D space [13], which results in a conic volume that contains object of interest visual hull. The term "visual hull" was coined by Laurentini in [14]. For our system, we constructed a cube containing the object of interest and the dimensions of cube found by trial and error. The main objective is to find the point in cloud cube that is part of the 3D object. This problem was solved by using an image space rather than an object space [15].

Figure 5 is the expected result of the visual hull of hand using the grid point cube shown in Figure 4. We projected onto the silhouette of each image in the region of interest or foreground in silhouette image. Otherwise the image is discarded. This process, when applied to all points in the bounding volume and all silhouettes, results in a visual hull.

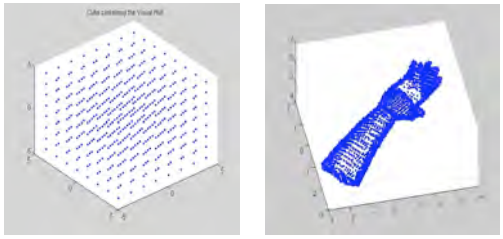

Figures 4, 5: Partitioned cube data of visual hull and hand

D. Surface extraction: The visual hull that has point cloud of objects contains all possible points. In our approach the point cloud is sliced to xy-plane of the 3D coordinate system. For each slice the interior points are removed based on simple neighborhood method.

E. Surface fitting: The surface point cloud of a 3D object may not show any abnormalities in the 3D object. We have found that the best way to observe the 3D object abnormalities is by looking at the surface that best fits the surface point cloud. For our research we used an application called Tight Cocone [16]. This application finds a water-tight surface to a given point cloud [17].

4 Experimental Input and Results

We have worked on several image-processing techniques to capture the hand motion. Figure 6 presents a sequence of input images of human hand from six different camera views that give details of the human hand. It is important to have the information of scene background, since it helps in extracting the foreground. Alignment of the hand is different at different intervals of time. This sequence of images is the initial input to our 3D system.

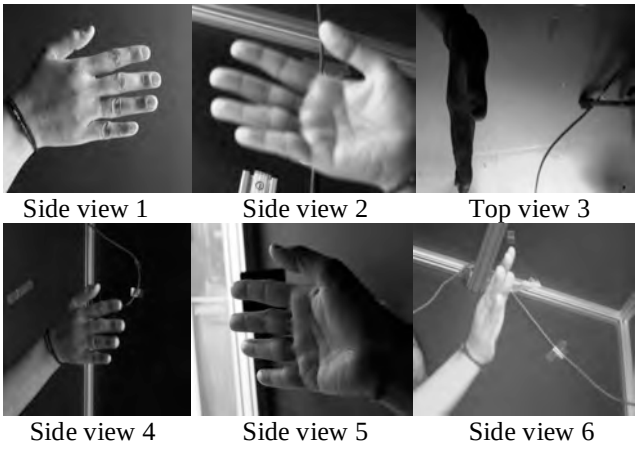

Figure 6: Captured images - camera views 1, 2, 3, 4, 5, 6

4.1 Hand Motion Tracking

Hand motion tracking is used in hand pose estimation. For our research, the main goal is to determine the location of the finger joints. For this we developed a 3D vision setup which includes six cameras as well as markers drawn on finger joints using ink pens. The input to this system is a sequence of gray-scale images captured from the cameras. When the image sequence of hand motion is captured (using LabVIEW), these markers must be visible in all cameras. Simple threshholding operation is performed so that only marker images are left, which store the 3D marker position information at particular intervals of time. Further, the distance between these marker positions is calculated using Euclidean distance between two points. For this marker-based method to work properly, the markers must not be affected by external lighting conditions, orientation and camera position, under which images are captured. The joint angles of the fingers are computed using formula 4.1. This is an off-line post-processing method.

$$\theta = \arccos\left(\frac{(x_2 - x_1)(x_3 - x_2) + (y_2 - y_1)(y_3 - y_2)}{\sqrt{((x_2 - x_1)^2 + (y_2 - y_1)^2)((x_3 - x_2)^2 + (y_3 - y_2)^2)}}\right) \quad (4.1)$$

where $(x_1, y_1), (x_2, y_2)$ and $(x_3, y_3) \in \mathbb{R}^2$ are the coordinates of the markers.

4.2 Background Subtraction Results

Figure 7 is the result of background subtraction in dynamic background. We needed to remove the background of the scene from these images and create a binary image with pixel values 0 for background and 1 for the object of interest. This resulted in silhouettes representing the accurate boundary of the object. We noticed some abnormalities in these results since image background is different for each camera.

Figure 7: Background subtraction results with six cameras

4.3 Discussion of Preliminary Results

Figure 8 shows the results of the automatic calibration method, which yields a complete camera projection. These projections of the light source shown in the form of circles are detected independently for each camera. Every time when the calibration is done, it is important to know whether the data is valid. If needed, we can always recalibrate the system completely. However, this takes time, and the resulting parameters will not be exactly the same as the old ones, even though the setup remained the same. This is a somewhat trial-and-error process. We need to strive for the results with the lowest reprojection error and variance.

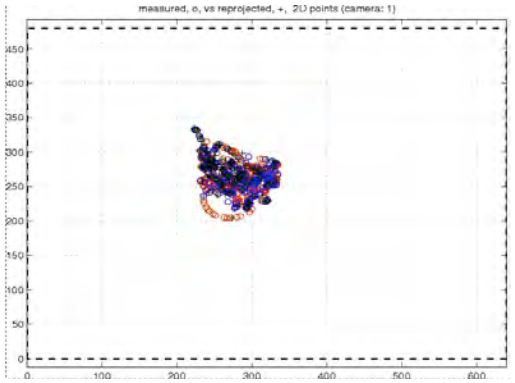

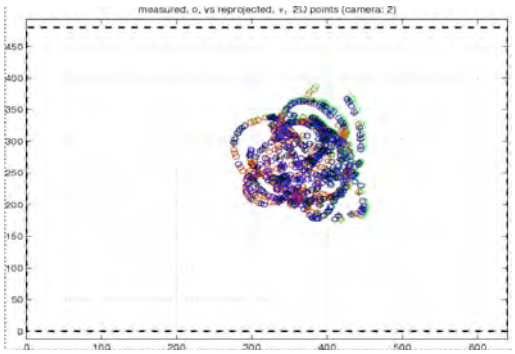

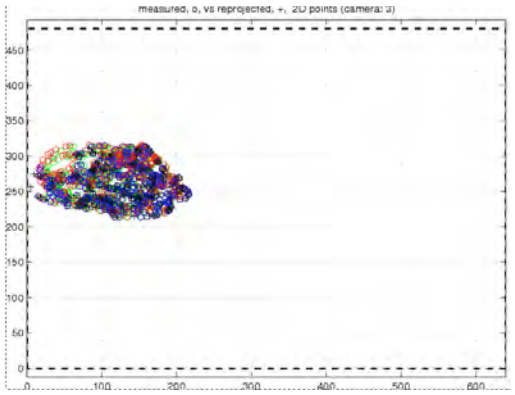

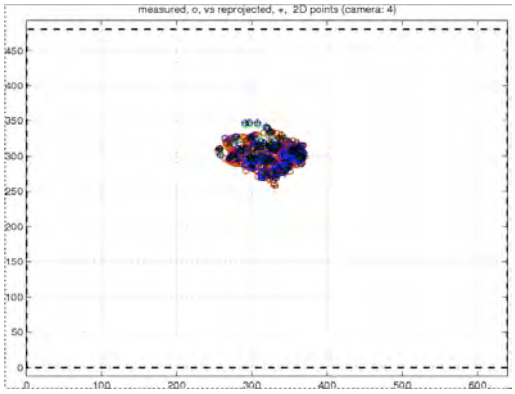

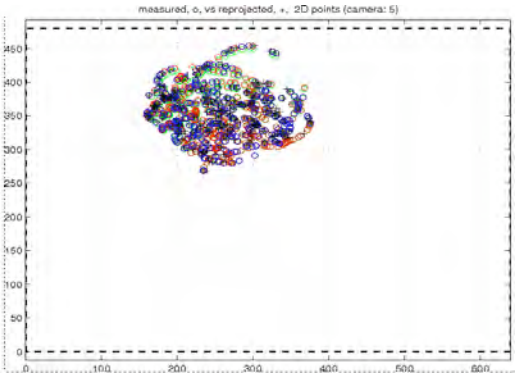

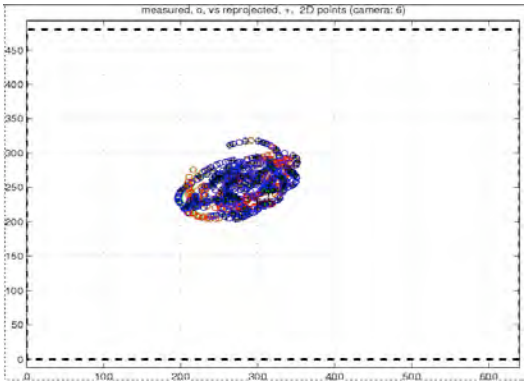

Figure 8: Reprojected outliers (RANSAC for 6 cameras)

Figure 9 shows the results of reconstructed setup of our six-camera system. Small blue circles with numbers denote the identification numbers and positions of the camera centers. Blue lines denote orientation of the cameras' optical axes. The red circles are the reconstructed positions of the laser pointer. From this we observe that camera alignment is not yet proper, the reason for this alignment being lens distortion. For the vision system, all cameras need to be closer to the hand so that most of the image is occupied by the hand. This is necessary to get detailed images of the hand with the working distance of the Fujinon lens.

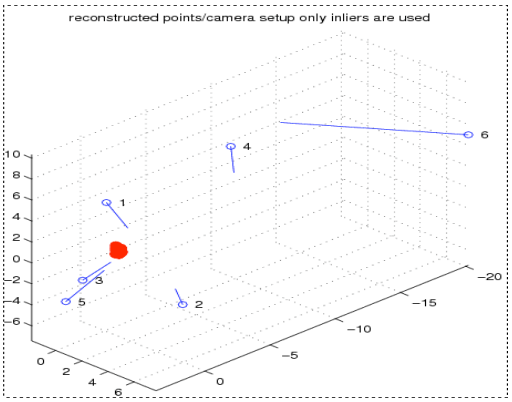

Figure 9: Reconstructed axes of the six-camera setup

Figure 10 shows the average reprojection errors and their standard deviations for each camera within the system. While the standard deviations are deemed acceptable, the mean errors are considered high. The purpose of system calibration is to minimize both the mean error and the standard deviation.

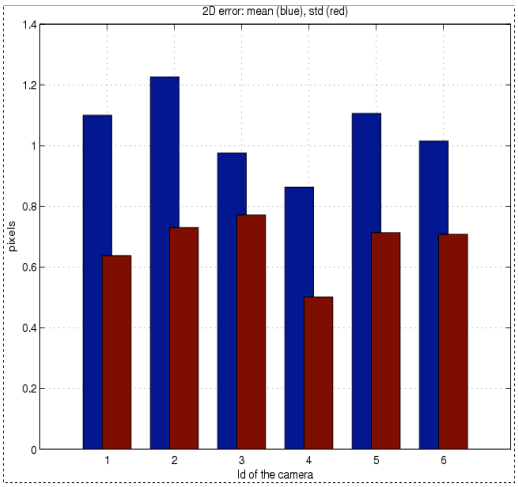

Figure 10: Reprojection errors of the cameras

5 Conclusion and Future Work

As we mentioned, this work is an extension of a previous system, where we used the techniques for 3D reconstruction and motion-tracking marker-based system, in which various image-analyzing techniques were applied to obtain the joint angle data. But there were several abnormalities in the 3D hand that was reconstructed. For example, two thumbs are visible and some fingers were altogether (this can be referred in [6]). These abnormalities exist because we are using only four camera views and background for all images is dynamic and it varies in instant interval of time. So, in our proposed system we introduced a six-camera design which can improve the system accuracy and reduce abnormalities by placing cameras as close as possible to the object, i.e. the hand.

For future work we plan to design and develop a real-time, fully automatic GUI-based 3D computer vision system that will capture the images in a dynamic background and give a better insight into the angle data. We will also be investigating any potential issues related to scaling up of the system.

6 Acknowledgement

We are grateful to all the MCERC students for being very supportive while we conducted the experiments. We want to thank Rajender Miyyapuram and Parmod Kumar for their help in the experiments and suggestions.

7 References

[1] Kihwan Kwon, Hong Zhang, and Fadi Dornaika. ‘‘Hand Pose Recovery with a single Video Camera’’ ; Department of Computer Science, University of Alberta, Canada. In IEEE International Conference on Robotics & Automation Proceedings, May, 2001.

[2] K. Hoshino and T. Tanimoto. ‘‘Real-time hand posture estimation without deviation of search time’’ ; In First IEEE/RAS-EMBS International Conference on Biomedical Robotics and Biomechatronics, 2006.

[3] Daniel Vlasic, Ilya Baran, Wojciech Matusiky, Jovan Popovi´c. ‘‘Articulated Mesh Animation from Multi-view Silhouettes’’; Computer Science and Artificial Intelligence Laboratory Adobe Systems Inc. Massachusetts Institute of Technology in Proceedings of ACM SIGGRAPH, August, 2008.

[4] Etsuko Ueda, Yoshio Matsumoto, Masakazu Imai, Tsukasa Ogasawara. ‘‘Hand Pose Estimation Using Multi-Viewpoint Silhouette Images’’; Nara Institute of Science and Technology. CREST, JST (Japan Science and Technology Corporation), In IEEE/RSJ International Conference on Intelligent Robots and Systems, November, 2001.

[5] Karthikeyan, Duraisamy AlbaPerez-Gracia, Marco P. Schoen. ‘‘Vision-Based Kinematic Synthesis of Hand Motion’’; MCERC, Idaho State University. In ASME International Mechanical Engineering Congress & Exposition (IMECE), 2006.

[6] Hidayatullah Ahsan. ‘‘3D Computer Vision System for Hand Joint Motion Calculation’’; Idaho State University. In Thesis defense, December, 2008.

[7] Y. Hwang, J. Kim, and I. Kweon. ‘‘Silhouette extraction for visual hull reconstruction”; In IAPR Conference on Machine Vision Applications, May, 2005.

[8] Point Gray Research Dragonfly image capturing device http://www.ptgrey.com/products/dragon_y2/index.asp, 2007.

[9] National Instrument http://www.ni.com/vision/, 2007.

[10] Tomas Svoboda, Hanspeter Hug, and Luc Van Gool. ‘‘ViRoom – Low Cost Synchronized Multicamera System and Its Self-calibration’’ ; Computer Vision Laboratory, Department of Information Technology and Electrical Engineering, Swiss Federal Institute of Technology, In MIT Press journal August ,2005.

[11] A. Hayden. ‘‘Handbook of Geometric Computing, chapter Three-Dimensional Geometric’’; Computer Vision. Springer, Berlin, Germany, 2005.

[12] H. Wang and D. Suter. ‘‘Background subtraction based on a robust consensus method’’; In ICPR '06 Proceedings of the 18th International Conference on Pattern Recognition, IEEE Computer Society, 2006.

[13] G. Slabaugh, B. Culbertson, T. Malzbender and R. Schafer. ‘‘A survey of methods for volumetric scene reconstruction from photographs’’; 2001.

[14] A. Laurentini. ‘‘The visual hull concept for silhouette-based image understanding’’; In IEEE Transactions on Pattern Analysis and Machine Intelligence, 1994.

[15] M. Potmesil. ‘‘Generating octree models of 3d objects from their silhouettes in a sequence of images’’; In Computer Vision Graph Image Processing, 1987.

[16] http://www.cse.ohio-state.edu/tamaldey/cocone.html, in 2008.

[17] T.K. Dey. ‘‘’Approximate medial axis as a voronoi sub complex’’; In ACM Press, 2002.

Genetic Algorithm Running Time Optimization Using OpenMP Parallel Computing

Parmod Kumar[1], Nikesh Joshi[2], Alex Jensen[1], Chandrasekhar Potluri[1],

Marco P. Schoen[1], Steve C. Chiu[1,2]

[1]Measurement and Control Engineering Research Centre, College of Engineering

[2]Department of Electrical Engineering and Computer Science, College of Engineering

Idaho State University

Pocatello, ID 83209 U.S.A.

[1]kumaparm@isu.edu, [2]joshnike@isu.edu, [1]jensalex@isu.edu, [1]potlchan@isu.edu, [1]schomarc@isu.edu, [2]chiustev@isu.edu

Abstract

Genetic Algorithm (GA) are biologically motivated evolutionary computation techniques used both as search methods for solving problems and for modelling evolutionary systems.GA has been used in a wide variety of optimization tasks, including numerical optimization and combinatorial optimization problems such as circuit design and job shop scheduling. Although there are many problems for which the genetic algorithm can evolve into a good solution in reasonable time, there are also problems for which it is inappropriate like the one in which it is important to find the exact global optimum. In addition, if the number of iteration increases the algorithm will take a long time to complete its computations. In this work, we are using GA to optimize the parameters of nonlinear Bayesian Filters for electromyographic (EMG) signal. OpenMP is a parallel programming model for shared memory and distributed shared memory multiprocessors. We are using OpenMP on four processors to improve the time of GA optimization for Bayesian Filter parameters.

Keywords: OpenMP, $Matlab^{®}$, MPI, EMG, GA, Gene, Mother Chromosome, Father Chromosome, Pairing Operator, Mating Operator, Mutation, Population Size.

1. Introduction

Principles of natural selection and genetics has been used to deduce some efficient search algorithms, GA is one of them. GA is used in different fields to obtain solutions to different problems, e.g. engineering, science, business and economics [1, 2]. Some of the applications of GA are in automotive design, engineering design, robotics, evolvable hardware, optimized telecommunication routing, joke and pun generation, bio-mimetic invention, traffic and shipment routing, computer gaming, encryption and code breaking, computer-aided molecular design, gene expression profiling, optimizing chemical kinetic analysis, finance and investment strategies, and marketing and merchandising. Although, for a general problem of normal size, GA is a good option to get the optimal solution in appropriate amount of time, whereas for bigger and complex problems GA takes more time to find optimal solution. Researchers have explored different approaches to minimize this computational time and cost and parallel processing came out to be one of the most promising approaches.

GA is based on the principle of natural selection. It uses a random search technique to find the optimal solution of a problem by manipulating a population of candidate solutions. To form next generation, GA selects the best solutions from the evaluated population. Good solutions and time to reach them by GA depends on the population size [3, 4], because if the population is too small, then the search space will not be sufficient explored and it will be difficult to identify good solutions. In the case when the population is too big, the GA will waste computational resources processing unnecessary individuals. Each individual in the population has a fitness value, which

is a payoff measure that depends on how well the individual solves the problem. Crossover and mutation are the two operators used by GA to explore the search space, here crossover is a primary and mutation is a secondary search operator. The probability of crossover is much higher than the probability of mutation. GA can be stopped based on different conditions, one is by using a predetermined number of generations and function evaluations, second is the average quality of the population gets saturated after some number of generations, and the third is when all the individuals are identical, which can only occur when mutation is not used. We are using predetermined number of generations and function evaluations to stop the GA in this research work. The generic GA flow chart is shown in Figure 1.

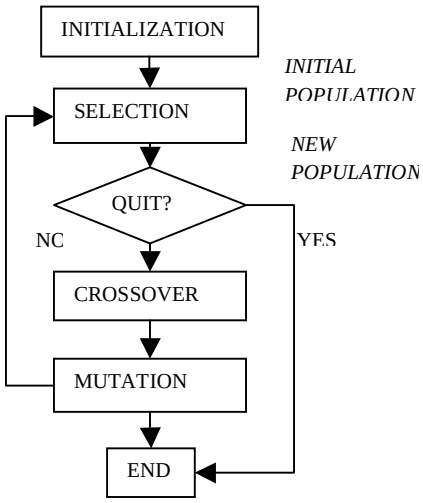

Figure 1: Generic GA Flow Chart.

The time taken by GA is directly proportional to the number of evaluations and generations, the more the number of evaluations the lager is the computational time for GA. On the other hand, this time can be minimized by paralleling the GA program on a parallel cluster. Most of the parallel programs divide the task in chunks and solve it simultaneously using multiple processors. On a parallel cluster, there are numerous processors, and they share the task, the larger the number of processors the faster the computation or lesser the time for the completion of the algorithm. In this research work we are using OpenMP parallel programming model and utilizing a cluster of four processors to run the GA and comparing its performance with the single processor in $Matlab^{®}$.

2. Background

Most of the parallel programs divide the task into chunks and solve it simultaneously using multiple processors. Similar approach can be used for GAs in different ways. These approaches can be using a single population, divide the population into several subpopulations, use of massively parallel architecture, or use of fewer multicomputer with fewer and more powerful processing units. Mainly there are three kinds of parallel GAs, and these are (a) global single-population master-slave GAs, (b) single-population fine grained, and (c) multiple-population coarse-grained GAs. The hierarchical parallel GAs combine the multiple demes with master-slave or fine-grained GAs. It has a higher level and a lower level, at the higher level they are multiple-deme algorithms and at the lower level they are single-population parallel GAs (either master-slave or fine-grained) [1].

The research work in [5] shows a method of parallel GA, in which a global parallel implementation of the conventional GA and a GA with a generation gap, where some part of the population is replaced. The efficiency of global parallel GA is close to 100 % in SIMD (single instruction multiple data) computers by [5]. Four prototypes for parallel GAs are proposed in [6] where the first three are variations of the master-slave GA, and the fourth is a multiple-population GA.

2.1 Master-Slave Parallelization

Same as in a simple GA, master-slave GA also have a single panmictic population. Figure 2 shows the schematic of master-slave GA, where the evaluation of fitness is distributed among the slave processors.

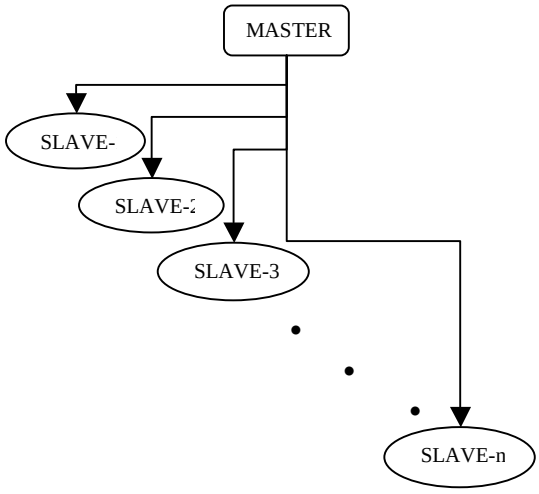

Figure 2: Master-Slave Parallel GA.

The master-slave GA considers full population size for selection and crossover, so it is known as global GA. The master-slave parallelization method for GA does not change the behavior of the algorithm while the single-population fine grained and multiple-population coarse-grained GA change the way the GA works [1]. The master-slave parallel GA considers all the population for selection, whereas the other parallel GAs considers only a subset of the population. In addition, in the master-slave parallel GA the mating is random, whereas in the other methods mating is restricted to a subset of individuals [1]. The majority of the global parallel GAs are implemented synchronously. If the multiprocessor architecture is of shared memory then each individual processor can share the information, reading and writing without any issue. In contrast, on distributed-memory architecture, the population is stored only at one processor and the master is responsible for sending the individuals to slaves for evaluation, collecting the results and applying GA for next generation. Encore Multimax is a shared-memory computer with 16 processors, a GA is implemented on this to search for efficient timetables for schools in [7]. This research in [7] gave a limited speed-up because of the critical path of the program serial code.

In 1993, Abramson, Mills, and Perkins added a distributed-memory machine "Fujitsu AP1000" with 128 processors to the experiments, changed the application to train timetables and modified the code [8]. In this research, the speed-up was significant up to 16 processors and then decreased because of the increase in communication as more processors are added.

Hauser and Männer used global GA on three different parallel processors and got good speed up only on NERV multiprocessor [9]. The speed-up of five using six processors is obtained with a very low communications overhead [9]. The reason of low performance on other processors a SparcServer and a KSR1 is because of the inadequate scheduling of computation threads to processors by the system. All the previous research results shows that the master-slave parallel GAs are easy to implement and very efficient method of parallelization especially when the evaluation needs considerable computations. Additionally the master-slave parallel GAs do not change the search behavior of the GA [1].

3. GA In *Matlab*®

The continuous number GA, which is used in this work, interprets the parameters of a problem as genes, where one set of parameters form a chromosome, $chromosome = \{gene_1, gene_2, \dots, gene_{Npar}\}$. Since one chromosome corresponds to a candidate solution, its evaluation is done by assessing the numerical value of that solution, which usually referred as the cost. Unlike traditional optimization, the function is not referred to as the cost function but as the fitness function or objective function. Using an initial population size with randomly generated chromosomes, where each gene is generated by a random number generator within the search space, the chromosome will take the dimension of $R^{Npar*population\ size}$. After evaluating each chromosome cost $c_i = f(chromosome_i), i = 1,2, \dots, population\ size$, the selection operator will select a subset of the chromosomes based on their cost value to survive for the next iteration.

For elitism based GA, the best performing chromosomes always survive. There are two options the population size, a steady-state or a performance based size. The first option maintains a certain number of chromosomes for each iteration – also referred to as a generation; while performance based size, selection sets a minimum criterion for chromosomes to survive. The latter option may cause the algorithm to end prematurely since not minimum criteria (cost value).

Pairing Operator: Genetic Algorithm may employ a number of pairing mechanisms. Among them are pairing from top to bottom, where the best performing chromosome is paired with the next best performing chromosome and so on; random pairing, where a uniform distribution is assumed to randomly pick the mother and father chromosome; weighted random pairing where the probability of selection is influenced by the performance of the individual chromosome; and rank weighing, where the probability of selection is influenced by the ranking of chromosome with respect to the others measured again by the performance. In this paper, the pairing is accomplished by determining the cumulative probability for each chromosome is

$P(n) = \frac{n}{\sum_{i=1}^{r} i}$, where

$r = \frac{population\ size - no.of\ chromosomes\ kept}{2}$,

and n is the index of chromosomes. Having computed the individual cumulative probabilities $P(n)$, the parent chromosomes are now selected by utilizing a random number generator and indexing this with the cumulative probability. Hence, the best performing chromosome has the best chance of being selected, but also, all chromosomes in the mating pool have a chance of being selected.

Mating Operator: In this work, the next generation chromosomes are created from the mother and father chromosome (which were selected as described above) by following equations given as:

$$gene_{new_1} = mother(\alpha) - \beta(mother(\alpha) - father(\alpha)),$$

$$gene_{new_2} = father(\alpha) + \beta(mother(\alpha) - father(\alpha)),$$

Where, $\alpha = integer(rand * N_{par})$, $\beta = random\ number\ between\ 0 - 1$, and N_{par} is number of parameters for complete solution. In this α can also be viewed as equivalent to the cross-over point utilized in the binary GA. Hence, the offspring (new chromosomes) are found as

$$chrom_{new_1} = (gene_{mother_1}, gene_{mother_2}, \dots, gene_{new_1}, \dots, gene_{dad_{N_{par}}}),$$

and

$$chrom_{new_2} = (gene_{dad_1}, gene_{dad_2}, \dots, gene_{new_2}, \dots, gene_{mother_{N_{par}}}).$$

Mutation: Mutation is an important operator that allows the search to escape local minima in order to find better areas on cost surface. Too much mutation will do opposite, i.e. if a chromosome approach an optimum point, it might mutate and be placed at an entirely different location of the cost surface. Mutation is accomplished by randomly changing a gene, i.e. substitute it with a random numbers.

4. GA In OpenMP

OpenMP is a parallel programming model, which uses some compiler directives and library routines to express shared-memory parallelism [10]. OpenMP uses Fortran and C++ interfaces, which is a standard feature. OpenMP API is designed and developed by a group, which represents the major vendors of high-performance computing hardware and software. A set of compiler directives is the major part of OpenMP interface. The programmer adds these compiler directives to a sequential program. The programmer specifies the synchronization points and tells the compiler what parts of the program to execute concurrently. As the directives can be added in a incremental fashion, the OpenMP gives a path and platform for the parallelization of existing software. In contrary, the Pthreads and MPI approaches are library routines. Pthreads and MPI are linked with and called from a sequential program, and the programmer is required to divide the computational work manually [11].

Literature does not show any evidence of the use of OpenMP parallel programming model for GA in specific. This work is using OpenMP to optimize the filter parameters of Bayesian filters using GA technique. The parallel cluster has four processors. The idea of the research is to implement the GA using OpenMP on this four processors cluster and compare the results with the output on $Matlab^{®}$ on a single processor. The OpenMP parallel programming model is given in Figure 3, where sequential parts and parallel regions are labelled clearly.

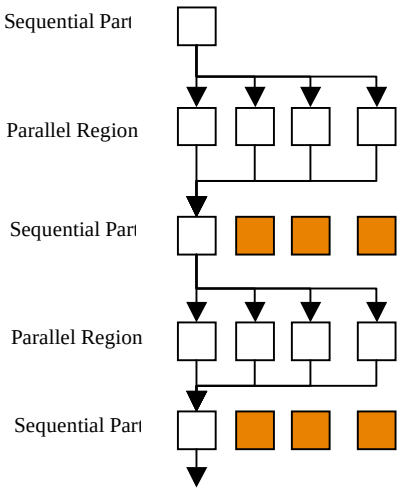

Figure 3: OpenMP Parallel Programming Model.

5. Results and Discussions

In this work, we are using GA to optimize the parameters of nonlinear Bayesian Filters for electromyographic (EMG) signals. OpenMP is a parallel programming model for shared memory and distributed shared memory multiprocessors. We are using OpenMP on four processors to improve the time of GA optimization for Bayesian Filter parameters.

First $Matlab^{®}$ is used to run GA on one processor, and the same algorithm is applied on OpenMP parallel processing model using four processors. Two sets of data captured at a sampling rate of 2000Hz are used, first data is for 30 seconds and the second is for 60 seconds. The total simulation time taken by the $Matlab^{®}$ and OpenMP is recorded precisely. Following tables shows the results obtained from simulations. Table 1, 2 and 3 shows the $Matlab^{®}$ simulation results for two different data sets of different lengths.

Table 1: Simulation time for 30 seconds and 60 seconds data sets in $Matlab^{®}$.

No. of Iterations	Simulation time seconds – 30 seconds of data set.	Simulation time seconds – 60 seconds of data set.
10,000	7.13	2393.06
15,000	16.95	2403.52
20,000	28.05	2416.66
25,000	42.66	2432.89
30,000	60.61	2452.34
35,000	82.41	2475.94
40,000	108.21	2503.69
45,000	139.35	2535.91
50,000	175.45	2571.72

Table 2: Simulation time for 30 seconds and 60 seconds data sets in $Matlab^{®}$.

No. of Iterations	Simulation time seconds – 30 seconds of data set.	Simulation time seconds – 60 seconds of data set.
60,000	208.65	2613.84
70,000	260.67	2741.73
80,000	331.85	2813.34
90,000	428.03	2913.25
100,000	550.89	3039.70

Table 3: Simulation time for 30 seconds and 60 seconds data sets in $Matlab^{®}$.

No. of Iterations	Simulation time seconds – 30 seconds of data set.	Simulation time seconds – 60 seconds of data set.
125,000	704.54	3193.36
150,000	943.89	3433.06
175,000	1288.28	3775.16
200,000	1755.77	4236.28

Figures 1, 2 and 3 are graphical representation of the results from the Table 1, 2 and 3 respectively. It is evident from Figure 1, 2 and 3 that CPU time is directly proportional to the data size and number of iterations. Therefore, increase in the data size and the number of iterations results in the increase in CPU time.

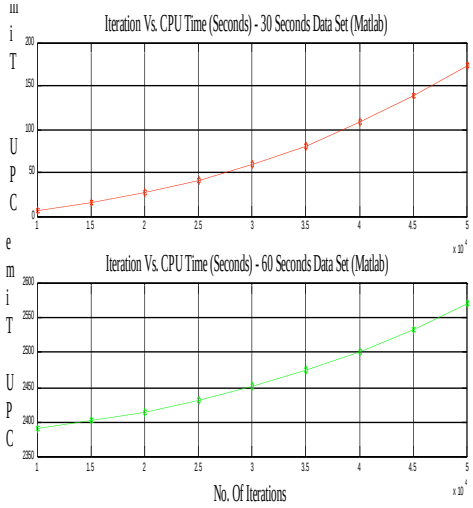

Figure 1: Iterations Vs. CPU Time – Table 1 Data.

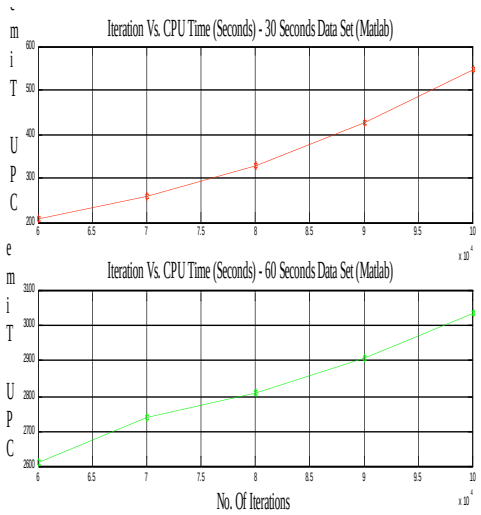

Figure 2: Iterations Vs. CPU Time – Table 2 Data.

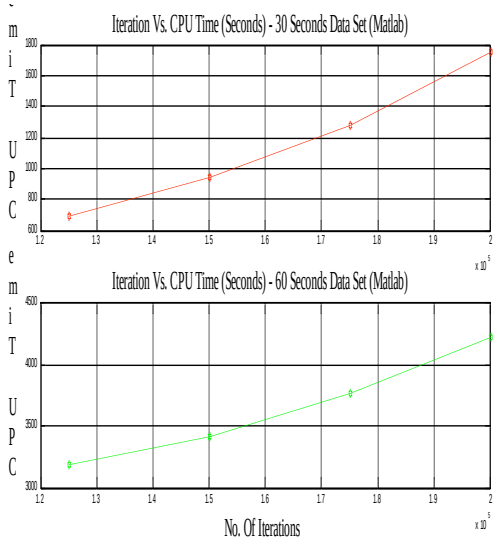

Figure 3: Iterations Vs. CPU Time – Table 3 Data.

The GA code from $Matlab^{®}$ is converted into C-code and OpenMP implementation is under pipeline. Results will be published in next reputed conferences. The code is available at http://www.isu.edu/~chiustev/.

6. Summary and Future Work

To conclude this work uses the idea of parallel processing and implement GA on OpenMP parallel programming model of four processors. First $Matlab^{®}$ GA code is converted to C code and then to OpenMP to implement on the parallel cluster. The algorithm is implemented both in OpenMP and $Matlab^{®}$ for 25, 50, 75 and 100 iterations and the time taken in execution is recorded. As expected the results shows the improvement of time in OpenMP implementation. In future work, similar approach will be applied using MPI and OpenMP and MPI combined for GA and more complex and advanced optimization algorithms.

Acknowledgement

The authors gratefully acknowledge the support of the Measurement and Control Engineering Research Center (MCERC) and College of Engineering, Idaho State University for using their recourses for this work.

References

[1] E. Cantú-Paz, "A survey of parallel genetic algorithms," *Calculateurs Parallèles,Réseaux et Systèmes Répartis*, vol. 10, no. 2, pp. 141–171, 1998.

[2] GOLDBERG D. E., « Genetic and evolutionary algorithms come of age ». *Communications of the ACM*, vol. 37, n 3, p. 113–119, 1994.

[3] GOLDBERG D. E., DEB K., CLARK J. H., « Genetic algorithms, noise, and the sizing of populations ». *Complex Systems*, vol. 6, p. 333–362, 1992.

[4] HARIK G., CANTÚ-PAZ E., GOLDBERG D. E., MILLER B. L., « The gambler's ruin problem, genetic algorithms, and the sizing of populations ». In *Proceedings of 1997 IEEE International Conference on Evolutionary Computation*, p. 7–12, IEEE Press (Piscataway, NJ), 1997.

[5] BETHKE A. D., « Comparison of Genetic Algorithms and Gradient-Based Optimizers on Parallel Processors: Efficiency of Use of Processing Capacity ». Tech. Rep. No. 197, University of Michigan, Logic of Computers Group, Ann Arbor, MI, 1976.

[6] GREFENSTETTE J. J., « Parallel adaptive algorithms for function optimization ». Tech. Rep. No. CS-81-19, Vanderbilt University, Computer Science Department, Nashville, TN, 1981.

[7] ABRAMSON D., ABELA J., « A parallel genetic algorithm for solving the school timetabling problem ». In *Proceedings of the Fifteenth Australian Computer Science Conference (ACSC-15)*, vol. 14, p. 1–11, 1992.

[8] ABRAMSON D., MILLS G., PERKINS S., « Parallelisation of a genetic algorithm for the computation of efficient train schedules ». *Proceedings of the 1993 Parallel Computing and Transputers Conference*, p. 139–149, 1993.

[9] HAUSER R., MÄNNER R., « Implementation of standard genetic algorithm on MIMD machines ». In DAVIDOR Y., SCHWEFEL H.-P., MÄNNER R., Eds., *Parallel Problem Solving fron Nature, PPSN III*, p. 504–513, Springer-Verlag (Berlin), 1994.

[10] [Online] Available: http://www.openmp.org.

[11] ENRIQUE A., MARCO T., << Parallelism and Evolutionary Algorithms >>. *IEEE Transactions on Evolutionary Computation, vol. 6, no. 5, October 2002.*

Synthesis of Spatial RPRP Closed Linkages for a Given Screw System

Alba Perez-Gracia
Institut de Robòtica i Informàtica Industrial (IRI) UPC/CSIC
Llorens i Artigas, 4-6, 08028 Barcelona, Spain;
And: College of Science and Engineering
Idaho State University
921 S. 8th Ave., Pocatello, ID 83209, USA.
Email: aperez@iri.upc.edu

The dimensional synthesis of spatial chains for a prescribed set of positions can be applied to the design of parallel robots by joining the solutions of each serial chain at the end effector. This design method does not provide with the knowledge about the trajectory between task positions and, in some cases, may yield a system with negative mobility. These problems can be avoided for some overconstrained but movable linkages if the finite screw system associated to the motion of the linkage is known. The finite screw system defining the motion of the robot is generated by a set of screws, which can be related to the set of finite tasks positions traditionally used in the synthesis theory. The interest of this paper lies in presenting a method to define the whole workspace of the linkage as the input task for the exact dimensional synthesis problem. This method is applied to the spatial RPRP closed linkage, for which one solution exists.

Nomenclature

S Line or dual vector, defined using Plücker coordinates.
$\mathbf{s}$ Vector
$\hat{S}$ Quaternion or dual quaternion
$\hat{w}$ Dual number
$[M]$ Matrix

1 Introduction

Synthesis of parallel robots has focused mainly on type or structural synthesis, using group theory, screw theory, or geometric methods, see for instance [1], [2], [3]. Dimensional synthesis examples exist, mainly for optimizing performance indices [4], [5], [6] or for reachable workspace sizing [7], [8], [9]; see also [10] for a comprehensive approach.

The dimensional synthesis of spatial serial chains for a prescribed set of positions can be used for the design of parallel robots by synthesizing all supporting legs for the same set of positions. There are a few examples of finite-position dimensional synthesis of parallel robots in the literature, most of them doing partial synthesis. Wolbrecht et al. [11] perform synthesis of 3-RRS, 4-RRS and 5-RRS symmetric parallel manipulators; Kim and Tsai [12] and Rao [13] solve the partial kinematic synthesis of a 3-RPS parallel manipulator. This method has been successfully applied mainly to special parallel systems with imposed symmetry. In general, the method does not allow the control of the final trajectory of the parallel system; in the most extreme cases, it may yield a system with negative mobility, that can be assembled at each task positions but cannot be driven from task position to task position.

The kinematic mapping is used for the synthesis of planar and spherical linkages in order to state design equations and to provide a tool for visualizing the workspace and trajectories of the linkage. See Ravani and Roth [14] and more recent applications by Hayes [15], Schröcker [16] and Wu and Ge [17]. For spatial motion, Study's kinematic mapping is used to obtain simplified equations for analysis and synthesis, see Husty et al. [18] and [19]. However, the kinematic image for the spatial motion is a six-dimensional quadric and that makes the visualization of workspaces and trajectories difficult for the designer.

In this paper, the workspace of the linkage is visualized as a set of finite screws corresponding to the set of finite displacements of the end-effector. One interesting question is whether the finite-screw surfaces generated by a set of task positions can give any information for the synthesis of parallel robots and, in particular, of some overconstrained closed linkages. Using Parkin's definition for pitch [20], the screws corresponding to finite displacements of some linkages can form screw systems. Huang [21] showed that the single RR chain forms a finite screw system of third order; however, the set of finite displacements of the coupler of the Bennett linkage form a cylindroid, which is a general 2-system of screws [22]. Baker [23] has also studied the motion of the Bennett linkage. Perez and McCarthy [24] used two arbitrary displacements to generate the cylindroid of finite screws associated to the Bennett linkage in order to perform dimen-

sional synthesis.

In this paper, the focus is on the simplest of the over-constrained linkages, the closed spatial RPRP linkage. This linkage is one of the Delassus linkages, later studied by Waldron [25] and Baker [26]. Recently, Huang [27] has shown that the set of screws corresponding to displacements of this linkage forms a 2-screw system. We use this result in order to synthesize RPRP linkages with positive mobility and for a given shape of the screw system of relative displacements. In order to do so, we state the design equations using the Clifford algebra of dual quaternions [28]. The dual quaternion expression can be easily related to the screw system and it is also used to assign the magnitude to the screws in order to obtain the correspondence between the screw system and the trajectory of the end-effector. The design yields a single RPRP linkage.

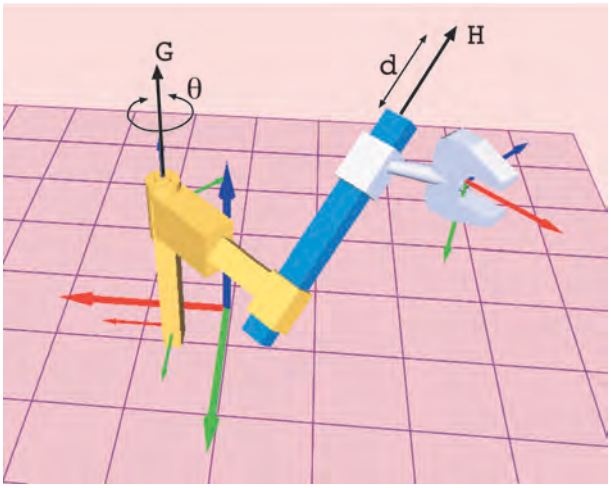

Fig. 1. The RP serial chain

2 Clifford Algebra Equations for the Synthesis

The approach used in this paper for stating design equations is based on the method of Lee and Mavroidis [29]. They equate the forward kinematics of a serial chain to a set of goal displacements and consider the Denavit-Hartenberg parameters as variables. A more efficient formulation for our purposes consists of stating the forward kinematics of relative displacements using the even Clifford subalgebra of the projective space $C^+(P^3)$, also known as dual quaternions [28].

The Plücker coordinates $\mathsf{S} = (\mathbf{s}, \mathbf{c} \times \mathbf{s})$ of a line can be identified with the Clifford algebra element $\mathsf{S} = \mathbf{s} + \varepsilon \mathbf{c} \times \mathbf{s}$, with $\varepsilon^2 = 0$. Similarly, a screw J becomes the element $\mathsf{J} = (1 + \mu\varepsilon)\mathsf{S}$, where μ is the pitch. Using the Clifford product we can compute the exponential of the screw $\frac{\theta}{2}\mathsf{J}$,

$$e^{\frac{\theta}{2}\mathsf{J}} = (\cos\frac{\theta}{2} - \frac{d}{2}\sin\frac{\theta}{2}\varepsilon) + (\sin\frac{\theta}{2} + \frac{d}{2}\cos\frac{\theta}{2}\varepsilon)\mathsf{S} = \cos\frac{\hat{\theta}}{2} + \sin\frac{\hat{\theta}}{2}\mathsf{S}. \tag{1}$$

The exponential of a screw defines a unit dual quaternion, which can be identified with a relative displacement from an initial position to a final position in terms of a rotation around and a slide along an axis.

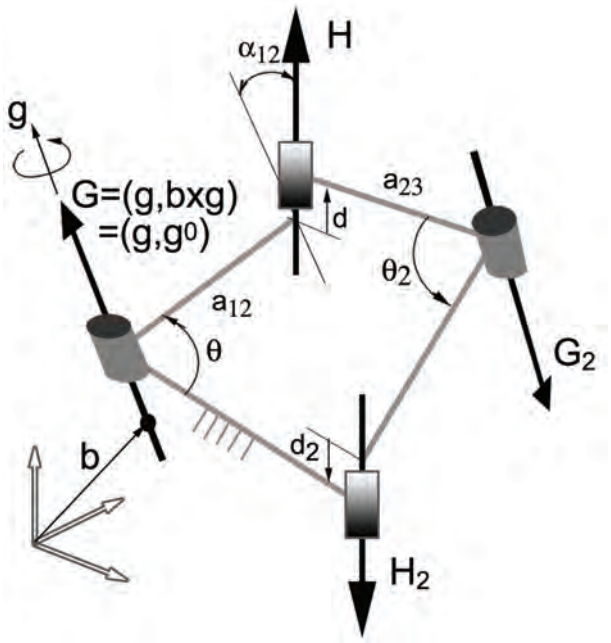

Fig. 2. The RPRP closed linkage

2.1 Forward Kinematics

For a serial chain with n joints, in which each joint can rotate an angle θ_i and slide a distance d_i, around and along the axis S_i, $i = 1, \ldots, n$, the forward kinematics of relative displacements (with respect to a reference position) can be expressed as the composition of Clifford algebra elements corresponding to the motion of each joint. Let $\vec{\theta}_0$ and $\vec{d}_0$ be the joint parameters of this chain when in the reference configuration, so we have $\vec{\Delta\hat{\theta}} = (\vec{\theta} - \vec{\theta}_0 + (\vec{d} - \vec{d}_0)\varepsilon)$. Then, the movement from this reference configuration is defined by

$$\hat{Q}(\vec{\Delta\hat{\theta}}) = e^{\frac{\Delta\hat{\theta}_1}{2}\mathsf{S}_1} e^{\frac{\Delta\hat{\theta}_2}{2}\mathsf{S}_2} \cdots e^{\frac{\Delta\hat{\theta}_n}{2}\mathsf{S}_n} = (\cos\frac{\Delta\hat{\theta}_1}{2} + \sin\frac{\Delta\hat{\theta}_1}{2}\mathsf{S}_1)$$
$$(\cos\frac{\Delta\hat{\theta}_2}{2} + \sin\frac{\Delta\hat{\theta}_2}{2}\mathsf{S}_2) \cdots (\cos\frac{\Delta\hat{\theta}_n}{2} + \sin\frac{\Delta\hat{\theta}_n}{2}\mathsf{S}_n) \tag{2}$$

The RPRP linkage has a mobility $M = -2$ using the Kutzbach-Gruebler formula; however, for certain dimensions of the links, it moves with one degree of freedom. Waldron [25] shows that the RPRP linkage will have positive mobility only if both revolute joints are parallel, and the directions of the prismatic joints are symmetric with respect to the plane containing the revolute joints.

The RPRP linkage can be seen as a serial RP chain and a serial PR chain joined at their end-effectors. The RP serial chain consists of a revolute joint followed by a prismatic joint. Figure 1 shows the RP serial chain and Figure 2 shows a sketch of the RPRP linkage with its axes. In the PR serial chain, the order of the joints in the chain is switched.

For both the RP and PR serial chains, let $\mathsf{G} = \mathbf{g} + \varepsilon\mathbf{g}^0$ be the revolute joint axis, with rotation θ, and $\mathsf{H} = \mathbf{h} + \varepsilon\mathbf{h}^0$ the prismatic joint axis, with slide d. Notice that, for synthesis

purposes, the location of the slider, given by $\mathbf{h}^0$, is irrelevant. The Clifford algebra forward kinematics equations for the RP chain are

$$\begin{aligned}\hat{Q}_{RP}(\Delta\theta,\Delta d) &= (\cos\frac{\Delta\theta}{2}+\sin\frac{\Delta\theta}{2}\mathsf{G})(1+\varepsilon\frac{\Delta d}{2}\mathsf{H})\\ &= (\cos\frac{\Delta\theta}{2}+\sin\frac{\Delta\theta}{2}\mathbf{g})+\varepsilon(\frac{\Delta d}{2}\cos\frac{\Delta\theta}{2}\mathbf{h}+\\ &\sin\frac{\Delta\theta}{2}\mathbf{g}^0+\frac{\Delta d}{2}\sin\frac{\Delta\theta}{2}(\mathbf{g}\times\mathbf{h}-\mathbf{g}\cdot\mathbf{h})).\end{aligned} \quad (3)$$

For the PR chain, the only difference is a negative sign in the cross product. In Eq. (3), the angle and slide are measured from a reference configuration.

2.2 Design Equations and Counting

Given a set of m task positions expressed as relative displacements, $\hat{P}_{1j}=\cos\frac{\Delta\hat{\phi}_{1j}}{2}+\sin\frac{\Delta\hat{\phi}_{1j}}{2}\mathsf{P}_{1j}$, $j=2,\ldots,m$, we equate them to the forward kinematics equations in Eq. (2),

$$\hat{P}_{1j}=e^{\frac{\Delta\hat{\theta}_{1j}}{2}\mathsf{S}_1}e^{\frac{\Delta\hat{\theta}_{2j}}{2}\mathsf{S}_2}\cdots e^{\frac{\Delta\hat{\theta}_{nj}}{2}\mathsf{S}_n},\quad j=2,\ldots,m \quad (4)$$

in order to create the design equations.

The result is $8(m-1)$ design equations. The design variables that determine the dimensions of the chain are the n joint axes S_i, $i=1,\ldots,n$, in the reference configuration. In addition, the equations cointain the $n(m-1)$ pairs of joint parameters $\Delta\hat{\theta}_{ij}=\Delta\theta_{ij}+\Delta d_{ij}\varepsilon$, which are also unknown.

For the RP (and similarly for the PR) serial chain, the design equations are

$$\hat{Q}_{RP}(\Delta\theta^j,\Delta d^j)=\hat{P}_{1j},\quad j=2,\ldots,m. \quad (5)$$

The counting of independent equations and unknowns defines the maximum number of arbitrary positions m that can be reached, based only on the type and number of joints of the serial chain, see [30] for details. Consider a serial chain with r revolute and p prismatic joints. The maximum number of task positions is given by

$$m=\frac{3r+p+6}{6-(r+p)}. \quad (6)$$

For serial chains with less than three revolute joints, the structure of semi-direct product of the composition of displacements needs to be considered, and the maximum number of rotations m_R needs to be calculated too. Assuming that the orientations are given and that both the directions of the revolute joints and the angles to reach the task orientations are known, we can count, in a similar fashion, the number of translations m_T that the chain can be defined for.

$$m_R=\frac{3+r}{3-r},\qquad m_T=\frac{2r+p+3}{3-p}. \quad (7)$$

In order to determine the maximum number of task positions for the RP and PR chains, we apply Eq. (6) to obtain $m=2.5$ task positions. Additional information is obtained using Eq. (7) to compute $m_R=2$ task rotations, and $m_T=3$ task translations. Hence, we can define one arbitrary relative displacement and a second relative displacement whose orientation is not general.

3 Screw System for the RPRP Linkage

In the context of this paper, a finite-screw surface is a ruled surface in which the lines with their associated pitch correspond to relative displacements. A screw surface will be a screw system if it is closed under addition and scalar multiplication, that is, if every screw of the set can be written as a linear combination of screws belonging to it.

3.1 The finite Screw System Generated by the Motion of the RPRP Linkage

The linear combination of two arbitrary screws representing relative displacements form a 2-system known as the cylindroid, which turns out to be the manifold for the relative displacements of the closed 4R linkage. Huang [27], by intersecting the 3-systems associated with the finite displacements of the RP and PR dyads, shows that the screw surface of the closed RPRP linkage forms a 2-system of a special type, the fourth special type according to Hunt [31], also known as 2-IB [32]. The screws of this system are parallel, coplanar screws whose pitches vary linearly with their distance.

The screw system corresponding to the RPRP linkage can be obtained in a quite straightforward way by using the composition of relative displacements at each joint, as expressed in Eq.(3). Let us denote the resulting displacements

$$\begin{aligned}\hat{Q}_{RP}(\Delta\theta,\Delta d) &= \cos\frac{\Delta\hat{\psi}}{2}+\sin\frac{\Delta\hat{\psi}}{2}\mathsf{S}_{RP}=\\ &(\cos\frac{\Delta\psi}{2}-\varepsilon\frac{\Delta t}{2}\sin\frac{\Delta\psi}{2})+\sin\frac{\Delta\psi}{2}(1+\varepsilon\frac{\frac{\Delta t}{2}}{\tan\frac{\Delta\psi}{2}})\mathsf{S}_{RP},\end{aligned} \quad (8)$$

where $\Delta\psi$ and Δt are the angle about and slide along the screw axis S_{RP} of the resulting relative displacement. Expand the product in Eq.(3) and separate the dual scalar and the dual vector part, so that

$$\begin{aligned}&\cos\frac{\Delta\psi}{2}-\varepsilon\frac{\Delta t}{2}\sin\frac{\Delta\psi}{2}=\cos\frac{\Delta\theta}{2}-\varepsilon\frac{\Delta d}{2}\sin\frac{\Delta\theta}{2}\mathsf{G}\cdot\mathsf{H}\\ &\sin\frac{\Delta\psi}{2}(1+\varepsilon\frac{\frac{\Delta t}{2}}{\tan\frac{\Delta\psi}{2}})\mathsf{S}_{RP}=\\ &\sin\frac{\Delta\theta}{2}\mathsf{G}+\varepsilon\frac{\Delta d}{2}\cos\frac{\Delta\theta}{2}\mathsf{H}+\varepsilon\frac{\Delta d}{2}\sin\frac{\Delta\theta}{2}\mathsf{G}\times\mathsf{H}.\end{aligned} \quad (9)$$

For studying the screw system, we are only interested in the dual-vector part of Eq.(9), which defines the lines with their associated pitch.

The resulting screw is parameterized by joint variables $\Delta\theta$ of the revolute joint and Δd corresponding to the prismatic joint. We denote the expression in Eq.(9) as the *finite kinematic generator* of the screw system. In the case of finite displacements, the screw systems correspond to subspaces of a projective space, and so we take the unit screws as representatives by dividing the dual vector of Eq.(9) by $\sin\frac{\Delta\psi}{2}$. From the real part of the first equation in (9) we can see that $\sin\frac{\Delta\psi}{2} = \pm\sin\frac{\Delta\theta}{2}$, so that

$$\pm(1+\varepsilon\frac{\frac{\Delta t}{2}}{\tan\frac{\Delta\psi}{2}})\mathsf{S}_{RP} = \mathsf{G}+\varepsilon\frac{\frac{\Delta d}{2}}{\tan\frac{\Delta\theta}{2}}\mathsf{H}+\varepsilon\frac{\Delta d}{2}\mathsf{G}\times\mathsf{H}. \quad (10)$$

If we give values to the joint variables $\Delta\theta$ and Δd, we will generate a screw surface of dimension 3 of a special type, in which all the screws have parallel directions.

It is easy to show that the set of screws generated by the motion of the RP serial chain is indeed a screw system, that is, closed under addition and multiplication by scalar. Generate two unit screws S_1 and S_2 using Eq.(10) and perform the linear combination with real constants k_1 and k_2. We normalize the resulting screw by dividing by k_1+k_2 to obtain

$$\begin{aligned}(1+\varepsilon\frac{\frac{\Delta t_3}{2}}{\tan\frac{\Delta\psi_3}{2}})\mathsf{S}_3 =& \frac{1}{k_1+k_2}(k_1S_1+k_2S_2)\\ =&\mathbf{g}+\varepsilon(\mathbf{g}^0+\varepsilon\frac{\frac{\Delta d_c}{2}}{\tan\frac{\Delta\theta_c}{2}}\mathbf{h}+\varepsilon\frac{\Delta d_c}{2}\mathbf{g}\times\mathbf{h}),\end{aligned} \quad (11)$$

where

$$\begin{aligned}\Delta d_c &= \frac{k_1}{k_1+k_2}\Delta d_1+\frac{k_2}{k_1+k_2}\Delta d_2,\\ \tan\frac{\Delta\theta_c}{2} &= \frac{k_1\frac{\Delta d_1}{2}+k_2\frac{\Delta d_2}{2}}{k_1\frac{\frac{\Delta d_1}{2}}{\tan\frac{\Delta\theta_1}{2}}+k_2\frac{\frac{\Delta d_2}{2}}{\tan\frac{\Delta\theta_2}{2}}},\end{aligned} \quad (12)$$

hence the linear combination belongs to the screw system generated by the relative motion of the RP chain. Next is to calculate the dimension of this screw system. Notice that the direction of all unit screws generated is equal to $\mathbf{g}$, then we just need to look at the dimension of the dual part. Generate three screws with values $\Delta\theta_i$ and Δd_i, $i=1,2,3$. For the three vectors corresponding to the dual part to be linearly independent, the determinant of the column vector matrix must be different from zero. We obtain the value for the determinant

$$\begin{aligned}\det([\mathbf{s}_i^0]) =&\mathbf{g}\cdot\mathbf{h}\quad \mathbf{g}^0\cdot\mathbf{h}(\frac{\frac{\Delta d_1}{2}}{\tan\frac{\Delta\theta_1}{2}}(\frac{\Delta d_3}{2}-\frac{\Delta d_2}{2})+\\ &\frac{\frac{\Delta d_2}{2}}{\tan\frac{\Delta\theta_2}{2}}(\frac{\Delta d_1}{2}-\frac{\Delta d_3}{2})+\frac{\frac{\Delta d_3}{2}}{\tan\frac{\Delta\theta_3}{2}}(\frac{\Delta d_2}{2}-\frac{\Delta d_1}{2})),\end{aligned} \quad (13)$$

which is different from zero when the angle θ and the slide d are independent, except for special parallel or perpendicular arrangements of the joints. Hence, a maximal set of independent screws has cardinality 3.

In order to generate the screw system of the RPRP linkage, we impose the motion constraint relations between the joint variables. The conditions are derived in [27] from the closure equations of the linkage, to obtain

$$\begin{aligned}&d = d_2,\\ &\theta = \pm(\theta_2-\pi),\\ &\frac{\tan\frac{\theta}{2}}{d} = \frac{\sin\alpha_{12}}{a_{12}\pm a_{23}} = k,\end{aligned} \quad (14)$$

where the twist angle α_{12} and link lengths a_{12}, a_{23} are shown in Figure 2; the angles θ, θ_2 and slides d, d_2, also shown in Figure 2, have to be measured according to the convention [27] from the previous common normal line. The plus/minus sign corresponds to folded and unfolded linkages. For our purposes, only the third condition is needed. It is important to notice that this condition applies to absolute values of the joint variables, measured from the previous common normal line as stated before.

In order to use this relation, substitute $\Delta d = d-d_0$, $\Delta\theta = \theta-\theta_0$ to apply Eq.(14) so that the resulting expression depends only on d, for instance. For all possible values of the slide d, this generates a 2-IB system of screws [31, 32]. This can be checked numerically by generating 6 random screws and computing the rank of the matrix that has the screws as columns. In this case, the rank is 2. It can also be shown that when the third condition in Eq.(14) holds, the determinant in Eq.(13) is equal to zero.

The unit screws of the system can be related to spatial displacements if we add the value of the magnitude of the screw. For finite displacement screws, the value of the magnitude related to each screw is unique; this is due to the fact that finite screw systems are projective subspaces [33]. The information about the magnitude corresponding to each screw can be extracted from the scalar part of the dual quaternion product in Eq.(9). This equation relates the rotation associated to the resulting screw, $\Delta\psi$, to the joint variables of the kinematic chain. For the RPRP chain, this yields $\sin\frac{\Delta\psi}{2} = \pm\sin\frac{\Delta\theta}{2}$ as noted before.

Figure 3 illustrates the nonlinear relation between the screws generated by an RPRP closed chain and the corresponding set of absolute positions of the end effector (for those positions we assume that the reference configuration is the identity). We use as values for the linkage those of an example from [27].

3.2 The Finite Screw System Generated as a Linear Combination of Two Screws

It has been shown that the relative displacements of the RPRP chain generate a 2-IB finite screw system. By definition, this same screw system can be generated as the linear combination of two screws with same direction and arbitrary

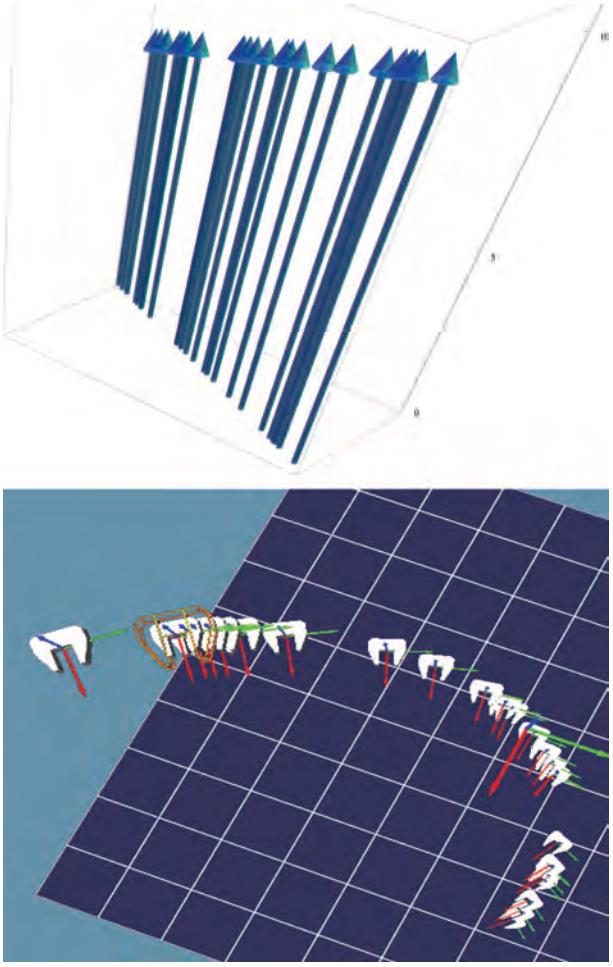

Fig. 3. Screw system generated by the RPRP linkage, above; corresponding absolute displacements, below

location and (possibly) finite pitches. From a synthesis point of view, the key is that this coincides with the results of the counting in section 2.2. The task positions defined for the synthesis of the RP (or PR) chain are two relative displacements with same direction and, in general, finite pitches.

The screw system is characterized by the pitch distribution as a linear function of the distance between screws along a common normal. In this derivation we can parameterize the results as a function of the angle θ or the slide d.

Consider the screw $S_{RP} = (1+\varepsilon p)\mathsf{S}_{RP} = \mathbf{s}_{RP} + \varepsilon \mathbf{s}^0_{RP}$.The pitch is obtained by computing $p = \frac{\mathbf{s}_{RP}\cdot\mathbf{s}^0_{RP}}{\mathbf{s}_{RP}\cdot\mathbf{s}_{RP}}$ in Eq.(10),

$$p = \frac{1+k^2 d d_0}{2k}\mathbf{g}\cdot\mathbf{h} = \frac{1}{2k}(1+\tan\frac{\theta_0}{2}\tan\frac{\theta}{2})\mathbf{g}\cdot\mathbf{h}. \tag{15}$$

For two screws S_A and S_B, the difference in the pitches is given by

$$p_B - p_A = \frac{k d_0 \mathbf{g}\cdot\mathbf{h}}{2}(d_B - d_A) = \frac{\tan\frac{\theta_0}{2}\mathbf{g}\cdot\mathbf{h}}{2k}(\tan\frac{\theta_B}{2} - \tan\frac{\theta_A}{2}) \tag{16}$$

The distance between two screws along the common normal is calculated by finding the perpendicular point on the axis, $\mathbf{c}_{RP} = \frac{\mathbf{s}_{RP}\times\mathbf{s}^0_{RP}}{\mathbf{s}_{RP}\cdot\mathbf{s}_{RP}}$ and computing the norm of the difference for two of them,

$$\begin{aligned}\mathbf{c}_B - \mathbf{c}_A &= (\frac{k d_0}{2}\mathbf{g}\times\mathbf{h} + \frac{1}{2}(\mathbf{g}\mathbf{g}\cdot\mathbf{h} - \mathbf{h}))(d_B - d_A) \\ &= \frac{1}{2k}(\tan\frac{\theta_0}{2}\mathbf{g}\times\mathbf{h} + \mathbf{g}\mathbf{g}\cdot\mathbf{h} - \mathbf{h})(\tan\frac{\theta_B}{2} - \tan\frac{\theta_A}{2}),\end{aligned} \tag{17}$$

and

$$\begin{aligned}\|\mathbf{c}_B - \mathbf{c}_A\| &= \frac{1}{2}\mid d_B - d_A \mid \sqrt{\sin^2\alpha_{12}(1+d_0^2k^2)} \\ &= \frac{1}{2}\mid (\tan\frac{\theta_B}{2} - \tan\frac{\theta_A}{2}) \mid \sqrt{\frac{\sin^2\alpha_{12}}{k^2\cos^2\frac{\theta_0}{2}}}\end{aligned} \tag{18}$$

The slope of the (linear) pitch distribution is computed as

$$K = \frac{p_B - p_A}{\|\mathbf{c}_B - \mathbf{c}_A\|}, \tag{19}$$

and for the RPRP chain we can simplify the expression to

$$K = \pm\frac{\cos\alpha_{12}}{\sqrt{d_0^2\sin^2\alpha_{12} + (a_{12}+a_{23})^2}} d_0 = \pm\frac{\cos\alpha_{12}}{\sin\alpha_{12}}\sin\frac{\theta_0}{2}. \tag{20}$$

Notice that the slope is constant and depends on the initial configuration. The sign is negative if $d_B < d_A$ or if $\tan\frac{\theta_B}{2} < \tan\frac{\theta_A}{2}$.

The screw system is related to the displacement of the RPRP linkage by computing the distribution of the magnitude with respect to the known pitch, distance and magnitude of the screws S_A and S_B used to define the distribution. Consider the magnitude of the screws as $m = \sin\frac{\Delta\psi}{2} = \pm\sin\frac{\Delta\theta}{2}$. Knowing the magnitude and pitch of screws S_A and S_B, we can solve for the magnitude m_C of a screw S_C using Eq.(18)

$$m_C = \pm\sin\frac{\Delta\theta_C}{2} = \frac{X}{\sqrt{1+X^2}}, \tag{21}$$

where the factor X is simplified using Eq.(15) to (20) to

$$X = \frac{\|\mathbf{c}_B - \mathbf{c}_A\| p_A \tan\frac{\Delta\theta_A}{2} - \|\mathbf{c}_C - \mathbf{c}_A\|(p_A\tan\frac{\Delta\theta_A}{2} \pm p_B\tan\frac{\Delta\theta_B}{2})}{\|\mathbf{c}_B - \mathbf{c}_A\| p_C} \tag{22}$$

The positive and negative signs in the expression of X correspond to the sign of the $\tan\frac{\theta_B}{2} - \tan\frac{\theta_A}{2}$ factor.

3.3 Defining the Kinematic Task as a Finite Screw System

It is now possible to define the screw system as the input task for the dimensional synthesis of the RPRP closed chain.

As a linear subspace, it is easy to shape the task at our convenience. Once we have a satisfactory screw system, any two screws from it can be selected to perform the dimensional synthesis and to obtain a finite number of solutions (in this case, just one).

We have several strategies for shaping the screw system. For instance, we can define a first relative displacement, $\hat{S}_{12} = \cos\frac{\hat{\Delta\psi}}{2} + \sin\frac{\hat{\Delta\psi}}{2}(\mathbf{s}_{12} + \varepsilon\mathbf{s}^0_{12})$. The rotation axis of the displacement, $\mathbf{s}_{12}$ is common to both $\hat{S}_{12}$ and the second relative displacement. We set $\mathbf{s}_{12} = \mathbf{s}_{13}$ and select a rotation angle to define the relative rotation $\hat{s}_{13}$.

We can then set the slope of the pitch distribution in order to shape the screw system. The pitch for the finite displacement screws is [20]

$$p_{1i} = \frac{\frac{\Delta t_{1i}}{2}}{\tan\frac{\Delta\psi_{1i}}{2}}, \tag{23}$$

directly calculated from the dual quaternion using $p_{1i} = \frac{\mathbf{s}_{1i}\cdot\mathbf{s}^0_{1i}}{\mathbf{s}_{1i}\cdot\mathbf{s}_{1i}}$. Similarly, a point on the screw axis is calculated as

$$\mathbf{c}_{1i} = \frac{\mathbf{s}_{1i}\times\mathbf{s}^0_{1i}}{\mathbf{s}_{1i}\cdot\mathbf{s}_{1i}}. \tag{24}$$

Define the slope of the distribution as $K = \frac{p_{13}-p_{12}}{\|\mathbf{c}_{13}-\mathbf{c}_{12}\|}$, according to Eq.(20). If we set the value of K, we can solve for Δt_{13} in order to define the pitch of the second relative displacement, the location of its screw axis being defined. This is one possible way of defining the screw system. Converting from this to absolute displacements we can easily check whether the trajectory for the synthesis is acceptable.

Any other strategy to basically define a triangle in space can be used. The purpose of this is to have a better control on the shape of the trajectory of the linkage than the one given by just two separate finite positions.

4 Dimensional Synthesis of the RPRP Linkage for a Prescribed Screw System

The synthesis of the RP, and similarly, PR chains, is simple and yields one solution. In general, the task positions are expressed as relative displacements $\hat{Q}_{1i} = \hat{Q}_i\hat{Q}_1^{-1}$ with respect to the first task position $\hat{Q}_1$.For the RP or PR chains, the maximum number of task positions that we can define is $i = 3$, as explained in section 2.2. Given an arbitrary relative displacement $\hat{Q}_{12} = (q^w_{12} + \mathbf{q}_{12}) + \varepsilon(q^{w0}_{12} + \mathbf{q}^0_{12})$ and a second displacement $\hat{Q}_{13} = (q^w_{13} + \mathbf{q}_{13}) + \varepsilon(q^{w0}_{13} + \mathbf{q}^0_{13})$ such that both have same direction and a given pitch distribution, we equate them to the forward kinematics in Eq.(3). We can solve for the direction of the revolute joint $\mathbf{g}$ and the rotation angles,

$$\mathbf{g} = \frac{\mathbf{q}_{12}}{\|\mathbf{q}_{12}\|}, \qquad \tan\frac{\Delta\theta_{1i}}{2} = \frac{\|\mathbf{q}_{1i}\|}{q^w_{1i}}, \quad i = 2,3. \tag{25}$$

The equations corresponding to the dual part are linear in the moment of the revolute joint, $\mathbf{g}^0$,

$$\mathbf{g}^0 = \frac{1}{\sin\frac{\Delta\theta_{1i}}{2}}\left(\mathbf{q}^0_{1i} - \frac{\Delta d_{1i}}{2}(\cos\frac{\Delta\theta_{1i}}{2}\mathbf{h} + \sin\frac{\Delta\theta_{1i}}{2}\mathbf{g}\times\mathbf{h})\right), \quad i = 1,2. \tag{26}$$

Equating the solution of $\mathbf{g}^0$ for both relative displacements, we can solve linearly for $\mathbf{h}$ as a function of the slides Δd_{12}, Δd_{13}. The relation between the slides is given by the pitch condition,

$$\frac{q^{w0}_{12}}{\frac{\Delta d_{12}}{2}\sin\frac{\Delta\theta_{12}}{2}} = \frac{q^{w0}_{13}}{\frac{\Delta d_{13}}{2}\sin\frac{\Delta\theta_{13}}{2}} \tag{27}$$

Imposing $\|\mathbf{h}\| = 1$, we can solve for the slides to obtain one solution. Using the same process, we can solve for the PR serial chain.

5 Examples

Two examples are presented below. The first one is performed to check the method, while for the second one, a fully general task is used.

5.1 First Example

In this first case, the two relative displacements are generated using the RP chain presented in Huang [27]. In this example, the revolute joint is located at the origin and the prismatic joint is located along the x direction with a twist angle of $\alpha_{12} = \pi/5$ and link length $a_{12} = 5$. We use the loop condition in Eq.(14) and random values for the slide to generate the set of relative displacements of the corresponding RPRP closed chain. From those, we randomly select two displacements, the ones in Table 1.

Table 1. Goal relative displacements for the RP and PR chains, Huang's example

$(0,0,-0.05,0.99) + \varepsilon(0.02,0.37,-0.51,-0.03)$
$(0,0,-0.34,0.94) + \varepsilon(0.80,2.23,-3.08,-1.10)$

The resulting screw system is shown in Figure 4, where the length of each screw is proportional to its pitch. Also the corresponding trajectory of absolute displacements, conisdering the reference position as the identity, is shown in same Figure.

Using the synthesis procedure explained in Section 4, we obtain the RP and PR chains of Table 2. Notice that they coincide with the values given in [27], which means this is a folded RPRP overconstrained movable linkage. Figure 5 shows the linkage reaching some of the positions. Notice that the shape of the coupler link attached to the end effector depends on the position chosen as reference configuration.

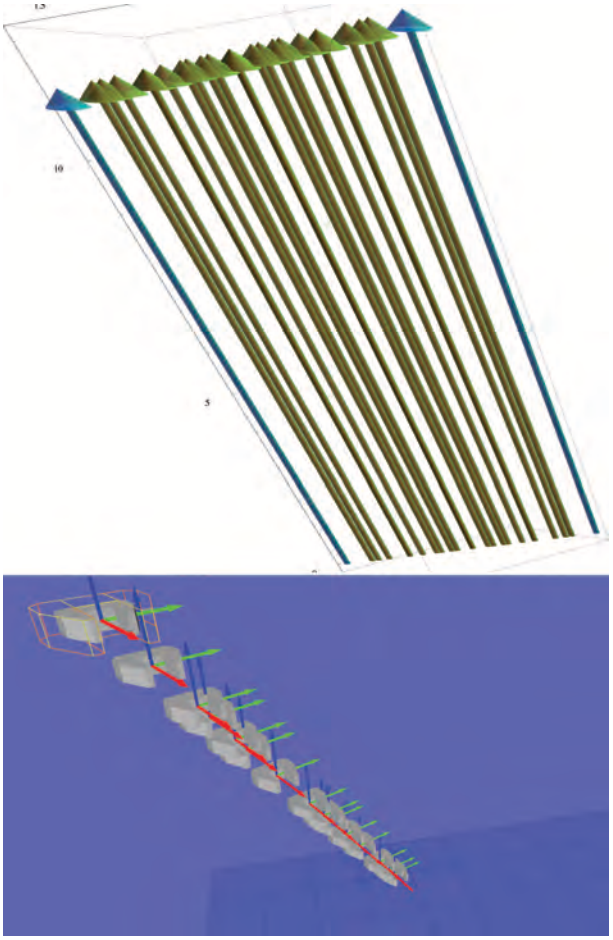

Fig. 4. Above, screw system generated by S_{12} and S_{13} (shown as first and last screws); below, corresponding absolute displacements with reference displacement being the identity

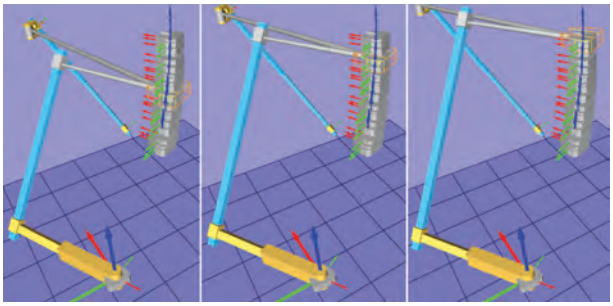

Fig. 5. RPRP linkage reaching three positions of the trajectory

5.2 Second example

For the second example, the dual quaternions in Table 3 have been generated as explained. $\hat{S}_{12}$ has been randomly generated, while the rotation in $\hat{S}_{13}$ is such that it belongs to the workspace of the chain.

We set the location of the second screw axis of the relative displacement with a point $\mathbf{p}_{13} = (0.083, 2.159, -3.226)$, randomly generated. Then we choose a value for the slope of the pitch distribution, $K = 0.480$, which allows us to create the second relative displacement.

The resulting screw system is shown in Figure 6, where

Table 2. Joint axes for the RPRP linkage at the reference configuration, Example 1

Chain	Revolute joint G	Prismatic joint **h**
RP axes	$\begin{Bmatrix} 0+0\varepsilon \\ 0+0\varepsilon \\ 1+0\varepsilon \end{Bmatrix}$	$\begin{Bmatrix} 0 \\ 0.59, \\ -0.81 \end{Bmatrix}$
RP Joint vars.	$\theta_{12} = -5.7$	$d_{12} = 1.27$
	$\theta_{13} = -39.4$	$d_{13} = 8.08$
PR axes	$\begin{Bmatrix} 0+5.38\varepsilon \\ 0+13.0\varepsilon \\ -1+0\varepsilon \end{Bmatrix}$	$\begin{Bmatrix} -0.42 \\ -0.42 \\ -0.81 \end{Bmatrix}$
PR Joint vars.	$\theta_{12} = 5.7$	$d_{12} = 1.27$
	$\theta_{13} = 39.4$	$d_{13} = 8.08$

Table 3. Goal relative displacements for the RP and PR chains

$(0.46, -0.13, -0.56, -0.67) + \varepsilon(1.66, 0.34, -0.02, 1.08)$
$(0.13, -0.04, -0.17, 0.98) + \varepsilon(0.02, -0.57, -0.92, -0.18)$

the length of each screw is proportional to its pitch. The corresponding trajectory of absolute displacements, conisdering the reference position as the identity, is shown in Figure 7.

We obtain one solution for the RPRP linkage, specified in Table 4 as the Plücker coordinates of the axes and the joint variables to reach the positions.

Again, the dimensions form an overconstrained movable RPRP linkage. Figure 8 shows the chain reaching three displacements along the trajectory, considering the reference displacement as the identity.

6 Conclusions

This papers presents the exact workspace synthesis of an overconstrained closed linkage, the RPRP. The knowledge of the screw system that corresponds to the finite displacements of the linkage is used to generate the workspace of the linkage, which in turn ensures that the solutions of the synthesis of the RP and PR serial chains can be assembled to create a movable system. The counting of the maximum number of positions for the finite-position synthesis of the serial chain turns out to fully define the finite screw system of the linkage. This provides an easy method to shape the whole trajectory of the RPRP linkage as an input for the synthesis process. Even though the method targets the whole motion of the linkage, the synthesis equations need to be stated only at

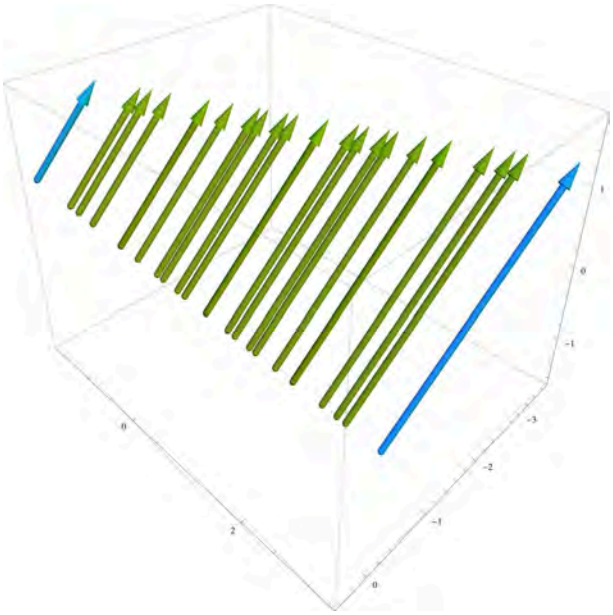

Fig. 6. Screw system generated by S_{12} and S_{13} (first and last screws)

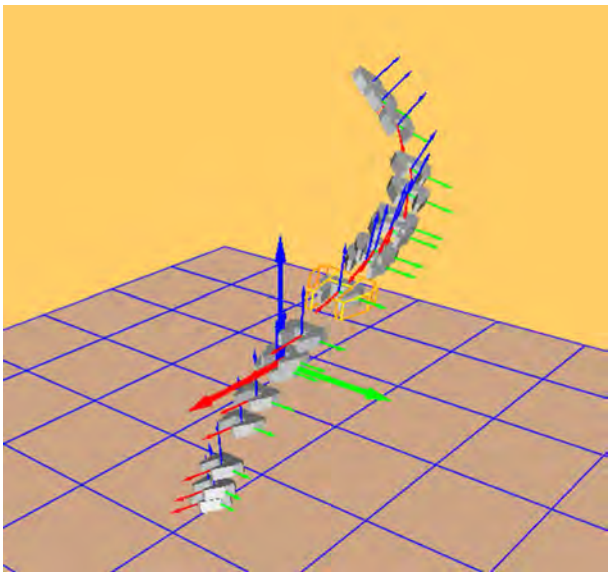

Fig. 7. The RPRP end-effector task trajectory

the task positions used to generate the linear combination of screws, hence the finite-position synthesis equations can still be used. The method yields a single RPRP linkage.

Achnowledgements

This work is supported by a Ramon y Cajal Research Fellowship from the Spanish Ministry of Science and Innovation.

Table 4. Joint axes for the RPRP linkage at the reference configuration, Example 2

Chain	Revolute joint G	Prismatic joint **h**
RP axes	$\begin{Bmatrix} -0.62-0.44\varepsilon \\ 0.18-3.17\varepsilon \\ 0.76+0.39\varepsilon \end{Bmatrix}$	$\begin{Bmatrix} -0.09 \\ 0.89 \\ 0.44 \end{Bmatrix}$
RP Joint vars.	$\theta_{12} = -264.5$	$d_{12} = 5.30$
	$\theta_{13} = -25.2$	$d_{13} = -3.05$
PR axes	$\begin{Bmatrix} 0.62+2.32\varepsilon \\ -0.18-1.83\varepsilon \\ -0.76+2.31\varepsilon \end{Bmatrix}$	$\begin{Bmatrix} -0.27 \\ 0.06 \\ -0.96 \end{Bmatrix}$
PR Joint vars.	$\theta_{12} = 264.5$	$d_{12} = -5.30$
	$\theta_{13} = 25.2$	$d_{13} = 3.05$

References

[1] Herve, J. M., 1999. "The lie group of rigid body displacements, a fundamental tool for mechanism design". *Mechanism and Machine Theory,* **34**, pp. 717–730.

[2] Angeles, J., 2002. "The qualitative synthesis of parallel manipulators". In Proceedings of the WORKSHOP on Fundamental Issues and Future Research Directions for Parallel Mechanisms and Manipulators, C. Gosselin and I. Ebert-Uphoff, eds.

[3] Gogu, G., 2007. *Structural Synthesis of Parallel Robots. Part 1: Methodology*, first ed. Springer.

[4] Huang, T., Li, M., Zhao, X. M., Mei, J., Chetwynd, D. G., and Hu, S. J., 2005. "Conceptual design and dimensional synthesis for a 3-dof module of the trivariant - a novel 5-dof reconfigurable hybrid robot". *IEEE Transactions on Robotics,* **21(3)**, pp. 449–456.

[5] Huang, T., Zhanxian, L., Li, M., Chetwynd, D. G., and Gosselin, C. M., 2004. "Conceptual design and dimensional synthesis of a novel 2-dof translational parallel robot for pick-and-place operations". *AMSE Journal of Mechanical Design,* **126**, pp. 449–455.

[6] Kim, H. S., and Tsai, L.-W., 2003. "Design optimization of a cartesian parallel manipulator". *ASME Journal of Mechanical Design,* **125**, pp. 43–51.

[7] Affi, Z., Romdhane, L., and Maalej, A., 2004. "Dimensional synthesis of a 3-translational-dof in-parallel manipulator for a desired workspace". *European Journal of Mechanics, A / Solids,* **23**, pp. 311–324.

[8] Kosinska, A., Galicki, M., and Kedzior, K., 2003. "Design and optimization of parameters of delta-4 parallel manipulator for a given workspace". *Journal of Robotic Systems,* **20(9)**, pp. 539–548.

[9] Chablat, D., and Wenger, P., 2003. "Architecture optimization of a 3-dof parallel mechanism for machining applications, the orthoglide". *IEEE Transactions on Robotics and Automation,* **19(3)**, pp. 403–410.

[10] Merlet, J.-P., 2005. "Optimal design of robots". In

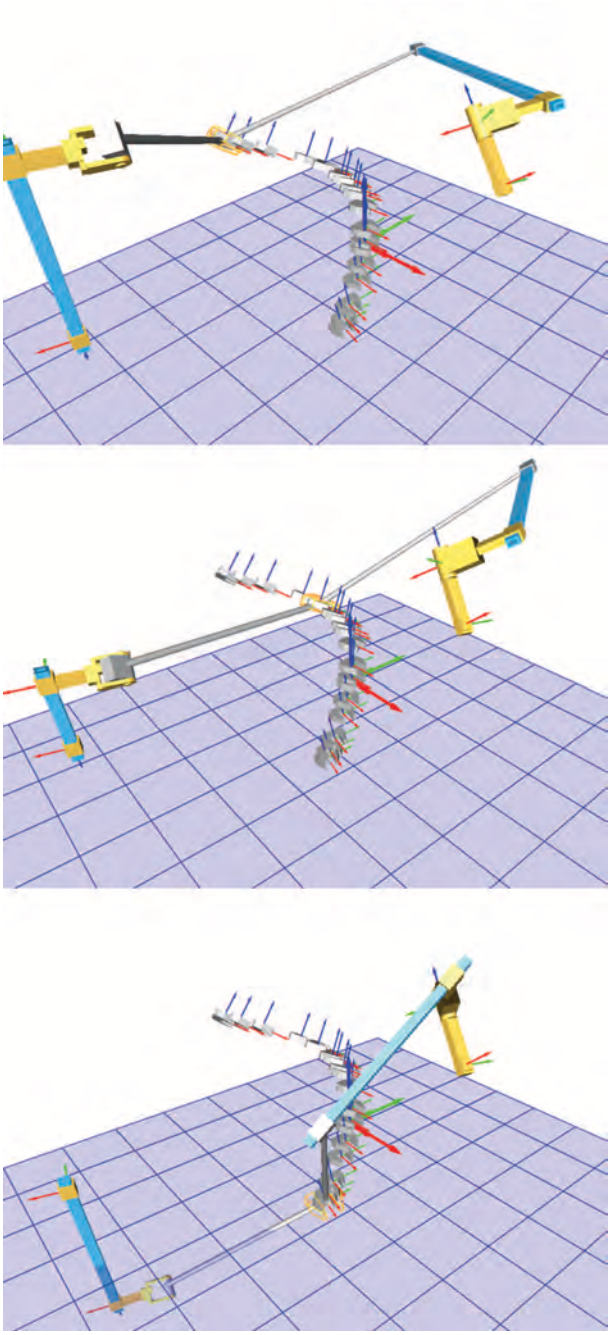

Fig. 8. The RPRP linkage reaching three positions along the trajectory

Proceedings of Robotics: Science and Systems.

[11] Wolbrecht, E., Su, H.-J., Perez, A., and McCarthy, J. M., 2004. "Geometric design of symmetric 3-rrs constrained parallel platforms". In Proceedings of the 2004 ASME International Mechanical Engineering Congress and Exposition, ASME, ed.

[12] Kim, H. S., and Tsai, L.-W., 2003. "Kinematic synthesis of a spatial 3-rps parallel manipulator". *ASME Journal of Mechanical Design,* **125**, pp. 92–97.

[13] Rao, N. M., and Rao, K. M., 2009. "Dimensional synthesis of a 3-rps parallel manipulator for a prescribed range of motion of spherical joints". *Mechanism and Machine Theory,* **44**, pp. 477–486.

[14] Ravani, B., and Roth, B., 1983. "Motion synthesis using kinematic mappings". *ASME Journal of Mechansims, Transmissions and Automation in Design,* **105(3)**, pp. 460–467.

[15] Hayes, M. J. D., Luu, T., and Chang, X. W., 2004. "Kinematic mapping application to approximate type and dimension synthesis of planar mechanisms". In On Advances in Robot Kinematics, J. Lenarcic and C. Galletti, eds., Kluwer Academic Publisher.

[16] Schrocker, H.-P., Husty, M. L., and McCarthy, J. M., 2007. "Kinematic mapping based assembly mode evaluation of planar four-bar mechanisms". *AMSE Journal of Mechanical Design,* **129**, pp. 924–929.

[17] Wu, J., Purwar, A., and Ge, Q. J., 2010. "Interactive dimensional synthesis and motion design of planar 6r single-loop closed chains via constraint manifold modification". *ASME Journal of Mechanisms and Robotics,* **2(3)**.

[18] Husty, M. L., Pfurner, M., Schrocker, H.-P., and Brunnthaler, K., 2007. "Algebraic methods in mechanism analysis and synthesis". *Robotica,* **25**, pp. 661–675.

[19] Brunnthaler, K., 2006. "Synthesis of 4r linkages using kinematic mapping". PhD thesis, Institute for Basic Sciences and Engineering, University of Innsbruck, Innsbruck, Austria.

[20] Parkin, I. A., 1992. "A third conformation with the screw systems: Finite twist displacements of a directed line and point". *Mechanism and Machine Theory,* **27**, pp. 177–188.

[21] Huang, C., 1994. "On the finite screw system of the third order associated with a revolute-revolute chain". *ASME Journal of Mechanical Design,* **116**, pp. 875–883.

[22] Huang, C., 1996. "The cylindroid associated with finite motions of the bennett mechanism". In Proceedings of the ASME Design Engineering Technical Conferences.

[23] Baker, J. E., 1998. "On the motion geometry of the bennett linkage". In Proc. 8th Internat. Conf. on Engineering Computer Graphics and Descriptive Geometry, pp. 433–437.

[24] Perez, A., and McCarthy, J. M., 2003. "Dimensional synthesis of bennett linkages". *ASME Journal of Mechanical Design,* **125(1)**, pp. 98–104.

[25] Waldron, K. J., 1972. "A study of overconstrained linkage geometry by solution of closure equations - part ii- four-bar linkages with lower pair joints other than screw joints". *Mechanism and Machine Theory,* **8**, pp. 233–247.

[26] Baker, J. E., 1975. "The delassus linkages". In Proc. of the 4th World Congress on the Theory of Machines and Mechanisms, p. 4549.

[27] Huang, C., 2006. "Linear property of the screw surface of the spatial rprp linkage". *ASME Journal of Mechanical Design,* **128**, pp. 581–586.

[28] Perez Gracia, A., and McCarthy, J. M., 2006. "The kinematic synthesis of spatial serial chains using clifford algebra exponentials". *Proceedings of the Institu-*

tion of Mechanical Engineers, Part C, Journal of Mechanical Engineering Science, **220(7)**, pp. 953–968.

[29] Lee, E., and Mavroidis, C., 2002. "Solving the geometric design problem of spatial 3r robot manipulators using polynomial homotopy continuation". *ASME Journal of Mechanical Design,* **124(4)**, pp. 652–661.

[30] Perez, A., and McCarthy, J. M., 2004. "Dual quaternion synthesis of constrained robotic systems". *ASME Journal of Mechanical Design,* **126(3)**, pp. 425–435.

[31] Hunt, K. H., 1978. *Kinematic Geometry of Mechanisms*. , Oxford University Press.

[32] Zlatanov, D., Agrawal, S., and Gosselin, C. L., 2005. "Convex cones in screw spaces". *Mechanism and Machine Theory,* **40**, pp. 710–727.

[33] Huang, C., Sugimoto, K., and Parkin, I., 2008. "The correspondence between finite screw systems and projective spaces". *Mechanism and Machine Theory,* **43**, pp. 50–56.

Proceedings of the ASME 2011 International Design Engineering Technical Conferences & Computers and Information in Engineering Conference
IDETC/CIE 2011
August 29-31, 2011, Washington, DC, USA

DETC2011/MECH-47818

DRAFT: DESIGN OF NON-ANTHROPOMORPHIC ROBOTIC HANDS FOR ANTHROPOMORPHIC TASKS

Edgar Simo-Serra
Inst. de Robòtica i Informàtica Ind.
Univ. Politècnica de Catalunya / CSIC
Llorens i Artigas, 4-6
08028 Barcelona, Spain
Email: esimo@iri.upc.edu

Francesc Moreno-Noguer
Inst. de Robòtica i Informàtica Ind.
Univ. Politècnica de Catalunya / CSIC
Llorens i Artigas, 4-6
08028 Barcelona, Spain
Email: fmoreno@iri.upc.edu

Alba Perez-Gracia*
Inst. de Robòtica i Informàtica Ind.
Univ. Politècnica de Catalunya / CSIC
Llorens i Artigas, 4-6
08028 Barcelona, Spain
And: College of Science and Engineering
Idaho State University
Pocatello, Idaho 83209
Email: aperez@iri.upc.edu

ABSTRACT

In this paper, we explore the idea of designing non-anthropomorphic, multi-fingered robotic hands for tasks that replicate the motion of the human hand. Taking as input data rigid-body trajectories for the five fingertips, we develop a method to perform dimensional synthesis for a kinematic chain with a tree structure, with three common joints and five branches.

We state the forward kinematics equations of relative displacements for each serial chain expressed as dual quaternions, and solve for all five chains simultaneously to reach a number of positions along the hand trajectory using a hybrid global numerical solver that integrates a genetic algorithm and a Levenberg-Marquardt minimization.

Although the number of candidate solutions in this problem is very high, the use of the genetic algorithm lets us to perform an exhaustive exploration of the solution space and retain a subset of them. We then can choose some of the solutions based on the specific task to perform. Note that these designs could exactly match the task while having a finger design radically different from that of the human hand.

*Address all correspondence to this author.

NOMENCLATURE

- r Number of revolute joints.
- b Number of kinematic chains.
- n Number of joints.
- m Number of task positions.

INTRODUCTION

There are many applications for which a robotic system is needed to work in human environments and to perform tasks that are designed for the human hand. In most cases, the solution adopted for grasping and manipulation consists of anthropomorphic robotic hands, which imitate to certain extent the topology and joint location of the human hand, see [1] for a review of applications and concept definition.

It is difficult to match the complexity of the human hand, commonly accepted to have 26 degrees of freedom when counting the motion at the wrist and the pronation/supination of the forearm. The anthropomorphic design must include a complex mechanical system, actuation and sensing in a small space [2]. In order to reduce complexity, actual designs limit the active degrees of freedom in many cases, through simplification of the mechanical structure or by designing underactuated hands [3].

The design of simplified grippers limits the tasks that the

robotic end-effector can perform to some grasping and manipulation actions. In order to perform some of the more complex functions of the human hand (not only grasping and manipulation, but also perception through surface exploration), it seems that an end-effector with several fingers may be needed. However, it may not be necessary that the robotic fingers mimic those of the human hand.

Kinematic design of robotic hands has focused on the design of individual motion of fingers or parts of the hand. Dai and Wang [4] use kinematic synthesis to design a spherical mechanism to act as a the palm of a metamorphic hand. Van Varseveld and Bone [5] designed a finger mechanism for a non-anthropomorphic dexterous hand. Walker et al. [6] also design planar linkages for the fingers of a non-anthropomorphic, dexterous hand. Schafer and Dillman [7] present the kinematic design of a humanoid robotic wrist.

In this paper, we explore the idea of designing the full non-anthropomorphic, multi-fingered robotic hand for tasks that replicate the motion of the human hand at the fingertips. Taking as input data rigid-body trajectories for the human fingertips, we develop a method to perform dimensional synthesis for a kinematic chain with a tree structure, with three common joints and five branches. As a whole, the process entails the simultaneous solution of five serial chains, two of them having four independent joints and three of them with five independent joints, plus three common joints for all of them. The total degrees of freedom of the non-anthropomorphic hand design is 26, similar to the human hand.

We state the forward kinematics equation of relative displacements for each serial chain expressed as dual quaternions, and solve for all five chains simultaneously to reach a number of positions along the hand trajectory. The synthesis of spatial serial chains for up to five degrees of freedom was developed in [8]. We use a similar methodology together with a hybrid global numeric solver, composed of a genetic algorithm paired with a Levenberg-Marquardt local solver. For the tree kinematic structure, a high number of positions can be defined to perform exact synthesis, obtaining a good approximation for the desired trajectory.

Finding the complete solution set for the synthesis of complex kinematic chains is an unsolved problem. Only dyads, such as the RR kinematic chain [9], [10], and some triads with particular characteristics [11], have been fully studied. Even the 3R kinematic chain has not been completely solved with a closed algebraic expression [12]. The complexity of a tree-like kinematic chain with a total of 26 revolute joints, and our numerical results, lead to believe that there will be a very large amount of solutions. This is an issue that has been found before even for simpler kinematic chains, see [11]. In order to deal with this, additional constraints may be added to help in the selection of the final design, depending on the task. We present one of the solutions for a hand task that was synthetically generated. The designs could exactly match the task while having a finger design radically different from that of the human hand.

KINEMATIC SYNTHESIS

The goal of the dimensional kinematic synthesis is to find the location and orientation of a set of joint axes able to perform a given motion, where the number and type of joints are predefined. In this paper, we follow the original idea of [13] of using the forward kinematics equations of the kinematic chain, but formulated as relative displacements and expressed as dual quaternions, see [8] for a complete description of this approach.

The input data for the synthesis are the $m-1$ relative transformations $\hat{P}_{1j} = \cos\frac{\Delta\hat{\phi}_{1j}}{2} + \sin\frac{\Delta\hat{\phi}_{1j}}{2}\mathsf{P}_{1j},\ j = 2,\ldots,m$, defining the task; the output are the Plücker coordinates $\mathsf{S}_i = \mathbf{s}_i + \varepsilon\mathbf{s}_i^0 = \mathbf{s}_i + \varepsilon\mathbf{c}_i \times \mathbf{s}_i$, $i = 1,\ldots,n$, of the n joints that define the kinematic chain, and also the joint variables $\Delta\vec{\hat{\theta}}_{ij} = \vec{\theta}_{ij} - \vec{\theta}_{i0} + (\vec{d}_{ij} - \vec{d}_{i0})\varepsilon$, $i = 1,\ldots,n,\ j = 2,\ldots,m$, used to reach the task positions, measured from the reference configuration.

Forward Kinematics

Given a kinematic serial chain with n joints, we can write the kinematics equations using the product of exponentials of the screws corresponding to the joint axes, as described in [14]. In this paper, instead of calculating the exponentials using matrix algebra, we do the exponentials for the Clifford even subalgebra of the projective space, in which the unit elements, also known as dual quaternions, express spatial displacements. The exponential of a screw represented by the Clifford algebra element $\mathsf{J} = (1 + \mu\varepsilon)\mathsf{S}$, where μ is the pitch relating the slide d and the rotation θ along and about the screw, and S is the screw axis, yields a finite displacement,

$$\begin{aligned} e^{\frac{\theta}{2}\mathsf{J}} &= (\cos\frac{\theta}{2} - \frac{d}{2}\sin\frac{\theta}{2}\varepsilon) + (\sin\frac{\theta}{2} + \frac{d}{2}\cos\frac{\theta}{2}\varepsilon)\mathsf{S} \\ &= \cos\frac{\hat{\theta}}{2} + \sin\frac{\hat{\theta}}{2}\mathsf{S}. \end{aligned} \tag{1}$$

For a serial chain with n joints, in which each joint can rotate an angle θ_i and slide a distance d_i, around and along the axis S_i, $i = 1,\ldots,n$, we calculate the forward kinematics of relative displacements (with respect to an arbitrary reference configuration),

$$\hat{Q}(\Delta\vec{\hat{\theta}}) = e^{\frac{\Delta\hat{\theta}_1}{2}\mathsf{S}_1} e^{\frac{\Delta\hat{\theta}_2}{2}\mathsf{S}_2} \cdots e^{\frac{\Delta\hat{\theta}_n}{2}\mathsf{S}_n} \tag{2}$$

$$= (\cos\frac{\Delta\hat{\theta}_1}{2} + \sin\frac{\Delta\hat{\theta}_1}{2}\mathsf{S}_1)\cdots(\cos\frac{\Delta\hat{\theta}_n}{2} + \sin\frac{\Delta\hat{\theta}_n}{2}\mathsf{S}_n), \tag{3}$$

where $\vec{\Delta\hat{\theta}}_i = (\vec{\theta}_i - \vec{\theta}_0 + (\vec{d}_i - \vec{d}_0)\varepsilon)$ contains the joint variables, as relative values with respect to the joint parameters of the chain $\vec{\theta}_0$ and $\vec{d}_0$ when in the reference configuration.

Synthesis Design Equations

The dimensioning of the articulated system has to be done so that the forward kinematics equations in Eqn.(3) can reach all the desired task positions $\hat{P}_{1j}$,

$$\hat{P}_{1j} = e^{\frac{\Delta\hat{\theta}_{1j}}{2}\mathsf{S}_1} e^{\frac{\Delta\hat{\theta}_{2j}}{2}\mathsf{S}_2} \cdots e^{\frac{\Delta\hat{\theta}_{nj}}{2}\mathsf{S}_n}, \quad j = 2, \ldots, m \tag{4}$$

This results in $8(m-1)$ design equations. The design variables that determine the dimensions of the chain are the n joint axes S_i, $i = 1, \ldots, n$, in the reference configuration. In addition, the equations contain the $n(m-1)$ pairs of joint parameters $\Delta\hat{\theta}_{ij} = \Delta\theta_{ij} + \Delta d_{ij}\varepsilon$, which are also unknown.

One important question when stating design equations such as those in Eqn.(4) is how many task positions can be imposed for the kinematic chain to reach exactly. This is easily computed by comparing the number of independent equations and unknowns, see [15] for details. The maximum number of task positions m to reach exactly depends on the topology of the chain,

$$m = \frac{3r + p + 6 - c}{6 - (r + p)}, \tag{5}$$

where r is the number of revolute joints, p is the number of prismatic joints and c is any additional constraint in the general position of the axes or in the joint variables.

Setting the design equations for the maximum number of task positions ensures that the number of solutions is finite. However, the resultant system of equations has a total degree that grows quickly with the number of joints, and so the number of solutions may be very high.

NON-ANTHROPOMORPHIC HAND SYNTHESIS

In this paper, we are interested in the synthesis of robotic grippers for human-hand tasks. We don't impose any limitation on the link dimensions or placement. The resulting design should be able to perform a given human-hand task while having a non-anthropomorphic aspect.

Hand Task Generation

In this paper, we want to design a mechanical system to replicate some of the motions of the human hand. In a first stage, we define this task using a robotics description of the human skeleton, considering dimensions from the literature [16, 17].

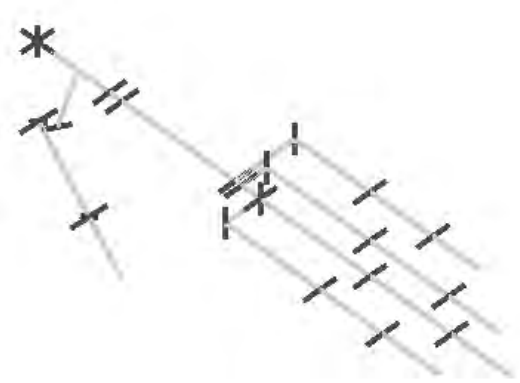

FIGURE 1: HAND SKELETON USED TO GENERATE POSITIONS.

TABLE 1: JOINT ANGLES USED TO GENERATE THE TRAJECTORY.

Chain	Hand task revolute joint limits [θ_{min}-θ_{max}]
Common	[-90°,90°],[-90°,90°],[-90°,90°]
Index	[-10°,90°],[-10°,10°],[0°,100°],[0°,90°]
Middle	[-10°,90°],[-10°,10°],[0°,100°],[0°,90°]
Third	[-10°,10°],[0°,20°],[-10°,10°],[0°,100°],[0°,90°]
Fourth	[-10°,10°],[0°,20°],[-10°,10°],[0°,100°],[0°,90°]
Thumb	[-25°,25°],[-25°,25°],[-10°,10°],[0°,70°], [-10°,85°]

The task is defined as a series of finite positions and orientations for each fingertip, creating by assigning a set of joint variables to the kinematic model. Figure 1 shows the draft of the hand skeleton used to generate the positions. The trajectories are generated from random positions with the joint angle ranges defined in Tab. 1 to simplify convergence.

System Topology

As input topology, we define a tree-like kinematic chain with three common joints in series at the base, connected to five serial chains arranged in parallel, two of them with four degrees of freedom and three of them with five degrees of freedom. This structure follows the generally accepted joint arrangement of the human hand plus the wrist motion. Figure 2 shows the topology

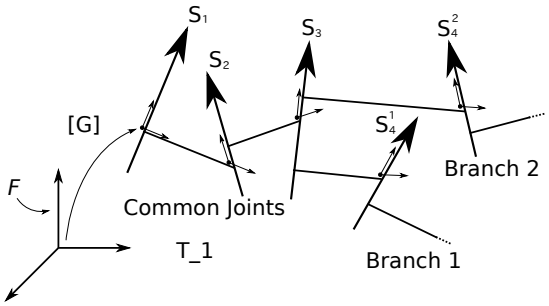

FIGURE 2: TOPOLOGY OF THE KINEMATIC CHAIN.

of the kinematic chain to be synthesized.

Design Equations

We state the design equations adapting Eq.(4) to our particular topology. For each one of the serial chains in the parallel arrangement we state a set of design equations, to obtain the total system of equations

$$\hat{P}^k_{1j} = e^{\frac{\Delta\hat{\theta}_{1j}}{2}\mathbf{S}_1} e^{\frac{\Delta\hat{\theta}_{2j}}{2}\mathbf{S}_2} e^{\frac{\Delta\hat{\theta}_{3j}}{2}\mathbf{S}_3} e^{\frac{\Delta\hat{\theta}^k_{4j}}{2}\mathbf{S}^k_4} \cdots e^{\frac{\Delta\hat{\theta}^k_{7j}}{2}\mathbf{S}^k_7}, k \in \{0,1\},$$
$$\hat{P}^k_{1j} = e^{\frac{\Delta\hat{\theta}_{1j}}{2}\mathbf{S}_1} e^{\frac{\Delta\hat{\theta}_{2j}}{2}\mathbf{S}_2} e^{\frac{\Delta\hat{\theta}_{3j}}{2}\mathbf{S}_3} e^{\frac{\Delta\hat{\theta}^k_{4j}}{2}\mathbf{S}^k_4} \cdots e^{\frac{\Delta\hat{\theta}^k_{8j}}{2}\mathbf{S}^k_8}, k \in \{2,3,4\},$$
$$j = 2,\ldots,m. \quad (6)$$

Here k identifies the kinematic chain and $j = 2,\ldots,m$ is the index of the task position.

Each of the five serial chains, taken individually, has a total of seven or eight degrees of freedom. Even though the exact dimensional synthesis does not apply to serial chains with six or more degrees of freedom, the fact of having three common degrees of freedom in this case allows us to state the design equations of the system as a whole. Using Eq.(5) with $r = 26$ revolute joints, three of them being common to all the branches, we obtain that we can solve exactly for a task defined by $m = 27$ finite positions for each finger. This gives a total of 156 structural parameters and 676 joint variables in our design equations.

Notice that, even though each individual finger have more than six degrees of freedom, the tree-like architecture is not kinematically redundant when defining the motion of several branches at the same time.

KINEMATIC SOLVER

In order to deal with the big system of equations presented in the previous section, the selected solver tries to minimize the error in Eqn.(6) for each kinematic chain. In principle, problems with selection of the metric does not apply to this case, as we are targeting exact synthesis.

Solver Implementation

Genetic algorithms have already been used in many kinematic problems [18, 19], however the complexity of the problem that we are tying to solve is especially challenging. Through the use of Clifford algebra the number of equations and variables can be reduced in comparison with the matrix algebra approach. This allows the entire equation system to be represented with only 832 input variables between both structural and joint variables.

The genetic algorithm performs an exhaustive exploration of the solution space in order find a solution. However, due to complexity of the system a pure genetic algorithm has trouble with convergence past a certain fitness. This problem was overcome but changing the solution space used by genetic algorithm to the local minima of the entire solution space. The local minima are found by a Levenberg-Marquardt minimizer.

The genetic algorithm chromosomes consist of sets of variables that belong to the full solution space. However after generation they are then converged on a local minima. This local convergence is also done when chromosomes are crossed between each other or mutated to ensure each chromosome always represents a local minima of the search space.

The fitness is calculated as the inverse of the sum of the error from Eqn.(6). This makes the fitness a continuous positive function, which allows roulette-wheel selection when choosing pairs from the genetic algorithm population to crossover. It also converts the genetic algorithm to a maximization problem. The crossover rate is kept low to encourage diversity in the population, since the strong convergence is provided by the Levenberg-Marquardt minimizer.

To avoid explicit constraints the chromosomes are generated in the proximity of the ideal kinematic solution. This acts as a soft limit for the possible shapes of the robotic hand. It is not unusual for the Levenberg-Marquardt minimizer to move far from the generation space and find extremely non-anthropomorphic solutions.

The solver is executed until the fitness surpasses the value of 10^{10} at which it is considered to have arrived to a solution. The error is attributed to the imprecision in the computer representation of real numbers.

Dimension of the Equation Set

The equations and variables obtained from Eqn.(6) are not all linearly independent; each dual quaternion has eight components, but in order to be unit quaternions, two constraints are imposed in each of them. Similarly, only four of the six Plücker components of each line are independent. Equation (7) gives the number of variables and independent variables represented as x

and x_0 respectively, while Eqn.(8) gives the number of equations and independent equations represented as f and f_0.

$$\begin{aligned} x &= r(6+(m-1)) \\ x^0 &= r(4+(m-1)) \end{aligned} \tag{7}$$

$$\begin{aligned} f &= 8b(m-1) \\ f^0 &= 6b(m-1) \end{aligned} \tag{8}$$

Notice that the number of positions, m, needed can be also obtained by imposing $f^0 = x^0$ and solving.

Kinematic Configurations

It is interesting to note is that it is possible to solve a reduced version of the kinematic chain tree. As long as the expression at Eq.(9),

$$6b - r > 0 \tag{9}$$

which is obtained from $f^0 = x^0$ and imposing $m > 0$, is met, the kinematic configuration will be solvable. Table 2 shows all the possible variations of the tree-like kinematic chain that can be solved.

The most interesting configurations to solve is the 5 kinematic chains at once to minimize the needed positions and the configuration with only two 4R branches to reduce the amount of variables needed. Afterwards the remaining fingers can be solved individually because the common revolute joints movement is known. There are still other systems that can be solved that are a compromise between number of positions and the number of variables needed.

RESULTS

Table 3 contains runtime information of example solutions. These results were obtained on an Intel®Core™i7-870 CPU at 2.93GHz. The algorithm has a parallel nature and can be adjusted to run on supercomputers or other distributed computing systems to increase the calculation speed. An example of a solution is shown in Fig.3. An example of the solver's converge can be seen in Fig.4.

Best results have been obtained with a population size of 100 and using very different positions in the task. The computational time and generations needed to find a solution vary greatly with different sets of positions. To minimize the computational time it is important to use very different positions as it simplifies the convergence of the algorithm.

TABLE 2: SOLVABLE SYSTEMS OF EQUATIONS FOR DIFFERENT COMBINATIONS OF CHAINS.

b	r	x	f	m	Notes
5	26	832	1092	27	Full model
4	22	1100	1452	45	(5R, 5R, 5R, 4R) fingers
4	21	714	938	29	(5R, 5R, 4R, 4R) fingers
3	17	1258	1666	69	(5R, 5R, 4R) fingers
3	16	608	800	33	(5R, 4R, 4R) fingers
2	11	550	726	45	(4R, 4R) fingers
1	5	130	170	21	5R finger, common solved
1	4	56	72	9	4R finger, common solved

TABLE 3: SOLVER EXECUTION INFORMATION.

Solution	Generations	Time (hours)
1	13	20.8
2	5	20.5
3	10	16.5
4	12	85.0

CONCLUSIONS

In this paper we present a method for the kinematic synthesis of tree-like articulated systems, with an application in the design of a robot to perform human-hand tasks. From the dimensional synthesis point of view, the interesting results is that, due to the tree structure, we can synthesize general serial chains with more than five degrees of freedom.We may conclude from this that, despite common believe that the human hand is a redundant mechanical system, it may not be so when we consider a task in which all fingers must act.

Dimensional synthesis for articulated systems like the one presented here, with a high number of joints, yield many solutions. A good process is required in order to select from the pool of candidates. For instance, for the application presented in this paper, additional constraints could be imposed either in the solving process or in the postprocessing phase in order to find a suitable design. Among others, we can cite size or location restrictions for exoskeletons mounted on the human hand, or

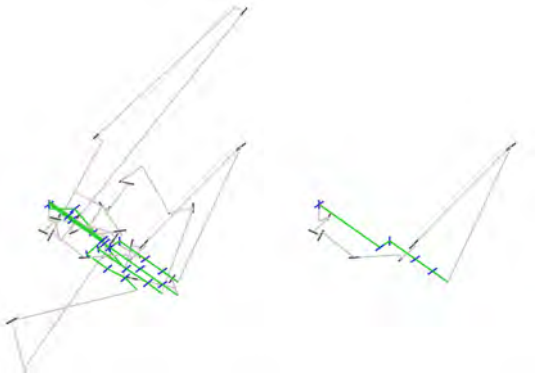

(a) Full Hand (b) Index Finger

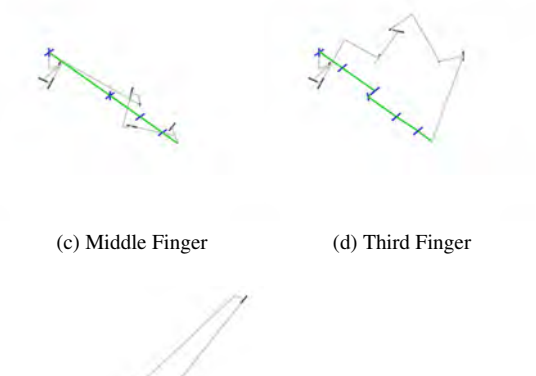

(c) Middle Finger (d) Third Finger

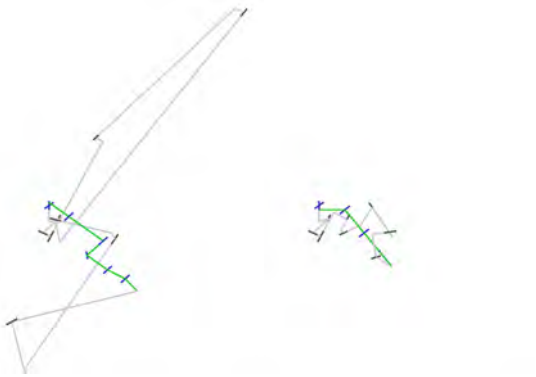

(e) Fourth Finger (f) Thumb

FIGURE 3: OVERVIEW OF A SOLUTION FOUND.

dexterity conditions at given configurations for manipulation in human environments. Future work will also include task velocities and accelerations in order to define grasping actions.

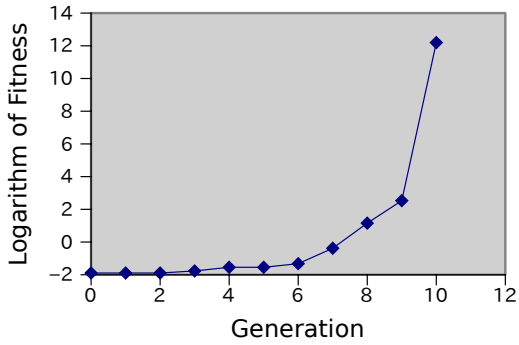

FIGURE 4: CONVERGENCE OF A SOLVER EXECUTION.

ACKNOWLEDGMENT

This work is supported by a Ramon y Cajal Research Fellowship from the Spanish Ministry of Science and Innovation.

REFERENCES

[1] Siciliano, B., and Khatib, O., 2008. *Handbook of Robotics*. Springer, Berlin.

[2] Soto Martell, J., and Gini, G., 2007. "Robotic hands: Design review and proposal of new design process". *World Academy of Science, Engineering and Technology,* ***26***.

[3] Briglen, L., Laliberte, T., and Gosselin, C., 2008. *Underactuated Robotic Hands*. Springer.

[4] Dai, J., and Wang, D., 2007. "Geometric analysis and synthesis of the metamorphic robotic hand". *ASME Journal of Mechanical Design,* ***129***, pp. 1191–1197.

[5] van Varseveld, R., and Bone, G., 1999. "Design and implementation of a lightweight, large workspace non-anthropomorphic dexterous hand". *ASME Journal of Mechanical Design,* ***121***.

[6] Ramos, A., Gravagne, I., and Walker, I., 2006. "Goldfinger: A non-anthropomorphic, dextrous robot hand". *ASME Journal of Mechanical Design,* ***128***, pp. 815–819.

[7] Schaffer, C., and Dillmann, R., 2001. "Kinematic design of a humanoid robot wrist". *Journal of Robotic Systems,* ***18(12)***, pp. 747–754.

[8] Perez Gracia, A., and McCarthy, J. M., 2006. "The kinematic synthesis of spatial serial chains using clifford algebra exponentials". *Proceedings of the Institution of Mechanical Engineers, Part C, Journal of Mechanical Engineering Science,* ***220(7)***, pp. 953–968.

[9] Perez, A., and McCarthy, J. M., 2003. "Dimensional synthesis of bennett linkages". *ASME Journal of Mechanical Design,* ***125(1)***, pp. 98–104.

[10] Brunnthaler, K., 2006. "Synthesis of 4r linkages using kinematic mapping". PhD thesis, Institute for Basic Sciences

and Engineering, University of Innsbruck, Innsbruck, Austria.

[11] Su, H., McCarthy, J. M., and Watson, L. T., 2004. "Generalized linear product homotopy algorithms and the computation of reachable surfaces". *ASME Journal of Computers and Information Science and Engineering,* ***4(3)***, pp. 226–235.

[12] Lee, E., Mavroidis, C., and Merlet, J. P., 2004. "Five precision point synthesis of spatial rrr manipulators using interval analysis". *ASME Journal of Mechanical Design,* ***126(5)***, pp. 842–850.

[13] Lee, E., and Mavroidis, C., 2002. "Solving the geometric design problem of spatial 3r robot manipulators using polynomial homotopy continuation". *ASME Journal of Mechanical Design,* ***124(4)***, pp. 652–661.

[14] Murray, R. M., Li, Z., and Sastry, S. S., 1994. *A Mathematical Introduction to Robotic Manipulation*. CRC Press, Inc., Boca Raton, FL.

[15] Perez, A., and McCarthy, J. M., 2004. "Dual quaternion synthesis of constrained robotic systems". *ASME Journal of Mechanical Design,* ***126(3)***, pp. 425–435.

[16] Fadi J. Beijjani, J. M. F. L., 1989. *Basic Biomechanics of the Musculoskeletal System*. Lea & Febiger, ch. Biomechanics of the hand, pp. 275–304.

[17] Chang, L., and Matsuoka, Y., 2006. "A kinematic thumb model for the act hand". In Robotics and Automation, 2006. ICRA 2006. Proceedings 2006 IEEE International Conference on, pp. 1000 –1005.

[18] Chocron, O., and Bidaud, P., 1997. "Evolutionary algorithms in kinematic design of robotic systems". In Intelligent Robots and Systems, 1997. IROS '97., Proceedings of the 1997 IEEE/RSJ International Conference on, Vol. 2, pp. 1111 –1117 vol.2.

[19] Yang, Y., Peng, G., Wang, Y., and Zhang, H., 2007. "A new solution for inverse kinematics of 7-dof manipulator based on genetic algorithm". In Automation and Logistics, 2007 IEEE International Conference on, pp. 1947 –1951.

Design of a Robotic Hand and Simple EMG Input Controller with a Biologically-Inspired Parallel Actuation System for Prosthetic Applications

Dr. Anthony L. Crawford, *Member, IEEE*, Jeffrey Molitor, *Member, IEEE*,
Dr. Alba Perez-Gracia *Member, IEEE,* Dr. Steve C. Chiu, *Member, IEEE*

***Abstract*—This paper presents the mechatronic design of a robotic hand for prosthetic applications. The main characteristic of this robotic hand is its biologically-inspired parallel actuation system, which is based on the behavior/strength space of the Flexor Digitorum Profundus (FDP) and the Flexor Digitorum Superficialis (FDS) muscles. The design separates the strength space of the FDS and FDP muscles into a lighter strength region where finer manipulation and general approach tasks are executed, and a higher strength region where the more robust grasps are achieved. Two parallel actuator types and kinematic structures are designed to complement the requirements of both strength space regions.**

This unique structure is intended to be driven by electromyographical (EMG) signals captured at the surface of the skin. The direct relation between signal and actuation system lends itself well to interpreting the EMG signals from the FDP and FDS muscles into effective task execution, with the goal of helping the user to achieve a good approximation of the full capabilities associated with the human hand, without compromising strength, dexterity, appearance, or weight; which are common issues associated with prosthetic hands.

The designed finger's capability of having a strength space similar to that of the FDS and FDP muscles is validated via direct inputs from a power supply and then via a controller using an actual EMG signal input from the human forearm. The controller is a simple feed forward system at this point in the research but provides the appropriate framework to integrate more elaborate control schemes and EMG signal conditioning as this portion of the research area matures.

Keywords – Prosthetics, Parallel Actuation Structure, Robotics, Hand, FDS and FDP Muscles

I. Introduction

THERE Have been many different approaches taken in the development of an effective prosthetic hand. These varying strategies often find themselves focusing on one of the following categories: implementing a new actuator type [11-16], developing a more effective kinematic structure [18,23,34], integrating effective compliance [18,23-25], generating effective control strategies [25-31], and interpreting/conditioning input signals [25]. Advances in these areas have resulted in robotic hands that perform many tasks with a high similarity to that of the human hand, such as the DLR hand [33], I-Limb hand [11], Shadow hand [12], and Fluidhand [32] to name a few. However, a prosthetic hand that is nimble, quick, strong, lightweight, quiet, and efficient [1] has yet to be achieved.

The primary reason for the current state of prosthetic hands has been the complexity associated with the human hand as a result of its multiple bones and joints (Fig 1). This is further compounded by the fact that the human hand as a functioning unit does not just embody the palm and its digits but also the wrist, forearm muscles, nervous system, and the body's energy generation system. As a result, the entire prosthetic hand actuation structure (inputs, power, strength, kinematics, etc.) must fit in a significantly reduced volume compared to the human hand that it is replacing.

To address some of the challenges described above, this research implements a unique perspective of the FDS and FDP muscles' strength space in the human forearm and proposes a novel design and parallel actuation structure that complements this perspective. The goal is to create a direct relation between the forearm's EMG signals and the actuation system, in order to help the user achieve a good approximation of the full capabilities associated with the human hand in a compact design.

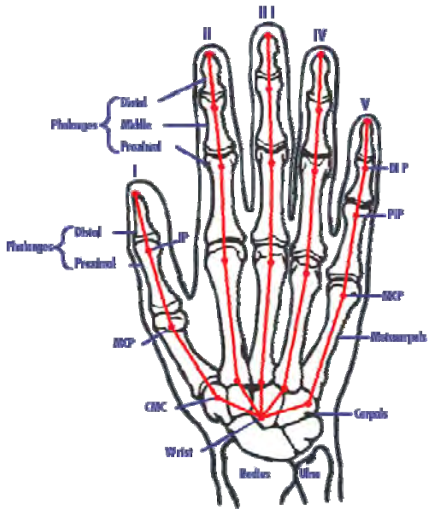

Fig 1: Joint/Bone composition of human hand [2]

Manuscript received May 24, 2010. this research was performed under an award/contract from Telemedicine Advanced Technology Research Center (TATRC), of the U.S. Army Medical Research and Materiel Command (USAMRMC) of the U.S. Department of Defense.

A. L. Crawford was a Ph.D. student at Idaho State University, Pocatello, ID 83209 (e-mail: crawanth@isu.edu)

J. Molitor is a Masters student at Idaho State University, Pocatello, ID 83209 (e-mail: molijeff@isu.edu)

M. A. Perez-Gracia is an assistant professor at Idaho State University, Pocatello, ID 83209 and is currently at Institut de Robotica i Informatica Industrial (UPC/CSIC), Barcelona, Spain (e-mail: perealba@isu.edu)

Sections 2 and 3 of this paper describe the FDS and FDP muscles' strength space, how it relates to the human hand's capabilities, as well as the actuators and actuation structures of current prosthetic/robotic hands. Sections 4 and 5 will provide a description of the mechanical design and testing results that justify the design's ability to execute the strength space perspective developed in this paper. The paper will finally present conclusions associated with the testing results and an identification of future work. The actuation structure's mechanical design presented here is an expansion of the content being published at the ASME IDETC 2010 conference with the inclusion of friction in the force calculations, implementation of the mechatronics, and the EMG inputs being an expansion of that presented research.

The FDS and FDP muscles are the primary flexor muscles in the human finger and are primarily opposed by the extensor digitorum (ED) muscle. As shown in Fig 2. The FDP muscle is attached to the distal phalanx and is capable of full hand closure; it is considered to be the more active of both finger flexion muscles. The FDS muscle is attached to the middle phalanx and its full capacity is primarily achieved when activation of the DIP joint is not required or when full hand closure tasks require additional strength [3].

The strength space of the FDS and FDP muscles is shown in Fig 3. The figure demonstrates the normalized maximal force exertion of the FDS and FDP muscles (y-axes) during maximum force execution of the hand (x-axes). The FDP muscle is shown to reach its maximal force execution (120N [5]) at approximately 35% of the total flexural effort; however, the FDS muscle continues to exert force until it reaches its maximal force execution (240 N [5]) at about 100% of the total flexural effort. The FDS and FDP behavior can be attributed to the learned neurological activation of these muscles [6] as well as the finger's associated kinematic structure.

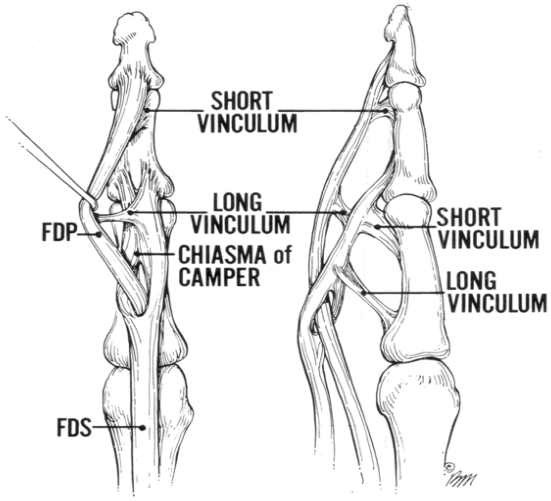

Fig 2: Graphic of FDS and FDP muscle in finger [4]

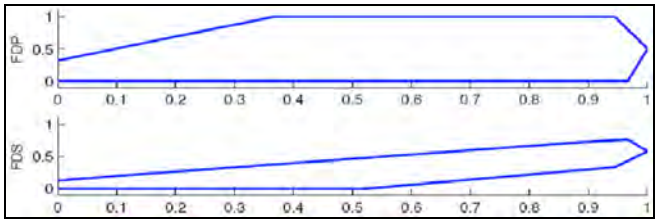

Fig 3: Strength space of FDS and FDP muscles (x-axis: normalized postion of hand from open (0) to closed (1), y-axis: normalized force)[7]

The FDS and FDP strength space comprises the strength requirements for all the tasks that a hand must execute [8][9]. In general, most everyday tasks don't require extensive force but do require a certain amount of dexterity. For manipulation or approaching an object, the finger can employ both the FDS and FDP muscles to nimbly accommodate various shapes and execute both general and complex movement paths. Fig 3 shows that the FDS and FDP muscles are both active for activities below 35% of the maximum force capacity of the hand and are most likely employed during manipulation/object approaching movements.

Gripping tasks generally require less dexterity and more strength than manipulation and general object approach. The size and weight of the object as well as the characteristics of the grasp (e.g. friction between pads or force closure) determines how much force is required from the finger's strength space shown in Fig 3. It is to be noted that the actual act of the grip also generally requires much less complex finger motion than that of manipulation. Based on these observations, we divided the FDS and FDP strength space into the regions shown in Fig 4. In Fig 4 region 1 is populated by the more frequent dexterous tasks and region 2 is populated by the less frequent and more strength-based tasks.

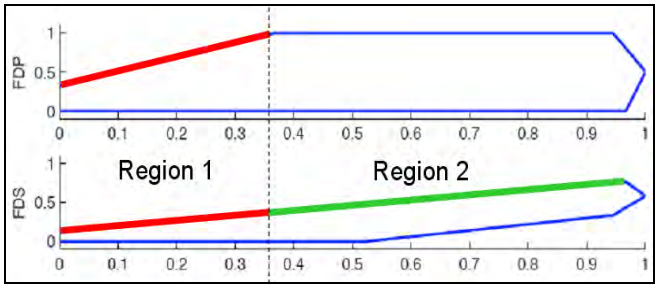

Fig 4: Divided Strength Space of FDS and FDP muscles (x-axis: normalized hand position from open (0) to closed (1), y-axis: normalized force)

Though the bones, joints, and muscles of the thumb are somewhat different than that of the finger, the same FDS and FDP strength space division philosophy is applied in the mechanical design of the prosthetic thumb.

II. Actuation Structures

To the authors' knowledge, all currently developed prosthetic/robotic hands use a single actuator type to execute all the tasks embodied in the FDS and FDP strength space.

This technique results in the shortcomings of the chosen actuator being carried throughout the strength space, let it be pneumatic, electromechanical, ultrasonic, or shape memory alloy. This could include excessive size and weight, or reduced time response and energy inefficiency to name a few.

The actuator types used in current robotic/prosthetic hands and considered in this design included electromagnetic [10][11], pneumatic [12][13], hydraulic [14], ultrasonic [15], and shape memory alloy [16]. Although all the listed actuator types have been employed in multiple prosthetic hand designs based on their advantageous features, one or more shortcoming (weight, noise, size, efficiency, and speed) have been accepted as well.

Prosthetic hands have employed the above actuator types into two general types of kinematic structures. These two structures are referred to as fully actuated and underactuated. The underactuated structure often uses a single input to actuate the multiple joints and essentially wraps the phalanges of the finger around an object [17]. Typically this is achieved by a flexible tendon routed through the finger structure which allows one of the finger's phalanges to be stopped by the object without preventing the remaining phalanges from continuing to wrap around the target

Some underactuated structures couple all three degrees of freedom associated with finger flexure to one actuator. However, there are structures where the underactuation exists only between the PIP and DIP joints. This behavior is typically executed by the human hand and will be referred to herein as nearly fully actuated. One example of this type of nearly fully actuated structure is that adopted by Yamano, Takemura and Maeno [15]. Dollar and Howe present many other types of couplings that have been employed in various underactuated hands [18]. The primary disadvantage of these structures is the lack of manipulation capabilities.

Fully actuated or nearly fully actuated structures do allow the greater manipulability lacking in underactuated structures. The consequence of this flexibility is the increased number of motors required to actuate these degrees of freedom, where each motor must also be of adequate size to apply the required forces. This in turn increases the size, weight, and control complexity of the prosthetic hand.

Few prosthetic hands are actually fully actuated. This could arise from the complexity that is introduced in the design or from the fact that the tasks which are to be performed are modeled after the underactuated human hand for grasping actions only. One hand that does fully actuate the finger's degrees of freedom is the UB-3 hand [19]. In this finger each phalange has a tendon attached to it and is able to actuate all flexing degrees of freedom independently.

In the design presented in this paper, the actuators and actuation structure were chosen to specifically complement the task characteristics of each region shown in Fig 4. The smaller, faster, and efficient electromagnetic motors are incorporated into a nearly fully actuated kinematic structure and chosen to perform the tasks associated with region 1. The quiet, lightweight, strong shape memory actuators implemented in a parallel underactuated structure were selected to provide sufficient strength to the system when required. The complementary function of both actuation systems provides the prosthetic hand with a broad capability for grasping and manipulating actions while trying to optimize actuator size and performance.

III. Prosthetic Hand Design

The developed design is shown in Fig 5. The design is dimensionally consistent with that of an average male human hand [2] and possesses the same degrees of freedom. The anthropomorphic aspect of the hand is intended to enhance the amputee's acceptance and usability. The DIP and PIP joints of the finger and the IP and MCP joints of the thumb are coupled. This is achieved by connecting a single actuator to both the PIP joint (bevel gears) and DIP joint (pulley connection on metacarpal phalange). This coupling technique is common among many prosthetic/robotic hands as noted in the section above.

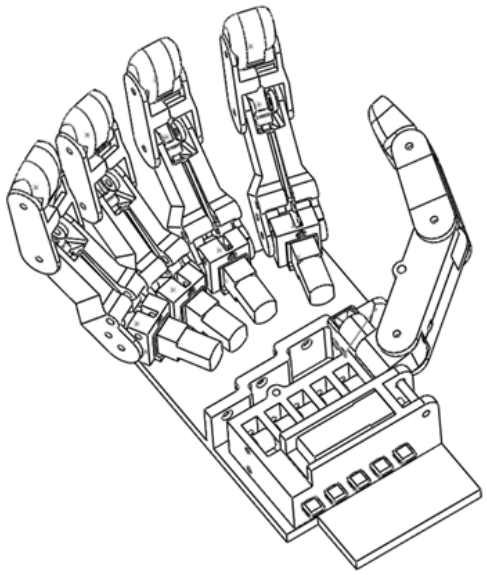

Fig 5: Prosthetic hand design

The developed parallel actuation structures discussed in the previous section are shown in Fig 6 and Fig 7 for the finger and Fig 8 and Fig 9 for the thumb. The movements associated with region 1 in Fig 4 are achieved by two DC motors. The DC motors actuating the coupled DIP/PIP joints of the finger and IP/MCP joints of the thumb are embedded in the proximal phalange of the finger and the metacarpal phalange of the thumb. The DC motor in the metacarpal phalange of the finger actuates the horizontal degree of freedom of the MCP joint. The DC motor at the base of the thumb actuates the CMC joint to obtain an approximation of the abduction/adduction motion. The second degree of freedom of the finger's MCP joint (abduction/adduction) is only subject to compliance without actuation. The second degree of freedom in the thumb's CMC joint (flexion/extension) is actuated by the region 2 actuation structure.

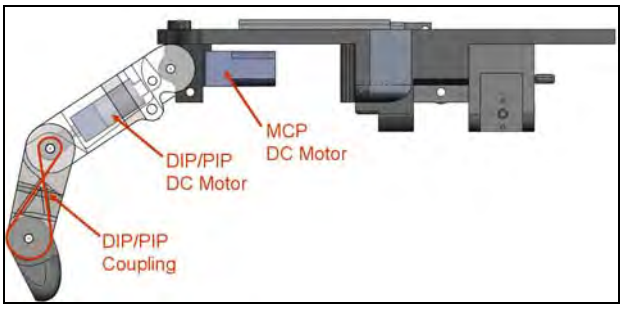

Fig 6: Region 1 actuation scheme for the finger

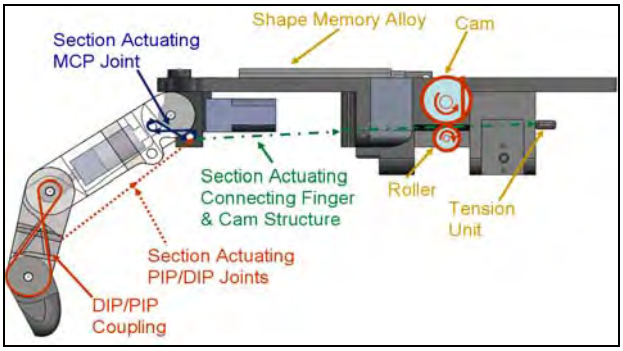

Fig 7: Region 2 actuation scheme for the finger

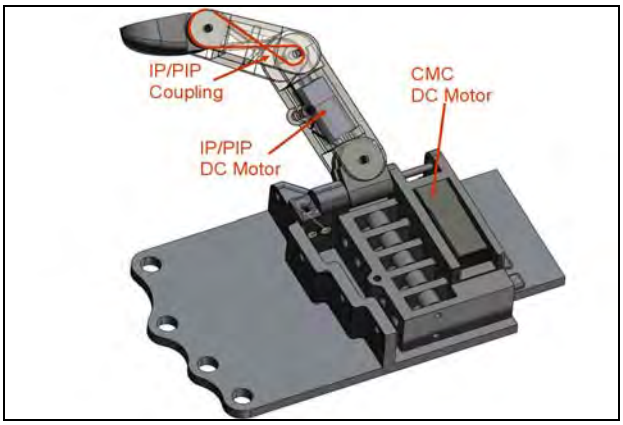

Fig 8: Region 1 actuation scheme for the thumb

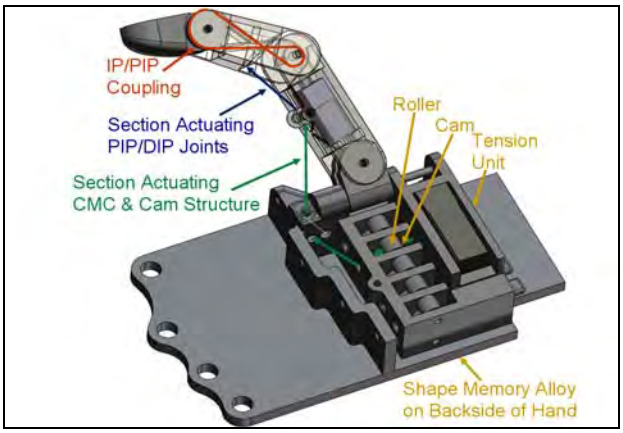

Fig 9: Region 2 actuation scheme for the thumb

The actuation structure corresponding to region 2 in Fig 4 for the finger includes a light cable that passes over two restraining shafts in the MCP joint of the finger, coils in the proximal phalange, and embeds in the middle phalange. The string is kept in light tension by a tension unit at the back of the hand while the region 1 actuation structure is active. When region 2 actuation is required the shape memory alloy actuates a spring loaded cam which in turn pinches the string between itself and a roller beneath it. As the shape memory alloy continues to actuate, the cam introduces the additional force required for region 2 tasks. At task completion the electric signal causing the shape memory alloy to heat up is stopped and the DC motors and cam spring extend the shape memory alloy back to its original state. The spring loaded cam mechanism is more definitively shown in Fig 10 and Fig 11.

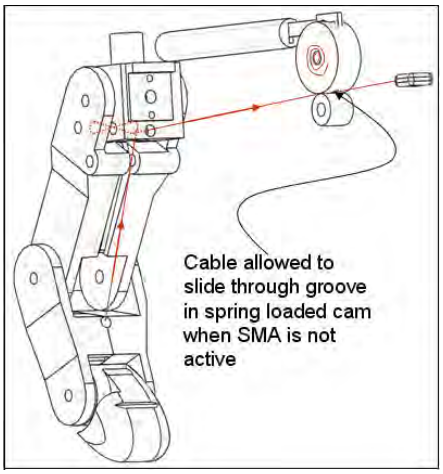

Fig 10: Region 2 spring loaded cam mechanism prior to SMA actuation (thinner line representing cable corresponds to lower tension applied by tensioner)

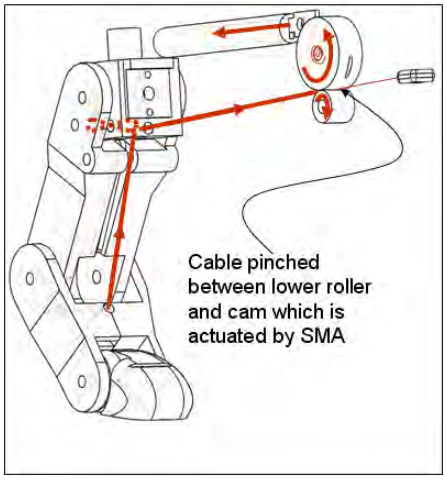

Fig 11: Region 2 spring loaded cam mechanism during SMA actuation (thicker line representing cable corresponds to additional tension applied by SMA via cam mechanism)

The thumb's region 2 actuation structure is similar to that of the finger's region 2 actuation structure. However, unlike the finger, this structure actuates the degree of freedom at the CMC joint that is not actuated by the DC motor. This is based on the observation that this degree of freedom is more apposing of the fingers during tasks that would require additional force (power grasp, high force pinch grasp, lateral grasp, etc. [8]).

The design shown in this section has been manufactured using a rapid prototyping machine. The prototype can be seen in the Results and Discussion section.

IV. Controller Details

The control of the DC motors in this research was accomplished through the use of pulse width modulation (PWM) and direction control. PWM allowed the applied voltage to be varied continuously which controlled the speed and torque of the motor. Direction control was used to determine the spin direction of the motor.

PWM and direction control functionality was provided by a Pololu Qik 2s12v10. The Qik motor controller provides two channels of speed and direction control for brushed DC motors and is controlled by a serial interface. In this research, the motor controller was connected to a PC running LabVIEW to provide the serial commands. The connection from the PC to the Qik was made through an intermediate device, the Pololu Jrk 21v3, to provide the conversion from USB to the required serial connection. The Jrk also provides motor control functionality, but it was not implemented in this research.

Additionally, EMG signal capturing capability was added to control the DC motors. The raw signals from the EMG sensor are shown in Fig 12 and Fig 13.

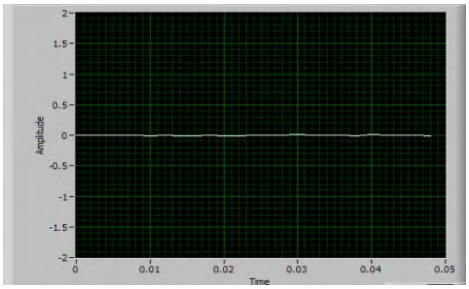

Fig 12: Raw EMG signal with finger in relaxed state

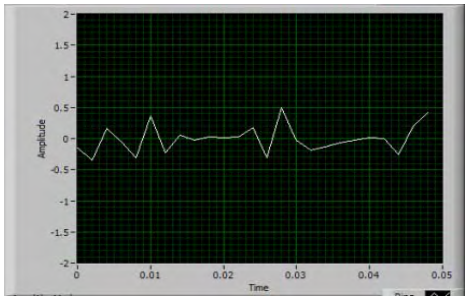

Fig 13: Raw EMG signal with finger in flexed state

The raw signals were processed by taking the maximum absolute value over a 100 sample interval and generating a new data set. In order to get the full flex and extend ability of the finger from this new data set two threshold levels where introduced. Above one threshold the motor would spin in one direction (flex) and below another the motor would spin in the opposite direction (extend). The deadzone was implimented as a buffer area to transition between the flexation and extention zones.

The EMG signal was acquired from the first author's digit III FDP muscle and supplied as an analog voltage from a separate PC incorporating a Delsys Bagnoli EMG system. The analog voltage was sampled through a National Instruments data acquisition card installed in the motor control PC. The analog signal was then filtered and scaled using LabVIEW to a value representing the amplitude of the EMG signal, which was then used to control the direction of the motors. A sample of the filtered and scaled signal with thresholds is shown in Fig 14.

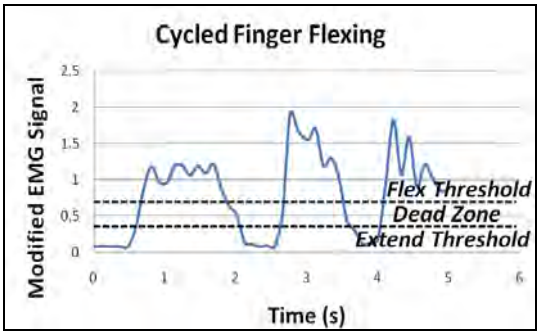

Fig 14: EMG signal as finger was flexed and relaxed

The entire controller setup can be seen in the schematic shown below in Fig 15.

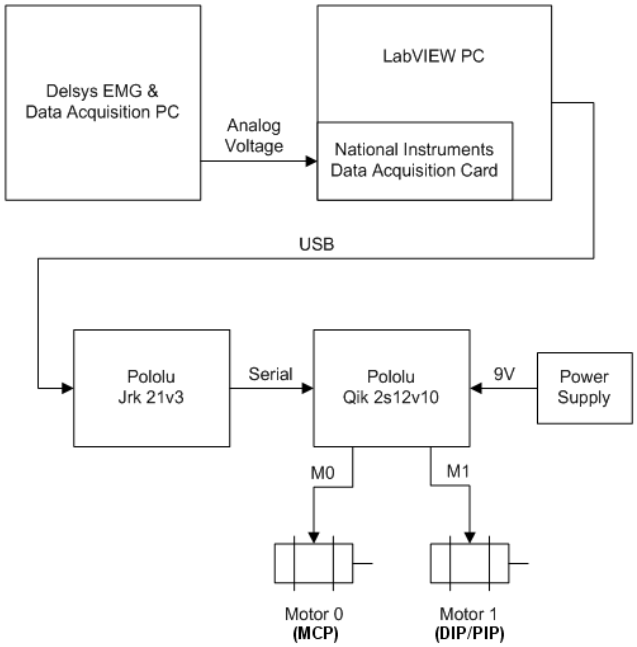

Fig 15: Motor controller setup

V. Experimental Setup

The experiment associated with this research was performed to validate the designed actuation structure's ability to span a two-region strength space similar to the one identified above for the human hand. The actuators used in the prototype were Pololu 298:1 Micro Metal Gearmotor HP DC motors [21] and the Electric Piston SMA actuator from Raychem [22]. These actuators are relatively inexpensive

and the implementation of more expensive actuators could further enhance the values reported below.

The experiment consisted of having the finger and the thumb grip a FSR sensor fastened to a dense foam ball in the large grip and then the close grip configurations as shown in Fig 16 through Fig 19. The large grip setup simulated the finger/thumb performing a more robust grasp on a larger object and the small grip setup simulated the actuation structure of the finger/thumb grasping smaller objects or performing the more dexterous pinch or lateral grasp. The values obtained experimentally are compared to the expected calculated values using a simple friction inclusive static calculation of the reaction force required at the FSR sensor to resist the stall torque of the DC motors and the measured tension provided by the SMA.

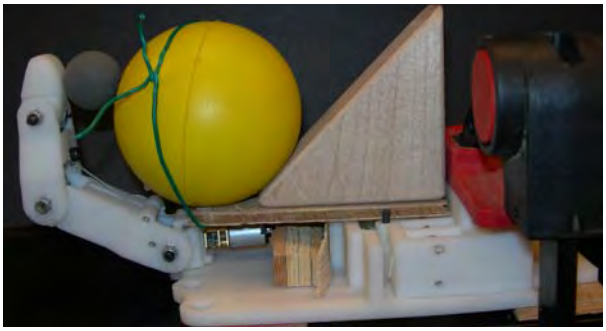

Fig 16: Finger in large grip configuration.

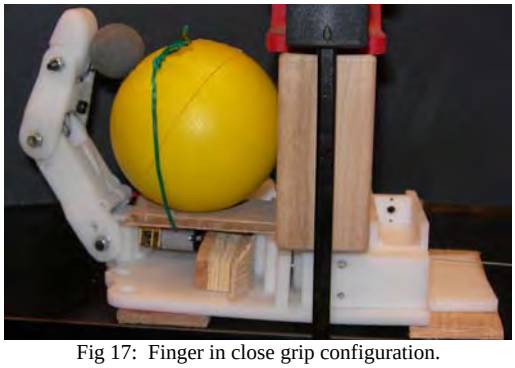

Fig 17: Finger in close grip configuration.

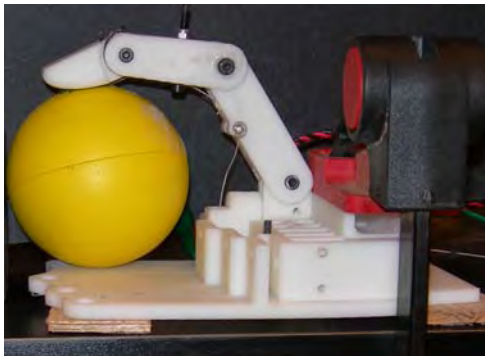

Fig 18: Thumb in close grip configuration.

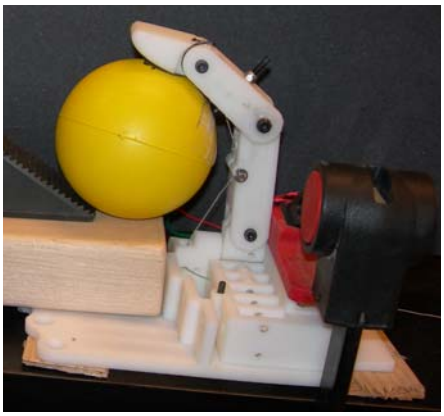

Fig 19: Thumb in large grip configuration.

The experimental values were compared to the expected ones using friction inclusive static calculations based on the free body and geometric diagrams shown in Fig 20 and Fig 21. The "T" vectors in the free body diagrams represent the tension in the cable. The tension values are calculated using (1) where the $\underline{V_i}$ and $\underline{V_j}$ are the geometric vectors of the cable on either side of a pivot point, t_i and t_j are the tension values in these vectors, and μ is the friction coefficient of the pivot point. Because t_j is the only unknown in this equation it is separated and solved for in order to determine the next tension vector in the system.

$$\left(\left|t_i \underline{V}_i\right| - \left|t_j \underline{V}_j + t_i \underline{V}_i\right|\mu\right) = \left|t_j \underline{V}\right| \qquad (1)$$

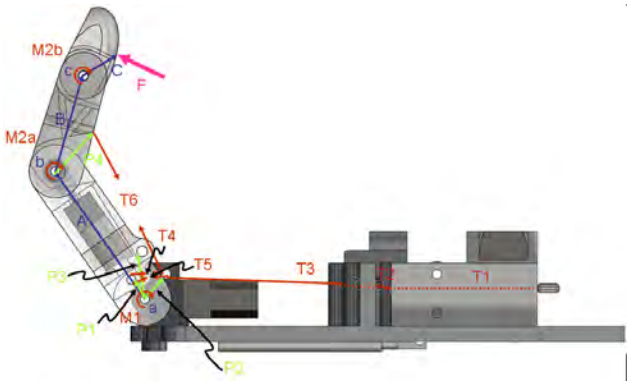

Fig 20: Primary variables used in friction inclusive static calculations of finger in both close and large grip configurations.

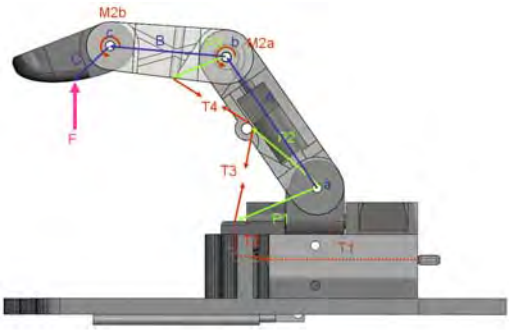

Fig 21: Primary variables used in friction inclusive static calculations of thumb in both close and large grip configurations.

With the tension vectors determined, the simple static equations (1) and (2) for the finger and thumb are used to solve for the forces/torques of each joint from the distal phalange to the knuckle in terms of the variable F value then using the equations to solve for F. The stall torque applied by the DC motors (90 oz-in) replaced the M1 and M2a/M2b variables. As described in the design section M2a and M2b are coupled and their relationship is shown in (3). The gravitational forces generated by each phalange was applied at the center of the link in the downward direction using the mass values for the finger of (M_{prox}=21.6g, M_{mid}=9.45g, M_{dist}=6.7g) and for the thumb of (M_{met}=33.3g, M_{prox}=10.5g, M_{dist}=8.5g).

$$\sum M = 0 \qquad (2)$$

$$\sum F = 0 \qquad (3)$$

$$M2a + \frac{8}{14} M2b = 90oz - in \qquad (4)$$

VI. Results and Discussion

Each of the four configuration setups were performed three times with each actuator type individually and then with them combined. The results are shown in Table 1 where the columns correspond to the resulting forces from the SMA, DC motors, the results of the SMA and DC motors column summed together, the experienced force when the two actuator types are physically applied at the same time, and the value calculated using basic statics. The table shows that when applied individually, the resulting forces from the SMA are for the most part larger than the applied DC motor forces for all four configurations. The average combined forces for the finger are generally greater than the experienced but the values for the thumb are approximately the same.

Table 1: Finger & Thumb Testing Results

Finger M1 & M2 & SMA (Newtons)

Finger CG	SMA	DC Motors	Combined (Sum)	Combined (Experimental)	Combined§ (Calculated)	Combined£ (Calculated)
Average	7.75	9.78	17.52	15.23	16.55	16.85
Std Dev	0.21	0.22	0.15	0.20	0.08	0.08
Finger LG	SMA	DC Motors	Combined (Sum)	Combined (Experimental)	Combined§ (Calculated)	Combined£ (Calculated)
Average	8.17	8.67	16.84	15.08	15.23	15.46
Std Dev	1.26	1.14	1.27	0.80	0.30	0.30

Thumb M1 & SMA (Newtons)

Thumb CG	SMA	DC Motor	Combined (Sum)	Combined (Experimental)	Combined§ (Calculated)	Combined£ (Calculated)
Average	4.70	1.24	5.94	5.60	5.14*	5.61*
Std Dev	0.90	0.35	0.86	1.14	0.05	0.06
Thumb LG	SMA	DC Motor	Combined (Sum)	Combined (Experimental)	Combined§ (Calculated)	Combined£ (Calculated)
Average	4.56	3.45	8.01	8.18	7.70*	8.27*
Std Dev	1.85	0.45	2.45	0.39	0.49	0.58

* Values combined from calculated SMA values and measured DC Motor values

§ Values where calculated using friction coefficients of μ(nylon)=0.102 and μ(steel)=0.09

£ Values where calculated using friction coefficients of μ(nylon)=0.52 and μ(steel)=0.09

The finger behavior is expected because the SMA was only partly isolated from the motors as the motors were still employed during the SMA test in order to maintain the structure of the finger against the ball prior to testing. This resulted in the SMA having to press against the ball and overcome the minor resistance presented by the motors. The thumb behavior was expected as well due to the slightly compliant units isolating the motor during the motor test absorbing some of the applied motor force. The calculated forces where also expectedly higher than the measured data as friction from the system was not incorporated in their development.

It is to be noted that the combined (calculated) values for the thumb are only calculated for the SMA input and the DC Motor experimental value has been added to the calculated value. This was done because a part of the component in the prototype thumb broke causing the gearing to not mesh appropriately, giving significantly smaller force values (approx. 3N) than those calculated (approx. 14N).

The controller was only applied to the DC motors of finger and thumb in their close grip configurations. The objective of these tests where to merely validate that the controller platform had the power and functional capacity to produce similar results to that of the power supply inputs using an EMG signal input.

The EMG voltage and current outputs for both the finger and thumb were consistent with that of the direct power supply inputs. The EMG thumb test resulted in a DC motor force of 0.95N which agreed with the 1.24N $\pm$ 0.35N generated by the direct power supply tests. It was also visually verified that the finger squeezed the ball to a similar degree with the EMG controller as the direct power supply test system. However, a later identified disconnect in the FSR sensor did not allow the generation of reliable force data for the finger. Successive experiments for the finger resulted in a break in the rapid prototyped proximal phalange. This experiment is being repeated immediately with a soon to be re-built proximal phalange

VII. Conclusions and Future Work

This paper presents a novel design and actuation system for a prosthetic hand. The actuation structure was shown to effectively span a two-region strength space to execute grip configurations similar to those found in the three primary grips of the human hand (power, pinch, and lateral). The design also showed the ability of an underactuated and nearly fully actuated kinematic structure to exist in a single actuation system using remarkably different types of actuators, without compromising the required size and weight of the prosthetic hand.

According to these results, the parallel actuation structure is a good starting point for the design. The results also validated that the design could be effectively driven by an EMG signal. Complete testing of the parallel actuation system's performance will require the expansion of the EMG inputs to perform different grasps and manipulations.

Future work includes further testing, development of the controller, fabrication of a prototype that is more robust yet

of the same form as the rapid prototype components tested here, and the use of the dynamical model of the hand for manipulation tasks, in order to improve the design. More precisely selected actuators will be used in the final design. The stronger actuators will add the appropriate scale to the developed strength space so as to mimic the force generation capabilities of the system as well as the strength space form.

ACKNOWLEDGMENT

This research was performed under an award/contract from Telemedicine Advanced Technology Research Center (TATRC), of the U.S. Army Medical Research and Material Command (USAMRMC) of the U.S. Department of Defense.

REFERENCES

[1] Bicchi, A., 2000, "Hands for dexterous manipulation and robust grasping: a difficult road toward simplicity", IEEE Transactions on Robotics and Automation, 16(6):652-662.

[2] Foegelle, M., Li, K., Pavacic, A., Moller, P., "Test & Measurement: Developing a Standard Hand Phantom for Wireless Testing," [Online]. Available: http://www.wirelessdesignmag.com/ShowPR.aspx?PUBCODE=055&ACCT=0029956&ISSUE=0811&RELTYPE=tm&PRODCODE=W0260&PRODLETT=A&CommonCount=0,

[3] Norkin, C., Levangie, P., 1992, *Joint Structure & Function: A Comprehensive Analysis: Second Edition*, F. A. Davis Publications, 262-299.

[4] Nelson, D. L. "Tendon Laceration Page," [Online]. Available: http://www.davidlnelson.md/Tendon_laceration.htm,

[5] Valero-Cuevas, F. J., Towles, J. D., Hentz, V. R., "Quantification of fingertip force reduction in the forefinger following simulated paralysis of extensor and intrinsic muscles," Journal of Biomechanics 33 (2000) 1601-1609.

[6] Kevin G. Keenan, K. G., Veronica J. Santos, V. J., Venkadesan, M. and Valero-Cuevas, F.J., Maximal Voluntary Fingertip Force Production Is Not Limited by Movement Speed in Combined Motion and Force Tasks, The Journal of Neuroscience, July 8, 2009 • 29(27):8784–8789.

[7] Kutch, J. J., Valero-Cuevas, F. J., "All muscles are redundant but some are less redundant than others," poster presentation for USC Viterbi School of Engineering Brain-Body Dynamics Lab.

[8] Perez-Gracias, M. A., http://progeny.isu.edu/~alba/, Idaho State University.

[9] Cutkosky, M.R., 1989, "On grasp choice, grasp models, and the design of hands for manufacturing tasks", IEEE Transactions on Robotics and Automation, 5(3):269-279.

[10] Butterfass, J.; Fischer, M.; Grebenstein, M.; Haidacher, S. and Hirzinger, G.., 2004, "Design and Experience with DLR Hand II", Proceedings of the World Automation Congress 2004, Seville, Spain, 2004.

[11] Touch Bionics Inc [Online]. Available: www.touchbionics.com

[12] Shadow Robot Company [Online]. www.shadowrobot.com/hand/papers.shtml

[13] Fite, K., Withrow, T., Shen, Z., Wait, K., Mitchell, J., Goldfarb, M., 2008, "A Gas-Actuated Anthropomorphic Prosthesis for Transhumeral Amputees," IEEE Transactions on Robotics, 24(1):159:169.

[14] Pylatiuk, C., Schulz, S., Kargov, A., Bretthauer, G., 2004, "Two Multiarticulated Hydraulic Hand Prostheses," Artifical Organs, 28(11),980:986.

[15] I. Yamono, T. Maeno, 2005, "Five-fingered Robot Hand using Ultrasonic Motors and Elastic Elements," Proceedings of the 2005 IEEE International Conference on Robotics and Automation, Barcelona, Spain, Aprill 2006.

[16] Andrianesis, K., Tzes, A., "Design of an Anthropomorphic Prosthetic Hand Driven by Shape Memory Alloy Actuators," Proceedings of the 2nd Biennial IEEE/RAS-EMBS International Conference on Biomedical Robotics and Biomechatronics, Scottsdale, AZ, USA, October 19-22, 08.

[17] Carrozza, M., Cappielo, G., Micera, S., Edin, B., Beccai, L., Cipriani, C., 2006, "Design of a cybernetic hand for perception and action," Biol Cybern (2006) 95:629-644.

[18] Dollar, A.M., and Howe, R.D., 2006, "Joint coupling design of underactuated grippers", Proc. of the ASME 2006 International Design Engineering Technical Conferences and Computers and Information in Engineering Conference, September 10-13, 2006, Philadelphia, PA, USA.

[19] Dollar Lotti, F., Tiezzi, P., Vassura, G., 2005, "Development of UB Hand 3: Early Results," Proceedings of the 2005 IEEE International Conference on Robotics and Automation, Barcelona, Spain, April 2005.

[20] Hollerbach, J., "ME 6220: Introduction to Robotics", Chapters 9 & 10 of Course Material, 2007.

[21] Pololu Robotics & Electronics, "298:1 Micro Metal Gearmotor HP," [Online] Available: http://www.pololu.com/catalog/product/994

[22] Electric Piston Instruction Manual, [Online]. Available: www.robotstore.com/download/EPiston_Instr_V12.pdf

[23] Carrozza, M., Cappiello, G., Stellin, G., Zaccone, F., Vecchi, F.,Micera, S., Dario, P., "A Cosmetic Prosthetic Hand with Tendon Driven Under- Actuated Mechanism and Compliant Joints: Ongoing Research and Preliminary Results," Proc. of the 2005 IEEE International Conference on Robotics and Automation, April 2005, Barcelona, Spain.

[24] Vanderniepen, I., Van Ham, R., Van Damme, M., Lefeber, D., "Design of a powered elbow orthosis for orthopaedic rehabilitation using compliant actuation," Proc. of the 2nd Biennial IEEE/RAS-EMBS International Conference on Bimedical Robotics and Biomechatronics, October 19-22, 2008, Scottsdale, AZ, USA.

[25] Zollo, L., Roccella, S., Guglielmelli, E., Carrozza, M., Dario, "Biomechatronic Design and Control of an Anthropomorphic Artificial Hand for Prosthetic and Robotic Applications," IEEE/ASME Transactions on Mechatronics, Vol. 12, No. 4, August 20007.

[26] Engeberg, E. D., Meek, S., "Improved Grasp Force Sensitivity for Prosthetic Hands Through Force-Derivative Feedback," IEEE Transactions on Biomedical Engineering, Vol. 55, No. 2, February 2008.

[27] Engeberg, E. D., Meek, S., "Model-Based Feedforward Derivative Compensation for Prosthetic Hands," Proc. of the 2nd Biennial IEEE/RAS-EMBS International Conference on Bimedical Robotics and Biomechatronics, October 19-22, 2008, Scottsdale, AZ, USA.

[28] Engeberg, E. D., Meek, S. G., Minor, M. A., "Hybrid Force-Velocity Sliding Mode Control of a Prosthetic Hand," IEEE Transactions on Biomedical Engineering, Vol. 55, No. 5, February 2008.

[29] Cipriani, C., Zaccone, F., Micera, S., Carrozza, M., "On the Shared Control of an EMG-Controlled Prosthetic Hand: Analysis of User-Prosthesis Interaction," IEEE Transactions on Robotics, Vol. 24, No. 1, February 2008.

[30] Blank, A., Okamura, A. M., Kuchenbecker, K. J., "Effects of Proprioceptive Motion Feedback on Sighted and Non-Sighted Control of a Virtual Hand Prosthesis," Symposium on Haptic Interfaces for Virtual Environments and Teleoperator Systems, March 13-14, 2008, Reno, Nevada, USA.

[31] Robinson, D. W., Pratt, G. A., "Force Controllable Hydro-Elastic Actuator," Proc. of the 2000 IEEE International Conference on Robotics and Automation, April 200, San Fransico, CA, USA.

[32] Pylatiuk, C., Schulz, S., Kargov, A., Bretthauer, G., 2004, "Two Multiarticulated Hydraulic Hand Prostheses," Artifical Organs, 28(11),980:986.

[33] Institute of Robotics and Mechatronics [Online]: http://www.dlr.de/rm/en/desktopdefault.aspx/tabid-3975/6161_read-245/

[34] Winfrey, Rex C., 2008, "Prosthetic Hand Having a Conformable, Compliant Grip, and Opposable, Functional Thumb," Patent 7,361,197, April 22, 2008.

International Journal of Nanomedicine

Dovepress
open access to scientific and medical research

Open Access Full Text Article

ORIGINAL RESEARCH

Treatment of human astrocytoma U87 cells with silicon dioxide nanoparticles lowers their survival and alters their expression of mitochondrial and cell signaling proteins

This article was published in the following Dove Press journal:
International Journal of Nanomedicine
18 September 2010
Number of times this article has been viewed

James CK Lai[1]
Gayathri Ananthakrishnan[1,2]
Sirisha Jandhyam[1]
Vikas V Dukhande[1]
Alok Bhushan[1]
Mugdha Gokhale[1]
Christopher K Daniels[1]
Solomon W Leung[3]

[1]Department of Biomedical and Pharmaceutical Sciences, College of Pharmacy and Biomedical Research Institute, [2]Department of Health and Nutrition Sciences, Kasiska College of Health Professions, [3]Department of Civil and Environmental Engineering, College of Engineering and Biomedical Research Institute, Idaho State University, Pocatello, ID, USA

Abstract: Recent evidence suggests silicon dioxide micro- and nanoparticles induce cytotoxic effects on lung cells. Thus, there is an increasing concern regarding their potential health hazard. Nevertheless, the putative toxicity of nanoparticles in mammalian cells has not yet been systematically investigated. We previously noted that several metallic oxide nanoparticles exert differential cytotoxic effects on human neural and nonneural cells. Therefore, we hypothesized that silicon dioxide nanoparticles induce cytotoxicity in U87 cells by lowering their survival by decreasing cell survival signaling and disturbing mitochondrial function. To investigate this hypothesis, we determined the activities of the key mitochondrial enzymes, citrate synthase and malate dehydrogenase, in astrocytoma U87 cells treated with silicon dioxide nanoparticles. In addition, we studied the expression of the mitochondrial DNA-encoded proteins, cytochrome C oxidase II and nicotinamide adenine dinucleotide (NADPH) dehydrogenase subunit 6, and cell signaling pathway protein extracellular signal-regulated kinase (ERK) and phosphorylated ERK in treated U87 cells. The activated form of ERK controls cell growth, differentiation, and proliferation. In parallel, we determined survival of U87 cells after treating them with various concentrations of silicon dioxide nanoparticles. Our results indicated that treatment with silicon dioxide nanoparticles induced decreases in U87 cell survival in a dose-related manner. The activities of citrate synthase and malate dehydrogenase in treated U87 cells were increased, possibly due to an energetic compensation in surviving cells. However, the expression of mitochondrial DNA-encoded cytochrome C oxidase subunit II and NADH dehydrogenase subunit 6 and the cell signaling protein ERK and phosphorylated ERK were altered in the treated U87 cells, suggesting that silicon dioxide nanoparticles induced disruption of mitochondrial DNA-encoded protein expression, leading to decreased mitochondrial energy production and decreased cell survival/proliferation signaling. Thus, our results strongly suggest that the cytotoxicity of silicon dioxide nanoparticles in human neural cells implicates altered mitochondrial function and cell survival/proliferation signaling.

Keywords: cytotoxicity, silicon dioxide nanoparticles, mitochondrial enzyme, extracellular signaling regulated kinase, cell signaling, neural cells

Introduction

According to the Environmental Protection Agency, exposure to nanomaterials can occur during the manufacturing or production process, and also has the potential to pollute the environment,[1] in this case the occupational environment. A case in point is exposure to silicon dioxide nanoparticles because silicon dioxide, including a range of its particle sizes, is being used in cosmetics, food,[2] and drug formulations.[3]

Correspondence: Solomon W Leung
Department of Civil and Environmental Engineering, College of Engineering and Biomedical Research Institute, Idaho State University, Pocatello, ID, USA
Email leunsolo@isu.edu

In general, silicon dioxide is viewed as a nontoxic substance and its industrial applications are numerous.[2–4] Nevertheless, there have been reports, at least in the last two decades, that silicon dioxide particles are not as harmless as they were previously assumed to be.

When the size of silicon dioxide is above the micrometer scale (ie, >1 μm), it appears to be benign to human, insects, and microorganisms. However, diatomaceous earth, which contains more than 85% of amorphous silicon dioxide, is used as insecticide in dust form,[4] but its toxicity to insects is not well defined. When the size of silicon dioxide is in the micrometer scale and below, several toxic effects have been observed in humans and animals. Most noticeable is the disease of silicosis in humans,[5] resulting from prolonged exposure to crystalline silica dust, and similar symptoms have also been reported in rats.[5] Thus far, silicon dioxide toxicity reports have been almost exclusively on particle sizes at the micrometer scale, and mostly concerning pulmonary injuries or lung inflammation.[5,6] Few studies have been conducted on silicon dioxide at the nanometer scale,[5,6] and even fewer studies so far reported have been conducted with human cells.

In macroscopic sizes, silicon dioxide is not known to be cytotoxic.[2,3,5,6] However, a recent study demonstrated that exposure of amorphous spherical silicon dioxide nanoparticles of different sizes induced decreases in viability of human endothelial cells, an expression of their cytotoxicity which was apparently dependent on their particle size.[7] Nevertheless, few, if any, studies have examined the putative cytotoxic effects of silicon dioxide nanoparticles on human neural cells.

There was an early study indicating that silica particles (in the micrometer and nanometer ranges) when introduced into the brains of rats and mice induced an inflammatory response in brain astrocytes and macrophages, and the degeneration of some adjacent axons and axon terminals, as elucidated by light and electron microscopy.[8] Furthermore, silicon and aluminum were found to be co-localized in the central region of senile plaque cores in the cortex of patients with senile dementia of the Alzheimer type,[9] and the accumulated silicon and aluminum appeared to be localized, at least in part, in lipofuscin granules in the brains of patients who died with Alzheimer's disease.[10] Consequently, these early studies[8–10] suggest that silicon dioxide nanoparticles may exert cytotoxic effects on neural cells.

We recently found that exposure to titanium dioxide and two other metallic oxide (namely, ZnO and MgO) nanoparticles induced differential cytotoxicity on human neural cells.[11] Because of our recent findings[11] and the increasing evidence that a variety of nanoparticles (including silicon dioxide-containing nanoparticles) can cross the blood–brain barrier,[12,13] we initiated this study to investigate the putative cytotoxic effect(s) of silicon dioxide nanoparticles on human neural cells. In particular, we focused on investigation of the putative cytotoxic effects of these nanoparticles on mitochondrial function and survival cell signaling in human astrocytoma U87 cells that are astrocyte-like in view of the fact that they are good models of astrocytes normally found in the brain in vivo[14,15] and that astrocytes in the brain are functionally coupled to endothelial cells and hence the functions of the blood–brain barrier.[16,17]

Because of the aforementioned considerations, we hypothesized that silicon dioxide nanoparticles induce cytotoxicity in U87 cells by disturbing mitochondrial function and by lowering cell survival via decreasing cell survival signaling. To investigate our hypothesis, we determined the effects of treatment with various concentrations of silicon dioxide nanoparticles on the activities of two key mitochondrial enzymes, ie, citrate synthase and malate dehydrogenase, and expression of the mitochondrial DNA-encoded proteins, cytochrome oxidase subunit II and NADH dehydrogenase subunit 6, and the cell survival signaling pathway protein ERK and phosphorylated ERK in U87 cells.

Materials and methods

Materials

Silicon dioxide nanoparticles (size 12 nm) were purchased from STREM Chemicals, Newburyport, MA. Dulbecco's modified Eagle's medium (DMEM) and other chemicals were purchased from Sigma-Aldrich (St. Louis, MO). U87 cells were obtained from American Type Culture Collection (Manassas, VA).

Cell culture

Human U87 astrocytoma cells were cultured using DMEM supplemented with 10% (v/v) fetal bovine serum and antimycotic solution. The cells were maintained in a 75 cm^2 flask containing 20 mL medium, incubated at 37°C in a CO_2 incubator. When the cells reached 70%–80% confluency, they were harvested either by scrapping or trypsinization and transferred to other flasks.

Preparation of stock suspension of silicon dioxide nanoparticles

The silicon dioxide nanoparticles stock suspension was first prepared by suspending 50 mg of silicon dioxide nanoparticles in a 100 mL conical flask containing sterile phosphate-buffered saline. The suspension was then placed

in a magnetic stirrer to allow the mixture to stir continuously at room temperature before further dilutions were made from the stock (which was being continuously stirred) to be used at specified concentrations and then mixed for use in treating cells.

MTT assay to assess cell viability

Cells were seeded (2000 cells/well) onto a 96-well plate and allowed to attach to the bottom of each well (inner diameter 0.6 cm) for an hour. Silicon dioxide nanoparticles were then added at specified concentrations (0.1–100 μg/mL) to each well containing 0.2 mL with the cells attached at the bottom and mixed. The plates so prepared were incubated for 48 hours at 37°C. MTT dye was then added to each well and the plate incubated for another four hours at 37°C. The purple crystals formed in cells were dissolved using dimethyl sulfoxide and the absorbance of the resultant material in the wells was measured at 567 nm using the microplate reader as described previously.[11]

Determination of mitochondrial enzyme activity

The U87 cells were cultured in DMEM in 75 cm^2 flasks. When the cells were 70%–80% confluent, silicon dioxide nanoparticle treatments were initiated. The mitochondrial function of the untreated and treated U87 cells was assessed by measuring activities of two tricarboxylic acid cycle enzymes, citrate synthase and malate dehydrogenase, in U87 cells treated with silicon dioxide nanoparticles at 0, 25, 50, or 100 μg/mL by previously published methods.[18] The untreated U87 cells served as the control. Citrate synthase and malate dehydrogenase activity in cell homogenates was measured at 412 nm and 340 nm, respectively, using an ultraviolet-VIS spectrophotometer.[18]

Western blot analysis

Expression of the mitochondrial DNA-encoded proteins, NADPH dehydrogenase subunit 6 and cytochrome C oxidase subunit II, and the cell signaling proteins ERK and phosphorylated ERK were determined by Western blot analysis. The U87 cells treated with or without (ie, control) silicon dioxide nanoparticles were collected and homogenized in a buffer containing 5 mM HEPES and 250 mM sucrose, along with protease inhibitors as described previously.[15] Protein content of the homogenates was then determined using the bicinchoninic acid technique with a microplate reader.[11] Briefly, equal amounts of protein from the samples were loaded onto the lanes of the gels, and the proteins were separated by polyacrylamide gel electrophoresis and transferred to a polyvinylidene fluoride membrane.[19] Monoclonal antibodies against the respective proteins were then used to probe the proteins of interest. The polyvinylidene fluoride membrane containing the target protein was then developed using the chemiluminescence technique on an X-ray film to assess the extent of expression of respective proteins.[19]

Assessment of cellular morphology

The morphology of the U87 cells, treated with silicon dioxide nanoparticles for 48 hours at 37°C using specified concentrations, were compared with that of the control or untreated U87 cells by using bright field light microscopy. The images were obtained using a Leica light microscope at 400 × magnification (Leica DM IRB; Leica, Bannockburn, IL) equipped with a digital camera (Leica DFC 300FX; Leica).[15]

Statistical analysis

Data analysis was performed employing one way ANOVA followed by Dunnett's post hoc test using SPSS software (SPSS Inc., Chicago, IL). All data reported are mean ± SEM of three individual experiments. Statistical significance was set at $P < 0.05$.

Results

Effect of nanoparticles on human U87 astrocytoma cell survival

To determine the effect of silicon dioxide nanoparticles on cell survival, U87 cells were exposed to silicon dioxide nanoparticles for 48 hours at concentrations ranging from 0.1 to 100 μg/mL. At lower treatment concentrations, from 0.1 to 10 μg/mL, the nanoparticles did not affect viability of the U87 cells (Figure 1). However, at treatment concentrations of 25 μg/mL and higher, silicon dioxide nanoparticles induced concentration-related decreases in survival of U87 cells.

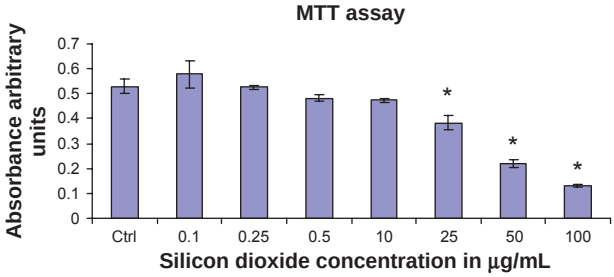

Figure 1 Effect of treatment with silicon dioxide nanoparticles on survival of human astrocytoma U87 cells. U87 cells were treated at specified concentrations of silicon dioxide nanoparticles for 48 hours. Values were the mean ± SEM of at least three separate experiments; CTRL represented the untreated (ie, control) U87 cells; *$P < 0.05$ versus control cells.

At the highest treatment level of 100 μg /mL, less than 30% of the cells survived (Figure 1).

Effect on mitochondrial function in human U87 astrocytoma cells

Because cell survival critically depends on mitochondrial functions being maintained at a normal physiologic level, we determined the effect of silicon dioxide nanoparticles on mitochondrial function in U87 cells by monitoring the activities of citrate synthase and malate dehydrogenase.[18] Both enzymes are nuclear DNA-encoded; these enzyme proteins are synthesized in the endoplasmic reticulum and then imported into the mitochondrial matrix compartment.

At treatment concentrations of 25–100 μg/mL for 48 hours, silicon dioxide nanoparticles induced dose-related increases in citrate synthase activities in U87 cells (Figure 2). On the other hand, although at the same concentrations the nanoparticles also induced significantly increased activity in malate dehydrogenase in U87 cells, the increases were not dose-related (Figure 3). Using the same nanoparticle concentrations for treatment of U87 cells, there was a dose-related decrease in cell survival (Figure 1), and it is likely that the remaining surviving U87 cells were compensating by upregulation of citrate synthase and, to a less extent, malate dehydrogenase, so as to maintain their energy production via tricarboxylic acid cycle metabolism for survival.

Effects of nanoparticles on mitochondrial DNA-encoded and cell signaling protein expression

Because silicon dioxide nanoparticles induced dose-related decreases in survival of U87 cells at concentrations of 25–100 μg /mL over 48 hours (Figure 1), we investigated the possibility that these decreases in survival can be attributed to the nanoparticle-induced alterations in expression of mitochondrial DNA-encoded and cell signaling proteins (Figures 4–6).

At treatment concentrations of 25–100 μg/mL for 48 hours, silicon dioxide nanoparticles induced dose-related decreases in the expression of cytochrome C oxidase subunit II and NADH dehydrogenase subunit 6 (two mitochondrial DNA-encoded peptides) in U87 cells (Figures 4 and 5). These results strongly suggested treatment with silicon dioxide nanoparticles altered the normal functioning of the mitochondrial genome in U87 cells. A likely consequence

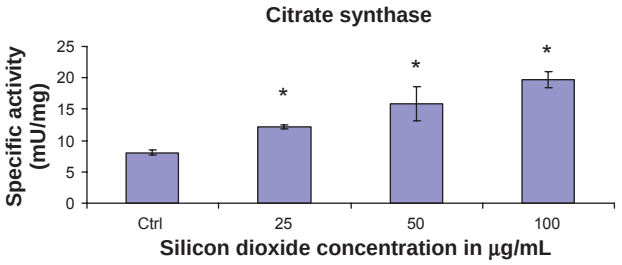

Figure 2 Effect of treatment with silicon dioxide nanoparticles on specific activities of citrate synthase in human astrocytoma U87 cells. U87 cells were treated at specified concentrations of silicon dioxide nanoparticles for 48 hours. Then the activities of citrate synthase in the homogenates of treated and untreated (ie, control, ctrl) U87 cells were determined as described in Materials and methods; the activities of citrate synthase were expressed per mg of homogenate protein as specific activities. The specific activities values were the mean ± SEM of at least three separate experiments; ctrl represented the value in untreated U87 cell homogenate; $^*P < 0.05$ versus that of control cells.

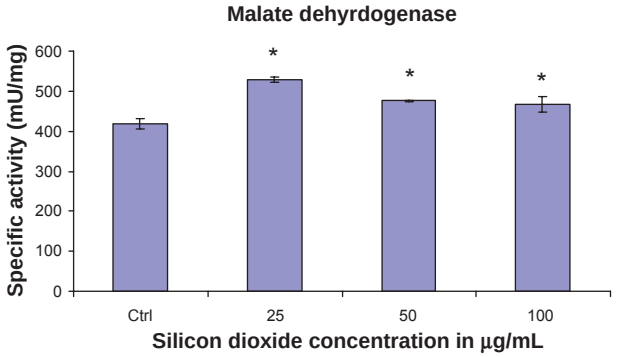

Figure 3 Effect of treatment with silicon dioxide nanoparticles on specific activities of malate dehydrogenase in human astrocytoma U87 cells. U87 cells were treated at specified concentrations of silicon dioxide nanoparticles for 48 hours. Then the activities of malate dehydrogenase in the homogenates of treated and untreated (ie, control, ctrl) U87 cells were determined as described in Materials and methods; the activities of malate dehydrogenase were expressed per mg of homogenate protein as specific activities. The specific activity values were the mean ± SEM of at least three separate experiments; ctrl represented the value in untreated U87 cell homogenate; $^*P < 0.05$ versus that of control cells.

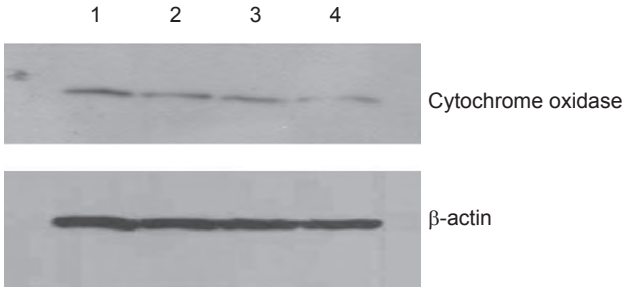

Figure 4 Effect of treatment with silicon dioxide nanoparticles on expression of cytochrome oxidase subunit II in human astrocytoma U87 cells. U87 cells were treated at specified concentrations of silicon dioxide nanoparticles for 48 hours. Then cell lysates of treated and untreated (ie, control) U87 cells were prepared as described in Materials and methods. The expression of cytochrome oxidase subunit II, encoded by mitochondrial DNA, was determined by Western blot analysis using β-actin as the loading control: Lane 1, lysate of untreated or control U87 cells; lane 2, lysate of U87 cells treated with silicon dioxide nanoparticles at 25 μg/mL; lane 3, lysate of U87 cells treated with silicon dioxide nanoparticles at 50 μg/mL; lane 4, lysate of U87 cells treated with silicon dioxide nanoparticles at 100 μg/mL. The blots were from a typical experiment. Two other experiments yielded essentially the same trend of results.

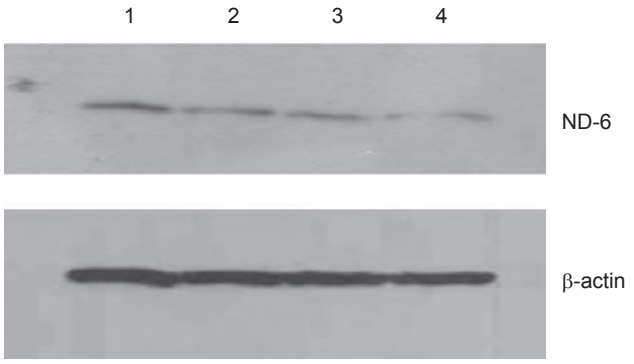

Figure 5 Effect of treatment with silicon dioxide nanoparticles on expression of nicotinamide adenine dinucleotide (NADH) dehydrogenase subunit 6 in human astrocytoma U87 cells. U87 cells were treated at specified concentrations of silicon dioxide nanoparticles for 48 hours. Then cell lysates of treated and untreated (ie, control) U87 cells were prepared as described in Materials and methods. The expression of NADH dehydrogenase subunit 6, encoded by mitochondrial DNA, was determined by Western blot analysis using β-actin as the loading control: Lane 1, lysate of untreated or control U87 cells; lane 2, lysate of U87 cells treated with silicon dioxide nanoparticles at 25 μg/mL; lane 3, lysate of U87 cells treated with silicon dioxide nanoparticles at 50 μg/mL; lane 4, lysate of U87 cells treated with silicon dioxide nanoparticles at 100 μg/mL. The blots were from a typical experiment. Two other experiments yielded essentially the same trend of results.

of this effect is impairment in the mitochondrial electron transport chain in U87 cells. Indeed, the nanoparticle-induced disruption of mitochondrial respiratory chain structure and function may be one cause of energy failure that ultimately led to the death of U87 cells.

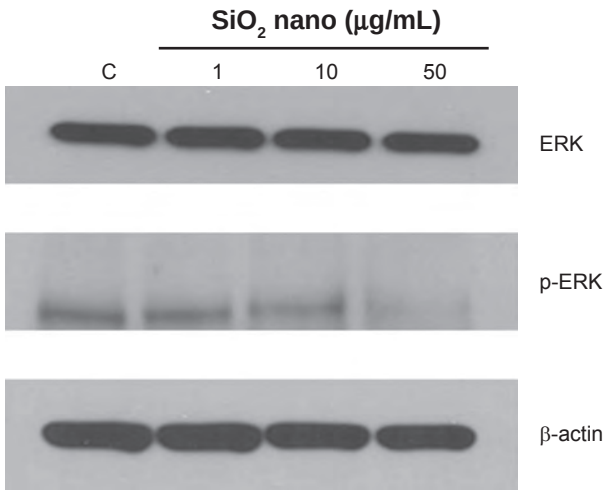

Figure 6 Effect of treatment with silicon dioxide nanoparticles on expression of extracellular signal regulated kinase (ERK) and phosphorylated ERK (p-ERK) in human astrocytoma U87 cells. U87 cells were treated at specified concentrations of silicon dioxide nanoparticles for 48 hours. Then cell lysates of treated and untreated (ie, control) U87 cells were prepared as described in Materials and methods. The expression of ERK and phosphorylated ERK was determined by Western blot analysis using β-actin as the loading control: Lane marked C, lysate of untreated or control U87 cells; lane marked 1, lysate of U87 cells treated with silicon dioxide nanoparticles at 1 μg/mL; lane marked 10, lysate of U87 cells treated with silicon dioxide nanoparticles at 10 μg/mL; lane marked 50, lysate of U87 cells treated with silicon dioxide nanoparticles at 50 μg/mL. The blots were from a typical experiment. Two other experiments yielded essentially the same trend of results.

Other than their effect of depressing the mitochondrial respiratory chain, thereby decreasing oxidative phosphorylation, treatment of U87 cells with silicon dioxide nanoparticles could also lower survival of U87 cells through altering cell signaling pathway(s) that regulate(s) cell survival and proliferation.[20] We therefore investigated this possibility by examining the effect of these nanoparticles on expression of ERK and phosphorylated ERK proteins. We observed that when U87 cells were treated with silicon dioxide nanoparticles 1–50 μg/mL for 48 hours, the protein expression of phosphorylated ERK showed a dose-related decrease, while that of ERK protein remained essentially unchanged (Figure 6), suggesting that a lowering of this cell survival/proliferation signaling mechanism could, at least in part, account for the dose-related decrease in U87 cell survival induced by these nanoparticles.

Effect on morphology of U87 cells

To ascertain whether or not treatment of U87 cells with silicon dioxide nanoparticles led to any gross changes in their morphology, we examined the cells under bright field light microscopy (Figure 7). We observed that as we exposed U87 cells to increasing concentrations of silicon dioxide nanoparticles higher than 25 μg/mL, the cells became more and more enlarged and swollen, suggesting that they assumed a pathologic appearance (Figure 7).

Discussion

Few, if any, recent studies have addressed the cytotoxic effects of silicon dioxide nanoparticles in neural cells. As far as we are aware, ours is the first to report the cytotoxic effects of silicon dioxide nanoparticles on human astrocytoma U87 cells and some of the underlying subcellular mechanisms. Consistent with our hypothesis that silicon dioxide nanoparticles induce cytotoxicity in U87 cells by disturbing mitochondrial function and by lowering cell survival via decreasing cell survival signaling, we found that treatment with silicon dioxide nanoparticles induced concentration-related lowering of protein expression of the mitochondrial DNA-encoded cytochrome C oxidase subunit II and NADH dehydrogenase subunit 6, two key components of the mitochondrial respiratory chain, and phosphorylated ERK, a key cell survival/proliferation signaling molecule in U87 cells. It is noteworthy that we found those changes in protein expression at concentrations of silicon dioxide nanoparticles that correlated with those inducing concentration-related decreases in survival of U87 cells.

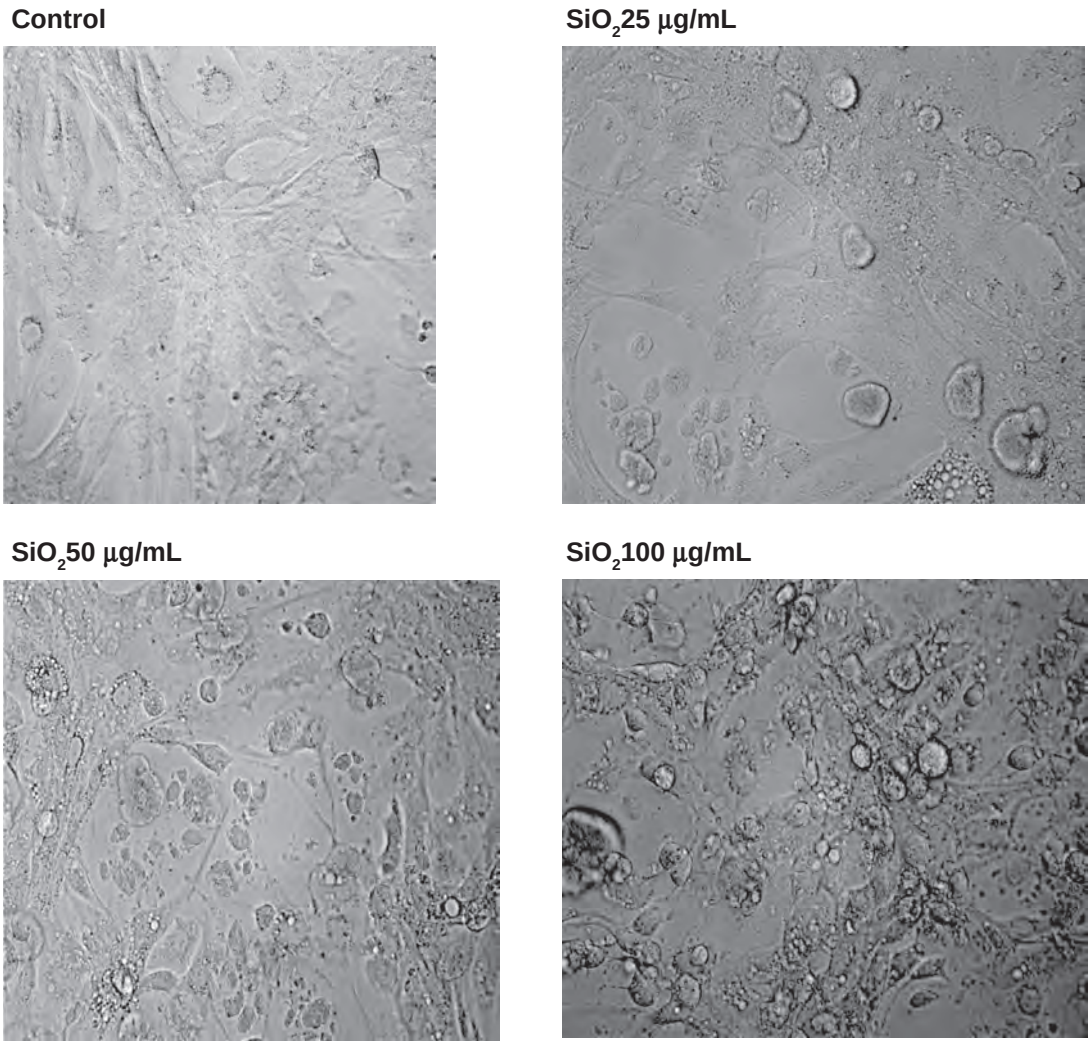

Figure 7 Effect of treatment with silicon dioxide nanoparticles on the morphology of human astrocytoma U87 cells. U87 cells were treated at specified concentrations of silicon dioxide nanoparticles for 48 hours. Then the morphology of treated and untreated (ie, control) U87 cells were assessed using bright field light microscopy at 400 × magnification as described in Materials and methods. The photomicrographs shown were representative of those obtained in several studies.

As emphasized earlier, the initial rationale for focusing our studies on U87 cells was that few studies have addressed the putative cytotoxic effects of silicon dioxide nanoparticles on neural cells, especially those from the human brain. More importantly, not only do astrocytes have many physiologic roles (eg, metabolic trafficking, neurotransmitter cycling, protecting neurons from pathophysiologic assaults),[15,21,22] they also play pathophysiologic roles in disease states (eg, neuroinflammation in neurodegenerative diseases such as Alzheimer's disease and Parkinson's disease).[22] Furthermore, it is relevant to note that although U87 are neurotumor cells, they possess many of the "normal" physiologic characteristics of astrocytes detected in primary cultures of astrocytes and astrocytes in the brain in vivo.[14,15] Thus, U87 cells constitute a good model system in vitro for brain astrocytes.[14,15] Consequently, we have employed U87 cells as a model system to elucidate the putative cytotoxicity of nanoparticles on neural cells in a systematic manner.[11]

One neurotoxic effect of a neurotoxicant, such as manganese, is via a lowering of cell survival/proliferation signaling molecule expression, leading ultimately to death of neural cells.[20] Consistent with this observation is our finding in this study that treatment of U87 cells with increasing concentrations of silicon dioxide nanoparticles induced a dose-related decrease in protein expression of phosphorylated ERK (Figure 6), one important cell survival/proliferation signaling molecule.[20] This effect correlated quite well with the dose-related decrease in survival of these cells (Figure 1) and alterations in their morphology (Figure 7) induced by the nanoparticles. Moreover, we also found that in U87 cells treated in the same nanoparticle dose

range, there was a concentration-related decrease in protein expression of mitochondrial DNA-encoded cytochrome C oxidase subunit II and NADH dehydrogenase subunit 6 (Figures 4 and 5).

Our present findings that exposure of human astrocytoma U87 cells to silicon dioxide induced dose-related decreases in cell survival and alteration of their mitochondrial structure and function (Figures 1–6) are similar to those of Chen et al[23] who demonstrated that exposure of human brain microvascular endothelial cells to aluminum oxide nanoparticles induced decreased viability of those cells, alteration in their mitochondrial membrane potential, and a lowering of their tight junction protein expression. Consequently, in this context, our finding that silicon dioxide nanoparticles induced a dose-related lowering of the expression of cytochrome C oxidase subunit II and NADH dehydrogenase subunit 6 is of pathophysiologic importance and interest in several respects. Because these two peptides are structural components of the mitochondrial respiratory chain complexes IV and I, respectively, and have key functional roles in that respiratory chain,[24] decreased expression of these peptides induced by the nanoparticles likely results in dysfunction in the mitochondrial respiratory chain and oxidative phosphorylation, leading ultimately to decreased adenosine triphosphate synthesis. Consequently, the decreased expression of the two mitochondrial DNA-encoded peptides could likely contribute to decreasing U87 cell survival induced by silicon dioxide nanoparticles through necrotic cell death as a result of energy failure.[11] This conclusion is certainly consistent with our observation that the U87 cells assumed an increasingly swollen appearance, a hallmark of necrosis, as we increased their treatment levels of silicon dioxide nanoparticles (Figure 7). The decreased expression of cytochrome C oxidase subunit II and NADH dehydrogenase subunit 6 peptides induced by the nanoparticles could reflect the effect of the nanoparticles on altering communication between the mitochondrial genome and the nuclear genome, decreasing mitochondrial peptide synthesis, disruption of protein targeting to mitochondria, and/or a combination of these mechanisms. The nanoparticle-induced decrease in protein expression of the two peptides could also result from the overall effect of the nanoparticles on survival/proliferation signaling in U87 cells. Clearly, these are novel but mechanistically relevant possibilities that deserve further investigation.

Unlike the downregulation of the protein expression of mitochondrial DNA-encoded cytochrome C oxidase subunit II and NADH dehydrogenase subunit 6, and the survival/proliferation signaling molecule phosphorylated ERK, treatment of U87 cells with silicon dioxide nanoparticles induced concentration-related increases in the activity of citrate synthase and malate dehydrogenase, both of which are located in the mitochondrial matrix (Figures 2 and 3). Because the increases in citrate synthase and malate dehydrogenase activity were observed at nanoparticle concentrations that also induced dose-related decreases in U87 cell survival (Figure 1), one possible, and likely, explanation for the increased citrate synthase and malate dehydrogenase activity is that the surviving cells were showing compensatory/adaptive mechanisms involving upregulation of tricarboxylic acid cycle enzymes in the mitochondrial matrix of surviving or dying cells, or both, in the face of downregulation of mitochondrial DNA-encoded respiratory chain components, such as cytochrome C oxidase subunit II and NADH dehydrogenase subunit 6. Consequently, this upregulation of tricarboxylic acid cycle enzymes may offset (or compensate for) the effect on mitochondrial energetics through the downregulation of respiratory chain components induced by the nanoparticles. Only future studies can elucidate whether this mechanistic possibility is tenable because they are beyond the scope of the present study.

Because ours is the first study to report on the cytotoxic effects of silicon dioxide nanoparticles on human neural cells, only a few comparisons can be made with the effects of silicon dioxide nanoparticles on neural and peripheral cell types because the literature in this area of research is rather scant.[11] For example, Napierska et al[7] demonstrated exposure of human endothelial cells to amorphous spherical silicon dioxide nanoparticles induced decreases in their viability and this effect was apparently dependent on their particle size. Several groups had also shown that silicon dioxide nanoparticles decreased viability of some peripheral human and other mammalian cell types.[5,25,26] Thus, recent reports,[5,7,25,26] as well as the findings of this study, are in accord in emphasizing that silicon dioxide nanoparticles induces decreased viability of a variety of human and other mammalian cell types. Nevertheless, more systematic studies are required to elucidate fully the molecular mechanisms underlying the cytotoxicity of these nanoparticles.

As we discussed previously, one early study indicated that when silicon nanoparticles were introduced directly into the brains of rats and mice, they induced an inflammatory response in brain astrocytes.[8] Furthermore, silicon was found in senile plaque cores and in lipofuscin granules in the cortex of patients who died of Alzheimer's disease.[9,10]

In view of these earlier findings,[8–10] because astrocytes play important roles in neuroinflammation,[22] and U87 cells constitute a good cell model for astrocytes, the results of this study may have pathophysiologic implications in the inflammation in astrocytes in Alzheimer's disease in particular and in neuroinflammation in general. Thus, the mechanistic connection between the inflammatory response in Alzheimer's disease, neuroinflammation, and the cytotoxic effects of silicon dioxide nanoparticles in neural cells merits further investigation.

Conclusion

This study is the first to report on the cytotoxic effects of silicon dioxide nanoparticles on human astrocytoma U87 cells, and some of the underlying subcellular mechanisms. Consistent with our hypothesis, we found that treatment with silicon dioxide nanoparticles induced concentration-related lowering of protein expression in the mitochondrial DNA-encoded cytochrome C oxidase subunit II and NADH dehydrogenase subunit 6, two key components of the mitochondrial respiratory chain, and phosphorylated ERK, a key cell survival/proliferation signaling molecule in U87 cells. We also noted those changes in protein expression induced by silicon dioxide nanoparticles correlated with concentration-related decreases in survival of U87 cells induced by the nanoparticles. On the other hand, we observed upregulation of citrate synthase and malate dehydrogenase, two key tricarboxylic acid cycle enzymes. Those changes were likely compensatory/adaptive mechanism of dying and/or surviving U87 cells. Thus, our findings may assume pathophysiologic importance in neuroinflammation and Alzheimer's disease and in the environmental health impact of human exposure to these nanoparticles. This is obviously a worthwhile area for further study.

Acknowledgments

Our studies were supported by a US Army Medical Research and Material Command Project Grant (Contract W81XWH-07-2-0078) and National Institutes of Health Grant P20 RR016454 from the Idaho IdeA Biomedical Research Excellence Program of the National Center for Research Resources. JCKL and GA contributed equally to this work.

Disclosure

The authors report no conflicts of interest in this work.

References

1. Environmental Protection Agency. Draft Nanomaterial Research Strategy. Available at: (http://epa.gov/ncer/nano/publications/nano_strategy_012408.pdf). Accessed August 3, 2010.
2. Martin KR. The chemistry of silica and its potential health benefits. *J Nutr Health Aging*. 2007;11:94–97.
3. Jonat S, Hasenzahl S, Gray A, Schmidt PC. Influence of compacted hydrophobic and hydrophilic colloidal silicon dioxide on tableting properties of pharmaceutical excipients. *Drug Dev Ind Pharm*. 2005; 31:687–696.
4. Ulrichs C, Krause F, Rocksch T, et al. Electrostatic applications of inert silica dust based insecticides onto plant surfaces. *Commun Agric Appl Biol Sci*. 2006;71:171–178.
5. Sayes CM, Reed KL, Warheit DB. Assessing toxicity of fine and nanoparticles: Comparing in vitro measurements to in vivo pulmonary toxicity profiles. *Toxicol Sci*. 2007;97:163–180.
6. Adams LK, Lyon DY, McIntosh A, Alvarez PJ. Comparative toxicity of nano-scale TiO_2, SiO_2, and ZnO water suspensions. *Water Sci Technol*. 2006;54:327–334.
7. Napierska D, Thomassen LC, Rabolli V, et al. Size-dependent cytotoxicity of monodisperse silica nanoparticles in human endothelial cells. *Small*. 2009;5:846–853.
8. Rees S, Cragg B. Is silica involved in neuritic (senile) plaque formation? *Acta Neuropathol*. 1983;59:31–40.
9. Candy JM, Oakley AE, Klinowski J, et al. Aluminosilicates and senile plaque formation in Alzheimer's disease. *Lancet*. 1986;1: 354–357.
10. Takutake S, Oyanagi S. Accumulation of aluminium and silicon in lipofuscin granules. *Gerontology*. 1995;41 Suppl 2:131–144.
11. Lai JC, Lai MB, Jandhyam S, et al. Exposure to titanium dioxide and other metallic oxide nanoparticles induces cytotoxicity on human neural cells and fibroblasts. *Int J Nanomedicine*. 2008;3:533–545.
12. Kim JS, Yoon T-J, Yu KN, et al. Toxicity and tissue distribution of magnetic nanoparticles in mice. *Toxicol Sci*. 2006;89:338–347.
13. Sharma HS, Hussain S, Schlager J, et al. Influence of nanoparticles on blood-brain barrier permeability and brain edema formation in rats. *Acta Neurochir Suppl*. 2010;106:359–364.
14. Malthankar GV, White BK, Bhushan A, et al. Differential lowering by manganese treatment of activities of glycolytic and tricarboxylic acid (TCA) cycle enzymes investigated in neuroblastoma and astrocytoma cells is associated with manganese-induced cell death. *Neurochem Res*. 2004;29:709–717.
15. Dukhande VV, Malthankar-Phatak GH, Hugus JJ, et al. Manganese induced neurotoxicity is differentially enhanced by glutathione depletion in astrocytoma and neuroblastoma cells. *Neurochem Res*. 2006;31:1349–1357.
16. Haseloff RE, Blasig IE, Bauer H-C, Bauer H. In search of the astrocytic factor(s) modulating blood-brain barrier functions in brain capillary endothelial cells in vitro. *Cell Mol Neurobiol*. 2005;25: 25–39.
17. Liebner S, Plate KH. Differentiation of the brain vasculature: The answer came blowing by the Wnt. *J Angiogenes Res*. 2010:2:1–10.
18. Clark JB, Lai JCK. Glycolytic, tricarboxylic acid cycle, and related enzymes in brain. In: Boulton AA, Baker GB, Butterworth RF (editors). *NeuroMethods Vol 11*. Clifton, NJ: Humana Press; 1989:233–281.
19. Isaac AO, Dukhande VV, Lai JCK. Metabolic and antioxidant system alterations in an astrocytoma cell line challenged with mitochondrial DNA deletion. *Neurochem Res*. 2007;32:1906–1918.
20. Puli S, Lai JCK, Edgley KL, et al. Signaling pathways mediating manganese-induced neurotoxicity in human glioblastoma cells (U87). *Neurochem Res*. 2006;31:1211–1218.
21. Faharani R, Pina-Benabou MH, Kyrozis A, et al. Alterations in metabolism and gap junction protein expression may determine the role of astrocytes as "Good Samaritans" or executioners. *Glia*. 2005;50: 351–361.

22. Sofroniew MV, Vinters HV. Astrocytes: Biology and pathology. *Acta Neuropathol*. 2010;119:7–35.
23. Chen L, Yokel RA, Hennig B, Toborek M. Manufactured aluminum oxide nanoparticles decrease expression of tight junction proteins in brain vasculature. *J Neuroimmune Pharmacol*. 2008;3:286–295.
24. Heales SJR, Gegg ME, Clark JB. Oxidative phosphorylation: Structure, function, and intermediary metabolism. *Int Rev Neurobiol*. 2002; 53:25–56.
25. Lin W, Huang YW, Zhou XD, Ma Y. In vitro toxicity of silica nanoparticles in human lung cancer cells. *Toxicol Appl Pharmacol*. 2006;217:252–259.
26. Adili A, Crowe S, Beaux II FM, et al. Differential cytotoxicity exhibited by silica nanowires and nanoparticles. *Nanotoxicology*. 2008;2:1–8.

A Cell Culture Model for Diabetic Neuropathy Studies

Ashvin R. Jaiswal[1], Alok Bhushan, Christopher K. Daniels and

James C.K. Lai[2]

Department of Biomedical and Pharmaceutical Sciences,

College of Pharmacy, and Biomedical Research Institute,

Idaho State University, Pocatello, ID 83209, USA

Fax: 208-282-4305;

Tel: 208-282-2275;

email: lai@pharmacy.isu.edu

[1]Presenting author.

[2]Corresponding author.

A Cell Culture Model for Diabetic Neuropathy Studies

Abstract :

Diabetic neuropathy is one of the most severe complications of chronic diabetes. Though several theories exist, the pathophysiology of the disease is poorly understood. We have therefore developed an *in vitro* model to elucidate its underlying pathophysiologic mechanisms. We believe our model allows us to gain new insights into such mechanisms. Moreover, our model improves on existing primary culture models because the latter change with passage number and have limited life-span. We hypothesize that high glucose treatment induces oxidative stress and decreases GSH level, ultimately leading to apoptosis in dorsal root ganglion (DRG) neurons and Schwann cells. Results of our ongoing studies suggest exposure of DRG neurons to high levels of glucose (e.g., 45 & 60 mM), conditions that favor increased ROS generation, decrease their survival, eventually leading to cell death whereas in co-culture, Schwann cells help protect DRG neurons and enhance their survival. Other studies are in progress to further characterize our cell model. Thus, results of our ongoing studies are consistent with the notion that our cell model is appropriate for investigation of diabetic neuropathy.

Keywords: Cell Culture Model, Diabetic Neuropathy, Neurodegeneration

Introduction:

Diabetes is the disease of high blood glucose and according to the American Diabetic Association, 23.6 million people (8% of United States populations) have diabetes. Diabetic neuropathy is one of the most severe complications of diabetes, an

inflammatory condition in which the nerves in the extremities of the body become damaged, ultimately resulting in death of nerve cells (Brownlee 2001, Figueroa-Romero et al. 2008, Leinninger et al. 2006). It affects more that 60% of diabetic population (Figueroa-Romero et al. 2008). Some of the serious complications of nerve damage as a result of diabetes include loss of sensation or pain in limbs, adverse effects on digestion, decreased sexual response, and urinary tract infection. Half of the foot amputations in the United States constitute the consequence of diabetic neuropathy. There is little advancement in the management and treatment of diabetic neuropathy because it is very difficult to predict and monitor nerve cell damage.

Various *in vivo* and *in vitro* models mimicking closely or approximately the diabetic pathologies in humans have been devised to investigate pathophysiological mechanisms of the disease. Each model has its own advantages and limitations. *In vivo* models are preferred in elucidating the etiology of the disease and for testing the efficacy of potential therapies. However, limitations of *in vivo* models include inability to tightly control their glycemic status and the fact that these models do not lend themselves readily for use in investigating the pathophysiology of the disease at the cellular and molecular levels (Apfel 2006).

Unlike *in vivo* models, *in vitro* models of diabetes in general and diabetic neuropathy in particular allow investigations of pathophysiological/pathogenic mechanisms at the cellular and molecular levels (Sango et al. 2006). For example, these models permit the examination of effects of high glucose on neurons in a controlled environment (Sango et al. 2006). Nevertheless, there is no *in vitro* cell model available whereby one could study the long-term exposure of dorsal root ganglion

(DRG) neurons and/or Schwann cells to high and pathologic levels of glucose. To address this need for such model(s), we have been systematically developing different co-culture models of DRG neurons and Schwann cells because the DRG neurons *in vivo* are always surrounded by Schwann cells and Schwann cells protect them from any damage or cell death (Vincent et al. 2005). We hypothesize that immortalized cell culture models using DRG neurons, Schwann cells and their co-cultures can be productively employed to elucidate the pathophysiological and/or pathogenic mechanisms of diabetic neuropathy. This study was initiated to investigate our hypothesis.

Materials and Methods:

Cell Cultures. The immortalized DRG neurons were a gift from Dr. Ahmet Hoke's laboratory at Johns Hopkins University (Baltimore, MD, USA) (Chen et al. 2007). The rat Schwann cell line was obtained from ATCC (Manassas, VA, USA). These cells and their co-culture were cultured in DMEM (Sigma; St Louis, MO, USA) supplemented with 10% (v/v) fetal bovine serum (FBS), 1% (w/v) sodium pyruvate, 0.292 g/l L-glutamine, 1.5 g/l sodium bicarbonate, 1% (v/v) anti-mycotic and various specified concentrations (5-45 mM) of glucose.

Cell Survival (MTT) Assay. 8000-10000 DRG neurons or Schwann cells were seeded per well in a 48-well plate in a medium with a normal or high glucose concentration. After incubation at 37^{o}C for 48 hours, 50 µl of MTT (5 mg/ml in PBS) reagent was added to each well. After incubation for another 4 hours, the medium was removed gently and the cellular reaction product was extracted in 200 µl DMSO. Then the optical density of

contents of each well was measured in a plate reader at 570 nm. The absorbance was proportional to the number of live cells previously present in each well.

Reactive Oxygen Species (ROS) Assay. Cells in a medium with normal or high glucose were incubated at 37^{o}C for 48 hours and then 200 µl of H_2DCF dye (10 µM in PBS) was added to each well. After another 45 minutes, the medium was removed gently and 200 µl of PBS was added in each well. The fluorescence output in each well was measured in the plate reader set at 489 nm excitation-521 nm emission in the fluorescence mode. The fluorescence output corresponded to the ROS produced by cells present in each well and was normalized with respect to cellular protein, which was determined using the BCA Protein Assay Kit.

Glutathione (GSH) Assay. GSH in cell homogenates was measured using Ellman's reagent (5,5'-dithiobis-(2-nitrobenzoic acid) or DTNB) as described previously (Dukhande et al. 2006).

Co-culture of DRG neurons and Schwann cells. Our co-culture model closely mimic the physiological conditions of DRG neurons & Schwann cells because Schwann cells always surround DRG neurons *in vivo* and protect them from pathophysiological assaults. DRG neurons & Schwann cells were cultured at 37^{o}C and 5% CO_2 in Dulbecco's Modified Eagle's Medium supplemented with 10% FBS and counted using a Coulter counter after 24 hours or at about 60-70 % confluence. DRG neurons were seeded on a Corning Costar 24-well plate. Schwann cells were then seeded on a Millipore hanging cell culture insert (pore size 0.4 µm) on a separate plate and then introduced to a DRG neuron-containing well after 4 hours to achieve the co-culture condition. DRG neurons (co-cultured with Schwann cells) were exposed to various

levels of glucose for specified periods and their survival determined employing the cell survival assay.

Statistical analysis of results. Statistical significance of experimental results was analyzed with one-way ANOVA followed by Dunnett's post-hoc test using SPSS 17 software package, with a minimum significance level set at $p < 0.05$.

Results and Discussion:

Diabetic neuropathy affects the peripheral nervous system (PNS) the most: dorsal root ganglion (DRG) neurons in PNS are especially susceptible to high glucose-induced cell damage and/or death. Therefore, we used DRG neurons to develop a cell culture model for diabetic neuropathy and have begun to characterize it. When we exposed DRG neurons to various glucose levels, we noted that these cells survived best at 25 mM of glucose (Fig. 1), a level higher than the physiological level of 5.5 mM. Relevant to our finding (Fig. 1) is the observation of Izawa et al. (2009) who found that lactate produced by Schwann cells may be a fuel for DRG neuronal energy metabolism.

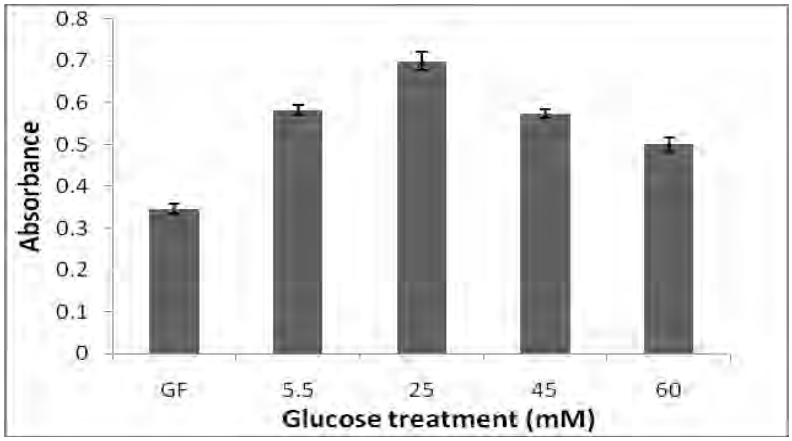

Fig. 1 Survival of DRG Neurons after 24-hour Exposure to Different Glucose Concentrations.

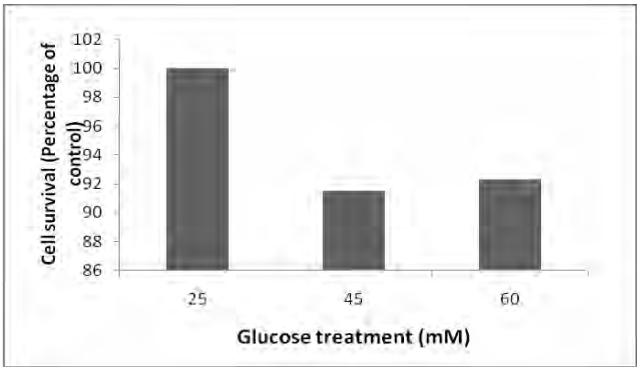

Fig. 2 Survival of DRG Neurons after exposure to high glucose for 24 hours. (*p<0.05 compare to 25 mM of glucose)

Schwann cells usually surround DRG neurons *in vivo*, provide them with glycolytic intermediates (Miller et al. 2002) and protect them from pathophysiological assaults. Consistent with this notion is our observation that both cell types survived better in co-culture than when they were cultured alone (data not shown). Furthermore, when DRG neurons are cultured alone, they need more glucose because of the absence of the glycolytic intermediates normally supplied to them by Schwann cells (Miller et al. 2002). Based on the above considerations and our finding that DRG neurons showed optimal survival with 25 mM glucose (Figs. 1 and 2), we employed 25 mM of glucose as a control parameter when DRG neurons and Schwann cells are cultured separately and 5.5 mM of glucose as a physiological control when we co-cultured them.

Exposure of neural cells to high glucose increases reactive oxygen species (ROS) production, a by-product of glucose metabolism and marker of diabetic neuropathy (Vincent et al. 2005). Consistent with this notion is our finding that ROS production by DRG neurons was increased whey they were exposed to glucose level higher than 25

mM (Fig. 3). Clearly the mechanisms underlying the increased ROS production by DRG neurons in high glucose merit further elucidation.

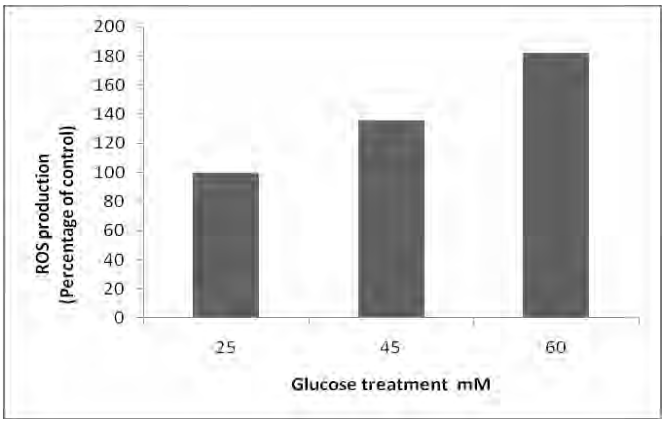

Fig. 3 ROS Production by DRG Neurons after Exposures to High Glucose Concentrations

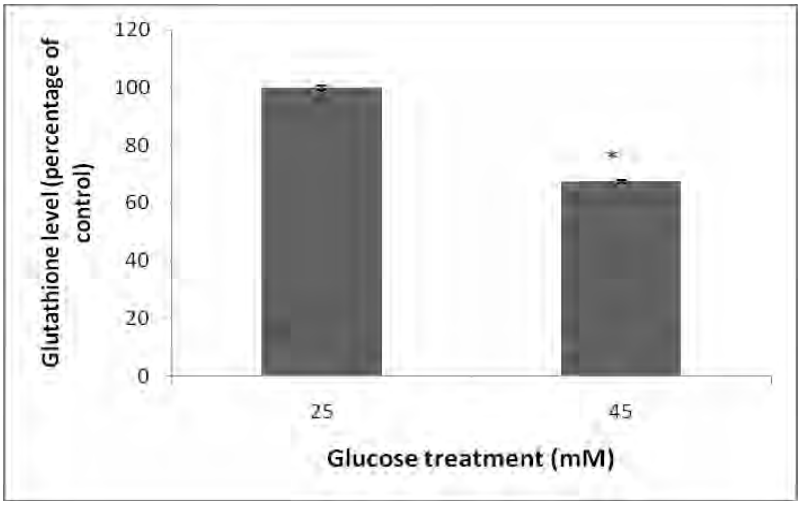

Fig. 4 Changes in Glutathione Level in Schwann Cells after Exposure to High Glucose for 24 hr (*p<0.05 compare to 25 mM of glucose)

Because glial cells in brain have a protective role on neurons (Dukhande et al. 2006), we investigated the possibility that under the stress of exposure to high glucose, Schwann cells may produce less glutathione (antioxidant) thereby decreasing their

ability to protect DRG neurons. We exposed Schwann cells to high glucose and measured their glutathione content. Consistent with this hypothesis is our finding that exposure to high glucose induced decreases in glutathione in Schwann cells compared to their levels when treated with 25 mM of glucose (Fig. 4).

In conclusion, results from this study strongly suggest our model is suitable for systematic investigation of mechanisms underlying pathophysiology and pathogenesis of diabetic neuropathy. Thus, these results (and those to be obtained in our ongoing studies) provide additional insights into cellular and molecular mechanisms relevant to diabetic neuropathy and as such may be implicated not only in this disease but also in other chronic diseases such as Alzheimer's disease and Parkinson's disease.

Acknowledgements:

We thank Dr. Ahmed Hoke (Johns Hopkins University School of Medicine) for his generous gift of DRG neurons. Our study was supported, in part, by an USAMRMC Project Grant (Contract #W81XWH-07-2-0078), and NIH Grant #P20 RR016454 from the Idaho INBRE Program of the National Center for Research Resource**s.**

References:

Apfel SC. 2006. Diabetic neuropathy models: Are they relevant? Drug Discovery Today: Disease Models 3: 397-402.

Brownlee M. 2001. Biochemistry and molecular cell biology of diabetic complications. Nature 414: 813-820.

Chen W, Mi R, Haughey N, Oz M, Höke A. 2007. Immortalization and characterization of a nociceptive dorsal root ganglion sensory neuronal line. Journal of the Peripheral Nervous System 12: 121-130.

Dukhande VV, Malthankar-Phatak GH, Hugus JJ, Daniels CK & Lai JCK 2006. Manganese-Induced Neurotoxicity is Differentially Enhanced by Glutathione Depletion in Astrocytoma and Neuroblastoma Cells. Neurochemical Research 31: 1349-1357.

Figueroa-Romero C, Sadidi M, Feldman E. 2008. Mechanisms of disease: The oxidative stress theory of diabetic neuropathy. Reviews in Endocrine & Metabolic Disorders 9: 301-314.

Izawa Y, Takahashi S, Suzuki N. 2009. Pioglitazone enhances pyruvate and lactate oxidation in cultured neurons but not in cultured astroglia. Brain Research 1305: 64-73.

Leinninger GM, Edwards JL, Lipshaw MJ, Feldman EL. 2006. Mechanisms of Disease: mitochondria as new therapeutic targets in diabetic neuropathy. Nat Clin Pract Neuro 2: 620-628.

Miller KE, Richards BA, Kriebel RM. 2002. Glutamine-, glutamine synthetase-, glutamate dehydrogenase- and pyruvate carboxylase-immunoreactivities in the rat dorsal root ganglion and peripheral nerve. Brain Research 945: 202-211.

Sango K, Saito H, Takano M, Tokashiki A, Inoue S, Horie H. 2006. Cultured Adult Animal Neurons and Schwann Cells Give Us New Insights into Diabetic Neuropathy. Current Diabetes Reviews 2: 169-183.

Vincent AM, McLean LL, Backus C, Feldman EL. 2005. Short-term hyperglycemia produces oxidative damage and apoptosis in neurons. FASEB J 19(6): 638-640.

Further Elucidation of Neuroprotective Properties of Astrocytoma (Astrocytes-like) Cells

Yin Yin Wendy Wong[1], Ashvin R. Jaiswal[2], Alok Bhushan[2], Solomon W. Leung[3], and James C.K. Lai[4]

[1]Presenting author: Department of Biomedical & Pharmaceutical Sciences, College of Pharmacy, and Biomedical Research Institute, Idaho State University, Pocatello, ID 83209, USA

[2]Department of Biomedical & Pharmaceutical Sciences, College of Pharmacy, and Biomedical Research Institute, Idaho State University, Pocatello, ID 83209, USA

[3]Department of Civil and Environmental Engineering, College of Engineering, and Biomedical Research Institute, Idaho State University, Pocatello, ID 83209, USA

[4]Corresponding author: Department of Biomedical and Pharmaceutical Sciences, College of Pharmacy, and Biomedical Research Institute, Idaho State University, Pocatello, ID 83209, USA Fax: 208-282-4305; Tel: 208-282-2275; email: lai@pharmacy.isu.edu

Further Elucidation of Neuroprotective Properties of Astrocytoma (Astrocytes-like) Cells

Abstract:

Astrocytes protect neurons against various assaults although the underlying pathophysiological and molecular mechanisms are poorly understood. Therefore, we have continued to develop cell models *in vitro* to further investigate the putative neuroprotective properties of astrocyte-like astrocytoma cells. We hypothesized that different stress factors can elicit and/or enhance the neuroprotective effects of astrocytes through the activation of astrocytic survival signaling and alteration of astroglial function. Employing cell models involving astrocytes-like U87 astrocytoma and neurons-like SK-N-SH cells, results of our previous and ongoing studies suggest that U87 cells protect SK-N-SH cells against cytotoxicity due to oxidative stress. Other ongoing studies target the putative neuroprotective effect(s) of U87 cells due to alterations of cell signaling and/or other astroglial function(s). Thus, our results may have implications for the pathophysiology of neuroprotection.

Keywords: Astrocytes; neuroprotection; astroglial function; U87 astrocytes-like astrocytoma cells; SK-N-SH neurons-like neuroblastoma cells

Introduction:

Astrocytes (non-neuronal, glial cells) in the brain are known to play important roles in protecting neurons (nerve cells) against various assaults although the

underlying mechanisms are incompletely understood (Sofroniew et al. 2010). Well known chronic neurodegenerative diseases, such as Alzheimer's disease (AD) and Parkinson's disease (PD), are correlated with neuronal cell death, which involves many factors alone or in combination (Przedborski et al. 2003). Among all neurodegenerative diseases, significant attention has been given to Alzheimer's disease (AD), following by Parkinson's disease (PD) (Przedborski et al. 2003). While the signs and symptoms of AD affect such patients' quality of life, the conditions that lead to memory loss and death of neurons in this disease state are not yet defined. AD remains one of the top ten leading causes of death in the elderly population in the United States and it is referred as the progressive and irreversible neurodegenerative disorder in human brain (Chung, 2009). Current therapy predominantly treats AD symptoms and, at best, helps the disease from worsening as there is no known cure available for AD. Hence, there is an urgent need to better understand how astrocytes exert their protective effects on neurons. Once the mechanisms for astrocyte-mediated neuronal protection are elucidated, one can design treatment strategies to prevent the occurrence of accelerated neuronal loss in neurodegenerative diseases such as AD and PD.

Our project seeks to examine the underlying neuroprotective properties offered by astrocytes to protect neurons employing a cell model system *in vitro.* We have therefore developed cell model systems to investigate cytotoxic and inflammatory mechanisms associated with induction of neuronal cell damage and cell death (Malthankar et al. 2004, Dukhande et al. 2006, Wang et al. 2008). We have previously shown that U87 astrocytoma and SK-N-SH neuroblastoma cells constitute good model systems for astrocytes and neurons, respectively, *in vitro* because of their close

functional resemblance to normal astrocytes and neurons and that U87 cells protect SK-N-SH cells from several pathological assaults (Malthankar et al. 2004, Dukhande et al. 2006). We therefore hypothesized that different stress factors (e.g. oxidative stress and nutrient depletion) can elicit and/or enhance the neuroprotective effects of astrocytes through the activation of astrocytic signaling and alteration of astroglial function. In this study, we have investigated this hypothesis further.

Materials and Methods:

Cell culture

The human astrocytoma (U87) and neuroblastoma (SK-N-SH) cell lines were obtained from (ATCC; Manassas, VA, USA) and cultured in Minimum Essential Medium (MEM) supplemented with 10% (v/v) fetal bovine serum (Atlanta Biologicals; Lawrenceville, GA), 1% (w/v) sodium pyruvate (Sigma Aldrich; St Louis, MO), 0.292 g/L L-glutamine (Sigma), 1.5g/L sodium bicarbonate (Sigma) and 1% (v/v) antimycotic (Atlanta Biologicals). Cells were maintained at 37°C and 5% (v/v) CO_2 as described previously (Malthankar et al. 2004, Dukhande et al. 2006).

Treatment of U87 cells

The U87 cells were cultured in T-75 tissue culture flasks until ~50% confluent in 20 ml of 10% FBS MEM medium. Then the medium was discarded and changed with 20 ml of 5% FBS-MEM medium and the cells incubated for 24 hours. After that, the medium was replaced with 20 ml of medium without FBS and the cells incubated for an additional 24 hours. Cells were treated with 5mM L-sulfoximine buthionine (BSO), or 20nM pioglitazone (PZ) or a combination of both frugs at the same concentrations. At

the end of another 24 hours of incubation, the media were first removed and frozen with liquid nitrogen immediately. The cells were collected subsequently and both cells and media collected were kept at -80°C until used for experiments.

Cell Survival (MTT) assay

The neuroprotective properties of U87 cells on SK-N-SH cells were determined in different combinations of regular media (RM) and conditioned media (CM) collected from U87 cells cultured (see above) with RC/CM ratios of 100/0, 70/30, 50/50, 40/60, 30/70, and 0/100. 5000 SK-N-SH cells were seeded per well in a 48-well plate. After 48 hours of incubation at 37°C, 50 µl thiazolyl blue tetrazolium bromide (MTT) (5 mg/ml in PBS) reagent was added to each well. The medium in each well was removed after 4 hours at 37°C and the purple formazan crystals formed were solubilized using DMSO. Optical densities (OD) of the contents of the wells were read in a plate reader at 570 nm; the OD corresponded to the proportion of live cells in each well (Dukhande et al. 2006).

Western Blot Analysis

Western blot analysis was used to assess protein expression in cell lysates to determine the effects of media, BSO and PZ. 10% SDS-PAGE gel electrophoresis was performed as described by Dukhande et al. (2006). The separated proteins were probed with anti-glutamine synthetase and anti-glial fibrillary acidic protein antibodies and then visualized using chemiluminesence detection kit with β-actin as the loading control.

Statistical Analysis of Data

Statistical significance of experimental results was analyzed with one-way ANOVA followed by Tukey's post-hoc test with a minimum significance level set at $p < 0.05$ using Kaleidagraph 4.0 software package.

Results and Discussion:

Being a selective inhibitor of glutathione (a naturally-occurring antioxidant) synthesis, L-buthionine sulfoximine (BSO) is used to induce oxidative stress in cells. Pioglitazone (PZ), a peroxisome proliferator activated receptor gamma (PPARγ) agonist, is used to block the inflammation which is usually unregulated in AD (Yamagishi 2000, Syversen et al. 2009). Consequently, we designed studies whereby we could use BSO and PZ to further elucidate the putative protective mechanism(s) on neurons-like SK-N-SH cells derived from conditioned media in which astrocytes-like U87 cells had been exposed to BSO or PZ or a combination of both drugs.

Serum depletion and drug treatment for U87 cell cultures were prepared as shown the flow chart below (Fig. 1). U87 cells cultured in medium containing 10% FBS were used as control (not shown in Fig. 1). Medium containing 0% FBS were defined as serum free (SF) medium.

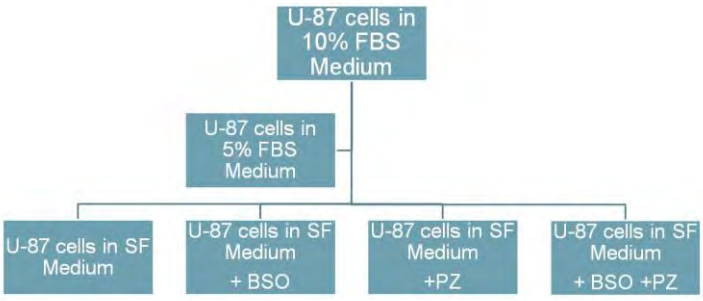

Figure 1. Experimental design of U87 cells treated with BSO, PZ or in combination.

Because oxidative and other environmental stresses can induce morphological and function changes/adaption in astrocytes *in vivo* and in culture, we employed light microscopy (by taking photomicrographs at 100x magnification) to examine the effects

of BSO treatment and FBS depletion to induce oxidative and environmental stress, respectively, on U87 cells and assess the effects of PZ treatment thereon.

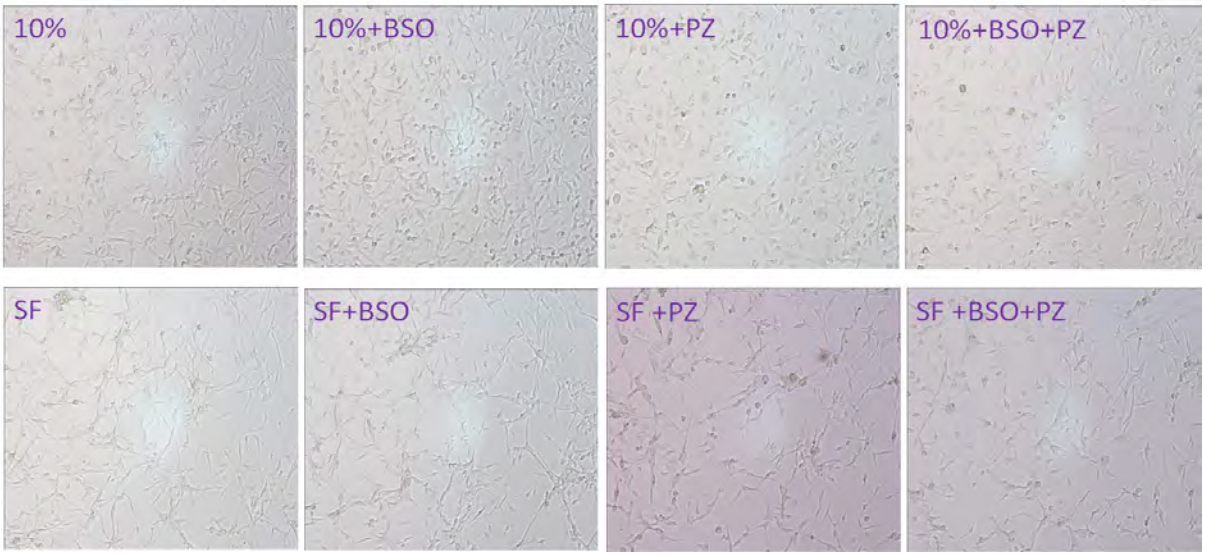

Figure.2 Treatment-induced cellular morphology changes in U87 cells (100X magnification).

In Figure 2, the top panel of photomicrographs shows U87 cells cultured in 10% FBS medium treated with or without drug or drug combination while those of the bottom panel represents U87 cells cultured in serum-deprived (SF) medium treated with or without drug or drug combination. In general, the photomicrographs revealed that treatment with SF medium induced U87 cells to extend multipolar processes. Moreover, treatment of U87 cells with or without drug treatment led to further changes in cellular morphology (e.g., extension of processes and shape changes) in addition to that noted in the U87 cells cultured in SF medium. Clearly, these observations raise interesting mechanistic questions that need to be addressed further: we were able to address two of these issues (see below) while others are beyond the scope of this study.

GFAP is an established marker for astrocytes: its altered expression is associated with changes in astroglial morphology. Thus, we employed Western blot to determine if the morphological changes in U87 cells exposed to SF medium with and

without BSO/PZ treatment were also associated with changes in glial fibrillary acid protein (GFAP) expression. GFAP expression was increased when U87 cells were cultured in SF medium compared to those cultured in 10% FBS medium, suggesting a correlation between changes its expression and cellular morphology (data not shown).

A key detoxification enzyme in astrocytes, glutamine synthetase (GS) can detoxify the exitotoxins glutamate and ammonia and its expression is modulated by changes in the surroundings of astrocytes. However, employing Western blot analysis we found little, if any, changes of GS expression in U87 cells exposed to the conditions employed (data not shown).

Growth factors and neuronal survival enhancers are putatively released into the medium by astrocytes to protect their surrounding neurons. To further investigate this neuroprotective mechanism, we collected media in which we grew U87 cells under the conditions specified in Figure 1 above and assessed their ability to influence survival of SK-N-SH cells employing the MTT cell survival assay (Fig. 3). Our results suggested that exposure of SK-N-SH cells to various combinations of SF media allowed them to survive better than when cultured in 10% FBS medium (control condition) alone (Fig. 3). Specifically, we found that exposure to PZ enhanced this protective effect, even under conditions of oxidative stress.

In conclusion, results from this study suggest changes in cell morphology of astrocytes-like U87 cells in various environmental conditions (e.g., serum deprivation & oxidative stress) can be correlated with up-regulation of GFAP in U87 cells.

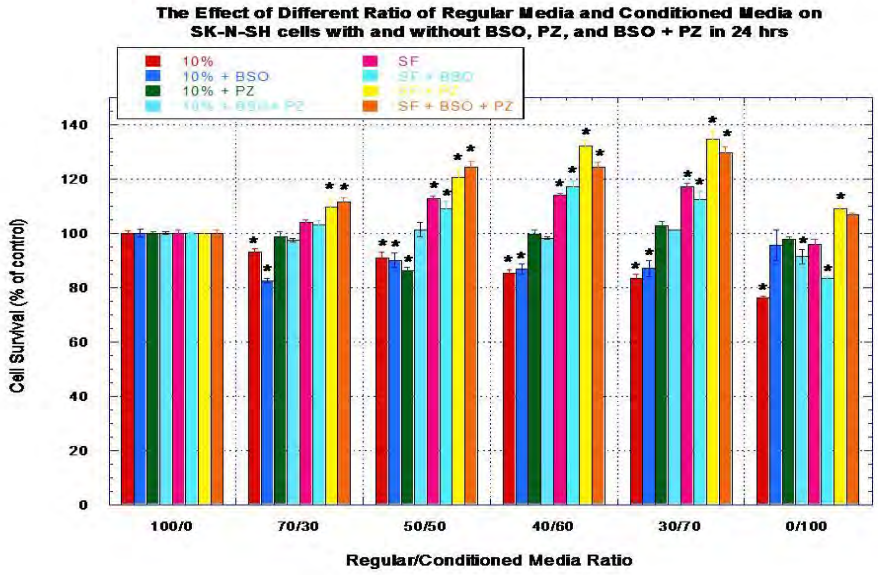

Figure 3. Treatment effects on SK-N-SH cell survival.

Our findings also suggest that conditioned medium has the ability to enhance the survival of neurons-like SK-N-SH cells and PZ treatment modulates this effect. Thus, our results provide additional evidence that our cell model can be productively employed to further elucidate the putative neuroprotective mechanisms of astrocytes. As such they assume pathophysiological importance in neuronal survival/death mechanisms in neurodegenerative diseases such as AD and PD. Clearly, this is an area that merits further study.

Acknowledgment:

Our studies were supported by NIH RO1 NS054038-01A1 subaward #A06474 and USAMRMC Project Grant (Contract #W81XWH-07-2-0078).

References:

Chung S. 2009. Aberrant phosphorylation in the pathogenesis of Alzheimer's disease. BMB Rep. 42(8): 467-474.

Dukhande VV, Malthankar-Phatak GH, Hugus JJ, Daniels CK, Lai JCK. 2006. Manganese induced neurotoxicity is differentially enhanced by glutathione depletion in astrocytoma and neuroblastoma cells. Neurochem Res. 31(11):1349-1357.

Malthankar GV, White BK, Bhushan A, Daniels CK, Rodnick KJ, Lai JCK. 2004. Differential lowering by manganese treatment of activities of glycolytic and tricarboxylic acid cycle enzymes in neuroblastoma and astrocytoma cells is associated with manganese-induced cell death. Neurochem Res. 29:709-717.

Przedborski S, Vila M, Jackson-Lewis V. 2003. Neurodegeneration: What is it and where are we? Journal of Clinical Investigation. 111(1): 3-10.

Sofroniew M V, Vinters H V. 2010. Astrocytes: biology and pathology. Acta Neuropathol. 119:7-35.

Syversen, U., Stunes, A K, Gustafsson, B I. et al. 2009. Different skeletal effects of the peroxisome proliferator activated receptor (PPAR) α agonist fenofibrate and the PPARγ agonist pioglitazone. *BMC Endocrine Disorders*. 9:10

Wang Y-H, Jandhyam S, Dukhande VV, Gao WJ, Gu H-Y, Lai MB, Leung SW, Lai JCK. 2008. A co-culture model for nanotoxicity and tissue engineering studies. In Technical Proceedings of the 2008 Nanotechnology Conference and Trade Show; Volume 2, Chapter 2: Environment, Health & Toxicology, pp. 164-167.

Yamagishi S. 2010. Protective role of PPARgamma agonists against cardiovascular disease. Nippon Rinsho. 68(2): 307-11.

Differential Cytotoxic Effects of Magnesium oxide Nanoparticles on Cisplatin Sensitive and Cisplatin Resistant Leukemia Cancer Cells

Prathamesh P. Patil[1,3], Maria B. Lai[1,3], Solomon W. Leung[2,3], James C.K. Lai[1,3], and Alok Bhushan[1,3]

[1]Department of Biomedical & Pharmaceutical Sciences, College of Pharmacy;

[2]Department of Civil and Environmental Engineering, College of Engineering; and

[3]Biomedical Research Institute,

Idaho State University, Pocatello, ID 83209-8334

Address for correspondence:

Alok Bhushan

Department of Biomedical and Pharmaceutical Sciences

College of Pharmacy

Idaho State University

Pocatello, ID 83209-8334

Email:abhushan@pharmacy.isu.edu

Differential Cytotoxic Effects of Magnesium oxide Nanoparticles on Cisplatin Sensitive and Cisplatin Resistant Leukemia Cancer Cells

Abstract:

Magnesium oxide (MgO) has many applications in pharmaceutical, cosmetic and food industry. It has been extensively used in these industries for decades. Magnesium oxide is used in preparation of antacid, laxatives and mineral supplements. It is also used in cosmetics in preparation of sunscreens, toothpastes and dental cements. Earlier studies from our laboratory have characterized the effects of different metal oxide nanoparticles on normal fibroblast cells and cancer cells. In this study, we compared the cytotoxicity of magnesium oxide nanoparticles on murine leukemia cells (L1210) and cisplatin resistant sub line (L1210/DDP). We found that magnesium oxide nanoparticles exhibit differential cytotoxicity in L1210 and L1210/DDP leukemia cells. Our results also suggested that cisplatin resistant cancer cells were cross resistant to MgO nanoparticles. These findings may assume pathophysiologic importance in elucidation of mechanisms underlying anti-cancer drug resistance and may aid future discovery of anti-cancer drugs.

Key Words: cancer, resistance, nanoparticles, leukemia

Introduction:

Approaches to treat cancers include surgery, chemotherapy and radiation therapy. Conventional chemotherapeutic agents like cisplatin, methotrexate, and 5-flurouracil are used extensively in the treatment of a variety of cancers. One major reason for the failure of chemotherapy is resistance to primary chemotherapeutic agents used in

treatment (Gottesman *et al. 2002*). Certain cancers, which develop resistance to primary cancer chemotherapeutic agent(s), also develop cross resistance to other unrelated chemotherapeutic agents (Bhushan *et al*. 1999).

Several mechanisms contribute to the development of resistance in cancers. Some of the mechanisms include increased efflux of the drug out of the cancer cell, decreased influx of into the cancer cell, and increase in altered cellular targets (Siddik *et al.* 2003, Liu *et al.* 2009). Other studies implicate the involvement of altered cellular signaling in the development of resistance to chemotherapy in cancer cells.

Overcoming cancer drug resistance is a major hindrance in effective use of chemotherapeutic drugs to treat cancers. Development of resistance in cancer cells is the major cause of failure of chemotherapy in treatment of cancer (Giaccone *et al.* 1996). Better understanding of the drug resistance mechanisms is necessary so that novel strategies can be devised for more effective treatment of cancer. In this study, we use a novel approach to target resistance in cancer by using metal-based nanomaterials.

Metallic nanoparticles are a subtype of nanoparticles which comprise of nanoparticles made from metals and their compounds (e.g., titanium dioxide, zinc oxide, MgO, gold, silver). The use of nanomaterials provides new technology and approaches to develop drugs for treatment of diseases. The metallic nanoparticles differ from their bulk counterparts in several properties like magnetic, surface electric, and their optical properties owing to their small size. These properties make metallic nanoparticles suitable candidates for developing treatment therapies and diagnostic and imaging agents (Bhattacharya *et al.* 2008).

Work in our laboratory emphasizes the biological and toxicological effects of nanomaterials. Previous studies from our laboratory have examined the effects of different metallic nanoparticles on neurotumor cells and normal human fibroblasts. We found while zinc oxide and titanium oxide nanoparticles induced high cytotoxicity in normal fibroblasts, magnesium oxide nanoparticles exhibited comparatively low cytotoxicity on these cells even at high concentrations (Lai e*t al. 2008*). Because MgO nanoparticles exhibited low cytotoxicity on normal fibroblasts, we selected them to determine if they could be used to overcome drug resistance in cisplatin resistant leukemia cancer cells. If resistant cells are susceptible to nanoparticles in influencing their proliferation, we can exploit this putative effect to develop novel ways to overcome anti-cancer drug resistance.

Materials and Methods: MgO nanopowder (Sigma-Aldrich Cat no: 549649, 50 nm particle size nanopowder) was dispersed in 100 ml of sterile saline in a sealed conical flask and stirred at ambient temperature for four hours prior to be diluted to the specified concentrations for treatment of cells. McCoy's 5A medium was purchased from Sigma-Aldrich. Mouse polyclonal antibodis for Akt and Erk, respectively, were obtained from Santa Cruz Biotechnology.

Cells and Culture Conditions: L1210 murine leukemia cells were purchased from Sigma-Aldrich and maintained under sterile conditions at 37°C and 5 % CO_2 in McCoy's 5A supplemented with 10% (v/v) horse serum. The L1210/DDP murine leukemia cells were obtained as a subline of L1210 cells resistant to cisplatin and were maintained under sterile conditions at 37°C and 5% CO_2 in McCoy's 5A supplemented with 10% (v/v) fetal bovine serum.

Dose Response Assay: L1210 and L1210/DDP cells were split at equal density in each well of 24-well plates. Cells in each well were treated with specified concentrations of MgO nanoparticles (ranging from 0.1 µg/ml to 100 µg/ml) for 72 hours at 37°C. After 72 hours, an aliquot was used for counting using a Z2 Beckman coulter counter.

Western Blot Analysis: L1210 cells were treated with various concentrations of MgO nanoparticles (10, 25, 50, or 100 µg/ml) for 72 hours. After treating the cells with MgO nanoparticles, cell lysates were prepared using the lysis buffer (1% (v/v) Triron X-100, 10 mM Tris base pH 7.6, 5 mM EDTA, 50 mM sodium chloride, 30 mM sodium pyrophosphate, 50 mM sofium fluoride, 0.1% (w/v) sodium azide, 50 mM phenyl methyl sulphonyl fluoride, 0.5 mg/ml aprotinin, 2.5 mg/ml leupeptin, and 100 mM sodium orthovanadate in distilled water, pH 7.6). BioRad reagents (Bradford assay) were used to determine the protein concentration. 25 µg of protein sample was loaded onto the wells in the sodium dodecyl sulphate polyacrylamide gel. The proteins separated by gel electrolysis were transferred to polyvinylidene fluoride membrane (PVDF), blocked (5% (w/v) Tris buffered saline with 0.01% (v/v) Tween or TBST in no-fat powdered milk). After washing, the blots were incubated in 1:500 primary antibody solution prepared in 5% bovine serum albumin (BSA) in distilled water. Membranes were washed and treated with the secondary antibody and developed using chemiluminescence kit (Pierce biotechnology, Rockford, Illinois), as recommended by the manufacturer. The blots were analyzed for the levels of Akt, pAkt, Erk and pErk. The scans were digitized suing Unscan-it-gel 6.1 software

Results:

Dose Response Studies: L1210 and L1210/DDP cells were treated with different concentrations of magnesium oxide nanoparticles for 72 hours. The dose response studies were performed following the procedure described above.

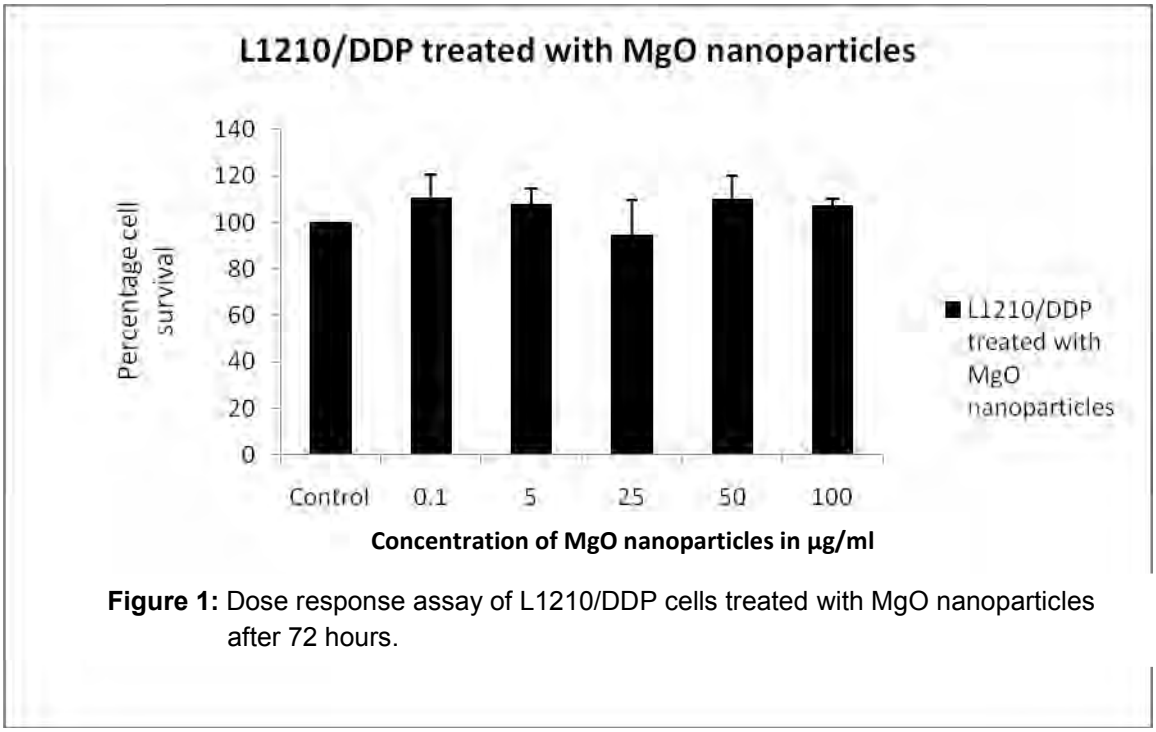

Figure 1: Dose response assay of L1210/DDP cells treated with MgO nanoparticles after 72 hours.

The results revealed that at the concentrations employed, MgO nanoparticles did not exert any cytotoxic effect on L1210/DDP cells after 72 hours treatment (Figure 1). By contrast, MgO nanoparticles did exert some cytotoxic effects on L1210 cells after 72 hours treatment (Figure 2). When the effects of MgO nanoparticles on the two cell lines were compared (Figure 3), it was evident that the resistant L1210/DDP cells was not susceptible to the cytotoxicity of the nanoparticles at the concentrations used while the sensitive L1210 cells showed dose-related decrease in survival upon treatment with the nanoparticles.

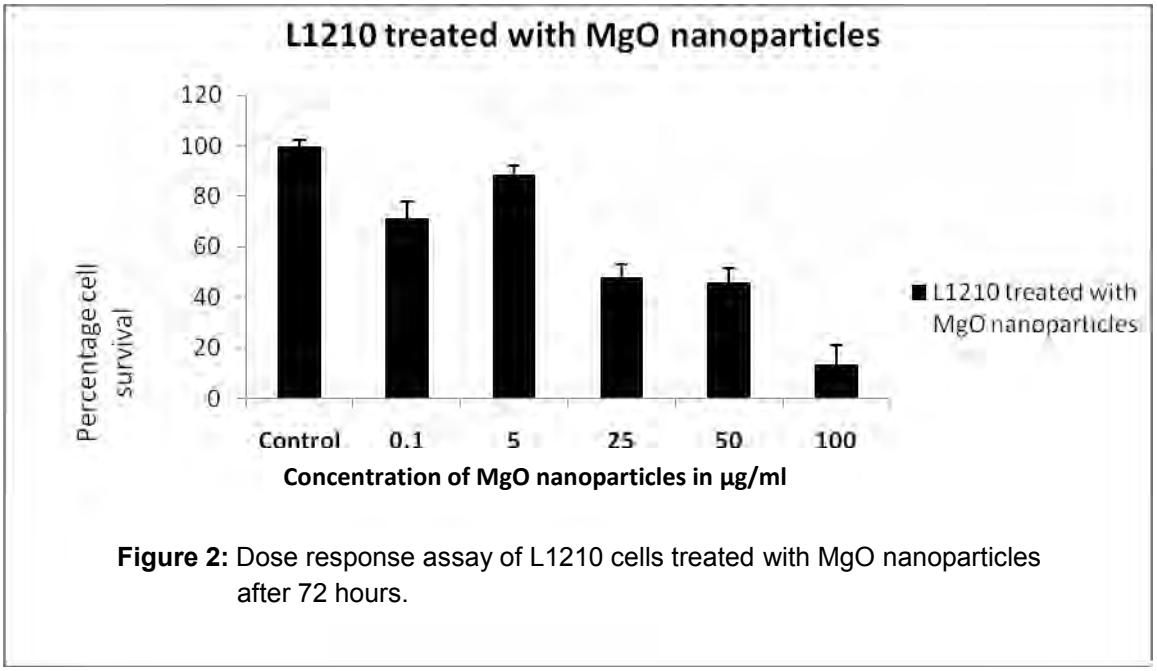

Figure 2: Dose response assay of L1210 cells treated with MgO nanoparticles after 72 hours.

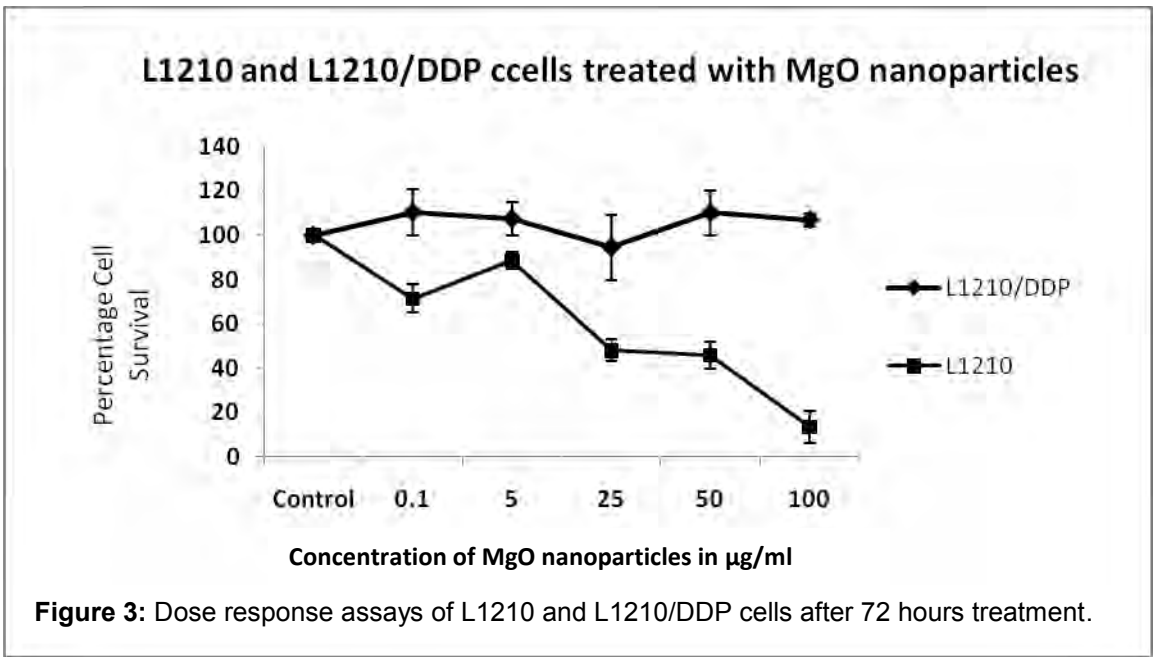

Figure 3: Dose response assays of L1210 and L1210/DDP cells after 72 hours treatment.

Akt and Erk expression: We performed western blot analysis to assess the change in expression of cell signaling elements like Akt, pAkt, Erk and pErk in L1210 cells after MgO nanoparticles treatment using a procedure described above. Our results showed that the expression of pAkt and pErk in these cells decreases when treated with increasing concentrations of MgO nanoparticles (Figure 4).

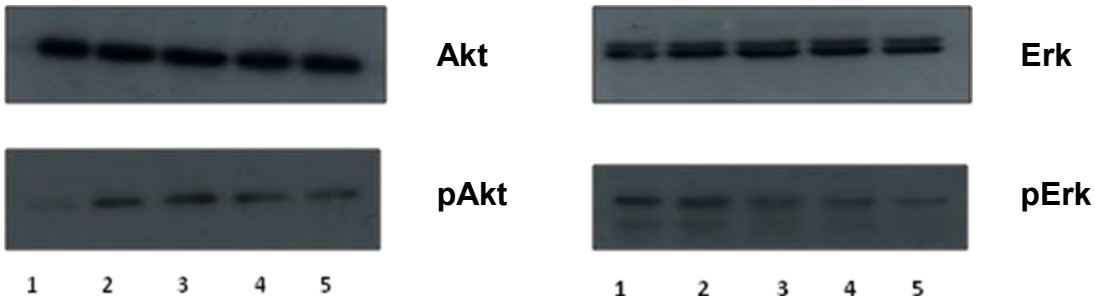

Figure 4: Western Blot Analysis of the effect of MgO nanoparticels on expression of AKT, pAKT, Erk and pErk in L1210 cells. In the above figure 1,2,3,4 and 5 represent the protein expression levels at control, 10 µg/ml, 25 µg/ml, 50 µg/ml and 100 µg/ml treatment of MgO nanoparticles.

In future we will examine the effects of these nanoparticles on expression of other cell signaling proteins like multiple drug resistance associated protein.

Discussion: The major reason for the failure of cancer chemotherapy is the development of resistance to chemotherapy in cancer cells. Few drug resistance mechanisms for cisplatin, which contribute to cisplatin resistance, include increase in intracellular glutathione, increase in MRP protein expression, and increase in DNA repair mechanisms. Despite these suggested mechanisms, a definitive mechanism for cisplatin drug resistance remains to be demonstrated. In our laboratory, we are developing a novel approach towards using metal-based nanoparticles in overcoming cancer drug resistance.

Although magnesium oxide nanoparticles did not overcome drug resistance in L1210/DDP cells, our results from the dose-response studies showed that the cisplatin resistant L1210/DDP leukemia cancer cells are cross resistant to MgO nanoparticles. We also observe that cisplatin sensitive leukemia cells are sensitive to MgO nanoparticles. These observations suggest that L1210/DDP may have similar mechanisms of drug resistance for cisplatin and for MgO nanoparticles.

Altered expression of signal transduction pathways are known to play a role in drug resistance. Our analysis of cell signaling proteins like Akt, pAkt, Erk and pErk by western blot analysis showed that the MgO nanoparticles decreased the expression of phosphorylated forms of Akt and Erk in the sensitive cell line. The decrease in the levels of phosphorylated forms of Akt and Erk with increasing concentrations of MgO nanoparticles in L1210 cells is highly suggestive of down-regulation of pathways leading to cellular proliferation and other processes critical for cancer progression. Clearly, this is an important area that merits further investigation.

Acknowledgements: Our study was supported, in part, by an USAMRMC Project Grant (Contract #W81XWH-07-2-0078), University Research Grant FY 2002-2009 and NIH P20RR016454.

References:

1. Bhattacharya, R., Mukherjee, P. (2008) Biological properties of “naked” metal nanoparticles. Adv. Drug Deliv. Rev. 60(11), 1289-306.
2. Bhushan, A., Hacker, M.P., Tritton T.R. (1999) Collateral methotrexate resistance in cisplatin-selected murine leukemia cells. Braz. J. Med. Biol. Res. 32, 827-33.
3. Giaccone, G., Pinedo H.M., (1996) Drug resistance. Oncologist, 1(1&2), 82-87.
4. Gottesman, M.M. (2002) Mechanisms of cancer drug resistance. Annu. Rev. Med. 53, 615-27.
5. Kartalou, M., Essigmann, J.M., (2001) Mechanisms of resistance to cisplatin. Mutat Res., 478(1-2), 23-43.
6. Lai, J. C., Lai, M.B., Jandhyam, S., Dukhande, V.V, Bhushan, A., Daniels,C.K., Leung, S.W., (2008) Exposure to titanium dioxide and other metallic oxide

nanoparticles induces cytotoxicity on human neural cells and fibroblasts. Int. J. Nanomedicine, 3(4), 533–545.

7. Liu, F.S. (2009) Mechanisms of chemotherapeutic drug resistance in cancer therapy-A quick review Taiwan J. Obstet. Gynecol. 48(3), 239-244.
8. Siddik, Z.H. (2003) Cisplatin: mode of cytotoxic action and molecular basis of resistance. Oncogene, 22(47), 7265-79.

Metallic Nanoparticles in Cancer Imaging and Therapy

*Alok Bhushan Ph.D., *Prathamesh P. Patil B.Pharm., M.S., **Solomon W. Leung Ph.D., and *James C.K. Lai Ph.D.

*Department of Biomedical & Pharmaceutical Sciences, College of Pharmacy and Biomedical Research Institute, Idaho State University, Pocatello, ID 83209, USA.

**Department of Civil & Environmental Engineering, School of Engineering, College of Science & Engineering and Biomedical Research Institute, Idaho State University, Pocatello, ID 83209, USA.

Correspond Author: Dr. Alok Bhushan, Department of Biomedical & Pharmaceutical Sciences, College of Pharmacy, 921 S 8th Avenue, Stop 8288, Pocatello, ID 83209; Fax: 208-282-4482; Tel: 208-282-4408; email:abhushan@pharmacy.isu.edu

Contents

Abstract Use of nanoparticles in cancer diagnosis, detection, and therapy is rapidly gaining impetus. This review focuses on the recent advances in the applications of metallic nanoparticles in cancer imaging and therapy. In particular, we discuss the uses of iron oxide nanoparticles, gadolinium-based nanoparticles, and multimodal metallic nanoparticles in cancer imaging and detection. Subsequently, we discuss the applications of several types of cancer therapies based on the use of metallic nanoparticles. The latter applications include: metallic nanoparticles in photodynamic therapy, in hyperthermia therapy, and in neutron capture therapy as well as surface-modified metallic nanoparticles in cancer therapy. Despite the possibility that advances in biomedical applications of such nanoparticles may ultimately lessen the suffering of cancer patients and improve their prospects for survival, we raise a strong note of caution regarding the safety of clinical use of metallic nanoparticles because of their putative or demonstrated toxicity.

Key Words: Metallic nanoparticles; cancer imaging; cancer therapy

1. Introduction

The diverse applications of nanotechnology in biomedical research and development have escalated exponentially in the last decade. This generalization is particularly pertinent when one considers the use of nanomaterials in the development of targeted drug delivery systems [1]. In light of growing interests in this and related areas, this review aims to highlight and discuss the recent and current advances of applications of one class of nanoparticles, namely metallic nanoparticles, in cancer imaging and therapy.

2. Applications of Metallic Nanoparticles in Cancer Imaging

Although various other techniques (e.g., X-ray imaging, CT-Scans, ultrasound imaging) exist, this review focuses on the current use of metallic nanoparticles (including iron oxide nanoparticles such as nanoparticles of super paramagnetic iron oxides (SPIO) and ultrasmall superparamagnetic iron oxides (USPIO), gadolinium nanoparticles, and manganese nanoparticles) in magnetic resonance imaging (MRI) in the detection and staging of cancer [2].

2.1 Iron Oxide Nanoparticles

Two subtypes of iron oxide nanoparticles are employed in the MRI applications — colloidal iron oxide nanoparticles and USPIO.

Colloidal Iron Oxide Nanoparticles

Colloidal iron oxides, also called superparamagnetic iron oxide (SPIO) nanoparticles constitute the first generation iron oxide nanoparticles and are comprised of colloidal iron oxides. Prepared by one-step alkaline precipitation of iron oxides (average size ~75 nm), they are stabilized by addition of polymers [3, 4].

Blood half life of SPIO nanoparticles is short because they are rapidly phagocytozed by mononuclear phagocyte system (MPS), leading to their accumulation in normal tissues but not in tumors [5]. This differential localization of phagocytozed SPIO nanoparticles facilitates the noninvasive and easy detection of tumors in the body by MRI.

SPIO nanoparticles have been successfully administered orally for imaging of the gastrointestinal tract [6]. Ferumoxsil (Lumirem) (i.e., SPIO nanoparticles coated with silicone) is approved for detecting cancer metastasis to the liver [7]. SPIO nanoparticles-enhanced MRI is superior to helical CT to detect liver metastases in candidates for hepatic resection [8] and superior to ultrasound and CT in detecting focal hepatic lesions and suspected cancer lesions [9].

Additionally, SPIO nanoparticles-enhanced MRI scans proved to be beneficial in planning surgeries of squamous cell carcinoma of head and neck [10].

Ferucorbotran (Resovist), another SPIO formulation, is currently under Phase III clinical trials in USA for detection of liver neoplasms. Ferumoxide (Endorem, Feridex) is an FDA-approved MRI contrasting agent for detection of neoplastic lesions in liver neoplasms.

Ultrasmall Superparamagnetic Iron Oxide (USPIO) Nanoparticles

The second generation iron oxide nanoparticles, USPIO nanoparticles are smaller in size (<50 nm): consequently, their circulating half life is increased, thereby enabling them to permeate through the vascular endothelium and reach the interstitium and the lymph nodes [11]. In the lymph nodes, USPIO nanoparticles are rapidly phagocytosed by lymphocytes: their differential accumulation in lymph nodes gives rise to a contrast in the imaging of normal versus metastatic lymph tissues using MRI.

Staging of cancer is essential for planning its treatment. In contrast to the current less precise techniques of CT and ultrasound, MRI using ferumoxtran-10 can identify the spread of cancer to lymph nodes with better sensitivity and specificity [12]. MRI using USPIO nanoparticles helps identify patients requiring salvage radiation therapy after prostatectomy [13]. USPIO nanoparticles (i.e., ferumoxytol-10)-enhanced MRI potentially can detect brain tumors [14].

2.2 Gadolinium

For some time, gadolinium chelates have been used as a MRI contrast agent [15]. Recently gadolinium-based nanparticles have been introduced into these MRI applications. Gadolinium oxide nanoparticles with fluorescence probes have been synthesized for use as contrast agents for MRI and fluorescence imaging [16]. Silica nanoparticles loaded with gadolinium have been used to detect nasopharyngeal cancer in nude mice [17]. Gadolinium dendrimers are being researched

for their efficiency as MRI contrast agents: the efficiency of gadolinium delivery depends upon the type of dendrimer used. Comparative study of gadolinium delivery to lymph nodes using polyamidoamine (PMAM) and diaminobutane (DAB) dendrimers showed that PMAM dendrimers were the more efficient in delivering gadolinium to the lymph nodes [18], thereby demonstrating their potential use in detecting lymph node involvement of tumors by MRI imaging [19]. However, the drawback associated with the use of PMAM dendrimers labeled with gadolinium is the intrinsic toxicity associated with PMAM and gadolinium [20, 21].

2.3 Multimodal Metallic Nanoparticles

Multi-modal imaging is sensitive, specific and yields more information than single-probe imaging. Multimodal metallic nanoparticles consist of magnetic nanoparticles as the core to which different functional moieties are tagged. The functional moieties can be fluorescence probes for fluorescence image analysis, antibodies for targeting a particular group of cells, or biomarker and radionucleotides for PET imaging [22]. For example, polysialic acid (PSA) is a cancer biomarker for neuroblastoma. HmenB1 antibody tagged with magnetic iron oxide nanoparticles having a dye doped silica core (for fluorescence imaging) can target PSA, thereby facilitating the detection of neuroblastoma in rats [23]. Similarly, iron oxide nanoparticles tagged with a fluorescence probe have been investigated for breast cancer detection in nude mice [24].

It is important to note that the current research trend on applications of metallic nanoparticles in cancer imaging strongly suggests that such applications can be coupled to or employed in conjunction with applications of metallic nanoparticles in cancer therapy.

3. Application of Metallic Nanoparticles in Cancer Therapy

Conventional cancer therapies include chemotherapy, radiation therapy, and surgery. These therapies have limitations that decrease their efficacy: anti-cancer drugs exhibit adverse effects

on normal cells and cross-resistance to other anti-cancer drugs [25] and radiation therapy also show deleterious side effects [26]. Thus, improved cancer therapies are needed. Metallic nanoparticles have demonstrated potential in several experimental cancer therapies, including photodynamic therapy (PDT), hyperthermia therapy (HT), neutron capture therapy (NCT), and surface-modified metallic nanoparticles for drug delivery or anti-proliferative activity [27].

3.1 Metallic Nanoparticles in Photodynamic Therapy

Photodynamic therapy (PDT) generally exploits a photosensitive compound that is subsequently activated using an external light source to kill the cancer cells [28]. When photons from the light source are incident upon the photosensitive material, the photosensitive drug is excited and produces reactive oxygen species that damage the cancer cells. Choice of the photosensitive compound depends upon the location of the tumor in the body [29,30].

Gold nanoparticles conjugated with epidermal growth factor receptor (EGFR) antibodies can induce cancer cell death after irradiation with light in the near-infrared (NIR) range. The conjugation of anti-EGFR antibodies to spherical gold nanoparticles facilitates their selective accumulation in cancer cells that over-express EGFR receptors [30]. The temperatures achieved upon NIR irradiation of gold nanoparticles *in vitro* were 70^0 - 80^0 C [31].

A comparison of the photothermal destruction of malignant cancer cells using gold nanoparticles with different surface dimensions and core material revealed that the efficiency of gold nanoparticles was dependent on the photothermal conversion efficiency and dimensions of nanoparticles [32]. Moreover, gold nanoshells can be used effectively for photodynamic therapy in cancer [33] and Au-Ag nanorods functionalized with aptamer exhibit specificity of these nanorods and their use for PDT in treating cancer [34].

The advantages of PDT include: 1) it is a noninvasive technique for killing cancer cells; 2) it induces tumor regression prior to surgery; and 3) it can target tumors located at inoperable areas (e.g., trachea). The main disadvantages of PDT therapy include, but are not limited to: 1) it uses near-IR light of limited power; 2) it does not penetrate more than 1 cm deep into the tissue; and 3) PDT therapy induces reddening or inflammation of the target tissue.

3.2 Metallic nanoparticles in Hyperthermia Therapy

Hyperthermia therapy (HT) is effected by exposing the cancerous tissues to high temperatures of up to 42-43^{0}C leading to damage or killing of cancer cells. Unlike PDT, where a light source is used to induce rise in target temperatures, HT utilizes radiofrequency, ultrasound, or microwave for raising the target temperatures [35]. HT is a conjugate therapy employed when the tumors are nonresponsive to chemotherapy and radiation therapy.

Conventional HT employing heating sources like microwave, radiofrequency or ultrasound is non-specific [36]. Metallic nanoparticles can help overcome this drawback: thus, the use of magnetic nanoparticles in HT was proposed [37]. Therapeutic potentials of iron oxide nanoparticulate formulations are being actively assessed in HT [38].

Use of magnetic iron oxide nanoparticles for HT is called "Magnetic Fluid Hyperthermia" (MFH) [39]. When iron oxide nanoparticles (dimensions < 10 nm) are subjected to an alternating external magnetic field, the heat so generated ultimately damages cancer cells. An *in vitro* and *in vivo* study demonstrated this MFH effect of Fe_2O_3 nanoparticles in cultured liver cancer cells and in xenograph liver cancers [40]. Similarly, MFH effect of dextran coated iron oxide and that of silane-coated nanoparticles were studied in normal and cancerous human cells *in vitro*: the consequent hyperthermia induced cytotoxicity in cancer cells [41]. Furthermore, conjugating iron oxide nanoparticles with folate, which binds to its receptors expressed by cancer cells, is

effective in inducing hyperthermia within the cancer cells [42]. MFH effect of Fe_2O_3, in combination with arsenic trioxide, was noted in human cervical cancer cells [43] and Au nanoparticles produced marked hyperthermia in gastrointestinal cancer cells *in vitro* [44].

Despite their utility in inducing hyperthermia, a major drawback of this application is that the temperature generated thus inside cells is difficult to control. A new class of magnetic nanoparticles, manganite perovskites show promise to overcome this limitation. The curie temperatures ($42^0 – 43^0$C) of silver-doped manganite pervoskites enable isothermal heating [45].

3.3 Metallic Nanoparticles in Neutron Capture Therapy

Neutron capture therapy utilizes a stable nuclide delivered to the tumor cells. Upon irradiation with neutrons, the stable nucleus produces ionizing radiations [46]. Boron Neutron capture therapy (BNCT) is a form of radiotherapy which utilizes neutron beam and boron-10: irradiation with neutron rays induces boron to form lithium and alpha rays. Although BNCT using boron-10 was investigated for treating glioblastoma multiforme [47], progress of BCNT in cancer treatment has been slow because few tumor-selective boron-containing drugs exist and the neutron beams employed are of the low-energy type [48, 49].

Use of gadolinium for NCT was recognized over two decades ago. Gadolinium emits gamma rays when irradiated with neutrons [50]. Currently, gadolinium nanoparticles (Gd-NP) are being invesgated for their application in NCT [51]. A comparison of Gd-NP and gadolinium solution revealed that Gd-NP showed significant accumulation and tumor growth suppression in cancer cells as compared to gadolinium solution [52]. Gd-NP can also target cancer cells by attaching to Gd-NP ligands or antibodies specific to the cancer cells. By attaching folate to the surface of Gd-NP, the uptake of Gd-NP into cancer cells *in vitro* and *in vivo* is enhanced [46, 53].

3.4 Surface-modified metallic nanoparticles in cancer therapy

Another type of application of metallic nanoparticles in cancer therapy exploits the intrinsic properties of the nanoparticles. That silver has been extensively commercialized in applications as anti-microbial agents [54] prompted investigations of anti-proliferative effect of silver nanoparticles on human glioblastoma cells [55]. Though the underlying mechanisms are incompletely understood, some researchers believe this anti-proliferative effect is attributable to oxidative stress induced by Ag nanoparticles [56]. Radioactive gold nanoparticles coated with gum arabica glycoprotein show promising results in targeting and treating prostate cancer: the nanoparticles passed through tumor vasculature to induce decrease in tumor volume [57].

One adverse effect of radiation therapy is its deleterious effects on normal cells. Cerium oxide nanoparticles have demonstrated selective radio-protective effect on normal cells [58]. For example, UV exposure of normal and tumor breast cells pretreated with cerium oxide nanoparticles induced more deaths in cancer cells compared to normal cells. Although the radio protective effect of nanoceria in normal cells is not understood, some researchers hypothesize this effect is due to superoxide dismutase enzyme mimetic activity of nanoceria [59].

Gadolium endohederal metallofullerenol nanoparticles have exhibited high anti-tumor activity in mice bearing liver tumors [60]. Gadolinium endohederal metallofullerenol nanoparticles owe their anti-tumor activity to their ability to scavenger reactive oxygen species [61, 62]. Metallic nanoparticles of motexafin gadolinium also have similar antioxidant properties. Clinical studies have indicated that they can prevent metastasis of cancer to brain when administered to patients in early stages of non-small cell lung cancer (NSCLC) [63, 64].

Metallic nanoparticles have improved the delivery of chemotherapeutic drugs, specifically at the tumor site. Metallic nanoparticles like iron oxide nanoparticles which have magnetic properties

can be targeted to the tumor site under the influence of external magnetic field [65]. For example, employing iron oxide nanoparticles as carriers for chemotherapeutic drugs such as doxorubicin and camptothecan resulted in improved therapeutic efficacy of these drugs in decreasing tumor size in rat cancer xenograft model [66].

4. Conclusions and Future Directions

The current rapid and explosive advances of nanotechnology herald a new age in cancer diagnosis and therapy. In this review, we have only highlighted the seminal roles of metallic nanoparticles in cancer imaging and therapy. Clearly one should appreciate the advances we have discussed above constitute only a small fraction of the applications of nanotechnology in cancer imaging and therapy. However, limitation of space does not allow us to even mention other important advances unrelated to the use of metallic nanoparticles.

Although mortality rates due to cancer have shown decreases in the recent two decades, cancer is still the leading cause of disease-related deaths in USA. The advances in development of newer cancer imaging and therapies based on metallic nanoparticles may help in early detection of cancer and thus contribute to decreasing deaths due to cancer. Various cancer imaging and therapies based on use of metallic nanoparticles are at different stages of preclinical and clinical development. Iron oxide nanoparticles, zinc oxide nanoparticles, gold nanoparticles, silver nanoparticles, and cerium oxide nanoparticles have tremendous potentials to be developed as novel diagnostic and therapeutic agents in cancer.

Enhanced cancer biomarker and genetic mutation detection techniques would help in identifying individuals at high risk for developing cancer. In this context, multi-functional metallic nanoparticles show exciting therapeutic potentials and these are currently under development for cancer therapy to be clinically applied in the near future. Metallic nanoparticles can be

engineered to enhance the efficacy of current diagnostic and imaging techniques in cancer. Furthermore, cancer therapies utilizing metallic nanoparticles as targeting vehicles for drug delivery, and other allied therapies using metallic nanoparticles would also play key roles in clinical management of cancer in the next decade.

Understandably, the advances of the biomedical applications of metallic nanoparticles discussed above strongly suggest that the clinical applications of such nanoparticles may ultimately lessen the suffering of cancer patients and improve their prospects for survival. Nevertheless, we cannot help but inject a strong note of caution here. As the ubiquitous and diverse applications of nanotechnology have become almost uncontrollable phenomena, humans are increasing exposed to nanoparticles and other nanomaterials although the health effects and environmental impact of their exposure have not been systematically assessed and are therefore largely unknown [67]. Moreover, recent advances in understanding the putative toxicity of nanoparticles and other nanomaterials [67-72] indicate that in developing metallic nanoparticles for cancer imaging and therapy, one needs to consider, and fully investigate in parallel, the putative toxicity of such nanoparticles prior to even adopting them for pre-clinical trial.

References

1. Arruebo M, Fernández-Pacheco R, Ibarra MR, Santamaría J. Magnetic nanoparticles for drug delivery. Nanotoday 2007;3:22-32.

2. Bonnemain B. Superparamagnetic agents in magnetic resonanceimaging: physicochemical characteristics and clinical applications. J Drug Target 1998; 6:167-174.

3. Qiu J, Yang R, Li M, Jiang. Preparation and characterization of porous ultrafine Fe_2O_3 particles. N Mater Res Bull 2005; 40:1968-1975.

4. Babes L, Denizot B, Tanguy G, Le Jeune JJ, Jallet P. Synthesis of Iron Oxide Nanoparticles Used as MRI Contrast Agents: A Parametric Study. J Colloid Interface Sci 1999;212:474-482.

5. Pouliquen D, Le Jeune, JJ, Perdrisot R, Ermias A, Jallet P. Iron oxide nanoparticles for use as an MRI contrast agent: pharmacokinetics and metabolism. Magn Reson Imaging 1991; 9: 275-255.

6. Rubin D.L., Muller HH, Young SW, Hunke WA, Gorman WG. Optimization of an oral gastrointestinal contrast agent for magnetic resonance imaging. Invest Radiol 1994;29: 81-86.

7. Kubaska S, Sahani DV, Hahn PF, Halpern E. Dual contrast enhanced magnetic resonance imaging of liver with superparamagnetic iron oxide followed by gadolinium for lesion detection and characterization. Clin Radiol 2001;56:410-415.

8. Ward J, Robinson PJ, Guthrie, JA, Downing S, Wilson D. Liver metastases in candidates for hepatic recesction: comparison of helical CT and gadolinium- and SPIOs – enhanced MR imaging. Radiol 2005;237:170-180.

9. Shah AJ, Parsons B, Pope I, Callaway M, Finch-Jones MD, Thomas MG. The clinical impoact of magnetic resonance imaging in diagnosing focal hepatic lesions and suspected cancer. Clin Imaging 2009;33:209-212.

10. Mack MG, Balzer JO, Straub R, Eichler K, Vogl TJ, Superparamagnetic iron oxide enhanced MR imaging of head and neck lymphnodes. Radiology 2002;222:239-244.

11. Iannone A, Magin RL, Walczak T, Fedrico M, Swartz HM, Tomasi A. Blood clearance of dextran magnetite particles determined by a noninvasive *in vivo* ESR method. Magn Reson Med 1991;22:435-442.

12. Tatsumi Y, Tanigawa N, Nishimura H, Nomura E, Mabuchi H, Matsuki M, Narabayashi I. Preoperative diagnosis of lymph node metastasis in gastric cancer by magnetic resonance imaging with ferumoxtran-10. Gastric Cancer 2006;9:120-128.

13. Ross RW., Zietman AL, Xie W, Coen JJ, Dahl DM, Shipley WU, Kaufman DS, Islam T, Guimaraes AR, Weissleder R, Harisinghani M**.** Lymphotropic nanoparticle-enhanced magnetic resonance imaging (LNMRI) identifies occult lymph node metastases in prostate cancer patients prior to salvage radiation therapy. Clin Imaging 2009; 33:301-305.

14. Neuwelt EA, Varallyay CG, Manninser S, Solymosi D, Haluska M, Hunt MA. The potential of ferumoxytol nanoparticle magnetic resonance imaging, perfusion, and angiography in central nervous system malignancy: A pilot study. Neurosurgery 2007; 60:601-612.

15. Sitharaman B, Kissell KR, Hartman KB, Tran LA, Baikalov A, Rusakova I, Sun Y, Khant HA, Ludtke SJ, Chiu W, Laus S, Tóth E, Helm L, Merbach AE, Wilson LJ. Superparamagnetic gadonanotubes are high-performance MRI contrast agents. Chem Commun (Camb) 2005;31:3915-3917.

16. Bridot JL, Faure AC, Laurent S, Rivière C, Billotey C, Hiba B, Janier M, Josserand V, Coll JL, Elst LV, Muller R, Roux S, Perriat P, Tillement O. Hybrid gadolinium oxide nanoparticles: multimodal contrast agents for in vivo imaging. J Am Chem Soc 2007;129:5076-5084.

17. Liu LZ, Guo GJ, Zeng MS, Lü YC, Liu XW, Cui CY, Wu PH, Li L. [Gadolinium-loaded nanoparticle as a novel molecular imaging contrast agent for magnetic resonance imaging] Zhonghua Yi Xue Za Zhi. 2007;87:240-243.

18. Kobayashi H, Kawamoto S, Bernardo M, Brechbiel MW, Knopp MV, Choyke PL. Delivery of gadolinium-labeled nanoparticles to the sentinel lymph node: Comparison of the sentinel node

visualization and estimations of intra-nodal gadolinium concentration by the magnetic resonance imaging. J Controlled Release 2006;111;343-351.

19. Kobayashi H, Kawamoto S, Sakai Y, Choyke PL, Star RA, Brechbiel MW, Sato N, Tagaya Y, Morris JC, Waldmann TA. Lymphatic drainage imaging of breast cancer in mice by micro-magnetic resonance lymphangiography using a nano-size paramagnetic contrast agent. J Natl Cancer Inst 2004;96:703-708.

20. Xu R, Wang Y, Wang X, Jeong EK, Parker DL, Lu ZR. In Vivo evaluation of a PAMAM-cystamine-(Gd-DO3A) conjugate as a biodegradable macromolecular MRI contrast agent. Exp Biol Med (Maywood) 2007;232:1081-1089.

21. Perazella MA. Gadolinium-contrast toxicity in patients with kidney disease: nephrotoxicity and nephrogenic systemic fibrosis. Curr Drug Saf 2008;3:67-75.

22. Cheon J, Lee JH. Synergistically integrated nanoparticles as multimodal probes for nanobiotechnology. Acc Chem Res 2008;41:1630-1640.

23. Lee JH, Jun YW, Yeon SI, Shin JS, Cheon J. Dual-mode nanoparticle probes for high-performance magnetic resonance and fluorescence imaging of neuroblastoma. Angew Chem Int Ed Engl 2006;45:8160-8162.

24. Shan L, Wang S, Sridhar R, Bhujwalla ZM, Wang PC. Dual Probe with Fluorescent and Magnetic Properties for Imaging Solid Tumor Xenografts. Mol Imaging 2007;6:85-95.

25. Assaraf YG. The role of multidrug resistance efflux transporters in antifolate resistance and folate homeostasis. Drug Resist Updat 2006;9:227-246.

26. Al-Mefty O, Kersh JE, Routh A, Smith RR. The long-term side effects of radiation therapy for benign brain tumors in adults. J Neurosurg 1990;73:502-512.

27. Liang S, Wang Y, Yu J, Zhang C, Xia J, Yin D. Surface modified superparamagnetic iron oxide nanoparticles: as a new carrier for bio-magnetically targeted therapy. J Mater Sci Mater Med 2007;18:2297-2302.

28. Dolmans D, Fukumara D, Jain RK. Photodynamic therapy for cancer. Nature Rev Cancer 2003;3:380-387.

29. Wilson BC. Photodynamic therapy for cancer: Principles. Can. J. Gastroenterol 2002;16:393-396.

30. Huang X, El-Sayed, IH, Qian W, El-Sayed MA. Cancer cell imaging and photothermal therapy in near IR region by using gold nanorods. J Am Chem Soc 2006; 128:2115-2120.

31. Huang X, Jain PK, El-Sayed IH, El-Sayed MA**.** Determination of the minimum temperature required for selective photothermal destruction of cancer cells with the use of immunotargeted gold nanoparticles. Photochem Photobiol 2006; 82:412-417.

32. Fong, YC, Chen TC, Chen SY. Comparative efficiencies of photothermal destruction of malignant cells using antibody cells using antibody-coated silica@Au nanoshells, hollow Au/Ag nanospheres and Au nanorods. Nanotechnology 2009;20:425104.

33. Gobin AM, Lee MH, Halas NJ, James WD, Drezek RA, West JL. Near-Infrared resonant nanoshells for combined optical imaging and photothermal cancer therapy. Nano Lett 2007;7:1929-1934.

34. Huang YF, Sefah K, Bamrungsap S, Chang HT, Tan W. Selective photothermal therapy for mixed cancer cells using aptamer-conjugated nanorods. Langmuir 2008;24:11860-11865.

35. Diederich CV. Thermal ablation and high-temperature thermal therapy: overview of technology and clinical implementation. Int J Hyperthermia 2005;21(8):745-753.

36. Kong G, Braun RD, Dewhirst MW. Hyperthermia enables tumor-specific nanoparticle delivery: effect of particle size. Cancer Res 2000;60:4440-4445.

37. Gilchrist R K. Selective Inductive Heating of Lymph. Ann Surg 1957;146(4): 596–606.

38. Xie J, Huang J, Li X, Sun S, Chen X. Iron oxide nanoparticle platform for biomedical applications. Curr Med Chem. 2009;16(10):1278-1294.

39. Latorre M, Rinaldi C. Applications of magnetic nanoparticles in medicine: magnetic fluid hyperthermia. P R Health Sci J 2009;28:227-238.

40. Therapeutic effect of Fe_2O_3 nanoparticles combined with magnetic fluid hyperthermia on cultured liver cancer cells and xenograft liver cancers. J Nanosci Nanotechnol 2005;5:1185-1192.

41. Jordan A, Scholz R, Wust P, Schirra H, Schiestel T, Schmidt H, Felix R. Endocytosis of dextran and silan-coated magnetite nanoparticles and the effect of intracellular hyperthermia on human mammary carcinoma cells in vitro. J Magnetism and Magnetic Materials 1999; 94:185-196.

42. Sonvico F, Mornet S, Vasseur S, Dubernet C. Folate-conjugated iron oxide nanoparticles for solid tumor targeting as potential specific magnetic hyperthermia mediators: synthesis, physicochemical characterization and, in vitro experiments. Bioconjugate Chem 2005;16:1181-1188.

43. Du Y, Zhang D, Liu H, Lai R. Thermochemotherapy effect of nanosized As_2O_3/Fe_3O_4 complex on experimental mouse tumors and its influence on the expression of CD44v6, VEGF-C and MMP-9. BMC Biotechnol 2009; 9:84.

44. Ganon CJ, Patra CR, Bhattacharya R, Mukherjee P, Curley SA. Intracellular gold nanoparticles enhance non-invasive radiofrequency thermal destruction of human gastrointestinal cancer cells. J Nanobiotechnol 2008;6:2.

45. Melnikov OV, Gorbenko Y, Markelova MN, Kaul AR, Atsarkin VA. Ag-doped manganite nanoparticles: New materials for temperature-controlled medical hyperthermia. J Biomed Mater Res A 2008;91(4);1048-1055.

46. Oyewumi MO, Mumper RJ. Engineering tumor-targetted gadolinium hexanedione nanoparticles for potential application in neutron capture therapy. Bioconjugate Chem 2002;13:1328-1335.

47. Yamamoto T, Nakai K, Matsumura A. Boron neutron capture therapy for glioblastoma. Cancer Lett 2008;262(2):143-152.

48. Barth, RF. Boron neutron capture therapy at the crossroads: challenges and opportunities. Appl Radiat Isot 2009;67(7-8 Suppl):S3-S6.

49. Barth RF. A critical assessment of boron neutron capture therapy: an overview. J Neuro-Oncol 2003;62:1-5.

50. Martin RF, D'Cunha G, Pardee M, Allen BJ. Induction of DNA double-strand breaks by 157Gd neutron capture. Pigment Cell Res 1989;2:330-332.

51. Tokumitsu H, Ichikawa H, Fukumori Y. Chitosan-gadopentetic acid complex nanoparticles for gadolinium neutron-capture therapy of cancer: preparation by novel emulsion-droplet coalescence technique and characterization. Pharm Res 1999;16:1830-1835.

52. Shikata F, Tokumitsu H, Ichikawa H, Fukumori Y. In vitro cellular accumulation of gadolinium incorporation into chitosan nanoparticles designed for neutron-capture therapy of cancer. Eur J BioPharm 2002;53:57-63.

53. Oyewumi MO, Yokel RA, Coakley T, Mumper RJ. Comparison of cell uptake, biodistribution and tumor retention of folate and PEG-coated gadolinium nanoparticles in tumor bearing mice. J Control Release 2004;95:613-626.

54. Percival SL, Bowler P.G., Dolman J. Antimicrobial activity of silver containing dressing on wound microorganisms using in vitro biofilm model. Int Wound J. 2007;4 :186-191.

55. Rahman MF, Wang J, Patterson TA, Saini UT, Robinson BL, Newport GD, Murdock R.C, Schlager JJ, Hussain SM, Ali SF. Expression of genes related to oxidative stress in the mouse brain after exposure to silver nanoparticles. Toxicol Lett 2009;187:15-21.

56. AshaRani PV, Hande MP, Valiyaveettil S. Anti-proliferative activity of silver nanoparticles. BMC Cell Biology 2009;10:65.

57. Chanda N, Kan P, Watkinson LD, Shukla R, Zambre A. *et al.* Radioactive gold nanoparticles in cancer therapy: therapeutic efficacy studies of GA-198AuNP nanoconstruct in prostate tumor-bearing mice. Nanomed 2010;6(2):201-209.

58. Tarnuzzer RW, Colon J, Patil S, Seal S. Vacancy Engineered Ceria Nanostructures for protection from Radiation-Induced cellular damage. Nano Lett 2005;5:2573-2577.

59. Heckert EG, Karakoti AS, Seal Sudipta, Self WT. The role of cerium redox state in the SOD mimetic activity of nanoceria. Biomaterials 2008;29:2705-2709.

60. Chen C, Xing G, Wang J, Zhao Y, Li B, Tang J, Jia G, Wang T, Sun J, Xing L, Yuan H, Gao Y, Meng H, Chen Z, Zhao F, Chai Z, Fang X. Multihydroxylated [Gd@C82(OH)22]n nanoparticles: antineoplastic activity of high efficiency and low toxicity. Nano Lett 2005;5:2050-2057.

61. Wang J, Chen C, Li B, Yu H, Zhao Y, Sun J, Li Y, Xing G, Yuan H., Tang J, Chen Z, Meng H, Gao Y, Ye C, Chai Z, Zhu C., Ma B, Fang X, Wan L. Anti-oxidative function and biodistribution of [Gd@C82(OH)22]n nanoparticles in tumor-bearing mice. Biochem Pharmacol 2006;71:872-881.

62. Yin JJ, Lao F, Meng J, Fu PP, Zhao Y, Xing G, Gao X, Sun B, Wang PC, Chen C, Liang XJ. Inhibition of tumor growth by endohedral metallofullerenol nanoparticles optimized as reactive oxygen species scavenger. Mol Pharmacol 2008;74:1132-1140.

63. Thomas SR, Khuntia D. Motexafin gadolinium injection for the treatment of brain metastases in patients with non-small cell lung cancer. Int J Nanomed 2007;2:79-87.

64. Mehta MP, Shapiro WR, Phan SC, Gervais R, Carrie C, Chabot P, Patchell RA. Motexafin gadolinium combined with prompt whole brain radiotherapy prolongs time to neurologic progression in non-small-cell lung cancer patients with brain metastases: results of a phase III trial. Int J Radiat Oncol Biol Phys 2009;73:1069-1076.

65. C. Alexiou, Jurgons R., Schmid R, Hilpert A, Bergemann C, Parak F, Iro H In vitro and in vivo investigations of targeted chemotherapy with magnetic nanoparticles. Journal of Magnetism and Magnetic Materials 2005;293:389-393.

66. Munnier E, Cohen-Jonathan S, Linassier C, Douziech-Eyrolles L, Marchais H, Soucé M, Hervé K, Dubois P, Chourpa I. Novel method of doxorubicin-SPION reversible association for magnetic drug targeting. Int J Pharm 2008;363:170-176.

67. Lai JCK, Schoen MP, Perez Gracia A, Naidu DS & Leung SW. Prosthetic devices: challenges and implications of robotic implants and biological interfaces: In: Proc I Mech E, Vol 221 Part H, J Engineering in Medicine, Special Issue entitled: "Micro and Nano Technologies in Medicine"; 2007, p 173-183.

68. Aghargar VA, Bhushan A, Lai JCK, Daniels CK. Cytotoxic Effects of Short Multiwall Caron Nanotubes: In: Technical Proceedings of the 2008 Nanotechnology Conference and Trade Show, Volume 2, Chapter 2: Environment, Health & Toxicology; 2008, p. 122-125.

69. Jandhyam S, Lai MB, Dukhande VV, Bhushan A, Daniels CK, Leung SW, Lai JCK. Silicon dioxide nanoparticles exert dissimilar cytotoxic effects on mammalian cell types: In: Technical Proceedings of the 2008 Nanotechnology Conference and Trade Show, Volume 2, Chapter 2: Environment, Health & Toxicology; 2008, p. 126-129.

70. Lai MB, Jandhyam S, Dukhande VV, Bhushan A, Daniels CK, Leung SW, Lai JCK. Differential cytotoxicity of metallic oxide nanoparticles in mammalian cells: In: Technical Proceedings of the 2008 Nanotechnology Conference and Trade Show, Volume 2, Chapter 2: Environment, Health & Toxicology; 2008, p. 130-133.

71. Lai JCK, Lai MB, Jandhyam S, Dukhande VV, Bhushan A, Daniels CK, Leung SW. Exposure to titanium dioxide and other metallic oxide nanoparticels induce cytotoxicity on human neural cells and fibroblasts. Int J Nanomed 2008;3:533-545.

72. Lai JCK, Ananthakrishnan G, Jandhyam S, Dukhande VV, Bhushan A, Gokhale M, Daniels CK, Leung SW. Treatment of human astrocytoma U87 cells with silicon dioxide nanoparticles lowers their survival and alters their expression of mitochondrial and cell signaling proteins. Int J Nanomed 2010;5:715-723.

A Noncontact Co-Culture Model of Peripheral Neural Cells for Nanotoxicity, Tissue Engineering and Pathophysiological Studies

A.R. Jaiswal[*], Yin Yin W. Wong[**], Alok Bhushan[***], Christopher K. Daniels[****] and James C.K. Lai[*****]

[*]Department of Biomedical and Pharmaceutical Sciences, College of Pharmacy, and Biomedical Research Institute, Idaho State University, Pocatello, ID 83209, USA Fax: 208-282-4305; Tel: 208-705-2447

[**]Department of Biomedical & Pharmaceutical Sciences, College of Pharmacy, and Biomedical Research Institute, Idaho State University, Pocatello, ID 83209, USA Fax: 208-282-4305; Tel: 469-463-5139, email: wongyin@pharmacy.isu.edu

[***]Department of Biomedical & Pharmaceutical Sciences, College of Pharmacy, and Biomedical Research Institute, Idaho State University, Pocatello, ID 83209, USA Fax: 208-282-4305; Tel: 208-282-4408, email: abhushan@pharmacy.isu.edu

[****]Department of Biomedical & Pharmaceutical Sciences, College of Pharmacy, and Biomedical Research Institute, Idaho State University, Pocatello, ID 83209, USA Fax: 208-282-4305; Tel: 208-282-3324, email: cdaniels@pharmacy.isu.edu

[*****]Corresponding author: Department of Biomedical & Pharmaceutical Sciences, College of Pharmacy, and Biomedical Research Institute, Idaho State University, Pocatello, ID 83209, USA Fax: 208-282-4305; Tel: 208-282-2275, E-mail: lai@pharmacy.isu.edu

ABSTRACT

Cell culture models *in vitro* have long served as tools for the elucidation of cellular and molecular mechanisms of diseases. Recently these versatile models have gained wide acceptance in toxicology and tissue engineering research. Although these models are not exactly the same as the models *in vivo*, they facilitate mechanistic insights pertaining to a particular cell type. Nevertheless, co-cultures of two different but functionally complementary cell types provide structural and functional perspectives single-cell-type models do not. We have initiated a systematic development of this model type employing dorsal root ganglion (DRG) neurons and Schwann cells. Our first model involves non-contact co-cultures of Schwann cells and DRG neurons employing the hanging cell culture insert. The results from our studies to date demonstrate that our non-contact co-culture model is suitable for both high throughput and mechanistic studies in nanotoxicological and pathophysiological research.

Keywords: Co-culture model, DRG neurons, Schwann cells, nanotoxicology, tissue engineering, pathophysiology.

Topic:

1 INTRODUCTION

The aim of our studies is to systematically develop and characterize cell culture models of neural cells of the peripheral nervous system *in vitro* for nanotoxicological and pathophysiological research. Once such models are developed, they may have wide applications in tissue engineering research. The need for such models is derived from the fact that the peripheral nervous system is most susceptible for the development of neuropathy. Some examples of peripheral neuropathies include drug-(chemotherapy) induced neuropathy [1], disease-induced neuropathy (e.g., diabetes) [2], immune and inflammatory neuropathies, inherited and genetic neuropathies, and other neuropathies induced by toxicity.

The applications of nanomaterials, including nanoparticles, have been increasing exponentially in the last decade and have infiltrated diverse fields. Once they enter the body by inhalation or other routes, nanoparticles may be toxic to one or more organ systems [3]. However, the toxicity of nanoparticles in mammals, especially humans, has not been systematically studied although there is increasing concern about the environmental and health impact of exposure to nanoparticles of different types [4].

Consequently, we have systematically initiated a series of studies to elucidate the putative cytotoxicity of nanoparticles in various mammalian cell types [4]. For example, once recent study of ours noted that several metal oxide (including titanium and zinc oxides) nanoparticles exert differential cytotoxic effects on human neural cells in cell model systems *in vitro* [4] .

There have been, however, extremely few cell model systems developed employing peripheral neural cell types for nanotoxicological and tissue engineering studies. We have therefore initiated a systematic development of this type of models employing Schwann cells and dorsal root ganglion (DRG) neurons. The first model we have developed involved a non-contact co-culture model of Schwann cells and DRG neurons using the hanging cell culture insert. Thus, this type of co-culture cell systems, consisting of two distinctly different but functionally complementary cell types, provide structural and functional perspectives that single-cell-type models do not.

We hypothesized that non-contact co-culture model of Schwann cells and DRG neurons can be useful in elucidating the putative toxic effects of various nanoparticles on the peripheral nervous system. Furthermore, the putative cytotoxic effects of nanoparticles could also influence/disrupt the cell-to-cell communications between the two cell types. To test our hypothesis, we have initially characterized the Schwann cells the DRG neurons in monotypic or single-cell-type cultures. In our ongoing studies, employing our new co-culture, non-contact model, we have recently demonstrated that the survival of DRG neurons is increased when co-cultured with Schwann cells in this construct. In this study, we compare the putative cytotoxic effects of SiO_2 and TiO_2 nanoparticles on dorsal root ganglion (DRG) neurons and Schwann cells employing established cytotoxicity testing [5-8]. Furthermore, we are investigating the putative toxic effect of these nanoparticles on interaction(s) between DRG neurons and Schwann cells in non-contact co-culture.

2 MATERIALS AND METHODS

2.1 Cells and Culture Conditions

The immortalized DRG neurons were a gift from Dr. Ahmet Hoke's Laboratory at Johns Hopkins University (Baltimore, MD, USA)[9]. The rat Schwann cell line was obtained from ATCC (Manassas, VA, USA). These cells and their co-culture were cultured in DMEM (Sigma; St Louis, MO, USA) supplemented with 10% (v/v) fetal bovine serum (FBS), 1% (w/v) sodium pyruvate, 0.292 g/l L-glutamine, 1.5 g/l sodium bicarbonate, 1% (v/v) anti-mycotic and various specified concentrations (5-45 mM) of glucose.

2.2 Co-culture Model System

DRG neurons were cultured on a Corning Costar 24-well plate. Schwann cells were then seeded on a Millipore hanging cell culture insert (pore size 0.4 µm) on a separate plate and then introduced to a DRG neuron-containing well after 4 hours to achieve the co-culture condition [7]. DRG neurons (co-cultured with Schwann cells) were exposed to various concentrations of SiO_2 nanoparticles for specified periods and their survival determined employing the cell survival assay.

2.3 Cell Survival (MTT) Assay

DRG neurons or Schwann cells were seeded per well in a 48-well plate in DMEM with specified concentrations of SiO_2 nanoparticles. After incubation at 37°C for 24 or 48 hours, 50 µl of MTT (5 mg/ml in PBS) reagent was added to each well. After incubation for another 4 hours, the medium was removed gently and the cellular reaction product was solubilized in 200 µl DMSO. Then the optical density of the contents of each well was measured in a plate reader at 570 nm [4]. The absorbance corresponds to live cells present in each well [4].

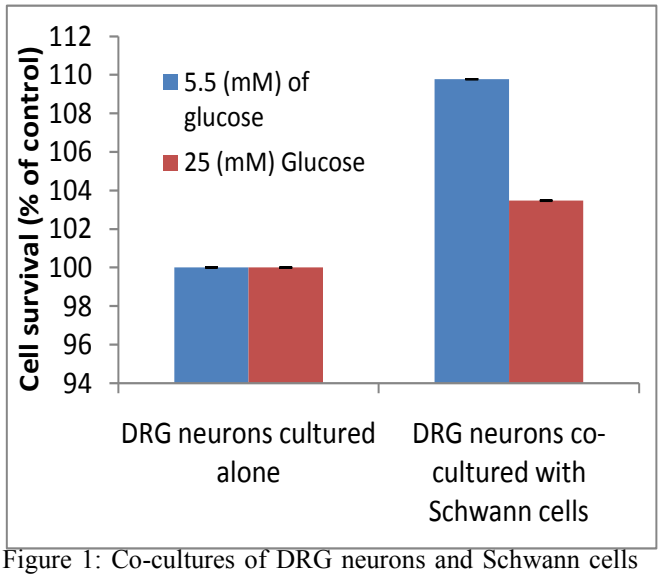

Figure 1: Co-cultures of DRG neurons and Schwann cells using hanging cell culture inserts (non-contact co-culture). Values are mean ± SEM of 2-3 determinations. DRG neurons cells treated with SiO_2 nanoparticles for 24 hours are arked with blue line and those treated for 48 hrs are marked with red line.

2.4 Cellular morphology

DRG neurons, Schwann cells and their co-culture was treated with SiO_2 specified concentration for 24 and 48 hours at 37^0 C as described above and bright field images were acquired by using a Leica light microscope (Leica DM IRB, Bannockburn, IL, USA) equipped with a digital camera (Leica DFC 300FX) [4].

2.5 Statistical analysis of results

Statistical significance of experimental results was analyzed with one-way ANOVA followed by Dunnett's post-hoc test with a minimum significance level set at $p < 0.05$ using the SPSS 17 software package.

3 RESULTS AND DISCUSSION

We are the first to employ dorsal root ganglion (DRG) neurons and Schwann cells to develop co-culture models *in vitro* because DRG neurons are the most susceptible nerve cells to developing pathologies in peripheral neuropathy. We have characterized the two cell types individually with respect to their optimum glucose requirement and activities of enzymes important in modulation of glutamate-glutamine cycling (e.g., glutamine synthetase) that is part of the metabolic and functional inter-dependence between DRG neurons and Schwann cells known to occur *in vivo* (data not shown). We have also studied the protein expression of various apoptosis-related proteins such as BCL-2, BCL-XL, BAX and cytohrome C in the two cell types (data not shown).

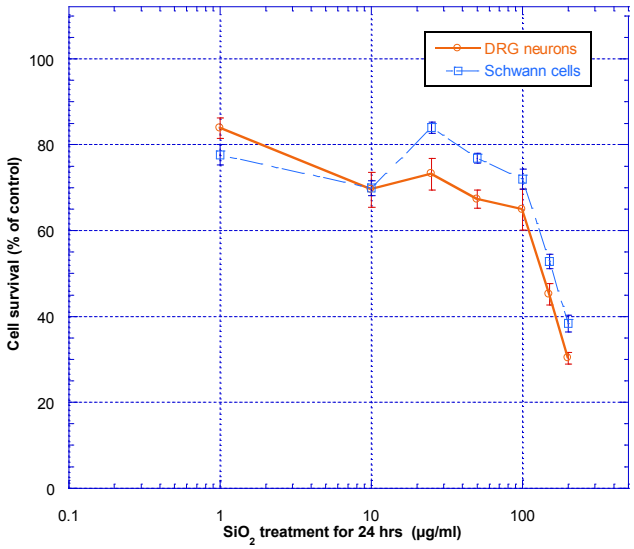

Figure 2: Effects of SiO_2 nanoparticles on DRG neurons and Schwann cells. Values are mean ± SEM of 12 determinations and replicate experiments show the same trend. DRG neurons and Schwann cells treated with SiO_2 nanoparticles for 24 hours are marked red and blue, respectively. treated with SiO_2 nanoparticles for 24 hrs are marked with blue line.

To our knowledge, we are the first to determine, in this study, the putative cytotoxic effects of SiO_2 and TiO_2 nanoparticles on neural cells of the peripheral nervous system (i.e., DRG neurons and Schwann cells).

As shown in Figure 2, treatment of DRG neurons or Schwann cells for 24 hours with SiO_2 induced a dose-related decreases in survival of those cells when we progressively increased the concentrations of the nanopartcles from 1 to 200 µM, with IC_{50} values of ~150 µM (Figure 2). At the highest concentration employed, less than 40% of the cells survived (Figure 2).

Because we had previously noted that TiO_2 nanoparticles exerted differential cytotoxic effects on central nervous system neural cells [4], we have investigated the possibility that these nanoparticles may also exert cytotoxic effects on neural cells from the peripheral nervous system. As shown in Figure 3, our on-going studies indicate that treatment with TiO_2 nanoparticles in the dose range so far employed (0.1 to 20 µM) appeared to lower the survival of both DRG neurons and Schwann cells: the effects seemed somewhat dose-related. Moreover, the Schwann cells appeared to be more susceptible to the effect of TiO_2 nanoparticles, suggesting they may exert differential effects on the neural cells of the peripheral nervous system.

We have also employed light microscopy to examine the effects of nanoparticles on DRG neurons and Schwann cells and assess the effects of SiO_2 and TiO_2 nanoparticles thereon (data not shown). In general, the photomicrographs revealed that treatment with the nanparticles induced dose-related changes in cellular morphology consistent with the nanoparticle-induced progressive decrease in cell viability (Figures 2 and 3).

As we have previous noted, treatment with TiO_2 nanoparticles induced dose-related increases in cell death of human central neural cells, marked by apoptosis, and necrosis, and an as yet uncharacterized cell death mechanism that appeared to be a mixture of apoptosis and necrosis [4]. Thus, the results of our ongoing studies with the peripheral nervous system neural cells such as DRG neurons and Schwann cells appear to show some similarity to those we obtained with central neural cells [4]. The DRG neurons and Schwann cells appear also to be susceptible to the cytotoxic effects of SiO_2 and TiO_2 nanoparticles. As we have indicated earlier, we are also determining the cell death mechanisms underlying the cytotoxic effects of SiO_2 and TiO_2 nanoparticles on DRG neurons and Schwann cells. Clearly, this is an important area that merits further study.

4 CONCLUSITIONS

Thus, the results from our studies to date as well as those from our ongoing studies demonstrate that our non-contact co-culture model is highly suitable for both high throughput and mechanistic studies in nanotoxicological and tissue engineering research. Moreover, this model is also relevant for the investigation of mechanistic issues associated with peripheral diabetic neuropathy and other disease states of the peripheral nervous system.

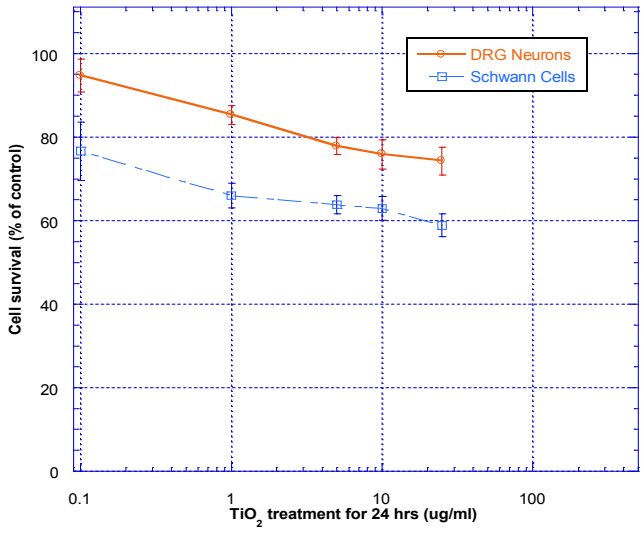

Figure 3: Effects of TiO_2 nanoparticles on DRG neurons or Schwann cells. Values are mean ± SEM of 12 determinations and replicate experiments show the same trend. DRG neurons and Schwann cells treated with TiO_2 nanoparticles for 24 hours are marked red and blue, respectively.

Results of our present and ongoing studies have confirmed that neural cells of the peripheral nervous system, similar to their counter parts in the central nervous system, are also susceptible to the cytotoxicity of SiO_2 and TiO_2 nanoparticles. Thus, these results are consistent with our hypothesis that our non-contact co-culture model of Schwann cells and DRG neurons can be useful to study toxic effects of various nanoparticles on peripheral nervous system.

The results of this and our ongoing studies suggest that nanoparticles may exert differential cytotoxic effects on neural cell types of the peripheral nervous system. As such, our results may assume pathophysiological importance in the environmental health impact of nanoparticles. Obviously, the is an important area that deserves further study.

5 ACKNOWLEDGEMENT

We thank Dr. Ahmed Hoke (Johns Hopkins University School of Medicine) for his generous gift of DRG neurons. Our study was supported, in part, by an USAMRMC Project Grant (Contract #W81XWH-07-2-0078), and NIH Grant #P20 RR016454 from the Idaho INBRE Program of the National Center for Research Resources.

6 REFERENCES

1. Chrissa, S. and A. Kyritsis, Cancer Chemotherapy and Pharmacology, 2009. **63**: p. 761–767.
2. Brownlee, M., *Biochemistry and molecular cell biology of diabetic complications.* Nature, 2001. **414**(6865): p. 813-820.
3. Cha K E and M. H, Journal of microbiology and biotechnology, Sep 2007. **17**(9): p. 1573-8.
4. James C K Lai1, et al., International Journal of Nanomedicine, Decmber 2008. **3(4)**.
5. Malthankar, G., et al., Neurochemical Research, 2004. **29**(4): p. 709-717.
6. Malthankar GV, White BK, and B. A, Neurochemistry Research, 2004. **29**: p. 709–17.
7. Puli S, Lai JCK, and Edgley KL, Neurochemistry Research, 2006. **31**: p. 1211–8.
8. Dukhande, V., et al.,
. Neurochemical Research, 2006. **31**(11): p. 1349-1357.
9. Lai JCK, Nguyen JV, and W. BK, Mol Biol Cell 1999. **10(Suppl)**: p. 445a.
10. Chen, W., et al., Journal of the Peripheral Nervous System, 2007. **12**(2): p. 121-130.

Elucidation of Neuroprotective Properties of Astrocytoma (Astrocytes-like) Cells in Neural Cell Culture Models *In Vitro*: Applications in Tissue Engineering and Nanotoxicology

Y.Y.W. Wong[*], A.R. Jaiswal[**], V.V. Dukhande[***], A. Bhushan[****], S.W. Leung[*****] and J.C.K. Lai[******]

[*]Presenting author: Department of Biomedical & Pharmaceutical Sciences, College of Pharmacy, and Biomedical Research Institute, Idaho State University, Pocatello, ID 83209, USA Fax: 208-282-4305; Tel: 469-463-5139, email: wongyin@pharmacy.isu.edu

[**] Department of Biomedical & Pharmaceutical Sciences, College of Pharmacy, and Biomedical Research Institute, Idaho State University, Pocatello, ID 83209, USA Fax: 208-282-4305; Tel: 208-705-2447, email: jaisashv@pharmacy.isu.edu

[***]Department of Molecular and Cellular Biochemistry, College of Medicine, University of Kentucky, Lexington, KY 40536-0509, USA Fax: 859-257-2283; Tel: 208-315-3370, email: vikas.dukande@gmail.com

[****]Department of Biomedical & Pharmaceutical Sciences, College of Pharmacy, and Biomedical Research Institute, Idaho State University, Pocatello, ID 83209, USA Fax: 208-282-4305; Tel: 208-282-4408, email: abhushan@pharmacy.isu.edu

[*****]Department of Civil and Environmental Engineering, College of Engineering, and Biomedical Research Institute, Idaho State University, Pocatello, ID 83209, USA Fax: 208-282-4538; Tel: 208-282-2524; email: leunsolo@isu.edu

[******]Corresponding author: Department of Biomedical and Pharmaceutical Sciences, College of Pharmacy, and Biomedical Research Institute, Idaho State University, Pocatello, ID 83209, USA Fax: 208-282-4305; Tel: 208-282-2275; email: lai@pharmacy.isu.edu

ABSTRACT

Evidence is accumulating that cell culture models *in vitro* facilitate high throughput and mechanistic studies in tissue engineering. Astrocytes are known to protect neurons against pathophysiological assaults *in vivo* and *in vitro* although the underlying mechanisms are not fully understood. Previously, we investigate several of the putative neuroprotective properties of astrocytes in cell culture model. Those studies led us to hypothesize that different stress factors can elicit and/or enhance the neuroprotective effects of astrocytes through the activation of astrocytic signaling and alteration of astroglial function. The results of this study suggest that U87 (astrocytes-like) astrocytoma cells exert some protective effects on SK-N-SH (neurons-like) neuroblastoma cells against pathophysiological assaults (e.g., oxidative stress) under several sets of culture conditions not previously studied. Thus, our results may have pathophysiological implications in neuroprotection and implications and applications in tissue engineering and nanotoxicological research.

Key Words: Cell culture models; human neural cells; U87 astrocytes-like astrocytoma cells; neuroprotection; tissue engineering; nanotoxicology

Topic Area:

1. INTRODUCTION

There is increasing evidence that cell model systems *in vitro* play vital roles in recent tissue engineering research. The additional structural and functional perspectives of co-culture cell systems *in vitro* start to gain prominence over

single cell type cell systems because unlike the latter, the former more closely resemble cell types in a tissue/organ *in vivo*.

Astrocytes (non-nerve, glial cells) in the brain play important roles in protecting neurons (nerve cells) against various assaults; yet, the cellular and molecular mechanisms underlying this protection is far more being understood [1]. Among the research on further elucidating such mechanisms, more efforts appear to center on commonly known neurodegenerative diseases such as Alzheimer's disease (AD), followed by Parkinson's disease (PD) [2]. AD is a progressive and irreversible neurodegenerative disorder in human brain leading to key symptoms of memory loss [3]. No known cure is available for AD as current therapy primarily treats AD symptoms and presents them from worsening. Thus, there is an urgent need to better understand how astrocytes exert their protective effects on neurons in a co-culture cell system *in vitro*. Once this protection is elucidated, then one could design treatment strategies and/or tissue engineering application to prevent the occurrence of accelerated neuronal loss in neurodegenerative diseases such as AD and PD.

Our project seeks to examine the underlying neuroprotective properties offered by astrocytes to protect neurons, employing a co-culture cell model system *in vitro*. We have been developing several model systems to investigate putative cytotoxic and inflammatory mechanisms associated with induction of neuronal cell damage and cell death [4-6]. Our previously data have shown that U87 astrocytoma and SK-N-SH neuroblastoma cells constitute good co-culture model systems for astrocytes and neurons, respectively, *in vitro* because of their close functional resemblance to normal astrocytes and neurons and that U87 cells protect SK-N-SH cells from several pathological assaults [4-5]. We therefore hypothesized that different stress factors can elicit and/or enhance the neuroprotective effects of astrocytes through the activation of astrocytic signaling and alteration of astroglial function. In this study, we have investigated this hypothesis further.

2. MATERIALS AND METHODS

2.1 Cell culture of U87 and SK-N-SH cells

The human astrocytoma (U87) and neuroblastoma (SK-N-SH) cell lines were obtained from (ATCC; Manassas, VA, USA) and cultured in MEM supplemented with 10% (v/v) fetal bovine serum (Atlanta Biologicals; Lawrenceville, GA), 1% (w/v) sodium pyruvate (Sigma Aldrich; St Louis, MO), 0.292 g/L L-glutamine (Sigma), 1.5g/L sodium bicarbonate (Sigma) and 1% (v/v) antimycotic (Atlanta Biologicals; Lawrenceville, GA). Cells were maintained at 37°C and 5% (v/v) CO_2 as described previously [4-5].

2.2 Treatment of U87 cells

The U87 cells were cultured in T-75 tissue culture flasks to ~50% confluent in 20 ml of 10% FBS-containing MEM medium. Then the medium was discarded and changed to 20 ml of 5% FBS-containing medium and the cells incubated for 24 hours. After that, the medium was replaced with 20 ml of medium containing 0% FBS and the cells incubated for an additional 24 hours. Cells were treated L-sulfoximine buthionine (BSO), or pioglitazone (PZ) or a combination of both. At the end of another 24 hours of incubation, the media were removed and frozen with liquid nitrogen immediately. The cell pellet was collected and both cell pellet and media collected were kept at -80°C until used for experiments.

2.3 Cell Survival (MTT) assay

The neuroprotective properties of U87 cells on SK-N-SH cells were determined in different combinations of regular medium (RM) and conditioned medium (CM) collected from U87 cells cultured under various conditions (see above). RC/CM ratio of 100/0, 70/30, 50/50, 40/60, 30/70, and 0/100 were used. SK-N-SH cell survival after the treatments was assessed employing the MTT assay [5].

2.4 Western Blot Analysis

Western blot analysis was employed to assess protein expression in cell lysates to determine the effects of media, BSO and PZ. SDS-PAGE electrophoresis was performed as previously described [7]. The separated proteins were visualized using chemiluminesence detection kit while β-actin was the loading control.

3. RESULTS AND DISCUSSION

Our culture model consists of U87 (astrocytes-like) cells and medium collected from U87 cells cultured under specified conditions to grow SK-N-SH (neurons-like) cells. This is a new modified co-culture strategy to allow the characterization of putative "protective factors" secreted by U87 cells to protect SK-N-SH cells in a non-contact cell culture setup. In addition, we can characterize the putative structural and functional properties of U87 cells under the different specified conditions.

A selective inhibitor of glutathione (naturally-occurring antioxidant) synthesis, L-buthionine sulfoximine (BSO), is used to induce oxidative stress in cells. A peroxisome proliferator activated receptor gamma (PPARγ) agonist, Pioglitazone (PZ), is used to block the inflammation which is usually unregulated in AD [8,9]. We have designed studies whereby we could utilize BSO and PZ in addition to serum depletion to further elucidate the putative protective mechanism(s) of U87 cells on neurons-like SK-N-SH cells. Serum depletion and drug treatment for U87 cell cultures were prepared as shown in the flow chart below (Fig. 1).

U87 cells cultured in medium containing 10% FBS were used as control (not shown in Fig. 1). Medium containing 0% FBS were defined as serum free (SF) medium.

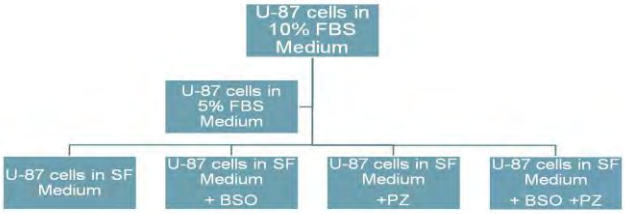

Figure 1. Experimental design of U87 cells treated with BSO, PZ or in combination. The U87 cells were grown to ~50% confluent in 10%-FBS containing medium and subsequently discarded and changed to 5% FBS-containing medium and incubated for 24 hours. After that, the medium was replaced with medium containing 0% FBS and incubated for an additional 24 hours. Cells were treated BSO or PZ or a combination of both for another 24 hours of incubation.

Morphological and functional changes/adaption in astrocytes *in vivo* and *in vitro* is known to associate with oxidative and other environmental stresses. We employed light microscopy to examine the effects of BSO treatment and FBS depletion to induce oxidative and environmental stress, respectively, on U87 cells and assess the effects of PZ treatment thereon.

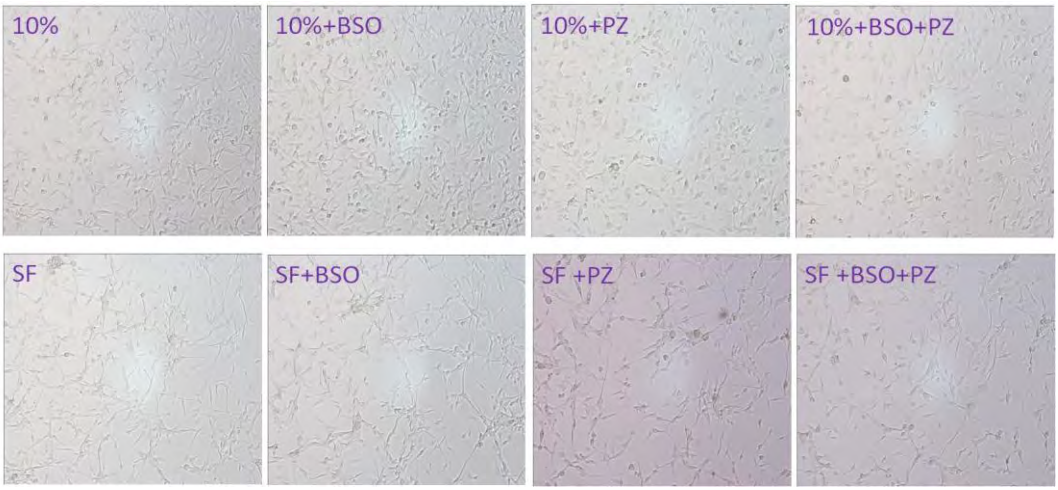

Figure. 2 Treatment-induced cellular morphology changes in U87 cells (100X magnification). Top panel of photomicrographs represents U87 cells cultured in 10% FBS medium treated with or without drug or drug combination while those of the bottom panel represents U87 cells cultured in serum-deprived (SF) medium treated with or without drug or drug combination.

Treatment with SF medium induced U87 cells to put out multipolar processes and the other treatments accentuated this effect (Fig. 2). Clearly, these observations raise interesting mechanistic questions that need to be addressed further (see below).

Glial fibrillary acid protein (GFAP) is a well-known and classical marker for astrocytes: its altered expression is associated with changes in astroglial morphology. Thus, we employed western blot to determine if the morphological changes in U87 cells exposed to SF medium with and without BSO/PZ treatment were seen also associated with changes in GFAP expression. An increased GFAP expression was observed when U87 cells were cultured in SF medium compared to those cultured in 10% FBS medium (data not shown), suggesting a correlation between changes in cellular morphology and GFAP expression.

Growth factors and neuronal survival enhancers are putatively released into the medium by astrocytes to protect their surrounding neurons. To investigate this possibility, we collected media in which we grew U87 cells under the conditions specified in Figure 1 above and assessed their ability to influence survival of SK-N-SH cells. Our results suggested that exposure of SK-N-SH cells to various combinations of SF media allowed them to survive better than when cultured in 10% FBS medium (control condition) alone (Fig. 3). Moreover, exposure to PZ enhanced this protective effect, even under conditions of oxidative stress.

4. CONCLUSIONS

When taken together, our results suggest astrocytes-like U87 cells changed their cell shape and morphology when cultured under serum-free media with and without drug treatment. Those morphological changes correlated with upregulation of GFAP in such cells.

Moreover, exposure of SK-N-SH cells to various combinations of SF media allowed them to survive better than when cultured in 10% FBS medium (control condition) alone and exposure to PZ enhanced this protective effect, even under conditions of oxidative stress. Thus, our results provide additional evidence that our cell model can be productively employed to further elucidate the putative neuroprotective mechanisms of astrocytes. As such they assume pathophysiological importance in neuronal

survival/death mechanisms in AD and PD. Clearly, this is an area that merits further study, especially in tissue engineering and nanotoxicological research and applications.

5. ACKNOWLEDGMENTS

This study was supported by an USAMRMC Project Grant (Contract #W81XWH-07-2-0078), NIH Grant #P20 RR016454 from the Idaho INBRE Program of the National Center for Research Resources.

REFERENCES

[1] Sofroniew M V, Vinters H V. Astrocytes: biology and pathology. Acta Neuropathol. 119:7-35,2010.

[2] Przedborski S, Vila M, Jackson-Lewis V. Neurodegeneration: What is it and where are we? Journal of Clinical Investigation. 111(1): 3-10, 2003.

[3] Chung S. Aberrant phosphorylation in the pathogenesis of Alzheimer's disease. BMB Rep. 42(8): 467-474, 2009.

[4] Malthankar GV, White BK, Bhushan A, Daniels CK, Rodnick KJ, Lai JCK. Differential lowering by manganese treatment of activities of glycolytic and tricarboxylic acid cycle enzymes in neuroblastoma and astrocytoma cells is associated with manganese-induced cell death. Neurochem Res. 29:709-717, 2004.

[5] Dukhande VV, Malthankar-Phatak GH, Hugus JJ, Daniels CK, Lai JCK. Manganese induced neurotoxicity is differentially enhanced by glutathione depletion in astrocytoma and neuroblastoma cells. Neurochem Res. 31(11):1349-1357, 2006.

[6] Wang Y-H, Jandhyam S, Dukhande VV, Gao WJ, Gu H-Y, Lai MB, Leung SW, Lai JCK. A co-culture model for nanotoxicity and tissue engineering studies. In Technical Proceedings of the 2008 Nanotechnology Conference and Trade Show; Volume 2, Chapter 2: Environment, Health & Toxicology, pp. 164-167, 2008.

[7] Isaac AO, Kawikova I, Bothwell ALM, Daniels CK & Lai JCK. Manganese Treatment Modulates the Expression of Peroxisomal Proliferator Activated Receptors (PPARs) in Astrocytoma and Neuroblastoma Cells. Neurochem. Res. 31(11):1305-1316, 2006.

[8] Yamagishi S. Protective role of PPARgamma agonists against cardiovascular disease. Nippon Rinsho. 68(2): 307-11, 2010.

[9] Syversen, U., Stunes, A K, Gustafsson, B I. et al. Different skeletal effects of the peroxisome proliferator activated receptor (PPAR) α agonist fenofibrate and the PPARγ agonist pioglitazone. *BMC Endocrine Disorders*.; 9:10,2009.

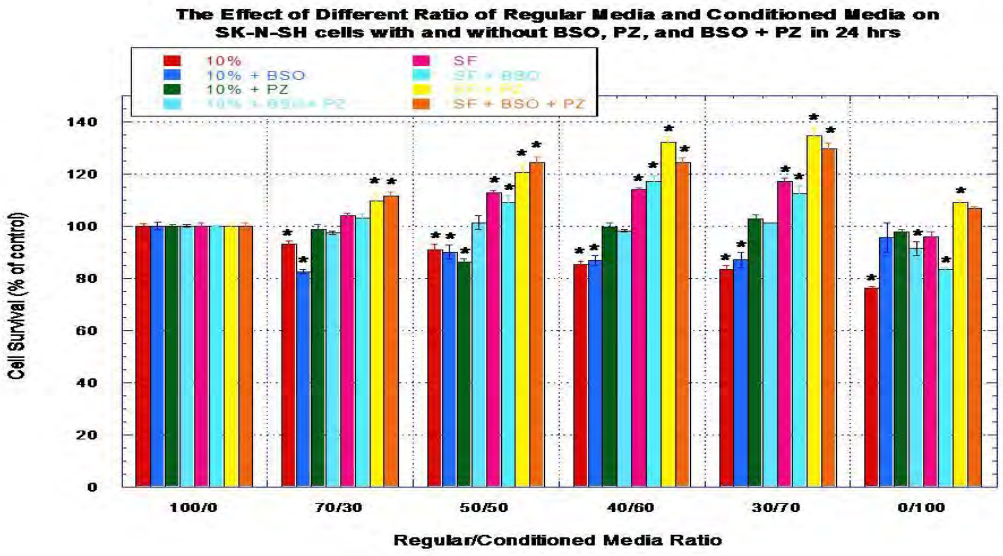

Figure 3. Treatment effects on SK-N-SH cell survival with different regular/conditioned media combination (see Fig. 1). SK-N-SH cells cultured in 10% FBS served as the control.
Values are expressed as % of the control and are given as mean ± SEM of separate determinations. *p<0.05 versus control.

Chitosan Membrane in Combinations with Nanoparticles and Adriamycin as a Treatment to Inhibit Glioma Growth and Migration

S. W. Leung*, W. Gao**, H. Gu***, A. Bhushan****, and J.C.K. Lai*****

*Corresponding author, Civil and Environmental Engineering Department, College of Engineering and Biomedical Research Institute, Idaho State University, Pocatello, ID 83209, USA Fax: 208-282-4538; tel: 208-282-2524; email: leunsolo@isu.edu
**Civil and Environmental Engineering Department, College of Engineering, Idaho State University, Pocatello, ID 83209, USA, email: gaowenj@isu.edu
***School of Public Health, Nantong University, Nantong, Jiangsu, 226007, P. R. China, email: hygu@ntu.edu.cn
****Biomedical & Pharmaceutical Sciences Department and Biomedical Research Institute, Idaho State University, Pocatello, ID 83209, USA, email: adhushan@pharmacy.isu.edu
*****Biomedical & Pharmaceutical Sciences Department and Biomedical Research Institute, Idaho State University, Pocatello, ID 83209, USA, email: lai@pharmacy.isu.edu

ABSTRACT

Chitosan exhibits antimicrobial activities through its interaction(s) with microbial cell surface thereby altering their gene expression and cellular function, leading to cell death. Nanometal particles exert many effects not previously expected on biological systems and thus can be explored for diverse biomedical applications. Our previous and on-going studies indicate that U87 cells cultured on chitosan film/membrane exhibited significantly slower growth and proliferation kinetics compared to U87 cells cultured alone. In this study we tested the hypothesis that the inhibitory effect of chitosan is enhanced if combined with nanometals and adriamycin, a common anticancer durg. Our results showed that combinations of metal nanoparticles, adriamycin and chitosan induced decreased survival of U87 glioma cells at different rates, more marked than those with chitosan alone. Thus, our results have pathophysiological implications in inhibiting human brain glioma invasion and migration.

Key words: Chitosan, nanoparticles, adriamycin, cancer therapy, U87 cells

1 INTRODUCTION

Chitosan, a polysaccharide biopolymer that combines a unique set of physicochemical and biological properties has increasingly gained popularity in biomedical applications [1, 2]. Our previous and on-going studies indicate that U87 cells (human brain glioblastoma cell line) cultured on chitosan film/membrane exhibite significantly slower growth and proliferation kinetics compared to U87 cells cultured in the absence of chitosan film/membrane [3]. Chitosan exhibits antimicrobial activities through its interaction(s) with microbial cell surface thereby altering their gene expression and cellular function and leading to cell death [4].

Nanometal particles, such as nanosilver, nanogold, are important material being utilized frequently. Recent studies of nanometal particles have revealed many properties that were not previously expected in biological systems and thus can be explored for various applications in biomedicine, such as tissue engineering [5] and wound dressing [6].

In this study, we hypothesized that the inhibitory effect of chitosan would be greatly modulated if we combine chitosan with nanometals and adriamycin, a common drug for cancer therapy. Similar treatments with a different cancer (PANC-1, human pancreatic cancer cell line) and normal cells (BJ, human fibroblast cell line) were also used to investigate this hypothesis.

2 MATERIALS AND METHODS

2.1 Materials

Human astrocytoma (astrocytes-like) U87 cells, human pancreatic PANC-1 cells and human fibroblast BJ cells were obtained from ATCC (Manassas,VA, USA). Chitosan (from crab shells, minimum 85% deacetylated), thiazolyl blue tetrazolium bromide (MTT), dimethyl sulfoxide (DMSO) and adriamycin were purchased from Sigma-Aldrich (St Louis, MO, USA). Fetal bovine serum (FBS) was obtained from Atlanta Biologicals (Lawrenceville, GA, USA). tetrachloroauric (III) acid ($HAuCl_4 \cdot 3H_2O$), trisodium citrate ($C_6H_5Na_3O_7 \cdot 2H_2O$) and silver nitrate ($AgNO_3$) were purchased from Fisher Scientific (Pittsburgh, PA, USA). Other chemicals were of analytical grade and were usually from Sigma-Aldrich (St. Louis, MO, USA) unless otherwise stated.

2.2 The Preparation of Nanosilver, Nanogold Particles

To prepare nanosilver, $AgNO_3$ and $C_6H_5Na_3O_7 \cdot 2H_2O$ solutions were filtered through a 0.22 µm microporous membrane filter, and nanosilver was prepared according to the literature [7] by adding $C_6H_5Na_3O_7 \cdot 2H_2O$ solution to boiling $AgNO_3$ aqueous solution.

To prepare nanogold, $HAuCl_4 \cdot 3H_2O$ and $C_6H_5Na_3O_7 \cdot 2H_2O$ solutions also need to be filtered through a 0.22 µm microporous membrane filter prior to use. Nanogold was prepared according to the literature [8] by adding $C_6H_5Na_3O_7 \cdot 2H_2O$ solution to boiling $HAuCl_4 \cdot 3H_2O$ aqueous solution.

2.3 Cell Culture

Chitosan membrane was prepared as described previously [3]. A certain amount of nanosilver or nanogold solution was added into each well of 24-well culture plates in which a sterile chitosan membrane had already been placed. After 12 hours, nanosilver or nanogold solution was aspirated and sterile phosphate-buffered saline (PBS) was added into each well to wash the membrane.

U87 cells were seeded with equal density in each well of the 24-well plates and cultured in an incubator at 37˚ C and 5 % CO_2 in modified Eagle's medium (MEM) supplemented with 10% fetal bovine serum (FBS). Adriamycin with a final concentration of 0.1 µm was added after cells were seeded. Culture of PANC-1 cells and BJ cells were similar with U87 cells whereas PANC-1 cells were grown in the RPMI 1640 medium.

2.4 MTT Assay

Cell survival and growth was determined using the MTT assay [9]. Cells (U87, PANC-1, and BJ) were cultured in 24-well plates as described in the preceding subsection. At the end of the incubation period (4, 7, 10, or 14 days), MTT dye (0.5%, w/v, in PBS) was added to each well and the plates were incubated for an additional 4 hours at 37°C. The purple-colored insoluble formazan crystals in viable cells were dissolved using dimethyl sulfoxide, and the subsequent absorbance of the content of each well was measured at 570 nm using a Bio-Tek Synergy HT Plate Reader (Winooski, VT, USA) [10].

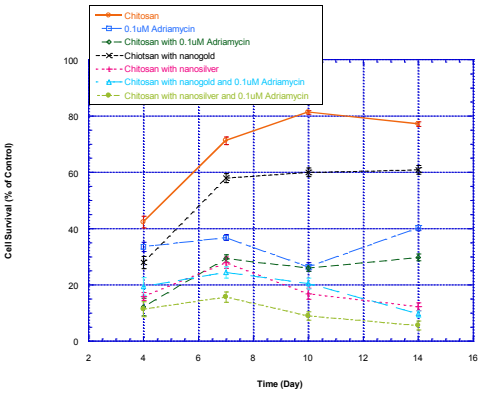

Figure 1: Effect of chitosan, chitosan/nanosilver, chitosan/nanogold and adriamycin on survival of U87 cells. Red circles: chitosan; Black cross signs: chitosan with nanogold; Blue squares: 0.1 µm adriamycin; Green squares: chitosan with 0.1 µm adriamycin; Red plus signs: chitosan with nanosilver; Blue triangles: chitosan with nanogold and adriamycin; Dark green circles: chitosan with nanosilver and 0.1 µm adriamycin. At the end of the specified incubation time, cell survival and growth was determined using the MTT assay. Values are the mean ± SEM.

2.5 Statistical Analysis of Data

Results are presented as mean ± standard error of the mean (S.E.M.) of 6 determinations in each experiment.

3 RESULTS AND DISCUSSION

As shown in Figure 1, all the treatments induced decrease in cell survival of U87 cells. There were apparent differences in the effects exerted by different treatments. After being treated for 14 days, chitosan with naosilver and 0.1 µm adriamycin was the most effective. This may enable lower doses of adriamycin to be used, with reduced toxicity. Chitosan with nanogold and 0.1µm adriamycin was the second most effective; chitosan alone was the least effective. Chitosan with nanosilver showed greater effect than chitosan with nanogold. Therefore, these results provided some support for our hypothesis that a combination of chitosan with nanometals and adriamycin was more effective than chitosan or adriamycin alone or chitosan with nanometals.

As shown in Figure 2, all the treatments showed an inhibitory effect on cell survival of PANC-1 cells. Similarly, after being treated for 14 days, chitosan with nanosilver and 0.1 µm adriamycin was the most effective; chitosan alone was the least effective. However, the effect was stronger on PANC-1 cells than on U87 cells. Compared with U87 cells, PANC-1 cells were considerably more sensitive to the effects of adriamycin alone.

Figure 3 showed the effect of different treatments on the survival of BJ cells. Chitosan with nanosilver and 0.1 µm adriamycin was the most effective, the same as U87 cells and PANC-1 cells. By day 14, however, there was no significant difference in the survival rate of cells treated with chitosan alone and chitosan with nanogold and untreated (control).

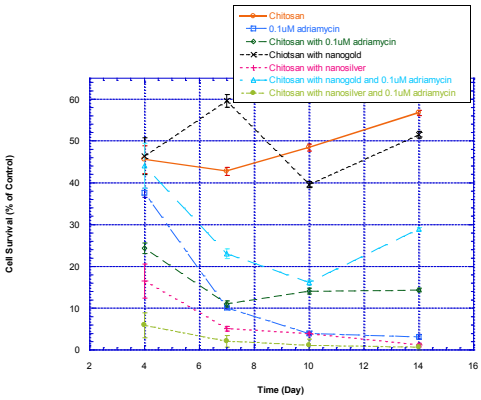

Figure 2: Effect of chitosan, chitosan/nanosilver, chitosan/nanogold and adriamycin on survival of PANC-1 cells. Red circles: chitosan; Black cross signs: chitosan with nanogold; Blue triangles: chitosan with nanogold and adriamycin; Green squares: chitosan with 0.1 µm adriamycin; Blue squares: 0.1 µm adriamycin; Red plus signs: chitosan with nanosilver; Dark green circles: chitosan with nanosilver and 0.1 µm adriamycin. At the end of the specified incubation time, cell survival and growth was determined using the MTT assay. Values are the mean ± SEM.

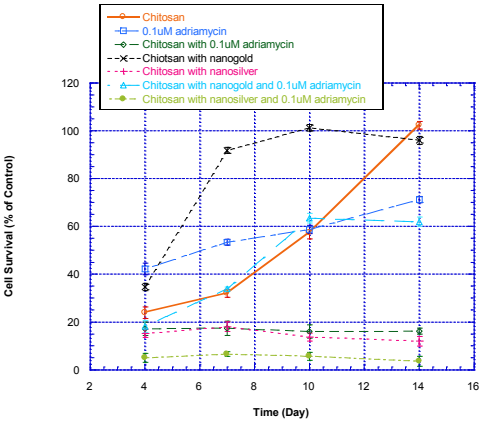

Figure 3: Effect of chitosan, chitosan/nanosilver, chitosan/nanogold and adriamycin on survival of BJ cells. Red circles: chitosan; Black cross signs: chitosan with nanogold; Blue squares: 0.1 µm adriamycin; Blue triangles: chitosan with nanogold and adriamycin; Green squares: chitosan with 0.1 µm adriamycin; Red plus signs: chitosan with nanosilver; Dark green circles: chitosan with nanosilver and 0.1 µm adriamycin. At the end of the specified incubation time, cell survival and growth was determined using the MTT assay. Values are the mean ± SEM.

4 CONCLUSIONS

Our previous and ongoing studies demonstrate that combinations of metal nanoparticles, adriamycin and chitosan induced cell death at different rates, with reference to U87 cells cultured in the absence of chitosan and with chitosan alone. Chitosan with nanosilver and 0.1 µm adriamycin showed the greatest cell survival reduction on all three cell lines. Chitosan with nanosilver showed greater effect than chitosan with nanogold. Taken together, these results suggest potentials for pathophysiological applications in inhibition of human brain glioma migration and invasion and in treatment of pancreatic cancer.

5 ACKNOWLEDGMENTS

Our studies were supported by a DOD USAMRMC Project Grant (Contract #W81XWH-07-2-0078).

REFERENCES

[1] Li Z, Cen L, Zhao L, Cui L, Liu W, Cao YL, "Preparation and evaluation of thiolated chitosan scaffolds for tissue engineering," Journal of Biomedical Materials Research Part A, 92A (3): 973 – 978, 2010.

[2] Wilson B, Samanta MK, Santhi K, Kumar KPS, Ramasamy M, Suresh B, "Chitosan nanoparticles as a new delivery system for the anti-Alzheimer drug tacrine," Nanomedicine: Nanotechnology, Biology and Medicine, 6(1):144-152, 2010.

[3] Gao WJ, Wang YH, Gu HY, Jandhyam S, Dukhande VV, Lai MB, Leung SW, Bhushan A, Lai JCK, "Chitosan Film/Membrane as a Surface to Alter Brain Glioma Growth and Migration," In Proceeding of the 12th NSTI (Nano Science and Technology Institute) Nanotech, Houston, USA, Volume 2, pp. 302-305, 2009.

[4] Raafat D, Bargen K, Haas A, Sahl H, "Insights into the mode of action of chitosan as an antibacterial compound," Appl Environ Microbiol, 74(12):3764-373, 2008.

[5] Zhang Y, He H, Gao WJ, Lu SY, Liu Y, Gu HY, "Rapid adhesion and proliferation of keratinocytes on the gold colloid/chitosan film scaffold," Materials Science and Engineering C, 29(3): 908-912, 2009.

[6] Lu SY, Gao WJ, Gu HY, "Construction, application and biosafety of silver nanocrystalline chitosan wound dressing," Burns, 34 (5): 623–628, 2008.
[7] Kamat PV, Flumiani M, Hartland GV, "Picosecond Dynamics of Silver Nanoclusters. Photoejection of Electrons and Fragmentation," J. Phys. Chem. B, 102(17): 3123-3128, 1998.
[8] Turkevich J, Stevenson PC, Hillier J, "A study of the nucleation and growth processes in the synthesis of colloidal gold," Discuss. Faraday Soc., 11: 55-75, 1951.
[9] Mossman T, "Rapid colorimetric assay for cellular growth and survival: Application to proliferation and cytotoxicity assays," Journal of Immunological Methods, 65(1-2): 55-63, 1983.
[10] Dukhande VV, Malthankar-Phatak GH, Hugus JJ, Daniels CK, Lai JCK, "Manganese induced neurotoxicity is differentially enhanced by glutathione depletion in astrocytoma and neuroblastoma cells," Neurochem Res., 31(11): 1349-1357, 2006.

Biomedical Applications of Modified Carbon Glassy Electrode Sensor with Nanoparticles and Dendrimers

S. W. Leung[1], Y. Wang[2], H. Gu[3], and J.C.K. Lai[4]

[1]Corresponding author, Civil and Environmental Engineering Department, College of Engineering and Biomedical Research Institute, Idaho State University, Pocatello, ID 83209, USA Fax: 208-282-4538; tel: 208-282-2524; email: leunsolo@isu.edu

[2]Civil and Environmental Engineering Department, College of Engineering, Idaho State University, Pocatello, ID 83209, USA

[3]School of Public Health, Nantong University, Nantong, Jiangsu, 226007, P. R. China.

[4]College of Pharmacy and Biomedical Research Institute, Idaho State University, Pocatello, ID 83209, USA

ABSTRACT

In our previous reports, we studied the development of biosensor platform that are capable of measuring biometabolites and environmental sensitive species, such as peroxide and nitrate/nitrate, to concentration in the order of ppb (parts per billion) or lower.

In our more recent development, we modified our platform with dendrimers to enhance its performance. Zero and second generation of dendrimers were coated on the surface of a carbon glassy platform electrode modified with GDH (glutamate dehydrogenase) and it was used to measured ammonium, a common biometabolite, at near neutral pH that is common for normal bioactivities.

The resulting electrode was tested with ammonium concentrations ranged from 0.002 to 0.3 µM with satisfactory results. Measurements at lower concentrations had better resolution than at higher concentrations and it is believed that the lower concentration limit can be better than the tested lower limit at 0.002 µM. Performance of the modified carbon glassy electrode was compared with other glassy electrodes that were modified differently, and the results will be reported.

The biosensor platform thus far was proven to be versatile and can be used in many biomedical and environmental applications.

Key words: biosensor, nanoparticle, GDH, ammonium, electrode, PAMAM

1 INTRODUCTION

In the past several years, our research group has been developing a platform for biosensor construction that are capable of detecting target species that are in nano and subnanomolar levels [1, 2].

In this study, we were developing a biosensor that can measure ammonia at submicromolar levels that cannot be detected by commercial ammonia electrodes or wet chemistry method easily.

1.1 Theory

As shown in the following equation, glutamate and NAD^+ can be hydrolyzed to form α-keto glutarate, NADH, and ammonium ion with the enzyme, glutamate dehydrogenase. The equilibrium constant is in favor of the formation of glutamate and thus the reverse reaction is faster kinetically.

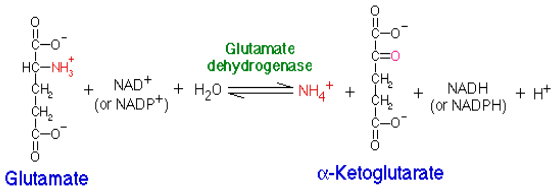

For many biological reactions, the end product or metabolite is ammonium, accumulation of high concentration of ammonium is toxic to the body. Environmentally, ammonium is a byproduct of many industrial processes, uncontrolled discharges of ammonium will lead to harmful consequence to the environment. Our goal here was to develop a sensor device that can measure ammonium ion at the lowest concentrations possible, its utilities can be in biomedical or environmental applications. Hence, it is the reverse of the reaction as shown above (glutamate formation) that we utilized.

2 MATERIALS AND METHODS

2.1 Materials

L-glutamic dehydrogenase (from bovine liver, solution in 50% glycerol) (GDH) was purchased from Sigma-Aldrich (St. Louis, MO, USA), the concentration of GDH is 28 mg protein/ml, and 46 units/mg. Cysteamine, polyamidoamine dendrimer generation 0 (PAMAM_0), polyamidoamine dendrimer generation 2nd (PAMAM_2nd), and α-keto glutarate, $AuCl_3HCl{\cdot}4H_2O$ (Au %> 48%) and Na_3citrate were purchased from Sigma. All the other chemicals were of analytical grade or highest grade available. All the experiments were carried out under deoxygenated condition in 0.1 M phosphate buffer solution.

2.2 Electrode Preparation

The cleaned glassy carbon electrode was first immersed in 0.1 M cysteamine solution in darkness. The resulting monolayer-modified electrode was rinsed thoroughly with twice-distilled water and soaked in water. Then, it was dipped into the colloidal gold. The gold colloid–cysteamine-modified electrode was dipped into the l-glutamate dehydrogenase (GDH) solution (pH 7.4) (or GDH solution containing NADH). In such a way, a GDH (/NADH) gold colloid–cysteamine-modified glassy carbon electrode was obtained.

In case that both cysteamine and PAMAM were coated onto electrodes, the cleaned glassy carbon electrode was first immersed in cysteamine solution, the resulting electrode was dipped into the PAMAM solution. The gold colloid–cysteamine/PAMAM-modified electrode was dipped into the GDH solution (pH 7.4) (or GDH solution containing NADH). In such a way, a GDH (/NADH) gold colloid–cysteamine/PAMAM-modified glassy carbon electrode was obtained.

2.3 Nanoparticles Solution Preparations

Nanoparticles Au was prepared by reacting $HAuCl_4$ with citric acid [2].

2.4 Detections

UV-VIS spectrophotometry was carried out by an Agilent diodearray spectrophotometer; cyclic voltammetry was conducted by using a Gamry 600 Potentiostat. Voltammetric potential was measured against a saturated chloride electrode (SCE).

3 RESULTS AND DISCUSSION

3.1 Stability of Electrodes

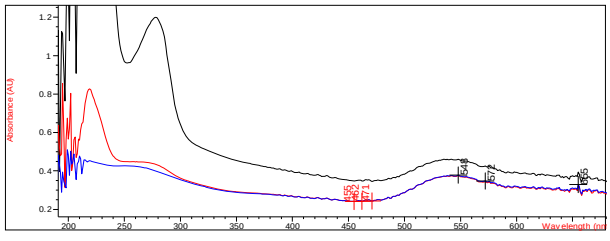

Figure 1. Cysteamine-PAMAM-Au-GDH coated on plastic UV-VIS cell with permanent absorption peak at 278 nm. Various lines indicated concentration differences.

As shown in Figure 1, PAMAMs can be attached to cysteamine to enhance the available sites for the electrons transfer between reactions, in this case, ammonium and α-keto glutarate, therefore increase the detection lower limit.

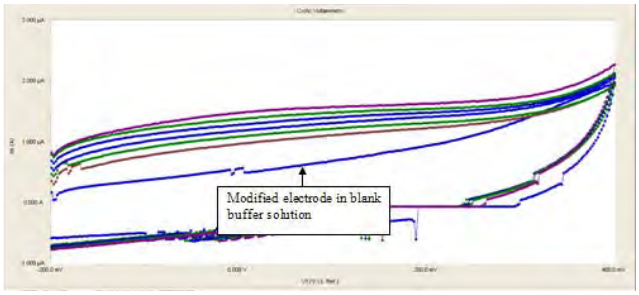

Figure 2. Cyclic voltammograms (i/v) of gold colloid-cysteamine/PAMAM_2ND-modified glassy carbon electrode measured from-0.2 to 0.4 V for the measurement of NH_4^+, the lowest concentration was 2 nM.

Figure 2 shows the cyclic voltammograms of various ammonium concentrations measured by the modified glassy carbon electrode, the lowest concentration was 2 nM. As indicated in the voltammogram in the reductive curves (upper lines), there was a big gap (current difference) between the blank (of buffer solution) and the first reductive curve (2 nM). Therefore, it is possible that the modified electrode can measure ammonium concentrations down to subnanomolar levels.

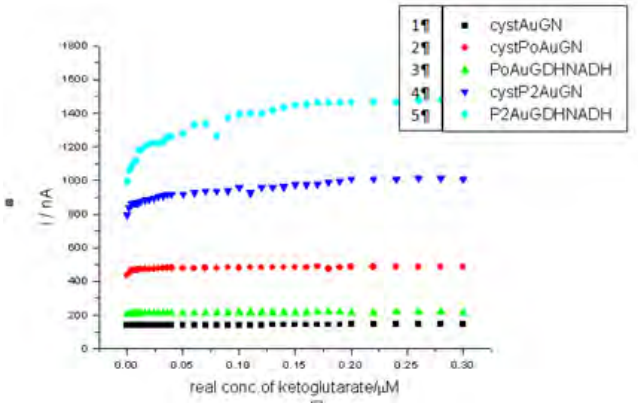

Figure 3. Performance differences of the glassy carbon electrode modified by different materials: 1. Modified with cysteamine-Au-GDH/NADH; 2. Cysteamine /PAMAM_0-Au-GDH/NADH; 3. PAMAM_0-Au-GDH/NADH; 4. Cysteamine /PAMAM_2nd-Au-GDH/NADH; 5. PAMAM_2nd -Au-GDH/NADH.

Figure 3 shows that there were distinctive current differences for the reaction of ammonium and α-keto glutarate when the electrode was modified by different

materials. From the stand point of detection, within the five modifications, sensor coated with second generation of PAMAM would have the highest sensitivity (current vs. concentration). The results were conceivably due to the higher branching property of PAMAM_2nd.

4 CONCLUSIONS

We successfully modified our glassy carbon electrode biosensor platform [2] for ammonium detection; we further modified the sensor platform with PAMAMs and the detection lower limit was enhanced. This highly modified electrode can detect ammonium concentrations down to 2 nM, or lower. The low detection limit of this biosensor is far more superior to most available methods, more research is needed for noise reduction and the stability of the electrode.

5 ACKNOWLEDGMENT

This study was supported by an USAMRMC Project Grant (Contract #W81XWH-07-2-0078).

REFERENCES

[1] S. W. Leung, Y. Wang, H. Gu, and J.C.K. Lai, “Characterization and Applications of Modified Gold Electrode Sensor with Nanoparticles”, in Technical Proceedings of the 2009 Nanotechnology Conference and Trade Show, Volume 2: Chapter 4: Biosensors and Diagnostics, pp. 233-235.

[2] J.C.K. Lai, Y. Wang, W. Gao, H. Gu, and S. W. Leung, “Performance Comparisons of Nanoparticle Modified Sensor Electrodes for the Detection of Nitrite and Peroxide”, in Technical Proceedings of the 2009 Nanotechnology Conference and Trade Show, Volume 2: Chapter 4: Biosensors and Diagnostics, pp. 233-235.

ISEIS 2010 International Conference on Environmental Informatics

Metallomic Distribution in Various Regions of the Brain as Influenced by Dietary Intakes and Their Implications

G.L. Wright[a], J.C.K. Lai[b], A.W.K. Chan[c], M.J. Minski[c], L. Lim[d] and S.W. Leung[e,*]

[a]*Civil and Environmental Engineering Department, College of Engineering, Idaho State University, Pocatello, ID 83209, USA*
[b]*Biomedical & Pharmaceutical Sciences Department, College of Pharmacy and Biomedical Research Institute, Idaho State University, Pocatello, ID 83209, USA*
[c]*Imperial College Reactor Centre, University of London, Silwood Park, Ascot, Berks., SL5 7PY, UK*
[d]*University College London, Institute of Neurology, University of London, London WCIN 1P3, UK*
[e]*Corresponding author: Civil and Environmental Engineering Department, and Biomedical Research Institute, Idaho State University, Pocatello, ID 83209, USA*

Abstract. Lifelong exposure to environmental factors can influence the risk of developing diseases according to recent research findings. Environmental stresses ultimately leading to neuronal cell death have been hypothesized as the causes of the increased occurrence in developing Alzheimer"s and Parkinson"s disease. Our daily diet is considered to be one of the most important environmental factors that can seriously affect the development and proper functions of the brain. Depending on the concentrations, metals and electrolytes can post some health concerns, especially for a prolonged consumption period. For example, it was reported that excess amounts of iron, zinc and copper in the human brain may cause oxidative damage and protein aggregation; the neurotoxicity induced by these metals may lead to cerebral and/or cerebellar degeneration. Other reports showed that there were differences in concentrations of five different elements (aluminum, zinc, copper, manganese, and iron) between normal human brain and brains of patients with Alzheimer"s disease. In this study, we investigated 30 elements, including electrolytes, and how dietary intake on a life-time basis would affect their concentrations and distributions in various regions of the rat brain (hypothalamus, cerebellum, pons and medulla, striatum, mid-brain, cerebral cortex, and hippocampus) and discussed their health implications. Information matrices of these 30 different elements (mostly metals) and their distributions in various regions of the rat brain were analyzed as a function of normal dietary intake at different ages during development. Our results showed that metallomic distribution in various regions of the rat brain is age-related. The results may help researchers to identify possible links between daily dietary intake of metals and electrolytes and diseases associated with aging (e.g., Alzheimer"s and Parkinson"s disease) and suggest such metallomic distributions may be used as neurological biomarkers of exposure to heavy metals.

Key words: Brain; elements; metals; electrolytes; distribution; metallomic; neurological; diseases

1. Introduction

Many of the metals around us are essential for life, but others are known to be highly toxic; even the essential metals can be toxic when their intakes are too high. For example, metals such as chromium, cobalt, copper, manganese, and zinc are essential for life. But, an excess intake of these essential metals can induce toxicity. Some metals such as arsenic, cadmium, lead, mercury, and vanadium, which are found throughout our environment, are toxic to humans and other animals. Some of these toxic metals are even capable of forming covalent bonds with carbon, resulting in metal-organic transformations. This type of transformation affects the mobility and toxicity of the element. Elements can come from naturally-occurring processes such as volcanoes, water, bacterial activity, and also from anthropogenic sources such as automobile exhaust, agricultural fertilizers, industrial activities, and many other sources. It has been shown that in highly industrialized areas, the exposure to metallic elements is extremely high [1].

Being a specialized organ of the body, the brain metabolizes and accumulates metals as part of its normal development and function. But in a rich metal environment, loss of metalloproteins and loss of defense against oxidative stress caused by one or more of the heavy metals could be responsible for neurodegenerative disorders such as Parkinson"s disease (PD) and Alzheimer"s disease (AD) [2]. The intake of these metals occurs via ingestion

* Solomon W. Leung. Tel.: +1-208-282-2524; fax: +1-208-282-4538.
E-mail address: leunsolo@isu.edu

of metal-containing food and water, and/or through inhaling metal-contaminated air. The elemental distributions in the different brain regions appear to vary for each element. Some of these metallic elements are known to increase or decrease in brains of humans with a neurodegenerative disorder.

The following are some of the more studied elements in brain; other elements are also found in brain, but research on the latter group has been scant. Although many metals are normally found in brain, over-accumulation of metals may lead to health problems. Moreover, an unbalanced increase or decrease could cause a major functional change and lead to a neurodegenerative disorder even though the underlying molecular mechanisms are largely unknown.

Aluminum

Aluminum (Al) is one of the more widely distributed metals in the environment. Approximately 8% of the earth‟s crust is Al. The exposure of Al normally occurs through air, food, and water [3]. The brain contains approximately 1% of the body‟s total Al; however, Al has no known function in normal mammalian brain.

During the life-span of a normal human brain, its Al levels appear to increase around age 40, and then plateau at about age 70. The Al levels then begin to increase again from age 80 to 90. The globus pallidus (GP), substantia nigra (SN) and the nucleus ruber appear to be the highest Al levels in the normal human brain [4]. The levels of Al increase in the grey matter in patients with dialysis encephalopathy [5]. Also, Al accumulations in the brain have been found to increase in patients with renal failure. Following oral exposure to this metal, retention of Al was reported in the hippocampus. This region of the brain is rich in cholinergic neurons. These and other observations suggest that Al has neurotoxic properties. Furthermore, following chronic exposure, Al has been shown to accumulate in all regions of the rat brain. There is evidence of a relationship between the high levels of Al and increased risk of neurodegenerative disorders, including AD and PD [3].

Calcium

Calcium (Ca) is the fifth most abundant element found in the earth‟s crust. Ca occurs most commonly in sedimentary rocks in the minerals calcite, dolomite, and gypsum. Ca is essential for life in most living organisms, including humans. Ca has been shown to be elevated in the brains of patients with AD: it concentrates in the amyloid plaques. These plaques are one of the neuropathological hallmarks of AD. However, PSAPP mice (a mouse model of AD) appear to accumulate less Ca in their plaques compared to their surrounding brain tissue [6].

Chromium

Chromium (Cr) is also found in the earth‟s crust and is mined as chromite ore. Because of chromium‟s high corrosion resistance and hardness, it is added to nickel to create stainless steel: this is the most common application of Cr. It is also used in dyes and pigments, as a gasoline additive, and in the tanning of leather. The pathophysiological role of Cr has not been elucidated. However, Cr has been shown to moderately increase in the parietal cortex of patients with AD when compared to that in normal brain [7].

Copper

Copper (Cu), like most elements, is mined from the earth‟s crust. Furthermore, Cu is recycled. Cu is commonly used in electrical applications, piping, many household products (e.g., sinks, plumbing, pots), architectural applications, coin-making, and chemical applications. Cu has been found to be vital in human and plant life. Cu is introduced into the body mostly via food intake. Some foods that are high in Cu are oysters, beef or lamb liver, Brazil nuts, cocoa, black pepper, lobster, sunflower seeds, green olives, avocados, and wheat bran. The brain contains approximately 7.3% of the total body Cu supply.

Cu has been an extensively studied metal in the brain [8]. In a normal brain, Cu is distributed in similar ways in the central and subcortical white matter of the cerebellum of both young and old brains; however, the periphery of the dentate nucleus is rich in Cu [2]. The higher Cu concentrations are mostly found in the cortex and hippocampus [8]. A normal aging brain has been shown to have increased Cu levels, especially in the substantia nigra and in some cerebellar regions [4]. However, when the levels of Cu in the cortex and hippocampus increase, Wilson‟s disease is said to result [9]. In AD, there is an abnormal brain Cu distribution, with large amounts in the amyloid plaques but a deficiency in the neighboring brain tissue. Other researchers also reported Cu to increase in the senile plaques [4]. These findings suggest the involvement of Cu in AD is multifactorial and complex.

Iron

Iron (Fe) is one of the most common metals found in everyday use. Fe makes up about 5% of the earth‟s crust. The earth‟s core is believed to consist largely of an iron-nickel alloy constituting 35% of the mass of the earth as a whole. Because of this distribution, Fe is thought to be the most abundant element on earth. Some popular food stuffs rich in Fe include red meat, fish, poultry, beans, vegetables, black-eye peas, wheat, and cereals.

Fe is another extensively studied metal in brain. Fe is necessary for normal brain function (e.g., in learning and memory) [10]. In a normal brain, Fe is distributed in similar ways in central and subcortical white matter of the cerebellum of both young and old brains; in the cerebellar cortex, there are high Fe levels, and the periphery of the dentate nucleus is also rich in Fe [2]. Fe appears to increase rapidly in the young brain and then remains stable until the later years; increases in Fe in the substantia nigra and globus pallidus have been reported [4]. Regions where brain Fe is high include substantia nigra, globus pallidus, red nucleus, caudate nucleus, and the putamen [11].

Like Cu and Ca, Fe has been shown to be elevated in brains of patients with AD. Elevated Fe is found in the amyloid plaques [6]. Fe is also moderately increased in the parietal cortex in AD patients [7]. In patients with Attention Deficit Hyperactivity Disorder (ADHD), Fe has been shown to increase in the substantia nigra [12].

Manganese

Manganese (Mn) is found in the earth‟s crust and in seawater. It is often found with Fe. Some of the more common usages of Mn are in steel, aluminum alloys, alkaline batteries, coins, and pigments. Some popular foods that contain Mn include tea, spinach, grains, rice, eggs, nuts, olive oil, green beans, and fish.

The majority of the human body‟s Mn is found in liver and kidneys; nevertheless, Mn is an important element for normal brain development and function [13]. In the aging brain, Mn has been shown to redistribute itself in different brain regions, including hypothalamus, thalamus, and corpus callosum [4]. High brain Mn concentrations are related to PD. There has been much research indicating that human striatum, globus pallidus, and substantia nigra show increases in Mn levels and are thought to be target sites for Mn neurotoxicity. The globus pallidus and pituitary glands are other regions where Mn preferentially accumulates. High exposures to Mn result in increases in Mn in the olfactory epithelium and olfactory bulb [14]. It is noteworthy that Mn levels in the cerebellum are similar in AD and normal brains while Mn increases in the parietal cortex of AD brains [7].

Magnesium

Magnesium (Mg) is the 8th most abundant element in the earth‟s crust and in found also in seawater. Mg is commonly used in structural building materials, automotive parts, electronic devices, aerospace construction, photography, and fireworks. Mg is an essential metal in human and plant life [13]. Human Mg deficiency has been linked to the development of asthma, ADHD, and osteoporosis. Foods that are high in Mg include spices, nuts, cereals, coffee, cocoa, tea, and vegetables. In neurodegenerative disorders such as AD and PD, Mg does not appear to play a major role. For example, Mg levels in the cerebellum and parietal cortex do not differ between patients with AD and normal humans [7].

Mercury

Mercury (Hg) is found in deposits throughout the world, mostly as cinnabar (a common ore of Hg). The more common uses of Hg are in barometers, thermometers, dental products (e.g., fillings), and electrical equipment (e.g., computers, telephones, etc.) [15]. Exposures to Hg most commonly occur from the consumption of marine species [1]. Other exposures to Hg may be from exhaust of coal-burning power plants, cement production, batteries, and gold production. The role of Hg in neurological diseases such as AD and PD has been controversial. Hg can cross the blood-brain and blood-placental barriers. It is then retained by the brain for years [16]. Hg tends to accumulate in lipid-rich regions of the brain. Human exposure to Hg usually results in kidney and neurological disorders [15].

Potassium & Rubidium

Potassium (K) occurs in nature as an ionic salt and is essential for humans and other animals. It is found dissolved in seawater and in other minerals. Some common food sources of K include orange juice, potatoes, bananas, avocados, tomatoes, broccoli, apricots, and many other fruits.

Rubidium (Rb) is not essential for humans, but is readily taken up by the body. It is found commonly mixed in with other elements, especially K. Rb is found in some plants as well. Some common uses of Rb are in fireworks, lasers, chemical applications, and electronic transmission. Rb is found in come brain tumors.

Exposure to K and Rb is not known to cause neurodegenerative disorders. For example, the concentrations of K and Rb are similar between AD and control brains [1; 7].

Sodium

Sodium (Na) is an essential element for humans and other animals. It is found in nature as a compound only; the most common forms are salt deposits. The most common form of Na that we know and use is sodium chloride, table salt. It does have many other industrial uses as well. Over- or under-exposure to Na has not been shown to cause neurological disorders. Nevertheless, Na has been shown to increase every brain region in AD patients [1].

Zinc

Zinc (Zn) is naturally found in the earth‟s crust and in seawater. It is normally found with Fe and Cu deposits. Zn is commonly used in batteries, production of brass, bronze, rubber, in pigments, fire retardant, nuclear weapons, automobile engines, and agricultural fungicides. The most common food source of Zn is red meats.

Zn is another essential element in mammals. Zn is distributed in similar ways in the central and subcortical white matter of both young and old brains; the interior of the dentate nucleus and the cerebellar cortex contain high levels of Zn [2]. The regions of the normal brain rich in Zn include the hippocampus, amygdala, and the cortex. As the brain ages, its Zn distribution changes, just in the regions mentioned above. Nevertheless, little or no decrease in brain Zn has been reported in aging humans or rats [4]. Zn is found to be elevated in human amyloid plaques while PSAPP mice (an AD mouse model that does not show neurodegeneration) only had a 29% increase of Zn in their plaques compared to the Zn in brain tissue surrounding the plaques [6]. The potential role of Zn as a cofactor in the pathogenesis of AD was strengthened when Zn enrichment was found in senile plaques and a Zn elevation in the neuropil of AD patients as compared to those in control individuals [4].

Of the 90 plus naturally-occurring elements, 26 are known to be essential for humans and animals [17]. These consist of 11 major elements or macro-elements. They are: C, H, O, N, S, Ca, P, K, Na, Cl, and Mg. Fifteen elements are known as trace elements or micro-nutrients. They include: Fe, Zn, Cu, Mn, Ni, Co, Mo, Se, Cr, I, F, Sn, Si, V, and As. The molecular bases for the essential element selection and rejection have not been elucidated, however. Major elements, such as Na, K, Ca, and Mg, are required for bodily functions such as body fluid buffer, active transport, ionic balance, electrical transmission, tissue development as well as the composition of body fluids and structures. Trace elements act primarily as catalyst in enzyme systems in cells where they serve a wide range of functions from weak ionic effects to highly specific associations such as metalloenzymes. In addition, the protein-metal interactions may increase the stability of the protein moiety to metabolic turnover.

In this study, we investigated 30 elements (including electrolytes) and how dietary intake on a life-time basis would affect their concentration and distribution in various regions of the rat brain (hypothalamus, cerebellum, pons and medulla, striatum, mid-brain, cerebral cortex, and hippocampus) and discussed their health implications. The 30 elements of interests were: Al, As, Ba, Br, Ca, Cd, Cl, Co, Cr, Cu, F, Fe, Hg, I, K, La, Mg, Mn, Mo, Na, Rb, S, Sb, Sc, Se, Si, Sm, Sr, V, and Zn. In the past, research has primarily focused on the effects of different elements on the brain and the neurological disorders they may cause. None of those studies, however, have examined simultaneously as many elements in a single study as we have presented here. The objective of this paper is to characterize the levels of major and selected trace elements in various regions of the rat brain during several critical stages of development. Because during the first 8-9 days of age postnatal, the rat hippocampus is extremely difficult to visually distinguish from the overlying cerebral cortex, we had included the hippocampus tissue together with the cerebral cortex for analysis in the case of 5-day-old tissue samples. The four postnatal age groups of rats we have studied include the following:

I. 5 days old;
II. 10 days old;
III. 22/23 days old; and
IV. 120 days old (i.e., adult).

While humans and rats are not identical neurologically and physiologically, there are more similarities between the two species as far as brain structure and functions are concerned. The four stages of the postnatal development of the rat chosen in this study closely parallel the postnatal development of humans. As our well being is largely impacted by the environment we are living in, dietary intake is definitely a major factor that posts a long-term effect on our health. This paper provides some insight into how our diet and pollutants in our diet may affect our neurological health. Consequently, our experimental results may allow us to take some preventative measures in determining how best to optimize and gauge our dietary intake of major and trace elements for the betterment of our health.

2. Experimental Methods

Wistar rats of the Portion strain (Animal Breeding Unit, Carshalton, Surrey, U.K.) bred in the Institute of Neurology, University of London, U.K. were used. All animals were kept on a 12-hour light/12-hour dark cycle with free access to food and water. Elemental concentrations in the rat food pellets had been determined (Table 1 below).

Table 1. Elemental Concentration of rat food pellet.

Element	Concentration (in mg/g)
Ca	6.39 ± 1.68
Cl	2.31 ± 0.49
Fe	0.25 ± 0.05
K	5.36 ± 0.95
Mg	1.17 ± 0.32
Na	1.48 ± 0.32
	Concentration (in µg/g)
Al	98.06 ± 8.05
Br	10.57 ± 2.26
Co	0.20 ± 0.04
Cr	1.50 ± 0.44
Cu	7.21 ± 2.12
F	ND(5.00)
Hg	ND (0.25)
I	ND (0.50)
Mn	49.34 ± 8.65
Mo	2.80 ± 0.45
Se	ND (0.25)
Rb	12.73 ± 2.61
V	ND (0.50)
Zn	47.73 ± 4.11

Thirty trace and major elements in different brain regions of rats at the four different age groups (i.e., I through IV as defined above) were analyzed by instrumental neutron activation analysis (INAA) [18]. The samples were irradiated by thermal neutrons using three different sets of conditions depending on the nuclear characteristics of the elements of interest [18]. Not all 30 elements were reported in the results because those not reported herein were either below the detection limits of our INAA technique [18] or the elements were not retained by the brain tissue. All values listed are mean ± S.D.; ND = not detectable, and values in brackets are the maximum elemental concentrations present in the diet.

As already noted above, in age group I, the hippocampal tissue had been included in the cerebral cortex and analyzed as such.

All the standard materials and samples for INAA were freeze-dried and pelleted. Dried samples (rat brain regions) were homogenized using a Glen Creston polystyrene ball-mill and pelleted. Other details of standard and sample preparations were as described previously [18; 19].

Standards and samples were irradiated in a 100 KW „Consort" Reactor Mark II at the Imperial College Reactor Centre. Irradiated standards and samples were then analyzed for their elemental contents by gamma ray spectrometry using various Ge(Li) detectors and ND6600 Multichannel Analyzer (Nuclear Data Inc., Schaumburg, Illinois, USA). Details of the elemental determinations were described in the methodology paper by Chan et al. (1983).

All laboratory chemicals used were of analytical grade (BDH Chemicals Limited, U.K.) and single element standards of trace elements were obtained from AAS (Ventron Division, Limited, U.K.); other elemental standards for F, Cl, Br, and P were obtained from Hopkin and Williams Chemical Ltd., U.K. Water for solution preparations and feeding was double-distilled.

3. Results

Cerebellum

The cerebellum is the "cauliflower-shaped" region of the brain located in the lower part of the brain next to the brain stem. The cerebellum controls movement, balance, and coordination. More recent evidence suggests that it plays roles in regulations of emotions and memory and learning. Figure 1 shows the elemental distributions in the cerebellum during rat postnatal development.

It can be noted from Figure 1 that the levels of different elements generally show a decreasing trend as the cerebellum develops and reaches adulthood: this trend may reflect the gradual closing of the blood-brain barrier between age 10 days through weanling and beyond. However, research on elemental distributions in cerebellum during development has been minimal: some of the more studied elements include magnesium, rubidium, and sodium.

Magnesium levels in the parietal cortex in AD patients do not differ from those in normal controls [7]. Similarly, rubidium levels in AD brains do not differ from those in control brains [1]. Consequently, the age-related changes in magnesium and rubidium levels in the cerebellum may not be have good predictive value of neurological diseases in later life. On the other hand, the sodium levels in the rat cerebellum decreases during the latter half of postnatal development as they approach the adult level. On the other hand, sodium levels in every regions of the human brain are significantly higher in the AD patients than those in control subjects [1]. These results taken together suggest that dietary intake of sodium may have some relevance in the causation and/or progression of AD.

Cerebral Cortex

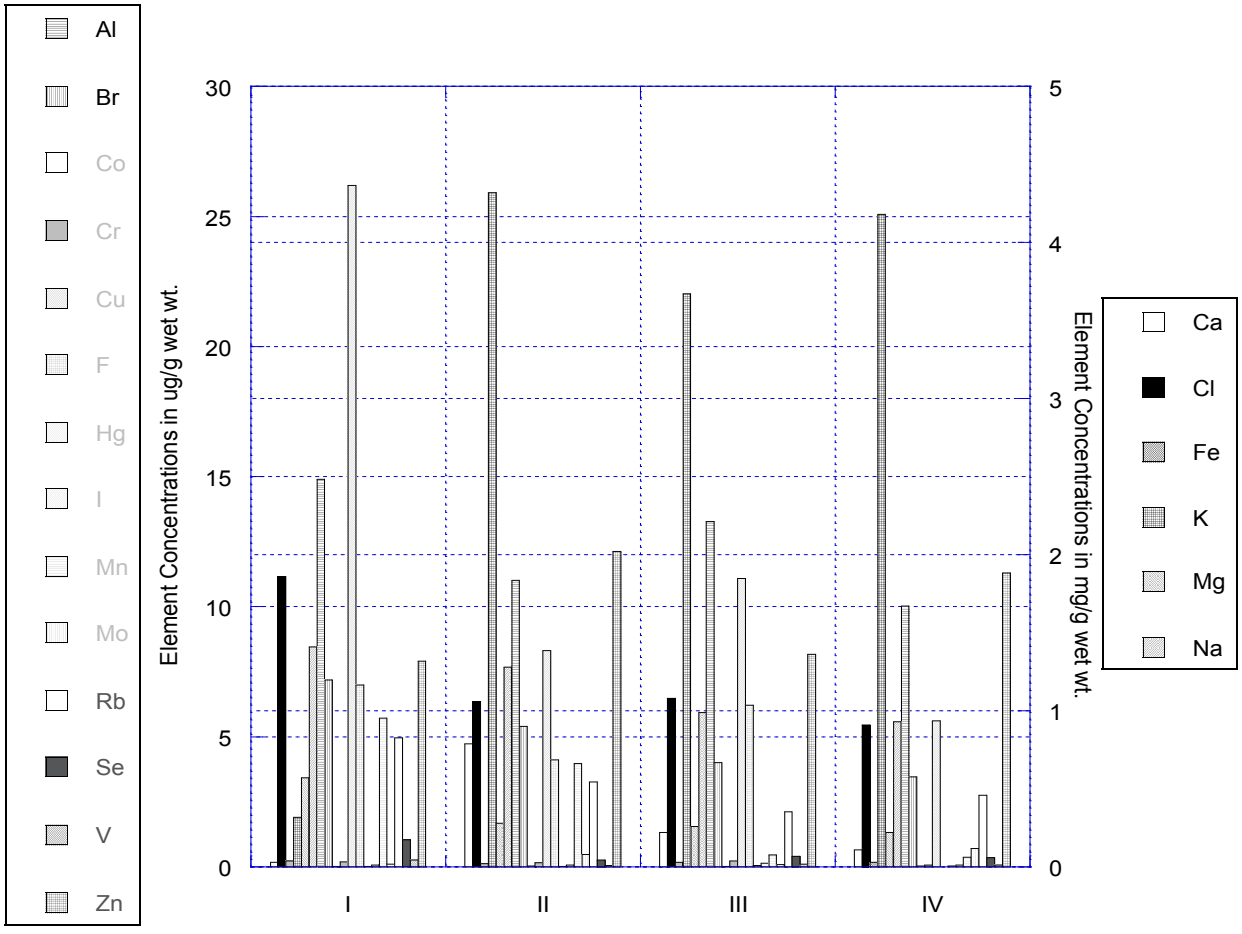

Fig. 1. Element Concentrations of Rat Cerebellum at Different Development Stages.

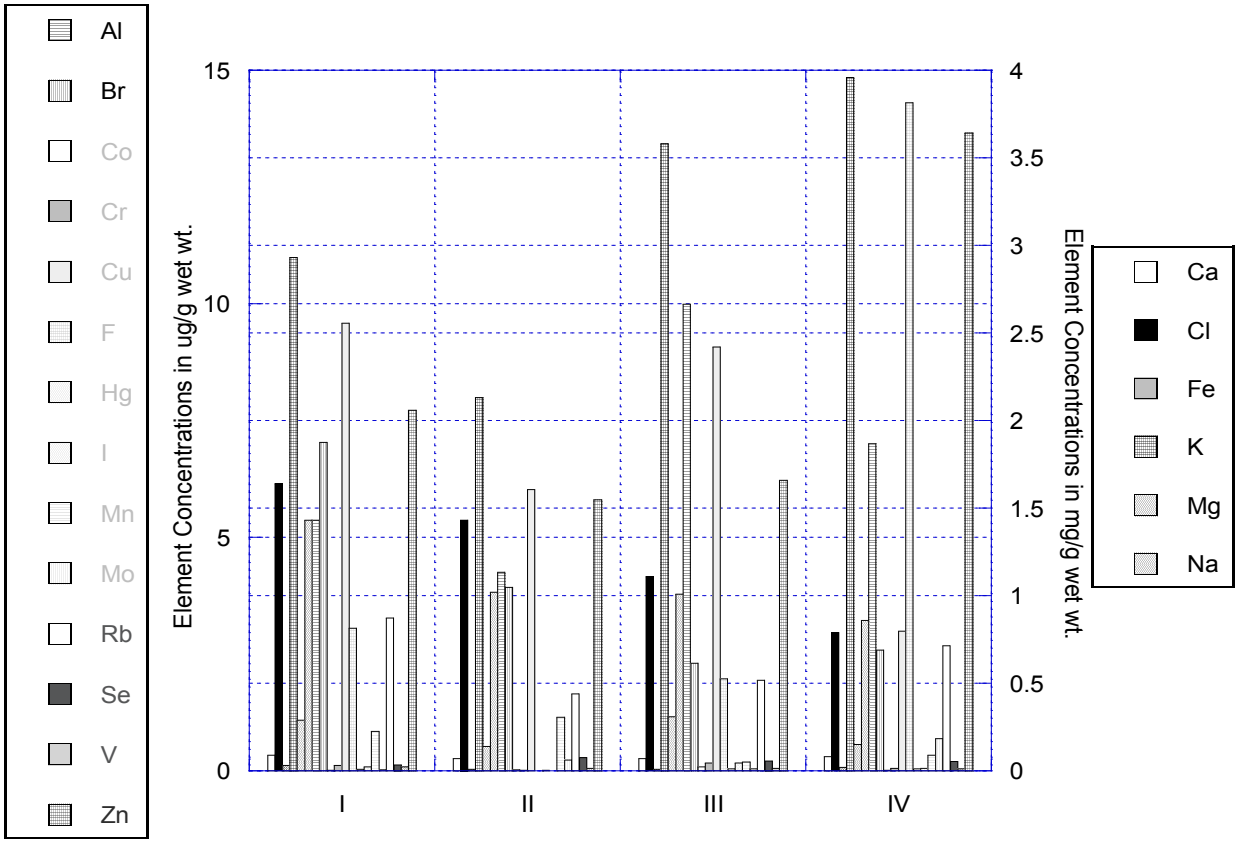

Fig. 2. Element Concentration of Rat Cerebral-Cortex at Different Developmental Stages

The cerebral cortex is responsible for all intellectual and other higher functions such as thinking, voluntary movements, language, reasoning, and perception. Figure 2 shows the elemental distributions in the cerebral cortex during postnatal development till adulthood. It can be gleaned from the results shown in Figure 2 that on average, about half of the concentrations of different elements increase with increasing age while about half of the levels of the other elements decrease as age advances toward adulthood.

Several elements in the human cerebral cortex have received more attention recently; they are described in further details in the following:

Even though the physiological role of aluminum (Al) in brain has not been identified, it is accumulated in the cerebral cortex of the rat as it matures to adulthood: presumably, this accumulation reflects dietary intake (Figure 2). Consequently, increasing brain accumulation of Al, which is known to be neurotoxic, could induce neurological problem(s) in the long term. For example, Al shows significantly higher level in the parietal cortex in AD patients compared to those in control individuals [7]. Similarly, Al accumulation in brain and other tissues, including bone, liver, and kidney, has also been shown to accompany renal failure [3].

Calcium (Ca) levels in the rat cerebral cortex do not markedly change during postnatal development (Figure 2). On the other hand, one of the pathological hallmarks of Alzheimer‟s disease (AD) is the accumulation of amyloid plaques between nerve cells (i.e., neurons) in different parts of human brain including cerebral cortex. Ca levels in human amyloid plaques in AD are elevated. Consistent with the latter observation is the finding that, in PSAAP mice (a mouse model of AD, which shows plaques but little neurodegeneration), Ca accumulation in their plaques is less than those in the surrounding brain tissue [6]. Consequently, age-related accumulation of Ca in this brain region could potentially serve as marker for the likelihood of developing neurodegeneration as age advances.

Chromium (Cr) shows a moderate increase in parietal cortex of AD patients compared to those in control subjects [7]. In rat cerebral cortex, Cr levels increase from day 10 to day 22/23 and thereafter decrease as adulthood is reached (Figure 2). Nevertheless, relations between brain Cr levels and neurological diseases have not been firmly established.

Copper (Cu) in amyloid plaques in AD is elevated [4]. In PSAAP mice (a mouse model of AD, which shows plaques but less neurodegeneration) Cu accumulation in their plaques is less than those in the surrounding brain tissue [6]. Consequently, increasing Cu accumulation in cerebral cortex as age advances can potentially herald the onset of neurological problems.

The magnesium (Mg) levels in rat cerebral cortex fluctuate during development and level off toward adulthood (Figure 2). Mg levels in parietal cortex and cerebellum in AD patients do not differ from those in control subjects. Taken together, these observations suggest Mg to be more predictor of neurological problems as age advances.

Manganese (Mn) shows significantly higher levels in the parietal cortex of AD patients compared to those in control subjects [7]. However, cerebellar Mn levels in AD are similar to those in control subjects [7]. Figure 2 shows that Mn levels in cerebral cortex of the rat show a general trend of decrease as its age increases. Nonetheless, whether this is a generalized trend of an essential element remains to be established.

Potassium (K) concentrations in the AD brain appear to be similar to those in control brain, especially in the regions examined [1]. K generally shows a trend of age-related increases in the rat cerebral cortex (Figure 2), perhaps reflecting increases in cellular material because intracellular K is higher than extracellular K.

Sodium (Na) levels in the rat cerebral cortex decrease with increasing age (Figure 2), reflecting the closing of the blood-brain barrier thereby excluding the entry of extracellular Na into cells. On the other hand, Na levels in every region of the AD brain are higher than corresponding levels in control brain [1]. Consequently, age-related increases in brain sodium may be considered at least a partial predictor of age-related neurological problems.

Zinc (Zn) is elevated in the amyloid plaques in AD and PSAPP mice (an AD mouse model that shows little or no neurodegeneration) only had a 29% increase of Zn in their plaques compared to the Zn in brain tissue surrounding the plaques [6]. By contrast, Zn levels in the rat cerebral cortex markedly increase between age 22/23 days and adulthood suggesting that the increase is associated with tissue growth. However, the increase in brain Zn during brain aging may be more predictive of onset and/or presence of neurological problems [6].

Hippocampus

The hippocampus is located deep within the temporal lobe and is part of the limbic system. This brain region is responsible for learning and formation of long-term memory. Figure 3 shows the elemental distributions in the rat hippocampus at different stages during postnatal development. We discuss below the elements that were emphasized in several recent reports.

Following oral exposure of rats to aluminum (Al), its retention has been noted in the hippocampus as occurs in other brain regions: rat hippocampal Al levels increase markedly after 10 days of age (Figure 3). In patients with PD, elevated Al levels have been found in several brain regions including the hippocampus, which is rich in cholinergic neurons [3]. Consequently, chronic accumulation of Al in this brain region over a life-span may lead to the development of neurodegenerative diseases such as PD because of Al is known to be neurotoxic.

Potassium (K) levels in the rat hippocampus increase from age day 10 till adulthood, likely reflecting the increase in cellular material during this developmental period (Figure 3). However, in the brain regions examined in AD, brain K remains essentially unchanged compared with corresponding levels in control subjects [1], suggesting that brain K may not be a good indicator of the likelihood of developing neurological diseases such as AD.

Rubidium (Rb) levels in rat hippocampus fluctuate between age day 10 and adulthood (Figure 3). However, Rb levels in the AD brain do not differ from those in control brain [1] suggesting that Rb levels in brain may not be a good predictor neurodegenerative diseases such as AD.

Sodium (Na) levels in the rat hippocampus decrease between ages day 10 and day 22/23 and level off at adulthood (Figure 3). However, Na levels in every part of the AD brain examined are higher than corresponding levels in the control brain [1].

Hypothalamus

The hypothalamus is located at the interior of the brain under the thalamus. It controls body temperature, emotion, thirst, hunger, appetite, digestion, and sleep. Figure 4 shows the elemental distributions in rat hypothalamus in the four developmental stages we have investigated. Even though this brain region is known to accumulate a variety of metals, their precise functional significance remains to be fully elucidated. Only few functionally important changes during development can be commented on (Figure 4).

The electrolytes in this rat brain region show fluctuating trends in the four age groups investigated, partly reflecting the closing of the blood-brain barrier. For example, sodium (Na) and chlorine (Cl) levels significant decrease in the first 22/23 days postnatal. On the other hand potassium (K) levels markedly increase between day 5 and day 10 postnatal.

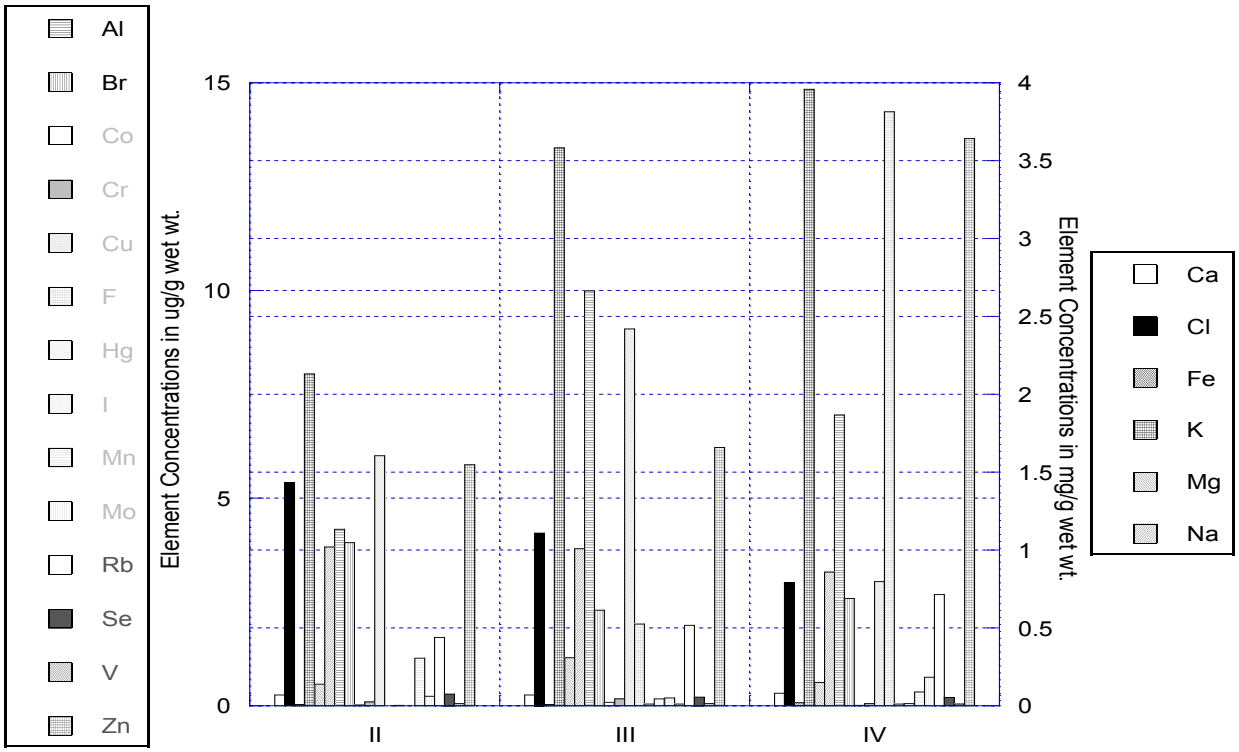

Fig. 3. Elemental Concentrations of Rat Hippocampus at Different Developmental Stages

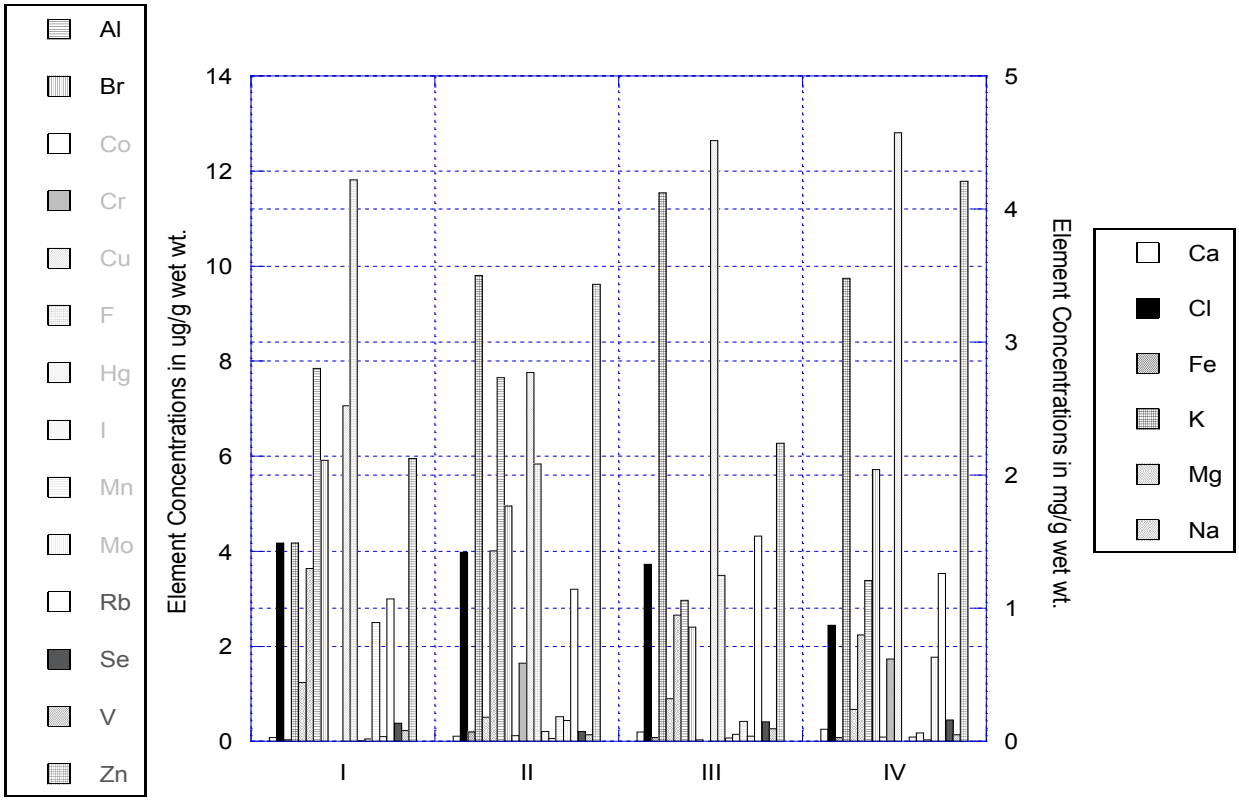

Fig. 4. Element Concentrations of Rat Hypothalamus at Different Developmental Stages

Although they show some age-related fluctuations, the essential trace elements copper (Cu), selenium (Se), and zinc (Zn) levels in the rat hypothalamus significantly increase between postnatal age 5 and adulthood (Figure 4). At present, one can only speculate about the functional significance of the postnatal increases of these essential metals in the rat hypothalamus because of the absence of relevant studies.

Mid-Brain

As its name implies, the mid-brain is located in the middle of the brain above the brain stem. The mid-brain generally acts as a relay station for both sensory and spinal cord signals and passes them on to the limbic system and the cortical areas. Figure 5 shows the elemental distributions in the rat mid-brain in the four age groups we have investigated. In the rat mid-brain, the levels of both major and trace elements studied show age-related fluctuations that differ from those in the rat cerebral cortex or hippocampus. However, the relevance of these fluctuations in the mid-brain to neurological diseases remains to be elucidated.

Pons and Medulla

Situated immediately below the mid-brain, pons and medulla constitute the brain stem which is connected to the spinal cord. Key functions of pons include motor control and sensory analysis and signal relay between the mid-brain and spinal cord. The medulla is known to be responsible for maintaining heart and breathing rates. Figure 6 shows the elemental distributions in the rat pons and medulla in the four age groups we have investigated. Most major and trace elements show age-related decreases in their levels in rat pons and medulla as adulthood approaches (Figure 6). Overall, the accumulation of metals in this brain region is not as quantitatively marked as those in the other brain regions, possibly due to the fact that this brain region is full of fiber tracts rather cell bodies. Moreover, the physiological significance of the distributions of metals in this brain region is still poorly understood.

Striatum

The striatum constitutes the sub-cortical parts of the forebrain: it includes the substantia nigra and the globus pallidus. Among its best known function is its role in the planning and modulation of movement pathways as well as roles in other cognitive functions. Figure 7 shows the elemental distributions in the rat striatum in the four age groups we have investigated. We discuss below the elements that were emphasized in several recent reports.

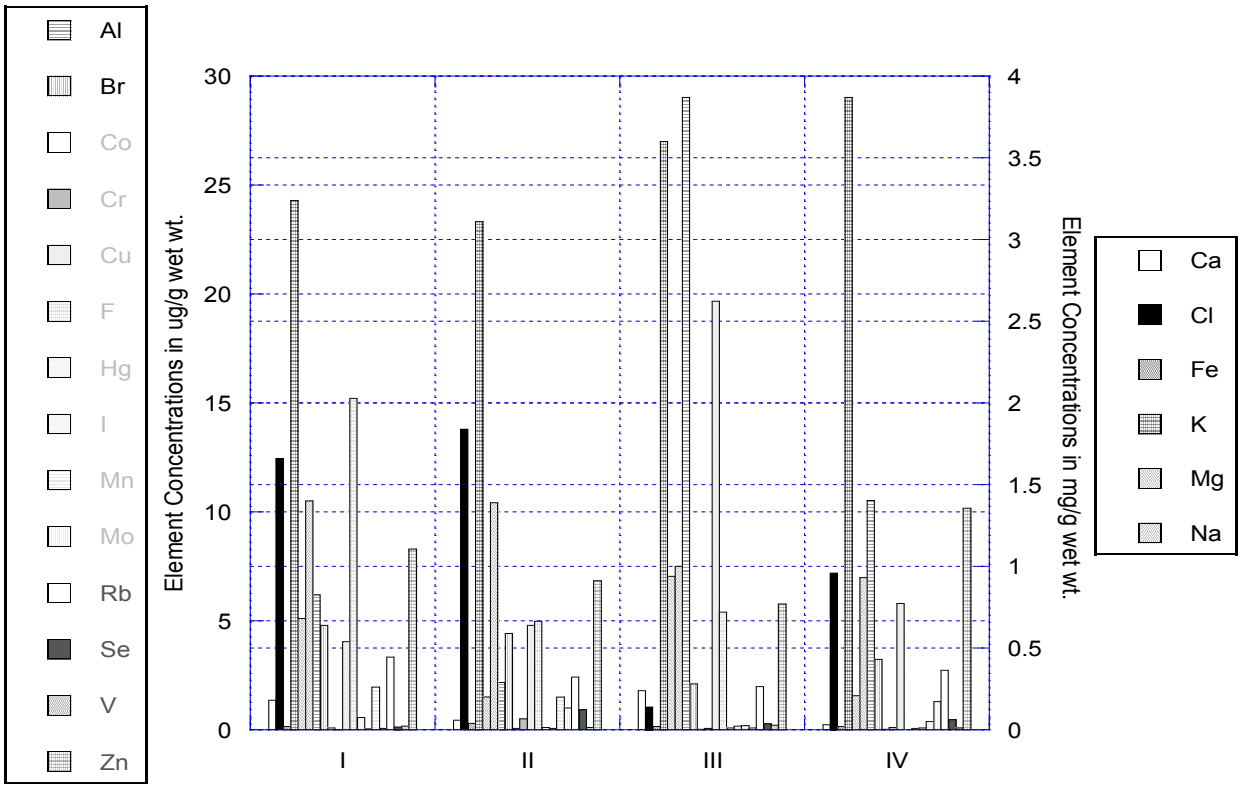

Fig. 5. Element Concentrations of Rat Mid-Brain at Different Developmental Stages

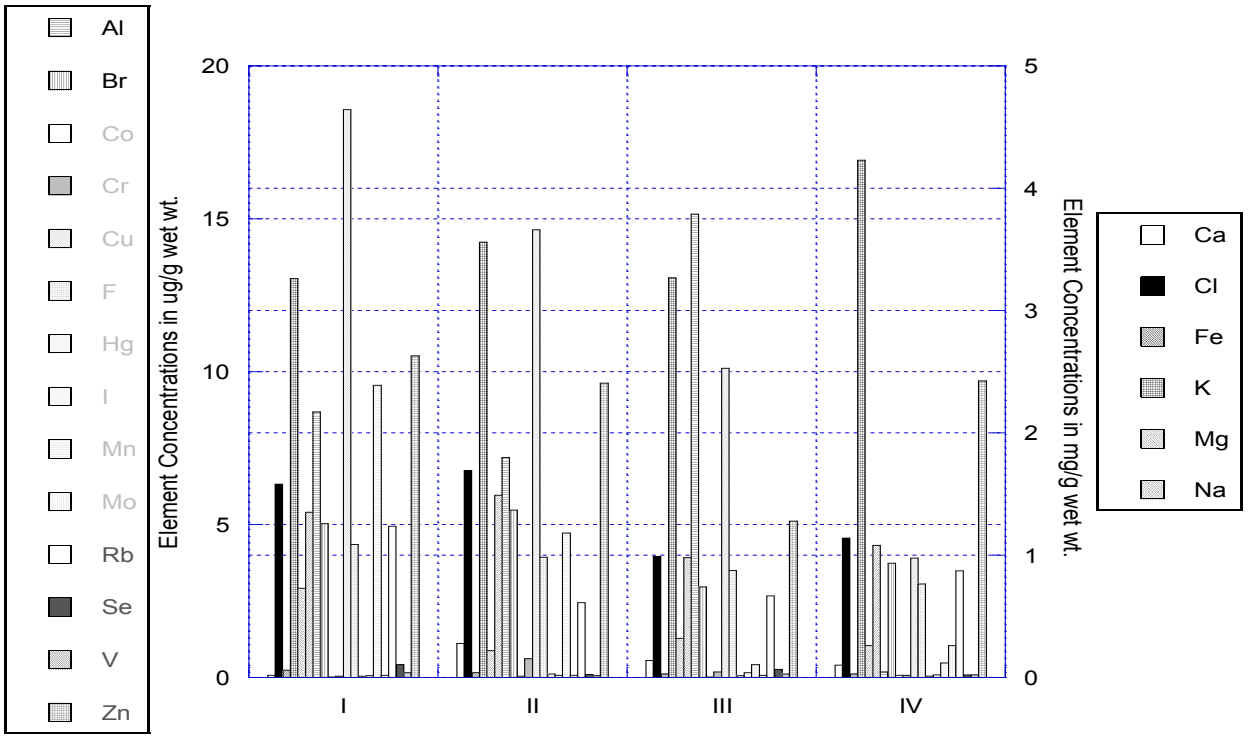

Fig. 6. Element Concentrations of Rat Pons & Medulla at Different Developmental Stages

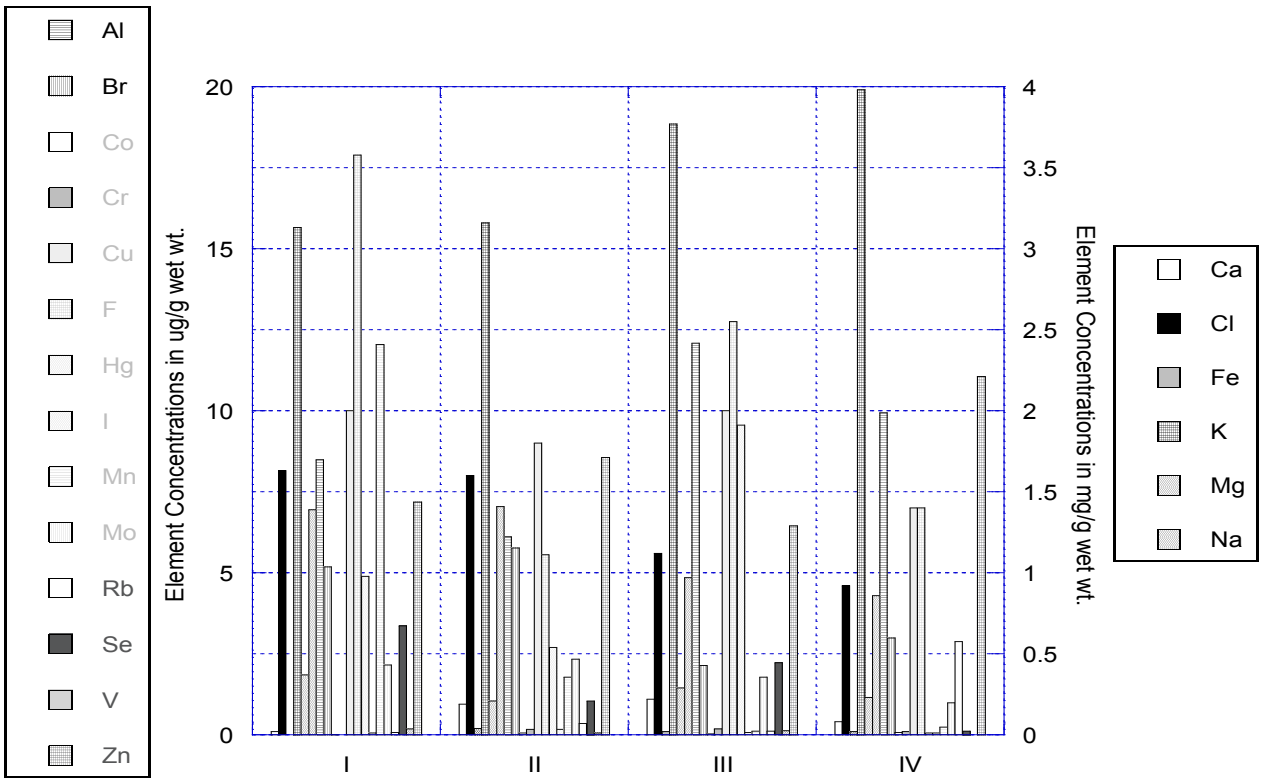

Fig. 7. Element Concentrations of the Striatum Different Developmental Stages

There is recent evidence that iron (Fe) plays a role in the consolidation of long-term memory. Brain Fe distribution overlaps with that of dopaminergic neurons. In rodent models of neurological disorders, Fe levels in the substantia nigra and basal ganglia increase. Because of those observations, increased striatal Fe has been suggested to be responsible for neuronal cell. Furthermore, Fe accumulates in brain as a function of age [19]. In rat striatum, Fe levels decrease between ages 10 days and 22/23 days and level off thereafter (Figure 7).

Brain Fe is highest in the substantia nigra, globus pallidus, red nucleus, caudate nucleus, and putamen. Increased brain Fe has been found in several neurodegenerative disorders although it has not been defined as the main cause [21]. Fe level in the substantia nigra increases in PD but total Fe in the substantia nigra zona reticulata does not change in either PD or AD [11]. Thus, these findings suggest that over accumulation of iron in striatum may lead to development of neurodegenerative diseases such as PD and AD and sources of Fe exposure could be environmental and dietary. However, it remains to be determined if the elevated Fe levels antedate injury of pigmented neurons or constitute a consequence of neuronal degeneration because the increased Fe in the substantia nigra may contribute to oxidative damage to neurons. Nevertheless, most brain Fe is stored in an inactive form bound to intracellular ferritin, which is thought to be mainly localized in microglia and oligodendroglia. Clearly, additional studies are needed to clearly delineate the pathophysiological role of Fe in neurodegenerative diseases.

Chronic manganese (Mn) toxicity in human induces signs and symptoms that closely resemble those noted in PD. There is a great deal of evidence that human striatum, globus pallidus, and substantia nigra show preferential increases in Mn and are believed to be the primary sites associated with Mn neurotoxicity. Moreover, exposure to high Mn leads to elevation of Mn levels in olfactory epithelium and olfactory bulb [14].

In every region of the brain examined, brain sodium (Na) is increased in AD compared with corresponding levels in control subjects [1]. On the other hand, Na levels in rat striatum decrease during postnatal development. Taken together, these observations suggest that high Na accumulation in brain may lead to pathological states and sources of the Na could be environmental and/or dietary in origin.

4. Conclusions

Our results strongly suggest that the metallomic distributions in various regions of the rat brain change markedly during the different stages of postnatal development. In conjunction with the reports in the literature, our findings also suggest that brain regional metallomic distribution can be influenced by dietary intake of metals and other elements and may pathophysiological implications in several key neurodegenerative diseases such as Parkinson‟s disease and Alzheimer‟s disease. A metallomic distribution model of various regions of the rat brain can be developed based on ours experimental results and statistical analysis. However, much remains to be discovered regarding the brain functional significance of metallomic distribution during development.

Acknowledgements

This study was partially supported a USAMRMC Project Grant (Contract #W81XWH-07-2-0078).

References

[1] Belavaria, C., Andresi, E., Molnar, Z., and Bertalan, E. (2005) Determination of Alkali Metals in Control and AD Brain Samples by Different Techniques. *Microchemical Journal*, 79(1-2), 367-373.

[2] Popescu, B. F. G., Robinson, C. A., Rajput, A., Rajput, A. H., Harder, S. L., and Nichol, H.. (2009) Iron, Copper, and Zinc Distribution of the Cerebellum. *Cerebellum*, 8(2), 74-79.

[3] Kumar, V., and Gill, K. D.. (2009) Aluminium Neurotoxicity; Neurobehavioural and Oxidative Aspects. *Archives of Toxicology*, 83(11), 965-978.

[4] Bolognin, S., Messori, L., and Zatta, P. (2009) Metal Ion Physiopathology in Neurodegenerative Disorders. *Neuromolecular Medicine*, 11(4), 223-238.

[5] Schafer, U., and Jahreis, G. (2006) Exposure, Bioavailability, Distribution, and Excretion of Aluminum and its Toxicological Relevance to Humans. *Trace Elements and Electrolytes*, 23(3), 162-172.

[6] Leskovjan, A. C., Lanzirotti, A., and Miller, L. M. (2009) Amyloid Plaques in PSAPP Mice Bind Less Metal Than Plaques in Human Alzheimer's Disease. *Neuroimage,* 47(4), 1215-1220.

[7]Srivastava, RAK., and Jain, JC. (2002) Scavenger Receptor Class B Type I Expression and Elemental Analysis in Cerebellum and Parietal Cortex Regions of the Alzheimer″s Disease Brain. *Journal of the Neurological Sciences*, 196(1-2), 45-52.

[8]Hung, YH., Bush, Al, and Cherny, RA. (2010) Copper in the Brain and Alzheimer″s Disease. *Journal of Biological Inorganic Chemistry*, 15(1), 61-76.

[9]Zhang, L., Lichtmannegger, J., Summer, K. H., Webb, S., Pickering, I. J., and George, G. N. (2009) Tracing Copper-Thiomolybdate Complexes in Prospective Treatment for Wilson″s Disease. *Biochemistry*, 48(5), 891-897.

[10] Gerlach, M., Benshachar, D., Riederer, P., and Youdim, MBH. (1994) Altered Brain Metabolism of Iron as a Cause of Neurodegenerative Diseases. *Journal of Neurochemistry*, 63(3), 793-807.

[11]Kienzl, E., Puchinger, L., Jellinger, K., Linert, W., Stachelberger, H., and Jameson, R.F. (1995) The Role of Transition Metals in the Pathogenesis of Parkinson″s Disease. *Journal of the Neurological Sciences*, 134, 69-78.

[12] Berg D., Gelach M., Youdim, MBH., Double, KL., Zecca, L., Riederer, P., and Becker, G. (2001) Brain Iron Pathways and Their Relevance to Parkinson″s Disease. *Journal of Neurochemistry*, 79(2), 225-236.

[13] Yokel, RA. (2009) Manganese Flux Across the Blood-Brain Barrier. *Neuromolecular Medicine*, 11(4), 297-310.

[14] Dorman, DC, Struve, MF, Wong, BA, Dye, JA, and Robertson, ID. (2006) Correlation of Brain Magnetic Resonance Imaging Changes with Pallidal Manganese Concentration in Rhesus Monkeys Following Subchronic Manganese Inhalation. *Toxicological Sciences*, 92(1), 219-227.

[15] Florea, AM, and Busselberg, D. (2006) Occurrence, Use, and Potential Toxic Effects of Metals and Metal Compounds. *Biometals*, 19(4) 419-427.

[16] Rooney, JPK. (2007) The Role of Thiols, Dithiols, Nutritional Factors and Interacting Ligands in the Toxicology of Mercury. *Toxicology*, 234(3), 145-156.

[17] Underwood, E.J. (1977) Trace Elements in Animal Nutrient. Academic Press.

[18] Chan, A.W.K., Minski, M.J., Lai, J.C.K. (1983) An Application of Neutron Activation Analysis to Small Biological Samples: Simultaneous Determination of Thirty Elements in Rat brain Regions. *Journal of Neuroscience Methods*, 7(4), 317-328.

[19] Chan, A.W.K. and Minski, M. J. (1981) U. L. R. C. Internal Report (RES/36), p 37-39.

[20] de Lima, MNM, Laranja, DC, Caldana, F, Grazziotin, MM, Garcia, VA, Dal-Pizzol, F., Bromberg, E., and Schroder, N. (2005) Selegiline Protects Against Recognition Memory Impairment Induced by Neonatal Iron Treatment. *Experimental Neurology*, 196(1), 177-183.

[21]Lee, DW., and Anderson, JK. (2010) Iron Elevations in the Aging Parkinsonian Brain: A Consequence of Impaired Iron Homeostasis. *Journal of Neurochemistry*, 112(2), 332-339.

ISEIS 2010 International Conference on Environmental Informatics

Effects of Diet Intakes on Metal and Electrolyte Distributions in Vital Organs

S. W. Leung[a, *], S. Siddhanti[b], B. Williams[b], A.W. K. Chan[c], M.K. Minski[c], C.K. Daniels[d], J.C.K. Lai[d]

[a]*Corresponding author: Civil and Environmental Engineering Department, and Biomedical Research Institute, Idaho State University, Pocatello, ID 83209, USA*

[b]*Civil and Environmental Engineering Department, College of Engineering, Idaho State University, Pocatello, ID 83209, USA*

[c]*Imperial College Reactor Centre, University of London, Silwood Park, Ascot, Berks., SL5 7PY, UK*

[d]*Biomedical & Pharmaceutical Sciences Department, College of Pharmacy and Biomedical Research Institute, Idaho State University, Pocatello, ID 83209, USA*

Abstract. The intake and concentration of metals and electrolytes from our diet are believed to be affecting our general health, in particular, the proper functions of vital organs. For example, in addition to other genetic and environmental factors, consuming water with high alkalinity for prolonged time is suspected to lead to diseases such as kidney stone. Evidence has been accumulating that excessive metal intakes would lead to organ failures. Once absorbed, minerals and electrolytes can travel freely throughout the body, and distribute at key organ systems such as the brain, lung, kidney, etc. By conducting experiments with animal models (e.g., rats), it is possible to not only determine where the organ distribution of various matrices of elements and minerals but also correlate such matrices with the overall physiological and behavioral status of such models. In this study, information matrices of 30 different elements (including heavy metals and some electrolytes) and their distributions in various vital organs (e.g., brain, lung, kidney, liver, heart, spleen, and uterus) were analyzed as a function of normal dietary intake at adulthood (120 days old). An elemental (metal and electrolyte) distribution model was then formulated based on experimental results. The study has high impact to our understanding of how environmental health would affect our well being. This study would also provide insights on how our diet would affect the accumulations of unwanted elements, such as heavy metals, in our vital organs. The results may help researchers and health practitioner to identify possible links between daily diet (metals and electrolytes) and diseases, and may also lead to a better understanding of diseases associated with aging such as Alzheimer's and Parkinson's diseases, and other neurological disorders.

Key words: Brain organs; elements; metals; distributions; diseases; diet; environment

1. Introduction

Since the era of industrial evolution, living conditions for humans have improved drastically; with the consequence of better living conditions and less physical activities, we are facing other aspects of health issues such as obesity and hyper immune responses (allergy). In modern living, considerable attention has been paid to dietary intake or supplement due to health concerns. On the other hand, involuntarily consumption of unwanted chemicals and preservatives via processed food and polluted water is also possible. One such example would be consumption of drinking water from sources that are laden with soluble ions and heavy metals. This occurs quite frequently for those that are living in rural areas with no treatment system for their drinking water in developing countries.

Attempts in understanding the homeostasis of different elements in brain and other major organs fell short significantly due to the vast complexity of mechanisms involved [1]. What cause this complexity are the multiple factors that can affect the dynamics of biological functions. For examples, an element of different compounds (chloride versus phosphate) would have various uptake rates by the body [2] and the uptake rate of elements in solution by the digestive system was proven to be faster than in food stuffs. Elemental accumulations are not solely related to exposure but likely have more to do with impairment of the relevant homeostasis mechanism [3]; conversely, a Cu deficiency in mice were able to be corrected by supplementation of Cu in drinking water [4],

* Solomon W. Leung. Tel.: +1-208-282-2524; fax: +1-208-282-4538.
E-mail address: leunsolo@isu.edu

2003). In addition, larger sample size is needed to observe statistical significance in the small changes over life time exposure [5]. Such constraint creates a vast obstacle to conduct research, and the hurdle is more difficult if human subjects are involved.

Currently, the understanding of homeostasis mechanisms for accumulation and control of individual element in our body is very limited; hence, the influence of elements with similar properties to each other is practically non-existent. However, results of Zn replacing Cu in a competitive homeostasis mechanism in rat's brain were recently reported by Maynard et al. [5]. Therefore, it can be concluded that our understanding of elemental homeostasis mechanisms in our body systems is still in the pioneer stage, and opportunities for further research and development are widely untouched.

There are chemicals (vitamins, for example) and elements needed to maintain proper bodily functions; in this study, we focused on the essence of major and selected trace elements and how these elements accumulated in our major organs. The major organs are: brain, lung, kidney, liver, heart, spleen, and uterus. Information matrices of 30 different elements (including heavy metals and some electrolytes) that were fed to rats as part of a regular diet were obtained from the seven major organs and analyzed. Measurements of the elements from the adult rats (120 days old) were compared with information obtained from healthy Japanese males [6]. A linear distribution model based on experimental results and statistical analysis for the elemental accumulations in the major organs was then developed to relate the accumulation ratio between rats and humans taking their respective regular diet. This model can be used as an assessment tool to evaluate elemental homeostasis in different organs for the initial screening of potential health issues and diseases.

2. Experimental Methods

The 30 elements included in this study were: Al, As, Ba, Br, Ca, Cd, Cl, Co, Cr, Cu, F, Fe, Hg, I, K, La, Mg, Mn, Mo, Na, Rb, S, Sb, Sc, Se, Si, Sm, Sr, V, and Zn. Analytical measurements of the elements from the organs of adult (120 days old) Wistar rats and diet pellets that were used to feed the rats were reported in a parallel paper at the same conference (Metallomic Distribution in Various Regions of the Brain as Influenced by Dietary Intakes and Their Implications) [7].

Information from the organs of healthy Japanese males was abstracted from Katoh et al. [5]: The data were collected from 64 persons ranging from 6 to 82 years of age with a mean age of 42 years. These data were assumed to be representatives of healthy humans regardless of race.

3. Results

3.1 Concentration of Elemental Accumulations with Rats

Table 1 tabulates the elemental concentrations obtained from 7 major organs of the rats which were feed with regular food pellets. Out of the 30 elements of interest, only 20 elements were detectable within the measurement limit by instrumental neutron activation analysis (INAA). This implies that either the concentrations of other (undetectable) elements were too low for the analytical method, or the organs did not retain those elements significantly. The latter observation was especially obvious for the brain that showed only 15 measureable elements.

Table 1. Measurements of elemental concentrations for the seven major organs. Noted that concentrations of the first 6 elements (above Al) were in mg/g of wet weight and concentrations of the rest of the elements were in μg/g of wet weight. ND indicates not detectable.

Element	Liver	Lung	Heart	Heart	Spleen	Uterus	Brain
Ca	0.05	0.08	0.16	0.04	0.06	0.09	0.054
Cl	1.01	1.39	1.35	0.8	0.94	1.99	0.95
Fe	0.28	0.14	0.1	0.1	1.06	0.09	0.019
K	3.6	1.94	2.15	2.39	3.61	2.35	2.677
Mg	0.24	0.11	0.14	0.15	0.19	0.22	0.103
Na	0.64	1.12	1.11	0.76	0.57	1.62	0.957

Al	6.57	3.98	4.13	5.68	7.17	3.43	5.87
Br	4.67	10.49	7.76	4.3	4.96	12.53	1.91
Co	0.1	0.03	0.22	0.04	0.05	0.02	0.011
Cr	0.05	0.06	0.44	0.33	0.13	0.58	ND
Cu	5.41	2.53	10.39	5.33	3.79	2.9	2.1
F	2.41	2.82	4.95	2.46	ND	6.15	ND
Hg	0.12	0.02	0.53	0.01	0.2	0	ND
I	0.06	0.05	0.08	0.05	ND	0.12	ND
Mn	2.76	0.2	0.78	0.32	0.35	0.19	0.51
Mo	1.11	1.37	0.61	0.28	0.61	0.71	ND
Rb	16.27	4.38	5.04	3.9	5.79	4.54	2.66
Se	1.26	0.4	1.54	0.39	0.72	0.44	0.64
V	0.08	0.01	0.1	0.07	0.04	0.08	ND
Zn	41.13	16.98	24.56	16.05	17.34	15.85	10.79

3.2 Elemental Accumulations in Human Organs

Similar to Table 1, Table 2 shows the corresponding elemental accumulations in 6 organs that were collected by Katoh et al. [6] and Magalhaes et al. [8]. Discussions with the brain is excluded from this paper but are discussed in a parallel study [7] due to the complexity of the brain. Katoh et al. have collected 21 elements of which 15 elements are common with the elements from the rat's study in Table 1. Magalhaes et al. have collected fewer elements, Table 2 only shows those that are of interested in this study. However, Magalhaes et al. also compared elemental concentrations of health tissues with cancerous tissues of the same individuals. It should be noted that samples of Magalhaes et al. were expressed in µg/g of dry weight instead of wet weight, but this relative weight ratio should be compatible for both approaches.

Table 2. Elemental concentrations of various organs reported by Katoh et al. [6], the concentrations were in µg/g of wet weight except as noted. *The elemental concentrations of uterus were abstracted from Magalhaes et al. [8] with samples of German origin, concentrations were reported as µg/g of dry weight, except otherwise specified.

Element	Liver	Lung	Kidney	Heart	Spleen	Uterus*
Al	11.3	130	10.4	11.4	12.5	
As(ng/g)	300	560	400	250	380	
Br	12.2	48.6	40.9	16.7	25.6	19
Ca	208	585	529	291	335	1590
Cd	16.7	4	237	1.2	5.4	
Cl(mg/g)	4.2	10.1	10.9	5	6.7	
Co(ng/g)	173	123	69	70	31	
Cs(ng/g)	69	88	120	113	77	
Cu	32.2	14.2	15.4	18	7.3	4
Fe	837	987	430	257	1400	59
K(mg/g)	9.4	9.9	10.4	15.5	15.9	0.571
La(ng/g)	285	311	64	32	650	
Mg	678	565	711	1070	729	
Mn	5.58	1.17	4.92	1.63	0.82	

Mo	2.1	1.37	1.55	0.69	0.96	
Na(mg/g)	4.2	10.4	10.7	5.7	5	
Rb	22.3	15.9	17	20.1	22	
Sb(ng/g)	52	242	69	16	49	
Sc(ng/g)	5	26	4	5	5	
Se	1.87	1.3	3.86	1.37	1.61	
Zn	228	62	238	126	83	40

3.3 Normalized Elemental Distribution Ratio in Various Organs between Rats and Humans

A normalized elemental distribution ratio can be obtained by dividing the concentration of an element in a rat organ by the concentration in the same human organ. Figure 1 shows the normalized elemental distribution ratio for the 6 organs and 15 elements that were common in our work and that of Katoh et al. [6]. As shown in Figure 1, the elemental distributions (homeostasis) for the 15 elements in the 6 major organs fit rather consistently in general. For examples, Na and Cl have nearly the same distribution ratio for all 6 organs, K is almost as consistent except for concentration in the uterus. This may be due to diet difference between rats and humans, or the difference is a factor of physiological/genetic origin; a proper explanation of the observation remains to be determined. In general, Co has the widest spread in distribution among organs.

The distribution model can be used to predict physiological development from rat (animal) to human. An abnormally high or low concentration of elements in organs can be a prelude of organ malfunction and/or cancer development. For example, samples of cancerous uterus tissue had 1.6 time the concentration of K when compared with that of normal uterus tissue from the same individual [8]. However, the general direction of increase or decrease in elemental concentration of cancerous tissue is not always the same for different elements and organs. The approach of normalized distribution ratios developed in this study can be used to find the general direction of elemental distribution of disease tissues, although there are genetic difference between rats and humans.

4. Conclusions

A normalized elemental distribution model is developed by comparing elemental measurements of the same organ in rats and humans. The model can be used to predict disease tissues based on their elemental measurements and to determine how well we can absorb elemental nutrients from food. This study has high impact on our understanding of how environmental health would affect our well being. This study would provide insights on how our diet would affect the accumulations of unwanted elements, such as heavy metals, in our vital organs. The results may help researchers and health practitioner to identify possible links between daily diet (metals and electrolytes) and diseases, and may also lead to a better understanding of diseases associated with aging such as Alzheimer's and Parkinson's diseases, and other neurological disorders.

Acknowledgment

This study was partially supported by NIH Grant P20RR16454 from the INBRE program of the National Center for Research Resources and USAMRMC Project Grant (Contract #W81XWH-07-2-0078).

References

[1] Pardridge, W. Blood-brain barrier drug targeting: the future of brain drug development. *Molecular Interventions*, **2003**;3(2):90-105

[2] Anderson, J.G., Fordahl, S.C., Cooney, P.T., Weaver, T.L., Colyer, C.L., and Erikson, K.M. Manganese exposure alters extracellular GABA, GABA receptor and transporter protein and mRNA levels in the developing rat brain. *Neurotoxicology*, **2008**;29(6) ;1044-53

[3] Bolognin, S., Messori, L., and Zatta, P. Metal ion physiopathology in neurodegenerative disorders. *Neuromolecular Medicine*, **2009**;11(4):223-38

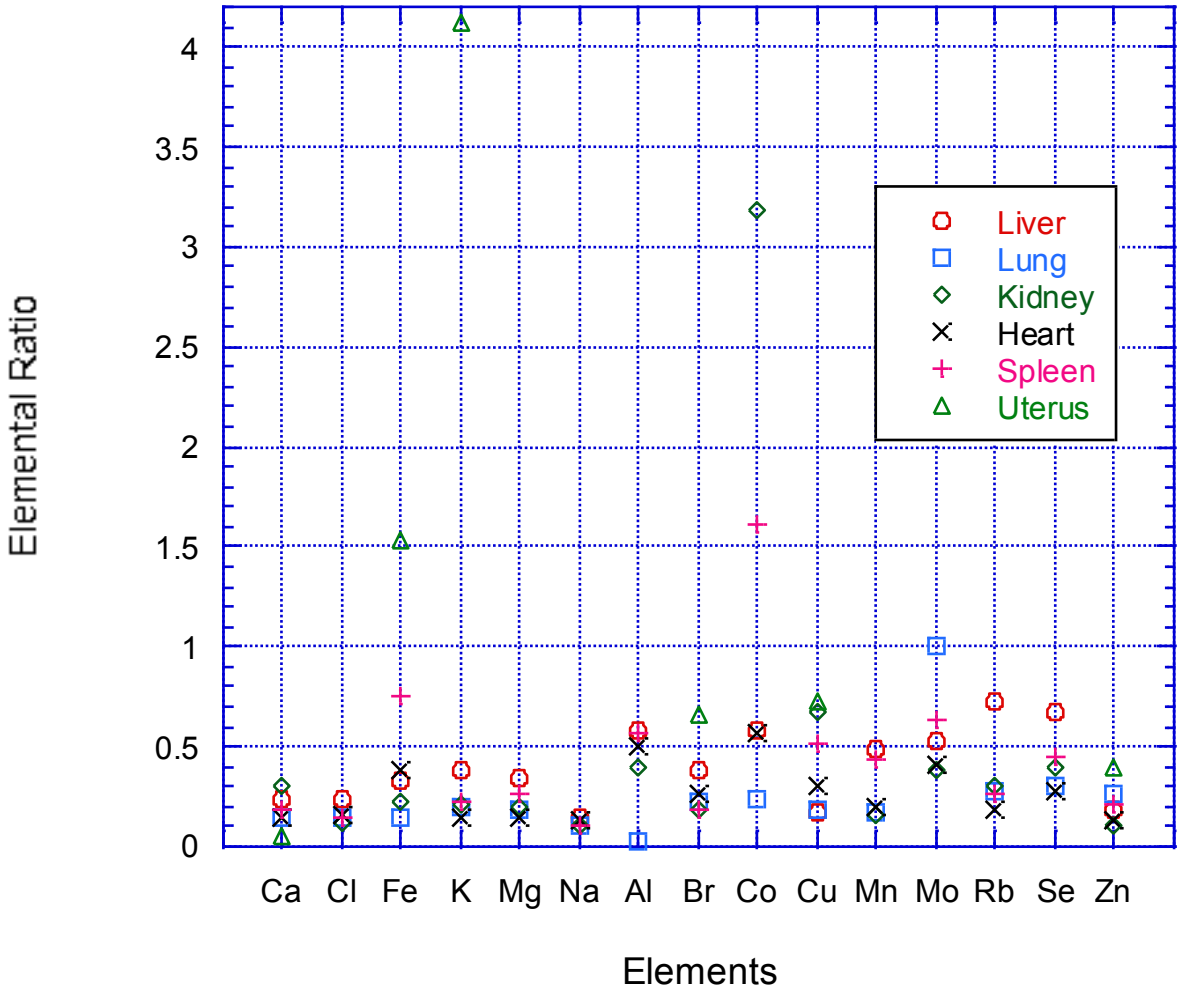

Fig. 1. Elemental concentration ratio of rat versus human for 6 major organs.

[4] Bayer T.A., Schafer S., Simons A., Kemmling A., Kamer T., Tepest R. et al. Dietary Cu stabilizes brain superoxide dismutase 1 activity and reduces amyloid abeta production in APP23 transgenic mice. *Proc Natl Acad Sci USA* **2003**;100(24):14187–92

[5] Maynard, C.J., Cappai, R., Volitakis, I., Laughton, K.M., Masters, C.L., Bush, A.I. et al. Chronic exposure to high levels of zinc or copper has little effect on brain metal homeostasis or a beta accumulation in transgenic APP-C100 mice. *Cellular and Molecular* **2009**;29(5):757-67

[6] Katoh, Y., Sato, T., and Yamamoto, Y. Determination of multielement concentration in normal human organs for the japanese. *Biological Trace Element Research* **2002**;90:57-70

[7] Wright, G., Lai, J. C. K., Chan, A.W.K., Minski, M.J., Lim, L., Leung, S. W. Metallomic distribution in various regions of the brain as influenced by dietary intakes and their implications. (ISEIS 100321), in proceedings of ISEIS 2010 International Conference on Environmental Informatics, **2010**, in press.

[8] Magalhaes, T., von Bohlen, A., Carvalho, M.L., Becker, M. Trace elements in human cancerous and healthy tissues from the same individual: A comparative study by TXRF and EDXRF. *Spectrochimica Acta Part B* **2006**;61:1185–3.

Cross Resistance of Magnesium Oxide Nanoparticles to Cisplatin in Leukemia Cells: Mechanistic Studies

By Alok Bhushan PhD, Prathamesh P Patil BPharm MS, Vikas Bhardwaj BPharm, Maria B Lai BS, Chrisotpher K Daniels PhD, Solomon W Leung* PhD, and James CK Lai PhD

Department of Biomedical and Pharmaceutical Sciences, College of Pharmacy, Idaho Biomedical Research Institute, Idaho State University, Pocatello, Idaho, USA and *College of Engineering, Idaho State University, Pocatello, Idaho 83209, USA

1. INTRODUCTION

The failure of cancer chemotherapy can be attributed to two major factors. The two major reasons are toxic effects of the drugs and secondly the resistance to the chemotherapeutic agents used in treatment of cancer. Although the design of the drugs is to get rid of cancer cells in the body, the normal cells also are exposed to the anti-cancer drugs resulting in toxic effects. The challenge to specifically target cancer cells continues and there have been many drugs designed and are now in use for specific cancer cells. Several drugs like herceptin and gleevec are in use in clinic with improvement of survival (1, 2). It becomes difficult to treat cancer when few of the cells in tumors acquire the ability to adapt to the toxic environment of the drugs that are used in chemotherapy (3). For the past 25 years, many laboratories around the world have focused efforts to unravel the mechanisms that contribute to the emergence of resistance in cancer. The hallmark of resistance was the discovery of P-glycoprotien by Dr.Victor Ling. P-glycoprotein was found to be an active transporter and pumped drugs outside the cells (4). This in turn decreased the intracellular concentration resulting in adaptation of cancer cells to toxic environment. A downside of this overexpression of P-glycoprotein was that it imparted cross resistance to several structurally unrelated drugs (5). Since the discovery of P-glycoprotein, several proteins have been identified which result in resistance in cancer. Multidrug Resistant related Proteins (MRPs) belong to a family of ATP cassette and about 7 MRPs have been identified with different substrate affinity (6). Studies in our laboratories have focused on many drug resistant cells from leukemias, sarcomas, multiple myelomas, breast cancer and pancreatic cancers. We have shown that cisplatin selected methotrexate resistant cells have a 66 kD protein that in its unphosphorylated state fails to transport the drug inside the leukemia cells resulting in resistance. Our studies with sarcoma cells selected for resistance to adriamycin has increased expression of c-fos indicating a role of this transcription factor in anthracycline resistance (7, 8, 9). Breast cancer cells resistant to adriamycin have higher expression of IL6 receptor (10). Studies with dexamethasone resistant multiple myeloma cells show changes in intracellular signaling. In addition, 5-fluorouracil resistant pancreatic cells have upregulated levels of mitogenic and drug metabolizing enzyme (unpublished data). All these findings from our laboratories indicate that resistance is a complex phenomenon and differs in different cell lines as well as mechanisms vary depending upon the exposure of the chemotherapeutic agent.

We took a different approach by utilizing nano materials to study the effect on various cancer cells. We exposed Leukemia cells and its subline that was selected for resistance to cisplatin as well as pancreatic cancer cells selected for resistance to 5-fluorouracil to MnO and ZnO nanoparticles that range in size from 30-80nm. The rationale of these studies was to determine if the resistant cells differ in sensitivity to nano particles and if the cellular signaling pathways were altered differentially in these cell limes. The data will provide us with information if cells resistant to anticancer drugs respond differently to nanoparticles so that we may design drugs using nanomaterials to specifically target resistant cells.

2. CYTOTOXICITY OF METALLIC OXIDE NANOPARTICLES AND THE UNDERLYING SIGNALING MECHANISMS

Nanomaterials have been increasingly used in industrial applications (e.g., drug delivery, additives to drugs and cosmetics). Because of their wide use, occupational exposure to nanomaterials and nanoparticles may pose as health risks. Recent studies have suggested that exposure to nanoparticles may induce cytotoxic effects in some mammalian cell types although these effects have not been systematically investigated (11).

In a series of studies, we tested the hypothesis that titanium oxide, magnesium oxide, and zinc oxide nanoparticles exert differential cytotoxic effects on human astrocytoma (U87) cells and human fibroblasts (HFF-1). Because the effects of such nanoparticles on human neural cells are unknown, we have determined the putative cytotoxic effects of these nanoparticles on human astrocytes-like astrocytoma U87 cells and compared their effects on normal human fibroblasts. We found that TiO_2 micro- and nanoparticles induced cell death on both human cell types in a concentration-related manner. We further noted that ZnO nanoparticles were the most effective, TiO_2 nanoparticles the second most effective, and MgO nanoparticles the least effective in inducing cell death in U87 cells. The cell death mechanisms underlying the effects of TiO_2 micro- and nanoparticles on U87 cells include apoptosis, necrosis, and possibly apoptosis-like and necrosis-like cell death types. Thus, our findings may have toxicological and other pathophysiological implications on exposure of humans and other mammalian species to metallic oxide nanoparticles. Furthermore, we are of the opinion that these mechanisms can be exploited to induce the death of cancer cells thereby enhancing the process of new anti-cancer drug discovery (11).

3. CYTOTOXIC EFFECTS OF METALLIC OXIDE NANOPARTICLES AND DRUG RESITANCE MECHANISMS

In this study, we determined the effect of MgO nanoparticles on murine leukemia cancer cells (L1210 cells) and a subline selected for resistance to cisplatin (L/DDP cells). The magnesium oxide nanoparticles showed differential effect on cell survival using different methods of assays. We further determined the effect of MgO on various cells signaling proteins (Akt, p-Akt and Erk and p-Erk) in L1210 and LDDP cells after magnesium oxide nanoparticles treatment. Our results indicate that the treatment with MgO nanoparticles increased the expression of p-Akt and decrease the expression of p-Erk expression in L1210 and L1210/DDP cells. The treatment of nanoparticles showed no effect on the level of expression of Erk and Akt in these cells indicating that the treatment of cells with MgO nanoparticals decreased activation of erk pathway but increased activation of Akt.

We further examined the expression of downstream transcription factors (c-fos and c-jun) as they are altered due to erk signaling. The western blot analysis shows that MgO nanoparticles decreased the expression of c-fos in L1210 and LDDP cancer cells. Expression of c-jun in L1210 cells showed some increase at treatment concentration of 25μg/ml. In L1210/DDP cells, the level of c-fos reduced in dose-related manner, however the level of c-jun was undetected.

4. CONCLUSIONS

We have presented an overview of our studies on anti-cancer drug resitance mechanisms as well as ongoing systematic studies of the nanotoxicity of metallic oxide nanoparticles. Our ongoing studies also

suggest that resistant cancer cells may exhibit cross-resistant to the cytotoxic effects of metallic oxide nanoparticles. The latter effects appear to be mediated by cell survival/proliferation signaling mechanisms. Clearly these are important and novel areas of anti-cancer drug discovery. As such they merit further investigation. We are currently pursuing these exciting new dormains of nanomedicine and nanocancer research.

5. ACKNOWLEDEMENTS

Our studies were supported by an USAMRMC Project Grant (Contract #W81XWH-07-2-0078) and NIH Grant #P20 RR016454 from the Idaho INBRE Program of the National Center for Research Resources.

6. REFERENCES

1) Arnold K. After 30 years of laboratory work, a quick approval for STI571 (2001). J Natl Cancer Inst. 4;93(13):972.
2) Miller JL. Progress in breast cancer treatment: prevention, new therapies come to forefront (1998). Am J Health Syst Pharm. 15;55(22):2326, 2328, 2330.
3) Gottesman MM. Mechanisms of cancer drug resistance (2002). Annu Rev Med. 53:615-27.
4) Juranka PF, Zastawny RL, Ling V. P-glycoprotein: multidrug-resistance and a superfamily of membrane-associated transport proteins (1989). FASEB J. 1989 3(14):2583-92.
5) Goda K, Bacsó Z, Szabó G. Multidrug resistance through the spectacle of P-glycoprotein (2009). Curr Cancer Drug Targets. ;9(3):281-97.
6) Toyoda Y, Hagiya Y, Adachi T, Hoshijima K, Kuo MT, Ishikawa T. MRP class of human ATP binding cassette (ABC) transporters: historical background and new research directions (2008). Xenobiotica. 38(7-8):833-62.
7) Bhushan A, Abramson R, Chiu JF, Tritton TR. Expression of c-fos in human and murine multidrug-resistant cells (1992). Mol Pharmacol. 42(1):69-74.
8) Bhushan A, Wroblewski D, Xuan Y, Tritton TR, Hacker MP. Correlation of altered tyrosine phosphorylation with methotrexate resistance in a cisplatin-resistant subline of L1210 cells (1996). Biochem Pharmacol. 1996 Feb 23;51(4):477-82.
9) Wroblewski DH, Bhushan A, Xuan Y, Brinton BT, Tritton TR, Hacker MP. Investigations on the mechanisms of methotrexate resistance in a cisplatin-resistant L1210 murine leukemia cell subline (1996). Cancer Chemother Pharmacol.37(4):337-42.
10) Conze D, Weiss L, Regen PS, Bhushan A, Weaver D, Johnson P, Rincón M. Autocrine production of interleukin 6 causes multidrug resistance in breast cancer cells (2001). Cancer Res. 2001 Dec 15;61(24):8851-8.
11) Lai JC, Lai MB, Jandhyam S, et al. 2008. Exposure to titanium dioxide and other metallic oxide nanoparticles induces cytotoxicity on human neural cells and fibroblasts (2008). Int J Nanomed, 3**,** 533-545.

Advanced Dehydrogenase Biofuel Cell Modified with Highly Branched Polymers and Nano Gold Sol-Gel

Solomon Leung
Civil and Environmental Engineering Department
Idaho State University
Pocatello, Idaho, 83209, USA
leunsolo@isu.edu

James Lai
Biomedical and Pharmaceutical Sciences Department
Idaho State University
Pocatello, Idaho, 83209, USA
Lai@pharmacy.isu.edu

***Abstract* – Highly branched polymers and nano Au particles sol-gel were used to construct an enzymatic biofuel cell system. The anode and cathode of this biofuel cell modified with the sol-gel were characterized. The sol-gel was very effective in anchoring and stabilizing lactate dehydrogenase (LDH) and glutamate dehydrogenase (GDH), the enzymes used in the biofuel cell system. This sol-gel modification would enable further enzymatic biofuel cell development that was not possible due to rapid deterioration of enzymes.**

Keywords - LDH; GDH; nanoparticle; biofuel cell; PAMAM

I. INTRODUCTION

Biochemical fuel cell drew heavy popularity among scientist and engineers in the early 1960s but the commercialization of it was not realized due to technical difficulties and the availability of inexpensive petroleum energy [1]. However, the recent energy crisis and the development of micro circuitry reiterate the interest of biofuel cell; with the aid of nano technology, biofuel cell has leapfrogged to a new horizon. In addition to the conventional application of waste conversion to energy recycling concept, the micro and nano technology enable the concept of biofuel cell to directly extract energy from organisms and plants [2, 3].

Our research group has started a biofuel fuel cell initiative, the objective of this initiative is to develop a biofuel cell system that is non-toxic and biological compatible that can be employed in a natural environment or human body. In this paper, we are reporting an enzymatic biofuel cell system that was constructed with electrodes that were enhanced with polymer and nanogold particles sol-gel that can be implanted into our body as power source for biomedical devices such as pacemaker and insulin pump; this cell/battery can be modified to generate electrical current to be utilized at point of generation or stored as battery power. The energy source or reactants were lactate, α-ketoglutarate, and ammonia that are all existing in our body or as parts of our body fluid.

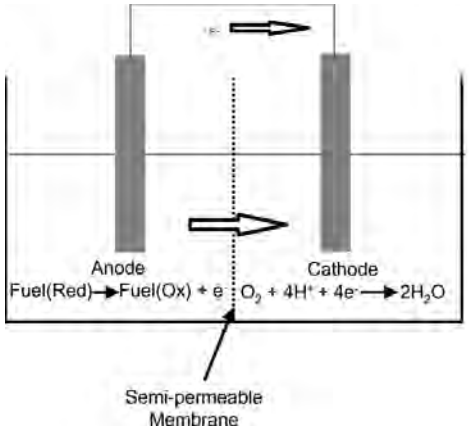

Fig. 1 A typical fuel cell, products of fuel cell reactants (fuel oxidants) can migrate to the cathode side through the semi-permeable membrane to complete the overall fuel cell reactions.

For our biofuel cell system, the anodic half-cell was made by an Au electrode coated with lactate dehydrogenase (LDH) submerged in solution containing lactate and nicotinamide adenine dinucleotide (NAD+), thus, for the anodic half reaction:

$$\text{Anode:} \quad \text{Lactate} + NAD^+ \xrightarrow{LDH} \text{pyruvate} + NADH + 2H^+ + 2e^- \quad (1)$$

As lactate was oxidized into pyruvate in the anode, the oxidative potential, E_0'(25 ˚C), would be 0.19 V.

The cathodic half-cell was made by a glassy carbon electrode (GCE) coated with glutamate dehydrogenase (GDH) submerged in solution containing ammonia and reduced nicotinamide adenine dinucleotide (NADH), the cathodic half reaction was:

$$\text{Cathode:} \quad \alpha\text{-Ketoglutarate} + NH_4^+ + NADH + H^+ + 2e^- \xrightarrow{GDH} \text{glutamate} + NAD^+ + H_2O \quad (2)$$

As α-ketoglutarate was reduced into glutamate in the cathode, it generated a reductive potential, E_0'(25 ˚C), of -0.14 V.

Combining (1) and (2), the total potential for the fuel cell with the anode and cathode above was 0.05 V (per mole). In general, biological reactions in nature do not release large amount of energy for each reaction step to preserve energy utilization efficiency. The overall reaction for the biofuel cell thus was [4]:

$$\text{Lactate} + \alpha\text{-ketoglutarate} + NH_4^+ \xrightarrow{LDH,GDH} \text{pyruvate} + \text{glutamate} + H^+ + H_2O \quad (3)$$

Since the ΔE_0' of (3) was greater than 0, the reaction was spontaneous and would proceed as written from left to right.

II. MATERIALS AND METHOD

A. Electrodes

Gold electrode had diameter of 0.3 cm and the GCE had diameter of 0.35 cm, they both were purchased from Tianjin Aida Heng Sheng Co, Tianjin, China.

B. Electrode Preparation

1). Anode: A clean gold electrode was immersed in 0.1 M cysteamine solution for 2 hours in the dark, then it was dipped into colloidal gold nanoparticles for 24 hours, finally the electrode was dipped into LDH solution for 20 hours before it was used for testing. This was a LDH-Au-cysteamine (sol-gel)-modified Au anode as shown in Fig. 2. LDH was embedded in the Au sol-gel matrix which also enabled electronic transfer.

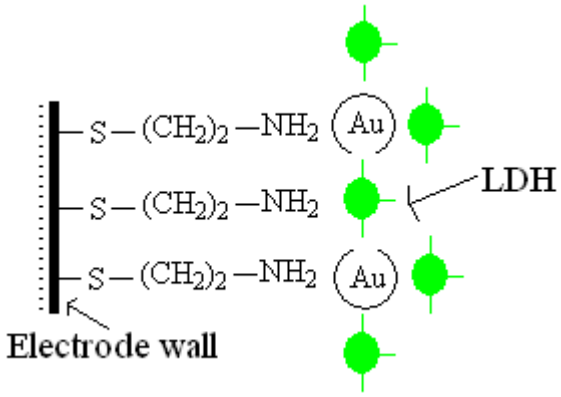

Fig. 2. A gold anode modified with cysteamine, Au nanoparticles (sol-gel) and LDH.

2). Cathode: Several combinations of ploymers (poly(amido amine) (PAMAM) of 0^{th} and 2^{nd} generation, and cysteamine) with GDH and nanogold particles were tested for their efficacies to enable the reductive reaction as in (2). A cleaned glassy carbon electrode was first immersed in 0.1 M cysteamine (or PAMAM) solution in darkness. The resulting monolayer-modified electrode was rinsed thoroughly with twice-distilled water and soaked in water. Then, it was dipped into the colloidal gold. The gold colloid–cysteamine-modified cathode was dipped into the l-glutamate dehydrogenase (GDH) solution (pH 7.4) (or GDH solution containing NADH). In such a way, a GDH (/NADH) gold colloid–cysteamine (or PAMAM)-modified glassy carbon cathode was obtained.

For cathode that both cysteamine and PAMAM were coated, the cleaned glassy carbon electrode was first immersed in cysteamine solution, the resulting electrode was dipped into the PAMAM solution. Then, it was dipped into the colloidal gold. The gold colloid–cysteamine/PAMAM-modified electrode was dipped into the GDH solution (pH 7.4) (or GDH solution containing NADH). In such a way, a GDH (/NADH) gold colloid–cysteamine/PAMAM-modified glassy carbon electrode was obtained

C. Nanoparticles Solution Preparations

Nanoparticles Au was prepared by reacting $HAuCl_4$ with citric acid [5].

All chemical reagents used in this study were analytical grade or the highest grade available, water was double deionized distilled water. All the experiments were carried out under deoxygenated condition in 0.1 M phosphate buffer solution. All enzymes and biochemicals were purchased from Sigma-Aldrich Chemical Co, St. Louis, MO, USA.

D. Detections

UV-VIS spectrophotometry was carried out by an Agilent diodearray spectrophotometer when needed; cyclic voltammetry was conducted by using a Gamry 600 Potentiostat. Voltammetric potential was measured against a saturated chloride electrode (SCE).

III. RESULTS AND DISCUSSIONS

A. Anodic half-cell

Fig. 3 shows the oxidative responses of the modified Au electrode with nanogold particles, cysteamine and LDH. As seen, the characteristic peak of lactate conversion to pyruvate was detected at 250 mV and the accumulative current increased linearly with added lactate instantaneously [6]. It verified that the modified anodic electrode was functioning as expected in (1).

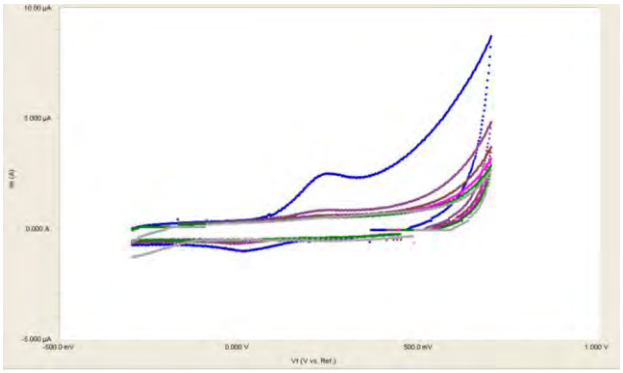

Fig. 3 Voltammetric responses of an Au electrode coated with cysteamine, Au nanoparticles, and LDH at pH 8. Responses were stepwise additions of lactate at $1.0x^{-4}$ mol/ml with linear current increments (oxidative peaks) at 250 mV.

B. *Cathodic half-cell*

Fig. 4 is the UV-VIS spectrum PAMAM-Au-GDH coated on a plastic cuvette that has no absorption in the UV-VIS range, the same procedures used to modify the cathode. As shown, PAMAM and Au have strong absorption at 278 and 548 nm, respectively. The red and blue line were absorption of the same coating after numerous rinses that indicated the self-assembling coating was stable, although some PAMAM were released after the initial rinses.

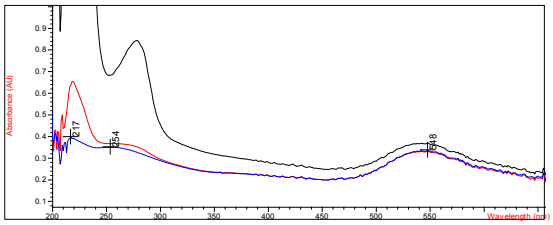

Fig. 5 is the reductive response of a GCE modified with 2nd generation of PAMAMs, nanogold particles, and GDH. The cathodic half-cell reaction functioned more efficiently at lower concentrations of α-ketoglutarate and became less effective as the accumulative concentration of α-ketoglutarate was higher (>0.025 mM). This could be an effect of saturation that the nanoAu particles could only support a limited amount of GDH for the conversion of α-ketoglutarate to glutamate. An alternative explanation is that some PAMAM was released by the Au sol-gel that resulted in less conversion efficiency. This also supported the general speculation that the Au sol-gel can only support a finite amount of "sorbed" molecules per unit of Au molecule. The near linear current versus α-ketoglutarate relationship appeared to support this observation.

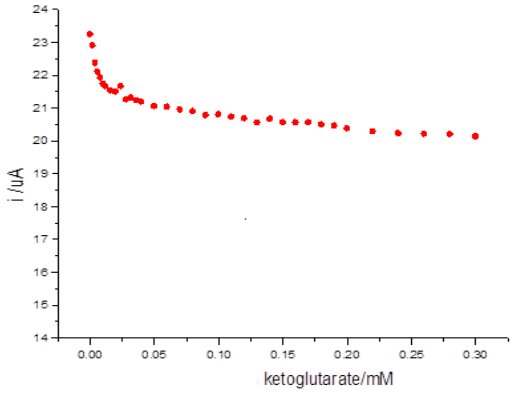

Fig. 5. Reductive responses of a glassy carbon electrode modified with PAMAM, Au nanoparticle and GDH measured at 0.7 V in solution of ammonia and α-ketoglutarate.

For the PAMAM-Au-GDH cathodic half-cell, the voltammetric responses of (3) at 0.7 V was shown in Fig. 5, the total current measured was 3.11 μA; Considering the electrode surface area of 0.0962 cm^2 (diameter of 0.35 cm) and reactants consumption of 0.3 mM, thus the current density (A/ cm^2) would be 32.3 μA/ cm^2 and the current generated from the reaction was 10.4 mA/M.

It was observed that with the different combinations of cysteamine and PAMAMs, polymers with the most branched structure would support the sol-gel nanogold structure with the most efficiency to anchor the embedded enzymes (LDH and GDH, for examples) for the enzymatic conversions [6]. In addition, this sol-gel structure on the electrodes could stabilize the enzymes that normally would easily decompose rapidly once they are in diluted solution, which was the case in our electrode preparation. Our anode and cathode performed repeatedly consistently as they were freshly prepared even after they were stored submerged in distilled water at 4 ˚C for 2 weeks. A stable and cost effective enzymatic system is very important for the realization of using enzymatic biofuel cell for practical applications.

Our biofuel cell system would generate a relative low potential (0.05V), but the reactants are all readily available from our body which make it closer to reality for the system to be implanted into our body as power source for biomedical devices. If this concept of enzymatic biofuel cell is to be employed to extract energy from an industrial waste containing high energy that is normally discarded, such as waste from potato processing

plant and cheese factory, then a more potential favorable redox reaction route should be chosen[7]. For example, the current cathode with (2) has a negative potential, one can choose a cathode made with cytochrome a that has a positive potential as shown in the following:

$$\text{Cytochrome a} + Fe^{3+} + e^{-} \rightarrow \text{cytochrome a} + Fe^{2+}$$

that will produce a reductive potential of 0.29 V per mole at 25 ˚C. Another half reaction with high positive potential:

$$^1/_2\, O_2 + 2H^{+} + 2e^{-} \rightarrow H_20$$

produces a reductive potential of 0.816 V [8].

IV. CONCLUSIONS

An enzymatic biofuel cell system consisted of anode and cathode modified with enzymes, highly branched polymers, and Au nanoparticles sol-gel was constructed and characterized. This enzymatic biofuel cell concept can be used to generate power for various biomedical and environmental applications, depending on the available energy sources. The energy sources also dictate the enzyme systems to be used, which could be a limiting factor for biofuel cell. The highly branched polymers and nanogold particles sol-gel proved to be effective in anchoring and stabilizing the enzymes used in the biofuel cell and should be explored further in the development of a practical biofuel cell system.

ACKNOWLEDGMENT

This study was supported by a DOD USAMRMC Project Grant (Contract #W81XWH-07-2-0078).

References

[1] Dieter Sell, “Bioelectrochemical Fuel Cells”, in Biotechnology: Special Processes, 2nd ed., vol. 10, H. Rehm and G. Reed, Eds., New York, Wiley and Sons, 2008, pp. 1-21.

[2] V. Flexer and N. Mano, “From Dynamic Measurements of Photosynthesis in a Living Plant to Sunlight Transformation into Electricity**, “**. Analytical Chemistry*,* vol 82, Apr. 2010, pp.1444-1449, doi**:** 10.1021/ac902537h.

[3] P. Cinquin, C. Gondran, F. Giroud, S. Mazabrard, A. Pellissier, F. Boucher, J.Alcaraz, K. Gorgy, F. Lenouvel, S. Mathé, P. Porcu, and S. Cosnier, “A Glucose BioFuel Cell Implanted in Rats,” 2010, PLoS ONE 5(5): e10476. doi:10.1371/journal.pone.0010476.

[4] Clarence Suelter and Larry Kricka, Methods of Biochemical Analysis, Volume 36, Bioanalytical Applications of Enzymes. New York, NY, Wiley and Sons, 1992.

[5] J. Lai, Y. Wang, W. Gao, H. Gu, and S. Leung, “Performance Comparisons of Nanoparticle Modified Sensor Electrodes for the Detection of Nitrite and Peroxide”, Technical Proceedings of the 2009 Nanotechnology Conference and Expo, volume 2: chapter 4: Biosensors and Diagnostics, NSTI, pp. 233-235.

[6] J. Cheng, J. Di, J. Hong, K. Yao, Y. Sun, J. Zhuang, Q. Xu, H. Zheng, and S. Bi, “The Promotion Effect of Titania Nanoparticles on the Direct Electrochemistry of Lactate Dehydrogenase Sol-Gel Modified Gold Electrode,” Talanta, vol 76, Sep 2008, pp. 1065-1069.

[7] K. Rabaey and W. Verstraete, “Microbial Fuel Cells: Novel Biotechnology for Energy Generation”, TRENDS in Biotechnology, vol 23, Jun 2005, pp. 291-298.

[8] Harry Clark, Standard Reduction Potentials, http://www.jesuitnola.org/upload/clark/refs/tables.html

Elemental Analyses in Organ Systems in a Small Animal after Life-Long Controlled Diet

Solomon Leung and Brad Williams
Civil and Environmental Engineering Department
Idaho State University
Pocatello, Idaho, 83209, USA
leunsolo@isu.edu

James Lai
Biomedical and Pharmaceutical Sciences Department
Idaho State University
Pocatello, Idaho, 83209, USA
lai@pharmacy.edu.edu

Alex Chan and Margret Minski
Imperial College Reactor Centre
University of London
Silwood Park, SL5 7PY Ascot, Berks, UK
lai@pharmacy.edu.edu

***Abstract* – The intake and concentration of metals and electrolytes from our diet are believed to be affecting our general health, in particular, the proper functions of vital organs. Other than genetic factors and environmental stresses, evidence has been accumulating that excessive metal intakes would lead to organ failure. Once absorbed, minerals and electrolytes can travel freely within the body, and deposit at key organ systems such as the brain, lung, kidney, etc. By conducting experiments with an established systematic animal model (e.g., rats), it is possible to determine the elemental distribution matrices within the organs, as well as to correlate such matrices with the overall physiological and behavioral status of the animal. In this study, rats were used as the testing animal with a controlled diet for their entire lifetime. Information matrices of 30 different elements (including heavy metals and electrolytes) associated with their distributions in various vital organs including brain, lung, kidney, liver, heart, spleen, and uterus were analyzed as a function of age at 5, 10, 23, and 120 days old. In addition, how excessive Mn intakes would affect the accumulation of other elements was also studied. It was found that the excessive Mn intakes would greatly affect the accumulation of most metals and electrolytes from the intake diet, although the diet only contained trace amount of some of these elements. For example, excessive amount of Hg was found in kidney issue compared to control sample. This multidimensional analysis of elemental accumulations in major organs provided groundbreaking information in our understanding of how dietary intakes, including pollutants, can directly affect our physiological condition and general health.**

Keywords - Metals, electrolytes, distribution, Mn, diet, accumulation.

I. INTRODUCTION

In the contemporary society, considerable attention has been paid to dietary intake or supplement due to health concerns. On the other hand, involuntarily consumption of unwanted chemicals and preservatives via processed foods and polluted water is also inevitable depending on the lifestyle and available resources of individuals; one such example would be consumption of drinking water source that is laden with soluble ions and heavy metals. This occurs quite frequently for those that are living in rural areas with no treatment system for their drinking water in developing countries.

Attempts in understanding the homeostasis of different elements in brain and other major organs fell short significantly due to the vast complexity of the mechanisms involved [1]. What cause this complexity are the multiple factors that can affect the dynamics of biological functions, and often these factors are not apparent until the advanced age of an animal. In addition, larger sample size is needed to observe statistical significance in the small changes over life time exposure [2]. Such constraint creates a vast obstacle to conduct research, and the hurdle is more difficult if human subject is involved, making studying such factors prohibitively costly.

There are chemicals and elements that we need to maintain proper bodily functions: in this study, we focused on the essence of major and selected trace elements and how these elements accumulated in our major organs. The major organs are: brain, lung, kidney, liver, heart, spleen, and uterus. Information matrices of 30 different elements (including heavy metals and some electrolytes) that were fed to rats as part of a regular diet were obtained from the seven major organs and analyzed. The 30 elements of interests were: Al, As, Ba, Br, Ca, Cd, Cl, Co, Cr, Cu, F, Fe, Hg, I, K, La, Mg, Mn, Mo, Na, Rb, S, Sb, Sc, Se, Si, Sm, Sr, V, and Zn.

Also, we investigated how intake of an excessive contaminant, such as a heavy metal ion (Mn^{2+}) in this study, would alter the accumulation of all other elements and electrolytes in the vital organs over the lifetime of the rats, that would directly affect the proper functions of these organs.

II. EXPERIMENTATION

Wistar rats of the Portion strain (Animal Breeding Unit, Carshalton, Surrey, U.K.) bred in the Institute of Neurology, University of London, U.K. were used. All

animals were kept on a 12-hour light/12-hour dark cycle with free access to food and water. Elemental concentrations in the rat food pellets have been determined as shown in Table 1 below.

TABLE I. Elemental Concentration of rat food pellet.

Element	Concentration (in mg/g)
Ca	6.39 ± 1.68
Cl	2.31 ± 0.49
Fe	0.25 ± 0.05
K	5.36 ± 0.95
Mg	1.17 ± 0.32
Na	1.48 ± 0.32
	Concentration (in µg/g)
Al	98.06 ± 8.05
Br	10.57 ± 2.26
Co	0.20 ± 0.04
Cr	1.50 ± 0.44
Cu	7.21 ± 2.12
F	ND(5.00)
Hg	ND (0.25)
I	ND (0.50)
Mn	49.34 ± 8.65
Mo	2.80 ± 0.45
Se	ND (0.25)
Rb	12.73 ± 2.61
V	ND (0.50)
Zn	47.73 ± 4.11

Thirty trace and major elements in different organs of rats at four different age groups (5, 10, 23, and 120 days) were analyzed by instrumental neutron activation analysis (INAA) [3]. The samples were irradiated by thermal neutrons using three different sets of conditions depending on the nuclear characteristics of the elements of interest. Not all 30 elements were reported in the results because those not reported herein were either below the detection limits of the INAA technique [3] or the element concentrations were not high enough in the samples (food pellets or organ) for detection.

All the standard materials and samples for INAA were freeze-dried and pelleted. Dried samples were homogenized using a Glen Creston polystyrene ball-mill and pelleted. Other details of standard and sample preparations were as described previously [3, 4].

Standards and samples were irradiated in a 100 KW 'Consort' Reactor Mark II at the Imperial College Reactor Centre. Irradiated standards and samples were then analyzed for their elemental contents by gamma ray spectrometry using various Ge (Li) detectors and ND 6600 Multichannel Analyzer (Nuclear Data Inc., Schaumburg, Illinois, USA). Details of the elemental determinations were described in the methodology paper by Chan et al. [3].

All laboratory chemicals used were of analytical grade (BDH Chemicals Limited, U.K.) and single element standards of trace elements were obtained from AAS (Ventron Division, Limited, U.K.); other elemental standards for F, Cl, Br, and P were obtained from Hopkin and Williams Chemical Ltd., U.K. Water for solution preparations and feeding was double-distilled.

The three concentrations of Mn^{2+} fed to the rats via drinking water were 1, 10, and 20 mg/ml.

III. RESULTS AND DISCUSSIONS

As shown in Fig. 1, there were only 20 elements detectable from the kidney tissue of the rats out of the 30 elements of interest. The rest of elements were either under the detectable limit of INAA, or the kidney did not retain these elements: As, Ba, Cd, La, S, Sb, Sc, Si, Sm, Sr. Notes that some of the undetectable elements from the food pellets showed up in the kidney tissue (such as F, Hg, I, Se, and V) which indicated that the elements would accumulate with time and the amounts would also depend on the organs, thus their functions.

Some elements increased with time (age); many elements would decrease slightly or level off with age, these variations were also organ dependent.

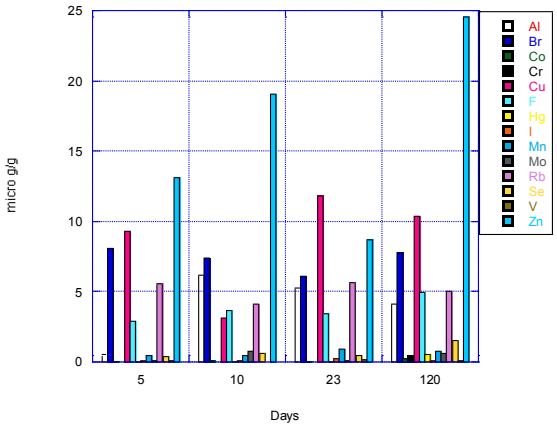

(a)

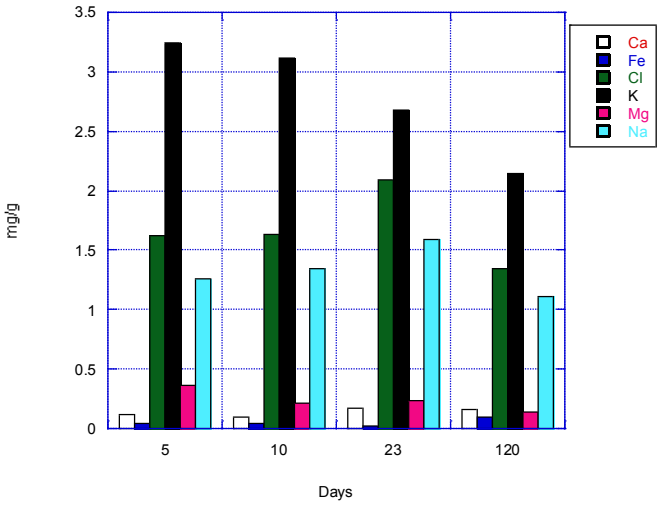

(b)

Fig.1 Elemental concentrations of rats' kidney at different developmental stages of 5, 10, 23, and 120 days. (a) The weight of elements in µg/g of organ in wet weight; (b). weight of elements in mg/g of organ in wet weight.

It was found that Mn^{2+} intake would definitely affect the retention of other elements in the major organs. Fig. 2 shows the fractional changes of different elements in the kidney tissue when 3 different concentrations of Mn^{2+} were fed to 120 days old rats, as compared to the 120 days old control without excessive Mn^{2+}. The intake of excessive Mn increased the accumulation of most heavy metals. More noticeably, it also increased the accumulation of I and Hg, and decreased the retention of Se and V, all of which were not detectable in the food pellet. Therefore, if we consume an excessive amount of an heavy metal (for example, Mn) for a lengthy period, it is likely that the total toxicity would be synergistically increase due to increased accumulation of other heavy metals induced by the excessive Mn. This synergistic effect has been observed consistently in all the organs we studied.

IV. CONCLUSIONS

Retention of elements from diet intake was found to be age and organ dependent. Excessive intake of a heavy metal can induce synergistic toxicity due to increased accumulation of other heavy metals presented in the diet, although the concentrations of these metals may be at trace level.

ACKNOWLEDGMENT

This study was supported by a DOD USAMRMC Project Grant (Contract #W81XWH-07-2-0078).

REFERENCES

[1] W. Pardridge, "Blood-Brain Barrier Drug Targeting: The Future of Brain Drug Development," Molecular Interventions, vol 3, Feb 2003, pp. 90-105.

[2] C. Maynard, R. Cappai, I. Volitakis, K. Laughton, C. Masters, A. Bush. et al. "Chronic Exposure to High Levels of Zinc or Copper Has Little Effect on Brain Metal Homeostasis or a Beta Accumulation in Transgenic APP-C100 Mice," Cellular and Molecular, vol 29, May 2009, pp. 757-67.

[3] A. Chan, M. Minski, and J. Lai, (1983) "An Application of Neutron Activation Analysis to Small Biological Samples: Simultaneous Determination of Thirty Elements in Rat brain Regions," Journal of Neuroscience Methods, vol 7, Apr 1983, pp. 317-328.

[4] A. Chan and M. Minski, U. L. R. C. Internal Report (RES/36), 1981, pp. 37-39.

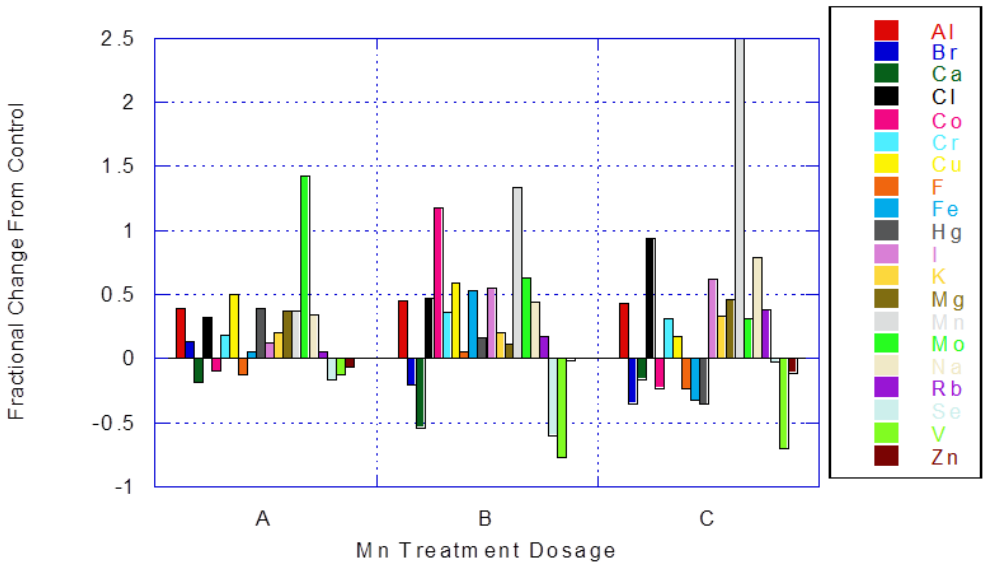

Fig. 2. Different concentration treatments with Mn^{2+} in water with % changes in adult kidney relative to control adult level: A).Life-long treatment with 1 mg/ml of Mn^{2+}; B.) 10 mg/ml of Mn^{2+}; C.) 20 mg/ml of Mn^{2+}.

ISSN 1726-5749

SENSORS & TRANSDUCERS

4 vol. 11 Special /11

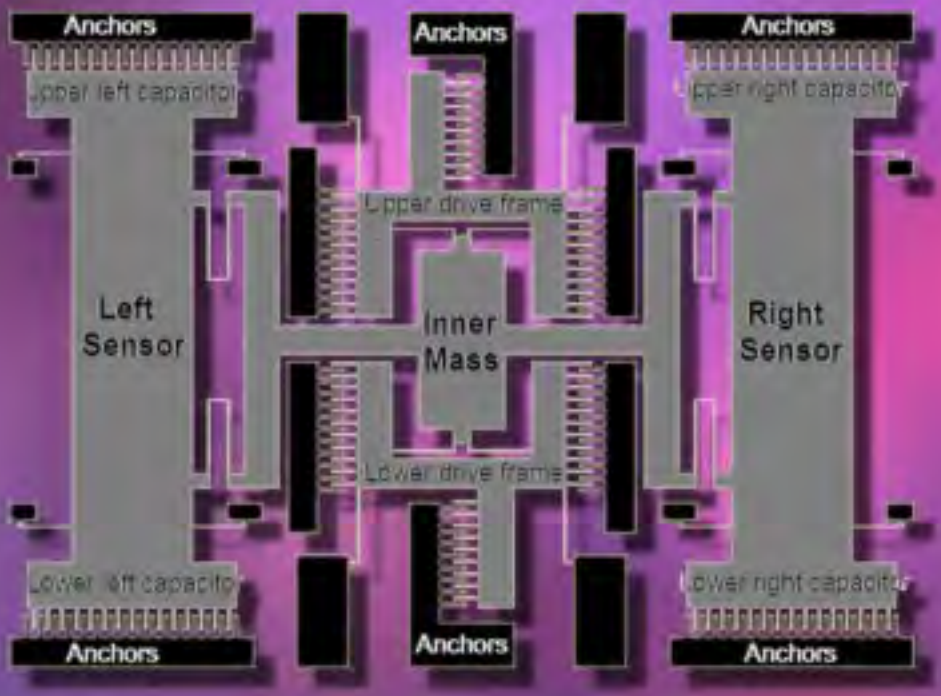

MEMS & NEMS: Devices and Technologies

International Frequency Sensor Association Publishing

IFSA

Sensors & Transducers

Volume 11, Special Issue, April 2011 | **www.sensorsportal.com** | **ISSN 1726-5479**

Sensors & Transducers Journal (ISSN 1726-5479) is a peer review international journal published monthly online by International Frequency Sensor Association (IFSA).
Available in electronic and on CD.

Sensors & Transducers Journal

Contents

Volume 11
Special Issue
April 2011

www.sensorsportal.com

ISSN 1726-5479

Research Articles

Authors are encouraged to submit article in MS Word (doc) and Acrobat (pdf) formats by e-mail: editor@sensorsportal.com
Please visit journal's webpage with preparation instructions: http://www.sensorsportal.com/HTML/DIGEST/Submition.htm

Sensors & Transducers Journal, Vol. 11, Special Issue, April 2011, pp. 74-83

www.sensorsportal.com

Sensors & Transducers

ISSN 1726-5479

http://www.sensorsportal.com

Biomedical Applications of Modified Carbon Glassy Electrode Sensor with Nanoparticles and Dendrimers

[1]Solomon W. LEUNG, [2]Yuanhong WANG and [3]James C. K. LAI

[1]Civil and Environmental Engineering Department, School of Engineering and Biomedical Research Institute, Idaho State University, Pocatello, ID 83209, USA
Tel.: 1-208-282-2524, fax: 1-208-283-4538

[2]Civil and Environmental Engineering Department, School of Engineering, Idaho State University, Pocatello, ID 83209, USA

[3]College of Pharmacy and Biomedical Research Institute, Idaho State University, Pocatello, ID 83209, USA

[1]E-mail: leunsolo@isu.edu

Received: 13 December 2010 /Accepted: 15 March 2011 /Published: 5 April 2011

Abstract: We previously reported the development of a biosensor platform that is capable of measuring biometabolites and environmental sensitive species, such as peroxide and nitrate/nitrate, to concentrations in the order of ppb (parts per billion) or lower. In this investigation, we modified our platform with dendrimers to enhance its performance. Zero and second generation of dendrimers were coated on the surface of a carbon glassy electrode which was then modified with l-glutamate dehydrogenase (GDH) and α-keto glutarate. The resulting electrode was tested with ammonium solutions, concentrations ranged from 2 to 300 nM at pH 7.4; the results were satisfactory. Measurements at lower concentrations had better resolution than at higher concentrations and it is believed that the measurement limit can be lower than 2 nM. This biosensor platform was proven to be versatile and can be employed as a platform for ultrasensitive detecting devices in many biomedical and environmental applications. *Copyright © 2011 IFSA.*

Keywords: Biosensor, GDH, Ammonium, Glassy carbon electrode, PAMAM.

1. Introduction

In the past several years, our research group has been developing a platform for biosensor construction that is capable of detecting target species that are in nano and subnanomolar levels [1, 2]. This sensor

platform is based on an Au electrode modified with sol-gel Au colloid and biocatalyst that is specific to the chemical species to be detected, the Au colloid comprises nano-size Au particles and cysteamine which binds strongly on the surface of the metal electrode and provide stable linkage with the nano gold particles and biocatalysts. Thus far, biometabolites and environmental sensitive chemicals such as nitrite/nitrate and peroxide were successfully detected at level of nM and below with this sensor platform.

In this study, we were developing another biosensor platform that can be used to measure biometabolites and environmental sensitive chemicals based on a non-metal glassy carbon electrode modified with sol-gel Au colloid that is similar to the sensor platform mentioned previously, except the binding polymer would be a dendrimer (polyamidoamine, PAMAM) instead of cysteamine. A dendrimer was chosen to be the linker between the electrode and Au particles/catalysts because of its low toxicity and highly branched structure that presumably can provide more anchoring sites for the Au particles and catalysts. Thus, the dendrimer can enhance the performance of the sensor platform. However, PAMAM does not have an S atom in the molecular structure and may not bind as well on the electrode's wall thus would be less durable. Performance of using cysteamine and dendrimer as a linker for the same sensor platform was compared in this study and the stability and durability of the senor would be investigated. Ammonia, which is a major biometabolite and environmental sensitive chemical, was used as the surrogate chemical to be tested by this sensor platform [3].

1.1. Theory

As shown in the following Equation (1), glutamate and nicotinamide adenine dinucleotide (NAD^+) can be hydrolyzed to form α-keto glutarate, β-nicotinamide adenine dinucleotide reduced (NADH), and ammonium ion with the enzyme, glutamate dehydrogenase (GDH). The equilibrium constant is in favor of the formation of glutamate and thus the reverse reaction is faster kinetically [4].

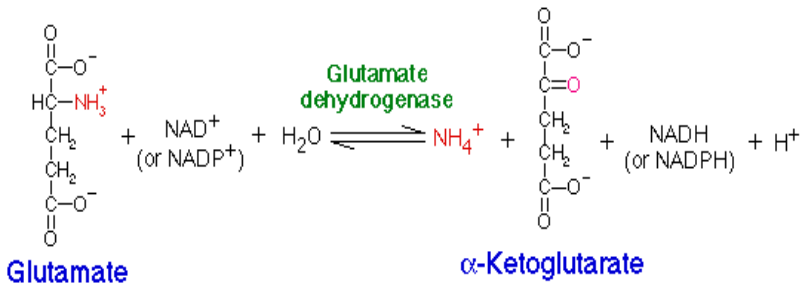

(1)

For many biological reactions, the end product or metabolite is ammonium; accumulation of a high concentration of ammonium is toxic to the body. Environmentally, ammonium is a byproduct of many industrial processes, uncontrolled discharges of ammonium will lead to harmful consequence to the environment. Our goal here was to develop a sensor device that is nontoxic and can measure the ammonium ion at the lowest concentration possible; its utilities can be found in many biomedical or environmental applications. Hence, it is the reverse reaction as shown above (glutamate formation) that we utilized in this study; however, the same sensor can be used to detect α-keto glutarate or glutamate with a slight alternation of the measuring approach. Measurements of these chemical species mentioned above that were reported in literature were mostly in the range of mM [5-7]. It should be noted that the motivation of this study was to develop a sensor that can measure low concentration of the target species, more specifically, it is to relate the current measurements exerted by the reacting species in a solution (with characteristics peaks of oxidation and/or reduction) by cyclic voltammetry

to concentrations of the species, rather than to determine the reaction kinetics of the measuring species of which in many instances are already known.

2. Materials and Methods

2.1. Materials

L-glutamic dehydrogenase (GDH, from bovine liver, solution in 50 % glycerol) was purchased from Sigma-Aldrich (St. Louis, MO, USA), the concentration of GDH was 28 mg protein/mL, and 46 units/mg. Cysteamine, polyamidoamine dendrimer generation 0 (PAMAM_0), polyamidoamine dendrimer generation 2nd (PAMAM_2), α-keto glutarate, β-nicotinamide adenine dinucleotide reduced disodium salt hydrate (NADH), $AuCl_3HCl{\cdot}4H_2O$ (Au %> 48 %) and Na_3citrate were purchased from Sigma. All the other chemicals were of analytical grade or highest grade available.

2.2. Electrode Preparation

The cleaned glassy carbon electrode (GCE) was first immersed in 0.1 M cysteamine solution in darkness. The resulting monolayer-modified electrode was rinsed thoroughly with twice-distilled water and soaked in distilled water. Then, it was dipped into the colloidal gold. The gold colloid–cysteamine-modified electrode was dipped into the l-glutamate dehydrogenase (GDH) solution (pH 7.4) (or GDH solution containing NADH). In such a way, a GDH (or GDH/NADH) gold colloid–cysteamine-modified glassy carbon electrode was obtained (GCE cysteamine-Au-GDH or cysteamine-Au-GDH/NADH).

For electrode that was modified by PAMAM only, either PAMAM _0 or PAMAM_2 was used in place of cysteamine, these resulting electrodes were termed GCE PAMAM _0 or PAMAM_2-Au-GDH or GDH/NADH. In cases that both cysteamine and PAMAM were coated onto electrodes, the cleaned glassy carbon electrode was first immersed in cysteamine solution, the resulting electrode was dipped into the PAMAM solution (PAMAM _0 or PAMAM_2). The gold colloid–cysteamine/PAMAM-modified electrode was dipped into the GDH solution (pH 7.4) (or GDH solution containing NADH). In such a way, a GDH (or GDH/NADH) gold colloid–cysteamine/PAMAM-modified glassy carbon electrode was obtained (GCE cysteamine/PAMAM _0 or PAMAM_2-Au-GDH or GDH/NADH).

2.3. Nanoparticles Solution Preparations

Nanoparticles Au was prepared by reacting $HAuCl_4$ with citric acid [2].

2.4. Detections

UV-VIS spectrophotometry was carried out by an Agilent diode-array spectrophotometer (Agilent Model 8453); cyclic voltammetry was conducted by using a Gamry 600 Potentiostat. Voltammetric potential was measured against a saturated chloride electrode (SCE). The experimental setup of the cyclic voltammetry is shown in Fig. 1.

Fig. 1. Cyclic voltammetry and the sensor measurement cell.

2.5. Experimental Procedures

For all experiments, the measurement cell contained 5 mL of 2.5 mM of NADH, then a combined solution of α-keto glutarate and NH_4^+ was injected into the reaction cell for measurement periodically, at 60 second intervals; injection volume varied from 10 to 1500 μL depending on the concentration required. The concentration of α-keto glutarate solution was $1x10^{-6}$ mol/L, NH_4^+ was $1x10^{-6}$ mol/L. All experiments were conducted at pH 7.4 in a 0.1 M phosphate buffer solution under deoxygenated condition and all solutions were prepared with double deionized distilled water.

Measurement of current (i) with time was usually at about 700 mV (vs. SCE) for the reduction reaction and at near 2.0 mV for the oxidation reaction. The resulting concentrations of α-keto glutarate and NH_4^+ in the reaction cell ranged from 2 to 300 nM after each injection unless otherwise stated.

3. Results and Discussion

3.1. Identification of PAMAM Binding with GDH in Sol-Gel Au Colloid

Fig. 2(a) shows the UV-VIS spectrum of PAMAM_2 solution at various concentrations. PAMAM's in general have major absorption peak at 227 nm, but a minor peak also appears at 278 nm. The peak at 278 disappears at dilute concentration as shown in blue in Fig. 2(a). GDH solution has similar spectrum as PAMAM_2 accept that its absorptivity is less intense at 278, as shown in black in Fig. 2(b). Fig. 2(b) also shows the spectra of a plastic cuvette (made for UV-VIS range) coated with cysteamine-Au-GDH, PAMAM_0-Au-GDH, and PAMAM_2-Au-GDH in red, green, and blue, respectively. The peak at near 548 nm is associated with Au particles. The peak at 227 nm would nearly disappear for the coating (sol-gel colloid) containing cysteamine (red line) after the cuvette was rinsed with deionized water numerous times, but a small peak at 278 nm would remain, that was believed to be a combined cluster layer of cysteamine and GDH situated in the Au colloid. The same can be observed if rinsing was done with the PAMAM's coating, however, the remaining cluster peak at 278 nm was much larger and the Au peak at 548 nm was accordingly higher. Hence, it can be reasoned from the magnitude of the absorbance at 278 nm that PAMAM's can bind better with the Au nanoparticles and GDH to form a colloid attached onto the electrode surface than cysteamine with Au nanoparticles and GDH in this self-assembly process.

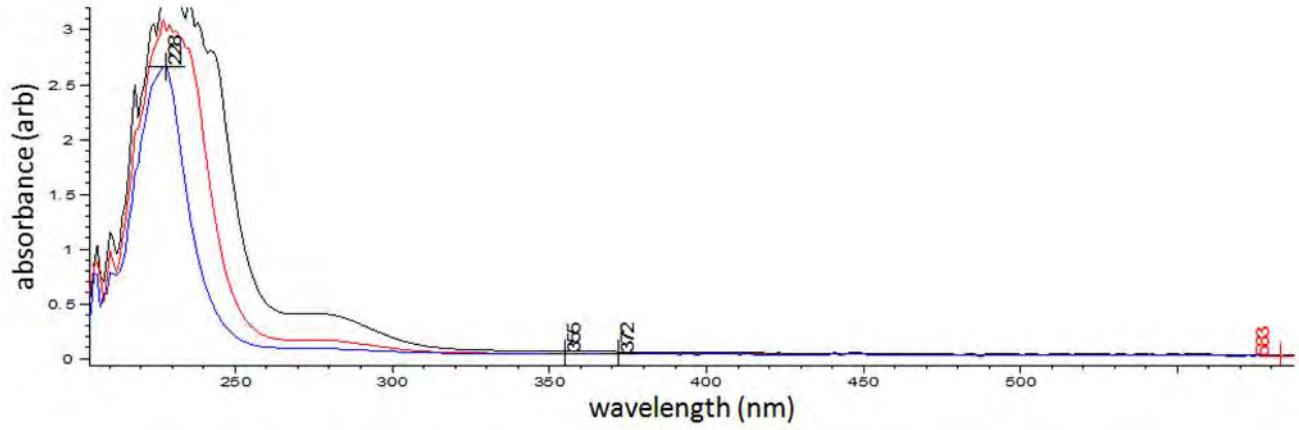

(a)

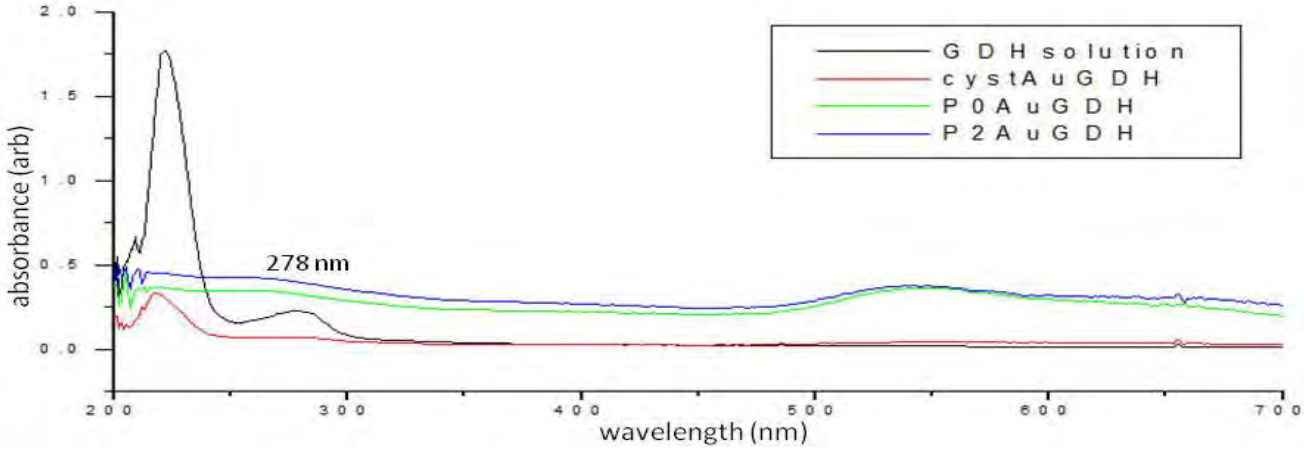

(b)

Fig. 2. UV-VIS spectra of PAMAM_2 and other senor materials coated on an UV-VIS cuvette: (a) Spectra of PAMAM_2 solutions at various concentrations, characteristic peaks of PAMAM's are at 227 and 278 nm. At lower concentration, as shown in blue, PAMAM_2 only has absorption peak at 227 nm; (b) Spectrum of GDH solution and spectra of an UV-VIS plastic cuvette coated with cysteamine-Au-GDH, PAMAM_0-Au-GDH, and PAMAM_2-Au-GDH in black, red, green, and blue, respectively.

3.2. Voltammetric Responses of the Modified GCE's for NH_4^+ Detection

We have explored several combinations of sol-gel Au colloids for the sensor development to detect ammonia, these combinations were: Cysteamine/PAMAM_0-Au-GDH, cysteamine/PAMAM_2-Au-GDH, cysteamine/PAMAM_0-Au-GDH/NADH, and cysteamine/PAMAM_2-Au-GDH/NADH. We have carried out a wide-range of ammonia concentrations from 2 nM to 300 nM with all the GCE's modified with different sol-gel Au colloid combinations in order to determine the champion performer. Trial measurements of the electrodes indicated that two distinguish characteristic peaks could be used to relate proportionally the concentrations of ammonia with heights of current peaks: a reductive peak at near 700 mV and an oxidative peak at 2 mV. Fig. 3 in the following is the voltammograms for the ammonia measurements generated by using a GCE modified with PAMAM_2-Au-GDH. The blue voltammogram is measurement of the blank in phosphate buffer solution. It should be noted that the reductive peaks at 700 mV shifted to higher positive voltage with increase of ammonia concentrations. The oxidative peaks at about 2 mV were also detected but were not obviously observed from the figure.

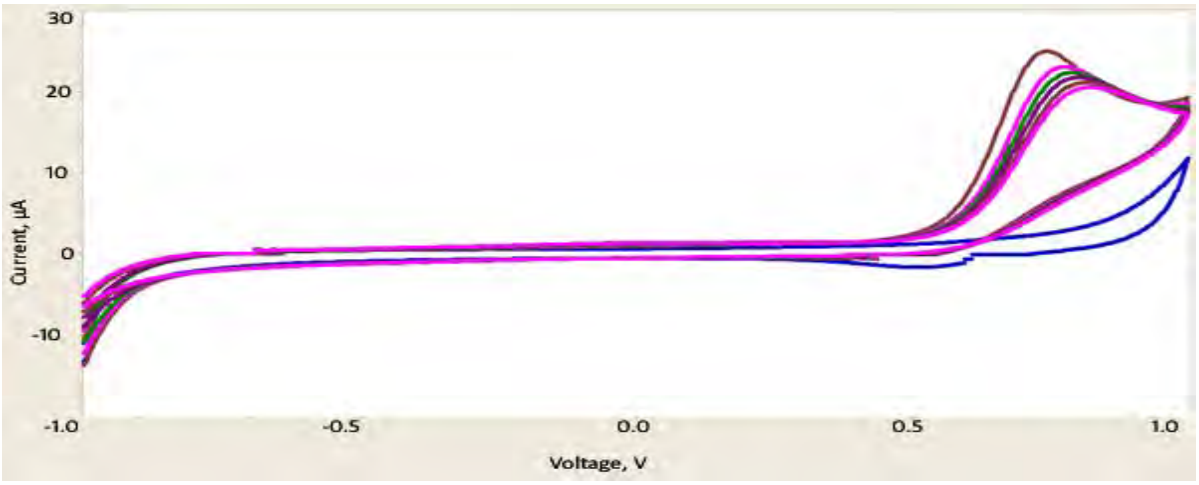

Fig. 3. Cyclic voltammograms of reaction of NH_4^+ with α-keto glutarate at pH 7.4 for concentrations from 2 to 300 nM.

Overall, GCE modified with either PAMAM_0 or PAMAM_2-Au- GDH/NADH worked best for the detection of ammonia with α-keto glutarate, although there was no significant detection advantage by using the more branched PAMAM_2 in the sensor preparation. Detection of NH_4^+ concentrations can be better demonstrated by using the oxidative peaks at 2 mV. Voltammograms of the oxidative peaks at 2 mV of the ammonia reaction with α-keto glutarate using GCE modified by PAMAM_2-Au-GDH/NADH and cysteamine-Au-GDH are shown in Fig. 4 (a) and Fig. 4 (b) respectively.

As shown in Fig. 4(a), there was about 0.45 µA difference between the blank buffer solution (in blue) and the measurement of 2 nM NH_4^+ solution (in brown), which indicated that the sensor platform is capable of measuring NH_4^+ concentration to subnanomolar level. Fig. 4(b) is the voltammograms of the same solutions, but current increments of the oxidative peaks were relatively small, which indicates that the PAMAM_2-Au-GDH/NADH modification makes a more superior sensor for low ammonia concentration detection. The more efficient of NADH oxidation in the system could also be attributed, at least partially, by the direct binding of NADH with GDH in the Au colloid.

Fig. 5 shows the amperometric responses measured by 5 sensors using the same platform with different modifications for the reaction of NH_4^+ with α-keto glutarate at 2 mV for concentrations ranged from 2 to 300 nM. It can be observed that there were two near linear regions that can be explored to be used for sensor design: a sensitive region at concentrations less than 20 nM, and a relatively less sensitive region at concentrations larger than 40 nM. One may conclude that this non-metal biosensor platform is ideal for making sensor for ammonia detection at extremely low concentrations (>20 nM). It is unclear at this time about the mechanisms why the modified GCE's become less sensitive at the higher concentration region, it is conceivable that there is a limited quantity of Au colloid attached to the GCE surface and its ability to transfer electrons is saturated and hence turns inefficient at higher concentration.

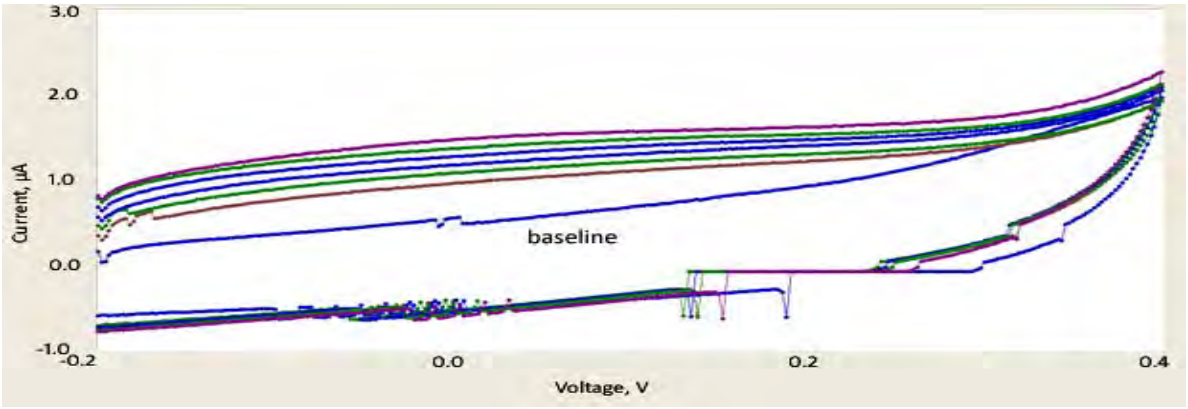

(a)

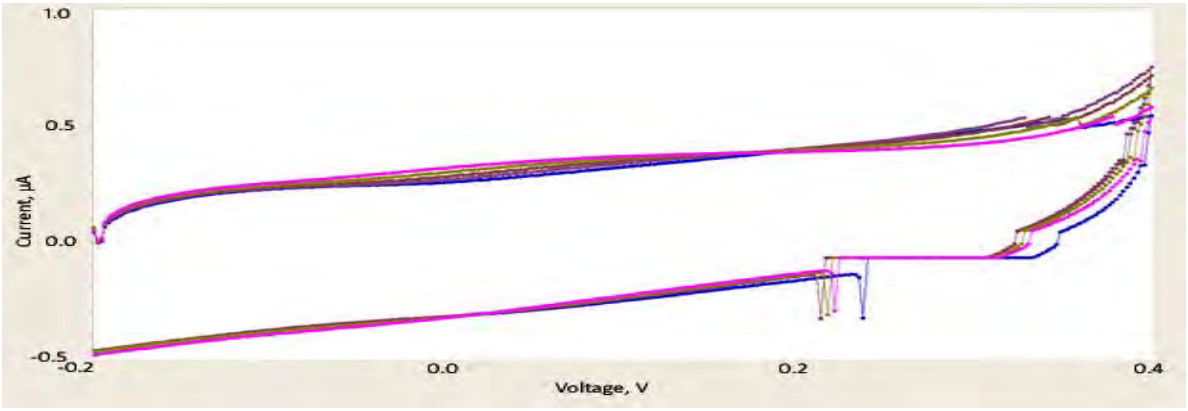

(b)

Fig. 4. (a) Cyclic voltammograms of PAMAM_2-Au-GDH/NADH modified GCE for detection of NH_4^+ at pH 7.4., concentrations of NH_4^+ varied from 2 to 300 nM. The bottom reduction line in blue was measurement for a blank. (b) Same measurements with a GCE modified with cysteamine-Au-GDH.

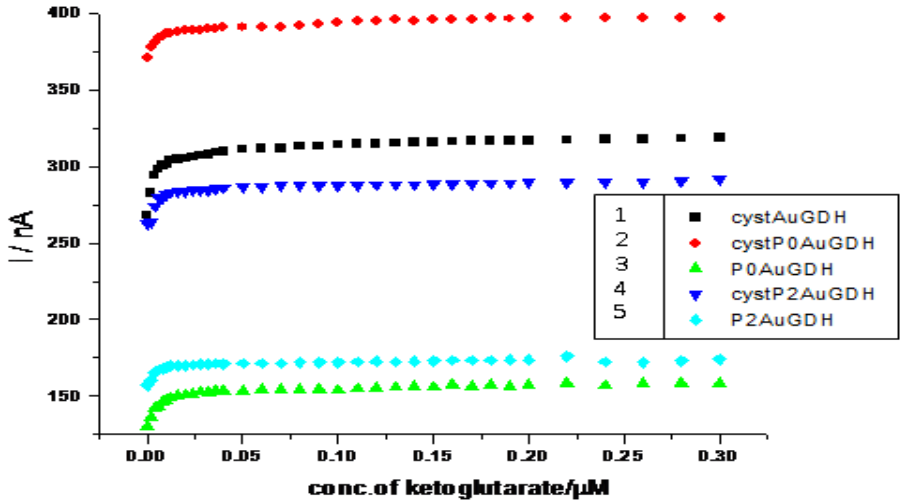

Fig. 5. Amperometric responses of ammonia reaction with α-keto glutarate from 5 different GCE sensors modified with similar platform materials: black is cysteamine-Au-GDH, red is cysteamine/PAMAM_0-Au-GDH, green is PAMAM_0-Au-GDH, blue is cysteamine/PAMAM_2-Au-GDH, light blue is PAMAM_2-Au-GDH.

3.2. Reproducibility and Stability of the Modified GCE's

An ideal sensor platform should be able to generate measurements that are reproducible and the system is stable with time, thus the measurements are consistent and reliable. Fig. 6 (a) shows the 50 cyclic responses of a typical modified GCE in the same ammonia solution. It can be seen that some deterioration occurred (as shown by the characteristic peaks at near 700 mV) after the 50 cycles but the results are relatively consistent. Fig. 6 (b) shows the amperometic responses of a GCE modified by PAMAM_0-Au-GDH/NADH at 2.0 mV after 2 weeks stored inside a refrigerator at 4 ˚C, the responses are nearly identified with the same trend, the measurements indicated that the sol-gel Au colloid stabilized the GDH/NADH within the cluster and prevented the bioenzyme/biochemical from deteriorating. It is well known that these bioenzyme/biochemical are very unstable, especially under dilute concentrations as they were in this study. These results demonstrated that the biosensor platform has reasonable reproducibility and stability.

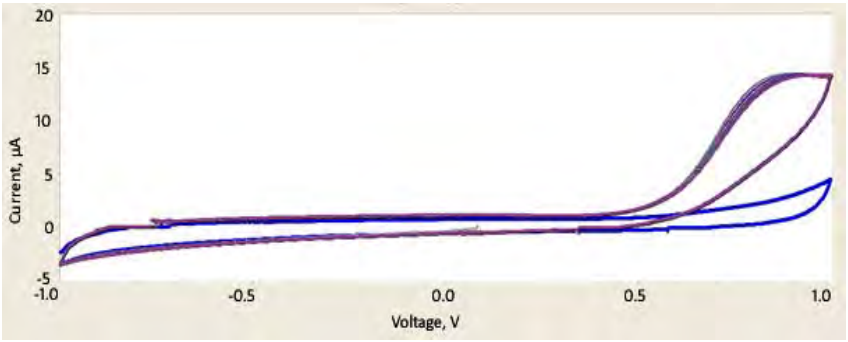

(a)

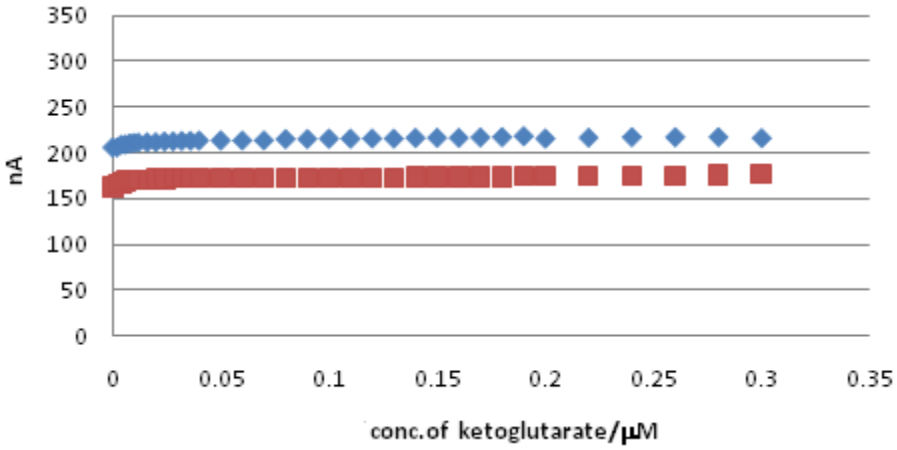

(b)

Fig. 6. (a) Voltammograms of a modified GCE with 50 measurement cycles of the same solution; (b) Amperometic respones of a GCE modified by PAMAM_0-Au-GDH/NADH at 1.8 mV, before (blue) and after (red) 2 weeks stored inside a refrigerator at 4 ˚C.

4. Conclusions

We successfully modified our glassy carbon electrode biosensor platform [2] for ammonium detection; we further modified the sensor platform with PAMAMs and the detection lower limit was enhanced. This highly modified electrode can detect ammonium concentrations down to 2 nM or lower. The low detection limit of this biosensor is far more superior than most available detection methods in the

public domain. This biosensor platform can be modified to be used for many measurement applications in biomedical and environmental field that require high sensitivity at low concentrations. Currently, the challenge of biosensor development is not in finding the right enzymes or conjugate reactions (Equation (1)) that govern the particular species to be detected, it is the portability, stability, and noise reduction that demand further research and development.

Acknowledgement

This study was supported by an USAMRMC Project Grant (Contract #W81XWH-07-2-0078).

References

[1]. S. W. Leung, Y. Wang, H. Gu, J. C. K. Lai, Characterization and Applications of Modified Gold Electrode Sensor with Nanoparticles, *in Proceedings of the 2009 Nanotechnology Conference and Trade Show*, Vol. 2, Chapter 4: Biosensors and Diagnostics, 2009, pp. 233-235.

[2]. J. C. K. Lai, Y. Wang, W. Gao, H. Gu, S. W. Leung, Performance Comparisons of Nanoparticle Modified Sensor Electrodes for the Detection of Nitrite and Peroxide, in *Proceedings of the 2009 Nanotechnology Conference and Trade Show, Volume 2: Chapter 4: Biosensors and Diagnostics*, 2009, pp. 233-235.

[3]. Y. Wang, L-glutamate Dehydrogenase Modified Biosensor Based with Gold Nanoparticles, M. S. Project Report, *Idaho State University*, Pocatello, Idaho, 2009.

[4]. P, Belenky, K. L. Bogan, C. Brenner, NAD^+ Metabolism in Health and Disease, *Trends in Biochemical Sciences*, Vol. 32, Issue 1, 2007, pp. 12-19.

[5]. A. K. Basu, P. Chattopadhyay, U Roychudhuri, Runu Chakraborty, A biosensor Based on Co-Immobilized L-glutamate Oxidase and L-glutamate Dehydrogenase for Analysis of Monosodium Glutamate in Food, *Biosensors and Bioelectronics*, Vol. 21, 2006, pp. 1968-1972.

[6]. K. Riedel, J. Huth, M. Kuehn, P. Liebs, Amperometric Determination of Ammonium ions with a Microbial Sensor, *Journal of Chemical Technology & Biotechnology*, Vol. 47, Issue 2, 1990, pp. 109-116.

[7]. N. Pasco, C. Jeffries, Q. Davies, A. J. Downard, A. D. Roddick-Lanzilotta, L. Gorton, Characterisation of a Thermophilic L-glutamate Dehydrogenase Biosensor for Amperometric Determination of L-glutamate by Flow Injection Analysis, *Biosensors & Bioelectronics*, Vol. 14, 1999, pp. 171-178.

The Second International Conference
on Sensor Device Technologies and Applications

SENSORDEVICES 2011

August 21-27, 2011 - French Riviera, France

IFSA
www.sensorsportal.com

Important deadlines:

Submission deadline	April 10, 2011
Notification	April 30, 2011
Registration	May 15, 2011
Camera ready	May 22, 2011

Tracks:
- Sensor devices
- Photonics
- Infrared
- Ultrasonic and Piezosensors
- Sensor device technologies
- Sensors signal conditioning and interfacing circuits
- Medical devices and sensors applications
- Sensors domain-oriented devices, technologies, and applications
- Sensor-based localization and tracking technologies

http://www.iaria.org/conferences2011/SENSORDEVICES11.html

The Fifth International Conference on Sensor
Technologies and Applications

SENSORCOMM 2011

August 21-27, 2011 - French Riviera, France

IFSA
www.sensorsportal.com

Important deadlines:

Submission deadline	April 10, 2011
Notification	April 30, 2011
Registration	May 15, 2011
Camera ready	May 22, 2011

Tracks:
- APASN: Architectures, protocols and algorithms of sensor networks
- MECSN: Energy, management and control of sensor networks
- RASQOFT: Resource allocation, services, QoS and fault tolerance in sensor networks
- PESMOSN: Performance, simulation and modelling of sensor networks
- SEMOSN: Security and monitoring of sensor networks
- SECSED: Sensor circuits and sensor devices
- RIWISN: Radio issues in wireless sensor networks
- SAPSN: Software, applications and programming of sensor networks
- DAIPSN: Data allocation and information in sensor networks
- DISN: Deployments and implementations of sensor networks
- UNWAT: Under water sensors and systems
- ENOPT: Energy optimization in wireless sensor networks

http://www.iaria.org/conferences2011/SENSORCOMM11.html

The Fourth International Conference on Advances
in Circuits, Electronics and Micro-electronics

CENICS 2011

August 21-27, 2011 - French Riviera, France

IFSA
www.sensorsportal.com

Important deadlines:

Submission deadline	April 10, 2011
Notification	April 30, 2011
Registration	May 15, 2011
Camera ready	May 22, 2011

Tracks:
- Semiconductors and applications
- Design, models and languages
- Signal processing circuits
- Arithmetic computational circuits
- Microelectronics
- Electronics technologies
- Special circuits
- Consumer electronics
- Application-oriented electronics

http://www.iaria.org/conferences2011/CENICS11.html

Guide for Contributors

Aims and Scope

Sensors & Transducers Journal (ISSN 1726-5479) provides an advanced forum for the science and technology of physical, chemical sensors and biosensors. It publishes state-of-the-art reviews, regular research and application specific papers, short notes, letters to Editor and sensors related books reviews as well as academic, practical and commercial information of interest to its readership. Because of it is a peer reviewed international journal, papers rapidly published in *Sensors & Transducers Journal* will receive a very high publicity. The journal is published monthly as twelve issues per year by International Frequency Sensor Association (IFSA). In additional, some special sponsored and conference issues published annually. *Sensors & Transducers Journal* is indexed and abstracted very quickly by Chemical Abstracts, IndexCopernicus Journals Master List, Open J-Gate, Google Scholar, etc. Since 2011 the journal is covered and indexed (including a Scopus, Embase, Engineering Village and Reaxys) in Elsevier products.

Topics Covered

Contributions are invited on all aspects of research, development and application of the science and technology of sensors, transducers and sensor instrumentations. Topics include, but are not restricted to:

- Physical, chemical and biosensors;
- Digital, frequency, period, duty-cycle, time interval, PWM, pulse number output sensors and transducers;
- Theory, principles, effects, design, standardization and modeling;
- Smart sensors and systems;
- Sensor instrumentation;
- Virtual instruments;
- Sensors interfaces, buses and networks;
- Signal processing;
- Frequency (period, duty-cycle)-to-digital converters, ADC;
- Technologies and materials;
- Nanosensors;
- Microsystems;
- Applications.

Submission of papers

Articles should be written in English. Authors are invited to submit by e-mail editor@sensorsportal.com 8-14 pages article (including abstract, illustrations (color or grayscale), photos and references) in both: MS Word (doc) and Acrobat (pdf) formats. Detailed preparation instructions, paper example and template of manuscript are available from the journal's webpage: http://www.sensorsportal.com/HTML/DIGEST/Submition.htm Authors must follow the instructions strictly when submitting their manuscripts.

Advertising Information

Advertising orders and enquires may be sent to sales@sensorsportal.com Please download also our media kit: http://www.sensorsportal.com/DOWNLOADS/Media_Kit_2011.pdf

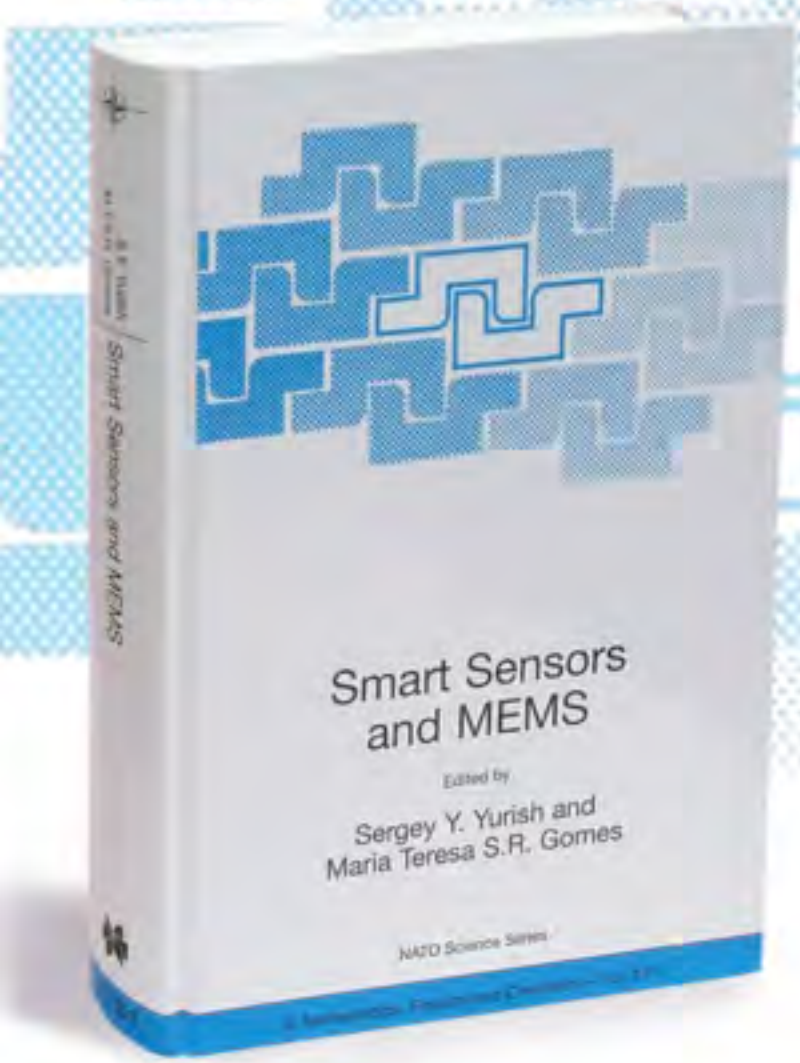

Smart Sensors and MEMS

Edited by

Sergey Y. Yurish and
Maria Teresa S.R. Gomes

The book provides an unique collection of contributions on latest achievements in sensors area and technologies that have made by eleven internationally recognized leading experts ...and gives an excellent opportunity to provide a systematic, in-depth treatment of the new and rapidly developing field of smart sensors and MEMS.

The volume is an excellent guide for practicing engineers, researchers and students interested in this crucial aspect of actual smart sensor design.

Kluwer Academic Publishers

Appendix 16. List of published Abstracts:

1. Jaiswal A, Wong YYW, Bhushan A, Daniels C & Lai JCK (2010) A Noncontact Co-Culture Model of Peripheral Neural Cells for Nanotoxicity, Tissue Engineering and Pathophysiological Studies. NSTI Nanotechnology Conference and Expo – Nanotech 2010, June 21-25, 2010, Anaheim, CA (in Abstracts Volume).

Abstract. Cell culture models *in vitro* have long serve as tools for the elucidation of the cellular and molecular mechanisms underlying the pathophysiology of diverse diseases. More recently these versatile model systems have permeated into the fields of toxicology and tissue engineering. Their attraction and utility for use in investigations in toxicology and tissue engineering appear to derive from the fact such model systems are particularly suitable for high throughput and mechanistic studies. Although these models do not exactly simulate the cellular architecture in tissues and organs *in vivo*, they have been well accepted for studies employing a single cell type. Their limitations notwithstanding, they facilitate gaining unique mechanistic insights regarding the role of a particular cell type, a position not easily attainable employing whole organ/tissue studies.

On the other hand, co-culture cell systems consisting of two distinctly different but functionally complementary cell types provide structural and functional perspectives that single-cell-type models do not offer. Consequently, there is a need for the development for more such model systems and applied them to nanotoxicological and tissue engineering studies. Our group have been emphasized the necessity of developing a variety of cell model systems using neural cells. We have recently demonstrated some of the utilities of such model systems in nanotoxicological and tissue engineering studies.

There have been, however, few cell model systems developed employing peripheral neural cell types for nanotoxicological and tissue engineering studies. We have therefore initiated a systematic development of this type of model systems using dorsal root ganglion (DRG) neurons and Schwann cells. The first model we have developed involved a non-contact co-culture model of Schwann cells and DRG neurons employing the hanging cell culture insert. Initially, we have partially characterized the DRG neurons and Schwann cells in single-cell-type cultures. In ongoing studies employing our new co-culture, non-contact model, we demonstrated that the cell survival of DRG neurons increased when co-cultured with Schwann cells in this construct. Thus, the results from our studies to date as well as those from our ongoing studies demonstrate that our non-contact co-culture model is highly suitable for both high throughput and mechanistic studies in nanotoxicological and tissue engineering research. Clearly this model is also germane for the investigation of mechanistic issues associated with peripheral diabetic neuropathy and other disease states of the peripheral nervous system.

2. Wong YYW, Jaiswal AR, Dukhande VV, Bhushan A, Leung SW & Lai JCK (2010) Elucidation of Neuroprotective Properties of Astrocytoma (Astrocytes-like) Cells in Neural Cell Culture Models *In Vitro*: Applications in Tissue Engineering and Nanotoxicology. NSTI Nanotechnology Conference and Expo – Nanotech 2010, June 21-25, 2010, Anaheim, CA (in Abstracts Volume).

Abstract. Evidence is accumulating that cell culture models *in vitro* facilitate high throughput and mechanistic studies in tissue engineering. More recently, our group as well as other researchers have developed several cell models for the systematic investigation of molecular mechanisms underlying the putative cytotoxicity of nanoparticles and other nanomaterials. These and other studies have drawn wide-spread interest in the possible environmental and occupational health impact of nanoparticles and other nanomaterials.

As part of a continuing effort to further develop and characterize cell models for cellular and molecular mechanistic studies, we have extended our previous investigation employing neural cell models because most studies have traditionally employed peripheral cell types but not neural cells.

Astrocytes are known to protect neurons against pathophysiological assults *in vivo* and *in vitro* although the underlying mechanisms are not fully understood. We have previously developed several cell culture models in vitro to systematically investigate several of the putative neuroprotective properties of astrocytes. For example, we have previously shown U-87 (astrocytes-like) astrocytoma cells afford SK-N-SH (neurons-like) neuroblastoma cells against several pathophysiological assaults such as oxidative stress induced by depletion of cellular glutathione.

Based on the results of our previous studies. we hypothesized that different stress factors can elicit and/or enhance the neuroprotective effects of astrocytes through the activation of astrocytic signaling and alteration of astroglial function. We have initiated a series of studies employing our cell models to test this hypothesis. The results of our ongoing studies demonstrate that U-87 (astrocytes-like) astrocytoma cells provide SK-N-SH (neurons-like) neuroblastoma cells against pathophysiological assaults (e.g., oxidative stress) under several sets of culture conditions not previously studied. Other studies are in progress to further elucidate the cellular and molecular mechanisms underlying these protective effects proffered by U-87 (astrocytes-like) astrocytoma cells to SK-N-SH (neurons-like) neuroblastoma cells. Thus, our results may have pathophysiological implications in neuroprotection but also implications and applications in tissue engineering and nanotoxicological research.

3. Leung SW, Gao W, Gu H, Bhushan A & Lai JCK (2010) Chitosan Membrane in Combinations with Nanoparticles and Adriamycin as a Treatment to Inhibit Glioma Growth and Migration. NSTI Nanotechnology Conference and Expo – Nanotech 2010, June 21-25, 2010, Anaheim, CA (in Abstracts Volume).

Abstract. Our previous and on-going studies indicated that U87 cells cultured on chitosan film/membrane exhibited significantly slower growth and proliferation kinetics compared to U87 cells cultured in the absence of chitosan film/membrane. Chitosan exhibits anti-microbial activities through its interaction(s) with microbial cell surface thereby altering their gene expression and cellular function and leading to cell death. Recent studies of nanometal particles have revealed many properties that were not previously expected in biological systems and thus can be explored for various applications in biomedical applications. In this study, we hypothesized that the inhibitory effect of chitosan would be greatly modulated if we combine chitosan with nanometals and adriamycin, a common drug for cancer therapy. Our results showed that combinations of metal nanoparticles, adriamycin and chitosan induced cell death at different rates, with reference to U87 cells cultured in the absence of chitosan and with chitosan alone. The results showed potentials for pathophysiological applications to inhibit human brain glioma migration and invasion. Results of similar treatments with different cancer and normal cells will also be presented.

4. Leung SW, Wang Y, Gu H & Lai JCK (2010) Biomedical Applications of Modified Carbon Glassy Electrode Sensor with Nanoparticles and Dendrimers. NSTI Nanotechnology Conference and Expo – Nanotech 2010, June 21-25, 2010, Anaheim, CA (in Abstracts Volume).

Abstract. In our previous reports, we studied the development of biosensor platform that are capable of measuring biometabolites and environmental sensitive species, such as peroxide and nitrate/nitrate, to concentration in the order of ppb (parts per billion) or lower.
In our more recent development, we modified our platform with dendrimers to enhance its performance. Zero and second generation of dendrimers were coated on the surface of a carbon glassy platform electrode modified with GDH (glutamate dehydrogenase) and it was used to measured ammonium, a common biometabolite, at near neutral pH that is common for normal bioactivities.
The resulting electrode was tested with ammonium concentrations ranged from 0.002 to 0.3 μM with satisfactory results. Measurements at lower concentrations had better resolution than at higher concentrations and it is believed that the lower concentration limit can be better than the tested lower limit at 0.002 μM. Performance of the modified carbon glassy electrode was compared with other glassy electrodes that were modified differently, and the results will be reported.
The biosensor platform thus far was proven to be versatile and can be used in many biomedical and environmental applications.

5. Wright GL, Lai JCK, Chan AWK, Minski MJ, Lim L & Leung SW (2010) Metallomic Distribution in Various Regions of the Brain as Influenced by Dietary Intakes and Their Implications. ISEIS 2010 International Conference on Environmental Informatics, Beijing, China, August 27-29, 2010 (in Abstracts Volume).

Abstract. Lifelong exposure to environmental factors can influence the risk of developing diseases according to recent research findings. Environmental stresses ultimately leading to neuronal cell death have been hypothesized as the causes of the increased occurrence in developing Alzheimer's and Parkinson's disease. Our daily diet is considered to be one of the most important environmental factors that can seriously affect the development and proper functions of the brain. Depending on the concentrations, metals and electrolytes can post some health concerns, especially for a prolonged consumption period. For example, it was reported that excess amounts of iron, zinc and copper in the human brain may cause oxidative damage and protein aggregation; the neurotoxicity induced by these metals may lead to cerebral and/or cerebellar degeneration. Other reports showed that there were differences in concentrations of five different elements (aluminum, zinc, copper, manganese, and iron) between normal human brain and brains of patients with Alzheimer's disease. In this study, we investigated 30 elements, including electrolytes, and how dietary intake on a life-time basis would affect their concentrations and distributions in various regions of the rat brain (hypothalamus, cerebellum, pons and medulla, striatum, mid-brain, cerebral cortex, and hippocampus) and discussed their health implications. Information matrices of these 30 different elements (mostly metals) and their distributions in various regions of the rat brain were analyzed as a function of normal dietary intake at different ages during development. Our results showed that metallomic distribution in various regions of the rat brain is age-related. The results may help researchers to identify possible links between daily dietary intake of metals and electrolytes and diseases associated with aging (e.g., Alzheimer's and Parkinson's disease) and suggest such metallomic distributions may be used as neurological biomarkers of exposure to heavy metals.

6. Leung SW, Siddhanti S, Williams B, Chan AWK, Minski MJ, Daniels CK & Lai JCK (2010) Effects of Dietary Intake on Metal and Electrolyte Distributions in Various Organs. ISEIS 2010 International Conference on Environmental Informatics, Beijing, China, August 27-29, 2010 (in Abstracts Volume).

Abstract. The intake and concentration of metals and electrolytes from our diet are believed to be affecting our general health, in particular, the proper functions of vital organs. For example, in addition to other genetic and environmental factors, consuming water with high alkalinity for prolonged time is suspected to lead to diseases such as kidney stone. Evidence has been accumulating that excessive metal intakes would lead to organ failures. Once absorbed, minerals

and electrolytes can travel freely throughout the body, and distribute at key organ systems such as the brain, lung, kidney, etc. By conducting experiments with animal models (e.g., rats), it is possible to not only determine where the organ distribution of various matrices of elements and minerals but also correlate such matrices with the overall physiological and behavioral status of such models. In this study, information matrices of 30 different elements (including heavy metals and some electrolytes) and their distributions in various vital organs (e.g., brain, lung, kidney, liver, heart, spleen, and uterus) were analyzed as a function of normal dietary intake at adulthood (120 days old). An elemental (metal and electrolyte) distribution model was then formulated based on experimental results. The study has high impact to our understanding of how environmental health would affect our well being. This study would also provide insights on how our diet would affect the accumulations of unwanted elements, such as heavy metals, in our vital organs. The results may help researchers and health practitioner to identify possible links between daily diet (metals and electrolytes) and diseases, and may also lead to a better understanding of diseases associated with aging such as Alzheimer's and Parkinson's diseases, and other neurological disorders.

7. Bhushan A, Patil PP, Bhardwaj V, Lai MB, Daniels CK, Leung SW & Lai JCK (2010) Cross Resistance of Magnesium Oxide Nanoparticles to Cisplatin in Leukemia Cells: Mechanistic Studies. Institution of Mechanical Engineers Seminar on Nanotechnology in Medicine and Biotechnology, October 2010, London, UK (in Program & Abstracts).

Abstract. We have presented an overview of our studies on anti-cancer drug resitance mechanisms as well as ongoing systematic studies of the nanotoxicity of metallic oxide nanoparticles. Our ongoing studies also suggest that resistant cancer cells may exhibit cross-resistant to the cytotoxic effects of metallic oxide nanoparticles. The latter effects appear to be mediated by cell survival/proliferation signaling mechanisms. Clearly these are important and novel areas of anti-cancer drug discovery. As such they merit further investigation. We are currently pursuing these exciting new dormains of nanomedicine and nanocancer research.